NUREG-xxxx

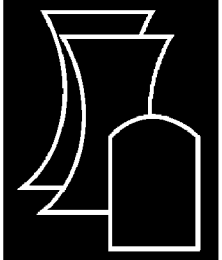

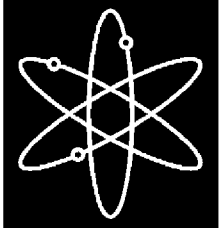

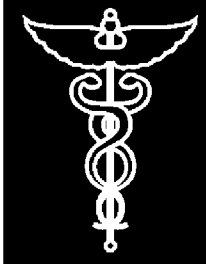

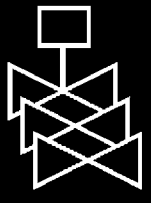

Technical Basis for Revision of Regulatory Guide 1.99: NRC Guidance on Methods to Estimate the Effects of Radiation Embrittlement on the Charpy V-Notch Impact Toughness of Reactor Vessel Materials

U.S. Nuclear Regulatory Commission
Division of Fuel, Engineering, and Radiological Research
Office of Nuclear Regulatory Research
Washington, DC 20555-0001

AVAILABILITY OF REFERENCE MATERIALS IN NRC PUBLICATIONS

NRC Reference Material

As of November 1999, you may electronically access NUREG-series publications and other NRC records at NRC's Public Electronic Reading Room at http://www.nrc.gov/reading-rm.html.
Publicly released records include, to name a few, NUREG-series publications; *Federal Register* notices; applicant, licensee, and vendor documents and correspondence; NRC correspondence and internal memoranda; bulletins and information notices; inspection and investigative reports; licensee event reports; and Commission papers and their attachments.

NRC publications in the NUREG series, NRC regulations, and *Title 10, Energy*, in the Code of *Federal Regulations* may also be purchased from one of these two sources:

1. The Superintendent of Documents
   U.S. Government Printing Office
   Mail Stop SSOP
   Washington, DC 20402–0001
   Internet: bookstore.gpo.gov
   Telephone: 202-512-1800
   Fax: 202-512-2250
2. The National Technical Information Service
   Springfield, VA 22161–0002
   www.ntis.gov
   1–800–553–6847 or, locally, 703–605–6000

A single copy of each NRC draft report for comment is available free, to the extent of supply, upon written request as follows:

Address: Office of the Chief Information Officer,
Reproduction and Distribution
Services Section
U.S. Nuclear Regulatory Commission
Washington, DC 20555-0001
E-mail: DISTRIBUTION@nrc.gov
Facsimile: 301–415–2289

Some publications in the NUREG series that are posted at NRC's Web site address http://www.nrc.gov/reading-rm/doc-collections/nuregs are updated periodically and may differ from the last printed version. Although references to material found on a Web site bear the date the material was accessed, the material available on the date cited may subsequently be removed from the site.

Non-NRC Reference Material

Documents available from public and special technical libraries include all open literature items, such as books, journal articles, and transactions, *Federal Register* notices, Federal and State legislation, and congressional reports. Such documents as theses, dissertations, foreign reports and translations, and non-NRC conference proceedings may be purchased from their sponsoring organization.

Copies of industry codes and standards used in a substantive manner in the NRC regulatory process are maintained at—

The NRC Technical Library
Two White Flint North
11545 Rockville Pike
Rockville, MD 20852–2738

These standards are available in the library for reference use by the public. Codes and standards are usually copyrighted and may be purchased from the originating organization or, if they are American National Standards, from—

American National Standards Institute
11 West 42nd Street
New York, NY 10036–8002
www.ansi.org
212–642–4900

Legally binding regulatory requirements are stated only in laws; NRC regulations; licenses, including technical specifications; or orders, not in NUREG-series publications. The views expressed in contractor-prepared publications in this series are not necessarily those of the NRC.

The NUREG series comprises (1) technical and administrative reports and books prepared by the staff (NUREG–XXXX) or agency contractors (NUREG/CR–XXXX), (2) proceedings of conferences (NUREG/CP–XXXX), (3) reports resulting from international agreements (NUREG/IA–XXXX), (4) brochures (NUREG/BR–XXXX), and (5) compilations of legal decisions and orders of the Commission and Atomic and Safety Licensing Boards and of Directors' decisions under Section 2.206 of NRC's regulations (NUREG–0750).

NUREG-xxxx

Technical Basis for Revision of Regulatory Guide 1.99: "NRC Guidance on Methods to Estimate the Effects of Radiation Embrittlement on the Charpy V-Notch Impact Toughness of Reactor Vessel Materials"

Manuscript Completed: October 1, 2007
Date Published: ???? 2007

Prepared by
Mark EricksonKirk

Office of Nuclear Regulatory Research
Division of Fuels, Engineering, and Radiological Research
U.S. Nuclear Regulatory Commission
Washington, DC 20555-0001

ABSTRACT

The U.S. Nuclear Regulatory Commission (NRC) promulgated Revision 2 of Regulatory Guide 1.99, "Radiation Embrittlement of Reactor Vessel Materials" [RG199R2], in May 1988. That guide details methods that the NRC staff considers acceptable for licensees to use in estimating the effects of radiation on the Charpy V-notch (CVN) impact energy (CVE) of the ferritic steels used in constructing the beltline region of a nuclear reactor pressure vessel (RPV). Radiation damage reduces the ability of these materials to carry load without failure. Consequently, any assessment of the operating safety of the RPV structure must account for the effects of radiation damage. However, since 1988, the NRC and the nuclear industry have made considerable advances in both the physical understanding of radiation damage processes and the empirical quantification of the effects these processes have on the mechanical properties of RPV steels. This report summarizes these advances in the state of knowledge and amalgamates them into a technical basis for an up-to-date version of RG 1.99.

FOREWORD

The U.S. Nuclear Regulatory Commission (NRC) promulgated Revision 2 of Regulatory Guide 1.99, "Radiation Embrittlement of Reactor Vessel Materials" [RG199R2], in May 1988. That guide details methods that the NRC staff considers acceptable for licensees to use in estimating the effects of radiation on the Charpy V-notch (CVN) impact energy (CVE) of the ferritic steels used in constructing the beltline region of a nuclear reactor pressure vessel (RPV). Radiation damage reduces the ability of these materials to carry load without failure. Consequently, any assessment of the operating safety of the RPV structure must account for the effects of radiation damage. By law, power reactor licensees are required to account for the effects of radiation damage in the following four situations:

(1) when assessing the ability of the RPV structure to resist fracture during postulated accident scenarios, such as pressurized thermal shock (PTS) [10CFR5061]

(2) when assessing the ability of the RPV structure to resist fracture during routine heatup, cooldown, and hydrotest conditions [10CFR50G]

(3) when determining which material samples need to be included in a surveillance program for the RPV beltline [10CFR50H]

(4) when assessing the ability of the RPV structure to continue safe operation in the presence of a flaw detected during either pre- or in-service inspection [ASME IWB3500, ASME IWB3600]

Since 1988, the NRC and the nuclear industry have made considerable advances in both the physical understanding of radiation damage processes and the empirical quantification of the effects these processes have on the mechanical properties of RPV steels. This report summarizes these advances in the state of knowledge and amalgamates them into a technical basis for an up-to-date version of RG 1.99.

Brian W. Sheron, Director
Office of Nuclear Regulatory Research
U.S. Nuclear Regulatory Commission

CONTENTS

Appendices

The following appendices appear in Volume 2 of this report:

Tables

Figures

EXECUTIVE SUMMARY

Background

The U.S. Nuclear Regulatory Commission (NRC) promulgated Revision 2 of Regulatory Guide 1.99, "Radiation Embrittlement of Reactor Vessel Materials" [RG199R2], in May 1988. That guide details methods that the NRC staff considers acceptable for licensees to use in estimating the effects of radiation on the Charpy V-notch (CVN) impact energy (CVE) of the ferritic steels used in constructing the beltline region of a nuclear reactor pressure vessel (RPV). Radiation damage reduces the ability of these materials to carry load without failure. Consequently, any assessment of the operating safety of the RPV structure must account for the effects of radiation damage. By law, power reactor licensees are required to account for the effects of radiation damage in the following four situations:

(1) when assessing the ability of the RPV structure to resist fracture during postulated accident scenarios, such as pressurized thermal shock (PTS) [10CFR5061]

(2) when assessing the ability of the RPV structure to resist fracture during routine hea-up, cooldown, and hydrotest conditions [10CFR50G]

(3) when determining what material samples need to be included in a surveillance program for the RPV beltline [10CFR50H]

(4) when assessing the ability of the RPV structure to continue safe operation in the presence of a flaw detected during either pre- or in-service inspection [ASME IWB-3500, ASME IWB-3600]

Motivation and Scope of Study

Since 1988, the NRC and the nuclear industry have made considerable advances in both the physical understanding of radiation damage processes and the empirical quantification of the effects these processes have on the mechanical properties of RPV steels. The objective of this report is to summarize these advances in the state of knowledge and amalgamate them into a technical basis for an up-to-date version of RG 1.99. Specifically, this report provides the basis of the staff's recommendations on the following matters:

- a formula that can be used to estimate the value of the transition temperature shift at the 30 ft-lb CVE level (ΔT_{30}) based on the composition of the steel of interest and the conditions under which it has been exposed to neutron irradiation
- a formula that can be used to estimate the value of the upper-shelf energy drop (ΔUSE) based on the composition of the steel of interest and the conditions under which it has been exposed to neutron irradiation
- the inadvisability of using material- and plant-specific surveillance data to influence or adjust ΔT_{30} and ΔUSE estimates for individual plant assessments
- the margins that should be assigned to the ΔT_{30} and ΔUSE estimates to account for uncertainties
- how the ΔT_{30} and ΔUSE estimates should be adjusted to account for the effects of neutron attenuation through the thick wall of the RPV

Investigative Approach

Based on the physical insights and literature data summarized herein, the NRC staff identified a candidate fitting function for ΔT_{30}. This function was fit to the U.S. light-water reactor (US-LWR) surveillance database using a least-squares approach. The staff then assessed the resultant best fit to evaluate its ability to predict data that were not used in developing the fit. Specifically, the staff used the following databases in this assessment:

(1) RADAMO Database: a database of test reactor irradiations performed on 14 commercial alloys with a focus on high fluences [Chaouadi 05a]

(2) IVAR Database: a database of test reactor irradiations performed on a wide array of both laboratory and commercial alloys with a controlled study of flux (see Appendix B to this report)

(3) JNES Databases: a database of both surveillance and test reactor irradiations performed by the Japan Nuclear Energy Safety Organization [JNES 07]

(4) French Database: a database of surveillance data from power reactors operated in France [Brillaud 92]

This assessment led to (1) a better understanding of the applicability limits of the best fit equation, (2) a modification of the best fit equation so that it applies to a larger range of conditions, and (3) the identification of certain steps that need to be taken to improve the predictive capability of the best fit equation for future conditions.

Major Technical Findings

Within the central range of composition and exposure conditions of the US-LWR surveillance database, the recommended model for ΔT_{30} [RM-6(2), as described in Section 9.4.1 of this report] predicts very well the embrittlement trends in all other databases examined in this study. However, when RM-6(2) is used to make either predictions at the peripheries of its calibration dataset or predictions that extrapolate from its calibrated range, its ability to represent embrittlement trends degrades in some cases. In particular, RM-6(2) cannot reliably predict embrittlement trends for the following conditions:

(1) **At high fluences**: As fluence increases beyond $\approx 3 \times 10^{19}$ n/cm^2, the predictive accuracy of RM-6(2) rapidly degrades, with the model systematically under-estimating the magnitude of embrittlement at these high fluences. This problem stems from the lack of a significant quantity of data above $\approx 3 \times 10^{19}$ n/cm^2 in the US-LWR calibration database, which appears to cause a systematic under-estimation of the matrix damage (MD) hardening rate coupled with a systematic over-estimation of the peak magnitude of copper-rich precipitate (CRP) hardening. Because matrix damage dominates embrittlement after CRP saturation, the net effect of these two errors is the systematic under-estimation at high fluences that was observed. While it is clear that RM-6(2) under-predicts embrittlement at fluences above 3×10^{19} n/cm^2, the apparent cause of this under-prediction advanced herein must be regarded as provisional, as it is based only on mechanical property data from the RADAMO and JNES test reactor databases. Microstructural examination of the alloys irradiated at high fluences using, for example, atom probe and small angle neutron scattering (SANS) techniques, is needed to determine which embrittlement mechanisms are active at high fluences.

(2) **At high and low nickel contents**: The bulk of the US-LWR surveillance data has between 0.5 and 1.0 wt-% Ni, so it is not surprising that RM-6(2) makes accurate predictions within this range of nickel content. However, at low nickel content (below ≈0.2 wt-%) and high nickel content (above ≈1.5 wt-%), respectively RM-6(2) systematically over-predicts or under-predicts embrittlement. Evidence supporting this finding is available in the RADAMO, JNES, and French surveillance databases.

(3) **As flux decreases from ≈8x10^{11} n/cm^2/sec**: Decreasing fluxes lead to a slight increase in the degree by which RM-6(2) under-predicts embrittlement. The slight effect of flux on the fluence at which CRP saturates (which appears in the controlled IVAR irradiations) cannot be resolved from any other database because of the strong correlations between flux and fluence in all other databases.

(4) **At high copper content**: Although RM-6(2) has a maximum copper content (Cu_{max}) term of 0.32 wt-%, this term is not a statistically essential feature of the model because the surveillance database has very limited data for high copper content. Nonetheless, information in the IVAR database demonstrates that above a copper content of ≈0.38 wt-%, RM-6(2) systematically over-estimates the magnitude of embrittlement.

These inadequacies of RM-6(2) are attributable to limitations in the US-LWR surveillance database that was used to calibrate the model. Thus, these limitations are shared by any similarly derived model (e.g., the model developed in Appendix A to this report, or the model described in [Eason 98]). Of these four inadequacies, the first presents the greatest practical concern because fluences above ≈3x10^{19} n/cm^2 have already occurred in operating pressurized-water reactors (PWRs), and will occur in approximately half of the PWRs in the currently operating fleet by the end of their original operating licenses. Additionally, reactors that may be constructed in the near future are likely to have peak fluences as high as ≈1x10^{20} n/cm^2 after 60–80 years of operation. Therefore, this report includes recommendations on treatment of high fluence situations. The latter three inadequacies present less practical concern because they are much smaller in magnitude, result in systematic over- (rather than under-) predictions of ΔT_{30}, and/or do not apply to the materials commonly encountered in power reactor service.

Recommendations

Based on the analyses presented herein, the NRC staff recommends the following formulae and procedures for adoption in Revision 3 of Regulatory Guide 1.99.

ΔT_{30} Trend Curve for Fluences At or Below 2x10^{19} n/cm^2

Eq. 4-21 (repeated) $\Delta T_{30} = \Delta T_{30(MD)} + \Delta T_{30(CRP)}$

where

$$\Delta T_{30(MD)} = PF_{MD} \cdot CF_{MD} \cdot TF_{MD} \cdot \phi F_{MD} \cdot \Phi F_{MD}$$

$$PF_{MD} = \left\{ \begin{array}{c} Weld = 6.7 \\ Plate = 8.1 \\ Forging = 4.75 \end{array} \right\} \times 10^{-9} \qquad CF_{MD} = \left[1 + 35 \cdot P\right]$$

$$TF_{MD} = \left(\frac{T}{550}\right)^{-14.64} \qquad \phi F_{MD} = \left(\frac{Log10(\phi)}{10.7}\right)^{-3.44} \qquad \Phi F_{MD} = \sqrt{\Phi}$$

$$\Delta T_{30(CRP)} = PF_{CRP} \cdot CF_{CRP} \cdot TF_{CRP} \cdot \Phi F_{CRP}$$

$$PF_{CRP} = \left\{ \begin{array}{c} Weld = 0.301 \\ Plate = 0.233 \\ Forging = 0.233 \end{array} \right\}$$

$$CF_{CRP} = \left[f(Cu) + 2500.3 \cdot \text{MIN}\{0.32, \text{MAX}(0, Cu - 0.048)\} \cdot Ni \right]$$

$$f(Cu) = -116.3 + 530.8\sqrt{Cu} \text{ , subject to } 0 \le f(Cu) \le 118.5$$

$$TF_{CRP} = \left(\frac{T}{550} \right)^{-1.74} \qquad \Phi F_{CRP} = \left\{ 1 - \exp\left(\frac{-\Phi}{2.38 \times 10^{18}} \right) \right\}$$

In this equation, the values of Cu, Ni, and phosphorous (P) are expressed in weight percent (wt-%), temperatures are expressed in degrees Fahrenheit (°F), fluence is expressed in n/cm^2 (E>1MeV), and flux is determined by dividing fluence by the time the reactor has been in operation (with time expressed in seconds). Thus, the uncertainty (standard deviation) of the RM-6(2) prediction of ΔT_{30} is 19 °F for materials having less than the minimum copper content (Cu_{min}=0.048 wt-%) and is 25 °F for materials having more copper than Cu_{min}.

Application of this model is expected to produce predictions within the stated uncertainties, provided that the conditions of the application meet all of the following criteria:

(1) Fluence is less than 3x10^{19} n/cm^2.
(2) Nickel is less than 1.25 wt-%.
(3) Nickel exceeds 0.25 wt-%.
(4) Copper is less than 0.38 wt-%.

If either of the first two criteria is not met, this model will most likely under-predict ΔT_{30}. Conversely, the model will most likely over-predict ΔT_{30} if either of the second two criteria is not met. Additionally, if the first criterion is met, the model described below as Eq. 4-22 should be used.

ΔT_{30} Trend Curve for Fluences Above 4x10^{19} n/cm^2

Eq. 4-22 (repeated) $$\Delta T_{30} = \left\{ \begin{array}{c} Weld = 1.39 \\ Plate = 1.18 \\ Forging = 0.84 \end{array} \right\} \cdot \left\{ \Delta YS_{(MD)} + \sqrt{\Delta YS^2_{(CRP)} + \Delta YS^2_{(PRP)}} \right\}$$

The product form-dependent constants convert the change in yield strength (ΔYS) values (with units of MPa), into ΔT_{30} values (with units of °F).

Matrix damage does not begin until an incubation fluence (Φ_o=1x10^{19} n/cm^2) has been achieved. Below Φ_o, $\Delta YS_{(MD)}$ is zero, and above Φ_o, $\Delta YS_{(MD)}$ is defined as follows:

$$\Delta YS_{(MD)} = \left\{585 \cdot \exp\left[-1250 \cdot \exp\left(-\frac{0.345}{kT}\right)\right] + (3880 - 6.3 \cdot T) \cdot Ni\right\} \sqrt{1 - \exp\left[-0.01(\Phi - \Phi_o)\right]}$$

where T is expressed in Kelvin, Ni is expressed in weight percent, and all fluences (both Φ and Φ_o) are divided by 1x10^{19} n/cm^2 before being used in this equation.

The magnitude of the **copper-rich precipitate** term is as follows:

$$\Delta YS_{(CRP)} = \Delta_{CRP(PEAK)}$$

where

If Cu $\leq$ Cu$_{min}$, then $\Delta_{CRP(PEAK)} = 0$

If Cu > Cu$_{min}$, then $\Delta_{CRP(PEAK)} = 215\left[1 - \exp\left\{-2.7\left(Cu - Cu_{\min}\right)\right\}\right]$

Cu$_{min}$ = 0.03 wt-%.

This relationship is simplified, insofar as this relationship for ΔYS_{CRP} reflects only the peak CRP hardening, rather than the evolution with fluence that is needed to achieve peak hardening. This simplification is possible because this formula will only be used at fluences above 2x10^{19} n/cm^2; which far exceed that needed to achieve peak hardening (see Figure 4-48).

Damage by **phosphorus-rich precipitates** is zero for alloys having less than 0.012 wt-% phosphorus. For higher-phosphorus alloys, the magnitude of the phosphorus-rich precipitate term is as follows:

$$\Delta YS_{(PRP)} = (44470.5 - 70T) \cdot (P - 0.012)$$

In this equation, T is expressed in Kelvin. It should be noted that, while suggested in [Chaouadi 05b], this relationship was not recommended for use because it is empirical and based on only two data sets. Nonetheless, our assessment of the RADAMO trend curve suggests that it is better to include this term than to omit it. This equation should only be used within its calibrated temperature range of 265–300 °C (509–572 °F). Additionally, it should not be applied to phosphorus levels that exceed 0.03 wt-%.

In Eq. 4-22, the uncertainty (standard deviation) with which ΔT_{30} is predicted is 33 °F. Application of this model is expected to produce predictions within this uncertainty bound, provided that the conditions of the application meet all of the following criteria:

(1) Phosphorus is less than 0.03 wt-%.
(2) Copper is less than 0.5 wt-%.
(3) Nickel exceeds 0.25 wt-%.
(4) Nickel is less than 1.25 wt-%.

If any of the first three criteria is not met, this model will most likely over-predict ΔT_{30}. Conversely, this model will most likely under-predict ΔT_{30} if last criterion is not met. However, none of these restrictions is expected to create a practical impediment to application of this model to currently operating materials, because these compositions are not typical of the RPV materials that are currently in service. Nonetheless, it should be noted that this model should be used only when fluence exceeds 2×10^{19} n/cm^2.

ΔT_{30} Trend Curve for Fluences Between 2 x10^{19} n/cm^2 and 4x10^{19} n/cm^2

For fluences between 2 x10^{19} n/cm^2 and 4x10^{19} n/cm^2, the ΔT_{30} estimates of Eq. 4-21 and 4-22 are combined according to the following weighting formula:

Eq. 4-23 (repeated) $$\Delta T_{30} = (1 - W) \cdot \Delta T_{30}^{RM-6(2)} + W \cdot \Delta T_{30}^{RADAMO}$$

where

$$W = \frac{1}{2}\left(\frac{\Phi}{1 \times 10^{19}} - 2\right)$$

and $\Delta T_{30}^{RM-6(2)}$ and ΔT_{30}^{RADAMO} represent the values of ΔT_{30} estimated using Eq. 4-21 and 4-22, respectively.

ΔUSE Equation

Eq. 5-1 (repeated) $$\Delta USE = 0.18 \cdot \Delta T_{30}$$

where ΔT_{30} is as predicted by Eqs. 4-21 to 4-23 and is expressed in degrees Fahrenheit (°F) and ΔUSE is expressed in foot-pounds. The uncertainty (standard deviation) in Eq. 5-1 is 13 ft-lbs.

Treatment of Surveillance Data

The complexity of the irradiation damage process makes it is impossible to obtain a reliable quantitative projection of the future embrittlement behavior of a particular material in a particular RPV based on small data sets. Surveillance programs conducted under the requirements of Appendix H to Title 10, Part 50, of the *Code of Federal Regulations* (10 CFR Part 50) result in the observation of far too few mechanical property changes to provide either reliable calibrations or adjustments of the recommended ΔT_{30} or ΔUSE values. In fact, nearly 80% of the reactor beltline materials that have been monitored under Appendix H have four ***or fewer*** surveillance observations, and no currently monitored material has greater than eight observations. Thus, the quantity of surveillance data available for a particular material is small in an absolute sense, and it is also small relative to the complexity of the embrittlement trend equations. For example, the recommended ΔT_{30} model (Eq. 4-15) includes seven independent variables and 18 parameters for which the numerical values were determined by fitting. Although it is possible on theoretical grounds to justify holding two of these parameters constant, this comparison suggests that, for the great majority of the materials in the surveillance database, a material-specific adjustment of either the ΔT_{30} or ΔUSE relationships would be under-determined (i.e., the number of unknown fitting parameters would exceed the number of experimental observations) by a factor of approximately four. As a result, plant-specific surveillance data (in the quantities currently available)

cannot be expected to provide an accurate plant-specific adjustment of the generic ΔT_{30} or ΔUSE relationships. Additionally, statistical justification for margin reduction is highly unlikely given the limited quantities of surveillance data that are now available.

In replacing the Revision 2 procedures for treatment of surveillance data, Revision 3 will require licensees to assess their plants using material-specific information on composition and exposure variables as inputs to the recommended ΔT_{30} and ΔUSE relationships. Also, as a defense-in-depth measure, collection of mechanical property change observations (i.e. ΔT_{30}, ΔUSE, and ΔYS data) as part of 10 CFR Part 50 Appendix H surveillance programs should continue to be required. These data provide advance indication of embrittlement mechanisms that have been (heretofore) unforeseen or unobserved, or have been observed only anecdotally. These data also provide the NRC staff with information that allows periodic assessment of (1) whether any plant-specific materials deviate from fleet-wide trends, and (2) whether the generic equations representing the overall trends need to be changed in view of the surveillance information. Section 9.5 discusses future plans to treat surveillance data beyond the recommendations of Revision 3 of Regulatory Guide 1.99.

Margins

Eq. 7-1 (repeated) $$\overline{\overline{\Delta T_{30}}} = \Delta T_{30(eq4-15)} + \alpha \cdot \sigma_{\Delta T_{30}}$$

Eq. 7-2 (repeated) $$\overline{\overline{\Delta USE}} = \Delta USE_{(eq5-1)} + \alpha \cdot \sigma_{\Delta USE}$$

In Eq. 7-1 and 7-2, the $\overline{\overline{\Delta T_{30}}}$ and $\overline{\overline{\Delta USE}}$ values indicate quantities that have been adjusted to account for the effects of uncertainty in a manner consistent with their intended application. In both equations, α is defined as follows:

α=0 if the estimate of ΔT_{30} or ΔUSE is needed as part of a probabilistic calculation where the analysis explicitly accounts for sources of uncertainty in ΔT_{30} or ΔUSE

α=0 if the estimate of ΔT_{30} or ΔUSE is needed for comparison to a prescribed limit that was arrived at based on a risk-informed probabilistic evaluation that accounted for the sources of uncertainty in ΔT_{30} or ΔUSE

α=2 if the estimate of ΔT_{30} or ΔUSE is needed for comparison to a prescribed limit that was arrived at deterministically

The value of $\sigma_{\Delta T_{30}}$ in Eq. 7-1 is 19 °F for alloys having a copper content below Cu_{min} of 0.048 wt-% and. For alloys having a copper content above Cu_{min} the value of $\sigma_{\Delta T_{30}}$ is 25 °F. If fluence exceeds $3x10^{19}$ n/cm^2, the value of $\sigma_{\Delta T_{30}}$ in Eq. 7-1 is 33 °F, irrespective of copper content. The value of $\sigma_{\Delta USE}$ in Eq. 8-2 is 13 ft-lbs.

Attenuation

The attenuation guidance in Revision 3 of Regulatory Guide 1.99 will remain the same as that provided in Revision 2, as follows:

Eq. 8-1 (repeated) $\Phi(z) = \Phi_{ID} \exp(-0.24z)$

where z is the distance from the inner diameter of the RPV (in inches) and fluence is expressed in n/cm^2 (E>1MeV).

Plans for Future Refinements in this Technical Area

The NRC envisions a two-pronged approach to continue to build on the advances to date, and to reconcile some of the inadequacies identified herein. Toward that end, the agency will undertake (or participate in) specifically focused research investigations to address inadequacies in the current equations. Additionally, the agency will initiate an ongoing data trending activity. The following sections detail the NRC's planned activities.

Planned Research Activities

The NRC is planning focused research and/or collaborative projects to address those technical inadequacies noted herein that have the greatest technical impact:

- High fluence: The NRC needs to better understand the under-prediction of the fit of the ΔT_{30} model fit to the US-LWR surveillance data at fluences above 3x10^{19} n/cm^2, so that the agency can adopt a single ΔT_{30} model for all fluences. This will allow confident projection of irradiation damage during the extended period of operating life (for existing reactors), as well as for new reactors. The agency also needs an assessment of the embrittlement mechanisms operating at these high fluences to allow the confident development of improved equations. Toward that end, the NRC's Office of Nuclear Regulatory Research (RES) is currently sponsoring research being conducted at the Belgian Nuclear Research Centre (SCK/CEN) and the Oak Ridge National Laboratory in the United States, which will include both mechanical property characterization (i.e., ΔT_{30}, ΔT_o, ΔUSE, and ΔYS data) and microstructural characterization (i.e., SANS, atom probe) of five RPV materials (three welds and two plates) having high copper content. These materials were exposed to fluences as high as 1x10^{20} n/cm^2; Appendix F is a report detailing work performed to date. Additional studies may be required to expand the scope of the investigation to low-copper materials, among other things.
- Nickel: While the inadequacy of RM-6(2) when applied to both high- and low-nickel materials is clear, the practical impact of these inaccuracies on new reactor materials is not. Therefore, the NRC will survey the planned materials of construction for Generation III+ reactors [e.g., the U.S. Evolutionary Power Reactor (US-EPR) or the 1,000-MWe AP1000 Advanced Passive Reactor] to determine whether the vendors plan to use high- or low-nickel materials. The outcome of this survey will inform the decision regarding the need to perform additional focused research related to nickel effects.
- Flux: As revealed by the IVAR database, flux has a slight effect that cannot be properly reflected in surveillance-calibrated models because of the strong correlation between the fluence and flux of surveillance materials. Although the magnitude of this effect is small, the development of physically sound and empirically informed flux models is fundamental to both properly designing surveillance programs and understanding

how accelerated test reactor irradiations inform surveillance-based trend curves. Therefore, the NRC will undertake a project that is specifically focused on developing validating a physically based flux model.

- Attenuation: As stated in Chapter 8, very limited data are available to inform the attenuation formula. Therefore, the NRC is co-sponsoring a collaborative project, being conducted at the Nuclear Research Institute at Řež in the Czech Republic, which features an extensive experimental quantification of attenuation effects using different RPV alloys. Current progress on this project is summarized in [Server ??]. In addition, the agency will pursue investigations of the practical implementation of approaches based on displacements per atom (dpa), as an alternative to fluence.
- Fracture toughness: Information on fracture toughness is needed as input to any structural integrity procedure; however, to date, only CVN information (which is not a measurement of fracture toughness) has been available in adequate quantities to permit the development of trend equations that express the effects of irradiation on mechanical properties. As a result, the NRC will undertake the development of trend curves based on fracture toughness using currently available data and, perhaps, newly generated data. Information from the flux studies (discussed above) is expected to support this effort, given that this information will provide physically appropriate rules to scale between test and power reactor irradiations. Additionally, continuation of recent work, which identified heretofore unrecognized commonalities between CVE and K_{Jc} transition characterizations [EricksonKirk 07], is expected to be helpful.

The NRC will undertake all of these activities as subtasks to an umbrella project focused on developing a fourth revision of Regulatory Guide 1.99 within 5 years. As part of that effort, the agency will pursue collaboration with the international research community whenever possible.

Ongoing Data Trending Activity

In nearly three decades since the NRC promulgated Revision 2 of Regulatory Guide 1.99, the agency has intermittently undertaken data trending activities, primarily focused on ΔT_{30}, which have invariably been viewed as activities having defined endpoints, rather than ongoing activities aimed at keeping estimation strategies current with the state of knowledge. By contrast, in the future, the NRC plans to replace this approach, as well as the occasional use of very limited quantities of surveillance data to adjust generic trends in a plant-specific way, by a systematic effort to continually evaluate new data (from both surveillance and research programs) as they become available. The agency will launch this effort as a staff activity, but will endeavor to organize and coordinate the work through a newly formed task group dedicated to this purpose, under the auspices of the American Society for Testing and Materials (ASTM) Subcommittee E10.02. Examining small sets of data within the context of larger databases and physical understanding gained from focused research programs offers the following advantages over current approaches, such as those advocated by Revision 2 of Regulatory Guide 1.99, which confer undue merit and significance to extremely limited data sets:

- Having a broader, physically based, framework within which to view new data permits more reliable discrimination of outliers from emergent trends.
- Insights gained from emergent trends can be rapidly communicated and applied to the entire reactor fleet in an evenhanded way.

- Undertaking a continuous effort ensures that embrittlement trends are kept up to date with the most recent research results, and the research being conducted is focused on the issues most important to the operating fleet.
- Broad maintenance and coordination of both research and surveillance databases, among various countries, operators, regulators, and research groups, offers the maximum benefit and leverage available from their respective investments of money and time.

ACKNOWLEDGEMENTS

The author is pleased and honored to acknowledge the valuable assistance in the preparation of this report provided by the following individuals:

- First and foremost, great thanks are due to Dr. Rachid Chaouadi of the Belgian Nuclear Research Centre (SCK/CEN). Dr. Chaouadi provided the author with copies of many relevant SCK/CEN research reports, as well as a complete electronic copy of the SCK/CEN RADAMO databank. These reports, RADAMO data, and Dr. Chaouadi's patient and insightful replies to the many questions posed by the author via email contributed significantly to the comprehensiveness and findings of this report.
- Thanks are also due to Dr. Robert Gérard of Tractebel. Dr. Gérard sponsored Dr. Chaouadi's work and authorized its release to the NRC.
- Finally, I would like to thank my supervisor, Mr. Robert Hardies, for his many helpful discussions and his tolerance of the time required to prepare this report.

1 SCOPE, OBJECTIVE, AND STRUCTURE OF THIS REPORT

The U.S. Nuclear Regulatory Commission (NRC) promulgated Revision 2 of Regulatory Guide 1.99, "Radiation Embrittlement of Reactor Vessel Materials" [RG199R2], in May 1988. That guide details methods that the NRC staff considers acceptable for licensees to use in estimating the effects of radiation on the Charpy V-notch (CVN) impact energy (CVE) of the ferritic steels used in constructing the beltline region of a nuclear reactor pressure vessel (RPV). Radiation damage reduces the ability of these materials to carry load without failure. Consequently, any assessment of the operating safety of the RPV structure must account for the effects of radiation damage. By law, power reactor licensees are required to account for the effects of radiation damage in the following four situations:

(1) when assessing the ability of the RPV structure to resist fracture during postulated accident scenarios, such as pressurized thermal shock (PTS) [10CFR5061]

(2) when assessing the ability of the RPV structure to resist fracture during routine heatup, cooldown, and hydrotest conditions [10CFR50G]

(3) when determining which material samples need to be included in a surveillance program for the RPV beltline [10CFR50H]

(4) when assessing the ability of the RPV structure to continue safe operation in the presence of a flaw detected during either pre- or in-service inspection [ASME IWB-3500, ASME IWB-3600]

Chapter 2 summarizes the provisions of Revision 2 of RG 1.99, assesses the accuracy of its predictions relative to currently available surveillance data, and discusses the motivations for its revision. Like Revision 2, Revision 3 of RG 1.99 will quantify radiation damage effects using the following two metrics of radiation embrittlement, which are illustrated in Figure 1.1:

(1) The transition temperature shift at the 30 ft-lb CVE level (ΔT_{30}) defines the increase in the Charpy 30 ft-lb transition temperature produced by radiation embrittlement.

(2) The upper-shelf energy drop (ΔUSE) defines the reduction in the CVE on the upper shelf produced by radiation embrittlement.

These two metrics can be correlated to the effects of radiation damage on the actual measurements of fracture toughness that are the inputs needed to assess structural integrity. Nonetheless, ΔT_{30} and ΔUSE are ***not*** direct measurements of fracture toughness. Additionally, although advancements in the field of fracture mechanics now make it possible to measure fracture toughness using mechanical test samples as small as those placed in nuclear surveillance capsules, there is, as yet, inadequate data and insufficient experience with this approach to allow Revision 3 of RG 1.99 to make use of direct fracture toughness measurements. Thus, **Chapter 3** of this report describes the background of the CVN test and its correlation with fracture toughness values.

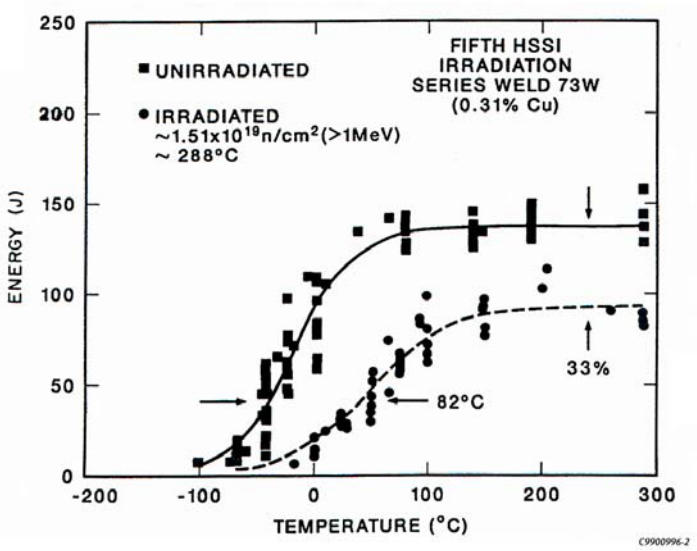

Figure 1.1. Effect of radiation damage on the CVN transition characterization of ferritic steels (from Chapter 1 of Appendix A to this report).

Since the NRC promulgated Revision 2 of the Regulatory Guide 1.99 in 1988, the agency and the nuclear industry have made considerable advances in both the physical understanding of the radiation damage processes and the empirical quantification of the effects these processes have on the mechanical properties of RPV steels. The objective of this report is to summarize these advances in the state of knowledge and amalgamate them into a technical basis for an up-to-date version of RG 1.99. Specifically, this report provides the basis of the staff's recommendations regarding the following matters:

- **Chapter 4** describes a formula that can be used to estimate the value of ΔT_{30} based on the composition of the steel of interest and the conditions under which it has been exposed to neutron irradiation.
- **Chapter 5** describes a formula that can be used to estimate the value of ΔUSE based on the composition of the steel of interest and the conditions under which it has been exposed to neutron irradiation.
- **Chapter 6** describes why material- and plant-specific surveillance data should be not influence the ΔT_{30} and ΔUSE estimates that are needed for individual plant assessments. This is a change from the provisions of RG 1.99R2, which permits limited material- and plant-specific data to influence the general ΔT_{30} and ΔUSE equations.
- **Chapter 7** describes the margins that should be assigned to the ΔT_{30} and ΔUSE estimates to account for uncertainties. These margins differ, depending on whether the ΔT_{30} or ΔUSE estimates are needed for comparison to a deterministically or probabilistically derived limiting value.
- **Chapter 8** describes how the ΔT_{30} and ΔUSE estimates should be adjusted to account for the effects of neutron attenuation through the thick wall of the RPV.

The recommendations presented in these chapters are informed by data taken from the technical literature (see **Chapter 10**), as well as data contained in two recently completed work products prepared by NRC contractors, which are attached as appendices to this report:

- **Appendix A** is a report by Eason, Odette, Nanstad, and Yamamoto, entitled "A Physically Based Correlation of Irradiation-Induced Transition Temperature Shifts for RPV Steels." That report contains an extensive amount of preliminary work on the development of a ΔT_{30} trend curve, and was one of the key documents that informed the development of Chapter 4 of this report. In addition, Chapter 2 of that report contains a review of the physical mechanisms of irradiation damage in RPV steels, while its Appendix C summarizes the U.S. light-water reactor (US-LWR) surveillance database.
- **Appendix B** is a report by Odette, Yamamoto, Klingensmith, Gragg, and Lucas, entitled "The UCSB Irradiation Variables Facility Database on Irradiation Induced Yield and Ultimate Tensile Stress Changes in the Reactor Pressure Vessel Steels." That report describes an extensive experimental effort conducted for the NRC at the University of California at Santa Barbara to measure the effects of irradiation damage on the yield strength of RPV steels and similar ferritic alloys. Toward that end, the report contains complete documentation of all yield strength shift measurements made as part of the **I**rradiation **VAR**iables database (**IVAR**) study. The trends seen, and not seen, in the IVAR data represent another key source of information for the recommendations presented in Chapter 4 of this report.

2 REVISION 2 OF REGULATORY GUIDE 1.99

This chapter summarizes the provisions of Revision 2 of Regulatory Guide 1.99, assesses the accuracy of its predictions relative to available data, and discusses the motivations for its revision.

2.1 Provisions of Revision 2 of Regulatory Guide 1.99

Revision 2 of Regulatory Guide 1.99 provides guidance regarding the following four matters:

(1) An embrittlement trend curve (ETC): a formula used to estimate the value of ΔT_{30} based on the composition of the steel of interest and the conditions under which it has been exposed to neutron irradiation

(2) An upper-shelf energy drop (USED) equation: a formula used to estimate the value of ΔUSE based on the composition of the steel of interest and the conditions under which it has been exposed to neutron irradiation

(3) Use of surveillance data: procedures for how material- and plant- specific surveillance data should be used to influence ΔT_{30} and ΔUSE estimates, and which margins should be assigned depending on whether surveillance data are used

(4) Attenuation: how the ΔT_{30} and ΔUSE estimates should be adjusted to account for the effects of neutron attenuation through the thick wall of the RPV

The following four subsections summarize this guidance.

2.1.1 Embrittlement Trend Curve (ΔT_{30} Equation)

Revision 2 of Regulatory Guide 1.99 includes the following ETC [Randall 87], which correlates the shift in the 30 ft-lb CVE transition temperature (ΔT_{30}) produced by radiation damage with exposure, composition, and categorical variables:

Eq. 2-1 $$\Delta T_{30} = (CF) f^{(0.28-0.1\log f)}$$

where

CF is a "chemistry factor" that characterizes the radiation sensitivity of the steel. *CF* depends on copper content, nickel content, and product form. Revision 2 of Regulatory Guide 1.99 includes tables of *CF* values.

f is the fast neutron fluence in neutrons per cm^2 (E>1Mev) divided by 10^{19}. The value of *f* is defined for the material and operational duration of interest.

[Randall 87] describes how Eq. 2-1 represents a compromise between two ETCs published by Odette and Guthrie [Odette 84, Guthrie 84] and how Eq. 2-1 was calibrated to the surveillance database of 177 shift values that were available at the time.

2.1.2 Upper-Shelf Energy Drop (ΔUSE)

The USED equation is a relationship that determines the degree by which the upper-shelf energy is reduced by the effects of neutron irradiation. As shown in Figure 2-1, the USED equation depends on fluence, copper, and product form. Revision 2 of Regulatory Guide 1.99 includes only a graphical depiction of this relationship.

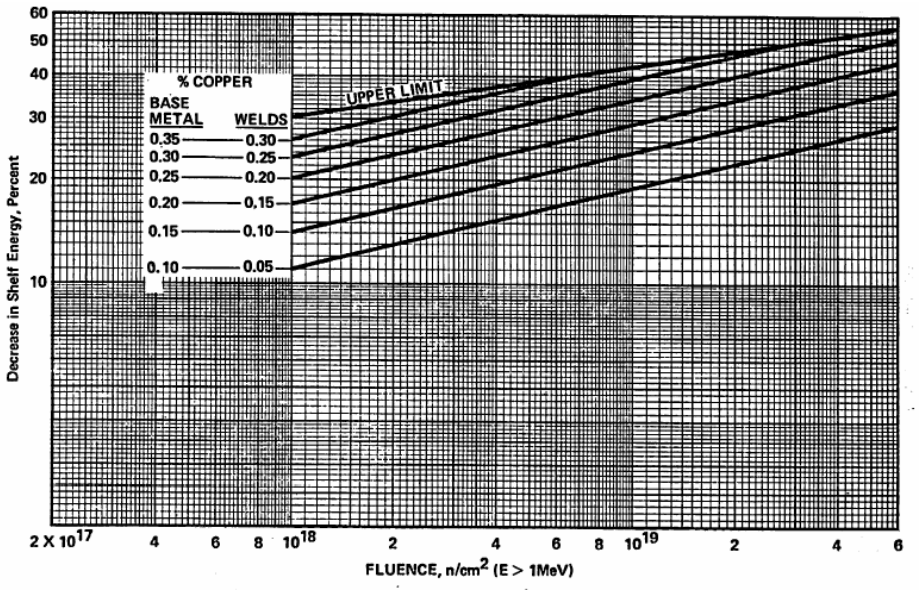

Figure 2-1. Graphical relation for upper-shelf energy drop from Revison 2 of Regulatory Guide 1.99.

2.1.3 Use of Surveillance Data, and Margins

The "Discussion" section in Revision 2 of Regulatory Guide 1.99 sets forth the criteria by which ΔT_{30} data from surveillance programs are judged to be "credible." (Although the guide does not set forth similar specific credibility criteria for ΔUSE data, it does imply that the credibility of those data should also be checked.) "Credible" surveillance data may then be used to adjust the generic relationship (described in the guide) between ΔT_{30} and fluence, copper content (Cu), nickel content (Ni), and product form. The following paragraphs summarize, in a step-by-step manner, the provisions of the "Discussion" section and Regulatory Position 2 in Revision 2 of Regulatory Guide 1.99 (including any ambiguities that may exist in the guide):

Step 1. **Credibility Check**: To establish that the ΔT_{30} data are "credible" for a particular heat, all of the following requirements must be met. (Note that to be allowed to check these requirements at all, two or more ΔT_{30} measurements must be available.)

a. The following credibility conditions assess how well the surveillance material and capsule irradiation conditions represent the material and irradiation conditions of the RPV:

i. The heat in question must be judged to have the largest adjusted reference temperature (i.e., $RT_{NDT(u)} + \Delta T_{30}$) of all of the beltline materials. This heat is called the "controlling" material.

ii. The irradiation temperature of the Charpy specimens must be within ±25 °F of the vessel temperature at the interface between the cladding and base metal.

iii. The surveillance data for the correlation monitor material in the capsule must fall within the scatter band of other data for that material.

b. The following credibility conditions require that the uncertainty in the Charpy data must be below certain limiting values:

i. Scatter in the variation of CVE with temperature should be sufficiently small in both the irradiated and unirradiated conditions that the T_{30} transition temperature can be "unambiguously" determined from the data.

ii. When the surveillance data are fit using the procedure in Step 3, the scatter in the ΔT_{30} measurements about the best-fit curve must be less than 28 °F for welds and 17 °F for base metal. If the fluence range exceeds 2 orders of magnitude, the maximum permissible scatter increases to 56 °F for welds and 34 °F for base metal.

Step 2. **Decision**: If the data are "credible" based on the criteria in Step 1, a heat-specific adjustment to the generic ΔT_{30} embrittlement trend is developed, as described in Steps 3–6 (below) and Regulatory Position 2 in Revision 2 of Regulatory Guide 1.99. If the data are not credible, the following equation is adopted to express generic embrittlement trends:

Eq. 2-2 $$\Delta T_{30(1.99R2)} = CF \cdot \left(\frac{\phi t}{10^{19}}\right)^{\left(0.28-0.10\cdot\log_{10}\left(\frac{\phi t}{10^{19}}\right)\right)}$$

Here, "CF" is a chemistry factor. The value of CF depends on copper content, nickel content, and product form, as described in Regulatory Position 1 in Revision 2 of Regulatory Guide 1.99.

Step 3. **ΔT_{30} Adjustment**: This step ensures that the ΔT_{30} measurements from surveillance best represent the material in the RPV. If there is evidence that the copper or nickel content of the surveillance weld (no mention is made of base metals) differs from that of the vessel weld, the following adjustment should be made to each of the measured ΔT_{30} values:

Eq. 2-3 $$\Delta T_{30(ADJ)} = \Delta T_{30(MEAS)} \cdot \frac{CF_{VESSEL}}{CF_{SURV}}$$

Here, CF_{VESSEL} and CF_{SURV} represent the chemistry factors for the vessel material and the surveillance material, respectively. Revision 2 of Regulatory Guide 1.99 provides tables of CF values that depend upon copper content, nickel content, and product form.

Step 4. **Estimate Best Fit to ΔT_{30} *vs.* Fluence for the Surveillance Data**: This step determines the best fit chemistry factor using the following formulae. This procedure minimizes the sum of squared residuals between the $\Delta T_{30(ADJ)}$ values that have been determined from the surveillance data and an ETC of the form assumed in Regulatory Position 1 in Revision 2 of Regulatory Guide 1.99.

Eq. 2-4 $$CF_{FIT} = \frac{\sum_{i=1}^{n} \left\{ \Delta T_{30(ADJ)_i} \cdot FF_i \right\}}{\sum_{i=1}^{n} FF_i}$$

Eq. 2-5 $$FF_i = \left(\frac{\phi t_i}{10^{19}} \right)^{\left(0.28 - 0.10 \cdot \log_{10} \left(\frac{\phi t_i}{10^{19}} \right) \right)}$$

Here, *n* is the number of ΔT_{30} measurements available from surveillance, and ϕt is fluence, which has units of n/cm^2. The best-fit relationship between ΔT_{30} and fluence, based on the surveillance measurements, can then be expressed as follows:

Eq. 2-6 $$\Delta T_{30(FIT)} = CF_{FIT} \cdot \left(\frac{\phi t}{10^{19}} \right)^{\left(0.28 - 0.10 \cdot \log_{10} \left(\frac{\phi t}{10^{19}} \right) \right)}$$

Step 5. **Use of ΔT_{30} *vs.* Fluence Determined from the Surveillance Data**: The ΔT_{30} values determined in Step 4 are then compared with those predicted using Regulatory Position 1.1 in Revision 2 of Regulatory Guide 1.99 (i.e., $\Delta T_{30(1.99R2)}$ values from Step 2). The following rules govern which of these two candidate ΔT_{30} values are used:

IF $\Delta T_{30(FIT)} > \Delta T_{30(1.99R2)}$ ***THEN*** $\Delta T_{30(FIT)}$ must be used.

IF $\Delta T_{30(FIT)} < \Delta T_{30(1.99R2)}$ ***THEN*** either $\Delta T_{30(FIT)}$ or $\Delta T_{30(1.99R2)}$ may be used.

Step 6. **Assigning Margins**: The term σ_Δ quantifies the uncertainty in the ΔT_{30} value. If $\Delta T_{30(FIT)}$ is used, σ_Δ is 14 °F for welds and 8.5 °F for base metal. Conversely, if $\Delta T_{30(1.99R2)}$ is used, σ_Δ is 28 °F for welds and 17 °F for base metal.

2.1.4 Attenuation

The attenuation function describes how fluence attenuates through the wall of a thick reactor vessel. Revision 2 of Regulatory Guide 1.99 adopts the following function:

Eq. 2-7 $$\phi t(z) = \phi t \exp(-0.24z)$$

where z is the distance from the inner diameter of the RPV. Eq. 2-7 conservatively assumes that fluence attenuates like displacements per atom (dpa) (i.e., more slowly than it actually does) [Randall 87].

2.2 Accuracy of Revision 2 of Regulatory Guide 1.99

The current availability of a surveillance database for ΔT_{30} containing 936 ΔT_{30} observations (see Appendix C to Appendix A) provides an ideal opportunity to assess the predictive accuracy of Eq. 2-1 from Revision 2 of Regulatory Guide 1.99. Figure 2-2 illustrates that the predictions of Eq. 2-1 over-estimate the effect of radiation on ΔT_{30} by, on average, approximately 8% for the survellience data that are now available. Figure 2-2 also shows that when a margin term of 1- or 2-σ is included in the estimated value of ΔT_{30}, as Revision 2 of Regulatory Guide 1.99 mandates for credible and non-credible surveillance data (respectively), the degree of over-prediction increases to 21 and 31% (respectively).

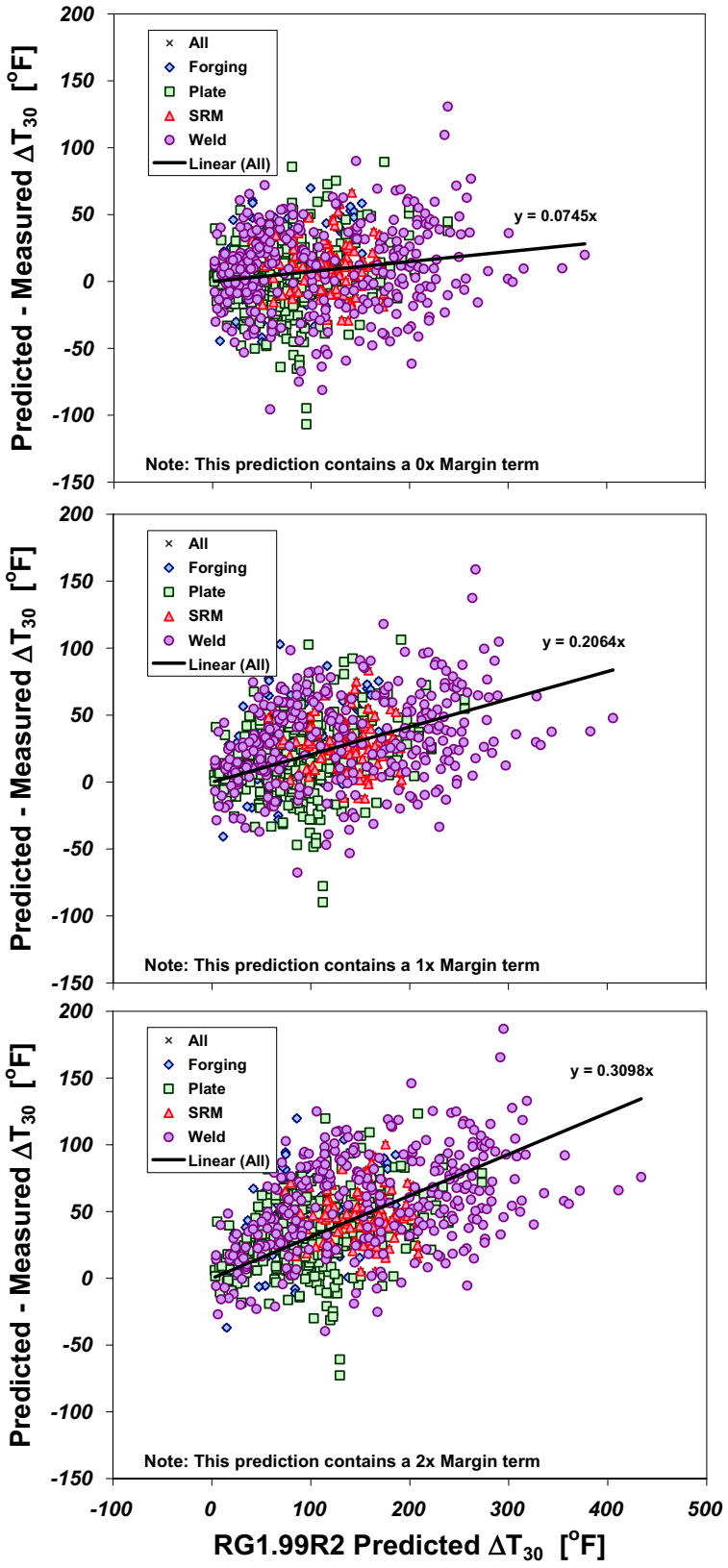

Figure 2-2. Comparison of ΔT_{30} values predicted by Regulatory Guide 1.99 Revision 2 with the currently available surveillance database.

The surveillance database also provides considerable information (859 values) on ΔUSE. However, because the upper-shelf energy drop equation in Revision 2 of Regulatory Guide 1.99 is available only graphically (see Figure 2-1), comparison of predictions to measured ΔUSE values is cumbersome and, therefore, is not performed here.

[English 02] provides a comprehensive assessment of the attenuation model (Eq. 2-7) set forth in Revision 2 of Regulatory Guide 1.99. That assessment demonstrates that Eq. 2-7 generally under-predicts the degree of attenuation relative to that shown in the data. English concluded that while the attenuation model in Revision 2 of Regulatory Guide 1.99 is appropriately regarded as conservative, no better alternative model exists at the current time.

2.3 Motivation for Revision of the Regulatory Guidance in Revision 2

Since the NRC promulgated Revision 2 of Regulatory Guide 1.99 in 1988, the state of knowledge has advanced substantially with regard to the physical mechanisms responsible for irradiation damage of the ferritic steels and welds used to construct the beltline of RPVs. The amount of data available to calibrate the equations used in the guide to estimate the effect of irradiation damage on the mechanical properties of RPV steel is also much greater than it was two decades ago. These advances in theoretical and empirical knowledge provide an opportunity to update the equations and procedures used in the guide and, in so doing, address the following issues:

- Comparison of existing surveillance data from U.S. pressurized-water reactors (PWRs) to the predictions in Revision 2 of Regulatory Guide 1.99 demonstrates that existing equations over-predict the degree of irradiation damage by 8% on average (see Figure 2-2). As the NRC migrates toward a risk-informed regulatory framework, it is important to remove this type of implicit conservatism from the equations and procedures that are used to assess plant safety and operability.
- The estimation equations used in Revision 2 of Regulatory Guide 1.99 are based on curve-fits to the surveillance data that were available in the mid 1980s. As such, those equations include features that are now understood to be physically incorrect. For example, the current fluence function predicts peak damage at a fluence of $\Phi \approx 2 \times 10^{20}$ n/cm^2 (see Figure 2-3), after which irradiation damage is predicted to decrease with increasing fluence. Furthermore, the existing equations do not differentiate between matrix damage and damage that occurs because irradiation causes copper and copper-rich second phases to precipitate from the ferrite matrix. This distinction is important to achieve accurate predictions of states that have not yet been observed (e.g., higher fluences) because matrix damage, for fluences of practical interest in LWR operations, increases in proportion to the square-root of fluence, while damage caused by precipitation saturates at fluences between approximately 1 and 3×10^{19} n/cm^2 [Chaouadi 05a]. Additionally, the equations used in Revision 2 of Regulatory Guide 1.99 did not account for the known effect of temperature on irradiation damage [Williams 86, Williams 87, Debarberis 05b].

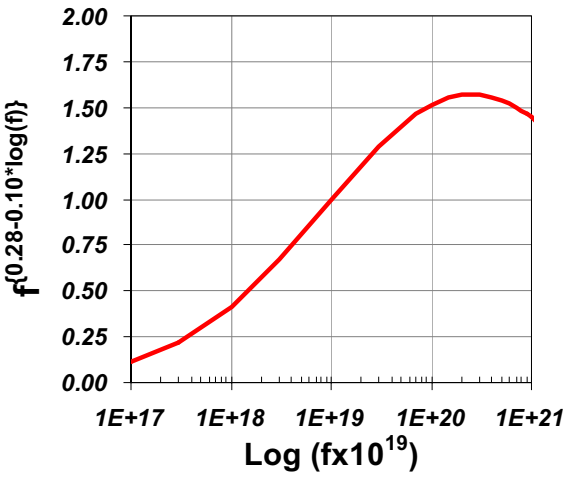

Figure 2-3. Fluence function from Revision 2 of Regulatory Guide 1.99.

- Revision 2 of Regulatory Guide 1.99 permits the use of a minimum of two credible surveillance measurements to (1) modify the predictions of the generic embrittlement equations, and (2) reduce the margin term by a factor of two. The current technical understanding demonstrates that radiation damage mechanics is a complex process driven by (at least) two competing embrittlement mechanisms, the dominance of which depends on the particular regime (i.e., fluence, flux, temperature) in which exposure to neutron irradiation occurs. This complexity is evidenced by the embrittlement trend curve equation recommended in Chapter 4 of this report, which depends on seven independent variables and includes 18 fit parameters. By contrast, in the existing surveillance database for domestic LWRs, nearly 80% of the monitored materials have four *or fewer* measurements of transition temperature shift. Given this limited quantity of surveillance data available on specific heats and the complexity of the prediction equations, it is necessary to modify the treatment of surveillance data recommended in Revision 2 of Regulatory Guide 1.99.
- Revision 2 of Regulatory Guide 1.99 recommends the use of a margin term to account for uncertainties. This provision was appropriate when the NRC promulgated Revision 2 because the structural integrity assessment procedures of the day were, nearly without exception, deterministic in nature. However, the NRC is in the process of risk-informing many of its regulatory products. In situations where regulatory limits have been established based on risk-informed probabilistic calculations that have accounted for the uncertainties that are important to embrittlement processes, the use of an additional margin term would represent an inappropriate double-counting of uncertainties. Therefore, as described in Chapter 7 of this report, the need for a margin term depends upon the application for which the estimate of embrittlement is needed.

This report addresses all of these motivating factors in a way that leads to either more accurate predictions or the use of procedures that are consistent with the current state of knowledge. However, the recommendations of this report do not address the following issues:

- As detailed in Chapter 3, the metrics that Revision 2 of Regulatory Guide 1.99 uses to measure radiation damage are based on changes to the CVE transition curve caused by radiation damage. However, CVE metrics cannot be used directly in structural integrity calculations because they do not measure fracture toughness; rather, they can only be correlated to true fracture toughness values such as those measured by the American Society for Testing and Materials (ASTM) Standard Test Method E1921-02, "Determination of the Reference Temperature, T_o, for Ferritic Steels in the Transition Range" [ASTM E1921]. While these correlations can be incorporated into probabilistic assessments of structural integrity, the use of correlations introduces uncertainties that can implicitly limit operational ability. Additionally, recent advances in fracture toughness characterization methods make the use of correlative approaches unnecessary [EricksonKirk 06a]. Moreover, ASTM E185-02, "Standard Practice for Design of Surveillance Programs for Light-Water Moderated Nuclear Power Reactor Vessels," recommends the placement of fracture toughness specimens into surveillance capsules [ASTM E185]. While these advances make it possible to measure fracture toughness using mechanical test samples as small as those placed in nuclear surveillance capsules, there is, as yet, inadequate data and insufficient experience with this approach to allow Revision 3 of Regulatory Guide 1.99 to make use of direct fracture toughness measurements.

- The equations recommended for use in Revision 3 are physically based and empirically calibrated. Thus, while the functional forms for the prediction equations were selected based on a physical understanding of the irradiation damage process, the numerical coefficients in the equations do not derive directly from physically expected/predicted trends; rather, they are merely the result of curve-fits to data. The resultant equations, therefore, cannot reliably predict trends that the calibration database does not exhibit. Also, scatter can obscure trends in the database to the point that those trends cannot be observed. For these reasons, the ΔT_{30} equation in Chapter 4 omits or does not properly reflect some known trends. (Specific trends that are not reflected in the recommended ΔT_{30} equation are discussed in Chapter 4.)

The staff anticipates that as the state of knowledge advances and additional data become available, it will be possible to address these issues in a future revision of Regulatory Guide 1.99.

3 THE CVN TEST AND CORRELATION OF CVN WITH FRACTURE TOUGHNESS TRANSITION TEMPERATURES

3.1 Characterization of Transition Temperature Using the CVN Specimen

The Charpy-V notch (CVN) specimen, illustrated in Figure 3-1, was first proposed at the beginning of the 20th century as a simple quality assurance (QA) test for use in steelmaking [Charpy 01]. The specimen contains a V-groove notch of finite root-radius cut to a depth equal to 20% of the specimen thickness. The CVN specimen is tested in a pendulum impact machine that measures the amount of energy needed to cause total failure of the specimen [ASTM E23]. Because of its small size and the ease with which it can be tested, use of the CVE specimen has grown beyond its initial application as a QA tool. Of particular interest here, in the 1940s and 1950s, the investigation of the catastrophic cleavage failures experienced by the Liberty Ships during World War II led to two significant findings:

(1) When tested at various temperatures, CVN specimens made from ferritic steels undergo a transition in their energy absorption behavior that is qualitatively similar to that experienced by fracture toughness (see Figure 3-2)[†].

(2) Index temperatures drawn from this transition curve (e.g., the temperature at which the mean absorbed energy equaled 15 ft-lbs) could be successfully correlated with the fracture performance of full-scale structures [Pellini 76].

Given the small size and blunt notch of the CVN specimen, these correlations with structural performance tended to depend on both the alloy and particulars of the structural design and loading. Nonetheless, by the mid-1950s, the CVN test was well-established as a useful tool for structural performance assessment.

3.2 Correlations Between CVE Transition Temperatures and Fracture Toughness Transition Temperatures

In the 1960s, various investigators studied the temperature dependence of the then-new fracture toughness metric K_{Ic} for the heavy section ferritic steels and welds that were being used to fabricate the then-new nuclear RPVs. These studies soon led to the realization that, in the transition temperature regime, the temperature dependence of K_{Ic} (see Figure 3.3) was qualitatively similar to that of the Charpy V-notch energy (*CVE*). This similarity set the scene for the incorporation of the CVN test into two different standards, as described in the following paragraphs. These decisions made the CVN test a critical element of the overall engineering framework used to ensure the structural integrity of nuclear RPVs throughout their operating lifetimes, a position the CVN test still occupies today.

[†] The form of the CVN energy transition curve is qualitatively similar to that of fracture toughness; however, this similarity was not known to the investigators of the Liberty Ship losses because modern concepts of fracture toughness had not yet been advanced by G.R. Irwin and others.

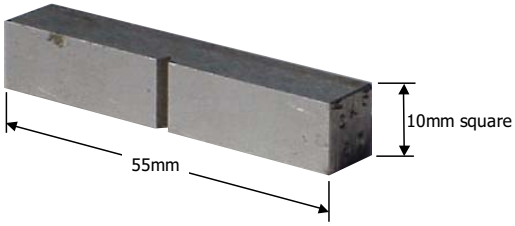

Figure 3-1. Charpy V-notch impact test specimen.

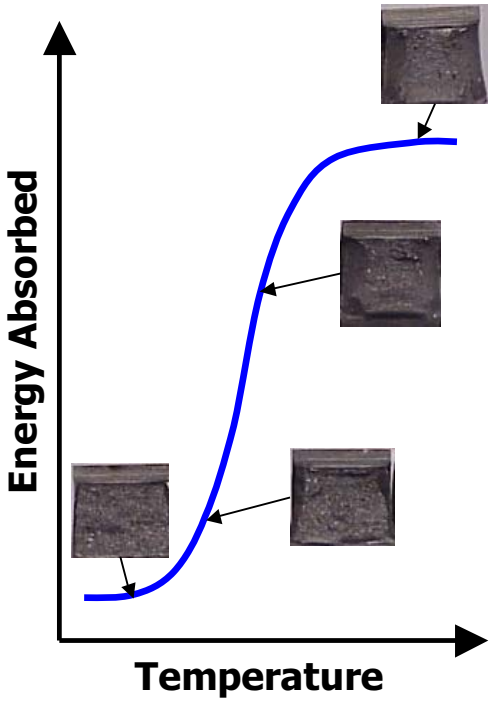

Figure 3-2. Charpy V-notch energy transition curve.

In 1961, the American Society for Testing and Materials (ASTM) published a document, designated as ASTM E185-61T and entitled “Standard Practice for Design of Surveillance Programs for Light-Water Moderated Nuclear Power Reactor Vessels” [ASTM E185]. That standard recommended that capsules of surveillance specimens should be bolted to the inner diameter (ID) of an operating reactor. These capsules were to be removed from the reactor at certain times during the reactor’s operating lifetime. The specimens within the capsules, which included samples of the materials used in the RPV beltline that were thought to be most susceptible to radiation damage, were then tested to quantify the effects of radiation on the properties of steels from which the vessel was constructed. The limited size of the water gap between the core and the vessel ID made the CVN specimen ideal for use in such surveillance programs.

By 1972, sufficient testing had been performed using both CVN and K_{Ic} specimens for the American Society of Mechanical Engineers (ASME) to recommend the use of a CVE transition temperature, along with a transition temperature defined by testing a "nil-ductility temperature" (NDT) specimen (see Figure 3-4 and Figure 3-5) [ASTM E208], to locate the K_{Ic} curve on the temperature axis for nuclear-grade ferritic steels and weldments [WRC 175]. The formula for the curve in Figure 3.3 is as follows:

Eq. 3-1 $$K_{Ic} = 33.2 + 2.806 \cdot \exp\left[0.02 \cdot \left(T - RT_{NDT} + 100\right)\right]$$

where

RT_{NDT} is defined in accordance with ASME NB2331, as $RT_{NDT} = MAX\left\{T_{NDT}, T_{35/50} - 60\right\}$.

T_{NDT} is the NDT determined by testing specimens in accordance with ASTM E208.

$T_{35/50}$ is the transition temperature at which CVN specimens tested in accordance with ASTM E23 exhibit lateral expansion of at least 0.035-in. (0.89-mm) and absorbed energy of at least 50 ft-lbs (68J).

In Eq. 3-1, RT_{NDT} serves as an "index temperature" (i.e., a single value that characterizes the combined effects of alloying heat treatment, radiation, etc. on fracture toughness).‡

Since the 1970s, numerous investigators have studied the relationship between CVN and cleavage fracture toughness transition temperatures. (cleavage fracture toughness is now quantified using K_{Jc} and the Master Curve index temperature T_o, as described in [ASTM E1921]). As illustrated in Figure 3-6, which is but one of many possible example results, these investigations invariably reveal that simple linear relationships exist between CVN and fracture toughness transition temperatures. These relationships link the fracture toughness data needed to perform a structural integrity assessment (see Figure 3.3) to the "trend curves" that relate CVN transition temperatures to composition and exposure variables. Chapter 4 of this report describes trend curves in further detail.

‡ While RT_{NDT} is an index temperature that has customarily been used along with the ASME K_{Ic} curve, RT_{NDT} is ***not*** a *fracture toughness* index temperature. As specified by ASME NB-2331 (and as represented in Eq. 3-1), RT_{NDT} is defined based on non-fracture toughness tests that can only be correlated with fracture toughness.

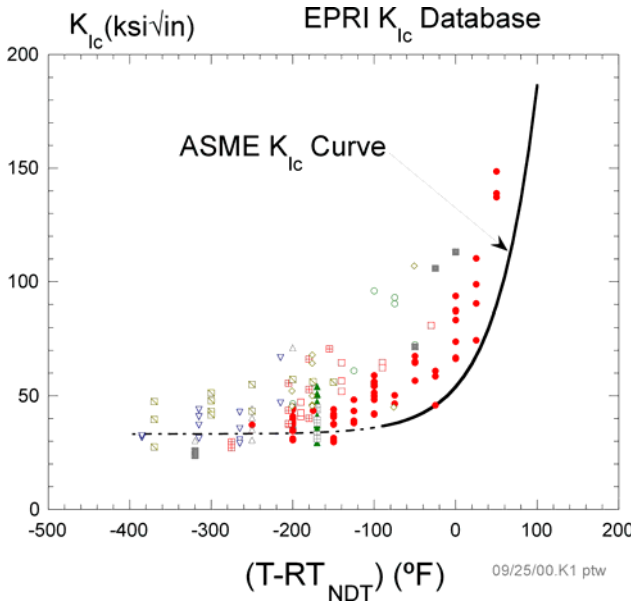

Figure 3.3. The empirical data used to establish the ASME K_{Ic} curve [Williams 04].

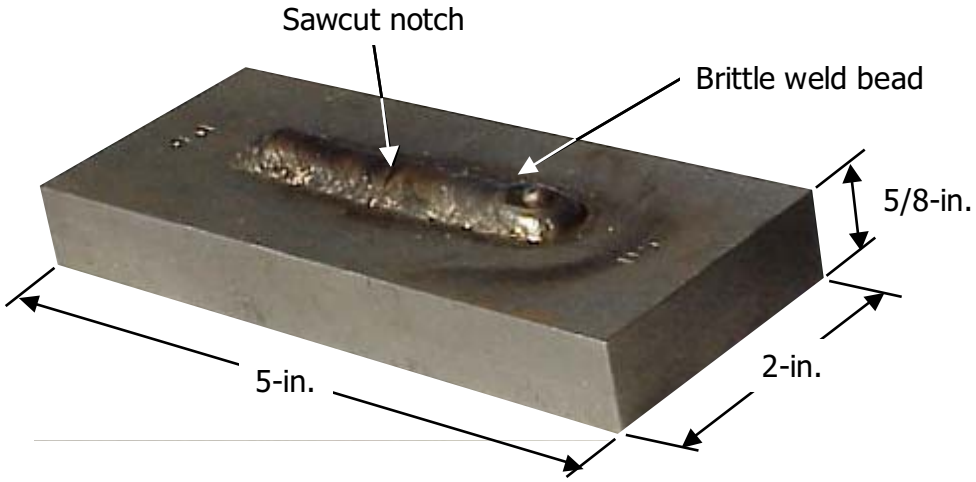

Figure 3-4. Nil-ductility temperature test specimen.

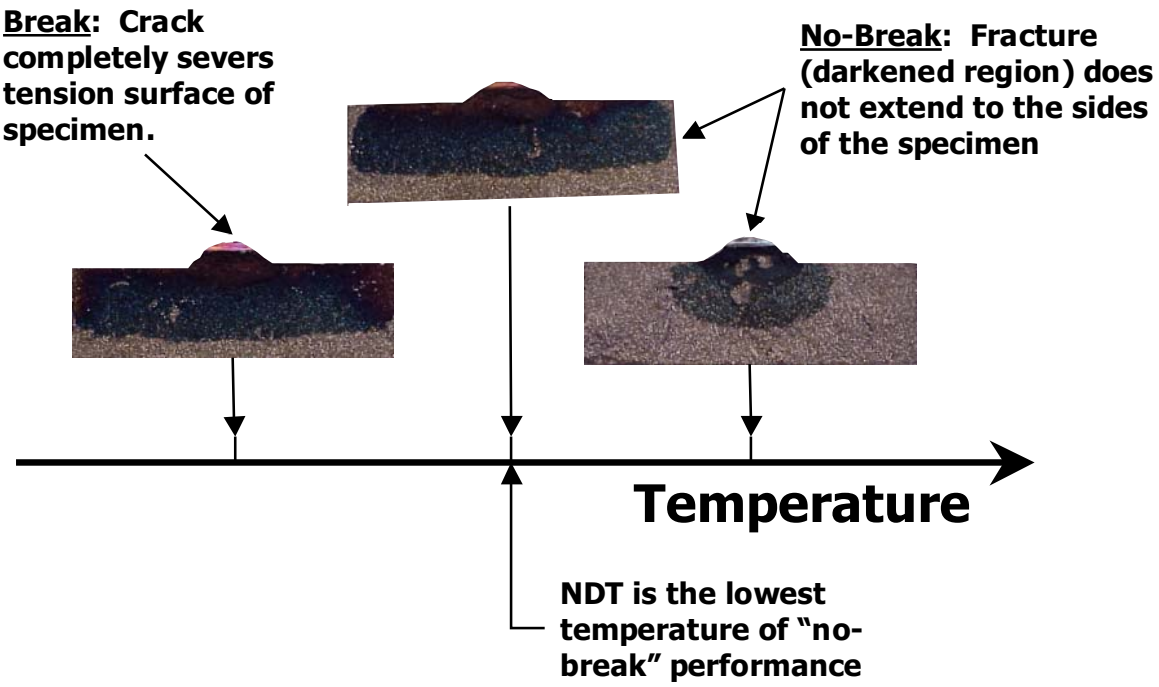

Figure 3-5. Definition of the NDT temperature.

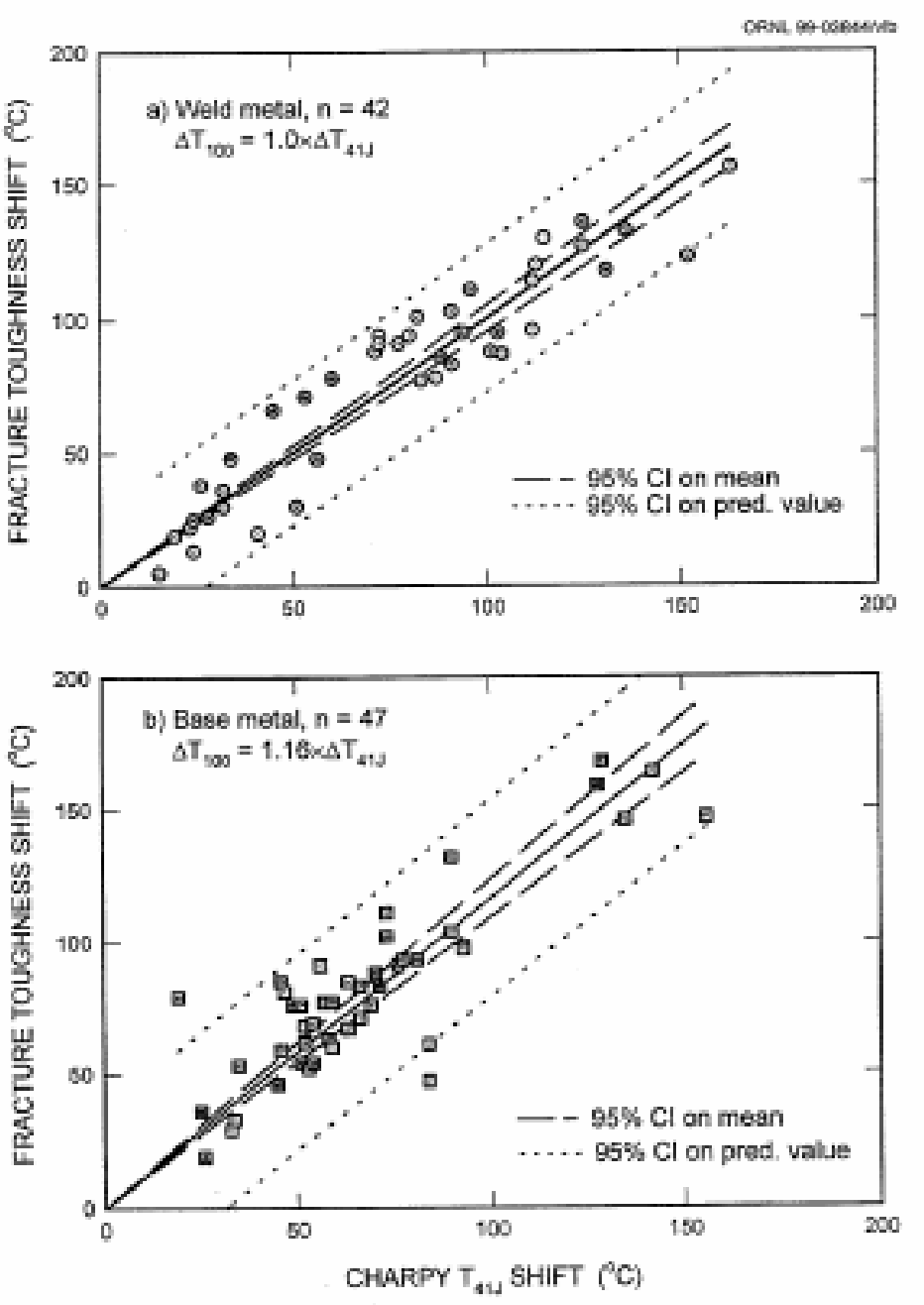

Figure 3-6. Examples of correlations between the shift in the fracture toughness transition temperature T_o as a result of radiation damage (vertical axis) and the shift in the CVE transition temperature at 41J absorbed energy (T_{41J}) attributable to radiation damage (horizontal axis) [Sokolov 00].

4 PREDICTION OF TRANSITION TEMPERATURE SHIFT (ΔT_{30})

This chapter concerns development an embrittlement trend curve (i.e., a relationship between ΔT_{30} and various composition, exposure, and categorical variables) that the NRC proposes for use in Revision 3 of Regulatory Guide 1.99. While similar in overall mathematical form, the trend curve developed in this chapter differs in some specific details from that developed in Appendix A to this report. These differences are attributable to differences in objective. The objective of the effort described Appendix A was to develop a trend curve that best fit the available surveillance database with the minimum possible error. In doing so, the investigators ensured that certain subsets of data were fit well by the ETC model. Conversely, the objective of the effort described in this chapter was to fit the overall database using as simple a model as possible. Consequently, there was less focus here (compared to the Appendix A effort) on fitting specific data subsets. Another consideration in developing the fit in this chapter was simplicity of regulatory implementation.

We begin in Section 4.1 with a review of the irradiation damage mechanisms that are expected in RPV steels. This review motivates the development of a fitting function, which is used in Section 4.2 along with the US-LWR surveillance database to develop candidate ETCs. These candidate trend curves are compared with other data (not contained in the US-LWR surveillance database) in Section 4.3. These comparisons motivate the selection of the recommended model, development of a model applicable at high fluences (see Section 4.4), and the restrictions placed on the use of these models, which are discussed in Section 4.5.

4.1 Expected Irradiation Damage Mechanisms

This section does not provide a comprehensive review of irradiation damage mechanisms; that topic is covered extensively by other authors (see, for example, Chapter 2 of Appendix A to this report, as well as [Chaouadi 01 and Chaouadi 05a]). Instead, the goal of this section is to summarize the physical and empirical evidence that has motivated our selection of a functional form to use in fitting the US-LWR surveillance database. Toward that end, this section is organized as follows:

- Section 4.1.1 summarizes the trends that may be expected to occur as a result of matrix damage (MD) and/or occur predominantly in steels having a low copper content.
- Section 4.1.2 summarizes the trends that may be expected to occur as a result of precipitation hardening (predominantly of copper or of second phases rich in copper) in steels having a higher copper content.
- Section 4.1.3 discusses the effects of initial properties on the ETC, and summarizes candidate rules for superposition of the separate hardening effects of matrix damage and copper-rich precipitation.
- Section 4.1.4 amalgamates the insights of the three preceding sections into a candidate fitting function for the US-LWR surveillance database.
- Section 4.1.5 discusses the implications of finding (or not finding) these physically anticipated trends in the empirical information contained within the US-LWR surveillance database.

This investigation does not address the non-hardening embrittlement, also referred to as "grain-boundary embrittlement," that is expected and commonly observed in the high-impurity-content steels used to construct the early VVER reactors [IAEA 1442]. The greater cleanliness associated with western RPV alloys such as ASTM Grades A302B, A302B Modified, A533B, A508 (with phosphorous of generally less than 0.02 wt-%, with a specified maximum of 0.025 wt-%) makes grain-boundary embrittlement unexpected, and indeed unobserved, for U.S. RPV steels.

In addition to drawing insights from the published literature, this section makes use of the IVAR database (see Appendix B) in motivating the functional form of (and terms selected in) the candidate fitting function. To facilitate the use of the IVAR data, each alloy and exposure condition in the IVAR database was fit using the following function, the form of which was motivated by the work of Debarberis et al. [Debarberis 05a]:

Eq. 4-1 $$\Delta\sigma_{ys} = A \cdot \sqrt{\Phi} + B\left[1 - \exp\left(-\Phi / \Phi_{SAT}\right)\right]$$

where

$\Delta\sigma_{ys}$ is the measured increase in yield strength attributable to irradiation (in MPa),
Φ is the neutron fluence greater than 1 MeV (in n/cm^2),
A is a fit coefficient quantifying the hardening caused by matrix damage (in $MPa/\sqrt{n/cm^2}$),
B is a fit coefficient quantifying the maximum possible hardening attributable to precipitation of copper and copper-alloyed second phases (in MPa), and
Φ_{SAT} is a fit coefficient quantifying the fluence at which 66% of the precipitation hardening has occurred (in n/cm^2).

This function was only fit to irradiations performed at 290 °C. While the IVAR study included exposures at both higher and lower temperatures, not enough observations were made at temperatures other than 290 °C to support the fitting of this equation. Least-squares fitting was performed using the *solver* function in Microsoft (MS) Excel®, and each fit was visually checked for reasonableness. Table 4.1 summarizes the values of the A, B, and Φ_{SAT} coefficients for the various alloys in the IVAR database.

4.1.1 Matrix Damage (Low-Copper) Mechanisms

Matrix hardening occurs when the defect clusters that are produced by neutron collisions act as barriers to dislocation motion. In addition to these nano-voids (or vacancy clusters), micro-features that include solute atoms have also been associated with matrix damage. Solutes can act either together with vacancies as dislocation barriers, or alone as second-phase "complexes" or "atmospheres" that remain after the vacancies have fully dissolved.

4.1.1.1 Fluence

[Seeger 58] demonstrated that, for the fluence range of interest in LWRs, the amount of hardening, as measured by the increase in yield strength varies (primarily) in proportion with the square-root of the number density of the obstacles to dislocation motion. Because fluence is a measure of the number of high-energy neutrons that pass through a unit area of material, it follows from Seeger's finding that matrix hardening should increase in proportion with the square-root of the neutron fluence. This theoretical expectation has been confirmed by experimental studies

[Chaouadi 05a]; indeed it forms the basis for our fitting of the IVAR database (see Section 4.1). Section 4.2.3 evaluates Seeger's prediction relative to the US-LWR database.

Despite its theoretical foundation and empirical success in predicting LWR irradiation, the Seeger $\sqrt{\Phi}$ model cannot be considered complete because it predicts that RPV steel could be hardened without bound, which is certainly not the case. Thus, the effect of MD should saturate above some fluence value. Indeed, data presented by Chaouadi (see Figure 4-1) demonstrate that MD will saturate, but only at fluences far above those that can be achieved in current and advanced LWRs [Chaouadi 05a]. This information demonstrates the adequacy of the Seeger $\sqrt{\Phi}$ model in representing fluence effects on MD for LWR conditions.

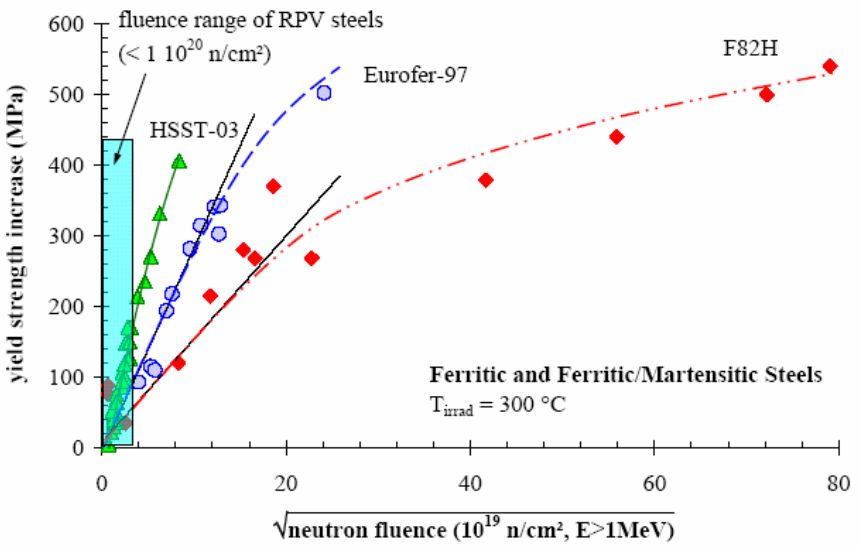

Figure 29. Radiation damage saturation at elevated neutron fluence levels.

Figure 4-1. Data showing that matrix damage does saturate, but at fluences far above those that can be encountered in LWR service [Chaouadi 05a].

4.1.1.2 Temperature

Temperature is expected to influence the amount of damage that irradiation imparts to a material. As temperature increases, the defects caused by irradiation can move more easily, thereby decreasing their hardening capacity because they are more prone to being annealed away. The effects of temperature on irradiation damage have long been recognized. Indeed, Revision 2 of Regulatory Guide 1.99 states that the capsule temperature must be close to the beltline temperature (within 25 °F, or 14 °C) because the ETC described in the guide does not explicitly account for temperature effects. Recent work by Chaouadi and by Debarberis provides an evaluation of temperature effects on MD over a wide range of temperatures (see Figure 4-2) [Chaouadi 05a, Debarberis 05b]. As noted by Chaouadi, both theoretical considerations and the available data indicate that the effect of temperature on radiation damage is non-linear. Nonetheless, over the limited range of temperatures typically encountered in U.S. LWR operation (usually 274–296 °C, or 525–565 °F), the effect of temperature can be well approximate using a linear function.

Table 4.1. Fits of Eq. 4-1 to the IVAR database.

Alloy ID	Chemical Composition [wt-%]					Flux Cat.*	# of $\Delta\sigma_{ys}$ Values	A [MPa/(n/cm^2)$^{0.5}$]	B [MPa]	Φ_{SAT} [n/cm^2]	MSE** [MPa]	Fit Notes
	Cu	Ni	Mn	P	Si							
CM1	0.01	0.01	1.67	0.003	0.15	H	#N/A	#N/A	#N/A	#N/A	#N/A	No shift apparent, just noise around no shift
CM1	0.01	0.01	1.67	0.003	0.15	M	#N/A	#N/A	#N/A	#N/A	#N/A	No shift apparent, just noise around no shift
CM1	0.01	0.01	1.67	0.003	0.15	L	#N/A	#N/A	#N/A	#N/A	#N/A	No shift apparent, just noise around no shift
CM2	0.01	0.01	1.65	0.041	0.16	H	5	1.31E-08	#N/A	#N/A	13.6	
CM2	0.01	0.01	1.65	0.041	0.16	M	4	1.50E-08	#N/A	#N/A	5.6	
CM2	0.01	0.01	1.65	0.041	0.16	L	3	1.81E-08	#N/A	#N/A	2.0	
CM3	0.02	0.85	1.6	0.006	0.16	H	8	5.72E-09	#N/A	#N/A	7.4	
CM3	0.02	0.85	1.6	0.006	0.16	M	6	6.54E-09	#N/A	#N/A	6.7	
CM3	0.02	0.85	1.6	0.006	0.16	L	4	9.47E-09	#N/A	#N/A	4.7	
CM4	0.02	0.86	1.53	0.031	0.16	H	5	1.29E-08	#N/A	#N/A	7.3	
CM4	0.02	0.86	1.53	0.031	0.16	M	4	1.68E-08	#N/A	#N/A	2.0	
CM4	0.02	0.86	1.53	0.031	0.16	L	3	1.81E-08	#N/A	#N/A	5.8	
CM5	0.02	0.86	1.61	0.05	0.16	H	5	1.34E-08	#N/A	#N/A	13.8	
CM5	0.02	0.86	1.61	0.05	0.16	M	4	2.32E-08	#N/A	#N/A	9.8	
CM5	0.02	0.86	1.61	0.05	0.16	L	3	2.32E-08	#N/A	#N/A	8.6	
CM6	0.02	1.68	1.5	0.007	0.17	H	5	9.76E-09	#N/A	#N/A	10.6	negative shifts at low fluence
CM6	0.02	1.68	1.5	0.007	0.17	M	4	1.30E-08	#N/A	#N/A	8.9	
CM6	0.02	1.68	1.5	0.007	0.17	L	3	1.58E-08	#N/A	#N/A	6.2	
CM7	0	1.7	1.55	0.047	0.17	H	5	1.50E-08	#N/A	#N/A	9.4	
CM7	0	1.7	1.55	0.047	0.17	M	4	1.62E-08	#N/A	#N/A	6.3	
CM7	0	1.7	1.55	0.047	0.17	L	3	2.44E-08	#N/A	#N/A	3.3	
CM8	0.01	0.86	0.01	0.004	0.14	H	#N/A	#N/A	#N/A	#N/A	#N/A	too much negative data, can't fit
CM8	0.01	0.86	0.01	0.004	0.14	M	4	4.13E-09	#N/A	#N/A	9.9	questionable fit
CM8	0.01	0.86	0.01	0.004	0.14	L	3	3.96E-09	#N/A	#N/A	1.2	
CM9	0.01	0.86	0.85	0.003	0.15	H	#N/A	#N/A	#N/A	#N/A	#N/A	too much negative data, can't fit
CM9	0.01	0.86	0.85	0.003	0.15	M	4	4.99E-09	#N/A	#N/A	4.2	negative shifts at low fluence
CM9	0.01	0.86	0.85	0.003	0.15	L	#N/A	#N/A	#N/A	#N/A	#N/A	too much negative data, can't fit
CM10	0.02	0.88	1.66	0.008	0.17	H	9	5.23E-09	#N/A	#N/A	7.0	
CM10	0.02	0.88	1.66	0.008	0.17	M	7	8.74E-09	#N/A	#N/A	5.6	
CM10	0.02	0.88	1.66	0.008	0.17	L	5	9.09E-09	#N/A	#N/A	2.8	
CM11	0.34	0.85	1.64	0.006	0.18	H	9	1.94E-08	102.03	9.35E+17	7.1	

Alloy ID	Chemical Composition [wt-%]					Flux Cat.*	# of $\Delta\sigma_{ys}$ Values	A [MPa/(n/cm^2)$^{0.5}$]	B [MPa]	Φ_{SAT} [n/cm^2]	MSE** [MPa]	Fit Notes
	Cu	Ni	Mn	P	Si							
CM11	0.34	0.85	1.64	0.006	0.18	M	7	1.31E-08	146.90	9.39E+17	2.7	
CM11	0.34	0.85	1.64	0.006	0.18	L	6	0.00E+00	170.05	7.08E+17	5.9	
CM12	0.86	0.84	1.65	0.006	0.17	H	6	4.24E-09	126.68	1.40E+18	5.3	
CM12	0.86	0.84	1.65	0.006	0.17	M	4	1.57E-08	104.66	7.84E+17	0.1	
CM12	0.86	0.84	1.65	0.006	0.17	L	3	0.00E+00	141.08	7.27E+17	3.7	
CM13	0.11	0.83	1.61	0.004	0.16	H	7	1.82E-10	68.66	4.45E+18	6.8	
CM13	0.11	0.83	1.61	0.004	0.16	M	6	1.96E-08	45.45	9.38E+18	5.9	
CM13	0.11	0.83	1.61	0.004	0.16	L	4	1.97E-08	60.80	8.28E+18	2.2	
CM14	0.11	0.83	1.62	0.04	0.17	H	5	0.00E+00	96.70	7.01E+18	9.4	
CM14	0.11	0.83	1.62	0.04	0.17	M	4	2.34E-08	12.94	2.67E+18	2.8	
CM14	0.11	0.83	1.62	0.04	0.17	L	3	0.00E+00	85.98	3.77E+18	3.5	
CM15	0.22	0.02	1.59	0.002	0.15	H	9	5.87E-10	44.91	8.12E+17	6.9	
CM15	0.22	0.02	1.59	0.002	0.15	M	7	0.00E+00	43.12	5.15E+17	6.7	
CM15	0.22	0.02	1.59	0.002	0.15	L	5	0.00E+00	40.12	2.63E+17	8.0	
CM16	0.22	0.82	1.58	0.004	0.25	H	10	4.80E-09	123.37	2.62E+18	3.6	
CM16	0.22	0.82	1.58	0.004	0.25	M	7	8.58E-09	142.78	1.82E+18	4.0	
CM16	0.22	0.82	1.58	0.004	0.25	L	5	0.00E+00	177.52	1.80E+18	7.3	
CM17	0.22	1.59	1.54	0.004	0.25	H	9	1.11E-08	209.93	3.69E+18	11.4	
CM17	0.22	1.59	1.54	0.004	0.25	M	7	2.29E-08	216.25	2.68E+18	4.0	
CM17	0.22	1.59	1.54	0.004	0.25	L	5	0.00E+00	270.58	1.68E+18	4.1	
CM18	0.43	0.02	1.7	0.002	0.15	H	10	3.94E-09	59.17	3.77E+17	6.5	
CM18	0.43	0.02	1.7	0.002	0.15	M	7	2.42E-09	62.47	2.69E+17	3.0	
CM18	0.43	0.02	1.7	0.002	0.15	L	5	0.00E+00	62.92	2.41E+17	4.5	
CM19	0.42	0.85	1.63	0.005	0.16	H	10	1.10E-08	127.72	8.70E+17	2.9	
CM19	0.42	0.85	1.63	0.005	0.16	M	7	1.49E-08	140.44	7.16E+17	3.1	
CM19	0.42	0.85	1.63	0.005	0.16	L	5	1.72E-08	143.54	5.62E+17	2.1	
CM20	0.43	1.69	1.63	0.006	0.16	H	10	2.63E-08	179.54	1.11E+18	4.5	
CM20	0.43	1.69	1.63	0.006	0.16	M	7	2.56E-08	217.31	1.02E+18	11.7	
CM20	0.43	1.69	1.63	0.006	0.16	L	5	4.60E-08	200.85	7.97E+17	7.5	
CM21	0.42	0.84	0.01	0.002	0.14	H	9	3.16E-09	90.88	5.87E+17	6.4	
CM21	0.42	0.84	0.01	0.002	0.14	M	7	3.20E-09	103.04	5.81E+17	5.1	
CM21	0.42	0.84	0.01	0.002	0.14	L	5	2.10E-08	68.28	3.19E+17	5.7	

Alloy ID	Chemical Composition [wt-%]					Flux Cat.*	# of $\Delta\sigma_{ys}$ Values	A [MPa/(n/cm^2)$^{0.5}$]	B [MPa]	Φ_{SAT} [n/cm^2]	MSE** [MPa]	Fit Notes
	Cu	Ni	Mn	P	Si							
CM22	0.42	0.84	0.84	0.002	0.14	H	9	7.76E-09	120.10	9.83E+17	7.4	
CM22	0.42	0.84	0.84	0.002	0.14	M	7	1.29E-08	119.38	8.33E+17	4.2	
CM22	0.42	0.84	0.84	0.002	0.14	L	5	6.32E-09	141.94	7.11E+17	4.1	
CM23	0.01	0.83	1.62	0.002	0.15	H	5	4.29E-09	#N/A	#N/A	5.1	
CM23	0.01	0.83	1.62	0.002	0.15	M	4	2.28E-09	#N/A	#N/A	4.4	
CM23	0.01	0.83	1.62	0.002	0.15	L	3	8.27E-09	#N/A	#N/A	8.6	negative shifts at low fluence
CM24	0.02	0.87	1.65	0.006	0.15	H	5	2.14E-09	#N/A	#N/A	5.7	negative shifts at low fluence
CM24	0.02	0.87	1.65	0.006	0.15	M	4	4.25E-09	#N/A	#N/A	6.9	negative shifts at low fluence
CM24	0.02	0.87	1.65	0.006	0.15	L	3	1.88E-09	#N/A	#N/A	4.1	scattered data, some negative
CM25	0.01	0.87	1.53	0.003	0.17	H	5	5.34E-09	#N/A	#N/A	7.3	
CM25	0.01	0.87	1.53	0.003	0.17	M	4	7.53E-09	#N/A	#N/A	6.2	
CM25	0.01	0.87	1.53	0.003	0.17	L	3	9.78E-09	#N/A	#N/A	3.5	
CM26	0.01	0.87	1.66	0.006	0.17	H	5	6.18E-09	#N/A	#N/A	2.0	
CM26	0.01	0.87	1.66	0.006	0.17	M	4	3.72E-09	#N/A	#N/A	3.1	
CM26	0.01	0.87	1.66	0.006	0.17	L	#N/A	#N/A	#N/A	#N/A	#N/A	No shift apparent, just noise around 0 shift
CM27	0.01	0.84	1.6	0.002	0.16	H	5	3.40E-09	#N/A	#N/A	10.3	negative shifts at low fluence
CM27	0.01	0.84	1.6	0.002	0.16	M	4	5.86E-09	#N/A	#N/A	7.0	
CM27	0.01	0.84	1.6	0.002	0.16	L	3	5.72E-09	#N/A	#N/A	5.3	
CM28	0.42	0.84	1.6	0.002	0.17	H	5	4.22E-09	162.10	1.53E+18	8.1	
CM28	0.42	0.84	1.6	0.002	0.17	M	4	9.35E-09	166.17	9.68E+17	1.2	
CM28	0.42	0.84	1.6	0.002	0.17	L	3	4.05E-08	87.96	3.07E+17	0.0	
CM29	0.21	0.02	1.68	0.002	0.14	H	5	2.74E-09	66.12	4.76E+17	4.3	
CM29	0.21	0.02	1.68	0.002	0.14	M	4	5.21E-09	60.97	5.17E+17	1.7	
CM29	0.21	0.02	1.68	0.002	0.14	L	3	5.89E-09	52.21	3.04E+17	0.0	
CM30	0.22	0.85	1.64	0.006	0.16	H	5	1.64E-08	75.20	1.88E+18	2.5	
CM30	0.22	0.85	1.64	0.006	0.16	M	4	1.11E-08	120.49	1.62E+18	2.1	
CM30	0.22	0.85	1.64	0.006	0.16	L	3	1.52E-08	113.77	1.12E+18	0.0	
CM31	0.01	0.86	1.65	0.006	0.17	H	5	4.98E-09	#N/A	#N/A	3.6	
CM31	0.01	0.86	1.65	0.006	0.17	M	4	6.01E-09	#N/A	#N/A	1.8	
CM31	0.01	0.86	1.65	0.006	0.17	L	3	9.75E-09	#N/A	#N/A	2.1	
LA	0.4	0	1.37	0.005	0.22	H	8	5.24E-09	63.94	4.84E+17	5.6	

Alloy ID	Chemical Composition [wt-%]					Flux Cat.*	# of $\Delta\sigma_{ys}$ Values	A [MPa/(n/cm^2)$^{0.5}$]	B [MPa]	Φ_{SAT} [n/cm^2]	MSE** [MPa]	Fit Notes
	Cu	Ni	Mn	P	Si							
LA	0.4	0	1.37	0.005	0.22	M	6	8.40E-09	56.52	1.00E+10	3.5	Sat fluence off - maybe bad YS(u) value? High sat flu looks OK
LA	0.4	0	1.37	0.005	0.22	L	7	1.93E-08	38.08	1.00E+10	10.5	Sat fluence off - maybe bad YS(u) value? High sat flu looks OK
LB	0.4	0.18	1.35	0.005	0.22	H	7	2.55E-09	83.36	3.67E+17	5.8	
LB	0.4	0.18	1.35	0.005	0.22	M	6	0.00E+00	90.55	4.37E+17	3.0	
LB	0.4	0.18	1.35	0.005	0.22	L	4	8.60E-09	65.68	1.00E+10	6.0	Sat fluence off - maybe bad YS(u) value? High sat flu looks OK
LC	0.41	0.86	1.44	0.005	0.23	H	8	1.16E-08	125.97	9.97E+17	6.2	
LC	0.41	0.86	1.44	0.005	0.23	M	7	1.61E-08	136.33	8.01E+17	2.5	
LC	0.41	0.86	1.44	0.005	0.23	L	9	4.59E-08	89.41	4.10E+17	5.5	
LD	0.38	1.25	1.38	0.005	0.23	H	9	1.98E-08	135.50	1.44E+18	10.0	
LD	0.38	1.25	1.38	0.005	0.23	M	7	2.65E-08	149.45	1.13E+18	3.7	
LD	0.38	1.25	1.38	0.005	0.23	L	8	6.53E-08	89.59	5.92E+17	6.6	
LG	0	0.74	1.37	0.005	0.22	H	8	1.07E-08	#N/A	#N/A	10.1	
LG	0	0.74	1.37	0.005	0.22	M	6	1.41E-08	#N/A	#N/A	12.0	
LG	0	0.74	1.37	0.005	0.22	L	4	2.07E-08	#N/A	#N/A	7.4	
LH	0.11	0.74	1.39	0.005	0.24	H	8	1.10E-08	12.51	5.31E+17	6.0	
LH	0.11	0.74	1.39	0.005	0.24	M	6	1.62E-08	11.10	3.60E+17	1.3	
LH	0.11	0.74	1.39	0.005	0.24	L	4	2.41E-08	0.00	2.29E+18	3.5	No CRP?
LI	0.2	0.74	1.37	0.005	0.24	H	8	1.07E-08	79.09	1.61E+18	5.7	
LI	0.2	0.74	1.37	0.005	0.24	M	6	1.34E-08	86.15	9.81E+17	4.8	
LI	0.2	0.74	1.37	0.005	0.24	L	4	4.03E-08	44.50	6.28E+17	0.0	
LJ	0.42	0.81	1.34	0.005	0.13	H	8	6.84E-09	123.87	1.03E+18	5.9	
LJ	0.42	0.81	1.34	0.005	0.13	M	6	7.75E-09	137.41	8.80E+17	1.2	
LJ	0.42	0.81	1.34	0.005	0.13	L	4	2.29E-08	106.05	5.53E+17	1.4	
LK	0.8	0.81	1.13	0.005	0.13	H	8	5.71E-09	99.47	9.05E+17	6.2	
LK	0.8	0.81	1.13	0.005	0.13	M	6	3.82E-09	117.40	7.78E+17	5.7	
LK	0.8	0.81	1.13	0.005	0.13	L	4	1.99E-08	84.30	5.82E+17	6.4	
LO	0.41	0.86	1.44	0.005	0.23	H	8	5.91E-09	185.13	1.89E+18	9.8	
LO	0.41	0.86	1.44	0.005	0.23	M	6	1.69E-08	147.12	1.26E+18	3.0	
LO	0.41	0.86	1.44	0.005	0.23	L	4	2.25E-08	146.92	9.47E+17	3.1	

Alloy ID	Chemical Composition [wt-%]					Flux Cat.*	# of $\Delta\sigma_{ys}$ Values	A [MPa/(n/cm^2)$^{0.5}$]	B [MPa]	Φ_{SAT} [n/cm^2]	MSE** [MPa]	Fit Notes
	Cu	Ni	Mn	P	Si							
BW-A	0.21	0.63	1.69	0.014	0.45	H	5	6.87E-09	88.87	1.69E+18	0.9	
BW-A	0.21	0.63	1.69	0.014	0.45	M	4	1.02E-08	85.82	1.43E+18	2.2	
BW-A	0.21	0.63	1.69	0.014	0.45	L	3	0.00E+00	100.59	7.40E+17	0.4	No MD?
BW-B	0.28	0.69	1.63	0.018	0.54	H	#N/A	#N/A	#N/A	#N/A	#N/A	Not enough data to fit
BW-B	0.28	0.69	1.63	0.018	0.54	M	#N/A	#N/A	#N/A	#N/A	#N/A	Not enough data to fit
BW-B	0.28	0.69	1.63	0.018	0.54	L	#N/A	#N/A	#N/A	#N/A	#N/A	Not enough data to fit
BW-C	0.06	0.62	1.3	0.009	0.37	H	#N/A	#N/A	#N/A	#N/A	#N/A	Not enough data to fit
BW-C	0.06	0.62	1.3	0.009	0.37	M	#N/A	#N/A	#N/A	#N/A	#N/A	Not enough data to fit
BW-C	0.06	0.62	1.3	0.009	0.37	L	#N/A	#N/A	#N/A	#N/A	#N/A	Not enough data to fit
62W	0.23	0.6	1.61	0.02	0.59	H	7	1.36E-08	65.37	8.75E+17	9.0	
62W	0.23	0.6	1.61	0.02	0.59	M	7	2.10E-08	49.07	4.61E+17	4.0	
62W	0.23	0.6	1.61	0.02	0.59	L	5	0.00E+00	111.26	9.27E+17	5.8	No MD?
63W	0.3	0.69	1.65	0.016	0.63	H	7	1.88E-08	91.41	8.67E+17	4.2	
63W	0.3	0.69	1.65	0.016	0.63	M	7	2.60E-08	86.08	7.89E+17	5.9	
63W	0.3	0.69	1.65	0.016	0.63	L	5	1.41E-08	125.06	7.12E+17	4.9	
65W	0.22	0.6	1.45	0.015	0.48	H	7	1.45E-08	58.51	1.01E+18	3.5	
65W	0.22	0.6	1.45	0.015	0.48	M	7	2.03E-08	53.78	6.64E+17	5.1	
65W	0.22	0.6	1.45	0.015	0.48	L	5	1.38E-08	71.18	6.15E+17	4.9	
67W	0.27	0.69	1.44	0.011	0.5	H	7	1.26E-08	43.52	7.31E+17	7.0	
67W	0.27	0.69	1.44	0.011	0.5	M	7	1.81E-08	35.63	3.10E+17	7.3	
67W	0.27	0.69	1.44	0.011	0.5	L	5	2.37E-08	31.00	4.51E+17	2.5	
73W	0.31	0.6	1.56	0.005	0.45	H	8	9.96E-09	111.54	1.13E+18	5.5	
73W	0.31	0.6	1.56	0.005	0.45	M	7	1.34E-08	117.04	8.23E+17	6.9	
73W	0.31	0.6	1.56	0.005	0.45	L	5	0.00E+00	141.01	6.06E+17	7.8	
Midland	0.27	0.57	1.61	0.017	0.62	H	5	1.59E-08	77.43	1.37E+18	3.8	
Midland	0.27	0.57	1.61	0.017	0.62	M	4	2.41E-08	65.45	1.05E+18	4.5	
Midland	0.27	0.57	1.61	0.017	0.62	L	3	4.55E-08	36.21	8.23E+17	0.0	
HSST02	0.14	0.67	1.55	0.009	0.2	H	7	1.30E-08	68.23	9.23E+17	5.6	
HSST02	0.14	0.67	1.55	0.009	0.2	M	7	2.68E-08	37.21	1.00E+07	9.2	Sat fluence off - maybe bad YS(u) value?
HSST02	0.14	0.67	1.55	0.009	0.2	L	5	3.26E-08	45.29	2.74E+17	2.1	
A302B	0.14	0.2	1.2	0.015	0.28	H	7	7.50E-09	8.49	1.17E+18	4.7	
A302B	0.14	0.2	1.2	0.015	0.28	M	#N/A	#N/A	#N/A	#N/A	#N/A	Data too scattered to fit

Alloy ID	Chemical Composition [wt-%]					Flux Cat.*	# of $\Delta\sigma_{ys}$ Values	A [MPa/(n/cm^2)$^{0.5}$]	B [MPa]	Φ_{SAT} [n/cm^2]	MSE** [MPa]	Fit Notes
	Cu	Ni	Mn	P	Si							
A302B	0.14	0.2	1.2	0.015	0.28	L	#N/A	#N/A	#N/A	#N/A	#N/A	Data too scattered to fit
JRQ	0.14	0.82	1.4	0.019	0.25	H	6	2.07E-08	8.37	1.00E+07	4.7	Sat fluence off - maybe bad YS(u) value?
JRQ	0.14	0.82	1.4	0.019	0.25	M	5	1.82E-08	41.50	2.96E+18	2.5	
JRQ	0.14	0.82	1.4	0.019	0.25	L	5	0.00E+00	57.10	8.52E+17	3.6	No MD?
RR-WP	0.04	1.65	1.43	0.011	0.5	H	4	1.78E-08	#N/A	#N/A	6.4	
RR-WP	0.04	1.65	1.43	0.011	0.5	M	4	1.91E-08	#N/A	#N/A	5.1	
RR-WP	0.04	1.65	1.43	0.011	0.5	L	3	2.62E-08	#N/A	#N/A	4.0	
RR-WG	0.24	1.71	1.21	0.008	0.6	H	6	3.52E-08	67.77	1.62E+18	4.6	
RR-WG	0.24	1.71	1.21	0.008	0.6	M	5	4.95E-08	50.34	1.12E+18	5.5	
RR-WG	0.24	1.71	1.21	0.008	0.6	L	4	4.97E-08	95.32	1.13E+18	3.2	
RR-WV	0.56	1.66	1.36	0.01	0.38	H	3	4.35E-08	173.58	9.66E+17	0.0	
RR-WV	0.56	1.66	1.36	0.01	0.38	M	3	3.65E-08	219.51	7.62E+17	0.0	
RR-WV	0.56	1.66	1.36	0.01	0.38	L	#N/A	#N/A	#N/A	#N/A	#N/A	Not enough data to fit
EPRI-C	0.4	0.6	1.36	0.006	0.51	H	7	7.06E-09	109.90	7.24E+17	5.4	
EPRI-C	0.4	0.6	1.36	0.006	0.51	M	7	6.78E-09	121.47	5.44E+17	2.8	
EPRI-C	0.4	0.6	1.36	0.006	0.51	L	5	0.00E+00	145.87	5.27E+17	3.9	No MD?
OV1	<0.02	<0.02	1.6	<0.002	<0.02	H	#N/A	#N/A	#N/A	#N/A	#N/A	Not enough data to fit
OV12	<0.02	<0.02	<0.02	<0.002	<0.02	H	#N/A	#N/A	#N/A	#N/A	#N/A	Not enough data to fit
OV9	<0.02	<0.02	<0.02	0.025	<0.02	H	#N/A	#N/A	#N/A	#N/A	#N/A	Not enough data to fit
OV10	<0.02	<0.02	1.6	0.025	<0.02	H	#N/A	#N/A	#N/A	#N/A	#N/A	Not enough data to fit
Palisades	0.2	1.2	1.3	0.01	0.18	H	6	1.43E-08	92.96	1.52E+18	6.9	
A508	0.06	0.8	1.3	0.005	0.02	H	6	5.21E-09	29.82	7.70E+17	2.4	
A508	0.06	0.8	1.3	0.005	0.02	M	5	2.92E-09	28.94	3.35E+17	4.2	
A508	0.06	0.8	1.3	0.005	0.02	L	4	0	37.08	3.11E+17	8.6	Data scattered, fit questionable.

Notes:
* - H = 9x10^{11} n/cm^2/s, M = 3x10^{11} n/cm^2/s, L = 1x10^1 n/cm^2/s.
** - MSE = Mean-Square Error.

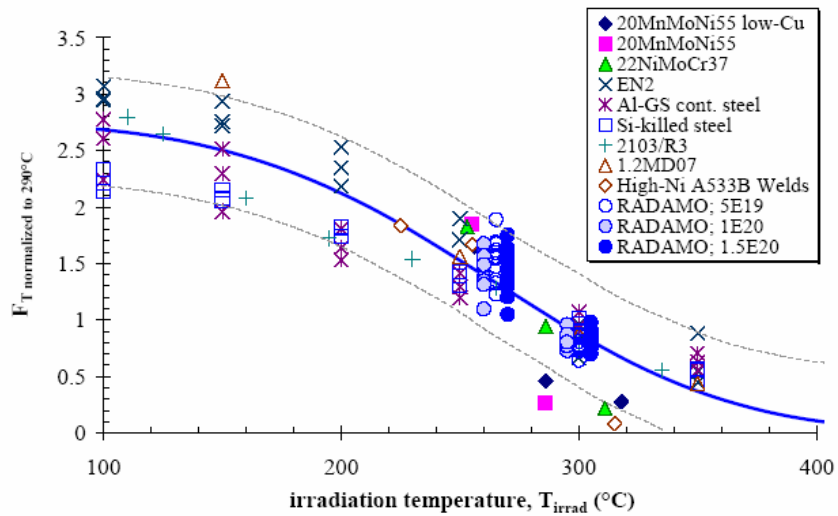

Figure 26. Relative yield strength increase as a function of irradiation temperature. The sensitivity factor is normalized to 290°C-irradiation (F_T=1 at T_{irrad}=290°C).

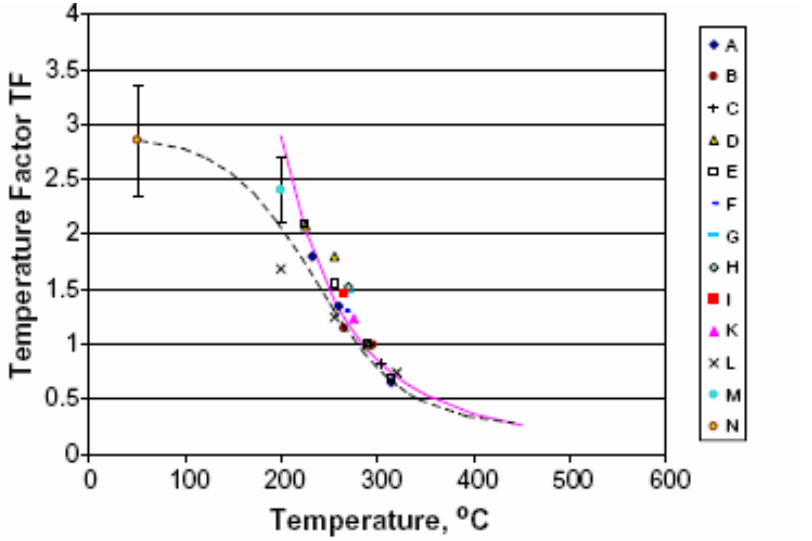

Fig. 5. Verification of temperature dependence at lower temperatures. Comparison with available data at 50 °C.

Figure 4-2. Temperature effects on matrix damage as reported by [Chaouadi 05a] and [Debarberis 05b] (left and right, respectively). In both graphs, the vertical axis is the ratio of the MD hardening at 290 °C to that occurring at some other temperature.

4.1.1.3 Flux

In 2002, an international symposium was held to review and summarize the then-current state of knowledge regarding dose-rate effects on RPV steel embrittlement [Soneda 02]. Prior to that symposium, the consensus technical view was that flux effects did not occur in low-copper steels. Jones and Bolton, for example, noted that "in the absence of precipitation effects, no influence of dose rate on irradiation hardening has been detected" [Jones 96]. Those researchers showed data indicating that MD hardening is unaffected by dose rate over the range of 10^{-13} to 10^{-6} dpa/s. Indeed, the findings of the symposium supported this view, as illustrated by the following statement in the symposium proceedings [Soneda 02]:

> Data from low-Cu C-Mn and MnMoNi steels support dose rate independence, provided that the:
>
> - Dose rate is below that for unstable matrix damage (UMD) formation. (UMD are additional defect clusters produced at high dose rate that… recover during irradiation. If follows that the UMD contribution to embrittlement will increase with increasing dose rate.)
> - Level of bulk Cu is less than 0.1 wt-%. (In certain cases, the threshold Cu level may be higher, e.g., at lower irradiation temperatures, or if copper is precipitated out in second phases during fabrication).
> - Irradiation temperature is between 150 and 300 °C.
>
> Dose rate dependence will be introduced once significant amounts of UMD forms. UMD is produced in high dose rate material test reactor (MTR) irradiations. The threshold dose rate [*above which dose rate dependence will be observed]* is approximately 10^{12} n/cm^2/s for E>1MeV at 290 °C.

However, recent evidence available from the IVAR database suggests that there may be a mild flux effect on MD. Figure 4-3 shows the variation of the A coefficient (matrix damage) from eq. 4-1 with flux for low-copper steels. (The plot has also been restricted in terms of nickel, manganese, and phosphorus to values that are typical of LWRs.) These data suggest that, over the flux range examined in IVAR, decreases in flux may increase the MD embrittlement rate by approximately a factor of two. Chapter 6 in Appendix A also notes the potential for flux effects on MD using the IVAR database.

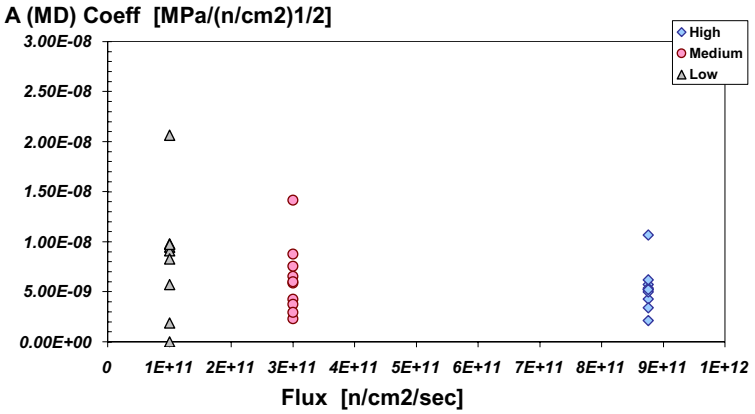

X-axis	Transform with square root?	FALSE
X-axis	Flux [n/cm2/sec]	7
Y-axis	A (MD) Coeff [MPa/(n/cm2)1/2]	8

Axis Code	Axis Lable	Min	Max
1	Copper [wt. %]	0	0.1
2	Nickel [wt. %]	0.5	1
3	Manganese [wt. %]	1	1.7
4	Phosphorus [wt. %]	0	0.025
5	Silicon [wt. %]	0	1000
6	Temperature [C]	290	291
7	Flux [n/cm^2/sec]		
8	A (MD) Coeff [MPa/(n/cm^2)$^{1/2}$]		
9	B (CRP) Coeff [MPa]		
10	Φ_{SAT} [n/cm^2]		
	Flux range to plot	ALL	
	Number of shift values fit	3	

Figure 4-3. Possible flux effect on the MD coefficient for low-copper IVAR data with irradiation at 290 °C.[§]

[§] Throughout the remainder of this section, plots of IVAR data (e.g. see Figure 4-3) are provided. The alloys plotted are restricted to having compositions similar to the majority of those in the US-LWR

4.1.1.4 Nickel

As is the case with many aspects of matrix damage, direct experimental evidence of nickel effects (for example, by atom probe observations) is lacking. Nonetheless, there is ample empirical evidence of nickel effects in controlled irradiation studies where yield strength increase or transition temperature shift is measured. Both Debarberis and Chaouadi report such information [Debarberis 05c, Chaouadi 05a]. Figure 4-4 shows Chaouadi's data for four different commercially available low-copper steels; the effect of increased nickel on increased matrix damage rate is clear. Chaouadi's evidence of nickel effects is consistent with that exhibited by the IVAR data, as shown in Figure 4-5.

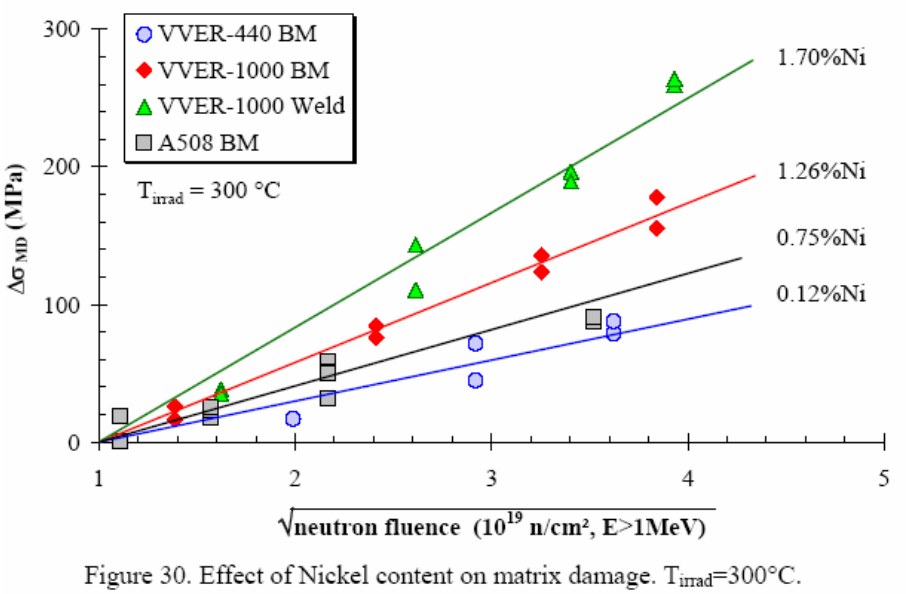

Figure 4-4. Nickel effect on the increase in yield strength attributable to irradiation for low-copper alloys (0.05 to 0.08 wt-%) in the RADAMO database [Chaouadi 05a].

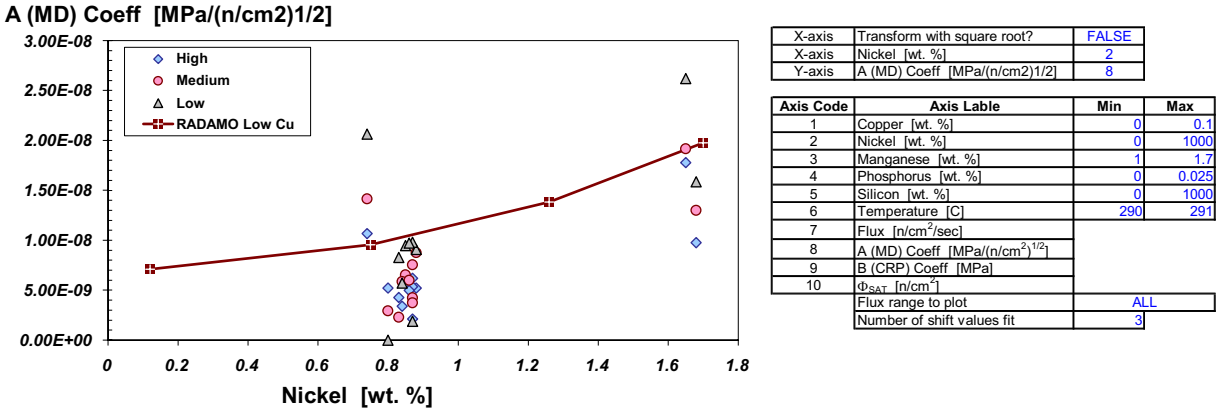

Figure 4-5. Nickel effect on the MD coefficient for low-copper alloys in the IVAR database, with irradiation at 290 °C.

database (i.e., Ni between 0.5 and 1.0 wt-%, Mn between 1.0 and 1.7 wt-%, and P less than 0.025 wt-%.

4.1.1.5 Phosphorus

When large amounts of phosphorus are available in the steel (≈0.3 wt-% and above), non-hardening embrittlement can occur as a result of grain-boundary segregation of the impurity elements. However, at the lower phosphorus concentrations typical of western RPV steels (below 0.025 wt-%), grain-boundary segregation is not expected and has not been observed. At these lower phosphorus levels, a physical mechanism for the formation of phosphorus-rich precipitates (PRP) is well established. The work of Miller [Miller 90, Miller 92, Miller 00], Beaven [Beaven 89], and Solt [Solt 93] all provide physical evidence (e.g., through atom probe studies) of the formation of PRPs in low-copper steels. Fabry's radiation damage model illustrates these results (see Figure 4-6), showing that in low-copper steels, the rate of hardening attributable to phosphorus exceeds that characteristic of higher-copper materials by nearly a factor of four [Fabry 95]. The IVAR data (Figure 4-7) illustrate that the effect of phosphorous is nearly constant (or indistinguishable from scatter) for low-copper materials. To the extent that IVAR is representative of the U.S. LWR surveillance data, the information in this figure indicates that it may be difficult to numerically establish the existence of a phosphorus effect in low-copper steels.

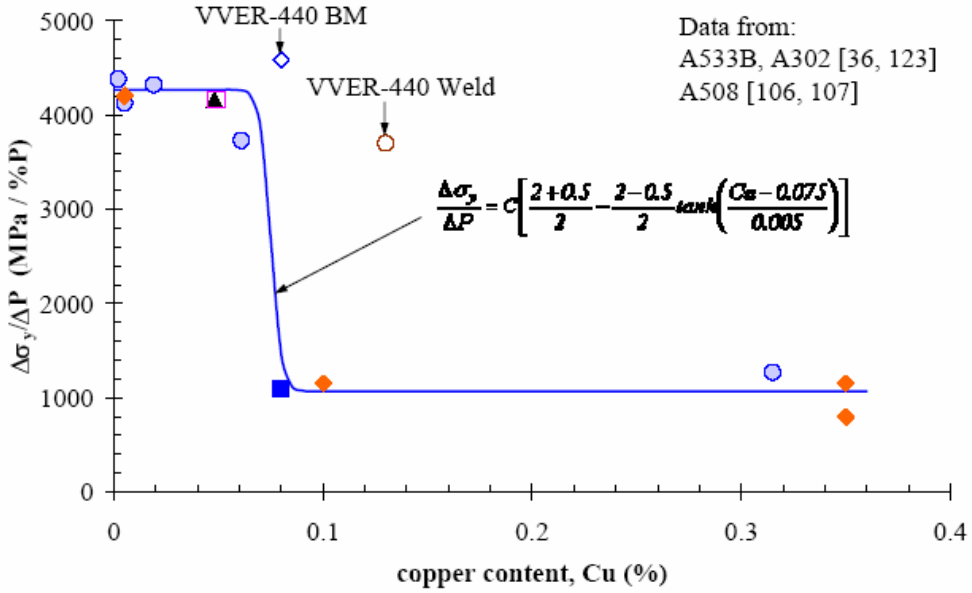

Figure 35. Effect of copper content on the phosphorus irradiation hardening sensitivity.

Figure 4-6. Fabry model of phosphorus overlaid on RADAMO data [Chaouadi 05a].

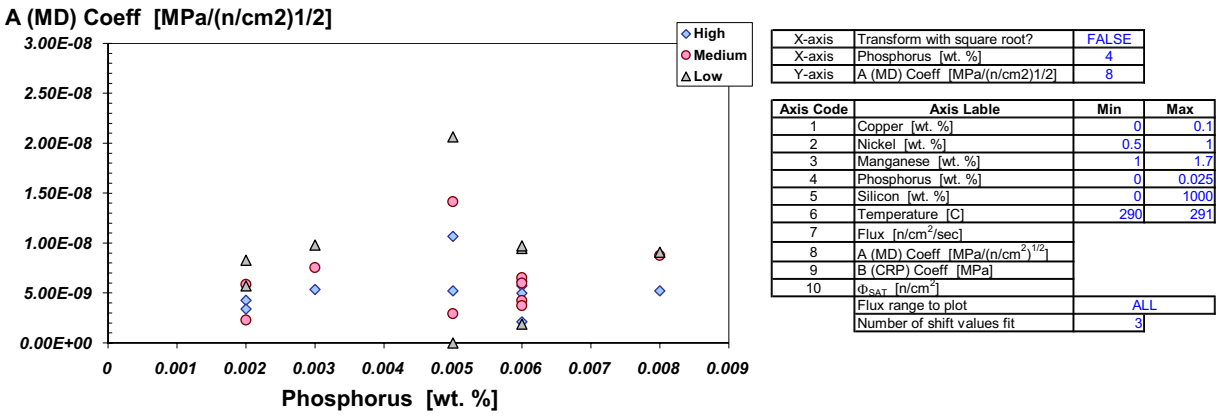

Figure 4-7. No perceptible phosphorus effect on the MD coefficient for low-copper IVAR data with irradiation at 290 °C.

4.1.1.6 Other Composition Variables

For completeness, Figure 4-8 shows the effect of copper, manganese, and silicon content on the matrix damage magnitude in low-copper steels. While no effect of either copper or manganese is evident, these data suggest a possible effect of silicon on matrix damage.

4.1.1.7 Product Form

Virtually all ΔT_{30} embrittlement trend curves in use imply that the magnitude of embrittlement, as measured by ΔT_{30}, varies depending on the product form (i.e., steels of identical composition exposed to identical irradiation exposure conditions are predicted to experience different amounts of ΔT_{30} depending on whether the steel is a weld, plate, or forging). However, when one examines the yield-strength increase behavior attributable to irradiation, such as that reported in RADAMO for low-copper materials (see Figure 4-9), there is no apparent effect of product form.
The categorical descriptor “product form” indicates the thermo-mechanical process experienced by a particular sample of steel before it was exposed to neutron irradiation. These different processes could, in principle, lead to different initial dislocation densities, and such differences in hardening prior to irradiation would produce physically expected differences in the radiation hardening behavior. However, RPV-grade welds, plates, and forgings are all procured to specifications that place controls on the permissible range of initial yield strength. Thus, differences in dislocation density attributable to product form seem unlikely to explain the observed product form effect in ΔT_{30} data within the population of construction-grade RPV steels in the current reactor fleet.

In a recent analysis of a large population of CVE transition curves, EricksonKirk reported that the product form effects appear to either disappear, or be significantly mitigated, if the CVE transition curve is fit using only an exponential curve restricted to the transition regime, instead of using the conventional hyperbolic tangent (*tanh*) fitting approach [EricksonKirk 07]. This finding suggests that the so-called product form effect may be a non-physical artifact of the linkage between upper-shelf and transition behavior that occurs when *tanh* fitting is used.

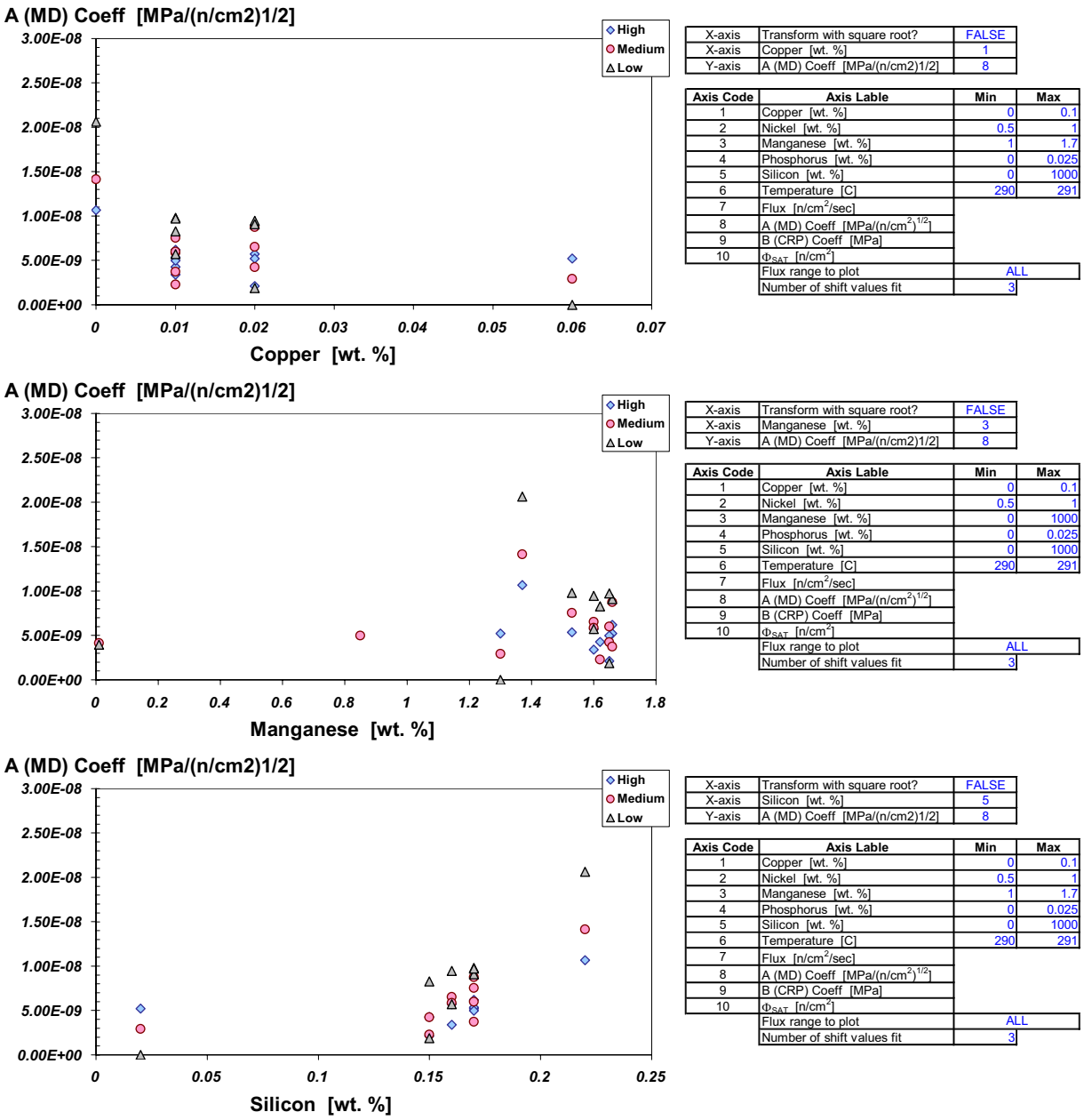

X-axis	Transform with square root?	FALSE
X-axis	Copper [wt. %]	1
Y-axis	A (MD) Coeff [MPa/(n/cm2)1/2]	8

Axis Code	Axis Lable	Min	Max
1	Copper [wt. %]	0	0.1
2	Nickel [wt. %]	0.5	1
3	Manganese [wt. %]	1	1.7
4	Phosphorus [wt. %]	0	0.025
5	Silicon [wt. %]	0	1000
6	Temperature [C]	290	291
7	Flux [n/cm^2/sec]		
8	A (MD) Coeff [MPa/(n/cm^2)$^{1/2}$]		
9	B (CRP) Coeff [MPa]		
10	Φ_{SAT} [n/cm^2]		
	Flux range to plot	ALL	
	Number of shift values fit	3	

X-axis	Transform with square root?	FALSE
X-axis	Manganese [wt. %]	3
Y-axis	A (MD) Coeff [MPa/(n/cm2)1/2]	8

Axis Code	Axis Lable	Min	Max
1	Copper [wt. %]	0	0.1
2	Nickel [wt. %]	0.5	1
3	Manganese [wt. %]	0	1000
4	Phosphorus [wt. %]	0	0.025
5	Silicon [wt. %]	0	1000
6	Temperature [C]	290	291
7	Flux [n/cm^2/sec]		
8	A (MD) Coeff [MPa/(n/cm^2)$^{1/2}$]		
9	B (CRP) Coeff [MPa]		
10	Φ_{SAT} [n/cm^2]		
	Flux range to plot	ALL	
	Number of shift values fit	3	

X-axis	Transform with square root?	FALSE
X-axis	Silicon [wt. %]	5
Y-axis	A (MD) Coeff [MPa/(n/cm2)1/2]	8

Axis Code	Axis Lable	Min	Max
1	Copper [wt. %]	0	0.1
2	Nickel [wt. %]	0.5	1
3	Manganese [wt. %]	1	1.7
4	Phosphorus [wt. %]	0	0.025
5	Silicon [wt. %]	0	1000
6	Temperature [C]	290	291
7	Flux [n/cm^2/sec]		
8	A (MD) Coeff [MPa/(n/cm^2)$^{1/2}$]		
9	B (CRP) Coeff [MPa]		
10	Φ_{SAT} [n/cm^2]		
	Flux range to plot	ALL	
	Number of shift values fit	3	

Figure 4-8. Low-copper IVAR data, with irradiation at 290 °C, showing that both copper and manganese have no discernable effect on the matrix damage (A) coefficient. The IVAR data indicate that silicon content has some effect on A.

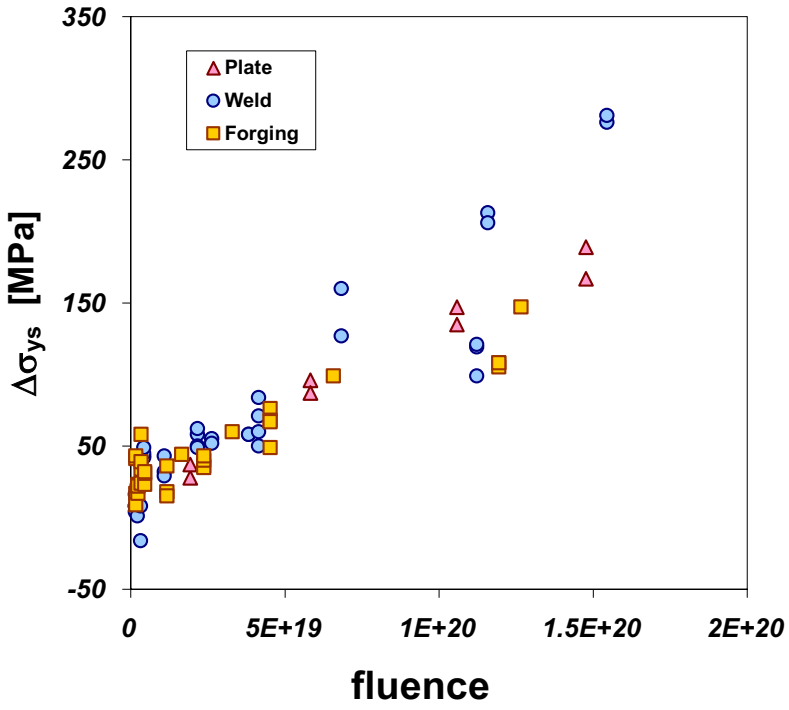

RADAMO Database

		Min	Max
Cu		0.05	0.08
Ni		0	1000
Mn		0	1000
P		0	1000
Si		0	1000
Temp		300	302
Flux		0.00E+00	1.00E+50
X-axis	Log10(fluence)		FALSE
	Sqrt(fluence)		FALSE
	Fluence		TRUE
Y-axis	Subtract MF		FALSE
	Subtract CRP		FALSE
	Subtract PRP		FALSE

Figure 4-9. No effect of product form on irradiation hardening for the low-copper materials in the RADAMO database, based on data from [Chaouadi 05a].

4.1.2 Copper-Rich Precipitation (High Copper) Mechanisms

Of the many alloying elements used in RPV-grade construction steels, copper is primarily responsible for precipitation hardening. Radiation enhances the diffusion and precipitation rates of supersaturated copper initially held in solid solution in the ferrite matrix. This process forms copper-rich precipitates (CRPs) that inhibit dislocation motion, thereby hardening the material. In contrast to MD hardening, CRP hardening has been recognized since the early days of RPV construction when, sadly, spools of weld wire were coated with copper to inhibit corrosion. Early construction plates and forgings also had higher copper contents than later construction because of the use of scrap (which included auto bodies with intact electrical systems) in the steel-making process.

Early recognition of the rapid and significant potential of radiation-enhanced precipitation processes to embrittle RPV steels motivated nearly 30 years of research aimed at understanding the physical mechanisms of this type of damage, as evidenced by review articles on this topic (see Chapter 2 of Appendix A, as well as [Chaouadi 05b]) and the discussions in the following subsections.

4.1.2.1 Fluence and Copper

As previously noted, radiation dramatically enhances the diffusion rate of copper and copper-alloyed second phase particles above the rates that can be expected based on temperature alone. Hardening by copper precipitation rises to a peak value and is then unaffected by subsequent radiation exposure because no copper remains in solid solution to precipitate out and cause further damage. This peak hardening is typically reported to occur in the fluence range of 1–2x10^{19} n/cm^2 (E>1MeV). The magnitude of the peak hardening depends on the amount of copper initially held in solid solution. Work by Fisher [Fisher 85, Fisher 87] demonstrates that the peak hardening magnitude scales in proportion to the square-root of the copper content (√Cu), in agreement with the model of Russell and Brown for thermally driven precipitation processes [Russell 72]. Information presented by Chaouadi (see Figure 4-10) suggests that the relation between peak hardening and √Cu may not be exactly linear [Chaouadi 05a, Chaouadi 05b]. Figure 4-11 shows Chaouadi's relation between peak hardening and √Cu overlaid on the peak hardening (B) coefficients calculated from the IVAR database. While the agreement is good, this comparison also suggests that it may be difficult to discern the non-linearity suggested by Chaouadi in the presence of data scatter. Data from IVAR shown in Figure 4-12 indicate that while the peak hardening magnitude depends strongly on copper content, copper content has little effect on the fluence at which peak hardening magnitude is achieved.

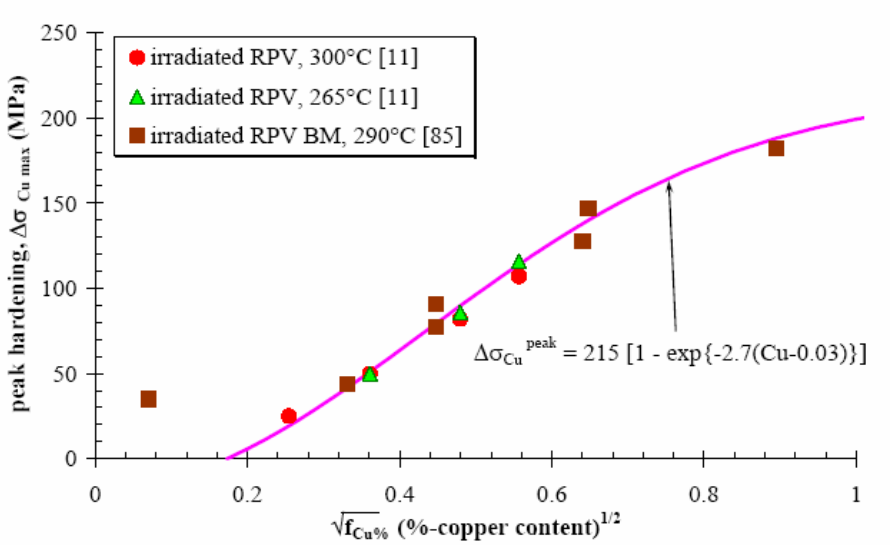

Figure 4-10. Relationship between peak CRP hardening and √Cu proposed in [Chaouadi 05b].

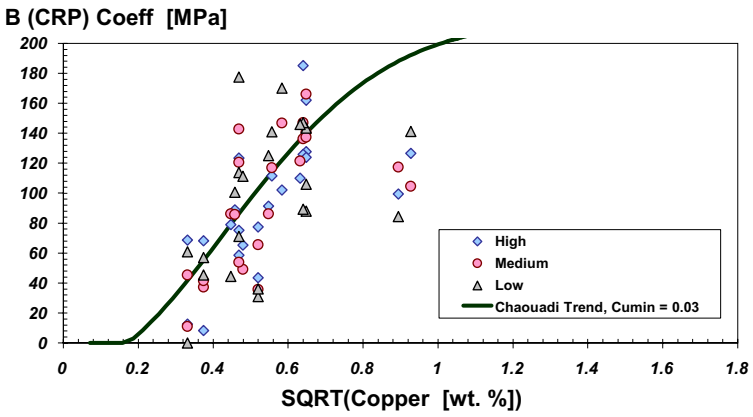

X-axis	Transform with square root?	TRUE
X-axis	SQRT(Copper [wt. %])	1
Y-axis	B (CRP) Coeff [MPa]	9

Axis Code	Axis Lable	Min	Max
1	Copper [wt. %]	0.1	1000
2	Nickel [wt. %]	0.5	1
3	Manganese [wt. %]	1	11.7
4	Phosphorus [wt. %]	0	0.025
5	Silicon [wt. %]	0	1000
6	Temperature [C]	290	291
7	Flux [n/cm^2/sec]		
8	A (MD) Coeff [MPa/(n/cm^2)$^{1/2}$]		
9	B (CRP) Coeff [MPa]		
10	Φ_{SAT} [n/cm^2]		
	Flux range to plot	ALL	
	Number of shift values fit	3	

Figure 4-11. Relationship between peak CRP hardening and √Cu proposed in [Chaouadi 05b] overlaid on the IVAR data for high-copper steels.

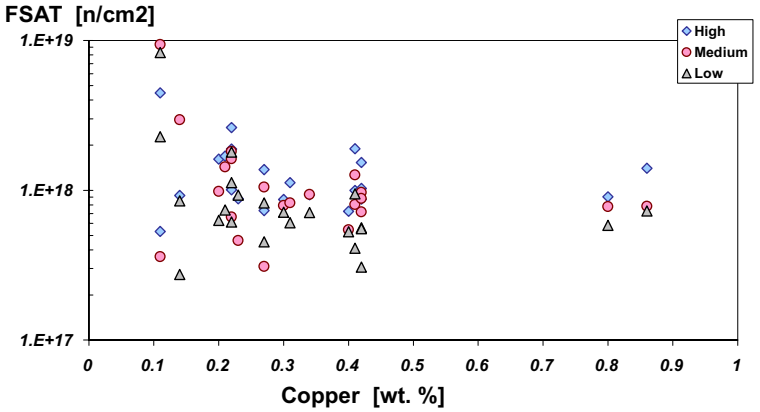

X-axis	Transform with square root?	FALSE
X-axis	Copper [wt. %]	1
Y-axis	FSAT [n/cm2]	10

Axis Code	Axis Lable	Min	Max
1	Copper [wt. %]	0.1	1000
2	Nickel [wt. %]	0.5	1
3	Manganese [wt. %]	1	1.7
4	Phosphorus [wt. %]	0	0.025
5	Silicon [wt. %]	0	1000
6	Temperature [C]	290	291
7	Flux [n/cm^2/sec]		
8	A (MD) Coeff [MPa/(n/cm^2)$^{1/2}$]		
9	B (CRP) Coeff [MPa]		
10	Φ_{SAT} [n/cm^2]		
	Flux range to plot	ALL	
	Number of shift values fit	3	

Figure 4-12. Relationship between the saturation fluence for CRP hardening and the copper content based on IVAR irradiations.

As is evident from the curve in Figure 4-10, the relationship between peak CRP hardening and √Cu has both lower and upper asymptotes. The upper asymptote occurs because, irrespective of the bulk amount of copper in the alloy, only a limited amount of copper can be held in solid solution in the ferrite matrix. The bulk copper above this solubility limit precipitates from the ferrite matrix at the final heat treatment temperature and, therefore, is not available for subsequent precipitation during irradiation. The solubility limit of copper in ferrite at the final heat treat temperature thereby establishes the amount of copper that can form into CRPs during irradiation. Post-weld heat treatment (PWHT) performed before the RPV is placed into service also precipitates copper, thereby removing some of it from solid solution and eliminating its ability to cause damage during irradiation. For typical RPV conditions, the maximum amount of copper that can remain in solution is approximately 0.3 wt-% [Odette 86, Odette 88]; however, McElroy and Lowe reported a lower value of 0.23 wt-% for Linde 80 welds [McElroy 96].

Empirical evidence strongly suggests that there is a minimum copper content required for CRP formation to occur. A range of minimum copper values have been suggested and used in trend curve modeling, as follows:

- [Chaouadi 05b] Cu_{min} = 0.03 wt-%
- [Debarberis 05a] Cu_{min} = 0.05 wt-%
- [IAEA 1442] Cu_{min} = 0.04 and 0.05 wt-%
- Appendix A, Chapters 4 and 7 Cu_{min} = 0.072 wt-%
- Appendix A, Chapter 6 Cu_{min} = 0.063 and 0.073 wt-%
- [Williams 86] Cu_{min} = 0.15 wt-%

Cu_{min} values between 0.03 and 0.15 wt-% produce x-intercept values in Figure 4-11 between 0.17 and 0.39. Thus, when calibrating Cu_{min} using an empirical database containing a range of compositions, any value within this range can be regarded as plausible. Physical arguments support the existence of a minimum copper content required for CRP formation to occur. Server suggested that a certain volume fraction of clustered Cu may be required before additional hardening is observed, while Fisher observed that small amounts of copper can be tied up as insoluble second-phase particles (e.g., the sulfides that form during casting and welding processes), making this copper unavailable for CRP formation [Server 01, Fisher 83].

4.1.2.2 Temperature

Empirical evidence for the effects of radiation damage on mechanical properties at various temperatures suggests that the effect of temperature on CRP hardening is either nonexistent or too small to distinguish from data scatter [Williams 86, Williams 87, Wirth 99]. Nonetheless, in Section 2.3.4 of Appenidx A to this report, Odette showed that, based on controlled IVAR irradiations, CRP temperature effects can be measured and, indeed, rationalized based on SANS data. Using data from a model alloy (Cu=0.4%, Ni=0.8%, Mn=1.4%), Odette showed that as irradiation temperature increases, both the volume fraction and the number density of precipitates decreases, while the size of precipitates increases. The integrated effect of these temperature-induced changes to the character of the CRPs is a reduction of ≈33% in the peak hardening capacity (B) of the alloy as the irradiation temperature increases from 270 to 290 °C.

4.1.2.3 Flux

In Section 2.3.1 of Appendix A to this report, Odette extensively discussed the effect of flux on CRP hardening. A flux of $\phi \approx 10^{10}$ n/cm^2/s is seen to be an approximate dividing line between a regime (at lower fluxes) where flux does not influence the radiation-enhanced diffusion rate versus (at higher fluxes) a regime where the radiation-enhanced diffusion rate is influenced by flux. While the US-LWR surveillance database spans the dividing line, with boiling-water reactors (BWRs) generally being exposed at lower fluxes and PWRs being exposed at higher fluxes, the IVAR experiments focused on the flux-dependent regime. Using data from a model alloy (Cu=0.4%, Ni=1.25%, Mn=1.4%), Odette showed that as flux decreases from 9×10^{11} to 1×10^{11} n/cm^2/s, both the volume fraction and size of precipitates increases. The integrated effect of these flux-induced changes is said to increase the saturation fluence for needed for CRP hardening (Φ_{SAT}), but leaves the peak CRP hardening potential (B) unaffected. Figure 4-13 and Figure 4-14 examine these ideas relative to both the high-Cu IVAR data and those alloys having Cu ≈0.3 wt-%. These data reveal that the increase of Φ_{SAT} with flux is modest over this flux range. Also, the effect of increasing flux on the peak CRP hardening potential (B) is either nonexistent, as expected from the discussion in Section 2.3.1 of Appendix A, or may in fact slightly reduce the peak hardening potential.

4.1.2.4 Solute Elements Other than Copper (Ni, Mn, P, and Si)

The presence of other solute elements in the alloy (e.g., nickel, manganese, phosphorus, and silicon) can further enhance its precipitation hardening capacity [Mader 95, Liu 97]. The effective energy of these atoms is lower in the precipitates than in the matrix, making conditions favorable for their precipitation [Odette 98]. Copper-alloyed second phases are both larger and more numerous than copper-only precipitates, making them greater impediments to dislocation motion and, thereby, enhancers of hardening. Using the IVAR database for high-copper alloys (above 0.1 wt-%) having compositions typical of US-RPV steels, Figure 4-15 and Figure 4-16 examine the potential effects of nickel, manganese, phosphorus, and silicon on the peak CRP hardening potential (B) and saturation fluence (respectively) for CRP hardening (Φ_{SAT}). Only nickel content has a clear effect on both variables.

4.1.2.5 Product Form

As previously noted in Section 4.1.1.7, virtually all ΔT_{30} embrittlement trend curves imply that the magnitude of embrittlement, as measured by ΔT_{30}, varies depending on the product form, despite the fact that such product form dependencies are not present in yield strength increase data. Figure 4-17 indicates that this same observation applies to higher-copper materials where irradiation damage by CRP occurs.

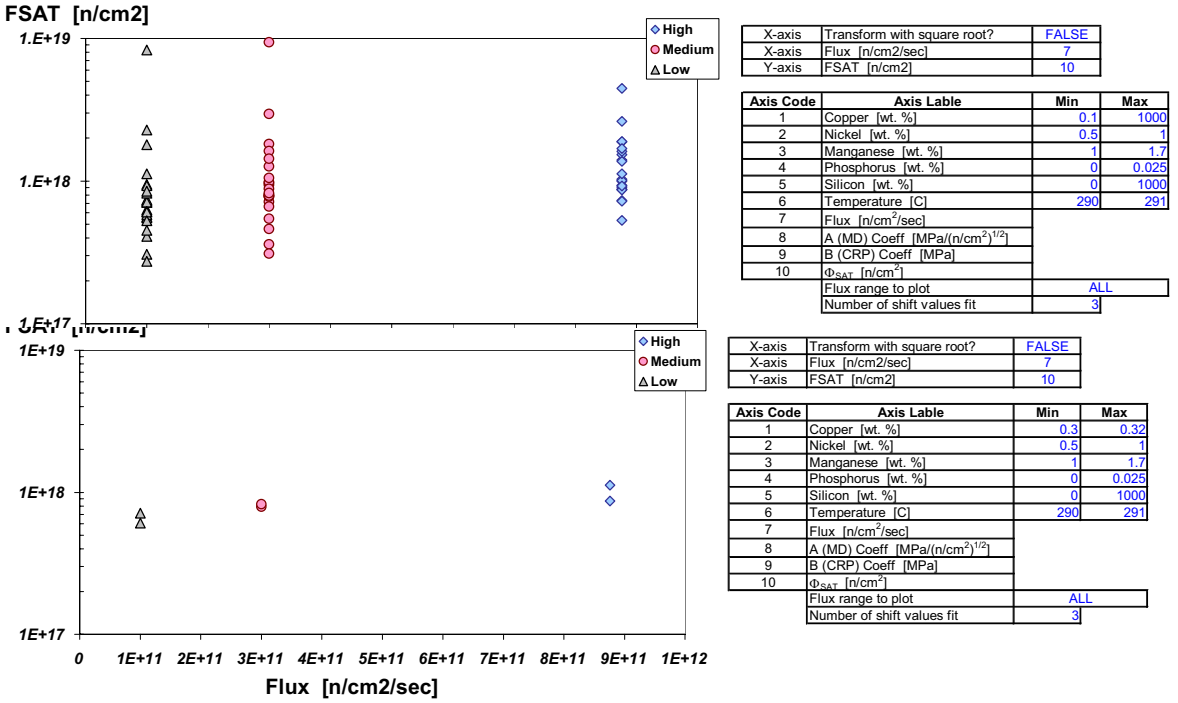

X-axis	Transform with square root?	FALSE
X-axis	Flux [n/cm2/sec]	7
Y-axis	FSAT [n/cm2]	10

Axis Code	Axis Lable	Min	Max
1	Copper [wt. %]	0.1	1000
2	Nickel [wt. %]	0.5	1
3	Manganese [wt. %]	1	1.7
4	Phosphorus [wt. %]	0	0.025
5	Silicon [wt. %]	0	1000
6	Temperature [C]	290	291
7	Flux [n/cm^2/sec]		
8	A (MD) Coeff [MPa/(n/cm^2)$^{1/2}$]		
9	B (CRP) Coeff [MPa]		
10	Φ_{SAT} [n/cm^2]		
	Flux range to plot	ALL	
	Number of shift values fit	3	

X-axis	Transform with square root?	FALSE
X-axis	Flux [n/cm2/sec]	7
Y-axis	FSAT [n/cm2]	10

Axis Code	Axis Lable	Min	Max
1	Copper [wt. %]	0.3	0.32
2	Nickel [wt. %]	0.5	1
3	Manganese [wt. %]	1	1.7
4	Phosphorus [wt. %]	0	0.025
5	Silicon [wt. %]	0	1000
6	Temperature [C]	290	291
7	Flux [n/cm^2/sec]		
8	A (MD) Coeff [MPa/(n/cm^2)$^{1/2}$]		
9	B (CRP) Coeff [MPa]		
10	Φ_{SAT} [n/cm^2]		
	Flux range to plot	ALL	
	Number of shift values fit	3	

Figure 4-13. Relationship between the saturation fluence (Φ_{SAT}) for CRP hardening and flux based on IVAR irradiations for (top) all high-copper alloys and (bottom) only alloys having ≈0.3 wt-% Cu.

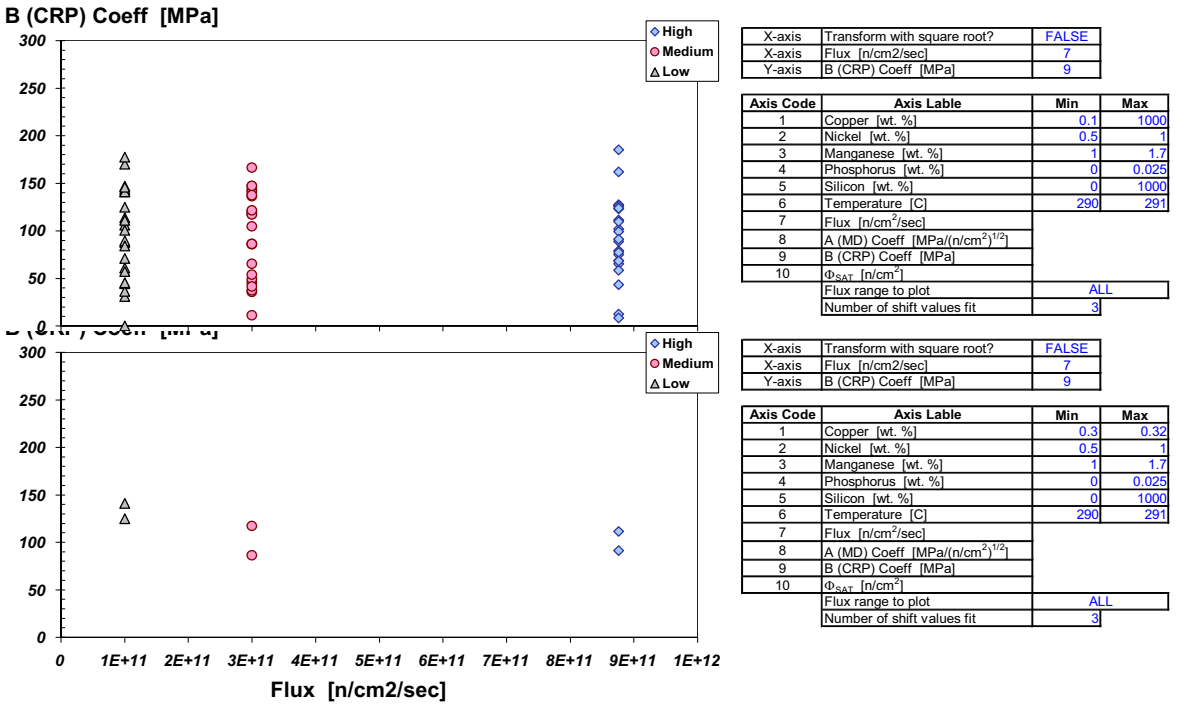

X-axis	Transform with square root?	FALSE
X-axis	Flux [n/cm2/sec]	7
Y-axis	B (CRP) Coeff [MPa]	9

Axis Code	Axis Lable	Min	Max
1	Copper [wt. %]	0.1	1000
2	Nickel [wt. %]	0.5	1
3	Manganese [wt. %]	1	1.7
4	Phosphorus [wt. %]	0	0.025
5	Silicon [wt. %]	0	1000
6	Temperature [C]	290	291
7	Flux [n/cm^2/sec]		
8	A (MD) Coeff [MPa/(n/cm^2)$^{1/2}$]		
9	B (CRP) Coeff [MPa]		
10	Φ_{SAT} [n/cm^2]		
	Flux range to plot	ALL	
	Number of shift values fit	3	

X-axis	Transform with square root?	FALSE
X-axis	Flux [n/cm2/sec]	7
Y-axis	B (CRP) Coeff [MPa]	9

Axis Code	Axis Lable	Min	Max
1	Copper [wt. %]	0.3	0.32
2	Nickel [wt. %]	0.5	1
3	Manganese [wt. %]	1	1.7
4	Phosphorus [wt. %]	0	0.025
5	Silicon [wt. %]	0	1000
6	Temperature [C]	290	291
7	Flux [n/cm^2/sec]		
8	A (MD) Coeff [MPa/(n/cm^2)$^{1/2}$]		
9	B (CRP) Coeff [MPa]		
10	Φ_{SAT} [n/cm^2]		
	Flux range to plot	ALL	
	Number of shift values fit	3	

Figure 4-14. Relationship between the peak CRP hardening (B) and flux based on IVAR irradiations for (top) all high-copper alloys and (bottom) only alloys having ≈0.3 wt-% Cu.

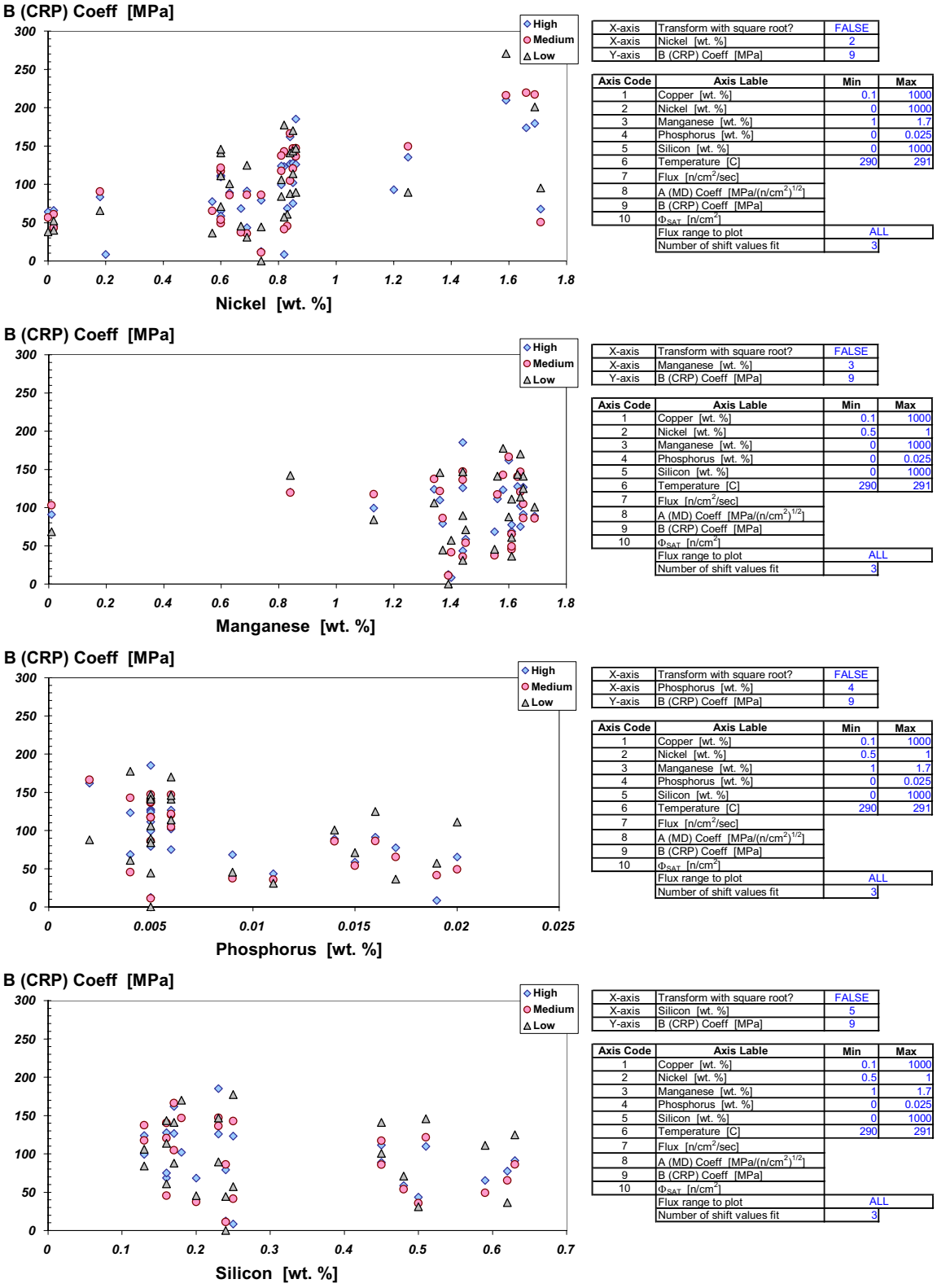

X-axis	Transform with square root?	FALSE
X-axis	Nickel [wt. %]	2
Y-axis	B (CRP) Coeff [MPa]	9

Axis Code	Axis Lable	Min	Max
1	Copper [wt. %]	0.1	1000
2	Nickel [wt. %]	0	1000
3	Manganese [wt. %]	1	1.7
4	Phosphorus [wt. %]	0	0.025
5	Silicon [wt. %]	0	1000
6	Temperature [C]	290	291
7	Flux [n/cm^2/sec]		
8	A (MD) Coeff [MPa/(n/cm^2)$^{1/2}$]		
9	B (CRP) Coeff [MPa]		
10	Φ_{SAT} [n/cm^2]		
	Flux range to plot	ALL	
	Number of shift values fit	3	

X-axis	Transform with square root?	FALSE
X-axis	Manganese [wt. %]	3
Y-axis	B (CRP) Coeff [MPa]	9

Axis Code	Axis Lable	Min	Max
1	Copper [wt. %]	0.1	1000
2	Nickel [wt. %]	0.5	1
3	Manganese [wt. %]	0	1000
4	Phosphorus [wt. %]	0	0.025
5	Silicon [wt. %]	0	1000
6	Temperature [C]	290	291
7	Flux [n/cm^2/sec]		
8	A (MD) Coeff [MPa/(n/cm^2)$^{1/2}$]		
9	B (CRP) Coeff [MPa]		
10	Φ_{SAT} [n/cm^2]		
	Flux range to plot	ALL	
	Number of shift values fit	3	

X-axis	Transform with square root?	FALSE
X-axis	Phosphorus [wt. %]	4
Y-axis	B (CRP) Coeff [MPa]	9

Axis Code	Axis Lable	Min	Max
1	Copper [wt. %]	0.1	1000
2	Nickel [wt. %]	0.5	1
3	Manganese [wt. %]	1	1.7
4	Phosphorus [wt. %]	0	0.025
5	Silicon [wt. %]	0	1000
6	Temperature [C]	290	291
7	Flux [n/cm^2/sec]		
8	A (MD) Coeff [MPa/(n/cm^2)$^{1/2}$]		
9	B (CRP) Coeff [MPa]		
10	Φ_{SAT} [n/cm^2]		
	Flux range to plot	ALL	
	Number of shift values fit	3	

X-axis	Transform with square root?	FALSE
X-axis	Silicon [wt. %]	5
Y-axis	B (CRP) Coeff [MPa]	9

Axis Code	Axis Lable	Min	Max
1	Copper [wt. %]	0.1	1000
2	Nickel [wt. %]	0.5	1
3	Manganese [wt. %]	1	1.7
4	Phosphorus [wt. %]	0	0.025
5	Silicon [wt. %]	0	1000
6	Temperature [C]	290	291
7	Flux [n/cm^2/sec]		
8	A (MD) Coeff [MPa/(n/cm^2)$^{1/2}$]		
9	B (CRP) Coeff [MPa]		
10	Φ_{SAT} [n/cm^2]		
	Flux range to plot	ALL	
	Number of shift values fit	3	

Figure 4-15. Relationship between the peak CRP hardening (B) and the content of nickel, manganese, phosphorus, and silicon based on IVAR irradiations. Of these elements, only nickel has a clear effect on B.

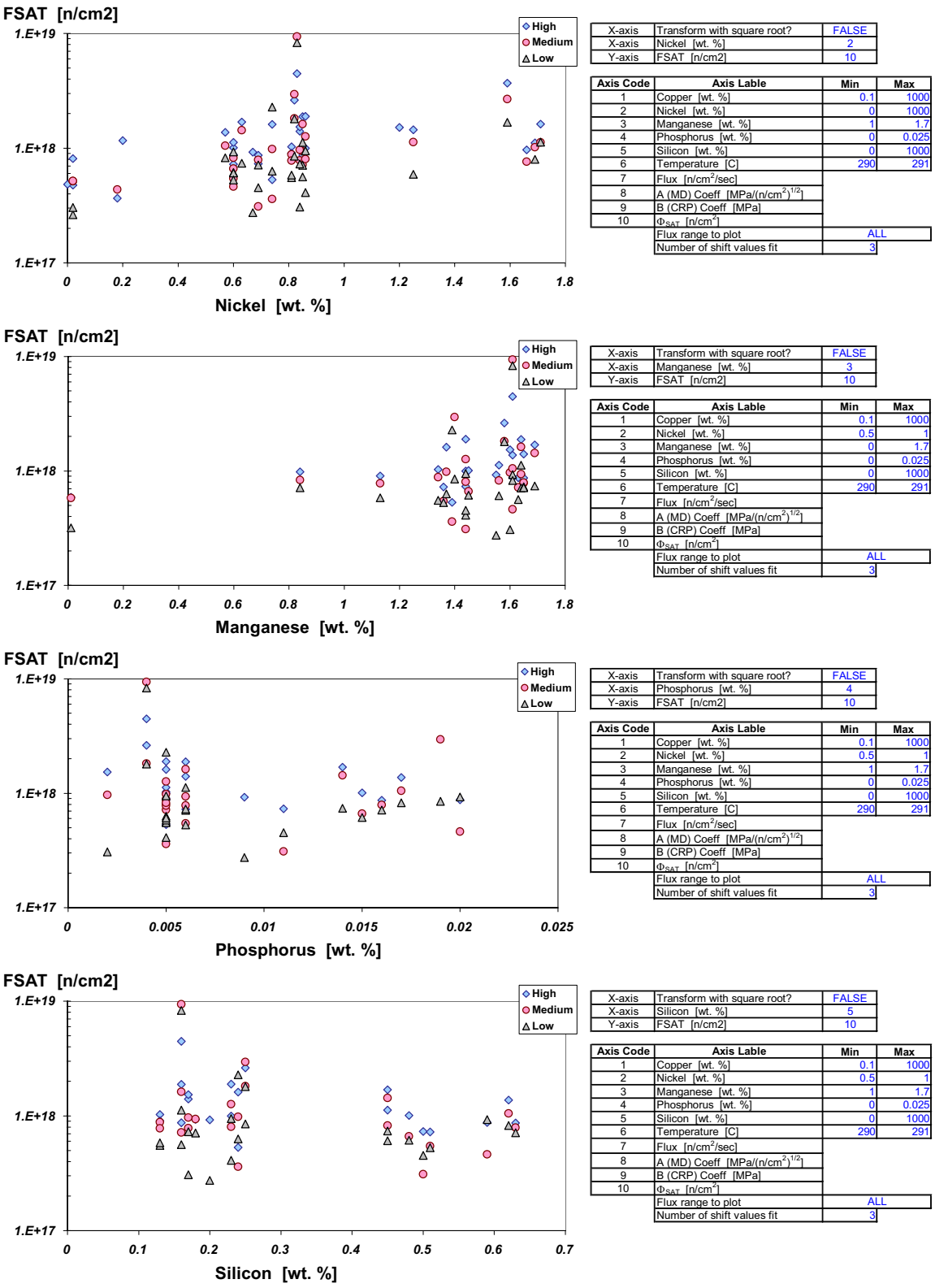

Figure 4-16. Relationship between the saturation fluence (Φ_{SAT}) for CRP hardening and the content of nickel, manganese, phosphorus, and silicon based on IVAR irradiations. Of these elements, only nickel has a clear effect on Φ_{SAT}.

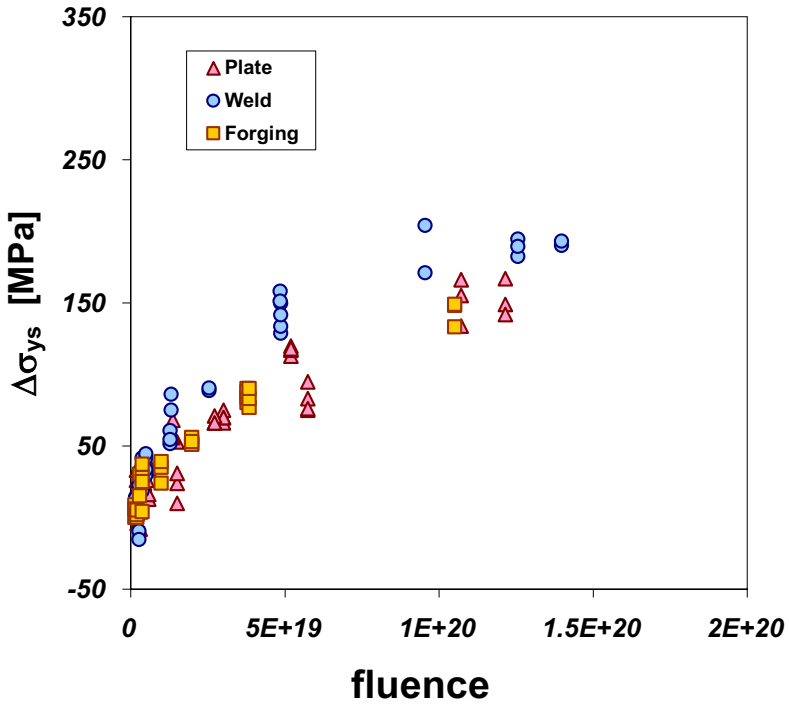

RADAMO Database

		Min	Max
Cu		0.11	0.14
Ni		0	1000
Mn		0	1000
P		0	1000
Si		0	1000
Temp		300	302
Flux		0.00E+00	1.00E+50
X-axis	Log10(fluence)		FALSE
	Sqrt(fluence)		FALSE
	Fluence		TRUE
Y-axis	Subtract MF		FALSE
	Subtract CRP		FALSE
	Subtract PRP		FALSE

Figure 4-17. No effect of product form on irradiation hardening for the higher-copper materials in the RADAMO database, based on data from [Chaouadi 05a].

4.1.3 Superposition Rule

The effects of matrix damage and precipitation of copper and copper-alloyed second phases both act to harden the material at the same time. Consequently, the proper way to combine these effects needs to be established so that the total hardening can be estimated. Section 2.2.2 of Appendix A to this report discusses superposition rules. Based on a model that accounts for the dislocation bowing angle produced by various obstacle sizes and densities, Section 2.2.2 of Appendix A concludes that if the hardening effects that are being added arise from defects of roughly equal size that produce hardening of roughly equal magnitude, the summed hardening should be the square-root of the sum of the squares of the individual hardening contributions. Conversely, if the hardening effects that are being added arise from defects of different sizes that produce hardening of different magnitudes, the summed hardening should be the simple linear sum of the individual hardening contributions. This model, which is shown (in Section 2.2.2 of Appendix A) to agree well with laboratory data, suggests that a linear sum approach is currently most appropriate for adding the effects of MD and CRP for U.S. LWR alloys because the hardening contribution of MD is usually much smaller than that resulting from CRP. This conclusion is consistent with Chaouadi's assessment of the RADAMO data [Chaouadi 05a]. However, it should be noted that Odette's model (in Section 2.2.2 of Appendix A) also suggests that the most appropriate superposition rule may change in the future as MD continues to accumulate, but CRP damage saturates.

4.1.4 Candidate Fitting Function

Table 4.2 summarizes the information presented in Sections 4.1.1 and 4.1.2 concerning the effects of various exposure, composition, and categorical variables on ΔT_{30}. The following two subsections use these insights to build candidate fitting functions for both a matrix damage and a copper-rich precipitate term which, in accordance with the observations in Section 4.1.3, are added linearly, as follows:

Eq. 4-2 $$\Delta T_{30} = \Delta T_{30(MD)} + \Delta T_{30(CRP)}$$

to estimate the total shift in the Charpy 30 ft-lb transition temperature caused by irradiation damage.

4.1.4.1 Matrix Damage Term

The matrix damage term in Eq. 4-2 is expressed as follows:

Eq. 4-3 $$\Delta T_{30(MD)} = PF \cdot CF \cdot TF \cdot \phi F \cdot \Phi F$$

where

the product form (PF) term is: $$PF = \begin{Bmatrix} Weld \\ Plate \\ Forging \end{Bmatrix}$$

the chemistry factor(CF) is: $$CF = \left[1 + A_1 \cdot Ni + A_2 \cdot Mn + A_3 \cdot P + A_4 \cdot Si + A_5 \cdot Cu\right]$$

the temperature factor (TF) is: $$TF = \left(\frac{T}{550}\right)^{E_{temp}}$$

the flux factor (ϕF) is: $$\phi F = \left(\frac{Log10(\phi)}{10.7}\right)^{E_{flux}}$$

the fluence factor (ΦF) is: $$\Phi F = \Phi^{E_{fluence}}$$

Based on the insights from Section 4.1.1, as summarized in Table 4.2, the following expectations exist regarding the fitting coefficients:

- The chemistry factor coefficients for nickel, phosphorous, and silicon (A_1, A_3, and A_4, respectively) are all positive and significantly greater than zero.
- The chemistry factor coefficients for manganese and copper (A_2 and A_5, respectively) are probably close to zero. These terms are retained in the fitting function for purposes of generality and to allow for calibration of a manganese or copper effect if such an effect is apparent in the surveillance data.
- The temperature exponent (E_{temp}) is negative, reflecting greater embrittlement at lower temperatures. The value of 550 °F is used in the denominator of the TF term because this is the nominal water temperature in most PWRs, and because it is close to the mean temperature of the surveillance database. Over the temperature range of the surveillance database (525–565 °F), a value of E_{temp} =-4 produces near-perfect agreement with the mean trend of the data presented by [Chaouadi 05a], as shown in Figure 4-2.

- The IVAR data suggest that the magnitude of MD increases slightly as flux is reduced. Therefore, the flux exponent (E_{temp}) should be negative. The value of 10.7 is used in the denominator of the ϕF term because this is the average of the $Log_{10}(\phi)$ values in temperature of the surveillance database.
- Both theoretical expectation and empirical evidence strongly suggests that the fluence exponent ($E_{fluence}$) should be ½, and this value will be attempted when fitting the surveillance database. $E_{fluence}$ is expressed as a variable in the fitting function for purposes of generality.

4.1.4.2 Copper-Rich Precipitate Term

The copper-rich precipitate term in Eq. 4-2 is expressed as follows:

Eq. 4-4 $$\Delta T_{30(CRP)} = PF \cdot CF \cdot TF \cdot \Phi F$$

where

the product form (PF) term is: $$PF = \left\{ \begin{array}{c} Weld \\ Plate \\ Forging \end{array} \right\}$$

the chemistry factor(CF) is:

$$CF = \left[1 + f(Cu) + B_2 \cdot Ni + B_3 \cdot MIN\left\{Cu_{\max}, MAX\left(0, Cu - Cu_{\min}\right)\right\} \cdot Ni + B_4 \cdot Mn + B_5 \cdot P + B_6 \cdot Si\right]$$

where $f(Cu) = B_{1b} + B_{1m} \cdot Cu^{E_{Cu}}$, subject to $0 \le f(Cu) \le B_{Cu(max)}$

the temperature factor (TF) is: $$TF = \left(\frac{T}{550}\right)^{E_{temp}}$$

the fluence factor (ΦF) is: $$\Phi F = \left\{1 - \exp\left(\frac{-\Phi}{\Phi_{SAT}}\right)\right\}$$

$$\Phi_{SAT} = C_0 + C_1 \cdot Ni + C_2 \cdot \left(\frac{Log_{10}(\phi)}{10.7}\right) + C_3\left(Cu - Cu_{\min}\right) + C_4 \cdot Mn + C_5 \cdot P + C_6 \cdot Si$$

Based on the insights from Section 4.1.2, as summarized in Table 4.2, the following expectations exist regarding the fitting coefficients:

- The dependence of the chemistry factor on copper is (approximately) as illustrated in Figure 4-18, which also illustrates the relationship between the various copper-based coefficients in Eq. 4-4. Values of Cu_{min} have been reported to range from 0.03 to 0.15 wt-% (see Section 4.1.2.1). Values of Cu_{Max} are typically around 0.3 wt-% [Odette 86, Odette 88]. Based on the theoretical model of Fisher, E_{Cu} should be ½ [Fisher 85, Fisher 87].
- The chemistry factor coefficient for nickel (B_2) is positive and significantly greater than zero. The copper/nickel interaction coefficient (B_3) appears in this equation based on the empirical need that arose during the fitting process described in Section 4.2.4.
- The chemistry factor coefficients for manganese, phosphorus, and silicon (B_4, B_5, and B_6, respectively) are probably close to zero. These terms are retained in the fitting function for purposes of generality and to allow for calibration of these effects on CRP hardening if such effects should be apparent in the surveillance data.

- The temperature exponent (E_{temp}) is negative and may be statistically indistinguishable from zero. As described in Section 4.1.2.2, the technical literature suggests that E_{temp} is close to zero; however, in Chapter 6 of Appendix A to this report, Odette provided evidence that E_{temp} may assume a negative value.
- The saturation fluence (C_0), at which 66% of the peak hardening attributable to CRP is reached, should be approximately $1x10^{18}$ n/cm^2.
- The saturation fluence is expected to be increased by both increasing nickel and increasing flux; therefore, C_1 and C_2 are both expected to be positive.
- The saturation fluence coefficients for manganese, phosphorus, and silicon (C_4, C_5, and C_6, respectively) are probably close to zero. These terms are retained in the fitting function for purposes of generality and to allow for calibration of these effects on CRP hardening if such effects should be apparent in the surveillance data.

The form of the fluence function selected in Eq. 4-4, which was motivated by the work of [Debarberis 05a], is but one of many "appropriate" mathematical functions that rise steeply and then level off at an asymptote. Other mathematical forms that have been used as CRP fluence functions include the hyperbolic tangent function (see Chapters 4 and 7 of Appendix A) and the Avrami function (see Chapter 2 of Appendix A). The form of Eq. 4-4 was adopted for this fitting exercise based on simplicity; the functionality with fluence in this function is controlled by only one fitting parameter (Φ_{SAT}), whereas the hyperbolic tangent and Avrami functions both have two fitting parameters.

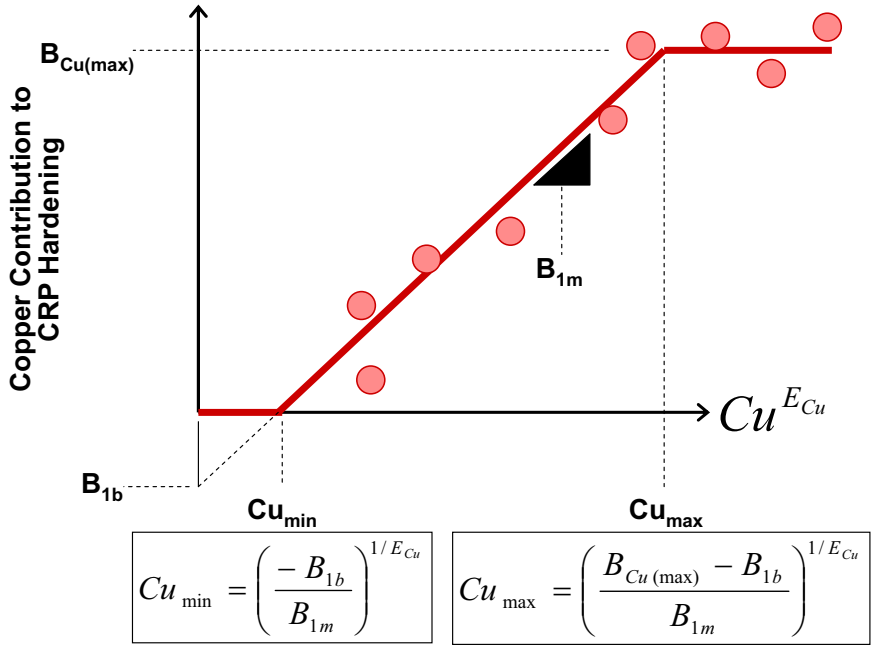

Figure 4-18. Dependence of the CRP chemistry factor on copper and relationships between fit variables.

Table 4.2. Summary of trends expected in developing an embrittlement trend curve for ΔT_{30} based on information presented in Sections 4.1.1 and 4.1.2.

Candidate Regressor Variable	Matrix Damage / Low Copper		Copper-Rich Precipitates / High Copper	
	Hardening Magnitude, A	Hardening Rate, $\sqrt{\Phi}$	Peak Hardening, B	Hardening Saturation Fluence, Φ_{SAT}
Fluence	N/A	Dependence on $\sqrt{\Phi}$ expected theoretically	CRP hardening increases rapidly to a plateau value of B $1.5 \cdot \Phi_{SAT}$.	
Temperature	↑T → ↓A Theoretically variation is non-linear, but over LWR temperatures a linear model appears adequate	N/A	No effect, or ↑T → ↓B	No effect
Flux	↑ϕ → ↓A (Slight Linear)		No effect, or ↑ϕ → ↓B (Slight Linear)	↑ϕ → ↑Φ_{SAT} (Slight Linear)
Copper	No effect		↑$\sqrt{Cu}$ → ↑B (Non Linear, with upper and lower asymptotes)	No effect
Nickel	↑Ni → ↑A (Linear)		↑Ni → ↑A (Linear)	↑Ni → ↑Φ_{SAT} (Linear)
Manganese	No effect		No effect	No effect
Phosphorus	No effect for the range of P in U.S. LWRs		No effect	No effect
Silicon	↑Si → ↑A (Non Linear)		No effect	No effect
Product Form	No effect is expected physically, but one is needed to model ΔT_{30} data		No effect is expected physically, but one is needed to model ΔT_{30} data	No effect

Note: A, B, and Φ_{SAT} are related to CRP shift as follows: $\Delta CRP = A \cdot \sqrt{\Phi} + B\left[1 - \exp\left(-\Phi / \Phi_{SAT}\right)\right]$

4.1.5 Physically Anticipated *vs.* Empirically Calibrated Trends

To this point, Section 4.1 has summarized the embrittlement trends that one can expect to find manifest in ferritic steels when subjected to the exposure conditions (i.e., combinations of fluence, flux, and temperature) that are characteristic of the beltline region of LWRs. The next section (Section 4.2) investigates the existence and magnitude (or lack thereof) of these effects in the US-LWR surveillance database. As the empirical fit is developed and described in Section 4.2, it is important to keep the following ideas in mind:

- **The absence of a physically anticipated trend from a particular empirical database does not prove that the expected trend does not exist, or is not real.** For example, as stated in Section 4.1, we cannot expect to observe non-hardening (grain-boundary) embrittlement in the US-LWR database because the impurity content (phosphorus, silicon, tin, antimony, and other tramp elements) of U.S. RPV steels is sufficiently low that preferential segregation of these elements to the grain boundaries will not occur for the exposure conditions of interest. Likewise, if we examine a database populated entirely by low-copper steels we should not expect to observe embrittlement by the precipitation of copper-rich second phases from the ferrite matrix; but such an observation would not mean that CRP embrittlement is not real. Thus, it is important to note when physically expected trends that are evident elsewhere cannot be found in the US-LWR surveillance database, in order to either (1) establish the applicability limits of the empirical calibration to the surveillance data, or (2) modify the calibration to improve its applicability to a larger range of service conditions.
- **The existence of an empirical trend does not provide conclusive proof of its physical existence.** Virtually all previously published embrittlement trend curves that relate Charpy transition temperature shift to exposure and composition variables include “product form” terms (i.e., different leading coefficients depending on whether the steel in question is a weld, a plate, or a forging). Indeed, different coefficients are sometimes used depending on the flux type used in weld fabrication (e.g., Linde 80). These “product form” effects on Charpy transition temperature suggest that, even with all other factors held constant, the pre-irradiation thermo-mechanical treatment of the steel affects its sensitivity to damage by neutron irradiation. (This idea stands in sharp contrast to the physical finding that the the initial mechanical properties have a very small effect on the embrittlement response [Chaouadi 05a].) Also, product form effects cannot be found in either yield-shift data (see Figure 4-9 and Figure 4-17) or fracture toughness data [Kirk 98, Sokolov 00]. These observations suggest that the product form effects found in Charpy transition temperature shift trend curves may, in fact, be an artifact of the Charpy *tanh* analysis methodology, as supported by recent work [EricksonKirk 07]. Another situation that can produce empirical trends where no physical expectation exists, or that can obscure physically anticipated trends, occurs when regressor variables are strongly correlated, or when they exist only over limited ranges. For example, in the US-LWR database, the only materials that have low Mn (<1 wt-%) are forgings, making it difficult to distinguish between a forging “product form” effect and potential Mn effects on embrittlement.

4.2 Fit of a ΔT_{30} Embrittlement Trend Curve to the US-LWR Surveillance Database

This section describes the development of an equation to express ΔT_{30} as a function of exposure, composition, and categorical variables. The numerical parameters in the equation, the form of which is based on the physical insights and literature data as discussed in Section 4.1, are established by calibrating the functional form established in Section 4.1.4 to the US-LWR ΔT_{30} surveillance database. This section provides details regarding the fitting procedure (Section 4.2.1), the database (Section 4.2.2), and the application of the fitting procedure to the database (Sections 4.2.3, 4.2.4, and 4.2.5). In addition, Section 4.3 presents an assessment of how well this fit represents other data available in the literature.

4.2.1 Fitting Procedure

This investigation employed the following five-step fitting procedure:

Step 1. Based on physical insights and literature data, a candidate fitting function was established as described in Section 4.1.

Step 2. The MD fitting function from Step 1 (Eq. 4-3) was fit to all records in the US-LWR surveillance database having Cu at or below 0.07 wt-%, using the method described in the remainder of this section. The 0.07 split value was adopted because it is near the midrange of the values reported in the literature, and because it is close to the 0.072 value used by Eason in previous analysis of this database [Eason 98]. The appropriateness of the 0.07 split value is assessed in Steps 3 and 4 of this procedure.

Step 3. The CRP fitting function from Step 1 (Eq. 4.4) was fit to all records in the US-LWR surveillance database having Cu above 0.07 wt-%, using the method described in the remainder of this section. In performing this fit, the MD function established in Step 2 was subtracted from the measured ΔT_{30} values to estimate the shift attributable only to CRP.

Step 4. The MD and CRP fits determined in Steps 2 and 3 were combined and assessed relative to the entire US-LWR surveillance database. The appropriateness of the 0.07 Cu split value to the entire database was also assessed in this step. In addition, this step included determining whether it is possible to simplify either the MD or CRP fits by removing terms.

Step 5. The best fit(s) from Step 4 were assessed for their predictive ability relative to data that were not used in developing the fit(s). This assessment may lead to either, or both, of the following:

- better understanding of the applicability limits of the best fit equation
- modification of the best fit equation so that it applies to a larger range of conditions.

Once a candidate model is established in each of Steps 2, 3, and 4, a criterion was needed to determine which combination of parameters constitutes a “best fit” to the data. When fitting simple models to data, a commonly used fitting strategy is to minimize the sum of squared residuals (where a “residual” is the difference between a measurement and the model’s prediction for the conditions of the given measurement). However, previous efforts to fit the US-LWR surveillance database revealed that additional and/or alternative criteria are needed because the mean-square error is not very sensitive to changes in a model of the complexity needed to represent the effects of both MD and CRP hardening [Eason 98, Server 01] (i.e., both good and not so good models can have mean-square error values that differ by only fractions of a degree Fahrenheit).

The goodness-of-fit criterion used in this investigation involved minimizing the T-statistics on slopes and intercepts of lines fit to {Y = ΔT_{30} Fit Error} *vs.* {X = Regressor Variable}. (Figure 4-19 shows a typical plot.) Slopes and intercepts (and their standard errors) were determined by fitting the following equation:

Eq. 4-5 $$\Delta T_{30(\mathrm{Predicted})} - \Delta T_{30(\mathrm{Measured})} = m\Theta + b$$

to data such as those illustrated in Figure 4-19 for a particular regressor variable Θ (e.g. flux, fluence, copper, etc.). The *m* and *b* values in Eq. 4-2 were estimated using the MS-Excel® *linest* function. The T-statistic values for *m* and *b* were determined as the ratio of the estimated value of the parameter to its standard error, both of which are output by *linest*. Specifically, the T-statistics were defined as follows:

Eq. 4-6 $$T_{m(\Theta)} = \frac{|m_\Theta|}{se(m)_\Theta}$$

$$T_{b(\Theta)} = \frac{|b_\Theta|}{se(b)_\Theta}$$

Here, "se" denotes the standard error of the parenthetically indicated parameter, while the subscript indicates the regressor variable of interest.

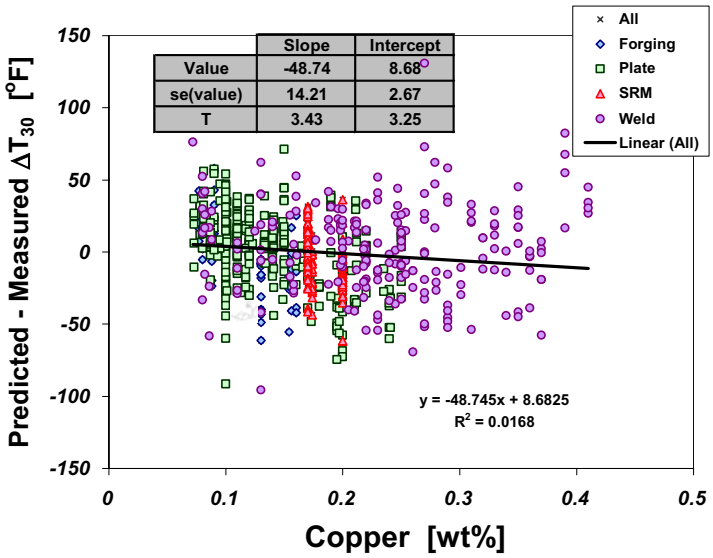

Figure 4-19. Calculation of T values for slope and intercept estimates from a residuals plot.

To assess the goodness-of-fit to the database as a whole, both total and maximum T values (T_{TOTAL} and T_{MAX}, respectively) were calculated for each fit performed to the data, as follows:

Eq. 4-7 $$T_{TOTAL} = \sum_i T_{m(i)} + \sum_i T_{b(i)}$$

Eq. 4-8 $$T_{MAX} = \underset{i}{MAX}\left\{T_{m(i)}, T_{b(i)}\right\}$$

In both equations, "i" is an indicator denoting, respectively, all of the following variables: fluence, flux, temperature, copper, nickel, phosphorus, manganese, product form, and $\Delta T_{30(PREDICTED)}$. Three specific points should be noted regarding Eq. 4-7 and 4-8:

- Product Form: The $T_{m(\Theta)}$ and $T_{b(\Theta)}$ values were established by defining an indicator variable for "X," where X=1 for forgings, X=2 for welds, and X=3 for plates.
- Silicon: The $T_{m(\Theta)}$ and $T_{b(\Theta)}$ values for silicon were not included in the T_{TOTAL} and T_{MAX} values because there were 16 records in the US-LWR database having no reported silicon value. An acceptable fit on silicon was established after an otherwise good fit was found by removing these 16 records from the database and computing the $T_{m(\Theta)}$ and $T_{b(\Theta)}$ values for silicon.
- $\Delta T_{30(PREDICTED)}$: $\Delta T_{30(PREDICTED)}$ is not a regressor variable, but rather the predicted result. Inclusion of $\Delta T_{30(PREDICTED)}$ in the T_{TOTAL} and T_{MAX} metrics was found to result in a better overall balance of errors between the different regressor variables than when $\Delta T_{30(PREDICTED)}$ was omitted from the T_{TOTAL} and T_{MAX} metrics.

Our fitting approach at Steps 2, 3, and 4 involved minimizing T_{TOTAL} using the *solver* routine in MS-Excel®. The *solver* "target" was set to T_{TOTAL}, "minimize" was selected, and "by changing" cells were assigned as the variable parameters in the fit being performed. No constraints were placed on any of the variable parameters. The starting conditions (or guesses) for the variable parameters of the models that were submitted to *solver* were established by trying various parameters, or combinations of parameters, and observing which parameters or parameter combinations led to the least statistically significant residual trends. Initial guesses were guided by both the insights and data summarized in Section 4.1, and statistical requirements for goodness of fit. Once an acceptable combination of parameters was established through this manual process, the parameter guesses were submitted to *solver* to further improve the statistical goodness of fit.

After running *solver* to minimize T_{TOTAL}, each candidate fit was classified as follows based on the value of T_{MAX}:

Unacceptable: $T_{MAX} > 1.97$. This indicates a statistically significant residual trend, at the 5% significance level, for at least one of the candidate regressor variables.

Provisional: $1.97 > T_{MAX} > 1$. These models have no statistically significant residual trends. However, several $T_{m(\Theta)}$ and $T_{b(\Theta)}$ values can be close to 1.97 in these models, and slightly different initial guesses for the parameters can lead to unacceptable models. Also, these models tend to exhibit an uneven distribution of errors among the regressor variables. For example, a provisional model may have $T_{m(\Phi)}$ and $T_{m(Cu)}$ both above 1.9, while all other $T_{m(\Theta)}$ and $T_{b(\Theta)}$ values are below 0.4. The instability of provisional fits (i.e., the ease with which they could be made "unacceptable") and the heterogeneity of their

error distribution among their regressor variables motivated further refinement.

Acceptable: $T_{MAX} < 1$. These models tend to have a reasonably homogeneous distribution of error across the regressor variables. They also tend to be sufficiently robust so that variations in parameter guesses cannot spawn "unacceptable" models.

The fitting process continued at Steps 2 and 3 (MD and CRP fitting, respectively) until it identified acceptable models, after which an effort was made to simplify the model (by removing parameters) while having it remain acceptable. If multiple acceptable models were found, a selection was made between them based on considerations of (1) the physical plausibility of the fit parameter values, and (2) the statistical stability of the fit. At Step 4 the acceptable models from Steps 2 and 3 were combined. Effort was again made to simplify the combined model (by removing parameters) while having it remain acceptable. The joint criteria of physical plausibility and statistical stability again guided the selection of the final combined model.

4.2.2 The US-LWR ΔT_{30} Surveillance Database

The database used was the same as that described in Appendix A, which includes all of the CVN surveillance (and associated) data collected from U.S. LWRs through 2003:

- 936 ΔT_{30} data records were used for fitting. This total included 247 observations that were used to fit the MF term (i.e., Cu $\leq$0.07 wt-%) and 689 observations that were used to fit the CRP term (i.e., Cu >0.07 wt-%). The total database includes 12 other ΔT_{30} data records, but these were not used because the value of Mn was unknown for these records.
- The data set sizes used in assessing the goodness of the combined fit were 920 for Si, and 936 for all other variables.
- 871 ΔUSE records were used for fitting (see Chapter 5).

Figure 4-20 and Figure 4-21 illustrate (respectively) the variation of exposure and composition variables contained within the surveillance database. The distribution of and between the various variables is uneven (e.g., the database does not represent all possible combinations of copper and nickel between the minimum and maximum observed values). This unevenness complicates fitting because the effects that are physically attributable to one regressor variable may be reflected in the database by a different variable because of correlations between two (or more) regressor variables. In addition, this unevenness may make it impossible to observe certain physically expected trends using this particular set of empirical data. Nonetheless, this unevenness occurs as a natural consequence of the physical metallurgy of the ferritic steels used for pressure vessel construction. As one might expect, the database contains a reasonably uniform distribution of the tramp and non-alloying elements (i.e., copper, phosphorus, and silicon) because these undesirable elements are never intentionally added to the melt for this class of steels. However, there is less uniformity in the distribution of nickel and manganese because these alloying elements are intentionally added to the melt to improve both fracture toughness and strength for this class of steels.

Figure 4-20 and Figure 4-21 support the following specific observations:

- The only data records that have low manganese (<0.75 wt-%) are for forgings. By contrast, plates and welds both have higher manganese and scatter over a similar range. For that reason, it may be difficult to differentiate between a manganese effect (if one exists) and a product form effect.
- Only welds exhibit a wide range of nickel content. By contrast, both forgings and plates exhibit nickel values that are much more tightly grouped and exist close to the midpoint of the nickel range exhibited by welds.
- Copper and phosphorus are roughly correlated (i.e., high-copper materials tend to have higher phosphorus content, while low-copper materials tend to have lower phosphorus) for all three product forms.
- In this database, flux and fluence are strongly correlated because they are not independent variables (i.e., flux is determined by dividing fluence by time). This may complicate or impede the resolution of physically expected flux trends because they are difficult to distinguish from fluence trends.
- While the database contains fluences as high as 7×10^{19} n/cm^2, high-fluence data are sparse above approximately $2–3 \times 10^{19}$ n/cm^2. This scarcity of high-fluence data may complicate good calibration of both the CRP saturation level and the magnitude of the matrix damage contribution to hardening.
- While the database contains copper values as high 0.42 wt-%, high-copper data are sparse above approximately 0.3 wt-%. This scarcity of high-copper data may complicate good calibration of the CRP copper saturation level.

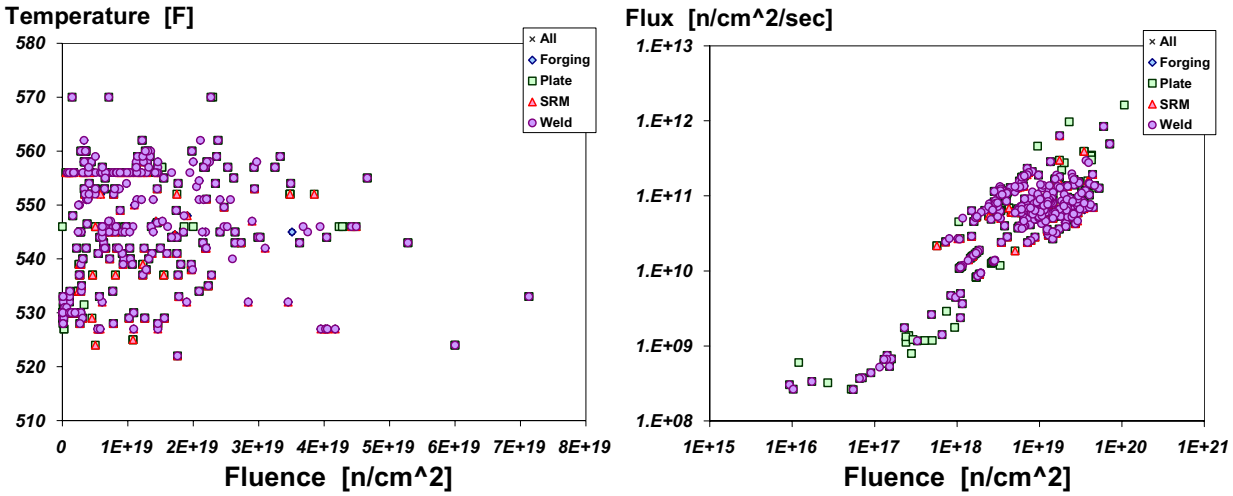

Figure 4-20. Variation of exposure variables within the surveillance database.

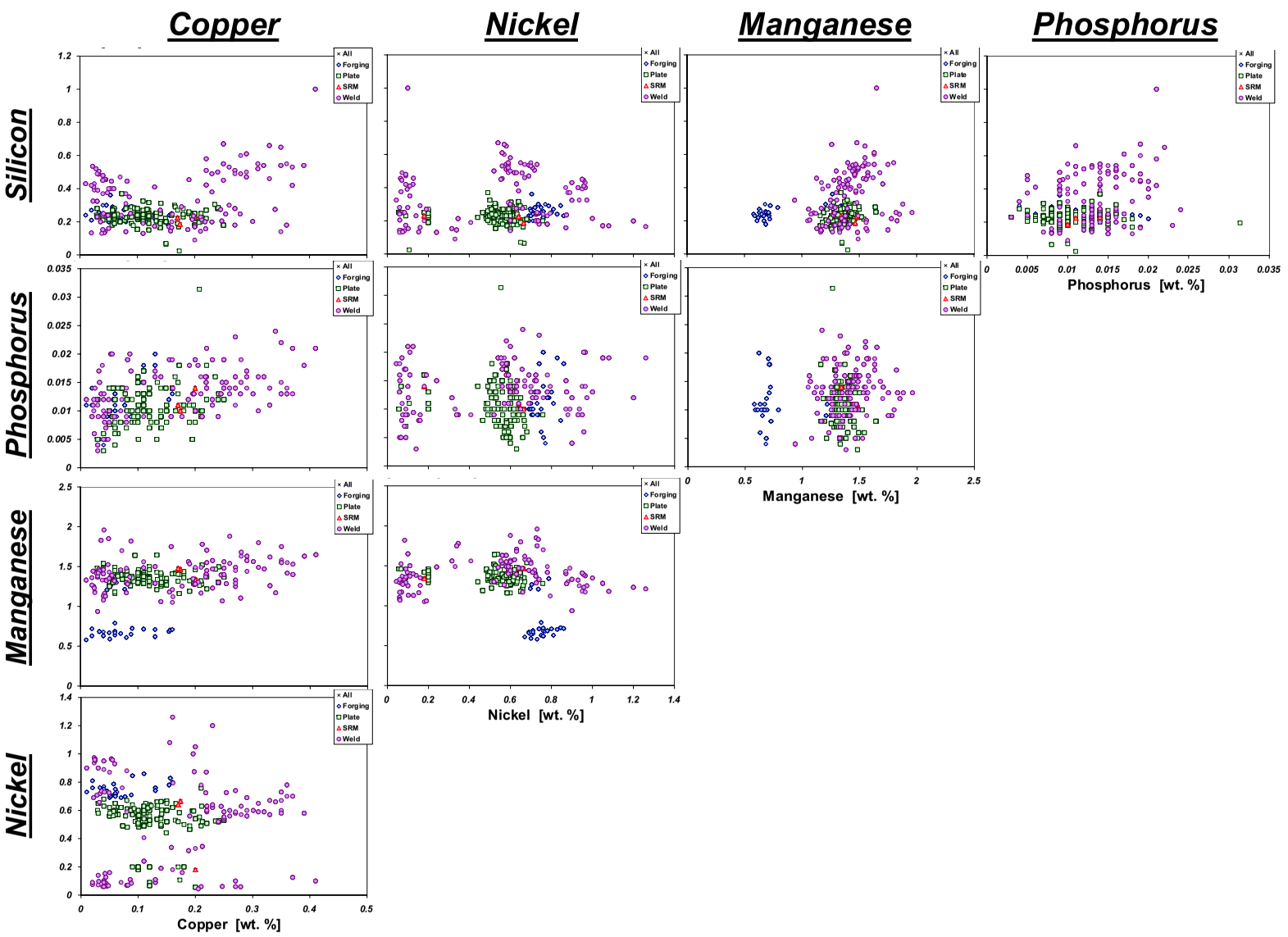

Figure 4-21. Variation of composition variables within the surveillance database.

4.2.3 Fit of the Matrix Damage Term

This section describes a fit of the MD term, Eq. 4-3, which is repeated below for ease of reference. This equation is fit to the 247 records in the US-LWR surveillance database having Cu ≤0.07 wt-%.

Eq. 4-3(repeated) $$\Delta T_{30(MD)} = PF \cdot CF \cdot TF \cdot \phi F \cdot \Phi F$$

where

$$PF = \left\{ \begin{array}{c} Weld \\ Plate \\ Forging \end{array} \right\} \qquad CF = \left[1 + A_1 \cdot Ni + A_2 \cdot Mn + A_3 \cdot P + A_4 \cdot Si + A_5 \cdot Cu\right]$$

$$TF = \left(\frac{T}{550}\right)^{E_{temp}} \qquad \phi F = \left(\frac{Log10(\phi)}{10.7}\right)^{E_{flux}} \qquad \Phi F = \Phi^{E_{fluence}}$$

Table 4.3 contains the coefficients and statistical assessments of the various models that were tried in the fitting process, while Figure 4-22 summarizes the statistical evaluation and classification of these fits. The fit ultimately developed as follows:

Model 1: Based on the physical insights summarized in Section 4.1.1, the first candidate fit had the following features:

- a product form coefficient that could be different for welds, plates, and forgings
- a chemistry factor that depends only on nickel content
- a dependence on temperature
- a dependence on flux
- a dependence on fluence that is fixed to $\sqrt{\Phi}$

As detailed in Table 4.3, this model has a T_{MAX} of 1.64 (making it provisional according to the model classification strategy described in Section 4.2.1); this value is controlled by the residual on phosphorus.

Model 2: Model 1 was modified by allowing the chemistry factor to depend on phosphorus, as well as nickel. As detailed in Table 4.3, this model has a T_{MAX} of 0.79, making it an acceptable model.

Models 3 and 3(2): Despite the strong evidence in the literature for a nickel effect on MD, the Model 2 chemistry factor for nickel in Table 4.3 is numerically small (0.03). This may be because the nickel content in the low-copper data only goes as high as 1 wt-%, as shown in Figure 4-23. Because of the weak nickel-dependence in the US-LWR low-copper database, the nickel term was removed in Model 3 and the model was re-calibrated. As detailed in Table 4.3, Model 3(2) has T_{MAX} and T_{TOTAL} values that are both less than those of Model 2.

Model 4: Model 3(2) was modified by allowing the fluence exponent to vary from the physically expected value of ½. The resulting best fit value was very close to ½. While Model 4 is classified as acceptable, it did not offer an empirical improvement over Model 3(2).

Models 5 and 5(2): Model 3(2) was modified by removing the effect of phosphorus from the chemistry factor. Model 5 was not optimized according to the T_{TOTAL} criteria of Eq. 4-7, whereas Model 5(2) was. Model 5 is provisional, with the $T_{m(P)}$ value being the highest and near statistical significance at 1.72. Distribution of the model errors over all of the regressor variables using the T_{TOTAL} criteria produced Model 5(2), which is unacceptable because it has statistically significant residual trends for phosphorus.

Models 6 and 7: These models both start from Model 3(2) but have (respectively) the effects of flux and temperature removed. After distribution of the model errors over all of the regressor variables using the T_{TOTAL} criteria, both models are seen to be unacceptable, having statistically significant residual trends.

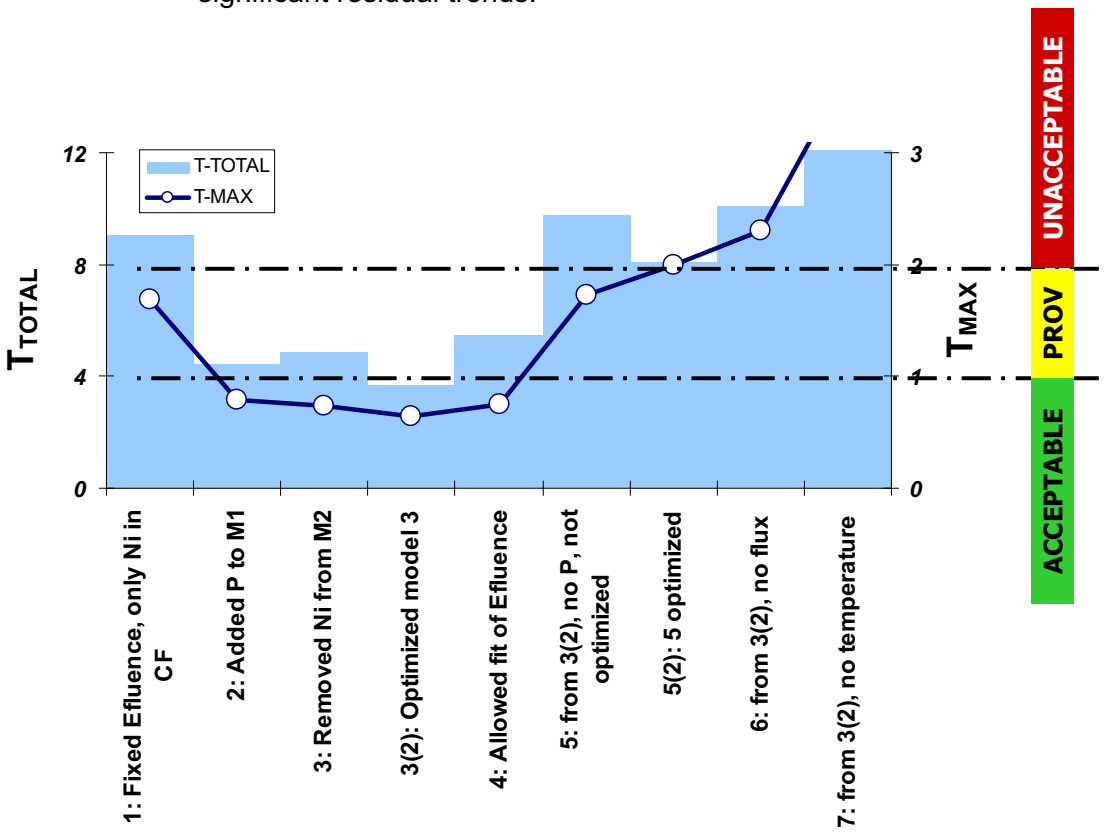

Figure 4-22. Statistical evaluation and classification of MD fits.

Based on this analysis, Model 3(2) was selected as the candidate matrix damage model. Model 3(2) has product form, flux, fluence, and temperature effects, as well as an effect of phosphorus. The following list summarizes Model 3(2) and provides an assessment of its trends relative to expectations:

- The dependence on fluence is fixed at the theoretical exponent of ½, with the empirical evidence in the US-LWR database providing strong support for this value.
- The temperature and flux effects in Model 3(2) are in the correct direction (i.e., lower values of flux and temperature are both seen to increases ΔT_{30}).

- As shown in Figure 4-24, the magnitude of the flux effect (E_{flux}=-3.46) is in good agreement with the IVAR data for low-copper materials.
- Figure 4-25 shows that the temperature effect in the LWR surveillance data is much larger than that reported in the literature. (The literature data support a value of E_{temp} of ≈-4, whereas Model 3(2) has a calibrated value of -14.6).
- Model 3(2) contains a phosphorous effect that, while difficult to see in the experimental data of the US-LWR database is nevertheless included in many embrittlement trend curves.
- Model 3(2) does not contain the expected and easily seen (in other empirical data) effect of nickel on matrix damage, perhaps due to the limited range of Ni in the low copper US-LWR database.

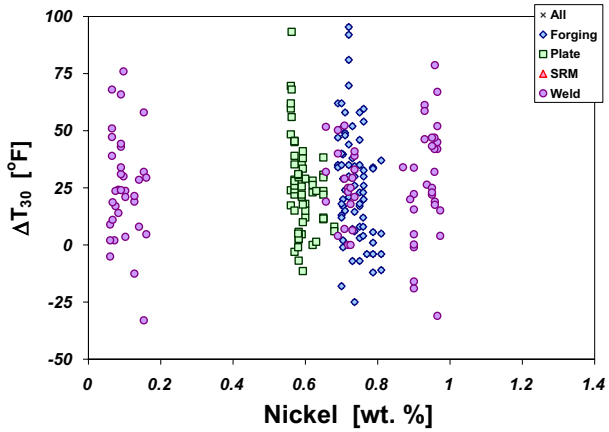

Figure 4-23. Variation of nickel content, and its effect on ΔT_{30}, in the low-copper portion of the US-LWR surveillance database

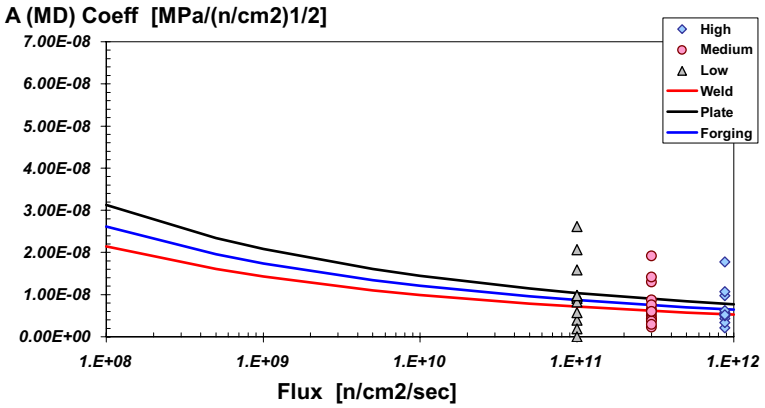

X-axis	Transform with square root?	FALSE
X-axis	Flux [n/cm2/sec]	7
Y-axis	A (MD) Coeff [MPa/(n/cm2)1/2]	8

Axis Code	Axis Lable	Min	Max
1	Copper [wt. %]	0	0.07
2	Nickel [wt. %]	0	1000
3	Manganese [wt. %]	0	1000
4	Phosphorus [wt. %]	0	0.02
5	Silicon [wt. %]	0	1000
6	Temperature [C]	290	291
7	Flux [n/cm^2/sec]		
8	A (MD) Coeff [MPa/(n/cm^2)$^{1/2}$]		
9	B (CRP) Coeff [MPa]		
10	Φ_{SAT} [n/cm^2]		
	Flux range to plot	ALL	
	Number of shift values fit	3	

Figure 4-24. Comparison of the Model 3(2) flux effect (curves) with the low-copper portion of the PVAR database (points). Comparison made over the flux range of the US-LWR surveillance database.

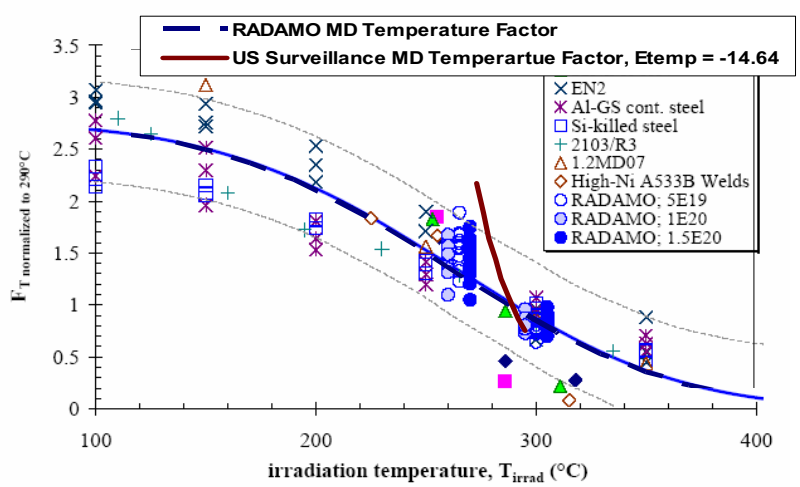

Figure 4-25. Comparison of the Model 3(2) temperature dependence (solid curve, shown only over the temperature range of the US-LWR surveillance database) with the temperature trend reported for the RADAMO database [Chaouadi 05a].

Table 4.3. Candidate fits of the US-LWR database to the MD equation. Models not part of the path to the final model appear in italics.

Model ID	Label	MD-1	MD-2	MD-3	MD-3(2)	*MD-4*	*MD-5*	*MD-5(2)*	*MD-6*	*MD-7*
	Action	Fixed $E_{fluence}$, only Ni in CF	Added P to M1	Removed Ni from M2	Optimized model 3	*From M3(2), fit $E_{fluence}$*	*from M3(2), no P, not optimized*	*5 optimized*	*from M3(2), no flux*	*from M3(2), no temperature*
Stats	Std Error	18.72	18.43	18.42	18.47	*18.40*	*18.72*	*18.81*	*18.57*	*19.37*
	T_{TOTAL}	9.04	4.47	4.89	3.71	*5.46*	*9.75*	*8.11*	*10.05*	*17.51*
	T_{MAX}	1.68	0.79	0.73	0.64	*0.75*	*1.72*	*2.00*	*2.30*	*3.73*
	Classification	P	A	A	A	*A*	*P*	*U*	*U*	*U*
	n	247	247	247	247	*247*	*247*	*247*	*247*	*247*
Fit Coefficients	$E_{fluence}$	0.5	0.5	0.5	0.5	*0.5006*	*0.5*	*0.5*	*0.5*	*0.5*
	E_{temp}	-13.458	-13.839	-13.839	-14.641	*-14.570*	*-15.900*	*-16.095*	*-16.000*	*0*
	E_{flux}	-3.804	-3.609	-3.609	-3.461	*-3.150*	*-2.850*	*-3.497*	*0*	*-7.123*
	Weld ($*10^9$)	8.277	6.734	6.734	6.661	*6.400*	*8.770*	*8.428*	*6.550*	*5.620*
	Plate & SRM ($*10^9$)	8.904	7.915	7.915	8.097	*7.200*	*9.500*	*10.086*	*7.370*	*6.335*
	Forging ($*10^9$)	6.181	4.956	4.956	4.755	*4.755*	*6.250*	*5.828*	*4.550*	*5.551*
	CF-Ni	0.16	0.03	0	0	*0*	*0*	*0*	*0*	*0*
	CF-Mn	0	0	0	0	*0*	*0*	*0*	*0*	*0*
	CF-P	0	31.082	31.082	31.238	*34.000*	*0*	*0*	*31.238*	*55.041*
	CF-Si	0	0	0	0	*0*	*0*	*0*	*0*	*0*
	CF-Cu	0	0	0	0	*0*	*0*	*0*	*0*	*0*
Fit Assessment	Log10(Φ)	OK	OK	OK	OK	*OK*	*OK*	*OK*	*OK*	*>1*
	Log10(ϕ)	OK	OK	OK	OK	*OK*	*OK*	*OK*	*Signif*	*OK*
	Temperature	OK	OK	OK	OK	*OK*	*OK*	*OK*	*OK*	*Signif*
	Copper	>1	OK	OK	OK	*OK*	*OK*	*OK*	*OK*	*>1*
	Nickel	OK	OK	OK	OK	*OK*	*OK*	*OK*	*OK*	*OK*
	Pred TTS	OK	OK	OK	OK	*OK*	*OK*	*OK*	*>1*	*>1*
	Phos	>1	OK	OK	OK	*OK*	*>1*	*Signif*	*OK*	*OK*
	Mn	OK	OK	OK	OK	*OK*	*OK*	*OK*	*OK*	*OK*
	Product Form	OK	OK	OK	OK	*OK*	*OK*	*OK*	*OK*	*OK*
T on Slope	Log10(Φ)	0.19	0.28	0.43	0.48	*0.24*	*0.17*	*0.78*	*0.71*	*1.59*
	Log10(ϕ)	0.45	0.46	0.44	0.38	*0.75*	*0.65*	*0.05*	*2.30*	*0.00*
	Temperature	0.03	0.01	0.12	0.00	*0.23*	*0.17*	*0.01*	*0.17*	*3.73*

Model ID	Label	MD-1	MD-2	MD-3	MD-3(2)	*MD-4*	*MD-5*	*MD-5(2)*	*MD-6*	*MD-7*
	Action	**Fixed $E_{fluence}$, only Ni in CF**	**Added P to M1**	**Removed Ni from M2**	**Optimized model 3**	***From M3(2), fit $E_{fluence}$***	***from M3(2), no P, not optimized***	***5 optimized***	***from M3(2), no flux***	***from M3(2), no temperature***
	Copper	1.05	0.68	0.73	0.64	*0.75*	*0.99*	*0.89*	*0.36*	*1.29*
	Nickel	0.25	0.14	0.01	0.01	*0.19*	*0.34*	*0.43*	*0.10*	*0.60*
	Pred TTS	0.00	0.00	0.20	0.00	*0.00*	*0.19*	*0.02*	*1.07*	*1.00*
	Phos	1.64	0.15	0.20	0.24	*0.12*	*1.72*	*2.00*	*0.19*	*0.12*
	Mn	0.80	0.20	0.19	0.00	*0.47*	*0.67*	*0.18*	*0.44*	*0.72*
	Product Form	0.02	0.00	0.04	0.00	*0.04*	*0.15*	*0.00*	*0.00*	*0.00*
T on Intercept	**Log10(Φ)**	0.42	0.50	0.40	0.39	*0.12*	*0.04*	*0.14*	*0.54*	*1.21*
	Log10(ϕ)	0.21	0.22	0.35	0.32	*0.72*	*0.69*	*0.36*	*2.06*	*0.00*
	Temperature	0.03	0.00	0.12	0.00	*0.23*	*0.17*	*0.00*	*0.17*	*3.73*
	Copper	1.13	0.79	0.73	0.62	*0.68*	*0.86*	*0.62*	*0.34*	*1.22*
	Nickel	0.07	0.04	0.03	0.00	*0.21*	*0.22*	*0.13*	*0.09*	*0.56*
	Pred TTS	0.19	0.21	0.23	0.02	*0.05*	*0.29*	*0.31*	*0.93*	*0.92*
	Phos	1.68	0.30	0.22	0.23	*0.15*	*1.52*	*1.62*	*0.17*	*0.11*
	Mn	0.88	0.31	0.21	0.00	*0.43*	*0.58*	*0.00*	*0.42*	*0.70*
	Product Form	0.02	0.07	0.16	0.21	*0.06*	*0.22*	*0.36*	*0.00*	*0.00*
T Quad	**PF Quad**	0.00	0.11	0.06	0.17	*0.04*	*0.12*	*0.21*	*0.00*	*0.00*
T Si	**Slope**	#N/A	#N/A	#N/A	1.57	*#N/A*	*#N/A*	*#N/A*	*#N/A*	*#N/A*
	Intercept	#N/A	#N/A	#N/A	1.42	*#N/A*	*#N/A*	*#N/A*	*#N/A*	*#N/A*

4.2.4 Fit of the Copper-Rich Precipitate Term

This section describes a fit of the MD term, Eq. 4-4, which is repeated below for ease of reference. This equation is fit to the 689 records in the US-LWR surveillance database having Cu >0.07 wt-%.

Eq. 4-4(repeated) $\Delta T_{30(CRP)} = PF \cdot CF \cdot TF \cdot \Phi F$

where

$$PF = \left\{ \begin{array}{c} Weld \\ Plate \\ Forging \end{array} \right\}$$

$$CF = \left[1 + f(Cu) + B_2 \cdot Ni + B_3 \cdot MIN\left\{Cu_{\max}, MAX(0, Cu - Cu_{\min})\right\} \cdot Ni + B_4 \cdot Mn + B_5 \cdot P + B_6 \cdot Si\right]$$

where $f(Cu) = B_{1b} + B_{1m} \cdot Cu^{E_{Cu}}$, subject to $0 \le f(Cu) \le B_{Cu(max)}$

$$TF = \left(\frac{T}{550}\right)^{E_{temp}}$$

$$\Phi F = \left\{1 - \exp\left(\frac{-\Phi}{\Phi_{SAT}}\right)\right\}$$

where $\Phi_{SAT} = C_0 + C_1 \cdot Ni + C_2 \cdot \left(\frac{Log_{10}(\phi)}{10.7}\right) + C_3(Cu - Cu_{\min}) + C_4 \cdot Mn + C_5 \cdot P + C_6 \cdot Si$

Table 4.4 contains the coefficients and statistical assessments of the various models that were tried in the fitting process, while Figure 4-26 summarizes the statistical evaluation and classification of these fits. The fit ultimately developed as follows:

Model 1 to 1(3): Based on the physical insights and other information summarized in Section 4.1.2, the first candidate fit had the following features:

- The product form coefficient could be different for welds, plates, and forgings,
- The chemistry factor depends only on copper, nickel, and a copper*nickel product. (This latter term was motivated by insights from preliminary modeling efforts). The magnitude of the chemistry factor scales with √Cu up to a maximum value that can be fit, but is not imposed in this model.
- Only steels having a copper content above some minimum value (in this model held fixed at 0.07 wt-%.) experience CRP, consistent with the MD model developed in Section 4.2.3.
- The saturation fluence is allowed to depend on both flux and nickel content, consistent with the data presented in Figure 4-13 and Figure 4-16.

As detailed in Table 4.4, after several different trials with various starting guesses, this model remains unacceptable, having a T_{MAX} value that always exceeds 1.97.

Model 2: Model 1(3) was modified by adding a temperature term. While successful in eliminating the statistical significance of the residual trend *vs*. temperature [which was the largest in Model 1(3)], overall this model remains unacceptable because the T_{MAX} value always exceeds 1.97.

Model 3: Model 2 was modified by eliminating the nickel effect on Φ_{SAT}. While successful in reducing the significance of the residual trend *vs*. nickel, overall this model remains unacceptable because the T_{MAX} value always exceeds 1.97.

Models 4 to 4(3): Model 3 was modified with the aim of eliminating the statistically significant trend *vs*. copper (the only residual trend that was not acceptable in Model 3) by allowing two copper-related coefficients to be fit rather than prescribed (Cu_{min} and the copper exponent) and by allowing Φ_{SAT} to vary with copper content. After several different initial guesses, an acceptable model, Model 4(3) was achieved with a T_{MAX} value of 0.62.

Model 5: Model 4(3) was simplified by eliminating the effect of flux on Φ_{SAT}. Model 5 is acceptable, with a T_{MAX} value of 0.85.

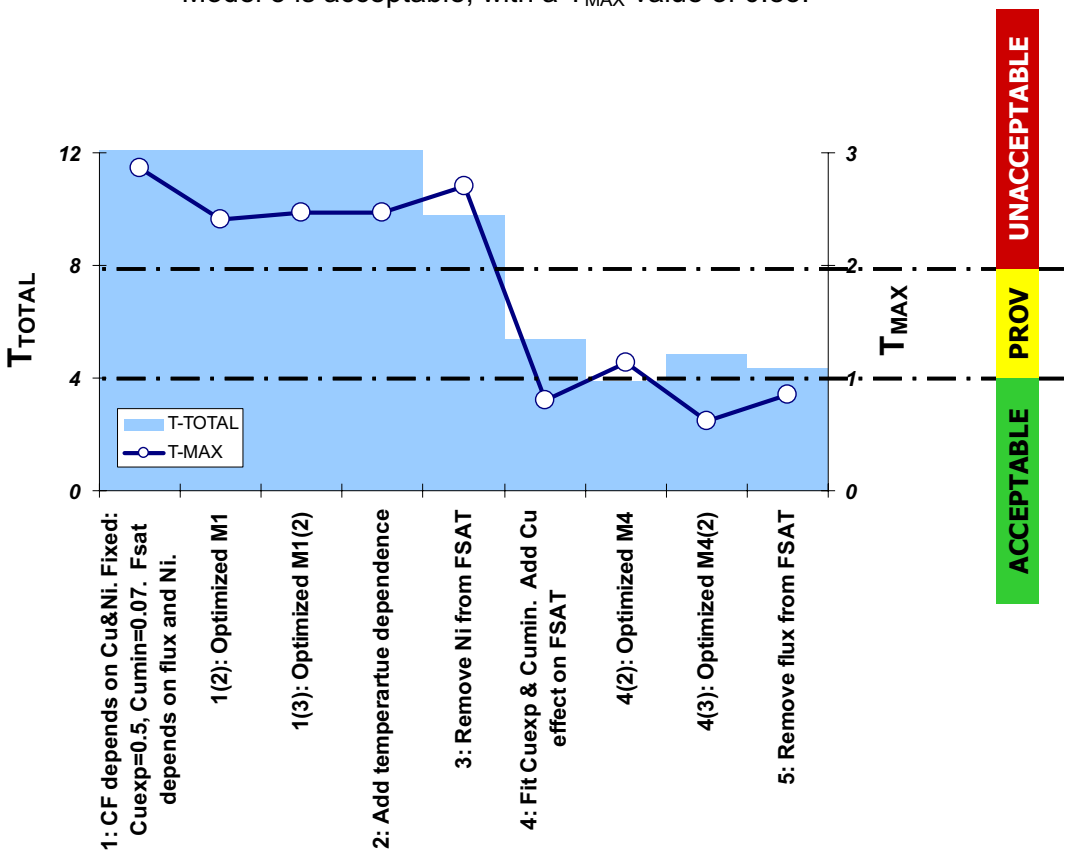

Figure 4-26. Statistical evaluation and classification of CRP fits.

While Model 5 should have been selected as the baseline CRP model, it was only realized after the combined models described in Section 4.2.5 had been developed based on Model 4(3) that Model 5 existed. It may, however, be noted that, like Model 5, the combined model recommended in Section 4.2.5 also has no effect of flux on Φ_{SAT}. It is, therefore, believed that this deviation from our modeling protocol did not have a significant effect on the final outcome.

Model 4(3), which was selected as the candidate CRP model to take forward to the combined analysis, has an embrittlement magnitude that depends on product form, copper, and nickel. The fluence at which CRP saturation occurs depends on both flux and copper content. The

following list summarizes Model 4(3) and provides an assessment of its trends relative to expectations:

- The dependence of CRP embrittlement magnitude on copper and nickel alone is as expected based on the information summarized in Sections 4.1.2.1 and 4.1.2.4.
  - While a dependence of embrittlement magnitude on $\sqrt{Cu}$ was expected theoretically, we did not find it possible to enforce this dependence and establish a fit without statistically significant prediction residuals vs. copper. However, the best-fit exponent for copper, 0.6, is reasonably close to the expected value of 0.5.
  - The minimum copper value for CRP precipitation was determined to be 0.083 (by fitting the LWR data). This value is in the range of values reported in the literature (see information summarized in Section 4.1.2.1).
  - It was not necessary to impose a maximum copper value on the f(Cu) function to achieve a statistically acceptable fit. This may be because of the limited number of data records that have copper values above the typically reported maximum copper value of $\approx$0.3 wt-%.
  - Overall, there is reasonable agreement between the magnitude of the CRP term in Model 4(3) and the information found in both the IVAR and RADAMO databases (see Figure 4-27).
- The slight dependence of CRP embrittlement magnitude on temperature was foreseen based on the IVAR data (see Chapter 2 of Appendix A) but, otherwise, has not been reported in the literature.
- Model 4(3) suggests that the saturation fluence, Φ_{SAT}, depends on copper, is weakly dependent on flux, and does not depend on nickel. This lack of dependence on nickel was unexpected based on the literature information summarized in Section 4.1.2.4, as was the dependence on copper. While small flux effects on Φ_{SAT} can be discerned for very limited ranges of composition, it is perhaps not surprising that these effects cannot be resolved relative to the scatter of the US-LWR database. The comparison of the calibrated Φ_{SAT} range from Models 4(3) and 5 to the IVAR data in Figure 4-28 suggests that the average calibrated value may be a bit high for the flux and nickel ranges of concern to LWR service.

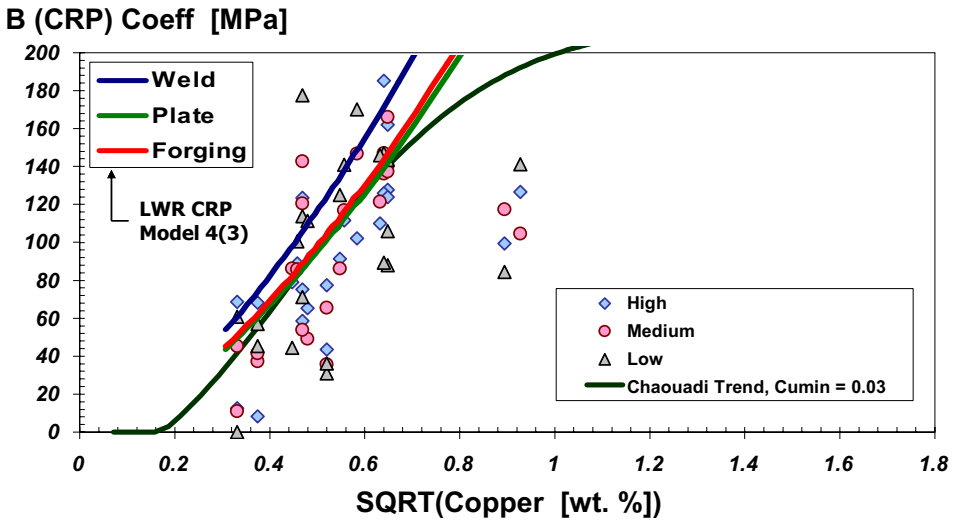

Figure 4-27. Comparison of the predictions of CRP Model 4(3) with the IVAR database and with the trend reported by Chaouadi based on the RADAMO data [Chaouadi 05a]. The IVAR data and the Model 4(3) trends are for normal Ni levels (0.5 to 1.0 wt-%) and an irradiation temperature of ≈550 °F.

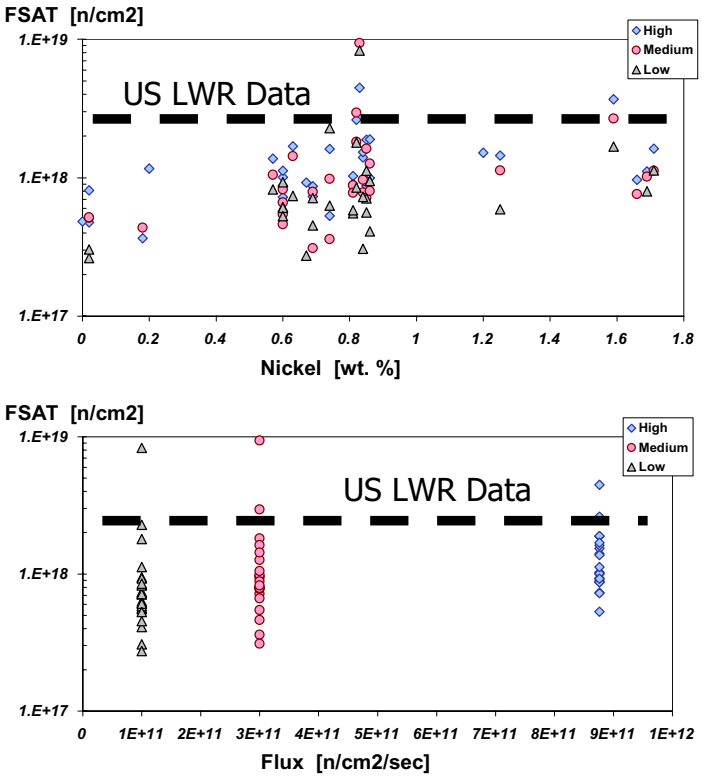

Figure 4-28. Comparison of the calibrated range for Φ_{SAT} from CRP Models 4(3) and (5) with the IVAR database.

Table 4.4. Candidate fits of the US-LWR database to the CRP equation. Models not on the path to the final model appear in italics

Model ID	Label	CRP-1	CRP-1(2)	CRP-1(3)	CRP-2	CRP-3	CRP-4	CRP-4(2)	CRP-4(3)	*CRP-5*
	Action	Starting model	Change red coefficients & optimize	Change red coefficients & optimize	Introduce E_{temp}, change red coefficients & optimize	Remove Ni effect on Φ_{SAT}, change red coefficients & optimize	Allowed Cu_{min} & Cu exponent to be fit introduced Cu effect on Φ_{SAT}, changed red variables & optimized	Change red coefficients & optimize	Change red coefficients, did not optimize	*Removed flux from Φ_{SAT}, changed red coefficients & optimized*
Stats	Std Error	26.34	26.59	26.66	26.28	26.15	25.66	25.69	25.68	*25.67*
	T_{TOTAL}	21.27	15.85	16.98	12.82	9.79	5.39	3.89	4.83	*4.33*
	T_{MAX}	2.87	2.40	2.47	2.47	2.70	0.80	1.14	0.62	*0.85*
	Classification	U	U	U	U	U	A	P	A	*A*
	N	689	689	689	689	689	689	689	689	*689*
Fit Coefficients	Weld	0.227	0.225	0.209	0.186	0.177	0.181	0.182	0.181	*0.181*
	Plate & SRM	0.142	0.135	0.124	0.112	0.111	0.132	0.133	0.132	*0.133*
	Forging	0.122	0.115	0.108	0.097	0.093	0.113	0.113	0.113	*0.113*
	Cu exponent	0.5	0.5	0.5	0.5	0.5	0.6003	0.6003	0.6003	*0.6003*
	Cu_{min}	0.07	0.07	0.07	0.07	0.07	0.083	0.082	0.083	*0.082*
	Cu: B_{1m}	1100	1100	1225	1400	1400	1400	1400	1400	*1400*
	Cu: $B_{Cu(max)}$	1000	1000	1000	1000	1000	1000	1000	1000	*1000*
	Ni: B_2	430	430	462	500	500	500	500	500	*500*
	Cu*Ni: B_3	1200	1200	1200	1200	1500	1500	1500	1500	*1500*
	Mn: B_4	0	0	0	0	0	0	0	0	*0*
	P: B_5	0	0	0	0	0	0	0	0	*0*
	Si: B_6	0	0	0	0	0	0	0	0	*0*
	Φ_{SAT}: C_0	10.0	16.5	16.5	16.5	22.0	25.0	25.0	26.0	*28.0*
	Φ_{SAT}: ϕ: C_2	2.02	2.02	2.02	2.02	2.02	2.02	4.00	2.02	*0*
	Φ_{SAT}: Ni: C_1	9.01	9.01	9.01	9.01	0	0	0	0	*0*
	Φ_{SAT}: Mn: C_4	0	0	0	0	0	0	0	0	*0*

Model ID	Label	CRP-1	CRP-1(2)	CRP-1(3)	CRP-2	CRP-3	CRP-4	CRP-4(2)	CRP-4(3)	*CRP-5*
	Action	Starting model	Change red coefficients & optimize	Change red coefficients & optimize	Introduce E_{temp}, change red coefficients & optimize	Remove Ni effect on Φ_{SAT}, change red coefficients & optimize	Allowed Cu_{min} & Cu exponent to be fit introduced Cu effect on Φ_{SAT}, changed red variables & optimized	Change red coefficients & optimize	Change red coefficients, did not optimize	*Removed flux from Φ_{SAT}, changed red coefficients & optimized*
	Φ_{SAT}: Cu : C_3	0	0	0	0	0	-40	-40	-40	*-40*
	Φ_{SAT}: P : C_5	0	0	0	0	0	0	0	0	*0*
	Φ_{SAT}: Si : C_6	0	0	0	0	0	0	0	0	*0*
	Etemp	0	0	0	-2.20	-2.20	-2.20	-2.00	-2.00	*-2.00*
Fit Assessment	Log10(Φ)	>1	OK	OK	OK	OK	OK	OK	OK	*OK*
	Log10(ϕ)	OK	OK	OK	OK	OK	OK	OK	OK	*OK*
	Temperature	Signif	Signif	Signif	OK	OK	OK	OK	OK	*OK*
	Copper	Signif	Signif	>1	Signif	Signif	OK	OK	OK	*OK*
	Nickel	>1	>1	>1	>1	OK	OK	OK	OK	*OK*
	Pred TTS	Signif	OK	OK	OK	OK	OK	>1	OK	*OK*
	Phos	>1	>1	>1	>1	OK	OK	OK	OK	*OK*
	Mn	OK	OK	OK	OK	OK	OK	OK	OK	*OK*
	Product Form	>1	>1	>1	>1	OK	OK	OK	OK	*OK*
T on Slope	Log10(Φ)	1.15	0.01	0.00	0.02	0.00	0.76	0.13	0.55	*0.50*
	Log10(ϕ)	0.01	0.17	0.16	0.05	0.00	0.34	0.01	0.28	*0.25*
	Temperature	2.26	2.40	2.47	0.06	0.17	0.27	0.09	0.00	*0.00*
	Copper	0.86	2.07	1.92	2.38	2.66	0.09	0.00	0.19	*0.04*
	Nickel	0.22	0.99	1.28	1.50	0.60	0.00	0.19	0.20	*0.12*
	Pred TTS	0.14	0.00	0.00	0.00	0.00	0.77	1.14	0.62	*0.85*
	Phos	1.88	1.19	1.39	1.19	0.75	0.37	0.16	0.18	*0.30*
	Mn	0.22	0.03	0.08	0.00	0.01	0.16	0.15	0.05	*0.13*
	Product Form	1.05	0.71	0.81	0.75	0.36	0.02	0.04	0.23	*0.04*
T on Intercept	Log10(Φ)	1.34	0.01	0.01	0.01	0.02	0.80	0.16	0.58	*0.54*
	Log10(ϕ)	0.29	0.14	0.14	0.01	0.04	0.41	0.07	0.32	*0.30*
	Temperature	2.16	2.39	2.46	0.05	0.18	0.29	0.07	0.01	*0.02*

Model ID	Label	CRP-1	CRP-1(2)	CRP-1(3)	CRP-2	CRP-3	CRP-4	CRP-4(2)	CRP-4(3)	*CRP-5*
	Action	**Starting model**	**Change red coefficients & optimize**	**Change red coefficients & optimize**	**Introduce E_{temp}, change red coefficients & optimize**	**Remove Ni effect on Φ_{SAT}, change red coefficients & optimize**	**Allowed Cu_{min} & Cu exponent to be fit introduced Cu effect on Φ_{SAT}, changed red variables & optimized**	**Change red coefficients & optimize**	**Change red coefficients, did not optimize**	***Removed flux from Φ_{SAT}, changed red coefficients & optimized***
	Copper	2.87	2.10	1.95	2.47	2.70	0.40	0.36	0.43	*0.35*
	Nickel	1.83	1.10	1.36	1.66	0.80	0.47	0.53	0.44	*0.48*
	Pred TTS	2.63	0.23	0.22	0.34	0.31	0.06	0.53	0.22	*0.26*
	Phos	0.24	1.00	1.20	0.94	0.53	0.01	0.11	0.02	*0.00*
	Mn	0.70	0.11	0.16	0.12	0.12	0.06	0.01	0.06	*0.04*
	Product Form	0.00	0.14	0.19	0.25	0.00	0.00	0.02	0.13	*0.00*
T Quad	**PF Quad**	1.42	1.05	1.18	1.02	0.55	0.11	0.13	0.33	*0.12*
T Si	**Slope**	#N/A	#N/A	#N/A	#N/A	#N/A	#N/A	#N/A	1.08	*#N/A*
	Intercept	#N/A	#N/A	#N/A	#N/A	#N/A	#N/A	#N/A	0.71	*#N/A*
Note: The (SAT coefficients in this table should all be multiplied by 10^{17}.										

4.2.5 Combination of MD and CRP Terms

The starting point for the combined model is MD Model 3(2) and CRP Model 4(3). Table 4.5 contains the coefficients and statistical assessments of the various models that were tried in the fitting process, while Figure 4-29 summarizes the statistical evaluation and classification of these fits. The fit ultimately developed as follows:

Model 1 and 1(2): Model 1 combines MD Model 3(2) and CRP Model 4(3); this combined model was optimized using *solver* to create Model 1(2). Both of these models are acceptable as they have T_{MAX} values below 1.

Model 2 and 2(2): Model 1(2) was simplified by removing the copper effect from Φ_{SAT}. After one iteration an acceptable version of this model, Model 2(2), was achieved.

Model 3 and 3(2): Model 2(2) was simplified by removing the flux effect from Φ_{SAT}. After one iteration an acceptable version of this model, Model 3(2), was achieved.

Model 4: Model 3(2) was simplified by shifting all of the temperature effect into the MD term. The resulting model, Model 4, was classified as provisional, but was not used because this approach increases the magnitude of the E_{temp} coefficient in the MD term. This increase moves E_{temp} further from the value of -4 suggested by the literature data. For this reason, Model 4 was not further pursued.

Other simplifications of the combined Model 3(2) were attempted, including removal (one at a time) of both phosphorus and flux from the MD term. These removals created unacceptable models with residuals that were difficult to null out by simple adjustment of a limited number of model parameters. These simplification attempts were, therefore, abandoned.

Model 3(2) was selected as the best combined model based on this modelling strategy. Table 4.5 provides rounded parameters for use in Model 3(2), and demonstrates that Model 3(2) does not have any statistically significant residuals with respect to silicon.

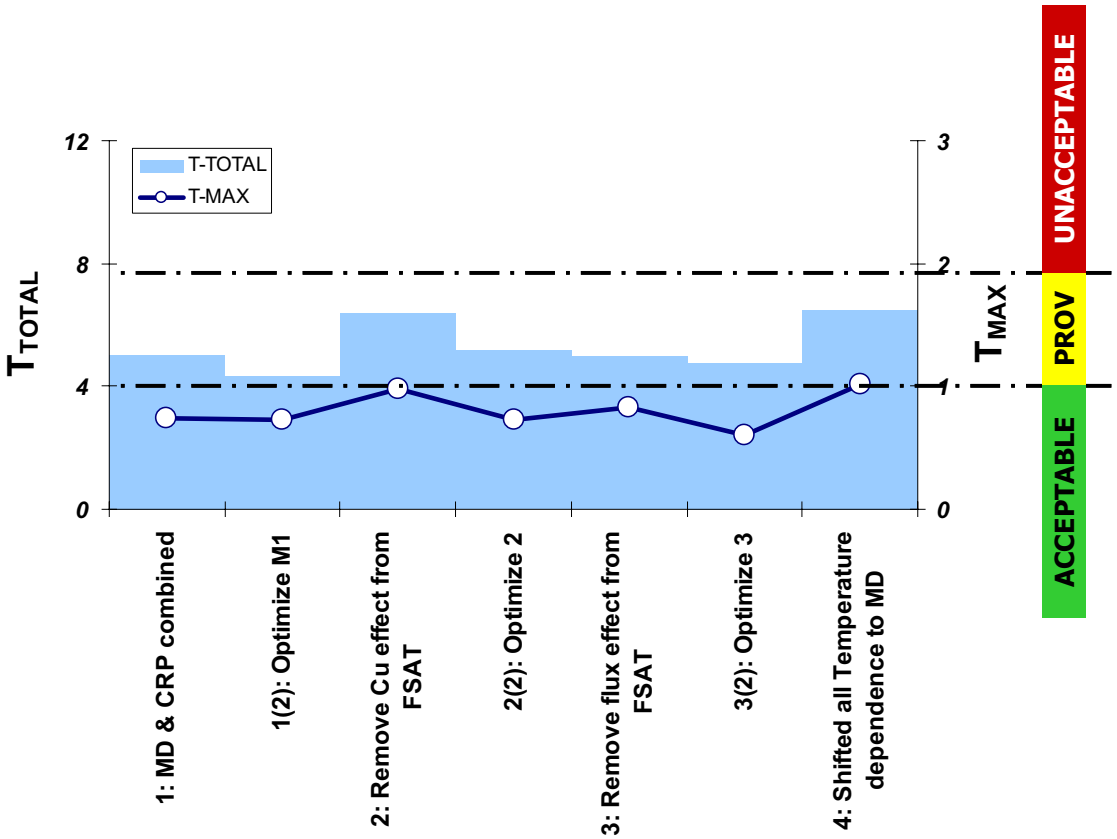

Figure 4-29. Statistical evaluation and classification of combined fits.

Table 4.5. Candidate fits of the US-LWR database to the combined MD and CRP equations. Models not on the path to the final model appear in italics

Model ID	Label	CM-1	CM-1(2)	CM-2	CM-2(2)	CM-3	CM-3(2)	*CM-4*	CM-3(2)
	Action	**Models MD 3(2) and CRP 4(3) combined, not optimized**	**M0 Optimized**	**Removed Cu effect from Φ_{SAT}, adjusted Φ_{SAT}** constant, & optimized	adjusted (SAT constant, & optimized	Removed flux effect on (SAT, adjusted (SAT constant, & optimized	Changed (SAT & Etemp(CRP) & did not optimize	Shifted all T-dependence in M3(2) to MD & optimized	Same as 3(2), Rounded coefficients
Stats	Std Error	23.97	23.98	23.93	23.94	23.95	23.96	*24.25*	23.96
	T_{TOTAL}	5.03	4.30	6.39	5.19	4.99	4.79	*6.48*	4.74
	T_{MAX}	0.74	0.73	0.98	0.73	0.83	0.60	*1.01*	0.66
	Classification	A	A	A	A	A	A	*P*	A
	n	936	936	936	936	936	936	*936*	936
Fit Coefficients - CRP	**Weld**	0.181	0.183	0.185	0.186	0.186	0.186	*0.188*	0.186
	Plate & SRM	0.132	0.134	0.133	0.132	0.132	0.132	*0.131*	0.132
	Forging	0.113	0.116	0.113	0.111	0.111	0.111	*0.111*	0.111
	Cu exponent	0.6003	0.6004	0.6004	0.6004	0.6005	0.6005	*0.6005*	0.6
	Cu_{min}	0.0829	0.0870	0.0860	0.0856	0.0852	0.0852	*0.0846*	0.085
	Cu: B_{1m}	1400	1400	1400	1400	1400	1400	*1400*	1400
	Cu: $B_{Cu(max)}$	1000	1000	1000	1000	1000	1000	*1000*	1000
	Ni: B_2	500	500	500	500	500	500	*500*	500
	Cu*Ni: B_3	1500	1500	1500	1500	1500	1500	*1500*	1500
	Mn: B_4	0	0	0	0	0	0	*0*	0
	P: B_5	0	0	0	0	0	0	*0*	0
	Si: B_6	0	0	0	0	0	0	*0*	0
	Φ_{SAT}: C_0	26.0	26.0	20.0	21.4	23.9	23.8	*23.8*	23.8
	Φ_{SAT}: ϕ: C_2	2.0	2.0	2.0	2.0	0	0	*0*	0
	Φ_{SAT}: Ni: C_1	0	0	0	0	0	0	*0*	0

	Φ_{SAT}: Mn: C_4	0	0	0	0	0	0	*0*	0
	Φ_{SAT}: Cu : C_3	-40	-40	0	0	0	0	*0*	0
	Φ_{SAT}: P : C_3	0	0	0	0	0	0	*0*	0
	Φ_{SAT}: Si : C_3	0	0	0	0	0	0	*0*	0
	Etemp	-2.00	-2.00	-2.00	-2.00	-2.00	-1.75	*0*	-1.75
Fit Coefficients - MD	Efluence	0.5	0.5	0.5	0.5	0.5	0.5	*0.5*	0.5
	Etemp	-14.64	-14.64	-14.64	-14.64	-14.64	-14.64	*-16.90*	-14.64
	E-Flux	-3.46	-3.46	-3.46	-3.46	-3.46	-3.46	*-3.46*	-3.46
	Weld (*10^9)	6.661	6.661	6.661	6.661	6.661	6.661	*6.661*	6.661
	Plate & SRM (*10^9)	8.097	8.097	8.097	8.097	8.097	8.097	*8.097*	8.097
	Forging (*10^9)	4.755	4.755	4.755	4.755	4.755	4.755	*4.755*	4.755
	CF-Ni	0	0	0	0	0	0	*0*	0
	CF-Mn	0	0	0	0	0	0	*0*	0
	CF-P	31.24	31.24	31.24	31.24	31.24	31.24	*31.24*	31.24
	CF-Si	0	0	0	0	0	0	*0*	0
	CF-Cu	0	0	0	0	0	0	*0*	0
Fit Assessment	Log10(Φ)	OK	OK	OK	OK	OK	OK	*OK*	OK
	Log10(ϕ)	OK	OK	OK	OK	OK	OK	*OK*	OK
	Temperature	OK	OK	OK	OK	OK	OK	*OK*	OK
	Copper	OK	OK	OK	OK	OK	OK	*OK*	OK
	Nickel	OK	OK	OK	OK	OK	OK	*OK*	OK
	Pred TTS	OK	OK	OK	OK	OK	OK	*>1*	OK
	Phos	OK	OK	OK	OK	OK	OK	*OK*	OK
	Mn	OK	OK	OK	OK	OK	OK	*OK*	OK
	Product Form	OK	OK	OK	OK	OK	OK	*OK*	OK
T on Slope	Log10(Φ)	0.63	0.73	0.95	0.62	0.49	0.55	*0.35*	0.52
	Log10(ϕ)	0.38	0.47	0.54	0.41	0.37	0.39	*0.47*	0.37
	Temperature	0.10	0.02	0.33	0.19	0.17	0.09	*0.39*	0.06
	Copper	0.04	0.01	0.15	0.49	0.49	0.59	*0.39*	0.55
	Nickel	0.22	0.02	0.22	0.07	0.05	0.01	*0.30*	0.02
	Pred TTS	0.74	0.65	0.77	0.73	0.83	0.60	*1.01*	0.66
	Phos	0.19	0.08	0.25	0.00	0.00	0.04	*0.30*	0.05
	Mn	0.11	0.01	0.02	0.00	0.00	0.05	*0.00*	0.02
	Product Form	0.11	0.15	0.00	0.04	0.08	0.02	*0.00*	0.02

T on Intercept	**Log10(Φ)**	0.65	0.73	0.98	0.62	0.49	0.55	*0.38*	0.52
	Log10(ϕ)	0.41	0.47	0.58	0.41	0.37	0.39	*0.50*	0.37
	Temperature	0.11	0.02	0.35	0.19	0.17	0.09	*0.41*	0.06
	Copper	0.29	0.04	0.51	0.50	0.49	0.50	*0.67*	0.53
	Nickel	0.44	0.00	0.08	0.00	0.00	0.00	*0.53*	0.05
	Pred TTS	0.23	0.49	0.19	0.49	0.59	0.49	*0.43*	0.47
	Phos	0.02	0.05	0.00	0.05	0.04	0.04	*0.07*	0.08
	Mn	0.01	0.00	0.17	0.03	0.03	0.05	*0.13*	0.04
	Product Form	0.07	0.05	0.15	0.24	0.27	0.22	*0.06*	0.22
T Quad	**PF Quad**	0.28	0.29	0.15	0.11	0.05	0.11	*0.09*	0.13
T Si	**Slope**	#N/A	#N/A	#N/A	#N/A	#N/A	#N/A	*#N/A*	0.17
	Intercept	#N/A	#N/A	#N/A	#N/A	#N/A	#N/A	*#N/A*	0.17
Note: The Φ_{SAT} coefficients in this table should all be multiplied by 10^{17}.									

4.3 Comparison of Combined Model to Other Data

Based on the information presented in Section 4.2, combined Model 3(2), hereafter referred to as CM-3(2) (see Table 4.5), was identified as the best fit to the US-LWR surveillance database. This section includes an assessment of how well CM-3(2) represents the trends seen in four other databases, two of which have already been discussed in this report:

(1) RADAMO Database: As reported by [Chaouadi 05a]. All irradiations were performed in a test reactor.

(2) IVAR Database: As reported in Appendix B of this report. All irradiations were performed in a test reactor.

(3) JNES Databases: This database contains both surveillance and test reactor irradiations. These data were supplied to the NRC by the Japan Nuclear Energy Safety Organization [JNES 07].

(4) French Database: This database contains surveillance data from power reactors operated in France. These data were reported by Brillaud and Hedin in 1992 [Brillaud 92].

Figure 4-30 compares the exposure conditions of these databases with that of the US-LWR surveillance database. While measured fluxes are reported for all of the test reactor irradiations, they are not routinely reported for the surveillence irradiations where only information on fluence is available. Therefore, the fluxes reported in Figure 4-30 for the surveillence databases were approximated as the reported value of fluence divided by the reported time that the specimens were subjected to irradiation in the power reactor.

The scope of both the RADAMO and IVAR databases is much more extensive than the JNES and French databases. Consequently, RADAMO and IVAR are used in Section 4.3.1 to assess how well CM-3(2) represents conditions beyond its calibration. Insights arising from this comparison suggest possible revisions to CM-3(2). These revisions are attempted in Section 4.3.2 by again fitting the US-LWR surveillance database. Finally, Section 4.3.3 assesses the revised fit developed in Section 4.3.2 by comparing its trends to the data in all four databases listed above.

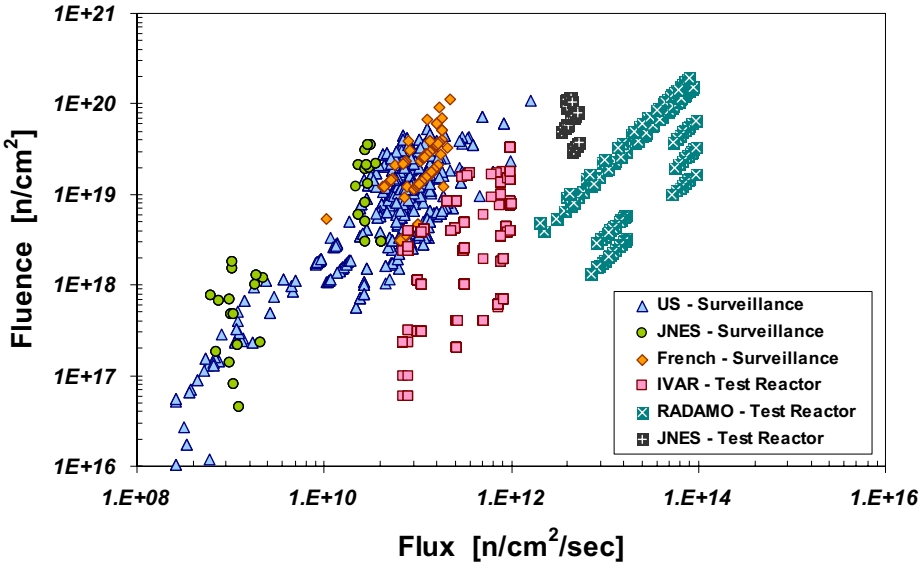

Figure 4-30. Exposure ranges for various embrittlement databases.

All four of these databases quantify the effects of irradiation embrittlement in terms of an increase in the room temperature yield strength; only the JNES and French databases also quantify irradiation embrittlement in terms of Charpy transition temperature shift. To enable comparison of the yield strength increase information in these databases to the values of ΔT_{30} predicted from CM-3(2), the following conversion was made:

Eq. 4-9 $$\Delta T_{30} = \beta \cdot \Delta YS$$

In Eq. 4-9, ΔT_{30} is expressed in °F, while ΔYS is expressed in MPa. The conversion constant β is as follows, based on data reported in [Kirk 01]:

Eq. 4-10 $$\beta = \begin{matrix} 1.242 & welds \\ 1.08 \ for & plates \\ 0.882 & forgings \end{matrix}$$

4.3.1 Initial Assessment

The method used to compare the predictions of CM-3(2) to the RADAMO and IVAR databases was as follows:

(1) A "data set" is identified as follows:

(a) In IVAR, a "data set" is composed of a particular alloy exposed at either a high, medium, or low flux. Only irradiations performed at 290 °C were included in this assessment. While the IVAR database includes information on irradiations performed at both 270 °C and 310 °C, at these temperatures, ΔYS data are available at only two different fluences. The limited data at 270 °C and 310 °C was judged to be an inadequate basis against which to assess CM-3(2).

(b) In RADAMO, a "data set" is composed of a particular alloy exposed at either 265 °C or 300 °C. (The RADAMO study did not include a controlled examination of flux effects.)

(2) The predicted variation of ΔT_{30} vs. fluence of CM-3(2), with uncertainty bounds, is overlaid on the measured values of ΔYS (scaled to ΔT_{30} using Eq. 4-9 and 4-10) *vs.* fluence.

(c) For IVAR, the measured ΔYS values represent the average of at least two measurements of irradiated yield strength for the alloy/flux combination being considered. Consequently, the ± uncertainty bounds added/subtracted to/from the mean prediction of CM-3(2) are estimated as follows:

Eq. 4-11 $$\Delta T_{30(uncertainty)} = 1.97\sqrt{\frac{\sigma}{2}}$$

The value of σ used in Eq. 4-11 is 18.5 °F for materials having Cu ≤0.083 wt-% and 26 °F for higher-copper materials. (See models MD-3(2) and CRP-4(3) in Table 4.3 and Table 4.4, respectively.)

(d) For RADAMO, the measured ΔYS values represent individual measurements of irradiated yield strength for the alloy/temperature combination being considered. Consequently, the ± uncertainty bounds added/subtracted to/from the mean prediction of CM-3(2) are estimated as follows:

Eq. 4-12 $$\Delta T_{30(uncertainty)} = 1.97\sigma$$

The σ values used in Eq. 4-12 are identical to those used in Eq. 4-11.

(e) As illustrated in Figure 4-31, the predictions of CM-3(2) are assessed as being high, OK, or low relative to the RADAMO and IVAR data. Because the aim of these comparisons is to assess broad ranges of conditions over which the predictions of CM-3(2) are (or are not) in acceptable accord with data, judgments were made on a case-by-case basis regarding the classification of, for example, situations where only one of several measured data lies outside of the uncertainty bounds. While every effort was made to be consistent, these judgments introduced a certain arbitrariness to the comparisons. For this reason, plots showing all of the comparisons can be found in Appendix C to this report, allowing individual readers to draw their own conclusions. For the RADAMO data, these comparisons were performed over two fluence ranges, below and above $\Phi=3x10^{19}$ n/cm^2. This fluence partition was selected because it corresponds approximately to both the highest fluence observed in IVAR and the highest fluence for which there is a reasonable amount of data in the US-LWR surveillance database.

Table 4.6 and Table 4.7 summarize the outcome of the comparisons between the predictions of CM-3(2) and, the IVAR and RADAMO databases, respectively. The plots that form the basis of the judgments summarized in these tables appear in Appendix C. To aid in consolidating the large amount of information presented in these tables, the various alloys were first assigned into the following copper bins:

- No CRP: below ≈0.07 wt-% copper
- CRP Increasing: above ≈0.07 wt-% copper and up to ≈0.3 wt-% copper
- CRP Saturated: above ≈0.3 wt-% copper

Each copper bin was further subdivided into the following three nickel bins:

- Low: below ≈0.2 wt-% nickel
- Typical: between ≈0.5 and 1.0 wt-% nickel; the great majority of the existing US-LWR surveillance database would fall into this category
- High: above ≈1.25 wt-% nickel

Binning the alloys in this way revealed the following situations where the predictions of CM-3(2) do not match well with the RADAMO or IVAR data. The supporting evidence is noted along with each observation.

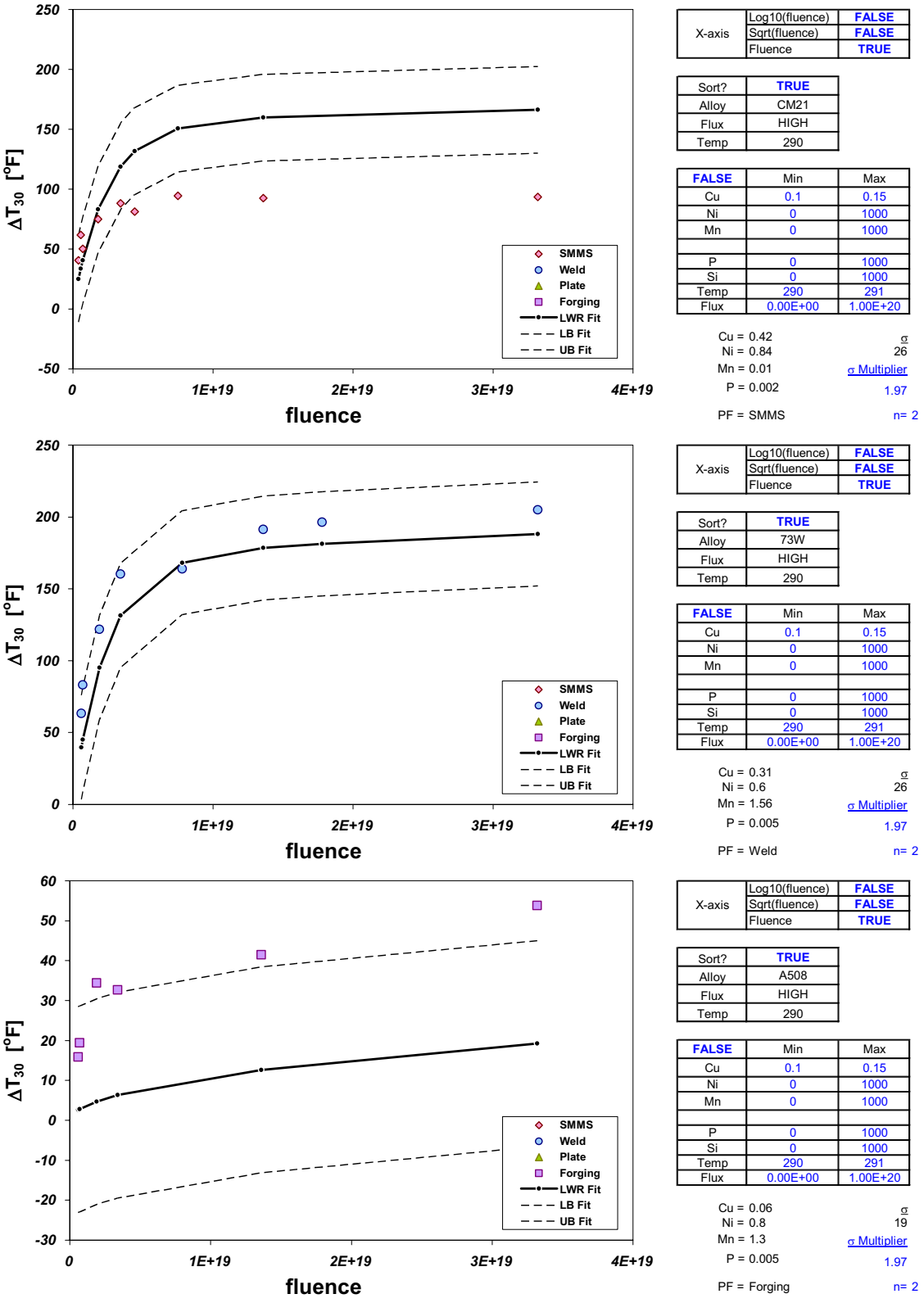

Figure 4-31. Illustration of comparisons between the prediction of CM-3(2) (lines) and IVAR data (points) that have been classified as high (top graph), OK (middle graph), and low (bottom graph).

Table 4.6. Assessment of comparisons between IVAR data and CM-3(2) predictions.

Bin		Alloy	Product Form	Composition [wt-%]					Assessment		
Cu	Ni			Cu	Ni	Mn	P	Si	LWR Fit is ___ Relative to data at this Flux		
									High ϕ	Med ϕ	Low ϕ
No CRP	Low	CM1	SMMS	0.01	0.01	1.67	0.003	0.15	OK	OK	OK
		CM2	SMMS	0.01	0.01	1.65	0.041	0.16	OK	OK	OK
	Typical	LG	SMMS	0	0.74	1.37	0.005	0.22	OK	OK	OK
		CM23	SMMS	0.01	0.83	1.62	0.002	0.15	OK	OK	OK
		CM27	SMMS	0.01	0.84	1.6	0.002	0.16	OK	OK	OK
		CM31	SMMS	0.01	0.86	1.65	0.006	0.17	OK	OK	OK
		CM8	SMMS	0.01	0.86	0.01	0.004	0.14	OK	OK	OK
		CM9	SMMS	0.01	0.86	0.85	0.003	0.15	OK	OK	OK
		CM25	SMMS	0.01	0.87	1.53	0.003	0.17	OK	OK	OK
		CM26	SMMS	0.01	0.87	1.66	0.006	0.17	OK	OK	OK
		CM3	SMMS	0.02	0.85	1.6	0.006	0.16	OK	OK	OK
		CM4	SMMS	0.02	0.86	1.53	0.031	0.16	OK	OK	OK
		CM5	SMMS	0.02	0.86	1.61	0.05	0.16	OK	LOW	OK
		CM24	SMMS	0.02	0.87	1.65	0.006	0.15	OK	OK	OK
		CM10	SMMS	0.02	0.88	1.66	0.008	0.17	OK	OK	OK
		BW-C	Weld	0.06	0.62	1.3	0.009	0.37	LOW	LOW	LOW
		A508	Forging	0.06	0.8	1.3	0.005	0.01	LOW	OK	OK
	High	CM7	SMMS	0	1.7	1.55	0.047	0.17	OK	OK	OK
		CM6	SMMS	0.02	1.68	1.5	0.007	0.17	LOW	LOW	OK
		RR-WP	Weld	0.04	1.65	1.43	0.011	0.5	LOW	LOW	LOW
CRP Increasing	Low	A302B	Plate	0.14	0.2	1.2	0.015	0.28	OK	OK	OK
		CM29	SMMS	0.21	0.02	1.68	0.002	0.14	HIGH	HIGH	HIGH
		CM15	SMMS	0.22	0.02	1.59	0.002	0.15	OK	OK	OK
	Typical	LH	SMMS	0.11	0.74	1.39	0.005	0.24	OK	OK	OK
		CM13	SMMS	0.11	0.83	1.61	0.004	0.16	OK	OK	OK
		CM14	SMMS	0.11	0.83	1.62	0.04	0.17	OK	OK	OK
		HSST02	Plate	0.14	0.67	1.55	0.009	0.2	LOW	LOW	LOW
		JRQ	Plate	0.14	0.82	1.4	0.019	0.25	OK	OK	OK
		LI	SMMS	0.2	0.74	1.37	0.005	0.24	OK	OK	LOW
		BW-A	Weld	0.21	0.63	1.69	0.014	0.45	OK	OK	OK
		65W	Weld	0.22	0.6	1.45	0.015	0.48	OK	OK	OK
		CM16	SMMS	0.22	0.82	1.58	0.004	0.25	OK	LOW	LOW
		CM30	SMMS	0.22	0.85	1.64	0.006	0.16	OK	LOW	LOW
		62W	Weld	0.23	0.6	1.61	0.02	0.59	OK	OK	LOW
		Midland	Weld	0.27	0.57	1.61	0.017	0.62	OK	OK	LOW
		67W	Weld	0.27	0.69	1.44	0.011	0.5	HIGH	HIGH	HIGH
		BW-B	Weld	0.28	0.69	1.63	0.018	0.54	OK	OK	no data
		63W	Weld	0.3	0.69	1.65	0.016	0.63	OK	OK	LOW
		73W	Weld	0.31	0.6	1.56	0.005	0.45	OK	OK	LOW
	High	Palisades	Weld	0.2	1.2	1.3	0.01	0.18	OK	no data	no data
		CM17	SMMS	0.22	1.59	1.54	0.004	0.25	LOW	LOW	LOW
		RR-WG	Weld	0.24	1.71	1.21	0.008	0.6	HIGH	OK	OK

Bin		Alloy	Product Form	Composition [wt-%]					Assessment		
Cu	Ni			Cu	Ni	Mn	P	Si	LWR Fit is ___ Relative to data at this Flux		
									High ϕ	Med ϕ	Low ϕ
CRP Saturated	Low	LA	SMMS	0.4	0	1.37	0.005	0.22	OK	OK	OK
		CM18	SMMS	0.43	0.02	1.7	0.002	0.15	OK	OK	OK
		LB	SMMS	0.4	0.18	1.35	0.005	0.22	OK	OK	OK
	Typical	CM11	SMMS	0.34	0.85	1.64	0.006	0.18	OK	LOW	LOW
		EPRI-C	Weld	0.4	0.6	1.36	0.006	0.51	HIGH	OK	LOW
		LC	SMMS	0.41	0.86	1.44	0.005	0.23	OK	OK	LOW
		LO	SMMS	0.41	0.86	1.44	0.005	0.23	OK	OK	LOW
		LJ	SMMS	0.42	0.81	1.34	0.005	0.13	OK	OK	OK
		CM21	SMMS	0.42	0.84	0.01	0.002	0.14	HIGH	HIGH	OK
		CM22	SMMS	0.42	0.84	0.84	0.002	0.14	OK	OK	OK
		CM28	SMMS	0.42	0.84	1.6	0.002	0.17	OK	OK	LOW
		CM19	SMMS	0.42	0.85	1.63	0.005	0.16	OK	OK	LOW
		LK	SMMS	0.8	0.81	1.13	0.005	0.13	HIGH	HIGH	HIGH
		CM12	SMMS	0.86	0.84	1.65	0.006	0.17	HIGH	HIGH	HIGH
	High	LD	SMMS	0.38	1.25	1.38	0.005	0.23	OK	OK	LOW
		CM20	SMMS	0.43	1.69	1.63	0.006	0.16	OK	OK	LOW
		RR-WV	Weld	0.56	1.66	1.36	0.01	0.38	HIGH	HIGH	OK

Table 4.7. Assessment of comparisons between RADAMO data and CM-3(2) predictions.

Bin		Alloy	Product Form	Composition [wt-%]					Assessment			
Cu	Ni			Cu	Ni	Mn	P	Si	LWR Fit is __ relative to data below Φ=3x10^{19} n/cm^2		LWR Fit is __ relative to data above Φ=3x10^{19} n/cm^2	
									265 °C	300 °C	265 °C	300 °C
No CRP	Low	VVER-440B	plate	0.08	0.12	0.4	0.012	0.29	OK	OK	HIGH	LOW
	Typical	A508-B	forging	0.05	0.75	1.43	0.008	0.28	OK	OK	LOW	LOW
		16MND5	forging	0.065	0.69	1.37	0.013	0.04	no data	LOW	no data	LOW
		A508-W	weld	0.07	0.83	1.57	0.015	0.22	OK	LOW	LOW	LOW
	High	VVER-1000B	plate	0.05	1.26	0.46	0.008	0.3	OK	LOW	LOW	LOW
		VVER-1000W	weld	0.06	1.7	0.73	0.006	0.14	LOW	LOW	LOW	LOW
CRP Increasing	Low	VVER-440W	weld	0.13	0.12	0.97	0.032	0.5	LOW	LOW	LOW	LOW
	Typical	20MnMoNi55	forging	0.11	0.8	1.29	0.007	0.2	OK	OK	LOW	LOW
		18MND5-W	weld	0.12	1.01	1.3	0.021	0.19	no data	HIGH	no data	LOW
		HSST-03	plate	0.12	0.62	1.36	0.011	0.26	OK	OK	LOW	LOW
		18MND5-BM	plate	0.13	0.64	1.55	0.008	0.25	OK	OK	LOW	LOW
		JRQ	plate	0.14	0.84	1.42	0.017	0.24	OK	OK	LOW	LOW
		72W	weld	0.23	0.6	1.6	0.006	0.44	OK	OK	LOW	LOW
		73W	weld	0.31	0.6	1.56	0.005	0.45	OK	OK	LOW	LOW

(1) At fluences below $\Phi=3x10^{19}$ n/cm^2, both RADAMO and IVAR data are available to assess how well CM-3(2) represents data that is not contained within the US-LWR surveillance database. CM-3(2) predicts both the RADAMO and IVAR data below $\Phi=3x10^{19}$ n/cm^2 remarkably well; 71% of the entries in Table 4.6 and Table 4.7 are "OK" for fluences below $\Phi=3x10^{19}$ n/cm^2. The following situations account for the 29% of the alloys for which the prediction of RADAMO or IVAR data using CM-3(2) is not judged to be within statistical scatter:

(a) CM-3(2) has a tendency to over-predict the irradiation hardening of alloys that have copper levels in the CRP saturation range (IVAR Alloys EPRI-C, LK, CM-12, and RR-WV; IVAR Alloy CM-21 is also over-predicted, but we believe this to be because it has no manganese). The amount of over-prediction increases as the copper content increases. We believe this difference between the CM-3(2) predictions and the IVAR alloys occurs because, owing to the limited amount of data with Cu >0.3 wt-% in the US-LWR database, a Cu_{max} value was not found to be statistically necessary using the fitting procedure adopted in this investigation.

(b) Irrespective of copper level, both the RADAMO and IVAR databases show better agreement with the CM-3(2) predictions for alloys having a "typical" nickel content (between 0.5 and 1.0 wt-%) than they do for alloys having either very high or very low nickel content. We believe this differences between the CM-3(2) predictions and the RADAMO and IVAR data are attributable to the previously noted inability to calibrate a nickel effect for MD, owing to the limited range of nickel content and fluence exposure in the US-LWR database (see discussion in Section 4.2.3).

(c) Model CM-3(2) does not adequately capture the slight flux effect seen in IVAR. This can be seen in Table 4.6 because the agreement of CM-3(2) with the IVAR data is better for the high-flux irradiations than it is for either the medium- or low-flux irradiations. If CM-3(2) adequately captured the flux dependence seen in IVAR, the agreement of the model to the IVAR data should be roughly equivalent, irrespective of flux.

(d) As previously noted (again see the discussion in Section 4.2.3), the temperature dependence of MD in CM-3(2) does not agree well with data in the literature. This can be seen in Table 4.7 because the no-CRP RADAMO alloys match the predictions of CM-3(2) much better at 300 °C than they do at 265 °C. If CM-3(2) adequately captured the temperature dependence seen in RADAMO, the agreement of the model to the RADAMO data should be roughly equivalent, irrespective of temperature.

(e) Two IVAR alloys, HSST-02 and 67W, that are (in all respects) well-contained within the US-LWR surveillance data ranges are not well predicted by CM-3(2). The cause for this difference is unclear; it may relate to an incorrect value of the unirradiated yield strength, but a technical case for this explanation is not advanced in this report.

The first three deviations can be attributed to the limited span of the US-LWR data combined with too low of a signal-to-noise ratio to permit calibration of a well-recognized physical phenomenon. Potential causes of the fourth deviation are discussed in further detail in Section 4.3.2 and, as previously noted, the cause of the fifth deviation is not explored herein.

(2) At fluences above $\Phi=3x10^{19}$ n/cm^2, only the RADAMO data are available to make an assessment. In contrast with the good agreement between CM-3(2) predictions and RADAMO data at lower fluences, at these high fluences, CM-3(2) under-predicts the magnitude of embrittlement for all but one of the RADAMO alloys. As shown in Figure 4-30, RADAMO irradiations were conducted at both higher fluxes and higher fluences than are characteristic of the US-LWR database. However, it appears that the cause of the under-prediction revealed in Table 4.7 is an inadequacy of the CM-3(2) model with respect to fluence rather than flux. The following observations support this conclusion:

(a) The predictions of CM-3(2) compare much more favorably with the RADAMO data below $\Phi<3x10^{19}$ n/cm^2 (70% agreement overall). This finding is consistent with comparisons made to IVAR, as previously discussed under Item 1.

(b) Gérard has published comparisons of Belgian PWR materials exposed in extended surveillance programs (these exposures are performed at fluxes characteristic of the US-LWR database) to the same materials exposed in the test reactor BR-2 (this is the same test reactor used for RADAMO, so the fluxes are similar) [Gérard 06]. Figure 4-32 shows Gérard's data; there is no effect of flux that is larger than the data scatter to fluences as high as $\Phi\approx2x10^{20}$ n/cm^2.

(c) Alloy 73W was studied in both IVAR and RADAMO. The top graph in Figure 4-33 compares the IVAR and RADAMO data for fluences below $\Phi=3x10^{19}$ n/cm^2. Over this fluence range, the slight effect of increasing flux increasing the saturation fluence noted previously in the IVAR database (see Figure 4-13) is evident; otherwise the data are in good agreement. However when the graph is expanded to fluences above $\Phi=3x10^{19}$ n/cm^2 so that the full range of the RADAMO data can be seen (middle graph in Figure 4-33), it is clear that embrittlement continues to increase as fluence increases; this trend was not obvious in the lower-fluence data. The bottom graph in Figure 4-33 compares the RADAMO 73W data exposed at 300 °C with the prediction of CM-3(2); the inadequacy of this, or indeed any, model fit solely to the existing US-LWR database to predict embrittlement trends at high fluences is obvious.

We believe that the poor predictive capability of CM-3(2) for fluences above $\approx3x10^{19}$ n/cm^2 is caused by the lack of significant data in the US-LWR calibration database above this fluence.

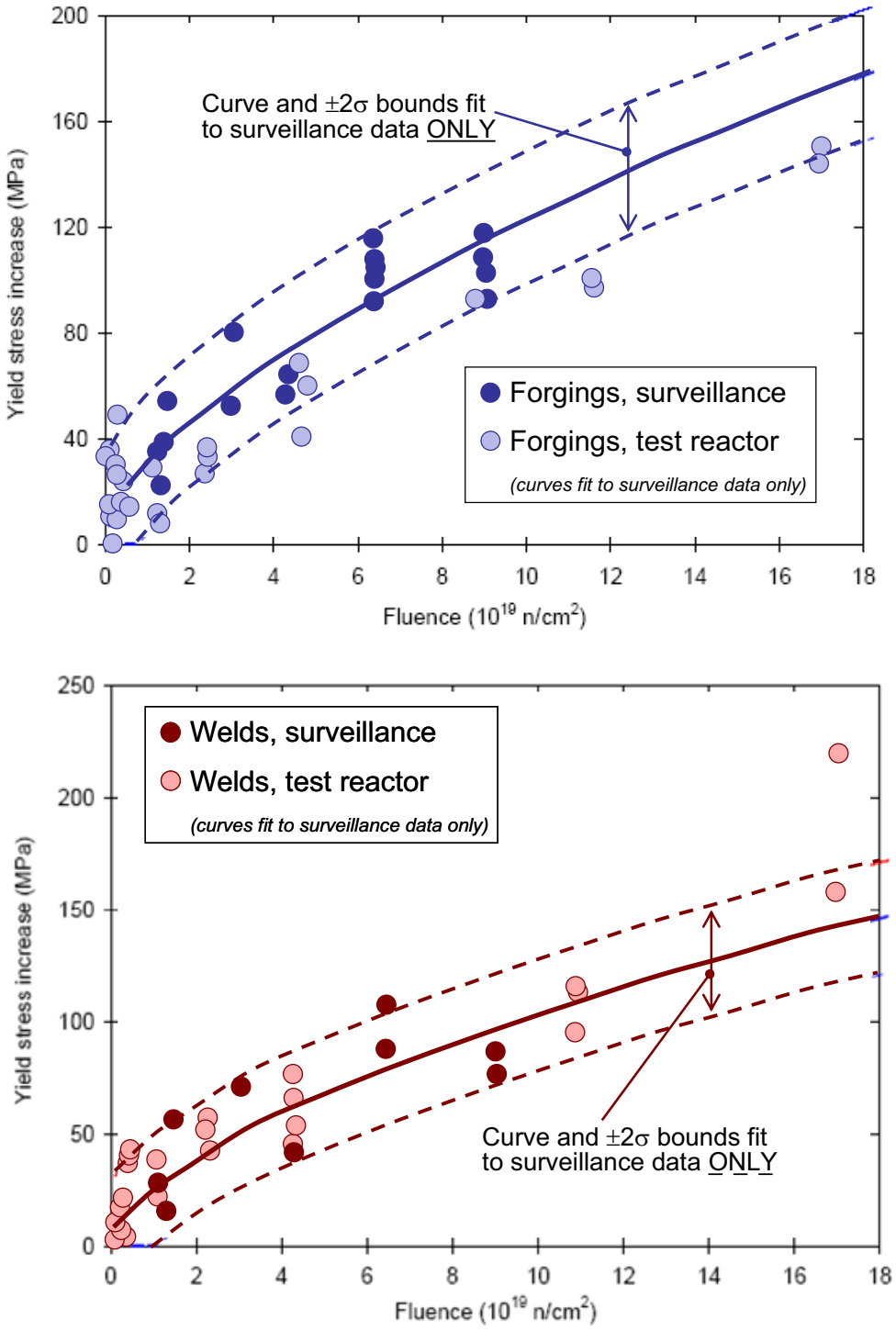

Figure 4-32. Data from [Gérard 06] showing good agreement between embrittlement trends for both low-flux (surveillance) and high-flux (BR-2) irradiations conducted to high fluences.

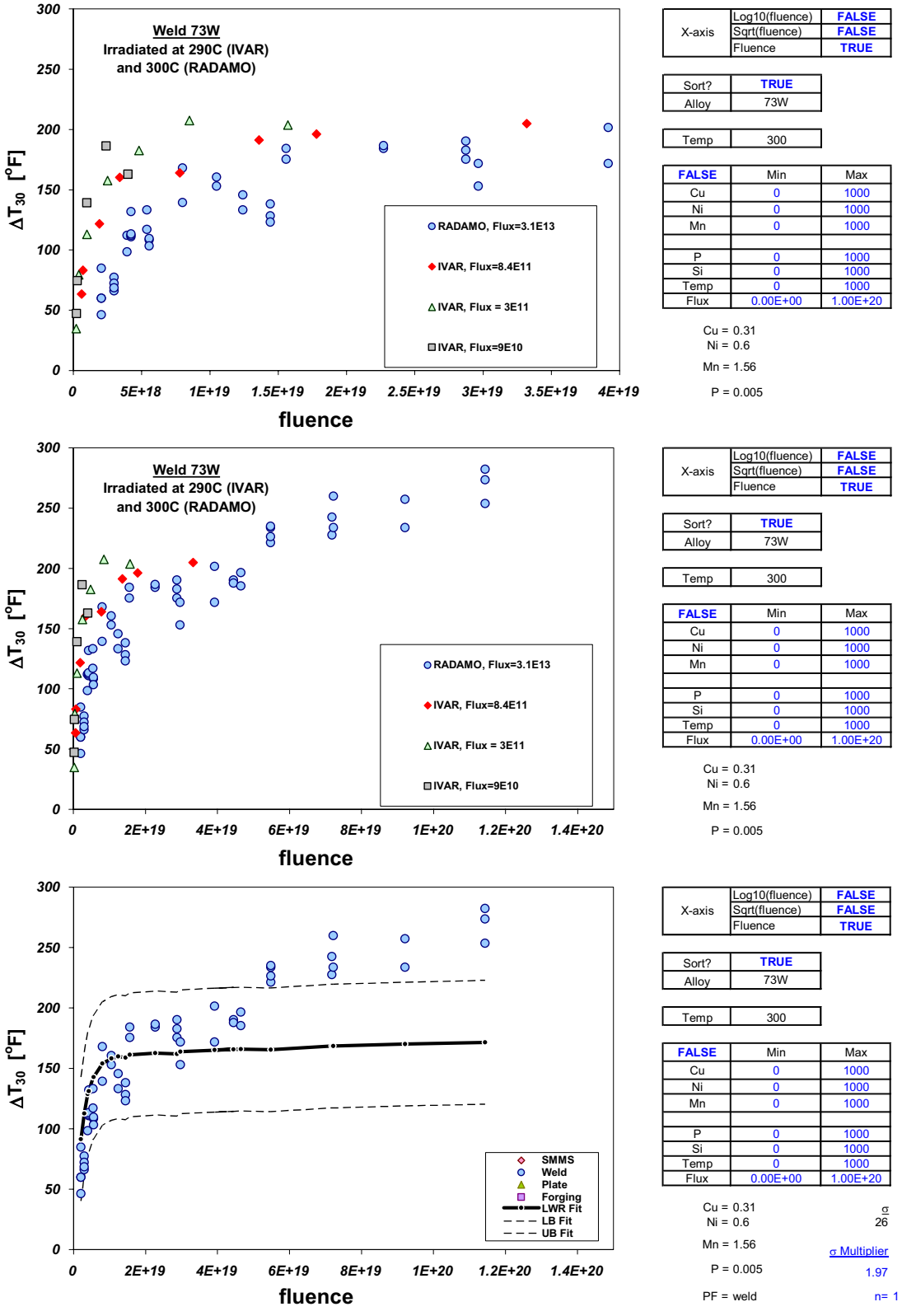

Figure 4-33. IVAR and RADAMO data for Alloy 73W. Top: Compared to a maximum fluence characteristic of both IVAR and the US-LWR database. Middle: Compared over the total fluence range examined in RADAMO. Bottom: RADAMO data compared to the prediction of CM-3(2).

An assessment was performed to determine whether the poor predictive capability of CM-3(2) for fluences above ≈3x10^{19} n/cm^2 is attributable to an inadequacy in the MD term (Eq. 4-3), the CRP term (Eq. 4-4), or both terms. The RADAMO data at 300 °C were fit to the following equation:

Eq. 4-13 $$\Delta T_{30(RADAMO=300C)} = D \cdot \Delta T_{30(MD)}^{CM-3(2)} + E \cdot \Delta T_{30(CRP)}^{CM-3(2)}$$

Table 4.8. Modification of CM-3(2) predictions based on RADAMO data at 300 °C.

Bins		Alloy	Product Form	Composition [wt-%]					CM-3(2) Modification Factors	
Cu	Ni			Cu	Ni	Mn	P	Si	D: MD	E: CRP
No CRP	Low	VVER-440B	plate	0.08	0.12	0.4	0.012	0.29	3.5	N/A*
	Typical	A508-B	forging	0.05	0.75	1.43	0.008	0.28	6	
		16MND5	forging	0.065	0.69	1.37	0.013	0.04	7	
		A508-W	weld	0.07	0.83	1.57	0.015	0.22	5.5	
	High	VVER-1000B	plate	0.05	1.26	0.46	0.008	0.3	6**	
		VVER-1000W	weld	0.06	1.7	0.73	0.006	0.14	12**	
CRP Increasing	Low	VVER-440W	weld	0.13	0.12	0.97	0.032	0.5	6.5	1
	Typical	20MnMoNi55	forging	0.11	0.8	1.29	0.007	0.2	8	0.1
		18MND5-W	weld	0.12	1.01	1.3	0.021	0.19	8	0.1
		HSST-03	plate	0.12	0.62	1.36	0.011	0.26	5	0.1
		18MND5-BM	plate	0.13	0.64	1.55	0.008	0.25	6	0.1
		JRQ	plate	0.14	0.84	1.42	0.017	0.24	6	0.1
		72W	weld	0.23	0.6	1.6	0.006	0.44	11	0.3
		73W	weld	0.31	0.6	1.56	0.005	0.45	11	0.4

* - There is no CRP component to the embrittlement of these alloys because their copper content is below Cu_{min} for CM-3(2).
** - Even with these modifications the predicted increase of embrittlement with fluence is not rapid enough for this alloy.

Here, $\Delta T_{30(MD)}^{CM-3(2)}$ and $\Delta T_{30(CRP)}^{CM-3(2)}$ are, respectively, the matrix damage and copper-rich precipitate predictions of CM-3(2), while D and E are fit factors determined by eye to provide good agreement between the predictions of Eq. 4-13 and individual alloys irradiated in RADAMO. Table 4.8 summarizes the resulting values of D and E; this information supports the following conclusions:

- Low-copper materials (Cu <0.083 wt-%) having nickel contents below 1 wt-% in the RADAMO database have a matrix damage rate exceeding that seen in the US-LWR database by a factor of approximately 5.
- Low-copper and high-nickel (Ni >1.25 wt-%) materials in the RADAMO database have matrix damage rates that are 6–12 times those seen in the US-LWR database. However, the increase of ΔYS with fluence in these alloys is more rapid than the $\sqrt{\Phi}$ dependence typically associated with a matrix damage mechanism.

- For alloys with enough copper to experience irradiation damage via a CRP mechanism, the materials in the RADAMO database have a matrix damage rate that exceeds that seen in the US-LWR database by a factor that ranges from ≈5 to ≈10 and increases with increasing copper content. These alloys also exhibit peak CRP hardening magnitudes that are lower than those seen in the US-LWR database. The peak CRP hardening magnitude of the higher-copper RADAMO materials increases from 10% to 40% of the CRP hardening magnitude exhibited by the US-LWR database as the copper content of the alloys increases from ≈0.1 to ≈0.3 wt-%.

These findings suggest that the limited fluence range of the US-LWR data combined with the practical need to calibrate physically motivated models using empirical data from reactor surveillance programs has resulted in a systematic under-estimation of the MD hardening rate coupled with a systematic over-estimation of the peak CRP hardening magnitude. Attempts were not made to correct for this inconsistency in the model revision discussed in Section 4.3.2 for the following reasons:

- While it is clear that CM3-(2) under-predicts embrittlement at fluences above $3x10^{19}$ n/cm^2, the cause of this under-prediction suggested by the analysis of Table 4.8 (i.e. that matrix damage is under-estimated and precipitation damage is over-estimated) must be regarded as provisional because it is based only on data fitting. Microstructural examination of the alloys irradiated at high fluences using, for example, atom probe and small angle neutron scattering (SANS) techniques, is needed to determine which embrittlement mechanisms are active at high fluences.
- Without augmenting the US-LWR surveillance database with high-fluence data, there is inadequate "signal" against which to calibrate a revised model. Attempts were made to combine the US-LWR, IVAR, and RADAMO databases to achieve this goal; however the different effect of temperature on irradiation damage previously noted in these databases (see Figure 4-25) and the different embrittlement damage metrics that were measured (ΔT_{30} and ΔYS) complicate this approach, making it difficult to express the combined databases on a common basis. Section 9.5 discusses future efforts at database combination and other activities that will be used to improve the performance of the ΔT_{30} model at high fluence.

4.3.2 Model Revision

In addition to the various inconsistencies between the predictions of CM-3(2) and IVAR/RADAMO databases noted in Section 4.3.1, a review of the CRP model, Eq. 4-3, also revealed an error in the functional form of the chemistry factor. For model CM-3(2), the best-fit chemistry factor is as follows (zero terms are omitted):

Eq. 4-14
$$CF = \left[1 + f\left(Cu\right) + 500Ni + 1500\left(Cu - Cu_{\min}\right) \cdot Ni\right]$$
where $f\left(Cu\right) = -343.8 + 1400Cu^{0.6}$, subject to $f(Cu) \geq 0$

The presence of the "1" and the "500Ni" terms in Eq. 4-14 allow for a step-function jump in the peak CRP hardening as the copper content increases from just below to just above the calibrated Cu_{min} value. As previously illustrated in Figure 4-27 the magnitude of this jump (calibrated to the US-LWR data) is approximately 50 MPa. Because such a sudden change in the hardening capacity seems physically unrealistic, both the "1" and the "500Ni" terms in Eq. 4-14 are eliminated in this model revision.

The following list summarizes the attempts made to resolve the various inconsistencies between the predictions of CM-3(2) and IVAR/RADAMO databases noted in Section 4.3.1 and to fix the modeling error noted in the preceding paragraph:

(1) The error in the CRP CF was addressed by removing the nickel and "1" terms from Eq. 4-14.

(2) We attempted to reduce the systematic over-prediction for high-copper alloys by re-calibrating the $B_{Cu(max)}$ term to reduce Cu_{max} to a value close to the ≈0.3 reported in the literature [Odette 86, Odette 88]. Also, we attempted to introduce a separate (lower) value of Cu_{max} for Linde 80 welds (value of 0.23 are often reported for Linde 80 because of the lower heat treatment temperatures used by Babcock and Wilcox) [McElroy 96].

(3) As noted in Figure 4-28 and Section 4.3.1, the calibrated value of Φ_{SAT} appears to be high, and the flux effect on Φ_{SAT} is missing. (Both of these observations are made relative to the IVAR data.) We attempted to reconcile both problems by re-introducing a flux dependence on Φ_{SAT}.

(4) The magnitude of matrix damage appears to be under-estimated, while the magnitude of CRP hardening appears to be over-estimated. This general observation was combined with the following specific observations:

- (a) There is no nickel effect on MD, but there is a strong nickel effect on CRP.
- (b) There is a flux effect on MD, but the flux effect on Φ_{SAT} is missing.
- (c) The temperature dependence of MD is too strong.

While all of these modifications to CM-3(2) were attempted, some were not successful. Specifically, the changes listed in Item 4 could not be made while retaining a model having statistically insignificant residual trends *vs*. all considered regressor variables. Correction of these modeling problems appears to await the availability of additional experimental data and/or the development of a new fitting procedure capable of making consistent and systematic tradeoffs between statistical goodness of fit *vs*. physically expected trends. However, both of these developments lie beyond the scope of the current study, so the Item 4 changes could not be addressed.

Table 4.9 contains the coefficients and statistical assessments of the various models that were tried to address Items 1–3, while Figure 4-34 summarizes the statistical evaluation and classification of these fits. The revised model fit ultimately developed as follows:

Model RM-1 & -1(2): In these models, the standalone Ni coefficient in the CRP chemistry factor (the B_2 value) was removed to eliminate the physically unrealistic step-jump in chemistry factor allowed by CM-3(2). A provisional model was achieved as the T_{MAX} value exceeded 1.0. The major effects of this change in the form of the CRP chemistry factor were (a) a re-arrangement of the magnitudes of the various PF and CF terms, and (b) a reduction in the calibrated Cu_{min} value from 0.085 to 0.045 wt-%.

Model RM-2 to -2(3): A limit on the maximum amount of copper available for CRP hardening was imposed by reducing the $B_{Cu(max)}$ value; a solution classified as acceptable was found. The calibrated Cu_{max} value of RM-2(3) is 0.35 wt-%.

Model RM-3: In RM-2(3), it was noted that the calibrated value of the copper exponent in the CRP chemistry factor is very close to the theoretically expected value

of ½. For this reason, the copper exponent was fixed at ½ in RM-3, and the model was optimized using *solver*. An acceptable model resulted.

Model RM-4 to -4(3): In these models, an attempt was made to introduce a different (lower) Cu_{max} value for the Linde 80 welds. [Linde 80 weld comprise approximately 10% of the US-LWR database (92 records).] A model classified as acceptable was found; that model had a calibrated Cu_{max} value for Linde 80 of 0.25. While this model change did reduce the magnitude of the residual trends for the 92 Linde 80 weld records, it failed to render these trends statistically insignificant (see Figure 4-35). Consequently, this modification was not retained in the continuing evolution of the revised model.

Model RM-5: Using RM-3 as a starting point, an attempt was made to reduce the overall Φ_{SAT} value by again permitting its variation with flux. While a model classified as acceptable was found, this model failed to achieve the goal of Φ_{SAT} reduction to bring it into better accord with the IVAR data. In fact, because fluence and flux are so strongly correlated in the US-LWR database (see Figure 4-30), a near infinity of statistically acceptable combinations of the C_0 and C_2 coefficients can be found. This modification was not retained in the continuing evolution of the revised model.

Model RM-6 to -6(2): Using RM-3 as a starting point, the "1" value in the CRP chemistry factor (see Eq. 4-13) was removed. A model classified as acceptable was found.

Model RM-7 to -7(2): Using RM-6(2) as a starting point, an attempt was made to remove the Cu_{max} term by increasing the $B_{Cu(max)}$ coefficient to a very high value. A model classified as acceptable was found.

Both the RM-6(2) and RM-7(2) models are acceptable alternatives to CM-3(2). The existence of RM-7(2) indicates that there is not enough high-copper data in the US-LWR surveillance database to calibrate a Cu_{max} value that is statistically essential to the model. Nevertheless, RM-6(2) is preferred because (1) the calibrated Cu_{max} value of 0.32 wt-% is in reasonable accord with values reported elsewhere [Odette 86, Odette 88], and (2) a model having a Cu_{max} limit is expected to perform better when extrapolated to conditions outside of the US-LWR database, thereby addressing a known deficiency in CM-3(2) (this belief is assessed in Section 4.3.3). As documented in Table 4.9, RM-6(2) has no statistically significant residuals with respect to silicon content. After rounding (again see Table 4.9), RM-6(2) was accepted as the final revised model. The uncertainty of RM-6(2) (standard deviation) is 19 °F below Cu_{min} and 25 °F above Cu_{min}.

In summary, there are four major differences between RM-6(2) and CM-3(2):

(1) The functional form of the CRP chemistry factor was revised to remove a physically unrealistic step-jump allowed by CM-3(2) (see Figure 4-27). Figure 4-36 illustrates that RM-6(2) has a peak magnitude of CRP hardening that rises as a smooth function of copper above Cu_{min}. Figure 4-36 also shows that the RM-6 model of CRP hardening magnitude is in reasonable agreement with that proposed by Chaouadi, and with the IVAR database.

(2) A calibrated value of Cu_{max} of 0.32 wt-% was determined from the database. This Cu_{max} value can also seen as the upper saturation point in Figure 4-36. As discussed in Section 4.3.2, the existence of alternative acceptable models without a Cu_{max} limit indicates that there is not enough high-copper data in the US-LWR surveillance database to calibrate a Cu_{max} value that is statistically essential to the model. Nevertheless,

RM-6(2) is preferred because (a) the calibrated Cu_{max} value of 0.32 wt-% is in reasonable accord with values reported elsewhere [Odette 86, Odette 88], and (b) a model having a Cu_{max} limit is expected to perform better when extrapolated to conditions outside of the US-LWR database.

(3) In RM-6(2), the theoretically expected dependence of peak CRP hardening on √Cu [Fisher 85] was successfully fit to the US-LWR data; in CM-3(2), the best-fit exponent on copper was 0.6 rather than 0.5.

(4) RM-6(2) has a lower copper value that signals the start of CRP hardening; the fit value of Cu_{min} is 0.048 in RM-6 vs. 0.085 in CM-3(2). As discussed in Section 4.1.2.1, both values are in good accord with other studies published in the literature. Figure 4-36 shows that the 0.048 Cu_{min} value agrees reasonably well with both IVAR data and the work of [Chaouadi 05b].

Other aspects of agreement, or lack thereof, between RM-6 and information in the literature remain unchanged from CM-3(2) (see discussions in Sections 4.2.3 and 4.2.4).

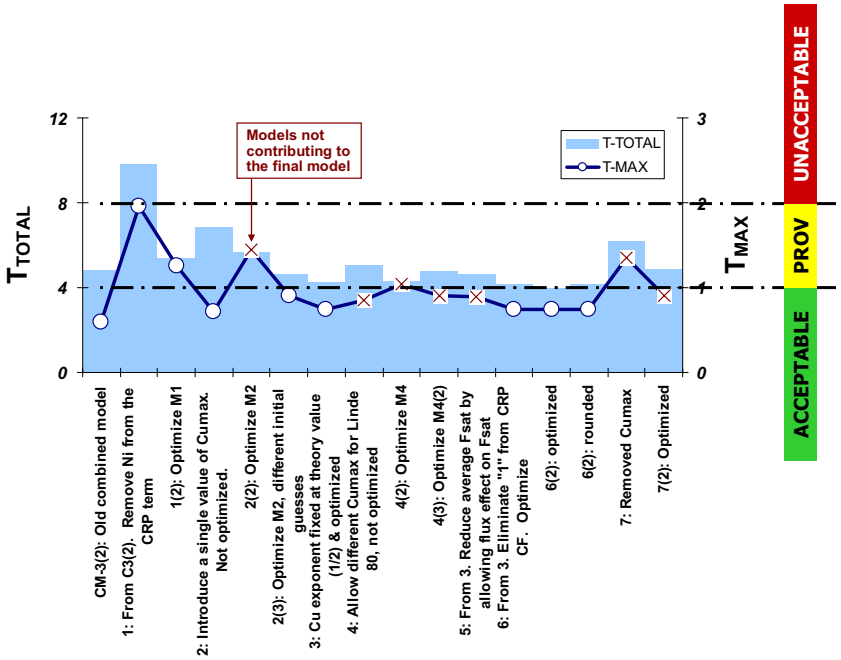

Figure 4-34. Statistical evaluation and classification of revised fits.

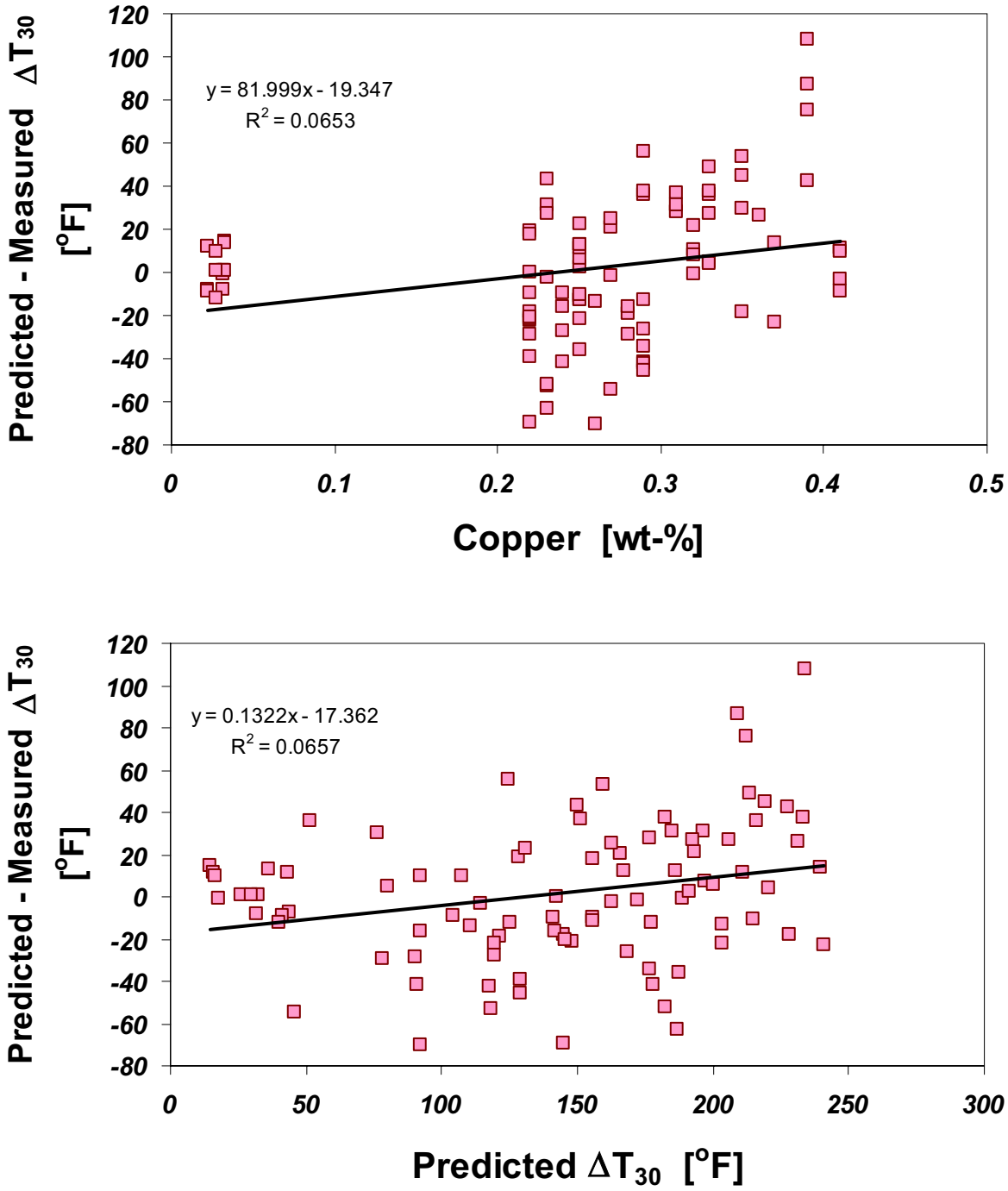

Figure 4-35. Residuals in RM-4(3) for the 92 Linde 80 weld records in the US-LWR database. Both of the trends shown are statistically significant at the 5% level.

Table 4.9. Candidate revised fits to the US-LWR database for the combined MD and CRP equations. Models that are not part of the path to the final model appear in italics.

	Label	CM-3(2)	RM-1	RM-1(2)	RM-2	*RM-2(2)*	RM-2(3)	RM-3	*RM-4*	*RM-4(2)*	*RM-4(3)*	*RM-5*	RM-6	RM-6(2)	*RM-7*	*RM-7(2)*	RM-6(2)
Model ID	**Action**	From Table 4.5	From CM-3(2). Eliminate stand alone Ni from the CRP term	Optimize RM-1	Introduce a single value of Cu_{max}, do not optimize	*Optimize RM-2*	From RM-2. Change red coefficients and optimize	Cu exp fixed at ½ theory value. Changed red and optimized	*Allow different Cu_{max} for Linde 80, not optimized*	*Optimize RM-4*	*Optimize RM-4(2)*	*From 3. Try to reduce average Φ_{SAT} by allowing ϕ to influence Φ_{SAT}*	From 3. Eliminate "1" from CRP CF. Optimize	optimized	*Removed Cu_{max}*	*Optimized*	Round coefficients
Stats	**Std Error**	23.96	24.81	24.73	24.55	*24.58*	24.61	24.47	*24.41*	*24.44*	*24.37*	*24.56*	24.46	24.47	*24.72*	*24.69*	24.45
	T_{TOTAL}	4.74	9.83	5.43	6.86	*5.67*	4.66	4.28	*5.10*	*4.30*	*4.77*	*4.65*	4.19	3.98	*6.21*	*4.88*	4.14
	T_{MAX}	0.66	1.96	1.26	0.71	*1.44*	0.90	0.74	*0.85*	*1.05*	*0.90*	*0.89*	0.75	0.74	*1.36*	*0.90*	0.75
	Classification	A	P	P	A	*P*	A	A	*A*	*P*	*A*	*A*	A	A	*P*	*A*	A
	n	936	936	936	936	*936*	936	936	*936*	*936*	*936*	*936*	936	936	*936*	*936*	936
Fit Coefficients - CRP	**Weld**	0.186	0.299	0.300	0.300	*0.305*	0.300	0.300	*0.300*	*0.302*	*0.302*	*0.300*	0.301	0.301	*0.301*	*0.298*	0.301
	Plate & SRM	0.132	0.239	0.236	0.236	*0.238*	0.234	0.233	*0.233*	*0.232*	*0.232*	*0.233*	0.233	0.233	*0.233*	*0.233*	0.233
	Forging	0.111	0.218	0.229	0.229	*0.232*	0.229	0.233	*0.233*	*0.234*	*0.234*	*0.234*	0.233	0.234	*0.234*	*0.235*	0.233
	Cu exponent	0.6	0.5811	0.5787	0.5787	*0.5778*	0.5001	0.5	*0.5*	*0.5*	*0.5*	*0.5*	0.5	0.5	*0.5*	*0.5*	0.5
	Cu_{min}	0.085	0.0445	0.0450	0.0450	*0.0455*	0.0488	0.0488	*0.0488*	*0.0495*	*0.0495*	*0.0484*	0.0484	0.0484	*0.0484*	*0.0483*	0.048
	Cu: B_{1m}	1400	422.40	513.47	513.47	*513.47*	530.81	530.81	*515.94*	*515.94*	*526.00*	*530.81*	530.81	530.81	*530.81*	*530.81*	530.8
	Cu: $B_{Cu(max)}$	1000	1000	1000	180	*180*	195	185	*186*	*186*	*183*	*185*	185	185	*1000*	*1000*	185
	Δ B $_{Cu(max)}$: L80	0	0	0	0	*0*	0	0	*-35*	*-35*	*-38*	*0*	0	0	*0*	*0*	0
	Ni: B_2	500	0	0	0	*0*	0	0	*0*	*0*	*0*	*0*	0	0	*0*	*0*	0
	Cu*Ni: B_3	1500	2746.9	2528.8	2528.8	*2528.8*	2500.3	2500.3	*2566.8*	*2566.8*	*2566.8*	*2500.3*	2500.3	2500.3	*2500.3*	*2500.3*	2500.3
	Mn: B_4	0	0	0	0	*0*	0	0	*0*	*0*	*0*	*0*	0	0	*0*	*0*	0
	P: B_5	0	0	0	0	*0*	0	0	*0*	*0*	*0*	*0*	0	0	*0*	*0*	0
	Si: B_6	0	0	0	0	*0*	0	0	*0*	*0*	*0*	*0*	0	0	*0*	*0*	0
	Φ_{SAT}: C_0	23.8	23.8	23.8	23.8	*23.8*	23.8	23.8	*23.8*	*23.8*	*23.8*	*10.0*	23.8	23.8	*23.8*	*23.8*	23.8
	Φ_{SAT}: ϕ: C_2	0	0	0	0	*0*	0	0	*0*	*0*	*0*	*13.0*	0	0	*0*	*0*	0
	Φ_{SAT}: Ni: C_1	0	0	0	0	*0*	0	0	*0*	*0*	*0*	*0*	0	0	*0*	*0*	0
	Φ_{SAT}: Mn: C_4	0	0	0	0	*0*	0	0	*0*	*0*	*0*	*0*	0	0	*0*	*0*	0
	Φ_{SAT}: Cu : C_3	0	0	0	0	*0*	0	0	*0*	*0*	*0*	*0*	0	0	*0*	*0*	0

Model ID	Label	CM-3(2)	RM-1	RM-1(2)	RM-2	*RM-2(2)*	RM-2(3)	RM-3	*RM-4*	*RM-4(2)*	*RM-4(3)*	*RM-5*	RM-6	RM-6(2)	*RM-7*	*RM-7(2)*	RM-6(2)
	Action	From Table 4.5	From CM-3(2). Eliminate stand alone Ni from the CRP term	Optimize RM-1	Introduce a single value of Cu_{max}, do not optimize	*Optimize RM-2*	From RM-2. Change red coefficients and optimize	Cu exp fixed at ½ theory value. Changed red and optimized	*Allow different Cu_{max} for Linde 80, not optimized*	*Optimize RM-4*	*Optimize RM-4(2)*	*From 3. Try to reduce average Φ_{SAT} by allowing ϕ to influence Φ_{SAT}*	From 3. Eliminate "1" from CRP CF. Optimize	optimized	*Removed Cu_{max}*	*Optimized*	Round coefficients
	Φ_{SAT}: P : C_3	0	0	0	0	*0*	0	0	*0*	*0*	*0*	*0*	0	0	*0*	*0*	0
	Φ_{SAT}: Si : C_3	0	0	0	0	*0*	0	0	*0*	*0*	*0*	*0*	0	0	*0*	*0*	0
	Etemp	-1.75	-1.74	-1.74	-1.74	*-1.74*	-1.74	-1.74	*-1.74*	*-1.74*	*-1.74*	*-1.74*	-1.74	-1.74	*-1.74*	*-1.74*	-1.74
Fit Coefficients - MD	**Efluence**	0.5	0.5	0.5	0.5	*0.5*	0.5	0.5	*0.5*	*0.5*	*0.5*	*0.5*	0.5	0.5	*0.5*	*0.5*	0.5
	Etemp	-14.64	-14.64	-14.64	-14.64	*-14.64*	-14.64	-14.64	*-14.64*	*-14.64*	*-14.64*	*-14.64*	-14.64	-14.64	*-14.64*	*-14.64*	-14.64
	E-Flux	-3.46	-3.44	-3.44	-3.44	*-3.44*	-3.44	-3.44	*-3.44*	*-3.44*	*-3.44*	*-3.44*	-3.44	-3.44	*-3.44*	*-3.44*	-3.44
	Weld	6.661	6.695	6.696	6.696	*6.697*	6.696	6.696	*6.696*	*6.696*	*6.696*	*6.696*	6.696	6.696	*6.696*	*6.696*	6.7
	Plate & SRM	8.097	8.113	8.113	8.113	*8.113*	8.113	8.113	*8.113*	*8.113*	*8.113*	*8.113*	8.113	8.113	*8.113*	*8.113*	8.1
	Forging	4.755	4.745	4.746	4.746	*4.746*	4.746	4.746	*4.746*	*4.746*	*4.746*	*4.746*	4.746	4.746	*4.746*	*4.746*	4.75
	CF-Ni	0	0	0	0	*0*	0	0	*0*	*0*	*0*	*0*	0	0	*0*	*0*	0
	CF-Mn	0	0	0	0	*0*	0	0	*0*	*0*	*0*	*0*	0	0	*0*	*0*	0
	CF-P	31.24	31.2	31.2	31.2	*31.2*	35.0	35.0	*35.0*	*35.0*	*35.0*	*35.0*	35.0	35.0	*35.0*	*35.0*	35
	CF-Si	0	0	0	0	*0*	0	0	*0*	*0*	*0*	*0*	0	0	*0*	*0*	0
	CF-Cu	0	0	0	0	*0*	0	0	*0*	*0*	*0*	*0*	0	0	*0*	*0*	0
Fit Assessment	**Log10(Φ)**	OK	OK	OK	OK	*OK*	OK	OK	*OK*	*OK*	*OK*	*OK*	OK	OK	*OK*	*OK*	OK
	Log10(ϕ)	OK	OK	OK	OK	*OK*	OK	OK	*OK*	*OK*	*OK*	*OK*	OK	OK	*OK*	*OK*	OK
	Temperature	OK	OK	OK	OK	*OK*	OK	OK	*OK*	*OK*	*OK*	*OK*	OK	OK	*OK*	*OK*	OK
	Copper	OK	OK	OK	OK	*OK*	OK	OK	*OK*	*OK*	*OK*	*OK*	OK	OK	*OK*	*OK*	OK
	Nickel	OK	>1	OK	OK	*OK*	OK	OK	*OK*	*OK*	*OK*	*OK*	OK	OK	*OK*	*OK*	OK
	Pred TTS	OK	>1	>1	OK	*>1*	OK	OK	*OK*	*>1*	*OK*	*OK*	OK	OK	*>1*	*OK*	OK
	Phos	OK	OK	OK	OK	*OK*	OK	OK	*OK*	*OK*	*OK*	*OK*	OK	OK	*OK*	*OK*	OK
	Mn	OK	OK	OK	OK	*OK*	OK	OK	*OK*	*OK*	*OK*	*OK*	OK	OK	*OK*	*OK*	OK
	Product Form	OK	OK	OK	OK	*OK*	OK	OK	*OK*	*OK*	*OK*	*OK*	OK	OK	*OK*	*OK*	OK
T on Slope	**Log10(Φ)**	0.52	0.12	0.06	0.12	*0.00*	0.01	0.01	*0.09*	*0.02*	*0.07*	*0.00*	0.01	0.01	*0.04*	*0.01*	0.05
	Log10(ϕ)	0.37	0.15	0.22	0.16	*0.26*	0.07	0.07	*0.15*	*0.07*	*0.12*	*0.25*	0.07	0.07	*0.12*	*0.08*	0.12
	Temperature	0.06	0.29	0.52	0.42	*0.37*	0.12	0.10	*0.16*	*0.11*	*0.23*	*0.16*	0.09	0.11	*0.24*	*0.25*	0.09

Model ID	Label	CM-3(2)	RM-1	RM-1(2)	RM-2	*RM-2(2)*	RM-2(3)	RM-3	*RM-4*	*RM-4(2)*	*RM-4(3)*	*RM-5*	RM-6	RM-6(2)	*RM-7*	*RM-7(2)*	RM-6(2)
	Action	From Table 4.5	From CM-3(2). Eliminate stand alone Ni from the CRP term	Optimize RM-1	Introduce a single value of Cu_{max}, do not optimize	*Optimize RM-2*	From RM-2. Changed coefficients and optimize	Cu exp fixed at ½ theory value. Changed red and optimized	*Allow different Cu_{max} for Linde 80, not optimized*	*Optimize RM-4*	*Optimize RM-4(2)*	*From 3. Try to reduce average Φ_{SAT} by allowing ϕ to influence Φ_{SAT}*	From 3. Eliminate "1" from CRP CF. Optimize	optimized	*Removed Cu_{max}*	*Optimized*	Round coefficients
	Copper	0.55	0.02	0.00	0.71	*0.00*	0.39	0.74	*0.82*	*0.71*	*0.80*	*0.39*	0.75	0.68	*0.12*	*0.29*	0.66
	Nickel	0.02	1.40	0.19	0.29	*0.44*	0.50	0.35	*0.03*	*0.01*	*0.02*	*0.31*	0.29	0.26	*0.37*	*0.46*	0.23
	Pred TTS	0.66	1.96	1.26	0.67	*1.44*	0.90	0.61	*0.85*	*0.92*	*0.89*	*0.89*	0.62	0.70	*1.36*	*0.90*	0.75
	Phos	0.05	0.45	0.06	0.43	*0.07*	0.00	0.07	*0.09*	*0.00*	*0.06*	*0.11*	0.07	0.00	*0.42*	*0.18*	0.00
	Mn	0.02	0.67	0.30	0.08	*0.25*	0.32	0.02	*0.05*	*0.00*	*0.05*	*0.11*	0.01	0.00	*0.26*	*0.11*	0.02
	Product Form	0.02	0.00	0.11	0.42	*0.00*	0.01	0.21	*0.29*	*0.08*	*0.16*	*0.15*	0.22	0.15	*0.19*	*0.16*	0.15
T on Intercept	**Log10(Φ)**	0.52	0.12	0.06	0.11	*0.01*	0.00	0.00	*0.09*	*0.00*	*0.08*	*0.01*	0.00	0.00	*0.04*	*0.00*	0.05
	Log10(ϕ)	0.37	0.15	0.22	0.17	*0.24*	0.08	0.08	*0.16*	*0.09*	*0.14*	*0.24*	0.08	0.08	*0.12*	*0.09*	0.13
	Temperature	0.06	0.29	0.52	0.43	*0.37*	0.12	0.10	*0.15*	*0.10*	*0.22*	*0.16*	0.10	0.11	*0.24*	*0.26*	0.09
	Copper	0.53	0.00	0.03	0.51	*0.13*	0.21	0.47	*0.62*	*0.34*	*0.52*	*0.43*	0.48	0.42	*0.11*	*0.13*	0.52
	Nickel	0.05	1.31	0.16	0.35	*0.31*	0.37	0.21	*0.09*	*0.20*	*0.10*	*0.35*	0.16	0.13	*0.34*	*0.34*	0.18
	Pred TTS	0.47	1.59	0.98	0.66	*1.01*	0.87	0.68	*0.78*	*1.05*	*0.90*	*0.61*	0.68	0.74	*1.11*	*0.86*	0.66
	Phos	0.08	0.41	0.08	0.35	*0.14*	0.08	0.03	*0.04*	*0.16*	*0.05*	*0.05*	0.03	0.10	*0.40*	*0.24*	0.03
	Mn	0.04	0.66	0.28	0.12	*0.20*	0.36	0.08	*0.02*	*0.10*	*0.01*	*0.07*	0.07	0.06	*0.26*	*0.15*	0.04
	Product Form	0.22	0.15	0.34	0.59	*0.27*	0.16	0.38	*0.47*	*0.26*	*0.34*	*0.38*	0.39	0.35	*0.09*	*0.37*	0.37
T Quad	**PF Quad**	0.13	0.10	0.05	0.29	*0.17*	0.11	0.07	*0.15*	*0.09*	*0.01*	*0.00*	0.07	0.01	*0.38*	*0.00*	0.01
T Si	**Slope**	0.17	#N/A	#N/A	#N/A	*#N/A*	#N/A	#N/A	*#N/A*	*#N/A*	*#N/A*	*#N/A*	#N/A	#N/A	*#N/A*	*#N/A*	1.38
	Intercept	0.17	#N/A	#N/A	#N/A	*#N/A*	#N/A	#N/A	*#N/A*	*#N/A*	*#N/A*	*#N/A*	#N/A	#N/A	*#N/A*	*#N/A*	1.36

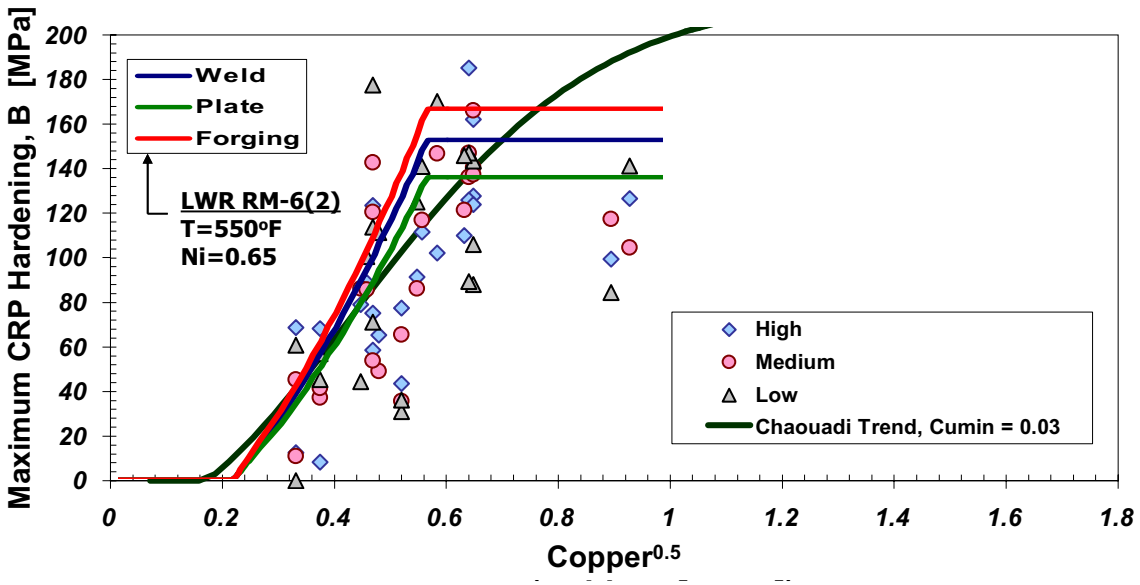

Figure 4-36. Variation of the peak CRP hardening with √Cu.
The predictions of RM-6(2) established by fitting the US-LWR surveillance database are compared with the IVAR data and also with the trend found by [Chaouadi 05b] for RPV steels of typical nickel content. Comparison is made for 290 °C exposures.

4.3.3 Final Assessment

4.3.3.1 Comparison of RM-6(2) to IVAR and RADAMO

The method described in Section 4.3.1 was again used to assess how well RM-6(2) represents the trends in both the IVAR and the RADAMO databases. While Appendix D presents the detailed comparisons, Table 4.10 and

Table 4.11 summarize the results of comparing the predictions of RM-6(2) to the 200 unique alloy/temperature/flux conditions explored in both IVAR and RADAMO. These comparisons show that RM-6(2) represents the embrittlement trends in these databases better than CM-3(2). At fluences below Φ=3x10^{19} n/cm^2, RM-6(2) represents 78% of these alloy/temperature/flux conditions "OK"; this is better than the 71% agreement rate of CM3-2. Even though agreement between predictions and data is good overall, the IVAR and RADAMO databases each highlight key areas for future improvements to embrittlement models, as illustrated by the following:

- Figure 4-37 shows the variation of ΔT_{30} prediction error with the predicted value of ΔT_{30} for all IVAR alloys having Cu $\leq$ 0.38 wt-% with the three different graphs partitioned by flux level. The overall agreement between RM-6(2) predictions and the IVAR data is very good for all alloys below this copper content, which exceeds Cu_{max} by 0.06 wt-% (the welds having ΔT_{30} prediction errors exceeding 50 °F are either high nickel alloys or are 67W, for which the cause of the poor prediction is not clear). The IVAR data do reveal a slight effect of flux that cannot be well calibrated from the LWR data due to the strong correlation between flux and fluence in the surveillance database.
- Figure 4-38 shows the variation of ΔT_{30} prediction error with the predicted value of ΔT_{30} for all IVAR alloys having Cu >0.38 wt-% with the three different graphs partitioned by flux level. While these ΔT_{30} prediction errors are less than those exhibited by alternative models that do not have a Cu_{max} term, these data reveal that RM-6(2) does not provide good predictions of the embrittlement trend in these higher copper alloys. This inadequacy of RM-6(2) stems from the lack of high-copper data in the US-LWR surveillance database used to calibrate RM-6(2).
- Figure 4-39 shows that RM-6(2) adequately predicts the 14 alloys in RADAMO for irradiations at both 265 and 300 °C, provided that the fluence remains below 3x10^{19} n/cm^2. However, at higher fluences, RM-6(2) significantly under-predicts the observed embrittlement magnitude. As discussed in Section 4.3.1, we believe this problem stems from the lack of significant data above this fluence in the US-LWR calibration database. This lack of data appears to be responsible for a systematic under-estimation of the MD hardening rate, coupled with a systematic over-estimation of the peak CRP hardening magnitude.

Table 4.10. Assessment of comparisons between IVAR data and RM-6(2) predictions.

Bin		Alloy	Product Form	Composition [wt-%]					Assessment		
Cu	Ni			Cu	Ni	Mn	P	Si	LWR Fit is ___ Relative to IVAR data at this Flux		
									High ϕ	Med ϕ	Low ϕ
No CRP	Low	CM1	SMMS	0.01	0.01	1.67	0.003	0.15	OK	OK	OK
		CM2	SMMS	0.01	0.01	1.65	0.041	0.16	OK	OK	OK
	Typical	LG	SMMS	0	0.74	1.37	0.005	0.22	OK	OK	OK
		CM23	SMMS	0.01	0.83	1.62	0.002	0.15	OK	OK	OK
		CM27	SMMS	0.01	0.84	1.6	0.002	0.16	OK	OK	OK
		CM31	SMMS	0.01	0.86	1.65	0.006	0.17	OK	OK	OK
		CM8	SMMS	0.01	0.86	0.01	0.004	0.14	OK	OK	OK
		CM9	SMMS	0.01	0.86	0.85	0.003	0.15	OK	OK	OK
		CM25	SMMS	0.01	0.87	1.53	0.003	0.17	OK	OK	OK
		CM26	SMMS	0.01	0.87	1.66	0.006	0.17	OK	OK	OK
		CM3	SMMS	0.02	0.85	1.6	0.006	0.16	OK	OK	OK
		CM4	SMMS	0.02	0.86	1.53	0.031	0.16	OK	OK	OK

Bin		Alloy	Product Form	Composition [wt-%]					Assessment		
Cu	Ni			Cu	Ni	Mn	P	Si	LWR Fit is ___ Relative to IVAR data at this Flux		
									High ϕ	Med ϕ	Low ϕ
		CM5	SMMS	0.02	0.86	1.61	0.05	0.16	OK	LOW	OK
		CM24	SMMS	0.02	0.87	1.65	0.006	0.15	OK	OK	OK
		CM10	SMMS	0.02	0.88	1.66	0.008	0.17	OK	OK	OK
		BW-C	Weld	0.06	0.62	1.3	0.009	0.37	LOW	LOW	LOW
		A508	Forging	0.06	0.8	1.3	0.005	0.01	OK	OK	OK
	High	CM7	SMMS	0	1.7	1.55	0.047	0.17	OK	OK	OK
		CM6	SMMS	0.02	1.68	1.5	0.007	0.17	LOW	OK	OK
		RR-WP	Weld	0.04	1.65	1.43	0.011	0.5	LOW	LOW	LOW
CRP Increasing	Low	A302B	Plate	0.14	0.2	1.2	0.015	0.28	OK	OK	OK
		CM29	SMMS	0.21	0.02	1.68	0.002	0.14	HIGH	HIGH	HIGH
		CM15	SMMS	0.22	0.02	1.59	0.002	0.15	OK	OK	OK
	Typical	LH	SMMS	0.11	0.74	1.39	0.005	0.24	OK	OK	OK
		CM13	SMMS	0.11	0.83	1.61	0.004	0.16	OK	OK	OK
		CM14	SMMS	0.11	0.83	1.62	0.04	0.17	OK	OK	OK
		HSST02	Plate	0.14	0.67	1.55	0.009	0.2	LOW	LOW	LOW
		JRQ	Plate	0.14	0.82	1.4	0.019	0.25	OK	OK	OK
		LI	SMMS	0.2	0.74	1.37	0.005	0.24	OK	OK	LOW
		BW-A	Weld	0.21	0.63	1.69	0.014	0.45	OK	OK	OK
		65W	Weld	0.22	0.6	1.45	0.015	0.48	OK	OK	OK
		CM16	SMMS	0.22	0.82	1.58	0.004	0.25	OK	LOW	LOW
		CM30	SMMS	0.22	0.85	1.64	0.006	0.16	OK	OK	LOW
		62W	Weld	0.23	0.6	1.61	0.02	0.59	OK	OK	OK
		Midland	Weld	0.27	0.57	1.61	0.017	0.62	OK	OK	OK
		67W	Weld	0.27	0.69	1.44	0.011	0.5	HIGH	HIGH	HIGH
		BW-B	Weld	0.28	0.69	1.63	0.018	0.54	OK	OK	no data
		63W	Weld	0.3	0.69	1.65	0.016	0.63	OK	OK	LOW
		73W	Weld	0.31	0.6	1.56	0.005	0.45	OK	OK	LOW
	High	Palisades	Weld	0.2	1.2	1.3	0.01	0.18	OK	no data	no data
		CM17	SMMS	0.22	1.59	1.54	0.004	0.25	LOW	LOW	LOW
		RR-WG	Weld	0.24	1.71	1.21	0.008	0.6	HIGH	OK	OK
CRP Saturated	Low	LA	SMMS	0.4	0	1.37	0.005	0.22	OK	OK	OK
		CM18	SMMS	0.43	0.02	1.7	0.002	0.15	OK	OK	OK
		LB	SMMS	0.4	0.18	1.35	0.005	0.22	OK	OK	OK
	Typical	CM11	SMMS	0.34	0.85	1.64	0.006	0.18	OK	OK	OK
		EPRI-C	Weld	0.4	0.6	1.36	0.006	0.51	HIGH	OK	OK
		LC	SMMS	0.41	0.86	1.44	0.005	0.23	OK	OK	OK
		LO	SMMS	0.41	0.86	1.44	0.005	0.23	OK	OK	OK
		LJ	SMMS	0.42	0.81	1.34	0.005	0.13	HIGH	OK	OK
		CM21	SMMS	0.42	0.84	0.01	0.002	0.14	HIGH	HIGH	HIGH
		CM22	SMMS	0.42	0.84	0.84	0.002	0.14	HIGH	HIGH	OK
		CM28	SMMS	0.42	0.84	1.6	0.002	0.17	OK	OK	OK
		CM19	SMMS	0.42	0.85	1.63	0.005	0.16	OK	OK	OK
		LK	SMMS	0.8	0.81	1.13	0.005	0.13	HIGH	HIGH	OK
		CM12	SMMS	0.86	0.84	1.65	0.006	0.17	HIGH	HIGH	OK

Bin		Alloy	Product Form	Composition [wt-%]					Assessment		
Cu	Ni			Cu	Ni	Mn	P	Si	LWR Fit is ___ Relative to IVAR data at this Flux		
									High ϕ	Med ϕ	Low ϕ
	High	LD	SMMS	0.38	1.25	1.38	0.005	0.23	HIGH	OK	OK
		CM20	SMMS	0.43	1.69	1.63	0.006	0.16	OK	OK	OK
		RR-WV	Weld	0.56	1.66	1.36	0.01	0.38	HIGH	OK	OK

Table 4.11. Assessment of comparisons between RADAMO data and RM-6(2) predictions.

Bin		Alloy	Product Form	Composition [wt-%]					Assessment			
Cu	Ni			Cu	Ni	Mn	P	Si	LWR Fit is __ relative to data below Φ=3x10^{19} n/cm^2		LWR Fit is __ relative to data above Φ=3x10^{19} n/cm^2	
									265 °C	300 C°	265 °C	300 °C
No CRP	Low	VVER-440B	plate	0.08	0.12	0.4	0.012	0.29	HIGH	OK	HIGH	LOW
	Typical	A508-B	forging	0.05	0.75	1.43	0.008	0.28	OK	OK	LOW	LOW
		16MND5	forging	0.065	0.69	1.37	0.013	0.04	no data	OK	no data	LOW
		A508-W	weld	0.07	0.83	1.57	0.015	0.22	OK	OK	LOW	LOW
	High	VVER-1000B	plate	0.05	1.26	0.46	0.008	0.3	OK	OK	LOW	LOW
		VVER-1000W	weld	0.06	1.7	0.73	0.006	0.14	LOW	LOW	LOW	LOW
CRP Increasing	Low	VVER-440W	weld	0.13	0.12	0.97	0.032	0.5	OK	LOW	LOW	LOW
	Typical	20MnMoNi55	forging	0.11	0.8	1.29	0.007	0.2	OK	OK	LOW	LOW
		18MND5-W	weld	0.12	1.01	1.3	0.021	0.19	no data	OK	no data	LOW
		HSST-03	plate	0.12	0.62	1.36	0.011	0.26	OK	OK	LOW	LOW
		18MND5-BM	plate	0.13	0.64	1.55	0.008	0.25	OK	OK	LOW	LOW
		JRQ	plate	0.14	0.84	1.42	0.017	0.24	OK	OK	LOW	LOW
		72W	weld	0.23	0.6	1.6	0.006	0.44	OK	OK	LOW	LOW
		73W	weld	0.31	0.6	1.56	0.005	0.45	OK	OK	LOW	LOW

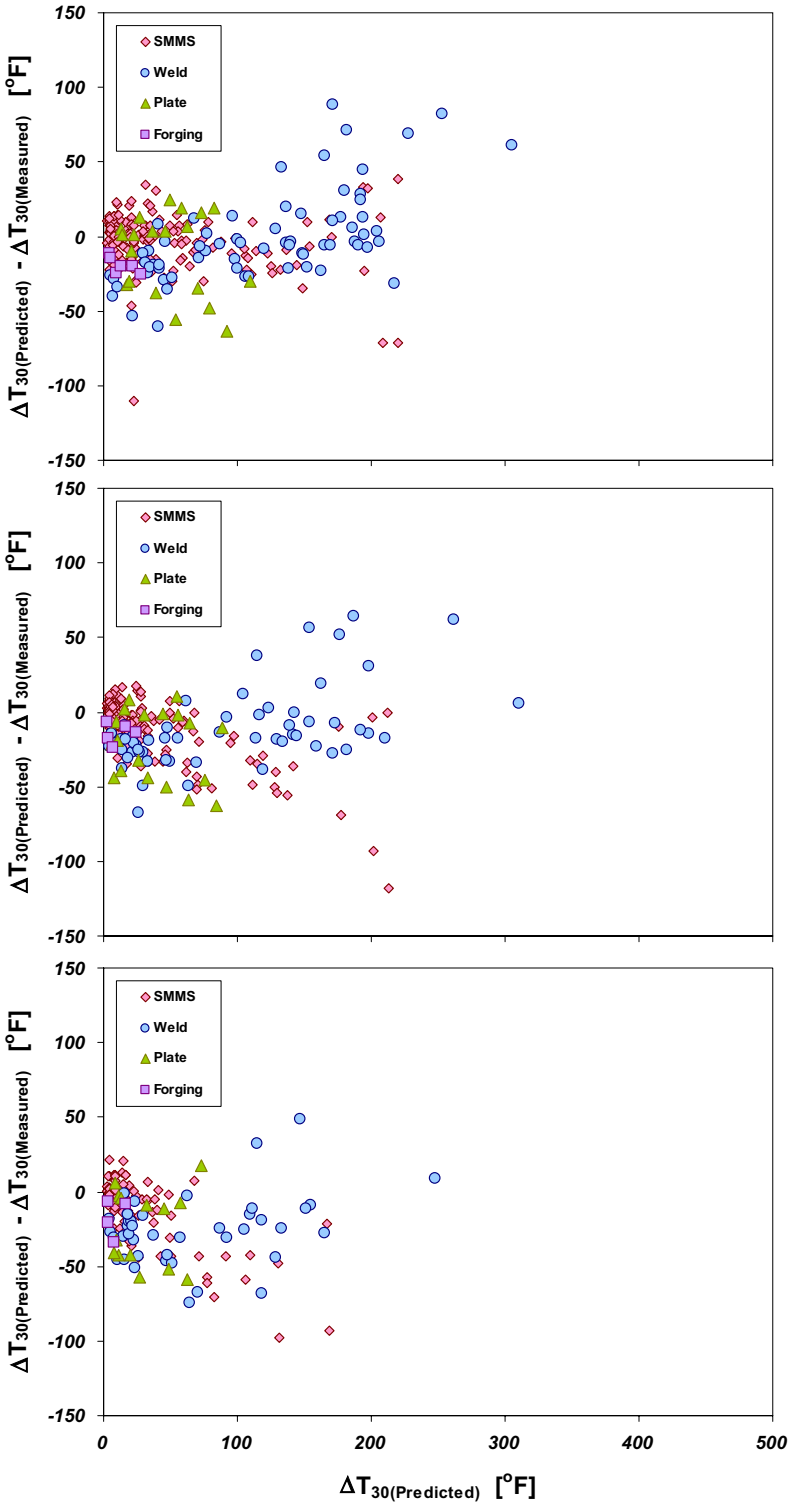

Figure 4-37. Assessment of the predictive capability of RM-6(2) relative to all of the alloys in the IVAR database having 0.38 wt-% copper or less irradiated at both 290 °C. The top, middle, and bottom plots show data from high ($\phi \approx 9 \times 10^{11}$ n/cm^2/s), medium ($\phi \approx 3 \times 10^{11}$ n/cm^2/s), and low ($\phi \approx 1 \times 10^{11}$ n/cm^2/s) flux irradiations, respectively.

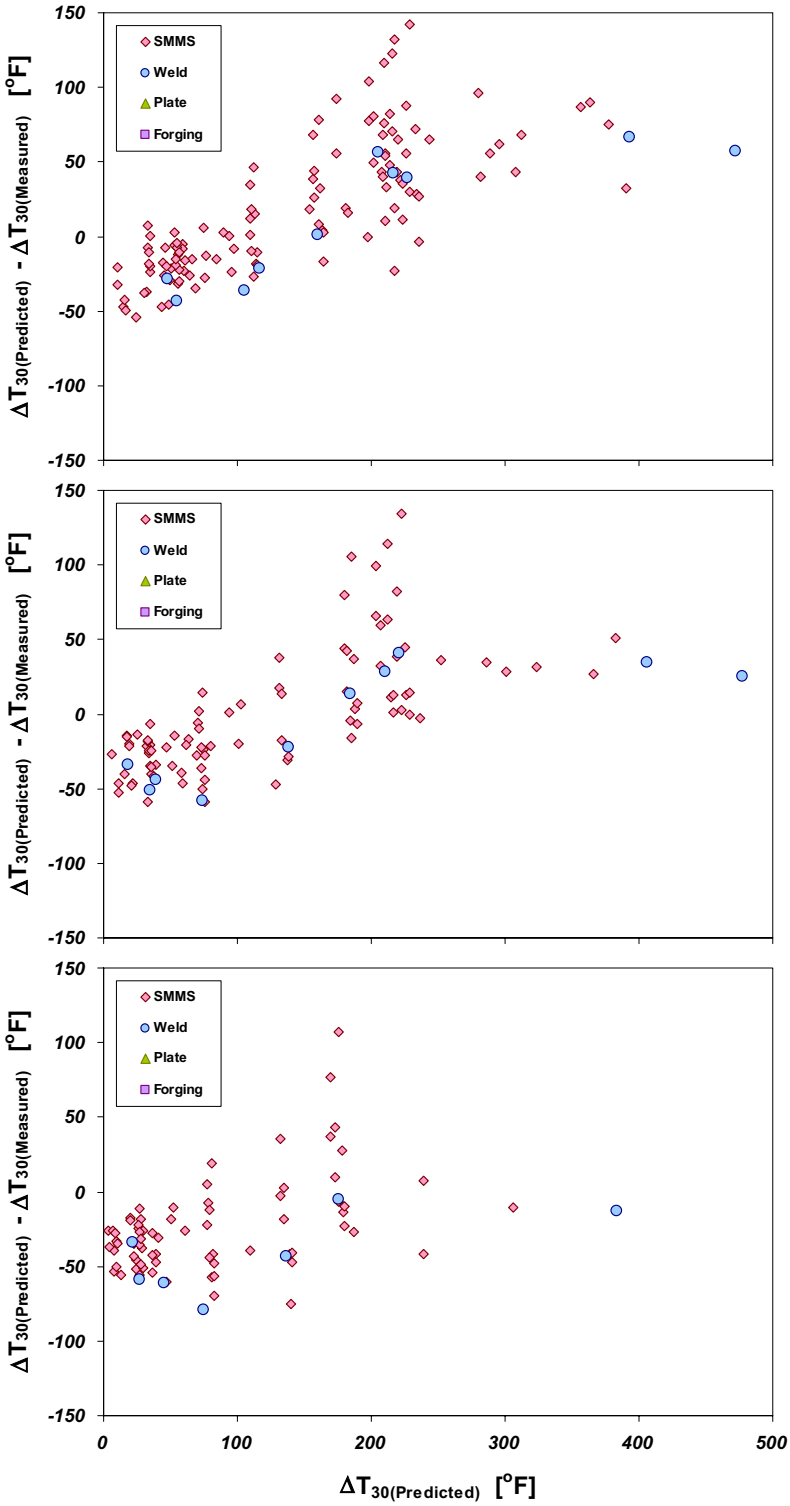

Figure 4-38. Assessment of the predictive capability of RM-6(2) relative to all of the alloys in the IVAR database having above 0.38 wt-% copper irradiated at both 290 °C. The top, middle, and bottom plots show data from high ($\phi \approx 9 \times 10^{11}$ n/cm^2/s), medium ($\phi \approx 3 \times 10^{11}$ n/cm^2/s), and low ($\phi \approx 1 \times 10^{11}$ n/cm^2/s) flux irradiations, respectively.

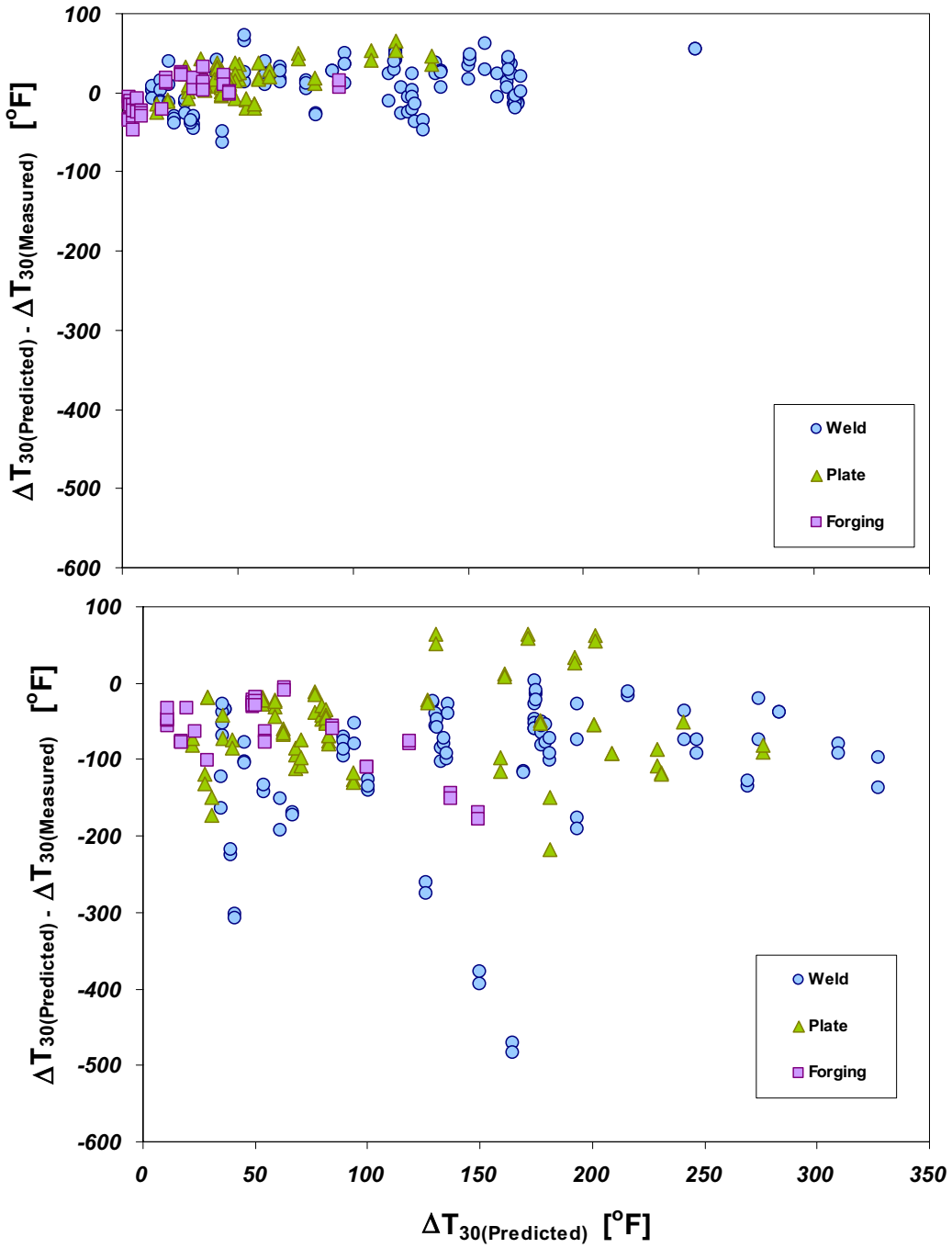

Figure 4-39. Assessment of the predictive capability of RM-6(2) relative to the 14 alloys in the RADAMO database irradiated at both 265 and 300 °C. The top graph is for fluence below $3x10^{19}$ n/cm^2, while the bottom braph is for fluences above $3x10^{19}$ n/cm^2.

4.3.3.2 Comparison of RM-6(2) to Japanese Test Reactor and Surveillance Data

Data from surveillance and test reactor irradiation programs were provided to the NRC by JNES [JNES 07]. These surveillance data were derived from 12 early-constructed plants, and are available in industry documents that are available to the public.

As previously illustrated in Figure 4-30, the JNES surveillance database covers approximately the same flux/fluence range as the US-LWR database. The JNES test reactor database samples both higher fluxes ($\phi > 10^{12}$ n/cm^2/s) and higher fluences (all but one shift value is above $\Phi = 3 \times 10^{19}$ n/cm^2). The surveillance database has 102 ΔT_{30} records, with these being approximately equally divided between plates, welds, and heat-affected zone (HAZ) specimens (the HAZ data were not included in the evaluation presented here). The test reactor database has 31 ΔT_{30} records, of which two-thirds are plates and the remainder are welds. Figure 4-40 shows that the materials in these databases have nickel contents that are comparable to the US-LWR data. The copper content of the materials in the JNES databases ranges from 0.02 to 0.24 wt-%, which is again similar to the US-LWR surveillance database. The phosphorus and manganese contents of these materials are also similar to those found in the US-LWR surveillance database.

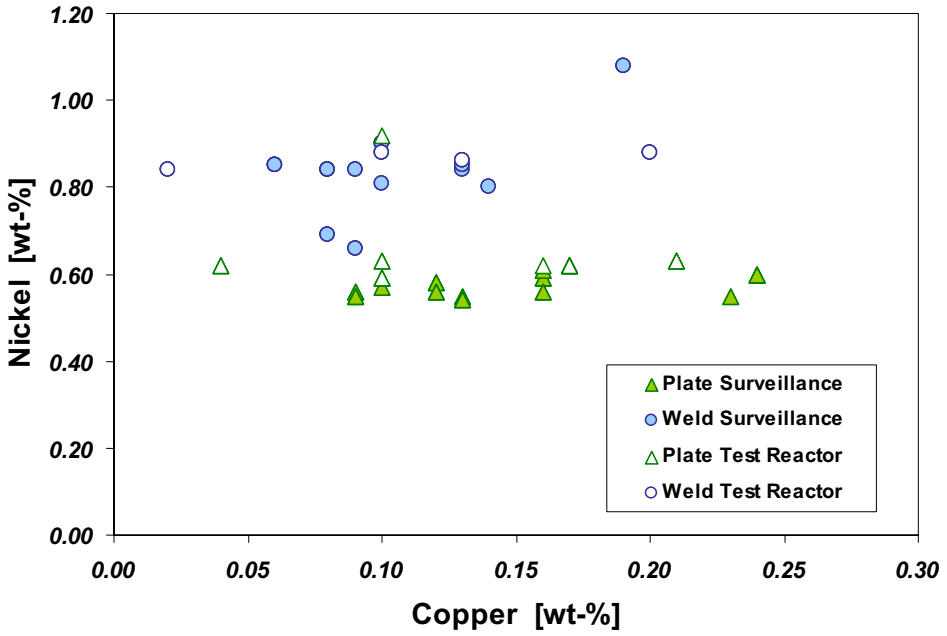

Figure 4-40. Copper and nickel contents of the plates and welds in the JNES databases [JNES 07].

Figure 4-41 shows the variation of ΔT_{30} prediction error with the value of ΔT_{30} predicted by RM-6(2) for all of the JNES surveillance data. The prediction error is well within the 2σ bounds for RM-6(2) of $\pm \approx 50$°F, indicating good agreement between the JNES data and the trends extracted from the US-LWR surveillance data that are reflected in RM-6(2).

Figure 4-42 shows the variation of ΔT_{30} prediction error with the value of ΔT_{30} predicted by RM-6(2) for all of the JNES test reactor data. In this case, the predictive capability of RM-6(2) is quite poor. We believe that the cause of this disagreement is that, with a singe exception, all of the data points in Figure 4-42 correspond to fluences above $\Phi = 3 \times 10^{19}$ n/cm^2. The poor predictive capability

of RM-6(2) at high fluences was previously noted using the RADAMO data (see the bottom graph in Figure 4-39). As previously stated, we believe this problem stems from the lack of significant data at high fluences in the US-LWR calibration database.

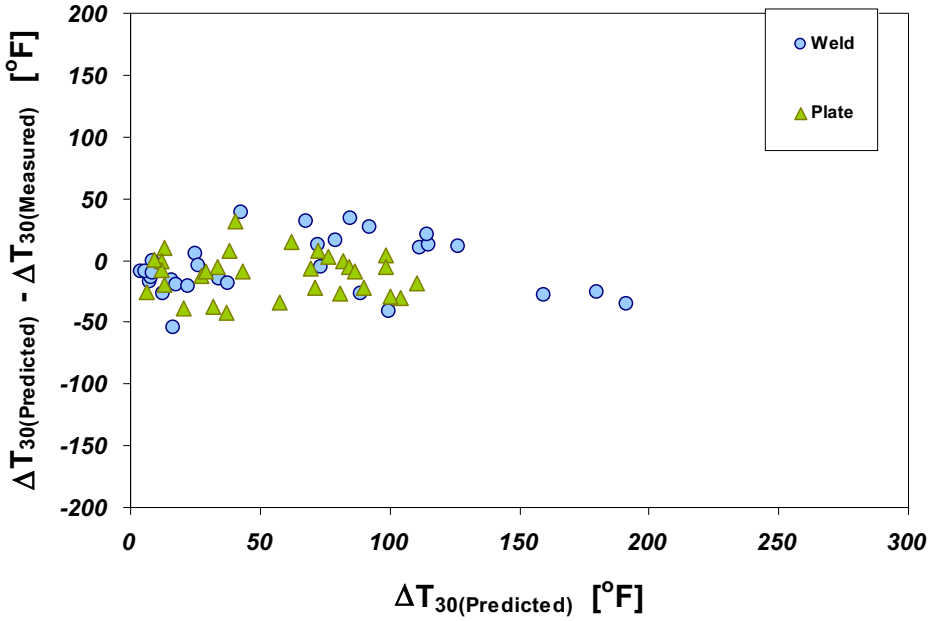

Figure 4-41. Assessment of the predictive capability of RM-6(2) relative JNES surveillance data.

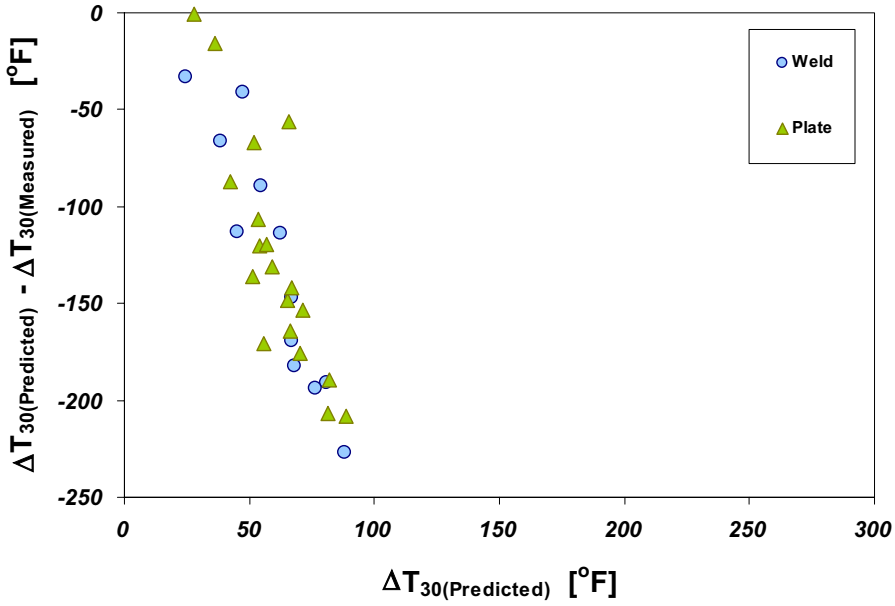

Figure 4-42. Assessment of the predictive capability of RM-6(2) relative JNES test reactor data.

4.3.3.3 Comparison of RM-6(2) to French Surveillance Data

Data from surveillance programs in French power reactors were detailed in a 1992 publication [Brillaud 92]. As previously illustrated in Figure 4-30, the fluxes and fluences of the French surveillance database nearly overlay those of the US-LWR database. The French database contains 123 ΔT_{30} records, of which 70 are forgings and the remainder welds. (Brillaud also reports HAZ data that were not included in the evaluation presented here.) Figure 4-43 shows that most of the French data have nickel contents that are comparable to the US-LWR data, but there is one weld with very low nickel. The French database is notably different from the US-LWR data in that the former consists almost exclusively of low-copper materials. The phosphorus and manganese contents of these materials are similar to those found in the US-LWR surveillance database.

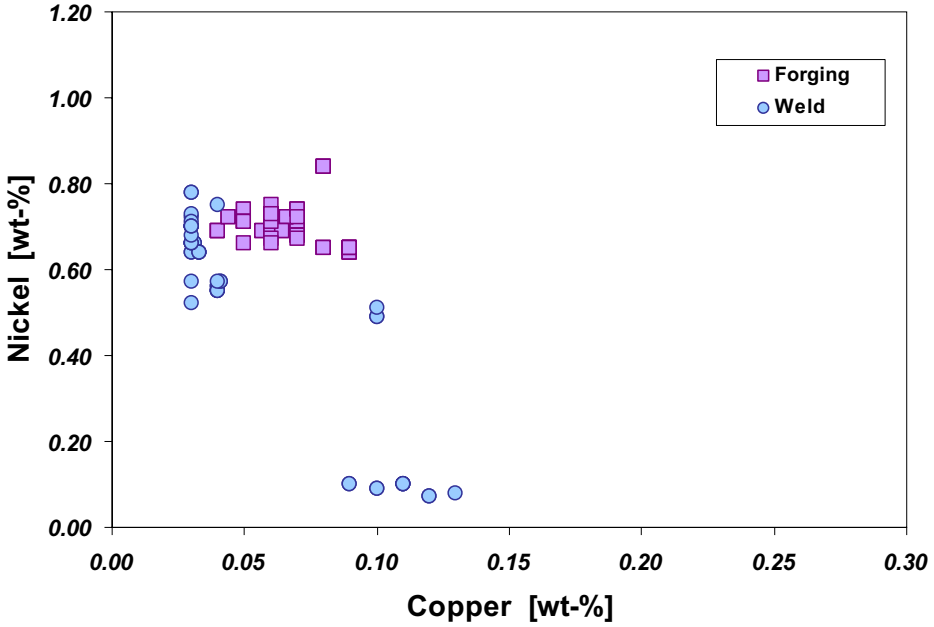

Figure 4-43. Copper and nickel contents of the forgings and welds in the French database [Brillaud 92].

Figure 4-44 shows the variation of ΔT_{30} prediction error with the value of ΔT_{30} predicted by RM-6(2) for all of the French surveillance data exposed at temperatures between 540 and 550 °F (this constitutes the bulk of the database). Similar to the bulk of the Japanese surveillance data, prediction error for these materials is within the 2σ bounds of $\pm \approx 50$ °F, indicating good agreement between the French surveillance data and the trends extracted from the US-LWR surveillance data that are reflected in RM-6(2). Conversely, Figure 4-45 shows that for the lower-temperature exposures achieved in the Chooz-A reactor, the predictive capability of RM-6(2) is not as good. This lack of agreement may be atttributable to the lower irradiation temperatures at Chooz-A (490 to 510 °F), which are outside of the range of temperatures in the US-LWR database. As previously noted, the temperature dependence of RM-6(2) (and all predecessor trend curves fit to the US-LWR surveillance database) differs from the temperature dependencies found in other large collections of data (see Figure 4-25 and associated discussion).

The preponderance of low-copper data in the French surveillance database provides an opportunity to test the observation, which arose during evaluation of the RADAMO database, that the magnitude of the matrix damage rate may be under-estimated by RM-6(2). Figure 4-46 restricts attention to the portion of the French surveillance database that has copper below the Cu_{min} value of 0.048 wt-% used in RM-6(2). These data show a clear trend of increasing under-prediction of embrittlement using RM-6(2) as the level of embrittlement increases; this observation further supports the observation made using the RADAMO database that the magnitude of matrix damage may be under-estimated by RM-6(2).

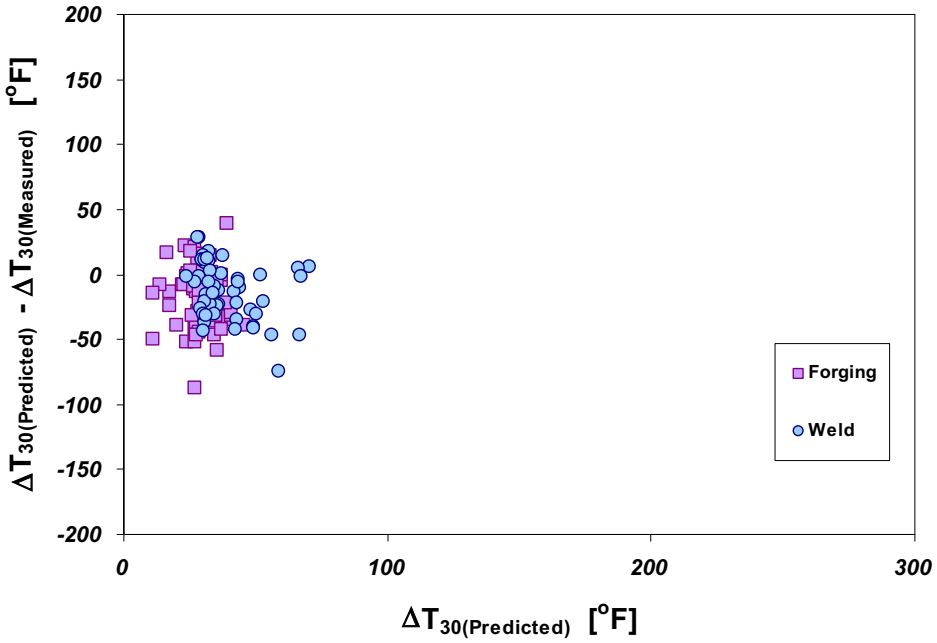

Figure 4-44. Assessment of the predictive capability of RM-6(2) relative to all of the French surveillance data having irradiation temperatures between 540 and 550 °F (i.e., the entire database other than Chooz-A).

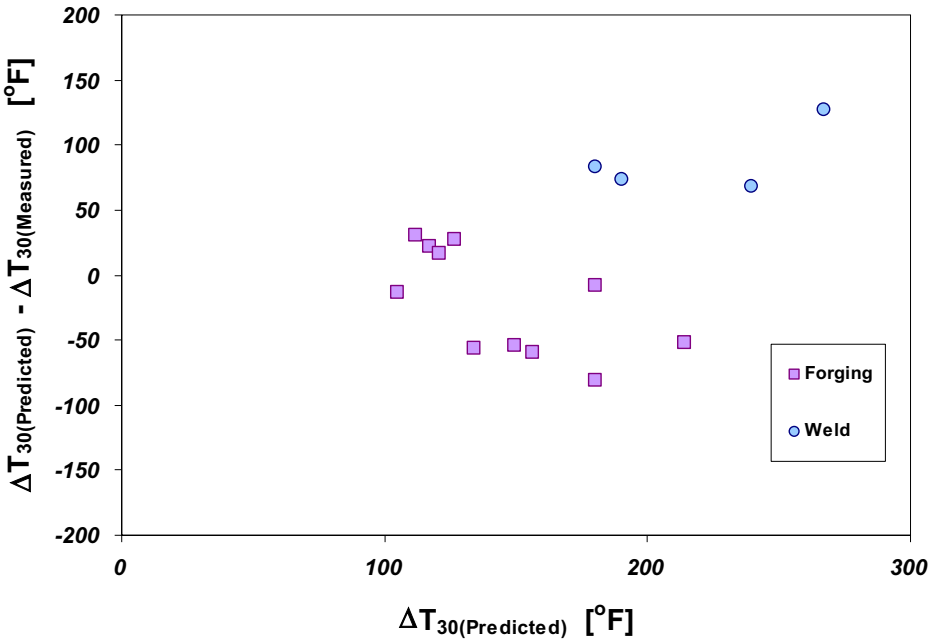

Figure 4-45. Assessment of the predictive capability of RM-6(2) relative to the Chooz-A surveillance data (irradiation temperature is between 490 and 510 °F).

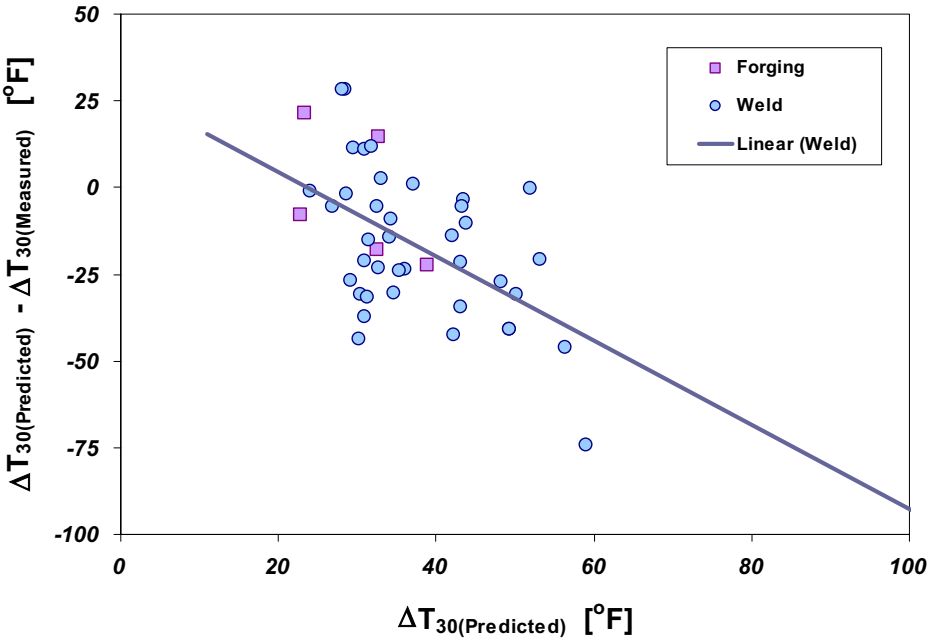

Figure 4-46. Assessment of the predictive capability of RM-6(2) relative to the French surveillance data having irradiation temperatures between 540 and 550 °F (i.e., the entire database other than Chooz-A) and copper content below the RM-6(2) Cu_{min} value of 0.048 wt-%.

4.4 Model for High Fluences

The information presented in Section 4.3 reveals one deficiency in RM-6(2) that is both significant and practically important — its under-prediction of ΔT_{30} at fluences above $\approx 3 \times 10^{19}$ n/cm^2. The data demonstrating this deficiency were obtained in Belgian and Japanese test reactor programs and, therefore, at flux levels above those seen in power reactor service. Nevertheless, the data in Figure 4-32 demonstrate that the difference between test- and power-reactor flux levels does not significantly alter the embrittlement trends at fluences above $\approx 3 \times 10^{19}$ n/cm^2. Fluences above $\approx 3 \times 10^{19}$ n/cm^2 will occur in both current and next-generation reactors. In the year of publication of this report (2007), nine PWRs have peak fluences above 3×10^{19} n/cm^2; by the end of the initial licensed lifetime (40 years), this number increases to 34. Additionally, some new reactor designs are projected to experience fluences as high as $\approx 1 \times 10^{20}$ n/cm^2 after 60–80 years of operation.

Because of the practical significance of high fluences for power reactor service, a ΔT_{30} trend curve equation is developed in this section for use beyond $\Phi = 3 \times 10^{19}$ n/cm^2. The following four options were considered:

A. Use RM-6(2), but add a margin to account for under-prediction of ΔT_{30} above $\Phi = 3 \times 10^{19}$ n/cm^2.

B. Modify RM-6(2) based on information of the type presented in Table 4.8, which suggests that the magnitude of the MD term may have been systematically under-estimated, while the magnitude of the CRP term may have been systematically over-estimated.

C. Modify the ΔYS trend curve developed by Chaouadi based on physical insights and the RADAMO database [Chaouadi 01, Chaouadi 05b] so that it can be used to predict ΔT_{30} for all fluences.

D. Modify the ΔYS trend curve developed by Chaouadi based on physical insights and the RADAMO database [Chaouadi 01, Chaouadi 05b] so that it can be used to predict ΔT_{30} for fluences above $\approx 3 \times 10^{19}$ n/cm^2.

Option A was not pursued because the data presented in Appendix D (see also Figure 4-33 for an example) demonstrate that the functional form of RM-6(2) does not match the high-fluence data. The margin would have to be extremely large to accommodate this, or it would have to be a function of fluence (and likely other variables) to provide a reasonable bound to the data. While such a margin approach would be adequate for use in deterministic structural integrity assessments, it would not provide the “best-estimate” model that is needed for probabilistic assessments. For these reasons, Option A was not pursued.

Option B would provide a better fit to the data and, therefore, would require a smaller margin than Option A. Nevertheless, the analysis presented in Table 4.8 was rudimentary and completely empirical. While this analysis *suggests* that the magnitude of matrix damage embrittlement has been under-estimated, while the magnitude of copper-rich precipitation embrittlement has been over-estimated, these suggestions have not yet been validated by microstructural observations. For these reasons, the robustness of the models that would result from Option B is viewed as questionable, so Option B was not pursued.

Options C and D were pursued, and are described in the remainder of this section. The advantage to these options is that Chaouadi developed the RADAMO trend curve with knowledge of high-fluence data, so it is known *a priori* that the RADAMO trend curve will provide a reasonable "best-estimate" model of embrittlement trends in the regime where RM-6(2) is deficient. The modeling strategy described in [Chaouadi 01, Chaouadi 05b] places strong emphasis on the adoption of mathematical forms that follow from a physical understanding of irradiation damage mechanisms, while placing less weight on the statistical goodness-of-fit considerations that drove the modeling effort described in this report. Therefore, it is hoped that even though Chaouadi's trend curve may not provide as good a fit, in a statistical sense, as the trend curves described in Sections 4.2 and 4.3, it will be more robust on extrapolation.

The RADAMO trend curve for ΔYS is as follows:

Eq. 4-15 $$\Delta YS = \Delta YS_{(MD)} + \sqrt{\Delta YS^2_{(CRP)} + \Delta YS^2_{(PRP)}}$$

Matrix damage does not begin until an incubation fluence (Φ_o=1x10^{19} n/cm^2) has been achieved; below Φ_o $\Delta YS_{(MD)}$ is zero. Above Φ_o $\Delta YS_{(MD)}$ is defined as follows:

Eq. 4-16

$$\Delta YS_{(MD)} = \left\{585 \cdot \exp\left[-1250 \cdot \exp\left(-\frac{0.345}{kT}\right)\right] + \left(3880 - 6.3 \cdot T\right) \cdot Ni\right\} \sqrt{1 - \exp\left[-0.01\left(\Phi - \Phi_o\right)\right]}$$

where T is expressed in Kelvin, Ni is expressed in wt-%, and all fluences, both Φ and Φ_o, are divided by 1x10^{19} n/cm^2 before being used in Eq. 4-16.

The magnitude of the copper-rich precipitate term (in MPa) is as follows.

Eq. 4-17 $$\Delta YS_{(CRP)} = \Delta_{CRP(PEAK)} \cdot f\left(\phi, t, T, Cu\right)$$

In this equation, t is expressed in years at full power, ϕ is expressed in n/cm^2/sec, T is expressed in Kelvin, and Cu is expressed in wt-%. The constants in this term are defined in Table 4.12.

Step 1: Establish the maximum possible hardening (in MPa) for the copper content of the alloy in question:

If Cu ≤ Cu$_{min}$, then $\Delta_{CRP(PEAK)} = 0$

If Cu > Cu$_{min}$, then $\Delta_{CRP(PEAK)} = 215\left[1 - \exp\left\{-2.7\left(Cu - Cu_{\min}\right)\right\}\right]$

Step 2: Establish the percentage of the maximum hardening (the value of f ranges from 0.0 to 1.0) that has been reached for the flux, time, temperature, and copper content of interest.

Step 2a: Determine the time to peak hardening, in years:

$$t_{peak} = \frac{10^{\left\{\frac{10684}{T} - (15.3 - 0.3/Cu)\right\}}}{1 + \frac{1\times10^{-32}\cdot\phi}{\exp\left(-\frac{E}{kT}\right)}}$$

If $\phi < \phi_{LIM}$ then $E = E_o$

If $\phi \geq \phi_{LIM}$ then $E = E_o - 0.03 \cdot LOG\left[\frac{\phi}{\phi_{LIM}}\right]$

Here, the activation energy for copper diffusion (E) is a constant value (E_o) below some limiting value of flux (ϕ_{LIM}); E decreases slightly with increasing flux above this limit. The formula for E_o is as follows:

$$E_o = -kT \cdot \ln\left\{\frac{1\times10^{-32}\cdot\phi_{LIM}}{\frac{10^{\left(\frac{10684}{T} - (15.3 - 0.3/Cu)\right)}}{t_{peak}^{Cu_{\max}}} - 1}\right\}$$

In the formula for E_o, the variable $t_{peak}^{Cu_{\max}}$ is defined as follows:

$$t_{peak} = \frac{10^{\left\{\frac{10684}{T} - (15.3 - 0.3/Cu)\right\}}}{1 + \frac{1\times10^{-32}\cdot\phi_{LIM}}{\exp\left(-\frac{2.8}{kT}\right)}}$$

Step 2b: Select the appropriate formula for f based on the time the reactor of interest has been in full-power operation.

If $t < \frac{1}{20}\cdot t_{peak}$, then $f = 0$

If $\frac{1}{20}\cdot t_{peak} \leq t < t_{peak}$, then $f = \frac{1}{LOG(20)}\cdot LOG\left\{20\cdot\frac{t}{t_{peak}}\right\}$

If $t \geq t_{peak}$, then $f = 1$

Damage by phosphorus precipitation does not occur unless the alloy has 0.012 wt-% phosphorus or greater. Above P = 0.012 wt-%, the magnitude of the phosphorus-rich precipitate term (in MPa) is as follows:

Eq. 4-18 $\Delta YS_{(PRP)} = (44470.5 - 70T)\cdot(P - 0.012)$

In this equation, T is expressed in Kelvin, and P is expressed in wt-%. It should be noted that this relationship, while suggested in [Chaouadi 05b], was not recommended for use because it is empirical and based on only two data sets. Nevertheless, our assessment of the RADAMO trend curve, which appears in the remainder of this section, suggests that it is better to include this term than to omit it. Eq. 4-18 should only be used within its calibrated temperature range of 265–300 °C (509–572 °F).

Table 4.12. Constants in the RADAMO copper-rich precipitate equation.

Variable	Value	Units	Description
Cu_{min}	0.03	wt-%	Minimum copper at which CRP hardening occurs.
Cu_{max}	0.425	Wt-%	Copper level above which increasing copper does not appreciably increase CRP hardening magnitude.
k	8.617×10^{-5}	eV/K	Boltzmann's constant
ϕ_{LIM}	6×10^{12}	$n/cm^2/sec$	Maximum flux for constant activation energy for copper diffusion (E). Above this value E decreases with increasing flux

Product form effects are not normally seen when embrittlement is quantified in terms of ΔYS, explaining the absence of product form terms in Eq. 4-15. Nevertheless, product form effects are almost always observed when embrittlement is quantified in terms of ΔT_{30}, and ΔT_{30} has been determined based on *tanh* fitting of the CVE *vs*. temperature data. Product form coefficients were developed to convert Eq. 4-15 into a trend curve for ΔT_{30} as follows:

(1) Eq. 4-15 was used to predict trends in the US-LWR database.

(2) A leading multiplier, which was allowed to be different for welds, plates, and forgings, was used to convert the equation from ΔYS (in MPa) to ΔT_{30} (in °F).

(3) The MS-Excel® *solver* routine was used to vary the weld, plate, and forging coefficients such that the mean sum of squared errors was minimized for the US-LWR database.

Table 4.13. Product form coefficients fit using the US-LWR surveillance database that convert the RADAMO trend curve from ΔYS (in MPa) to ΔT_{30} (in °F).

Product Form	Best-fit Coefficient relating RADAMO trend curve to US-LWR data [°F/MPa]	Coefficients from [Kirk 01] in [°F/MPa]	Difference
Weld	1.39	1.24	+11%
Plate	1.18	1.08	+9%
Forging	0.84	0.88	-6%

Table 4.13 provides the results of this analysis, which are close to coefficients estimated by directly regressing ΔT_{30} *vs*. ΔYS [Kirk 01]. Combining Eq. 4-15 with the information in Table 4.13 produces the following estimation equation for ΔT_{30}:

Eq. 4-19
$$\Delta T_{30} = \left\{ \begin{array}{l} Weld = 1.39 \\ Plate = 1.18 \\ Forging = 0.84 \end{array} \right\} \cdot \Delta YS$$

In Eq. 4-19, the constants in the { … } convert the ΔYS values taken from Eq. 4-15 (which have units of MPa) into ΔT_{30} values (which have units of °F).

Our analysis compared the ΔYS and ΔT_{30} data from the four databases described in Section 4.3 to the predictions of Eq. 4-15 and 4-19, respectively. Plots of prediction residuals were made against all of the following variables:

- fluence
- flux
- temperature
- copper
- nickel
- phosphorus
- manganese
- silicon

Appendix E to this report presents the detailed results of this analysis. Observations based on the graphs in Appendix E are summarized below, separated in terms of the regressor variable:

- Fluence
  - Above $\Phi \approx 1 \times 10^{18}$ n/cm^2, the RADAMO trend curve provides a good fit, all the way to the highest fluence measured in any of the databases ($\Phi \approx 2 \times 10^{20}$ n/cm^2).
  - Below this fluence, the RADAMO trend curve under-predicts the shift by increasing amounts as fluence decreases.
- Flux
  - Above $\phi \approx 1 \times 10^{11}$ n/cm^2/sec, the RADAMO trend curve provides a good fit.
  - Below this flux, the RADAMO trend curve under-predicts the shift by increasing amounts as flux decreases.
- Temperature
  - The temperature dependence of the French and US-LWR power reactor irradiations appears to be different than that of the test reactor irradiations (e.g., RADAMO, IVAR) as characterized by the RADAMO data and trend curve.
  - At temperatures close to those characteristic of PWR operation (i.e., close to 550 °F), the RADAMO trend curve provides a reasonable representation of power reactor data.
  - For the test reactor irradiations, the RADAMO trend curve provides a good fit to the data above temperatures of ≈260 °C (≈500 °F). At lower irradiation temperatures, the RADAMO trend curve under-predicts the shift by an increasing amount as irradiation temperature decreases.
- Copper
  - All databases examined (even the RADAMO database) show a slight, but consistent, trend toward increasing under-prediction of shift by the RADAMO trend curve as copper content increases. However, this effect does not become large until copper levels exceed those typical of RPV steels (i.e., above ≈0.5 wt-%).

- Nickel
  - Relative to the RADAMO data, the RADAMO trend curve shows a slight trend toward increasing over-prediction as nickel increases.
  - Relative to US-LWR surveillance, IVAR test reactor, and French surveillance databases, an opposite trend is observed (i.e., the RADAMO trend curve over-predicts the shift of low-nickel materials and under-predicts the shift of high-nickel materials).
  - Over the range of nickel most often commonly encountered in western RPV steels (between 0.5 and 1.0 wt.-%) the RADAMO trend curve provides a good representation of all available data.
- Phosphorus
  - For phosphorus below 0.03 wt-%, the empirical phosphorus term developed in [Chaouadi 05] significantly improves the fit in all databases examined.
  - For phosphorus above 0.03 wt-%, the IVAR data show that the phosphorus term developed in [Chaouadi 05] significantly over-predicts the observed shift values.
  - As the maximum specification limits on phosphorus for A533B plates and A508 forgings are both below 0.03 wt-%, the phosphorus term developed in [Chaouadi 05] appears adequate to represent the embrittlement trends in these RPV steels.
- Manganese
  - No data set examined shows a significant residual trend relative to the un-modeled element manganese.
  - However, the IVAR data demonstrate that if both manganese and nickel contents are high (above 1.5 and 1.6 wt-%, respectively), the RADAMO trend curve will under-predict the shift.
- Silicon
  - The data examined indicate a slight trend toward an increasing degree of over-prediction by the RADAMO trend curve as the value of the un-modeled element silicon increases.

Figure 4-47 shows the cumulative effects of all of these observations on the predictive capability of the RADAMO trend curve for both the RADAMO and US-LWR databases. For a blind prediction, the RADAMO trend curve provides a very good overall representation of the trends in the US-LWR, and other, databases. Most important, the RADAMO trend curve provides accurate predictions at fluences above $3x10^{19}$ n/cm^2 (see figures in Appendix E to this report), a regime where RM-6(2) consistently under-predicts all available data (see the discussion and graphs in Section 4.3.3). Nevertheless, RM-6(2) performs statistically better as an interpolator in the well-populated areas of the US-LWR database. This is, of course, not surprising because RM-6(2) was fit to the US-LWR database.

To combine the best aspects of the RM-6(2) and the RADAMO trend curves for regulatory applications, both relationships are recommended for use (i.e., Option D is recommended), as follows:

- If $\Phi \leq 2x10^{19}$ n/cm^2, RM-6(2) is recommended for use.
- If $2x10^{19} < \Phi \leq 4x10^{19}$ n/cm^2, ΔT_{30} is estimated using the following formula. In this formula, $\Delta T_{30}^{RM-6(2)}$ and ΔT_{30}^{RADAMO} represent the values of ΔT_{30} estimated using RM-6(2) and Eq. 4-19, respectively.

Eq. 4-20 $$\Delta T_{30} = (1-W)\cdot \Delta T_{30}^{RM-6(2)} + W \cdot \Delta T_{30}^{RADAMO} \text{ where } W = \frac{1}{2}\left(\frac{\Phi}{1\times 10^{19}} - 2\right)$$

- If $\Phi > 4x10^{19}$ n/cm^2, the RADAMO trend curve, with ΔYS scaled to ΔT_{30}, is recommended for use.

The combination of the RM-6(2) and RADAMO estimates for fluences between 2 and $4x10^{19}$ n/cm^2 is recommended to smooth out the abrupt change in the predicted value of ΔT_{30} that would otherwise result at a fluence of $3x10^{19}$ n/cm^2. The effect of the combination formula (Eq. 4-20), which is completely empirical, is illustrated in Figure 4-48. As expected from previous comparisons (see Table 4.8), RM-6(2) generally under-predicts the value of ΔT_{30} for steels where embrittlement is dominated by matrix damage (i.e., low-copper materials), while it generally over-predicts the value of ΔT_{30} for steels where embrittlement is dominated by percipitation of copper, and copper-rich, second phases (i.e., high-copper materials). Combination of RM-6(2) with the RADAMO equation mitigates these errors, especially at high fluences where RM-6(2) produces non-conservative estimates of ΔT_{30}. Figure 4-49 demonstrates reasonable agreement between the prediction of the combined formula and the measured values of ΔT_{30} and ΔYS data from the US-LWR and RADAMO databases, respectively.

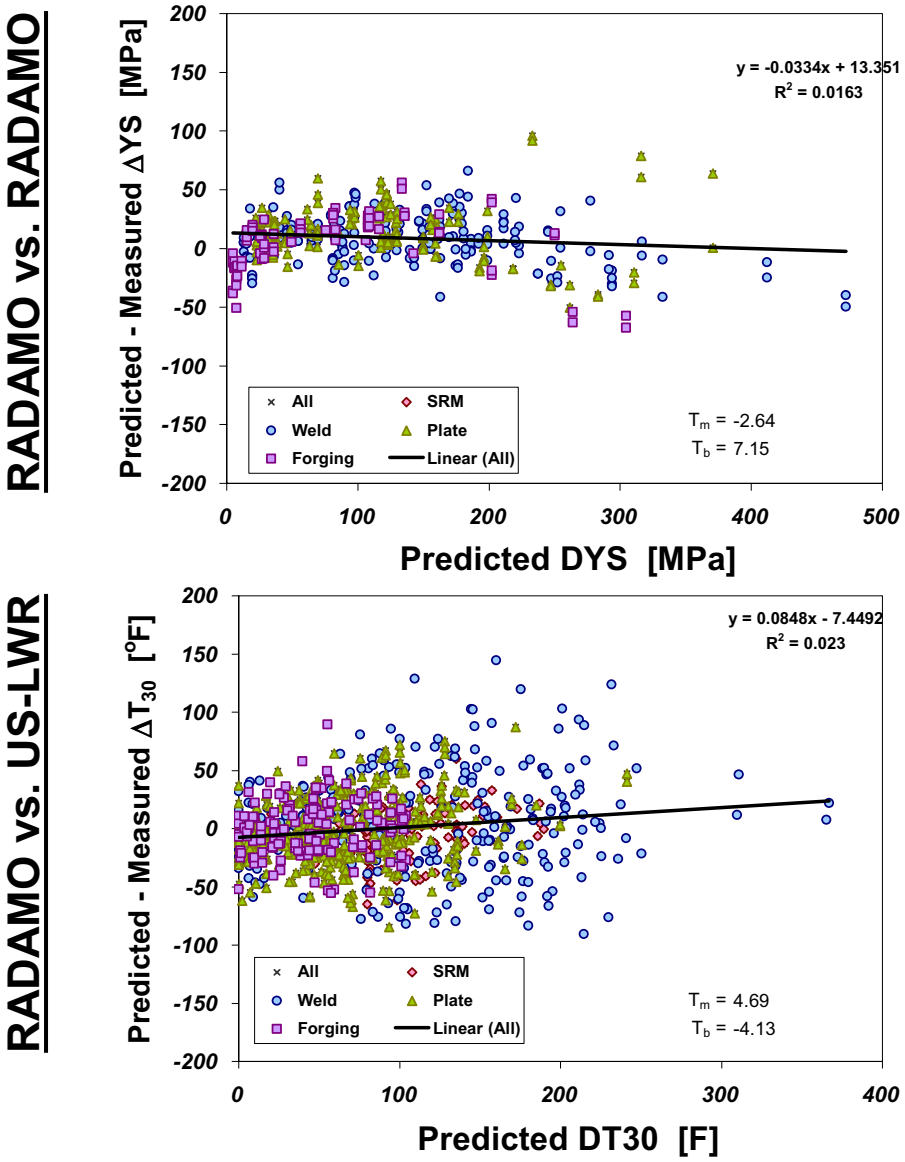

Figure 4-47. Comparison of the predictions of the RADAMO trend curve with the RADAMO ΔYS database (top), and the US-LWR surveillance database (bottom).

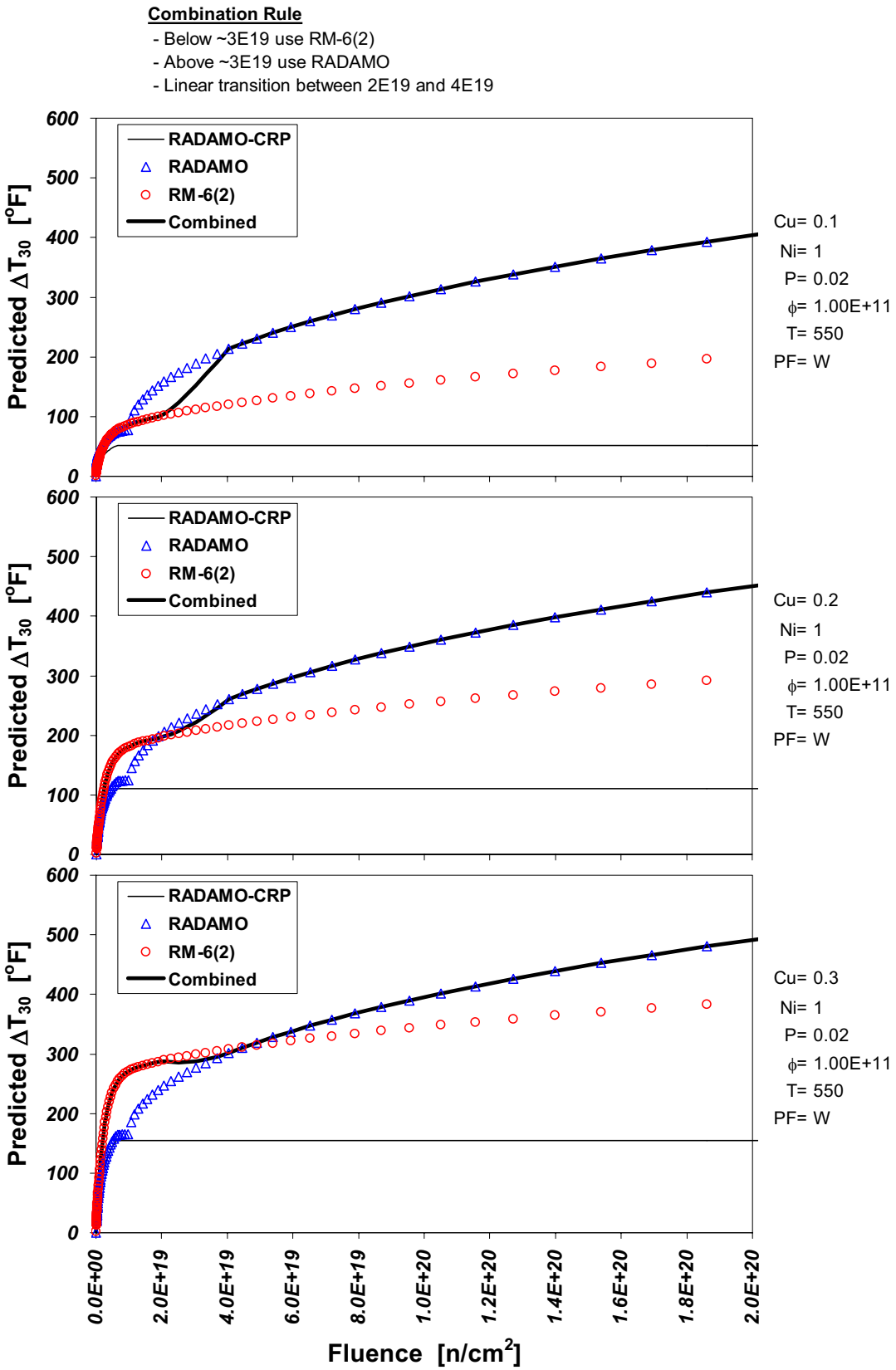

Figure 4-48. Illustration of combined ΔT_{30} prediction (Eq. 4-20) for a range of copper contents.

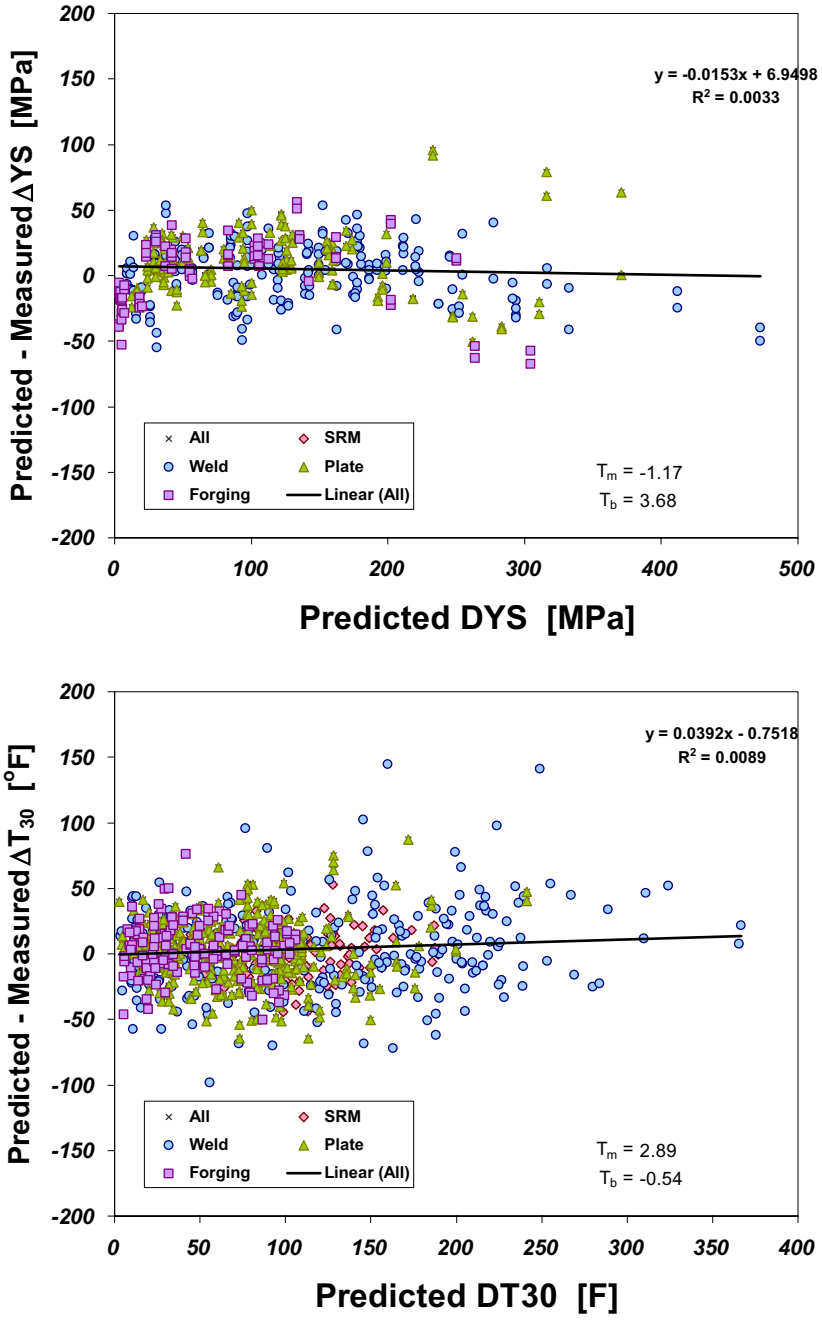

Figure 4-49. Comparison of the predictions of the combined ΔT_{30} prediction (Eq. 4-20) with the RADAMO ΔYS database (top), and the US-LWR surveillance database (bottom).

4.5 Recommended Model and Limitations

In this chapter, we have developed various relationships between ΔT_{30} and the composition, exposure, and categorical variables that can be applied to estimate the effects of neutron irradiation embrittlement on the Charpy V-Notch transition temperature of ferritic pressure vessel steels. The physical processes responsible for radiation-induced hardening of these steels motivate the functional form of these relationships. The numerical coefficients that quantify the relative magnitudes of the various embrittlement processes and the relative importance of the various regressor variables were established by calibrating the selected functional form to the US-LWR surveillance database using a least-squares approach. The form of these models was also guided by information available in both the RADAMO and IVAR test reactor databases. Comparison of the predictions of the RM-6(2) model to information in four different test reactor and surveillance databases established the accuracy/limits of the recommended model to conditions outside of its calibrated range.

The model recommended for use in Revision 3 of Regulatory Guide 1.99 depends on the fluence in question, as described in the following sections.

4.5.1 For Fluences At or Below 2×10^{19} n/cm^2

For fluences at or below 2×10^{19} n/cm^2, RM-6(2) is recommended for use, as follows:

Eq. 4-21 $$\Delta T_{30} = \Delta T_{30(MD)} + \Delta T_{30(CRP)}$$

where

$$\Delta T_{30(MD)} = PF_{MD} \cdot CF_{MD} \cdot TF_{MD} \cdot \phi F_{MD} \cdot \Phi F_{MD}$$

$$PF_{MD} = \left\{ \begin{array}{c} Weld = 6.7 \\ Plate = 8.1 \\ Forging = 4.75 \end{array} \right\} \times 10^{-9} \qquad CF_{MD} = \left[1 + 35 \cdot P\right]$$

$$TF_{MD} = \left(\frac{T}{550}\right)^{-14.64} \qquad \phi F_{MD} = \left(\frac{Log10(\phi)}{10.7}\right)^{-3.44} \qquad \Phi F_{MD} = \sqrt{\Phi}$$

$$\Delta T_{30(CRP)} = PF_{CRP} \cdot CF_{CRP} \cdot TF_{CRP} \cdot \Phi F_{CRP}$$

$$PF_{CRP} = \left\{ \begin{array}{c} Weld = 0.301 \\ Plate = 0.233 \\ Forging = 0.233 \end{array} \right\}$$

$$CF_{CRP} = \left[f(Cu) + 2500.3 \cdot \mathrm{MIN}\{0.32, \mathrm{MAX}(0, Cu - 0.048)\} \cdot Ni\right]$$

$$f(Cu) = -116.3 + 530.8\sqrt{Cu}\ \text{, subject to } 0 \le f(Cu) \le 118.5$$

$$TF_{CRP} = \left(\frac{T}{550}\right)^{-1.74} \qquad \Phi F_{CRP} = \left\{1 - \exp\left(\frac{-\Phi}{2.38\times10^{18}}\right)\right\}$$

In this equation, the values of Cu, Ni, and P are expressed in wt-%, temperature is expressed in degrees Fahrenheit, fluence is expressed in n/cm^2 (E>1MeV), and flux is determined by dividing fluence by the time the reactor has been in operation (with time expressed in seconds). The uncertainty (standard deviation) of RM-6(2) is 19 °F below Cu_{min}=0.048 wt-% and 25 °F above Cu_{min}.

RM-6(2) reflects the following physically expected trends:

- a linear addition of the embrittlement contribution of matrix damage (MD) and precipitation of copper-rich phases (CRP)
- a magnitude of matrix damage that increases in proportion to the square-root of the fluence
- a magnitude of peak CRP hardening that increases in proportion to the square-root of the copper content, with lower and upper asymptotes
- an effect of nickel content on the magnitude of peak CRP hardening that is synergistic with copper content
- an effect of temperature on the magnitude of matrix damage, and a slight additional effect of temperature on peak CRP hardening that was anticipated based on information in the IVAR database; however, it should be noted that the temperature effect on hardening in the US-LWR database that is reflected in RM-6(2) (and all precursor models fit to the US-LWR data) is much larger than reported in most other irradiation damage studies

Due to limitations in the span of the US-LWR surveillance database, the following physically expected trends could not be revealed by the calibration procedure employed herein:

- The slight effect of flux on the fluence at which CRP saturation occurs that is evident in the IVAR database could not be resolved because of the strong correlation between flux and fluence in the US-LWR surveillance dataset.
- The recognized effect of nickel on matrix damage could not be resolved because the bulk of the US-LWR surveillance data has between 0.5 and 1.0 wt-% nickel. There is a relatively small amount of data with low-nickel content (below 0.2 wt-%), and no data with high-nickel content (1.5 to 1.75 wt-%).

We also compared the predictions of RM-6(2) with information available in the following databases:

- IVAR test reactor database of ΔYS values,
- RADAMO test reactor database of ΔYS values,
- JNES test reactor database of ΔT_{30} values,
- JNES power reactor database of ΔT_{30} values, and
- French power reactor database of ΔT_{30} values

This comparison revealed that, within the central range of composition and exposure conditions of the US-LWR surveillance database, RM-6(2) predicts the embrittlement trends in all other databases very well. However, when RM-6(2) is used to make predictions at the peripheries of its calibration dataset or predictions that extrapolate from its calibrated range, its ability to represent embrittlement trends degrades in some cases.

Information presented in this chapter demonstrates the inability of RM-6(2) to reliably predict embrittlement trends for the following conditions:

(1) **At high fluences**: As fluence increases beyond ≈$3x10^{19}$ n/cm^2, the predictive accuracy of RM-6(2) rapidly degrades, with the model systematically under-estimating the magnitude of embrittlement at these high fluences. This problem stems from the lack of significant data above ≈$3x10^{19}$ n/cm^2 in the US-LWR calibration database, which appears to cause a systematic under-estimation of the matrix damage (MD) hardening rate coupled with a systematic over-estimation of the peak magnitude of copper-rich precipitate (CRP) hardening. Because matrix damage dominates embrittlement after CRP saturation, the net effect of these two errors is the systematic under-estimation at high fluences that was observed. While it is clear that RM-6(2) under-predicts embrittlement at fluences above $3x10^{19}$ n/cm^2, the apparent cause of this under-prediction advanced herein must be regarded as provisional, as it is based only on mechanical property data from the RADAMO and JNES test reactor databases. Microstructural examination of the alloys irradiated at high fluences using, for example, atom probe and small angle neutron scattering (SANS) techniques, is needed to determine which embrittlement mechanisms are active at high fluences.

(2) **At high and low nickel contents**: The bulk of the US-LWR surveillance data has between 0.5 and 1.0 wt-% Ni, so it is not surprising that RM-6(2) makes accurate predictions within this range of nickel content. However, at low nickel content (below ≈0.2 wt-%) and high nickel content (above ≈1.5 wt-%), respectively RM-6(2) systematically over-predicts or under-predicts embrittlement. Evidence supporting this finding is available in the RADAMO, JNES, and French surveillance databases.

(3) **As flux decreases from ≈$8x10^{11}$ n/cm^2/sec**: Decreasing fluxes lead to a slight increase in the degree by which RM-6(2) under-predicts embrittlement. As previously noted, the effect of flux on the fluence at which CRP saturates (which is evident in the controlled IVAR irradiations) cannot be resolved from any other database because of the strong correlations in all other databases between flux and fluence.

(4) **At high copper content**: Although RM-6(2) has a maximum copper content (Cu_{max}) term of 0.32 wt-%, this term is not a statistically essential feature of the model because the surveillance database has very limited data for high copper content. Nonetheless, information in the IVAR database demonstrates that above a copper content of ≈0.38 wt-%, RM-6(2) systematically over-estimates the magnitude of embrittlement.

Of these four inadequacies, the first presents the greatest practical concern and, therefore, is addressed by the recommendations presented in Sections 4.5.2 and 4.5.3. Fluences above ≈$3x10^{19}$ n/cm^2 have already occurred in operating PWRs, and will occur in approximately half of the PWRs in the current operating fleet by the end of their original operating licenses. Moreover, end-of-license-extension fluences for the existing reactor fleet are projected to be ≈$7x10^{19}$ n/cm^2 after 60 years of operation, and reactors that may be constructed in the near future are likely to have peak fluences as high as ≈$1x10^{20}$ n/cm^2 after 60–80 years of operation. Issue 1 also suggests a possible under-estimation in the matrix damage part of RM-6(2); this is a practical concern because matrix damage will be the dominant embrittlement mechanism in new reactors as they are expected to be fabricated from low-copper materials.

The latter three inadequacies present less practical concern because they are much smaller in magnitude, result in systematic over- (rather than under-) predictions of ΔT_{30}, and/or do not apply to the materials commonly encountered in power reactor service. The inadequacy of the RM-6(2) nickel model (Issue 2) will only matter if significant quantities of high- or low-nickel materials are used in fabricating new reactors. The inadequacy of the RM-6(2) flux model (Issue 3) is a relatively small effect, but needs to be better demonstrated with surveillance data before its practical impact can be assessed. Finally, the failure of RM-6(2) to accurately predict embrittlement magnitudes for high-copper (above ≈0.38 wt-%) alloys is not considered a practical concern because such materials do not exist in the operating reactor fleet, and are not likely to be introduced in the future.

Section 9.5 discusses methods to address these inadequacies in both the short- and long-term.

4.5.2 For Fluences Above 4x10^{19} n/cm^2

For fluence above 4x10^{19} n/cm^2, the RADAMO trend curve is recommended for use. The equations presented below are a consolidation and simplification of Eq. 4-15 through 4-19, which were presented earlier:

Eq. 4-22
$$\Delta T_{30} = \left\{ \begin{array}{c} Weld = 1.39 \\ Plate = 1.18 \\ Forging = 0.84 \end{array} \right\} \cdot \left\{ \Delta YS_{(MD)} + \sqrt{\Delta YS^2_{(CRP)} + \Delta YS^2_{(PRP)}} \right\}$$

The product form-dependent constants convert ΔYS (with units of MPa) into ΔT_{30} values (with units of °F).

Matrix damage does not begin until an incubation fluence (Φ_o=1x10^{19} n/cm^2) has been achieved; below Φ_o, $\Delta YS_{(MD)}$ is zero. Above Φ_o, $\Delta YS_{(MD)}$ is defined as follows:

$$\Delta YS_{(MD)} = \left\{ 585 \cdot \exp\left[-1250 \cdot \exp\left(-\frac{0.345}{kT} \right) \right] + \left(3880 - 6.3 \cdot T \right) \cdot Ni \right\} \sqrt{1 - \exp\left[-0.01 \left(\Phi - \Phi_o \right) \right]}$$

where T is expressed in Kelvin, Ni is expressed in wt-%, and all fluences (both Φ and Φ_o,) are divided by 1x10^{19} n/cm^2 before being used in this equation.

The magnitude of the **copper-rich precipitate** term is as follows:

$$\Delta YS_{(CRP)} = \Delta_{CRP(PEAK)}$$

where

If Cu ≤ Cu$_{min}$, $\quad \Delta_{CRP(PEAK)} = 0$

If Cu > Cu$_{min}$, $\quad \Delta_{CRP(PEAK)} = 215\left[1 - \exp\left\{-2.7\left(Cu - Cu_{\min}\right)\right\}\right]$

Cu$_{min}$ = 0.03 wt-%

This relationship is simplified relative to that presented in Section 4.4, insofar as this relationship for ΔYS_{CRP} reflects only the peak CRP hardening, rather than the evolution with fluence that is needed to achieve peak hardening. This simplification is possible because this formula will only be used at fluences above 2×10^{19} n/cm^2, which far exceeds that needed to achieve peak hardening (see Figure 4-48).

Damage by **phosphorus-rich precipitates** is zero for alloys having less than 0.012 wt-% phosphorus. For higher-phosphorus alloys, the magnitude of the phosphorus-rich precipitate term is as follows:

$$\Delta YS_{(PRP)} = (44470.5 - 70T) \cdot (P - 0.012)$$

In this equation, T is expressed in Kelvin. It should be noted that this relationship, while suggested in [Chaouadi 05b], was not recommended for use because it is empirical and based on only two data sets. Nonetheless, our assessment of the RADAMO trend curve suggests that it is better to include this term than to omit it. This equation should only be used within its calibrated temperature range of 265–300 °C (509–572 °F). Additionally, it should not be applied to phosphorus levels that exceed 0.03 wt-%.

4.5.3 For Fluences Between 2 and 4×10^{19} n/cm^2

For fluences between 2 and 4×10^{19} n/cm^2, the ΔT_{30} estimates of Eq. 4-20 and 4-21 are combined according to the following weighting formula:

Eq. 4-23 $\Delta T_{30} = (1 - W) \cdot \Delta T_{30}^{RM-6(2)} + W \cdot \Delta T_{30}^{RADAMO}$ where

where

$$W = \frac{1}{2}\left(\frac{\Phi}{1 \times 10^{19}} - 2\right)$$

$\Delta T_{30}^{RM-6(2)}$ and ΔT_{30}^{RADAMO} represent the values of ΔT_{30} estimated using Eq. 4-21 and 4-22, respectively.

5 PREDICTION OF UPPER-SHELF ENERGY DROP

In NUREG/CR-6551, which was the last systematic attempt to develop upper-shelf energy fits using the surveillance data from U.S. power reactors, Eason et al. investigated the following two fitting approaches [Eason 98]:

(1) One approach was similar to that taken to fit ΔT_{30} data in which the functional relationship between ΔUSE and both exposure and composition variables are explicitly fit, accounting separately for the embrittling effects of matrix damage *vs*. hardening by copper-rich precipitation. However, the lack of physical studies of ΔUSE made the assumed functional forms empirical, rather than physically motivated.

(2) The second (simpler) approach was to develop a linear correlation between the fit values of ΔT_{30} and the measured values of ΔUSE.

In NUREG/CR-6551, Eason reported that, from a statistical viewpoint, the second approach was nearly as good as the first. (The first fit had a standard error of 11.2 ft-lbs, while the second had a standard error that was only slightly larger at 12.9 ft-lbs.) It can also be noted that more recent work on fracture toughness data shows a systematic relationship between transition fracture toughness (K_{Jc}) and upper-shelf fracture toughness (J_{Ic}), which appears to be common to a wide variety of ferritic steels [EricksonKirk 06b]. This finding suggests that Eason's second approach to fitting ΔUSE data is defendable on a physical basis. In this analysis, we therefore adopted the approach of developing a linear correlation between ΔUSE and ΔT_{30}.

The US-LWR surveillance database from was filtered to remove any records that did not have recorded values for either the unirradiated or the irradiated value of upper-shelf energy. This left a total of 859 observations of ΔUSE to fit. The unirradiated and irradiated USE values that were used to estimate ΔUSE were themselves estimated from the parameters of the *tanh* fit to the entire CVE transition curve, as described in [Eason 98]. This procedure for estimating ΔUSE differs from that recommended by ASTM-E185, which is to average the CVE of all Charpy tests that exhibit at least 95% shear fracture area [ASTM E185]. The Eason procedure was adopted herein because it is less-influenced by the scatter in individual energy measurements made on the upper shelf. In well-populated data sets, the difference between the Eason and ASTM E185 USE values is very small (typically less than a single foot-pound).

As shown in Figure 5-1, the correlation between ΔT_{30} and ΔUSE is as follows:

Eq. 5-1 $$\Delta USE = 0.18 \cdot \Delta T_{30}$$

where ΔT_{30} is as predicted by Eqs. 4-21, 4-22, and 4.23 and is expressed in degrees Fahrenheit, and ΔUSE is expressed in foot-pounds. The uncertainty (standard deviation) in Eq. 5-1 is 13 ft-lbs. The relationship between ΔUSE and ΔT_{30} expressed in Eq. 5-1 is recommended for use in Revision 3 of Regulatory Guide 1.99.

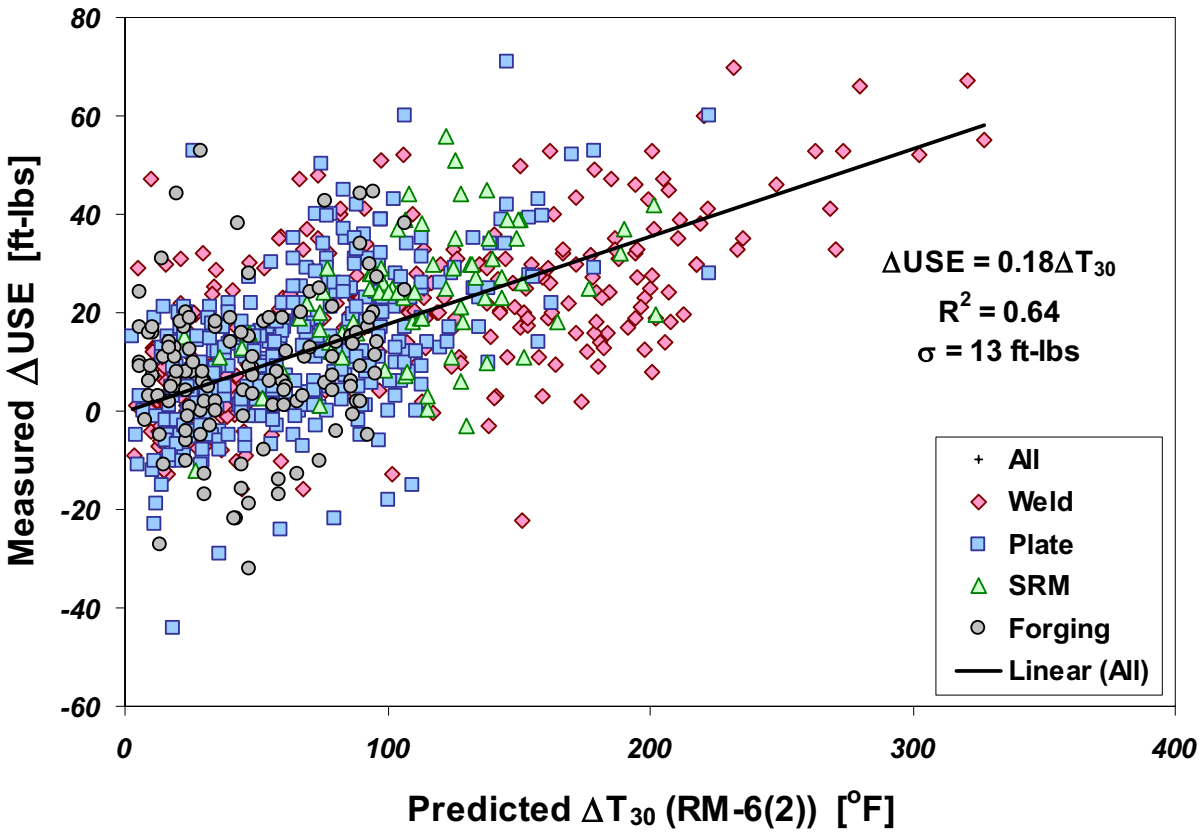

Figure 5-1. Relationship between measured values of ΔUSE from the surveillance database and the value of ΔT_{30} predicted using Eq. 4-15 from Chapter 4.

6 TREATMENT OF SURVEILLANCE DATA

6.1 Current Guidance

Regulatory Position 2 in Revision 2 of Regulatory Guide 1.99 describes procedures for estimating ΔT_{30} and ΔUSE when a minimum of two "credible" surveillance data points are available. This guidance allows the following manipulations:

- Modify the generic ΔT_{30} and ΔUSE relationships (Eq. 2-1 and Figure 2-1, respectively), based on the surveillance data.
- Reduce the margin term by a factor of two.

This section discusses the appropriateness of these procedures in view of the current state of knowledge of irradiation damage mechanisms.

6.2 Discussion

The state of knowledge regarding irradiation damage mechanisms and magnitudes in the ferritic steels and welds used to construct the beltline of reactor pressure vessels (RPVs) has advanced substantially since the NRC promulgated Revision 2 of Regulatory Guide 1.99 nearly two decades ago. As a result, it is now apparent that the physical mechanisms responsible for the irradiation hardening of ferritic steels are complex. As described in Section 4.1, Appendix A, and many publications in the literature, irradiation hardening depends on an array of composition and exposure variables. Moreover, the functional dependence of embrittlement (as measured by ΔT_{30} or ΔUSE) on composition and exposure is known to differ over various composition and exposure regimes because different embrittlement mechanisms are active in various regimes.

The complexity of the irradiation damage process makes it is impossible to obtain a reliable quantitative projection of the future embrittlement behavior of a particular material in a particular RPV based on small data sets. Surveillance programs conducted under the requirements of Appendix H to Title 10, Part 50, of the *Code of Federal Regulations* (10 CFR Part 50) result in the observation of far too few mechanical property changes to provide either reliable calibrations or adjustments of the recommended ΔT_{30} or ΔUSE relationships developed in Chapters 4 and 5, respectively. In fact, as illustrated in Figure 6-1, nearly 80% of the reactor beltline materials that have been monitored using Appendix H have four ***or fewer*** surveillance observations, and no currently monitored material has greater than eight observations. Thus, the quantity of surveillance data available for a particular material is small in an absolute sense, and it is also small relative to the complexity of the embrittlement trend equations. For example, the ΔT_{30} model recommended in Chapter 4 (Eq. 4-15) includes seven independent variables and 18 parameters for which the numerical values were determined by fitting. Although it is possible on theoretical grounds to justify holding two of these parameters constant, this comparison suggests that, for the great majority of the materials in the surveillance database, a material-specific adjustment of either the ΔT_{30} or ΔUSE relationships would be under-determined (i.e., the number of unknown fitting parameters would exceed the number of experimental observations) by a factor of approximately four. As a result, plant-specific surveillance data (in the quantities currently available) cannot be expected to provide an accurate plant-specific adjustment of the generic ΔT_{30} or ΔUSE

relationships. Additionally, statistical justification for margin reduction is highly unlikely given the limited quantities of surveillance data that are now available (see Figure 6-1).

While plant-specific trends are difficult to discern, significant advances in both understanding and quantitative prediction capability have arisen when large quantities of surveillance data from operating plants are considered together with other information concerning the mechanisms of irradiation damage in ferritic steels (e.g., information from theoretical considerations and information from test reactor irradiations). Chapter 4 and Appendix A of this report provide examples of this type of study.

6.3 Recommendation

The information presented in Section 6.2 suggests that the practice recommended in Revision 2 of Regulatory Guide 1.99 (i.e., allowing the very limited amounts of currently available data from 10 CFR Part 50 Appendix H surveillance programs to modify overall embrittlement trends) is no longer technically defensible. A far more robust and stable regulatory framework can be achieved by requiring licensees to assess their plants using material-specific information on composition and exposure variables as inputs to physically informed equations that are fit to large databases, such as the equations recommended in Chapters 4 and 5. However, as a defense-in-depth measure, collection of mechanical property change observations (i.e., ΔT_{30}, ΔUSE, and ΔYS data) as part of 10 CFR Part 50 Appendix H surveillance programs should continue to be required. These data provide advance indication of embrittlement mechanisms that have been (heretofore) unforeseen or unobserved, or have been observed only anecdotally. These data also provide the NRC staff with information that allows periodic assessment of (1) whether any plant-specific materials deviate from fleet-wide trends, and (2) whether the generic equations representing the overall trends need to be changed in view of the surveillance information. Section 9.5 discusses future plans to treat surveillance data beyond the recommendations of Revision 3 of Regulatory Guide 1.99.

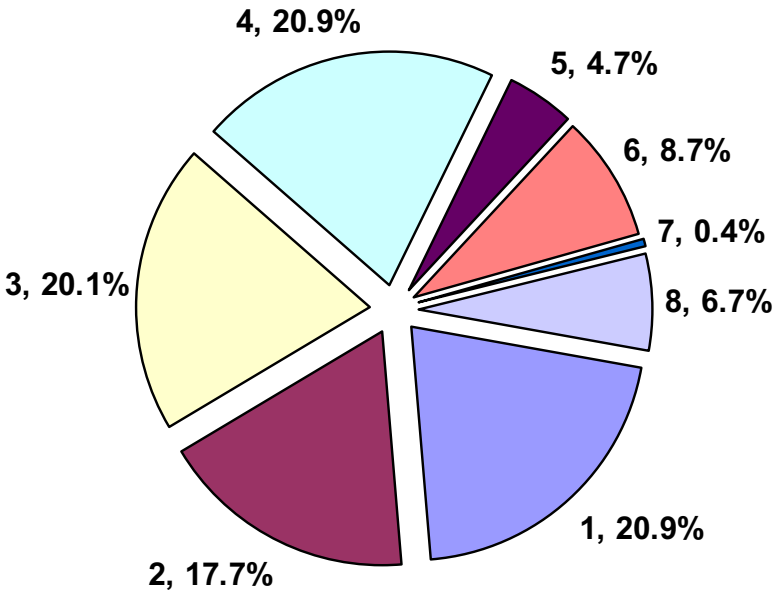

Figure 6-1. Variation of surveillance dataset size for the ΔT_{30} database summarized in Appendix C to Appendix A.

7 MARGINS

Revision 2 of Regulatory Guide 1.99 recommends the use of a margin term to account for uncertainties. This provision was appropriate when the NRC promulgated Revision 2 because the structural integrity assessment procedures of the day were, nearly without exception, deterministic in nature. However, the NRC is in the process of risk-informing many of its regulatory products. In situations where regulatory limits have been established based on risk-informed probabilistic calculations that have accounted for the uncertainties that are important to embrittlement processes, the use of an additional margin term would represent an inappropriate double-counting of uncertainties. Therefore, in Revision 3 of Regulatory Guide 1.99 the recommended margin term will depend upon the application for which the estimate of embrittlement is needed, as follows:

Eq. 7-1 $$\overline{\overline{\Delta T_{30}}} = \Delta T_{30(eqs\,4-21\,to\,4-23)} + \alpha \cdot \sigma_{\Delta T_{30}}$$

Eq. 7-2 $$\overline{\overline{\Delta USE}} = \Delta USE_{(eq\,5-1)} + \alpha \cdot \sigma_{\Delta USE}$$

In Eq. 7-1 and 7-2 the $\overline{\overline{\Delta T_{30}}}$ and $\overline{\overline{\Delta USE}}$ values indicate quantities that have been adjusted to account for the effects of uncertainty in a manner consistent with their intended application. In both equations, α is defined as follows:

α=0 if the estimate of ΔT_{30} or ΔUSE is needed as part of a probabilistic calculation where the analysis explicitly accounts for sources of uncertainty in ΔT_{30} or ΔUSE.

α=0 if the estimate of ΔT_{30} or ΔUSE is needed for comparison to a prescribed limit that was arrived at based on a risk-informed probabilistic evaluation that accounted for the sources of uncertainty in ΔT_{30} or ΔUSE.

α=2 if the estimate of ΔT_{30} or ΔUSE is needed for comparison to a prescribed limit that was arrived at deterministically.

The value of $\sigma_{\Delta T_{30}}$ in Eq. 7-1 is 19 °F below Cu_{min} of 0.048 wt-%, and 25 °F above Cu_{min}.

If fluence exceeds $3x10^{19}$ n/cm^2, the value of $\sigma_{\Delta T_{30}}$ in Eq. 7-1 is 33 °F irrespective of copper content.

The value of $\sigma_{\Delta USE}$ in Eq. 7-2 is 13 ft-lbs.

8 PREDICTION OF THE THROUGH-WALL ATTENUATION OF RADIATION DAMAGE

Limited information is available regarding how fluence attenuates through the wall of a thick reactor vessel. Revision 2 of Regulatory Guide 1.99 adopts the following attenuation function:

Eq. 8-1 $$\Phi(z) = \Phi_{ID} \exp(-0.24z)$$

where z is the distance from the inner diameter of the RPV (in inches), and fluence is expressed in n/cm^2 (E>1MeV). Eq. 8-1 conservatively assumes that fluence attenuates like displacements per atom (dpa) (i.e., Eq. 2-7 assumes that fluence attenuates more slowly than it actually does [Randall 87]).

The Electric Power Research Institute (EPRI) recent performed review of this topic, entitled "Attenuation in U.S. RPV Steels (MRP-56)" [English 02]. In MRP-56, EPRI provided an excellent discussion of the physical process by which neutron irradiation damage is attenuated by steel between the neutron source (i.e., the core) and the location of interest in the vessel wall (designated by z in Eq. 8-1). MRP-56 also summarized all of the test data available to provide insight on the magnitude by which neutron damage is attenuated by steel. Based on this review, MRP-56 stated the following conclusion:

> *The best available parameter to express neutron exposure damage is displacements per atom (dpa). Plant-specific calculation of dpa through the RPV wall is the best method to be used for neutron exposure. Alternatively, the fluence attenuation function provided in Regulatory Guide 1.99, Rev. 2, can be used. The current regulatory method uses dpa as the neutron exposure parameter and relates it to the inside wall fluence of neutron energies greater than 1 MeV, which is consistent with the surveillance database.*

Additionally, MRP-56 presented data demonstrating the conservatism of Eq. 8-1. For these reasons, Eq. 8-1 is recommended for use in Revision 3 of Regulatory Guide 1.99.

9 SUMMARY, RECOMMENDATIONS, AND FUTURE PLANS

9.1 Motivation and Scope of Study

Since Revision 2 of Regulatory Guide 1.99 was promulgated in 1988, the NRC and the nuclear industry have made considerable advances in both the physical understanding of the radiation damage processes and the empirical quantification of the effects these processes have on the mechanical properties of RPV steels. The objective of this report is to summarize these advances in the state of knowledge and amalgamate them into a technical basis for an up-to-date version of RG 1.99. Specifically, this report provides the basis of the staff's recommendations on the following matters:

- a formula that can be used to estimate the value of the transition temperature shift at the 30 ft-lb CVE level (ΔT_{30}) based on the composition of the steel of interest and the conditions under which it has been exposed to neutron irradiation
- a formula that can be used to estimate the value of the upper-shelf energy drop (ΔUSE) based on the composition of the steel of interest and the conditions under which it has been exposed to neutron irradiation
- the inadvisability of using material- and plant-specific surveillance data to influence or adjust ΔT_{30} and ΔUSE estimates for individual plant assessments
- the margins that should be assigned to the ΔT_{30} and ΔUSE estimates to account for uncertainties
- how the ΔT_{30} and ΔUSE estimates should be adjusted to account for the effects of neutron attenuation through the thick wall of the RPV

9.2 Investigative Approach

Based on the physical insights and literature data summarized herein, the NRC staff identified a candidate fitting function for ΔT_{30}. This function was fit to the US-LWR surveillance database using a least-squares approach. The staff then assessed the resultant best fit to evaluate its ability to predict data that were not used in developing the fit. Specifically, the staff used the following databases in this assessment:

(1) RADAMO Database: a database of test reactor irradiations performed on 14 commercial alloys with a focus on high fluences [Chaouadi 05a]

(2) IVAR Database: a database of test reactor irradiations performed on a wide array of both laboratory and commercial alloys with a controlled study of flux (see Appendix B to this report)

(3) JNES Databases: a database of both surveillance and test reactor irradiations performed by the Japan Nuclear Energy Safety Organization [JNES 07]

(4) French Database: a database of surveillance data from power reactors operated in France [Brillaud 92]

This assessment led to (1) a better understanding of the applicability limits of the best fit equation, (2) a modification of the best fit equation so that it applies to a larger range of conditions, and (3) the identification of certain steps that need to be taken to improve the predictive capability of the best fit equation for future conditions, particularly high fluences (see Section 9.5).

9.3 Major Technical Findings

Within the central range of composition and exposure conditions of the US-LWR surveillance database, model RM-6(2) for ΔT_{30} [as described in Section 9.4.1 of this report] predicts very well the embrittlement trends in all other databases examined in this study. However, when RM-6(2) is used to make either predictions at the peripheries of its calibration dataset or predictions that extrapolate from its calibrated range, its ability to represent embrittlement trends degrades in some cases. In particular, RM-6(2) cannot reliably predict embrittlement trends for the following conditions:

(1) **<u>At high fluences</u>**: As fluence increases beyond $\approx 3 \times 10^{19}$ n/cm^2, the predictive accuracy of RM-6(2) rapidly degrades, with the model systematically under-estimating the magnitude of embrittlement at these high fluences. This problem stems from the lack of a significant quantity of data above $\approx 3 \times 10^{19}$ n/cm^2 in the US-LWR calibration database, which appears to cause a systematic under-estimation of the matrix damage (MD) hardening rate coupled with a systematic over-estimation of the peak magnitude of copper-rich precipitate (CRP) hardening. Because matrix damage dominates embrittlement after CRP saturation, the net effect of these two errors is the systematic under-estimation at high fluences that was observed. While it is clear that RM-6(2) under-predicts embrittlement at fluences above 3×10^{19} n/cm^2, the apparent cause of this under-prediction advanced herein must be regarded as provisional, as it is based only on mechanical property data from the RADAMO and JNES test reactor databases. Microstructural examination of the alloys irradiated at high fluences using, for example, atom probe and small angle neutron scattering (SANS) techniques, is needed to determine which embrittlement mechanisms are active at high fluences.

(2) **<u>At high and low nickel contents</u>**: The bulk of the US-LWR surveillance data has between 0.5 and 1.0 wt-% Ni, so it is not surprising that RM-6(2) makes accurate predictions within this range of nickel content. However, at low nickel content (below ≈0.2 wt-%) and high nickel content (above ≈1.5 wt-%), respectively RM-6(2) systematically over-predicts or under-predicts embrittlement. Evidence supporting this finding is available in the RADAMO, JNES, and French surveillance databases.

(3) **<u>As flux decreases from $\approx 8 \times 10^{11}$ n/cm^2/sec</u>**: Decreasing fluxes lead to a slight increase in the degree by which RM-6(2) under-predicts embrittlement. The slight effect of flux on the fluence at which CRP saturates (which appears in the controlled IVAR irradiations) cannot be resolved from any other database because of the strong correlations between flux and fluence in all other databases.

(4) **<u>At high copper content</u>**: Although RM-6(2) has a maximum copper content (Cu_{max}) term of 0.32 wt-%, this term is not a statistically essential feature of the model because the surveillance database has very limited data for high copper content. Nonetheless, information in the IVAR database demonstrates that above a copper content of ≈0.38 wt-%, RM-6(2) systematically over-estimates the magnitude of embrittlement.

These inadequacies of RM-6(2) are attributable to limitations in the US-LWR surveillance database that was used to calibrate the model. Thus, these limitations would be shared by any similarly derived model (e.g., the model developed in Appendix A to this report, or the model described in [Eason 98]). Of these four inadequacies, the first presents the greatest practical concern because fluences above $\approx 3 \times 10^{19}$ n/cm^2 have already occurred in operating pressurized-water reactors (PWRs), and will occur in approximately half of the PWRs in the currently operating fleet by the end of their original operating licenses. Additionally, reactors that may be constructed in the near future are likely to have peak fluences as high as $\approx 1 \times 10^{20}$ n/cm^2 after 60–80 years of operation. Therefore, Section 9.4.1 of this report includes recommendations on treatment of high fluence situations. The latter three inadequacies present less practical concern because they are much smaller in magnitude, result in systematic over- (rather than under-) predictions of ΔT_{30}, and/or do not apply to the materials commonly encountered in power reactor service.

9.4 Recommendations

Based on the analyses presented herein, the staff recommends the following formulae and procedures for adoption in Revision 3 of Regulatory Guide 1.99.

9.4.1 ΔT_{30} Trend Curve

9.4.1.1 For Fluences At or Below 2×10^{19} n/cm^2

Eq. 4-21 (repeated) $\Delta T_{30} = \Delta T_{30(MD)} + \Delta T_{30(CRP)}$

where

$$\Delta T_{30(MD)} = PF_{MD} \cdot CF_{MD} \cdot TF_{MD} \cdot \phi F_{MD} \cdot \Phi F_{MD}$$

$$PF_{MD} = \left\{ \begin{array}{c} Weld = 6.7 \\ Plate = 8.1 \\ Forging = 4.75 \end{array} \right\} \times 10^{-9} \qquad CF_{MD} = \left[1 + 35 \cdot P\right]$$

$$TF_{MD} = \left(\frac{T}{550}\right)^{-14.64} \qquad \phi F_{MD} = \left(\frac{Log10(\phi)}{10.7}\right)^{-3.44} \qquad \Phi F_{MD} = \sqrt{\Phi}$$

$$\Delta T_{30(CRP)} = PF_{CRP} \cdot CF_{CRP} \cdot TF_{CRP} \cdot \Phi F_{CRP}$$

$$PF_{CRP} = \left\{ \begin{array}{c} Weld = 0.301 \\ Plate = 0.233 \\ Forging = 0.233 \end{array} \right\}$$

$$CF_{CRP} = \left[f(Cu) + 2500.3 \cdot \mathrm{MIN}\{0.32, \mathrm{MAX}(0, Cu - 0.048)\} \cdot Ni\right]$$

$$f(Cu) = -116.3 + 530.8\sqrt{Cu} \text{ , subject to } 0 \le f(Cu) \le 118.5$$

$$TF_{CRP} = \left(\frac{T}{550}\right)^{-1.74} \qquad \Phi F_{CRP} = \left\{1 - \exp\left(\frac{-\Phi}{2.38 \times 10^{18}}\right)\right\}$$

In this equation, the values of Cu, Ni, and P are expressed in weight percent (wt-%), temperatures are expressed in degrees Fahrenheit (°F), fluence is expressed in n/cm^2 (E>1MeV), and flux is determined by dividing fluence by the time the reactor has been in operation (with time expressed in seconds). Thus, the uncertainty (standard deviation) of RM-6(2) is 19 °F below the minimum copper content (Cu_{min}=0.048 wt-%) and 25 °F above Cu_{min}.

Application of this model is expected to produce predictions within the stated uncertainties, provided that the conditions of the application meet all of the following criteria:

(1) Fluence is less than 3x10^{19} n/cm^2.
(2) Nickel is less than 1.25 wt-%.
(3) Nickel exceeds 0.25 wt-%.
(4) Copper is less than 0.38 wt-%.

If either of the first two criteria is not met, this model will most likely under-predict ΔT_{30}. Conversely, the model will most likely over-predict ΔT_{30} if either of the second two criteria is not met. Additionally, if the first criterion is met, the model described in the following section as Eq. 4-22 should be used.

9.4.1.2 For Fluences Above 4x10^{19} n/cm^2

Eq. 4-22 (repeated) $$\Delta T_{30} = \left\{ \begin{array}{c} Weld = 1.39 \\ Plate = 1.18 \\ Forging = 0.84 \end{array} \right\} \cdot \left\{ \Delta YS_{(MD)} + \sqrt{\Delta YS^2_{(CRP)} + \Delta YS^2_{(PRP)}} \right\}$$

The product form-dependent constants convert the ΔYS, which have units of MPa, into ΔT_{30} values, which have units of °F.

Matrix damage does not begin until an incubation fluence (Φ_o=1x10^{19} n/cm^2) has been achieved; below Φ_o, $\Delta YS_{(MD)}$ is zero. Above Φ_o, $\Delta YS_{(MD)}$ is defined as follows:

$$\Delta YS_{(MD)} = \left\{ 585 \cdot \exp\left[-1250 \cdot \exp\left(-\frac{0.345}{kT} \right) \right] + (3880 - 6.3 \cdot T) \cdot Ni \right\} \sqrt{1 - \exp\left[-0.01 (\Phi - \Phi_o) \right]}$$

where T is expressed in Kelvin, Ni is expressed in wt-%, and all fluences (both Φ and Φ_o,) are divided by 1x10^{19} n/cm^2 before being used in this equation.

The magnitude of the **copper-rich precipitate** term is as follows:

$$\Delta YS_{(CRP)} = \Delta_{CRP(PEAK)}$$

where

If Cu ≤ Cu_{min}, $\Delta_{CRP(PEAK)} = 0$

If Cu > Cu_{min}, $\Delta_{CRP(PEAK)} = 215\left[1 - \exp\left\{-2.7\left(Cu - Cu_{\min}\right)\right\}\right]$

Cu_{min} = 0.03 wt-%

This relationship is simplified, insofar as this relationship for ΔYS_{CRP} reflects only the peak CRP hardening, rather than the evolution with fluence that is needed to achieve peak hardening. This simplification is possible because this formula will only be used at fluences above $2x10^{19}$ n/cm^2; which far exceed that needed to achieve peak hardening (see Figure 4-48).

Damage by **phosphorus-rich precipitates** is zero for alloys having less than 0.012 wt-% phosphorus. For higher-phosphorus alloys, the magnitude of the phosphorus-rich precipitate term is as follows:

$$\Delta YS_{(PRP)} = (44470.5 - 70T)\cdot(P - 0.012)$$

In this equation, T is expressed in Kelvin. It should be noted that, while suggested in [Chaouadi 05b], this relationship was not recommended for use because it is empirical and based on only two data sets. Nonetheless, our assessment of the RADAMO trend curve suggests that it is better to include this term than to omit it. This equation should only be used within its calibrated temperature range of 265–300 °C (509–572 °F). Additionally, it should not be applied to phosphorus levels that exceed 0.03 wt-%.

In Eq. 4-22, the uncertainty (standard deviation) with which ΔT_{30} is predicted is 33 °F. Application of this model is expected to produce predictions within this uncertainty bound, provided that the conditions of the application meet all of the following criteria:

(5) Phosphorus is less than 0.03 wt-%.
(6) Copper is less than 0.5 wt-%.
(7) Nickel exceeds 0.25 wt-%.
(8) Nickel is less than 1.25 wt-%.

If any of the first three criteria is not met, this model will most likely over-predict ΔT_{30}. Conversely, this model will most likely under-predict ΔT_{30} if last criterion is not met. However, none of these restrictions is expected to create a practical impediment to application of this model to currently operating materials, because these compositions are not typical of the RPV materials that are currently in service. Nonetheless, it should be noted that this model should be used only when fluence exceeds $2x10^{19}$ n/cm^2.

9.4.1.3 For Fluences Between 2 4x10^{19} n/cm^2 and 4x10^{19} n/cm^2

For fluences between 2 and $4x10^{19}$ n/cm^2, the ΔT_{30} estimates of Eq. 4-20 and 4-21 are combined according to the following weighting formula:

Eq. 9-1 $$\Delta T_{30} = (1 - W)\cdot \Delta T_{30}^{RM-6(2)} + W \cdot \Delta T_{30}^{RADAMO}$$ where

where

$$W = \frac{1}{2}\left(\frac{\Phi}{1\times 10^{19}} - 2\right)$$

$\Delta T_{30}^{RM-6(2)}$ and ΔT_{30}^{RADAMO} represent the values of ΔT_{30} estimated using Eq. 4-21 and 4-22, respectively.

9.4.2 ΔUSE Equation

Eq. 5-1 (repeated) $\Delta USE = 0.18 \cdot \Delta T_{30}$

where ΔT_{30} is as predicted by Eq. 4-15 or 4-21 and is expressed in degrees Fahrenheit, and ΔUSE is expressed in foot-pounds. The uncertainty (standard deviation) in Eq. 5-1 is 13 ft-lbs.

9.4.3 Treatment of Surveillance Data

The complexity of the irradiation damage process makes it is impossible to obtain a reliable quantitative projection of the future embrittlement behavior of a particular material in a particular RPV based on small data sets. Surveillance programs conducted under the requirements of Appendix H to Title 10, Part 50, of the *Code of Federal Regulations* (10 CFR Part 50) result in the observation of far too few mechanical property changes to provide either reliable calibrations or adjustments of the recommended ΔT_{30} or ΔUSE values. In fact, nearly 80% of the reactor beltline materials that have been monitored under Appendix H have four ***or fewer*** surveillance observations, and no currently monitored material has greater than eight observations. Thus, the quantity of surveillance data available for a particular material is small in an absolute sense, and it is also small relative to the complexity of the embrittlement trend equations. For example, the recommended ΔT_{30} model (Eq. 4-15) includes seven independent variables and 18 parameters for which the numerical values were determined by fitting. Although it is possible on theoretical grounds to justify holding a few of these parameters constant, this comparison suggests that, for the great majority of the materials in the surveillance database, a material-specific adjustment of either the ΔT_{30} or ΔUSE relationships would be under-determined (i.e., the number of unknown fitting parameters would exceed the number of experimental observations) by a factor of approximately four. As a result, plant-specific surveillance data (in the quantities currently available) cannot be expected to provide an accurate plant-specific adjustment of the generic ΔT_{30} or ΔUSE relationships. Additionally, statistical justification for margin reduction is highly unlikely given the limited quantities of surveillance data that are now available.

In replacing the Revision 2 procedures for treatment of surveillance data, Revision 3 will require licensees to assess their plants using material-specific information on composition and exposure variables as inputs to the recommended ΔT_{30} and ΔUSE relationships. Also, as a defense-in-depth measure, collection of mechanical property change observations (i.e. ΔT_{30}, ΔUSE, and ΔYS data) as part of 10 CFR Part 50 Appendix H surveillance programs should continue to be required. These data provide advance indication of embrittlement mechanisms that have been (heretofore) unforeseen or unobserved, or have been observed only anecdotally. These data also provide the NRC staff with information that allows periodic assessment of (1) whether any plant-specific materials deviate from fleet-wide trends, and (2) whether the generic equations representing the overall trends need to be changed in view of the surveillance information. Section 9.5 discusses future plans to treat surveillance data beyond the recommendations of Revision 3 of Regulatory Guide 1.99.

9.4.4 Margins

Eq. 7-1 (repeated) $\overline{\overline{\Delta T_{30}}} = \Delta T_{30(eq4-15)} + \alpha \cdot \sigma_{\Delta T_{30}}$

Eq. 7-2 (repeated) $\overline{\overline{\Delta USE}} = \Delta USE_{(eq5-1)} + \alpha \cdot \sigma_{\Delta USE}$

In Eq. 7-1 and 7-2, the $\overline{\overline{\Delta T_{30}}}$ and $\overline{\overline{\Delta USE}}$ values indicate quantities that have been adjusted to account for the effects of uncertainty in a manner consistent with their intended application. In both equations, α is defined as follows:

α=0 if the estimate of ΔT_{30} or ΔUSE is needed as part of a probabilistic calculation where the analysis explicitly accounts for sources of uncertainty in ΔT_{30} or ΔUSE

α=0 if the estimate of ΔT_{30} or ΔUSE is needed for comparison to a prescribed limit that was arrived at based on a risk-informed probabilistic evaluation that accounted for the sources of uncertainty in ΔT_{30} or ΔUSE

α=2 if the estimate of ΔT_{30} or ΔUSE is needed for comparison to a prescribed limit that was arrived at deterministically

The value of $\sigma_{\Delta T_{30}}$ in Eq. 7-1 is 19 °F for alloys having a copper content below Cu_{min} of 0.048 wt-% and. For alloys having a copper content above Cu_{min} the value of $\sigma_{\Delta T_{30}}$ is 25 °F. If fluence exceeds $3x10^{19}$ n/cm^2, the value of $\sigma_{\Delta T_{30}}$ in Eq. 7-1 is 33 °F, irrespective of copper content. The value of $\sigma_{\Delta USE}$ in Eq. 8-2 is 13 ft-lbs.

9.4.5 Attenuation

The attenuation guidance in Revision 3 of Regulatory Guide 1.99 will remain the same as that provided in Revision 2, as follows:

Eq. 8-1 (repeated) $\Phi(z) = \Phi_{ID} \exp(-0.24z)$

where z is the distance from the inner diameter of the RPV (in inches) and fluence is expressed in n/cm^2 (E>1MeV).

9.5 Plans for Future Refinements in this Technical Area

The NRC envisions a two-pronged approach to continue to build on the advances to date, and to reconcile some of the inadequacies identified herein. Toward that end, the agency will undertake (or participate in) specifically focused research investigations to address inadequacies in the current equations. Additionally, the agency will initiate an ongoing data trending activity. The following sections detail the NRC's planned activities.

9.5.1 Planned Research Activities

The NRC is planning focused research and/or collaborative projects to address those technical inadequacies noted herein that have the greatest technical impact:

- High fluence: The NRC needs to better understand the under-prediction of the fit of the ΔT_{30} model fit to the US-LWR surveillance data at fluences above $3x10^{19}$ n/cm^2, so that the agency can adopt a single ΔT_{30} model for all fluences. This will allow confident projection of irradiation damage during the extended period of operating life (for existing reactors), as well as for new reactors. The agency also needs an assessment of the embrittlement mechanisms operating at these high fluences to allow the confident development of improved equations. Toward that end, the NRC's Office of Nuclear Regulatory Research (RES) is currently sponsoring research being conducted at the Belgian Nuclear Research Centre (SCK/CEN) and the Oak Ridge National Laboratory in the United States, which will include both mechanical property characterization (i.e., ΔT_{30}, ΔT_o, ΔUSE, and ΔYS data) and microstructural characterization (i.e., SANS, atom probe) of five RPV materials (three welds and two plates) having high copper content. These materials were exposed to fluences as high as $1x10^{20}$ n/cm^2; Appendix F is a report detailing work performed to date. Additional studies may be required to expand the scope of the investigation to low-copper materials, among other things.
- Nickel: While the inadequacy of RM-6(2) when applied to both high- and low-nickel materials is clear, the practical impact of these inaccuracies on new reactor materials is not. Therefore, the NRC will survey the planned materials of construction for Generation III+ reactors [e.g., the U.S. Evolutionary Power Reactor (US-EPR) or the 1,000-MWe AP1000 Advanced Passive Reactor] to determine whether the vendors plan to use high- or low-nickel materials. The outcome of this survey will inform the decision regarding the need to perform additional focused research related to nickel effects.
- Flux: As revealed by the IVAR database, flux has a slight effect that cannot be properly reflected in surveillance-calibrated models because of the strong correlation between the fluence and flux of surveillance materials. Although the magnitude of this effect is small, the development of physically sound and empirically informed flux models is fundamental to both properly designing surveillance programs and understanding how accelerated test reactor irradiations can be used to inform the surveillance-based trend curves that are used in regulatory decision-making. Therefore, the NRC will undertake a project that is specifically focused on developing validating a physically based flux model.
- Attenuation: As stated in Chapter 8, very limited data are available to inform the attenuation formula. Therefore, the NRC is co-sponsoring a collaborative project, being conducted at the Nuclear Research Institute at Řež in the Czech Republic, which features an extensive experimental quantification of attenuation effects using different RPV alloys. Current progress on this project is summarized in [Server ??]. In addition, the agency will pursue investigations of the practical implementation of approaches based on displacements per atom (dpa), as an alternative to fluence.
- Fracture toughness: Information on fracture toughness is needed as input to any structural integrity procedure; however, to date, only CVN data (which does not provide a measurement of fracture toughness) has been available in adequate quantities to permit the development of trend equations that express the effects of irradiation on mechanical properties. As a result, the NRC will undertake the development of trend curves based on fracture toughness using currently available data and, perhaps, newly generated data. Information from the flux studies (discussed above) is expected to support this effort, given that this information will provide physically appropriate rules to scale between test and power reactor irradiations. Additionally, continuation of recent work,

which identified heretofore unrecognized commonalities between CVE and K_{Jc} transition characterizations [EricksonKirk 07], is expected to be helpful.

The NRC will undertake all of these activities as subtasks to an umbrella project focused on developing a fourth revision of Regulatory Guide 1.99 within 5 years. As part of that effort, the agency will pursue collaboration with the international research community whenever possible.

9.5.2 Ongoing Data Trending Activity

In nearly two decades since the NRC promulgated Revision 2 of Regulatory Guide 1.99, the agency has intermittently undertaken data trending activities, primarily focused on ΔT_{30}, which have invariably been viewed as activities having defined endpoints, rather than ongoing activities aimed at keeping estimation strategies current with the state of knowledge. By contrast, in the future, the NRC plans to replace this approach, as well as the occasional use of very limited quantities of surveillance data to adjust generic trends in a plant-specific way, with a systematic effort to continually evaluate new data (from both surveillance and research programs) as they become available. The agency will launch this effort as a staff activity, but will endeavor to organize and coordinate the work through a newly formed task group dedicated to this purpose, under the auspices of the American Society for Testing and Materials (ASTM) Subcommittee E10.02. Examining small sets of data within the context of larger databases and physical understanding gained from focused research programs offers the following advantages over current approaches, such as those advocated by Revision 2 of Regulatory Guide 1.99, which confer undue merit and significance to extremely limited data sets:

- Having a broader, physically based, framework within which to view new data permits more reliable discrimination of outliers from emergent trends.
- Insights gained from emergent trends can be rapidly communicated and applied to the entire reactor fleet in an evenhanded way.
- Undertaking a continuous effort ensures that embrittlement trends are kept up to date with the most recent research results, and the research being conducted is focused on the issues most important to the operating fleet.
- Broad maintenance and coordination of both research and surveillance databases, among various countries, operators, regulators, and research groups, offers the maximum benefit and leverage available from their respective investments of money and time.

10 REFERENCES

10CFR5061 Title 10, Section 50.61, of the *Code of Federal Regulations*, "Fracture Toughness Requirements for Protection Against Pressurized Thermal Shock Events," promulgated June 26, 1984.

10CFR50G Appendix G to Title 10, Part 50, of the *Code of Federal Regulations*, "Fracture Toughness Requirements {for Normal Operations}," promulgated June 26, 1984.

10CFR50H Appendix H, to Title 10, Part 50, of the *Code of Federal Regulations*, "Reactor Vessel Material Surveillance Program Requirements," promulgated December 19, 1995.

ASME NB2331 ASME NB-2331, "1998 ASME Boiler and Pressure Vessel Code, Rules for Construction of Nuclear Power Plants, Division 1, Subsection NB, Class 1 Components," American Society of Mechanical Engineers, 1998.

ASME IWB3500 ASME Section XI Article IWB-3500, "Acceptance Standards," ASME Boiler and Pressure Vessel Code, American Society of Mechanical Engineers, 2007.

ASME IWB3600 ASME Section XI Article IWB-3600, "Analytical Evaluation of Flaws," ASME Boiler and Pressure Vessel Code, American Society of Mechanical Engineers, 2007.

ASTM E23 ASTM E23, "Standard Test Methods for Notched Bar Impact Testing of Metallic Materials," American Society for Testing and Materials, 1998.

ASTM E185 ASTM E185-94, "Standard Practice for Conducting Surveillance Tests for Light-Water Cooled Nuclear Power Reactor Vessels," American Society for Testing and Materials, 1998.

ASTM E208 ASTM E208, "Standard Test Method for Conducting Drop-Weight Test To Determine Nil-Ductility Transition Temperature of Ferritic Steels," American Society for Testing and Materials, 1998.

ASTM E399 ASTM E399, "Test Method for Plane-Strain Fracture Toughness Testing of Metallic Materials," American Society for Testing and Materials, 1998.

ASTM E1921 ASTM E1921, "Test Method for Determination of Reference Temperature, T_o, for Ferritic Steels in the Transition Range," American Society for Testing and Materials, 2002.

Beaven 89 Beaven, P.A., F. Frisius, R. Kampmann, R. Wagner, and J.R. Hawthorne, "SANS Investigation of Irradiated A533-B Steels Doped with Phosphorus," *Radiation Embrittlement of Nuclear Reactor Pressure Vessel Steels: An International Review*, ASTM STP 1011, L.E. Steele, Ed., American Society for Testing and Materials, 1989, pp. 243–256.

Brillaud 92 Brillaud, C., and Hedin, F., "In-Service Evaluation of French Pressurized-Water Reactor Vessel Steel," *Effects of Radiation on Materials, 15th International Symposium,* ASTM STP-1125, R.E. Stoller, A.S. Kumar, and D.S. Gelles, Eds., American Society for Testing and Materials, 1992, pp. 23–49.

Chaouadi 01 R. Chaouadi, "Status Report on Radiation Damage Modeling of Reactor Pressure Vessel Steels," SCK/CEN Report R-3538, June 2001.

Chaouadi 05a R. Chaouadi, "An Engineering Radiation Hardening Model for RPV Materials," SCK/CEN Report R-4235, September 2005.

Chaouadi 05b R. Chaouadi, and R. Gérard, "Copper Precipitate Hardening of Irradiated RPV Materials and Implications on the Superposition Law and Re-Irradiation Kinetics," *Journal of Nuclear Materials,* **345** (2005), pp. 65–74.

Charpy 01 Charpy, M.G., "Note sur l'Essai des Metaux a la Flexion par Choc de Barreaux Entailles," *Soc. Ing. Francais*, June 1901, p. 848.

Debarberis 05a L. Debarberis, A. Kryukovb, F. Gillemotc, B. Acosta, and F. Sevinia, "Semi-Mechanistic Analytical Model for Radiation Embrittlement and Re-Embrittlement Data Analysis," *International Journal of Pressure Vessels and Piping* **82** (2005), pp. 195–200.

Debarberis 05b L. Debarberis, B. Acosta, A. Zeman, F. Sevini, A. Ballesteros, A. Kryukov, F. Gillemot, and M. Brumovsky, "Effect of Irradiation Temperature in PWR RPV Materials and Its Inclusion in Semi-Mechanistic Model," *Scripta Materialia* **53** (2005), pp. 769–773.

Debarberis 05c L. Debarberis, B. Acosta, F. Sevini, A. Kryukov, F. Gillemot, M. Valo, A. Nikolaev, and M. Brumovsky, "Role of Nickel in a Semi-Mechanistic Analytical Model for Radiation Embrittlement of Model Alloy," *Journal of Nuclear Materials* **336** (2005), pp. 210–216.

Eason 98 Eason, E.D., J.E. Wright, and G.R. Odette, "Improved Embrittlement Correlations for Reactor Pressure Vessel Steels," NUREG/CR-6551, U.S. Nuclear Regulatory Commission, Washington DC, 1998.

English 02 English, C., and W. Server, "Attenuation in US RPV Steels – MRP-56," Electric Power Research Institute, Palo Alto, California, June 2002.

EricksonKirk 06a EricksonKirk, M.T., and EricksonKirk, M.A., "Use of a Unified Model for the Fracture Toughness of Ferritic Steels in the Transition and on the Upper Shelf in Fitness-For-Service Assessment and in the Design of Fracture Toughness Experiments," PVP2006-ICPVT11-93652, *Proceedings of the 2006 Pressure Vessel and Piping Conference*, Vancouver, British Columbia, Canada, July 2006.

EricksonKirk 06b EricksonKirk, M.A., and EricksonKirk, M.T., "The Relationship Between the Transition and Upper-Shelf Fracture Toughness of Ferritic Steels," *Fatigue and Fracture of Engineering Materials and Structures* **29** (2006), pp. 672–684.

EricksonKirk 07 EricksonKirk, M.A., EricksonKirk, M.T., Rosinski, S., and Spanner, J., "Insights Arising from a Comparison of the *tanh* and Exponential Fitting

Methods for Charpy V-Notch Energy Data," PVP Paper 2007-26305, *Proceedings of the 2007 Pressure Vessel and Piping Conference*, San Antonio, Texas, USA, July 2007.

Fabry 95 — Fabry, A., "Modeling-Based Embrittlement Trend Curve for KWO Vessel Submerged-Arc Weld," SCK.CEN Report R-3090, December 1995.

Fisher 83 — Fisher, S.B., J.R. Harbottle, and N. Aldridge, in *Proceedings of BNES Conference of Dimensional Stability and Mechanical Behaviour of Irradiated Metals and Alloys*, Brighton, 1983, Vol. 2., British Nuclear Energy Society, p. 87.

Fisher 85 — Fisher, S.B., J.E. Harbottle, and N. Aldridge, "Radiation Hardening in Magnox Pressure Vessel Steels," *Philosophical Transactions of the Royal Society London*, A315, 1985, pp. 301–332.

Fisher 87 — Fisher S.B., and J.T. Buswell, "A Model for PWR Pressure Vessel Embrittlement," *International Journal of Pressure Vessel and Piping*, Vol. 27, 1987, pp. 91–135.

Gérard 06 — Gérard, R., E. Lucon, M.Scibetta, R.Chaouadi, and E. Van Walle, "Reactor Pressure Vessel Steels Embrittlement at Very High Neutron Doses," *Fontevraud 6th International Symposium on Contribution of Material Investigations to Improve Safety and Performance of LWRs*, September 18–22, 2006, Fontevraud-L'Abbaye, France

Guthrie 84 — Guthrie, G.L., "Charpy Trend Curves Based on 177 PWR Data Points, LWR Pressure Vessel Surveillance Dosimetry Improvement Program, Quarterly Progress Report April 1983 – June 1983, Hanford Engineering Development Laboratory, NUREG/CR-3391, Vol. 2, HEDL-TME-83-22, April 1984.

IAEA 1442 — *Guidelines for Prediction of Irradiation Embrittlement of Operating WWER-440 Reactor Pressure Vessels*, prepared within the framework of the coordinated research project, IAEA TECHDOC 1442, June 2005.

JNES 07 — JNES database composed of the open data from the industry's Aging Evaluation Reports to the Public, and "Nuclear Plant Integrated Management Technology, Summary Report," JNES, March 2003.

Jones 96 — Jones R.B., and C.J. Bolton, "Neutron Radiation Embrittlement Studies in Support of Continued Operation and Validation of Sampling of Magnox Reactor Steel Pressure Vessels and Components," *Proceedings of the U.S. Nuclear Regulatory Commission 24th Water Reactor Safety Meeting*, NUREG/CP-0157-2, 1996, pp. 25–49.

Kirk 98 — Kirk, M., R. Lott, C. Kim, and W. Server, "Empirical Validation of the Master Curve for Irradiated and Unirradiated Reactor Pressure Vessel Steels," *Proceedings of the 1998 ASME/JSME Pressure Vessel and Piping Symposium*, July 26–30, 1998, San Diego, California.

Kirk 01 — Kirk, M., and M.E. Natishan, "Shift in Toughness Transition Temperature Due to Radiation: ΔT_o *vs.* ΔT_{41J}, A Comparison and Rationalization of Differences," *Proceedings of the IAEA Specialists Meeting on Master Curve Technology*, Prague, Czech Republic, September 2001.

Liu 97 — Liu, C.L., G.R. Odette, B.D. Wirth, and G.E. Lucas, "A Lattice Monte Carlo Simulation of Nanophase Compositions and Structures in Irradiated Pressure Vessel Fe-Cu-Ni-Mn-Si Steels," *Matls Sci and Eng.*, A238, 1997, pp.202–209.

Mader 95 — Mader, E., "Kinetics of Irradiation Embrittlement and the Post-Irradiation Annealing of Nuclear Reactor Pressure Vessel Steels," PhD. Thesis, UC Santa Barbara, 1995.

McElroy 96 — McElroy, R.M., and A. L. Lowe, "The Dependence of Radiation Hardening and Embrittlement on Irradiation Temperature." *Effects of Radiation on Materials: 17th International Symposium, ASTM 1270*, D.S. Gelles, R.K. Nanstad, A.S. Kumar, and E.A. Little, Eds., ASTM, 1996, p. 68.

Miller 90 — Miller, M.K., and M.G. Burke, "Fine-Scale Microstructural Characterization of Pressure Vessel Steels and Related Materials Using APFIM," *Effects of Radiation on Materials: 14th International Symposium, (Volume II),* ASTM STP 1046, N.H. Packan, R.E. Stoller, and A.S. Kumar, Eds., American Society for Testing and Materials, 1990, pp. 107–126.

Miller 92 — M.K. Miller and M.G. Burke, "An Atom Probe Field Ion Microscopy Study of Neutronirradiated Pressure Vessel Steels," *Journal of Nuclear Materials*, **195** (1992), pp. 68–82.

Miller 00 — Miller, M.K,. P. Pareige, and M.G. Burke, "Understanding Pressure Vessel Steel: An Atom Probe Perspective", *Materials Characterization*, **44** (2000), pp. 235–254.

Odette 84 — Odette, G.R., Lombrozo, P.M., Perrin, J.F., and Wullaert, R.A., "Physically Based Regression Correlations of Embrittlement Data from Reactor Pressure Vessel Surveillance Programs," EPRI NP-3319, Electric Power Research Institute, Palo Alto, California, January 1984.

Odette 86 — Odette, G.R., and G.E. Lucas "Recent Advances in Predicting Embrittlement of Reactor Pressure Vessel Steels," *Proceedings of the 2nd International Symposium on Environmental Degradation in Nuclear Reactors-Water Reactors*, J.T.A. Roberts, J.R. Weeks, G.J Theus, Eds., American Nuclear Society, La Grange Park, IL, 1986, p. 345.

Odette 88 — Odette, G.R. and G.E. Lucas "The Effect of Heat Treatment on Irradiation Hardening of Pressure Vessel Steels," *Proceedings of the 3rd International Symposium on Environmental Degradation in Nuclear Reactors-Water Reactors*, J.R. Weeks, G.J Theus, Eds., The Metallurgical Society, Warrendale, Pennsylvania, 1988, p. 95.

Odette 98 — Odette, G.R., "Modeling of Irradiation Embrittlement in Pressure Vessel Steels," *Irradiation Effects on Pressure Vessel Steels*, IAEA IRRWG-LMNPP98-3, International Atomic Energy Agency, Vienna, Austria, 1998.

Pellini 76 — Pellini, W.S., "Principles of Structural Integrity Technology," Office of Naval Research, Arlington, Virginia, 1976.

Randall 87 — Randall, P.N., "Basis for Revision 2 of the U.S. Nuclear Regulatory Commission's Regulatory Guide 1.99," *Radiation Embrittlement in Nuclear Pressure Vessel Steels: An International Review* (Second Volume), ASTM STP-909, L.E. Steele, Ed., 1987.

RG199R2 — Regulatory Guide 1.99, "Radiation Embrittlement of Reactor Vessel Materials," Rev. 2, U.S. Nuclear Regulatory Commission, Washington, DC, May 1988.

Russell 72 Russell K.C., and L.M. Brown, "Dispersion Strengthening in Iron-Copper System," *Acta Metallurgica*, **20** (1972), pp. 969–974.

Seeger 58 Seeger, A.K., "On the Theory of Radiation Damage and Radiation Hardening," *Proceedings of the U.N. International Conference on the Peaceful Uses of Atomic Energy*, Vol. 6, United Nations, New York, New Yor, 1958, pp. 250–273.

Server 01 Server, W., C. English, D. Naimon, and S. Rosinski, "Charpy Embrittlement Correlations—Status of Combined Mechanistic and Statistical Bases for U.S. RPV Steels – MRP-45," PWR Materials Reliability Program (PWRMRP), Electric Power Research Institute, Palo Alto, California, 2001.

Server?? Attenuation study

Sokolov 00 Sokolov, M.A., and Nanstad, R.K., "Comparison of Radiation-Induced Shifts of K_{Jc} and Charpy Impact Toughness for Reactor Pressure Vessel Steels," NUREG/CR-6609, U.S. Nuclear Regulatory Commission, Washington, DC, November 2000.

Solt 93 Solt, G., F. Frisius, W.B. Waeber, and P. Tipping, "Irradiation-Induced Precipitation in Model Alloys with Systematic Variation of Cu, Ni and P Content: A Small Angle Neutron Scattering Study", *Effects of Radiation on Materials,: 16th International Symposium,* ASTM STP 1175, A.S. Kumar, D.S. Gelles, R.K. Nanstad, and E.A. Little, Eds., American Society for Testing and Materials, 1993, pp. 444–461.

Soneda 02 Soneda N., and R.G. Carter, "Dose Rate Effects in RPV Materials", *Proceedings of an EPRI-CRIEPI Workshop*, CD-ROM, 2002.

Williams 86 Williams T.J., et al., "The Influence of Copper, Nickel and Irradiation Temperature on the Irradiation Shift of Low Alloy Steels," *Proceedings of 2nd International Symposium on Environmental Degradation of Materials in Nuclear Power Systems —Water Reactors*, September 1985, American Nuclear Society, 1986.

Williams 87 Williams, T.J., P.R. Burch, C.A. English, and P.H.N. Ray, "The Effect of Irradiation Dose Rate and Temperature, and Copper and Nickel Content on the Irradiation Shift of Low Alloy Steel Submerged Arc Welds," *Proceedings of the 3rd International Symposium on Environmental Degradation of Materials in Nuclear Power Systems—Water Reactor*s, Traverse City, July 1987, The Metallurgical Society, 121.

Williams 04 Williams, P.T., and T.L. Dickson, "Fracture Analysis of Vessels—Oak Ridge, FAVOR v04.1, Computer Code: Theory and Implementation of Algorithms, Methods, and Correlations," NUREG/CR-6854, U.S. Nuclear Regulatory Commission, Washington, DC, 2007.

Wirth 99 Wirth, B.D., G.R. Odette, W.A. Pavinich, G.E. Lucas and S.E. Spooner, "Small Angle Neutron Scattering Study of Linde 80 RPV Welds", *Effects of Radiation on Materials, 18th International Symposium*, ASTM STP 1325, R.K. Nanstad, M.F. Hamilton, F.A. Garner, and A.S. Kumar, Eds., American Society for Testing and Materials, 1999, pp. 102–121.

WRC 175 "PVRC Recommendations on Toughness Requirements for Ferritic Materials." *Welding Research Council Bulletin No. 175*, PVRC Ad Hoc Group on Toughness Requirements, August 1972.

Appendix A

A Physically Based Correlation of Irradiation-Induced Transition Temperature Shifts for RPV Steels

Prepared by
E. D. Eason, Modeling and Computing Services, LLC
G. R. Odette, University of California, Santa Barbara
R. K. Nanstad, Oak Ridge National Laboratory
T. Yamamoto, University of California, Santa Barbara

Contents

Figures

Tables

Appendix A

Abbreviated Terms, Nomenclature, and Unit Conversions

Acronyms and Abbreviations

ASTM	American Society for Testing and Materials
B&W	Babcock and Wilcox
BWR	boiling water reactor
CDM	cluster dynamics model
CE	Combustion Engineering
CF	chemistry factor
CRP	copper-rich precipitate
DBT	ductile-brittle transition
dpa	displacements per atom
EPRI	Electric Power Research Institute
FRM	fitted recombination model
IAEA	International Atomic Energy Agency
IGF	intergranular fracture
IVAR	Irradiation Variable (program)
JRQ	Japanese designation for a specific heat of RPV steel
LBP	late-blooming phase
LSE	lower shelf energy
LWR	light water reactor
M&CS	Modeling and Computing Services
MC	Monte-Carlo
MD	molecular dynamic
MF	matrix feature
MNP	Mn-Ni-Si-rich precipitate
NRC	U.S. Nuclear Regulatory Commission
ORNL	Oak Ridge National Laboratory
PP	phosphide phases
PR-EDB	Power Reactor Embrittlement Database
PWHT	postweld heat treatment
PRA	primary recoiling atom
PWR	pressurized water reactor
RED	radiation-enhanced diffusion
RPV	reactor pressure vessel
RSC	resistivity-Seebeck coefficient
RSS	square root of the sum of the squares
SANS	small-angle neutron scattering
SAW	submerged arc weld
SIA	self-interstitial atom
SMF	stable matrix feature
SMMS	split metal model steel
SRM	standard reference material
SSP	Supplemental Surveillance Program
TTS	transition temperature shift
UCSB	University of California, Santa Barbara
USE	upper shelf energy
VSR	variable stress relief

Nomenclature

α_j	obstacle strength of hardening feature j
$\alpha(n)$	the rate at which the cluster of the size, n, emits a mobile monomer
β	precipitation kinetics parameter depending on the controlling mechanism
$\beta(\nu)$	the rate at which the cluster of the size, n, absorbs a mobile monomer
δ	lattice parameter mismatch between precipitate and matrix
$\Delta\rho$	change in resistivity
ΔS	change in Seebeck coefficient
$\Delta\sigma_y$	change in yield strength
$\Delta\sigma_{yj}$	change in yield strength due to hardening feature j
ΔUSE	change in Charpy upper shelf energy due to irradiation (= USE_i-USE_u)
γ_{pm}	precipitate-matrix interface energy
μ	shear modulus
ϕ	flux, n/cm^2/s, E > 1 MeV
ϕ_r	reference flux
$\phi(E)$	spectrum
ϕt	fluence, n/cm^2, E > 1 MeV
ϕt_e	effective fluence
Γ_{ij}	thermodynamic activity coefficient of solute i in phase j (= a_{ij} / X_{ij})
μ	shear modulus
σ^*	microcleavage fracture stress
σ_v	neutron spectrum averaged vacancy production cross section
σ_{yj}	intrinsic contribution of hardening feature j to yield strength before superposition
σ_{ypm}	maximum CRP hardening
ρ	dislocation density
A	product form parameter for TTS_{mf}
a_{ij}	thermodynamic activity of solute i in phase j
b	Burger's vector
B	product form parameter for TTS_{crp}
C_c	ratio of TTS to $\Delta\sigma_y$ (ºC/MPa)
C_{Cue}	effective Cu concentration
C_p	P coefficient for TTS (ºC/wt % P)
C_T	irradiation temperature coefficient for irradiation hardening
CF	Chemistry factor quantifying the effect of the composition of MF hardening
CF_P	Phosphorus CF
Cu_{min}	minimum Cu needed for CRP formation
Cu_{max}	maximum effective dissolved Cu prior to irradiation
Cu_e	effective Cu
D*	radiation-enhanced diffusion coefficient of Cu
D_{Cu}	thermal diffusion coefficient of Cu
D_i	diffusion coefficient of SIAs
D_{sd}	diffusion coefficient for Fe self-diffusion
D_S	diffusion coefficient of a species S
D_v	vacancy diffusion coefficient (= $1.1\text{x}10^{-16}$m^2/s @290 ºC)
f_j	volume fraction of hardening feature j
f_{pm}	maximum precipitate volume fraction
fluence	n/cm^2, E > 1 MeV
flux	n/cm^2/s, E > 1 MeV
G_i	generation rate of SIAs

g_r	fraction of vacancies that recombine with SIAs before reaching sinks
g_s	fraction of vacancies that reach sinks
G_S	generation rate of a species S
G_v	generation rate of vacancies
H_{ij}	heat of solution of solute i in phase j
i	solute index for precipitation thermodynamics
j	hardening feature index; by type (mf, p, crp, mnp, pp for MF, precipitate, CRP, MNP, PP) or by strength (w, m, o for weak, medium, high strength)
j	thermodynamics index for the j phase containing element i
k	Boltzmann's constant
K	radiation-enhanced diffusion factor
M	constraint factor >1
M_ϕ	effective fluence multiplier reflecting flux effect ($=\phi t_e / \phi t$)
n	number of atoms in a cluster
N_j	number density of hardening feature j
N(n)	number density of the cluster of size, n
p, p(ϕ)	dose rate effect exponent, which varies from 0 to 1 depending on the flux regime
R	gas constant
R_f	recombination factor
r_j	radius of hardening feature j
r_n	radius of a cluster of n Cu atoms
r_r	recombination radius
S	superposition factor to control the balance between LS and RSS laws
S_d	standard deviation
S_e	standard error
S_S	total defect sink strength
S_t	total defect sink strength for a species S
SS	Cu supersaturation
T	temperature
T_{30}	temperature at 30 ft-lb (41 J) in Charpy tests
T_{ann}	annealing temperature
T_c	elastic cleavage temperature
T_i	irradiation temperature
t_{sr}	stress relief time
t_t	overall time constant for precipitate formation (time for f_p to reach $0.63f_{pm}$)
T_{sr}	stress relief temperature
tanh	hyperbolic tangent
TF	Taylor Factor (≈ 3)
TT_{10i}	transition temperature measured at ≈10J for irradiatetd material
TT_{10u}	transition temperature measured at ≈10J for unirradiated material
TTS_{10}	TTS measured at 10 J $=TT_{10i}-TT_{10u}$
TTS_p	TTS due to hardening feature p
TTS_u	TTS measured at 41 J due to the reduction in USE
TTS_{mf}	TTS due to MF
TTS_{crp}	TTS due to CRP
USE_i	Charpy upper shelf energy for irradiated material
USE_u	Charpy upper shelf energy for unirradiated material
$V_{cu/fe}$	the volume of a Cu or Fe atom
V_{Cu}	the volume of a mole of Cu atoms
X_{Cu}	initial Cu in solution
X_{Cue}	effective atomic fraction of Cu initially in solution

X_{Cup}	precipitate Cu content
X_{Cur}	residual Cu in solution in equilibrium with precipitates
X_{ij}	atomic fraction of solute i in phase j
X_S	atomic fraction of a species S
X_v	atomic fraction of vacancies under irradiation
X_{ve}	atomic fraction of vacancies at thermal equilibrium

Unit Conversions

Fahrenheit to Celsius: $T_C = (T_F - 32)/1.8$

Foot-pounds to Joules: 1 ft-lb = 1.356 J

Note: The U.S. RPV surveillance database is maintained in English units. Thus, the modeling task was performed and is reported in English units. Other parts of this report, namely Chap. 2 on embrittlement mechanisms and Chap. 6 on comparisons of the IVAR data with the TTS model, are reported in SI units.

Acknowledgments

The authors extend their appreciation to the members of ASTM E10.02.02 for extensive reviews of the surveillance database, to J. A. Wang for assistance and advice regarding the PR-EDB database, to Thomas M. Rosseel, Program Manager of the Heavy-Section Steel Irradiation Program, Mikhail Sokolov and Roger Stoller for helpful discussions and technical reviews of the report, to Walter Koncinski for technical editing, and to Brenda Phillips for preparation of the manuscript. We also gratefully acknowledge the very significant contributions of UCSB student Mr. Jonathan Smith to the analysis of the IVAR database and comparison of the IVAR database with the TTS model predictions. We also thank the members of the UCSB Materials Reliability and Performance Group, especially Mr. Doug Klingensmith and Mr. David Gragg, whose tireless efforts made developing the IVAR database possible. We also wish to express our appreciation for the contributions of our many collaborators around the world, who helped to develop an improved fundamental understanding of embrittlement mechanisms that forms the foundation of Chapter 2, with special thanks going to Professor Brian Wirth (UC Berkeley), Mike Miller (ORNL) and the staff of the National Institute of Standards and Technology Center for Neutron Research. The research at UCSB was supported by the US NRC Contract Number 04-01-064. Finally, appreciation is also extended to Carolyn Fairbanks, Mark EricksonKirk, Bob Hardies, Allen Hiser, Cayetano Santos, and Simon Sheng of the U.S. Nuclear Regulatory Commission for their advice, encouragement, and financial support.

Appendix A

1. Introduction

1.1 Background

Pressure vessels for light water reactors (LWRs) are designed and fabricated in accordance with the requirements in consensus codes that are based on mechanical and physical properties of the steels used to construct the vessels. In the absence of radiation damage to the reactor pressure vessel (RPV), fracture of the vessel is difficult to postulate because the fracture toughness of the RPV in the unirradiated condition is generally very high at and above room temperature. However, exposure to high-energy neutrons can result in embrittlement of radiation-sensitive RPV materials. The degrading effects of neutron irradiation on carbon and low-alloy pressure vessel steels have been recognized and investigated since the early 1950s. In those steels at LWR operating temperatures [~ 520–570ºF (~ 270–300ºC)], radiation damage is produced when neutrons of sufficient energy displace atoms; the displacements result in displacement cascades, which produce large numbers of vacancy and interstitial-type defects. Although the inside surface of the RPV is exposed to neutrons of varying energies, the higher-energy neutrons produce the bulk of the damage. In a typical LWR, the flux of such high-energy neutrons (> 1 MeV) is from about 10^{13} to 10^{16} $n \cdot m^{-2} s^{-1}$.

Irradiation embrittlement of RPV beltline materials is currently evaluated according to U.S. Nuclear Regulatory Commission (NRC) Regulatory Guide 1.99, Revision 2 [1], which presents methods (based on data correlations) for estimating the Charpy transition temperature shift (TTS) at 30 ft-lb (41 J) as well as the drop in upper shelf energy (USE). Figure 1.1 shows an example for one particular RPV weld with high copper content [2].

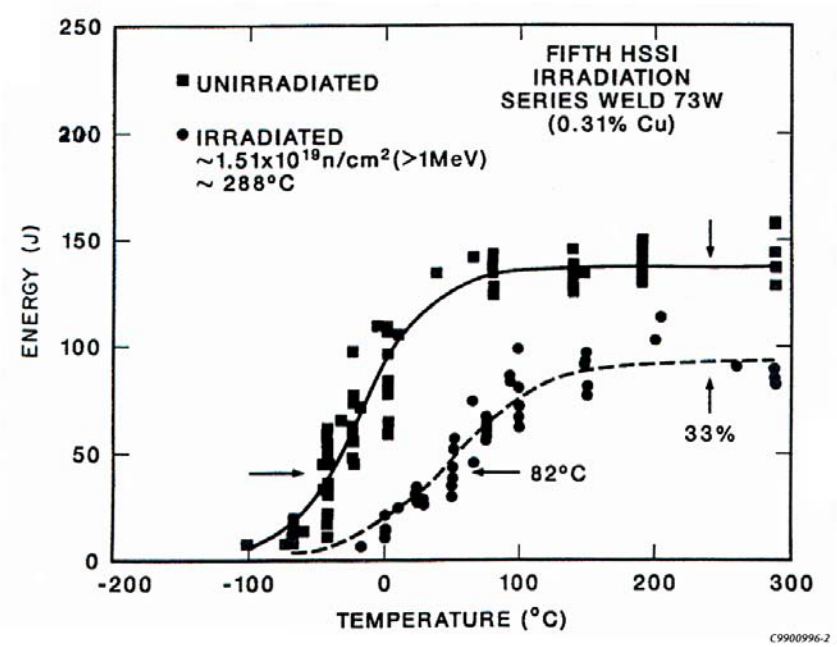

Fig. 1.1. Plot of Charpy impact results showing the effects of irradiation at 288ºC to a fluence of 1.5 × 10^{23} $n \cdot m^{-2} s^{-1}$ (>1 MeV) on the CVN impact toughness.

Improved correlation models, based on a broader database and a better understanding of embrittlement mechanisms, are presented in NUREG/CR-6551, published in November 1998 [3]. The models incorporate material chemical composition and various exposure variables to enable predictions of TTS and USE changes. The embrittlement shift model in NUREG/CR-6551 was updated in July 2000 with additional surveillance data collected since the earlier work; this is referred to in this report as the Draft 2000 model [4]. Another embrittlement shift model was developed at about the same time on the same mid-2000 database under the auspices of the Electric Power Research Institute (EPRI) and the American Society for Testing and Materials (ASTM) E10.02 subcommittee (the E900 model [5]), published as E900-02 [6] in 2002. Similar correlation models were developed on different databases in the United Kingdom [7,8]. A large database of test reactor data from single-variable experiments is being analyzed in terms of a physically motivated model with some features similar to the correlation models [9,10].

Motivation for a new modeling effort came from the fact that 62 additional low-flux boiling water reactor (BWR) shifts became available in 2003. These data were significantly underpredicted by the previous shift models [4,5], so it was necessary to investigate the cause of the underprediction. Additional pressurized water reactor (PWR) data from surveillance reports (about 140 shifts) were also added to the database in 2003 and 2004. Finally, the reliability of the database was improved when all old and new surveillance data were reviewed for completeness, duplicates, and discrepancies during summer and fall 2004, in cooperation with the ASTM Subcommittee E10.02 on Radiation Effects in Structural Materials. Thus a larger, better balanced and, therefore, more reliable database was made available for analysis.

This report is a record of work performed in part by the Heavy Section Steel Irradiation Program (see Appendix A).

1.2 Objectives and Scope of Work

The present work is an update to the earlier embrittlement shift correlation models [3,4], based on the expanded surveillance database and on the continuing advances in mechanistic understanding. The objective is to produce an improved embrittlement shift correlation model with demonstrated predictive capability.

The work reported here includes several steps:

- collection of new data that have become available since the last database revision in 2000;
- review and updating of both new and previously collected data, including identifying duplicates and discrepancies;
- model development to address the low-flux data that were not well fitted by previous models and to improve the agreement with recent physical insights and the expanded database;
- calibration of the revised model;
- validation of the model on surveillance data not used for fitting, to the extent possible; and
- comparison with test reactor results not used for fitting.

The model revision presented here is calibrated to the surveillance data from U.S. power reactors; so data from test reactor irradiations were used only for insight during the calibration process. After the model was calibrated to surveillance data, an extensive comparison was made between the model and the Irradiation Variable (IVAR) program test reactor data, as described in Chap. 6. (See Appendix B, "Irradiation Variable [IVAR] Program Data Base.") Subsequent sensitivity studies on surveillance data led to minor simplifications of the model as discussed in Chap. 7.

The revised model is able to fit both PWR and BWR data, within a format similar to earlier models, using a modification of the "effective fluence" (ϕt_e) approach to flux effects that has been previously suggested by Odette and others [9–11]. The revised model contains, sometimes in different form, all

effects that were in earlier models by the same authors [3,4], except the "long-time" effect in [4], which became clearly nonsignificant with the latest expansion of the database and the use of a separate standard reference material (SRM) coefficient. The revised model (discussed in detail in Chap. 4) combines two terms, the first of which depends on irradiation temperature (T_i), material chemical composition, and effective fluence (ϕt_e), while the second depends only on those latter two factors. The general form of the model is shown in Eq. (1-1); the complete model includes various coefficients to account for material specific product forms, chemical composition ranges, and weld flux types:

$$TTS = f(T_i, P, Mn, \phi t_e) + g(Ni, Cu, P, \phi t_e). \quad (1\text{-}1)$$

The Mn effect in the revised model is an example of a change in model form – the effect of Mn was implicitly included in the prior models via the product form coefficients, while in the revised model it is also incorporated explicitly. The revised model also incorporates the variation in fluence at which copper-rich precipitate (CRP) damage becomes important as a function of Cu and Ni, a known effect (see p. 87 in [3] that could not be calibrated reliably before the recent database expansions; see also [7],[9],[10]).

1.3 Overview and Organization of Report

This report presents the revised embrittlement shift model and discusses its quality of fit, both of data used for model calibration and of other data that were not used for calibration. The focus of the report is on the revised model and its quality of fit. The model development process has been an iterative effort over several years as the surveillance database has increased in size and the understanding of radiation damage has matured. Two of the previous iterations are described in [3,4] and more recent iterations are summarized in this report.

The report is organized to provide some background on radiation damage and statistical terminology in the remainder of Chap. 1, followed by a more detailed description in Chap. 2 of the radiation damage mechanisms relevant to the revised model. Chapter 3 describes the surveillance database and the subsets used for model calibration and analysis. Chapter 4 summarizes the model development process, presents the model, and demonstrates quality of fit and validation on surveillance data not used for fitting. The individual variable effects are described and plotted and their statistical significance is discussed in Chap. 5. Then, the model of surveillance data is compared to an independent database of test reactor results, the IVAR database, in Chap. 6. The agreement with the independent IVAR database provides additional validation of predictive capability and illuminates some limitations of the surveillance database and the effects of those limitations on the model. Chapter 7 discusses minor simplifications and supporting sensitivity analysis, and presents the revised model in the form recommended for application. Chapter 8, the final chapter, provides a brief summary and conclusions.

1.4 Radiation Damage Mechanisms Background

The mechanisms of irradiation embrittlement are discussed in Chap. 2 and are only briefly described in this section. Reactor spectrum neutrons generate high-energy primary recoil atoms. The primary recoil atoms slow down in a branching series of collisions with atoms that are ejected from their lattice sites, in what is known as a displacement cascade. This produces a large concentration of vacancies and self-interstitial atoms in the cascade region. Many self-interstitial atoms quickly recombine with vacancies, thus healing the damage, or form clusters of like defects, typically in the form of complexes with various solute atoms. At RPV operating temperatures, the residual vacancies and interstitials subsequently diffuse long distances relative to the size of the cascade. The migrating single vacancies, interstitials, and small interstitial clusters, as well as vacancies emitted by the dissolution of vacancy clusters, recombine during long-range diffusion, or are absorbed at sinks. So-called "matrix features" (MFs), which mainly form in

the cascades, produce hardening in both low- and high-Cu steels. They are believed to be vacancy-solute cluster complexes or their solute remnants; MFs may also grow by the long-range diffusion of solutes and vacancies. The hardening from MF increases with decreasing irradiation temperature and roughly with the square root of fluence. The excess concentration of vacancies under irradiation also accelerates precipitation of Cu, along with Ni, Mn, and Si, from the supersatured solution (the Cu solubility limit is less than 100 appm at 290°C) above threshold levels of about 0.07 wt % Cu. This precipitation results in the formation of CRPs, or at high levels of these elements, manganese-nickel rich precipitates (MNPs) [12,13]. The causes, character, and consequences of the MFs are not as well understood as are those of CRPs and MNPs, and improved treatments of their contributions to TTS are the subject of continuing study by the research community.

Evolution of CRPs or MNPs is the most important mechanism of embrittlement in irradiation sensitive western LWR steels [12]. Radiation-enhanced diffusion is a result of the much higher concentration of vacancies in the steel under irradiation, compared with that under thermal conditions. Thus, a given solute atom (e.g., Cu, Ni, Mn, and Si) has a much higher probability of having a neighboring vacancy during irradiation. With or without irradiation, diffusion of solutes, such as copper, takes place by thermal jumps into adjacent vacancies, but the number of these jumps in a given time interval is much higher during irradiation, corresponding to the increased concentration of vacancies. Subsequent repetition of this vacancy-solute exchange process results in random diffusion of copper. When a diffusing Cu atom encounters another Cu atom (or cluster of Cu atoms), they bind with one another. Small Cu clusters can redissolve, but at a sufficient size the Cu clusters form coherent precipitates that continue to grow by radiation-enhanced diffusion up to the point when the Cu is depleted from the matrix. The effective energy of Ni, Mn, and Si atoms is lower in the precipitates than in the matrix, so these elements also flow into CRPs along with Cu. The resulting high number density of CRPs ($> 10^{23}/m^3$) with typical diameters on the order of 1 to 3 nm efficiently pin dislocations, resulting in significant hardening in RPV steels, which increases with Cu contents above about 0.10 wt %. The amount of solute diffusion under irradiation that occurs at a specified fluence increases with increasing dose rate (neutron flux). This results in a strong dose rate effect in the CRP hardening and TTS regime (due to matrix solute depletion).

At high levels the actual copper remaining in solid solution that is available for irradiation-induced precipitation may be less than the measured bulk copper content, due to pre-precipitation during postweld heat treatment (PWHT) performed during the fabrication of an RPV. As a result the maximum amount of copper that remains in solution following typical PWHT is about 0.25 to 0.3 wt % [12].

The synergistic interaction among Cu, Mn, and Ni is the reason why Ni enhances the effects of Cu on TTS, as reflected in the predictive embrittlement formulas based on the U.S. LWR surveillance database [1,3,6], that of the Japanese LWR surveillance database [14], and in other commercial reactor vessel steels [15,16]. Moreover, atom probe tomography has observed the enrichment of CRPs with Ni, Mn, P, and Si as well as segregation of solutes such as P, Ni, and Mn to grain and lath boundaries in the microstructure [17]. In *Effects of Nickel on Irradiation Embrittlement of Light Water Reactor Pressure Vessel Steels*, a report by the International Atomic Energy Agency (IAEA) Cooperative Research Project, it was noted that, "for a given high level of nickel in the material and all other factors being equal, high manganese content leads to much greater radiation-induced embrittlement than low manganese content for both VVER-1000 and PWR materials"[18]. Notably, these interactions were long ago predicted based on theoretical models that were subsequently verified by careful single-variable experiments and very detailed nano-analytical characterization studies [19]. Some further references that discuss the effects of nickel with copper and manganese are [20-27].

While the existence of MNPs in Cu-bearing steels has long been well established, the models also predicted the possible formation of Mn-Ni-Si precipitates even in very low Cu steels. Since these precipitates were expected to be slow to nucleate relative to CRPs, thus requiring high fluence to cause hardening and TTS, they were called "late-blooming phases (LBPs)." Recently, careful experimental

studies have verified the existence of LBPs, even in nominally Cu-free alloys [28]. The significance of LBP to the steels and irradiation conditions pertinent to the fleet of western RPVs is a topic of ongoing research.

Irradiation hardening results in TTS, which can be understood from the basic micromechanics of fracture. Body-centered cubic alloys, such as RPV steels, undergo a transition from cleavage to ductile fracture over a range of temperature known as the "ductile-brittle transition" (DBT), shown in Fig. 1.1. In the higher-temperature region, the yield stress of the alloy is insufficient to produce a stress concentration near the tip of a notch or crack that reaches the cleavage fracture stress. In this case, ductile fracture occurs by the nucleation, growth, and coalescence of internal voids that form on inclusion particles. The position and range of the DBT is controlled by the magnitude and rate of increase in the yield stress with decreasing temperature and the local critical stress-volume conditions leading to cleavage. As a result of irradiation-induced increases in yield stress, higher temperatures are required to keep the internal stress concentrations below the cleavage fracture stress, resulting in TTS.

For some steels, nonhardening embrittlement can be caused by radiation-enhanced solute segregation of elements such as phosphorus to grain boundaries that are effectively weakened to the point where they become the primary path for the propagation of brittle cracks. Thus this type of embrittlement, typically defined as irradiation-assisted temper embrittlement [29], is manifested as an intergranular (grain boundary) fracture rather than the usual transgranular cleavage fracture. In this case, TTS can occur even if the yield strength does not increase; in principle, combinations of irradiation hardening and grain boundary embrittlement can interact synergistically to produce very large TTS. In general, however, the amount of radiation-induced intergranular fracture in U.S. RPV steels (Mn-Mo-Ni steels) is low, probably due to their generally low sensitivity to temper embrittlement [30,31]. Consequently, intergranular fracture is not discussed in this report.

1.5 Modeling and Statistical Background

1.5.1 Basis of Modeling

The model presented in Chap. 4 is a hybrid incorporating both physically motivated features and empirical calibration. In this type of model, features of the model may be based on statistical significance in the modeling database, physical understanding, observations from independent sources (including data from controlled experiments), or all of these types of evidence. Most of the effects incorporated in the model presented are supported by more than one form of evidence. However, as a key ground rule for the modeling effort, the only data used in this report for calibration and statistical analysis are the U.S. reactor surveillance data, described in more detail in Chap. 3.

The calibration and much of the analysis of the model are inherently statistical, so the following paragraphs highlight a few statistical definitions and issues intended to help nonspecialists with the statistical details given in the report.

1.5.2 Definition of Residuals

Much of the discussion of models in this report refers to residuals. A residual is the difference between the model estimate and the measured TTS value:

$$Residual = Model\ TTS - Measured\ TTS\ . \tag{1-2}$$

In this calculation, the values of the independent variables that were recorded for the measured TTS (e.g., fluence, Cu, Ni) are used to make the model estimate. The residuals are just as often defined with the opposite sign (*residual = measured TTS − model TTS*), so it is important to be sure which definition is

used when interpreting the direction of trends in residuals. Both definitions are used in this report, in sections prepared by different authors, and the corresponding definition is shown. As defined in Eq. (1-2), residuals are negative if the model underestimates the measured shift.

The least squares method finds the best fit by minimizing the sum of squared residuals, so by definition, a good fit will have relatively small residuals overall. Moreover, a good model will show no obvious trends if the residuals are plotted against model variables and against variables not included in the model.

1.5.3 Statistical Significance

Statistical significance, although not the only basis of the model, is frequently mentioned throughout this report. Statistical significance implies that the variable effect or difference in shift or residual slope that is being analyzed is large enough relative to the uncertainty from data scatter and limited sample size that it is unlikely to be caused by random variations. Any reference to "significant" in this report refers to statistical significance unless otherwise noted. Differences in shift and variable effects that are practically important (i.e., having cost, operational, or other consequences) may or may not be statistically significant, Two types of questions are frequently asked about statistical significance: (1) is A significantly different from B? or (2) is A significantly larger (or smaller) than B?

The first question gives rise to what is called a two-tail or two-sided significance test, in which a result is significant if the probability is small that the difference, in either direction, is due to random variation. The second question gives rise to what is called a one-tail or one-sided test, in which a result is significant if the probability is small that the difference, in a preselected direction, is due to random variation. The usual practice in statistical analysis is that a two-sided test is appropriate if the direction of an effect or comparison is not known in advance and if neither direction is substantially more important than the other. A one-sided test is appropriate if the direction of an effect or comparison is known in advance, or if differences in one direction are clearly more critical than in the other [32,33]. As a practical matter, a difference must be larger to show a specified level of significance on a two-sided basis than on a one-sided basis.

Both two-sided and one-sided tests of significance are used in this report, following the usual practice noted in the last paragraph, and the type of test used is stated. It could be argued that enough research and prior modeling has been done that by now most questions about the significance of embrittlement variable effects should be one-sided questions, as the direction of most variable effects is well known in advance of the statistical analysis. For instance, Cu is known to enhance embrittlement, so it makes little sense to ask if the data show that high-Cu shifts are significantly different from the low-Cu shifts; instead, if the question were raised at all, it would be asked whether the high-Cu shifts are significantly greater than the low-Cu shifts, hence a one-sided test. But some questions are more appropriate for two-sided tests. For example, throughout this report, tests on the significance of the slope of residual trends are two-sided unless otherwise noted, asking the question whether the slope of the residual trend is significantly different from zero. The reason is that the modeling objective is to make the model accurately fit the data trends (i.e., zero slopes to the residuals when plotted against modeling variables), so in most cases a significant residual trend for a variable in the model represents a modeling issue whether its slope is positive or negative. Moreover, although the direction of the physical variable effect is often known in advance, the direction of residual modeling error depends on the model and the specific data that are available and may not be known in advance.

An exception to the use of two-sided tests for residuals is appropriate if the residual offset or slope is caused by intentionally leaving out or disabling the effect of a term in the model to see whether it is significant. In this case, the expected direction of the residual slope or offset is known in advance because the analyst intentionally took out a previously calibrated effect, thus causing the residual slope or offset to occur in a predictable direction. The question in this case is whether the slope or offset is large enough in

the predictable direction to imply a significant variable effect relative to the uncertainty, so a one-sided test is appropriate.

The level of probability (p) used in this report for concluding that an effect is significant is $p < 0.05$ unless otherwise stated. This is a typical significance level for engineering, where it is sometimes referred to as the 95% significance level. That level of significance means that the chance the observed effect or difference could arise from random variation is estimated to be less than 5%. In the case of a two-sided test, such as the test for significance of residual slope, a slope that is significantly different from zero at $p < 0.05$ implies it is far enough from zero in one direction that there is less than 2.5% chance that it could occur by random variation. The same would be true of a slope of the same magnitude in the opposite direction, and hence the chance of observing that magnitude of slope in either direction due to random variation is less than 5%.

1.5.4 Treatment of Outliers

Despite best efforts, anomalous data points occur in engineering databases, in many cases because of measurement or documentation errors that cannot be identified or resolved by the available information. The question from an analyst's point of view is whether an apparent outlier is different enough from the bulk of the data to suggest that the point is in error. The risk in using such a point for model calibration can be substantial because extreme outliers produce large residuals, which can have a disproportionate effect on the sum of squared residuals that is minimized by least squares, thus biasing the fit. The risk in not using such points is the possibility that they are valid; hence, by omitting them the fitted model or the estimates of data scatter could be somewhat unrealistic. A biased fit from leaving outliers in a calibration set is the greater risk, particularly in large datasets as analyzed here. Since the purpose of the modeling is usually to characterize the average trend in the data, that can be accomplished using about 99% of the data nearest the average trend while ignoring the few points furthest away.

The procedure followed in this analysis was to calibrate a preliminary model, then apply an objective statistical criterion (Chauvenet's) to identify potential outliers among the residuals. These outlier points were investigated to the extent possible with the available documentation and with help in many cases from the ASTM E10.02 subcommittee (on Behavior and Use of Nuclear Structural Materials), in an attempt to determine whether there were recording errors, physical causes for the anomalous behavior, or extremes in test or irradiation conditions or composition. If a correctable error or other cause of the anomaly could be found, appropriate corrections were made and documented; otherwise, the points were set aside based on Chauvenet's criterion and the models were recalibrated without the identified outliers, producing the results presented in this report.

Chauvenet's criterion provides a quantitative and objective means of deciding whether or not an outlier point may be discarded [34,35]. Chauvenet's criterion calls for rejection of an outlier if the estimated probability of observing it is less than $1/(2N)$, where N is the total number of points being analyzed. In other words, an outlier is rejected if the expected number of observations in the database as far from the mean as the outlier is less than ½. In the modeling application, the mean of the distribution is typically set to be equal to the mean residual (or to zero), and the residuals relative to the model are the observations. If the standard deviation of the residuals is estimated by the model standard error (S_e), the critical multiple of S_e from the model, beyond which the data are suspect, can be calculated from the normal distribution. For example, if 100 points are used for calibration, an outlier might be rejected if further than $2.8S_e$ from the model, whereas if 1000 points are used, an outlier must be further than about $3.5S_e$ from the model to be rejected on that basis.

Chauvenet's criterion was used to justify removal of several surveillance data points in previous modeling efforts and in the present analysis. The outliers removed in previous modeling efforts were reconsidered in the present analysis and all remained Chauvenet outliers. A few points were also removed because they were irradiated under unusual conditions, including irradiation in two different reactors at

substantially different flux and/or temperature and irradiation at flux values higher than the usual range for surveillance materials. One point could be removed on either basis. The points not used in the fit amounted to about 1% of the available data.

1.5.5 Variable Confounding

In data from statistically designed experiments, variables may be confounded by the experimental design such that their effects cannot be separately estimated, as discussed in many statistics texts (e.g., Chap. 14 of. [32]). Partial confounding may occur, in which estimation of the effects of two or more variables is feasible, but the estimates are affected to some degree by the other variable(s) [36]. In databases that are not from a single statistically designed experiment, such as the surveillance database, partial confounding often occurs from patterns in the data. For example, the only product form in the surveillance database with relatively low Mn values (below about 1 wt %) is forging, so the analysis reported in later chapters found that the Mn variable is partially confounded with the product form variable.

The problem with variable confounding is that effects that are nominally attributed to one physical variable may be caused in part by one or more other variables, and the effect of some variables may not be readily calibrated because of relationships with other variables. This situation is noted where detected in the following chapters.

1.6 References

1. U.S. Nuclear Regulatory Commission, *Radiation Embrittlement of Reactor Vessel Materials*, Regulatory Guide 1.99 Revision 2, 1988.
2. Nanstad, R. K., McCabe, D. E., Menke, B. H., Iskander, S. K., Haggag, F. M., "Effects of Radiation on K_{Ic} Curves for High Copper Welds," pp. 214–33 in Effects of Radiation on Materials: 14th International Symposium (Volume II), ASTM STP 1046, N. H. Packan, R. E. Stoller, and A. S. Kumar, Eds., American Society for Testing and Materials, Philadelphia, 1990.
3. Eason, E. D., J. E. Wright, and G. R. Odette, *Improved Embrittlement Correlations for Reactor Pressure Vessel Steels*, NUREG/CR-6551, U.S. Nuclear Regulatory Commission, Washington D.C., 1998.
4. Kirk, M., C. Santos, E. Eason, J. Wright, and G. R. Odette, "Updated Embrittlement Trend Curve for Reactor Pressure Vessel Steels," in *Transactions of the 17th International Conference on Structural Mechanics in Reactor Technology (SMiRT 17), Prague, Czech Republic, August 17-22, 2003,* 2003.
5. Server, W., C. English, D. Naiman, and S. Rosinski, "Charpy Embrittlement Correlations—Status of Combined Mechanistic and Statistical Bases for U.S. RPV Steels (MRP-45)," EPRI Report 1000705, 2001.
6. ASTM International, "Standard Guide of Predicting Neutron Radiation Damage to Reactor Vessel Materials," E706 (IIF), E900-02, *Annual Book of ASTM Standards*, ASTM International, 2002.
7. Williams, T. J., and D. Ellis, "A Mechanistically-Based Model of Irradiation Damage in Low Alloy Steel Submerged Arc Welds," pp. 8–27 in *Effects of Radiation on Materials: 20th International Symposium*, ASTM STP 1405, Ed. S.T. Rosinski, et al., ASTM, 2001.
8. Williams, T. J., D. Ellis, C. A. English, and J. Hyde, "A Model of Irradiation Damage in High Nickel Submerged Arc Welds," *Int. Jour. of Pressure Vessels and Piping* 79, 649–60, 2002.
9. Odette, G. R., T. Yamamoto, and D. Klingensmith, *The Effect of Dose Rate on Irradiation Hardening of RPV Steels: A Comprehensive Single Variable Database and Model Based Analysis*, Letter Report UCSB-NRC-03/1, 2003.

10. Odette, G. R., T. Yamamoto, D. Klingensmith, and H. Kishimoto, *The Effect of Flux and Irradiation Temperature on Hardening in RPV Steels*, Letter Report UCSB-NRC-03/2, 2003.

11. Electric Power Research Institute, Workshop on Dose Rate Effects in Reactor Pressure Vessel Materials Held November 12-14, 2001, Olympic Valley Calif., Conference Proceedings (CD), Ed. N. Soneda and R. G. Carter, EPRI 1006981, CRIEPI T02904, 2002.

12. Odette, G. R., and G. E. Lucas, "Embrittlement of Nuclear Reactor Pressure Vessels," *J. of Metals* 53 (7), 18–22, 2001.

13. Odette, G. R., and G. E. Lucas, "Recent Progress in Understanding Reactor Pressure Vessel Embrittlement," *Rad. Effects and Defects in Solids* 144, 189–231, 1998.

14. Japanese Electric Association (JEA), *Method of Surveillance Tests for Structural Materials of Nuclear Reactors*, Japanese Electric Association Code (JEAC) 4201-2000, 2000.

15. Kryukov, A. M., Y. A. Nikolaev, and A. V. Nikolaeva, "Behavior of Mechanical Properties of Nickel-Alloyed Reactor Pressure Vessel Steel under Neutron Irradiation and Post-Irradiation Annealing," *Nuclear Engineering and Design* 186 (3), 353–59, 1998.

16. Williams, T. J., P. R. Burch, C. A. English, and P. H. N. de la Cour Ray, "The Effect of Irradiation Dose Rate and Temperature, and Copper and Nickel Content, on the Irradiation Shift of Low Alloy Steel Submerged Arc Welds," pp. 121–131 in *Third International Symposium on Environmental Degradation of Materials in Nuclear Power Systems—Water Reactors, 1987*, Ed. G. J. Theus and J. R. Weeks, 1988.

17. Miller, M. K., P. Pareige, and M. G. Burke, "Understanding Pressure Vessel Steels: An Atom Probe Perspective," *Materials Characterization* 44, 235–54, 2000.

18. International Atomic Energy Agency, *Effects of Nickel on Irradiation Embrittlement of Light Water Reactor Pressure Vessel Steels*, IAEA-TECDOC-1441, Vienna, June 2005.

19. Odette, G.R. and Lucas, G.E. "The Effect of Nickel on Radiation Hardening of Pressure Vessel Steels", *Effects of Irradiation on Materials-14th Symposium, ASTM-STP-1046,* American Society for Testing and Materials, Philadelphia, 323-347, 1989.

20. Nanstad, R. K., M. A. Sokolov, and M. K. Miller, "Comparison of Nickel Effects on Embrittlement Mechanisms in a Radiation-Sensitive Weld and in Prototypic WWER-1000 and A533B Steels," *Proceedings of IAEA Specialists' Meeting on Effects of Radiation on Reactor Pressure Vessels and Internals*, Gus-Khrustalny, Russia, May, 2004.

21. Odette, G. R., and G. E. Lucas, "The Effect of Nickel on Irradiation Hardening of Pressure Vessel Steels," pp. 323–47 in *Effects of Radiation on Materials: 14th International Symposium* (Volume II), ASTM STP 1046, Ed. N. H. Packan, R. E. Stoller, and A. S. Kumar, American Society for Testing and Materials, Philadelphia, 1990.

22. Odette, G. R., "Radiation Induced Microstructural Evolution in Reactor Pressure Vessel Steels," pp. 137–48 in *Microstructure of Irradiated Materials*, MRS Symposium Proceedings, Volume 373, Pittsburgh, 1995.

23. Gerard, R., A. Fabry, J. Van de Velde, J. L. Puzzolante, A. Verstrepen, T. Van Ransheeck, and E. van Walle, "In-Service Embrittlement of the Pressure Vessel Welds at the Doel I and II Nuclear Power Plants," pp. 294–319 in *Effects of Radiation on Materials: 17th International Symposium* (Volume II), ASTM STP 1046, Ed. David S. Gelles, R. K. Nanstad, A. S. Kumar, and E. A. Little, American Society for Testing and Materials, 1996.

24. Odette, G. R., C. L. Liu, and B. D. Wirth, On the Composition and Structure of Nanoprecipitates in Irradiated Pressure Vessel Steels," pp. 457–69 in *Microstructure Evolution During Irradiation*, MRS Symposium Proceedings, Volume 439, Pittsburgh, 1997.

25. S. M. Rekhson, M. J. Leitman, Y. A. Nikolaev, A. M. Kryukov, V. I. Levit, Y. N., Korolyov, and A. V. Nikolaeva, "Radiation Embrittlement and Thermal Annealing Behavior of Cr-Ni-Mo Reactor Pressure Vessel Materials," *J. Nuc. Matls*. 226, 144–55, 1995.

26. Burke, M. G., R. J. Stofanak, J. M. Hyde, C. A. English, and W. L. Server, "Irradiation Damage Investigation of A508 Grade 4N Steels: Ni and Flux Effects," pp. 13-1 through 13-30 in Workshop on Dose Rate Effects in Reactor Pressure Vessel Materials Held November 12-14, 2001, Olympic Valley Calif., Conference Proceedings (CD), Ed. N. Soneda and R. G. Carter, EPRI 1006981, CRIEPI T02904, 2002.

27. Burke, M. G., R. J. Stofanak, J. M. Hyde, C. A. English, and W. L. Server, "Microstructural Aspects of Irradiation Damage in A508 Gr 4N Forging Steel: Composition and Flux Effects," pp. 194-207 in *The Effects of Radiation on Materials: 21st International Symposium, ASTM STP 1447*, Ed. M. L. Grossbeck, ASTM, 2003.

28. G. R. Odette, T. Yamamoto, and B. D. Wirth, "Late Blooming Phases and Dose Rate Effects in RPV Steels: Integrated Experiments and Models," *Proceedings of the Second International Conference on Multiscale Materials Modeling*, edited by N. M. Ghoniem, University of California (2004) 355.

29. McMahon, Jr., C. J., V. Vitek, and J. Kameda, "Mechanics and Mechanisms of Intergranular Fracture," Chap. 4 in *Developments in Fracture Mechanics-2*, Ed. G. G. Chell, Applied Science Publishers, Englewood, N.J., 1981.

30. McElroy. R. J., C. A. English, A. J. E. Foreman, G. Gage, J. M. Hyde, P. H. N. Ray, and I. A. Vatter, "Temper Embrittlement, Irradiation Induced Phosphorus Segregation and Implications for Post-Irradiation Annealing of Reactor Pressure Vessels," pp. 296–316 in *Effects of Radiation on Materials: 18th International Symposium, ASTM STP 1325*, Ed. R. K. Nanstad, M. L. Hamilton, F. A. Garner, and A. S. Kumar, American Society for Testing and Materials, West Conshohocken, Pennsylvania, 1999.

31. Nanstad, R. K., D. E. McCabe, M. A. Sokolov, C. A. English, and S. R. Ortner, "Investigation of Temper Embrittlement in Reactor Pressure Vessel Steels Following Thermal Aging, Irradiation, and Thermal Annealing," pp. 356–82 in *Effects of Radiation on Materials: 20th International Symposium, ASTM STP 1405*, Ed. S. T. Rosinski, M. L. Grossbeck, T. R. Allen, and A. S. Kumar, American Society for Testing and Materials, West Conshohocken, Pennsylvania, 2001.

32. Miller, I. and J. E. Freund, pp. 162–65 in *Probability and Statistics for Engineers*, Englewood Cliffs, N.J.: Prentice-Hall, 1965.

33. Milton, J. S. and J. C. Arnold, pp. 234–37 in *Probability and Statistics in the Engineering and Computing Sciences*, New York: McGraw-Hill, 1986.

34. Taylor, J. R., *An Introduction to Error Analysis*, University Science Books, Mill Valley, California, 1982.

35. Young, H. D., *Statistical Treatment of Experimental Data*, McGraw-Hill Book Company, Inc., New York, 1962.

36. Haaland, P. D., pp. 85-92 in *Experimental Design in Biotechnology*, New York, Marcel Dekker, 1989.

2. Embrittlement Mechanisms and Physical Models Underpinning the TTS Model

2.1 Background and Context

Irradiation hardening and embrittlement of RPV steels depend on the combination of a large number of metallurgical and irradiation variables [1–23]. Physical models and experimental insight on mechanisms are helpful in identifying potentially important embrittlement variables and their interactions, as well as in developing simplified embrittlement model equations that can be fitted to the TTS data base. (See Appendix C, "Analysis Data Base.")

To begin we note that this chapter and Chap. 6 were both written *after* work on the TTS model (presented in Chaps. 3 to 5) had been basically completed. The foundation for what follows is a large literature on embrittlement that has developed over the recent years, including the results of a number of controlled single variable and variable combination experiments and mechanism studies, as well as extensive modeling efforts. The experimental studies include the Irradiation Variable (IVAR) program that is extensively discussed in Chap. 6. However, it must be emphasized that the current state of understanding of embrittlement is not complete, and that the overview that follows represents the author's own experience and viewpoints, that will be extended and refined in the future. It is also important to note that, while basic understanding of embrittlement mechanisms was used as a guide, the quantitative TTS model was derived by non-linear least square fitting of necessarily simplified analytical expressions to the scattered and non-ideally distributed surveillance database. Thus some differences between the TTS model and the description of the physics that follows are almost inevitable. (See Appendix D for an explanation of the specialized terms used in Chaps. 2 and 6.)

The basic mechanisms of irradiation embrittlement are illustrated in the block diagram shown in Fig. 2.1 [8]. High-energy neutrons interactions with atomic nuclei create energetic primary recoil atoms (PRAs) with energies up to several tens of keV. The PRAs produce displacement cascades by a branching series of atomic collisions until the energies of the final generation of secondary recoiling atoms fall below that needed to displace atoms from their crystal lattice sites. The defects created in the cascade are in the form of single and small clusters of vacancies and self-interstitial atoms (SIAs). SIA defects are two atoms sharing one crystal lattice site. A molecular dynamics simulation of a cascade is shown in Fig. 2.2 [24]. The green atoms are displaced from the vacant lattice sites marked as the red symbols. The primary vacancy and SIA defects that remain after tens of ps, illustrated in Fig. 2.3, are the basic sources of radiation damage [12,24,25]. These point defects and small defect clusters are mobile and diffuse through the ferrite matrix at RPV operating temperatures. A fraction of the vacancies and SIA recombine and like defects quickly cluster in the cascade region, but most eventually migrate to sinks or undergo SIA-vacancy recombination (self-healing) reactions during long-range diffusion [3,7-9,12,13,24-27]. Sinks are sites where the individual vacancies and SIA are destroyed, like at dislocation jogs, free surfaces and grain boundaries. Larger vacancy clusters dissolve over varying time scales [26,27]. Larger SIA clusters: (a) migrate one dimensionally to sinks; (b) shrink by absorbing excess vacancies; or (c) grow by absorbing an excess flux of SIAs to form dislocation loops [8,24,26,27]. The primary vacancies also locally interact with various solutes during the long-term aging of the cascades, as illustrated in the kinetic lattice Monte Carlo simulation shown in Fig. 2.4, to form defect-solute cluster complexes and their solute remnants, which are known as matrix features (MFs) [3,8,26,27].

Substitutional solutes diffuse by a vacancy exchange mechanism, as schematically illustrated in Fig. 2.5 (a). Thus the excess concentration of vacancies created by irradiation greatly accelerates solute diffusion rates. As illustrated by the kinetic lattice Monte Carlo simulation in Fig. 2.5 (b) for a Fe-0.3 at.% Cu alloy [27], at highly supersaturated dissolved Cu concentrations (more than about 0.05 to 0.1 wt % Cu), radiation-enhanced diffusion (RED) leads to the accelerated precipitation of a high number density of nanometer-scale coherent bcc copper-rich precipitate (CRP) phases [3,6–9,12,22,28–34]. The

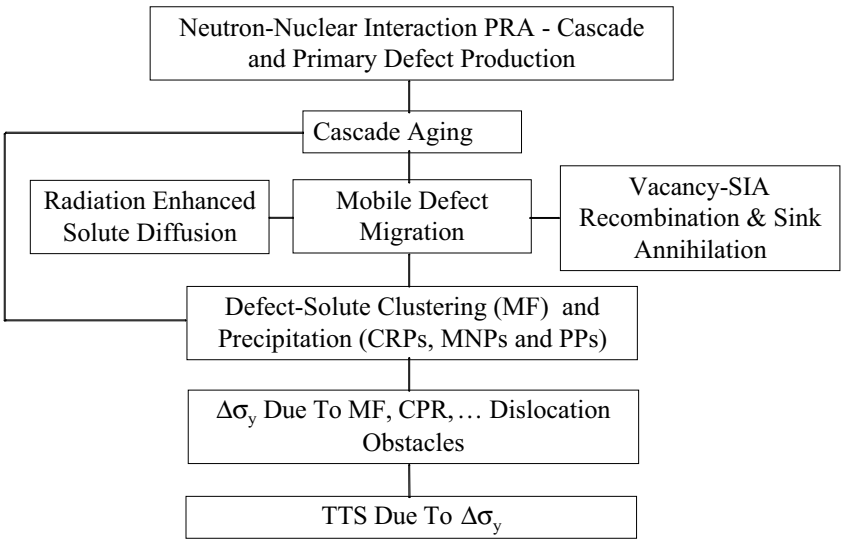

Fig. 2.1. A simplified description of the sequence of events leading to irradiation-induced TTS.

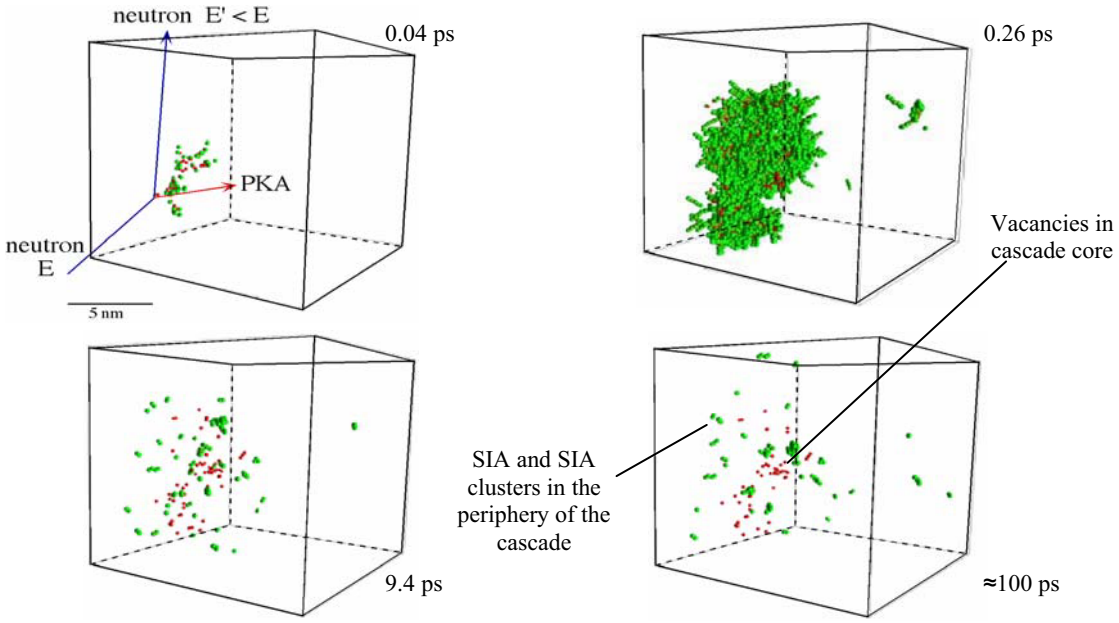

Fig. 2.2. A molecular dynamics simulation of displacement cascade in Fe produced by primary recoil atoms (PRAs) created by high-energy neutrons. The figures represent a time sequence starting from the initial PRA collisions (upper left) to the defects remaining after the thermal energy has dissipated from the cascade (lower right) after ≈ 100 ps. The green dots are SIA and the red dots are vacancies. Note the positions of the lattice Fe atoms are not shown.

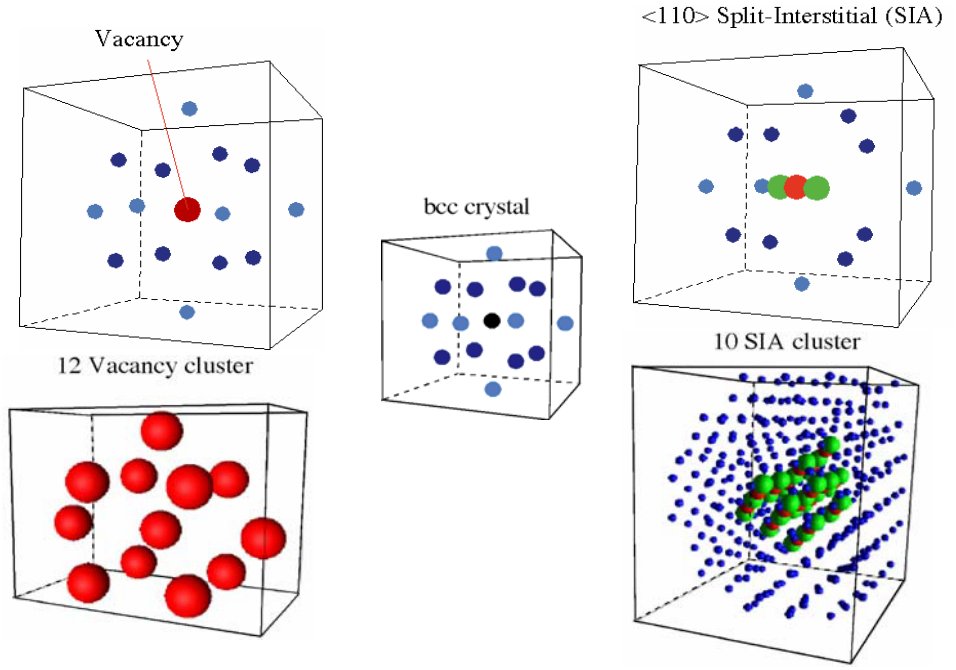

Fig. 2.3. Primary vacancy and SIA defects and defect clusters created in cascades by PRAs.

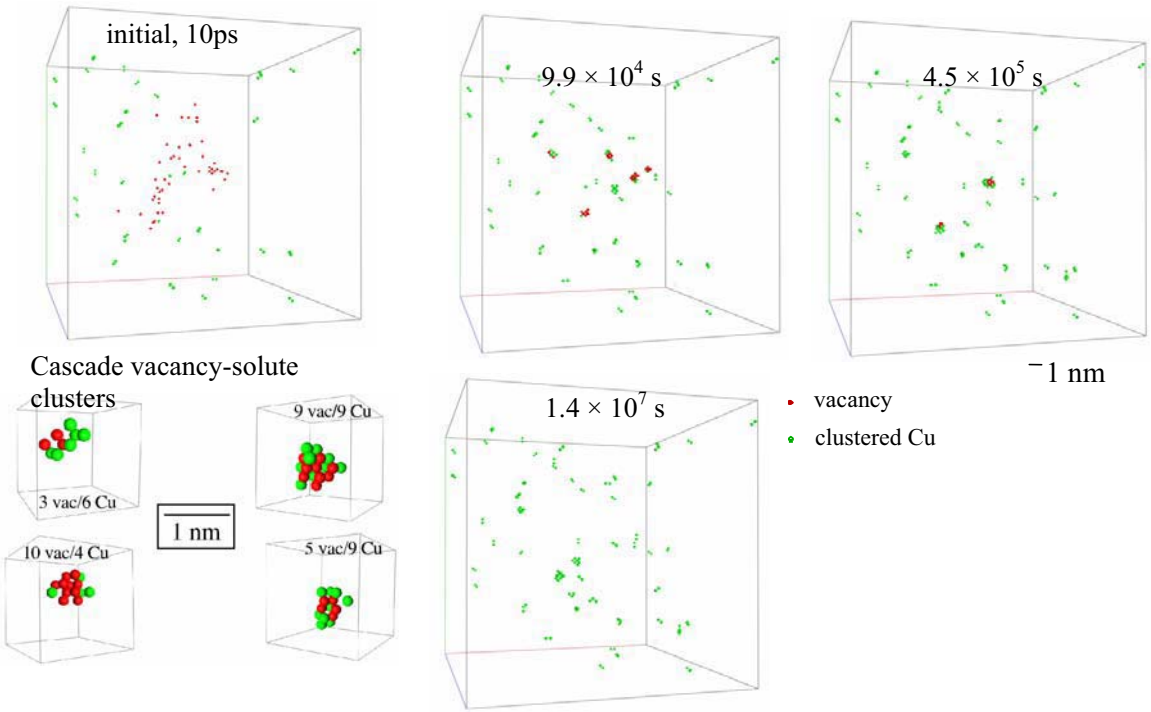

Fig. 2.4. Kinetic lattice Monte Carlo simulations of cascade aging to form vacancy solute (Cu) cluster complexes and their remnants that are believed to be the primary source of MF hardening. Note the positions of the Fe atoms are not shown.

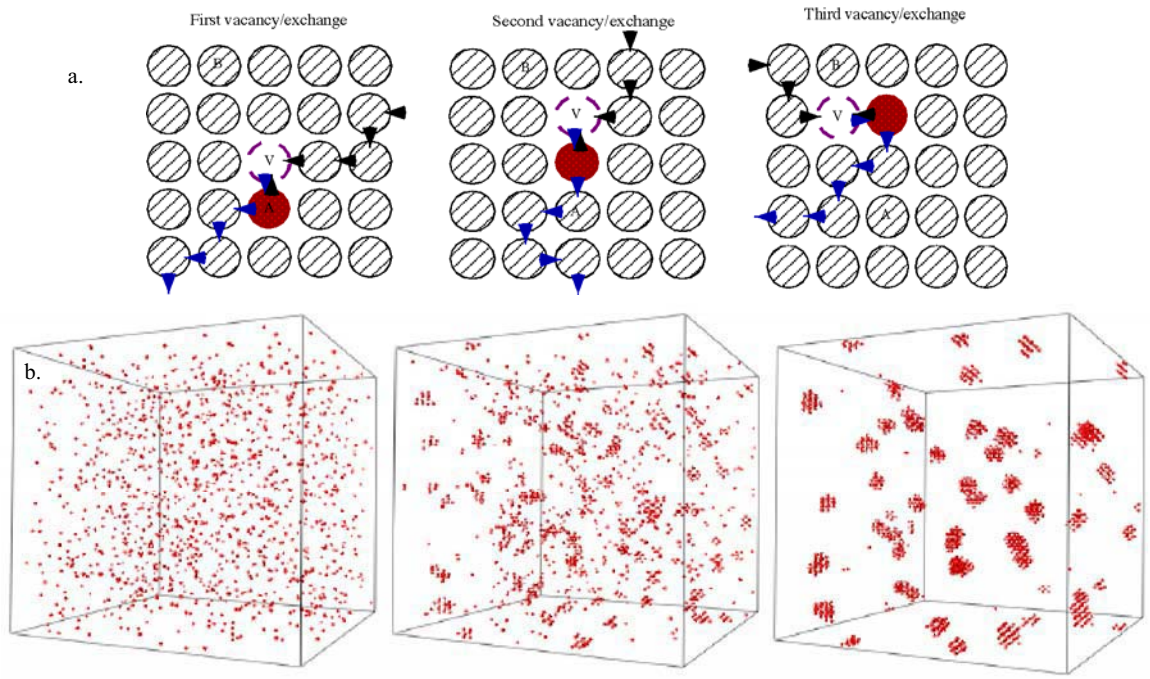

Fig. 2.5. (a) Schematic illustration of the vacancy exchange mechanism that resuts in diffusional motion of a substitutional solute. Note the path of the vacancies are shown by the arrows and, in this illustration, a new vacancy participates in each solute exchange; (b) a kinetic lattice Monte Carlo simulation of Cu clustering and precipitation in an Fe-0.3Cu alloy at 300°C based on the effects for a sequence of a large number of jumps of a single vacancy (not shown), corresponding to increasing time. The time scales roughly with the inverse of the number of vacancies per lattice site, hence is reduced under irradiation compared to thermal aging conditions. The Cu-clusters would eventually coarsen into a single precipitate. Note the positions of the Fe atoms are not shown.

CRPs are also enriched with varying amounts of Mn, Ni, Si, and P in RPV steels containing these elements. In addition to CRPs, nanometer-scale Mn-Ni-Si rich precipitates (MNPs) also form under some conditions [3,6–9,12,22,28–33]. The nanometer-scale features, that are primarily responsible for irradiation hardening, are illustrated in Fig. 2.6. In addition to CRPs, MNPs, MFs, and dislocation loops, other potential hardening features include alloy phosphide precipitates (PPs) and dislocation solute atmospheres [34,35].

The defect cluster complex MF and fine-scale precipitates (or solute clusters) act as obstacles to dislocation glide, resulting in an increase in the yield ($\Delta\sigma_y$) and flow stress of the steel. The $\Delta\sigma_y$ results in the elevation of the Charpy impact test transition temperature, typically defined as the 41 J (30 ft-lb) transition temperature shift (TTS). Thus, the sequence of embrittlement mechanisms is

$$\text{Irradiation and metallurgical variables} \rightarrow \text{Evolution of hardening features} \rightarrow \Delta\sigma_y \rightarrow \text{TTS}$$

Hierarchical multiscale-multiphysics models and experiments have been used to link these various mechanisms and ultimately to relate the TTS to the combination of metallurgical and irradiation variables [8,36]. However, accurate TTS predictions require that simplified analytical representations of these models be fitted to the TTS surveillance database (or other embrittlement databases

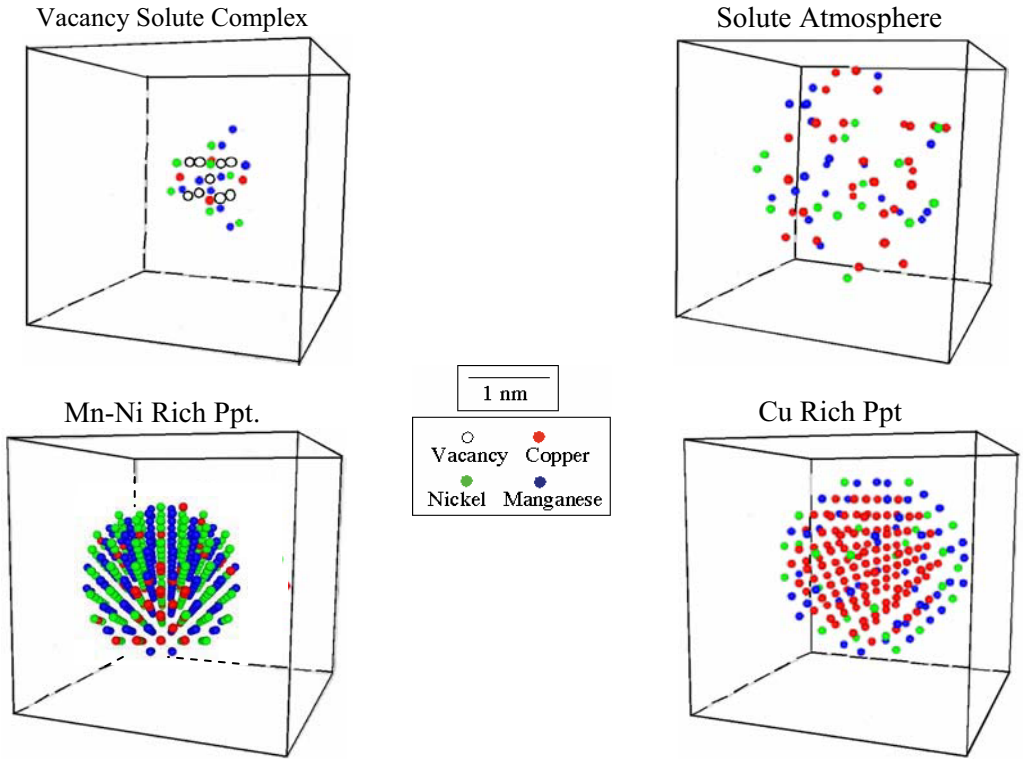

Fig. 2.6. Schematic illustration of the primary types of nanometer-scale features that cause the irradiation hardening and embrittlement of RPV steels. Note the positions of the Fe atoms are not shown.

In the following sections, the various mechanisms leading to embrittlement are briefly discussed in a sequence aimed both to frame an understanding of embrittlement and to provide a mechanistic foundation for the formulation of the physically motivated TTS models. The discussion starts with the basic hardening mechanism of embrittlement and its underlying microstructural basis. Next, the effects of thecombination of metallurgical and irradiation variables on the hardening microstructures are discussed, first for CRPs. Representative examples of the effect of some metallurgical and irradiation variables on the CRP microstructure from the Irradiation Variables (IVAR) program are then presented. This is followed by a discussion of MFs, which form in both low-Cu and higher-Cu steels.

2.2 Key Embrittlement Mechanisms

2.2.1 The Basic Hardening Mechanism of Embrittlement and Primary Hardening Features

The primary mechanism of irradiation embrittlement in Mn-Mo-Ni RPV steels is an increase in the yield stress ($\Delta\sigma_y$), produced by a high number density of nanometer-scale hardening features that develop as a consequence of irradiation. The nanofeatures include coherent Cu-Mn-Ni-rich CRPs, although in some cases they contain more Mn, Ni, and Si than Cu, and so are referred to as MNPs. In low-Cu alloys (Cu less than about ≈ 0.07 wt %), the primary hardening features are believed to be defect cluster-solute complex MFs. Dislocation loops, phosphide (PPs) and other fine-scale precipitates, as well as solute dislocation atmospheres may also contribute to the hardening in some cases. Irradiation hardening, as quantified by $\Delta\sigma_y$, depends on the combination of metallurgical and irradiation variables (alloy

composition, heat treatment, product form, irradiation temperature, and neutron flux, fluence and spectra) and may exceed 350 MPa in very irradiation-sensitive steels.

The following sections aim to provide a more quantitative, model-based descriptions of key embrittlement mechanisms. It must be emphasized that even these more detailed models are simplified and do not represent a fully comprehensive description of all the complexities involved in the embrittlement process. However, they do provide a good physical framework for assessing the strengths and limitations of necessarily even more simplified TTS models used to fit the surveillance database, as described in Chaps. 3 and 4.

2.2.2 Irradiation Hardening

The hardening features act as obstacles to dislocation glide, increasing the critical resolved shear stress for plastic deformation [37]. As expressed in Eq. 2-1, the strengthening produced by a specific type of feature depends on its radius (r_j), number density (N_j), volume fraction (f_j), structure and composition (where j = p for CRPs and = mf for MFs) and can be characterized by an obstacle strength parameter, α_j, as:

$$\Delta\sigma_{yj} \approx [0.55TF\alpha_j\mu b\sqrt{f_j}]/r_j \qquad (2\text{-}1)$$

Here TF is the Taylor factor ≈ 3, μ is the shear modulus of Fe ≈ 80 GPa, and b is the Burger's vector ≈ 0.248 nm. The MFs are relatively weak obstacles ($\alpha_{mf} \approx 0.05$-0.1), since they are small and may be loose aggregates of solutes, while the well-formed CRPs have a range of medium strengths ($\alpha_{crp} \approx 0.1$ to 0.3), which increases with the precipitate radius, r_p [3]. This means that dislocations cut through the CRPs and MFs at a maximum local pinning force, corresponding to a critical bowing angle, characterized by the α_j, which is controlled by the detailed obstacle-dislocation interaction mechanism. Obstacle-dislocation interaction mechanisms have been characterized experimentally, and modeled, most recently, by computer simulations. Figure 2.7 (a) shows the molecular dynamics simulations of the critical bowing angle, reported by Bacon and Osetskiy [38], when the dislocation cuts though a small coherent Cu precipitate with a radius r_p. Figure 2.8 (b) shows that the corresponding prediction of $\sigma_{yp}/\sqrt{f_p}$ vs r_p is reasonably consistent with experimental data (various symbols) from the IVAR irradiations, where f_p and r_p have been measured by small-angle neutron scattering (SANS). Figure 2.7 also shows $\sigma_{yp}/\sqrt{f_p}$ for a fitted Russell-Brown model, which is in slightly better agreement with the data [3,39]. These pinning mechanisms involve dislocations cutting through the obstacles, in contrast to hardening by high strength, Orowan type obstacles, which require bypass by dislocation looping, with a corresponding maximum $\alpha_o \approx 1$ [3,37]. Strong obstacles, particularly Mo_2C precipitates, are responsible for producing a significant fraction of the pre-existing strength of unirradiated steels [3].

In developing embrittlement models, the individual hardening contributions from various irradiation-induced obstacles must be combined with one another, as well as with the various sources of the unirradiated alloy strength [3,40]. The limiting rules for such superposition are a linear sum (LS) law and a square root of the sum of the squares (RSS) law [40]. The RSS law accounts for the spacing of obstacles with similar strength on a slip plane. However, if mixtures of high- and medium-strength obstacles are present, the high-strength obstacles result in larger dislocation bowing angles [3,40]. The bowed and extended dislocation segments thus encounter more of the medium-strength obstacles than would be the case if only the latter were present. Thus the net σ_y for mixtures of medium- and high-strength obstacles is larger than is predicted by the simple RSS law. In the other limit, numerous very low strength obstacles do not significantly change the shape of gliding dislocations; hence, they act more like a lattice friction stress that simply adds to higher-strength obstacle contributions by an LS law. These concepts are schematically illustrated in Fig. 2.8.

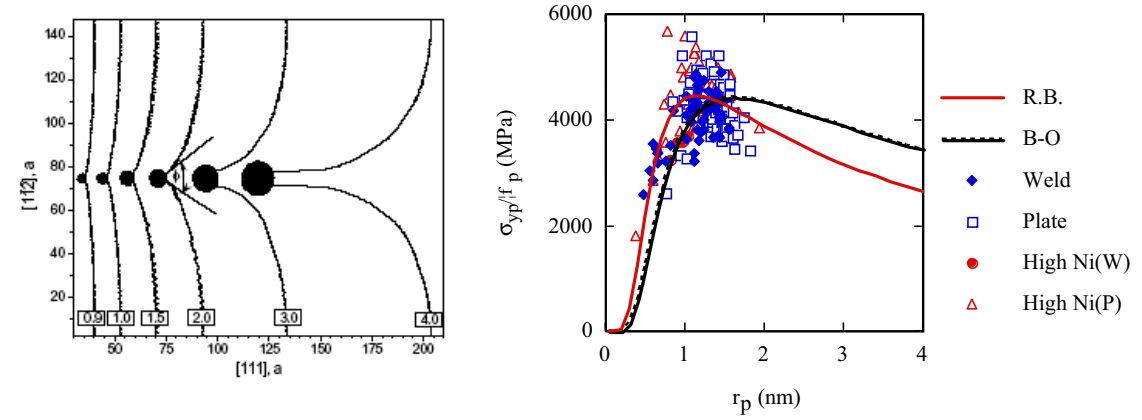

Fig. 2.7. (a) Molecular dynamics simulation of the critical dislocation bowing angle for penetrating coherent Cu precipitates with various r_p by Bacon and Osetskiy (BO). (b) The precipitate hardening efficiency ($\sigma_{yp}/\sqrt{f_p}$) vs r_p showing both a fitted Russell-Brown model (RB) along with the BO model compared to pairs of $\sigma_{yp}/\sqrt{f_p}$ and r_p data from a combination of SANS measurements (f_p and r_p) and tensile tests (σ_{yp}).

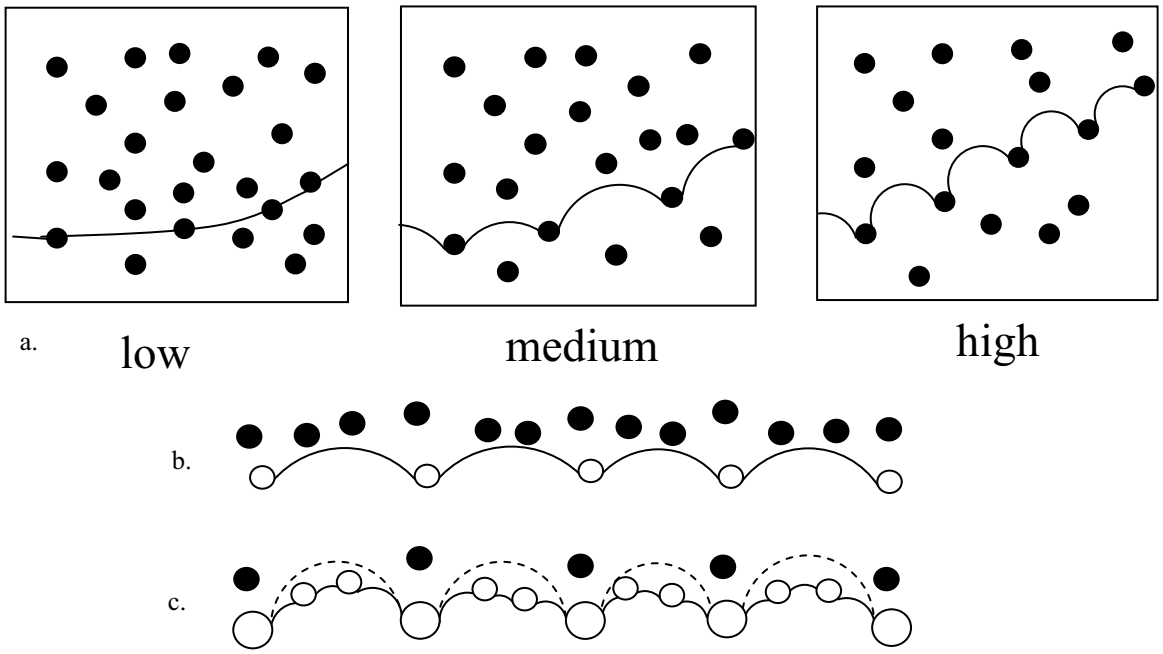

Fig. 2.8. Schematic illustration of the effect of the critical dislocation bowing angle on strength superposition. (a) Critical dislocation angle shapes for low-, medium- and high-strength obstacles. (b) The bowing for dislocation pinned by five medium-strength obstacles. The dislocation has not yet encountered obstacles shaded black at the critical bowing angle. (c) The dislocation bowing when high-strength obstacles have replaced the medium-strength obstacles. The dislocation is now also pinned by eight medium-strength obstacles instead of five as in Fig. 2.8b. The dashed line shows the bowing for strong obstacles alone at the critical bowing angle.

Computer simulations have been developed to evaluate the net $\Delta\sigma_y$ [36,41] for various populations of obstacles with different α_j [3,36,41]. In one study, the resulting computational database was fitted by an analytical model that can be used to calculate the net $\Delta\sigma_y$ based on the individual yield stress contributions and α_i of weak ($\alpha_w < 0.1$, σ_{yw}), medium ($0.1 < \alpha_m < 0.6$, σ_{ym}) and high ($\alpha_o > 0.6$, σ_{yo}) strength obstacles. The net σ_y is given by

$$\sigma_y \approx \sigma_{yw} + (1\text{-}S)(\sigma_{ym}^2 + \sigma_{yo}^2)^{1/2} + S(\sigma_{ym} + \sigma_{yo}) \quad (2\text{-}2)$$

Here the superposition factor S is given by [3]

$$S \approx \alpha_o - \alpha_m(5.0 - 3.3\alpha_o) \quad (2\text{-}3)$$

Thus, features with similar α_j (all fairly low, medium, or high strength) obey an RSS superposition law, while those with very different α_j (low and high strength) obey an LS law. The superposition of the strengthening contributions of medium strength and strong obstacles falls in between.

The LS law is most appropriate for adding the contribution of medium-strength irradiation-induced precipitates to simple model alloys, which initially have low unirradiated σ_{yu} due to the absence of preexisting medium- and high-strength obstacles. The resulting $\Delta\sigma_y \approx \sigma_{yp}$ in this case is greater than if the same irradiation induced features were added to a complex steel alloy, with a large contribution from pre-existing high-strength obstacles, where the net superposition falls between the LS and RSS limits. Figure 2.9 plots the net yield stress increase, $\Delta\sigma_y$, vs the individual strengthening contribution of 1-nm CRPs, σ_{yp}, assuming the pre-existing strengthening is due to strong obstacles with $\alpha_o = 0.9$ is $\sigma_{yo} =$ 180 MPa. A curve for pure Cu precipitates, which are somewhat weaker than CRPs in RPV steels, is also shown for comparison, along with the bounding LS and RSS laws. For example, if the $\sigma_{yp} = 100$ MPa, the $\Delta\sigma_y = 48$ MPa for 1 nm CRPs, falling between the limiting cases of 100 MPa (LS) and 23 MPa (RSS).

Thus, if the details of a material's microstructure are known, the strengthening and superposition models described above can be applied rigorously, and have been shown to work well [3,8,27,42]. This is illustrated in Fig. 2.10 which shows, predicted vs measured CRP hardening for two medium-strength ≈ 0.4 wt % Cu-bearing RPV split melt model alloys with ≈ 0.8 wt % (LC) and ≈ 1.3 wt % (LD) Ni as well as a high-Cu ≈ 0.55 wt % and high-Ni ≈ 1.66 wt % weld (WV) for a variety of irradiation conditions [3,27,42]. Here, the values of f_p and r_p were again determined from SANS measurements, and the $\Delta\sigma_{yp}$ was predicted based on the Russell Brown model (see Fig. 2.7) and Eqs. (2-2) and (2-3), again assuming a pre-irradiation $\sigma_{yo} = 180$ MPa and $\alpha_o = 0.9$. The added MF contribution was based on the measured $\Delta\sigma_y$ in alloys with the same nominal composition as the three alloys cited above, except that they do not contain Cu.

Such detailed information is generally not available. Thus obstacle interaction and superposition effects must be effectively incorporated into the chemistry, product form and fluence function terms in the TTS model and fitting parameters. Since the MFs are fairly weak obstacles, a linear sum (LS) of $\Delta\sigma_{mf}$ from MFs plus the net $\Delta\sigma_p$ from CRPs roughly account for superposition effects and is a common approximation, leading to the so-called two-feature model adopted in the following chapters. In addition to these theoretical considerations, as illustrated in Fig. 2.11, the two-feature model appears to work well in practice. Figure 2.11a plots $\Delta\sigma_y$ vs the square root of fluence for intermediate flux, 290°C irradiations (see Chap. 6) of the LC alloy, cited above, along with a Cu-free alloy (LG), which otherwise has the same nominal composition as LC. Subtracting the $\Delta\sigma_y$ for LG from that for LC gives an estimate of the net CRP hardening, shown as the long dashed line. As expected the CRP contribution approaches saturation. Figure 2.11b plots corresponding SANS measurements of the CRP f_p and r_p for LC. The dotted line in

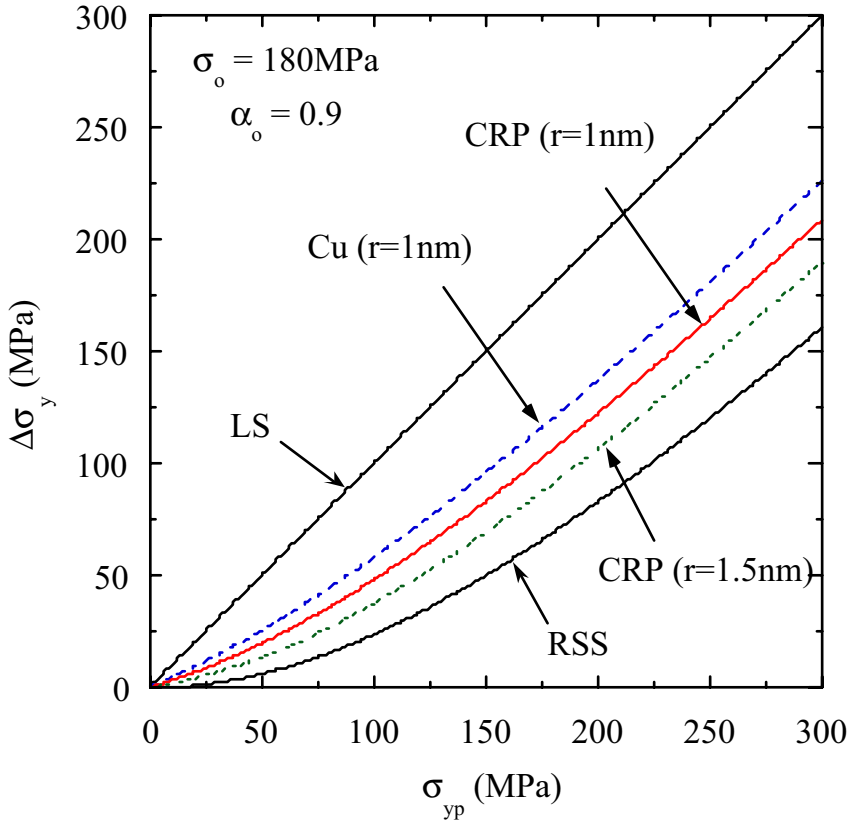

Fig. 2.9. Superposition of various levels of strengthening from 1-nm pure Cu precipitates and CRPs with 180 MPa of pre-existing strong obstacle strengthening and α_o = 0.9.

Fig. 2.11a shows the predictions of σ_{yp} based on the Russell Brown hardening and superposition models described above. The general consistency of these results clearly supports the use of a two-feature model.

2.2.3 Irradiation Hardening and TTS

The transition temperature shift (TTS) in the Charpy temperature at 41 J (30 ft-lb) can be related to $\Delta\sigma_y$ based on well-established micromechanical models. There are two hardening contributions to the TTS [23]. The largest contribution is the shift in the maximum elastic cleavage fracture temperature typically occurring at about 10 J, ΔTTS_{10}, which correlates directly with $\Delta\sigma_y$. Figure 2.12 schematically illustrates this mechanism in terms of the so-called Davidenkov diagram. Here, M (>1) is a constraint factor that elevates the internal tensile stresses near the notch tip to values greater than σ_y, and σ^* is the microcleavage fracture stress. Based on the conventional assumption that σ^* does not vary with temperature and, for purposes of illustration, assuming a simple linear relation between the yield stress σ_y and T, $[d\sigma_y/dT]$, the TTS_{10} is simply [23]

$$TTS_{10} = TT_{10i}(\text{irradiated}) - TT_{10u}(\text{unirradiated}) = \Delta\sigma_y/[d\sigma_y/dT] \qquad (2\text{-}4)$$

The actual non-linear relation between σ_y and T can be accounted for by using the average $\langle[d\sigma_y/dT]\rangle$ over the unirradiated, TT_{10u}, to irradiated, TT_{10i}, temperature interval. More generally, the elastic cleavage

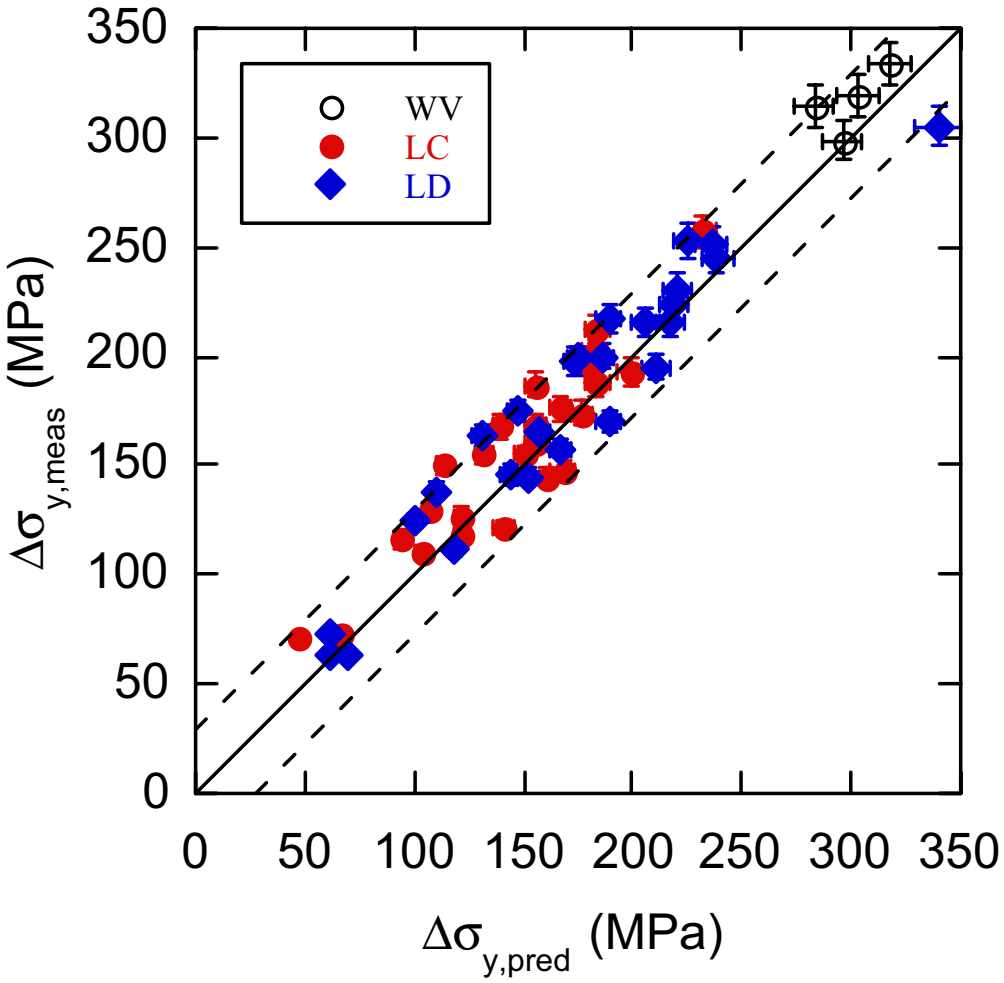

Fig. 2.10 Measured versus predicted $\Delta\sigma_y$ from CRPs based on SANS measurements of f_p and r_p used in a modified Russell-Brown precipitate hardening and computer simulation derived superposition model [Eqs. (1) to (3)]. The MF hardening is based on the addition of a much smaller $\Delta\sigma_y$ for alloys with similar compositions, except that they contained little or no Cu [27,42].

temperature shift can be specified by the difference in the temperatures at which the unirradiated and irradiated σ_y are equal [23],

$$\sigma_{yu}(T_{cu}) = \sigma_{yu}(T_{ci}) + \Delta\sigma_y \qquad (2\text{-}5)$$

Equation (2-5) accounts for the actual nonlinear relation between σ_y and T, and predicts a corresponding nonlinear relation between the TTS that depends on TT_{10u} and $\Delta\sigma_y$.

There is also a generally smaller contribution, TTS_{use}, to the overall TTS at 41 J, due to the reduction in the Charpy upper shelf energy, ($\Delta USE = USE_i - USE_u < 0$) and the associated layover of the Charpy energy temperature curve in the ductile-brittle transition region. A previous study showed that the lower-

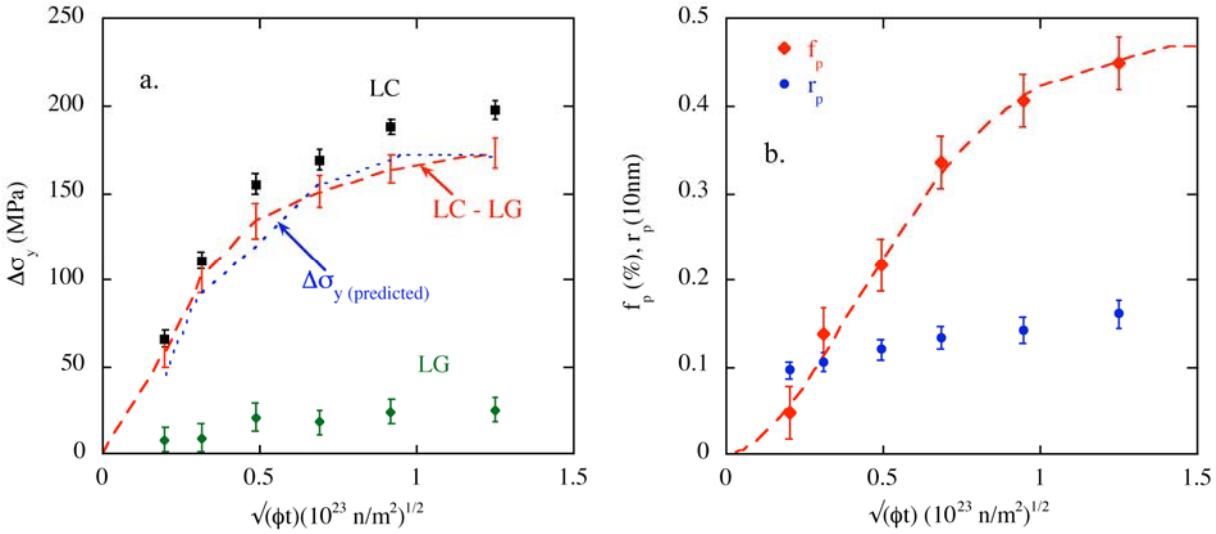

Fig. 2.11 Two feature model hardening analyses for a 0.4% Cu LC alloy irradiated at 290ºC (a) $\Delta\sigma_y$ vs the square root of fluence for intermediate flux irradiations (see Chap. 6) of the LC alloy, along with a Cu-free alloy (LG), which otherwise has the same nominal composition as LC, and the net CRP hardening (LC-LG), as shown as the long dashed line. (b) The corresponding SANS measurements of the CRP f_p and r_p for LC. The dotted line in Fig. 2.11a shows the predictions of σ_{yp} based on the Russell Brown hardening and superposition models. The general consistency of these results clearly supports the use of a two-feature model.

to-upper shelf transition occurs over an approximately constant temperature interval of 120±25°C [23] as illustrated in Fig. 2.12 (b). Note, that a recent unpublished study suggests that this transition temperature interval is not constant, but rather increases with radiation damage; the generality of this behavior willbe assessed in the future. However, even if confirmed, this detail would have little effect on the current discussion. The ΔUSE can also be related empirically to $\Delta\sigma_y$ based on a simple fitting model [23]. Thus the assumption of a constant transition interval combined with the empirical $\Delta USE(\Delta\sigma_y)$ model is used to estimate TTS_{use} and TTS with an expression of the general form

$$TTS = TTS_{10} + TTS_{use} = C_c(TT_{10u}, USE_u, \Delta\sigma_y)\Delta\sigma_y \qquad (2\text{-}6)$$

Fig. 2.13 shows the predicted $C_c(\Delta\sigma_y)$ for TT_{cu} = -75°C and USE_u = 100 J. Notably, C_c increases with $\Delta\sigma_y$. C_c also increases at higher TT_{cu} and lower initial USE_u. Observed C_c values of ≈ 0.6±0.2°C/MPa, are consistent with these predictions [23].

The mechanisms and models described in this and the previous section provide the underpinning for the so-called two-feature TTS embrittlement model given by Eq. (2-7), which was calibrated to the surveillance data and presented in Chap. 4 of this report:

$$TTS = TTS_{mf} + TTS_{crp} \qquad (2\text{-}7)$$

As in the case of superposition of strengthening contributions, the nonlinear relation between C_c and $\Delta\sigma_y$ is approximately incorporated in the TTS model equations and effective fitting parameters.

In summary, the relations between TTS and $\Delta\sigma_y$ are reasonably well understood and can be modeled. Standard micromechanical models predict weakly nonlinear relations between TTS and $\Delta\sigma_y$ that depend

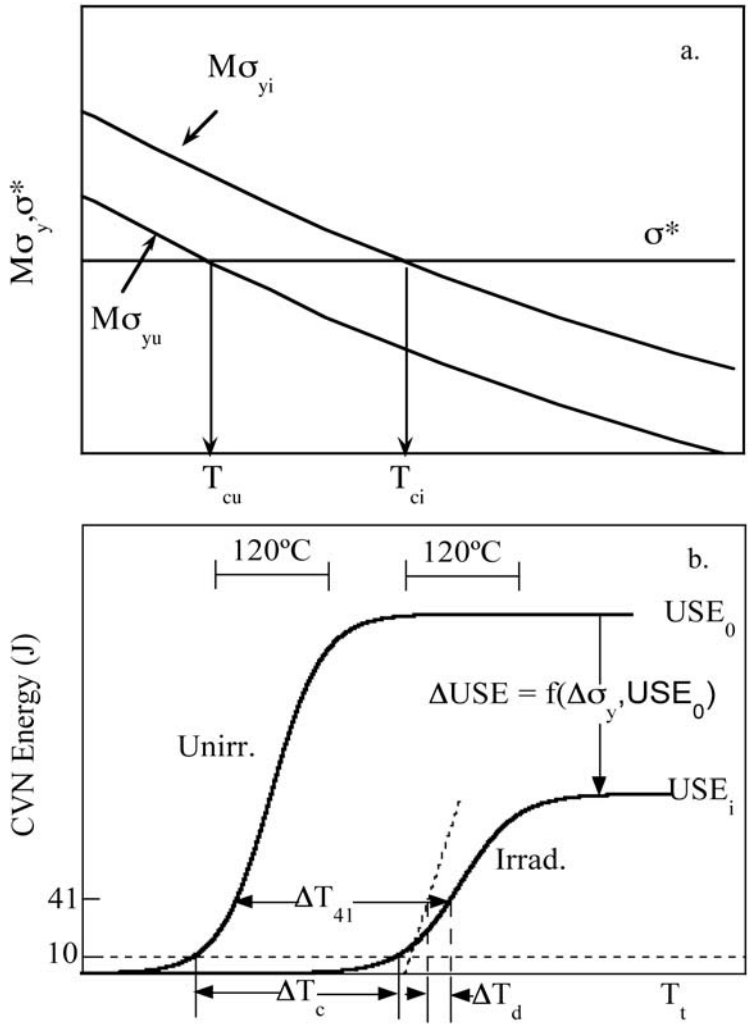

Fig. 2.12. Illustration of the basis for determining TTS from $\Delta\sigma_y$. The model assumes that the critical cleavage stress and $\Delta\sigma_y$ are both independent of temperature. The $\Delta\sigma_y$ is used to estimate the shift in the elastic cleavage temperature (T_c) defined at 10 J. The extra TTS increment at 41 J, due to the layover of the energy-temperature curve, is based on the observation that the temperature interval of the transition is ≈ 120°C and the use of an empirical relation between the reduction in the upper shelf energy (ΔUSE) and $\Delta\sigma_y$.

on the unirradiated properties of a particular steel. Such physical complexities are approximately incorporated in the two-feature TTS model presented in Chap. 4 of this report, in terms of averaged behavior, since the TTS equations are fit to the surveillance database.

2.3 Copper-Rich Precipitates

2.3.1 Radiation-Enhanced Diffusion and Flux Effects on CRP Hardening

Trace quantities of Cu (Cu ≈ 0.3 wt.% or less) are left in solution after stress-relief treatments that are typically performed at around 600°C [3,4,6,7,12]. However, as illustrated in Fig. 2.14, even at these low levels, Cu is highly supersaturated at the much lower vessel operating temperatures around 290°C [4,43] where the solubility of Cu is ≈ 74 appm, or ≈ 8.4×10^{-3} wt %. Thus Cu precipitates, first forming nm-scale coherent bcc transition phases, akin to so-called GP zones in aluminum alloys. Because of low

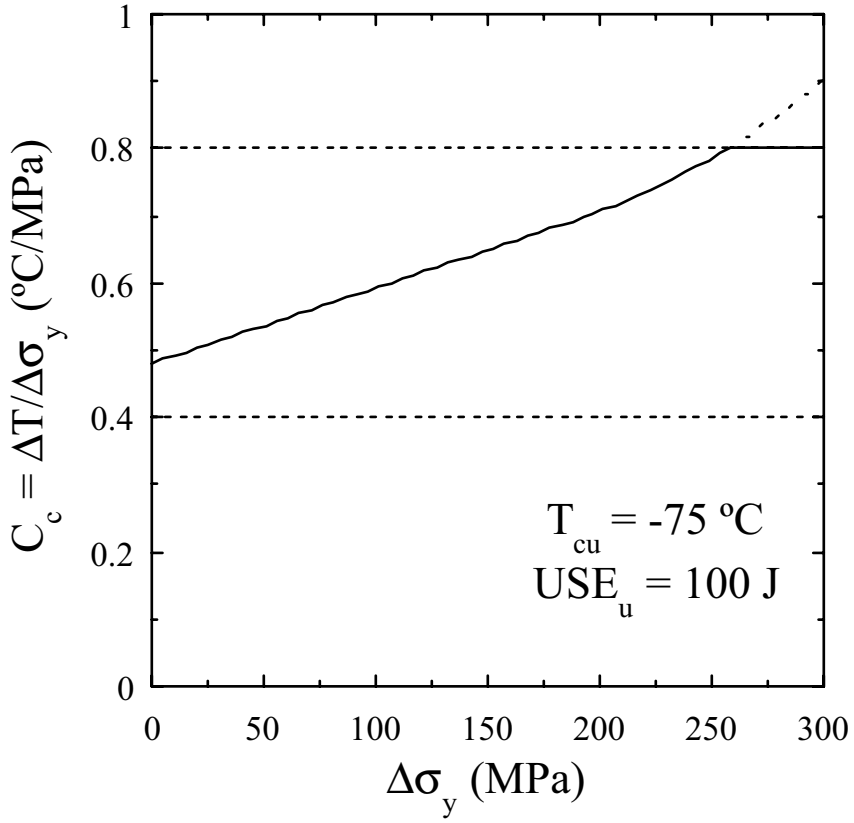

Fig. 2.13. The C_c = TTS/$\Delta\sigma_y$ derived from the model described in Fig. 2.12 and the text. The $\Delta\sigma_y$ dependence is primarily due to the variation in the slope of the σ_y-T curve, with smaller contributions from the reduction in the USE. The value of C_c depends on the unirradiated Charpy properties of the steel and $\Delta\sigma_y$. The dashed lines mark the estimated bounds of the applicability of the model consistent with the range of observed C_c values.

rates of thermal diffusion, Cu precipitation is relatively sluggish in the absence of irradiation. However, CRP nucleation and growth rates are greatly accelerated by radiation-enhanced diffusion (RED).

In the following section we estimate the magnitude of the radiation enhanced diffusion coefficient, D*, and model how it changes with variables such as the alloy composition and microstructure, irradiation temperature and, especially, the neutron flux. Substitutional solutes, like Cu, diffuse by a vacancy exchange mechanism. Thus, the solute diffusion coefficient is proportional to the fractional concentration of vacancies, X_v. In the absence of irradiation, thermodynamics dictates an equilibrium concentration of vacancies, X_{ve}, which controls the rate of both solute and self-diffusion. Under irradiation, there is an excess concentration of vacancies, $X_v > X_{ve}$, leading to a radiation enhanced diffusion coefficient, $D^* > D_{cu}$, where D_{cu} is the thermal diffusion coefficient of Cu. Assuming all other variables are specified, the variation of D* with flux is non-linear and exhibits four general regimes of behavior.

- At very low flux $D^* \approx D_{cu}$ since $X_v \approx X_{ve}$
- At somewhat higher flux - when recombination is minimal - $D^* > D_{cu}$ is independent of flux
- At still higher flux - when recombination is dominant - $D^* >> D_{cu}$ varies with the square root of flux

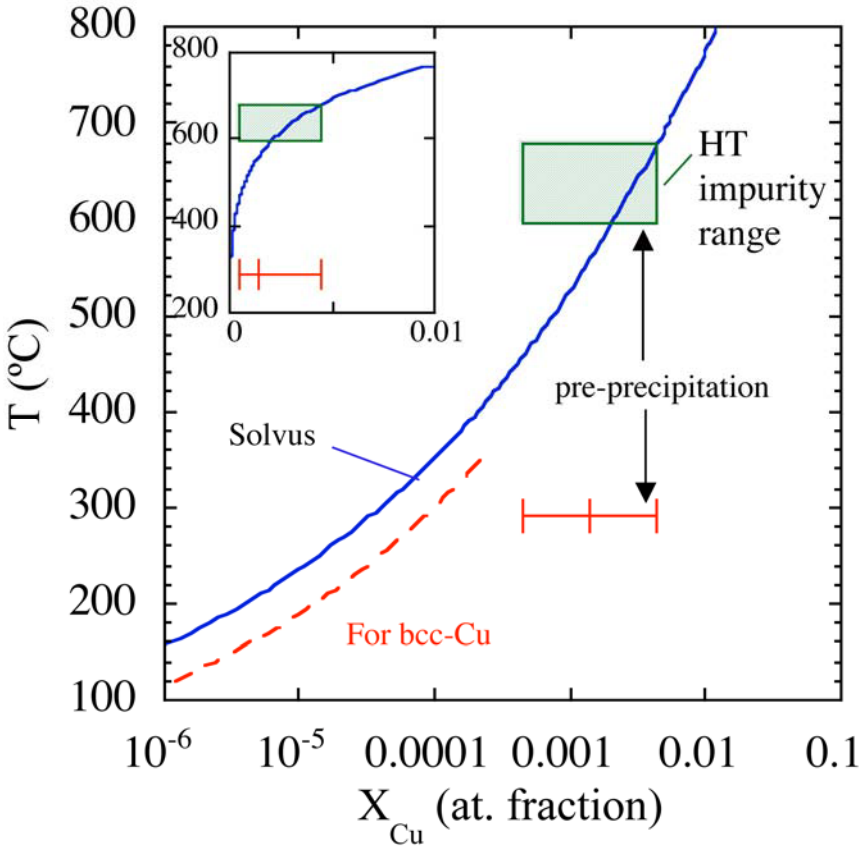

Fig. 2.14. The solubility of Cu in α-Fe in equilibrium with the fcc (solid line) and bcc Cu phases (dashed line) as a function of temperature. The typical range of Cu impurity content is shown by the shaded box. At high-Cu levels beyond the solubility limit at the stress-relief temperature pre-precipitation limits the amount in solution prior to irradiation to a lower effective value, Cu_{max}. The Cu_{max} depends on the heat treatment time and temperature history and the alloy composition, as well as the Ni content. The Cu remaining dissolved in the α-Fe matrix is highly supersaturated around 290°C with respect to the coherent bcc phase. The supersaturated Cu undergoes accelerated precipitation under irradiation due to radiation enhanced diffusion (RED).

- At very high flux—when SIA-vacancy recombination occurs a high density of transient vacancy clusters is produced in displacement cascades—$D^* >> D_{cu}$ is once again constant and independent of flux [11]

The first three regimes are pertinent to surveillance and most test reactor irradiation conditions, hence, they will be the focus of the subsequent discussion. Rate theory can be used to model RED [12,13, 25] and D* by calculating the excess concentration of vacancies under irradiation. More details on the model described in this section are given in Ref. [13]. In the most basic sense, however, rate theory models determine the concentrations of reacting species by accounting for their generation, transport and fates that establish the kinetic balances between production, cluster accumulation (storage) and loss processes. The balances are expressed in terms of conservation equations containing the products of

concentrations and rate coefficients, similar to those used to model chemical reaction kinetics. The fates of vacancies include recombination with SIA, self-clustering, cluster complex formation with solutes and annihilation at sinks, especially dislocations.

As a simple illustrative example, consider a species S that is generated at a rate G_s (S/atom-s) that undergoes diffusion to sinks where it is annihilated at a rate $X_sD_sS_s$ (S/atom-s). Here X_s (S/atom), D_s (m^2/s) and S_s (m^{-2}) are the fractional concentration, diffusion coefficient and total sink strength for S, respectively. At steady-state, the production and loss of S must balance, thus $G_s = X_sD_sS_s$, hence,

$$X_s = G_s/D_sS_s \tag{2-8}$$

The sink strength, S_s, is determined by solving the diffusion equation for the particular geometry. For example, for a specified dilute concentration of spherical sinks, with a number density, N_s, and a radius r_s, the sink strength $S_s \approx 4\pi r_sN_s$ [25]. Thus the concentration of S, X_s, is determined by the rate of generating S, the sink microstructure, N_s and r_s, and the diffusion coefficient of S, D_s. In the case of radiation damage the S species are vacancies and SIA.

Displacement damage creates an equal number of vacancies and SIAs, sometimes called Frenkel pairs, at a rate

$$G_v = G_i = \phi\sigma_v \tag{2-9}$$

Here ϕ is the neutron flux (n/m^2-s, typically reported in terms of neutrons with energies > 1 MeV) and σ_v (vacancies-m^2/n-atom) is the neutron spectrum averaged vacancy production cross section [12,24]. A cross section can be thought of as an effective area per atomic nucleus for producing a nuclear reaction, in this case, generation of vacancies. Computer simulations of the formation and subsequent short-term rearrangement of displacement cascades leading to recombination, combined with neutron cross-section and reaction kinematics models, have been used to derive σ_v as a function of the neutron energy [24]. At higher fluxes, RED is primarily due to the excess vacancy concentration, X_v. The RED coefficient (D*) can be expressed in terms of the ratio of atomic fraction of vacancies under irradiation (X_v) to that at thermal equilibrium (X_{ve}) and the thermal diffusion coefficient of Cu, D_{cu}, as

$$D^* \approx D_{cu}[X_v/X_{ve}] \tag{2-10}$$

At steady state, X_v is constant; thus, as noted previously, vacancies (and SIAs) must be destroyed at the same rate as they are created. Vacancies are destroyed when they are absorbed at sinks, like dislocation jogs, or when they recombine with SIAs, which are both self-healing processes. In the simplest case, the vacancy and SIA destruction rates at sinks are $D_vX_vS_t$ and $D_iX_iS_t$, where D_v and D_i (>> D_v) are the vacancy and SIA diffusion coefficients, respectively, and S_t is the total defect sink strength, taken here to be the same for vacancies and SIA. Thus the creation-destruction balance equation for vacancies is

$$D_vX_vS_t + \text{recombination rate} = \phi\sigma_v \tag{2-11}$$

The recombination rate is RX_vX_i, where R (s^{-1}) is a recombination factor $\approx 4\pi r_r(D_i + D_v)$, where r_r is the recombination radius. Without recombination,

$$X_v = \phi\sigma_v/S_tD_v + X_{ve} \quad (2\text{-}12)$$

Thus, X_v increases linearly with flux, and in the very low flux limit of no irradiation, $X_v = X_{ve}$.

The fraction of vacancies ($g_r \leq 1$) that recombine with SIAs before reaching sinks is proportional to X_iX_v, or X_v^2, since X_i is proportional to X_v. Hence, recombination rates increase with increasing flux (ϕ), since X_v also increases, but not in direct proportion. In the limit where recombination dominates, ignoring defect annihilation at sinks,

$$G_v = \phi\sigma_v = RX_vX_i = [D_v/D_i]RX_v^2 \quad (2\text{-}13)$$

Thus, X_v varies with the square root of flux as

$$X_v = \sqrt{(\phi\sigma_v/[(D_v/D_i)R]} \quad (2\text{-}14)$$

Trapping of vacancies bound to solute atoms also increases recombination and g_r, since this lowers the effective diffusion coefficient (D_v) for vacancies compared to alloys that do not contain such traps. Recombination rates also increase with decreasing irradiation temperature (T_i) due to the lower D_v and de-trapping rates. Combining Eqs. (2-11) and (2-12),

$$X_v = (1\text{-}g_r)\phi\sigma_v/S_tD_v + X_{ve} = [g_s(\phi,T_i,S_t,X_t,H_t)\phi\sigma_v]/[S_tD_v] + X_{ve}, \quad (2\text{-}15)$$

Here g_s is the fraction of vacancies that reach sinks, ($g_s = 1 - g_r \leq 1$), X_t is the concentration of solute traps and H_t is the corresponding trapping energy. Noting that the self-diffusion coefficient is $D_{sd} \approx D_vX_{ve}$, and using Eq. (2-10):

$$D^* \approx D_{cu}\{\phi[g_s\sigma_v]/[S_tD_{sd}] + 1\} = K\phi + D_{cu} \quad (2\text{-}16)$$

Here K (m^4) is the RED factor, defined as

$$K = [g_s\sigma_v/S_t][D_{cu}/D_{sd}] \quad (2\text{-}17)$$

Thus, both g_s and K are functions of flux, irradiation temperature, and the total sink strength, S_t, as well as the parameters describing solute vacancy trapping enhanced recombination. In the absence of recombination, g_s = 1 and K is inversely proportional to S_t, which is primarily determined by the dislocation density, and K is independent of flux if $\phi K >> D_{cu}$. The ratio of the Cu to self-diffusion coefficients term $[D_{cu}/D_{sd}]$ is a temperature and composition-dependent property of an alloy, and can be both modeled and measured [13, 43-46]. Both theory and experiment show that $[D_{cu}/D_{sd}]$ is greater than 1, and has relatively large values at low temperatures, due to a high copper-vacancy binding energy [47]. As a result, both D_{cu} and D* may be much larger at low temperatures than estimates based on extrapolations of D_{cu} data from high temperature data [13,43-45]. However, the low temperature values of $[D_{cu}/D_{sd}]$, and hence, K, are uncertain, even in simple Fe-Cu alloys.

Experimental estimates of the maximum K_m at 290°C for g_s = 1 (no recombination) range from $K_m \approx 10^{-37}$ to 10^{-38} m^4 [13]. An average $K_m = 5 \times 10^{-38}$ m^4 and nominal values of $S_t = 2 \times 10^{14}/m^2$ and $\sigma_v = 6 \times 10^{-26}$ m^2/neutron-atom, corresponds to $[D_{cu}/D_{sd}] \approx 33$ at 290°C. Thus, for a typical PWR surveillance capsule flux of 5×10^{14} n/m^2-s, $D^* \approx 2.5 \times 10^{-23}$ m^2/s. This value compares to a *high* estimate (see below)

of D_{cu} at 290°C of ≈ 3×10^{-25} m^2/s, or an RED acceleration factor of $D^* \approx 84D_{cu}$. At a typical BWR capsule flux of 2×10^{13} n/m^2, $D^* \approx 4.3D_{cu}$ Thus, at low flux, thermal diffusion may make a significant contribution to precipitation under irradiation.

Before further quantification of D*, we turn to the question of how RED affects Cu precipitation. For a specified alloy, fluence and irradiation temperature, the precipitate volume fraction, f_p, scales with D*t given by

$$D^*t = \phi t K(\phi, T_i) + D_{cu}t \qquad (2\text{-}18)$$

Note, that $(D^*t)^{1/2}$ is a measure of the average *distance* that Cu diffuses under RED and that the initial rate of diffusion controlled growth of the Cu precipitate volume fraction, df_p/dt, approximately scales with $(D^*t)^{3/2}$ [13].

The $D^* \approx \phi K$ is much greater than the thermal D_{cu} at flux levels characteristic of PWR surveillance and test reactor irradiations. In this case, the effect of flux is controlled by $g_s(\phi) \leq 1$. At higher flux, in the recombination-dominated regime, g_s is much less than 1, and K scales as $1/\sqrt{\phi}$, since recombination reduces X_v and hence K. Thus the D*t, or amount of precipitation, at a specified fluence, also varies as $1/\sqrt{\phi}$. At lower dose rates, when recombination is not important, $g_s \approx 1$, and both K and D*t at a specified fluence are independent of flux. However, at very low flux, D_{cu} is similar in magnitude to ϕK, and in the limit, $D^* \approx D_{cu}$ is independent of flux. In this case $D^*t \approx D_{cu}t$ depends only on time, t; since time at a specified fluence depends on $1/\phi$, the corresponding D*t also varies as $1/\phi$.

Solutes like Mn and Ni have a positive binding energy with vacancies (that is, the vacancy energy decreases near a solute) [13,47]. The resulting trapping of vacancies at solutes increases the recombination rate, hence, decreases g_s. Figure 2.15 schematically illustrates this mechanism, which figuratively makes deeply trapped vacancies *"sitting ducks"* for recombination with SIA. Analytical expressions for g_s are available, including treatment of solute trapping [13].

The solid lines in Fig. 2.16 (a) plot $D^*t/\phi t = D^*/\phi = K$ vs ϕ, neglecting D_{cu}, for a typical set of recombination model parameters at 290°C: $S_t = 2 \times 10^{14}/m^2$; $H_t = 30$ kJ/mole; $X_t = 0.01$ and 0.03; $D_v = 1.13 \times 10^{-16}$ m^2/s and $[D_{cu}/D_{sd}] = 33$ [13]. These curves flatten out at low flux, so it is important to properly represent the effects of thermal diffusion (D_{cu}) on D*. Unfortunately, estimates of D_{cu} are highly uncertain at low temperature. Values of D_{cu} based on extrapolation of tracer diffusion data from high temperatures range from ≈ 2×10^{-28} and 6×10^{-27} m^2/s at 290°C [43]. Atomistic models predict similar D_{cu} values between ≈ 3×10^{-28} and 9×10^{-27} m^2/s. Extrapolating the lowest values of measured tracer D_{cu} with activation energies from the atomistic models that are also thought to be appropriate for lower temperatures (≈ 222 to 242 kJ/mole), yields tracer D_{cu} values between ≈ 8×10^{-27} and 5×10^{-26} m^2/s.

However, these tracer diffusion coefficients do not account for either the effects of interstitial and substitutional solutes, or the thermodynamic factor that multiplies the tracer diffusion coefficient to account for chemical diffusion. The thermodynamic factor is approximately given by ≈ $-2\ln X_{Cue}$; for Cu at 290°C the factor is estimated to be about 20. The effect of a solute j on D_j is approximately given by the expression $D_j(X_j) \approx D_j(X_j = 0)(1 + b_j X_j)$. For Cu the atomistic model predicts that b increases with decreasing temperature and that b ≈ 43 at 290°C [44]. However, experimental estimates at high temperature give a much higher b ≈ 1760 at 778°C [43]. Assuming b is the geometric mean of these values ≈ 275 and that a typical total alloy concentration of solutes of X ≈ 0.04 behaves like Cu, (1 + bX) ≈ 12. The geometric mean of the limiting experimental values of the tracer diffusion coefficient is ≈ 1.1×10^{-27} m^2/s; multiplying this value by the product of the thermodynamic and solute (1 + bX) factors ≈ 240 yields a chemical $D_{cu} \approx 2.6 \times 10^{-25}$ m^2/s.

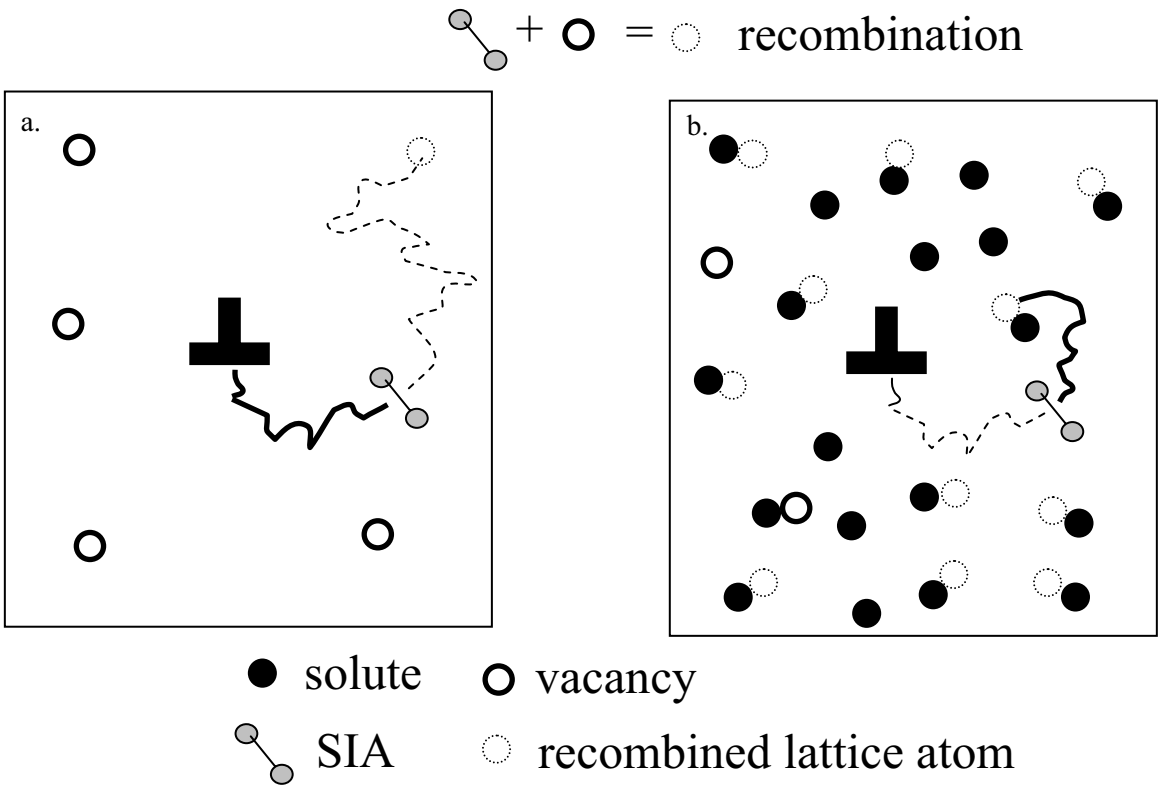

Fig. 2.15. Schematic illustration of solute vacancy trap enhanced recombination. (a) The SIA is more likely to annihilate at sinks like dislocations (the inverted T) when there are no vacancy traps; thus the concentration of mobile vacancies is higher. (b) The SIA is more likely to annihilate at solute (filled circles)-trapped vacancies, shown by the dashed open circles, than sinks, and the concentration of mobile vacancies, shown by the solid line circles, escaping recombination is lower.

Low temperature values of chemical D_{cu} can also be indirectly estimated by fitting a diffusion controlled growth model to thermal precipitation data based on measured values of N_p and f_p [13,48]. Analysis of a Fe-0.9 wt % Cu binary alloy thermally aged at 290°C for 7200 h yields a very high estimate of the chemical D_{cu} of $\approx 5 \times 10^{-24}$ m^2/s. However, excess quench vacancies may produce a transient enhancement of D_{cu} in this case. Nevertheless, Cu precipitation, and corresponding hardening, have also been observed in slowly cooled complex steels with high Ni and Cu contents including alloys aged at $\approx$ 290°C for $\approx$ only 7200 h [48,49]. Thus the thermal aging data for complex alloys also qualitatively indicates a very high value of D_{cu} of order 10^{-24} m^2/s, or possibly greater.

The dashed lines in Fig. 2.16 (a), for $X_t = 0.03$ and 0.01, are based on nominally low and high values of the chemical D_{cu} of 10^{-26} and 3×10^{-25} m^2/s, respectively, although possibly lower and, even more likely, higher D_{cu} values are certainly possible. However, these nominal low and high values of D_{cu} give some sense of the possible role of thermal diffusion in extrapolating embrittlement models to very low flux.

It should be added that, in addition to RED, other radiation damage mechanisms may interact with thermal aging processes leading to accelerated embrittlement rates at very low flux. For example, formation of solute-defect cluster complexes directly in displacement cascades may combine synergistically with long-range thermal diffusion of solutes. The potential for, what might be called, *radiation assisted thermal precipitation hardening*, under long time-very low flux irradiation conditions, is not understood for the range of alloys and compositions in the TTS database. Thus, these various

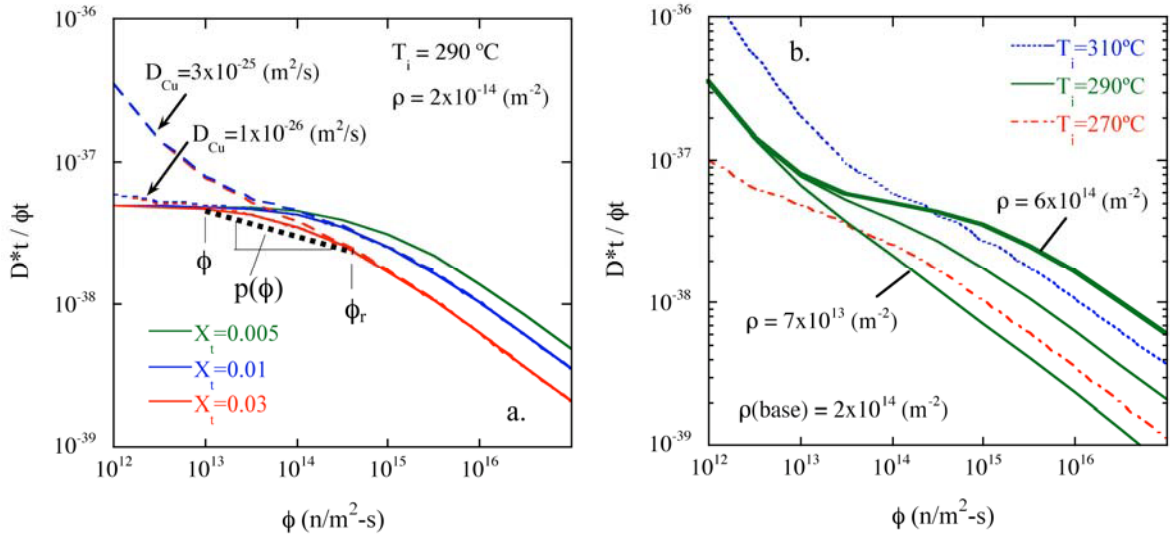

Fig. 2.16. The diffusion scaling parameter, $D^*t/\phi t = K + D_{Cu}/\phi$, as a function of flux for the solute trap enhanced recombination-D_{Cu} model. Larger values of this parameter mean that more precipitation occurs at a given fluence. (a) The base model at 290°C with estimated low and high-Cu thermal diffusion coefficients, D_{cu}. (b) The effect of variations in the recombination model parameters for the high D_{cu}.

considerations suggest that the nominally high D_{cu} curves in Fig. 2.16 (a) provides the most reasonable basis to extrapolate experimentally estimated values of D* to lower flux.

Figure 2.16 (b) shows the effect of variations in the irradiation temperature and sink strength on $D^*t/\phi t$ curves assuming the high value of D_{cu}. Lower irradiation temperatures (T_i) shift the $D^*t/\phi t$ curves down and to the left due to enhanced recombination; higher solute vacancy trap binding energies have the same effect. Higher sink densities (S_t) reduce recombination, but also shift the curves down and to the left, since X_v is reduced [13]. However, the general shapes of the curves remain similar and the magnitude of K is still in the range of $\approx 10^{-38}$ to 10^{-37} m^4, in the pertinent flux range or slightly higher at 310°C.

The effect of flux shown in the curves in Fig. 2.16 (a) can also be represented in terms of a flux dependent effective fluence, ϕt_e, as

$$\phi t_e = \phi t(\phi_r/\phi)^{p(\phi)} \qquad (2\text{-}19)$$

Here ϕ_r is an arbitrary reference flux. Note, $\phi t_e = \phi t$ at ϕ_r. As illustrated in Fig. 2.16 (a), the flux-scaling exponent, $p(\phi)$, is the average slope of a line connecting $\ln[K(\phi)]$ with $\ln[K(\phi_r)]$. Hence, p depends on both ϕ and ϕ_r. Figure 2.17 (a) plots $p(\phi)$ for $\phi_r = 4.4 \times 10^{14}$ n/m^2, which is the reference flux in the TTS model, versus ϕ for the $K(\phi)$ curves shown in Fig. 2.16 (a). The p-curves decrease in going from high to intermediate flux, but go through a minimum whose position depends on D_{cu}.

Assuming a constant average p as in Eq. (2-20) provides a simplified formulation for the flux effect that can be readily incorporated into analytical expressions calibrated by fits to the TTS database.

$$\phi t_e = \phi t(\phi_r/\phi)^{p} \qquad (2\text{-}20)$$

While the value of p in Fig. 2.17 (b) explicitly depends on flux (as well as the alloy composition, microstructure and irradiation temperature), the variation between dose rates of 10^{13} and 10^{15} n/m^2-s is not

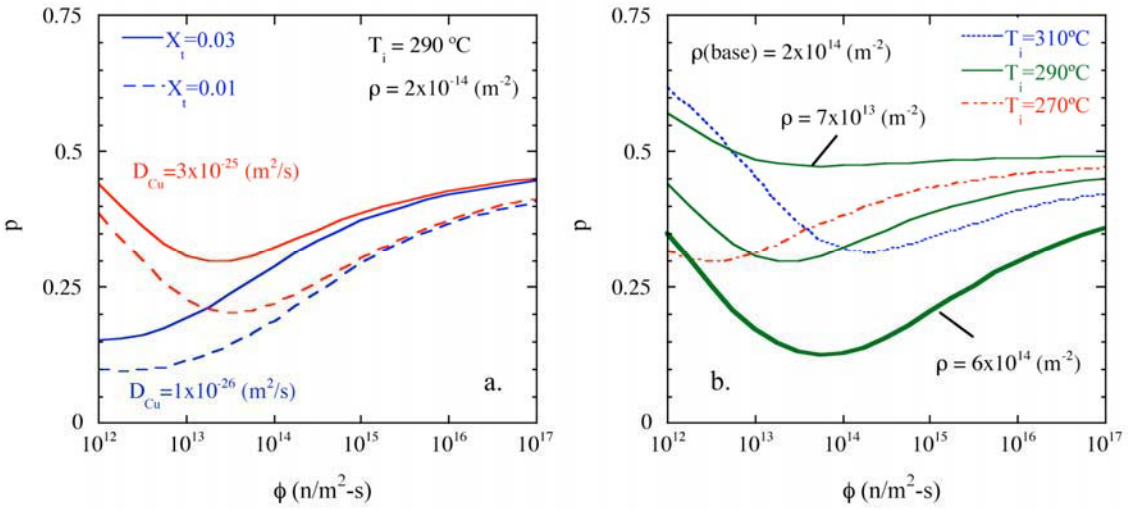

Fig. 2.17. The dose rate effect scaling parameter p for $\phi_r = 4.45 \times 10^{14}$ n/m^2 versus ϕ for the K(ϕ) curves shown in Fig. 2.16 (a). (a) The base recombination model parameters and X_t = 0.01 to 0.03 for low and high D_{Cu}. (b) The effect of variations in the model parameters for X_t = 0.03.

extremely large. For the high D_{cu} case the average value and range of p are 0.33±0.05 and 0.24±0.07 for X_t = 0.03 and 0.01, respectively. For the low D_{cu} model, the corresponding averages are 0.29±0.09 and 0.20±0.10. Thus, using an *effective average* fitted p to fit and interpolate between embrittlement data at low and high flux, as is done in the TTS model, is a reasonable engineering approximation. Again note that, in the TTS model, the fitted effective flux scaling exponent p is also the average for a range of alloy compositions and microstructures, as well as irradiation temperatures.

Figure 2.18 shows SANS measurements of the effect of flux on the CRP f_p, and r_p for a split melt model alloy containing 0.4 wt % Cu, 1.4 wt % Mn and 1.25 wt % Ni irradiated at 290°C. The diamonds, circles and squares are for fluxes of ≈ 8, 3 and 0.8 × 10^{15} n/m^2-s respectively. The f_p and r_p are plotted vs both the actual fluence (Fig. 2.18a and c), ϕt, and the effective fluence (Fig. 2.18b and d), ϕt_e, assuming p = 0.5 and $\phi_r = 3 \times 10^{15}$ n/m^2-s. The shifts in the precipitation curves to higher fluence with higher flux is clear, while these data collapse onto one curve on the effective fluence, ϕt_e, scale. This flux effect is also clearly reflected in the corresponding $\Delta\sigma_y$ data shown in Chap. 6. Table 2.1 summarizes the various flux regimes described in this section.

In summary, within the framework of the solute trap enhanced recombination model, the effect of flux on CRP precipitation and hardening is manifested in the pre-saturation regime. Higher flux shifts the CRP hardening curves to higher fluence, as schematically illustrated in Fig. 2.19. The plateau hardening does not depend on the flux. The observed effects of flux can be modeled based on a solute-enhanced recombination mechanism. Recombination models show that dose rate effects depend on flux, irradiation temperature, alloy composition, and microstructure. These conclusions are consistent with analysis of the IVAR database discussed in Chap. 6 and in Ref. [13]. However, flux effects can be approximately incorporated in TTS models using an effective fluence, $\phi t_e = \phi t(\phi_r/\phi)^p$, by fitting a constant average effective flux scaling exponent, p. This provides a reasonable basis to fit low flux BWR and high PWR flux surveillance data, and, more approximately, for interpolating between these extremes in dose rate. Extrapolation to even lower fluxes is uncertain, due to corresponding uncertainties in the thermal diffusion coefficient, D_{cu}, of Cu. Nevertheless, using a nominally low value of D_{cu} to extrapolate to very low fluxes is likely to under predict hardening and embrittlement, which may be further enhanced by synergisms between irradiation and thermal precipitation processes.

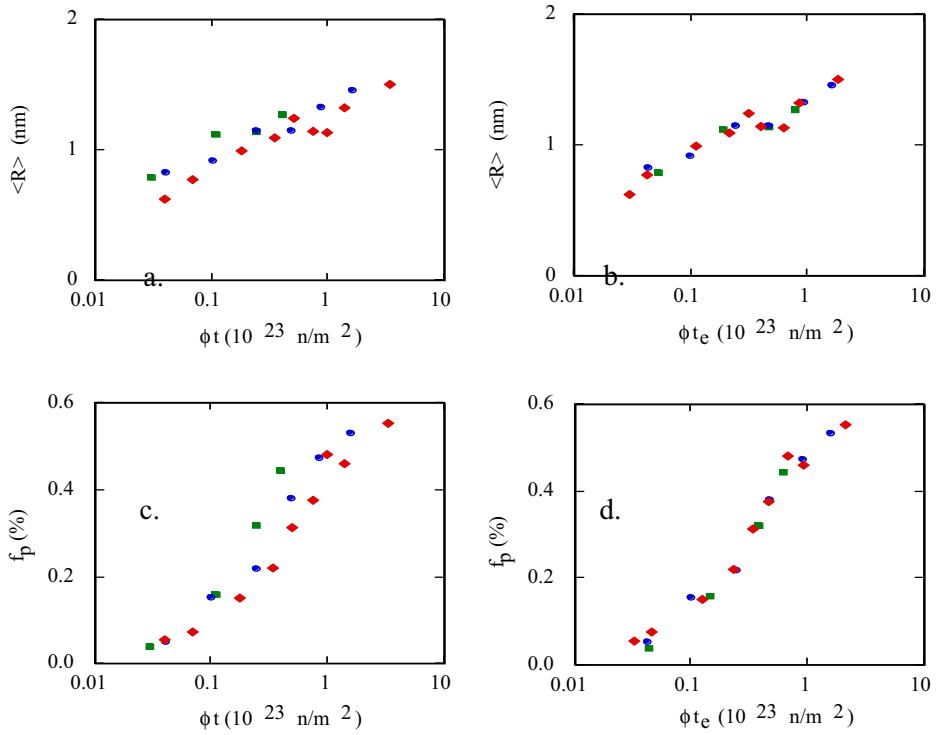

Fig. 2.18 SANS data on f_p and r_p for a 0.4 wt % Cu, 1.25 wt % Ni split melt model steel alloys (LD) irradiated at three flux levels between 0.6 to 10 × 10^{15} n/m^2-s in IVAR at 290°C, plotted on both fluence, ϕt, and effective fluence, ϕt_e, scales using a value of p = 0.5.

Table 2.1. Flux dependence mechanisms, regimes, and scaling laws for T_i = 290°C

Dominant Mechanism	ϕ-regime (n/m^2-s)	$\phi t_{pm/2}$–ϕ Scaling[a]	Comments[b]
Thermal diffusion assisted	$< \approx 10^3$	D*t @ $\phi t \alpha 1/\phi$	Depends on low temperature D_{cu}. Thermal precipitation is observed in sensitive model alloys and sensitive steels at 290 to 350°C.
Fixed sink	$< 10^{14}$	D*t @ $\phi t \neq f(\phi)$	This flux range is pertinent to BWR vessels and some low flux surveillance capsules. There may be no purely sink dominated regime - depends on alloy Ni & Mn contents, microstructure and low temperature D_{cu}.
Solute trap recombination	$> 10^{14}$	D*t @ $\phi t \alpha 1/\sqrt{\phi}$	May be pertinent to PWR vessels at lower flux levels. Depends on alloy Ni & Mn contents, microstructure Pertinent to PWR surveillance capsules and test reactor irradiations as well as higher flux regions in PWR vessels.

[a]In regime dominated by the specified mechanism. Note the flux-scaling varies smoothly in transitions between regimes that are dominated by a specific mechanism. Also note that more than one mechanism may be important in the overlap between some regimes.

[b]The flux levels at actual surveillance and vessel locations vary greatly, depending on details of the design and fuel assembly arrangements. For perspective, the peak flux in U.S. PWR and BWR RPVs are roughly 10^{15} and 10^{13} n/m^2-s, respectively. The flux levels are about two to four times higher in corresponding surveillance locations.

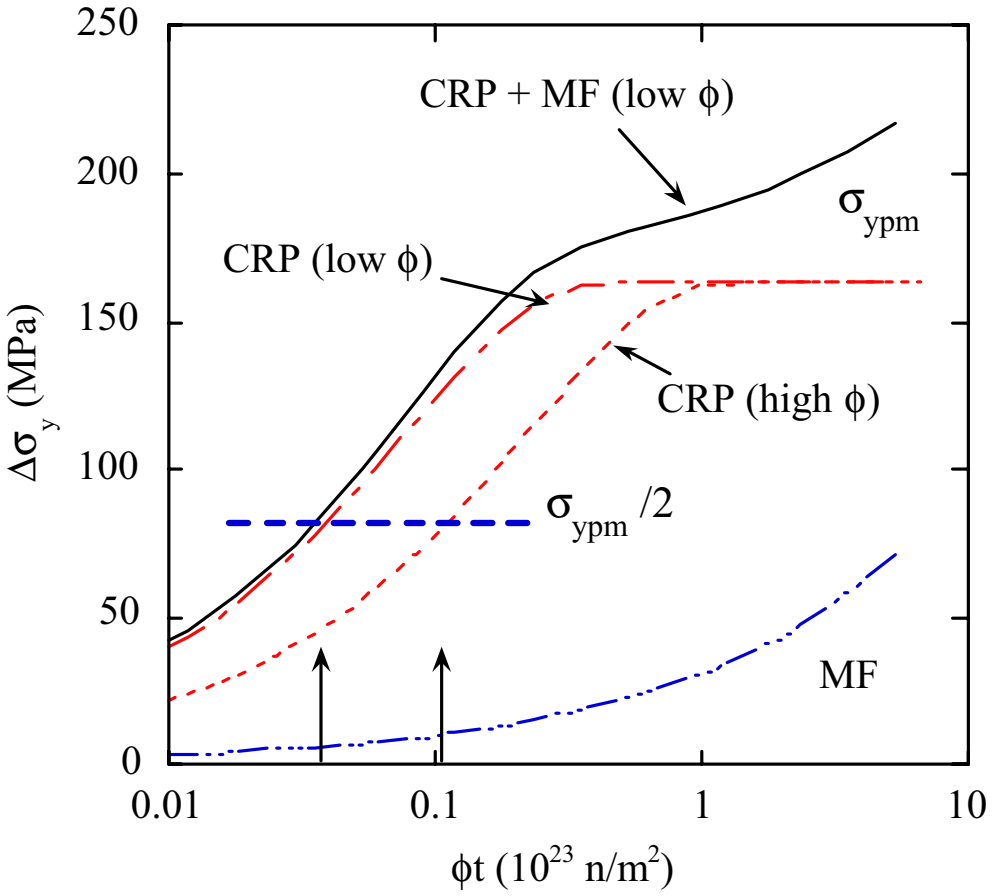

Fig. 2.19. Illustration of the two feature hardening model and the effect of flux, ϕ, on the fluence, ϕt, dependence of the CRP hardening contribution. The value of $\sigma_{ypm}/2$, which marks the fluence at 50% of the maximum CRP hardening, increases with increasing flux due to recombination.

2.3.2 The Composition Dependence of CRPs

We now turn our attention to the composition of the CRPs. At levels more than Cu ≈ 0.1 wt %, the nucleation of CRPs is primarily driven by the high supersaturations of dissolved Cu. Once nucleated, CRPs grow by RED of solutes. The CRPs are also enriched in Mn, Ni, Si, and P, depending on the alloy content of these elements [3,8,9,12,27–33].* The CRP enrichment in solutes, such as Mn, can be understood and modeled within the framework of both classical thermodynamics [12] and atomistic

*A number of atom probe (AP) studies suggest that the precipitates contain up to 50% or more Fe. However, this interpretation is inconsistent with thermodynamic principles and data, as well as the results of other characterization methods such as SANS. Recent local area atom probe (LEAP) studies on Cu bearing IVAR alloys indicate a highly enriched Cu core (>80 - 90% solute at sub nm dimensions) surrounded by shells enriched in Ni, Mn and Si. However, the outer shells may be somewhat ragged or diffuse and may also contain some thermodynamically dictated Fe. For nm scale precipitates almost all the atoms are at or near the interface, thus even small uncertainties in the positions of atoms (0.3 to 0.5 nm) lead to an artifact of higher than actual precipitate Fe contents. Hence, some of the differences are due to the definition of what constitutes a precipitate. Note, in general, there is much better agreement on the total number of solute atoms in the precipitates which is the most important observation since it is the solutes that control the obstacle strength of the precipitate and provide an overall mass balance for various elements.

simulations [31]. As an example, consider a simple A-B-C system (e.g., Fe-Cu-Mn). The activity coefficient Γ_{ij} is the ratio of the thermodynamic activity of solute i in phase j, a_{ij}, to the corresponding atomic fraction, X_{ij}, $\Gamma_{ij} = a_{ij}/X_{ij}$. Assume the primary matrix and precipitate phases are A (matrix, m) and B (precipitate, p) rich (e.g., Fe and Cu), respectively, and that C (e.g., Mn) partitions between them at different X_{Cm} and X_{Cp}.

If the solute C has a limited solubility (forms a dilute solution) in the A matrix phase, Γ_{Cm} is approximately constant (Henry's law) and is given by

$$\Gamma_{Cm} \approx \exp(H_{Cm}/RT) \tag{2-21}$$

where H_{Cm} is the heat of solution for dissolving C in the matrix phase (note, small thermal entropy effects have been neglected). For simplicity, assume that the precipitate-phase is an ideal B-C solution, with Γ_{Cp}= 1 (Rault's Law). Equilibrium requires that $a_{Cp} = a_{Cm}$, thus

$$X_{Cp}/X_{Cm} = \Gamma_{Cm}/\Gamma_{Cp} = \exp(H_{Cm}/RT) \tag{2-22}$$

For example, $X_{Cp}/X_{Cm} = 10$ at 290°C corresponds to $H_{Cm} = 10.8$ kJ/mole. Equation (2-22) also shows that solute enrichment in the precipitate phase decreases with increasing temperature.

The thermodynamics of real RPV alloys are more complex than in this simple example, and evaluation of CRP compositions requires the use of empirical thermodynamic parameters that can be found in the literature [27,31]. For example, in the Fe-Cu-Mn case, Γ_{Mnp} is less than Γ_{Mnm}; thus $X_{Mnp}/X_{Mnm} > 1$. At 290°C and $X_{MnFe} = 0.016$, $X_{Mnp}/X_{Mnm} \approx 12$; thus, $X_{Mnp} \approx 0.2$ and $X_{Cup} \approx 0.8$. In other words, if initially pure Cu precipitates in a Fe-Mn matrix are to approach equilibrium, Mn must flow out of the Fe-rich matrix phase and into the Cu-rich precipitate phase until $a_{Mnm} = a_{Mnp}$.

As schematically illustrated in Fig. 2.20, these basic thermodynamic and atomistic bonding concepts can be extended to treating additional solutes. Strong Mn-Ni, Cu-P, and Ni-Si interactions lead to the co-enrichment of these elements in the CRPs along with Mn. If the Mn plus Ni content of the precipitates exceeds that of Cu they are called manganese-nickel rich precipitates (MNPs). These models also treat the effects of the CRP-Fe matrix interface excess free energy, which scales as $1/r_p$, which is important at nanometer size scales. Higher Ni, Mn, Si, and P decrease the precipitate-matrix interface energy, resulting in additional non-equilibrium solute enrichment and increasing the nucleation rates and number densities of the CRPs.

However, the major effect of solutes is to increase the volume fraction of precipitates, f_p. Thus, $f_p = f_{Cup}/X_{Cup}$, where f_{Cup} is the volume fraction of precipitated Cu and X_{Cup} is the fraction of Cu in the precipitates. Since almost all the copper eventually precipitates, the maximum f_{pm} can be estimated from the fraction of Cu initially in solution in the matrix X_{Cu}, as $f_p \approx (X_{Cu} - X_{Cur})/X_{Cup}$, where X_{Cur} is the residual Cu in solution in local equilibrium at the precipitate of radius r_p. The residual Cu, X_{Cur}, is greater than X_{Cue} due to three sources of excess free energy in precipitates relative to bulk Cu: 1) the excess free energy due to the precipitate-matrix interface energy (γ_{pm}), which is important for nanometer-size scales (the Gibbs Thompson effect); 2) the higher energy of the bcc coherent Cu precipitates versus the equilibrium fcc phase (see Fig. 2.14); and 3) the coherency strain energy associated with a lattice parameter mismatch between bcc Cu and Fe. The X_{Cur} can be estimated as

$$X_{Cur} = X_{Cue}(bcc)\exp([(2\gamma_{pm}/r_p + 4\mu\delta^2)V_{Cum}]/[RT]) \tag{2-23}$$

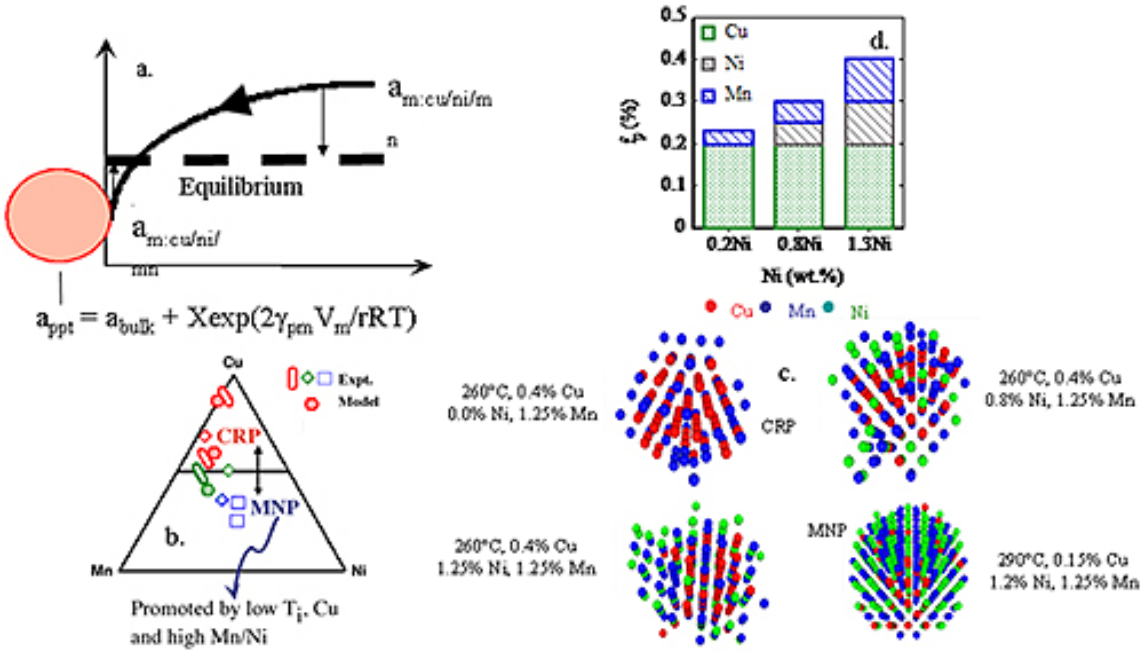

Fig. 2.20. Illustration of the thermodynamics leading to CRP enrichment on Mn and Ni. (a) The Cu, Ni and Mn activities are initially higher in the matrix than in the precipitate. As these elements flow into the CRP their activities decrease in the matrix and increase in the precipitate until equilibrium is established when they are equal in both phases. At small sizes the solute activity in the precipitate must include the contribution of the interface, which also depends on composition (b) A Gibb's triangle indicating the CRP and MNP composition ranges in Cu-bearing alloys. (c) Atomistic Monte Carlo simulations of CRPs and MNPs. (d) Illustration of the Cu, Ni and Mn contributions to the CRP volume fraction as a function of alloy composition.

For pure copper precipitates at 290°C, assuming an interface energy, $\gamma_{pm} \approx 0.4$ J/m^2, a molar volume of Cu, $V_{Cum} \approx 7.1 \times 10^{-6}$ m^3/mole, a solubility of copper in equilibrium with coherent bcc precipitates, $X_{Cue} \approx 7.4 \times 10^{-5}$, $\delta = 0.03$ and $\mu = 70$ GPa (the weighted mean of Cu and Fe), $X_{Cur} = \approx 0.042$ wt. % for a precipitate with $r_p = 1$ nm at 290°C. While X_{Cur} is fairly small, it is significant for steels with lower copper levels and, as discussed below, results in a threshold copper content, Cu_{min}, for forming CRPs.

The Mn and Ni enriched CRPs and MNPs can be very large, resulting in large f_p and high levels of hardening and embrittlement as illustrated in Fig. 2.20 (d). For alloys with 1.3 to 1.6 wt % Mn, typical precipitate copper contents are $X_{Cup} \approx 0.7$ to 0.9 for low Ni (< 0.5 wt %), $X_{Cup} \approx 0.5$ to 0.7 for medium Ni (0.5 to 0.9 wt %), and $X_{Cup} \approx 0.25$ to 0.5 for high Ni (> 0.9 wt %). Hence, CRPs give way to Mn-Ni(-Si,..) rich precipitates (MNPs) in alloys with high Ni and Mn contents. The Mn and Ni enrichment in precipitates also increases with decreasing irradiation temperature.

Figure 2.21 shows SANS measurements of the mean radius, number density, and volume fraction of CRPs and MNPs as a function the alloy Ni and Mn contents, for alloys with ≈ 0.4 wt % Cu irradiated at high flux at 290°C to 3.4×10^{23} n/m^2. The alloys with variations in Ni contain nominal concentrations of about 1.4 to 1.6 wt % Mn. The alloys with variations in Mn contain nominal concentrations of 0.8 wt % Ni. The pie charts in the volume fraction plots are estimates of the precipitate composition based on the measured magnetic to nuclear scattering ratio [27,32]. The radius increases and decreases slightly with increasing Ni and Mn, respectively. However, there are much larger increases in the corresponding number densities and volume fractions in both cases. At high alloy Ni and Mn the MNPs replace CRPs. Since the Mn and Ni activities decrease in the precipitates with decreasing Cu, highly enriched MNPs are also favored over CRPs at lower Cu levels. Indeed, it has been recently shown that MNPs can even form

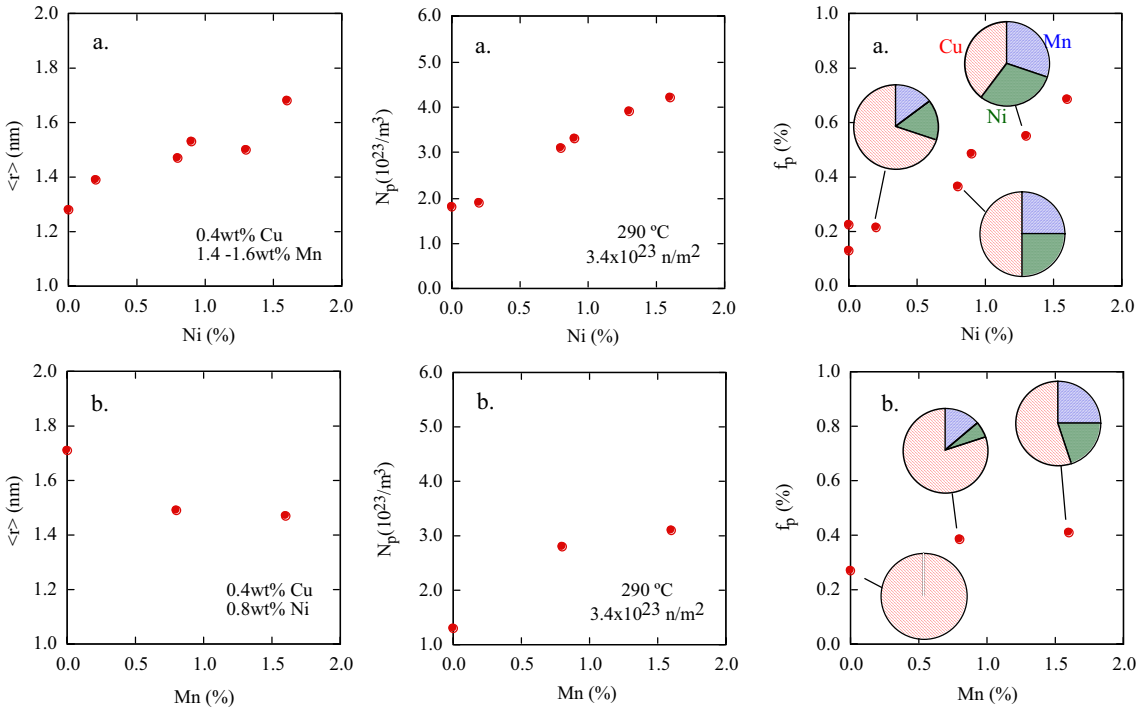

Fig. 2.21. SANS data on r_p, N_p, and f_p for a 0.4 wt % Cu split melt model steels irradiated at high IVAR flux at 290°C. (a) Effects on Ni variations in alloys with 1.4 to 1.6 wt % Mn; (b) Effects on Mn variations in alloys with ≈ 0.8 wt.% Ni.The pie charts in the f_p plots show the estimated precipitate compositions.

in Cu-free steels [50]. In this case X_{Cup} < to << 0.1. Since these nearly pure MNPs are slow to nucleate, they have been called "late-blooming" phases. These (and other) experimental observations are consistent with the thermodynamic concepts outlined above.

Thus, large volume fractions of CRPs and MNPs can form under irradiation. Fortunately, pre-precipitation during stress relief heat treatments at around 600°C limits the maximum dissolved copper prior to irradiation at start-of-life, to an effective Cu_{max}, that may be lower than the bulk alloy copper content if the latter exceeds the solubility limit. An extensive study of pre-precipitation kinetics [4] yielded estimates of $Cu_{max} \approx 0.25 \pm 0.05$ wt % in medium Ni (Ni ≈ 0.8 wt.%) steels. This start-of-life copper increases to $Cu_{max} \approx 0.3$ wt %, or slightly more, at high Ni levels ≈ 1.6 wt %. The apparent influence of Ni on the start-of-life Cu_{max} may have both thermodynamic and kinetic origins. Thermodynamically, the bond strength between low solubility Cu and Fe is smaller than between high solubility Ni and both Fe and Cu. Thus, as Ni replaces Fe atoms as neighbors of Cu, the latter's solubility increases. The decrease in the matrix activity of Cu with increasing Ni also reduces the rate of Cu pre-precipitation. The actual Cu_{max} depends on the heat-treatment time-temperature history, as well as the alloy composition. In general Cu_{max} may approach, but does not reach the equilibrium solubility limit. These estimates of Cu_{max} are consistent with the parameters obtained by fitting the TTS model to the welds with high Cu and medium and higher Ni in the surveillance database.

Test reactor data also show there is a minimum Cu threshold for forming CRPs, Cu_{min}, between ≈ 0.06 and 0.09 wt.% Cu [3,5,8]. This can be simply understood based on Eq. 2-23 and conservation of Cu requiring that

$$f_p + X_{cur} = X_{cu} \tag{2-24}$$

A given N_p and r_p specify the precipitate f_p and X_{Cur}, hence, the initial dissolved Cu, X_{Cu}, that is required to establish the balance in Eq. 2.24. As shown by the unfilled symbols in Fig. 2.22, assuming pure Cu precipitates and using Eq. 2-23 to determine X_{Cur}, X_{Cu} goes through a minimum as a function of r_p that depends on N_p. Figure 2.22 shows that for $N_p = 10^{23}/m^3$ the minimum is greater than the threshold for forming CRPs in the TTS model, $X_{Cu} \approx 0.063$ at %, which is equivalent to 0.072 wt % Cu. The minimum X_{Cu} is slightly less than 0.063 at % for $N_p = 10^{22}$ and $5 \times 10^{22}/m^3$; however, as shown by the filled symbols for the corresponding $\Delta\sigma_y$ curves, the hardening is small in these cases. Further, the homogeneous nucleation rates of Cu precipitates, as well as heterogeneous nucleation rates on small sub-critical Cu clusters that may form in cascades, also very rapid drop-off very rapidly below ≈ 0.05 to 0.09 wt. % Cu. These theoretical considerations are consistent with the minimum Cu for CRP formation that is in the TTS model of Cu=0.072 wt %.

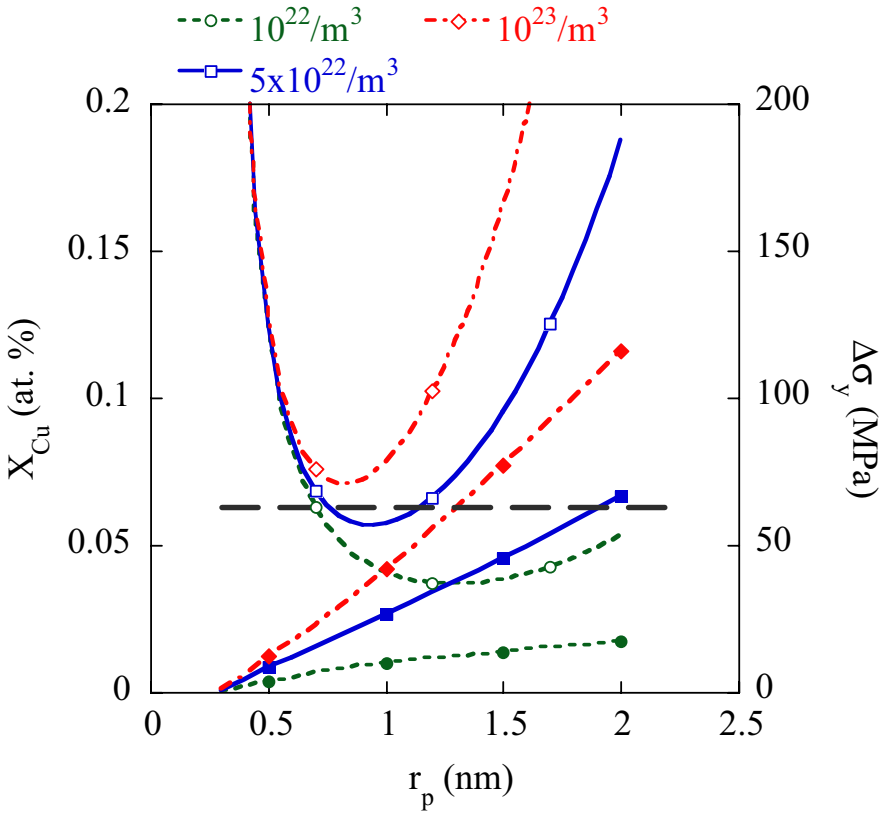

Fig. 2.22. The total Cu (X_{Cu}) required for a balance between that contained in the precipitates (f_p) plus that dissolved in the Fe matrix in local equilibrium with the bcc phase of Cu, for an interface energy γ_{pm} = 0.4 J/m^2 and lattice coherency mismatch parameter δ = 0.03, plotted vs r_p for various N_p (open symbols) and the corresponding estimated hardening $\Delta\sigma_y$ (filled symbols). The horizontal dashed line represents the threshold for forming CRPs in the TTS model.

In summary, the synergistic interactions between Cu-Mn-Ni (and by extension P and Si) are experimentally fairly well characterized and can be thermodynamically modeled. Most notably, higher-alloy Mn and Ni increase the precipitate volume fraction, f_p. Pre-precipitation limits the maximum effective dissolved Cu prior to irradiation, Cu_{max}, depending on both the stress-relief time and temperature and the alloy composition. Experimental estimates suggest that, following typical stress relief times around 600°, $Cu_{max} \approx 0.25 \pm 0.05\%$ for medium Ni steels and ≈ 0.30 wt %, or slightly more, in very high-Ni steels, Both independent experimental observations and theory indicate that a threshold Cu content in the range of $Cu_{min} \approx 0.05$ to 0.09 wt % is required for CRP formation. These conclusions are broadly consistent with the treatment of alloy composition in the CRP term in the TTS model.

2.3.3 The Fluence Dependence of CRP Hardening

Precipitates evolve by long-range diffusion and clustering of Cu and other solute atoms. Rate theory can also be used to model the evolution of Cu precipitates as a function of fluence. The most detailed treatment is based on so-called cluster dynamics models (CDMs). CDMs represent the number clusters in each size category, N(n), from the mobile monomer species n = 1, up to a maximum number of atoms n = n_{max} , with a set of ordinary differential equations. In the simplest form,

$$dN(n)/dt = \beta(n-1)N(n-1) + \alpha(n+1)N(n+1) - [\alpha(n) + \beta(n)]N(n) \quad (2\text{-}25)$$

In this formulation, clusters with sizes > 1 are assumed to be immobile. The α and β coefficients are the rates at which the cluster of the indicated sizes, n-1, n and n+1, emit or absorb a mobile monomer species, respectively. Note slightly different equations are used for the monomer and largest cluster. For diffusion controlled growth of spherical Cu clusters and using the capillary approximation for the Gibbs-Thompson effect,

$$\beta(n) = 4\pi r_n D^* X_{cum}/V_{Cu} \quad (2\text{-}26a)$$

$$\alpha = [4\pi r_n D^* X_{cue}/V_{Cu}]\exp(2\gamma_{pm} V_{Cu}/r_n kT) \quad (2\text{-}26b)$$

Here r_n is the radius of a cluster of n Cu atoms. The set of n =1 to n_{max} coupled equations are integrated over time from an initial condition of supersaturated Cu in solution, typically with no clusters with n > 1. Note, these simplifying assumptions are not necessary, and there are many elaborations of CDMs to treat effects such as heterogeneous nucleation, mobile clusters and interface controlled kinetics.

Figure 2.23 shows a CDM prediction of a 300°C irradiation induced evolution of Cu precipitates in a Fe-0.3 at. % Cu alloy with overlapping regimes of nucleation (N), growth (G) and coarsening (C) [3]. At low fluence, nucleation dominates, as manifested by a rapid increase in N_p and f_p, At intermediate fluence, nucleation, growth and coarsening overlap, as manifested by a more rapid increase in r_p, a peak in N_p and a continued increase in f_p until it approaches an approximate plateau, when the matrix Cu is almost depleted. At still higher fluence, the precipitate evolution is dominated by coarsening, with a slowly decreasing N_p and increasing r_p. The only adjustable parameter in these calculations is K factor in the RED diffusion coefficient D*, which sets the absolute fluence scale. The thermodynamic models described in the previous section can be used to properly enrich the precipitates with other solutes, assuming that Cu clustering controls the basic kinetics. The overall predictions of CDM are in good qualitative agreement with experimentally observed trends and provide a foundation for much simpler models used to fit the TTS database.

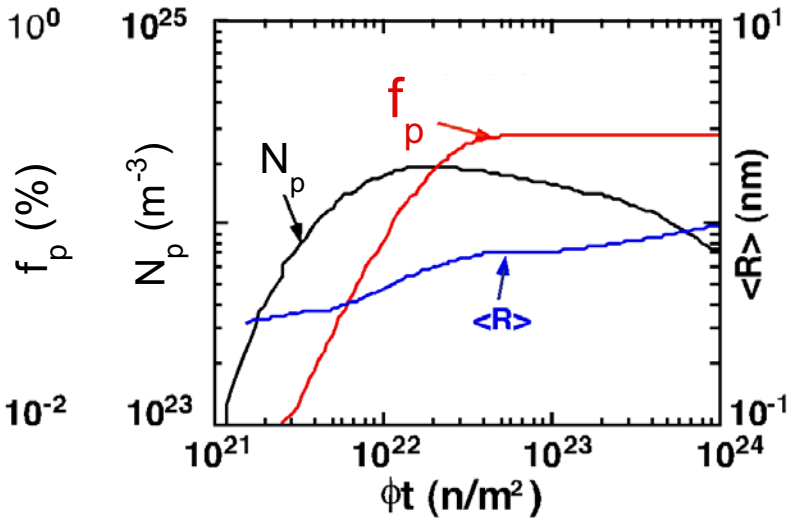

Fig. 2.23. Example of a cluster dynamics model of the nucleation-growth and coarsening Cu precipitation kinetics for an Fe 0.3 wt % Cu alloy irradiated at 300°C. Nominal thermodynamic parameters for the Fe-Cu system were used. The only adjustable parameter in this model is the radiation enhanced diffusion factor K, which sets the fluence scale.

The factors that control the precipitation processes can be understood on a conceptual basis. There is a free energy activation barrier to CRP nucleation that is very sensitive to the Cu supersaturation. The CRP nucleation barrier has two apparent effects. First, the incubation fluence, marking the initiation of hardening by CRPs, increases with decreasing Cu, due to correspondingly lower nucleation and growth rates and number densities (N_p) [1,13]. Second, below a threshold Cu_{min}, well-developed CRPs do not form; the threshold is $Cu_{min} \approx 0.05$ to 0.09 wt % Cu at ≈ 290°C [3,5,13,18]. The CRP number densities also decrease with increasing irradiation temperature, due to the lower Cu supersaturation. However, the precipitate number densities increase with higher alloy Ni, Mn, Si and P contents, due to the reduction of the CRP-Fe matrix interface energy by these solutes [12].

Once nucleated, the CRPs grow by RED of solutes. A standard expression to analytically represent precipitation (and other transformations) kinetics is the so-called Avrami (or Johnson-Mehl) equation, which has a general form [13,51]

$$f_p(t) = f_{pm}\{1 - \exp[-(t/t_t)^{\beta}]\} \qquad (2\text{-}27)$$

where f_{pm} is the maximum precipitate volume fraction, t_t is the time for f_p to reach $0.63f_{pm}$ and β is a parameter that depends on the rate controlling precipitation kinetics mechanism. For example, in the case of diffusion-controlled growth of a fixed number density of precipitates from very small size to saturation due to solute depletion, β is 3/2. In contrast, if the precipitate interface mobility is rate controlling, β = 3. The maximum precipitation rate at short times is $f_p(t) = f_{pm}(t/t_t)^{\beta}$, and df_p/dt decreases at larger times due to depletion of solute from the matrix.

As illustrated by the CDMs, actual kinetics of CRP evolution is much more complex than can be described by any simple analytical expression such as Eq. (2-27). However, by considering β to be an effective fit parameter, some of the missing physics can be captured [13]. As shown in Fig. 2.24, β sets

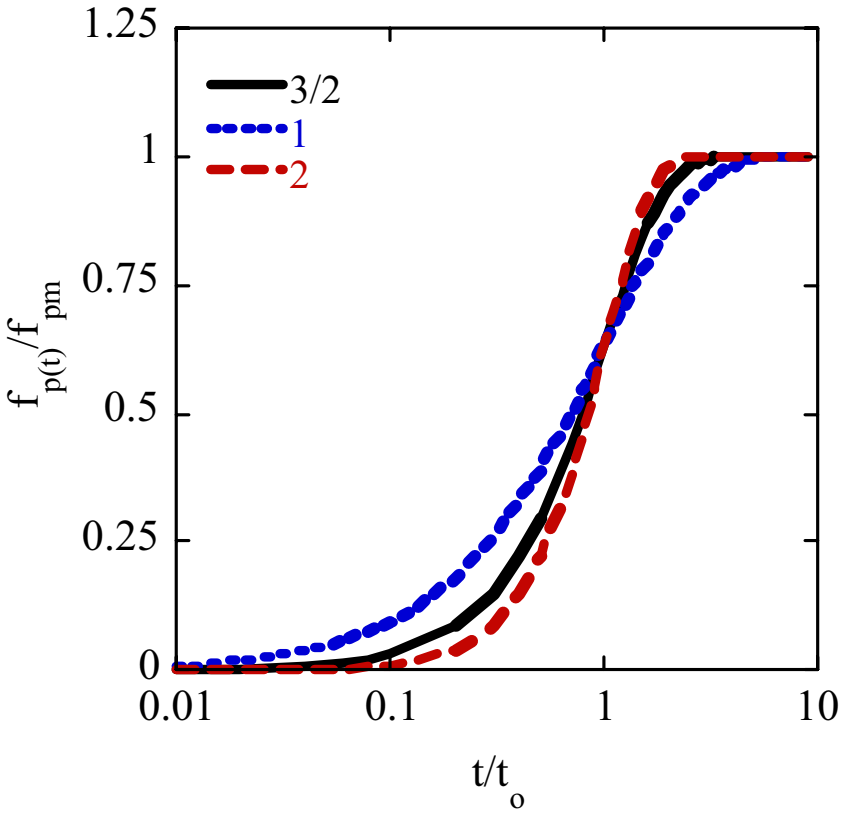

Fig. 2.24 The Avrami equation for different values of β.

the effective shape of the $f_p(t)$ curve between 0 and f_{pm}; decreasing β increases the time interval for the precipitation.

The corresponding ϕt_e dependence of f_p under irradiation can be approximately represented by [13]

$$f_p(\phi t_e) \approx f_{pm}\{1 - \exp[(-\phi t_e/\phi t_{et})^{\beta}]\} \quad (2\text{-}28)$$

In the case of pure diffusion-controlled growth, β = 3/2 and ϕt_{et} can be related to X_{Cu}, X_{Cup}, N_p, and D* [13]. Fitted values of β (≈ 1) are typically less than 3/2, suggesting that other mechanisms influence CRP growth [13]. For example, this could reflect a slow decrease in the RED coefficient, D*, due to the buildup of additional defect sinks and recombination centers. Assuming that almost all the Cu initially in solution, X_{Cu}, precipitates, and accounting for enrichment by other elements, such as Ni and Mn,

$$f_{pm} \approx X_{Cu}/X_{Cup} \quad (2\text{-}29)$$

The effective ϕt_{et} and β can be determined by fitting data for f_p as a function of the effective fluence at the reference flux, $f_p(\phi t_e)$ [13]. For a specified alloy ϕt_e can be approximated by

$$\phi t_e = \phi t(\phi_r/\phi)^p \quad (2\text{-}30)$$

Recall, however, that this simple constant p scaling is not fully rigorous over a wide range of flux and that p also depends on the alloy composition and irradiation temperature as well as flux (as discussed in Sect. 2.2.3). Thus, p must also be considered an effective fitting parameter. Ignoring the detailed effects of the precipitate size in the peak hardening regime and superposition effects, the corresponding CRP hardening, $\Delta\sigma_{yp}$, is simply given by [13]

$$\Delta\sigma_{yp}(\phi t_e) \approx \Delta\sigma_{ypm}[f_p(\phi t_e)/f_{pm}]^{1/2} \tag{2-31}$$

Thus,

$$\Delta\sigma_{yp}(\phi t_e) = \Delta\sigma_{ypm}[1 - \exp(-\phi t_e/\phi t_{et})^{\beta}]^{1/2} \tag{2-32}$$

Here $\Delta\sigma_{ypm}$ is the maximum, or saturation, CRP hardening. The CRP contribution to the TTS, or TTS_p, is given by

$$TTS_p = C_c\Delta\sigma_{yp} \tag{2-33}$$

Equations (2-30) to (2-33) represent physically based $\Delta\sigma_y$ and TTS models that can be fit to experimental data. The p, β, ϕt_{et}, and $\Delta\sigma_{ypm}$, or TTS_{pm}, are effective fitting parameters that depend on metallurgical and irradiation variables in a way that can be physically understood and modeled. While these analytical expressions are greatly simplified relative to the complexities of the underlying embrittlement mechanisms, they can empirically reflect at large part of the physics that is not explicitly included when fitted to the TTS database. Hyperbolic tangent and error function (erf) equations can also be used to approximate $\Delta\sigma_{yp}(\phi t_e)$ and $TTS_p(\phi t_e)$.

Based on both the physics of the CRP nucleation and growth mechanisms and a large body of data, any $\Delta\sigma_{yp}$ or TTS model should reflect the following systematic variable effects:

- The $\Delta\sigma_{yp}(\phi t)$ curve should manifest both low dose incubation and high dose saturation fluence. A $\ln(\Delta\sigma_{yp})$ versus $\ln(\phi t)$ plot should be sigmoidal, with an approximately linear shape in the transition. If simple diffusion controlled growth is rate controlling, the log-log transition slope is ≈ 3/4.
- Threshold and maximum effective Cu contents for CRP formation are ≈ 0.06 to 0.09 and ≈ 0.25 to 0.30 wt %, respectively.
- The saturation CRP hardening, $\Delta\sigma_{ypm}$, increases rapidly with higher Ni and, to a lesser extent, Mn.
- The CRP hardening curve is shifted to higher fluence with increasing flux in the PWR and test reactor regime in a way that can be represented by an effective fluence, ϕt_e, that accounts for solute enhanced recombination. The recombination rate decreases with increasing irradiation temperature and decreasing alloy solute content flux. However, thermal Cu diffusion coefficients may be important at low flux, in and below the BWR regime.
- The CRP hardening curve is shifted to higher fluence with decreasing Cu.
- The width of the CRP hardening curve transition increases with higher Ni.

The effects of Ni and Cu on the shape of TTS curves and their and position on the fluence scale are schematically illustrated in Fig. 2.25.

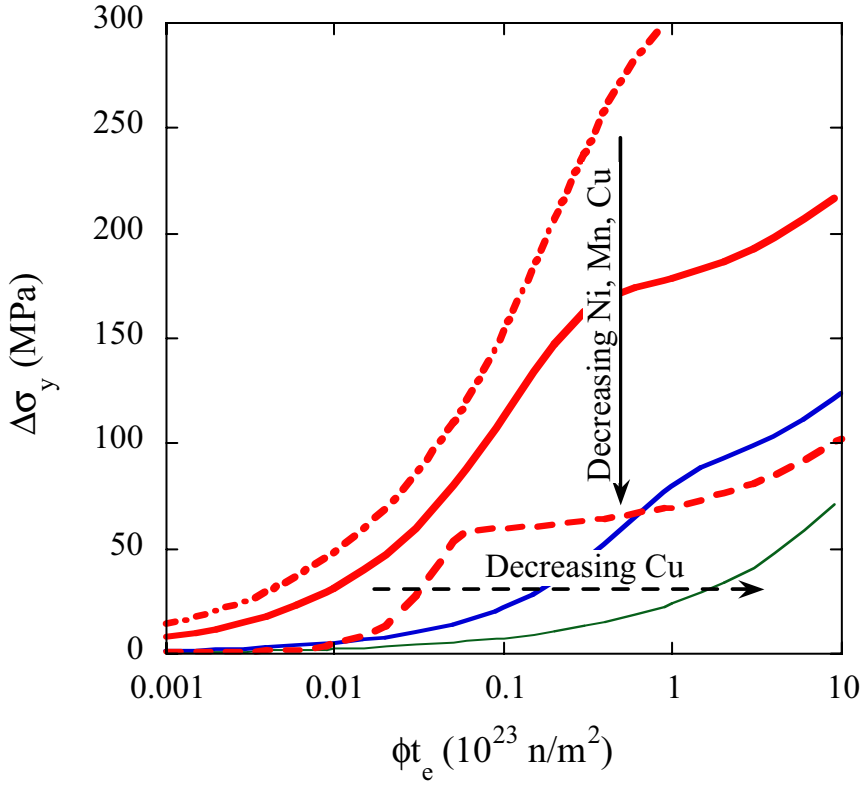

Fig. 2.25 Illustration of the effects of alloy composition on the shape and position of the CRP/MNP effective fluence function.

In summary, the fluence dependence of $\Delta\sigma_y(\phi t_e)$ and $TTS(\phi t_e)$ can be modeled by the Avrami-type equation, as well as with roughly equivalent tanh or erf representations. The effective fluence, ϕt_e, depends on the flux and other irradiation and material variables. The simplest flux scaling is given by $\phi t_e = \phi t(\phi_r/\phi)^p$, where ϕ_r is a reference flux, and the fitting parameter p is assumed to be constant. The model fit parameters include p, which controls the flux scaling; β, which sets the width and shape of the precipitation hardening function; ϕt_{et}, which provides an effective fluence scale; and $\Delta\sigma_{ypm}$ or TTS_{pm}, which are the saturation CRP hardening and transition temperature shift due to precipitation, respectively. The p and β parameters generally depend on the alloy composition, flux and irradiation temperature, but are fitted averages in the TTS model.

2.3.4 Effects of Irradiation Temperature, T_i, on CRP Hardening

It has often been assumed that hardening and embrittlement due to irradiation-induced CRPs do not depend on the irradiation temperature, T_i [2,7,9,16,22]. However, this is not actually the case [5,18]. The irradiation temperature dependence of $\Delta\sigma_{yp}$ and TTS_p is due to a number of mechanisms.

- The CRP nucleation rates, hence N_p and, to a lesser extent f_p, decrease with increasing irradiation temperature due to higher Cu solubility. The CRPs are larger at higher irradiation temperature and, if

they grow beyond a radius of about 1.2 nm, their hardening efficiency ($\Delta\sigma_{yp}/\sqrt{f_p}$) gradually decreases with increasing r_p.

- The f_p also decreases with increasing irradiation temperature, T_i, partly due to the reduction of Ni, Mn and Si in the CRPs.
- At higher fluxes, the previous effects are somewhat offset by decreased recombination at higher irradiation temperature.

The effect of irradiation temperature on the CRP r_p, N_p, f_p, and estimated compositions is illustrated by the SANS data in Fig. 2.26 for an 0.4 wt % Cu, 0.8 wt % Ni, 1.4 wt % Mn split melt model steel irradiated at medium flux to 1.6 × 10^{23} n/m^2 at 270, 290, and 310ºC. The corresponding effects of irradiation temperature on $\Delta\sigma_y$ are also shown along with a plot of the predicted value based on the SANS data are shown in Figure 2.26d.

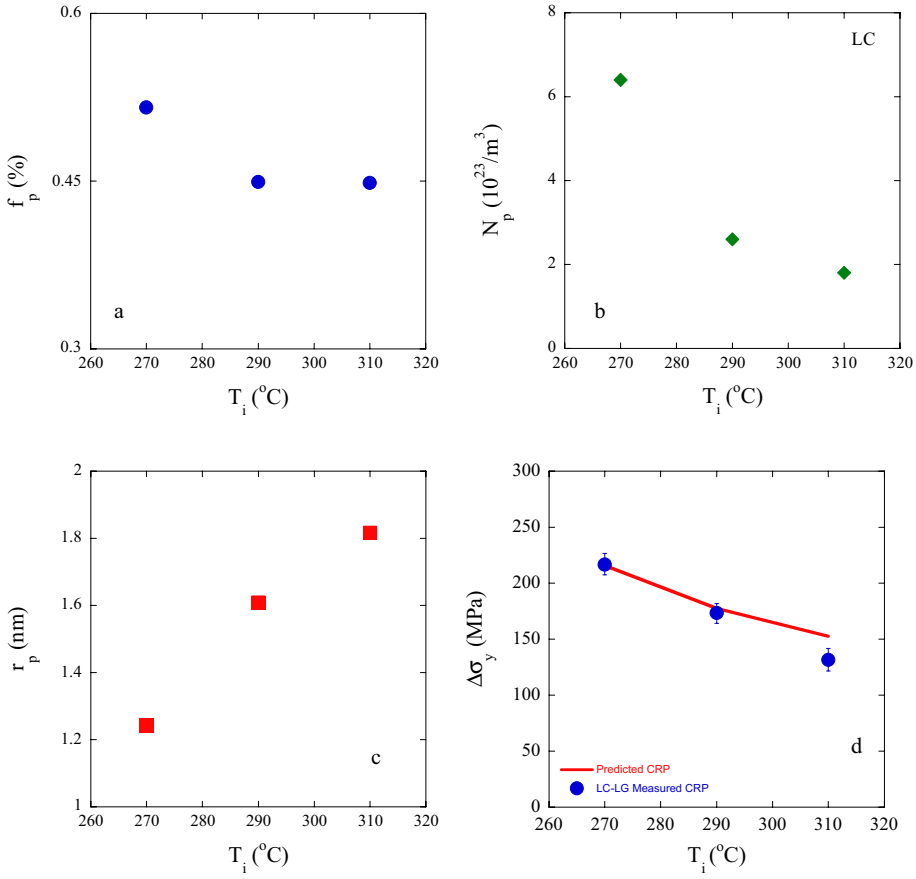

Fig. 2.26. SANS data on r_p, N_p, and f_p for a 0.4 wt % Cu, 0.8 wt % Ni, 1.4 wt % Mn SMMS irradiated at three temperatures in IVAR. Figure 2.26d shows the measured $\Delta\sigma_y$ along with predictions of the model and procedures described previously.

The irradiation temperature dependence for CRP hardening can be modeled by a $f_T(T_i)$ function as

$$\Delta\sigma_y(T_i) = \Delta\sigma_y(290°C)[1 + C_T(290 - T_i)] \quad (2\text{-}34)$$

For higher fluence and intermediate flux irradiations, typical values of C_T is ≈ 0.015±0.05/°Cin Cu-bearing alloys, while in lower-Cu steels the corresponding C_T is ≈ 0.020±0.05/°C. The highest irradiation temperature sensitivity is observed in steels that have Cu contents that are slightly greater than Cu_{min}. Equation (2-34) is equivalent to the linear form used in the TTS model for the temperature dependence of the MF term.

In summary, CRP hardening is not athermal, as is often assumed. The irradiation temperature dependence of the hardening can be treated using a linear $C_T(T_i)$ function.

2.4 Matrix Features

Matrix features (MFs) are generally defined as the dislocation obstacles that produce hardening in low Cu (≤ 0.072 wt %) alloys. As noted previously, the general category of MFs includes dislocation loops, vacancy-solute clusters, dislocation atmospheres and fine-scale precipitates enriched in P or Mn, Ni and Si. At low P levels and typical low to intermediate flux irradiation conditions the dominant MFs are believed to be Mn-Ni-Si-P-Cu vacancy solute complexes or their remnants. However, at higher P levels alloy phosphide precipitates are observed. The effects of P and role of phosphide phases are discussed in the next section followed by a discussion of solute vacancy complex MFs.

2.4.1 Phosphide Phases (PPs)

It is well established that P contributes to the hardening and embrittlement of RPV steels [1–4,9,22,52,53]. While the amount of dissolved P in RPV alloys is generally very small, (< 0.05 wt %), it is very insoluble, and remains supersaturated following typical stress-relief heat treatments [12]. Thus, P can undergo accelerated precipitation due to RED to form phosphide phases [3,4,12,34,54]. This is illustrated in Fig. 2.27 (a) where the tomographic atom probe map shows phoshide precipitates in a Fe-0.025 wt % P binary model alloy irradiated in IVAR at ≈ 290°C and high flux to $\phi t \approx 1.8 \times 10^{23}$ n/m^2 [54].

The contribution of P to embrittlement is greatly enhanced by Mn in the TTS model. Jones proposed that the hardening associated with P is due to Mn_3P precipitates [52]. Figure 2.27 (b) shows the corresponding APT P and Mn maps for a Fe-0.025%-1.6 wt % Mn ternary model alloy. In this case, the P clusters appear to be more diffuse, and significant segregation of both P and Mn to dislocations is observed. Notably, Mn doers not appear to be associated with the P clusters in this case, which is a puzzling observation in need of further examination. However, irradiation hardening in the same set of simple model alloys also reflects both a P precipitation and P-Mn interaction: for the 1.6 wt % Mn and 0.025 wt % P alloy, $\Delta\sigma_y$ = 151 MPa; for the Fe-0.025% P alloy, $\Delta\sigma_y$ = 76 MPa; for an Fe ≈ .0125 wt % N alloy, $\Delta\sigma_y$ = -31 MPa; and for a Fe-1.6% wt % Mn alloy, $\Delta\sigma_y$ = 46 MPa. Note the hardening from P in these cases may be partly due to formation of dislocation atmospheres, as well as precipitation. The softening in the Fe alloy containing N is probably the result of the dissolution of fine scale quench defects during long-term irradiation. We have also recently observed unusually low magnetic to nuclear scattering ratios (<0.5) in a SANS study of a Cu free, ≈ 0.8 wt % Ni, ≈ 1.6 wt % Mn, ≈ 0.040 wt % P split melt model steel that are also consistent with the presence of the $Mn_{2\text{-}3}P$ precipitates for medium flux irradiations to ≈ 1.6×10^{23} n/m^2 at 270°C and 290°C.

The effect of Mn can be theoretically understood based on the strong bonding between P and various alloying elements, such as Mo, Cu, and especially Mn. The alloy phosphides reduce P solubility in the ferrite matrix compared with that in pure Fe [12,55]. The stability and bonding strength of a phase is

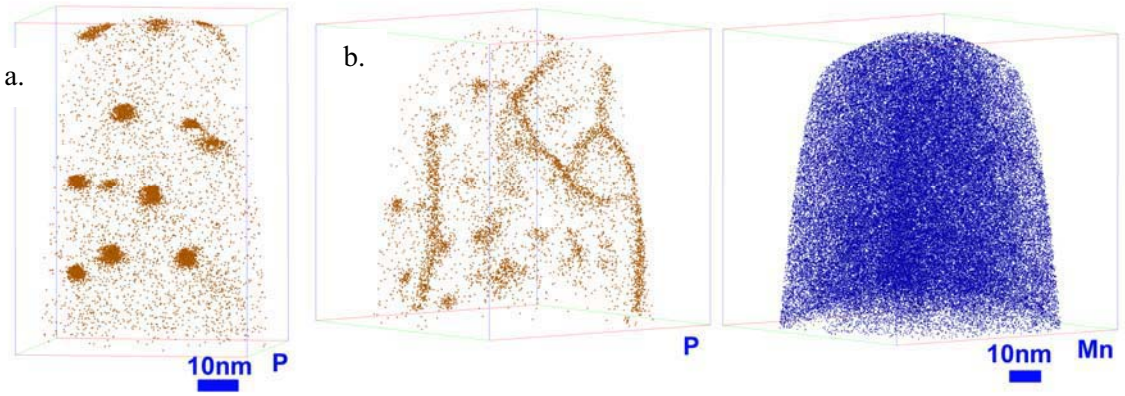

Fig. 2.27. Three-dimensional tomographic atom probe data on for model alloys irradiated in IVAR to 1.77 × 10^{19} n/cm^2 at 290°C and high flux. (a) An Fe-0.025 wt % P alloy; (b) an Fe-0.025 wt % P-1.6 wt % Mn alloy. Note the extensive P segregation to dislocations in Fig. 2.27 (b).

reflected in its melting temperature. Thus it is notable that the Mn_2P phase has the highest melting point in the Mn-P binary system. Assuming a mix of Mn_2P and Mn_3P phases, the maximum volume fraction of phosphide precipitates, is roughly three to four times the supersaturated atomic concentration of P. Phosphorous precipitation kinetics are expected to be roughly similar to those for CRPs. Phosphorous also bonds with vacancies, hence it is expected to increase the thermal stability and hardening efficiency of MF vacancy solute (Cu-Ni-Mn-P) cluster complexes, discussed in the next section. Finally, segregation of P to form dislocation atmospheres by RED would also result in additional hardening.

Thus, the general form of the P-Mn contribution to the TTS MF term for low Cu steels is consistent with hardening by some combination of fine scale alloy phosphides, vacancy-solute complexes and dislocation atmospheres. Phosphorous may also enhance the formation of dislocation loops. However, the TTS MF P term is not consistent with expectation that phosphide hardening ultimately saturates due to depletion of P from the matrix.

There are several other complications to treating P effects on hardening and embrittlement. First, P also segregates to grain boundaries [34,54], as well as dislocations. Grain boundary P segregation reduces the amount of P available for precipitation under irradiation. However, accelerated grain boundary P segregation due to RED can also cause irradiation enhanced temper embrittlement, typically associated with brittle intergranular fracture [54,56]. Fortunately, irradiation enhanced temper embrittlement and intergranular fracture do not appear to be a very significant embrittlement mechanisms in irradiated LWR RPV steels [56,57].

The TTS model also includes an additional contribution of P to embrittlement in the CRP term. This would seem to be at odds with several early studies showing that the effect of P decreases with increasing Cu [52,53], as well as results of the IVAR irradiations, discussed in Chap. 6. The Cu-P synergism may be due to the fact that P is also enriched in CRPs due to strong P-Mn and P-Cu bonding. At higher Cu levels the effect of a relatively small amount of P adding to the larger CRP volume fraction (f_p) has little effect on net hardening. So the net consequence, in this case, may be a reduced $\Delta\sigma_y$ since less P is available to form phosphides. Further, the net effect of strength contributions of phosphide precipitates decreases when superposed with a larger CRP contribution.

However, there are other mechanisms that could result in more CRP hardening at higher P. For example, at lower Cu levels, not too much above the Cu threshold for CRP hardening, the proportionately larger f_p, and especially N_p, due to the added P would result in a larger increase of the CRP $\Delta\sigma_y$, perhaps offsetting any corresponding decrease in phosphide hardening. Further, since P decreases the size and

increases the number density of CRPs, the CRPs may remain near their peak hardening efficiency radius of ≈ 1 nm, especially at low flux levels typical of surveillance conditions.

In summary, a variety of mechanisms may lead to increases in hardening by P from both enhanced MF (phosphide precipitates, vacancy-solute complexes and dislocation atmospheres) and CRP (larger volume fractions and higher number densities) contributions. Significant P-Mn interactions are supported by both thermodynamic considerations and experimental observations. These conclusions are generally consistent with the treatment of P in the TTS model. However, phosphorous depletion leading to hardening saturation and a reduced effect of P due to Cu-P interactions are expected in some cases, but are not reflected in the TTS model.

2.4.2 Defect Solute Cluster Complexes: The Temperature and Flux Dependence of MF Hardening

Nanometer-scale SIA dislocation loops develop in RPV steels at sufficiently high flux and fluence [35]. However, the significance of SIA loops for the lower flux and fluence irradiation conditions pertinent to RPV embrittlement has not been established (for example, by conclusive electron microscopy observations). In addition to loops and phosphide precipitates, MFs are believed to be primarily vacancy-solute (Mn, Ni, Cu, P,..) cluster complexes, or their remnants left after the vacancy clusters have fully dissolved, forming solute aggregates in their wake [3,12,26–28,58,59]. Hence, MF hardening can be expected to depend on the alloy composition. This has been confirmed by studies showing that hardening in low Cu steels increases with Cu, Ni, P and Mn, as discussed in Chap. 6. The MFs initially form by local spatially correlated vacancy and solute diffusion during long-term aging of displacement cascades. The MFs, and their remnants, may continue to grow by both the overlap of additional cascades [59] and by absorbing additional solutes and vacancies arriving by long-range RED. These concepts are schematically illustrated in Fig. 2.28. Simple dispersed barrier dislocation theory predicts that the MF are relatively weak obstacles, thus they would produce hardening in an additive term that increases with the square root of fluence.

Hardening in low Cu RPV steels caused by MF generally decreases with increasing irradiation temperature. The conventional view, reflected in all previous two-feature embrittlement models, has been that MF hardening is independent of flux. A combination of irradiation temperature dependence and flux independence is physically puzzling, since time-temperature kinetics usually go hand in hand. This behavior might be rationalized if an irradiation temperature dependent fraction of primary cascade features transform into MFs that are thermally stable at intermediate to high flux levels. However, to the extent that MFs recover in situ during irradiation, or grow by long range RED, some sensitivity to flux is to be expected. Both in-situ recovery and growth by long-range RED increase with decreasing flux. However, only the latter may be important at very low flux surveillance irradiation conditions. That is, at very low flux almost all the vacancies dissolve anyway; hence, the net hardening increases due to the rearrangement and growth of MF into stronger dislocation obstacles.

Observation of flux effects on MF is also complicated by the fact that the hardening levels are small; hence, it is difficult to establish reliable trends in data that are scattered. Further, it has proven to be difficult to characterize the precise character of MFs in RPV steels. Low-temperature post-irradiation annealing ($T_{ann} = T_i$ to $T_i + 50°C$) recovery measurements have been used to characterize the effects of various irradiation variables on MF hardening [60,61]. These studies clearly showed that MF hardening increases with decreasing irradiation temperature and increasing alloy Ni content. More recently, the presence of Mn and Ni in MF has been shown by combined electrical resistivity–Seebeck coefficient measurements that can be used to track solute (e.g., Mn and Ni) clustering and precipitation [58]. This is illustrated in Fig. 2.29, where $\Delta\sigma_y$ for a Cu-free, ≈ 0.8 wt % Ni, ≈ 1.4 wt % Mn, ≈ 0.005 wt % P alloy (LG) is plotted against measured changes in both the electrical resistivity ($\Delta\rho$) and the Seebeck coefficient (ΔS) for a range of flux, fluence, and irradiation temperatures.

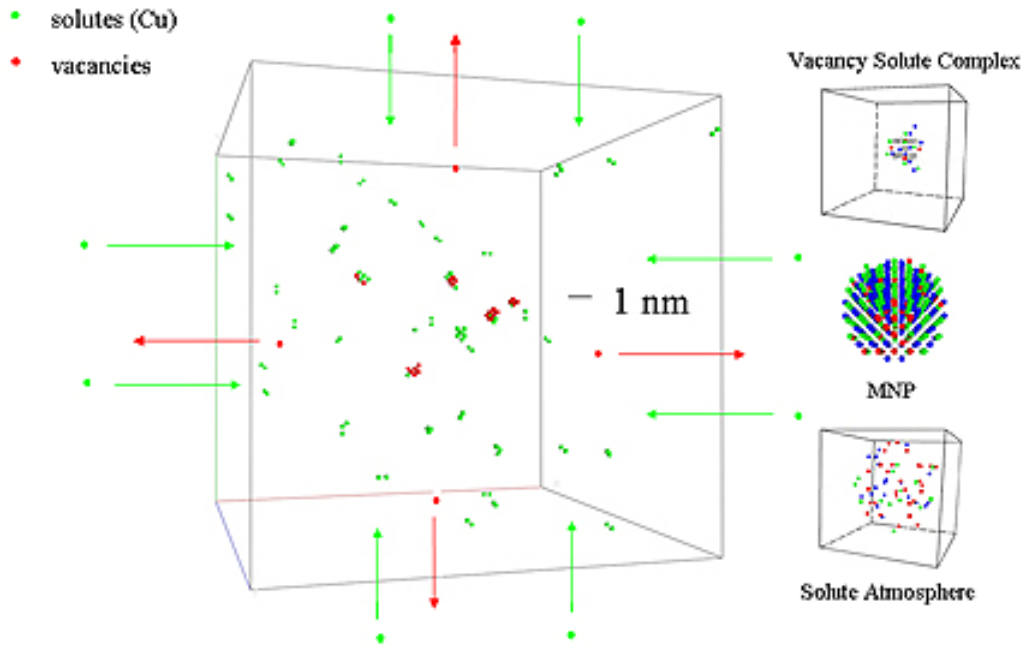

Fig. 2.28. Illustration of vacancy-solute (Cu surrogate) cluster complexes that form in cascades from lattice Monte Carlo simulations and the further evolution of these features by a solute flux from long range RED. The cascade vacancy clusters eventually dissolve and the emitted vacancies migrate to sinks or recombine with SIA. Cascade overlap also plays a role in the MF evolution. The residual features that form in both low-Cu and Cu-bearing steels represent a continuum that includes solute vacancy complexes, solute atmospheres, and MNP - depending on the alloy composition and irradiation conditions.

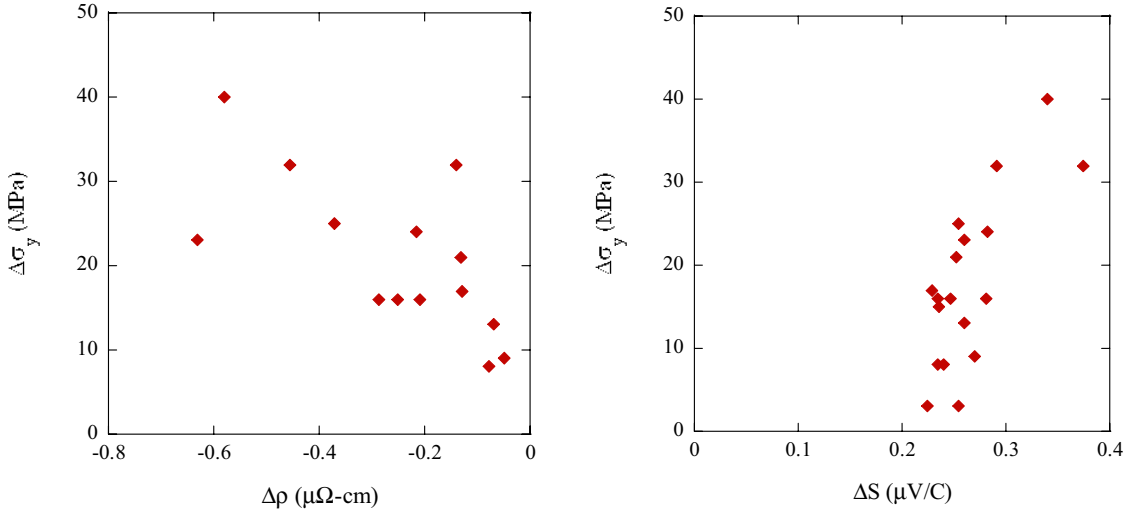

Fig. 2.29. Electrical resistivity and Seebeck coefficient changes in a Cu-free alloy with 0.8 wt % Ni, 1.4 wt % Mn, and 0.005 wt % P irradiated at various fluxes and temperatures over a range of fluence plotted against $\Delta\sigma_y$. These changes can be related to clustering of Mn and Ni.

Additional support for the hypothesis that MF hardening may depend on flux is provided by recent experimental studies that confirmed early model-based predictions that, under some conditions, well-defined Mn-Ni(-Si) late blooming precipitate phases (LBPs) form in both complex pressure vessel type steels and simple model alloys that have very low Cu contents or that are Cu free [50]. For example, LBPs were observed in two high-Ni split melt Cu free model steels after intermediate flux irradiations at 270°C resulting in substantial hardening ranging from 160 to 190 MPa. Smaller volume fractions of similar features have been found in recent SANS studies for a variety of irradiation conditions. The LBPs are precipitates and are distinguished from MNPs by the definition that they do not require significant Cu to form. Taken together, studies of both low Cu and Cu bearing steels suggest that CRPs, MNPs, MFs and LBPs *represent a continuum of radiation-induced nanoscale features*, involving both cascade defect accumulation processes and long-range, dose-rate-dependent RED of solutes leading to cluster growth and precipitation. The effects of flux on RED contributions to MF hardening can also be represented in terms of an effective fluence, $\phi t_e \approx \phi t(\phi_r/\phi)^p$. The IVAR data supporting this conclusion are discussed in Chap. 6.

In summary, MF hardening increases with the square root of fluence and with decreasing irradiation temperature. Higher, Cu, P, Mn and Ni concentrations increase MF hardening. While the conventional view has been that the MF hardening does not depend on flux, both theoretical consideration and new empirical evidence suggest that this may not be true in all situations, especially at low flux.

2.5 Summary and Conclusions

The implications of the overview of embrittlement mechanisms in this chapter can be summarized as follows. Transition temperature shifts are due to irradiation hardening ($\Delta\sigma_y$), primarily produced by nanometer-scale precipitates (CRPs), vacancy-solute complexes (MFs) and alloy phosphide precipitates (PPs). A MF plus CRP two-feature model provides an approximate, but reasonable, formulation for simple, parameterized, analytical equations for fitting the TTS surveillance database. It should be noted, however, that these simplified models can not practically be expected to treat all detailed mechanisms of embrittlement. For example, it would be very difficult to formulate simple analytical models that treat the complexities such as: strengthening superposition from multiple hardening features; the effects of the magnitude of hardening and unirradiated properties on the $\Delta\sigma_y$-TTS relation; the multiple potential roles of P and its synergisms with Cu and Mn; and the detailed kinetics of CRP evolution. In part, the effects of simplifications are mitigated by fitting the TTS models to the surveillance database, which enforces adherence to important data trends, as represented by averaged effective fit parameters. Based on the information presented in this chapter, the following physical trends are expected to appear respectively in the MF and CRP terms of such a simplified TTS model. However, it should be emphasized that all these trends may not be observed in practice, in part due to limitations of both the surveillance database and fitting models.

For the MF term:

- The MF TTS term is expected to increase approximately with the square root of fluence and with decreasing irradiation temperature.
- MF embrittlement in low-Cu and Cu-free steels (< 0.072 wt % Cu) increases with the alloy Mn, Ni, P and Cu contents.
- Large volume fractions of Mn-Ni rich MNPs can form under some conditions in low-Cu and Cu-free steels, and these late-blooming phases produce high levels of hardening.
- The MF contribution in low-Cu steels also appears to depend on flux in a way that can be represented by an effective fluence, $\phi t_e \approx \phi t(\phi_r/\phi)^p$, where ϕ_r is a reference flux and p is a fitting constant.
- The flux dependences of MF and CRP hardening are similar.

For the CRP term:

- The CRP hardening depends on flux due to a solute vacancy-trap-enhanced recombination mechanism.
- The effect of flux depends on the irradiation temperature and flux itself, as well as the alloy composition and microstructure.
- The flux effect can be treated in terms of an effective fluence, $\phi t_e \approx \phi t(\phi_r/\phi)^p$, where ϕ_r is a reference flux and where, in principle, the scaling exponent p depends on flux, irradiation temperature, and alloy composition and microstructure.
- In fitting the TTS database it is a reasonable approximation to treat flux scaling with an effective average p, where p is assumed to be a constant and independent of the irradiation and metallurgical variables.
- Higher flux shifts the CRP TTS curves to higher fluence.
- The maximum, plateau CRP TTS increases with the alloy Cu, Ni, and Mn contents in a way that can be understood and modeled based on fundamental thermodynamic principles.
- Most notably, higher-alloy Mn and Ni increase the precipitate volume fraction, f_p.
- Pre-precipitation limits the maximum effective dissolved Cu prior to irradiation, Cu_{max}, depending on the stress-relief time and temperature and on the alloy composition.
- Best estimates suggest $Cu_{max} \approx 0.25 \pm 0.05\%$ for medium Ni steels and $Cu_{max} \approx 0.30$ wt % (or higher) in high-Ni steels following typical stress relief times around 600°C.
- A threshold Cu content for forming CRPs that contribute to hardening is ≈ 0.05 to 0.09 wt %.
- CRP embrittlement is not athermal and decreases with increasing irradiation temperature.

For P contributions to the TTS:

- Phosphorous also increases embrittlement in low Cu steels, by a variety of mechanisms, including forming phosphide precipitates and enhancing MF contributions.
- The hardening kinetics of phosphide precipitates are expected to be qualitatively similar to that for CRPs.
- The phosphorous contribution to hardening would be expected to saturate at high fluence.
- Strong P-Mn interactions are consistent with the formation of stable Mn_2P and Mn_3P alloy phosphides;
- Phosphorous also affects CRP hardening by increasing the CRP volume fractions (slightly) and number densities (significantly).
- However, several other studies suggest that the effect of P decreases with increasing Cu at and above about 0.1 wt %.
- This negative P-Cu synergism may be due to a combination of strength superposition reductions in the net phosphide contribution to TTS in steels with CRPs, as well as larger reductions in the phosphide TTS itself, compared to the corresponding smaller increases in the CRP contribution.
- Complex P-Cu synergisms are not well understood and may enhance or retard TTS, depending on the combination of other variables.
- It may be necessary to include phosphorous in both the MF and CRP terms or to use a separate phosphorous term in TTS fitting models.

2.6 References

1. Odette, G. R., and G. E. Lucas, *Irradiation Embrittlement of Reactor Pressure Vessel Steels*, EPRI NP 6114, 1989.
2. Eason, E. D., J. E. Wright and G. R. Odette, *Improved Embrittlement Correlations for Reactor Pressure Vessel Steels*, NUREG/CR-6551, U.S. Nuclear Regulatory Commission, Washington, DC, 1998.
3. Odette, G. R., and G. E. Lucas, "Recent Progress in Understanding Reactor Pressure Vessel Embrittlement," *Radiation Effects and Defects in Solids* 144, 189, 1998.
4. Odette, G. R., G. E. Lucas, R. D. Klingensmith, et al., *The Effects of Composition and Heat Treatment on Hardening and Embrittlement of Reactor Pressure Vessel Steels*, NUREG/ CR-6778, U.S. Nuclear Regulatory Commission, Washington, DC, 2003 .
5. Odette, G. R., T. Yamamoto, R. D. Klingensmith, et al., *The Effect of Flux and Irradiation, Temperature on Hardening in RPV Steels*, UCSB-NRC-LR-03/2, 2003 .
6. Odette, G. R., "On the Dominant Mechanism of Irradiation Embrittlement of Reactor Pressure Vessel Steels," *Scripta Met*. 17, 1183, 1983 .
7. Fisher, S. B., and J. T. Buswell, "A Model For PWR Pressure-Vessel Embrittlement", *Int. J. of Pressure Vessels and Piping* 27-2, 91(1988 .
8. Odette, G. R., B. D. Wirth, D. J. Bacon and N. M. Ghoneim, "Multiscale-Multiphysics Modeling of Radiation-Damaged Materials: Embrittlement of Pressure Vessel Steels," *MRS Bulletin* 26, 176, 2001 .
9. Williams, T. J., and D. Ellis, "A Mechanistically-Based Model of Irradiation Damage in Low Alloy Submerged Arc Welds," *Effects of Radiation on Materials: 20th International Symposium*, ASTM STP 1405, ed. S. T. Rosinski et al., American Society for Testing and Materials, West Conshohocken, PA, 8, 2001 .
10. Carter, R.G., and N. Soneda, *Workshop on Dose Rate Effects in Reactor Pressure Vessel Materials*, Electric Power Research Institute Conference Proceedings, EPRI 1006981, CD,, 2002 .
11. Odette, G., R. E. V. Mader, G. E. Lucas, et al., "The Effect of Flux on the Irradiation Hardening and Embrittlement of Pressure Vessel Steels", *Effects of Radiation on Materials: 16th International Symposium*, ASTM-STP 1175, ed. A.S. Kumar et al., American Society for Testing and Materials, West Conshohocken, PA, 373, 1994 .
12. Odette, G. R., "Modeling of Irradiation Embrittlement in Pressure Vessel Steels", *Irradiation Effects on Pressure Vessel Steels*, IAEA IRRWG-LMNPP98-3, International Atomic Energy Agency, Vienna, Austria, 438, 1998 .
13. Odette,G. R., T. Yamamoto, and R. D. Klingensmith, "On the Effect of Dose Rate on Irradiation Hardening of RPV Steels," *Phil. Mag.* 85, 2005 779.
14. English, C.A., W. L. Server, and S. T. Rosinski, "Critical Review of Through-Wall Attenuation of Mechanical Properties in RPV Steels," *Effects of Radiation on Materials: 21st International Symposium*, ASTM STP 1447, ed. M. L. Grossbeck et al., American Society for Testing and Materials, West Conshocken, PA, 221, 2004 .
15. Langer, R., R. Bartsch and G. Nagel, "Irradiation Behavior of Submerged Arc Welding Materials with Different Copper Content," *Effects of Radiation on Materials: 19th International Symposium*, ASTM STP 1366, ed. M. L. Hamilton et al., American Society for Testing and Materials, West Conshocken, PA, 2000 235.

16. R. B. Jones and T. J. Williams, "The Temperature Dependence of Radiation Hardening and Embrittlement on Irradiation Temperature," Effects of Radiation on Materials: 17th International Symposium, ASTM STP 1270, ed. D. S. Gelles et al., American Society for Testing and Materials, West Conshocken, PA, 569,1996.

17. Odette, G. R., and G. E. Lucas, "Embrittlement of Nuclear Reactor Pressure Vessels," *J. of Metals*, 18, July 2001.

18. G. R. Odette, G. E. Lucas and R. D. Klingensmith, "The Influence of Metallurgical Variables on the Temperature Dependence of Irradiation Hardening in Pressure Vessel Steels," *Effects of Radiation on Materials: 17th International Symposium*, ASTM STP 1270, ed. D. S. Gelles et al., American Society for Testing and Materials, West Conshocken, PA, 606, 1996.

19. McElroy, R. J., and A. L. Lowe, Jr., "Irradiation Embrittlement Modeling of Linde 80 Weld Metals," *Effects of Radiation on Materials: 17th International Symposium*, ASTM STP 1270, ed. D. S. Gelles et al., American Society for Testing and Materials, West Conshocken, PA, 68, 1996.

20. Lucas, G. E., G. R. Odette, P. M. Lombrozo and J. W. Sheckherd, "Effects of Composition, Microstructure, and Temperature on Irradiation Hardening of Pressure Vessel Steels," *Effects of Radiation on Materials: 12th International Symposium*, ASTM STP 870, ed. F. A. Garner et al., American Society for Testing and Materials, West Conshocken, PA, 900, 1985.

21. Bolton, C. J., J. T. Buswell, R. B. Jones, R. Mskovic, and R. H. Priest, "The Modeling of Irradiation Embrittlement in Submerged Arc Welds, *Effects of Radiation on Materials: 17th International Symposium*, ASTM STP 1405, ed. D. S. Gelles et. al. American Society for Testing and Materials, West Conshohocken, PA, 103, 2001.

22. Williams, T. J., D. Ellis, C. A. English, and J. Hyde, "A Model of Irradiation Damage in High Nickel Submerged Arc Welds," *Int. J. of Pressure Vessels and Piping* 79, 964, 2002.

23. Odette, G. R., P. M. Lombrozo and R. A. Wullaert, "Relationship Between Irradiation Hardening and Embrittlement of Pressure Vessel Steels," *Effects of Radiation on Materials: 12th International Symposium*, ASTM STP 870, ed. F. A. Garner et al., American Society for Testing and Materials, West Conshocken, PA, 840, 1985.

24. Stoller, R. E., G. R. Odette and B. D. Wirth, "Primary Damage Formation in bcc Iron," *J. of Nuc. Mater.*, 251, 49, 1997.

25. Mansur, L. K., A. D. Brailsford and W. G. Wolfer, "On The Meaning Of Sink Capture Efficiency and Sink Strength for Point-Defects," *J. Nuc. Mater.*, 105, 1982.

26. Wirth, B. D., and G. R. Odette, "Kinetic Lattice Monte Carlo Simulations of Cascade Aging in Iron and Dilute Iron-Copper Alloys," *Microstructural Processes in Irradiated Materials*, MRS Soc. Symp. Proc. 540, ed. S. J. Zinkle et. al., Materials Research Society, Warrendale, PA, 637, 1999.

27. Wirth, B. D., "On the Character of Nano-Scale Features in Reactor Pressure Vessel Steels Under Neutron Irradiation," PhD. Thesis UC Santa Barbara, 1998.

28. Odette, G. R., and B. D. Wirth, "A Computational Microscopy Study of Nanostructural Evolution in Irradiated Pressure Vessel Steels," *J. Nuc. Mat.* 251, 157, 1997.

29. Odette, G. R., C. L. Liu, and B. D. Wirth, "On the Composition and Structure of Naonoprecipitates in Irradiated Pressure Vessel Steels," *Microstructural Evolution During Irradiation*, MRS Symp. Proc. 439, ed. I. M. Robertsonet. al. Materials Research Society, Warrendale, PA, 457, 1997.

30. Odette, G. R., "Radiation Induced Microstructural Evolution in Reactor Pressure Vessel Steels," *Microstructural Evolution During Irradiation*, Mat Res. Soc. Symp. Proc. 373, ed. I. M. Robertson et. al., Materials Research Society, Warrendale, PA, 137, 1995.

31. Liu, C. L., G. R. Odette, B. D. Wirth, and G. E. Lucas, "A Lattice Monte Carlo Simulation of Nanophase Compositions and Structures in Irradiated Pressure Vessel Fe-Cu-Ni-Mn-Si Steels," *Mat. Science & Engin. A-Struct.* 238-1, 202, 1997.

32. Wirth, B. D., G. R. Odette, W. A. Pavinich, G. E. Lucas, and S. Spooner, "Small Angle Neutron Scattering Study of Linde80 RVSP Welds," *Effects of Radiation on Materials: 18th Symposium*, ASTM STP 1325, ed. R. K. Nanstad et. al., American Society for Testing and Materials, West Conshohocken, PA, 102, 1999.

33. Odette, G. R., and G. E. Lucas, "The Effect of Nickel in Irradiation Hardening of Pressure Vessel Steels," E*ffects of Radiation on Materials: 14th International Symposium*, ASTM STP 1046, ed. N. H. Packan et al., American Society for Testing and Materials, West Conshocken, PA,, 323, 1990.

34. Miller, M. K., and M. G. Burke, "An APFIM Survey of Grain Boundary Segregation and Precipitation in Irradiated Pressure Vessel Steels," *Effects of Radiation on Materials: 16th International Symposium*, ASTM STP 1175, ed. A. S. Kumar et al., American Society for Testing and Materials, West Conshocken, PA, 492, 1994.

35. Nicol, A. C., M. L. Jenkins, and M. A. Kirk, "Matrix Damage in Iron," *Microstructural Processes in Irradiated Materials-2000*, MRS Symp. Proc. 650, ed. G. E. Lucas et. al., Materials Research Society, Warrendale, PA, R1. 3, 2001.

36. Jumel, S., C. Domain, J. Ruste et al., "Simulation of Irradiation Effects in Reactor Pressure Vessel Steels: The Reactor for Virtual Experiments, REVE Project," *J. Test. Eval.*, 30-1, 37, 2002.

37. Martin, J. W., *Micromechanisms in Particle-Hardened Alloys*, Cambridge University Press, 1980

38. Bacon, D. J., and Y. N. Osetsky, "Hardening Due to Copper Precipitates in α-iron Studied by Atomic-Scale Modeling," *J. Nuc. Mat.* 329-333, 1233, 2004.

39. Russell, K. C., and L. M. Brown, "A Dispersion Strengthening Model Based on Differing Elastic Moduli Applied to the Iron-Copper System," *Acta Met.*, 20, 969, 1972.

40. Foreman, A. J. E., and M. J. Malkin, "Dislocation Movement Through Random Arrays of Obstacles," *Phil. Mag.* 14, 911, 1966.

41. Jumel, S., J. C. Van Duysen, J. Ruste and C. Domain, "Interactions Between Dislocations and Irradiation-Induced Defects in Light Water Reactor Pressure Vessel Steels," *J. Nuc. Mat.*, 346, 79, 2005.

42. Odette, G. R., B. D. Wirth, and T. Yamamoto, unpublished analysis of a large body of recent SANS data.

43. Salje, G., and M. Feller-Kneipmeier, "The Diffusion and Solubility of Copper in Iron," *J. Appl. Phys*., 48-5, 1833, 1977.

44. Marian, J., B. D. Wirth G,R, Odette et al, "Cu Diffusion in Alpha-Fe: Determination of Solute Diffusivities using Atomic-Scale Simulations," *Computational Materials Science* 31:3-4, 347, 2005.

45. le Claire, A. D., "Solvent Self-Diffusion in Dilute B. C. C. Solid Solutions," *Phil. Mag.* 172, 819, 1970.

46. Lê, T. N., Barbu, A., Liu, D., and Maury, F., "Precipitation Kinetics of Dilute Fe-Cu and Fe-Cu-Mn Alloys Subjected To Electron-Irradiation," *Scripta Metall. et Mater*. 26, 771, 1992.

47. Moslang, A., E. Albert, E. Recknagel and A. Weidinger, "Interaction of Vacancies With Impurities in Iron," *Hyperfine Interactions*, 15/16, 409, 1983.

48. Miller, M. K., K. F. Russell, G. R. Odette and D. Klingensmith, *Precipitation in Thermally Aged and Neutron Irradiated Fe-Cu and Fe-Cu-Mn Model Alloys*, ORNL/NRC/LTR-03/01, 2003 .

49. Odette, G. R., G. E. Lucas and D. Klingensmith, "Anomalous Hardening in Model Alloys and Steels Thermally Aged at 290°C and 350°C: Implications to Low Flux Irradiation Embrittlement," *Effects of Radiation on Materials: 18th International Symposium*, ASTM STP 1325, ed. R. K. Nanstad et al., American Society for Testing and Materials, West Conshocken, PA, 1089, 1999.

50. Odette, G. R., T. Yamamoto, and B. D. Wirth, "Late Blooming Phases and Dose Rate Effects in RPV Steels: Integrated Experiments and Models," *Proceedings of the Second International Conference on Multiscale Materials Modeling*, ed. N. M. Ghoniem, Univeristy of California, 355, 2004.

51. Machlin, E. S., *An Introduction to Thermodynamics and Kinetics Relevant to Materials Science*, 2nd ed., Giro Press, Croton-on Hudson, NY, 1999.

52. Jones, R. B., and J. T. Buswell, "The Interactive Roles of Phosphorus, Tin and Copper in the Irradiation Embrittlement of PWR Pressure Vessel Steels," *Environmental Degradation of Materials in Nuclear Power Systems – Water Reactors*, Proceedings of the 3rd International Symposium, ed. G. T. Theus et al., Metallurgical Society, Warrendale, PA, 111, 1988.

53. Hawthorne, J. R., *Exploratory Studies of Element Interactions and Composition Dependences in Radiation Sensitivity Development*, NUREG/CR-4437,U. S. Nuclear Regulatory Commission, Washington, DC, 1985.

54. *Smithells Metals Reference Book 8th Edition*, ed. E. W. F. Gale and T. C. Totemeir, ASM/Elsevier, 2004.

55. Miller, M. K., K. Russell, and G. R, Odette, "Clustering and Precipitation in Low Copper and Copper Free Steels and Model Alloys," International Field Emission Symposium, 2006.

56. English, C. A., S. R. Ortner, G. Gage, W. L. Server and S. T. Rosinkski, "Review of Phosphorus Segregation and Intergranular Embrittlement in Reactor Pressure Vessel Steels," *Effects of Radiation on Materials: 20th International Symposium*, ASTM STP 1405, ed. S. T. Rosinski et al., American Society for Testing and Materials, West Conshohocken, PA, 151, 2001.

57. Nanstad, R. K., D. E. McCabe, M. A. Sokolov, C. A. English, and S. R. Ortner, "Investigation of Temper Embrittlement in Reactor Pressure Vessel Steels Following Thermal Aging, Irradiation, and Thermal Annealing," *Effects of Radiation on Materials: 20th International Symposium,* ASTM STP 1405, ed. S. T. Rosinskiet. al., American Society for Testing and Materials, West Conshohocken, Pennsylvania, 2001.

58. Odette, G. R., and C. Cowan, "Use of Combined Electrical Resistivity and Seebeck Coefficient Measurements to Characterize Solute Redistribution Under Irradiation and Thermal Aging," *Proceedings of the 10th International Symposium on Environmental Degradation of Materials in Light Water Reactors*, Ed. G. S. Was et. al., NACE, CD, 2001.

59. Wirth, B. D., G. R. Odette and R. E. Stoller, "Recent Progress Toward an Integrated Multiscale-Multiphysics Model of Reactor Pressure Vessel Embrittlement," Multiscale Modeling of Materials, *MRS Soc. Symp. Proc.* 677, ed. V. Bulatov et. al., Materials Research Society, Warrendale, PA, AA5. 2, 2001.

60. Mader, E., G. E. Lucas, and G. R. Odette, "The Effects of Metallurgical and Irradiation Variables on the Postirradiation Annealing Kinetics of Pressure Vessel Steels," *Effects of Radiation on Materials: 15th International Symposium*, ASTM STP 1125, ed. R. E. Stoller et al., American Society for Testing and Materials, West Conshocken, PA, 151, 1992.

61. Mader, E. V., "Kinetics of Irradiation Embrittlement and the Post-Irradiation Annealing of Nuclear Reactor Pressure Vessel Steels," PhD. Thesis, UC Santa Barbara, 1995.

3. Transition Temperature Shift (TTS) Database

This chapter identifies the main sources of data utilized in this report and describes how the datasets used for model calibration and validation were prepared. The key databases include the Power Reactor Embrittlement Database (PR-EDB), which is an archive of information from U.S. reactor surveillance programs, the Irradiation Variable (IVAR) data, which are results from a major research program on irradiation effects, and the TTS database used for the analysis and modeling reported in Chaps. 4, 5, and 7. The TTS analysis database was developed from the PR-EDB and later surveillance reports as described in Sects. 3.3 and 3.4. (See Appendix B, "Irradiation Variable [IVAR] Program Data Base," and Appendix C, "Analysis Data Base.")

3.1 Power Reactor Embrittlement Database (PR-EDB)

The PPR-EDB as reported in NUREG/CR-4816 [1] is an archival database that includes considerable detail on surveillance capsules that have been irradiated in U.S. power reactors. It is a relational database containing many linked attributes associated with surveillance data. In many cases, the PR-EDB includes multiple entries when data are presented in multiple sources, and generally more complete and detailed information than is needed specifically for embrittlement correlation development. Version 2 of the PR-EDB through Update 12[1] was a primary source of data for the analysis and for cross-checking, identifying, and resolving discrepancies. Input data for the PR-EDB come from various surveillance reports, data logs, and official memorandums from nuclear power plants. Raw data files are constructed, and the input data are subjected to a rigorous quality assurance review prior to inclusion in the database. The data are categorized into (1) material history, (2) radiation environments, and (3) mechanical test results, along with the associated detailed references. The ORNL Radiation Safety Information Computational Center (865-574-6176, pdc@ornl.gov) is responsible for NRC software distribution, including the distribution of PR-EDB Version 2.

Newer results not yet in Version 2 (Update 12) to the PR-EDB were extracted in 2003 and 2004 from industry reports [2,3] and individual surveillance capsule reports. The latter reports were identified and provided by C. Santos, who searched the ADAMS document-indexing facilities at the NRC through about March 2004.

3.2 Guidance from Research Programs (IVAR Database)

The Irradiation Variable (IVAR) database [4] is mentioned at various points in this report, particularly in Chap. 6, where it is directly compared with the transition temperature shift (TTS) model calibrated to the surveillance database. The IVAR materials, database, irradiations and testing program are described in some detail in Sect. 6.1; the IVAR database results from an extensive program, producing a large set of data from controlled, replicated experiments, using many different materials, including some that are typical of commercial RPV materials and others that have been remelted and heat-treated in order to explore individual and combined material variable trends. The key irradiation exposure variables were varied to clarify effects of fluence, flux, and irradiation temperature.

The significance of the IVAR database is that it provides independent evidence of variable trends, in many cases with less uncertainty, without confounding effects from other variables and with better signal to noise ratios than can the surveillance data. Some preliminary IVAR results were available and were used for modeling insight as the TTS model was developed, and additional details have since emerged from the comparison of the TTS model with the IVAR data presented in Chap. 6. Although some of the theory in Chap. 2 and some trends from IVAR data and other sources were used for insight, the TTS

[1]Update 12 to Version 2 of the PR-EDB was provided to the USNRC in 2004.

model described in Chap. 4 was calibrated solely on the surveillance database, so the comparison with IVAR data in Chap. 6 provides an independent check on predictive capability for data not used in fitting.

3.3 Development of Charpy TTS Estimates

The PR-EDB includes reported transition temperature shifts (TTSs) and upper shelf energy (USE) drops taken directly from surveillance reports. However, multiple entries appear for some heats, making it unclear which values to use. Additionally, the reported values were determined using various techniques over the years, including visual inspection of raw Charpy plots and various fitting techniques. To ensure that mean estimates of shift and drop determined on a consistent, repeatable basis were used, a computer program, FITCV, was written to fit the raw Charpy datasets from PR-EDB or other sources and to compute TTS and USE based on those fits. FITCV was first used and described in Sect. 2 of NUREG/CR-6551 [5] and is only summarized here. The same program has been used to estimate TTS for the additions to the database in 2000 and 2003–2004, so all shifts used in the present analysis are self-consistent and consistent with those used in the Draft 2000, ASTM E900-02 and NUREG/CR-6551 models.

The general approach in FITCV is to fit modified hyperbolic tangent (tanh) curves to each set of raw Charpy data from the same heat of material tested in the same orientation and with the same neutron exposure. The program evaluates the two tanh fitting forms given by Eqs. (3-1) and (3-2) (and an exponential form if no upper shelf data are available), each calibrated by two independent least squares algorithms as an automatic check on convergence. The unirradiated and irradiated curves for the same heat and orientation are matched, and shifts and drops are computed from the difference of the fitted curves. The program chooses the best fit (minimum sum of squared residuals) automatically, but plots of the data and fits are also printed, showing the choice and the alternatives, and the choices are confirmed by individual review of the plots.

The general symmetric tanh model form often used for modeling Charpy curves [6] is one of the options fitted by FITCV:

$$C_v = a_3 \tanh\left(\frac{T - a_1}{a_2}\right) + (a_3 + LSE) \tag{3-1}$$

where

C_v = Charpy impact energy
a_3 = fitting parameter equal to $(USE - LSE)/2$
T = test temperature
a_1 = fitting parameter equal to temperature at the inflection point of the fitted curve
a_2 = fitting parameter related to the slope of the transition region
LSE = lower shelf energy; LSE = 1.28 ft-lbs (see Appendix B in [5]).

The symmetric tanh form in Eq. (3-1) does not do a good job of fitting the Charpy data for sets of data that exhibit an abrupt transition from the lower shelf and a more gradual transition to the upper shelf, which frequently occur. In such sets, the symmetric tanh curve does not agree well with the data in the lower transition region, near the 30 ft-lb (41J) temperature (T_{30}), which is the part of the curve needing the best possible fit because it is where the irradiation-induced shift is calculated. An asymmetric form of the tanh model fits the data better than the usual tanh model in those cases.

The form of the asymmetric tanh is:

$$C_v = c_3 \tanh\left(\frac{T - c_1}{c_4 T + c_2}\right) + (c_3 + LSE) \tag{3-2}$$

where c_1, c_2, and c_3 are analogous to a_1, a_2, a_3 in Eq. (3-1), and c_4 is a positive fitting parameter causing the hyperbolic tangent fit to have a more sharply curved transition in the lower region than in the upper region. The examples in Fig. 3.1 show that the asymmetric tanh is often able to come closer to the data than the symmetric tanh fit in the lower transition region. However, the symmetric tanh usually provides a better fit to sets with limited upper shelf data.

Note that Eq. (3-1) is a special case of Eq. (3-2), where $c_4 = 0$; hence, given sufficient data, Eq. (3-2) always fits the lower transition region at least as well as Eq. (3-1). Thus most of the shifts in the analysis database described in this report use Eq. (3-2).

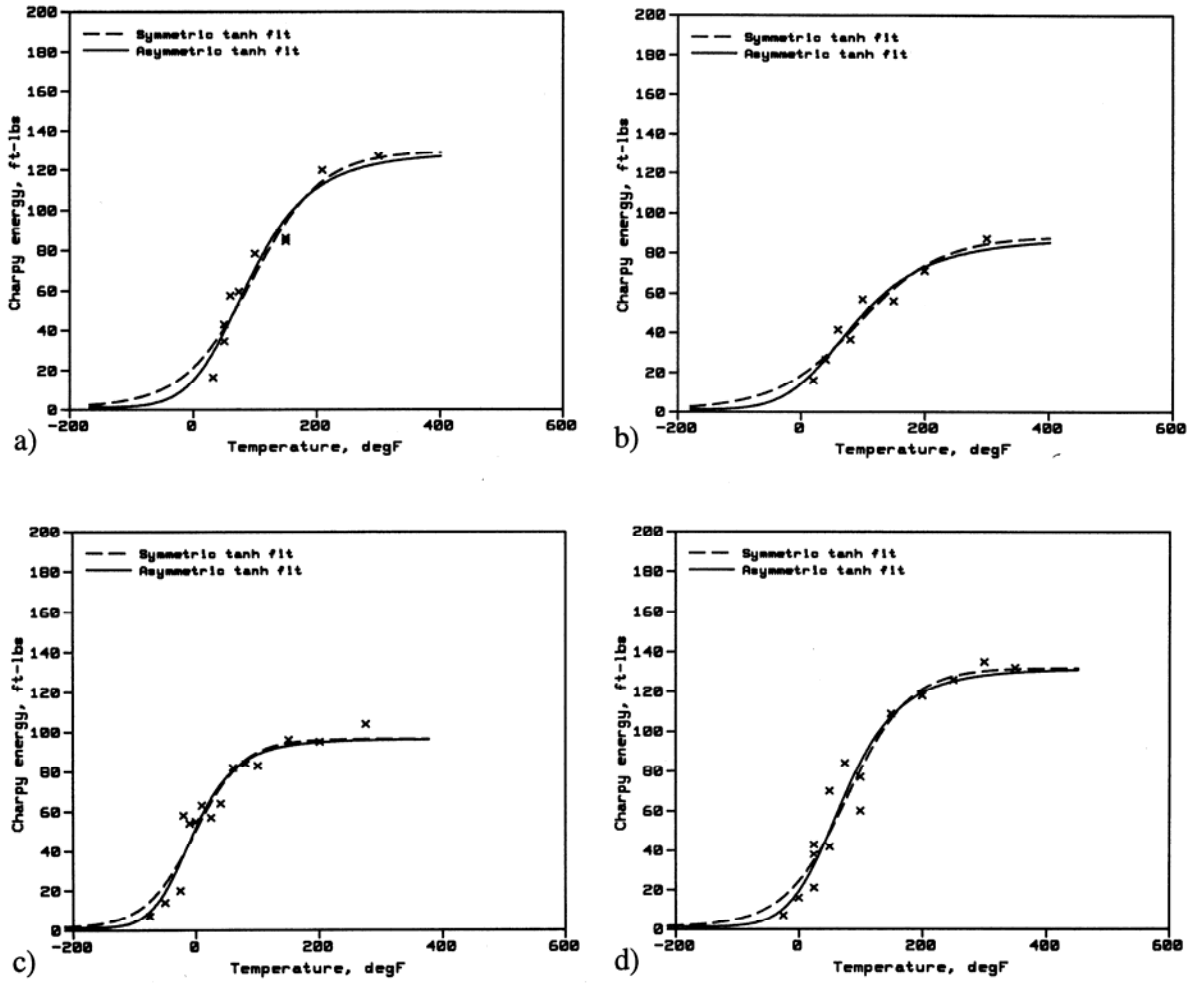

Fig. 3.1. Examples of symmetric and asymmetric tanh curve fits (from Fig. 2.1 in Eason, E. D., J. E. Wright, and G. R. Odette, *Improved Embrittlement Correlations for Reactor Pressure Vessel Steels*, NUREG/CR-6551, U.S. Nuclear Regulatory Commission, Washington, D.C., 1998).

Most sets of raw Charpy data include only specimens from a single plant that are either unirradiated or irradiated in a single capsule. However, in the case of unirradiated standard reference materials, raw Charpy data associated with different plants were pooled together, so that one unirradiated C_v vs. T curve was fitted for each standard reference material (SRM). The basis for this approach is that the unirradiated SRMs are the same three heats, regardless of which plant they were sent to, so combining the data from all plants gives the best average characterization of the heat in the unirradiated condition. This heat-based approach may have inadvertently increased the scatter for one of the SRMs, as discussed in Sect. 4.3.5 of this report, although it did not affect the correlation for plant materials.

Plate and forging materials were often tested in two orientations, TL and LT [7]. The shift for each orientation is about the same, although the unirradiated and irradiated values of T_{30} are not. The two orientations contribute independent measurements of unirradiated and irradiated T_{30}, so they were treated as separate observations in the statistical analysis. The same approach was used in calibrating earlier surveillance models [5,8–10].

3.4 Analysis Database

The term "analysis database" is used to denote the information used for analysis, model development, and calibration. It is a subset of the more complete details available in PR-EDB and surveillance reports. The analysis database is in the form of an Excel spreadsheet where each row is an individual shift observation for one heat and the columns contain the details that are used for identifying that shift and all the independent variables used for developing the embrittlement shift correlation. The analysis database includes data on surveillance welds, plates, and forgings, but heat-affected-zone data (which are in PR-EDB) are not included. This exclusion was deliberate and was made in conjunction with the ASTM E10.02 committee because of concerns regarding the heat-affected zone results. The same heat-affected zone exclusion was invoked for the same reasons in the earlier modeling efforts back to NUREG/CR-6551.

The analysis database used in the current modeling effort is contained in Appendix C of this report and is the result of the most recent cycle of updating, and was largely derived from the PR-EDB [1] as supplemented by recent capsule reports and corrections by members of the ASTM E10.02 committee. The steps in the updating process were (1) use the latest version of the PR-EDB (Version 2, Update 12), (2) search the available NRC documents for more recent surveillance reports, (3) tabulate and submit the extracted data for detailed review by the ASTM E10.02 committee in meetings held in January and June 2004, and (4) collaborate with Jy-An Wang of ORNL regarding data verification.

3.4.1 Database for Developing the Matrix Feature (MF) Term

The July 16, 2004 analysis database file, DupsDiscreps7-04.xls (which contains Version 7-04 of the data), was the starting point for the initial matrix feature (MF) modeling, although it was revised before that round of modeling was complete. The only result presented in this report that came from Version 7-04 is the analysis of the threshold separating low-Cu and high-Cu subsets. All other results presented in this report are from the database in file TTSDatabase8-04.xls (Version 8-04 of the data), completed August 23, 2004. Extensive comments are provided in TTSDatabase8-04.xls documenting the detailed changes to the data, including those made between Version 7-04 and Version 8-04. The main difference between the two databases is that some additional low-Cu points are included in Version 8-04. This difference arose because there were unknown values of irradiation temperature (T_i) that initially eliminated nine points from Vogtle unit 2, all of which are at low Cu. A value of T_i was provided for those points before completing Version 8-04 of the database, and they were included for all subsequent modeling work. The omitted points do not affect the threshold Cu level determined in the analysis below because the Vogtle 2 Cu values are not near the threshold.

Preliminary analysis and modeling using the Version 7-04 dataset also identified anomalies in composition and apparent low-Cu outliers (see Appendix E). Requests were made to members of the ASTM E10.02 committee to check the unusual and questionable points. The responses from committee members included revised values of S for the plate and welds from San Onofre Units 2 and 3, which were incorporated into the Version 8-04 database. Two of the Chauvenet outlier points identified in low-Cu materials are from weld WFA201, for which the unusually low Mo values (lowest in the database) were reviewed and confirmed. Another outlier had the largest negative shift (−35°F) in the database; possible reasons for negative shifts include incorrect values of unirradiated T_{30} and fitting anomalies in the irradiated Charpy data. The four low-Cu outliers relative to the preliminary model remained Chauvenet outliers relative to the final model presented below. The revised PWR low-Cu fitting set contains 219 points after the nine VO2 data points were added and the four outliers were removed.

3.4.2 Database for Developing the Copper-Rich Precipitate (CRP) Term

The Version 8-04 database (August 2004) was used for the preliminary copper-rich precipitate (CRP) term modeling and for all of the final models presented here (both MF term and CRP term). The database incorporates the additional data, corrections, and low-Cu outlier deletions made during the preliminary low-Cu analysis discussed in Sect. 3.4.1. Additionally, the high-Cu Chauvenet outliers identified in the NUREG/CR-6551 and the July 2000 modeling efforts [5,8] were still Chauvenet outliers and were removed, along with three points with unusual irradiation conditions and one point that was identified by Chauvenet analysis but also reflects unusual irradiation conditions. The Version 8-04 database is given in Appendix C, which is a CD containing the electronic file TTSDatabase8-04R1.xls. The details of all points removed as outliers or anomalies are in Appendix E.

Previous modeling efforts had identified issues related to the SRM or correlation monitor data. Three SRM plates, referred to as ASTM, HSST-01, and HSST-02, are included in U.S. commercial reactor surveillance programs, each of which has been irradiated in many reactors. All three are in the high-Cu category (Cu > 0.072 wt %). The first modeling issue with the SRMs is that they unbalance the database for modeling heat chemistry effects because a large fraction of all the available surveillance data comes from these three heats, which are similar in composition except for Ni. A second issue is that including them in one or the other group of plate data can affect the results for those groups [note that plates in Combustion Engineering (CE)-manufactured vessels and non-CE-manufactured vessels are separated because they have significantly different shifts]. Furthermore, grouping the SRMs with either the CE or non-CE plate groups cannot be justified because in fact the three plates are not part of actual plant pressure vessels. A third issue is that the heat treatment of the plates may differ somewhat from plates that were welded into vessels and then postweld heat treated. Finally, concerns have been expressed for Plate HSST-02 because the unirradiated T_{30} value used in the analysis database (which is an average of values from several sources) may not be representative of the samples sent to some specific plants due to inhomogeneity of that plate. An error in unirradiated T_{30} would show up as a consistent offset between the model and measured shift TTS for that plate over a range in fluences. Such errors are of less concern for plates with an average amount of available data, but they could bias the correlation if the plate in question contributes much more data to the fit than most plates, as would be the case with HSST-02.

To address the SRM issues, the data on standard reference materials were initially removed from the high-Cu dataset, and a randomly selected subset of SRM data was added back into the calibration and validation datasets as described in the following paragraphs. The objective was to sample the SRMs to obtain a similar number of shifts as in the typical surveillance heats from plant vessels (usually two to five shifts in each orientation or four to ten shifts total for each plate or forging heat chemistry). Without such sampling, the SRMs would get undue weight in the fit, and the effects of the SRM chemistry or of uncertainties in unirradiated T_{30} would be magnified. The sampling plan shown in Table 3.1 was used.

Table 3.1. Sampling of standard reference material data

Heat ID	TL or LT	Plant type	Total shifts available	Sample size	
				Calibration set	Validation set
SASTM	LT	PWR	21	5	1
SASTM	LT	BWR	1	1	0
SASTM	TL	PWR	4	4	0
SHSS01	LT	PWR	17	5	1
SHSS02	LT	PWR	61	5	1
SHSS02	TL	PWR	1	1	0
SHHS02	TL	BWR	2	2	0
Total			107	23	3

The random sampling of each of the three heats in the LT orientation was performed by first listing the data by increasing exposure time, assigning a uniformly distributed random number between 0 and 1 to each shift, then dividing the data on each heat into five subsets. For example, the SASTM LT PWR data were divided into five subsets, with the five lowest-time shifts in the first subset, the five next lowest-time shifts in the next subset, and so on up to the four highest time shifts in the last subset. Then one shift was picked from each of the five subsets by taking the shift in that subset with the smallest random number. Because the numbers were assigned randomly, it would also be random which shift would have the smallest random number. The choice of the smallest random number is arbitrary; any other unbiased method of picking one number (e.g., the largest random number, the random number nearest 0.5) should work as well. This procedure ensured that there would be five shifts, including at least one with high, medium, and low exposure time, from each SRM heat. All shifts from the heat/orientation combinations with fewer than five shifts (e.g., SASTM TL) were included in the calibration set without sampling.

The total number of SRM shifts after sampling is 23 in the calibration set, so a 10% validation sample should have no more than 3 shifts. The three validation shifts were selected by picking the shift in each heat in the LT orientation with a random number nearest to an arbitrary number, in particular, 0.55. Without the sampling, the three SRM heats would have contributed a total of 104 shifts to the PWR high-Cu dataset and 3 shifts to the BWR high-Cu dataset, amounting to over 18% of all the available high-Cu PWR data. With the sampling, the 3 SRM heats contribute a more reasonable 23 out of 485 shifts (less than 5%) in the PWR high Cu dataset.

It should be noted that a different random sample of SRMs could produce slightly different results, but any such differences would be expected to affect mainly the SRM coefficient. Any difference in the SRM coefficient would also be small, based on the fact (shown in Sect. 4.3.5 and Fig. 4.12) that all SRM data, including points that are not included in the calibration and validation samples, are reasonably consistent with the model and generally within the 5% and 95% bounds estimated for plate materials. The effect of a different SRM sample on the other parts of the embrittlement shift model would be negligible for several reasons. First, the number of points with the SRM chemical compositions would be unchanged in a different sample, and the same chemistry is used for all shifts from each of the three heats; hence there would be no change in chemistry input to the model. Second, the sample of SRM data is less than 5% of the calibration data, so since they are a small subset and in reasonable agreement with the model, sampling the SRM data differently cannot have much effect. Finally, the SRM sample only affects the CRP term, since the materials are all high Cu, and the SRM heats have their own CRP coefficient specifically so that they cannot bias other parts of the model.

3.4.3 Calibration and Validation Datasets

After the Chauvenet outliers, unusual irradiation points, and SRMs were removed, the database was partitioned into calibration and validation sets. The split was made on all remaining data, including PWR and BWR, with both high Cu (Cu > 0.072 wt %) and low Cu (Cu ≤ 0.072 wt %). The validation set is nominally 10% of the data, selected randomly by assigning uniform random numbers between 0 and 1, then selecting the data with random numbers in the range 0.45 to 0.55 (the middle tenth). The choice of the middle tenth was arbitrary; any other arbitrarily-selected tenth should work as well because the random numbers are approximately uniformly distributed. The data not selected in the process became the 90% calibration set. The SRM samples defined in Table 3.1 were then added back into the appropriate calibration and validation sets.

As shown in Table 3.2, the splits in the PWR datasets have nearly the desired 90% : 10% proportions, as does the split in the BWR high-Cu dataset. The BWR low-Cu set is really too small for the random sampling to give the desired proportions. (There should be two or three points in the BWR low-Cu validation set; random sampling produced only one.) However, even if the ideal 10% fraction were selected, the BWR low-Cu validation set would be too small.

Table 3.2. Distribution of data by dataset (including SRM samples)

Dataset[a]	Total shifts available	Sample size (%)	
		Calibration set	Validation set
PWR, high Cu	485	440 (91%)	45 (9%)
PWR, low Cu	219	196 (89%)	23 (11%)
BWR, high Cu	124	113 (91%)	11 (9%)
BWR, low Cu	27	26 (96%)	1 (4%)
Total	855	775	80

[a]High Cu: > 0.072 wt %; low Cu: ≤ 0.072 wt %.

A different random partitioning of the data into calibration and validation sets would be expected to make little or no difference in the results. The reason is that all the data, both calibration and validation sets, are reasonably consistent with the model as shown in Table 4.2 and in Figs. 4.8, 4.10, and 4.11. The greatest possible change in the calibration dataset would come from replacing 1/9 of the calibration points with the 10% validation set (any other change would reuse more than 8/9 of the calibration set). There is no significant difference between the calibration and validation sets as measured by the residuals relative to the model, (see Table 4.2) so replacing 1/9 of the calibration set by the validation data should have little or no effect on the model.

3.4.4 Range of Data by Independent Variable

The independent variables used in the TTS model, together with the range and mean value of each variable, are shown in Table 3.3. An additional independent variable not listed in Table 3.3 is product form, which can take on the values forging, plate (in CE manufactured vessels or other vessels), weld (Linde 80, Linde 1092, or other), and standard reference material (SRM). Note that three exposure variables, fluence, time-averaged flux, and effective full power exposure time, are mathematically related such that any two of the three can be considered independent variables for modeling; the two that are used in the model given in Chap. 4 are fluence and flux.

The statistics in Table 3.3 are based on 855 datapoints, including all calibration and validation data, both PWR and BWR. Only the SRM data that were included in either calibration or validation sets have been included; there are additional SRM data that were not in those sets. Adding in the rest of the SRM

Table 3.3. Independent variables in the embrittlement shift model and their ranges and mean values over all calibration and validation data (855 datapoints)

Variable	Description	Range	Mean
Cu	Copper content (wt %)	0.01–0.41	0.136
Mn	Manganese content (wt %)	0.58–1.96	1.300
Ni	Nickel content (wt %)	0.044–1.26	0.565
P	Phosphorous content (wt %)	0.003–0.031	0.0119
ϕt	Neutron fluence, E > 1 MeV (n/cm^2)	9.26×10^{15}–7.13×10^{19}	6.50×10^{18}
ϕ	Neutron flux, E > 1 MeV (n/cm^2/s)	1.81×10^{8}–9.71×10^{11}	5.13×10^{10}
T_i	Irradiation temperature (°F)	522–570	545

data would change the count and perhaps slightly bias the mean chemistry but would not affect the ranges because all data on each SRM heat have the same heat-average chemistry.

Some additional information about the variables in Table 3.3 is needed. The chemical composition variables are intended to represent the best available estimate of actual measured composition at the location where the shift is being analyzed. This is consistent with the use of average measured composition on surveillance samples from each heat (to the extent available) to develop the calibration database.

The values of fluence and flux variables are intended to be estimates at the actual location where the shift is to be estimated, with the flux estimate averaged over the total effective full power operating time. This is consistent with the estimates for the surveillance specimens, for which dosimetry was based on the actual capsule location and the time averaging was done by dividing total accumulated fluence by the effective full power operating time to estimate time-averaged flux.

The irradiation temperature is also intended to be a time-averaged estimate for the metal at the specific location where the shift is to be estimated. The best available metal temperature estimate for the surveillance specimens was the temperature of the coolant near the surveillance capsule, but coolant temperature may not be the best estimate of metal temperature in other cases.

The range of data given in Table 3.3 is not by itself sufficient for estimating the limits of applicability of the model given in Chap. 4. The actual coverage of the data over the fitting variables and combinations of variables varies considerably, so it is necessary to review the actual distribution of data in TTSDatabase8-04.xls to determine the ranges of variables and variable combinations that are supported by a reasonable amount of data. For instance, forgings with Cu > 0.16 wt % or plates with Cu > 0.25 wt % are simply not available in the database, and the upper limit of Cu = 0.41 wt % in Table 3.3 applies only to welds. As another example, there are no low Mn (Mn < 0.93 wt %) materials in the database except A508 class 2 forgings, and the range of other chemistry variables in such forgings is limited ($0.67 \le$ Ni ≤ 0.86 wt %, $0.01 \le$ Cu ≤ 0.16 wt %, and $0.004 \le$ P ≤ 0.02 wt %). Thus, application of the model to any materials with Mn < 0.93 and values of Ni, Cu, or P outside the ranges corresponding to A508 class 2 forgings would be an extrapolation beyond the available data.

As an example of limits on exposure variable combinations, Table 3.3 shows that there are both high-fluence and low-fluence data, and high-flux and low-flux data, so one might assume that the full range of the fluence/flux space is reasonably covered by data. Unfortunately, this assumption is not true. In fact, there are no high-fluence data at low flux. The highest available fluence in the database decreases as flux decreases, so in all the data with $\phi < 1 \times 10^{10}$ n/cm^2/s, the highest available fluence is $\phi t = 1.9 \times 10^{18}$ n/cm^2. The highest available fluence in all the data with $\phi < 1 \times 10^{9}$ n/cm^2/s is only $\phi t = 2.8 \times 10^{17}$ n/cm^2. Thus, estimating the shift at any fluence greater than 1.9×10^{18} n/cm^2 for $\phi \cong 1 \times 10^{10}$ n/cm^2/s (and similarly for lower flux levels) is an extrapolation beyond the available data.

3.4.5 Comparison with Prior Databases

The dataset used in the final calibration of most constants in the current model is larger (at 775 points) than the datasets used in prior modeling efforts. Some specific comparisons include

- The July 2000 draft model [8] and ASTM E900-2 models [10] were calibrated on 736 points
- The shift calibration set used in NUREG/CR-6551 [5] contained 609 points
- Regulatory Guide 1.99 Rev. 2 was based on 177 points.

In addition to the calibration data, there are additional data in the current TTS database that were not used for calibration but can be used to provide evidence of predictive capability of the TTS model. An additional 80 datapoints were randomly selected before the model development and reserved for validation purposes (see Table 3.2). An additional 81 randomly selected SRM shifts were excluded from the calibration and validation sets in the modeling effort discussed in this report, as shown in Table 3.1. These data are also available for comparison with the model, providing additional evidence of predictive capability. By comparison, all available non-outlier data were used in the earlier modeling efforts, leaving no independent surveillance data for validation and comparison.

Counting both the calibration points and the additional data available for validation and comparison, the calibration dataset for the current model is actually a sample of data from a 27% larger database (200 more usable points) than the one used in July 2000. The total TTS database is more than 5 times the size of the database used to develop Regulatory Guide 1.99 Rev. 2. More important than the gross increase in size, the additional points helped fill in areas of the database that were notably sparse in the earlier modeling efforts, including low copper, high fluence and long exposure time, and low flux data from BWR surveillance capsules. The imbalance in the NUREG/CR-6551 and July 2000 databases caused by a large number of points from just three SRM heats has also been addressed. Thus, the current calibration dataset, although only 5% larger than the one used for calibration in July 2000, is much better balanced.

3.5 References

1. Stallmann, F. W., J. A. Wang, F. B. K. Kam, and B. J. Taylor, "PR-EDB: Power Reactor Embrittlement Data Base, Version 2," NUREG/CR-4816 (ORNL/TM-10328/R2), U.S. Nuclear Regulatory Commission, Washington, D.C., 1994.
2. Tilly, L., and T. Hardin, *BWRVIP-87: BWR Vessel and Internals Project Testing and Evaluation of BWR Supplemental Surveillance Program Capsules D, G, and H*, EPRI Report TR-1000890, 2000.
3. Burgos, B., K. Hour, C. Potze, and K. Watkins, *BWRVIP-111: BWR Vessel and Internals Project Testing and Evaluation of BWR Supplemental Surveillance Program Capsules E, F, and I*, EPRI Report TR-1003553, 2002.
4. Odette, G. R., T. Yamamoto, and D. Klingensmith, *The Effect of Dose Rate on Irradiation Hardening of RPV Steels: A Comprehensive Single Variable Database and Model Based Analysis*, Letter Report UCSB-NRC-03/1, U.S. Nuclear Regulatory Commission, Washington, D.C., 2003.
5. Eason, E. D., J. E. Wright, and G. R. Odette, *Improved Embrittlement Correlations for Reactor Pressure Vessel Steels*, NUREG/CR-6551, U.S. Nuclear Regulatory Commission, Washington, D.C., 1998.
6. McConnell, P., W. L. Server, W. Oldfield, and F. M. Oldfield, *Irradiated Nuclear Pressure Vessel Steel Data Base*, EPRI NP-2428, Electric Power Research Institute, Palo Alto, Calif., June 1982.
7. ASTM, "Standard Test Method for Plane-Strain Fracture Toughness of Metallic Materials, E399-90, "*Annual Book of ASTM Standards*, Vol. 03.01ASTM International, 2005.

8. Kirk, M., C. Santos, E. Eason, J. Wright, and G. R. Odette, "Updated Embrittlement Trend Curve for Reactor Pressure Vessel Steels," in *Transactions of the 17th International Conference on Structural Mechanics in Reactor Technology (SMiRT 17), Prague, Czech Republic, August 17–22, 2003*, 2003.

9. Server, W., C. English, D. Naiman, and S. Rosinski, *Charpy Embrittlement Correlations—Status of Combined Mechanistic and Statistical Bases for U.S. RPV Steels (MRP-45)*, EPRI Report 1000705, 2001.

10. ASTM, "Standard Guide of Predicting Neutron Radiation Damage to Reactor Vessel Materials, E706 (IIF), E900-02, "*Annual Book of ASTM Standards*, ASTM International, 2002.

4. Transition Temperature Shift (TTS) Model

The primary objective of this chapter is to present the revised embrittlement shift model and to demonstrate that it is a good fit to the calibration data and to other data not used for calibration. The main steps that produced the model, summarized in Sects. 4.1 and 4.2, should be viewed as just the latest steps in an iterative process of data collection and review, use of physical insight, empirical model calibration, and post-calibration analysis that has now gone through four major iterations, dating back to and including the NUREG/CR-6551modeling effort [1]. The emphasis in this chapter on the final baseline model and its quality of fit on relevant sets of data is deliberate, since intermediate models and preliminary significance tests on subsets of the relevant data, though useful during the modeling process, do not fairly characterize the final model and can be misleading.

In addition to information presented in this chapter, the model is further justified by information in Chap. 5 on the shape and statistical significance of individual variable effects on relevant datasets, and by comparisons with an independent set of data showing similar trends, given in Chap. 6. The model presented in this chapter is considered the baseline model, and a slightly simplified model is presented in Sect. 7.3 that reflects the comparisons in Chap. 6 and subsequent sensitivity studies.

4.1 TTS Analysis Methodology

The following modeling guidelines were generally followed in developing the TTS model:

1. use results of mechanistic studies to guide the overall model and help identify variable effects that should be looked for in the TTS data;
2. use only the U.S. power reactor surveillance data for choosing appropriate mathematical fitting forms and calibrating the adjustable parameters;
3. fit each part of the model to the most relevant data, considering numerical trade-off issues as well as physical mechanism issues; and
4. make sure the model provides a reasonable fit in each of the key datasets, including high and low Cu; high and low flux; and forging, plate, and weld.

The surveillance database has a very uneven distribution of data, signal-to-noise issues, and variable confounding, which limit what can be done under guideline 2. The imposed square root dependence of fluence in the MF term is an example where guideline 2 was relaxed in the present effort, and further relaxation of this guideline may be appropriate in the future to better reflect well-established results of mechanistic studies. Also, guidelines 3 and 4 are effectively constraints on the fit that imply that the sum of squares might be lower and that the calibrated constants might be somewhat different if they were simultaneously fitted to the entire database. Guidelines 3 and 4 were imposed because of lessons learned in past modeling iterations and because use of a single function to describe the entire database is not justified when different physical mechanisms are known to be active in different subsets of data (e.g., following from guideline 1, MF and CRP in low- and high-Cu subsets).

The revised model presented in this report is based on multiple radiation damage features identified in mechanistic studies, as discussed in Chaps. 1 and 2. The best-understood damage features are MFs and copper-rich precipitates CRPs, which are represented by separate terms in the model. Other damage features have been identified, involving Ni, Mn, Si and P, which occur in materials both with and without Cu (see Sects. 2.1, 2.3.2, 2.4.1 and [2,3]). The MFs are important in materials with low Cu while both the MF and precipitation mechanisms are important in higher-Cu materials. In this report, the two terms are referred to as the “MF term” and the “CRP term,” but it should be noted that in an empirically calibrated model, the model terms will reflect all the physical embrittlement mechanisms that are active in the data and not necessarily according to the labels used to refer to the model terms. Thus, associating one term

with MFs and the other with precipitation mechanisms is a useful concept that is physically motivated, but it does not restrict the features each empirically calibrated model term may reflect.

The sum of the MF and CRP model terms estimates the total Charpy TTS at 30 ft-lb (41J). The U.S. surveillance TTS data are traditionally reported in degrees Fahrenheit, the same units used in the embrittlement model in Eq. (4-1). TTS may be converted by °C = (°F-32)/1.8.

$$TTS = MF\ term + CRP\ term \tag{4-1}$$

The modeling guidelines specify that each part of the model should be calibrated on the most relevant subset of data. First, the MF term was initially developed on the low-Cu data, where, based on insights from guideline 1, it is the only term that applies. Then the MF term was held fixed while developing the CRP term. This approach provides temporary independence of the data domains for calibrating MF and CRP terms, preventing the fitting constants for fluence, temperature, chemistry, and product form variables that are present in both MF and CRP terms from trading off numerically during the nonlinear least squares iteration. Second, all available low-flux data, at both low and high Cu, were used to calibrate the two effective fluence fitting constants, which apply at all Cu levels. A similar rationale led to use of both low- and high-Cu data for calibrating the P*Mn term, which also applies at all Cu levels. Because low-flux data are scarce, all available low-flux data were used rather than setting aside a validation sample. Third, SRM plates were modeled as a separate product form so that the large number of measured TTS values for the three SRM plates could not unduly bias the model. By using a separate coefficient, the SRM plates, which are not part of any operating reactor vessel, cannot affect the calibration of coefficients for plates that are used in operating vessels. Finally, the PWR dataset[1] is almost five times the size of the BWR dataset and so would dominate any model calibrated to the combined PWR and BWR data, so most of the preliminary model development was conducted on the PWR data; then the differences between the resulting PWR model and the BWR data were analyzed. This approach avoids the possibility that BWR trends could be masked by the much larger amount of PWR data, and it avoids confounding T_i and flux, which both have relatively low values in the typical BWR data.[2] The PWR data have a substantial range in T_i and are not as much affected by flux, adequately separating these effects.

4.1.1 Summary of Steps Taken to Develop a Draft Model

The first step in the data analysis was to confirm the earlier definition of the border between low-Cu and high-Cu data for separating the MF and CRP mechanisms. The threshold value of 0.072 wt % for high-Cu behavior had been calibrated in earlier modeling efforts on smaller databases, so the purpose was to check that value on the current database. Then the MF part of the model was calibrated to all the available low-Cu PWR data. Calibration and validation samples were not used in this preliminary MF calibration step because the low-Cu PWR dataset (219 points) is not considered large enough to set aside a statistically meaningful number of data values for later use in a model validation step. Next, the CRP term was developed on the 90% calibration sample of the high-Cu PWR data, holding the MF term fixed. Then the BWR data were compared to the resulting PWR model to determine what changes to the PWR model would be needed to predict BWR data. The only change that was necessary was to add a flux effect (effective fluence) in both terms of the model, which was then calibrated to all BWR data and 90% of the PWR data at medium and lower flux. Then the flux-related fitting constants were held fixed, and the rest

[1] "Database" refers to the complete set of surveillance data while "dataset," "subset," or just "set" refer to part of the database.

[2] "Typical BWR" data are those with flux < 2×10^{10} n/cm^2/s and T < 535°F. There are other data from surveillance specimens irradiated inside the shroud in BWR plants, and in an unusual BWR plant (Big Rock Point), that have flux and/or temperatures comparable to and higher than typical PWR irradiations.

of the fitting parameters in the CRP term were calibrated to a 90% sample of PWR and BWR high-Cu data. This produced a draft model.

The draft model was reviewed in some detail, and several issues with it were identified. The P effect in the draft model (initially applicable only to higher Cu material) was contrary to clear P effects in low- or no-Cu materials tested in single-variable IVAR experiments [as shown in Ref. [4,5], Sect. 6.4.2, and Fig. 6.12 (c)] and to observations of P effects in low-Cu material worldwide, as discussed in Sect. 2.4.1. A significant interaction of P and Mn subsequently identified in the low-Cu surveillance data is the likely cause of the initial lack of an observed P effect in that subset of data. Potential improvements were identified for the draft method of choosing Cu saturation limits. An improved form for modeling P precipitation was also introduced. During the draft model review, the need for flux effects modeled by effective fluence in both MF and CRP terms, which was originally noted in the surveillance data, was confirmed on the independent IVAR database. The flux effects in both low and higher Cu IVAR materials are discussed in Sect. 6.6, and the flux effects in both low and higher Cu surveillance data are discussed in Sect. 5.2. These observations led to a second iteration of model calibration which is described in Sect. 4.1.2.

4.1.2 Summary of Steps Taken to Calibrate the Baseline TTS Model

In the second modeling iteration, the MF part of the model was again calibrated initially to all the available low-Cu PWR data. A preliminary MF term consisting of only a single calibrated coefficient, the temperature term from the draft model, and square root of fluence, was used in an attempt to model the interaction of P and Mn explicitly on the low-Cu PWR data without confounding that effect with product form effects and the effects of flux in BWR data. (Confounding of Mn and product form arises mainly from the lower average Mn in forging materials, as shown in more detail in Chap. 5, where effects of individual variables on TTS are discussed.) Then the resulting P*Mn term was held fixed while three coefficients were calibrated on the low-Cu PWR data to account for all other effects of chemistry and microstructure in the low-Cu forging, plate, and weld materials. Because of this procedure, the proper interpretation of the MF coefficients is that they reflect composition and other differences between product forms, given that an interaction effect of P and Mn is explicitly modeled. In particular, a significant relationship between P, Mn, and Ni can be found by regression analysis in the low-Cu data, so the P*Mn term and coefficients in the MF term implicitly contain an effect of Ni as well as product form and Mn. Efforts to explicitly model the known Ni effect in low-Cu data [shown in Sect. 6.4 and Fig. 6.12 (a)] were unsuccessful, probably because of confounding.

The MF term, including the P and Mn fitting constants, was then held fixed while updating the coefficients and constants of the CRP term on a 90% sample of the high-Cu PWR and BWR data. The other 10% sample of high-Cu data had been selected by random sampling as a validation set and were not used in this step. For this preliminary CRP update, the effective fluence fitting constants were held fixed at the values that had been calibrated in the draft model, to be updated in the next step for compatibility with the updated MF and CRP terms. Exploratory CRP term modeling was conducted in two forms, both with a single CRP coefficient, used to attempt to calibrate the Mn effect explicitly,, and with separate CRP coefficients for forgings, plates in Combustion Engineering (CE) and non-CE manufactured vessels (which are significantly different in their shifts), welds, and SRMs. It was found that an explicit effect of Mn could not be calibrated in the CRP term, given the fact than the P*Mn effect and different coefficients for forgings, plates and welds were already included in the MF term. As in the MF term, regression analysis found that Mn is strongly correlated with and can be estimated from Cu and Ni in the high-Cu data, complicating the modeling of Mn in the surveillance data. The Mn effects on higher Cu materials are discussed in more detail in Sects. 5.1, 6.4, and 6.7.

The next step was to update the preliminary effective fluence (flux) fitting constants for compatibility with the updated MF and CRP terms. This was done in conjunction with an update to the P

and Mn coefficients in the MF term. It was by then clear that the effective fluence and P*Mn terms would be the only terms used for modeling those effects in both low- and high-Cu data, and thus they should be calibrated to both low- and high-Cu data. The dataset used for calibrating the four constants included all available low-flux data ($< 5 \times 10^{10}$ n/cm^2/s), all low-Cu data (≤ 0.072 wt %), and 90% of the high-Cu PWR and BWR data. Better balance in the dataset is achieved by using all data in the subsets where data are relatively scarce (low flux and low Cu) and a random sample of the data at high Cu and higher flux, which are more plentiful. The updated flux-related and P*Mn fitting constants (four total) were held fixed for the remaining modeling.

The MF fitting constants (other than the four effective fluence and P*Mn constants) were then updated on the 90% calibration set of low-Cu data (BWR and PWR). This produced the final MF term coefficients and temperature slope. The final MF term and effective fluence constants were held fixed while the final constants for the CRP term were updated using the 90% sample of high-Cu BWR and PWR data as the fitting set. Thus, except for the four effective fluence and P*Mn fitting constants, all fitting constants can be validated on the 10% samples of low- and high-Cu data reserved for that purpose. There is also partial validation of the two P*Mn fitting constants on the 10% random sample of high-Cu data. There is no validation set for the flux-related constants, as the low-flux data are so scarce that all available data were used to calibrate them. However, the comparison with flux effects in the IVAR data in Sect. 6.6 indicates that the physically based extrapolation of IVAR data to the BWR flux range is reasonably consistent with the flux-sensitive part of the TTS model. (see Fig. 6.20). The last remaining capsules (A, B, C) from the BWR Supplemental Surveillance Program (SSP) may provide additional low-flux surveillance data for validation when available [6].

The result of the fitting process described above is that the 2 flux-related constants in the model are based on all low flux data (and most of the high flux data), the 2 constants in the P*Mn part of the MF term are based on all available low-Cu data (and most of the high-Cu data) and the 22 other fitting constants are calibrated on a 90% sample of BWR & PWR data. The CRP fitting constants are based on a fixed MF model calibrated mainly to low-Cu data, which means that the P and T_i terms and the product form coefficients in the CRP part of the model should be interpreted as the *additional* effect of those variables in high-Cu material, relative to the effects present in low-Cu material. This fitting approach provides both a good fit to both the low Cu data and to the higher Cu data, as is shown in Sect. 4.3.

4.2 TTS Model

Throughout this section, selected results are presented in the order originally developed, following the steps summarized above. Most preliminary models have been omitted to avoid confusion with the final model. The statistical justification for the final model form given in this section is presented in Sect. 4.3, in the form of non-significant residual trends in all variables using the model, and in Chap. 5, in the form of significance analyses of the key variable effects.

4.2.1 Threshold for High-Cu Behavior

This subsection reports a preliminary study performed to see if the previously calibrated value of Cu threshold is reasonable for the enlarged dataset. This check is needed because the first step in the modeling effort is to split the data into low- and high-Cu sets based on a Cu threshold value, then calibrate an MF model on the low Cu data. Thus, the threshold value of Cu is needed to define “low Cu” before doing any calibration on the TTS data. The temperature dependence from the Jones & Williams model [7], based on a completely separate set of data, is used to help confirm the threshold.

Some lack of precision in determining the threshold copper level for separating low-Cu and high-Cu behavior is unavoidable. For example, there is no practical difference between splitting the surveillance data at 0.07 and 0.072 wt % Cu, as there is only one datapoint in that range. The datapoint happens to be

in the BWR subset, so that splitting on either 0.07 or 0.072 wt % Cu produces identical results on the PWR subset. Thus, the uncertainty in the threshold is at least 0.002 wt %, and, based on the method of determining it below, the actual uncertainty is probably at least ±0.005 wt %.

To determine the best value of copper for the split, the simple low-Cu model of Jones and Williams [7] (which was not used in the original calibration of the 0.072 value in [1]) was used to approximately account for the effects of temperature and fluence. The Jones and Williams model is usually presented in terms of Celsius temperature and dose measured by dpa. After conversion to Fahrenheit temperature and fluence in n/cm^2, it takes the form

$$\textit{Preliminary MF term} = 2.766 \times 10^{-8}(1 - 0.001302 * T_i)\sqrt{\phi t} \tag{4-2}$$

where the coefficient 2.766×10^{-8} is fitted to the 214 PWR points in the Version 7-04 database with Cu ≤ 0.072 wt %. The temperature coefficient was not fitted; it was merely converted from the Jones and Williams value.

To determine whether 0.072 wt % Cu is a reasonable splitting value, the available PWR data were split by Cu into categories in the range 0.02 to 0.10 wt % Cu. The lowest categories had an increment of 0.01 in copper, and categories above 0.05 wt % Cu (where the threshold was expected to be) had an increment of 0.005. For each category, the standard deviation and average value of the residuals relative to Eq. (4-2) were evaluated, and the average copper for each category was calculated. The coefficient $a_1 = 2.766 \times 10^{-8}$ in Eq. (4-2) was also refitted to the data in each Cu category, holding the temperature coefficient and fluence exponent fixed.

Plotting the results, one can identify the approximate transition from MF to MF + CRP behavior by abrupt changes in three different measures: the best fit coefficient a_1, the standard deviation of residuals about Eq. (4-2), and the average residual relative to Eq. (4-2). Up to about 0.07 wt % Cu in the PWR data, the results on all three measures, although scattered, do not show a consistent trend with Cu. For Cu categories above 0.07 wt %, the best fit coefficient increases, the average residual becomes increasingly negative, and the standard deviation increases, all indications that the CRP term must be added to reasonably fit the data. The results are shown in Figs. 4.1 through 4.3. The conclusion from this study is that 0.072 wt % Cu is a reasonably good threshold for high copper behavior in the updated surveillance database. The same value was used in the NUREG/CR-6551 modeling effort [1] and all model revisions since then. An independent analysis of Cu threshold (Cu_{min}) in the IVAR database found values in the range 0.06 to 0.08 wt %, which are consistent with this estimate [see Sect. 6.4.1 and Fig. 6.8 (d)].

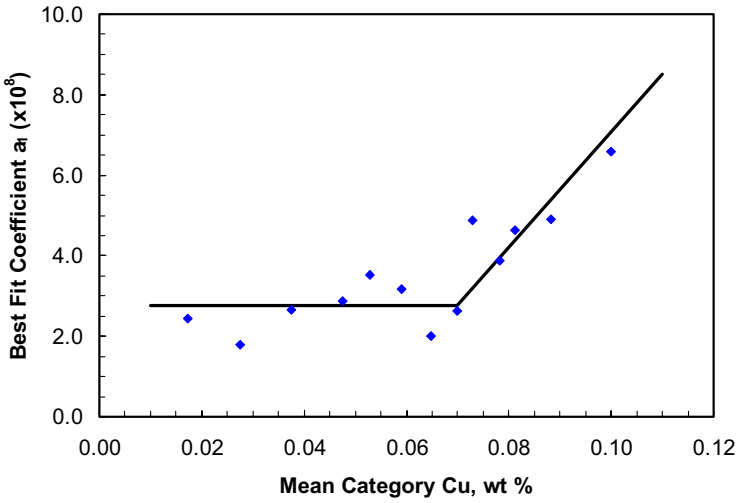

Fig. 4.1. Apparent location of Cu threshold based on coefficient in Eq. (4-2) fitted to each Cu category.

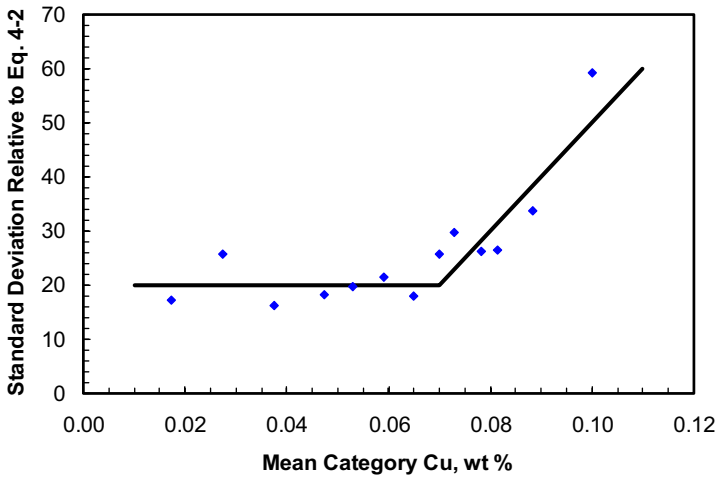

Fig. 4.2. Apparent location of Cu threshold based on standard deviation of residuals relative to Eq. (4-2) for each Cu category.

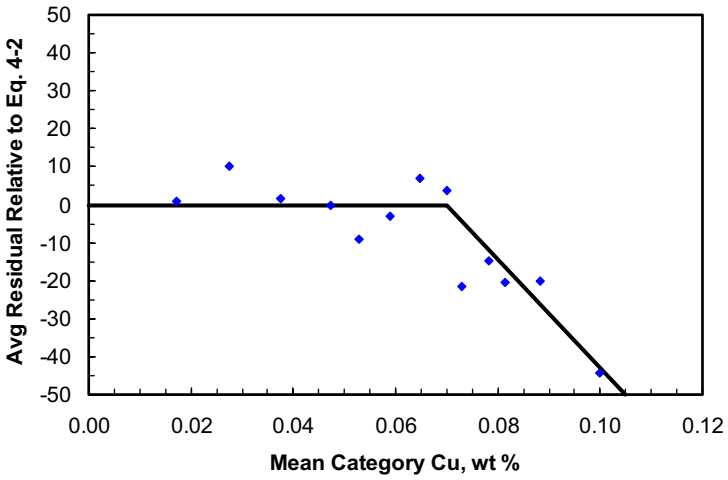

Fig. 4.3. Apparent location of Cu threshold based on average residual relative to Eq. (4-2) for each Cu category.

4.2.2 Matrix Feature (MF) Term

Having established that Cu = 0.072 wt % is a reasonable value for separating low-Cu behavior (which can be modeled by just an MF term) from high-Cu behavior (which requires both MF and CRP terms), the next task is to calibrate an appropriate MF term for the low-Cu data. While fitting the Jones and Williams model in the preliminary work, it was apparent that the linear temperature term in that model is numerically more stable than the exponential (Arrhenius) form that had been previously used [1,8]. The ability to fit over the limited range of irradiation temperatures in surveillance data (522–562°F for PWRs) is comparable. Considering the comparable fitting capability, numerical stability advantages, and common use of the linear form in the radiation damage field (e.g., Ref [7] and Sect. 2.3.4), a decision was made to use the linear temperature term for the revised low-Cu model.

A decision was also made to hold the fluence exponent at the theoretical value of 0.5 for MF, rather than fit it to the data as in prior modeling efforts. This decision follows current common practice in the radiation damage field (see Sect. 2.4.2), and it was supported by preliminary models that gave fitted exponents slightly greater than 0.5 on the expanded low-Cu dataset. The fitted exponent in the July 2000 modeling effort [8] was slightly less than 0.5, so the current and prior results of fitting the exponent could be viewed as clustering about 0.5, depending on the database. A final advantage to fixing the MF term exponent at 0.5 is that it then cannot trade off numerically with the fluence function in the CRP term.

As a preliminary study, an MF term containing a single calibrated coefficient, the temperature term from the draft model, and the square root of fluence was calibrated to the Version 8-04 PWR low-Cu fitting set (219 points). The low-Cu residuals relative to this model [defined in Eq. (1-1)] show apparent trends with P, Mn, and P*Mn. The slope of the low-Cu residuals is statistically significant for Mn and P*Mn but not for P. However, the slope of the residuals with P is significant on the broader set of data affected by the final P*Mn interaction term (both low and high Cu), as discussed in Sect. 5.1.4. Moreover, the P effect in the MF term is in a direction consistent with the P effects previously calibrated in NUREG/CR-6551 [1] and Draft 2000 models [8], as shown in Fig. 4.4, such that increased P appears to produce increased shift in low-Cu steels. The slope of the residuals throughout this section is always opposite in sign to the slope of the effect that is missing from the model. Thus, the negative slope to the residuals in Fig. 4.4 can be cured by adding to the model a term with a positive slope with P.

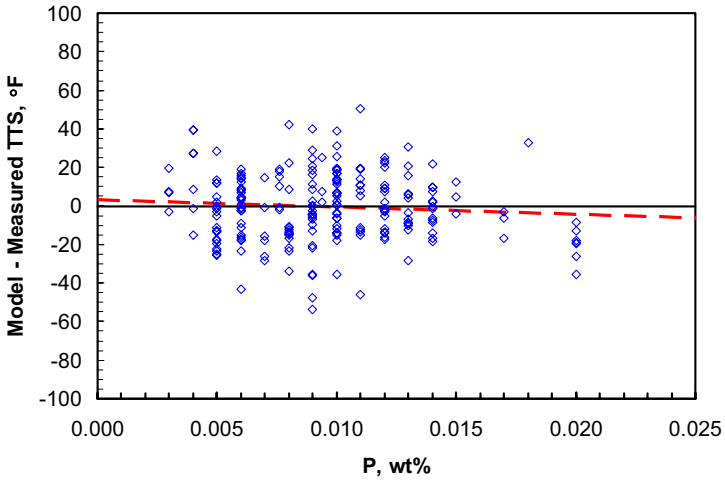

Fig. 4.4. Residuals in low-Cu PWR data relative to single coefficient model, plotted against P. Dashed trend is not statistically significant.

The observation that the slope of the P residuals is not statistically significant in the preliminary models of the low-Cu surveillance database is contrary to studies worldwide that have found significant effects of P in low-Cu data [5,7], NUREG/CR-6551 and the previous Draft 2000 models [1,8], and controlled single-variable studies of the effect of P on no-Cu steel shown in Sect. 6.4 and Fig. 6.12c, which clearly show an effect of P. The reason for the lack of statistical significance for the P effect in low-Cu PWR surveillance data appears to be the interaction of P with Mn that is observed in the current surveillance database. The residual effect of P is significant in high-Mn, low-Cu steels, as shown in Fig. 4.5, but not in low-Mn, low-Cu steels, as shown in Fig. 4.6. When those two sets are combined, the trend with P is not significant over the low-Cu PWR data currently available (all two sided tests on slope of fitted residual trend, $p < 0.05$ for significance). The high-Mn plot is for Mn > 1.35 wt %, while the low-Mn plot is for Mn ≤ 1.35 wt %, with Ni in the typical range (Ni > 0.5 wt %) in both plots. The value of 1.35 wt % for Mn is approximately mid-range for the allowable content in the specification for RPV plates of SA 533 grade B class 1 steel, and is also approximately mid-range in the Mn values for a number of PWR data subsets evaluated in the analysis. Thus, the choice of 1.35 wt % is arbitrary but reasonable as a split for low- and high-Mn groups in these preliminary analyses. Moreover, the final calibrated term for Mn in the model is not dependent on the preliminary splits used for the various data subsets because it was calibrated to a broader dataset (see Sect. 5.1.5). The no-Cu IVAR materials showing a strong effect of P in controlled experiments had reasonably high Mn = 1.6 wt %, so these observations are reasonably consistent.

In addition to the residual trends with chemistry, there are statistically significant differences in average residual among the different product forms. This was determined by t-tests on the low-Cu residuals relative to a preliminary single-coefficient MF term model (without a P*Mn term). Specifically, there is a statistically significant difference in average residuals for forging and plate and for forging and weld based on two sided t-tests and $p < 0.05$. Plate and weld average residuals are also significantly different on the broader dataset to which the MF coefficients apply (both low and high Cu materials), as discussed in Sect. 5.1. Thus, three separate MF coefficients were used for forging, plate, and weld.

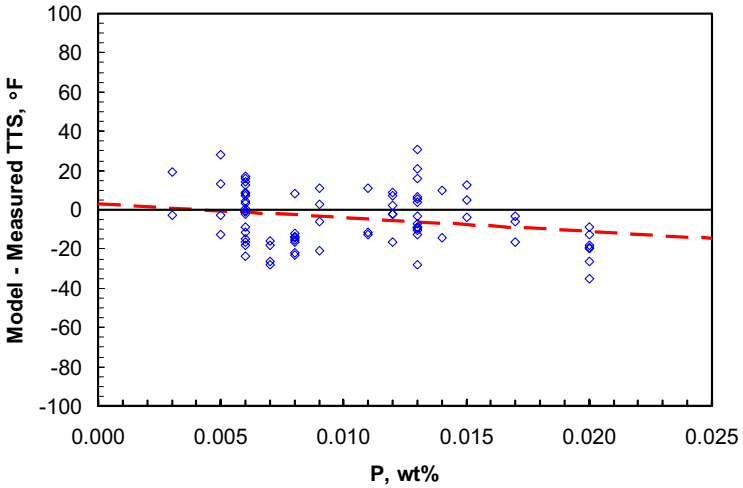

Fig. 4.5. Residuals in low-Cu PWR data with Mn > 1.35 wt % relative to single coefficient model, plotted against P.
Dashed trend is statistically significant.

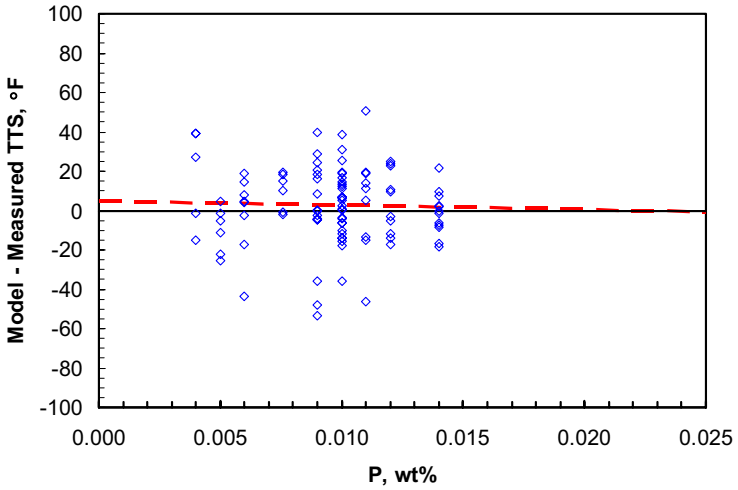

Fig. 4.6. Residuals in low-Cu PWR data with Mn ≤ 1.35 wt % relative to single coefficient model, plotted against P.
Dashed trend is not statistically significant.

The MF term was modified from the form shown in Eq. (4-2) to include a P*Mn term and three separate product form coefficients for forging, plate, and weld. These enhancements eliminated the significant residual trends with Mn and P*Mn, flattened further the trend with P, and eliminated the significant differences in average residual between the three product form groups. The final MF term, calibrated to a 90% sample of PWR and BWR low-Cu data in the analysis process described above, is

$$MF\ term = A\left(1 - 0.001718T_i\right)\left(1 + 6.13PMn^{2.47}\right)\sqrt{\phi t_e} \tag{4-3a}$$

Where

$$A = \left\{ \begin{array}{l} 1.140\times10^{-7} \ \text{ for forgings} \\ 1.561\times10^{-7} \ \text{ for plates} \\ 1.417\times10^{-7} \ \text{ for welds} \end{array} \right\} \tag{4-3b}$$

Both MF and CRP terms use an effective fluence, calculated from fluence ϕt and flux ϕ as

$$\phi t_e = \left\{ \begin{array}{c} \phi t \quad for\ \ \phi \geq 4.39\times10^{10} \\ \phi t\left(\dfrac{4.39\times10^{10}}{\phi}\right)^{0.259} \quad for\ \ \phi < 4.39\times10^{10} \end{array} \right\} \tag{4-4}$$

The effective fluence in Eq. (4-4) is greater than actual fluence for flux below 4.39×10^{10} n/cm^2/s, while above that breakpoint value, the fluence and effective fluence are the same (see Sect. 5.2.1 for discussion of effective fluence). The breakpoint, 4.39×10^{10}, and the exponent, 0.259, were fitted simultaneously to all available low-flux data (< 5×10^{10} n/cm^2/s), all low-Cu data (< 0.072 wt %), and 90% of the high-Cu PWR and BWR data, as described in Sect. 4.1.2. Moreover, the fitted breakpoint, 4.39×10^{10}, remained relatively stable in preliminary and final calibration. The breakpoint approach was the result of preliminary analysis that showed only a slight residual trend with flux, in the expected direction but not statistically significant, in the PWR calibration data (which are mainly in the range $3 \times 10^{10} \leq \phi \leq 2 \times 10^{11}$ n/cm^2/s). This may have been due to the narrow flux range and other limitations of the PWR data, as there is strong evidence of flux effects in the PWR range in IVAR data, as discussed in more detail in Sect. 6.6.

Figure 4.7 shows typical curves based on Eq. (4-3) using the effective fluence form in Eq. (4-4) at assumed flux values of 1×10^9 and 1×10^{10} and for any flux greater than 4.39×10^{10} n/cm^2/s. The shifts estimated by the MF term at 1×10^9 and 1×10^{10} n/cm^2/s, respectively, are factors of 1.63 and 1.21 times the shift at 4.39×10^{10} n/cm^2/s or higher flux. The statistical justification for including the effective fluence term in the MF term is given in Sect. 5.2, and additional supporting evidence is given in Sect. 6.6.2.

The MF term model given by Eq. (4-3) is a good fit to the low-Cu data, as shown by the plot of model TTS vs measured TTS in Fig. 4.8. In that figure, a perfect fit with no scatter would put all data along the 1:1 diagonal line. In any real case, there is scatter, but Fig. 4.8 shows the scatter is evenly distributed around the 1:1 line with no consistent deviation above or below. Both PWR and BWR points are shown, with open symbols for the calibration data and filled symbols for validation data. The good fit is confirmed by analyzing the residuals relative to Eq. (4-3), using all available low-Cu data (calibration and validation subsets, PWR and BWR, a total of 246 points). The residuals do not show statistically significant trends in fluence, flux, T_i, time, chemistry variables, product form, or the chemical interactions P*Mn, P*Ni, or Mn*Ni. Further details on the quality of fit and comparison of calibration and validation data are given in Sect. 4.3.

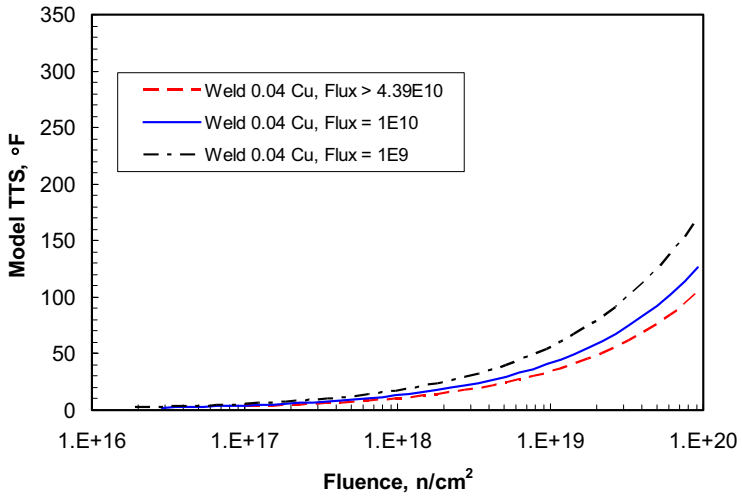

Fig. 4.7. Effect of effective fluence on MF term at various flux values.

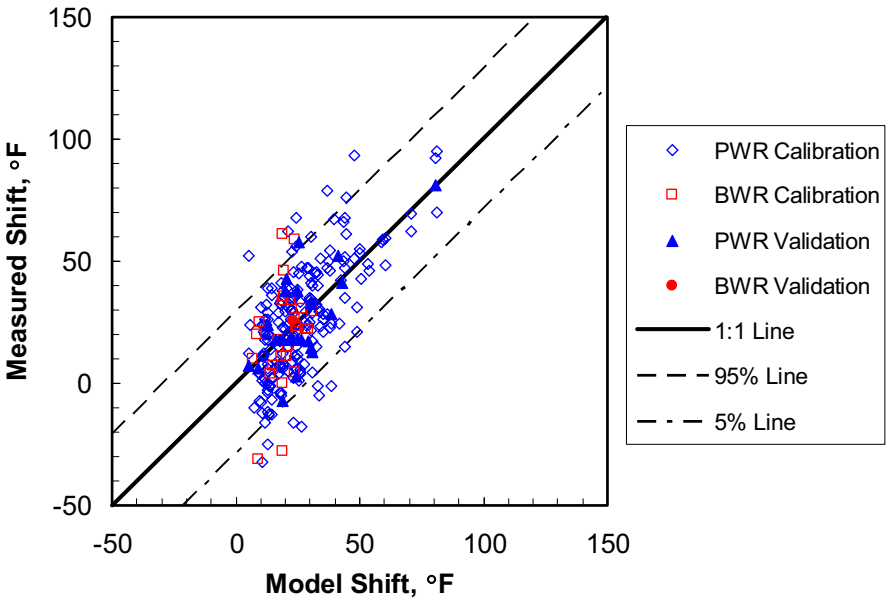

Fig. 4.8. Model shift vs measured shift, Eq. (4-3), all data with Cu ≤ 0.072 wt %.

The T_i term in Eq. (4-3a) has a steeper slope in the low-Cu surveillance data [–0.001718 in Eq. (4-3)] than in the Jones and Williams model [-0.001302 in Eq. (4-2)]. The different slopes may reflect differences in the materials used for calibration, different average values of fluence and other variables, or the fact that the temperature range of the surveillance data is smaller. The possibility of partial confounding of flux and temperature effects when fitting both effects simultaneously was ruled out by separately calibrating the temperature slope in narrow ranges of flux. The average of these subset values was the same as the overall calibration, and there was no obvious trend with flux, proving no apparent confounding of those variables.

The effective fluence form shown in Eq. 4-4 is used in both MF and CRP terms; it is presented here because it is used in Eq. 4-3a. The effective fluence form was originally developed to cause the high Cu BWR data to agree with the preliminary model calibrated to high Cu PWR data. During preliminary modeling, using effective fluence in both the MF and CRP terms produced better fits to the high-Cu, low-flux data than using the effective fluence form in the CRP term only, as well as improving the fit to the low-Cu, low-flux data. Based on this empirical observation, the draft model from the first round of modeling had effective fluence in both terms. Significance tests on the draft model showed that disabling the flux effect by using fluence instead of effective fluence, in either the MF or CRP terms separately or both terms together, would produce significant mean residual errors on the low-flux BWR data with fluence > 10^{17} n/cm^2. This provided a preliminary statistical justification for using effective fluence in both terms in the model, which was later confirmed on the baseline model as reported in Sect. 5.2.

There are only 27 low flux ($\phi < 2 \times 10^{10}$ n/cm^2/s) data points, all from exposure in BWRs, in the low-Cu dataset. Four of those points are at such low fluence ($< 2 \times 10^{17}$ n/cm^2) that very small shifts would be expected with or without a flux effect (see Fig. 4.7). Thus, the ability to statistically identify significant fitting trends or residual effects with respect to flux using just the low-Cu dataset is quite limited – there are not enough data, and the shifts in low-Cu data at such low fluence values are generally small. Using effective fluence in the MF term is justified on the broader dataset to which the MF term applies (both low and higher Cu materials) where the effective fluence term is significant, as shown in Sect. 5.2.

The flux effect in low Cu data was first identified in the surveillance data, but additional analysis of the low-Cu and no-Cu IVAR data confirmed that there is a statistically significant effect of flux in that dataset under controlled experimental conditions. The evidence in IVAR for a flux effect in no-Cu steels is shown in Sect. 6.6.2, providing independent support for a flux effect in the MF term. The IVAR data also show substantial effects of flux in the high-Cu materials, as has been known for some time (see Sect. 6.6.1 and [4,9]). The TTS and IVAR flux effects are in different flux ranges, reflecting the different flux ranges in those databases, but the physically based extrapolation of IVAR data to the BWR flux range is reasonably consistent with the flux-sensitive part of the TTS model (see Fig. 6.20).

4.2.3 Copper-Rich Precipitate (CRP) Term

As discussed in Sect. 2.2.3, the CRP term models the shift due to precipitation of Cu, P, and other elements, which is negligible at low fluence, rises rapidly over a higher range of fluence and saturates at high fluence. The appearance of the shift vs fluence curve is a plateau as shown in Fig. 4.9, with amplitude that depends on temperature, material chemistry, and product form, but not on fluence (above the saturation value) or on flux. The fluence values at which the CRP-related shift makes the transition to full amplitude depend on chemistry and flux (see Sects. 2.3.1, 2.3.2, and 2.3.3). High Cu, low Ni, or low flux causes the transition to move toward lower fluence, while high Ni, low Cu, and higher flux cause the transition to move toward higher fluence. The saturating behavior and the effect of the variables is well known, shown with independent controlled experiments in IVAR data [4] and in British data [10], as discussed in Sect. 2.3.3. The precipitation behavior can be reasonably modeled by a tanh function, in the same form as Eq. (2-1) with LSE = 0 and $a_3 = ½$, as is shown in Fig. 4.9, or by Avrami functions [4,11] which are similar in appearance to the tanh function. The alternative tanh form used in [12] to model the Cu effect was also tried, but it gave a substantially higher standard error (Se) than that used here.

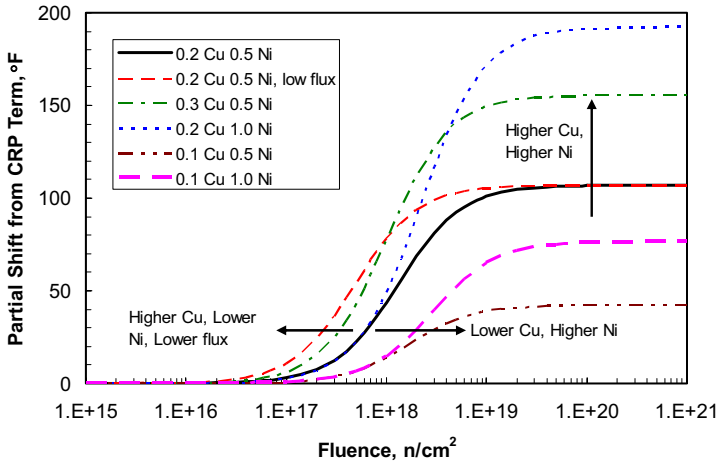

Fig. 4.9. Schematic of CRP term showing effect of key variables on changes in plateau height and location. Low flux is 10^9 n/cm^2/s; all others are 10^{11} n/cm^2/s.

Following the steps summarized in Sect. 4.1, preliminary CRP term models were developed based on high-Cu PWR calibration data, which were then extended to adequately model the BWR data by simply incorporating an effective fluence (flux) model in both MF and CRP terms. Then both MF and CRP terms were recalibrated in a second round of modeling that addressed several issues in the preliminary models. The final result of this process is the following CRP term:

$$CRP\,term = B\left(1 + 3.77Ni^{1.191}\right)\left(\frac{T_i}{543}\right)^{1.10} f\left(Cu_e, P\right)g\left(Cu_e, Ni, \phi t_e\right) \qquad (4\text{-}5a)$$

Where

$$B = \left\{\begin{array}{c} 102.3 \;\; for\;\; forgings \\ 102.5 \;\; for\;\; plates\; in\; non\text{-}CE\; mfg.\; vessels \\ 135.2 \;\; for\;\; plates\; in\; CE\; mfg.\; vessels \\ 155.0 \;\; for\;\; welds \\ 128.2 \;\; for\;\; SRM\;\; plates \end{array}\right\} \qquad (4\text{-}5b)$$

It is clear in Eq. (4-5b) that calculations involving forgings and non-CE plates could use the same compromise coefficient of 102.4 with negligible (~ 0.1%) error. As in other recent model development efforts [8,13], the shifts for plates in CE-manufactured vessels are statistically significantly larger than in non-CE manufactured vessels, an empirical observation for which an accepted physical explanation is not yet available. There is also a special SRM coefficient, used for matching results with the surveillance data on standard reference materials but not used for calculations related to materials in actual vessels (see Sects. 5.1.5 and 5.1.6 for detailed discussions of product form effects, 5.1.2 for Ni effect, and 5.2.2 for Ti dependence).

The copper and phosphorus precipitation term in the model, $f(Cu_e, P)$, is built up from several functions. First, the effective Cu in solution, Cu_e, which is the amount of Cu available for precipitation, is zero below a threshold value of 0.072 and is also limited by a maximum saturation value that reflects the amount of Cu available for precipitation. The Cu_{max} value appears to depend on Ni concentration, heat treatment details, and possibly other factors (see Sects. 2.3 and 4.2.1). Hence, an effective Cu is defined as

$$Cu_e = \begin{Bmatrix} 0 \quad for\ Cu \le 0.072\ wt\% \\ \min[Cu, Max(Cu_e)] \quad for\ Cu > 0.072\ wt\% \end{Bmatrix} \tag{4-5c}$$

where the upper limits

$$Max(Cu_e) = \begin{Bmatrix} 0.243 \quad for\ typical\ (Ni > 0.5 wt\%)\ Linde\ 80\ welds \\ 0.301 \quad for\ Linde\ 1092\ welds \\ 0.370 \quad for\ all\ other\ materials \end{Bmatrix} \tag{4-5d}$$

The Cu saturation limits, $Max(Cu_e)$, can only be calibrated for materials with Cu above the limits. Only the materials that have very high Cu (Cu > 0.243 wt % for the lowest limit in the current database) can affect the calibrated saturation limits because materials with Cu below the limits show only increasing shifts with higher Cu, with no limit behavior at all. The Linde 80 weld group is the only subset that has enough high-Cu data, with high enough Cu levels, to have confidence in the calibrated limits. This situation is discussed in detail in Sects. 5.1.3 and 7.2.

None of the forging materials in the surveillance database and only one of the plates have nominal Cu values above 0.243 wt % (and that plate is just above the limit at 0.25 wt %), so the upper limits on Cu available for precipitation cannot be determined from the TTS database. Base metals should use the full Cu level, at least up to Cu = 0.25 wt %. This point is reiterated in Sect. 7.2.3, where the issue is further discussed under "Treatment of base metals."

The two large weld groups that have at least six welds with Cu > 0.243 wt % (Linde 80 and Linde 1092) have individually calibrated Cu limits. It must be noted that the weld flux is only used as a means of grouping welds—there is no implication that weld flux directly affects the Cu limits. Most of the Linde 80 weld group have 0.52 ≤ Ni ≤ 0.72 wt %, although one Linde 80 weld has much lower Ni (~ 0.1 wt %). The "typical Linde 80" group is defined as those welds with nominal Ni > 0.5 to distinguish the usual Linde 80 welds from the unusual low-Ni weld. The Linde 1092 weld group is generally in a higher Ni range than Linde 80 welds range, but some Linde 1092 welds have Ni values as low as 0.6 wt %. The "all other" welds are generally at lower Ni (≤ 0.5 wt %). An attempt was made to consider Ni in calibrating the Cu_{max} limits, but it was unsuccessful, as discussed in Sects. 5.1.3 and 7.2.

The effective Cu and P concentrations are simply combined on the basis that the observed precipitates generally include both Cu and P (see Sects. 2.3.2 and 2.4.1; see also [14,15]). Williams has noted that the mechanistic role of P appears to be similar to that of Cu in the precipitates, so that the sum of Cu and some multiple of P should be considered as the effective Cu available for precipitation[3]. The precipitation model includes a threshold concentration of both Cu (0.072) and P (0.008), below which precipitation is assumed to be negligible. The Cu threshold was calibrated in earlier studies and confirmed as reported above, while the P threshold (0.008) is a current calibrated (fitted) value determined along with the other CRP fitting constants using the high-Cu calibration set and least squares. Consequently, P – 0.008 was linearly combined with the effective Cu – 0.072 as in Eq. (4-5e).

[3]Williams, T. J., email to E. D. Eason, 6/18/2004

The chemistry term of the shift model in Regulatory Guide 1.99 Rev. 1 contained a linear combination of (Cu – 0.08) and (P – 0.008) terms, somewhat similar to the Cu and P terms in Eq. (4-5e).

$$f(Cu_e, P) = \left\{ \begin{array}{c} 0 \quad for\ Cu \le 0.072 \\ [Cu_e - 0.072]^{0.668} \quad for\ Cu > 0.072\ and\ P \le 0.008 \\ [Cu_e - 0.072 + 1.359(P - 0.008)]^{0.668} \quad for\ Cu > 0.072\ and\ P > 0.008 \end{array} \right\} \qquad (4\text{-}5e)$$

The remaining CRP term is the saturating fluence function, which depends on Cu and Ni as well as flux and fluence.

$$g(Cu_e, Ni, \phi t_e) = \frac{1}{2} + \frac{1}{2}\tanh\left[\frac{\log_{10}(\phi t_e) + 1.139 Cu_e - 0.448 Ni - 18.120}{0.629}\right] \qquad (4\text{-}5f)$$

The effective fluence from Eq. (4-4) and the effective Cu [limited by the values in Eqs. (4-5c) and (4-5d)] are used in the saturating term, not fluence and bulk Cu values.

The Cu and Ni effects inside the tanh function, which move the location of the transition laterally as shown on Fig. (4-9), are known physical effects as discussed in Sect. 2.3.3. These effects were previously explored as part of the NUREG/CR-6651 modeling effort, with similar results for the Ni term (see [1], p. 87). The database at the time was inadequate for calibrating the Cu effect, and numerical trade-offs were noted between Cu and Ni terms inside and outside of the tanh function, so including those terms was deferred. With the current database there was no difficulty calibrating the effects, and the Cu and Ni terms outside the tanh function did not change much as Cu and Ni terms inside the tanh function were calibrated. However, some change was noted, so the Cu and Ni fitting constants that control amplitude and those that control location of the transition are not completely numerically independent.

The model of high-Cu behavior (Cu > 0.072 wt %) is given by Eqs. (4-1), (4-3), (4-4), and (4-5). It is a good fit, as shown by comparing model shifts and actual shifts for all PWR high-Cu data in Fig. 4.10 and for all BWR high-Cu data in Fig. 4.11. In the BWR plot, two symbols (small square or circle, larger diamond) are plotted for some points. These are the atypical BWR data, which were irradiated at unusual locations for a BWR (denoted BWb in database) and in an unusual BWR (Big Rock Point, denoted BWa in database) such that the flux levels are more typical of PWR than BWR exposure. Indeed, some of the flux levels in this atypical BWR set are higher than in most PWR surveillance capsules.

As detailed in Sect. 4.3, a further indication of the good fit is the fact that there are no significant residual trends in the high-Cu data with fluence, flux, T_i, exposure time, chemistry variables, and interactions P*Mn, P*Ni, Cu_e*Ni, Cu_e*Mn, and Mn*Ni. There is also no significant difference in average residual with product form variables or between high-flux (> 4.39×10^{10} n/cm^2/s) and low-flux (≤ 4.39×10^{10} n/cm^2/s) subsets. The high flux and low flux comparison is for plate and weld, since only one of the BWR low flux observations is high-Cu forging material.

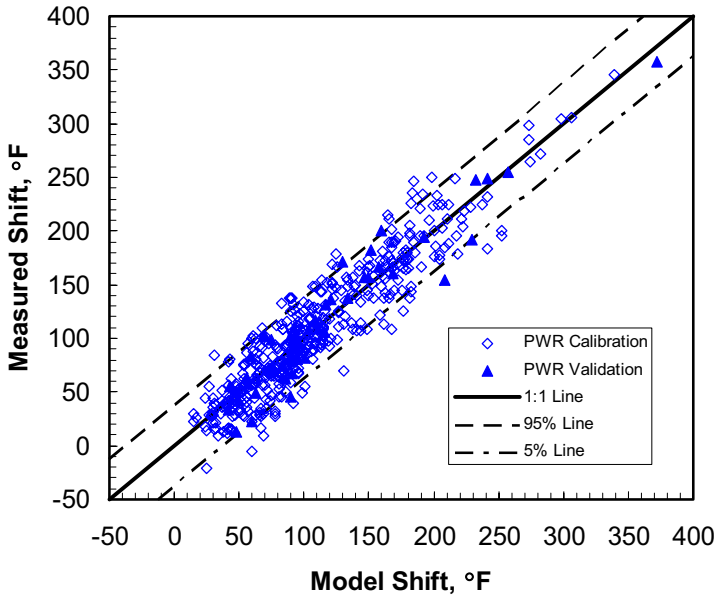

Fig. 4.10. Model shift vs measured shift, all PWR calibration and validation data with Cu > 0.072 wt %.

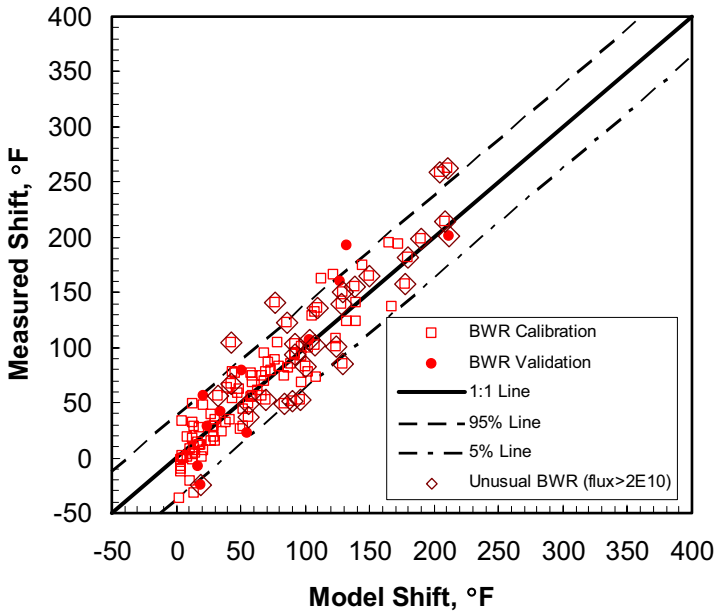

Fig. 4.11. Model shift vs measured shift, all BWR calibration and validation data with Cu > 0.072 wt %.

4.3 Quality of Fit of Revised TTS Model

This section presents several measures of goodness of fit of the revised TTS model and demonstrates predictive capability on surveillance data not used for fitting. Additional details on the TTS model trends, including analysis of their statistical significance on the available surveillance data, are given in Chap. 5.

4.3.1 Model TTS vs Measured TTS Plots

There are several ways to assess the quality of fit of the multivariable TTS model given above. The first, and perhaps clearest overall assessment, is given in the model shift vs measured shift plots, Fig. 4.8 for low-Cu steels and Figs. 4.10 and 4.11 for high-Cu PWR and BWR data, respectively. Separate plots are given for those three subsets, both to avoid an overly dense cloud of points that cannot be interpreted easily and also to demonstrate the good fit in these important subsets of the surveillance database. A good model should be a reasonable fit to each of these major subsets (among others). The fact that the cloud of points on each of these plots is reasonably centered on the 1:1 line over the available range of measured shifts shows a reasonable fit. The plots also show that the fit is comparable on the calibration data used for model development (open symbols) and the validation sample used to show predictive capability (filled symbols).

4.3.2 Statistical Measures

Another typical indicator of the quality of fit is the standard error (S_e), which is the standard deviation of residuals about the model, adjusted for the number of fitted constants in the model. Values of overall S_e are given for the earlier models in [1,8], for example. However, with the expansion of the database in 2003–2004, it became apparent that S_e is considerably smaller in the low-Cu data than in the high-Cu data. Thus, the overall S_e depends on the relative amount of low-Cu and high-Cu data in the calibration set and hence has no validity as an indicator of quality of fit across different databases. Simply including less high-Cu data or increasing the amount of low-Cu data would have the same effect as improving the fit, in all cases causing the value of the overall S_e to decrease. A similar result would be obtained by changing the proportion of forging and plate material (smaller S_e) relative to weld material (larger S_e). Because comparisons to the S_e values found for the earlier models or possible future models on different databases would not be valid, the overall S_e is not given for the revised model presented in this report.

A more valid measure than overall S_e is the standard deviation (S_d) of residuals about the model in the various subsets that have significantly different S_d, as given in Table 4.1. Standard deviation is used rather than standard error because many of the fitting constants in the model are fitted overall, not to the particular subsets shown in Table 4.1, and also because the S_d values are based on both calibration data used for fitting and validation data that were not used in fitting. The traditional standard error concept is not well suited to these complexities. The SRM data have not been included in the plate S_d values in Table 4.1, so that the tabulated values would be representative of plates in actual pressure vessels. The values of S_d in Table 4.1 should be considered when setting margins or analyzing uncertainties in applications.

In Table 4.1, the standard deviation of high-Cu welds is significantly greater than the standard deviation for high-Cu plates and forgings. The standard deviation of low-Cu welds is significantly greater than the standard deviation for low-Cu plates (but not low-Cu forgings). The standard deviation of forging and plate are not significantly different from each other in either high or low-Cu material. The standard deviation in the high-Cu subset is significantly greater than the corresponding value for the same product form in the low-Cu subset for both plate and weld. All of these significance tests used the F-test on variance with significance if $p < 0.05$.

Table 4.1 Standard deviation (S_d) of residuals about the embrittlement shift model in various subsets, all PWR and BWR calibration and validation data except SRM
All entries are TTS values measured in °F

Product Form	S_d (points)	
	Cu ≤ 0.072 wt %	Cu > 0.072 wt %
Forging	17.5 (75)	19.8 (61)
Plate	15.0 (78)	20.9 (309)
Weld	18.6 (93)	26.3 (213)

4.3.3 Residual Analysis

Another way to assess the quality of fit is by analyzing residual plots for variables that are in the model and variables that are not. Residual plots show the difference between the model estimate and the actual shift, plotted against variables of interest. A good multivariable fit shows residuals scattered about the zero residual line with no apparent trend when plotted against the variables that are in the model and those that are not. Interactions of key variables can also be analyzed, and a fit that adequately reflects interaction nonlinearities will show no significant trend in the interactions. If the slope of the residual trend were significantly different from zero for a variable in the model, it would indicate that the model does not accurately reflect the first-order (linear) effect of that variable. Similarly, a nonlinear pattern in the residuals for a variable in the model would indicate a model inaccuracy of a nonlinear form. Finally, if the slope of the residual trend were significantly different from zero for a variable that is not in the model, it would indicate that the variable should be added to the model for a better fit.

The result of the residual analysis on the TTS model presented in this report is that there are no linear residual trends with slopes that are significantly different from zero, in either high- or low-Cu data, for all of the variables in the model and for all others that were analyzed. The statistical tests were two-sided, looking for a significant difference from zero slope in either direction. The residual plots are presented in Appendix F as Figs. F.1 through F.13 for low-Cu material and Figs. F.14 through F.28 for high-Cu material. The dashed line on each residual plot is the linear trend of the residuals, fitted to the residuals by least squares. Many of the trend lines are barely distinguishable from the zero residual line over the range of data. Moreover, there is no clear evidence of nonlinear trends in the residual plots for the modeling variables. Because the low-Cu residual indicates the quality of fit of the MF term separate from the CRP term, while both MF and CRP terms are reflected in the high-Cu residuals, it is useful to look at both measures of the fit. When the plots are interpreted, it is important to recall that the residual for these plots is defined as model TTS – measured TTS, so the residual and model slopes are reversed in sign. That is, a negative slope on these residual plots can be eliminated by making the slope of that variable more positive in the model.

The residual plots in Figs. F.1 through F.28 also show both calibration and validation points. Overall, there is no obvious difference between the residual trends in calibration and validation data. A statistical comparison of the fit to calibration and validation sets is presented in Sect. 4.3.4.

Additional residual analysis was performed by comparing the mean residuals of selected sets using Student-t tests. No significant differences in mean residual were found for different product forms, in either low-Cu or high-Cu material. If there had been significant differences, they would suggest calibration issues with the MF or CRP coefficients. The residuals for the product form groups that were analyzed are plotted in Figs. F.10 for low-Cu and F.23 for high-Cu data. None of the mean residuals for these product form groups were significantly different from zero. An additional comparison found no significant difference in mean residual in high-flux ($\phi > 4.39 \times 10^{10}$) vs low-flux ($\phi \leq 4.39 \times 10^{10}$ n/cm^2/s) categories in either low-Cu or high-Cu material. The low-Cu flux comparison was conducted on all product forms combined because the amount of low-flux, low-Cu data is relatively small and all three product forms are represented in both high- and low-flux categories. That is not the case in the high-Cu data, so high-Cu comparisons were made on plate and weld separately, and not for forging material (there are not enough forging data with low-flux and high-Cu). As in the slope tests for continuous variables discussed above, the statistical tests were two-sided, looking for a significant difference between group means and from zero mean residual at $p < 0.05$.

4.3.4 Calibration vs Validation Datasets and Predictive Capability

The purpose of validation is to determine whether the model has predictive capability for data that were not used for calibrating it. In the present modeling effort, the validation is partial because there are insufficient data in the low-flux regime to be able to reserve a statistically meaningful sample of low-flux

data for validation. However, all of the model except the two flux-related fitting constants can be validated on a significant sample of data that were randomly selected prior to the modeling effort and that were not used in fitting. Future quantitative validation of the flux effect on surveillance data may be possible when data become available from the last remaining capsules of the BWR SSP [6]. An overall validation of many effects in the TTS model, including the effects of flux in both MF and CRP terms, is provided by comparison with the IVAR data in Chap. 6.

The validation set consists of a 10% random sample of data that was not used in developing most of the model or in the final calibration of most of the fitting constants. The parts of the model that did use points from the 10% sample during development and final calibration are the two constants in the effective fluence submodel and the two constants in the P*Mn submodel. Those four fitting constants were calibrated to the broadest possible dataset intended to reflect all low and high-Cu data, at both low and high flux. Because two of those subsets, low flux and low Cu, are much smaller than the high-Cu subset of the surveillance data, all available data at medium to low flux ($\phi < 5 \times 10^{10}$ n/cm^2/s) and all available data at low-Cu were used to better balance the 90% sample of high-Cu data for this purpose.

The two flux-related constants are not validated on the surveillance data because the flux effect is mainly evident in the range $\phi < 4.39 \times 10^{10}$ n/cm^2/s, and all available data in that range were needed and used for flux effect calibration. But the P*Mn term applies to all data, and the two constants in that term are validated by the 40 high-Cu validation points with $\phi > 5 \times 10^{10}$ n/cm^2/s which were not used to develop or calibrate the two constants. Additional confidence in the P*Mn term comes from theory and independent data that show strong P, Mn, and P-Mn interaction effects in low-Cu data (see Sects. 2.4.1 and 6.7.1). Additional confidence also comes from the fact that similar values for the P*Mn constants were calibrated during development on the PWR low-Cu data (219 points) and in the final calibration of those constants on the broadest possible set of high and low-Cu, high and low flux points (830 points).

Some comparisons of calibration and validation data have been discussed previously (see Figs. 4.8, 4.10, and 4.11), and they also appear on the model vs actual shift plots and the residual plots in Appendix F. Qualitative comparisons of that sort show reasonable agreement of calibration and validation data. A more quantitative method of validation is to compare mean residual and S_d of residuals between key calibration and validation subsets.

Table 4.2 shows reasonable agreement of the mean and standard deviation of residuals between high- and low-flux, high- and low-Cu calibration and validation subsets. None of the differences between mean residuals and only one of the differences between S_d in corresponding calibration and validation subsets is statistically significant, as indicated by the superscript a in Table 4-2 (two-sided t test on means, F test on S_d, significant if $p < 0.05$). The one difference in S_d that is significant involves only two points in the validation set, a clearly inadequate sample for comparing S_d values. So the statistics on validation sets generally confirm the calibrated model and the estimated S_d values. Also, none of the mean residuals in Table 4.2 is significantly different from zero, confirming the overall quality of fit on these 8 subsets. The one validation mean that might appear different from zero, –7.9 in the high-Cu, low flux group, is for a small sample (15 points) and is not significantly different from zero based on a t test (which accounts for the greater uncertainty in small samples).

Table 4.2. Comparison of calibration and validation subsets by mean and standard deviation (S_d) of residuals

The number of points is shown for subsets smaller than 40 points

Subset	Mean (points)		S_d (points)	
	Calibration	Validation	Calibration	Validation
Cu ≤ 0.072, $\phi > 4.39 \times 10^{10}$	0.0	0.9[a] (22)	17.0	14.6[a] (22)
Cu ≤ 0.072, $\phi \leq 4.39 \times 10^{10}$	1.7	−2.1[a] (2)	19.5	0.2 (2)
Cu > 0.072, $\phi > 4.39 \times 10^{10}$	0.5	1.4[a]	23.1	22.7[a]
Cu > 0.072, $\phi \leq 4.39 \times 10^{10}$	0.6	−7.9[a] (15)	21.2	26.7[a] (15)

[a]The difference from the calibration value is not statistically significant.

4.3.5 Comparison with SRM Data

Although not set up as a statistical validation study, the SRM data provide additional insight on the predictive capability of the model, because about two-thirds of the SRM datapoints were not used in any way for calibrating any part of the model. The three SRM heats have their own CRP coefficients, so any partial validation from the SRM data is not necessarily representative of all plates or of the forgings and welds. The comparison of measured and model estimates of shift for the SRM data in Fig. 4.12 shows that the model is a reasonable representation of embrittlement behavior for all the data on the three SRM heats, with almost all SRM data falling within the 5% and 95% bounds (which were based on S_d for high-Cu plates).

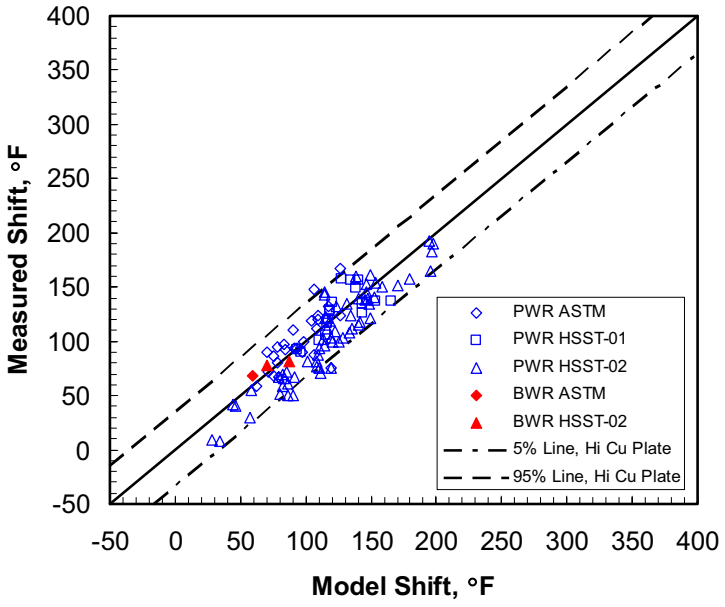

Fig. 4.12. Model shift vs measured shift for all SRM data.

Looking closer at Fig. 4.12, it appears that some of the points from Plate HSST-02 (triangle symbols) are reasonably distributed about the 1:1 line and others are offset below the 1:1 line (over-predicted) by an amount that is similar over a range of fluence (or shift). This evidence provides some support for the concept expressed at an ASTM E10.02 meeting in January 2004 that the average value of unirradiated T_{30} used for all shifts with this heat may not be representative of the specific piece of material sent to some of the plants because of inhomogeneity in the plate. Due to the SRM sampling, which limited the impact of this heat on the model, and the separate coefficient for SRM materials, which isolated all SRM materials from the coefficients fitted to other materials, the effect of this uncertainty on the predictions for vessel materials is considered to be negligible.

4.3.6 Numerical Convergence Checks

The calibration of the model relies on nonlinear least squares. As with any nonlinear solution algorithm, convergence is not guaranteed, and the solution to a nonlinear problem may not be unique. These uncertainties were addressed by fitting all the key intermediate and final models more than once, using different initial estimates of the fitting parameters and two completely different least squares solution algorithms. The solutions agreed to several digits, converging from different initial estimates and using different algorithms. This information provides a check on model implementation and inputs (which are quite different for the two solution algorithms) and reasonable confidence in the convergence of the results.

4.3.7 Comparison with Prior Models

The present model is similar in overall format to the NUREG/CR-6551 and July 2000 draft models [1,8], although differing in details. It includes all the effects except one from the prior models, although sometimes in different form. The linear MF temperature term is somewhat simpler than the Arrhenius term previously used. The P term in the MF part of the earlier models has been replaced by a P*Mn interaction in the MF part and a P precipitation term in the CRP part. The explicit use of Mn is new, but as in previous models, Mn is implicitly present in the form of lower coefficients for forgings, which have generally lower Mn compared to plates and welds.

The flux-time effect inside the tanh function in the July 2000 model has been replaced by a stronger flux effect in both MF and CRP terms, using the effective fluence form, which is a better fit to the larger set of low-flux data now available and is supported by mechanistic understanding and studies of an independent database (see Sects. 2.3.1, 2.4.2, and 6.6). The previously identified long-time bias, represented by a constant offset in the July 2000 model, is not evident in the data now available (see Figs. C.4 and C.17), so it is omitted from the present model. It appears that roughly doubling the amount of long time data and using a separate SRM coefficient caused that bias to disappear. The location of the transition to CRP plateau behavior now varies with Cu, Ni, and flux; it varied only with flux or time in the earlier models. These well-established effects are evident in the IVAR data [4,5], had been previously considered in the NUREG/CR-6551 fitting effort [1], and have been observed and calibrated in other databases [12].

4.4 References

1. Eason, E. D., J. E. Wright, and G. R. Odette, *Improved Embrittlement Correlations for Reactor Pressure Vessel Steels*, NUREG/CR-6551, U.S. Nuclear Regulatory Commission, Washington D.C., 1998.

2. Odette, G. R., "Radiation Induced Microstructural Evolution in Reactor Pressure Vessel Steels," pp. 137–48 in *Microstructure of Irradiated Materials*, MRS Symposium Proceedings, Volume 373, Pittsburgh, 1995.

3. Odette, G. R., and G. E. Lucas, "Embrittlement of Nuclear Reactor Pressure Vessels," *J. of Metals* 53 (7), 18–22, 2001.

4. Odette, G. R., T. Yamamoto, and D. Klingensmith, The Effect of Dose Rate on Irradiation Hardening of RPV Steels: A Comprehensive Single Variable Database and Model Based Analysis, Letter Report UCSB-NRC-03/1, U.S. Nuclear Regulatory Commission, Washington, D.C., 2003.

5. Odette, G. R., G. E. Lucas, R. D. Klingensmith et al., *The Effects of Composition and Heat Treatment on Hardening and Embrittlement of Reactor Pressure Vessel Steels*, NUREG/ CR-6778, U.S. Nuclear Regulatory Commission, Washington, D.C., 2003.

6. Chap. 3 (p. 3-3 regarding status of SSP Capsules A, B, C) in *BWR Vessel and Internals Project Updated BWR Integrated Surveillance Program (ISP) Implementation Plan*, BWRVIP-86-A, EPRI Report 1003346, October 2002.

7. Jones, R. B., and T. J. Williams, "The Dependence of Radiation Hardening and Embrittlement on Irradiation Temperature," pp. 569–90 in *Effects of Radiation on Materials: 17th International Symposium*, ASTM STP 1270, Ed. D. S. Gelles et al., American Society for Testing and Materials, 1996.

8. Kirk, M., C. Santos, E. Eason, J. Wright, and G. R. Odette, "Updated Embrittlement Trend Curve for Reactor Pressure Vessel Steels," in *Transactions of the 17th International Conference on Structural Mechanics in Reactor Technology (SMiRT 17), Prague, Czech Republic, August 17–22, 2003* (2003).

9. EPRI, Workshop on Dose Rate Effects in Reactor Pressure Vessel Materials Held November 12–14, 2001, Olympic Valley Calif., Electric Power Research Institute Conference Proceedings (CD), EPRI 1006981 (2002).

10. Williams, T. J., D. Ellis, C. A. English, and J. Hyde, "A Model of Irradiation Damage in High Nickel Submerged Arc Welds," *Int. Jour. of Pressure Vessels and Piping*, 79 649–60, 2002.

11. Odette, G. R., T. Yamamoto, D. Klingensmith, and H. Kishimoto, *The Effect of Flux and Irradiation Temperature on Hardening in RPV Steels*, Letter Report UCSB-NRC-03/2, 2003.

12. Williams, T. J., and D. Ellis, "A Mechanistically Based Model of Irradiation Damage in Low Alloy Steel Submerged Arc Welds," pp. 8–27 in *Effects of Radiation on Materials: 20th International Symposium*, ASTM STP 1405, ed. S. T. Rosinski et al. ASTM, 2001.

13. Server, W., C. English, D. Naiman, and S. Rosinski, Charpy Embrittlement Correlations – Status of Combined Mechanistic and Statistical Bases for U.S. RPV Steels (MRP-45), EPRI Report 1000705, 2001.

14. Miller, M. K., P. Pareige, and M. G. Burke, "Understanding Pressure Vessel Steels: An Atom Probe Perspective," *Materials Characterization* 44, 235–54, 2000.

15. Sokolov, M. A., R. K. Nanstad, and M. K. Miller, "Fracture Toughness and Atom Probe Characterization of a Highly Embrittled RPV Weld," *Effects of Radiation on Materials: 21st International Symposium*, ASTM STP 1447, Ed. M. L. Grossbeck, T. R. Allen, R. G. Lott, and A. S. Kumar, ASTM International, West Conshohocken, PA, 2004.

5. Effects of Individual Variables on TTS

In this chapter, individual variable effects in the TTS model given by Eqs. (4-1), (4-3), (4-4), and (4-5) are discussed in more detail. Plots are presented that show the trends in TTS as a function of variables that are in the TTS model, in most cases for various values and combinations of other variables. These are the same variable effects on which the residual plots in Appendix F are based. The fact that the residuals are reasonably distributed about the zero residual lines implies that the measured data are reasonably distributed about the TTS model trends shown in this chapter.

The second objective of this chapter is to show that the individual variable effects in the TTS model are statistically significant on the applicable surveillance data. The level of probability (p) used in this report for concluding that an effect is significant is $p < 0.05$ unless otherwise stated. This is a typical significance level for engineering, where it is sometimes referred to as the 95% significance level. That level of significance means that the chance the observed effect or difference could arise from random variation is estimated to be less than 5%. Statistical significance is one form of evidence supporting the TTS model, and most effects in the model are also supported by physical understanding and other independent data, as indicated below by cross-references to the relevant parts in Chaps. 2 and 6.

5.1 Material Variables

5.1.1 Copper

Copper affects embrittlement in several ways. The matrix features in materials with Cu ≤ 0.072 wt % show a simple square root dependence on fluence (as shown in Fig. 4.7) without much effect of Cu. Materials with higher Cu have the same matrix features as low-Cu materials plus a saturating precipitation effect that depends on Cu, shown by the CRP term in Fig. 5.1. The CRP plateau in Fig. 5.1 both increases in amplitude and shifts to lower fluence as the Cu level increases. The lateral shift is somewhat easier to see by focusing on the point on the transition that is halfway to full amplitude, marked by dots on Fig. 5.1. The transition occurs over a similar range in fluence at all Cu levels, which has the effect of increasing the slope of the transition as the Cu level increases. The sum of the square root dependence in Fig. 4.7 and the saturating plateau in Fig 5.1 is a rather "bumpy" curve for total shift in higher Cu materials, as shown in Fig 5.2.

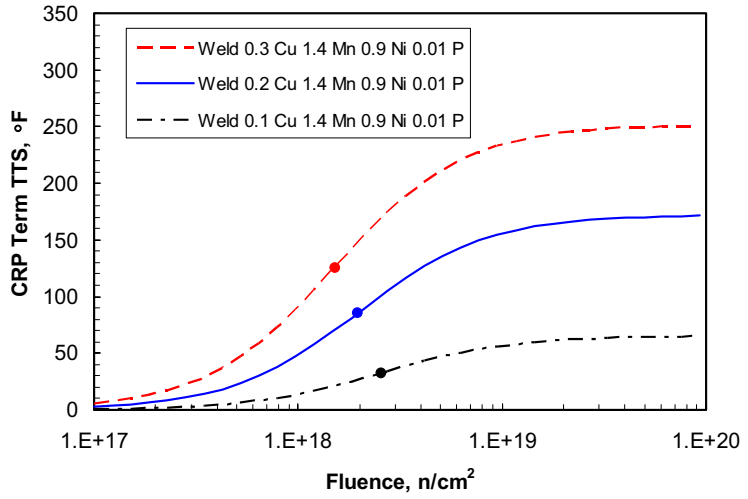

Fig. 5.1. Effect of Cu on CRP term amplitude and transition fluence. Dots indicate half amplitude location.

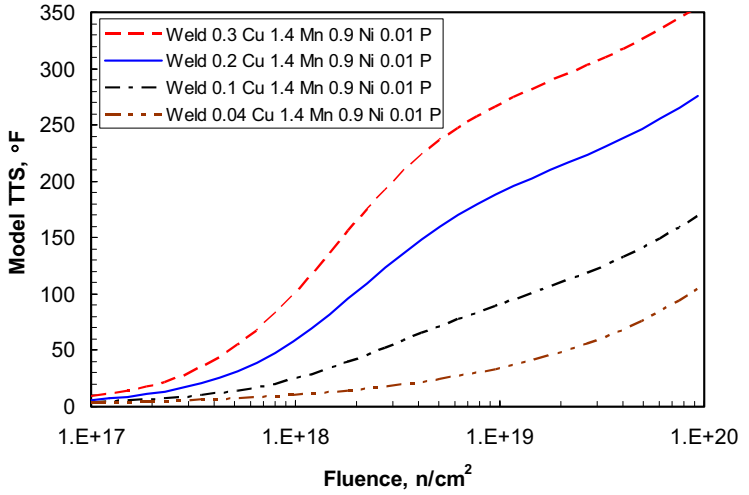

Fig. 5.2. Effect of Cu and fluence on TTS Model (MF term + CRP term).

The same effect shown in Figs. 5.1 and 5.2 can be plotted against Cu, as shown for average Ni in Fig. 5.3. There is also an interaction of Cu and Ni, such that the effect of Cu is enhanced at high Ni. The synergistic effect of Cu and Ni occurs with all product forms but is somewhat more complicated for high-Cu welds because different Cu saturation levels apply in the three weld groups, which also have different ranges of Ni, as shown in Fig. 5.4. The saturation levels of Cu are discussed in Sect. 5.1.3. Because of the strong Cu-Ni interaction, it is important to have no significant residual trend relative to the interaction variable Cu_e*Ni, as is the case with the TTS model (see Fig. C.27). Note in both Figs. 5.3 and 5.4 the initial flat segment of the curve corresponds to low-Cu material, where the shift does not vary much with Cu, and the final flat segment at high Cu reflects the limit of Cu available for precipitation, Cu_{max}.

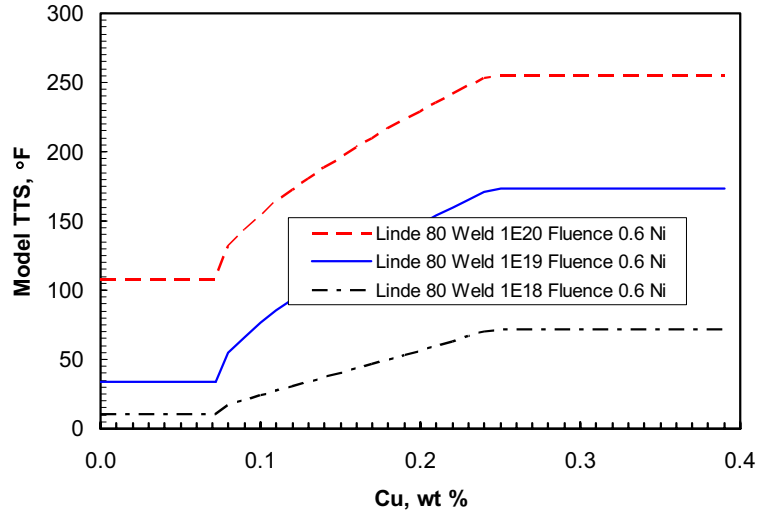

Fig. 5.3. Effect of Cu on TTS for average Ni Linde 80 welds at three fluence values.

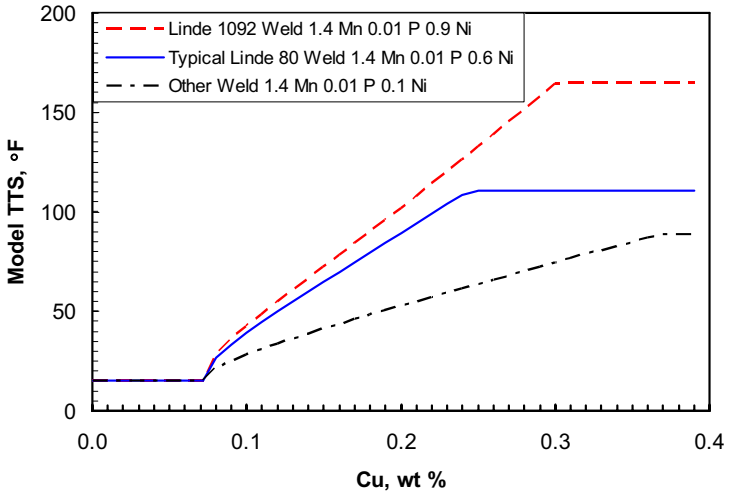

Fig. 5.4. Effect of Cu on TTS for three weld groups and 2×10^{18} n/cm^2 fluence.

The effect of Cu on the amplitude of the CRP term can be easily shown to be statistically significant by disabling it, using the average Cu value (0.1729 wt %) in the Cu term for all the high-Cu calibration and validation data. The residual slope that results from disabling the term is significant on the high-Cu calibration and validation data. A one-sided test is appropriate because the direction of the residual slope from disabling the effect is known in advance. Similarly, the Cu effect on the CRP term plateau location can be shown to be significant by using the average Cu value in the tanh term while continuing to use the actual Cu values in the amplitude of the CRP term. As both effects of Cu are separately significant, the combined effect of taking Cu entirely out of the TTS model is also significant.

5.1.2 Nickel

There are effects of Ni on CRP amplitude and plateau location, as there are for Cu. There is an overall enhancement of shift by increasing Ni for any particular Cu, as shown in Fig. 5.5. The CRP plateau in Fig. 5.5 both increases in amplitude and shifts to higher fluence as the Ni level increases. The lateral shift due to increasing Ni is in the opposite direction to that caused by increasing Cu, as can be seen by focusing on the point on the transition that is halfway to full amplitude, marked by dots on both Figs. 5.1 and 5.5. Because of the lateral shift, the fluence effect curves at various Ni converge essentially to a single curve at low fluence, as shown in Fig. 5.5 for the CRP term and in Fig. 5.6 for total shift (MF term + CRP term).

The convergence to essentially a single curve at low fluence corresponds to very small effects of Ni at low fluence and much larger effects at higher fluence, as shown for medium Cu levels in Fig. 5.7. Another implication is that the fluence at which the precipitation effect begins to be important varies more strongly with Cu than with Ni (compare the range in the fluence at TTS = 10°F on Figs. 5.1 and 5.5). For the higher Cu levels in welds, where the Cu saturation limits apply, there are different Ni curves within weld groups based on the different maximum Cu levels, as shown by the dashed curves in Fig. 5.8. Note that the curve segments for maximum Cu in Fig. 5.8 are upper bounds on TTS under the conditions used for plotting, and many materials within those weld categories will have lower Cu than the maximum and, hence, smaller shifts.

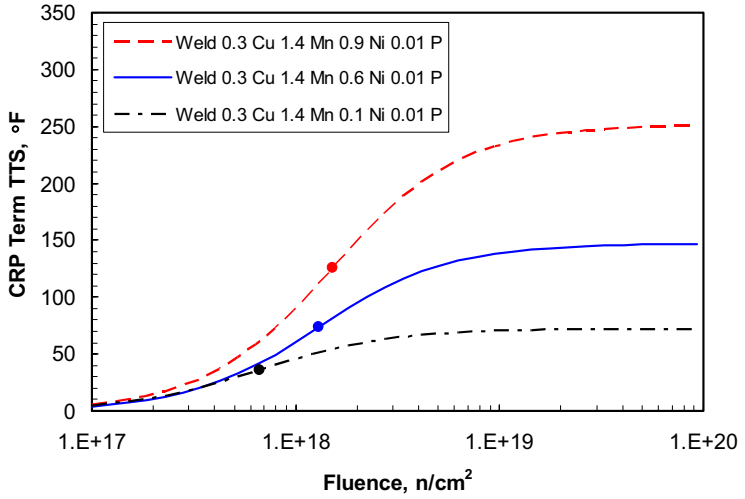

Fig. 5.5. Effect of Ni on CRP term amplitude and transition fluence. Dots indicate half amplitude location.

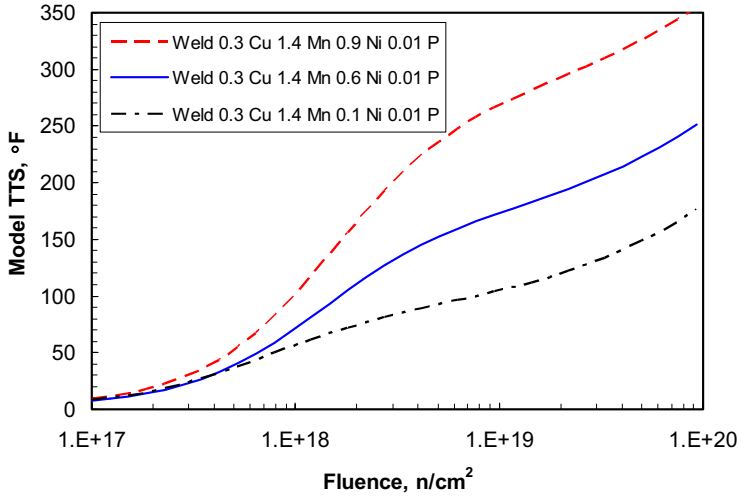

Fig. 5.6. Effect of Ni and fluence on TTS (MF term + CRP term).

Both the effect of Ni on CRP amplitude and the effect of Ni on plateau location are statistically significant, as can be shown by temporarily disabling the effects by using the average Ni in each of those places (separately), then testing the significance of the resulting residual trend slope. The procedure is exactly as described above for Cu, and the average Ni value on the high-Cu calibration and validation data is 0.5444 wt %.

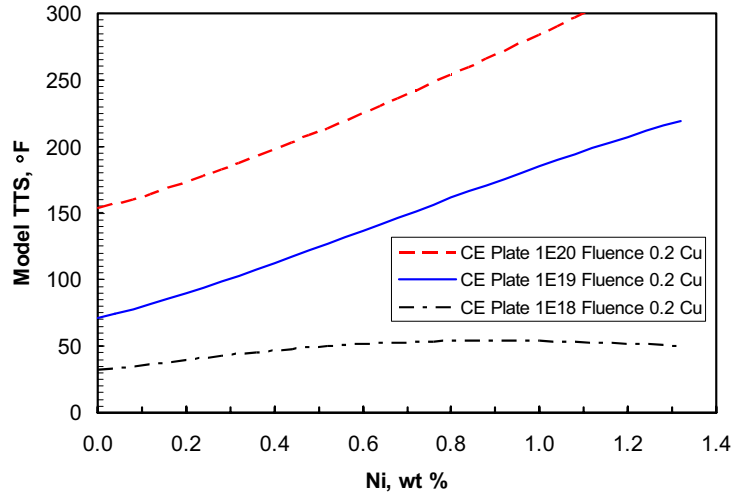

Fig. 5.7. Effect of Ni on TTS at typical Cu and three fluence values.

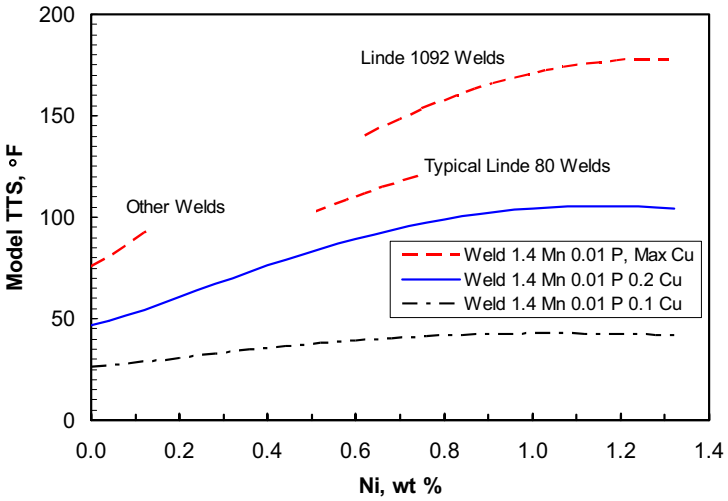

Fig. 5.8. Effect of Ni on TTS at various Cu levels and 2 × 10^{18} n/cm^2 fluence. The curves at Cu_{max} for each weld group are plotted over representative Ni ranges.

5.1.3 Maximum Cu Limits, Cu_{max}

Calibration of the limits on the maximum copper available for precipitation present several challenges due to limited data, including insufficient data to calibrate limits applicable to base metals. None of the forging materials in the surveillance database has nominal Cu high enough to be usable for calibrating Cu_{max}; only one of the plates does, and that plate is just above the lowest calibrated limit for welds of 0.25 wt %. The reason that lower-Cu materials are unusable for calibration is that the maximum Cu limit for a group of materials is determined solely by the materials with Cu values equal to or greater than the limit. The materials with lower Cu levels show only an increasing effect of Cu, with no limit behavior at all. Because of this, maximum Cu limits can only be determined if there are several materials that have Cu levels at and above the calibrated limit. There are only two weld groups, identified by their weld flux (Linde 80 and Linde 1092), for which there are at least six different material chemistries with

Cu > 0.243 wt % (the value of the lowest calibrated limit). The limits for any other welds must be based on very sparse data and information from other research, since there are insufficient data in the surveillance database for calibration.

The information available at this time suggests that the maximum Cu available for precipitation depends on the Ni concentration, postweld heat treatment, and possibly other factors as discussed in Sect. 2.3.2 and [1]. Thus, it is appropriate to consider Ni content as a possible way to group materials in large enough groups for estimating Cu maxima, and it is also appropriate to consider the two large high-Cu weld groups, within which individual welds have similar welding and heat treatment details. Weld flux is just a way of grouping welds that may have similar welding procedure and heat treatment, with no implication that the particular flux used for the welding directly affects the embrittlement of the steel. Thus, the two weld groups with sufficient high-Cu data to be separately considered, Linde 80 and Linde 1092, were examined in more detail, and Ni categories were also considered.

Three statistically justifiable categories are presented for the baseline model in Chap. 4: typical Linde 80 welds (the most common Linde 80 welds with nominal Ni > 0.5), Linde 1092 welds, and other welds. Low-Ni, medium-Ni, and high-Ni categories were also considered, but the current surveillance database is not adequate for calibrating Ni-based categories. A key difficulty with Ni categories in the surveillance database is that the Ni ranges of the particular Linde 80 and Linde 1092 datapoints that establish the Cu limits overlap substantially, yet those two weld categories have statistically significantly different limits. An additional difficulty with a Ni approach is that there are very few datapoints outside the medium-Ni range (nominally 0.5 to 0.75 wt % Ni) that have high enough Cu to be usable. Calibrating Cu_{max} as a continuous function of Ni is not feasible at this time, either. The detailed discussion of these issues is given in Sect. 7.2, where a two-category version of the three Cu_{max} categories in the baseline model is recommended for the simplified model presented in Sect. 7.3. All results in Chaps. 4, 5, and 6 were generated with the baseline model containing 3 Cu_{max} values.

The baseline Cu_{max} effect is statistically significant, as can be shown by taking out the variation of Cu_{max} by weld group and analyzing the residuals that result from this change. The simplest way to take out the effect is to calibrate a model with a single best-fit value of Cu_{max} (0.2646 wt % Cu) that is otherwise exactly like the baseline model. The average residual for the single-value Cu_{max} model in the "other welds" category (−11.8°F) is significantly below the average residual of typical Linde 80 welds (8.7°F), which is significantly above the average residual of Linde 1092 welds (−6.3°F). It should be noted that the "other welds" and Linde 1092 weld groups do not have significantly different average residuals in this analysis, so there is also statistical merit in a slightly simpler "typical Linde 80" vs "all other" grouping, as discussed in Sect. 7.2.

Only two welds establish the calibrated Cu_{max} value for the baseline "other welds" category. One is an atypical Linde 80 weld in Crystal River 3 with very low Ni (0.1 wt %) and high Cu (0.41 wt %). The other is a Rotterdamse weld from Sequoyah 1 with Ni = 0.125 wt % and Cu = 0.37 wt %. Since it is effectively based on just two dissimilar welds, the limit on Cu for the baseline "other welds" should be considered highly uncertain. Although there are many Linde 1092 welds in the database, the Cu_{max} value for the baseline Linde 1092 weld category is also not very well established, as there are only three Linde 1092 welds at and above the calibrated Cu_{max} level (0.301 wt % Cu). The only weld group that has a well-established Cu_{max} value is the typical Linde 80 weld group, which is calibrated on at least 21 Linde 80 welds that have Cu levels at and above the calibrated Cu_{max} value.

5.1.4 Phosphorus

The P effect in low-Cu surveillance materials ranges from almost no effect for low-Mn materials like ASTM A508 class 2 forgings to a clear linear effect of P for higher-Mn materials. This is a consequence of the P–Mn interaction, as shown in Fig. 5.9. The P effect in high-Cu material is the sum of the effect given by the MF term and an increase in the amplitude of the CRP plateau as P increases.

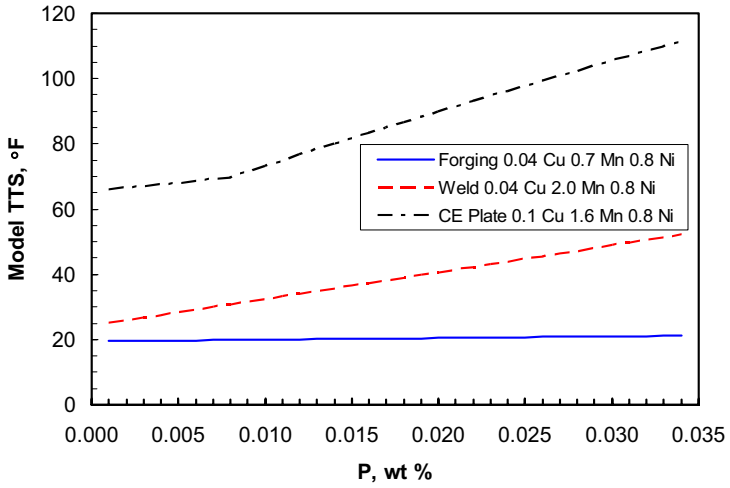

Fig. 5.9. Effect of P on TTS at high- and low-Cu and 6.5×10^{18} n/cm^2 fluence.

The increase in CRP term plateau amplitude due to increased P is similar in form but smaller in magnitude compared to the effects of Cu and Ni on plateau amplitude as described previously. In fact, based on Eq. (4-5e), increasing P from the threshold level of 0.008 wt % to the maximum value observed in the surveillance data, 0.031 wt %, will increase the CRP plateau amplitude the same amount as an increase in Cu from 0.072 to 0.103 wt %. P does not produce a lateral shift in the location of the plateau on the fluence plot, as do Cu and Ni. There will be an additional increase in TTS from the P* $Mn^{2.47}$ term in the MF term, depending on the material Mn. Thus, there are two slopes on the curve of TTS vs. P for high-Cu material, a flatter slope coming from the MF term (at a slope that depends on Mn), which extends from P = 0 to the threshold value P = 0.008 wt %, then a steeper slope at higher P, where both the MF and CRP terms contribute some effect. This is shown by the CE plate curve in Fig. 5.9.

The incorporation of phosphorus in the CRP term during model development was partly justified during model development by the fact that doing so eliminates the otherwise statistically significant residual trend with phosphorus in the high-Cu data. Similarly, incorporating phosphorus in the MF term was partly justified by the fact that doing so addresses the otherwise statistically significant residual trend with P*Mn and the significant trend with P in the low-copper data at above-average Mn (Figs. 4.5 and 4.6 depict these residual effects graphically). In both cases additional justification came from theory and results of independent research on other databases, as discussed in Sects. 2.3.2 and 2.4.1. The other data show P effects in both low-Cu and high-Cu data, as shown in Sects. 6.4 and 6.7. Hardening features that are enriched in P are also observed in the radiation-damaged microstructure (see Sect. 2.4.1 and [2]). The way in which the empirical terms were incorporated in the model is also supported by the fact that the model produces no significant residual trends with phosphorus or its interactions with other key chemistry variables (P*Ni and P*Mn), both in low- and high-Cu surveillance data, as discussed in Sect. 4.3, and shown in the figures in Appendix F.

After the model was completed, the significance of the P effects in both terms of the model was evaluated. If the final P*$Mn^{2.47}$ effect in the MF term is disabled by setting P and Mn to their average values (0.0119 and 1.30 respectively over all calibration and validation data) for the MF term but not the CRP term, the slopes of the resulting three residual trends for P, Mn, and P*Mn (over all calibration and validation data) are all statistically significant. The same result is obtained if the value of P*$Mn^{2.47}$ is set equal to its average value 0.02463 instead of setting P and Mn to their separate averages, while leaving P at its actual value in the CRP term. The significance tests are one-sided in this case because the directions

of the residual slopes from disabling the P term are known in advance. If the P effect in the CRP term is disabled by using the average value of P, but the $P*Mn^{2.47}$ term in the MF term is still active, using actual P and Mn, the slope of the residuals is also statistically significant. Disabling both $P*Mn^{2.47}$ in the MF term and the P effect in the CRP term also produces significant residual slope errors. This is evidence that both P terms, individually and together, are statistically significant in the final model.

5.1.5 Manganese, Product Form

The effect of Mn is partly explicit, via the $P*Mn^{2.47}$ part of the MF term, and partly implicit in the MF and CRP term coefficients and correlations with other composition variables. As noted in the discussion of P in Sect. 5.1.4, the explicit effect of Mn can be shown to be statistically significant by putting the average values of P and Mn in the MF term and analyzing the residual slopes relative to Mn and P*Mn over all affected data. But an additional effect of Mn (and probably other variables) is included in the MF and CRP term coefficients. This is shown in Fig. 5.10, which plots the effect of Mn for selected product forms in high-Cu and low-Cu materials. The explicit effect of Mn, coming from the MF term, is shown by the curves identified in the legend, each of which is plotted over the corresponding range of Mn in the surveillance database for high-Cu or low-Cu materials and for the particular product form group. The apparent implicit effect of Mn (and probably other variables) in the MF and CRP term coefficients is suggested by the arrows, which approximately pass through the mid-range Mn values for each product form group (see Sect. 5.1.6 for additional product form information). Note that the apparent implicit effect of Mn is at least as large as the explicit effect in low-Cu material and clearly larger than the explicit effect in high-Cu material for the examples shown on Fig. 5.10.

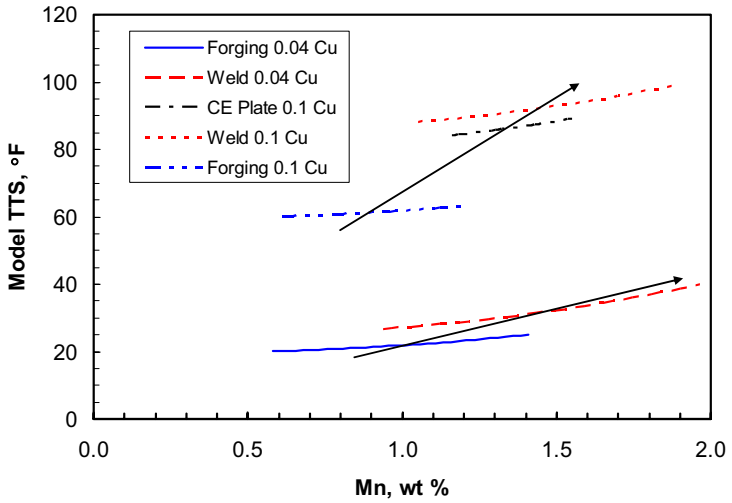

Fig. 5.10. Effect of Mn on TTS at high- and low-Cu and 6.5×10^{18} n/cm^2 fluence, 0.8 wt % Ni and 0.02 wt % P. Curves represent the explicit Mn effect from the MF term, arrows suggest the apparent effect of average Mn implicit in the MF and CRP term coefficients.

As noted in Sect. 4.1, attempts were made to capture as much of the Mn effect as possible explicitly, by initially calibrating Mn effects with single MF and CRP coefficients. The fact that this effort did not take out more of the apparent Mn trend in the coefficients may indicate confounding of variables and suggests that other variables in addition to Mn may contribute to the apparent Mn trend in the product form groups.

Most of the apparent Mn effect for typical high-Cu surveillance materials is in the TTS model coefficients, not the explicit $P*Mn^{2.47}$ term, as shown in Fig. 5.10. Thus, although the coefficients are identified in Eqs. (4-3b) and (4-5b) by product form labels, they also may be surrogates for average composition. For this reason, comparisons of the TTS model with plates or welds from other databases, which may have substantially lower Mn than typical surveillance materials, should use the most appropriate coefficient for the average composition, as is done for IVAR SMMS materials with Mn = 0 and 0.8 in Fig. 6.8(c). The justification is the fact that the forgings have considerably lower average Mn than plates or welds in the surveillance database. The coefficients may also include unmodeled effects of Ni, particularly affecting the MF coefficients, as noted in Sect. 5.1.6.

The hypothesis that the "product form" effect in previous TTS models could be a manganese effect (at least in part) was supported during the present analysis by the finding that either a manganese term or coefficients that vary by product form (or both) could reduce the residual difference between forging and other material groups. Introducing a P–Mn interaction effect in the MF term helped to account for the otherwise significant residual trend with Mn in the low-Cu surveillance data, but there is still a significant difference in the coefficients for forgings and other materials, where the main composition difference is Mn.

5.1.6 Additional Comments on Composition and Product Form

The surveillance database contains numerical dependencies and confounding among the composition and product form variables used for fitting, of which the Mn issues discussed above are but one example. Independent variation of composition variables is possible, and some composition variables can and do vary reasonably independently within and between product forms (e.g., wide variations in Cu in some welds, depending on the weld wire copper coating or lack of copper coating, ~10× variation in P across the database, ~2× variation in Mn between A 508 class 2 and class 3 forgings, ~ 6× variation in Ni between low Ni and typical Linde 80 welds). Composition variables have been intentionally varied independently over moderate ranges in RPV-like research materials, as in IVAR (see Sect. 6.1), which allows separation of variables in those studies. But the composition values in the surveillance materials do tend to occur in "clumps" and limited ranges corresponding to typical steelmaking practice for some materials, as shown in Appendix G.

The effect of typical steelmaking practices is to reduce the independence of composition and "product form" variables. Mn can be roughly estimated from Ni in both low-Cu and high-Cu data, using a statistically significant linear regression model. Mn can also be roughly estimated from Cu content in the high-Cu data by a statistically significant regression, and from forging vs plate and weld. Additional evidence includes the fact that the various product form groups do have different average values of Ni (see Appendix G). The average values of Cu also vary considerably by product form, but the average values of P do not. Other composition, microstructural, and mechanical property (e.g., unirradiated yield strength, upper shelf energy) variables may also be incorporated in what is referred to as the "product form effect." These numerical dependencies that exist in the surveillance database must be accepted and worked around in calibrating the TTS model, as it is not feasible now to include different steels in the surveillance capsules to help separate the effects of composition variables. The result is that the explicit Mn effect in the MF term may be partly confounded with a Ni effect, and the Ni and Cu effects in the CRP term may be partly confounded with a Mn effect, and all composition effects may be partially confounded with the product form effect.

As long as the TTS model is applied to estimate shifts in steels that are the same or similar to the steels represented in the surveillance database, the dependencies among the composition variables and coefficients cause no problems and the model should be directly applicable. The design of surveillance programs is intended to ensure that the surveillance materials are the same as, or as similar as possible to, the limiting materials in plants. However, the correlations among theoretically independent variables in

the TTS model should be considered when trying to reconcile results with other databases that have more independent variables, such as IVAR. In particular, the inability to calibrate an explicit Ni effect in the MF term on surveillance data, despite IVAR results [Figs. 6.10, 6.11, and 6.12(a)] suggesting there should be one, may be caused by the partial confounding of Ni with Mn and product form in the surveillance data. Similarly, Mn is known to affect high-Cu shifts [Figs. 6.7 and 6.8(c)] , so the inability to calibrate an explicit Mn effect in the CRP term may be related to partial confounding of Mn with Ni, Cu, and product form as well as to the explicit Mn effect contribution from the MF term.

Fortunately, over the range of compositions that are present in both the surveillance and IVAR databases, the agreement with the TTS model is generally good, as shown in Sects. 6.3 and 6.4. This suggests that the numerical dependencies in the surveillance data discussed above have not prevented the calibration of a reasonably robust model. The TTS model provides both a reasonable representation of the surveillance data and a reasonable approximation of the main independent composition trends indicated by IVAR results, as shown and discussed in Chap. 6.

The product form effects are statistically significant, as can be demonstrated by taking out the variation in coefficients. If a single coefficient is used in the MF term, all differences in mean residual between forging, plate, and weld are statistically significant over the data affected by that change (all calibration and validation data). If a single coefficient is calibrated in the CRP term, all product forms (including CE vs non-CE plates discussed in more detail in the following paragraphs) have significantly different mean residuals over the relevant data (high-Cu calibration and validation). These are all one-sided comparisons because the previously calibrated effect was intentionally disabled by using a single coefficient. Clearly the product form effect, including both microstructural variations and all related implicit composition effects, is a significant contribution in the model.

As first identified in the July 2000 modeling effort [3], there is a statistically significant difference between plates in CE-manufactured vessels and plates in other vessels, with the CE plates having greater shifts. The significant difference was independently noted by Professor Naiman in [4]. This difference was thought possibly to be caused by the grouping of SRMs with other plates (which was done in 2000). The current analysis proves otherwise because the difference between CE and non-CE plates is still significant in the present TTS model, where SRMs have their own coefficient in the CRP term to ensure that they could not affect the CE or non-CE plate coefficients.

The physical cause of the “CE plate effect” has not yet been identified, but the empirical evidence of it is strong. The coefficients in Eq. (4-5b) indicate that for the same composition and exposure, the CRP contribution to shift is about a third larger for plates in CE manufactured vessels, producing a difference in mean shift that is significant ($p < 0.0001$) on a substantial amount of data (181 CE points, 128 non-CE points). Possible causes include any of the physical differences that could be associated with different manufacturers, including vessel fabrication and heat treatment practices, any material differences that may not be fully accounted for in the composition terms in the model, differences in surveillance programs including testing, capsule placement, and exposure variable estimates, and possibly differences in plant operation that may be associated with the manufacturer of the vessel. Some have questioned the statistical association of the plate differences with different manufacturers on the basis that any effects associated with the vessel manufacturer should also show up in weld data. However, the Linde 1092 and Linde 80 weld groups have significantly different Cu saturation limits in Eq. (4-5d), and they are in fact associated with CE and non-CE vessel manufacturers, respectively, with the highest-Cu members of the CE weld group having greater shifts because of the higher Cu_{max} limit. Thus, broadly consistent CE vs non-CE shift differences are observed in both plates and welds. Differences in Ni content may contribute to this weld difference, although the substantial overlap in Ni content of the specific Linde 80 and Linde 1092 welds that have high enough Cu to establish the significance of Cu_{max} limits suggests that other factors may also be relevant (see Sect. 7.2.2). At this point, the difference in shift of CE and non-CE plates is adopted and accepted as a purely empirical part of the model.

5.2 Exposure Variables

5.2.1 Fluence, Effective Fluence, and Flux

The effect of fluence on radiation damage is well known and has been shown in several previously discussed plots, including Fig. 4.7 for the MF term, Figs. 4.9, 5.1, 5.5 for the CRP term, and Figs. 5.2 and 5.6 for both terms combined. The effective fluence approach adjusts the fluence effect to account for greater embrittlement damage at the same fluence under lower flux conditions. The effect of a lower flux in the effective fluence approach is numerically equivalent to the effect of a higher fluence, hence the name.

For the MF term, lower flux in the effective fluence form has the same effect as multiplying the MF shift by a factor greater than 1. The magnitude of the fluence multiplier can be determined by introducing Eq. (4-4) into Eq. (4-3) and working through the algebra. For instance, the effective fluence for a flux value of 1×10^9 n/cm^2/s is a factor of 2.67 times the nominal fluence. The multiplier on shifts estimated by the MF term at a flux of 1×10^9 is a factor of 1.63 (= $\sqrt{2.67}$) times the shift at 4.39×10^{10} n/cm^2/s or higher flux. The multiplier on MF shift arising from a particular lower value of flux is the same at any fluence, for any temperature, composition or product form. The effect of flux on the fluence plot is shown in Fig. 4.7.

For the CRP term, lower flux causes the CRP plateau to be reached at a lower nominal fluence, but it does not increase the amplitude of shift at high fluence after reaching the CRP plateau. The effect of flux on CRP plateau location at various flux levels is shown in Fig. 5.11. Lower flux shifts the plateau to lower fluence without changing its amplitude. Combined with the MF term effect, the total shift is as shown in Fig. 5.12.

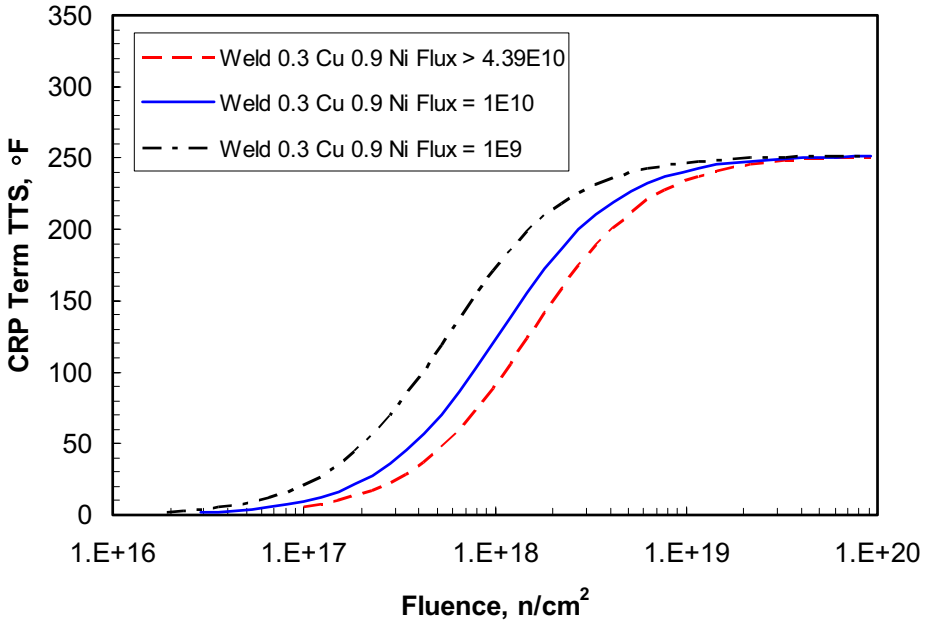

Fig. 5.11. Effect of flux on TTS in CRP term.

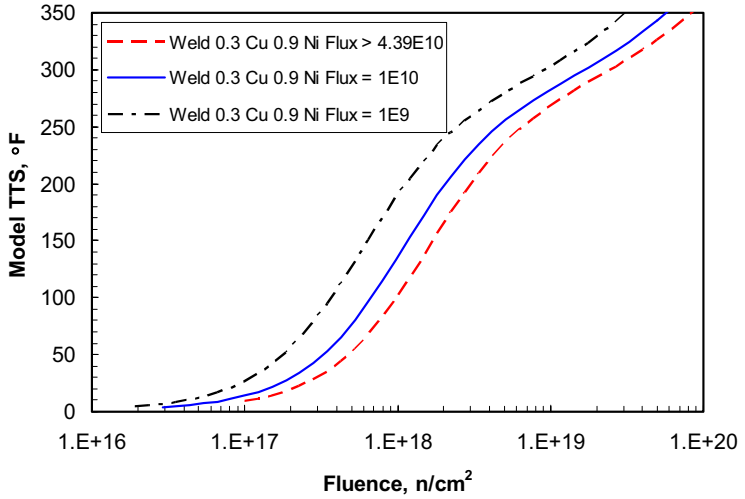

Fig. 5.12. Effect of flux on total TTS (MF term + CRP term) for $\phi t < 8 \times 10^{16}$ n/cm^2.

In the surveillance data, the apparent effect of flux above 4.39×10^{10} n/cm^2/s has a flatter slope compared to the effect below that value. This can be seen in the flat residuals on Figs. F.2 and F.15, which would show a residual slope above 4.39×10^{10} n/cm^2/s if there were a strong effect of flux in that range. The observation of a much flatter, nonsignificant slope in PWR data motivated the piecewise form of effective fluence used in the TTS model. The break point is a calibrated value from the fit to both low- and high-flux data, and a completely flat function above the break point was assumed for the calibration, based on the observed nonsignificant effect in the PWR surveillance data. Note that the lack of a strong flux effect in the PWR data may be caused by limitations of the surveillance data, as discussed in Sect. 6.6.1. The piecewise form differs somewhat from a simple power law form, although they can give roughly similar results over the range in flux found in surveillance data ($\phi > 4 \times 10^8$ n/cm^2/s) as shown in Fig. 5.13.

Both curves in Fig. 5.13 are approximations of the fitted recombination model applied to individual materials in Sect. 6.6. The main difference is that the exponents for the curves in Fig. 5.13, though different from each other, are both constant values that would apply to many materials, while in the fitted recombination model the exponent is fitted to individual materials and is (theoretically) a function of flux, Cu diffusion rates, and other variables. Additional discussion of the flux effect, including the similarities and likely reasons for the differences between surveillance and IVAR results, is provided in Sect. 6.6. Figure 6.20 is a key result, showing that the extension of the flux dependent trend in the TTS model to higher flux levels is in reasonable agreement with the IVAR results, and the physically based extrapolation of the IVAR recombination model to the BWR flux range is in reasonable agreement with the TTS model.

It is easy to check the significance of effective fluence in each term of the TTS model separately and the combined effect in both terms. For the MF term, the relevant data includes both low-Cu and high-Cu data with sufficiently high fluence ($\phi t > 8 \times 10^{16}$ n/cm^2) to exhibit measurable effects. The significance test is done by simply using fluence instead of effective fluence in the MF term, while continuing to use effective fluence in the CRP term. The significance test asks whether the slope of the residuals is significantly greater than zero on all data with $\phi < 4.39 \times 10^{10}$ n/cm^2/s and $\phi t > 8 \times 10^{16}$ n/cm^2. The first condition arises because only the data with $\phi < 4.39 \times 10^{10}$ n/cm^2/s show a substantial flux effect, while the second condition is based on the fact that measured shift is essentially zero below $\phi t = 8 \times 10^{16}$ n/cm^2, even at low flux, as shown in Fig. 5.14. Thus, data that do not meet both conditions are not useful for

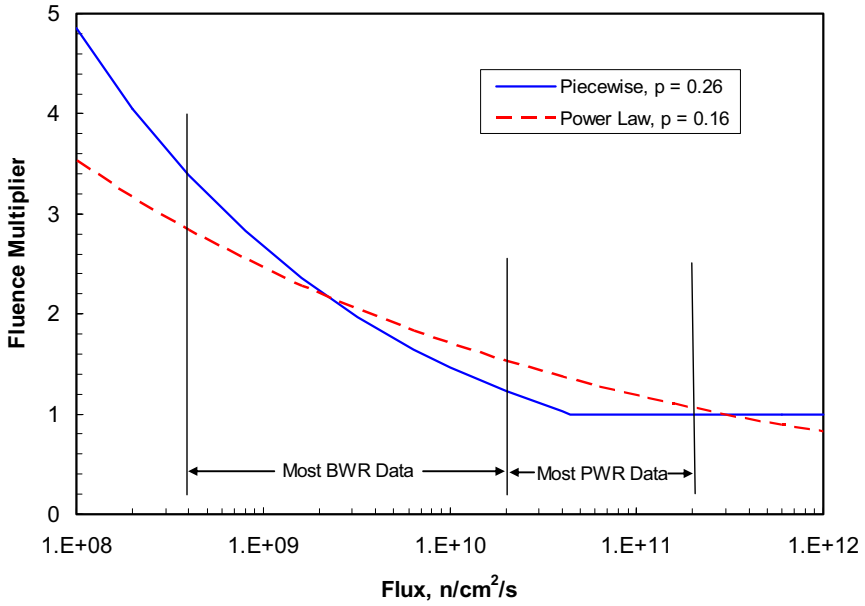

Fig. 5.13. Schematic of effective fluence in the TTS model (solid curve) and a power law form with p = 0.16 (dashed curve).

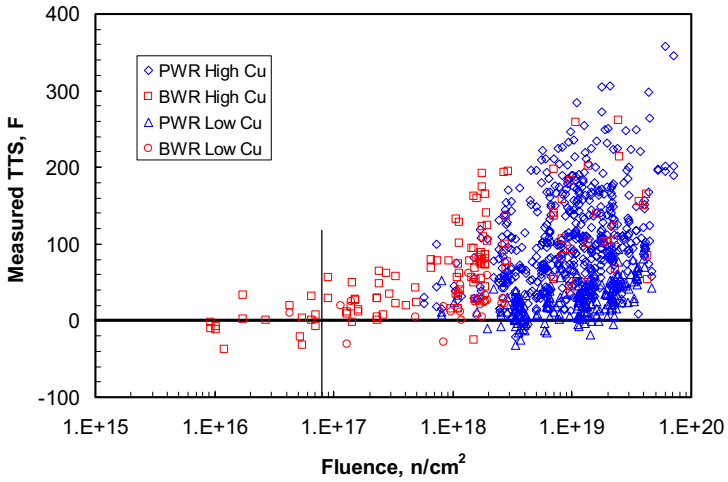

Fig. 5.14. Measured shift is essentially zero (avg. = –1.3 °F) for $\phi t < 8 \times 10^{16}$ n/cm^2.

determining whether fluence or effective fluence should be used. The significance test is one-sided because the direction of the residual slope resulting from taking out the flux effect is known in advance. The slope of the residuals is statistically significant, confirming the significance of using effective flux in the MF term. Without flux in the MF term, there is also a statistically significant mean residual, –7.5°F, in the 103 BWR datapoints with $\phi < 2 \times 10^{10}$ n/cm^2/s and $\phi t > 8 \times 10^{16}$ n/cm^2, again showing the need for using effective fluence in the MF term.

Similarly, one can test for the significance of the flux effect on high Cu data, using effective fluence in the MF term and nominal fluence in the CRP term, or just use fluence (no flux effect) in both terms for

all data. Those analyses show that flux, modeled as effective fluence, is also significant in the CRP term and in both terms used together. The residuals for the latter case, again meeting the two tests $\phi < 4.39 \times 10^{10}$ n/cm^2/s and $\phi t > 8 \times 10^{16}$ n/cm^2, are shown in Fig. 5.15, where there is no doubt that the use of fluence rather than effective fluence leads to large negative residuals at low flux and a significant unmodeled trend with flux. Without a flux effect in either term, the average residual in the 103 BWR datapoints with $\phi < 2 \times 10^{10}$ n/cm^2/s and $\phi t > 8 \times 10^{16}$ n/cm^2 is –15.9°F, which is significantly less than zero. A large cloud of higher-flux ($\phi > 4.39 \times 10^{10}$ n/cm^2/s) data has been omitted from Fig. 5.15. Because the effective fluence term in Eq. (4-4) has no effect on those data, the residuals are the same with or without effective fluence. Therefore, Figs. C.2 and C.15 show the residuals from $\phi > 4.39 \times 10^{10}$ n/cm^2/s points for both fluence and effective fluence.

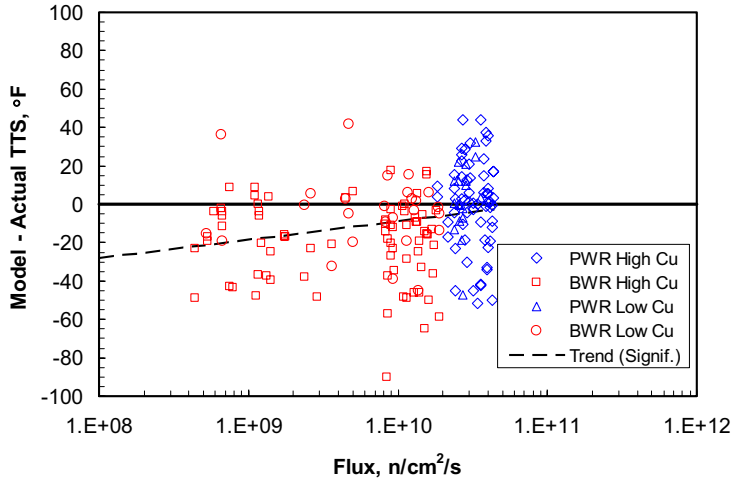

Fig. 5.15. Significant residual trend using fluence instead of effective fluence, $\phi < 4.39 \times 10^{10}$ n/cm^2/s and $\phi t > 8 \times 10^{16}$ n/cm^2.

The flux effect, implemented as effective fluence in both MF and CRP terms, is also supported by significant trends with flux in the independent IVAR database. As in the surveillance data, the effects of flux are apparent in both the no-Cu steels (see Sect. 6.6.2) and the Cu-bearing steels (see Sect. 6.6.1) that are in the IVAR database.

Although the calibration data range included a few flux observations as low as $\phi = 1.8 \times 10^8$ n/cm^2/s, as shown in Table 3.3, the flux values in the surveillance database below about 4 to 6 $\times 10^8$ n/cm^2/s correspond to fluence below about 8×10^{16} n/cm^2, where the observed shifts are near zero with or without the effective fluence term, as shown in Fig. 5.14. Thus, the useful flux range in the calibration data is $\phi \geq 4 \times 10^8$ n/cm^2/s (the range of the data shown on Fig. 5.15), and applications to lower flux should be considered extrapolations beyond the currently available and usable data. Moreover, as noted in Chap. 3, the highest fluence that is available in surveillance data decreases as flux decreases, such that there are no data in the surveillance database with $\phi < 2 \times 10^{10}$ n/cm^2/s and $\phi t > 5.1 \times 10^{18}$ n/cm^2. Applications at $\phi < 2 \times 10^{10}$ n/cm^2/s and fluences higher than 5.1×10^{18} n/cm^2 (and, similarly, above lower fluence values at lower flux levels) are also extrapolations beyond the currently available data.

5.2.2 Irradiation Temperature

The TTS model presented in Chap. 4 requires values of T_i, the average temperature of the metal during irradiation. The surveillance database uses the time-averaged coolant temperature in the vicinity of the surveillance capsule as the best available estimate of Charpy specimen metal temperature during irradiation. This choice was one of necessity - the only other direct information on surveillance specimen temperature during irradiation is thermal monitor (melt wire) results, which only give an approximation of the maximum temperature reached over a period of time, not the average. In applications of the model, one should use the best available estimate of time-averaged metal temperature at the specific location in the vessel wall being analyzed, which will not be coolant temperature in many applications (e.g., at the tip of an assumed buried flaw or at any other location in the vessel wall).

The temperature effect in the MF term is in the same form as that used by Jones and Williams [5], but the calibrated coefficient on temperature is somewhat larger than in their studies. The temperature coefficient in the MF term for surveillance data is also larger than the value found in IVAR, though the overall trends with temperature in the most similar steels are similar (see Sect. 6.5). The fact that the temperature effect in the TTS model adequately fits the surveillance data is supported by the zero residual slopes in Figs. C.3 and C.16.

The temperature effect is shown for low-Cu and high-Cu cases on Fig. 5.16. The magnitude of the effect in this example is about 0.88 degrees increased shift per degree temperature decrease for the low-Cu conditions (MF term only) and 0.65 degrees increased shift per degree temperature decrease for the high-Cu conditions shown on Fig. 5.16 (using both terms). These “degree shift per degree temperature” estimates depend on the conditions assumed when estimating them and would be different under other conditions (e.g., other product forms, different chemistry, different fluence).

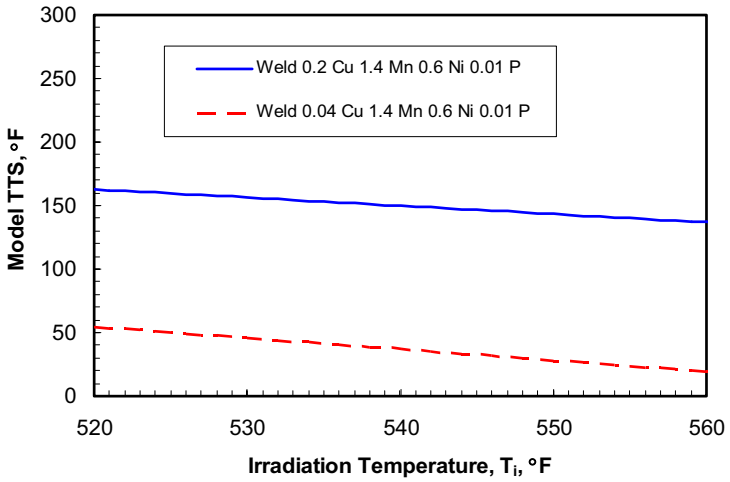

Fig. 5.16. Effect of estimated irradiation temperature.

The T_i effect is statistically significant in the MF term, as can be demonstrated by noting the significant slope to the residuals that results from disabling it (setting T_i equal to the average value over all calibration and validation data).

The T_i effect in the CRP term is just a small empirical correction factor, partially counteracting the MF T_i effect to approximate the somewhat flatter overall temperature effect observed in high-Cu surveillance data compared to low Cu surveillance data. The T_i correction in the CRP term has little effect on estimated shift, amounting to –4.3%, +5.5% of the value of the CRP term (and hence a smaller percentage of total TTS) over the full range of temperatures in the database. The form of the correction

term was designed to facilitate removal without recalibration by setting it equal to 1 for all T_i, because CRP T_i terms were found to be small in prior calibration efforts.

A linear residual analysis finds that the baseline T_i term is not statistically significant, as shown by setting the CRP T_i term equal to 1 and checking the significance of the slope of the line fitted to residuals over all the high-Cu data (both calibration and validation). However, additional analysis of the data that are most affected by the CRP T_i term (the points at least ±15°F from average T_i), again with no T_i term in the CRP part, indicates a significant difference in low- and high-T_i residuals, suggesting a nonlinear trend in the same direction as the baseline T_i term and a significant average residual at low temperature. The direction of the apparent temperature trend in the surveillance data is a slightly flatter slope in the high-Cu data than in low-Cu data, as shown in Fig. 5-16, while the IVAR data from controlled experiments show the opposite trend—a steeper slope in high-Cu data than in low-Cu data, as shown in Figs. 6.13 and 6.14. The questionable significance and contrary direction of the trend led to additional analysis reported in Sect. 7.1. The CRP T_i term is included in the baseline model used for the results in Chaps. 4, 5, and 6 but has been dropped from the simplified model presented in Sect. 7.3 based on that analysis.

It should be noted that the way the temperature effect is implemented in the TTS model, with a strong temperature term in the MF part and a small correction in the CRP term (or no CRP T_i term), works because (a) the temperature trend in low Cu surveillance materials is relatively strong and (b) the CRP term contribution to total shift is roughly comparable to the MF term contribution to total shift in the surveillance data. If some plant applications have much larger CRP contributions relative to the MF contributions than in the surveillance data, and if those applications are at temperatures far from the average in the surveillance database, the TTS model may underestimate the temperature effect.

5.3 References

1. Odette, G. R., and G. E. Lucas, "Embrittlement of Nuclear Reactor Pressure Vessels," *J. of Metals* 53(7), 18–22, 2001.
2. Miller, M. K., P. Pareige, and M. G. Burke, "Understanding Pressure Vessel Steels: An Atom Probe Perspective," *Materials Characterization* 44, 235–54, 2000.
3. Kirk, M., C. Santos, E. D. Eason, J. E. Wright, and G. R. Odette, "Updated Embrittlement Trend Curve for Reactor Pressure Vessel Steels," in *Proc. Structural Mechanics in Reactor Technology (SMiRT) Conference*, 2003.
4. Server, W., C. English, D. Naiman, and S. Rosinski, *Charpy Embrittlement Correlations—Status of Combined Mechanistic and Statistical Bases for U.S. RPV Steels (MRP-45)*, EPRI Report 1000705, 2001.
5. Jones, R. B., and T. J. Williams, "The Dependence of Radiation Hardening and Embrittlement on Irradiation Temperature," pp. 569–90 in *Effects of Radiation on Materials: 17th International Symposium*, ASTM STP 1270, Ed. D. S. Gelles et. al., American Society for Testing and Materials, 1996.

6. Comparison of the IVAR Database with the Calibrated TTS Model Predictions

The purpose of this chapter is to compare the trends in the Irradiation Variable (IVAR) database with the TTS model described in Chap. 4. The direct comparison was performed after the modeling effort in Chaps. 3 to 5 was completed, though preliminary IVAR results on some of the variable trends were available earlier.

6.1 The IVAR Program and Database

The main objective of the IVAR program was to develop an irradiation hardening and microstructure database that provides a high-accuracy and high-resolution map of the individual and combined effects of key RPV steel embrittlement variables, including: irradiation temperature (T_i), flux (ϕ), fluence (ϕt), alloy composition (Cu, Ni, Mn, P, C, N, Mo, Sn/As/Sb, B), heat treatment and product form. Other IVAR objectives were to study embrittlement mechanisms, to explore phenomena like late-blooming Mn-Ni rich phases, and to develop a better understanding of deformation and fracture micromechanics in irradiated RPV steels. The main focus of this chapter is to compare the IVAR yield stress change ($\Delta\sigma_y$) database to the predictions of the TTS model fitted to the surveillance data described in Chap. 4.

The IVAR database includes stress-strain curves determined by testing sub-sized tensile specimens and associated information on CRPs and MFs derived from a variety of microanalytical characterization techniques, with special emphasis on the small-angle neutron scattering (SANS) and resistivity-Seebeck coefficient (RSC) methods [1,2]. The irradiations were carried out in three flux (ϕ) regimes and three irradiation temperatures (T_i) in the IVAR facility at the University of Michigan Ford Research Reactor [3]. The IVAR facility was designed by UCSB and ORNL and was operated by ORNL and University of Michigan staff for a total of 27,650 reactor hours. The high- and low-flux irradiation assemblies and the specimen subcapsule configuration are shown in Fig. 6.1. The nominal flux levels were $\approx 8 \times 10^{10}$ (low), $\approx 3 \times 10^{11}$ (medium) and $\approx 8 \times 10^{11}$ (high) n/cm^2-s, E > 1 MeV. The irradiation temperatures were 270, 290 and 310°C. The irradiations at different fluxes were carried out over overlapping fluence ranges from ≈ 0.006 to 3.6×10^{19} n/cm^2.

The specimens were contained in a total of 80 individual capsules, which occupied one of the 54 IVAR locations for various periods of time. Capsules were inserted and removed during scheduled reactor shutdown periods by using a transfer cask to move the entire irradiation assembly to a nearby hot cell. When not occupied by an actual capsule, a dummy block was inserted in the location to provide a stable neutronic environment. Extensive 3-D neutronics calculations were carried out by ORNL to provide a flux map of the entire IVAR facility [4]. The map was validated and calibrated by multiple activation reaction measurements. The flux map was found to be consistent with individual capsule Ni and Fe dosimetry wire measurements, made as part of the IVAR program, to within ≈ ±7%. The specimens in a capsule were assigned a fluence corresponding to the full power irradiation time and the nominal flux at the center of each capsule. The capsule temperatures were continuously monitored by 49 thermocouples, that also provided feedback control for achieving the prescribed conditions, which remained extremely stable and close to the nominal set points. Coupled with the thermocouple monitors, extensive heat transfer calculations showed that the specimen temperatures were within ±5°C of the nominal values [5].

The IVAR alloy matrix included 41 split melt model steels (SMMS) with systematic single and combined variations in the alloy Cu, Mn, Ni, and P and other compositional variables. The balance of elements was nominally the same and was selected to match typical A533B RPV plate steels. The SMMS were melted in final (approximately) 10-kg batches. One set of alloys with controlled composition variations, from Laval University, was hot-rolled to 27-mm plate (LV alloys) and the other set, produced at Sheffield University and acquired in collaboration with AEA Technology, was hot-rolled to 18-mm plate (CM alloys). The baseline heat treatment for the LV SMMS was as follows: austenitize at 900°C for 1 h, air cool, temper at 664°C for 4 h, air cool, stress relieve at 600°C for 40 h, and air cool. The baseline heat treatment for the CM SMMS was as follows: austenitize at 900°C for 30 min, salt quench to 450°C

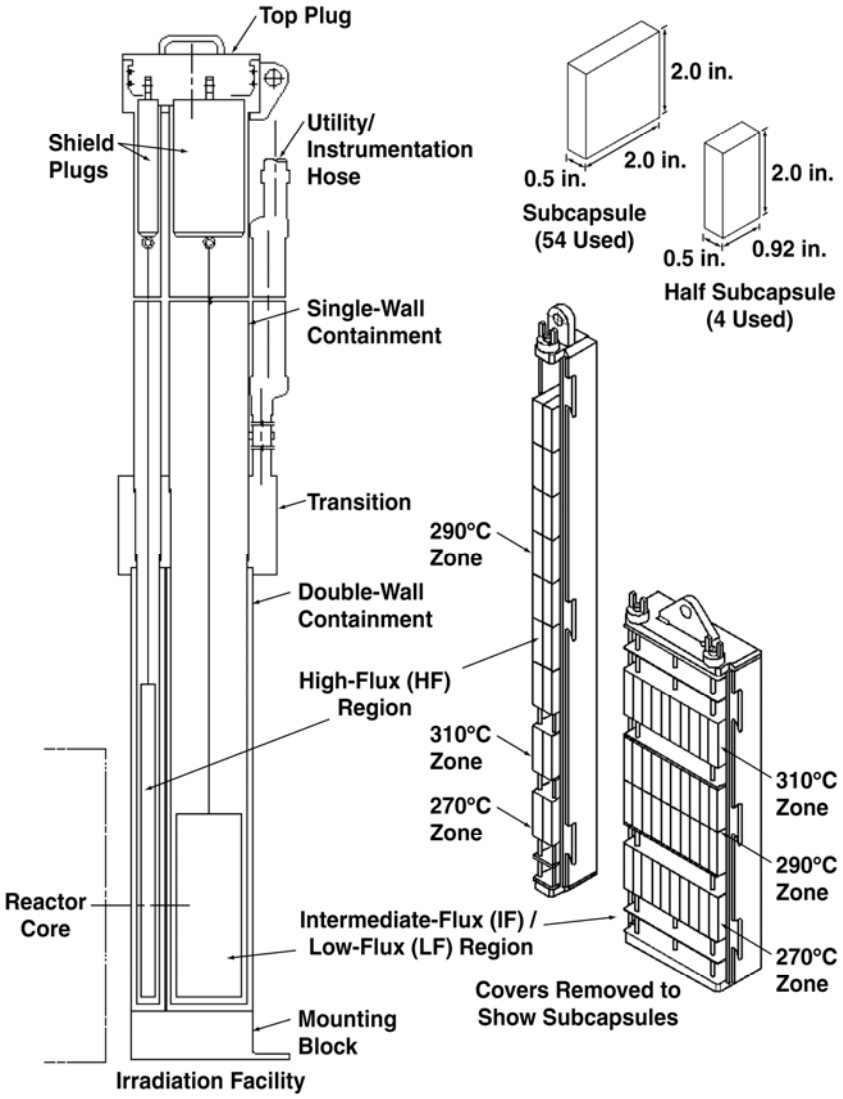

Fig. 6.1. The IVAR irradiation facility and specimen capsules.

and hold for 10 min, temper at 660°C for 4 h, air cool, stress relieve at 607°C for 24 h, cool at 8ºC/h to 300°C, and air cool. Additionally, a set of 9 CM SMMSs were heat treated to 15 combinations of stress relief times and temperatures and then irradiated at high flux and at 290°C to 0.85×10^{19} n/cm^2 [6]. The SMMS experiments were complemented by irradiations of 14 commercial or program steels, including 10 welds, 3 plates, and 1 forging. Further perspective on the objectives and character of the SMMS is given in the following paragraphs.

A subset of the IVAR data is compared with the TTS model predictions in the remainder of this chapter. The IVAR data used in this report are summarized in Appendix B. The compositions and heat treatments of the alloys are shown in Table 6.1; the irradiation conditions are summarized in Table 6.2. The alloys include the following; their nominal compositions are noted.

- Twelve Cu-bearing SMMSs: Cu ≈ 0.11 to 0.43 wt %, Ni ≈ 0.18 to 1.7 wt %, Mn ≈ 0.0 to 1.69 wt %, and P ≈ 0.002 to 0.008 wt %
- Nine nominally Cu-free SMMSs plus one SMMS with Cu = 0.05: Cu ≈ 0.01 to 0.05 wt %, Ni = 0 to 1.68 wt %, Mn = 0.01 to 1.67 wt %, and P = 0.003 to 0.035 wt %

Table 6.1. Alloy compositions and heat treatments

	Composition (wt %)									
Alloy	Cu%	Ni%	Mn%	Cr%	Mo%	P%	C%	Si%	HT #[a]	Prod. Form
CM1	0.01	0.01	1.67	0.04	0.56	0.003	0.13	0.15	1	SMMS[b]
CM3	0.02	0.85	1.60	0.00	0.49	0.006	0.13	0.16	1	SMMS
CM4	0.02	0.86	1.53	0.05	0.55	0.031	0.16	0.16	1	SMMS
CM5	0.02	0.86	1.61	0.04	0.53	0.035	0.15	0.16	1	SMMS
CM6	0.02	1.68	1.50	0.05	0.54	0.007	0.15	0.17	1	SMMS
CM8	0.01	0.86	0.01	0.04	0.55	0.004	0.13	0.14	1	SMMS
CM9	0.01	0.86	0.85	0.04	0.55	0.003	0.15	0.15	1	SMMS
CM10	0.02	0.88	1.66	0.05	0.53	0.008	0.16	0.17	1	SMMS
CM13	0.11	0.83	1.61	0.00	0.51	0.004	0.15	0.16	1	SMMS
CM14	0.11	0.83	1.62	0.00	0.52	0.040	0.16	0.17	1	SMMS
CM19	0.42	0.85	1.63	0.01	0.51	0.005	0.16	0.16	1	SMMS
CM21	0.42	0.84	0.01	0.02	0.58	0.002	0.14	0.14	1	SMMS
CM22	0.42	0.84	0.84	0.02	0.56	0.002	0.14	0.14	1	SMMS
CM31	0.01	0.86	1.65	0.05	0.51	0.006	0.16	0.17	1	SMMS
LB	0.40	0.18	1.35	0.06	0.53	0.005	0.16	0.22	2	SMMS
LC	0.41	0.86	1.44	0.06	0.55	0.005	0.14	0.23	2	SMMS
LD	0.38	1.25	1.38	0.07	0.53	0.005	0.19	0.23	2	SMMS
LG	0.01	0.74	1.37	0.05	0.55	0.005	0.16	0.22	2	SMMS
LH	0.11	0.74	1.39	0.05	0.55	0.005	0.16	0.24	2	SMMS
LI	0.20	0.74	1.37	0.05	0.55	0.005	0.16	0.24	2	SMMS
MD	0.27	0.57	1.61	0.10	0.41	0.017	0.08	0.62	3	Weld
62W	0.23	0.60	1.61	0.12	0.39	0.020	0.08	0.59	4	Weld
63W	0.30	0.69	1.65	0.10	0.43	0.016	0.10	0.63	5	Weld
65W	0.22	0.60	1.45	0.09	0.39	0.015	0.08	0.48	6	Weld
BWA	0.21	0.63	1.69	0.14	0.40	0.014	0.08	0.45	7	Weld
BWC	0.08	0.62	1.30	0.08	0.31	0.009	0.08	0.37	8	Weld
WP	0.04	1.65	1.43	0.05	0.39	0.011	0.06	0.50	9	Weld
A302	0.14	0.20	1.20	0.24	0.60	0.015	0.21	0.28	10	Plate
JRQ	0.14	0.82	1.40	0.12	0.50	0.019	0.18	0.25	11	Plate
OV1	<0.02	<0.02	1.60	<0.02	<0.02	<0.002	<0.02	<0.02	12	Model alloy
OV12	<0.02	<0.02	<0.02	<0.02	<0.02	<0.002	<0.02	<0.02	12	Model alloy
OV9	<0.02	<0.02	<0.02	<0.02	<0.02	0.025	<0.02	<0.02	12	Model alloy
OV10	<0.02	<0.02	1.60	<0.02	<0.02	0.025	<0.02	<0.02	12	Model alloy

[a]Heat Treatments:

1. Heat treatment for CM alloys: austenitize 900°C 30 min/ salt quench 450°C 10 min/ temper 660°C 4 h air cool/stress relief 607°C 24 h followed by slow cool @8*C/h to 300°C air cool.
2. Heat treatment for Laval alloys: austenitize 900°C 1 h/air cool/temper 664°C 4 h air cool/stress relief 600°C 40 h to 300°C/air cool.
3. PWHT 607˚C, 22.5.
4. Submerged Arc Weld (SAW)(stress relieved (SR) 8 cycles of 6 h at 593–621˚C.
5. SAW, SR 48 h at 593–621°C.
6. SAW, SR 80 h at 593–621°C.
7. PWHT, 607˚C for 15 h, furnace cool.
8. PWHT, 607˚C for 13.5 h, furnace cool.
9. Austenitized 920˚C, water quench; tempered 600˚C, 42 h, 650°C, 6 h; slow cooled.
10. Normalized and tempered; 1700°F 6.5h/warer quench/1625°F 6.5h/warer quench/1200°F 6.5h/warer quench/1125°F 6.5 h/furnace cool.
11. Normalized @ 900°C, quenched @ 880°C, tempered at 665˚C for 12 h, SR at 620˚C 40 h.
12. Normalize @ 775°C, 17 h; forced helium quench.

[b]SMMS are Split Melt Model Steels

Table 6.2. Irradiation conditions

Capsule ID	T_i (°C)	ϕ (n/cm^2-s)	ϕt (n/cm^2)
A5	290	5.1×10^{11}	4.0×10^{17}
T1	290	7.8×10^{11}	7.0×10^{17}
T2	290	7.8×10^{11}	1.8×10^{18}
T3	290	7.8×10^{11}	3.4×10^{18}
T4	290	9.7×10^{11}	7.5×10^{18}
SR1	290	9.7×10^{11}	8.5×10^{18}
Piggyback[a]	290	7.7×10^{11}	1.0×10^{19}
T5	290	7.8×10^{11}	1.4×10^{19}
T6	290	9.7×10^{11}	3.3×10^{19}
T7	270	9.2×10^{11}	3.8×10^{18}
T8	270	9.2×10^{11}	1.5×10^{19}
T9	310	9.8×10^{11}	4.0×10^{18}
T10	310	9.8×10^{11}	1.5×10^{19}
T11	290	2.6×10^{11}	4.0×10^{17}
T12	290	3.2×10^{11}	1.0×10^{18}
T13	290	3.1×10^{11}	2.4×10^{18}
T14	290	3.2×10^{11}	4.8×10^{18}
T15	290	2.6×10^{11}	8.5×10^{18}
T16	290	3.0×10^{11}	1.6×10^{19}
T17	270	2.5×10^{11}	4.3×10^{18}
T18	270	3.6×10^{11}	1.7×10^{19}
T19	310	2.3×10^{11}	4.0×10^{18}
T20	310	3.4×10^{11}	1.6×10^{19}
A1	290	7.0×10^{10}	6.0×10^{16}
A2	290	7.0×10^{10}	1.0×10^{17}
A3	290	7.0×10^{10}	2.3×10^{17}
A4	290	7.0×10^{10}	3.2×10^{17}
T21	290	1.0×10^{11}	3.0×10^{17}
T22	290	1.0×10^{11}	1.1×10^{18}
T23	290	8.0×10^{10}	2.4×10^{18}
T24	290	8.0×10^{10}	4.0×10^{18}

[a]Piggyback irradiations were not part of the IVAR program. These ORNL irradiations were carried out in space-compatible subcapsules prepared by UCSB in the mouths of large CT specimens in the Tenth HSSI Irradiation Series capsules.

- Five commercial welds: Cu ≈ 0.21 to 0.30 wt %, Ni ≈ 0.6 to 0.69 wt %, Mn ≈ 1.45 to 1.69 wt. %, and P ≈ 0.014 to 0.020 wt %
- Two low-copper commercial welds: Cu ≈ 0.04 to 0.06 wt %, Ni ≈ 0.6 to 1.65 wt %, Mn ≈ 1.3 to 1.43 wt %, and P ≈ 0.009 to 0.011 wt %
- Two program plates: Cu ≈ 0.14 wt %, Ni ≈ 0.2 to 0.82 wt %, Mn ≈ 1.2 to 1.4 wt %, and P ≈ 0.015 to 0.019 wt%
- Four simple ferritic model alloys: Fe, Fe + 1.6 wt. % Mn, Fe + 0.025 wt % P, and Fe + 1.6 wt % Mn + 0.025 wt % P

Tests on flat tensile specimens with 9 × 2 × 0.5 mm gauge section were conducted on a computer-controlled, semiautomated tensile instrument designed and constructed by UCSB on an Instron 1100 tabletop load frame. Cartridges of 29 specimens were loaded and tested in sequence. Each cartridge included two unirradiated reference steels with precisely known yield and ultimate stresses to provide a continuous system calibration. Except in a few cases, a minimum of two tensile tests was carried out for

each alloy-irradiation condition. Replicate tensile tests showed an average standard deviation in $\Delta\sigma_y$ to be $\approx \pm 15$ MPa.

Some additional perspective on the objectives and character of SMMSs is useful. The use of SMMS was specifically intended to provide precise and controlled variations in key compositional variables and variable combinations. The SMMS baseline composition, fabrication route, and heat treatment schedule were selected to produce microstructures and properties that closely match those found in "typical" RPV plates. The baseline heat treatment generally produced prior austenite grain sizes of ≈ 50 μm and plate microstructures ranging from tempered bainite to mixed tempered bainite-ferrite. The corresponding unirradiated σ_y ranged from 400 to 525 MPa, again very similar to the range of strength levels of typical A533B-type RPV steels. Thus, the SMMS are similar to their commercial counterparts, except that (1) they are generally likely to exhibit less melt-to-melt variability than is characteristic of the wide range of heavy- section RPV plates, and (2) the variation of key elements is intentionally wider than in typical commercial steelmaking practice in order to identify variable trends and interactions. Thus, the matrix includes some chemistry combinations that do not generally occur in commercial plates, such as higher-than-typical Ni and Cu and lower-than-typical P and Mn and high P with low Cu.

Given their wide range of compositions, there may be some differences in the microstructures of the SMMSs compared to what might characterize the corresponding range and average of plates in the TTS database. For example, some SMMS microstructures may differ somewhat from the average for the plates in the TTS database in particular details, such as dislocation densities. Thus, the SMMSs can be thought of as a unique product form or as a small set of product forms that differ from those found in the TTS database. The TTS database itself has three product form coefficients for plate as well as additional product form coefficients for welds and forgings, so calibrating different coefficients for different product forms is a normal feature of the TTS model.

Further details on the IVAR facility and materials are provided in Ref. [6].

6.2 Comparison of TTS Model Predictions and IVAR Data Trends—The TTS to $\Delta\sigma_y$ Conversion

The objective is to compare predictions of the TTS model developed in Chap. 4 to various subsets of the IVAR database. To make this comparison, it is necessary to convert the TTS model predictions to $\Delta\sigma_y$ by using a relation,

$$\Delta\sigma_y = \mathrm{TTS}/C_c \tag{6-1}$$

As discussed in Chap. 2, the conversion factor C_c depends on a number of variables, including the unirradiated Charpy properties and the $\Delta\sigma_y$ itself. Eq. (6-1) can be expressed as

$$C_c = C_0 + C_1\mathrm{TTS} + C_2\mathrm{TTS}^2 \ldots \tag{6-2}$$

Here the units are °C/MPa, MPa, °C for C_c, $\Delta\sigma_y$ and TTS, respectively.

Previous studies have shown that the C_c for welds is typically somewhat larger than for plates [6]. For welds the expression was based on slightly modifying a fit to $\Delta\sigma_y$ – TTS data in Ref. [6] with data reported by English from the PSF experiment [7], yielding

$$C_{cw} = 0.55 + 1.2 \times 10^{-3}\mathrm{TTS} - 1.33 \times 10^{-6}\mathrm{TTS}^2 \ldots \tag{6-3}$$

This expression is also approximately equivalent to the model-based C_c described in Chap. 2, as well as and the formulation reported in NUREG/CR-6778 [6]. For plates, Eq. (6-2) was least-square fit to a compilation of ç – TTS data in Ref. [8], yielding

$$C_{cp} = 0.45 + 1.945 \times 10^{-3}\mathrm{TTS} - 5.496 \times 10^{-6}\mathrm{TTS}^2 + 8.473 \times 10^{-9}\mathrm{TTS}^3 \tag{6-4}$$

The corresponding $\Delta\sigma_y$-TTS relations are shown in Fig. 6.2. While Eqs. (6-3) and (6-4) provide reasonable conversions of TTS to $\Delta\sigma_y$, the actual values for any particular alloy, and the effective average for the TTS database, may vary from these "generic" estimates, which adds an element of uncertainty to any quantitative TTS model IVAR $\Delta\sigma_y$ comparisons. Based on the fits of available data, estimated conversion uncertainties for the $\Delta\sigma_y$ derived from the TTS model predictions are on average $\oplus\pm$10% up to 20% in some individual cases.

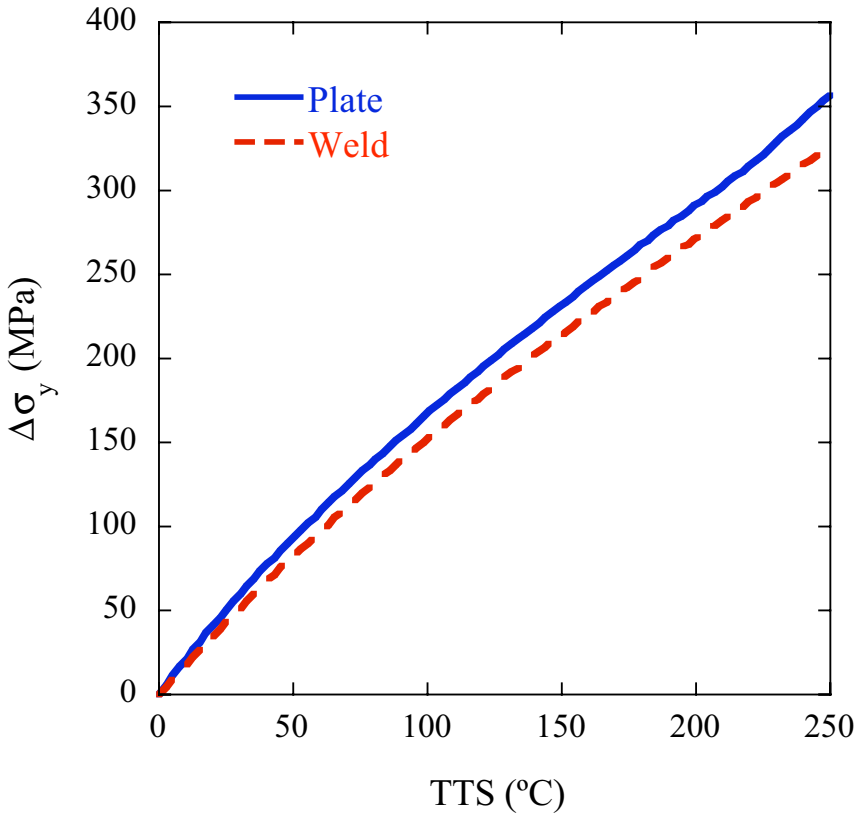

Fig. 6.2. The relations used to convert TTS predictions to $\Delta\sigma_y$ data for welds and plates.

6.3 The Fluence and Irradiation Temperature Dependence of $\Delta\sigma_y$ in Welds and Plates

Given the TTS to $\Delta\sigma_y$ conversion uncertainties noted above, coupled with possible product form differences, especially for the IVAR SMMS case, modest differences between the TTS model predictions and the IVAR $\Delta\sigma_y$ are not unexpected. The welds and plates discussed in this section are among the IVAR alloys that are the most similar to the steels in the TTS database. Figures 6.3a–f show the IVAR data and the corresponding Chap. 4 TTS model predictions converted to $\Delta\sigma_y$ curves plotted against square root fluence for six submerged-arc welds. The irradiations were carried out at 290°C at three dose rates, representing the low (squares $\approx 8 \times 10^{10}$ n/cm^2), intermediate (circles $\approx 3 \times 10^{11}$ n/cm^2), and high (diamonds $\approx 8 \times 10^{11}$ n/cm^2) IVAR flux regimes, respectively. Five of these welds (MW, 62W, 63W, 65W, and BWA) contain more than 0.2 wt % Cu, while one weld (BWC) contains only ≈ 0.06 wt % Cu, which is below the 0.072 wt % threshold for CRP contributions to TTS. Figures 6.3g–h show similar plots for the A302B and JRQ plates with intermediate Cu (≈ 0.14 wt % in both cases) using the CE-plate

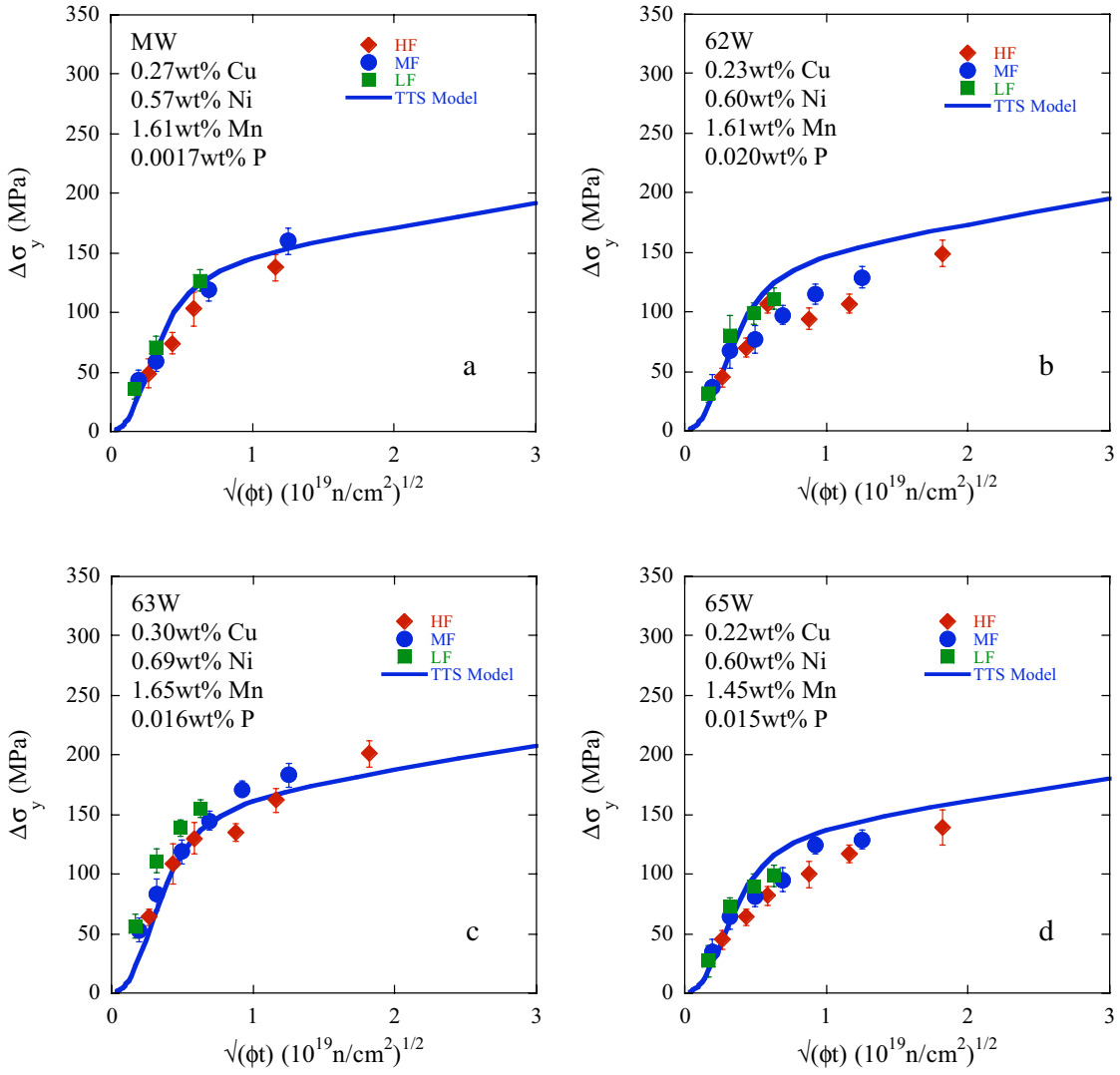

Fig. 6.3 a–d. The TTS model predictions and the IVAR $\Delta\sigma_y$ data plotted against the square root of fluence for four commercial Cu-bearing welds.

coefficients in the TTS model. In the case of the Cu bearing welds, the TTS model is in generally good agreement with IVAR weld $\Delta\sigma_y$ data, especially at low flux and fluence. However, the TTS model tends to slightly over predict the IVAR $\Delta\sigma_y$ data at higher flux and fluence in 3 out of the 5 cases (62W, 65W, BWA). These differences are generally within the expected TTS model and IVAR $\Delta\sigma_y$ data uncertainties. The TTS model prediction is also in good agreement with the IVAR $\Delta\sigma_y$ for the low Cu weld as well as for the plate $\Delta\sigma_y$ data at low and intermediate flux.

The TTS model does not predict the systematic dose-rate effects observed in comparing HF, MF, and LF subsets in Fig. 6.3, or those found in the SMMS comparison that are discussed below. (Note: due to the expanded fluence scale the dose rate effects do not appear to be large in these figures. The effects of dose rate are more clearly shown in Sect. 6.6 [see Figs. 6.15 to 6.18].) The TTS model does include a dose rate effect, but it applies to the effect of flux noted when comparing typical BWR with PWR surveillance data. The typical BWR flux range is well below the range of the IVAR flux levels, which

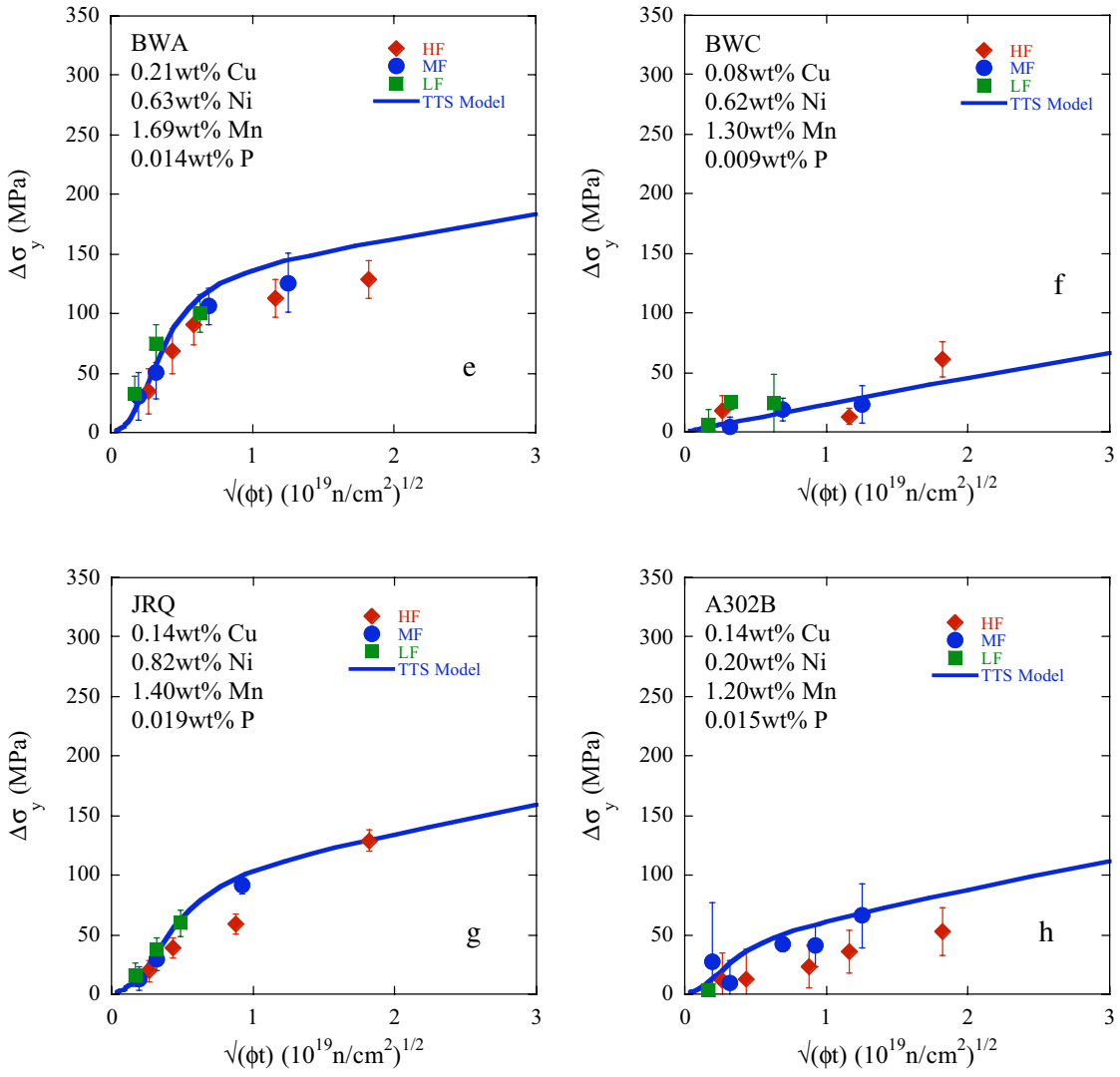

Fig. 6.3 e–h. The TTS model predictions and the IVAR $\Delta\sigma_y$ data plotted against the square root of fluence for a Cu-bearing, and low-Cu weld and two commercial plates.

overlap the PWR range. This different range of flux effects captured in the TTS model vs the flux effects present in the IVAR data affects many of the comparisons throughout this chapter, as discussed in some detail in Sect. 6.6.

Figure 6.4 compares the TTS model predictions to the available $\Delta\sigma_y$ data for the same welds and plates at ≈ 0.43 and ≈ 1.6×10^{19} n/cm^2, for medium flux IVAR irradiations at 270, 290 and 310°C. MW and JRQ IVAR data are not available at higher and lower irradiation temperatures. The TTS model lines are plotted only over the range of T_i in the surveillance database. The irradiation temperature dependence predicted by the TTS model is somewhat stronger than for the low-Cu IVAR $\Delta\sigma_y$ data and is, on average, slightly weaker than the IVAR data for Cu bearing welds. However, the overall agreement is again generally good and within the expected TTS model and IVAR data uncertainties.

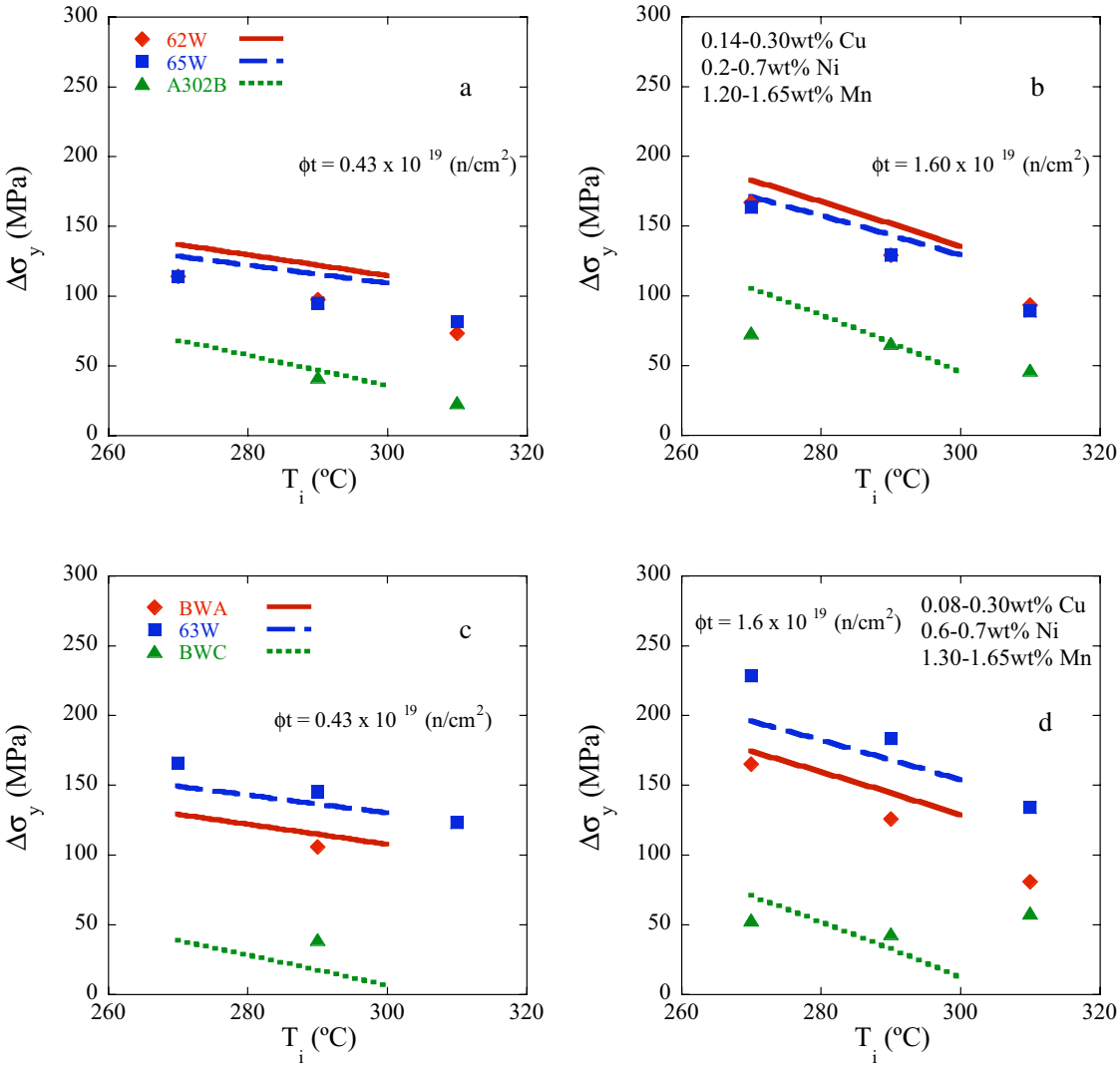

Fig. 6.4. The TTS model predictions and the IVAR $\Delta\sigma_y$ data at two fluences for intermediate flux irradiations of five commercial welds and a plate at 270, 290, and 310°C.

6.4 The Fluence Dependence of $\Delta\sigma_y$ in the SMMS Irradiated at 290°C

6.4.1 Cu-Bearing SMMS Irradiated at 290°C

For comparisons with SMMS, the Cu_{max} categories and coefficients used in the TTS model must be determined in part by expert judgment. The SMMS with Ni ≥ 0.75 wt % are assigned Cu_{max} = 0.30 wt %, the value for the higher Ni weld category (Linde 1092) in the TTS database. Lower Ni SMMS (Ni < 0.75 wt %) are assigned Cu_{max} = 0.24 wt %, the value for the medium Ni weld group (typical Linde 80) in the TTS data.

The nominal baseline composition for the SMMS described in the following paragraphs and elsewhere in this chapter are as follows: medium 0.8 wt % Ni; higher 1.4 (LV) to 1.6 (CM) wt % Mn; and low 0.005 wt % P. The results are described in terms of composition variations with respect to these

baseline values. Figure 6.5 compares TTS model $\Delta\sigma_y$ vs square root fluence curves to the IVAR data for the three baseline medium-Ni SMMS compositions with varying Cu ≈ 0.1, 0.2 and 0.4 wt % Cu (bulk)

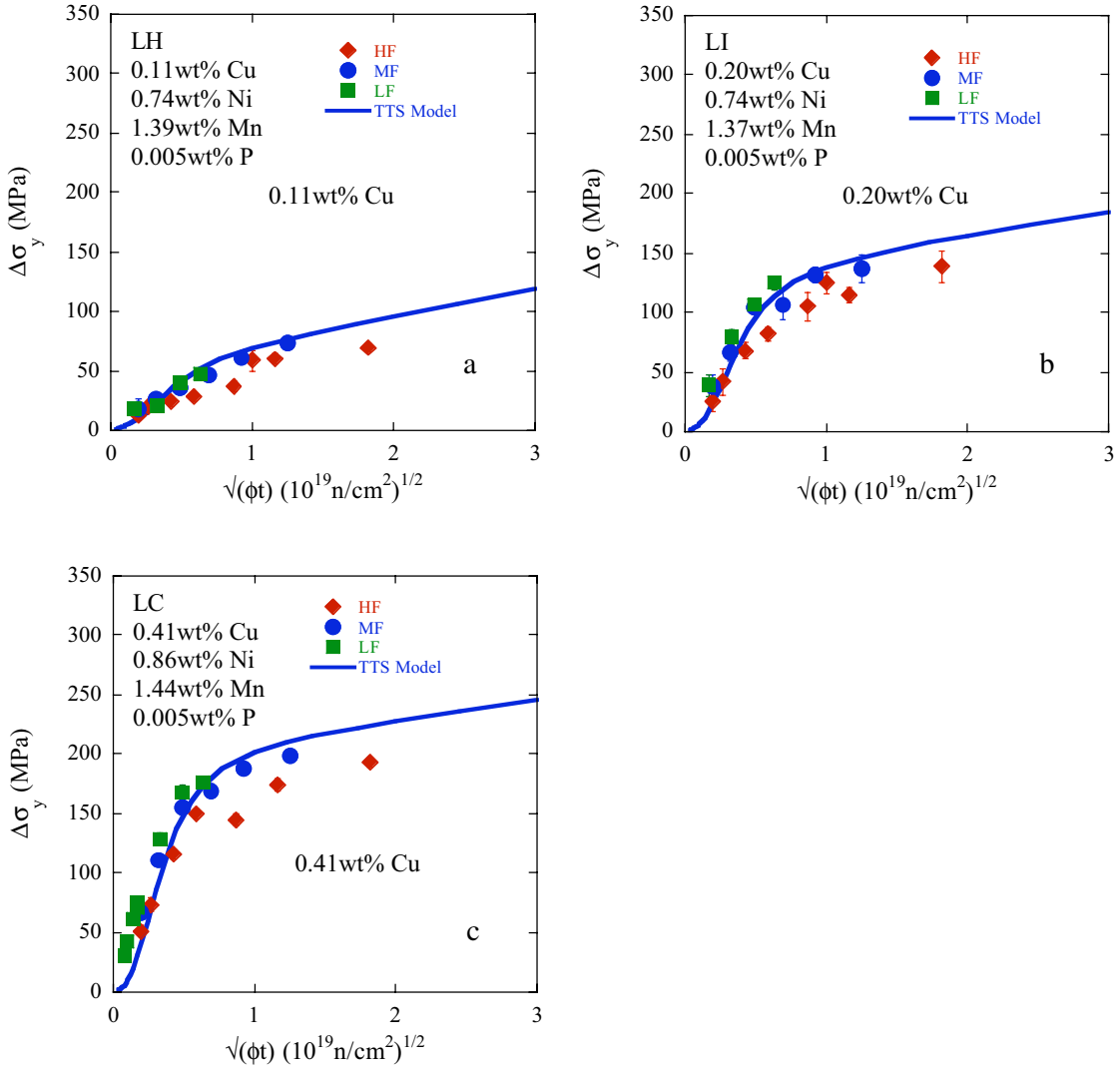

Fig. 6.5 a–c. The TTS model predictions and the IVAR $\Delta\sigma_y$ data plotted against the square root of fluence for three 0.8 wt % Ni SMMS with 0.1 (a), 0.2 (b), and 0.4 (c) wt % Cu.

irradiated at 290°C at low, medium, and high IVAR flux levels. The solid line is the TTS model prediction, with the set of plate product form coefficients that provide the best agreement. As noted above, the Cu_{max} was 0.30 wt % Cu for Ni ≥ 0.75 wt % and 0.24 wt % Cu for Ni < 0.75 wt %. Figure 6.6 shows similar plots for a high ≈ 0.4 wt % Cu (bulk) SMMS composition with varying Ni ≈ 0.2, 0.8, and 1.3 wt %. Note the 0.4% Cu and 1.3 wt % Ni SMMS is outside the range of all surveillance plates, although there are welds with similar compositions. Figure 6.7 shows the corresponding plots for a high ≈ 0.4 wt % Cu (bulk), medium-Ni SMMS baseline composition with varying Mn ≈ 0, 0.8 and 1.6 wt %. The coefficients for forgings were used for the 0 and 0.8 wt % Mn SMMS because a substantial part of the Mn effect in the TTS model is implicit in the differences between forging and other coefficients. With the exception of the 0.0 wt % Mn alloy, whose composition is far outside the TTS database, the overall agreement is good.

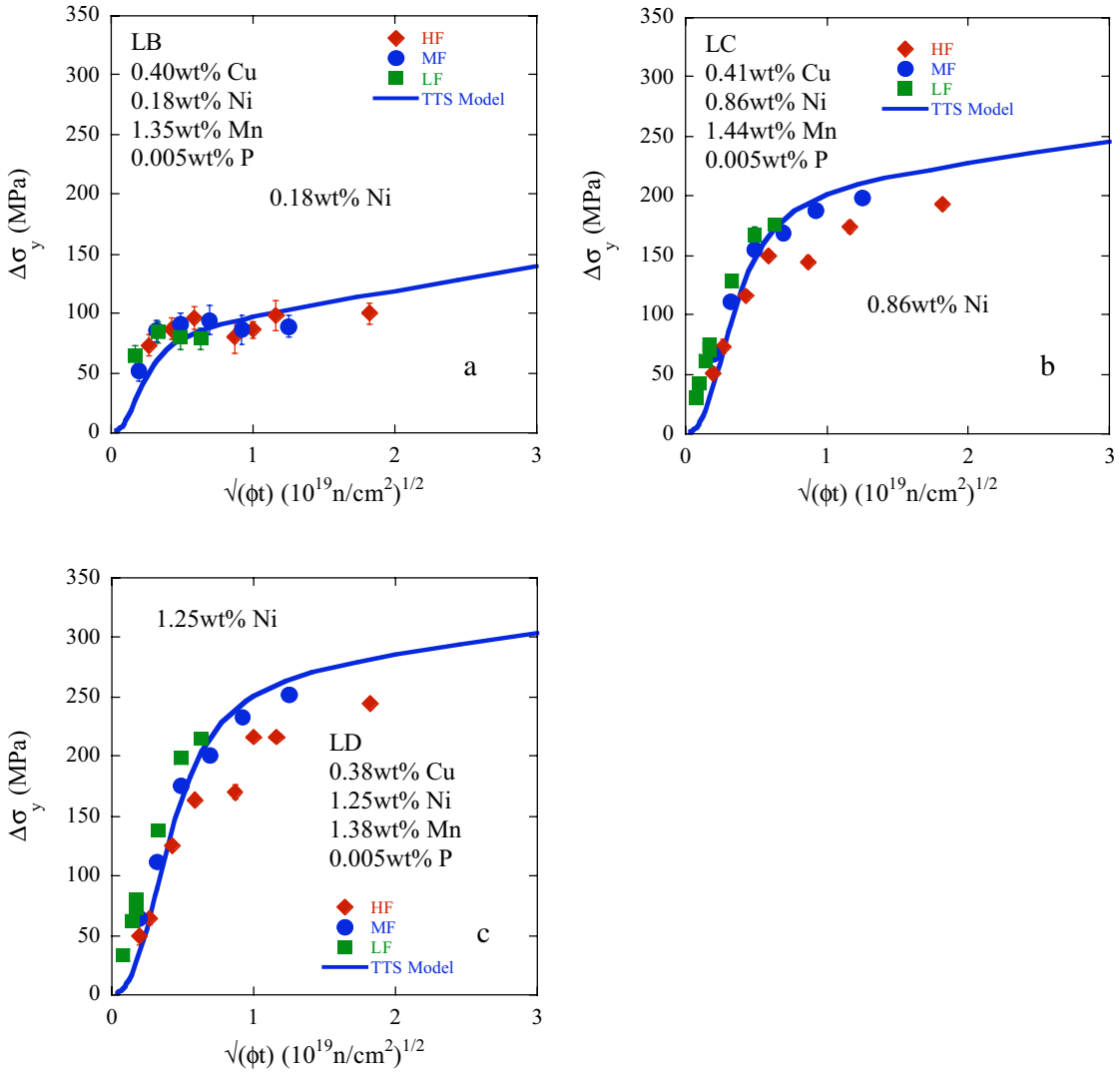

Fig. 6.6 a–c. The TTS model predictions and the IVAR $\Delta\sigma_y$ data plotted against the square root of fluence for three 0.4 wt % Cu SMMS with 0.2 (a) 0.4 (b) and 1.25 (c) wt % Ni.

Figure 6.8a cross plots the Cu dependence predicted by the TTS model for CE-Plate coefficient (B=135.2) and Cu_{max} = 0.30 wt %, and the IVAR $\Delta\sigma_y$ data for SMMS baseline composition at 0.24 and 1.6 × 10^{19} n/cm^2 for 290°C irradiations at the intermediate IVAR flux. The lines are the TTS model predictions covering the range of compositions in the surveillance plate database. A similar cross plot for Ni variations is shown in Fig. 6.8b for the SMMS with 0.4 wt % Cu, 1.4 wt % Mn, and 0.005 wt % P. In this case curves are given for both Cu_{max} = 0.24 (dashed) and 0.30 wt % (solid). Figure 6.8c shows the corresponding Mn cross plot for the SMMS medium-Ni baseline composition, assuming Cu_{max} = 0.30 wt %. The effect of Mn shown in Fig. 6.8c is based on using the CE-Plate coefficient (solid lines) for higher Mn and forging coefficient (B = 102.3, dashed lines) for lower Mn. The arrows in Fig. 6.8(a-c) show the average Cu, Ni, and Mn contents of the steels in the TTS plate database. Overall, the TTS model

predictions of the effects of Ni, Cu and Mn (as reflected in the forging coefficients), are in reasonably good agreement with the IVAR $\Delta\sigma_y$ data trends.

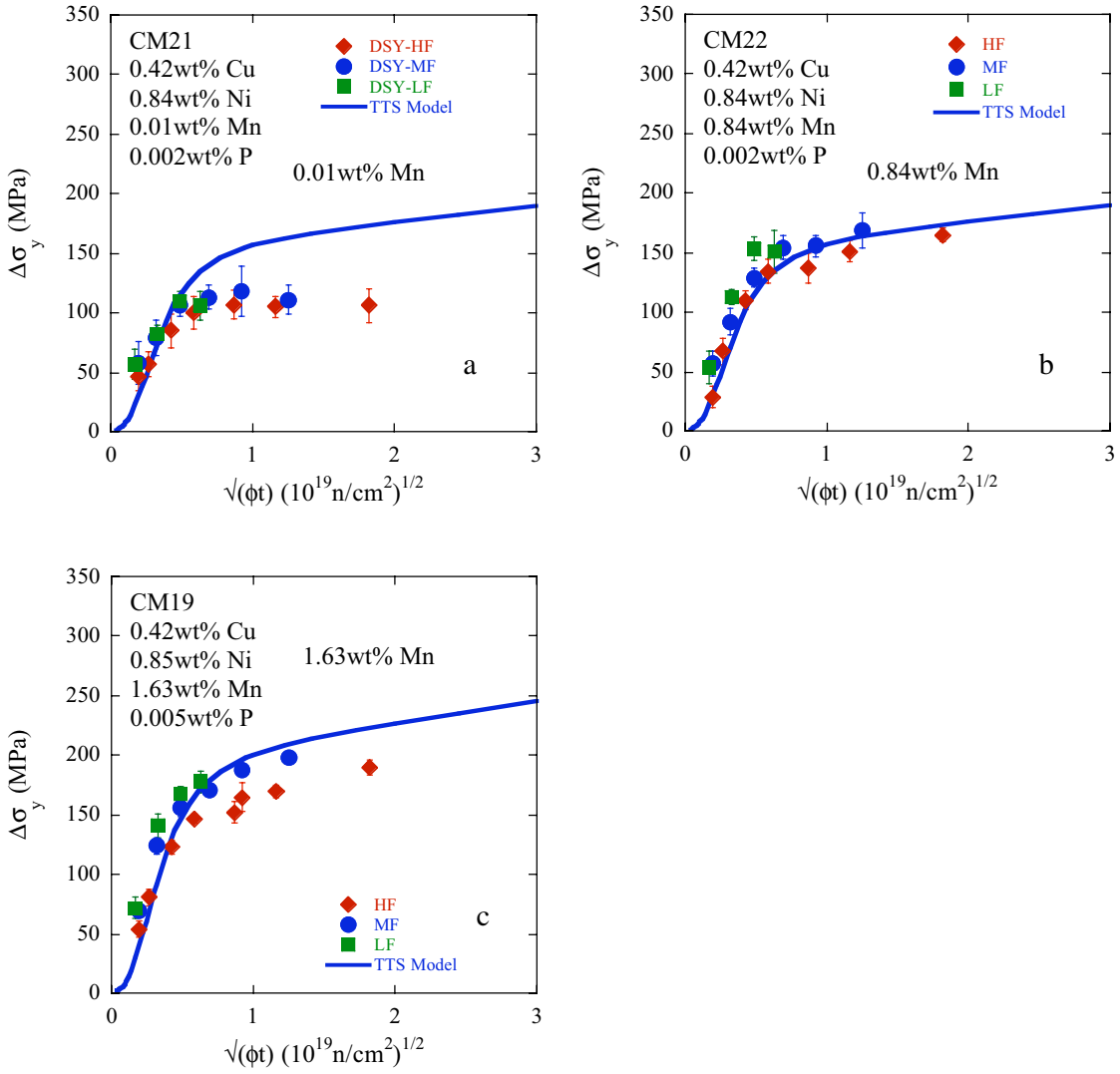

Fig. 6.7 a–c. The TTS model predictions and the IVAR $\Delta\sigma_y$ data plotted against the square root of fluence for three 0.4 wt % Cu SMMS with 0.0 (a), 0.8 (b), and 1.6 (c) wt % Mn.

Figure 6.8 also supports the TTS fit of a Cu_{max} between ≈ 0.24 and 0.3 wt. %. Figure 6.8d shows that the IVAR data are also consistent with a minimum Cu for CRP formation, Cu_{min}. Here, the CRP hardening of LV SMMS baseline composition is estimated by subtracting the $\Delta\sigma_y$ for the Cu free alloy (LG), from the corresponding $\Delta\sigma_y$ for alloys with 0.1 (LH), 0.2 (LI) and 0.4 (LC) wt. % Cu alloys, and plotting the result against the square root of Cu. These data are for irradiations to 0.48 and 1.56 × 10^{19} n/cm^2 at intermediate flux and 290°C. For the SMMS with 0.4 wt % Cu (bulk) two values of Cu_{max} = 0.24 and 0.30 wt % are shown. The $\Delta\sigma_y$ scales with the square root of the precipitate volume fraction, hence, the dissolved Cu content. Thus the intercepts of the least-square lines with the with $\Delta\sigma_y$ = 0 axis provide estimates of the Cu_{min}, of 0.073 and 0.063 (rounded) wt % Cu for the lower and higher fluences, respectively. Note: the values of √Cu = 0.25 and 0.5 correspond to Cu contents of 0.0625 and 0.25 wt %,

respectively. As expected, the Cu_{min} threshold decreases slightly with increasing fluence, and is in good agreement with the value in the TTS model of 0.072 wt % Cu.

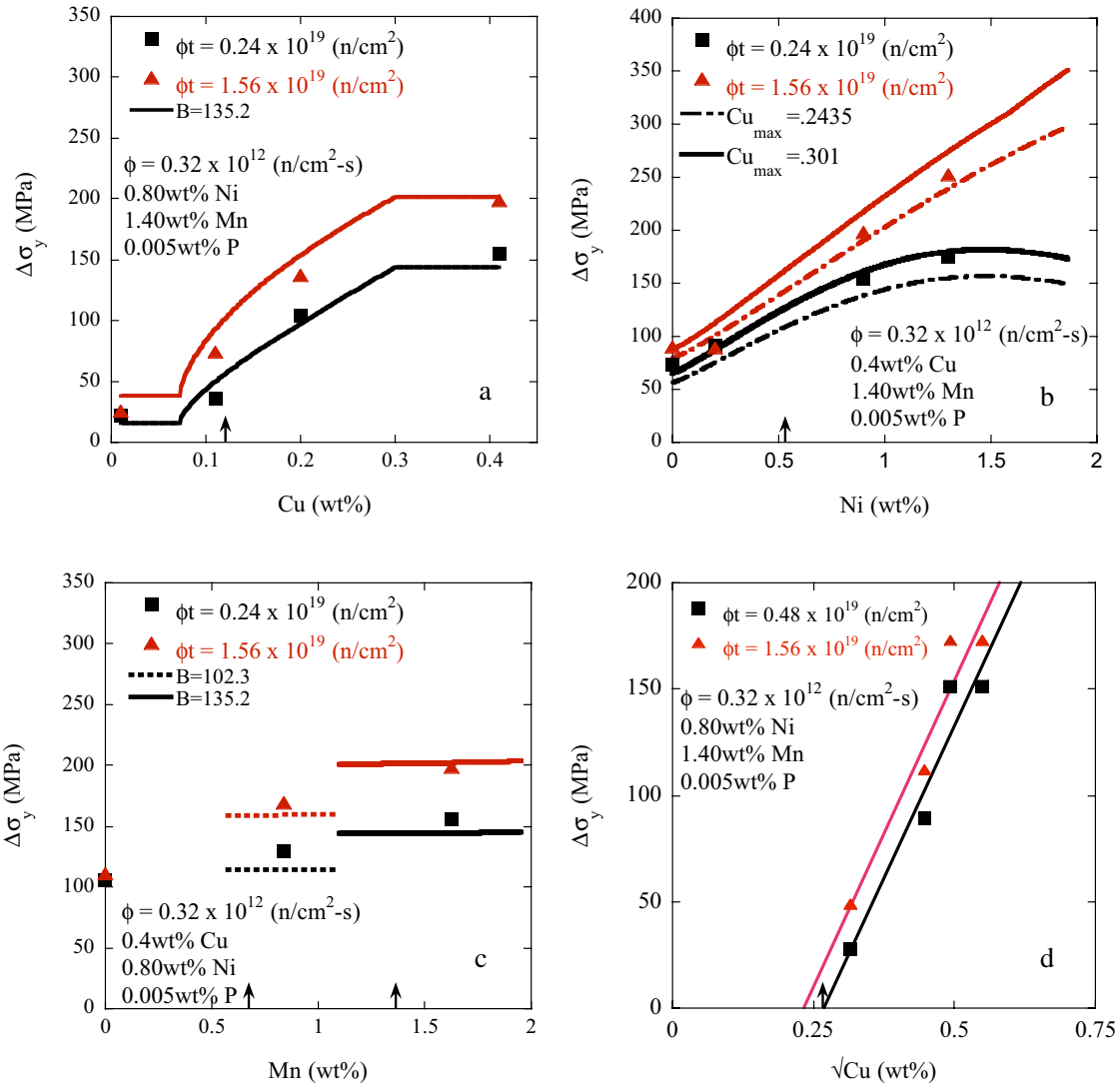

Fig. 6.8 a–d. The solid lines in a-c are TTS model predictions for a nominal CE plate product form coefficients (B = 135) and the IVAR $\Delta\sigma_y$ data at two fluences plotted against Cu (a), Ni (b), and Mn (c). The vertical arrows show the average compositions of these elements in the TTS plate database. The horizontal dotted lines in Fig. 6.8c are for the coefficients and average Mn composition of forgings in the TTS database. Fig. 6.8d plots the estimated CRP hardening versus the square root of the dissolved Cu content to estimate Cu_{min}.

In summary, there is generally good agreement between the TTS model predictions and the IVAR $\Delta\sigma_y$ data. However, there is a systematic effect of flux observed in the IVAR $\Delta\sigma_y$ data shown in Figs. 6.3, 6.5, 6.6 and 6.7, that is not captured by the TTS model. The TTS model does predict flux dependence of $\Delta\sigma_y$ but only below the range of the IVAR data. The probable reasons that the TTS model does not fully capture the effect of flux in the IVAR (and also the PWR surveillance) regimes are discussed in Sect. 6.6.

6.4.2 Low-Cu SMMS Irradiated at 290°C

Figure 6.9 compares the nominal TTS model $\Delta\sigma_y$ curves plotted versus the square root of fluence (solid lines) to IVAR data for four nominally Cu-free SMMS with similar compositions (≈ 0.8 wt % Ni, ≈ 1.3 to 1.7 wt % Mn and ≈ 0.005 wt % P) for 290°C irradiations at low, medium, and high flux. The slight curvature of these predicted lines is due to the nonlinear TTS-to-$\Delta\sigma_y$ conversion. The dashed lines are least squares fits to the IVAR $\Delta\sigma_y$ data, using the simple form, $\Delta\sigma_y = CF\sqrt{(\phi t)}$, where CF is a fitted chemistry factor. The short dashed line in Fig. 6.9b is the fit to the data leaving out the seemingly anomalous high-flux, high-fluence data point. Note there is a general trend for the measured $\Delta\sigma_y$ for this irradiation condition to fall below the TTS model predictions. We believe this is due in part to a flux effect discussed in Sect. 6.6.2. Overall, the TTS MF model systematically over predicts the CF, and thus the $\Delta\sigma_y$, for Cu-free IVAR data by a factor of about 1.33. However, the overall absolute average deviation ≈ 6.4 MPa is not large.

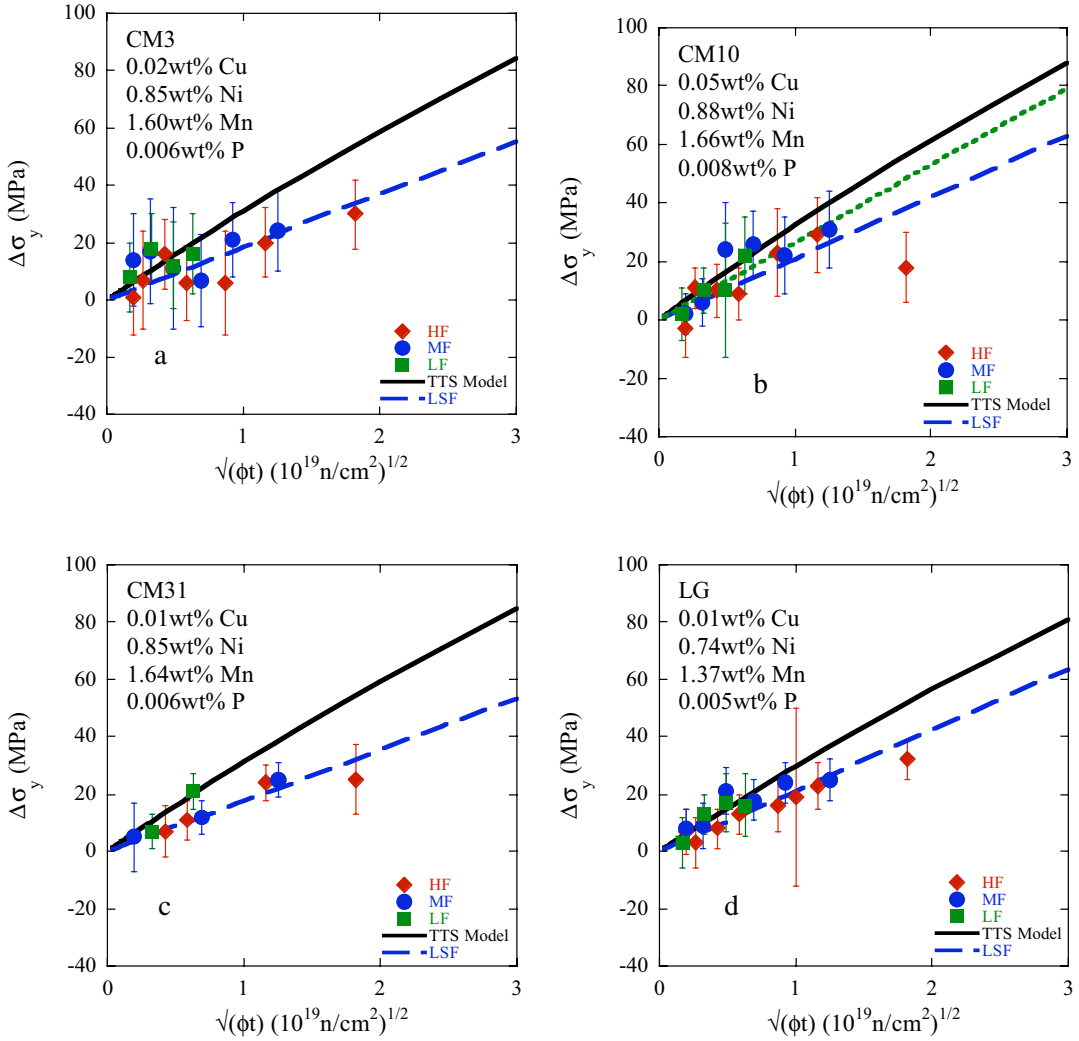

Fig. 6.9 a-d. The TTS model predictions (solid lines) and best fit chemistry factor (dashed lines) for the IVAR $\Delta\sigma_y$ data plotted against the square root of fluence for Cu-free SMMS. The dotted line in Fig. 6.9b is the best fit ignoring the highest fluence data point. The TTS models over predict the $\Delta\sigma_y$ in the lower sensitivity Cu-free SMMS.

Figures 6.10a and b show that the TTS model greatly over predicts and slightly under predicts the $\Delta\sigma_y$ in Cu-free SMMS with ≈ 1.6 wt % Mn and ≈ 0.0 and ≈ 1.68 wt % Ni, respectively. These very low-and high-Ni contents are outside the TTS database composition limits. Figures 6.10c and d show that the TTS model greatly and somewhat over predicts the IVAR $\Delta\sigma_y$ for Cu-free SMMS with ≈ 0.8 wt % Ni for ≈ 0.0 and 0.8 wt % Mn, respectively. In this case the forging MF coefficient, that is appropriate for alloys with lower Mn contents, was used in the TTS model. Again, the SMMS with no Mn is well outside the TTS database composition limits.

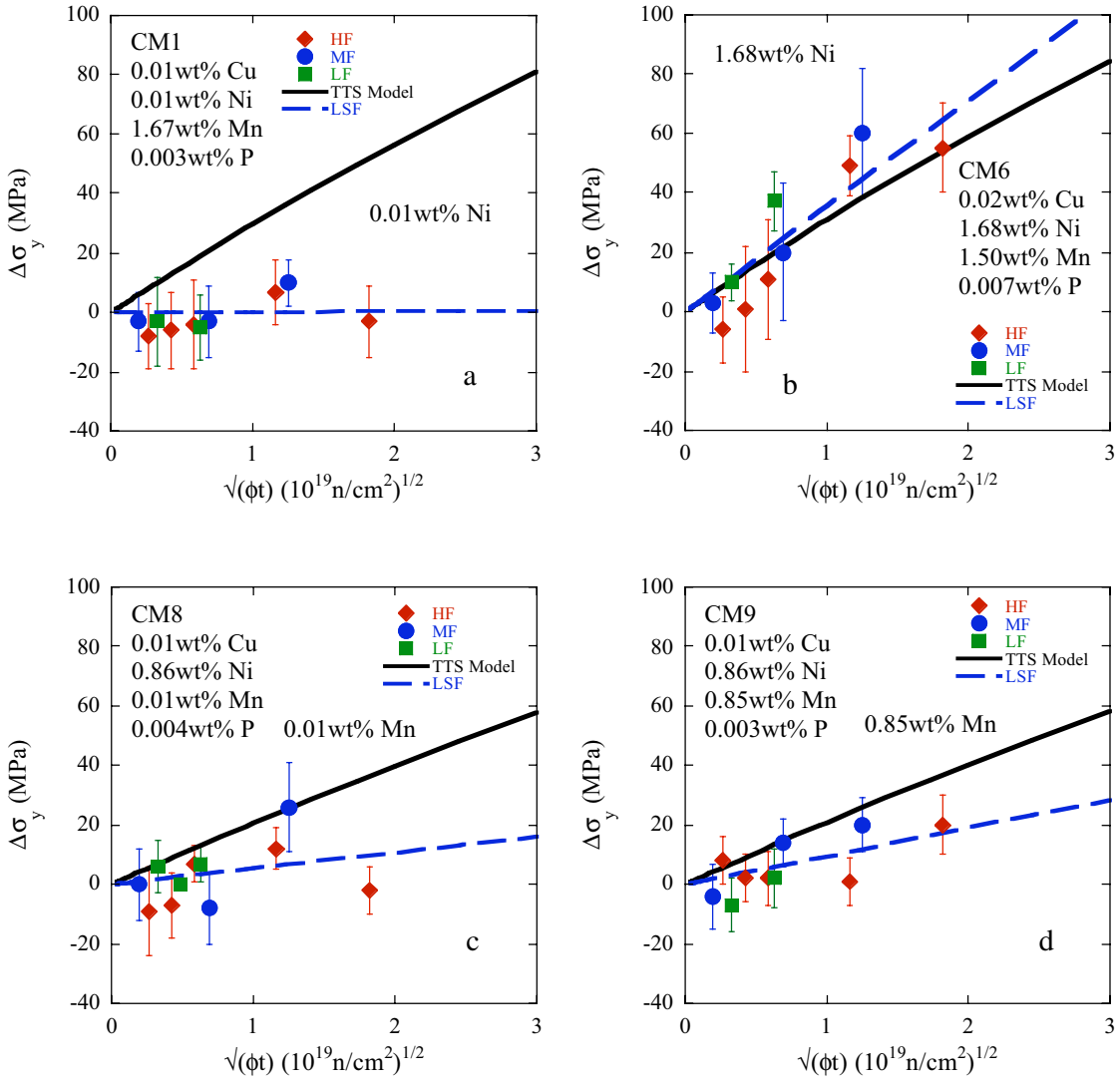

Fig. 6.10 a–d. The TTS model predictions (solid lines) and best fit chemistry factor (dashed lines) for the IVAR $\Delta\sigma_y$ data plotted against the square root of fluence for (a) and (b) 0.0 and 1.6 wt % Ni Cu-free SMMS and (c) and (d) 0.0.and 1.6 wt % Mn. The TTS model over predicts $\Delta\sigma_y$ in the three low-sensitivity steels and slightly under-predicts the $\Delta\sigma_y$ for the high Ni SMMS.

Figures 6.11a and b show that the TTS model slightly to significantly under predicts σ_y in ≈ 0.8 wt % Ni, ≈ 1.6 wt % Mn, Cu free SMMS with ≈ 0.031 and 0.035 wt % P. The underprediction is more severe relative to the dotted line in Fig. 6.11b, which is the fit without the high flux, high fluence data point. These P compositions are slightly outside the composition limits of the TTS plate database. Figure 6.11c shows that the TTS model also significantly under predicts $\Delta\sigma_y$ for a very high Ni ≈ 1.65 wt % weld with ≈ 0.04 wt % Cu, 1.43 wt % Mn, and 0.011 wt % P. Since the Ni content in this case is far beyond the TTS database composition limits, these differences are not a specific matter of concern. However, these results reaffirm the importance of Ni in MF hardening that was found in the SMMS data.

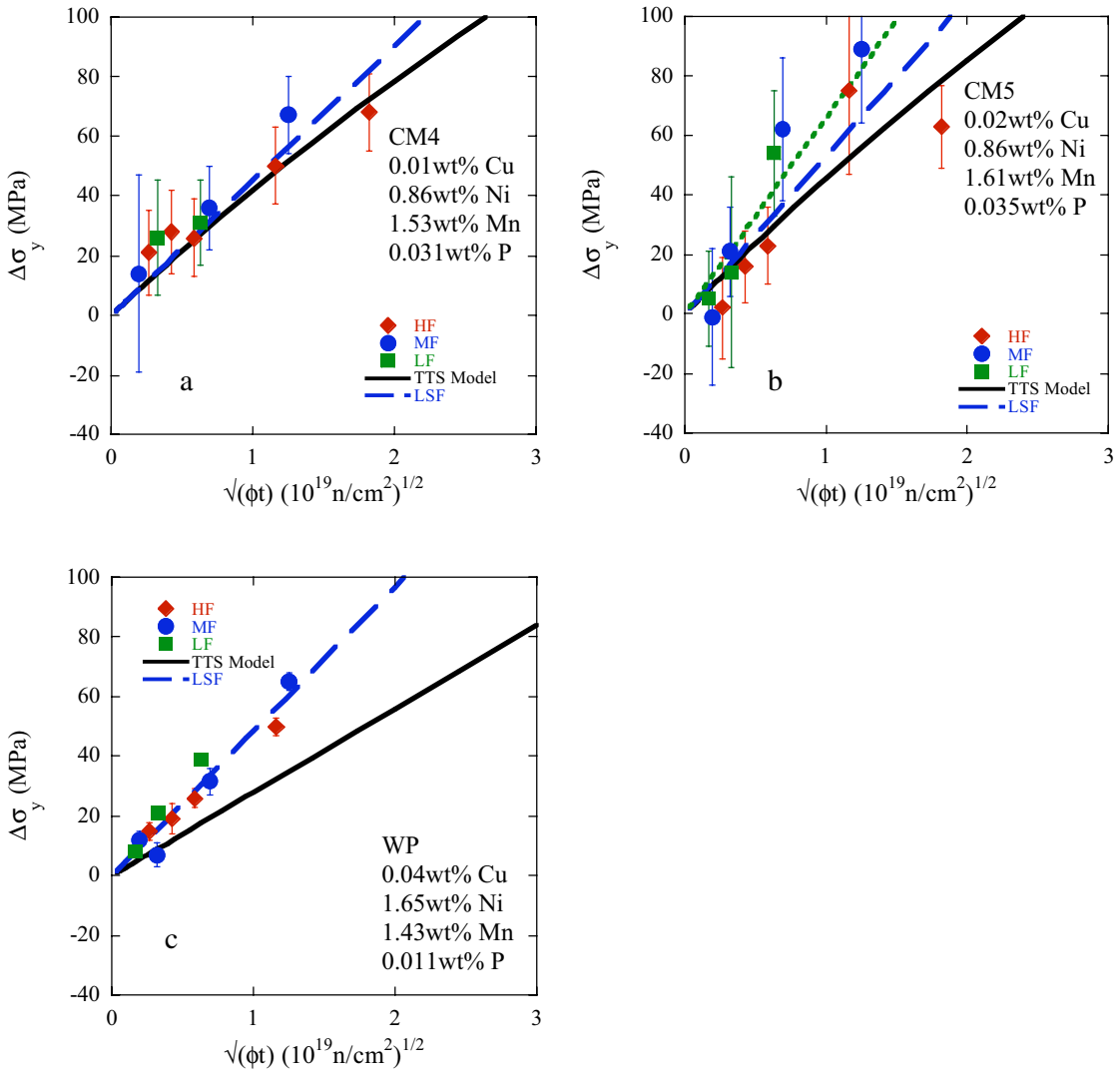

Fig. 6.11 a–c. The TTS model predictions (solid lines) and best fit chemistry factor (dashed lines) for the IVAR $\Delta\sigma_y$ data plotted against the square root of fluence: (a) and (b) for Cu-free SMMS with 0.031 (a) and 0.35 wt % P (b); and a high Ni (1.6 wt % Ni) low Cu weld (c). The dotted line in Figs. 6.11b is the best fit ignoring the highest fluence data point. The TTS model under-predicts $\Delta\sigma_y$ in these sensitive steels.

Figure 6.12 summarizes Figs. 6.9, 6.10, and 6.11 with cross-plots the fitted CF slopes of the IVAR data against Ni (Fig. 6.12a), Mn (Fig. 6.12b), P (Fig. 6.12c) and Cu (Fig. 6.12d). The open diamonds are for the CF fits after dropping the high flux and high fluence data point. The solid lines are the corresponding TTS model predictions. The arrows show the average composition of the plates (and where pertinent, forgings) in the surveillance database. The strong effect of Ni in Fig. 6.12a in the IVAR $\Delta\sigma_y$ data is not reflected in the TTS MF model predictions. The effect of Mn shown in the IVAR $\Delta\sigma_y$ data in Fig. 6.12b is primarily reflected in the TTS MF model coefficient differences between plate (higher Mn)

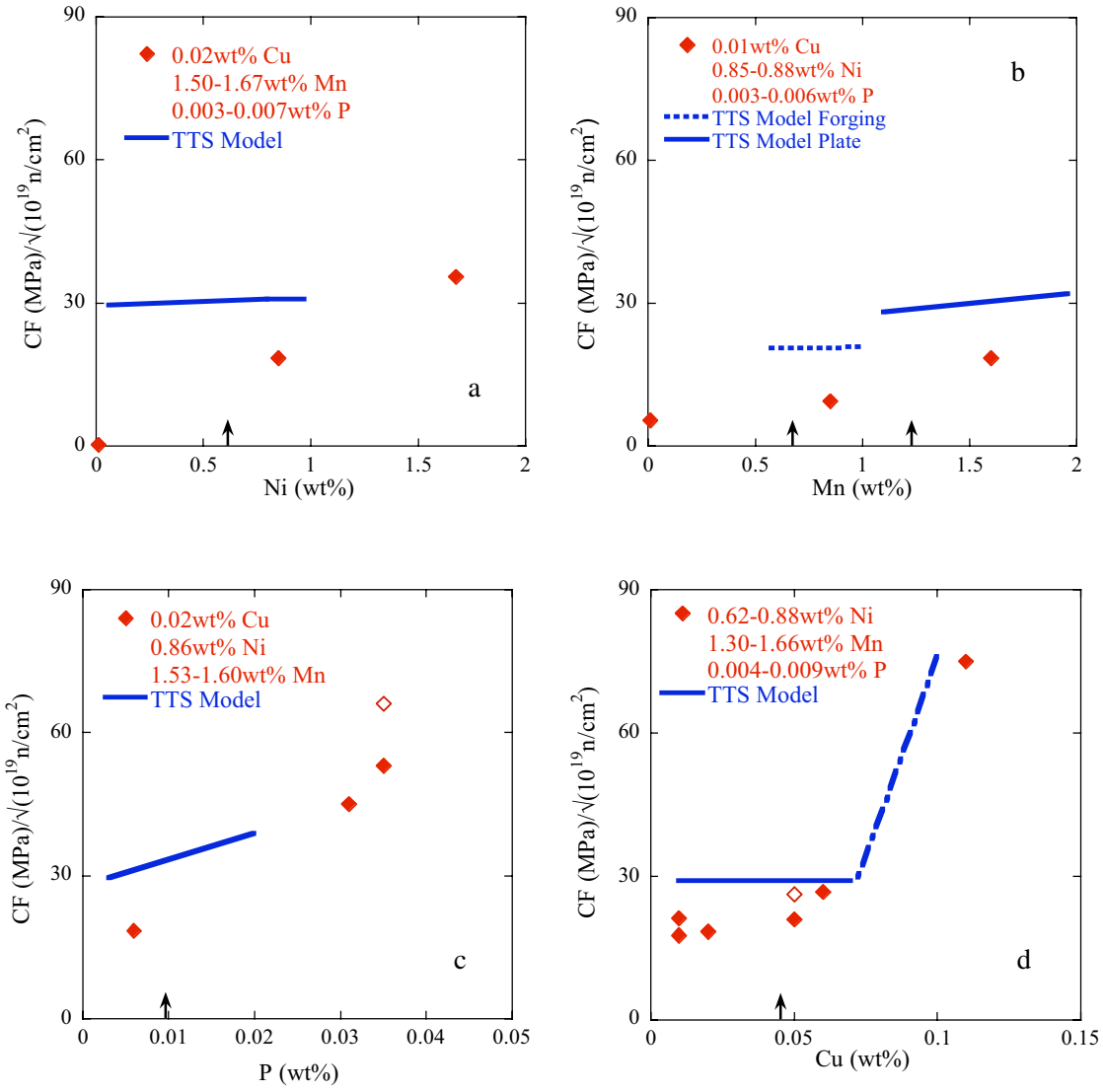

Fig. 6.12 a–d. The solid lines are TTS model predictions at 290°C for IVAR SMMS compositions, including one low-Cu weld, several Cu-free SMMS and a 0.1 wt % Cu SMMS. The filled diamond symbols are the corresponding CF fits to the IVAR σ_y data plotted against Ni (a), Mn (b), P (c), and Cu (d). The vertical arrows show the average compositions of these elements in the TTS plate database. The horizontal dotted line in Fig. 6.12b is for the TTS forging model. The open symbols are the IVAR data fits ignoring the highest fluence data points. The dashed dotted line in Fig. 12d includes the TTS model CRP contribution to hardening for > 0.072 wt % Cu.

and forgings (lower Mn). The effect of P shown in Fig. 6.12c is stronger in the IVAR $\Delta\sigma_y$ data than predicted by the TTS model. The IVAR $\Delta\sigma_y$ data in Fig. 6.12d shows there is a weak effect of Cu below the threshold for CRP formation that is not reflected in the TTS model. Note, the 0.1 wt % Cu data is included to show the rapid increase of $\Delta\sigma_y$ above the threshold for CRP formation of 0.072 wt %.

Indeed, the effects of Cu that are not treated in the TTS MF model, as well as the corresponding weaker effect of P, at least partially explain the apparent systematic TTS model over prediction of the low Cu IVAR $\Delta\sigma_y$ data. This is due to the fact that the IVAR SMMS are generally cleaner than the low Cu alloys in the TTS database, which contain on average about 0.05 wt % Cu and 0.011 wt % P. However, the generally higher Ni in the IVAR $\Delta\sigma_y$ has the opposite effect in making the IVAR steels slightly more sensitive to irradiation hardening. The CF values fitted to the IVAR data are also generally biased to lower values by the high flux IVAR $\Delta\sigma_y$ data. The analysis in Sect. 6.6.2 shows that high flux leads to systematically lower $\Delta\sigma_y$, even in low Cu steels. If the influence of the composition differences and flux effects are accounted for, the TTS MF model predictions and the IVAR $\Delta\sigma_y$ data are in much better agreement. Details of this analysis will be presented in a future report.

Finally, we note that the TTS MF model also includes flux dependence, but only below the range of the IVAR data. Although the absolute flux dependent differences in the $\Delta\sigma_y$ are much smaller than for the Cu-bearing alloys, as noted previously and discussed in Sect. 6.6.2, a systematic effect of flux is also observed in the low Cu and Cu free IVAR $\Delta\sigma_y$ data. The reasons that the TTS MF model does not capture the effect of flux in the IVAR and PWR surveillance regimes are discussed in Sects. 6.6.1 and 6.6.2.

6.5 The Irradiation Temperature Dependence of $\Delta\sigma_y$ in the SMMS

Figures 6.13 and 6.14 show intermediate flux IVAR $\Delta\sigma_y$ data plotted against the irradiation temperature (T_i) for several of the same SMMS shown in Sect. 6.4 at fluences of ≈ 0.48 and 1.6 × 10^{19} n/cm^2, along with the corresponding TTS model curves using the coefficients for the CE plates. As shown in Fig. 6.13, the TTS model predicts stronger irradiation temperature dependence than is observed in the IVAR data for the four Cu-free SMMS. In contrast, Fig. 6.14 shows that the opposite is the case in the more sensitive Cu-bearing SMMS. The absolute irradiation temperature dependence (slope) of IVAR $\Delta\sigma_y$ data increases with the alloy Cu, Ni, and Mn contents, as well as with fluence.

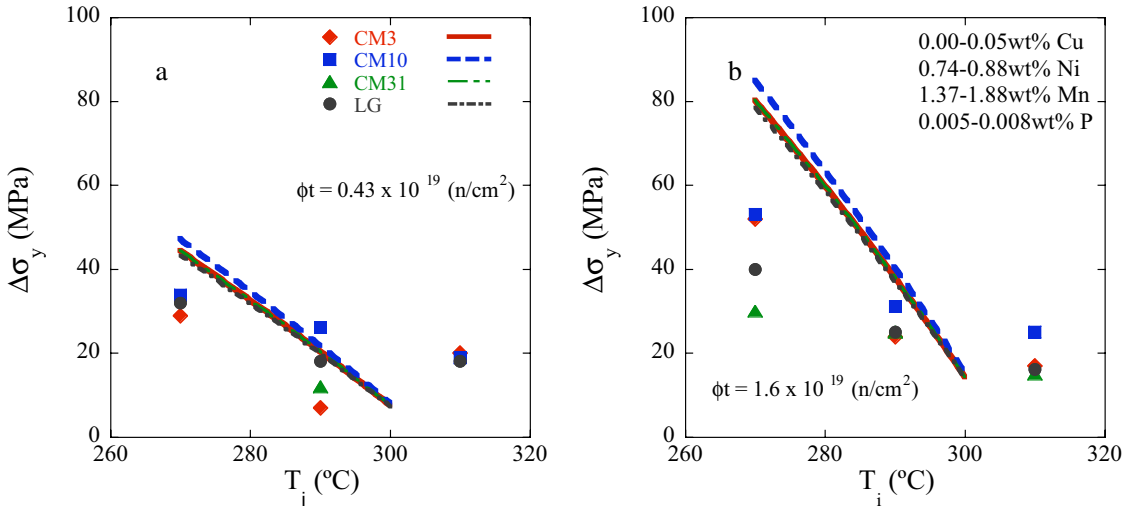

Fig. 6.13 a–b. TTS model predictions and the $\Delta\sigma_y$ data for four Cu-free SMMS irradiated in IVAR at 270, 390, and 310°C at intermediate flux to two fluences. The TTS model predicts a stronger irradiation temperature dependence of $\Delta\sigma_y$ than observed in the IVAR SMMS.

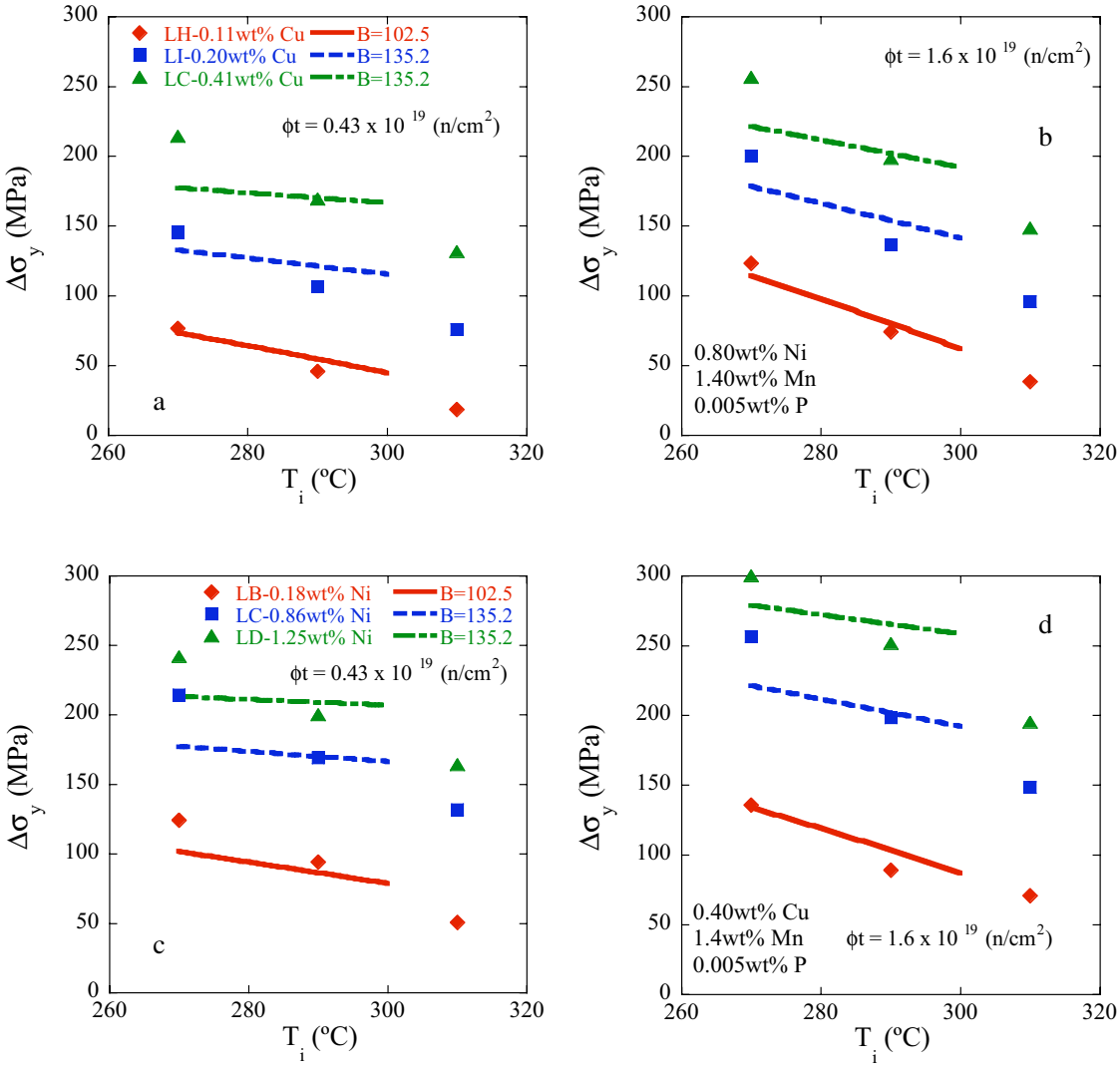

Fig. 6.14 a–d. TTS model predictions and the $\Delta\sigma_y$ data for intermediate flux IVAR irradiations to two fluences at 270, 290, and 310°C: (a) and (b) SMMS with 0.8 wt % Ni, 1.4 wt % Mn and 0.1, 0.2, and 0.4 wt % Cu; (c) and (d) SMMS with 0.4 wt % Cu, 1.4 wt % Mn and 0.2, 0.8 and 1.25 wt % Ni. The TTS model generally predicts weaker irradiation temperature dependence of σ_y than observed in the Cu-bearing IVAR SMMS.

The reasons for the decrease in CRP contribution to hardening with increasing irradiation temperature were discussed in Chap. 2. In contrast, the TTS model predicts a weak increase in the CRP contribution to $\Delta\sigma_y$ with increasing irradiation temperature. Possible reasons for this difference, and a recommended simplification which reduces the discrepancy, are discussed in Chap. 7. However, as shown in Fig. 6.4, the irradiation temperature dependence of the $\Delta\sigma_y$ data for the lower-sensitivity IVAR welds and plates, which are most like the steels in the surveillance database, are more consistent with the TTS model predictions, compared to the $\Delta\sigma_y$ vs T_i trends in the higher-sensitivity IVAR SMMS shown here.

In summary, the IVAR database shows that both MF and CRP hardening contributions decrease with increasing irradiation temperature. This observation is consistent with the TTS model MF term but is not consistent with the TTS model CRP term presented in Chap. 4, that shows a weak, but opposite, trend.

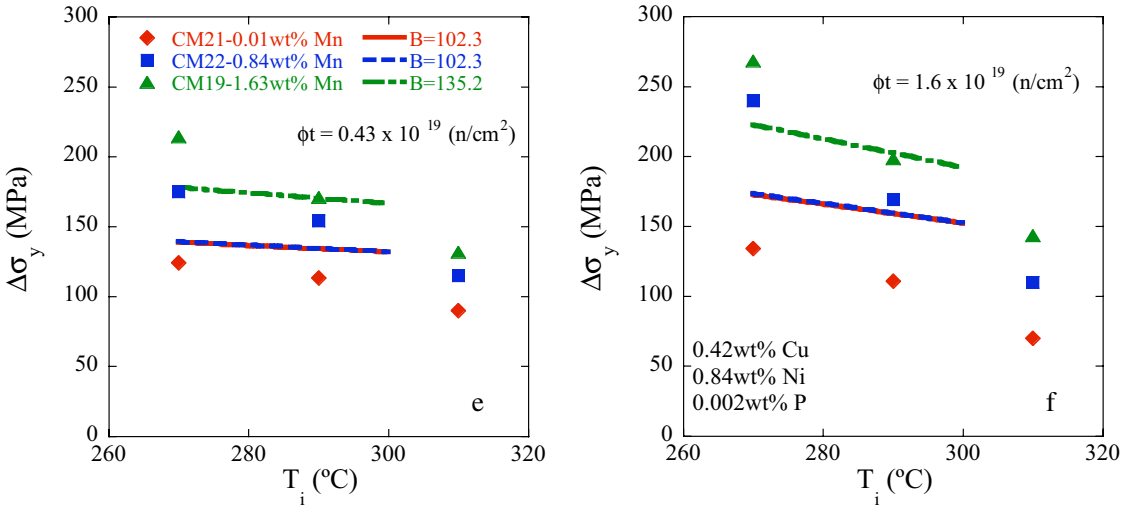

Fig. 6.14 e–f. The TTS model predictions and the $\Delta\sigma_y$ data for intermediate flux IVAR irradiations to two fluences at 270, 290, and 310°C for SMMS with 0.4 wt % Cu; 0.8 wt % Ni; and 0.0, 0.8, and 1.6 wt % Mn. The TTS model generally predicts weaker irradiation temperature dependence than observed in the IVAR results.

However, the CRP contribution in the TTS model is so small that the overall trend (MF plus CRP terms) in high Cu TTS model predictions follows the expected trend of decreasing $\Delta\sigma_y$ with increasing irradiation temperature. The absolute irradiation temperature dependence predicted by the TTS model is stronger than observed in the low Cu SMMS and weaker than observed in Cu-bearing IVAR SMMS. However, the agreement between the IVAR data and the TTS model is better for the welds and plates that are most similar to surveillance steels.

6.6 Flux Effects

6.6.1 Flux Effects on Hardening in Cu-Bearing Steels

The systematic flux effect on CRP hardening observed in the IVAR database has been described in detail elsewhere [9] and will be only summarized briefly here. Examples of such flux effects were shown in Figs. 6.3, 6.5, 6.6, and 6.7. All these data show that the pre-plateau CRP hardening regime is shifted to lower fluence with decreasing flux. Note, while these effects may look small on an expanded $\Delta\sigma_y$ vs log fluence scale, the average difference between the $\Delta\sigma_y$ in the pre-plateau region for the highest and lowest flux measure in IVAR is ≈ 40%.

As discussed in Chap. 2, flux effects in the IVAR data are believed to be primarily due to recombination enhanced by solute vacancy trapping, which reduces the efficiency of radiation enhanced diffusion (RED) of solutes. The net Cu diffusion per unit fluence, given by $D^*t/\phi t$, is smaller at higher flux. Thus, the hardening curves are shifted to higher fluence with increasing flux. The flux effect can be modeled using an effective fluence, ϕt_e, as

$$\phi t_e = \phi t(\phi_r/\phi)^p \qquad (6\text{-}8)$$

The ϕ_r is an arbitrary reference flux that was taken as the intermediate IVAR flux of 3×10^{11} n/cm^2-s [9]. Since p is the slope of the log[$D^*t/\phi t$](ϕ) curve between log[ϕ] and log[ϕr] in principle the flux depends on the irradiation temperature, and the alloy composition and microstructure [9]. For example, recombination, hence p, increases with higher alloy Mn and Ni contents because these solutes are vacancy

traps. Also, p decreases with increasing irradiation temperature because the corresponding vacancy de-trapping rates increase. The value of p also depends on the choice of the reference flux, ϕ_r (see Fig. 2.16), decreases from a limiting, high flux value of 0.5 in the recombination-dominated regime, and may approach 0 if the thermal diffusion coefficient of Cu, D_{Cu}, is very small. However if, as expected, the low-temperature D_{Cu}, is larger than estimates based on extrapolations of tracer diffusion data from high temperature, as indicated by thermal precipitation kinetics data in the range of 290 to 350°C, p goes through a minimum and may reach values greater than 0.5 at low flux; in the limiting case where $D^* \approx D_{Cu}$, p may approach 1 at very low flux. These limiting values of p occur only if the actual and reference flux are in the same mechanism regime, in which p is independent of flux. More generally p is lower than the recombination limit of 0.5 and higher than the minimum flux independent value of 0. To reiterate, the flux effect completely resides in D*; there is not flux effect if D* is independent of flux.

Figures 6.15 to 6.18 show the same Cu-bearing IVAR steel data presented in Figs. 6.3, 6.5, 6.6, and 6.7. The figures on the far left-hand side of Figs. 6.15 to 6.18 are for a solute vacancy trap enhanced recombination model for the CRP contribution to $\Delta\sigma_y$ fitted to the individual alloy data sets and plotted on a common effective fluence, ϕt_e, scale. In this case the MF term was modeled as $\Delta\sigma_y = CF\sqrt{(\phi t_e)}$ where the CF is the fitted value for the individual alloy that has the same nominal composition, except for being Cu free, as the corresponding Cu bearing steel. In the cases where Cu free alloy data were not directly available, a simple linear correlation model, accounting for Cu, Ni, Mn and P effects in the MF for the Cu bearing alloy, was used to estimate the MF CF. As expected, the fitted recombination model (FRM) greatly reduces the flux dependence of $\Delta\sigma_y$ in Cu bearing steels.

The systematic effect of flux is more clearly shown in the corresponding measured minus predicted $\Delta\sigma_y$ vs flux residuals shown in Figs. 6.15 to 6.18. The figures in the middle show that the residuals for the FRM are generally well centered and, as expected, do not depend strongly on flux. In contrast, the figures on the far right hand side of Figs. 6.15 to 6.18 show that the residuals for the TTS model has a strong flux dependence, in some cases tending to slightly under predict the $\Delta\sigma_y$ data at the low IVAR flux (squares), while over predicting the $\Delta\sigma_y$ at the high IVAR flux (diamonds). In a number of cases, there is an overall bias in the average residual for the TTS model.

The TTS model also includes a flux effect on CRP and MF hardening, but with some key differences with respect to the IVAR data. Although the flux ranges of IVAR and surveillance data overlap, the calibrated TTS model has a flux effect only below 4.4×10^{10} n/cm^2-s, which is lower than the flux range of the IVAR data. Note, above this threshold, a residual trend with flux can be detected in some surveillance datasets that is in the same direction as shown by the IVAR data. However, the magnitude of the effect in the TTS model residuals is not sufficiently large relative to the scatter in the data to be statistically significant. Possible reasons for this difference between the effects of dose rate in the TTS model and IVAR $\Delta\sigma_y$ are discussed in Sect. 6.6.1.

The TTS model also assumes a fitted constant effective fluence scaling exponent, p = 0.26. Figure 6.19 plots p vs flux the recombination model shown previously in Fig. 2.16, taking $\phi_r = 4.4 \times 10^{10}$ n/cm^2-s, using the same parameters that were described in Chap. 2. Curves are shown for trap concentrations, X_t, of 0.03 and 0.01, effectively spanning the range of typical RPV steels with various Ni, Mn. Cu,… solute contents. Figs 6.19a and 6.19b are for nominally high and low values of D_{Cu}, respectively. The constant p = 0.26 from the TTS model shown as the horizontal dashed line is in reasonable agreement with the physically based recombination model predictions in the flux range from 10^9 and 10^{11} n/cm^2-s: the average values of the predicted p are 0.29 and 0.20 for X_t = 0.03 and 0.01, respectively, for the low D_{Cu} case; the corresponding values for the high D_{Cu} case are 0.33 and 0.24. Overall, the FRM with the high D_{Cu} is most consistent with the TTS model.

The fitted FRM can also be used to physically extrapolate the IVAR data to lower fluxes. The flux effect can be represented by a fluence-multiplier, $M_\phi(\phi) = \phi t_e/\phi t$, that is normalized to unity at a specified flux. Figure 6.20 plots M_ϕ curves normalized at $\phi_r = 8 \times 10^{10}$ n/cm^2-s, in the borderline region of over-

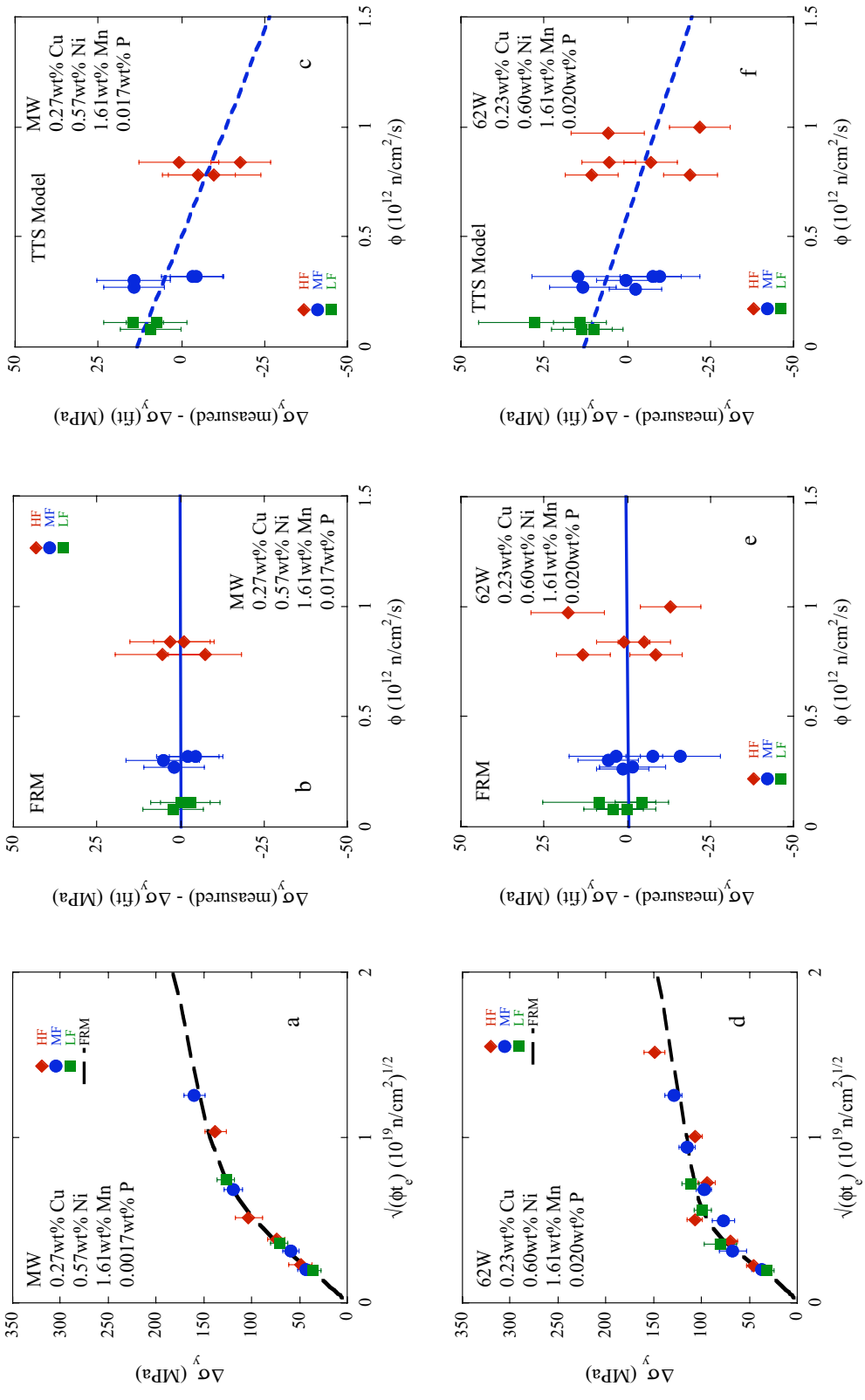

Fig. 6.15 a–f. (a, d) The fitted recombination model (FRM) predictions and the 290°C IVAR $\Delta\sigma_y$ data for two Cu-bearing commercial welds on an effective fluence, ϕt_e, scale; (b, e) the corresponding measured minus predicted residuals for the FRM that are well centered and approximately independent of flux; (c, f) the corresponding residuals for the TTS model, showing a systematic effect of flux that is not accounted for in the TTS model developed in Chap. 3.

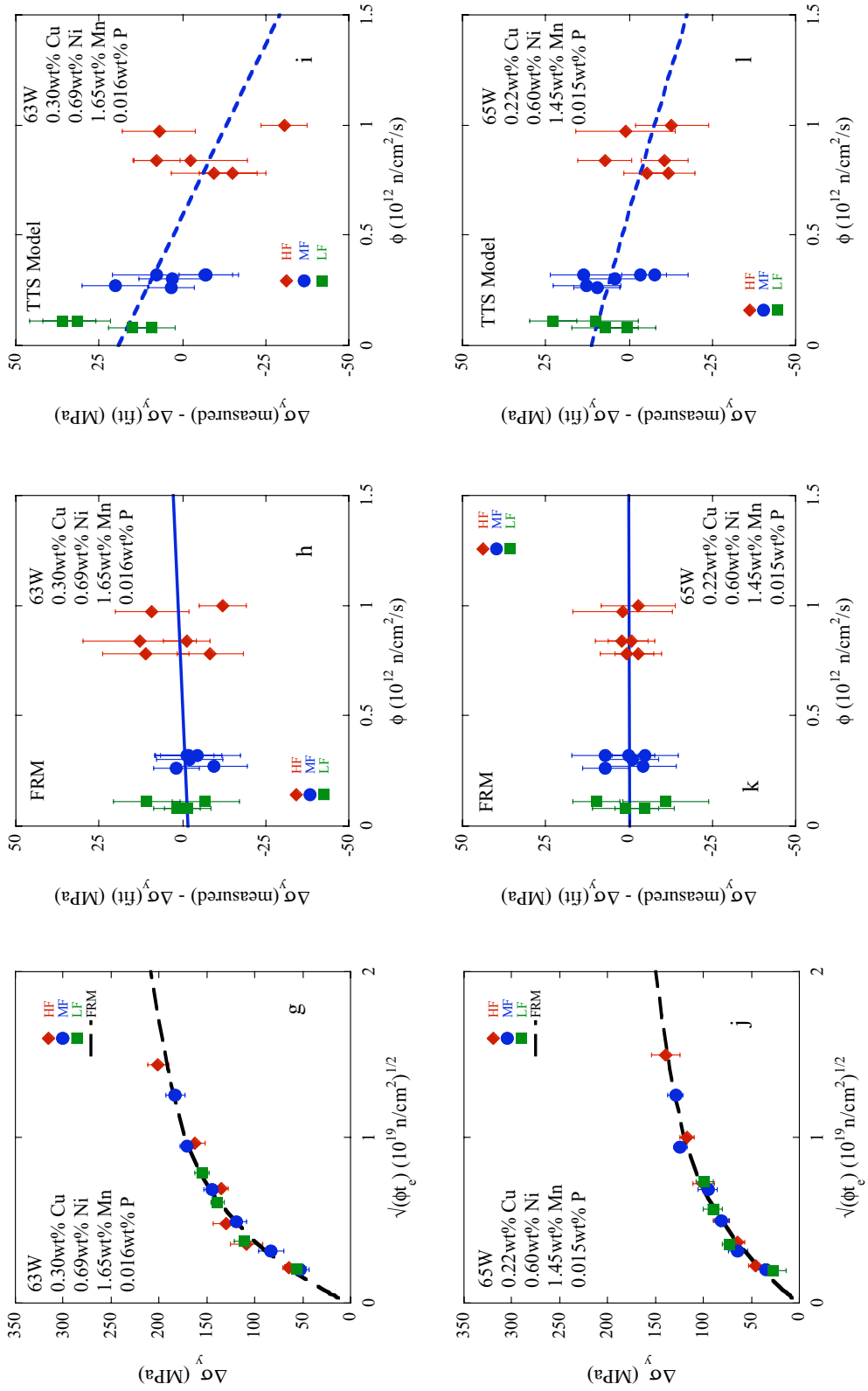

Fig. 6.15 g–l. (g, j) The fitted recombination model (FRM) predictions and the 290°C IVAR $\Delta\sigma_y$ data for two Cu-bearing commercial welds on an effective fluence, ϕt_e, scale; (h, k) the corresponding measured minus predicted residuals for the FRM that are well centered and approximately independent of flux; (i, l) the corresponding residuals for the TTS model, showing a systematic effect of flux that is not accounted for in the TTS model developed in Chap. 3.

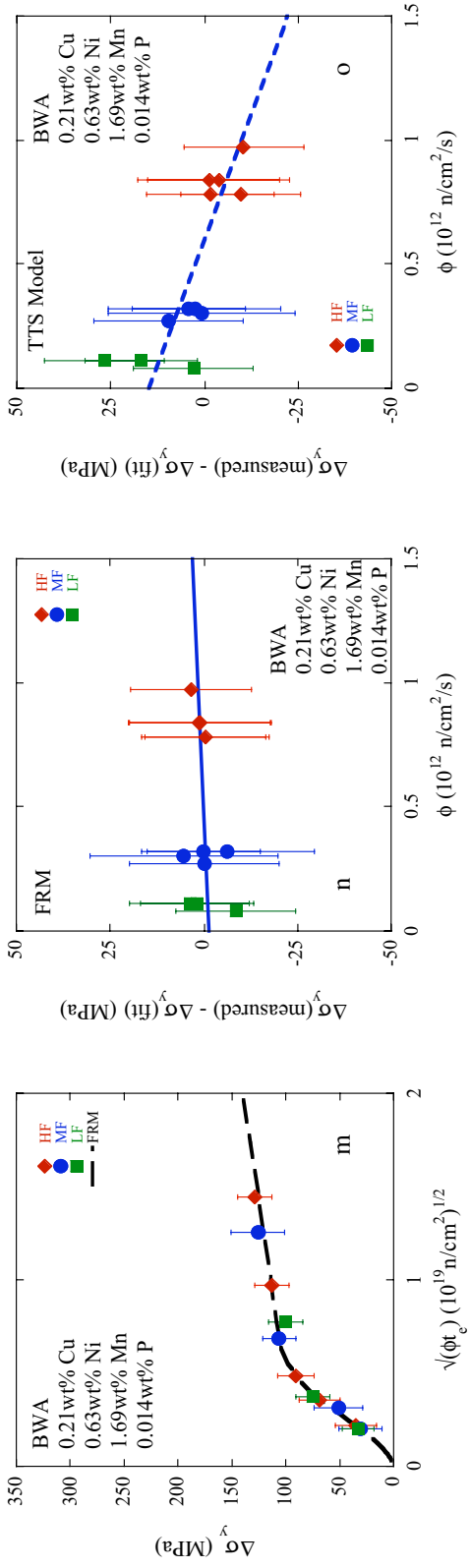

Fig. 6.15 m-o. (m) The fitted recombination model (FRM) predictions and the 290°C IVAR $\Delta\sigma_y$ data for a Cu-bearing commercial welds on an effective fluence, ϕt_e, scale; (n) the corresponding measured minus predicted residuals for the FRM that are well centered and approximately independent of flux; (o) the corresponding residuals for the TTS model, showing a systematic effect of flux that is not accounted for in the TTS model developed in Chap. 3.

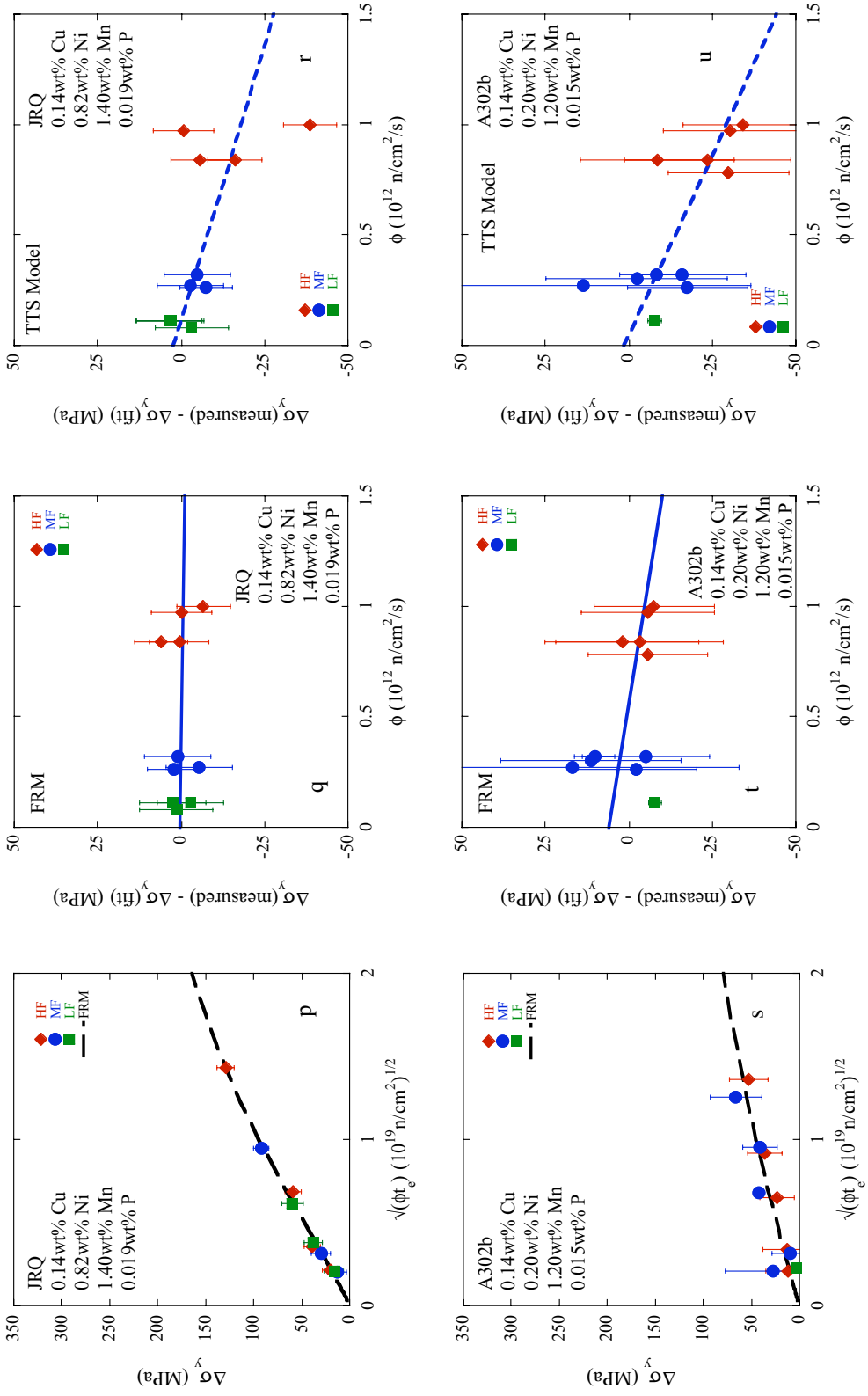

Fig. 6.15 p-u. (p, s) The fitted recombination model (FRM) predictions and the 290°C IVAR $\Delta\sigma_y$ data for two Cu-bearing commercial plates on an effective fluence, ϕt_e, scale; (q, t) the corresponding measured minus predicted residuals for the FRM that are well centered and approximately independent of flux; (r, u) the corresponding residuals for the TTS model, showing a systematic effect of flux that is not accounted for in the TTS model developed in Chap. 3.

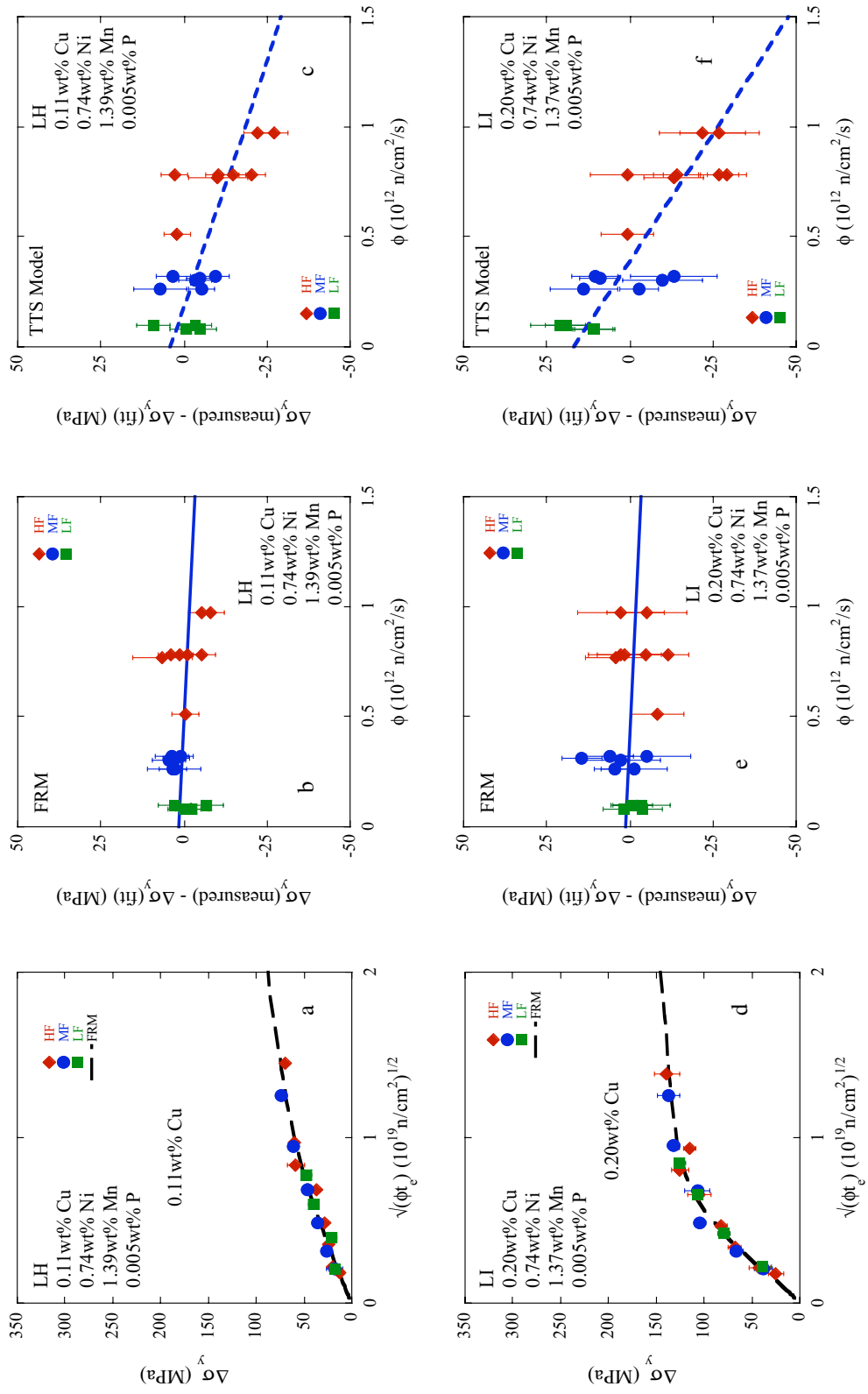

Fig. 6.16 a–f. (a, d) The fitted recombination model (FRM) predictions and the 290°C IVAR $\Delta\sigma_y$ data for two SMMS with 0.8 wt % Ni, 1.4 wt % Mn and 0.1 and 0.2 wt % Cu on an effective fluence, ϕt_e, scale; (b, e) the corresponding measured minus predicted residuals for the FRM that are well centered and approximately independent of flux; (c, f) the corresponding residuals for the TTS model, showing a systematic effect of flux that is not accounted for in the TTS model developed in Chap. 3.

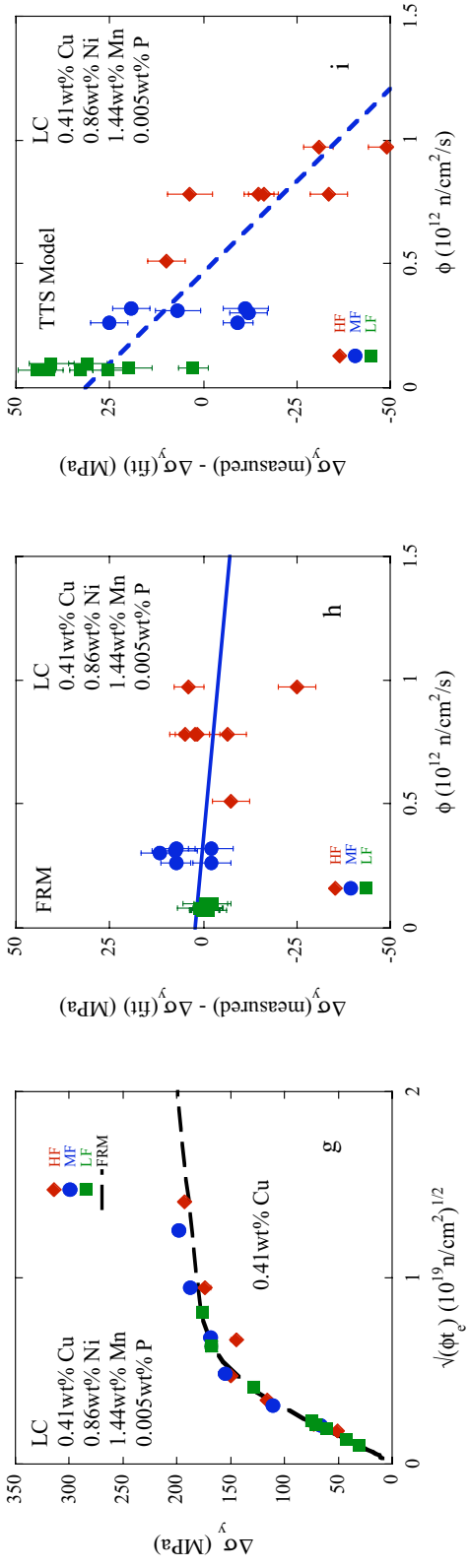

Fig. 6.16 g-i. (g) The fitted recombination model (FRM) predictions and the 290°C IVAR $\Delta\sigma_y$ data for a SMMS with 0.8 wt % Ni, 1.4 wt % Mn and 0.4 wt % Cu on an effective fluence, ϕt_e, scale; (h) the corresponding measured minus predicted residuals for the FRM that are well centered and approximately independent of flux; (i) the corresponding residuals for the TTS model, showing a systematic effect of flux that is not accounted for in the TTS model developed in Chap. 3.

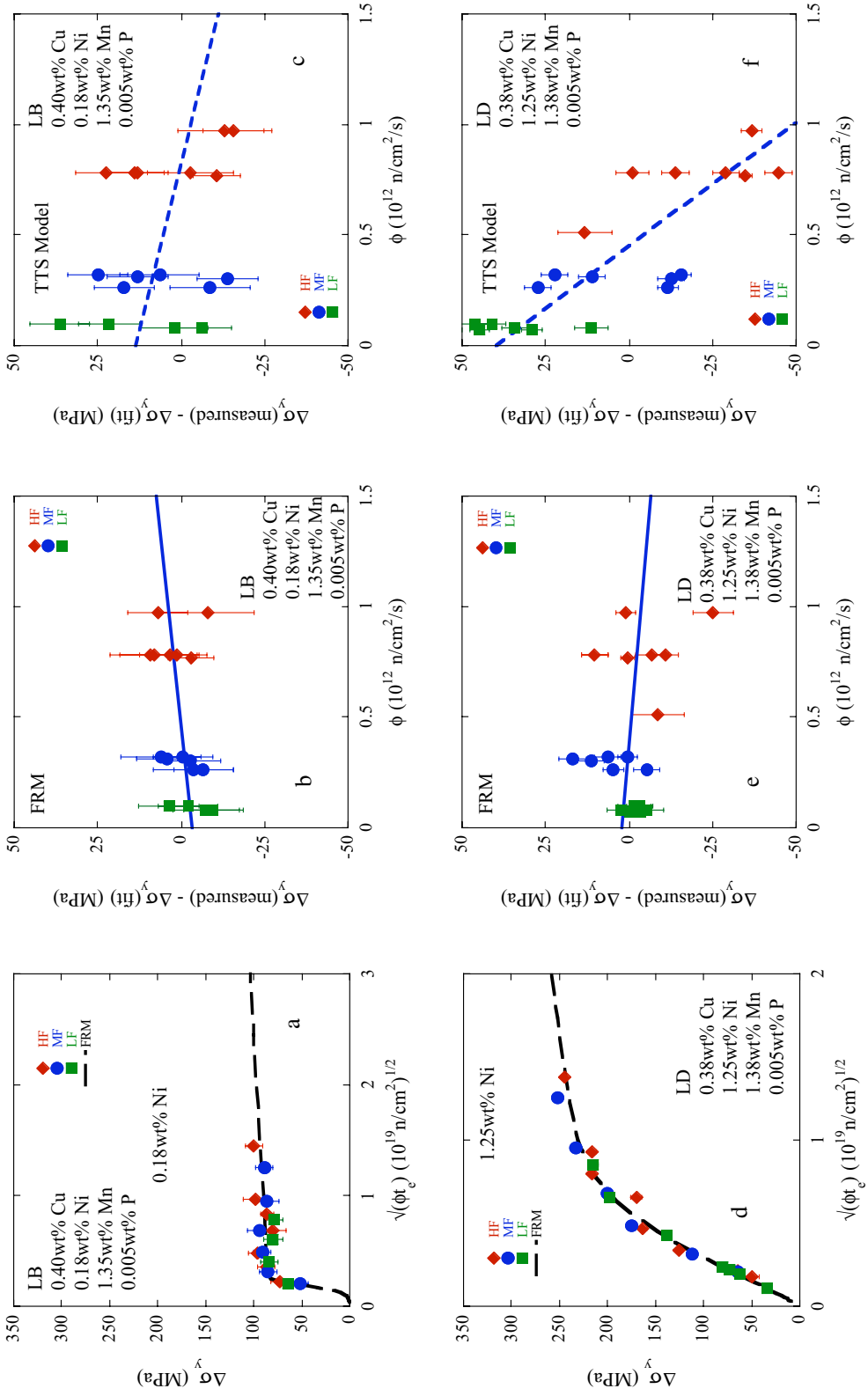

Fig. 6.17 a–f. (a, d) The fitted recombination model (FRM) predictions and the 290°C IVAR $\Delta\sigma_y$ data for two SMMS with 0.4 wt % Cu, 1.4 wt % Mn, and 0.2and 1.25 wt % Ni on an effective fluence, ϕt_e, scale; (b, e) the corresponding measured minus predicted residuals for the FRM that are well centered and approximately independent of flux; (c, f) the corresponding residuals for the TTS model, showing a systematic effect of flux that is not accounted for in the TTS model developed in Chap. 3.

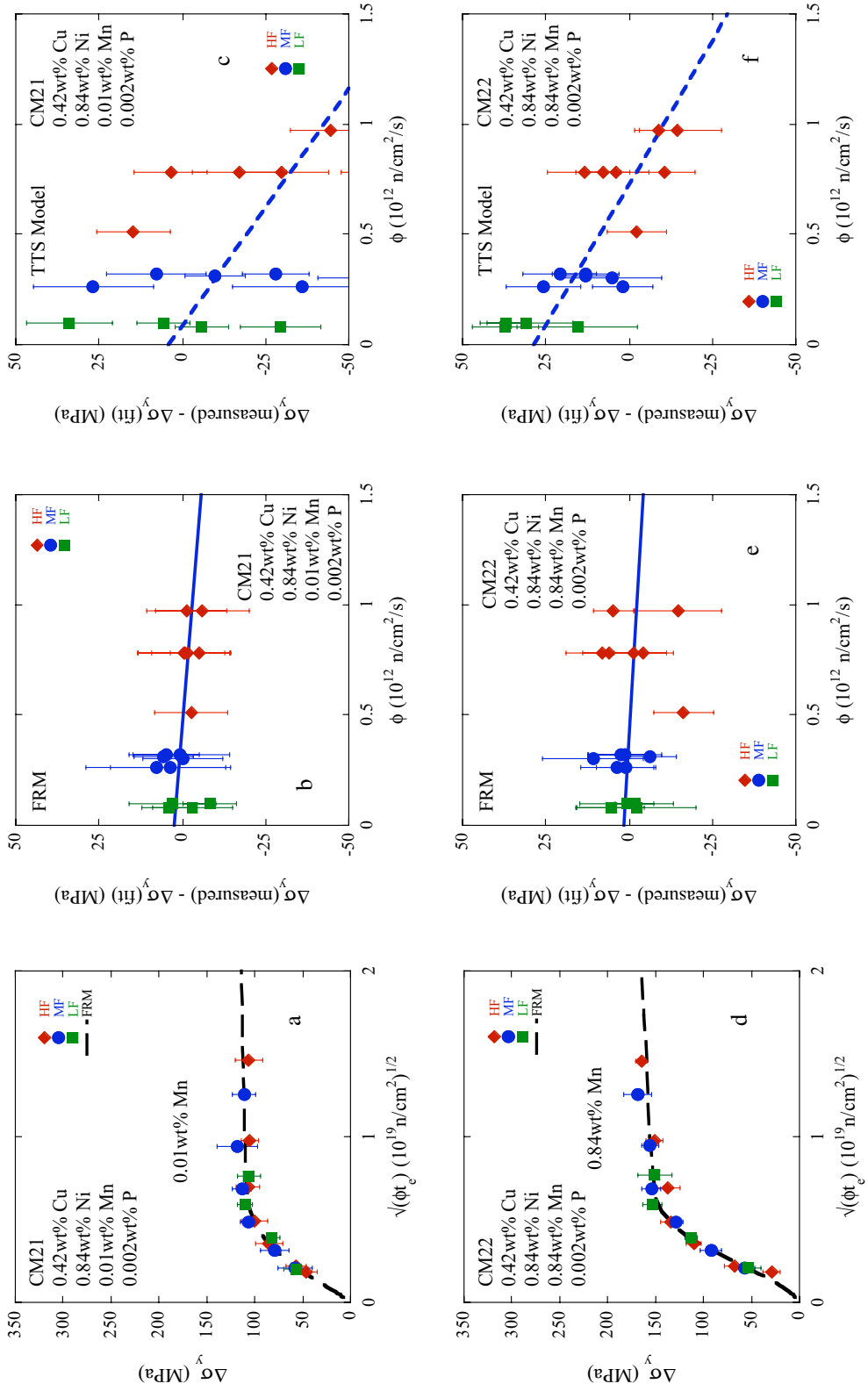

Fig. 6.18 a–f. (a, d) The fitted recombination model (FRM) predictions and the 290°C IVAR $\Delta\sigma_y$ data for two SMMS with 0.4 wt % Cu, 0.8 wt % Ni, and 0.0 and 0.8 wt % Mn on an effective fluence, ϕt_e, scale; (b, e) the corresponding measured minus predicted residuals for the FRM that are well centered and approximately independent of flux; (c, f) the corresponding residuals for the TTS model, showing a systematic effect of flux that is not accounted for in the TTS model developed in Chap. 3.

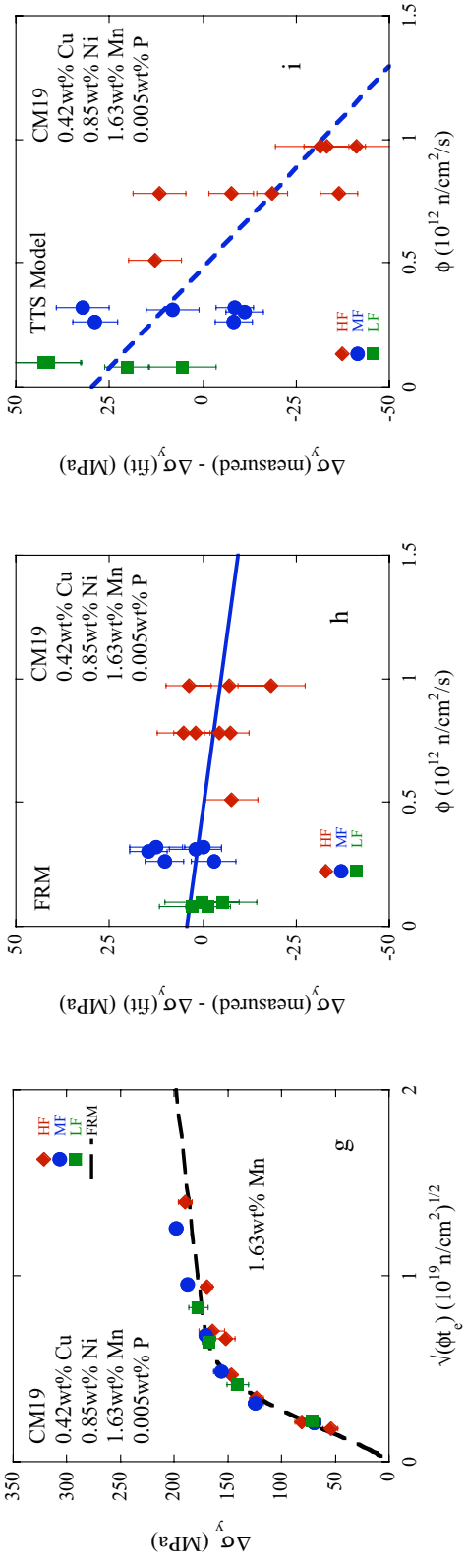

Fig. 6.18 g–i. (g) The fitted recombination model (FRM) predictions and the 290°C IVAR $\Delta\sigma_y$ data for two SMMS with 0.4 wt % Cu, 0.8 wt % Ni, and 1.6 wt % Mn on an effective fluence, ϕt_e, scale; (h) the corresponding measured minus predicted residuals for the FRM that are well centered and approximately independent of flux; (i) the corresponding residuals for the TTS model, showing a systematic effect of flux. that is not accounted for in the TTS model developed in Chap. 3.

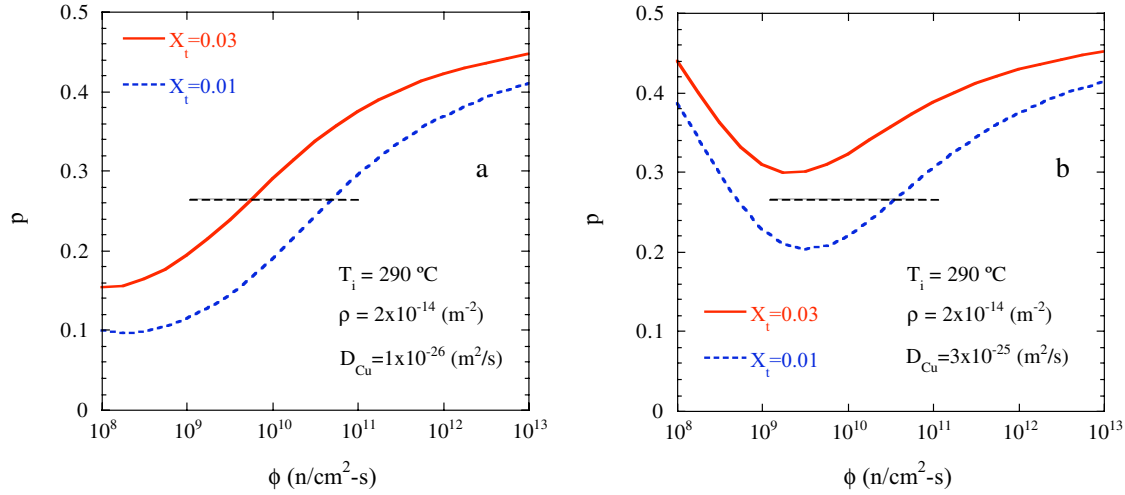

Fig. 6.19. The flux scaling p values for a range of X_t and low and high nominal D_{Cu}. The horizontal dashed line represents the fitted value in the TTS model.

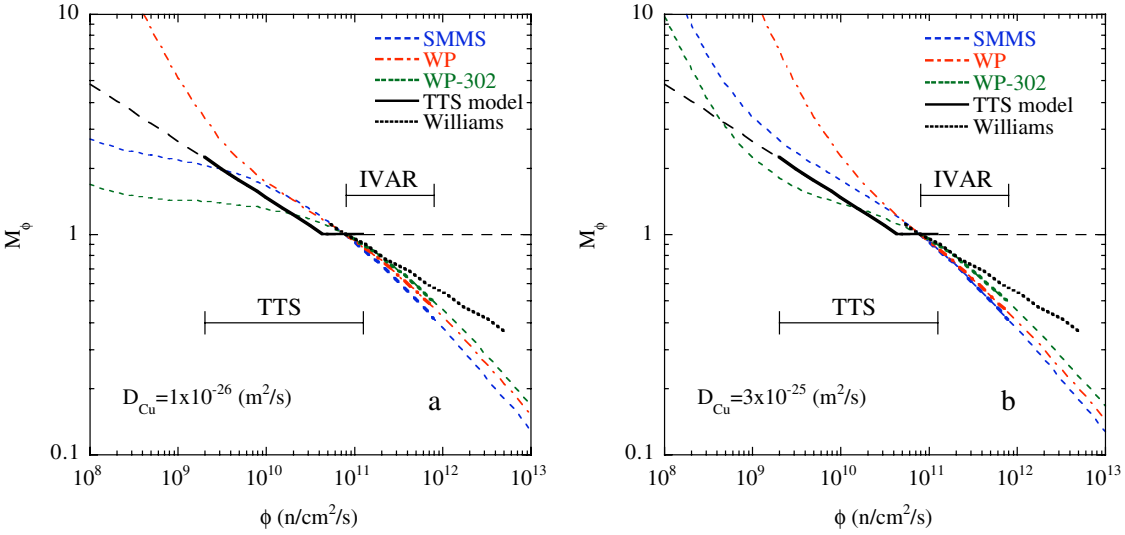

Fig. 6.20. The $M_\phi = \phi t_e/\phi t$ effective fluence multiplying factor as a function of flux for the TTS model, the FRM for various subsets of IVAR data and the corresponding M_ϕ reported by Williams. The M_ϕ is normalized at 8×10^{10} n/cm^2-s. The solid line is the TTS model plotted over the approximate range of TTS data: the dashed extensions indicate how the TTS model would extrapolate. Notably, the M_ϕ curves are similar at a low flux (2×10^9 n/cm^2-s).

overlapping fluxes between the IVAR and TTS surveillance databases. Figures. 6.20a and 6.20b assume the nominal low and high estimates of D_{Cu} (see Chap. 2). Separate averages are shown for the SMMS (solid line) and weld plus plate (long dashed line) alloy groupings. With one exception, the FRM $M_\phi(\phi)$ curves compare favorably with that for the TTS model, in spite of the latter's "hockey stick" shape. The exception is the high D_{Cu} FRM fitted to the weld and plate alloys. The M_ϕ in this case is significantly larger than for the TTS model at low flux. However, this is due to an anomalously large M_ϕ in the A302B plate, hence, this curve is not considered to be very reliable. The corresponding curve that does not include the A302B data in the normalization is in better agreement with the TTS M_ϕ curve. Figure 6.20 also shows that the M_ϕ function reported by Williams [10] is in good agreement with the IVAR results. Note, this figure also demonstrates the modest effect of flux predicted by the FRM in the region between 4.45×10^{10} and 2×10^{11} n/cm^2-s, where a flux effect is not included in the TTS model because, for reasons discussed below, it did not appear to be significant in the surveillance data. Note, the effect of flux on ϕt_e is stronger than that of the corresponding $\Delta\sigma_y$ which scales with dose to a power that is less than 1. For example, if $\Delta\sigma_y$ varies with $\sqrt{\phi t_e}$, then a ±20% variation in ϕt_e results in a ±10% difference in $\Delta\sigma_y$.

The FRM $\Delta\sigma_y$ hardening curves for the SMMS and welds tend to be shifted to slightly lower fluence compared to the TTS model predictions. The opposite is the case for the plates. This effect can be simply quantified in terms of the fluence at 50% of the maximum CRP hardening, $\phi t_{0.5}$. Figure 6.21 shows the average $\phi t_{0.5}$ for both models at 2×10^9 and 2×10^{11} n/cm^2-s for separate SMMS, weld and plate alloy groupings. As noted above, the FRM $\phi t_{0.5}$ are lower for the SMMS and welds and higher for the plates compared with the TTS model.

The fact that the TTS model does not find a strong flux effect in the range of the IVAR experiment is not very surprising since:

- The PWR surveillance data and IVAR data have overlapping flux ranges, but the higher flux surveillance data are sparse. About 95% of the surveillance data have flux $< 2 \times 10^{11}$ n/cm^2-s, which is below the medium flux level (3×10^{11} n/cm^2-s) in the IVAR irradiations. Thus, the TTS model calibration reflects mainly lower flux levels and only a small fraction of the IVAR flux range.
- It is inherently difficult to resolve an influence of any variable over the narrow range, in this case flux, especially since the effects are relatively small compared to the scatter in the TTS database.
- The TTS model is necessarily simplified and must compromise to provide average fits for p for a wide range of alloys and irradiation conditions, while the FRM model is physically based and is fitted to individual alloys, each with a large set of high quality data.
- Most of the high Cu TTS data in the IVAR flux range are at high fluence on, or approaching, the flux independent CRP hardening plateau, while the IVAR database explicitly explores a wide range of fluence, with many experimental observations for each alloy. Since the main effect of flux is to shift the fluence to reach rather than the magnitude of the CRP hardening plateau, it is not surprising that the TTS data do not show a flux effect.
- The Ni and Mn solute contents of the IVAR SMMS are, on average, somewhat higher than in the TTS database, thus enhancing recombination and flux effects.

In summary, as schematically illustrated in Fig. 6.22, it appears that a flux effect in the TTS surveillance database can be detected only over the wide range of fluxes corresponding to typical BWR and PWR surveillance capsule conditions. However, the more precise and well-controlled IVAR database shows a systematic flux effect that is remarkably consistent with simply extrapolating the flux dependence found in the TTS model to higher flux, in the region where the effect apparently flattens in fitting the surveillance database. There is no physical basis to expect an abrupt end to the flux dependent regime. Indeed, physical considerations suggest that the effect of flux should increase with increasing

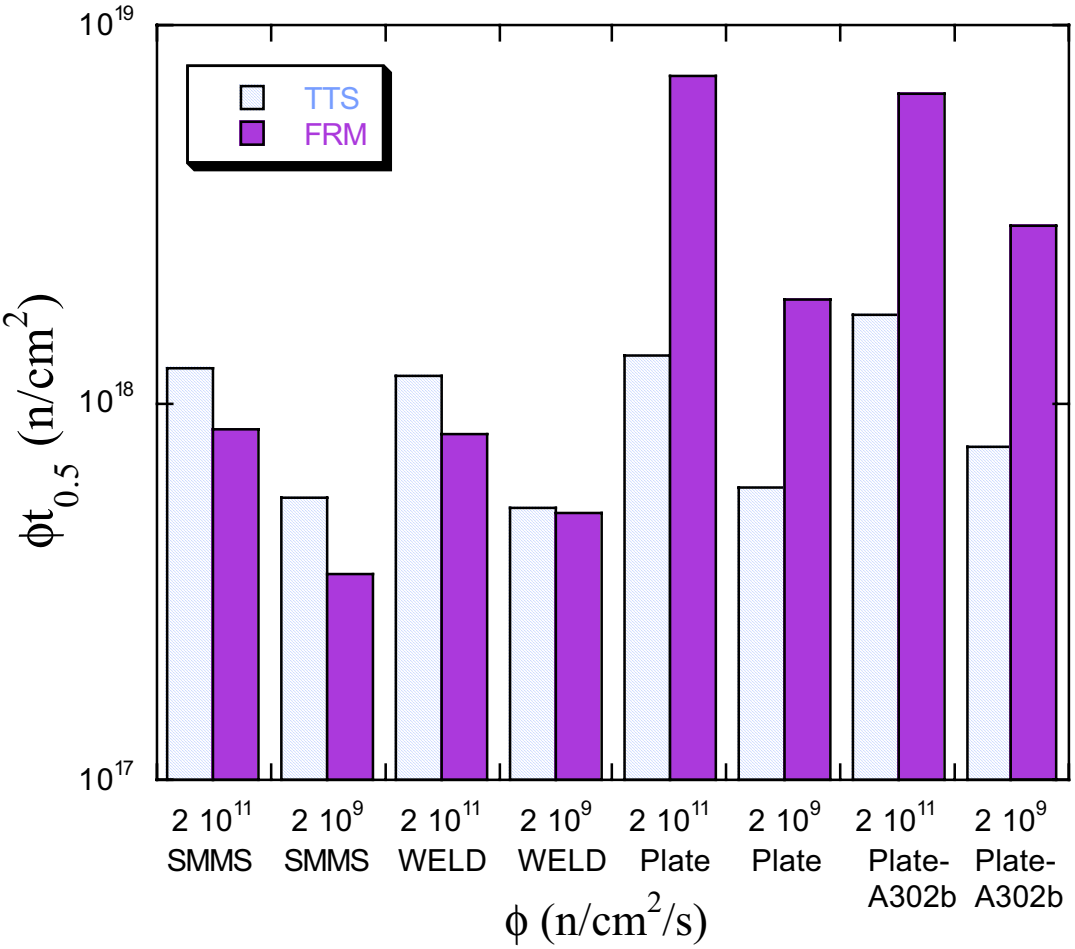

Fig. 6.21. The fluence at 50% of the maximum CRP hardening, $\phi t_{0.5}$, for the TTS and FRM models and various subsets of IVAR data ignoring the effect of the TTS to $\Delta\sigma_y$ conversion. The $\phi t_{0.5}$ is somewhat lower for the IVAR SMMS and commercial welds and higher for plates for the FRM vs TTS model.

dose rate. The use of a constant p approximation is supported by the analysis provided in this section. However, it must be recognized that the fitted p in the TTS model is a compromise average that does not account for any of the relevant variables that affect p such as the alloy composition, microstructure and irradiation temperature. The overall trends in the FRM and TTS models represented by a flux multiplier $M_\phi(\phi)$ function are remarkably consistent over a wide range of flux, and are supported by independent results reported by Williams. Extrapolation of the TTS model to low flux, below the surveillance database, is clearly uncertain, since there are no relevant TTS data. However, it is notable that the TTS model extrapolation is bounded by the predictions of the FRM models that assume the high and low values for D_{Cu}. This suggests that from a mechanistic perspective, extrapolating the TTS model to low flux is justified by the current state of knowledge.

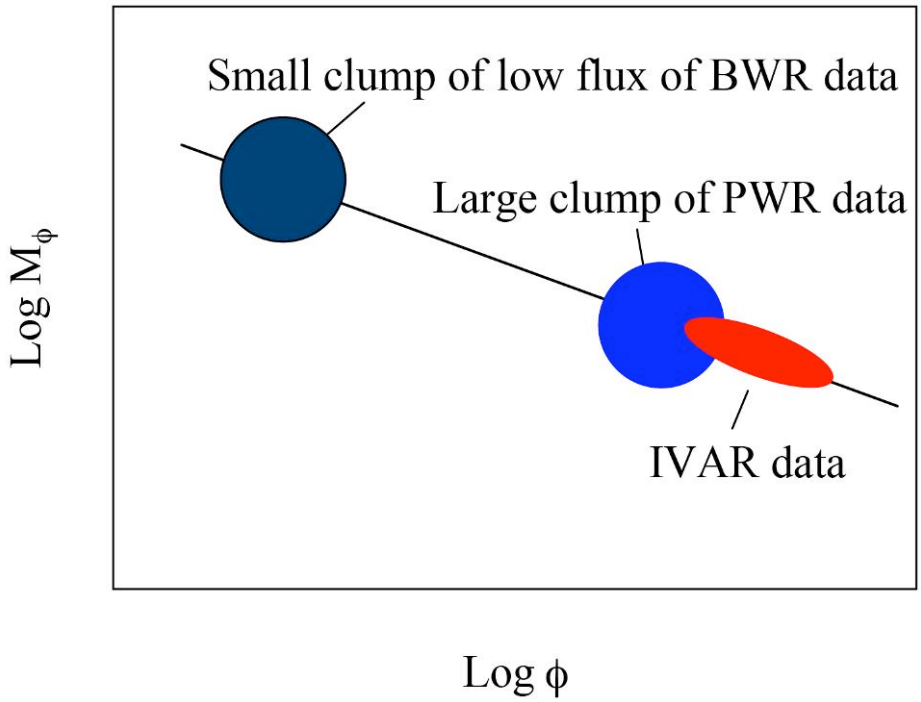

Fig. 6.22. Schematic illustration of the ability of the TTS model to fit a flux effect in scattered data over a wide range of dose rates compared to the more precise data from the controlled IVAR experiment.

6.6.2 Flux Effects on MF Hardening

The conventional view is that the MF contribution to hardening does not depend on flux. However, as in the case of the CRP contribution, the MF hardening in the IVAR database on low Cu steels systematically increases with decreasing flux, as shown in Figs. 6.9 to 6.11. The effect of flux can also be accounted for by the effective fluence, ϕt_e, by least square fitting the scaling exponent, p, in Eq. (6-8) and CF parameters models for each alloy with the expression

$$\Delta\sigma_y = CF\sqrt{\phi t_e} = CF\sqrt{[\phi t(\phi_r/\phi)^p]} \quad (6\text{-}9)$$

Figures 6.23 to 6.25 show plots similar to those Figs. 6.15 to 6.18, except that in this case they are for the low-Cu IVAR steels. The figures on the left are again the fits to the IVAR $\Delta\sigma_y$ data plotted on an effective fluence, ϕt_e, scale. The figures in the middle are the measured minus predicted $\Delta\sigma_y$ residuals plotted against flux for the effective fluence MF model in Eq. (6-9). The figures on the right are the corresponding residuals for the TTS model, which does not have a flux effect in the MF term in the flux range of the IVAR experiment, although it does at lower flux. As expected, the residuals for the fitted effective fluence MF model are generally well centered around 0, and show neither a significant average net bias nor any strong, systematic effect of flux. In contrast, the TTS model residuals show a systematic flux effect and are sometimes not well centered around 0. The average fitted p is 0.42 for the data in Fig. 6.23, which represent steels most like those in the IVAR database. The corresponding p for fits to low and high sensitivity data in Figs 6.24 and 6.25 are 0.47 and 0.44, respectively. The p for the single low Cu IVAR medium Ni weld is 0.125. These p values are broadly consistent with the observed effect of flux on the CRP contribution to hardening.

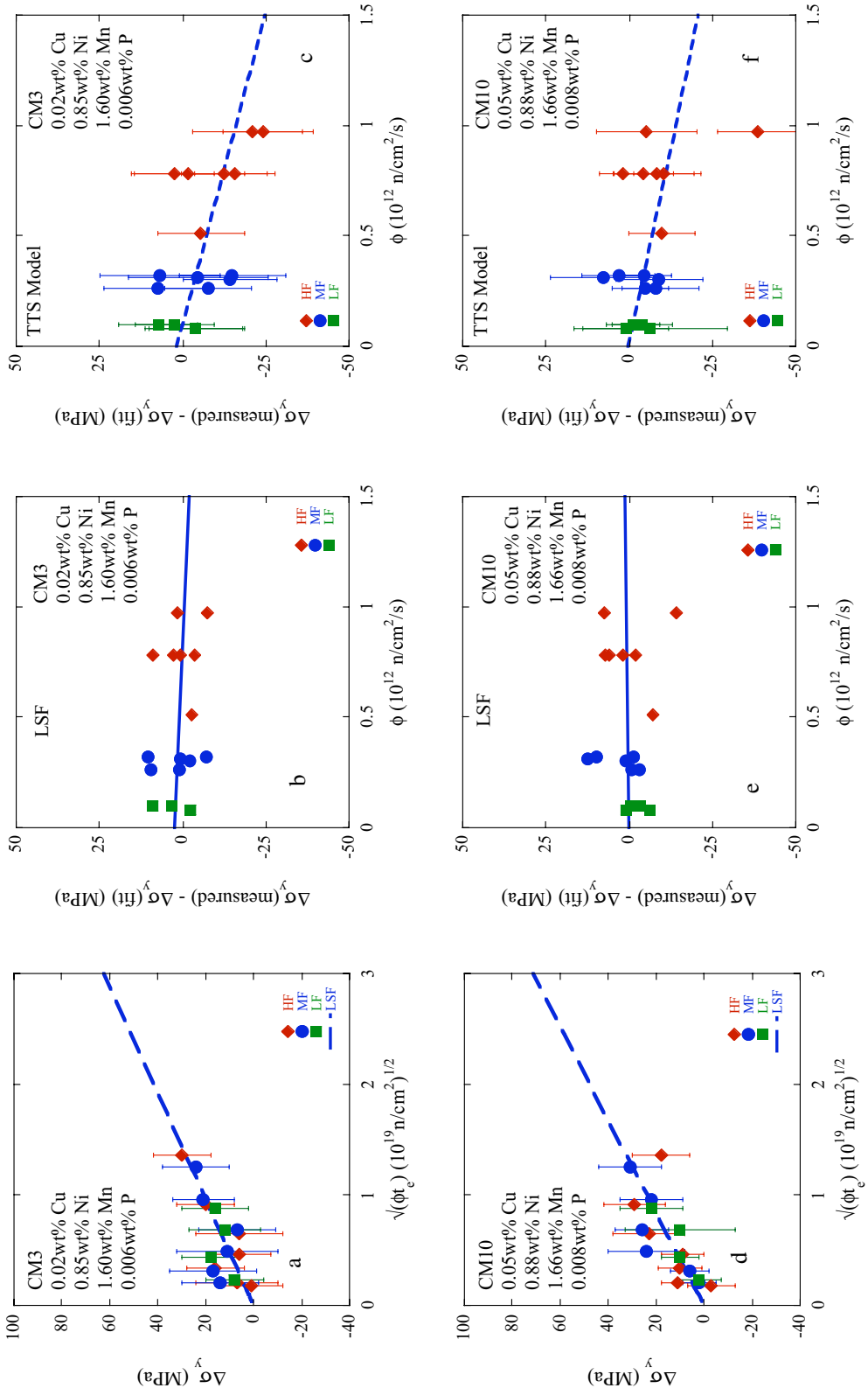

Fig. 6.23 a–f. (a, d) The fitted MF model for the 290°C IVAR $\Delta\sigma_y$ data on two Cu-free SMMS with 0.8 wt % Ni, 1.6 wt % Mn, and 0.005 wt % P on an effective fluence, ϕt_e, scale; (b, e) The corresponding measured minus predicted residuals for the FRM that are reasonably well-centered and approximately independent of flux; (c, f) The corresponding residuals for the TTS model, showing a systematic effect of flux.

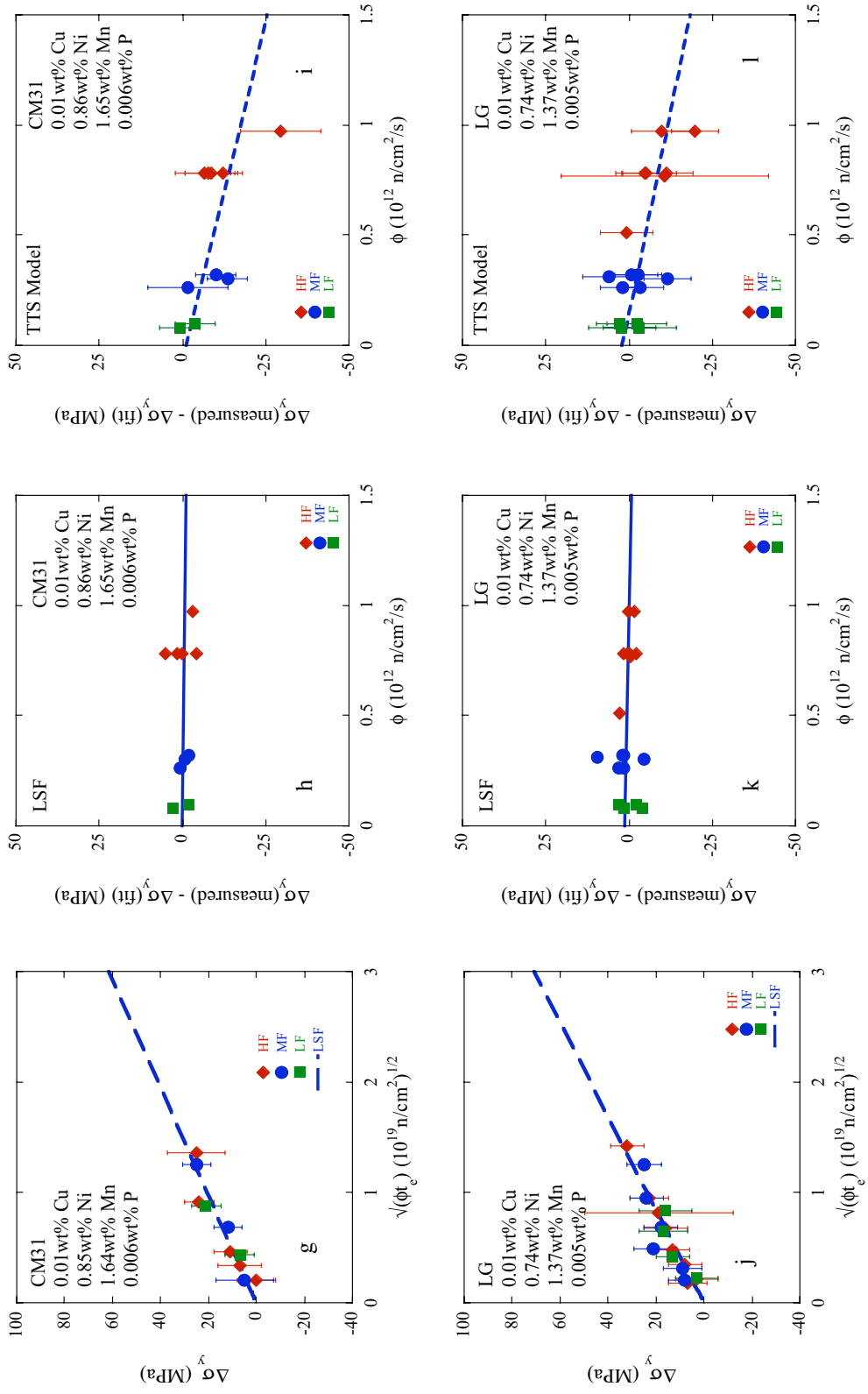

Fig. 6.23 g–l. (g, j) The fitted MF model for the 290°C IVAR $\Delta\sigma_y$ data on two Cu-free SMMS with 0.8 wt % Ni, 1.4 to1.6 wt % Mn, and 0.005 wt % P on an effective fluence, ϕt_e, scale; (h, k) The corresponding measured minus predicted residuals for the FRM that are reasonably well-centered and approximately independent of flux; (i, l) The corresponding residuals for the TTS model, showing a systematic effect of flux.

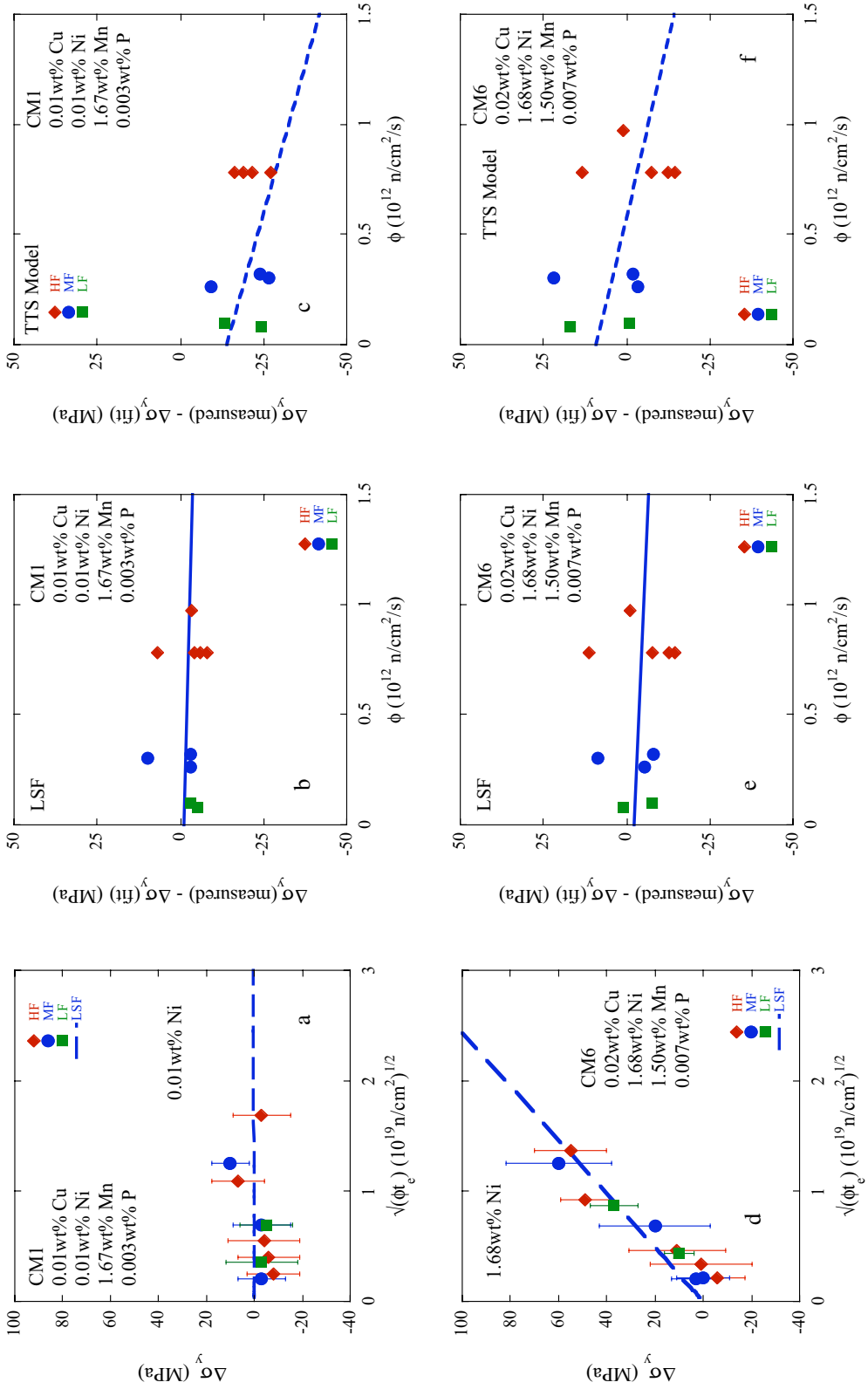

Fig. 6.24 a–f. (a, d) The fitted MF model for the 290°C IVAR $\Delta\sigma_y$ data on two Cu-free SMMS with 0.8 and 1.6 wt % Ni , 1.6 wt % Mn, and 0.005 wt % P on an effective fluence, ϕt_e, scale; (b, e) The corresponding measured minus predicted residuals for the FRM that are reasonably well-centered and approximately independent of flux; (c, f) The corresponding residuals for the TTS model, showing a systematic effect of flux.

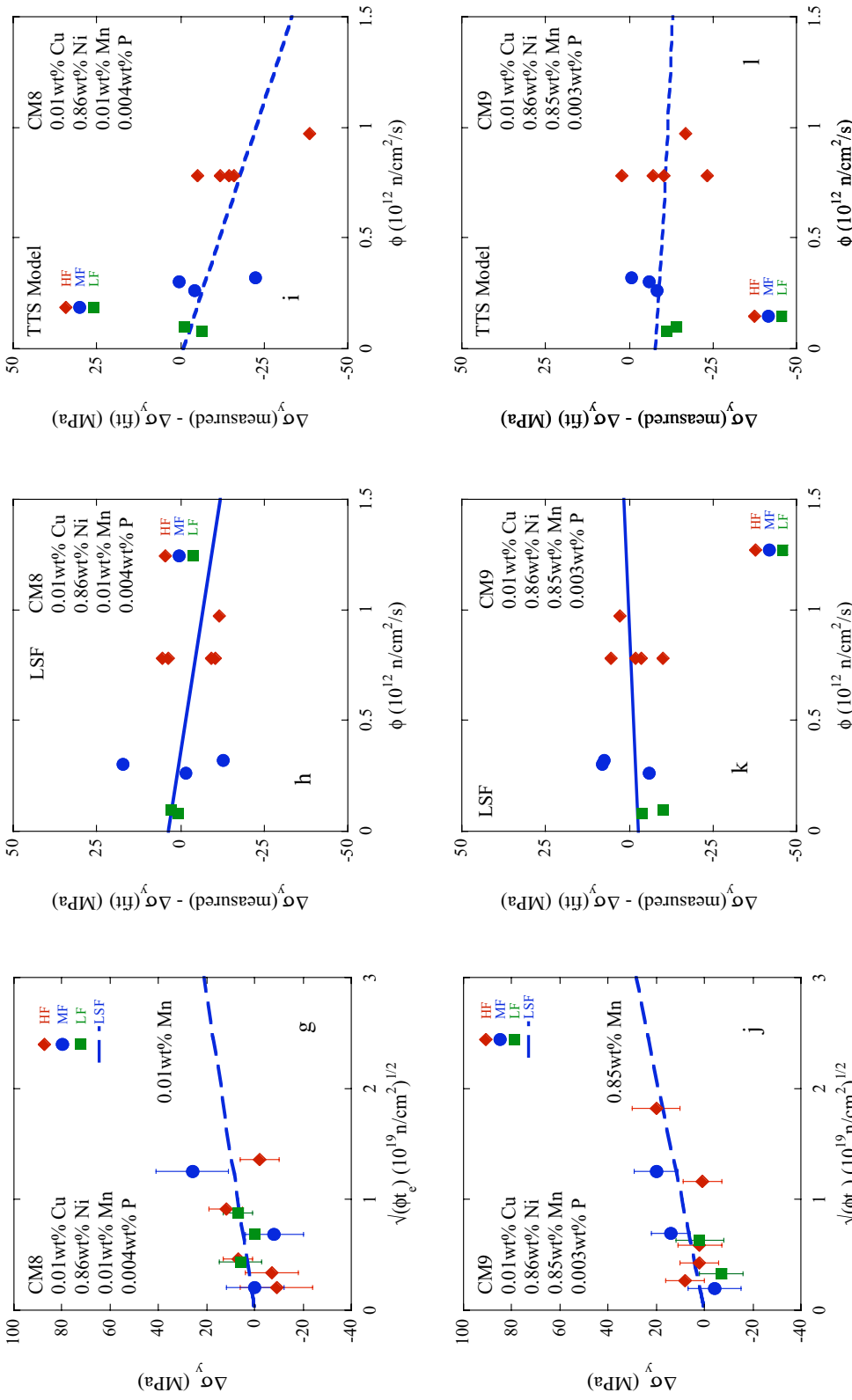

Fig. 6.24 g–l. (g, j) The fitted MF model for the 290°C IVAR $\Delta\sigma_y$ data on two Cu-free SMMS with 0.8 wt % Ni, 0.005 wt % P, and 0.0 and 0.8 wt % Mn on an effective fluence, ϕt_e, scale; (h, k) The corresponding measured minus predicted residuals for the FRM that are reasonably well-centered and only moderately sensitive to flux in the 0.0 wt,% Mn alloy; (i, l) The corresponding residuals for the TTS model, showing a systematic effect of flux.

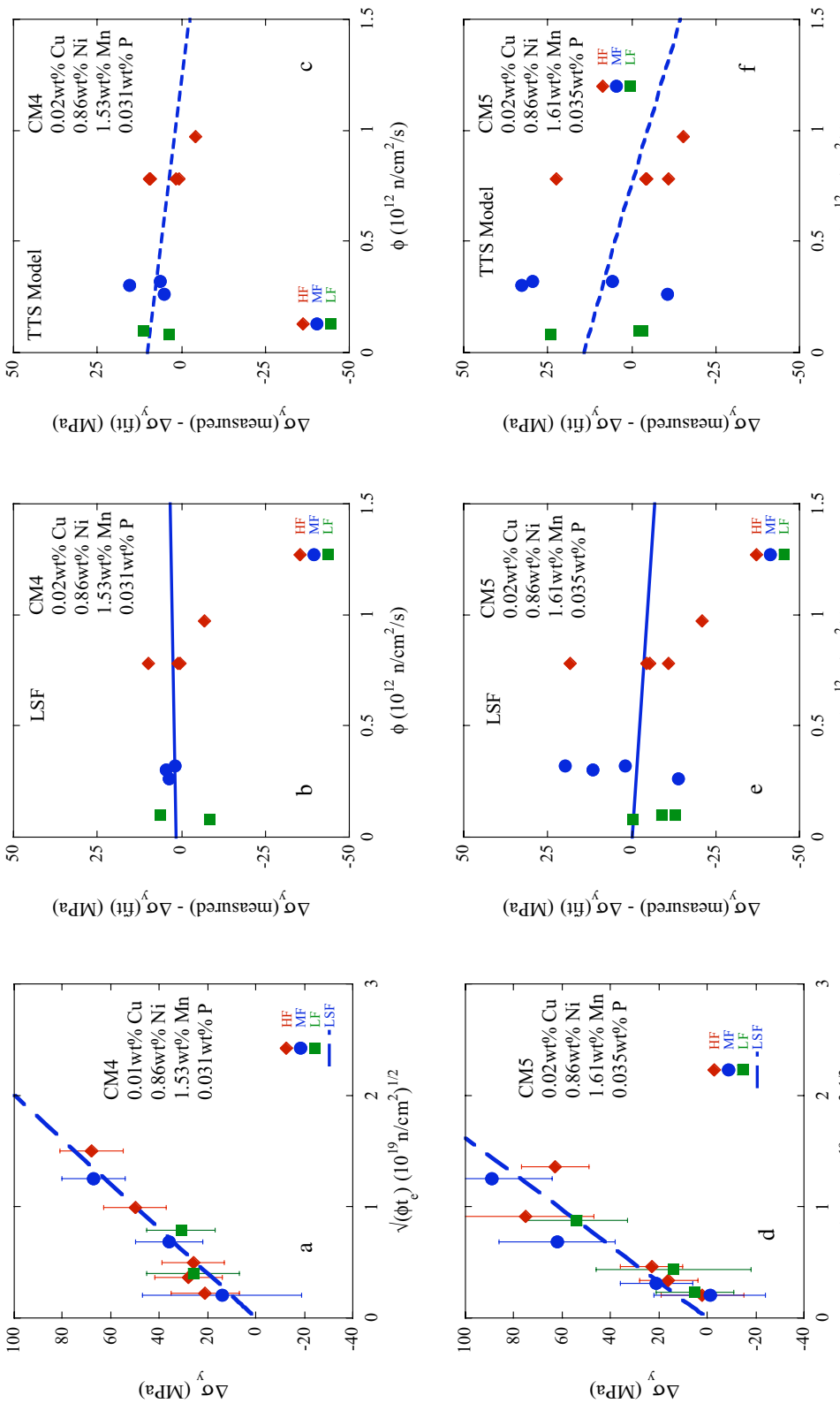

Fig. 6.25 a–f. (a, d) The fitted MF model for the 290°C IVAR $\Delta\sigma_y$ data for two Cu-free SMMS with 0.8 wt % Ni, 1.6 wt % Mn, and 0.031 and 0.35 wt % P on an effective fluence, ϕt_e, scale; (b, e). The corresponding measured minus predicted residuals for the FRM that are reasonably well centered and approximately independent of flux; (c, f) The corresponding residuals for the TTS model, showing a systematic effect of flux.

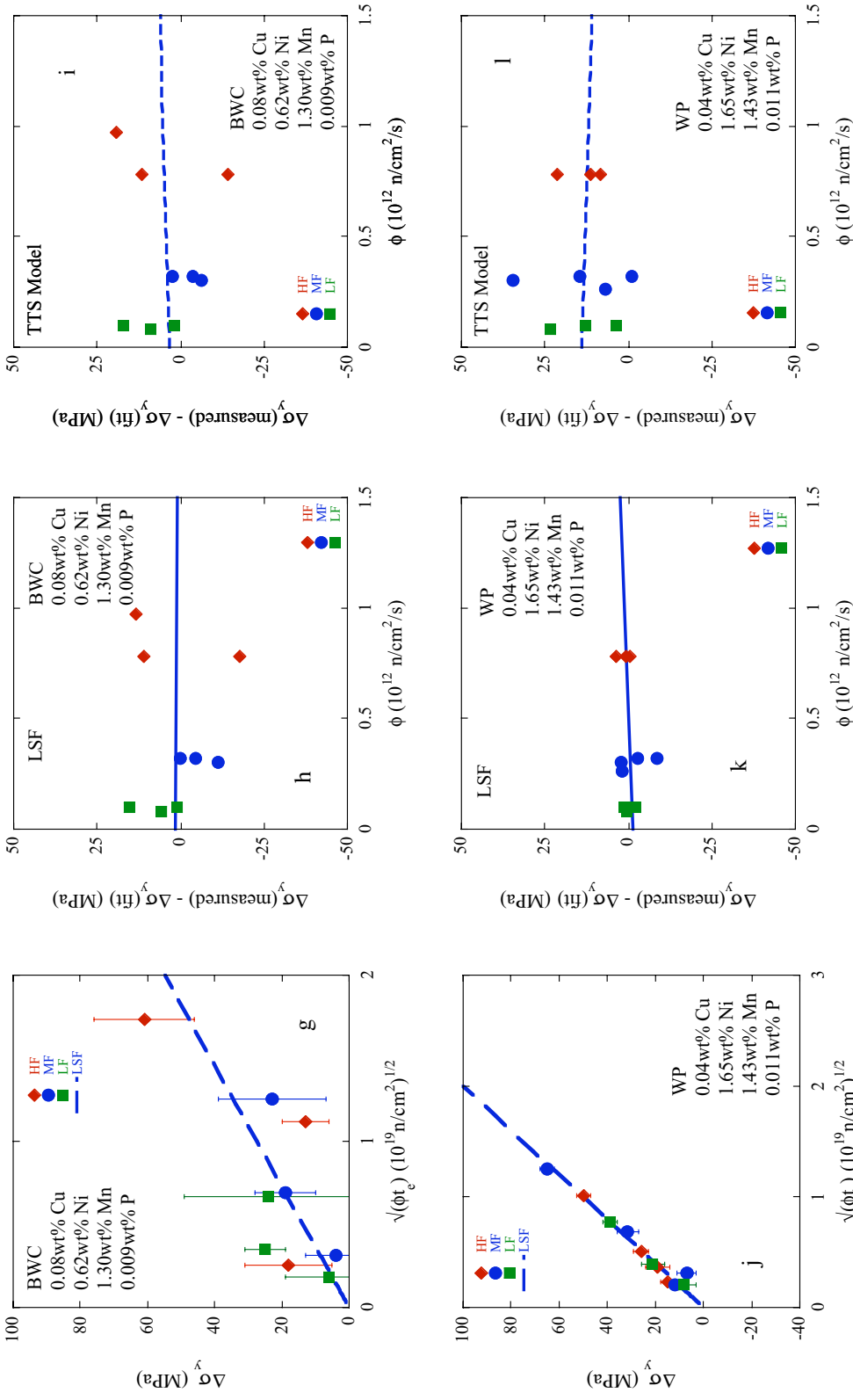

Fig. 6.25 g–l. (g, j) The fitted MF model for the 290°C IVAR $\Delta\sigma_y$ data for two low-Cu welds with 0.8–1.6 wt % Ni on an effective fluence, ϕt_e, scale; (h, k) The corresponding measured minus predicted residuals for the FRM that are reasonably well-centered and approximately independent of flux; (i, l). The corresponding residuals for the TTS model, showing a systematic effect of flux for the high Ni weld.

It is also clear that while the relative effect is fairly large, the absolute magnitude of the influence of flux on the MF hardening is small to modest because of the corresponding low values of $\Delta\sigma_y$. Thus, given the minimal signal-to-noise ratio, a more detailed and quantitative analysis of flux effects on MF hardening has not yet been attempted. However, as discussed in Chap. 2, the effects are likely to be due to long-range solute diffusion. Thus, the physical arguments supporting a flux effect for the CRP contribution also apply to the MF as well.

In summary, weak but systematic flux effects are observed in low Cu IVAR steels. The IVAR results are broadly consistent with the use of a dose-rate-dependent effective fluence in the TTS MF model.

6.7 Effects of Other Variables

The TTS model includes a contribution to embrittlement from P in both the MF and CRP terms. The P effect in the MF term simply adds to the composition independent contributions and depends strongly on the alloy's Mn content. Since the IVAR SMMS with systematic variations on P all contained ≈ 1.6 wt % Mn, the corresponding data cannot be used to directly address the specific issue of how P contributions in low Cu steels vary with Mn. However, as shown in Fig. 6.26, IVAR irradiations of simple model alloys do support an Mn-P interaction. Fe alloyed with 0.0125 wt % N softens by $\Delta\sigma_y \approx -31$ MPa. This softening is probably due to some recovery of quench hardening vacancy-N clusters and, perhaps, annealing of a small amount of surface strain hardening introduced in preparing tensile specimens of this low strength material, as well as data scatter. Adding 0.025 wt % P to Fe results in a $\Delta\sigma_y = 76$ MPa, while the model alloy with 1.6 wt. % Mn and 0.025 wt % P hardens by a $\Delta\sigma_y = 151$ MPa. The corresponding $\Delta\sigma_y$ for the Fe-1.6 wt % Mn model alloy is 46 MPa. Thus, there is clearly an additional contribution from a P-Mn interaction, beyond the individual contributions of P and Mn.

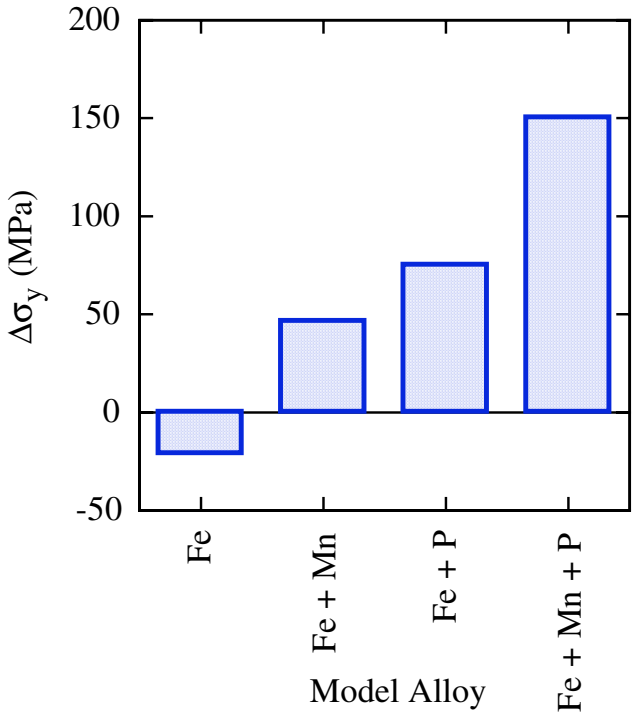

Fig. 6.26. The $\Delta\sigma_y$ for three simple model alloys irradiated in IVAR at high flux and 290°C to 1.77 × 10^{19} n/cm^2, showing a Mn-P interaction leading to higher hardening.

The TTS model also includes a contribution of P to CRP embrittlement. In this case, P in excess of the empirically determined threshold of 0.008 wt %, (note, the solubility of P is much lower than 0.008 wt %) adds to the CRP hardening above the threshold of 0.072 wt % Cu. This TTS model contribution can be viewed as P adding to the hardening by CRPs, or, alternately, by forming separate phosphide precipitates whose flux, fluence, irradiation temperature, and Ni dependence approximately mirror those of the CRPs. However, as noted in Chap. 2, several earlier studies also showed that the effect of P decreases with increasing Cu [11,12].

As shown in Fig. 6.27, P effects, including P-Cu synergisms, are also observed in the IVAR database. Here the average σ_y at the four highest fluence data points for the high and intermediate flux IVAR irradiations at 290°C are plotted against P for both Cu free and 0.1 wt % Cu SMMS. Least square fits yield P hardening chemistry factors, CF_p, which are the slopes of $\Delta\sigma_y$ versus P fits in Fig. 6.27, of 1450 and 666 MPa/wt % P for Cu contents well below (≈ 0.0 wt % Cu) and just above (0.1 wt % Cu) the CRP threshold (0.072 wt. % Cu), respectively. The IVAR CF_p are smaller than the equivalent values found by Jones [11], who also reported that 0.1 wt % Cu reduced CF_p by about 75%, compared to about 55% in the subset of the Jones data shown in Fig. 6.27. Note, other subsets of the IVAR data also suggest a greater reduction in the CF_p at 0.1 wt % Cu than for the high fluence data shown in Fig. 6.27. Analyzing the IVAR results is somewhat complicated by the larger-than-average scatter in the unirradiated yield stress in the steels with higher P. However, the IVAR data, as well as all the test reactor results summarized in Chap. 2, are consistent with a significant effect of P in low-Cu steels that is reduced at higher Cu.

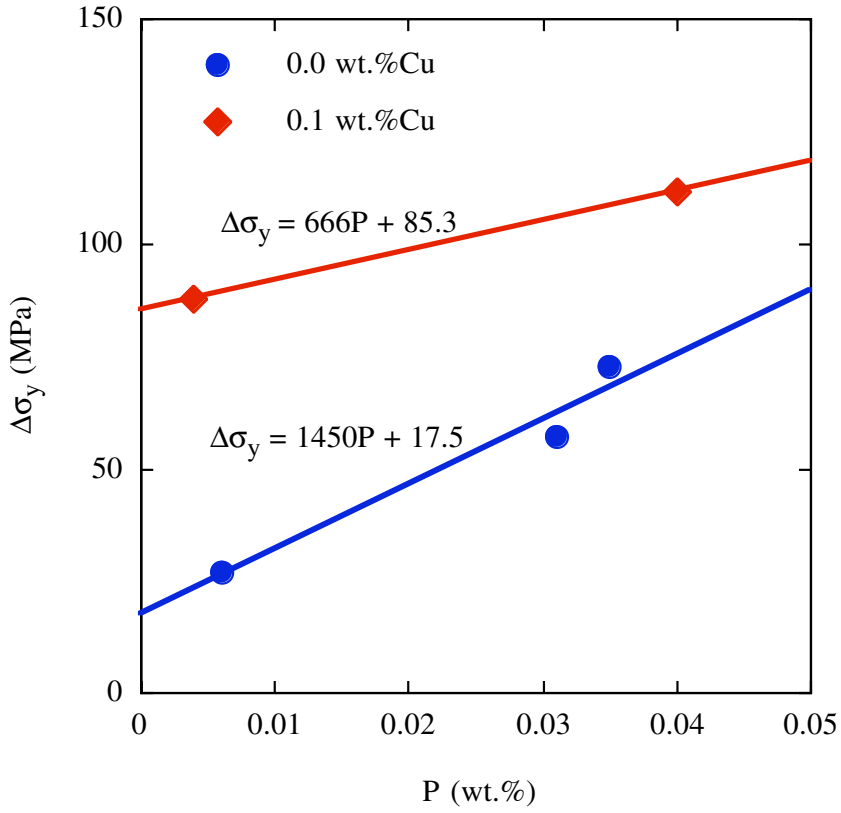

Fig. 6.27. Averaged high fluence σ_y data for IVAR irradiations at intermediate and high flux at 290°C plotted as a function of P for SMMS with 0.8 wt % Ni, 1.6 wt % Mn and 0.0 and 0.1 wt % Cu. The data show a Cu-P synergism leading to decreased hardening due to P at higher Cu, consistent with some previous observations.

It is useful to compare the P chemistry factor (CF_p) estimates from the IVAR data to those predicted by the TTS model. The CF_p estimated from the TTS model depends on the flux, fluence, irradiation temperature, the alloy Cu and Mn contents, as well as the $\Delta\sigma_y$/TTS conversion factor. In the case of low Cu steels, using nominal IVAR parameters of 1.6 wt % Mn, T_i = 290°C, $\phi t = 1.5 \times 10^{19}$ n/cm^2 and $\Delta\sigma_y$/TTS = 1.82 MPa/°C, the TTS model estimate is $CF_p \approx 660$ MPa/% P. This is lower than the value of CF_p for the IVAR Cu free SMMS of 1450 MPa/wt % P. For the ≈ 0.1 wt % Cu, ≈ 0.8 wt % Ni and ≈ 1.6 wt % Mn alloy and a $\Delta\sigma_y$/TTS = 1.65 MPa/°C, the TTS model estimate is $CF_p \approx 1820$ MPa/wt % P, which is higher than the corresponding IVAR CF_p estimate of 666 MPa/wt % P. Using the approximate average compositions of Cu-bearing surveillance database plates of ≈ 0.14 wt % Cu, ≈ 0.6 wt % Ni and ≈ 1.3 wt % Mn, the TTS model estimate is $CF_p \approx 1050$ MPa/wt % P. The TTS model estimate of CF_p decreases further at higher Cu; for example 0.25 wt % Cu, the TTS estimate is $CF_p \approx 880$ MPa/wt % P. These values compare reasonably with the estimated value $CF_p \approx 1060$ MPa/wt % P found by averaging the slopes for the IVAR data shown in Fig. 6.27.

In summary, both the IVAR data and information in the literature support a significant contribution of P to $\Delta\sigma_y$, especially in low Cu steels. Both theoretical considerations and IVAR model alloy data discussed in Chap. 2 are also consistent with a strong P-Mn interaction. Previous results in the literature, as well as the IVAR SMMS data, also indicate a significant P-Cu synergism, leading to a smaller P effect at higher Cu levels. The TTS model predicts that the effect of P is larger just above the CRP threshold of 0.072 wt % Cu. However the effect of P in the TTS model decreases with further increases in Cu beyond this threshold. Overall the effects of P predicted by the TTS model fall either somewhat on the low side (low Cu) or within the expected range (for > 0.072 wt % Cu) found in other evaluations. The average contribution of P to hardening derived from the IVAR data and predicted by the TTS model are generally similar.

6.8 Conclusions

1. With the exception of the systematic effect of flux observed in the range of the IVAR database, the overall agreement between the TTS model predictions and the IVAR $\Delta\sigma_y$ is reasonably good for the weld and plate alloys most like those in the TTS database.

2. The predictions of the TTS CRP model are also in remarkably good agreement with the IVAR $\Delta\sigma_y$ data for Cu-bearing (≥ 0.072 wt % Cu) SMMS. However, the systematic dose rate effects observed in the SMMS $\Delta\sigma_y$ data in the range of IVAR fluxes, are not explicitly captured by the TTS model. The effect of Mn observed in the IVAR database is reflected in product coefficients, rather than being treated directly.

3. While the absolute values are much smaller than the corresponding effects in the Cu-bearing alloys, the systematic effect of flux observed in the range of the IVAR database for the low-Cu IVAR $\Delta\sigma_y$ data are also not captured in the TTS MF model.

4. As noted above, the IVAR database indicates a systematic flux effect in the range of ≈ 0.8 to 8×10^{11} n/cm^2-s, which is not predicted by the TTS model, which finds a flux effect that begins below 4.4×10^{10} n/cm^2-s. However, the predicted dose rate effects at lower fluxes are generally similar in both models. This observation suggests that detecting flux effects in the TTS surveillance database is difficult except over the widest range of dose rates. The IVAR results suggest that flux effects continue above 4.4×10^{10} n/cm^2-s, where the fitted TTS model flattens. Use of a constant average p flux scaling approximation in the TTS model is generally supported by the analysis in this chapter as well as in Chap. 2. With the exception of the flux effect noted above, the predictions of the TTS MF model are in reasonably good agreement with the IVAR data, especially for alloys with compositions comparable to the preponderance of the low-Cu TTS plate database (like CM10 and BWC). However, a simple direct comparison shows that the TTS model tends to over predict the $\Delta\sigma_y$ in Cu-free medium-Ni, low-P SMMS. The differences are probably due to (a) the fact that the IVAR SMMS are, on average, cleaner than the alloys in the TTS

surveillance database; and, (b) unaccounted for flux effects, that occur in the TTS database at fluxes below the IVAR range.

5. The TTS MF model does not reflect the significant effects of the wider range of Ni that are observed in the SMMS and $\Delta\sigma_y$ data, or explicitly treat the effects of Mn. The effects of P are discussed below.

6. The IVAR database shows that both MF and CRP hardening contributions decrease with increasing irradiation temperature. The absolute irradiation temperature dependence predicted by the TTS model is generally stronger than observed in the low-Cu SMMS and weaker than observed in Cu-bearing SMMS. However, the agreement is reasonably good for the welds and plates that are most similar to steels in the TTS surveillance database. The IVAR data shows that the CRP contribution to $\Delta\sigma_y$ decreases with increasing irradiation temperature, while the TTS model predicts a weak, but opposite effect.

7. The TTS model, IVAR data and information in the literature all support a significant contribution of P to $\Delta\sigma_y$. Both theoretical considerations and IVAR model alloy data are also consistent with a strong P-Mn interaction that is found in the TTS MF model. Previous results in the literature, as well as the IVAR SMMS data, also indicate a significant P-Cu synergism, leading to a smaller P effect at higher Cu levels. In contrast, the TTS model predicts that the effect of P is larger above the CRP threshold of 0.072 wt % Cu and 0.008 wt % P. However the effect of P in the TTS model decreases with increasing Cu beyond this threshold. Overall the effects of P predicted by the TTS model fall either on the low side (low Cu) or within the expected range (for > 0.072 wt % Cu) found in other evaluations.

6.9 References

1. Wirth, B. D., On the Character of Nano-Scale Features in Reactor Pressure Vessel Steels Under Neutron Irradiation, Ph.D. Thesis, the University of California, Santa Barbara (1998).
2. Odette, G. R. and Cowan, C., *Use of Combined Electrical Resistivity and Seebeck Coefficient Measurements to Characterize Solute Redistribution Under Irradiation and Thermal Aging*, Proceedings of the 10th International Symposium on Environmental Degradation of Materials in Light Water Reactors, ed. G. S. Was et. al., NACE CD (2001).
3. Heatherly, D. W., Hurst, M. T., Thoms, K. R., Lucas, G. E., Odette, G. R. and Simpson, P. A., *A New Versatile Materials Irradiation Facility*, Trans 14th Int Conf on Structural Mechanics in Reactor Technology 4G, SMIRT 341.
4. Remec, I., Baldwin, C. A. and Blakeman, E. D., Characterization of the Neutron Field in the HSSI/UCSB Irradiation Facility at the Ford Nuclear Reactor, NUREG/CR-6646 (U.S. Nuclear Regulatory Commission, Washington, DC, 1999).
5. Heatherly, D. W., K. R. Thoms, M. T. Hurst, and G. E. Giles, *Heavy-Section Steel Irradiation Program's Reusable Irradiation Facilities*, ORNL/TM-2002/77, Oak Ridge National Laboratory, Oak Ridge, Tennessee, 2004.
6. Odette, G. R., et al., *The Effects of Composition and Heat Treatment on Hardening and Embrittlement of Reactor Pressure Vessel Steels*, NUREG/CR-6778 (U.S. Nuclear Regulatory Commission, Washington, DC, 2003).
7. Odette, G. R., Lombrozo, P. M. and Wullaert, R. A., *Relationship Between Irradiation Hardening and Embrittlement of Pressure Vessel Steels*, pp. 840–62 in Effects of Radiation on Materials: 12th International Symposium, ASTM STP 870, ed. F.A. Garner et al. (American Society for Testing and Materials, West Conshohocken, Pa., 1985).

8. English, C. A., Server, W. L. and Rosinski, S. T., *Critical Review of Through-Wall Attenuation of Mechanical Properties in RPV Steels*, pp. 221-243 Effects of Radiation on Materials: 21th International Symposium, ASTM STP 1447, ed. M. L Grossbeck et al. (American Society for Testing and Materials, West Conshohocken, Pa., 2004).

9. Odette, G., Yamamoto, R., T. and Klingensmith, R. D., *On the Effect Of Dose Rate on Irradiation Hardening of RPV Steels*, Philosophical Magazine 85, 779 (2005).

10. Williams, T. and Ellis, D., *A mechanistically-Based Model of Irradiation Damage in Low Alloy Steel Submerged Arc Welds*, pp. 8-27 in Effects of Radiation on Materials: 20th International Symposium, ASTM STP 1405, ed. S. T. Rosinski et al. (American Society for Testing and Materials, West Conshohocken, Pa., 2001).

11. Jones, R. B. and Buswell, J. T., *The Interactive Roles of Phosphorus, Tin, and Copper in the Irradiation Embrittlement of PWR Pressure Vessel Steels*, p. 111 in Environmental Degradation of Materials in Nuclear Power Systems—Water Reactors, Proceedings of the 3rd International Symposium, ed. G.T. Theus et al. (Metallurgical Society, Warrendale, Pa., 1988).

12. Hawthorne, J. R., Exploratory Studies of Element Interactions and Composition Dependences in Radiation Sensitivity Development, NUREG/CR-4437 (U.S. Nuclear Regulatory Commission, Washington, DC, 1985).

Appendix A

7. Discussion and TTS Model Simplification

The summary of current mechanistic understanding in Chap. 2 and the detailed comparison of the baseline model and IVAR data in Chap. 6 were completed after the development and analysis of the baseline model presented in Chaps. 3, 4, and 5. Two sensitivity studies were then conducted, which motivated minor changes to Eqs. (4-5a) and (4-5d) of the baseline model, as discussed in this chapter. These changes both simplify the baseline model and bring it into better agreement with the current mechanistic understanding and other data presented in Chaps. 2 and 6. The changes also address the two aspects of the baseline model that have the least statistical support from the surveillance database, the T_i term and Cu_{max} values in the CRP part of the model.

This chapter has two main purposes, to discuss the results of the sensitivity studies and to present a simplified model that implements the recommendations from those studies. All related information needed to properly apply the simplified model (e.g., the definitions of variables, units, revised standard deviation values for material groups) are also collected in Sect. 7.3 for ready reference.

7.1 Discussion of the Irradiation Temperature Term in the CRP Part of the Baseline Model

7.1.1 Background

During the development of the embrittlement shift model, it was assumed that there could be some effect of irradiation temperature, T_i, on both MF and CRP features based on prior theory and on observations discussed in Sect. 2.3.4. The effect of T_i in the MF term has been studied by many authors; it is known to be a strong effect, and the accepted linear form presented by Jones and Williams [1] was used in the shift model. The best fitting form for the T_i effect in the CRP part of the model has been studied much less, but a linear form appears to work, as given by Eq. (2-34).

Past experience with TTS models calibrated to the surveillance database suggested that the CRP T_i term might turn out to be small relative to the stronger T_i effect in the MF term, which applies to all materials. Consequently, the fitting form that was chosen for modeling the CRP T_i effect was designed to allow removal of the term without recalibration. In particular, the effect was expressed as a multiplicative term in the CRP part that is a power law in the ratio of actual irradiation temperature, T_i, to the average irradiation temperature of the high-Cu calibration set (T_{avg} = 543.1°F); i.e.,

$$CRP\ T_i\ term = \left[\frac{T_i}{T_{avg}}\right]^n \tag{7-1}$$

This term is capable of representing linear or nonlinear effects with either increasing or decreasing shifts as temperature increases, depending on the value and sign of the exponent. It should be considered an empirical "fix-up" term, adjusting the stronger MF T_i term (which was calibrated to low-Cu data) as needed to better fit the high-Cu surveillance data. No claim is made that the CRP T_i term is an optimal fitting function for the surveillance data, but it is reasonably flexible and should be adequate for modeling a relatively small effect.

When the value of the CRP temperature term is unity, which will happen if the exponent, n, calibrates (or is set equal) to zero, the term has no effect on the calculated shift. For any exponent, if the T_i term is removed from the model by setting the term equal to 1, the result would be an unbiased estimate overall, giving the same results as if the average irradiation temperature of the high-Cu calibration set were used for all CRP calculations at any T_i.

The calibrated shift model confirmed the assumption that the CRP T_i term might be a small contribution, as the calibrated exponent turned out to be 1.10. Thus, the CRP contribution from the T_i term is only –4.3% to +5.5% of the CRP term value at average temperature, over the entire range of temperatures (522–570°F) in the surveillance database. Since the CRP term is just part of the estimate of total shift, the contribution of the CRP T_i term to total shift is always less than ±5%. Moreover, the direction of the calibrated CRP term is to increase the CRP contribution to shift as irradiation temperature increases, which is opposite to the direction of the MF term temperature effect, indicating that the high-Cu surveillance data have a slightly flatter temperature trend than the low-Cu surveillance data, as shown in Fig. 5.16 (the difference in slope is hard to see). The effect of the CRP T_i term in the shift model is typically much smaller than the MF T_i term, so the slope of the overall irradiation temperature trend is in the same direction for both low- and high-Cu surveillance materials, tending to decrease the shift as T_i increases.

The IVAR data and other data show a different trend, in which the higher Cu materials have a steeper temperature trend than the low-Cu materials, again with increasing irradiation temperature tending to decrease the hardening in both low- and high-Cu materials. Figures 6.14(a) and 6.14(b) show this trend, for example. Thus, the incremental CRP contribution from T_i in controlled IVAR experiments is opposite in direction to the incremental CRP contribution from T_i in surveillance materials. The overall temperature trend (combining both MF and CRP trends) is in the same direction and reasonably consistent between the IVAR data and surveillance data for materials with similar compositions, as shown in Fig. 6.4.

Because of the relatively small calibrated CRP T_i effect and the questionable statistical significance (discussed in the next section), and because the effect of the calibrated CRP term is to flatten the overall temperature trend slope for high-Cu data rather than steepen it as shown in data from controlled experiments, a question was raised as to what the effect would be of removing the CRP T_i term. That effect is analyzed in the next section as a sensitivity study, in which the only change from the baseline model was to remove the CRP T_i term.

7.1.2 Sensitivity Study on the CRP T_i Term

The irradiation temperature term from the CRP part of the TTS model was effectively removed from the model by temporarily setting its exponent $n = 0$ in Eq. 7-1, which causes the value of the CRP temperature term to be unity for all temperatures. The effect of removing the temperature term was analyzed using all high-Cu calibration and validation data. This was done for direct comparison with the analysis done earlier for the baseline model in Chap. 4, which includes the temperature term in the CRP part. The analysis of the baseline model had shown a reasonably flat, nonsignificant residual trend with temperature in the high-Cu data, as shown in Fig. C.16.

After removing the temperature term from the CRP part of the model, there appears to be a small residual trend, as shown by the fitted linear residual trend line in Fig. 7.1. However, considering all high-Cu calibration and validation data, the slope of this linear residual trend is not significantly less than zero. Deleting the CRP temperature term affects all high-Cu points to some extent, but the effect is predictably greatest at the high and low temperatures furthest from the average temperature. Thus, the planned approach for this sensitivity study was to examine the effect of removing the CRP temperature term on the residuals of points that are at least some ΔT_i interval above and below the average temperature. This approach can provide insight into whether removing the term would cause previously nonsignificant trends in variables other than T_i to become significant. It also can determine whether there might be a trend in the T_i residuals that is nonlinear. Such a trend would not necessarily be detected in the significance test on the slope of the CRP T_i term because that test assumes a linear trend in the temperature residuals.

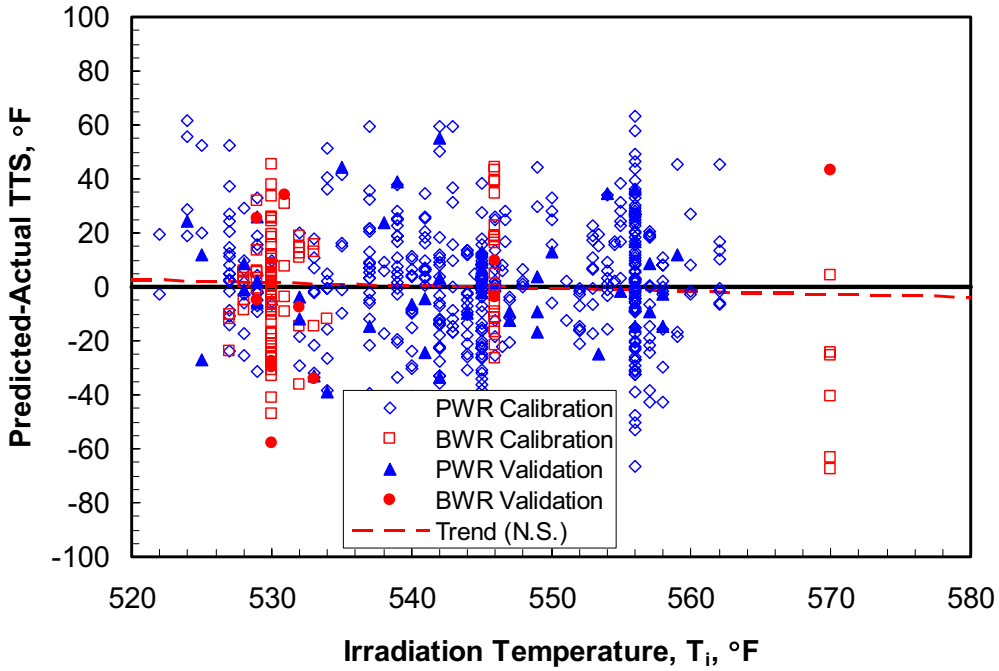

Fig. 7.1. Residual trend with temperature for high-Cu data, modified model without CRP T_i term, showing apparent residual effect (slope is not significant).

The particular limiting values initially chosen for analysis, ±10°, ±15°, and ±20°F from the average value of T_i for high-Cu calibration data, were arbitrarily chosen to explore the competing issues of (a) being far enough from average temperature to show effects of deleting the term, if there are any, vs (b) having enough points to check significance using t-tests. If one does not go far enough out from the average temperature, a small effect should be expected to be nonsignificant, which is what is observed for the 312 points that are at least ±10° F from the average temperature. If one goes too far from average temperature, there are not enough points for a credible significance analysis, which is what is observed for the nine points that are at least ±20°F from the average temperature. The ±15° F analysis is a reasonable compromise that spreads the high- and low-temperature sets adequately and retains 83 points in the analysis (about 14% of the high-Cu data).

The CRP T_i term was removed, producing a modified model, and residuals relative to the modified model were calculated for each point. The results of t-tests for points at least ±15° F from the average temperature are shown in Table 7.1. Two types of significance tests are summarized in Table 7.1. The first test determines whether the average residual at low temperatures is significantly greater than the average residual at high temperatures. If this difference in residuals at low and high temperatures is statistically significant, that is evidence that there may be a real T_i trend in the high-Cu surveillance data, and as stated that trend would be in the same direction as the baseline CRP T_i term. The second test determines whether the average residual at low temperature is significantly greater than zero, and whether the average residual at high temperature is significantly less than zero. These tests determine if the average deviation from the model at low and high temperatures is large relative to the scatter. It is possible for a significant trend to exist when comparing the low- and high-temperature data, whether or not the average residuals are individually far enough from zero to be significant.

As shown in Table 7.1, the average residual of the low-temperature set is significantly greater than the average residual of the high temperature set. The significant difference is in the direction that suggests that the baseline CRP temperature trend may be real. That is, an effect that increases the incremental CRP

contribution to shift as temperature increases would reduce both the under-prediction of high temperature points and the over-prediction of low-temperature points, thus counteracting the residual pattern that is observed after removing the CRP T_i term. The average residuals at least 15°F above and below the average temperature are a factor of 2 different in absolute value (8.1 vs 3.7), an indication of nonlinearity. The fact that the low-temperature residual is significantly different from zero but the high temperature residual is not is another indication of nonlinearity. Thus, it appears that the residual trend from deleting the CRP T_i term, which was not significant over the full range of T_i when assumed to be linear, is statistically significant in the high and low-temperature data analyzed for Table 7.1. The significant difference in residuals and the significant average residual in the low-temperature data are visible in Fig. 7.1, where the points with Ti ≤ 528°F do appear to be high relative to the zero residual line, and some points with $T_i \geq 558$°F (especially at $T_i = 570$°F) do appear to be low.

Table 7.1. Residual analysis of the points that are at least 15°F above and below average temperature, modified model without CRP T_i term

	Data with $T_i \leq 528$°F	Data with $T_i \geq 558$°F
Average residual	8.1 °F	–3.7 °F
Sd of residuals	20.9 °F	25.8 °F
Number of points	48	35
Significant difference in average residual at high and low T_i	Yes, 8.1 > –3.7	Yes, 8.1 > –3.7
Significant average residual?	Yes, average residual 8.1 > 0	No, average residual -3.7 ~ 0

The fact that significant residual differences exist in the low- and high-T_i data does not prove that a missing T_i term is the cause. What it does suggest is that there are some apparently real differences in the average residuals of those subsets of data, which may be due to unmodeled temperature effects or other causes. The fact that the high-Cu data show a flatter T_i trend than the low-Cu data in the collected surveillance data while the reverse is true in the controlled experiments is a strong indication that this particular residual trend may be due to causes other than an unmodeled T_i trend.

The CRP T_i term that is in the baseline model reduces the apparent temperature residual trend, but not by much, as can be shown using the same low- and high-temperature data and the same analysis as in Table 7.1. The absolute values of the average residuals at high and low temperature are each reduced by less than 2°F by incorporating the baseline T_i term, which is not enough to be a significant reduction. The low-temperature average residual is still significantly greater than zero with or without the baseline T_i term. Thus, by either the linear residual analysis or the analysis of low- and high-temperature subsets presented here, the baseline CRP T_i term is not a significant improvement over having no CRP T_i term at all.

7.1.3 Detailed Review of Low-T_i and High-T_i Surveillance Data

The points in the low- and high-temperature datasets from Table 7.1 were examined in some detail, looking for data-related anomalies that could explain the apparent T_i trend in the surveillance data. In the high temperature subset, with $T_i \geq 558$°F, the points at 570°F appear to be unusual, as shown by Fig. 7.1. These points are all from the Big Rock Point reactor, an early 67 MW BWR demonstration plant that was not typical of later BWR designs and that has now been decommissioned. The Big Rock Point data are the main cause of the negative average residual at $T_i \geq 558$°F, as can be seen from the fact that the 7 Big Rock Point datapoints have an average residual of -25°F, while the average residual of the 28 other points with $T_i \geq 558$°F is 1.6°F, not significantly different from zero. Because of the small amount of Big Rock Point data and its relatively large scatter, the difference between the mean residuals of Big Rock Point and the other $T_i \geq 558$°F data is not statistically significant in a t-test. No other plant, BWR or PWR, has

estimated surveillance capsule temperature close to 570°F, as is clear in Fig. 7.1. The Big Rock Point temperature is far above mean temperature, so those points have more influence on the slope of the T_i term (more "leverage") than points nearer the mean temperature. Thus, there appear to be ample reasons, based on the unusual plant, the unusually large residual, and the T_i value that is unusually higher than the mean temperature, to consider the data at 570°F to be possibly atypical and to consider the effect of excluding those seven points from T_i term considerations. The underlying hypothesis that the Big Rock Point data may be different cannot be proven with the small sample of data, so this must be considered an exercise in exploring the implications of a hypothesis.

If the Big Rock Point data were excluded from consideration, the residual difference from low to high temperature groups with no CRP T_i term would be reduced from 11.8 = 8.1 - (-3.7) to 6.5 = 8.1 - 1.6. The reduced difference (6.5°F) between average residuals at low and high T_i is not statistically significant. Thus, the exclusion of 7 datapoints from one atypical plant would change the statistical situation from an apparently real but nonlinear trend to no significant trend on either a linear or nonlinear (grouped data) basis.

There is no single plant in the low-temperature data group that has as much effect on significance as Big Rock Point does, but there is a possibly relevant pattern. The average residual in the $T_i \leq 528$°F data is based on 9 BWR observations and 39 PWR observations. The significant positive average residual in the low-temperature group (8.1°F in Table 7.1) is caused by the PWR data, as can be seen from the fact that the average BWR residual in the $T_i \leq 528$°F range is -4.7°F, which is not significantly different from zero (on 9 points), while the average PWR residual in the $T_i \leq 528$°F range is +11.0°F, which is significantly greater than zero. Note that $T_i \leq 528$°F is an unusually low irradiation temperature range for PWRs, most of which have reported surveillance temperatures in the range 540 – 560°F. Some of these unusually low PWR temperatures were reviewed by a working group of ASTM E10.02 subcommittee members in the 2004 data review, as indicated by comments in the appropriate cells of the database. But if some of these values are underestimates of the actual irradiation temperatures at the capsule locations, the shifts would be over-estimated, consistent with the positive average residual that is observed. This possibility of underestimated T_i in the PWR data has not been resolved and would affect any future modeling activity.

7.1.4 Conclusions and Recommendations from the CRP T_i Term Sensitivity Study

Removing the CRP temperature term from the TTS model contributes to an overall residual trend that is visible as shown in Fig. 7.1. Under a linear regression assumption, that residual trend is not significant, but analysis of the average residuals for the data furthest from (≥ 15°F above and below) the average temperature show a significant difference, and for $T_i \leq 528$°F the average residual is significantly greater than zero. The average residuals of the surveillance data at high and low T_i are consistent with the direction of the trend in the baseline model, in which the high-Cu surveillance data show a flatter T_i trend than the low-Cu data, and the significance results suggest this trend may be real, though the baseline CRP T_i term does not adequately reflect the nonlinearity or strength of the trend. However, finding a significant difference between sets of data at low and high temperature does not prove that temperature causes the difference.

Data from controlled experiments show that high-Cu data have a steeper T_i trend slope than low-Cu data, just opposite to the surveillance data. The IVAR temperature effect data are believed to be more reliable because they come from controlled experiments in which T_i was deliberately varied for the same material and the irradiation temperatures were measured. By comparison, the different temperatures in the surveillance data also correspond to different heats and plants, possibly confounding the effects of multiple variables, and all of the surveillance T_i values are estimates from coolant temperature. Thus, the IVAR results are the better indication of the actual T_i trend, strongly suggesting that the surveillance data pattern may be due to other factors.

Possible data issues have been identified that could explain the apparent trend in surveillance data, including unusual data from an unusual decommissioned plant (Big Rock Point) at the highest T_i value in the database. Without the data from this one plant, the difference in average residuals at low and high T_i in the surveillance data would become nonsignificant, though the average residual at low T_i would still be significant. The positive average residual in the low-T_i group is due to PWR data with unusually low T_i values compared to typical PWR plants. Some of these temperature data have been recently reviewed, but additional checking may be warranted, since an underestimate of the actual T_i values at the surveillance capsule in these PWR plants could explain the significant positive average residual. The possible contributions from these specific data issues must be regarded as unproven hypotheses.

A simplified model is recommended, in which the CRP T_i term is removed from the baseline model by setting it to 1 for all T_i. The decision to present a simplified model is justified on the basis of the small, nonsignificant contribution of the baseline CRP T_i term to shift estimates and the contrary direction of the baseline CRP T_i term relative to controlled experiments. The fact that a statistically significant pattern exists in the surveillance data that suggests the need for a stronger, more nonlinear CRP T_i term in the same direction as the baseline term was considered in forming this recommendation. That data pattern is not believed to be caused by a temperature effect, based on the contrary evidence from controlled experiments and the unusual nature of the particular datapoints responsible for the surveillance data pattern.

The baseline CRP T_i term has little effect, so there is no motivation to revise all the results showing the baseline model in earlier chapters. Instead, the effects of the CRP T_i term deletion and the recommended change to Cu_{max} values discussed in Sect. 7.2 are analyzed together in Sect. 7.3, where a simplified model incorporating both changes is presented. Deleting the CRP T_i term from the simplified model will slightly improve the agreement between the surveillance model and the IVAR data by slightly steepening the slopes of the TTS model plotted on Figs. 6.4, 6.14(a), and 6.14(b). The difference would be difficult to see, just as the change to exactly parallel lines (the result after deleting the CRP T_i term) would be difficult to see in Fig. 5.16.

7.2 Discussion of the Maximum Cu_e Values for Material Groups

7.2.1 Background

The baseline model includes calibrated maximum Cu values at which the Cu effect in the CRP term of the model saturates, referred to here as Cu_{max} values. The values were calibrated originally in both Ni and weld flux categories, based on the understanding that the Ni level and heat treatment control the Cu saturation values (see Sect. 2.3.2) plus successful experience using weld flux categories in previous models. The Cu_{max} values and categories were considered both based on Ni ranges and weld categories, with the latter approach being used in Eq. (4-5d) of the baseline model. The reasons why a Ni-based approach did not work on the surveillance data are discussed in Sects. 7.2.2 and 7.2.3.

The three categories in Eq. (4-5d) of the baseline model are typical Linde 80 welds (those with nominal Ni > 0.5 wt %), Linde 1092 welds, and all other materials. These categories apply to the CRP term, so they are only relevant to materials with higher Cu (Cu > 0.072 wt %). There are many materials in each of the three categories with Cu > 0.072 wt %, but most do not have high enough Cu to be affected by a saturation limit. The lowest calibrated saturation limit is 0.243 (typical Linde 80 category) so all materials with Cu < 0.243 wt % are unaffected by any of the calibrated Cu limits because the limit is never reached. Materials with Cu levels below-Cu_{max} show only an increasing shift as Cu increases, with no limit behavior at all. Thus, for calibrating Cu_{max} values, only the data with Cu > 0.243 wt % are potentially usable.

After calibrating the baseline model, it became apparent that more discussion is needed on the basis and description of the Cu_{max} categories. The value of Cu_{max} depends on Ni, and for medium Ni materials

$Cu_{max} \cong 0.25$ wt % while for higher Ni materials, Cu_{max} is higher, up to a solubility limit of about 0.3 wt % Cu, as described in Sect. 2.3.2. The value of Cu_{max} in the surveillance database for low-Ni materials is contrary to this expectation, with a calibrated value ($Cu_{max} = 0.37$ wt %) that exceeds both the solubility limit and the values of Cu_{max} calibrated for the higher Ni materials. The Linde 1092 welds generally have higher Ni than the typical Linde 80 welds, so a higher calibrated value of Cu_{max} is expected (and observed) for the Linde 1092 welds. But closer examination reveals that the higher calibrated value of Cu_{max} is based on a small set of Linde 1092 welds with Ni values that substantially overlap the Ni range of the Linde 80 welds, thus casting doubt on Ni as the reason for the difference. It appears that the surveillance data are simply inadequate to confirm or calibrate the expected Ni effect on Cu_{max}, because of data limitations. The next section shows these limitations by a detailed examination of the surveillance data available for confirmation or calibration of the Cu_{max} values.

7.2.2 Analysis of Surveillance Data Usable for Calibrating the Cu_{max} Values

Table 7.2 shows the total number of Cu > 0.072 wt % materials in each of the baseline Cu_{max} categories and provides additional details on the materials with Cu > 0.243 that are potentially usable for calibrating the Cu_{max} values. The baseline categories correspond roughly to the Ni ranges shown in parentheses, though all the Linde 1092 welds have been included in the high Ni category even though a few have medium Ni. The "all other" category only contains low-Ni materials in Table 7.2, so it will also be referred to as the "low-Ni" category in the following discussion.

Some of the difficulties in estimating Cu_{max} limits from the surveillance data are readily apparent in Table 7.2. There are only 6 different weld chemistries available for low-Ni materials that have a high enough Cu level (Cu > 0.243) to possibly help establish a Cu_{max} value, despite the fact that there are 52 heats in the "all other" category with Cu > 0.072 and Ni ≤ 0.5. Only two of those 6 welds have Cu values at and above the calibrated limit of $Cu_{max} = 0.37$ wt %, thus, the calibrated value for the category is effectively determined by only two welds from different vessel manufacturers, a clearly inadequate sample. Similarly, there are many Linde 1092 welds, spanning the Ni range from 0.6 to 1.26 wt %, but only 6 different chemistries are available in the Linde 1092 welds with Cu > 0.243 wt %, and only 3 of those welds have Cu values at and above the calibrated limit of $Cu_{max} = 0.301$ wt %. There are no high Ni (Ni ≥ 0.75 wt %) materials other than Linde 1092 welds that have a high enough Cu value (Cu > 0.243 wt %) to affect the value of Cu_{max} for any category. Clearly, the samples available for calibrating two of the Cu_{max} values are very small, both for the low-Ni data (two welds) and the Linde 1092 group (three welds).

Looking in more detail at Linde 1092 welds, despite the generally higher Ni level of most Linde 1092 welds (0.6 ≤ Ni ≤ 1.26 wt %) compared to typical Linde 80 welds (0.52 ≤ Ni ≤ 0.73 wt %), there are only 2 of the 6 Linde 1092 welds with Cu > 0.243 that have Ni values higher than the Linde 80 welds, and one of those has Cu = 0.270 so it does not affect the calibrated $Cu_{max} = 0.301$ for Linde 1092 welds. Thus, there is almost total overlap in Ni range of the typical Linde 80 points and the Linde 1092 points that are actually relevant to the calibrated Cu_{max}. That overlap and the significant difference between Linde 80 and Linde 1092 calibrated Cu_{max} values are the reasons why pure Ni categories were not used in the baseline model.

The quantity of usable data is much larger for typical Linde 80 welds than for any other category. "Typical Linde 80" implies the usual high-Cu, medium Ni Linde 80 welds, which nominally have Ni > 0.5 wt %, as opposed to a low-Ni Linde 80 weld in the database with Ni = 0.1 wt % and a few Linde 80 welds with Cu < 0.07 wt %. There are 25 different heat chemistries in the medium Ni/typical Linde 80 category that are at and above the calibrated limit for that category ($Cu_{max} = 0.243$ wt %). 21 of the 25 are identified specifically as Linde 80 welds and 3 more are B&W welds that may be Linde 80 (the plant records should show whether they are or not, but requests to fill in this missing information during the 2004 ASTM review were not met, so the database used for analysis is missing the weld flux for those 3 welds). The only medium Ni heat that is clearly <u>not</u> Linde 80 is the plate heat with Cu = 0.25 wt %,

which is not far enough above the calibrated Cu_{max} = 0.243 wt % to make any difference. Obviously, the Cu_{max} value for the typical Linde 80 category is far better established than for any other category.

The low-Ni "all other" category is not so easy to identify with a particular weld group, because the two welds that establish the Cu_{max} value are different (an unusual B&W Linde 80 weld with Ni = 0.1 wt % and high-Cu and a Rotterdamse weld with SMIT 89 flux and high Cu). There are several Linde 0091 welds in the category, and two of them have Cu > 0.243 wt % (the two unknown weld flux cases shown in Table 7.2 also may be Linde 0091), but the known and possible Linde 0091 welds did not affect the calibrated limit for the low-Ni category, so it should not be described as a Linde 0091 Cu_{max} value.

Table 7.2. Distribution of data for calibrating Cu saturation limits (calibration and validation data)

	All other materials (Ni ≤ 0.5 wt %)	**Typical Linde 80 welds (0.5 < Ni < 0.75 wt %, excluding Linde 1092 welds)**	**Linde 1092 welds (Ni ≥ 0.75 wt %)**
Product forms with data in the Category and Cu > 0.072	P, SRM, W	F, P, SRM, W	F, P, W
Number of heats or welds in the Category with Cu > 0.072	52	98	21
Number of heats or welds in the Category with Cu > 0.243 wt %	6	25	6
Number of TTS observations with Cu > 0.243 wt %	19	65	20
Description of heats or welds in the Category with Cu > 0.243 wt %	1 – Linde 80 weld 2 – Linde 0091 welds, PWR vessels 1 – Rotterdamse SMIT 89 weld 2 – CE welds (unknown weld flux, BWR vessels)	1 – CE plate 21 – Typical Linde 80 welds 3 – B&W welds (unknown weld flux, may also be Linde 80)	6 – Linde 1092 welds (Note: only one of these six Linde 1092 welds has Ni ≥ 0.75, and there are no other materials with Ni ≥ 0.75 and Cu > 0.243 wt % in the TTS database)

7.2.3 Specific Issues Regarding the Cu_{max} Limits

Using strict Ni categories to specify Cu_{max}. Because of the overlap in the Ni ranges for Linde 80 and Linde 1092 welds, strictly imposing the Ni limits shown in Table 7.2, rather than using the weld group categories, would penalize the many Linde 80 welds by increasing their Cu_{max} limit, just to accommodate a few medium Ni Linde 1092 welds. There would also be inadequate statistical basis for a high Ni value of Cu_{max} if this were done. In fact there are only 2 materials in the entire surveillance database (both Linde 1092 welds) that have Ni levels above 0.73 wt % (the high end of the Linde 80 range) and high enough Cu (> 0.243 wt %) to possibly contribute to a Cu_{max} value. There is only one Linde 1092 weld that actually falls in the originally-defined high Ni range (Ni ≥ 0.75 wt %) and has high enough Cu. Thus, if the Linde 1092 welds were strictly divided by Ni level, most of the subset that affects Cu_{max} would go into the medium Ni category (where they would increase the calibrated Cu_{max} for all the Linde 80 welds) and the Cu_{max} value for the high Ni category would be based on just 1 or 2 welds. It would then be highly uncertain, just as the Cu_{max} value for the low-Ni "all other" category is.

Fitting Cu_{max} as a continuous function of Ni. If feasible, it would be preferable to have a continuous function of Ni for estimating Cu_{max} rather than the discrete categories shown in Table 7.2. Unfortunately, a continuous function of Ni for predicting Cu_{max} is not feasible because the currently-available

surveillance data are inadequate for such an approach. The main problem is lack of data, which is evident in Table 7.2, where the lack of sufficiently high-Cu data at high and low-Ni is clear. Another problem is the pattern of the available data, which is evident when analyzing the residuals relative to a model that is otherwise like the baseline model but recalibrated for the best-fit single value of Cu_{max} = 0.2646 wt %, as shown in Fig. 7.2. The points on Fig. 7.2 are the residuals relative to the single-value Cu_{max} model for all the points in the surveillance database with Cu > 0.243 wt %, which are the only points that could possibly produce a Cu_{max} function that spans a range similar to the baseline Cu_{max} values. A linear function would be the obvious choice of fitting function in Fig. 7.2, because there are really only two clumps of data that have high enough Cu to be usable for a saturation limit. Fitting anything other than a linear function to the two clumps of data would be debatable at best.

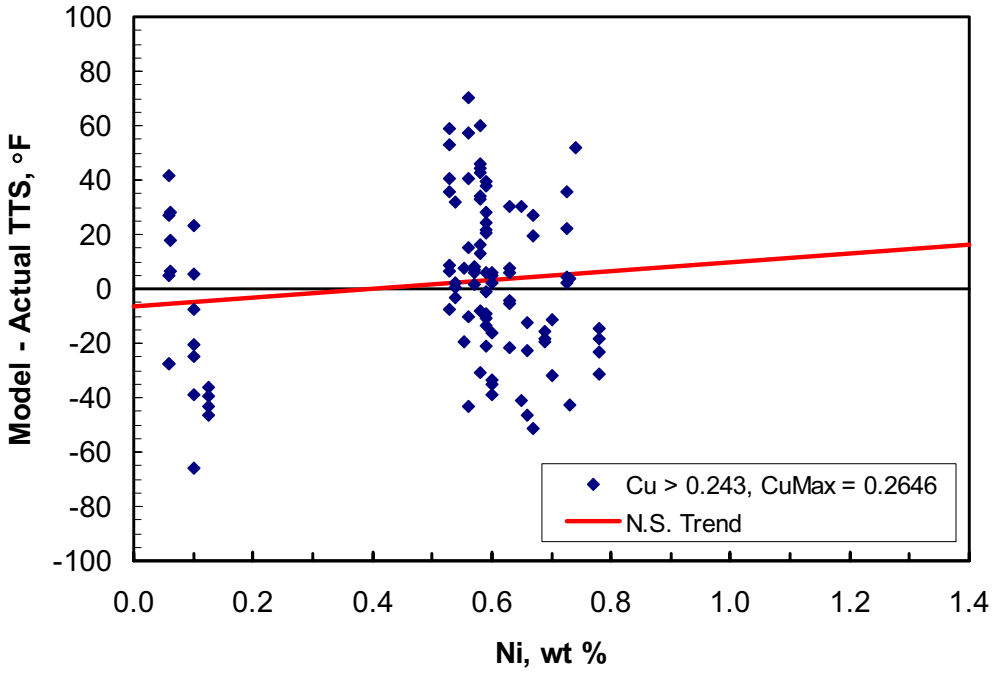

Fig. 7.2. Nonsignificant linear residual trend when a single calibrated Cu_{max} value is used, all available data with Cu > 0.243 wt %.

In order to justify calibrating Cu_{max} as a linear function of Ni, there should be a significant linear trend in the residuals on Fig. 7.2. Instead, the slope of the apparent linear residual trend line is not statistically significant. The lack of significance does not prove that there is no effect of Ni on Cu_{max}, only that the effect, if any, is not large relative to the scatter in the surveillance data. For the residual definition used in Fig. 7.2, the positive apparent slope of the residual plot implies decreasing Cu_{max} as Ni increases, opposite in sign relative to other results showing that higher Ni causes higher Cu_{max} values (see Sect. 2.3.2). The results showing higher Cu_{max} with higher Ni that are presented in Sect. 2.3.2 are based on controlled experiments and are considered more reliable than the surveillance residual trend. Thus, the facts that (a) the surveillance data show no significant effect of Ni on Cu_{max} and (b) the slight apparent trend that is visible is contrary to the direction of the trend in controlled experiment data are both evidence that the surveillance data are inadequate to calibrate a continuous function Cu_{max}(Ni).

Significant differences in Cu > 0.243 wt % residuals by weld group. Though the trend line shown in Fig. 7.2 does not indicate a significant trend of residuals with Ni, significant differences are revealed when grouped by Linde 1092 welds, typical Linde 80 welds, and all other. The average residuals of the grouped data are statistically significantly different in t-tests. In particular, with a single Cu_{max} value the average residual of the low-Ni "all other" data, (-11.8°F), is significantly below the average residual of typical Linde 80 welds (8.7°F), which is significantly above the average residual of Linde 1092 welds (-6.3°F). Thus, there is a statistical justification for 3 grouped Cu_{max} values but a lack of statistical justification for a linear function of Ni on the same set of surveillance data. It should be noted that the low-Ni and Linde 1092 groups do not have significantly different average residuals in the weld group analysis, so there is also statistical merit in a two-category "typical Linde 80" vs "all other" grouping, as discussed below.

Several possible reasons why the significant difference by weld group does not translate into a significant continuous trend with Ni have been identified. They include the known importance of post-weld heat treatment details, the near-total overlap in Ni range of the high-Cu members of the Linde 1092 and Linde 80 weld groups, and the relative lack of surveillance data outside the medium Ni range. Additional possibilities include the fact that the overall difference in average residual of the two clumps of surveillance data is small relative to the scatter within each clump, making it difficult to justify any continuous function, and possible nonlinearity in the Ni effect that does not show up clearly in Fig. 7.2 because of the limited number of very high-Cu heats that are available. All the possibilities mentioned in this paragraph should be considered hypotheses, as the actual reasons are not yet established.

Uncertainty from medium Ni B&W welds that may or may not be typical Linde 80 welds. Three of the medium Ni welds that were used for determining the value Cu_{max} = 0.243 were not specifically identified as Linde 80 (weld flux is blank, vessel manufacturer is Babcock & Wilcox), and they contribute 7 of the 65 points used in the Cu_{max} calibration for that category. The Cu values for these welds are 0.26, 0.31, and 0.35. There is also a CE plate at Cu = 0.25 wt % that contributes another 7 points. The plate at 0.25 wt % Cu and the weld at 0.26 wt % Cu had little effect on the calibrated value of Cu_{max} = 0.243 because the fitted Cu_{max} value is close to the maximum actual Cu values for these materials (limiting Cu makes little difference when the unlimited value is nearly the same). Thus, there are really only 5 points from welds WDR302 and WQC102 that could have affected the calibrated value substantially. If those two welds are in fact Linde 80 welds, there is no issue and the calibrated value of Cu_{max} = 0.243 is the best value to use. If not, there may be a slight inaccuracy in the calibrated value of Cu_{max} for typical Linde 80 welds.

To bound the possible inaccuracy, all the data in the medium Ni category in Table 7.2 that are not specifically listed as Linde 80 welds were moved into the "Other" category, including the plate and the three B&W welds that may be Linde 80. The value of Cu_{max} for the typical Linde 80 category was recalibrated, and it changed only slightly, from 0.243 to 0.247. The third digit of the calibrated Cu_{max} value is in any case somewhat uncertain and the measured composition is often only given to two digits, so whether the medium Ni welds with missing weld flux are in fact Linde 80 makes little difference.

Treatment of base metals. The proper value of Cu_{max} for base metals is not adequately established by the surveillance data, because there is only one plate heat with high enough Cu to affect any of the Cu_{max} values (and it is barely high enough, at Cu = 0.25 wt % so it cannot substantially affect the calibrated Cu_{max} limit). Cu levels in all other base metals do not exceed the Cu_{max} limit calibrated for any of the groups, so no Cu limit behavior is observed. Thus, the base metals are assigned to the "all other" group, which means that their full Cu value is used without limit. This is an adequate approach up to Cu ≅ 0.25 wt % ,which includes all current surveillance base metals and most or all plant base metals.

Unusually high value of Cu_{max} in the low-Ni category. The calibrated value of Cu_{max} in the low-Ni or "all other" category is higher (0.37 wt % Cu) than the expected value of about 0.3 wt % based on the solubility of Cu (see Sect. 2.3.2 and [2]). The low-Ni Cu_{max} value is also higher than the calibrated value

for the typical Linde 80 category, which has substantially higher Ni, contrary to the evidence that increased Ni generally causes a higher Cu_{max} limit. Moreover, the statistical case for the particular calibrated value in the low-Ni category is based on so few datapoints (8 points from 2 welds) that it is highly uncertain. Finally, the grouped statistical analysis described in the preceding subsection found no significant difference between residuals in the low-Ni and Linde 1092 data. Consequently, a sensitivity study was conducted to determine the effect of combining the low-Ni data into a larger "all other" category.

7.2.4 Sensitivity Study on Combining the Low-Ni Group in a Larger "All Other" Grouping

A sensitivity approach was taken, in which the only change from the baseline model was to combine the low-Ni data with one of the other groups, without recalibration. The low-Ni group has only 19 high-Cu datapoints (Cu > 0.243 wt %), and those are the only points that can be affected by the re-grouping changes being analyzed. Depending on the final Cu_{max} value, not all of the 19 points will be affected. Thus, the approach used in the study was to apply the previously calibrated values of Cu_{max} for either the typical Linde 80 or Linde 1092 weld group to the low-Ni data and analyze the effects on the 19 points, without recalibration.

Combining the low-Ni and typical Linde 80 groups and using $Cu_{max} = 0.243$ for all materials in those groups is not a reasonable choice. All 19 of the TTS points from the 6 welds with Ni < 0.5 and Cu > 0.243 are affected by this choice, and the average residual for those points is large (–15.2°F), in the unconservative direction, and significantly less than zero. The average residual of the low-Ni group after combination is also significantly less than the average residual of the typical Linde 80 and Linde 1092 groups. Thus, this combination is not recommended.

Combining the low-Ni and Linde 1092 weld groups and using $Cu_{max} = 0.301$ for all materials in those groups is a reasonable choice. The two Cu_{max} values that would result in this case could be interpreted as values for typical Linde 80 welds ($Cu_{max} = 0.243$) and "all other" ($Cu_{max} = 0.301$). Only the 8 points from the 2 welds that currently establish the low-Ni Cu_{max} value are affected by this choice, because all the other low-Ni welds have Cu ≤ 0.279 wt %. Thus, the average residual for the 19 high-Cu points in the low-Ni group is -7.1°F in this case, which is not significantly less than zero.

The standard deviation of residuals for all welds with Cu > 0.072 wt % would increase slightly due to combining the Linde 1092 and "all other" categories in Table 7.2. The increase would be reduced if both the Cu_{max} change and the deletion of the CRP T_i term are implemented, as these two recommended changes partially offset in the weld category. The two-category approach with typical Linde 80 and "all other" has an advantage over the similar two-category approach in the ASTM E 900-2 model, because the only weld group that has a well-established Cu_{max} value (typical Linde 80) would be the only weld group that would be specifically mentioned in the model. The value used for Linde 1092 welds would still be the best available estimate for that weld group, so the change from three to two values of Cu_{max} would not affect the second-largest group of very high-Cu welds. The only other weld group that has 2 or more welds with Cu > 0.243 wt % (Linde 0091) is also unaffected by the change, because the highest Cu level in such welds (0.279 wt %) is below both the baseline three category "all other" limit and the revised two-category "all other" limit.

It is better to use the calibrated Linde 1092 value ($Cu_{max} = 0.301$ wt %) for the two-category "all other" group rather than to recalibrate a new value for the combined group. This can be seen by analyzing the consequences of a recalibration. There are only 12 welds with Cu > 0.243 wt % in the Linde 1092 and low-Ni categories combined. The shifts calculated for 7 of these 12 welds will not be affected by a recalibration, because their actual Cu values are below the Cu_{max} values calibrated for both Linde 1092 and low-Ni categories, and hence below any recalibrated compromise value. If a single value were re-calibrated for the remaining 5 welds in the combined category with Cu > 0.243 wt %, it would be somewhat high for the 3 Linde 1092 welds and somewhat low for the 2 low-Ni welds. Thus, while the

original Linde 1092 value would be a best estimate for 3 out of 5 welds and statistically acceptable on the other two welds, the recalibrated result would not be a best estimate for either the Linde 1092 or the low-Ni subsets. More importantly, the particular Cu_{max} value calibrated to the low-Ni welds is higher than expected based on Cu solubility, so the net effect of a recalibration would be to penalize the Linde 1092 welds by increasing their Cu_{max} value to accommodate physically-questionable data.

In a two-Cu_{max} approach, the model trends shown in Figs. 5.4 and 5.8 would be modified as shown for "other materials" in Fig. 7.3 and 7.4. The corresponding curve for typical Linde 80 welds would look similar to the 0.6 Ni curve on Fig. 7.3, except the curve would be flat for any Cu > 0.243 instead of Cu > 0.301. The 0.3 Cu curve on Fig. 7.4 would be plotted somewhat lower for the typical Linde 80 group, plotting at Cu_{max} = 0.243 instead of 0.3, and it would be plotted only over the relevant Ni range 0.52 ≤ Ni ≤ 0.73.

The 8 points in the baseline "all other" group that are affected by the change from three to two Cu_{max} categories are shown in Fig. 7.5, with small filled diamond symbols for the baseline model plotting location and large filled diamond symbols for the plotted location after incorporation in the revised "all other" category. The trend line has been updated, and it remains nonsignificant and almost indistinguishable from the baseline residual Ni trend (and almost indistinguishable from the horizontal "no-trend" line) after making the change. The same 8 points would move by the same amount on all other residual plots for materials with Cu > 0.072. None of the residual plots is affected by the change to such a degree that previously nonsignificant trends would become significant, as shown in Sect. 7.3.3.

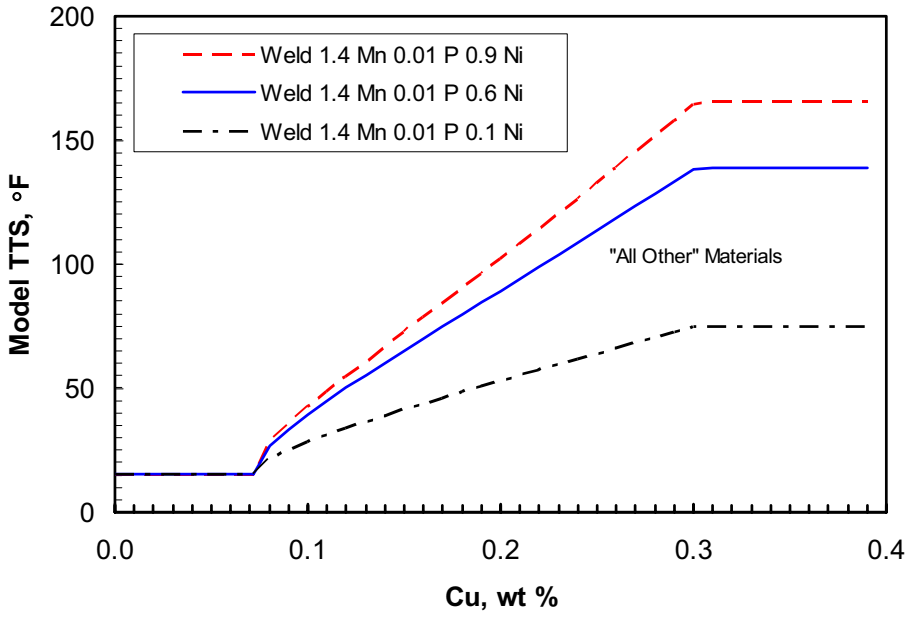

Fig. 7.3. Effect of Cu on TTS for various Ni levels, "all other" materials (similar to Fig. 5-4 but revised for two material group categories).

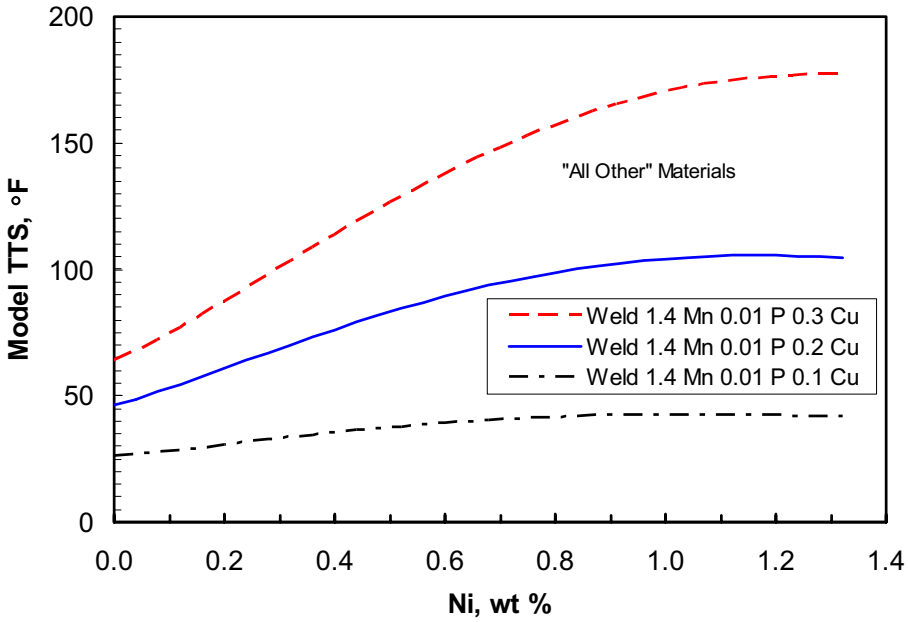

Fig. 7.4. Effect of Ni on TTS for various Cu levels, "All Other" group, and 2×10^{18} n/cm^2 fluence.

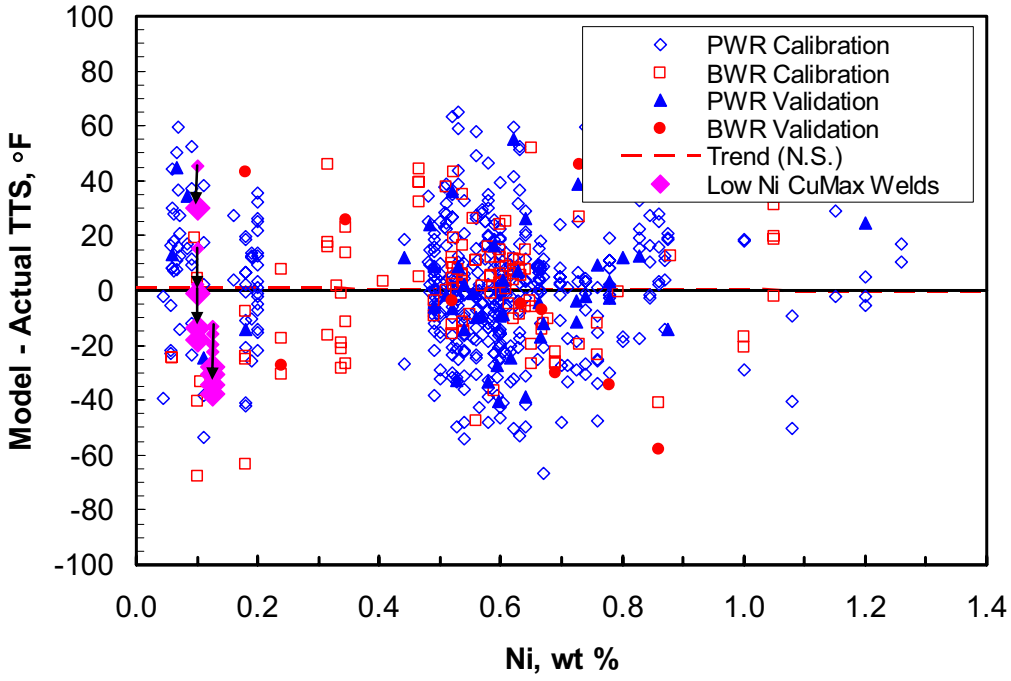

Fig. 7.5 Effect of using Cu_{max} = 0.301 on the low-Ni welds that determined the Cu_{max} = 0.37 value for the "other weld" category in the baseline model.

7.2.5 Conclusions and Recommendations Regarding Cu_{max}

Limitations of the surveillance data for establishing Cu_{max} values. The baseline values of Cu_{max} for the Linde 1092 and "all other" categories in Eq. (4-5d) are not well established, being determined by only three and two welds respectively. The value of Cu_{max} for the typical Linde 80 category is reasonably well established, calibrated to at least 21 different Linde 80 welds. The surveillance database is simply lacking in enough materials with sufficiently high Cu to reasonably establish the Cu_{max} limits for materials other than typical Linde 80 welds.

The lack of sufficient surveillance data with high enough Cu and either low or high levels of Ni prevents the confirmation or calibration of the Ni effect on Cu_{max} that has been identified in other data. The possibility of expressing Cu_{max} as a continuous function of Ni has been evaluated, and it also is not feasible with the present database.

The surveillance database also does not contain enough plate or forging materials with high enough Cu levels to directly establish a Cu_{max} limit for base metals. The assumption has been made that the full Cu level (which is ≤ 0.25 wt %) should be used for all base materials.

Recommended change from three Cu_{max} values to two Cu_{max} values. Based on the additional analysis in Sect. 7.2.4, the baseline "all other" category should be combined with the baseline Linde 1092 weld category in a new category labeled "all other materials". The typical Linde 80 category in the baseline model should be maintained. The Cu_{max} value for the revised "all other" category would be 0.301 wt %, which is equal to the calibrated value for the Linde 1092 welds. The value $Cu_{max} = 0.301$ is somewhat low for the two low-Ni welds that determined Cu_{max} in the baseline "all other" category, but not low enough to cause a statistically significant error in that category. No other materials are affected by the revised "all other" Cu_{max} value, because they are all either included in the typical Linde 80 weld group or they have Cu levels below 0.301 wt %. In particular, the four other very high-Cu welds from the baseline "all other" category all have Cu ≤ 0.279 wt %, so they are not affected by the revision.

7.3 Simplified TTS Model

In this section, a simplified model is presented incorporating the recommended changes of the previous two sections. The quality of fit and predictive capability of the simplified model are updated as well. All additional information needed to apply the model is included here for ready reference, even though some of this material was presented in earlier Chapters.

7.3.1 Simplified Model Equations

Implementing the recommendations in both Sects. 7.1.4 and 7.2.5 produces the following simplified model.

$$TTS = MF\ term + CRP\ term \tag{7-2}$$

$$MF\ term = A(1 - 0.001718T_i)(1 + 6.13PMn^{2.47})\sqrt{\phi t_e} \tag{7-3a}$$

$$A = \begin{Bmatrix} 1.140\text{x}10^{-7} & \text{for forgings} \\ 1.561\text{x}10^{-7} & \text{for plates} \\ 1.417\text{x}10^{-7} & \text{for welds} \end{Bmatrix} \tag{7-3b}$$

$$CRP\ term = B\left(1 + 3.77Ni^{1.191}\right) f\left(Cu_e, P\right) g\left(Cu_e, Ni, \phi t_e\right) \tag{7-4a}$$

$$B = \left\{ \begin{array}{c} 102.3 \;\; for \;\; forgings \\ 102.5 \;\; for \;\; plates \; in \; non\text{-}CE \; mfg. \; vessels \\ 135.2 \;\; for \;\; plates \; in \; CE \; mfg. \; vessels \\ 155.0 \;\; for \;\; welds \\ 128.2 \; for \; SRM \;\; plates \end{array} \right\} \tag{7-4b}$$

$$Cu_e = \left\{ \begin{array}{c} 0 \quad for \; Cu \le 0.072 \; wt\% \\ \min[Cu, Max(Cu_e)] \;\; for \; Cu > 0.072 \; wt\% \end{array} \right\} \tag{7-4c}$$

$$Max(Cu_e) = \left\{ \begin{array}{c} 0.243 \; for \; typical \; (Ni > 0.5) \; Linde \; 80 \; welds \\ 0.301 \;\; for \; all \; other \; materials \end{array} \right\} \tag{7-4d}$$

$$f(Cu_e, P) = \left\{ \begin{array}{c} 0 \;\; for \; Cu \le 0.072 \\ [Cu_e - 0.072]^{0.668} \;\; for \; Cu > 0.072 \; and \; P \le 0.008 \\ [Cu_e - 0.072 + 1.359(P - 0.008)]^{0.668} \;\; for \; Cu > 0.072 \; and \; P > 0.008 \end{array} \right\} \tag{7-4e}$$

$$g(Cu_e, Ni, \phi t_e) = \frac{1}{2} + \frac{1}{2} \tanh\left[\frac{\log_{10}(\phi t_e) + 1.139 Cu_e - 0.448 Ni - 18.120}{0.629} \right] \tag{7-4f}$$

The effective fluence form in Eq. (7-5) applies to both the MF and CRP terms, Eqs. (7-3) and (7-4).

$$\phi t_e = \left\{ \begin{array}{c} \phi t \quad for \;\; \phi \ge 4.39 \times 10^{10} \\ \phi t \left(\dfrac{4.39 \times 10^{10}}{\phi} \right)^{0.259} \quad for \;\; \phi < 4.39 \times 10^{10} \end{array} \right\} \tag{7-5}$$

7.3.2 Variables, Units, Definitions, and Ranges of Applicability

The units and descriptions of independent variables in Eqs. (7-2) through (7-5) are given in Table 7.3. The dependent variable, transition temperature shift (TTS), is estimated by Eq. (7-2) in degrees Fahrenheit. Both TTS and T_i may be converted by the usual formula T(°C) = [T(°F)-32]/1.8.

Table 7.3. Independent variables in the embrittlement shift model and their ranges and mean values over all calibration and validation data (855 datapoints)

Variable	Description	Range	Mean
Cu	Copper content (wt %)	0.01–0.41	0.136
Mn	Manganese content (wt %)	0.58–1.96	1.300
Ni	Nickel content (wt %)	0.044–1.26	0.565
P	Phosphorous content (wt %)	0.003–0.031	0.0119
ϕt	Neutron fluence, E > 1 MeV (n/cm^2)	9.26×10^{15}–7.13×10^{19}	6.50×10^{18}
ϕ	Neutron flux, E > 1 MeV (n/cm^2/s)	1.81×10^{8}–9.71×10^{11}	5.13×10^{10}
T_i	Irradiation temperature (°F)	522–570	545

Two quantities are derived from the independent variables given in Table 7.3, the effective Cu in solution, Cu_e as defined in Eq. (7-4c), and the effective fluence (or flux-adjusted fluence) ϕt_e as defined by Eq. (7-5). An additional independent variable not listed in Table 7.3 is product form, which can take on the values for forging, plate (in CE manufactured vessels or other vessels), weld (typical Linde 80 or other), and SRM as defined in Eqs. (7-3b) and (7-4b).

Some additional information about the variables is needed for application of the model. The chemical composition variables are intended to represent the best available estimate of actual measured composition at the location where the shift is being analyzed. This is consistent with the use of average measured composition on surveillance samples from each heat (to the extent available) to develop the calibration database. Generic default chemical composition values could be considered if measurements or better estimates are unavailable. The average composition does vary significantly in high-Cu (> 0.072 wt %) and low-Cu categories and by class of forging or plate material, weld group etc. so it is necessary to define any default values on statistically-relevant material groupings. A list of mean, standard deviation, minima, and maxima of composition variables for various material groups in the surveillance database is given in Appendix G.

The values of fluence and flux variables to be used in the model should be estimated at the actual location where the shift is to be estimated, with the flux estimate averaged over the relevant effective full power operating time. This is consistent with the estimates for the surveillance specimens, for which dosimetry was based on the actual capsule location and the time averaging was done by dividing total accumulated fluence by the effective full power operating time to estimate time-averaged flux. If an analysis is performed partway through the wall of the vessel, the average flux and fluence estimates should be made first at that specific location in the wall, using appropriate attenuation models, then those attenuated flux and fluence estimates should be used in the shift model. The location of greatest sensitivity to embrittlement will depend generally on both fluence and flux in the lower flux range.

The irradiation temperature used in the model should also be a time-averaged estimate for the metal at the specific location where the shift is to be estimated. The best available metal temperature estimate for the surveillance specimens was the temperature of the coolant near the surveillance capsule, but coolant temperature is not necessarily the best estimate of metal temperature in applications.

The overall range of data given in Table 7.3 is not by itself sufficient for estimating the limits of applicability of the model. The actual coverage of the data over the fitting variables and combinations of variables varies considerably, so it is necessary to review the actual distribution of data in TTSDatabase8-04.xls (Appendix C) to determine the ranges of variables and variable combinations that are supported by a reasonable amount of data. Some information on the ranges of chemical composition variables in the database is tabulated by product form in Appendix E, where, for instance, it is clear that forgings with Cu > 0.16 wt % or plates with Cu > 0.25 wt % are simply not available in the database, and the upper limit of Cu = 0.41 wt % in Table 7.3 applies only to welds. As another example, there are no low Mn (Mn < 0.93 wt %) materials in the database except A508 class 2 forgings, and the range of other chemistry variables in such forgings is limited (0.67 ≤ Ni ≤ 0.86 wt %, 0.01 ≤ Cu ≤ 0.16 wt %, and 0.004 ≤ P ≤ 0.02 wt %). Thus, application of the model to any materials with Mn < 0.93 and values of Ni, Cu, or P outside the ranges corresponding to A508 class 2 forgings would be an extrapolation beyond the available data.

As an example of limits on exposure variable combinations, Table 7.3 shows that there are both high-fluence and low-fluence data, and high-flux and low-flux data, so one might assume that the full range of the fluence/flux space is reasonably covered by data. Unfortunately, this assumption is not true. The highest available fluence in the database decreases as flux decreases, so in all the data with $\phi < 1 \times 10^{10}$ n/cm^2/s, the highest available fluence is $\phi t = 1.9 \times 10^{18}$ n/cm^2. The highest available fluence in all the data with $\phi < 1 \times 10^{9}$ n/cm^2/s is only $\phi t = 2.8 \times 10^{17}$ n/cm^2. Thus, estimating the shift at any fluence greater than 1.9×10^{18} n/cm^2 for $\phi \cong 1 \times 10^{10}$ n/cm^2/s (and similarly for lower flux levels) is an extrapolation beyond the available data.

7.3.3 Goodness of Fit of the Simplified Model

After deleting the CRP T_i term and choosing two Cu_{max} values instead of three, the quality of fit of the simplified model in Eqs. (7-2) through (7-5) is not significantly changed from the baseline model. Only the results for higher Cu materials (Cu > 0.072 wt %) are affected by these simplifications, so that is the only subset of data discussed here; the results for lower Cu materials remain as given in Chap. 4. The model prediction vs actual shift plots for Cu > 0.072 wt % data are similar to the baseline model, as shown by comparing Figs. 7.6 and 7.7 below with Figs. 4.10 and 4.11.

The table of standard deviations by product form is slightly changed from Table 4.1 which corresponds to the baseline model with the CRP T_i term. After the simplifications, the high-Cu standard deviations change slightly, with the values decreasing slightly for forgings and increasing slightly for plates and welds, as highlighted in Table 7.4. The sum of squared residuals over the Cu > 0.072 wt % calibration data increases about 1% with the simplifications. The mean residuals for the product forms listed in Table 7.4 are not significantly different from zero and pairs of means (forging vs plate, plate vs weld, forging vs weld) are not significantly different from each other.

Table 7.4. Standard deviation (S_d) of residuals about the simplified embrittlement shift model in various subsets, all PWR and BWR calibration and validation data except SRM

All entries are TTS values measured in °F

Product Form	S_d (points)	
	Cu ≤ 0.072 wt %	Cu > 0.072 wt %
Forging	17.5 (75)	19.6 (61)
Plate	15.0 (78)	21.2 (309)
Weld	18.6 (93)	26.4 (213)

None of the lines fitted to residual trends have a significant slope after the simplifications, both for variables in the model and for those variables not in the model that were checked. The plots showing this fact are given in Appendix H. These can be compared directly to the corresponding plots for the baseline model (See Appendix F, Figs. F.14 through F.28). The differences are not easy to see, and both baseline and simplified models have reasonably flat residual plots that indicate a good fit.

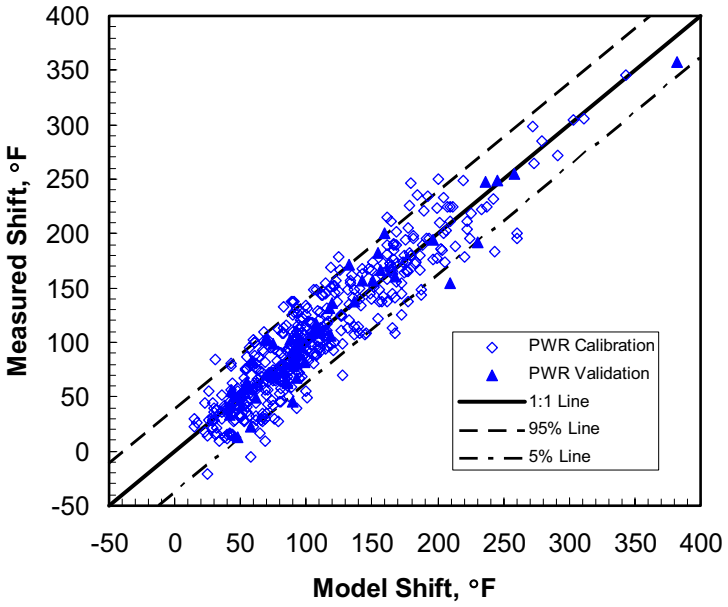

Fig. 7.6. Simplified Model shift (Eq. 7-2 through 7-5) vs measured shift, all PWR calibration and validation data with Cu > 0.072 wt %.

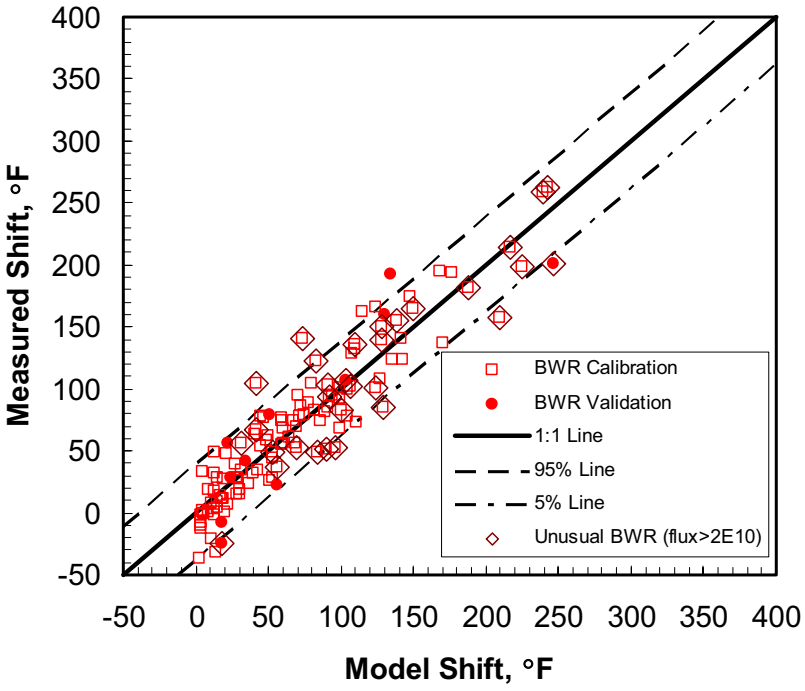

Fig. 7.7. Simplified Model shift (Eq. 7-2 through 7-5) vs measured shift, all BWR calibration and validation data with Cu > 0.072 wt %.

7.3.4 Predictive Capability

The simplified model retains the predictive capability of the baseline model on the high-Cu data, and the prediction of low-Cu data is not affected by the simplifications. Table 7.5 shows the statistical comparison of calibration and validation data for the simplified model, which can be compared to Table 4.2 for the baseline model. Though the highlighted numbers changed somewhat, the conclusion is the same – there is no significant difference between means or standard deviations of high-Cu (Cu > 0.072 wt %) calibration and validation data at either low or high flux. None of the mean residuals is significantly different from zero, either. Thus, the simplified model predicts data not used in fitting about as well as it fits the calibration data used to develop the model.

Table 7.5. Comparison of calibration and validation subsets by mean and standard deviation (S_d) of residuals for the simplified TTS model

The number of points is shown for subsets smaller than 40 points

Subset	Mean (points)		S_d (points)	
	Calibration	Validation	Calibration	Validation
Cu ≤ 0.072, $\phi > 4.39 \times 10^{10}$	0.0	0.9[a] (22)	17.0	14.6[a] (22)
Cu ≤ 0.072, $\phi \leq 4.39 \times 10^{10}$	1.7	-2.1[a] (2)	19.5	0.2 (2)
Cu > 0.072, $\phi > 4.39 \times 10^{10}$	0.4	2.9[a]	23.2	23.7[a]
Cu > 0.072, $\phi \leq 4.39 \times 10^{10}$	1.4	-7.5[a] (15)	21.3	26.1[a] (15)

[a]The difference from the calibration value is not statistically significant.

7.4 References

1. Jones, R. B., and T. J. Williams, "The Dependence of Radiation Hardening and Embrittlement on Irradiation Temperature," pp. 569–90 in *Effects of Radiation on Materials: 17th International Symposium*, ASTM STP 1270, Ed. D. S. Gelles et al., American Society for Testing and Materials, 1996.
2. Odette, G. R., et al., *The Effects of Composition and Heat Treatment on Hardening and Embrittlement of Reactor Pressure Vessel Steels*, NUREG/CR-6778, U.S. Nuclear Regulatory Commission, Washington, D.C., 2003.

Appendix A

8. SUMMARY AND CONCLUSIONS

The primary result of the present work is the physically motivated, empirically calibrated model of transition temperature shift (TTS) and the associated demonstration of the quality of fit and ability to predict data not used for fitting. This model is based on using separate terms for matrix features (MFs) and copper-rich precipitates (CRPs). It is a revision of earlier models of similar form, based on the larger surveillance database now available and on the continuing advances in mechanistic understanding. Following a detailed comparison in Chap. 6 of the baseline model given in Chap. 4 and the IVAR data, two sensitivity studies were conducted on the TTS data that resulted in a simplified model presented and discussed in Chap. 7. The following summary and conclusions are applicable to both models because the differences between the two models are slight and statistically nonsignificant.

The embrittlement mechanisms underlying the revised TTS model are reviewed in Chap. 2, noting practical simplifications of the set of complex, interacting processes controlling TTS. The TTS model reflects reasonably well-understood physical effects of composition, particularly the main effects and interactions of Cu, Ni, P, and Mn, and the exposure variables fluence, flux, and irradiation temperature. These variables cause changes in the magnitude and fluence dependence of the shift, especially the CRP contribution that is a saturating function of Cu, Ni, and flux. The model also includes empirical treatment of product form by using different coefficients, which reflect several physical variables, including heat treatment, preirradiation microstructure, and unmodeled effects of alloy composition, especially for Mn and for the likely effects of Ni on matrix features. The coefficients also reflect other factors not yet explained physically, such as the difference in shifts between plates in CE and non-CE-manufactured vessels.

The database used to calibrate the TTS model was updated in 2003–2004 to include an important set of 62 additional low-flux BWR shifts and an additional 140 PWR shifts. All available surveillance data, both old and new, were reviewed for completeness, discrepancies, and duplicates, and the database was improved in quality by addressing the issues identified in this review. Random sampling was used to ensure better balance of the standard reference material (SRM) data relative to the data from actual vessel materials and to reserve a 10% sample of data for validating the predictive capability of the model on data not used for fitting. The combined effect of the database expansion, review, and sampling effort was to produce a TTS calibration set that is larger than any dataset that was previously modeled, as well as being better balanced and of generally higher data quality.

The overall philosophy in calibrating the model was to fit the MF and CRP contributions to the most relevant data, which helps to avoid numerical tradeoffs between the various model terms. Thus, most of the MF constants are calibrated to low-Cu data (Cu ≤ 0.072 wt %) since there is no CRP contribution in that case. The MF term, which applies at all Cu levels, is then held fixed while calibrating the CRP term, again to avoid trade-offs between variables that appear in both terms. A few constants were calibrated to the entire range of Cu, either because of the scarcity of data (in the case of flux) or because the MF term is used for all data and there is no corresponding CRP term that can adjust for any differences in the low- and higher-Cu data (in the case of the P-Mn interaction term). Insights from prior research on embrittlement mechanisms are reflected in the model form and variables, and the fitting functions and calibrated constants are chosen to produce a reasonable empirical fit to the key TTS datasets, including high- and low-Cu material, PWR and BWR irradiations, and forging, plate, and weld product forms.

The revised model contains, sometimes in different form, all effects that were in the earlier NUREG/CR-6551 model [1], which was based on a substantially smaller database, plus additional effects that have been subsequently characterized. The main differences from earlier models are

- the use of a theoretical square root dependence on fluence and a linear temperature dependence in the MF term;

- inclusion of an explicit P-Mn interaction in the MF term and a P precipitation term in the CRP term;
- separate CRP coefficients for plates in CE-manufactured vessels, plates in other vessels, and SRM plates (which are not part of any vessels);
- variation in the fluence at which the CRP term becomes important as a function of Cu, Ni, and flux; and
- incorporation of flux effects in both the MF and CRP terms by an effective fluence approach.

The goodness of fit of the model to the calibration and validation data is displayed in predicted vs measured plots, tabulated standard deviations within product form groups, and residual plots that separately consider the low-Cu data, where only the MF term applies, and the higher-Cu data, where both MF and CRP terms apply. Based on all of these measures, the fit to surveillance data is good, with no statistically significant residual trends found for any of the variables used for modeling or for other variables that were not.

The predictive capability of most aspects of the model is validated on a subset of surveillance data not used in model development, comparing means and standard deviations of residuals and predicted vs measured plots. The model also compares favorably with SRM data, most of which were not used in the calibration. The two fitting constants in the effective fluence part of the model are not validated by the sample of data set aside for validation because all of the relatively scarce low-flux data were needed for calibration. However, the effective fluence (flux effect) part of the model, as well as all other variable effects, are generally supported by comparisons with the IVAR data, which were also not used in calibrating the model.

The rather complex variable trends in the model are shown in a series of plots in Chap. 5, and each variable effect is discussed in some detail, including analysis of the statistical significance of the effect and discussion of variable confounding. All key terms in the TTS model are statistically significant for the relevant data, and most also have support from the physical understanding described in Chap. 2 and the separate set of data generated in the controlled IVAR experiments discussed in Chap. 6. The temperature correction in the CRP part of the baseline model presented in Chap. 4, a small adjustment that partially counteracts the temperature effect of the MF term to slightly improve the fit to the high-Cu surveillance data, is contrary to trends observed in controlled experiments; hence, this term is not included in the simplified model presented in Chap. 7.

The TTS model is compared in Chap. 6 to data from the controlled IVAR experiments, which are completely independent of the surveillance data used for calibrating the TTS model. The form of the TTS model is also reasonably independent of the IVAR data, although it was based in part on physical insights from the literature on embrittlement, which includes some previous results of IVAR experiments. However, specific fitting functions used in the TTS model, such as the saturating CRP function and effective fluence form, differ from the functions previously used to characterize IVAR data. Thus, the comparison with IVAR data in Chap. 6 can be considered an independent check on the TTS model.

Notably, the IVAR database is a very large collection of results from test reactor irradiations and postirradiation testing of materials selected to systematically study the effects of variables that influence radiation hardening and embrittlement. A quantitative comparison is made, using an empirical conversion between the TTS that characterizes the surveillance data and the yield strength increase that characterizes the IVAR data. Generally good agreement is shown between the TTS model and the IVAR results on welds and plates that are very similar to the surveillance materials. Good agreement is also found with IVAR results on the split-melt model steels over the range of compositions that encompass the surveillance database. Where some disagreements occur, they are generally associated with the wider variation of composition variables in the IVAR database and known limitations of the available surveillance data. The IVAR data generally provide more precise evaluations of the effects of individual

variables and variable combinations under controlled conditions, while the TTS model reflects average effects of many variables over a wide range of alloys and irradiation conditions.

The main difference between the TTS and IVAR data trends is the range of flux over which significant dose rate effects are observed. This difference arises in part from the fact that the majority of observations in the IVAR database have higher flux than the 95th percentile flux in the TTS database, and there is a relatively narrow overlapping flux range in which both databases have substantial data. Physically based extrapolation of the flux effect identified in IVAR down to the lower flux levels of BWR surveillance data, based on an enhanced recombination mechanism, shows good agreement with the calibrated TTS flux effect, and numerical extrapolation of the flux-dependent part of the empirical TTS model to the higher flux levels in IVAR also shows agreement, suggesting that the two databases emphasize different parts of the same continuum of flux effects, as discussed in Sect. 6.6.1.

The key new insight in the TTS modeling effort, that flux effects are evident in both low-Cu (or no-Cu) and higher-Cu materials, is supported by the IVAR data, as discussed in Sect. 6.6.2. The flux effect in the MF term was originally incorporated in the TTS model because it is statistically significant in fitting the surveillance data. Since that empirical observation was made, a broadly similar MF flux effect was found in the low-Cu (no-Cu) data from controlled experiments in the IVAR database, as described in Sect. 6.4.2. While the absolute flux effect on the MF term in the IVAR data is relatively small, it is systematic and can be rationalized based on mechanistic considerations discussed in Sect. 2.4.2. Thus, flux effects have been found to affect both MF and CRP terms in two independent databases and are included in the revised model.

In conclusion, the TTS model presented in this report is a good fit to the available surveillance data, with no significant residual trends in the model variables or in other variables that were considered, on both low- and higher-Cu subsets of the data. The slightly simplified version of the model given in Sect. 7.3 is recommended for applications. All major variable effects in the model are statistically significant, and most variable trends are also supported by physical understanding and quantitative agreement with trends in the independent IVAR database. The model has predictive capability for data not used in fitting, including a 10% random sample of surveillance data reserved for validation, SRM data not used in fitting, and the independent IVAR database of test reactor irradiations.

8.1 Reference

1. Eason, E. D., J. E. Wright, and G. R. Odette, *Improved Embrittlement Correlations for Reactor Pressure Vessel Steels*, NUREG/CR-6551, U.S. Nuclear Regulatory Commission, Washington D.C., 1998.

Appendix A

Appendix A. Publications List

Irradiation embrittlement of RPV beltline materials is currently evaluated using Regulatory Guide 1.99 Revision 2 (RG1.99/2), which presents methods for estimating the shift in Charpy transition temperature at 30 ft-lb (TTS) and the drop in Charpy upper shelf energy (ΔUSE). The purpose of the work reported here is to improve on the TTS correlation model in RG1.99/2 using the broader database now available and current understanding of embrittlement mechanisms.

This report is also a record of work performed in part at ORNL under the Heavy-Section Steel Irradiation (HSSI) Program, which is sponsored by the NRC Office of Nuclear Regulatory Research. A list of publications for the ORNL HSSI Program is given in Sect. A.1.

The HSSI Program includes both follow-on research and the direct continuation of work that was performed under the Heavy-Section Steel Technology (HSST) Program. Previous HSST reports related to irradiation effects in pressure vessel materials and those containing unirradiated properties of materials used in HSSI and HSST irradiation programs are listed in Sect. A.2.

A.1 HSSI Program Reports

1. F. M. Haggag, W. R. Corwin, and R. K. Nanstad, Martin Marietta Energy Systems, Inc., Oak Ridge Natl. Lab., Oak Ridge, Tenn., *Irradiation Effects on Strength and Toughness of Three-Wire Series-Arc Stainless Steel Weld Overlay Cladding*, USNRC Report NUREG/CR-5511 (ORNL/TM-11439), February 1990.
2. L. F. Miller, C. A. Baldwin, F. W. Stallman, and F. B. K. Kam, Martin Marietta Energy Systems, Inc., Oak Ridge Natl. Lab., Oak Ridge, Tenn., *Neutron Exposure Parameters for the Metallurgical Test Specimens in the Sixth Heavy-Section Steel Irradiation Series*, USNRC Report NUREG/CR-5409 (ORNL/TM-11267), March 1990.
3. S. K. Iskander, W. R. Corwin, and R. K. Nanstad, Martin Marietta Energy Systems, Inc., Oak Ridge Natl. Lab., Oak Ridge, Tenn., *Results of Crack-Arrest Tests on Two Irradiated High-Copper Welds*, USNRC Report NUREG/CR-5584 (ORNL/TM-11575), December 1990.
4. R. K. Nanstad and R. G. Berggren, Martin Marietta Energy Systems, Inc., Oak Ridge Natl. Lab., Oak Ridge, Tenn., *Irradiation Effects on Charpy Impact and Tensile Properties of Low Upper-Shelf Welds*, HSSI Series 2 and 3, USNRC Report NUREG/CR-5696 (ORNL/TM-11804), August 1991.
5. R. E. Stoller, Martin Marietta Energy Systems, Inc., Oak Ridge Natl. Lab., Oak Ridge, Tenn., *Modeling the Influence of Irradiation Temperature and Displacement Rate on Radiation-Induced Hardening in Ferritic Steels*, USNRC Report NUREG/CR5859 (ORNL/TM-12073), August 1992.
6. R. K. Nanstad, D. E. McCabe, and R. L. Swain, Martin Marietta Energy Systems, Inc., Oak Ridge Natl. Lab., Oak Ridge, Tenn., *Chemical Composition RTNDT Determinations for Midland Weld WF-70*, USNRC Report NUREG/CR-5914 (ORNL-6740), December 1992.
7. R. K. Nanstad, F. M. Haggag, D. E. McCabe, S. K. Iskander, K. O. Bowman, and B. H. Menke, Martin Marietta Energy Systems, Inc., Oak Ridge Natl. Lab., Oak Ridge, Tenn., *Irradiation Effects on Fracture Toughness of Two High-Copper Submerged-Arc Welds*, USNRC Report NUREG/CR-5913 (ORNL/TM-12156/V1), October 1992.
8. S. K. Iskander, W. R. Corwin, and R. K. Nanstad, Martin Marietta Energy Systems, Inc., Oak Ridge Natl. Lab., Oak Ridge, Tenn., *Crack-Arrest Tests on Two Irradiated High-Copper Welds*, USNRC Report NUREG/CR-6139 (ORNL/TM-12513), March 1994.

9. R. E. Stoller, Martin Marietta Energy Systems, Inc., Oak Ridge Natl. Lab., Oak Ridge, Tenn., *A Comparison of the Relative Importance of Copper Precipitates and Point Defects in Reactor Pressure Vessel Embrittlement*, USNRC Report NUREG/CR-6231 (ORNL/TM-6811), December 1994.

10. D. E. McCabe, R. K. Nanstad, S. K. Iskander, and R. L. Swain, Martin Marietta Energy Systems, Inc., Oak Ridge Natl. Lab., Oak Ridge, Tenn., *Unirradiated Material Properties of Midland Weld WF-70*, USNRC Report NUREG/CR-6249 (ORNL/TM-12777), October 1994.

11. P. M. Rice and R. E. Stoller, Lockheed Martin Energy Systems, Oak Ridge Natl. Lab., Oak Ridge, Tenn., *Microstructural Characterization of Selected AEA/UCSB Model FeCuMn Alloys*, USNRC Report NUREG/CR-6332 (ORNL/TM-12980), June 1996.

12. J. H. Giovanola and J. E. Crocker, SRI International, *Fracture Toughness Testing with Cracked Round Bars: Feasibility Study*, USNRC Report NUREG/CR-6342 (ORNL/SUB/94-DHK60), April 2000.

13. F. M. Haggag and R. K. Nanstad, Lockheed Martin Energy Systems, Oak Ridge Natl. Lab., Oak Ridge, Tenn., Effects of Thermal Aging and Neutron Irradiation on the Mechanical Properties of Three-Wire Stainless Steel Weld Overlay Cladding, USNRC Report NUREG/CR-6363 (ORNL/TM-13047), May 1997.

14. M. A. Sokolov and D. J. Alexander, Lockheed Martin Energy Systems, Oak Ridge Natl. Lab., Oak Ridge, Tenn., *An Improved Correlation Procedure for Subsize and Full-Size Charpy Impact Specimen Data*, USNRC Report NUREG/CR-6379 (ORNL/TM-13088), March 1997.

15. S. K. Iskander and R. E. Stoller, Lockheed Martin Energy Research Corporation, Oak Ridge Natl. Lab., Oak Ridge, Tenn., Results of Charpy V-Notch Impact Testing of Structural Steel Specimens Irradiated at ~30°C to 1×10^6 Neutrons/cm2 in a Commercial Reactor Cavity, USNRC Report NUREG/CR-6399 (ORNL-6886), April 1997.

16. S. K. Iskander, P. P. Milella, and A. Pini, Lockheed Martin Energy Research Corporation, Oak Ridge Natl. Lab., Oak Ridge, Tenn., *Results of Crack-Arrest Tests on Irradiated A 503 Class 3 Steel*, USNRC Report NUREG/CR-6447 (ORNL-6894), February 1998.

17. P. Pareige, K. F. Russell, R. E. Stoller, and M. K. Miller, Lockheed Martin Energy Research Corporation, Oak Ridge Natl. Lab., Oak Ridge, Tenn., *Influence of Long-Term Thermal Aging on the Microstructural Evolution of Nuclear Reactor Pressure Vessel Materials: An Atom Probe Study*, USNRC Report NUREG/CR-6537(ORNL-13406), March 1998.

18. I. Remec, C. A. Baldwin, and F. B. K. Kam, Lockheed Martin Energy Research Corporation, Oak Ridge Natl. Lab., Oak Ridge, Tenn., *Neutron Exposure Parameters for Capsule 10.05 in the Heavy-Section Steel Irradiation Program Tenth Irradiation Series*, USNRC Report NUREG/CR-6600 (ORNL/TM-13548), October 1998.

19. I. Remec, C. A. Baldwin, and F. B. K. Kam, Lockheed Martin Energy Research Corporation, Oak Ridge Natl. Lab., Oak Ridge, Tenn., *Neutron Exposure Parameters for the Dosimetry Capsule in the Heavy-Section Steel Irradiation Program Tenth Irradiation Series*, USNRC Report NUREG/CR-6601 (ORNL/TM-13549), October 1998.

20. D. E. McCabe, R. K. Nanstad, S. K. Iskander, D. W. Heatherly, and R. L. Swain, Lockheed Martin Energy Research Corporation, Oak Ridge Natl. Lab., Oak Ridge, Tenn., *Evaluation of WF-70 Weld Metal from the Midland Unit 1 Reactor Vessel—Final Report*, USNRC Report NUREG/CR-5736 (ORNL/TM-13748), November 2000.

21. Mikhail A. Sokolov and Randy K. Nanstad, Lockheed Martin Energy Research Corporation, Oak Ridge Natl. Lab., Oak Ridge, Tenn., *Comparison of Irradiation-Induced Shifts of K_{Jc} and Charpy*

Impact Toughness for Reactor Pressure Vessel Steels, USNRC Report NUREG/CR-6609 (ORNL/TM-13755), November 2000.

22. S. K. Iskander, C. A. Baldwin, D. W. Heatherly, D. E. McCabe, I. Remec, and R. L. Swain, UT-Battelle, LLC, Oak Ridge Nat'l. Lab., Oak Ridge, Tenn., *Detailed Results of Testing Unirradiated and Irradiated Crack-Arrest Toughness Specimens from the Low-Upper-Shelf-Energy, High-Copper Weld, WF-70*, USNRC Report NUREG/CR-6621 (ORNL/TM-13764), to be published (submitted July 2004).
23. D. J. Alexander, K. B. Alexander, M. K. Miller, and R. K. Nanstad, Lockheed Martin Energy Research Corporation, Oak Ridge Natl. Lab., Oak Ridge, Tenn., *The Effect of Aging at 343°C on the Microstructure and Mechanical Properties of Type 308 Stainless Steel Welds*, USNRC Report NUREG/CR-6628 (ORNL/TM-13767), November 2000.
24. M. K. Miller, P. Pariege, K. F. Russell, and R. E. Stoller, Lockheed Martin Energy Research Corporation, Oak Ridge Natl. Lab., Oak Ridge, Tenn., *An Atom Probe Tomography Characterization of the Solute Distributions in a Neutron Irradiated and Annealed Pressure Vessel Steel*, USNRC Report NUREG/CR-6629 (ORNL/TM-13768), November 2000.
25. I. Remec, C. A. Baldwin, and E. D. Blakeman, Lockheed Martin Energy Research Corporation, Oak Ridge Natl. Lab., Oak Ridge, Tenn., *Characterization of the Neutron Field in the HSSI/UCSB Irradiation Facility at the Ford Nuclear Reactor, USNRC Report NUREG/CR-6646* (ORNL/TM-1999/140), to be published (submitted September 1999).
26. P. M. Rice and R. E. Stoller, UT-Battelle, LLC, Oak Ridge Natl. Lab., Oak Ridge, Tenn., *Hardening Behavior of Ferritic Alloys at High Doses and After Thermal Aging*, USNRC Report NUREG/CR-6643 (ORNL/TM-1999/297), to be published (submitted August 2000).
27. S. K. Iskander, J. T. Hutton, L. E. Creech, M. Suzuki, K. Onizawa, E. T. Manneschmidt, R. K. Nanstad, T. M. Rosseel, and P. S. Bishop, UT-Battelle, LLC, Oak Ridge Natl. Lab., Oak Ridge, Tenn., *Attenuation of Charpy Impact Toughness Through the Thickness of a JPDR Pressure Vessel Weldment*, USNRC Report NUREG/CR-6709 (ORNL/TM-2000-343), to be published (submitted January 2001).
28. K. Onizawa, E. van Walle, W. Pavinich, and R. K. Nanstad, UT-Battelle, LLC, Oak Ridge Natl. Lab., Oak Ridge, Tenn., *Results and Analysis of The ASTM Round Robin On Reconstitution*, USNRC Report NUREG/CR-6777, (ORNL/TM-2001/34) August 2002.
29. D. W. Heatherly, K. R. Thoms, M. T. Hurst, and G. E. Giles, UT-Battelle, LLC, Oak Ridge Natl. Lab., Oak Ridge, Tenn., *Heavy-Section Steel Irradiation Program's Reusable Irradiation Facilities*, USNRC Report NUREG/CR-6779, (ORNL/TM-2002/77) to be published (submitted February 2002).
30. R. K. Nanstad and D. E. McCabe, UT-Battelle, LLC, Oak Ridge Natl. Lab., Oak Ridge, Tenn., Preliminary Evaluation of Precracked Charpy Specimens for Determining Fracture Toughness of Reactor Pressure Vessel Weldment, New Coordinated Research Program, USNRC Report NUREG/CR-XXXX (ORNL/TM-2001/YYY), to be published (submitted July 2001).
31. M. A. Sokolov, R. K. Nanstad, I. Remec, C. A. Baldwin, and R. L. Swain, UT-Battelle, LLC, Oak Ridge Natl. Lab., Oak Ridge, Tenn., *Fracture Toughness of an Irradiated, Highly Embrittled Reactor Pressure Vessel Weld*, USNRC Report NUREG/CR-XXXX (ORNL/TM-2002/293), to be published (submitted December 2003).
32. M. K. Miller et al., UT-Battelle, LLC, Oak Ridge Natl. Lab., Oak Ridge, Tenn., *APT Characterization of Highly Irradiated High-Nickel RPV Welds and Low-Upper-Shelf Midland Weld Materials*, USNRC Report NUREG/CR-XXXX, ORNL/TM-2006/531), to be published.

33. M. A. Sokolov et al., UT-Battelle, LLC, Oak Ridge Natl. Lab., Oak Ridge, Tenn., *The Effects of Radiation on Fracture Toughness Curve Shape on a Low-Upper-Shelf Weld*, USNRC Report NUREG/CR-XXXX, ORNL/TM-2006/532), to be published.

34. This report. E. D. Eason, M&CS; R. K. Nanstad, UT-Battelle, LLC, Oak Ridge Natl. Lab., Oak Ridge, Tenn; G. R. Odette, UCSB; and T. Yamamato, *A Physically Based Correlation of Irradiation-Induced Transition Temperature Shifts for RPV Steels,* USNRC Report NUREG/CR-XXXX, ORNL/TM-2006/530).

35. S. K. Iskander, R. K. Nanstad, C. A. Baldwin, D. W. Heatherly, M. K. Miller, and I. Remec, UT-Battelle, LLC, Oak Ridge Natl. Lab., Oak Ridge, Tenn., *Reirradiation Response of Irradiated and Thermally Treated Reactor Pressure Vessel Steels*, USNRC Report NUREG/CR-XXXX, ORNL/TM-2006/533), to be published.

A.2 Reports Related to Irradiation Effects in Pressure Vessel Materials and to the Properties of Unirradiated Materials Used in the HSSI and HSST Programs

C. E. Childress, Union Carbide Corp. Nuclear Div., Oak Ridge Natl. Lab., Oak Ridge, Tenn., Fabrication History of the First Two 12-in.-Thick A-533 Grade B, Class 1 Steel Plates of the Heavy-Section Steel Technology Program, ORNL-4313, February 1969.

T. R. Mager and F. O. Thomas, Westinghouse Electric Corporation, PWR Systems Division, Pittsburgh, Pa., *Evaluation by Linear Elastic Fracture Mechanics of Radiation Damage to Pressure Vessel Steels*, WCAP-7328 (Rev.), October 1969.

P. N. Randall, TRW Systems Group, Redondo Beach, Calif., *Gross Strain Measure of Fracture Toughness of Steels*, HSSTP-TR-3, Nov. 1, 1969.

L. W. Loechel, Martin Marietta Corporation, Denver, Colo., *The Effect of Testing Variables on the Transition Temperature in Steel*, MCR-69-189, Nov. 20, 1969.

W. O. Shabbits, W. H. Pryle, and E. T. Wessel, Westinghouse Electric Corporation, PWR Systems Division, Pittsburgh, Pa., *Heavy-Section Fracture Toughness Properties of A533 Grade B Class 1 Steel Plate and Submerged Arc Weldment*, WCAP-7414, December 1969.

C. E. Childress, Union Carbide Corp. Nuclear Div., Oak Ridge Natl. Lab., Oak Ridge, Tenn., *Fabrication History of the Third and Fourth ASTM A-533 Steel Plates of the Heavy-Section Steel Technology Program*, ORNL-4313-2, February 1970.

P. B. Crosley and E. J. Ripling, Materials Research Laboratory, Inc., Glenwood, Ill., *Crack Arrest Fracture Toughness of A533 Grade B Class 1 Pressure Vessel Steel*, HSSTP-TR-8, March 1970.

F. J. Loss, Naval Research Laboratory, Washington, D.C., Dynamic *Tear Test Investigations of the Fracture Toughness of Thick-Section Steel*, NRL-7056, May 14, 1970.

T. R. Mager, Westinghouse Electric Corporation, PWR Systems Division, Pittsburgh, Pa., *Post-Irradiation Testing of 2T Compact Tension Specimens*, WCAP-7561, August 1970.

F. J. Witt and R. G. Berggren, Union Carbide Corp. Nuclear Div., Oak Ridge Natl. Lab., Oak Ridge, Tenn., *Size Effects and Energy Disposition in Impact Specimen Testing of ASTM A533 Grade B Steel*, ORNL/TM-3030, August 1970.

D. A. Canonico, Union Carbide Corp. Nuclear Div., Oak Ridge Natl. Lab., Oak Ridge, Tenn., *Transition Temperature Considerations for Thick-Wall Nuclear Pressure Vessels*, ORNL/TM-3114, October 1970.

T. R. Mager, Westinghouse Electric Corporation, PWR Systems Division, Pittsburgh, Pa., *Fracture Toughness Characterization Study of A533, Grade B, Class 1 Steel*, WCAP-7578, October 1970.

W. O. Shabbits, Westinghouse Electric Corporation, PWR Systems Division, Pittsburgh, Pa., *Dynamic Fracture Toughness Properties of Heavy-Section A533 Grade B Class 1 Steel Plate*, WCAP-7623, December 1970.

C. E. Childress, Union Carbide Corp. Nuclear Div., Oak Ridge Natl. Lab., Oak Ridge, Tenn., Fabrication Procedures and Acceptance Data for ASTM A-533 Welds and a 10-in.-Thick ASTM A-543 Plate of the Heavy Section Steel Technology Program, ORNL-TM-4313-3, January 1971.

D. A. Canonico and R. G. Berggren, Union Carbide Corp. Nuclear Div., Oak Ridge Natl. Lab., Oak Ridge, Tenn., *Tensile and Impact Properties of Thick-Section Plate and Weldments*, ORNL/TM-3211, January 1971.

C. W. Hunter and J. A. Williams, Hanford Eng. Dev. Lab., Richland, Wash., *Fracture and Tensile Behavior of Neutron-Irradiated A533-B Pressure Vessel Steel*, HEDL-TME-71-76, Feb. 6, 1971.

C. E. Childress, Union Carbide Corp. Nuclear Div., Oak Ridge Natl. Lab., Oak Ridge, Tenn., *Manual for ASTM A533 Grade B Class 1 Steel (HSST Plate 03) Provided to the International Atomic Energy Agency*, ORNL/TM-3193, March 1971.

P. N. Randall, TRW Systems Group, Redondo Beach, Calif., *Gross Strain Crack Tolerance of A533-B Steel*, HSSTP-TR-14, May 1, 1971.

C. L. Segaser, Union Carbide Corp. Nuclear Div., Oak Ridge Natl. Lab., Oak Ridge, Tenn., Feasibility Study, Irradiation of Heavy-Section Steel Specimens in the South Test Facility of the Oak Ridge Research Reactor, ORNL/TM-3234, May 1971.

H. T. Corten and R. H. Sailors, University of Illinois, Urbana, Ill., Relationship Between Material Fracture Toughness Using Fracture Mechanics and Transition Temperature Tests, T&AM Report 346, Aug. 1, 1971.

L. A. James and J. A. Williams, Hanford Eng. Dev. Lab., Richland, Wash., Heavy Section Steel Technology Program Technical Report No. 21, The Effect of Temperature and Neutron Irradiation Upon the Fatigue-Crack Propagation Behavior of ASTM A533 Grade B, Class 1 Steel, HEDL-TME 72-132, September 1972.

P. B. Crosley and E. J. Ripling, Materials Research Laboratory, Inc., Glenwood, Ill., *Crack Arrest in an Increasing K-Field*, HSSTP-TR-27, January 1973.

W. J. Stelzman and R. G. Berggren, Union Carbide Corp. Nuclear Div., Oak Ridge Natl. Lab., Oak Ridge, Tenn., *Radiation Strengthening and Embrittlement in Heavy-Section Steel Plates and Welds*, ORNL-4871, June 1973.

J. M. Steichen and J. A. Williams, Hanford Eng. Dev. Lab., Richland, Wash., *High Strain Rate Tensile Properties of Irradiated ASTM A533 Grade B Class 1 Pressure Vessel Steel*, HEDL-TME 73-74, July 1973.

J. A. Williams, Hanford Eng. Dev. Lab., Richland, Wash., The Irradiation and Temperature Dependence of Tensile and Fracture Properties of ASTM A533, Grade B, Class 1 Steel Plate and Weldment, HEDL-TME 73-75, August 1973.

J. A. Williams, Hanford Eng. Dev. Lab., Richland, Wash., Some Comments Related to the Effect of Rate on the Fracture Toughness of Irradiated ASTM A553-B Steel Based on Yield Strength Behavior, HEDL-SA 797, December 1974.

J. A. Williams, Hanford Eng. Dev. Lab., Richland, Wash., The Irradiated Fracture Toughness of ASTM A533, Grade B, Class 1 Steel Measured with a Four-Inch-Thick Compact Tension Specimen, HEDL-TME 75-10, January 1975.

J. G. Merkle, G. D. Whitman, and R. H. Bryan, Union Carbide Corp. Nuclear Div., Oak Ridge Natl. Lab., Oak Ridge, Tenn., *An Evaluation of the HSST Program Intermediate Pressure Vessel Tests in Terms of Light-Water-Reactor Pressure Vessel Safety*, ORNL/TM-5090, November 1975.

J. A. Davidson, L. J. Ceschini, R. P. Shogan, and G. V. Rao, Westinghouse Electric Corporation, Pittsburgh, Pa., *The Irradiated Dynamic Fracture Toughness of ASTM A533, Grade B, Class 1 Steel Plate and Submerged Arc Weldment,* WCAP-8775, October 1976.

J. A. Williams, Hanford Eng. Dev. Lab., Richland, Wash., *Tensile Properties of Irradiated and Unirradiated Welds of A533 Steel Plate and A508 Forgings*, NUREG/CR-1158 (ORNL/SUB-79/50917/2), July 1979.

J. A. Williams, Hanford Eng. Dev. Lab., Richland, Wash., T*he Ductile Fracture Toughness of Heavy-Section Steel Plate*, NUREG/CR-0859, September 1979.

K. W. Carlson and J. A. Williams, Hanford Eng. Dev. Lab., Richland, Wash., *The Effect of Crack Length and Side Grooves on the Ductile Fracture Toughness Properties of ASTM A533 Steel*, NUREG/CR-1171 (ORNL/SUB-79/50917/3), October 1979.

G. A. Clarke, Westinghouse Electric Corp., Pittsburgh, Pa., *An Evaluation of the Unloading Compliance Procedure for J-Integral Testing in the Hot Cell, Final Report*, NUREG/CR-1070 (ORNL/SUB-7394/1), October 1979.

P. B. Crosley and E. J. Ripling, Materials Research Laboratory, Inc., Glenwood, Ill., *Development of a Standard Test for Measuring KIa with a Modified Compact Specimen*, NUREG/CR-2294 (ORNL/SUB-81/7755/1), August 1981.

H. A. Domian, Babcock and Wilcox Company, Alliance, Ohio, *Vessel V-8 Repair and Preparation of Low Upper-Shelf Weldment*, NUREG/CR-2676 (ORNL/SUB/81-85813/1), June 1982.

R. D. Cheverton, S. K. Iskander, and D. G. Ball, Union Carbide Corp. Nuclear Div., Oak Ridge Natl. Lab., Oak Ridge, Tenn., *PWR Pressure Vessel Integrity During Overcooling Accidents: A Parametric Analysis*, NUREG/CR-2895 (ORNL/TM-7931), February 1983.

J. G. Merkle, Union Carbide Corp. Nuclear Div., Oak Ridge Natl. Lab., Oak Ridge, Tenn., *An Examination of the Size Effects and Data Scatter Observed in Small Specimen Cleavage Fracture Toughness Testing*, NUREG/CR-3672 (ORNL/TM-9088), April 1984.

W. R. Corwin, Martin Marietta Energy Systems, Inc., Oak Ridge Natl. Lab., Oak Ridge, Tenn., *Assessment of Radiation Effects Relating to Reactor Pressure Vessel Cladding*, NUREG/CR-3671 (ORNL-6047), July 1984.

W. R. Corwin, R. G. Berggren, and R. K. Nanstad, Martin Marietta Energy Systems, Inc., Oak Ridge Natl. Lab., Oak Ridge, Tenn., *Charpy Toughness and Tensile Properties of a Neutron Irradiated Stainless Steel Submerged-Arc Weld Cladding Overlay*, NUREG/CR-3927 (ORNL/TM-9709), September 1984.

J. J. McGowan, Martin Marietta Energy Systems, Inc., Oak Ridge Natl. Lab., Oak Ridge, Tenn., *Tensile Properties of Irradiated Nuclear Grade Pressure Vessel Plate and Welds for the Fourth HSST Irradiation Series*, NUREG/CR-3978 (ORNL/TM-9516), January 1985.

J. J. McGowan, Martin Marietta Energy Systems, Inc., Oak Ridge Natl. Lab., Oak Ridge, Tenn., *Tensile Properties of Irradiated Nuclear Grade Pressure Vessel Welds for the Third HSST Irradiation Series*, NUREG/CR-4086 (ORNL/TM-9477), March 1985.

W. R. Corwin, G. C. Robinson, R. K. Nanstad, J. G. Merkle, R. G. Berggren, G. M. Goodwin, R. L. Swain, and T. D. Owings, Martin Marietta Energy Systems, Inc., Oak Ridge Natl. Lab., Oak Ridge, Tenn., *Effects of Stainless Steel Weld Overlay Cladding on the Structural Integrity of Flawed Steel Plates in Bending, Series 1*, NUREG/CR-4015 (ORNL/TM-9390), April 1985.

W. J. Stelzman, R. G. Berggren, and T. N. Jones, Martin Marietta Energy Systems, Inc., Oak Ridge Natl. Lab., Oak Ridge, Tenn., *ORNL Characterization of Heavy-Section Steel Technology Program Plates 01, 02, and 03*, NUREG/CR-4092 (ORNL/TM-9491), April 1985.

G. D. Whitman, Martin Marietta Energy Systems, Inc., Oak Ridge Natl. Lab., Oak Ridge, Tenn., Historical Summary of the Heavy-Section Steel Technology Program and Some Related Activities in Light-Water Reactor Pressure Vessel Safety Research, NUREG/CR-4489 (ORNL-6259), March 1986.

R. H. Bryan, B. R. Bass, S. E. Bolt, J. W. Bryson, J. G. Merkle, R. K. Nanstad, and G. C. Robinson, Martin Marietta Energy Systems, Inc., Oak Ridge Natl. Lab., Oak Ridge, Tenn., *Test of 6-in.-Thick Pressure Vessels. Series 3: Intermediate Test Vessel V-8A - Tearing Behavior of Low Upper-Shelf Material*, NUREG-CR-4760 (ORNL-6187), May 1987.

D. B. Barker, R. Chona, W. L. Fourney, and G. R. Irwin, University of Maryland, College Park, Md., A Report on the Round Robin Program Conducted to Evaluate the Proposed ASTM Standard Test Method for Determining the Plane Strain Crack Arrest Fracture Toughness, K_{Ia}, of Ferritic Materials, NUREG/CR-4966 (ORNL/SUB/79-7778/4), January 1988.

L. F. Miller, C. A. Baldwin, F. W. Stallman, and F. B. K. Kam, Martin Marietta Energy Systems, Inc., Oak Ridge Natl. Lab., Oak Ridge, Tenn., *Neutron Exposure Parameters for the Metallurgical Test Specimens in the Fifth Heavy-Section Steel Technology Irradiation Series Capsules*, NUREG/CR-5019 (ORNL/TM-10582), March 1988.

J. J. McGowan, R. K. Nanstad, and K. R. Thoms, Martin Marietta Energy Systems, Inc., Oak Ridge Natl. Lab., Oak Ridge, Tenn., Characterization of Irradiated Current-Practice Welds and A533 Grade B Class 1 Plate for Nuclear Pressure Vessel Service, NUREG/CR-4880 (ORNL-6484/V1 and V2), July 1988.

R. D. Cheverton, W. E. Pennell, G. C. Robinson, and R. K. Nanstad, Martin Marietta Energy Systems, Inc., Oak Ridge Natl. Lab., Oak Ridge, Tenn., *Impact of Radiation Embrittlement on Integrity of Pressure Vessel Supports for Two PWR Plants*, NUREG/CR-5320 (ORNL/TM-10966), February 1989.

J. G. Merkle, Martin Marietta Energy Systems, Inc., Oak Ridge Natl. Lab., Oak Ridge, Tenn., *An Overview of the Low-Upper-Shelf Toughness Safety Margin Issue*, NUREG/CR-5552 (ORNL/TM-11314), August 1990.

R. D. Cheverton, T. L. Dickson, J. G. Merkle, and R. K. Nanstad, Martin Marietta Energy Systems, Inc., Oak Ridge Natl. Lab., Oak Ridge, Tenn., *Review of Reactor Pressure Vessel Evaluation Report for Yankee Rowe Nuclear Power Station (YAEC No. 1735)*, NUREG/CR-5799 (ORNL/TM-11982), March 1992.

Appendix B. Irradiation Variable (IVAR) Program Data Base

Irradiation Variable (IVAR) program test reactor data, as described in Chap. 6, is collected in the IVAR Data Base (filename IVAR_database.doc).

The compact disc included in the pocket on the back cover of this report contains a copy of the IVAR Data Base, along with the Analysis Data Base (See Appendix C) and a pdf version of this report.

All three files are transmitted together if sent electronically.

Appendix C. Analysis Data Base

The complete surveillance data base used for the modeling and analysis, as described in Chap. 3 of this report, is TTSDatabase8-04R1.xls, a file in Microsoft Excel format.

The compact disc included in the pocket on the back cover of this report contains a copy of TTSDatabase8-04R1.xls, along with the IVAR Data Base (See Appendix B) and a pdf version of this report.

All three files are transmitted together if sent electronically.

Appendix D. Explanations of the Specialized Terms and Parameters Used in Chapters 2 and 6

D.1 Terms related to radiation damage production, point defects and defect clusters

Cascade: The small (several tens of nm) region of the crystal lattice where the primary and secondary recoiling atoms slow down and initially produce a dense concentration of vacancies and self interstitial atom (SIA) and small clusters of these defects.

Cascade aging: The spatially correlated rearrangement of the cascade over the period of time from about 100 ps up to a gs, involving additional recombination and clustering of vacancies, SIA and solutes. The residual SIA and SIA clusters quickly leave the cascade region. The vacancy clusters coarsen and form complexes with solutes. However, the vacancy clusters eventually dissolve leaving behind solute cluster remnants that can be very stable, and can even grow by the long-range diffusion of additional solutes. The solute clusters may be somewhat diffuse relative to well-formed precipitates. Vacancy cluster solute complexes and their solute remnants are believed to be one of the primary matrix features that contribute to hardening in both low Cu and Cu-bearing steels.

Dislocation loop: A dislocation line that closes on itself to form a nearly circular loop; a prismatic loop is composed of edge dislocation segments.

Displacements-per-atom (dpa, nd): A measure of the neutron damage dose that represents the computed fraction of atoms that have been displaced from their atomic lattice positions. Also, in ASTM E 170: the mean number of times each atom of a solid is displaced from its lattice site during an exposure to displacing radiation, as calculated following standard procedures.

Fraction of vacancies that recombine and the fraction that escape recombination to reach sinks (g_r and g_s, nd): The fraction of vacancies that recombine versus vacancies that escape recombination during long range diffusion and annihilate at sinks thus determining the steady-state vacancy concentration

Frenkel pair: The SIA and vacancy produced by an atomic displacement event.

Primary recoiling atom (PRA): The high-energy ionized atom that is created by interactions between neutrons and the atomic nucleus that slows down by collisions with other atoms and with electrons. The multiplying chain reaction atomic collisions continue until the n'th generation of collided atoms has insufficient energy to create additional displaced atoms.

Cascade recombination: The reaction between a vacancy and SIA in a displacement cascade that annihilates both defects, thus healing the crystal lattice. Cascade recombination rapidly annihilates about 60 to 70 percent of the vacancies SIA created by atomic displacements.

Self-interstitial atom (SIA): Two atoms sharing a single crystal lattice site

SIA clusters: Two-dimensional platelet shaped aggregates of SIA that are equivalent to a prismatic dislocation loop.

Vacancy: A crystal lattice site that is missing an atom.

Vacancy production cross-section (σ_v, vacancies-m^2/atom): The effective area per atom for a neutron to produce a vacancy that, when multiplied by neutron flux (ϕ, n/m^2-s), gives the generation rate per lattice

site of creating vacancies, G_v (atom fraction of vacancies created/s). The rate of creating SIA, G_i, is the same as that for vacancies.

Vacancy cluster: Compact spherical or polyhedral three-dimensional aggregates of vacancies

Vacancy-solute cluster complex: A vacancy cluster with solutes segregated to and near the surface. These features form in aged cascades.

D.2 Terms related to irradiation-induced changes in the yield stress, $\Delta\sigma_y$ (MPa), and transition temperature shifts, TTS (°C).

Critical stress for cleavage fracture (σ^*, MPa): The internal tensile stress near the tip of a notch or crack required to initiate cleavage fracture. In the case of Charpy tests, σ^* has generally been found to be independent of temperature and irradiation.

Dislocations and dislocation density (ρ, m^{-2}): Line defects that glide to propagate slip between atomic planes at a critical value of a resolved shear stress. Dislocations also serve as sinks for SIA and vacancies, especially at jogs which are short dislocation segments connecting longer dislocation segments that do not lie entirely in the same glide plane. The dislocation density, ρ, is the total length of dislocations per unit volume.

Dislocation Burger's vector (b m or nm, 0.248 nm): The close packed spacing in the ferrite lattice that defines the unit distance of slip.

Elastic shear modulus of Fe (μ, 80 GPa)

Obstacle strength parameters α_i (nd): The numerical coefficient ($\leq$1) that characterizes the strength of the i'th-type obstacle for retarding the glide of dislocations. Obstacles are classified as being weak (w), medium strength (m) or strong (o).

Orowon obstacle: A strong obstacle to dislocation glide, with α_o up to 1, which is bypassed by a dislocation looping around, rather than shearing through, the feature. Fine scale Mo_2C precipitates in low alloy steels are Orowon obstacles.

Parameters that characterize irradiation induced features - f_i (nd), N_i ($/m^3$), r_i (m or nm): The volume fraction, number density and radius of feature i that retards dislocation glide and increases the critical resolved shear stress

Superposition and the superposition parameter (S, nd): The method used to combine the strengthening contributions from various obstacles to dislocation slip needed to predict the total σ_y and $\Delta\sigma_y$. Superposition can be modeled by a superposition parameter, S, that depends on the strengths (α_i) of the different obstacles. The limiting superposition laws are linear sum (LS) and root sum of the squares (RSS) combinations of the individual contributions, σ_{yi}. The S parameter can be used along with the medium strength *(σ_{ym})* and strong *(σ_{yo})* obstacle yield stress contributions to interpolate between LS and RSS laws to determine the net σ_y and $\Delta\sigma_y$. The yield stress contribution from weak obstacles follows the LS law.

Taylor factor (nd, T $\approx$ 3): The factor that relates the critical resolved shear stress to the uniaxial yield stress.

Maximum elastic fracture temperature TT_{10} and TTS_{10} shifts [TTS_{10} = TT_{10i} (irradiated) - TT_{10u} (unirradiated), °C]: The highest temperature at which Charpy specimens undergo cleavage fracture in the linear elastic loading regime, prior to plastic yielding. This also marks the highest elastic load. At higher temperatures, if cleavage occurs, it is only after general plastic yielding. At lower temperatures the fracture is in the linear elastic regime, but occurs at a lower load compared to that at TT_{10}. The TT_{10} condition typically occurs at about 10J of absorbed energy. Irradiation hardening increases TT_{10}, and TTS_{10} can be related to the temperature dependence of $\sigma_y(T)$.

TTS due to the irradiation induced reduction in the Charpy upper shelf energy (TTS_{use}, °C): Irradiation induced decreases in the Charpy upper shelf energy (*ΔUSE*) lead to reductions in the slope of the energy-temperature curve. This adds an increment of TTS_{use} to the TTS_{10} in the TTS at 41 J. The ΔUSE can be correlated with $\Delta\sigma_y$ and TTS_{use} from the observation that the lower-to-upper shelf transition occurs over an approximately constant temperature interval.

TTS to $\Delta\sigma_y$ ratio (C_c, °C/MPa): The overall coefficient relating TTS to $\Delta\sigma_y$. C_c can be predicted by semi-empirical models (Chap. 2) and represented by a polynomial with coefficients (C_0, C_1, C_2,..) fitted to pairs of TTS-$\Delta\sigma_y$ data (Chap. 6).

D.3 Terms related to the concentrations and diffusion of solutes and defects and the annihilation of defects by sinks.

Atomic volume of Cu and Fe atoms (v_{cu} and v_{fe}, m^3): Volume occupied by a Cu or Fe atom ≈ $1.18\text{x}10^{-29}$ and ≈ $1.15\text{x}10^{-29}$ m^3, respectively.

Chemical Cu diffusion coefficient (D_{cu} or D_{Cu}, m^2/s): The diffusion coefficient for Cu (and other solutes) that accounts for the effects of both finite concentrations of multiple alloying elements and the non-ideal solution behavior of the diffusing species. The effects of solutes on diffusion are due to their corresponding effect of solute j on vacancy concentrations and various atomic jump frequencies and can be approximately characterized by a factor ($1 + X_j b_j$) that multiplies the by the intrinsic diffusion coefficient. The effects of non-ideality are represented by the solution thermodynamic factor (TDF) that also multiplies the solute modified diffusion coefficient.

Weight fraction concentration of species i, (C_i , wt %): The weight fraction of the species in %.

Atomic fraction concentration of species i, (X_i, atom fraction): The atomic fraction of the species. The species include solutes, vacancies, SIA and solute vacancy traps that can have units of the absolute atom fraction, %, or atomic parts per million (appm).

Concentration of vacancies under irradiation (X_v, nd): The excess steady-state fractional concentration of vacancies that just balances vacancy production by displacements and their annihilation at sinks.

Effective fluence (ϕt_e, n/m^2): The actual fluence adjusted for dose rate effects at a flux, ϕ, different than a specified reference flux, ϕ_r. The choice of ϕ_r is arbitrary. However, once ϕ_r is selected, the effective fluence at other fluxes can by determined by a scaling relation in the form $\phi t_e = (\phi_r/\phi)^p$ (see next definition for exponent p).

Effective fluence scaling exponent (p, nd): The exponent ($p \leq 1$) that scales the actual to effective fluence. The value of p depends of the flux, reference flux, irradiation temperature and the alloy composition and microstructure. However, in fitting the TTS model to the surveillance database it is assumed that p is an average constant.

Equilibrium concentration of vacancies (X_{ve}, nd): The concentration of vacancies in the absence of irradiation.

Intrinsic Cu tracer diffusion coefficient (D_{cu} or D_{Cu}, m^2/s): The coefficient for the diffusion of Cu (and other solutes) at very low concentrations.

Molar volume of Cu (V_{cu}, $m^3/mole$): Volume occupied by a $6.02x10^{23}$ of Cu atoms ≈ $7.15x10^{-6}$ m^3/mole.

Radiation enhanced Cu diffusion (RED) and the RED diffusion coefficient (D, m^2/s):* The enhancement of the diffusion rate of Cu (and other solutes) due to the excess concentration of vacancies under irradiation, that is characterized by a RED coefficient D*.

RED factor (K, m^4): The factor that when multiplied by flux gives the enhancement term for Cu (and other solute) diffusion under irradiation that adds to the thermal Cu coefficient of Cu, D_{cu}.

Ratio of the Cu to self-diffusion coefficient [D_{cu}/D_{sd}, nd]: The diffusion coefficients of solutes, such as Cu, are generally not the same as those for the self-diffusion of matrix (Fe) atoms. The corresponding ratio [D_{cu}/D_{sd}] is much less temperature dependent than D_{cu}, and when multiplied by the irradiation enhanced self-diffusion coefficient, which can be estimated with some accuracy, provides a good means to model D* at low temperatures.

Lattice recombination and recombination coefficient (R, nd): The reaction between a vacancy and SIA during long-range diffusion that annihilates both defects, thus healing the crystal lattice, where R is characterized by a recombination radius *(r_r, nm)*, D_v, D_i and the atomic volume of Fe, v_{fe}.

Molar volume of Cu (V_{cu}, $m^3/mole$): Volume occupied by a $6.02x10^{23}$ of Cu atoms.

Self-diffusion coefficient (D_{sd}, m^2/s): The diffusion coefficient for an Fe atom in the ferrite matrix.

Vacancy and SIA sinks and sink strength (S_t, m^{-2}): A site where SIA and vacancy defects lose their individual identity (are annihilated). The total sink strength, S_t, is used in defect conservation equations. Dislocations are the primary defect sinks in RPV steels, and S_t is often approximated as the total dislocation density, ρ.

Vacancy and SAI diffusion coefficients (D_v and D_i, m^2/s): The diffusion coefficients for thermally activated migration of vacancies and SIA that control the steady state concentration of these species that balances their production, recombination and annihilation rates. Within the framework of the rate theory models described in Chapter 2, for technical reasons it is not necessary to know D_i, which is much higher than D_v.

Solute vacancy trapping energy (X_t and H_t, kJ/mole): The trap concentration (X_t) and binding energy (H_t) between a vacancy and a solute atom trap, that adds to the activation energy for the jumps of vacancies between lattice sites.

Substitutional solute: A solute that replaces an Fe atom on a crystal lattice site.

Spherical cluster sink strength (S_s, m^{-2}): The sink strength for a dilute concentration of spherical sinks rate $S_s \approx 4\pi r_s N_s$. Note features that act as sinks can also act as sources by emitting vacancies or solutes at a rate proportional to the sink strength

D.4 Terms related to irradiation induced features and their evolution under irradiation as well as fitting the IVAR $\Delta\sigma_y$ Data

Activity (a_{ij}, nd) and activity coefficient Γ_{ij} (nd) of a element i in phase j: The activity, a_{ij}, of an element in solution is a measure of its effective thermodynamic concentration relative to its actual concentration as described by the activity coefficient $\Gamma_{ij} = a_{ij}/X_{ij}$ that can be related to the solutes enthalpy of solution, H_{ij}.

Avrami transformation equation: A simple representation of the ϕt (or time) dependence of precipitate volume fraction *(f_p)* and precipitate hardening $\Delta\sigma_{yp}$ that varies between 0 and 100% of the maximum values of f_{pm} and $\Delta\sigma_{ypm}$. The parameters in Avrami model used to fit the IVAR $\Delta\sigma_y$ data are $\Delta\sigma_{ypm}$, ϕt_e at 63% precipitation and maximum hardening, p that scales the effective fluence, ϕt_e and β that sets the ϕt_e interval for the transformation.

Chemistry factor for matrix features [CF, MPa/$\sqrt{(10^{23}$ n/m^2)]: The composition dependent coefficient for matrix feature hardening that multiplies the square root of the fluence (or effective fluence) in fitting the low Cu IVAR data.

Coherency misfit strain parameter ($\delta \approx 0.03$, nd): The ratio of the difference between the lattice parameters for Cu and Fe divided by the lattice parameter of Fe.

Cluster dynamics models are based on the rates of absorbing and emitting Cu by CRP clusters of size n up to a maximum n_{max} [β(n) and α(n), number/cluster-s]: In the simplest cluster dynamics models of nucleation, growth and coarsening, CRPs (and MNPs) simultaneously dissolve by emitting [α(n)] and grow by absorbing [β(n)] mobile Cu atoms (n = 1), and other solute atoms, respectively.

Cu in equilibrium with CRP with a radius r_p (X_{cur}, nd): The solubility of Cu is higher for small precipitates due to the interface (Gibbs-Thompson effect) and misfit strain energies, as well as the bcc vs fcc crystal structure.

Cu rich precipitates (CRPs): Coherent bcc phases of Cu alloyed with varying amounts of Mn, Ni, Si and P with a fraction of Cu in the precipitate, $X_{cup} \geq 0.5$.

Cu supersaturation (SS, nd): The ratio of the Cu in solution, X_{cu}, to the equilibrium solubility of Cu, X_{cue}.

Effective fluence factor (M_ϕ, nd): The flux dependent factor that multiplies the actual fluence to determine the effective fluence, normalized to 1 at a reference flux. M_ϕ provides a convenient basis to compare different models of flux effects.

Enthalpy of solution of solute i (H_i, kJ/mole): The thermodynamic parameter that governs the activity and solubility limit of a solute.

Equilibrium solubility of Cu (X_{cue}, nd): The solubility limit of Cu in equilibrium with nearly pure bcc Cu phase.

Fitted recombination model (FRM): The Avrami effective fluence model fit to IVAR $\Delta\sigma_y$ data to optimize the parameters β, ϕt_{et}, $\Delta\sigma_{ypm}$ and p for individual alloys.

Fluence at 50% of the maximum CRP hardening ($\phi t_{0.5}$, 10^{23}n/m^2): The fluence at $\Delta\sigma_{ypm}/2$.

Irradiation temperature coefficient (C_T, $°C^{-1}$): The temperature sensitivity coefficient in a function $\Delta\sigma_y(T_i) = \Delta\sigma_y(290)[1 - C_T(T_i - 290)]$.

Late blooming phases (LBPs): Mn, Ni, Si, P phases (MNPs) that form in low or Cu free RPV steels that contain little or no Cu. The LBP nucleation rate is low compared to those for CRPs and MNPs with significant contents of Cu.

Manganese-nickel rich precipitates (MNPs): Coherent bcc phases of Mn, Ni, Cu and P with a fraction of Cu in the precipitate, $X_{cup} < 0.5$.

Matrix Features (MF): MF are defined as the obstacles to dislocation slip that form in both low Cu and Cu-bearing steels. Possible MF include dislocation loops, dislocation solute atmospheres, phosphide precipitates (PP, separately defined) and especially vacancy cluster solute complexes and their solute cluster remnants.

Nucleation barrier: Below a critical size Cu clusters shrink faster than they grow, so CRPs (and other phases) must nucleate by statistical fluctuations. The rate of nucleation can be described by equations containing a pseudo activation energy barrier or directly simulated using cluster dynamics models.

Particle matrix interface energy (γ_{pm}, J/m^2): The energy of the generally coherent interface separating CRPs and MNPs from the Fe matrix. The γ_{pm} depends on the composition of the precipitate.

Precipitate volume fraction and maximum volume fraction (f_p and f_{pm}, nd): The volumetric fraction of precipitates up to a solute (Cu) limited maximum.

Phosphide precipitates (PP): Solute atom-P precipitates such as Mn_2P and Mn_3P.

D.5 Terms related to experimental facilities and characterization methods

Irradiation variable facility (IVAR): The facility at the University of Michigan Ford Research Reactor that was used to irradiate specimens that were tested to produce the IVAR database. The IVAR facility had three temperature zones in each of three flux regimes. The facility had 54 locations for subcapsules that were inserted and removed during reactor shutdown periods. Each subcapsule held up to several hundred specimens.

Resistivity-Seebeck coefficient characterization (RSC): Dissolved solutes contribute to the electrical resistivity and Seebeck coefficient of an alloy. The effects of an individual element, i, can be represented by individual coefficients k_i and κ_i for the resistivity and Seebeck coefficient, respectively. Clustering and precipitation removes solutes from solution and, thus, results in changes in the resistivity ($\Delta\rho$) and Seebeck (ΔS) coefficient. The k_i and κ_i can be used along with the measured $\Delta\rho$ and ΔS to estimate the total amount of precipitation.

Model Alloys: Simple Fe-Mn-Ni-P-… ferritic alloys used to study embrittlement mechanisms.

Small angle neutron scattering characterization (SANS): Small microstructural features, like CRPs, produce scatter of a well-collimated cold neutron beam at small angles. The scattering intensity as a function of both the scattering angle and the angle from the direction of a strong imposed magnetic field is reduced to magnetic and nuclear scattering cross sections. These scattering cross sections are analyzed to provide CRP (and MNP) r_p, N_p and f_p parameters, as well as estimates of the CRP (and MNP)

composition. MF can also be detected by SANS in some cases, but generally produce only weak scattering. Well defined PPs and LBP MNPs can also be characterized by SANS.

Split melt model steels (SMMS): Special small melt heats of low alloy steels with controlled variations in combinations of Cu, Ni, Mn, P and other minor elements heat treated to produce mechanical properties and microstructures very similar to RPV plates.

Appendix E. Points Excluded from Fitting Sets

Twelve points were removed from the database during the model development process, as listed by group below.

E.1 Low Cu Chauvenet Outliers

See the description of Chauvenet outlier analysis in the Introduction for information on this analysis technique.

- Heat FGIN02, plant Ginna, forging in capsule T (1 point),
- Heat WFA201, plant Farley 2, weld in capsules X and Z (2 points),
- Heat WCL101, plant Callaway 1, weld in capsule U (1 point)

The above four points were identified as Chauvenet outliers during preliminary low-Cu modeling and remained Chauvenet outliers relative to the revised model. FGIN02 has the largest recorded negative shift (–35°F) in all the PWR data (the physical impossibility of such a large negative shift suggests a possibly incorrect value of unirradiated T_{30}), and WFA201 has the lowest recorded Mo of all materials in the database (the Mo value was checked by a member of ASTM E10.02 and is believed to be correct).

E.2 High-Cu Chauvenet Outliers

- Heat PBR_01, plant Big Rock Point, plate in capsule 124 (1 point)

This is one of the atypical BWR points, with the highest flux, fluence, and temperature of all data in the database (1.63×10^{12} n/cm^2/s flux, 1.07×10^{20} n/cm^2 fluence, 570°F). It was found to be a Chauvenet outlier in the preliminary amplitude study of high-Cu, high-fluence ($> 2 \times 10^{19}$ n/cm^2) data and was excluded from further consideration. It could also be excluded on the basis of its unusual irradiation, which is well beyond the flux and fluence values expected in applications, so it is listed below as well.

The four Chauvenet outliers identified in the NUREG/CR-6551 [1] and July 2000 [2] modeling efforts remained outliers relative to the revised model:

- Heat WCK101, plant Cook 1, weld in capsules U and T (2 points)
- Heat WSQ201, plant Sequoyah 2, weld in capsule U (1 point)
- Heat WTM201, plant Surry 2, weld in capsule W1 (1 point)

E.3 Unusual Irradiations

Three points in the high-Cu subset were excluded from the modeling sets because they were irradiated in two reactors at substantially different irradiation temperatures (T_i) or in both a PWR and a BWR reactor at different flux values. Since the damage accumulation varies with T_i and flux, representative values of T_i and flux for these three points were considered more uncertain than usual:

- Heat PMON01, plants Monticello (BWR) and Prairie Island 1(PWR), plate in capsule W
- Heat WTP301, plants Turkey Point 3 and Davis Besse 1, weld in capsules V and A5
- Heat WZN101, plants Zion 1 and Davis Besse 1, weld in capsules Y and A5

Other points irradiated in two reactors were left in the modeling datasets if the reactors were of like kind and similar T_i. Where small T_i variations occurred during irradiation, usually due to operating condition changes, a time-weighted average T_i was used.

As noted above, the following point can be considered both an unusual irradiation and a Chauvenet outlier, so it is listed in both places.

- Heat PBR_01, plant Big Rock Point, plate in capsule 124 (1 point)

This is one of the atypical BWR points, with the highest flux, fluence, and temperature of all data in the database (1.63×10^{12} n/cm^2/s flux, 1.07×10^{20} n/cm^2 fluence, 570°F).

E.4 References

1. Eason, E. D., J. E. Wright, and G. R. Odette, *Improved Embrittlement Correlations for Reactor Pressure Vessel Steels*, NUREG/CR-6551, U.S. Nuclear Regulatory Commission, Washington D.C., 1998.

2. Kirk, M., C. Santos, E. D. Eason, J. E. Wright, and G. R. Odette, "Updated Embrittlement Trend Curve for Reactor Pressure Vessel Steels," *Proc. Structural Mechanics in Reactor Technology (SMiRT) Conference, 2003*, 2003.

Appendix F. Residual Plots for Low-Cu and High-Cu Datasets, Baseline Model

The plots in Figs. F.1 through F.28 are based on the following definition of residual:

$$Residual = Model\ TTS - Measured\ TTS, \tag{F-1}$$

which implies that a negative residual is an underestimate by the model of the actual shift. The linear trend of the residuals fitted by least squares is shown by a dashed line on each plot. A residual plot for a variable in the model that shows no significant residual slope trend, denoted "N.S." in the legend, indicates that the model correctly captures the trend of the variable to first order. A similar result for a variable not included in the model implies that the variable would be unlikely to improve the fit significantly if it were added.

The residual plots for the low-Cu data, Figs. F.1 through F.13, are based on the matarix feature (MF) term model, Eqs. (4-3) and (4-4). The residual plots for the high-Cu data, Figs. F.14 through F.28, are based on the complete model, including both MF and copper-rich–precipitate (CRP) terms, i.e., Eqs. (4-1), (4-3), (4-4), and (4-5).

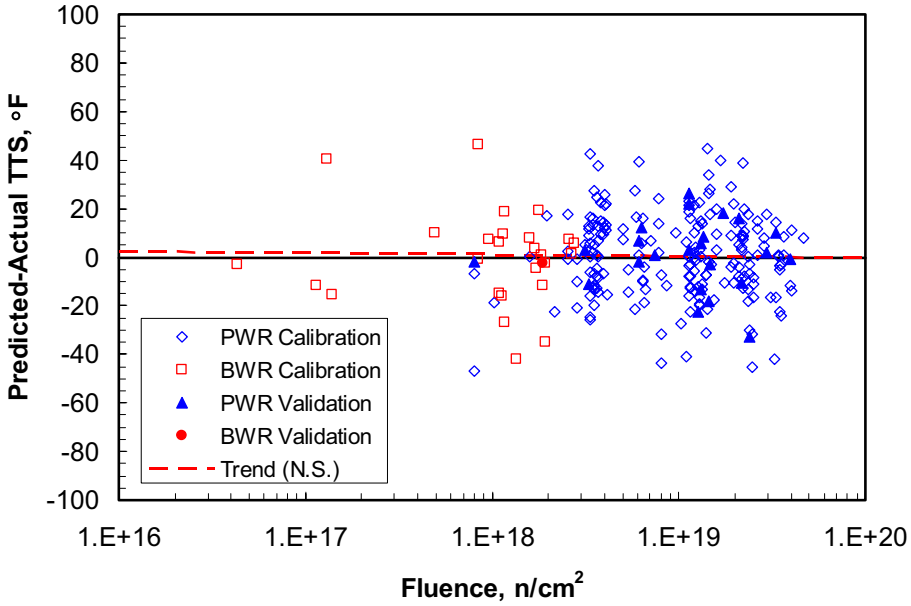

Fig. F.1. Residuals plotted against fluence, calibration and validation data with Cu ≤ 0.072 wt %.

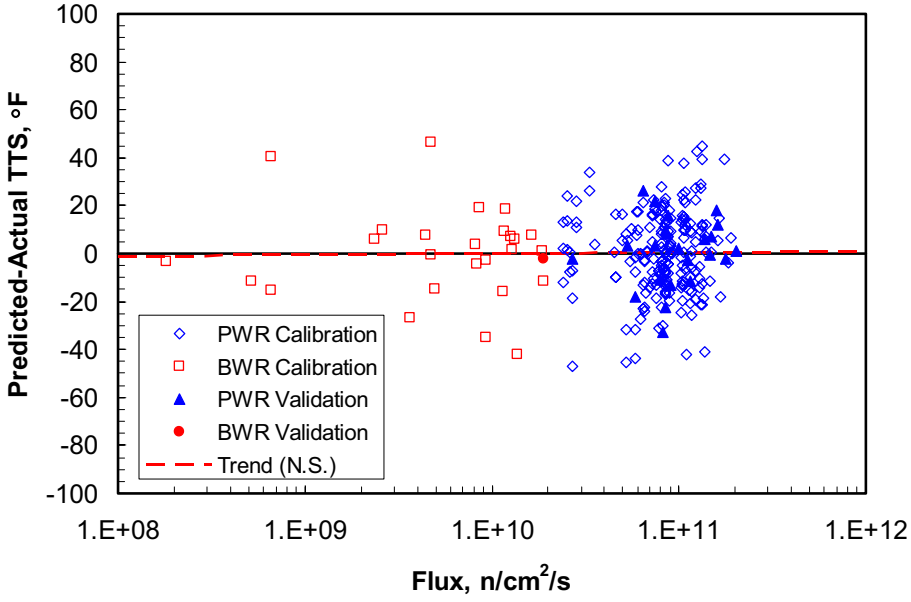

Fig. F.2. Residuals plotted against flux, calibration and validation data with Cu ≤ 0.072 wt %.

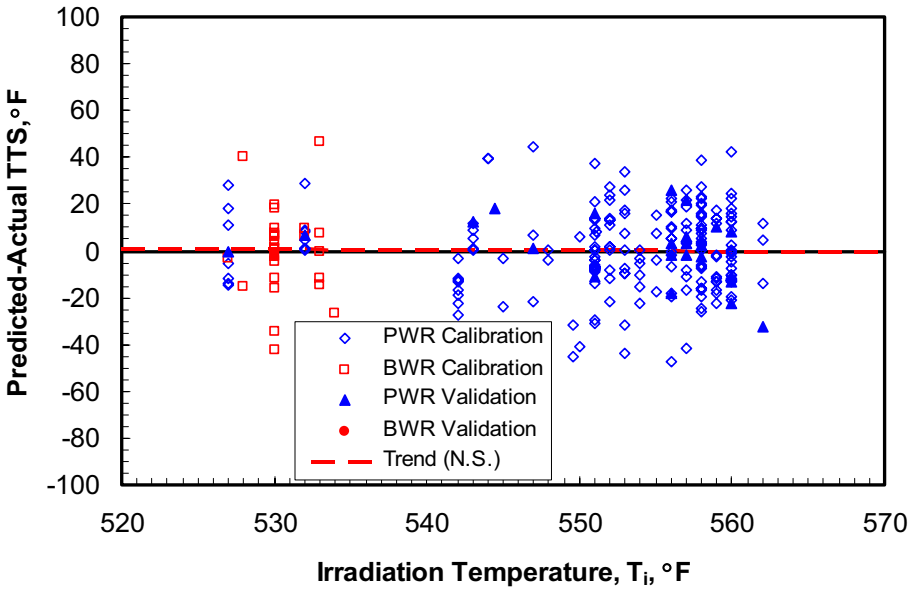

Fig. F.3. Residuals plotted against T_i, calibration and validation data with Cu ≤ 0.072 wt %.

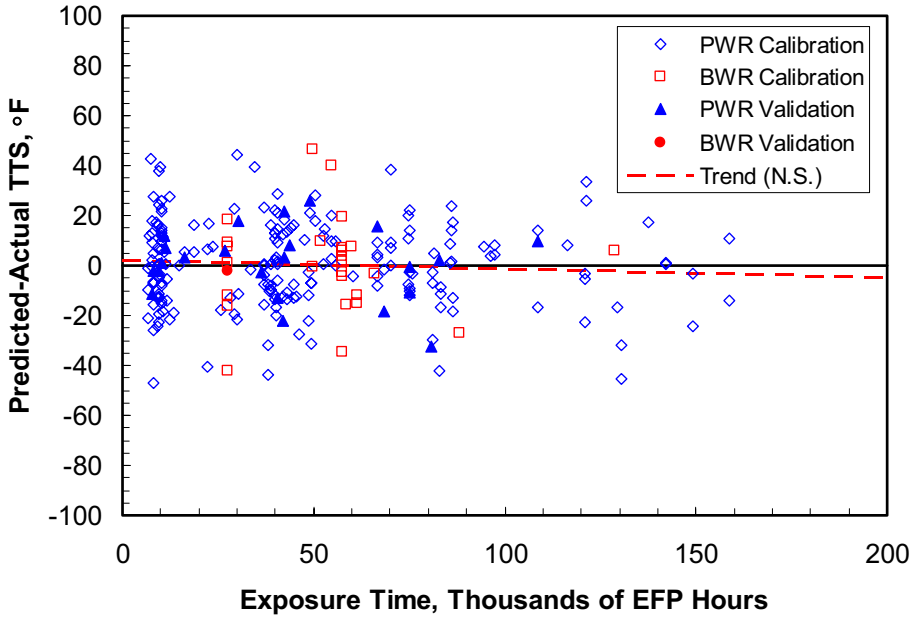

Fig. F.4. Residuals plotted against time, calibration and validation data with Cu ≤ 0.072 wt %.

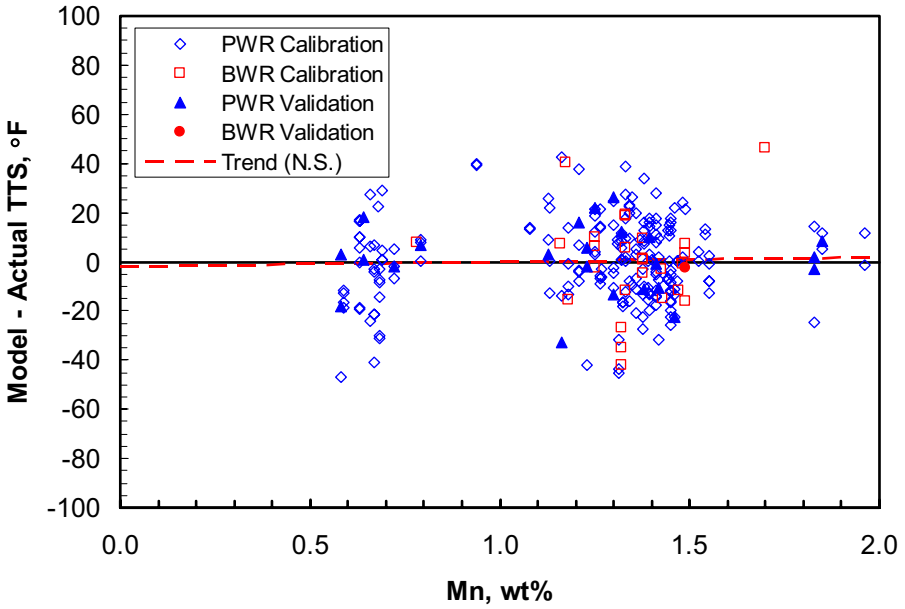

Fig. F.5. Residuals plotted against Mn, calibration and validation data with Cu ≤ 0.072 wt %.

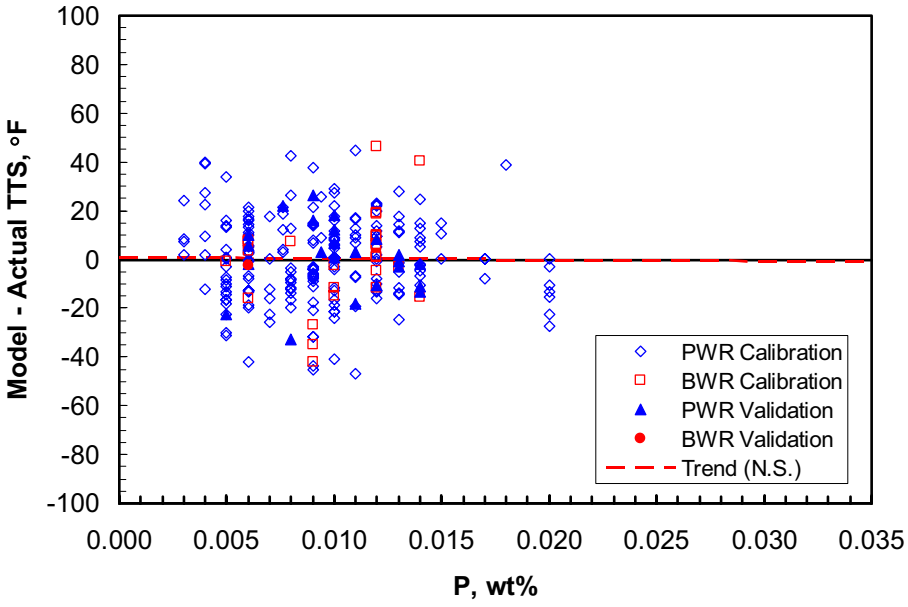

Fig. F.6. Residuals plotted against P, calibration and validation data with Cu ≤ 0.072 wt %.

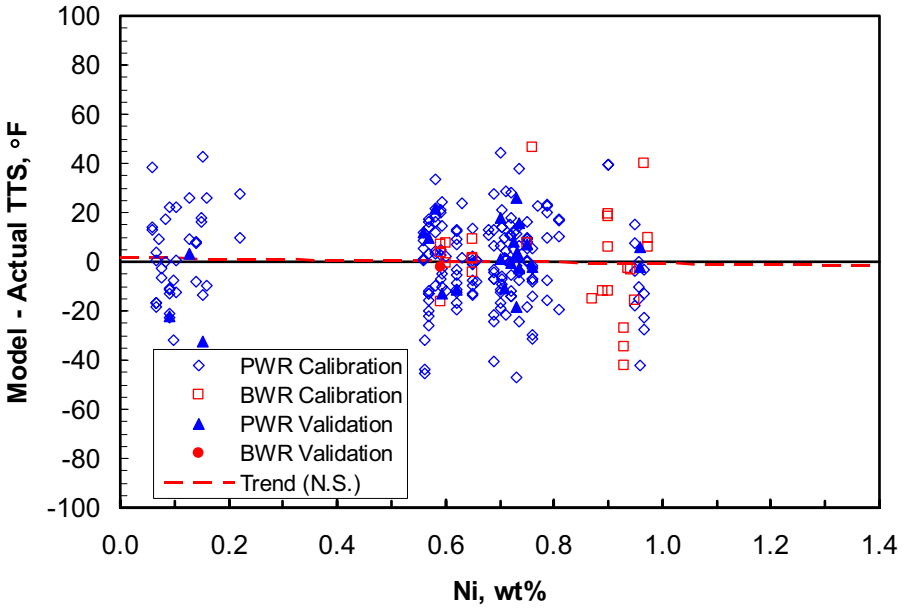

Fig. F.7. Residuals plotted against Ni, calibration and validation data with Cu ≤ 0.072 wt %.

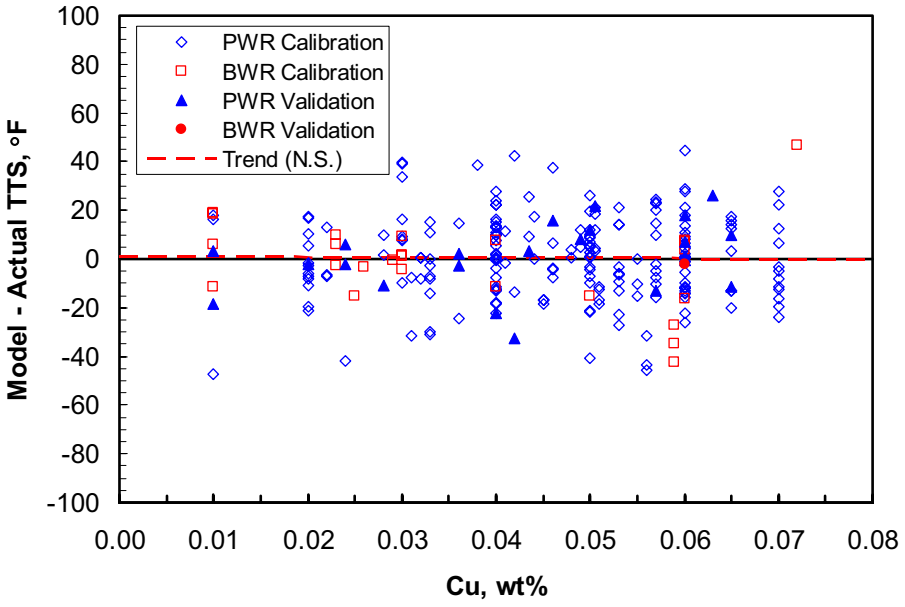

Fig. F.8. Residuals plotted against Cu, calibration and validation data with Cu ≤ 0.072 wt %.

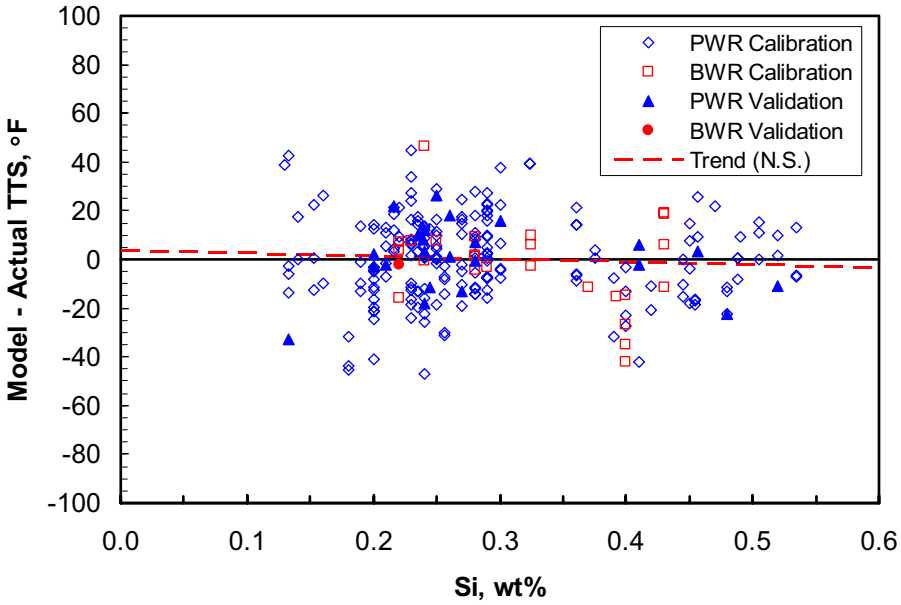

Fig. F.9. Residuals plotted against Si, calibration and validation data with Cu ≤ 0.072 wt %.

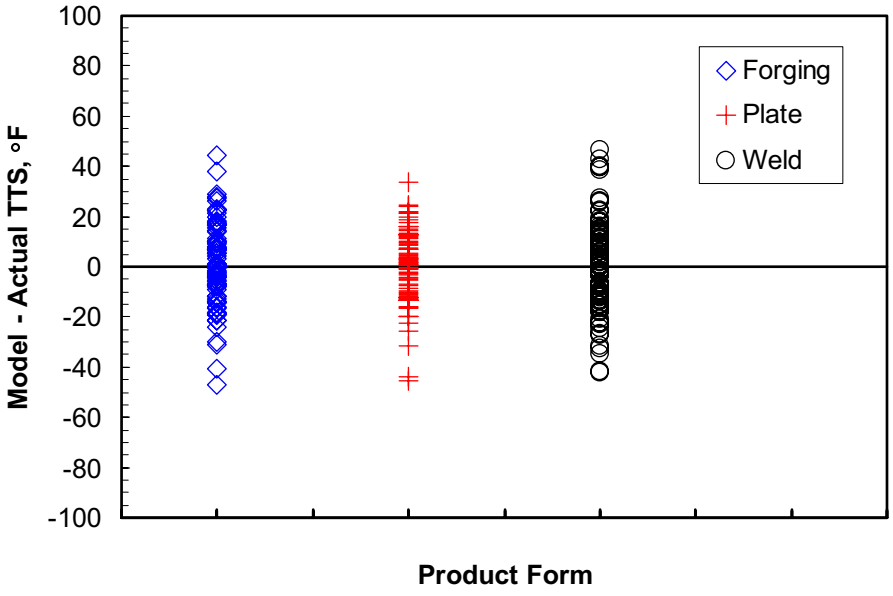

Fig. F.10. Residuals plotted against Product Form, calibration and validation data with Cu ≤ 0.072 wt %.

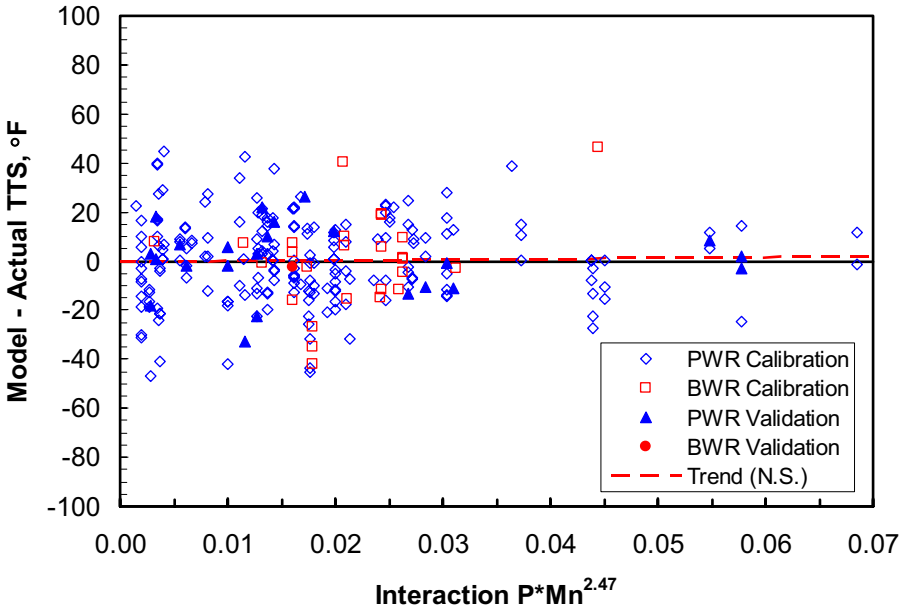

Fig. F.11. Residuals plotted against P*Mn$^{2.47}$, calibration and validation data with Cu ≤ 0.072 wt %.

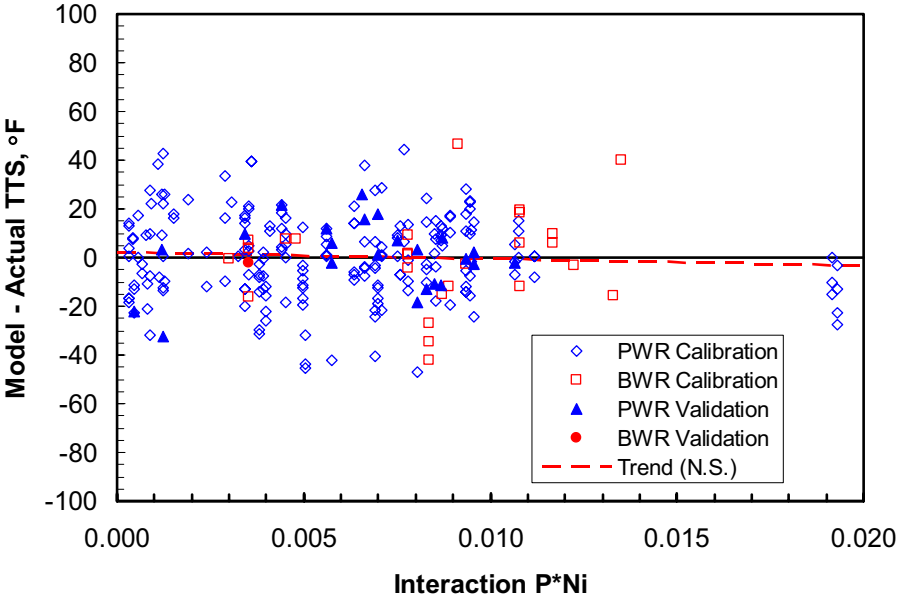

Fig. F.12. Residuals plotted against P*Ni, calibration and validation data with Cu ≤ 0.072 wt %.

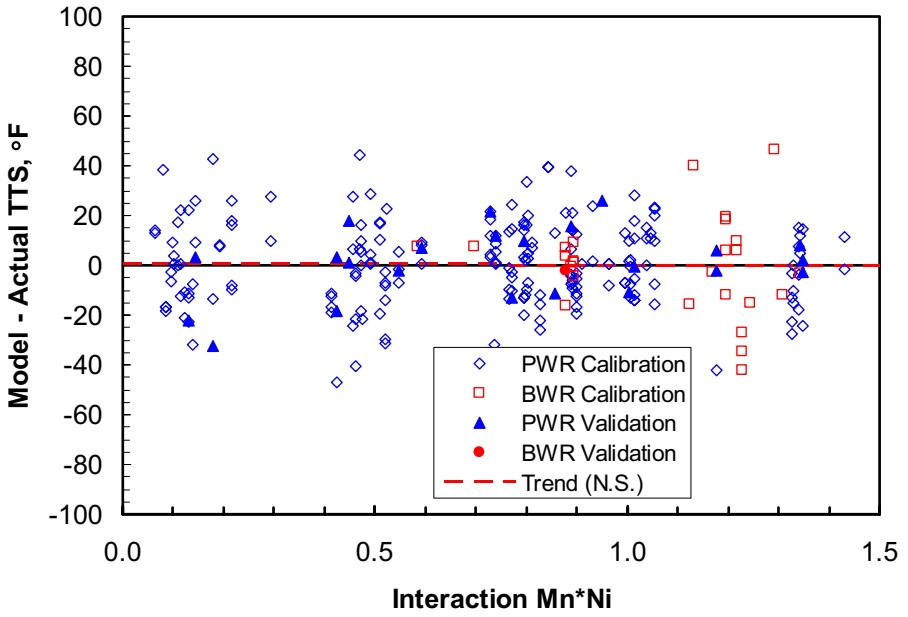

Fig. F.13. Residuals plotted against Mn*Ni, calibration and validation data with Cu ≤ 0.072 wt %.

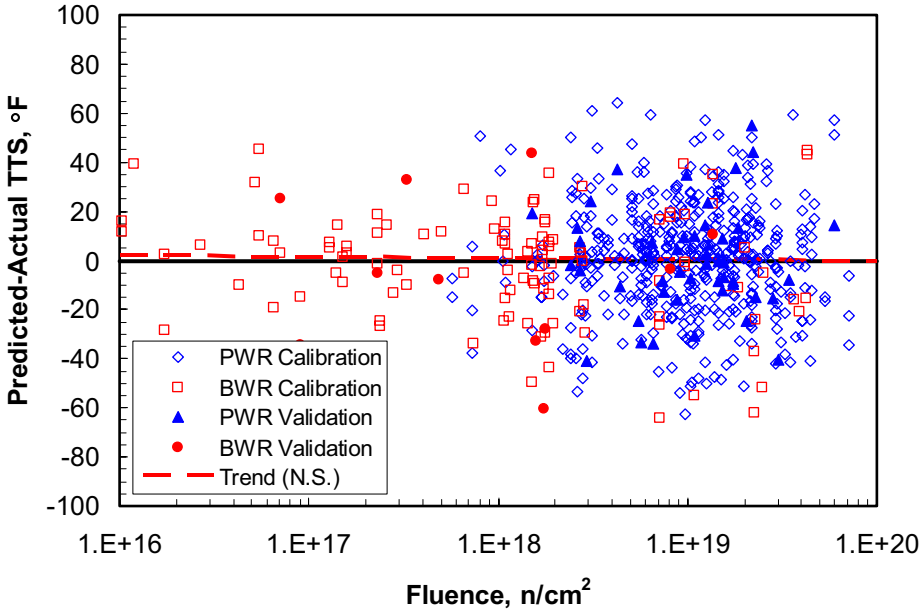

Fig. F.14. Residuals plotted against Fluence, calibration and validation data with Cu > 0.072 wt %.

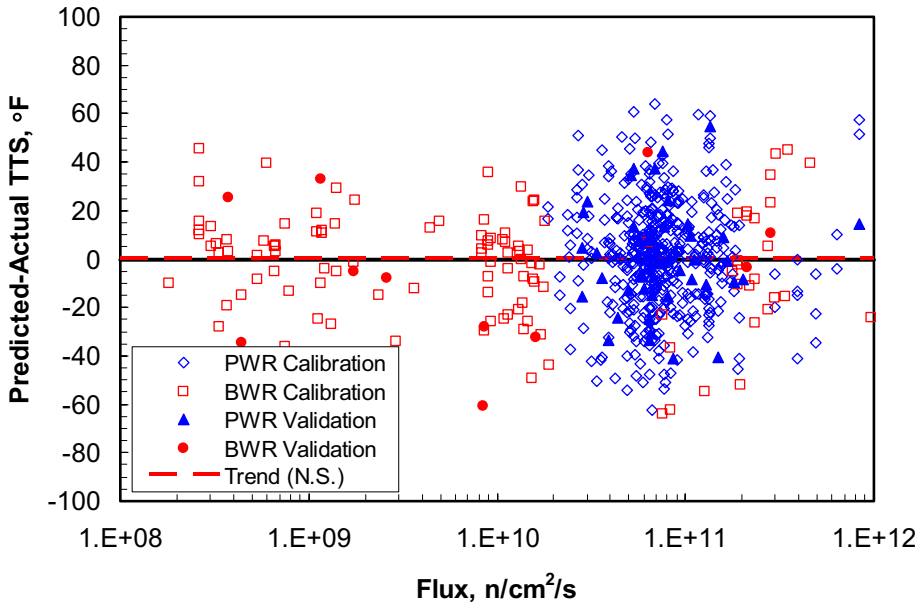

Fig. F.15. Residuals plotted against Flux, calibration and validation data with Cu > 0.072 wt %.

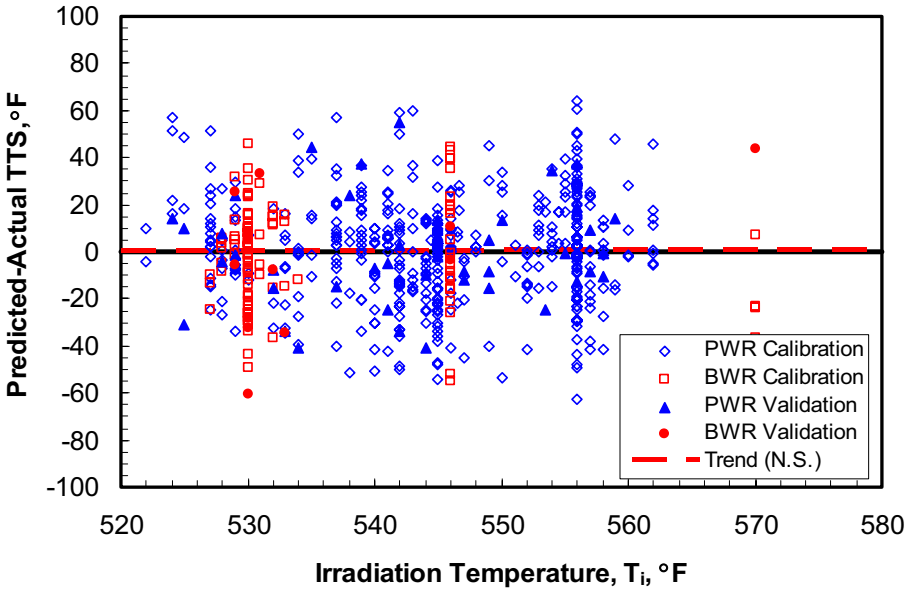

Fig. F.16. Residuals plotted against T_i, calibration and validation data with Cu > 0.072 wt %.

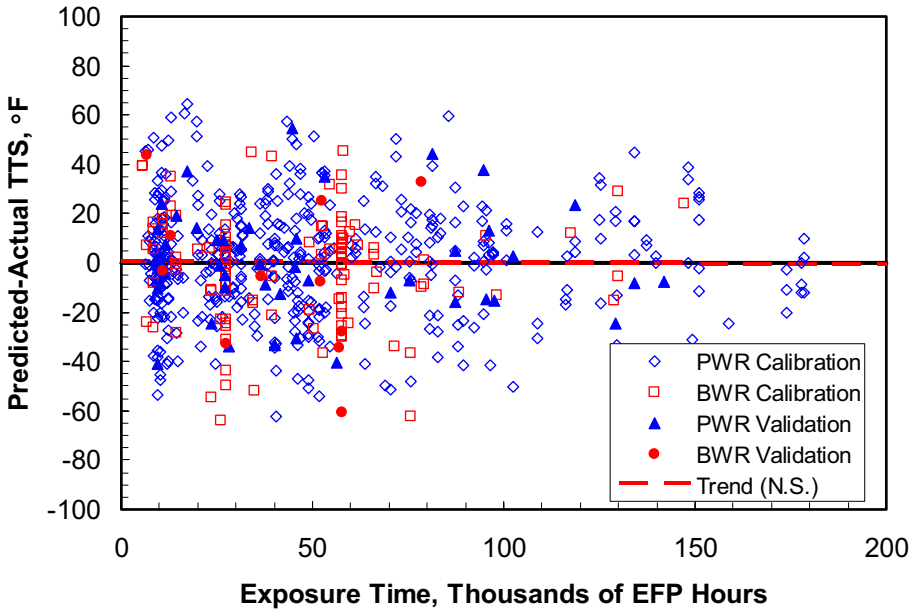

Fig. F.17. Residuals plotted against Time, calibration and validation data with Cu > 0.072 wt %.

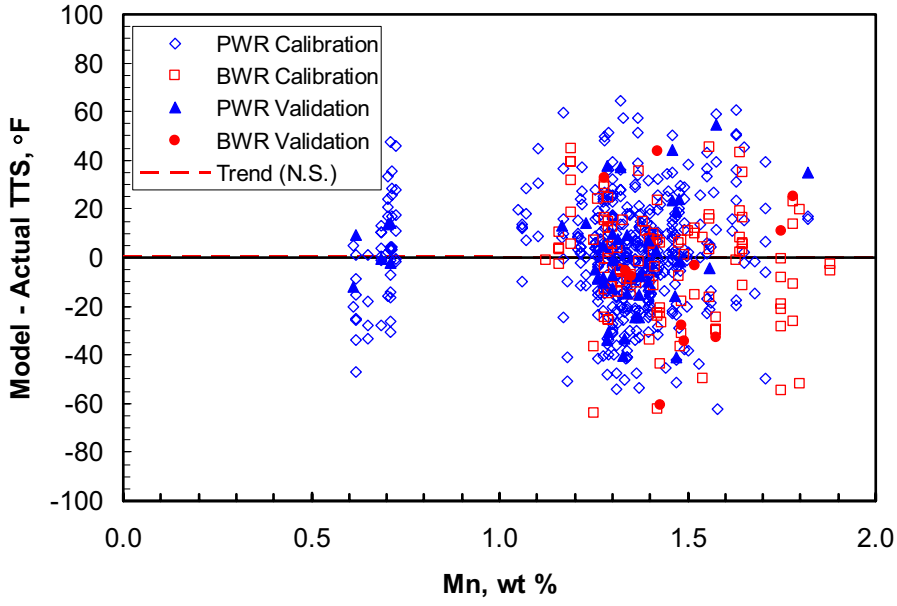

Fig. F.18. Residuals plotted against Mn, calibration and validation data with Cu > 0.072 wt %.

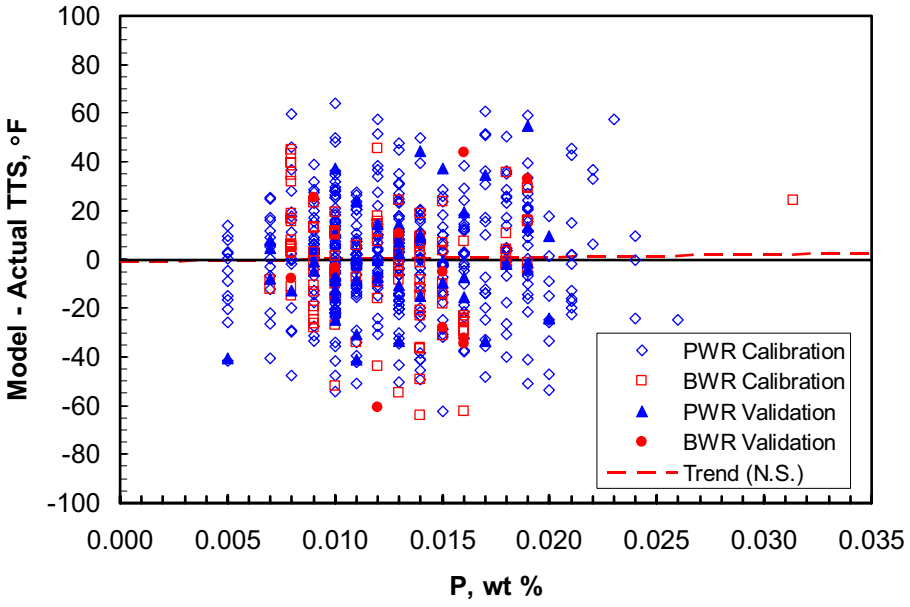

Fig. F.19. Residuals plotted against P, calibration and validation data with Cu > 0.072 wt %.

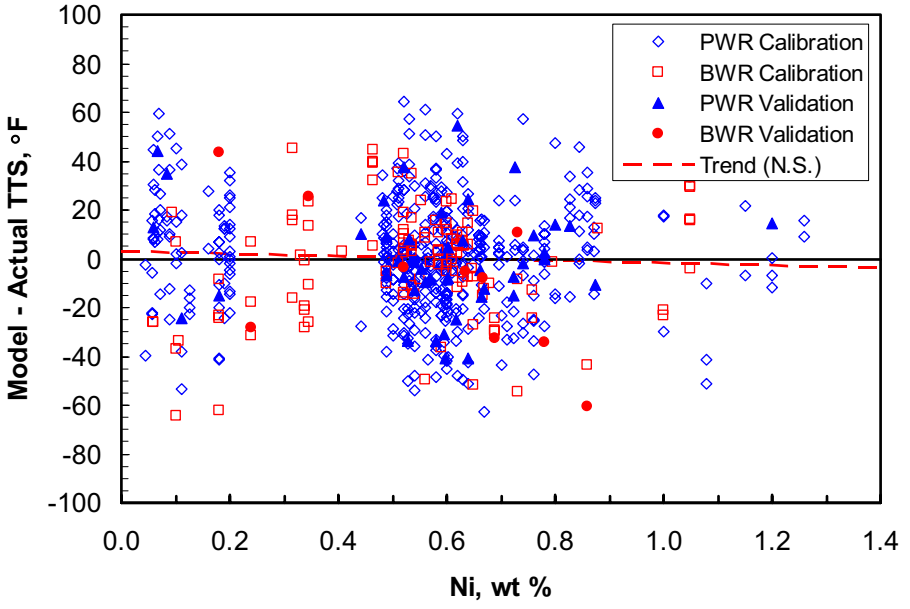

Fig. F.20. Residuals plotted against Ni, calibration and validation data with Cu > 0.072 wt %.

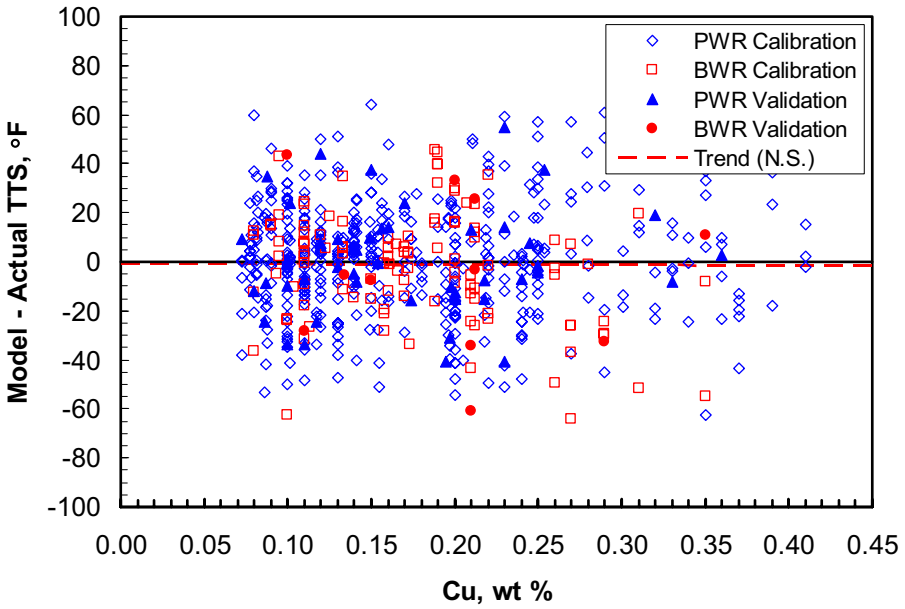

Fig. F.21. Residuals plotted against Cu, calibration and validation data with Cu > 0.072 wt %.

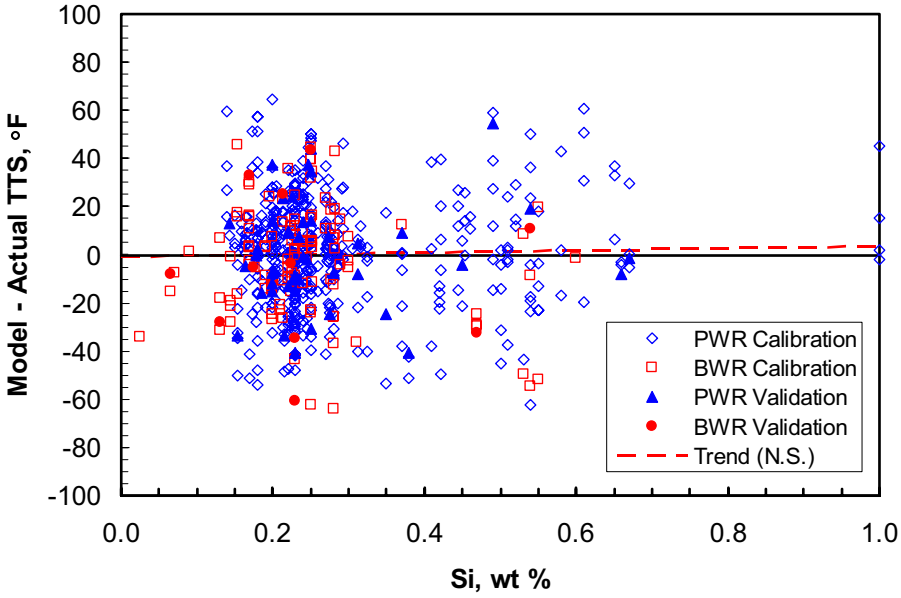

Fig. F.22. Residuals plotted against Si, calibration and validation data with Cu > 0.072 wt %.

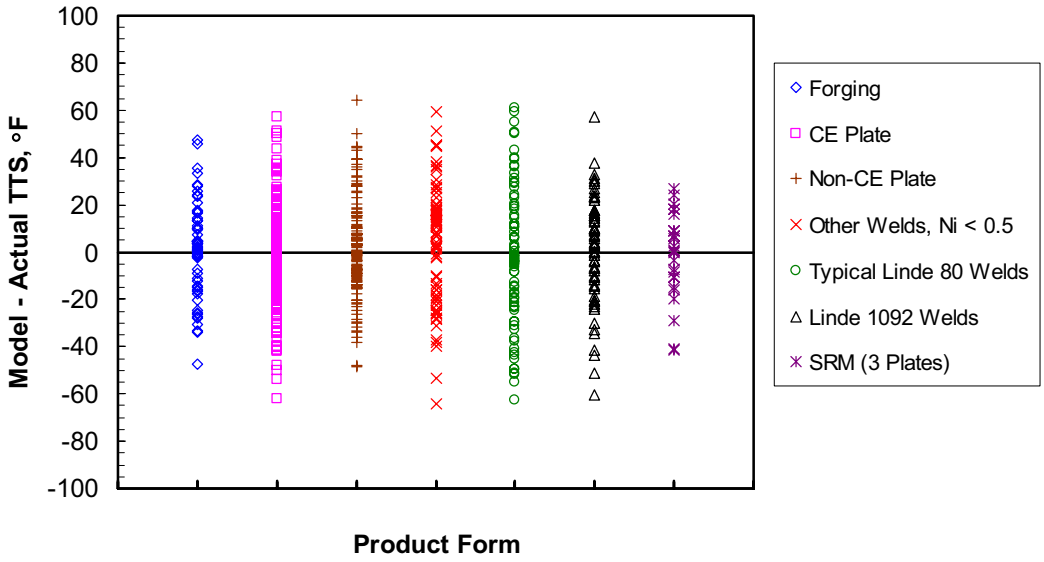

Fig. F.23. Residuals plotted against Product Form, calibration and validation data with Cu > 0.072 wt %.

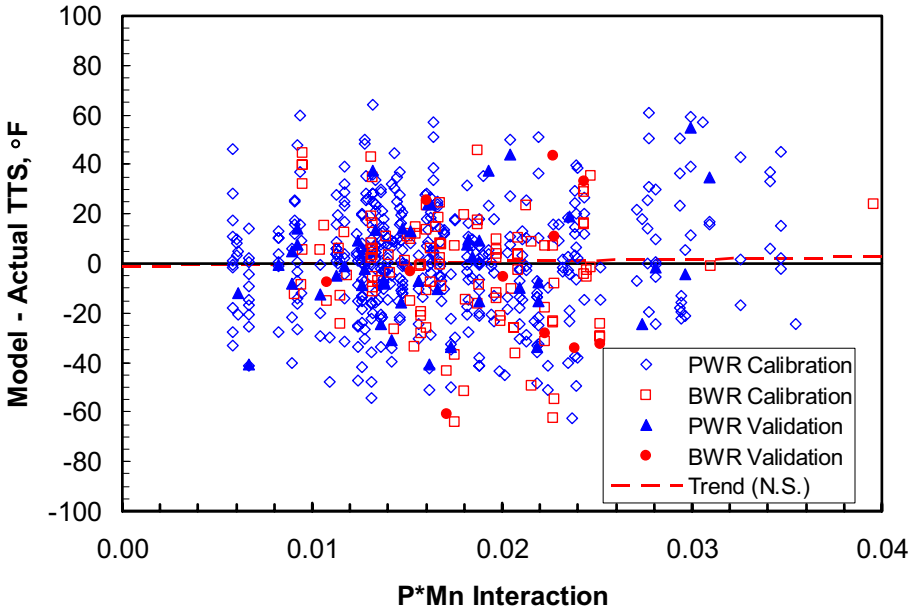

Fig. F.24. Residuals plotted against P*Mn, calibration and validation data with Cu > 0.072 wt %.

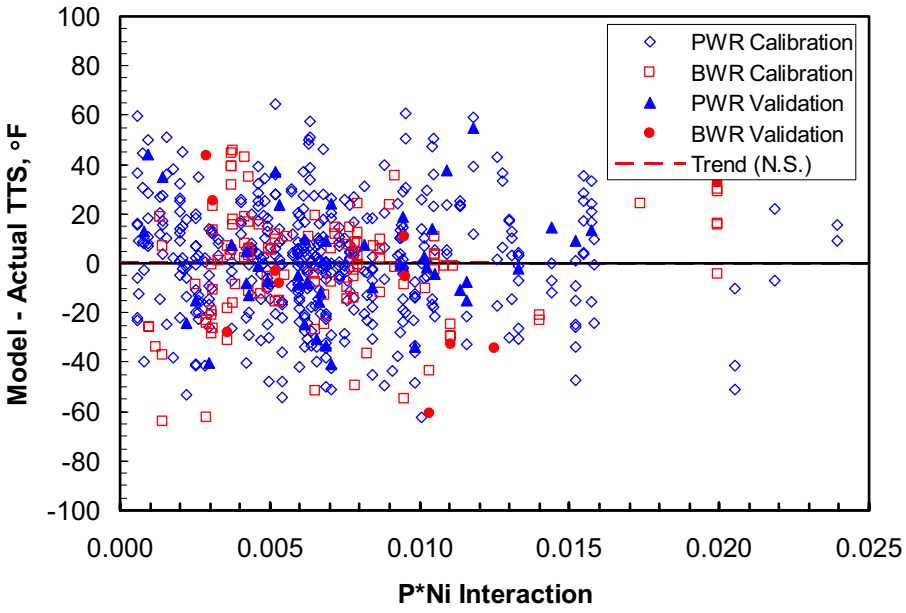

Fig. F.25. Residuals plotted against P*Ni, calibration and validation data with Cu > 0.072 wt %.

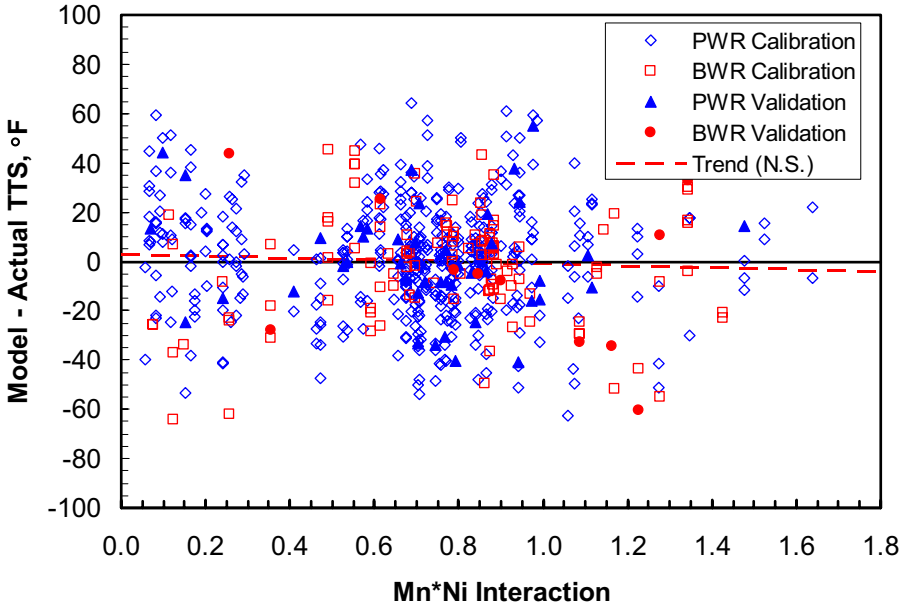

Fig. F.26. Residuals plotted against Mn*Ni, calibration and validation data with Cu > 0.072 wt %.

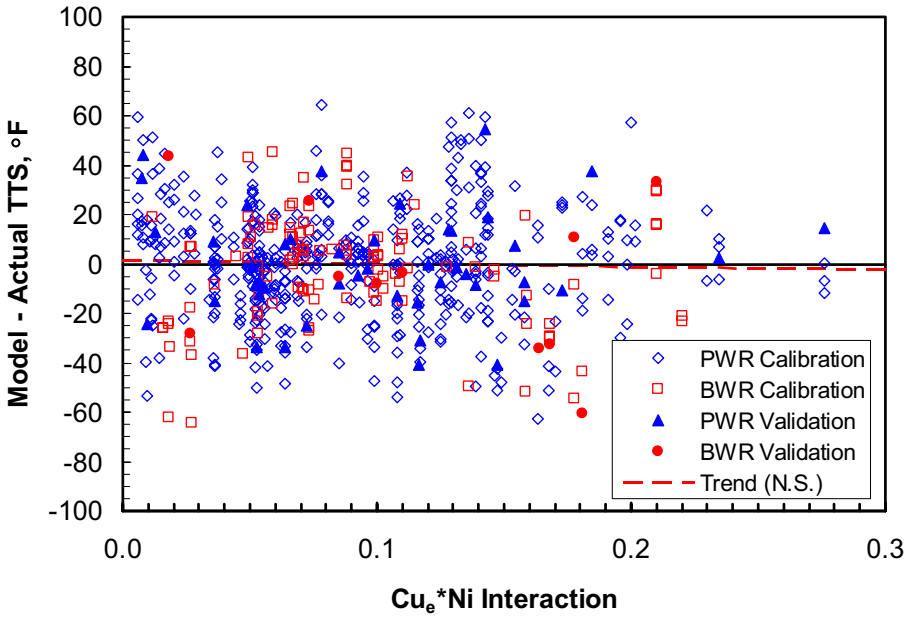

Fig. F.27. Residuals plotted against Cu_e*Ni, calibration and validation data with Cu > 0.072 wt %.

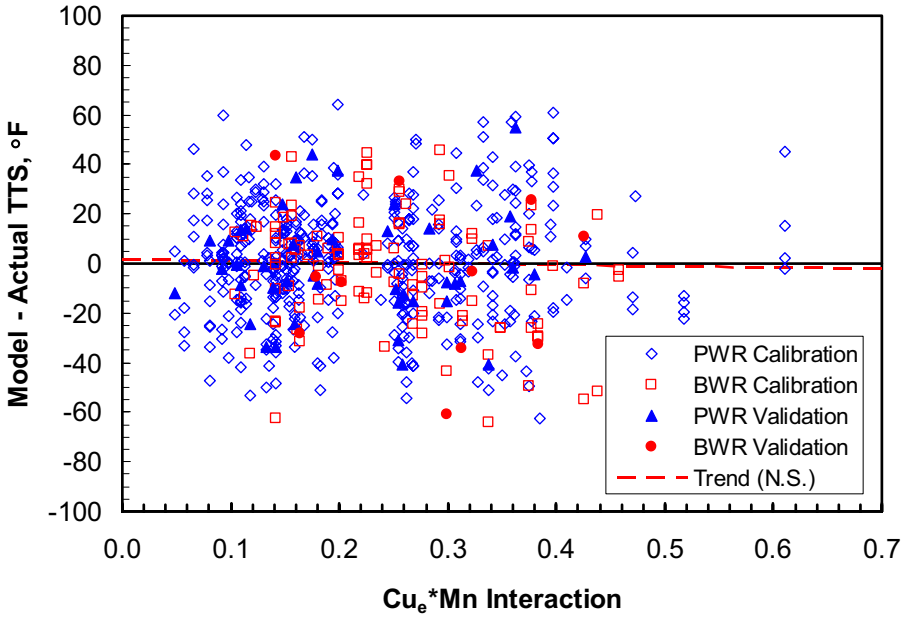

Fig. F.28. Residuals plotted against Cu_e*Mn, calibration and validation data with Cu > 0.072 wt %.

Appendix G. Means, Standard Deviations, and Range of Chemistry Variables by Material Group, Surveillance Data

The statistics in the following tables were calculated for the referenced material groups in the surveillance database, giving each heat in each group equal weight regardless of the number of shift estimates available for that heat. The number of heats used in the statistics for each sample is given by n.

Table G.1. Low-Cu Materials

Cu ≤ 0.072 wt % except as noted

	Mn	P	Ni	Cu
Forging A508 Class 2 (low Cu), n = 15				
Minimum	0.5800	0.0040	0.6900	0.0100
Mean	0.6646	0.0092	0.7321	0.0443
Std deviation	0.0525	0.0027	0.0356	0.0175
Maximum	0.7900	0.0140	0.8100	0.0700
Forging A508 Class 3 (1 heat has Cu > 0.072 wt %), n = 6				
Minimum	1.2070	0.0090	0.6970	0.0460
Mean	1.2897	0.0105	0.7290	0.0593
Std deviation	0.0776	0.0018	0.0321	0.0105
Maximum	1.4100	0.0130	0.7870	0.0770
Plate A533B1 (low Cu), n = 21				
Minimum	1.1600	0.0030	0.5600	0.0290
Mean	1.3759	0.0080	0.6079	0.0506
Std deviation	0.1058	0.0034	0.0339	0.0124
Maximum	1.5500	0.0140	0.6800	0.0700
Low-Cu welds Ni ≤ 0.5 (some Linde 0091 & Linde 124), n = 19				
Minimum	1.0800	0.0030	0.0600	0.0100
Mean	1.3372	0.0082	0.1074	0.0369
Std deviation	0.1338	0.0035	0.0433	0.0136
Maximum	1.5500	0.0180	0.2200	0.0700
Low-Cu welds 0.5 < Ni < 0.75 (some Linde 80 & LW320), n = 7				
Minimum	1.4170	0.0110	0.6570	0.0220
Mean	1.6303	0.0133	0.7091	0.0344
Std deviation	0.2375	0.0021	0.0276	0.0088
Maximum	1.9600	0.0170	0.7360	0.0490
Low-Cu welds Ni ≥ 0.75 (most Linde 124, 1 has Cu > 0.072 wt %), n = 16				
Minimum	0.9370	0.0040	0.7600	0.0100
Mean	1.3164	0.0115	0.9203	0.0397
Std deviation	0.1692	0.0043	0.0540	0.0199
Maximum	1.7000	0.0200	0.9730	0.0800

Table G.2. High-Cu Materials
Cu > 0.072 wt %

	Mn	P	Ni	Cu
Forging A508 Class 2 (high Cu), n = 9				
Minimum	0.6100	0.0080	0.6700	0.0800
Mean	0.6810	0.0141	0.7770	0.1220
Std deviation	0.0433	0.0047	0.0635	0.0313
Maximum	0.7250	0.0200	0.8600	0.1600
Plate A302B and A302B1, n = 18				
Minimum	1.2626	0.0070	0.0560	0.0900
Mean	1.3878	0.0134	0.2524	0.1400
Std deviation	0.0585	0.0060	0.1794	0.0468
Maximum	1.4600	0.0314	0.6300	0.2400
Plate A302BM, n = 19				
Minimum	1.1600	0.0070	0.4410	0.0950
Mean	1.3669	0.0111	0.5407	0.1812
Std deviation	0.1297	0.0033	0.0571	0.0449
Maximum	1.6450	0.0180	0.6300	0.2500
Plate A533B1 (high Cu), n = 52				
Minimum	1.2100	0.0050	0.4810	0.0730
Mean	1.3505	0.0108	0.5755	0.1303
Std deviation	0.0686	0.0029	0.0616	0.0412
Maximum	1.5000	0.0170	0.7580	0.2410
Other high Cu welds (Ni < 0.5) (some Linde 0091, others), n = 24				
	Mn	P	Ni	Cu
Minimum	1.0500	0.0080	0.0440	0.0800
Mean	1.3685	0.0144	0.1560	0.1849
Std deviation	0.2320	0.0040	0.1113	0.0883
Maximum	1.8200	0.0210	0.4070	0.4100
Typical Linde 80 welds (Ni > 0.5), n = 32				
Minimum	1.2600	0.0090	0.5200	0.0800
Mean	1.5475	0.0152	0.6073	0.2800
Std deviation	0.1291	0.0031	0.0508	0.0624
Maximum	1.8800	0.0220	0.7300	0.3900
Linde 1092 welds, n = 20				
Minimum	1.1220	0.0120	0.6000	0.1550
Mean	1.3316	0.0158	0.8689	0.2349
Std deviation	0.1323	0.0036	0.2024	0.0610
Maximum	1.5700	0.0240	1.2600	0.3600

Appendix H. Residual Plots for the Simplified Model

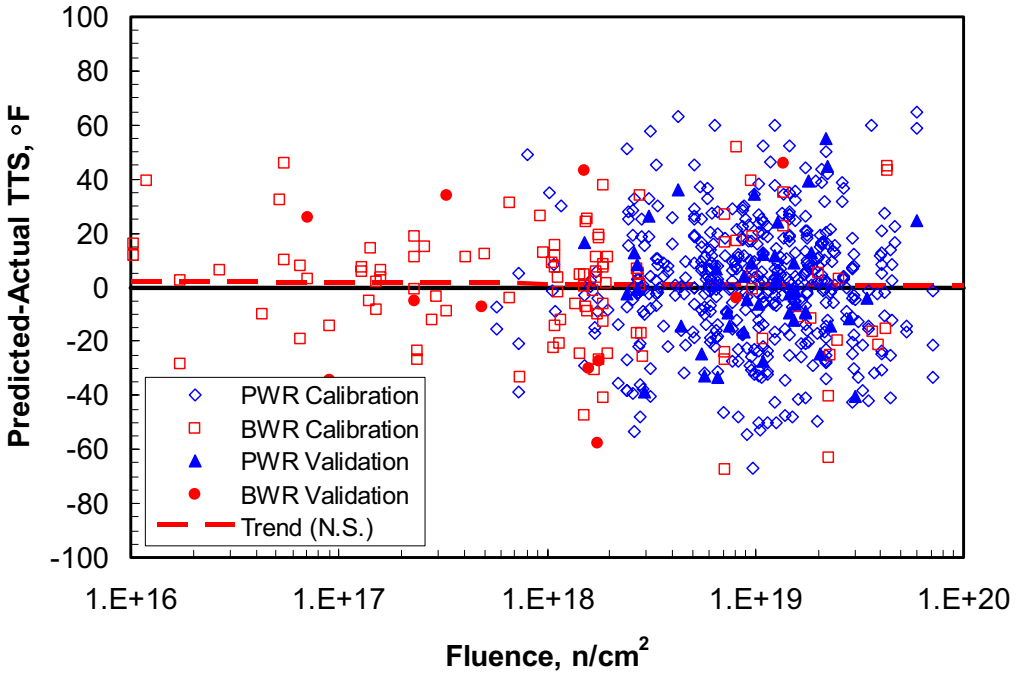

Fig. H.1. Residuals plotted against fluence, calibration and validation data with Cu > 0.072 wt %.

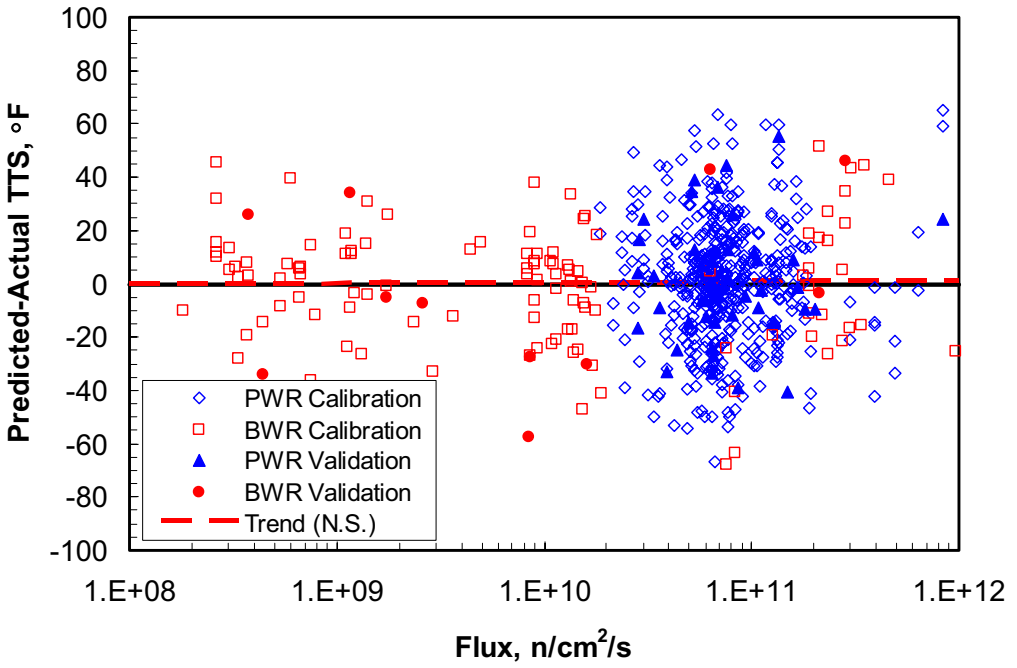

Fig. H.2. Residuals plotted against Flux, calibration and validation data with Cu > 0.072 wt %.

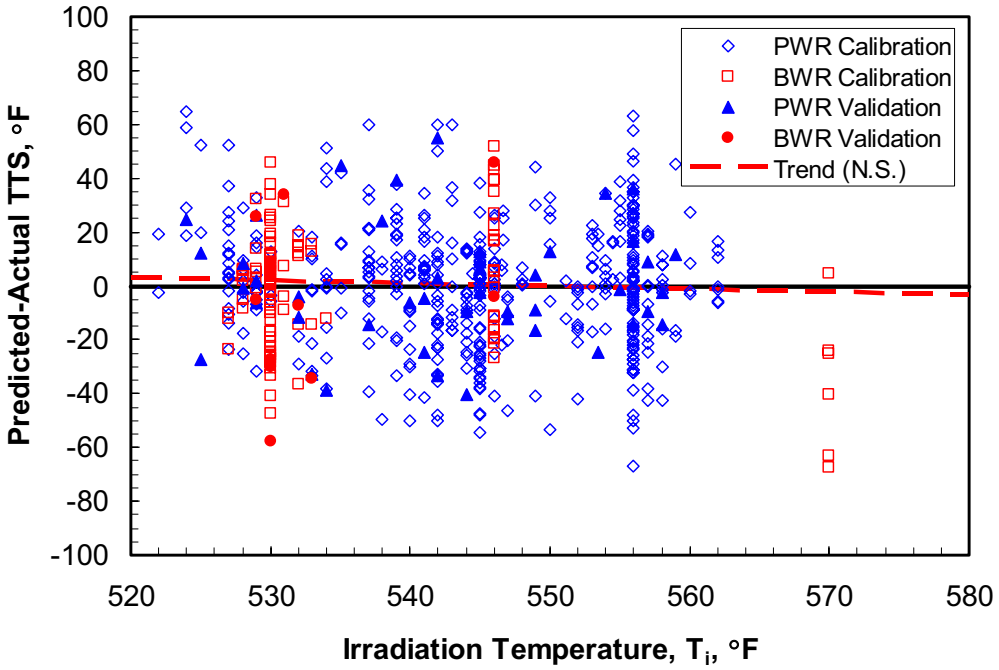

Fig. H.3. Residuals plotted against T_i, calibration and validation data with Cu > 0.072 wt %.

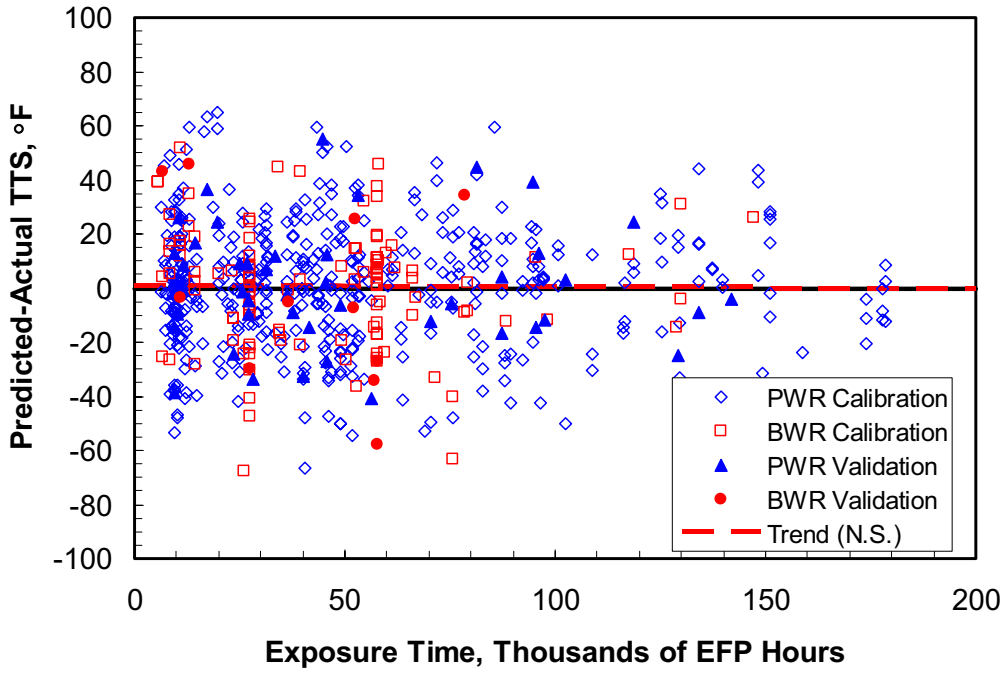

Fig. H.4. Residuals plotted against exposure time, calibration and validation data with Cu > 0.072 wt %.

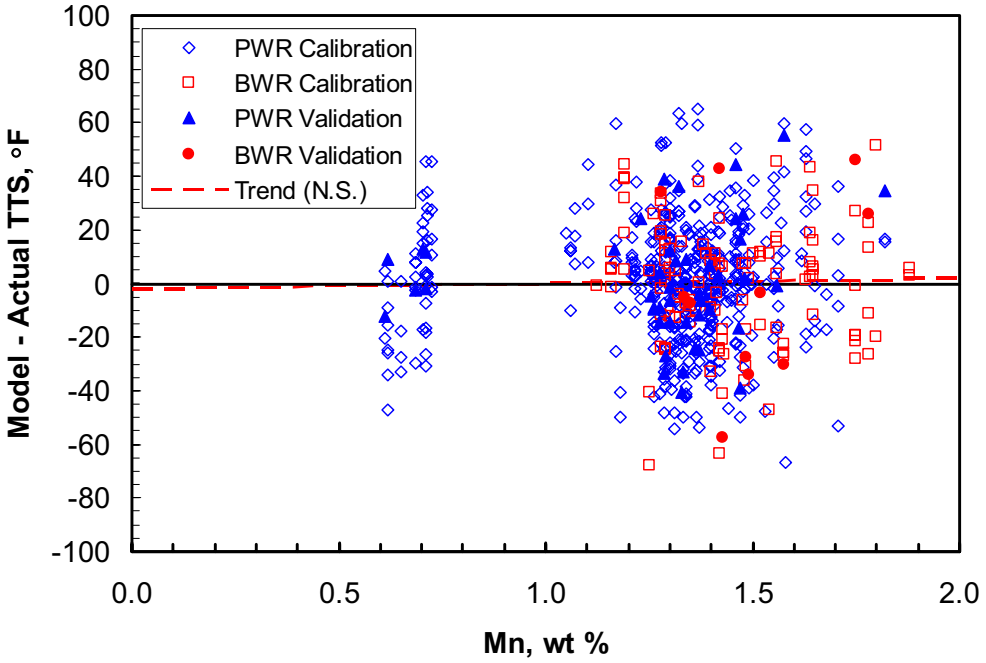

Fig. H.5. Residuals plotted against Mn, calibration and validation data with Cu > 0.072 wt %.

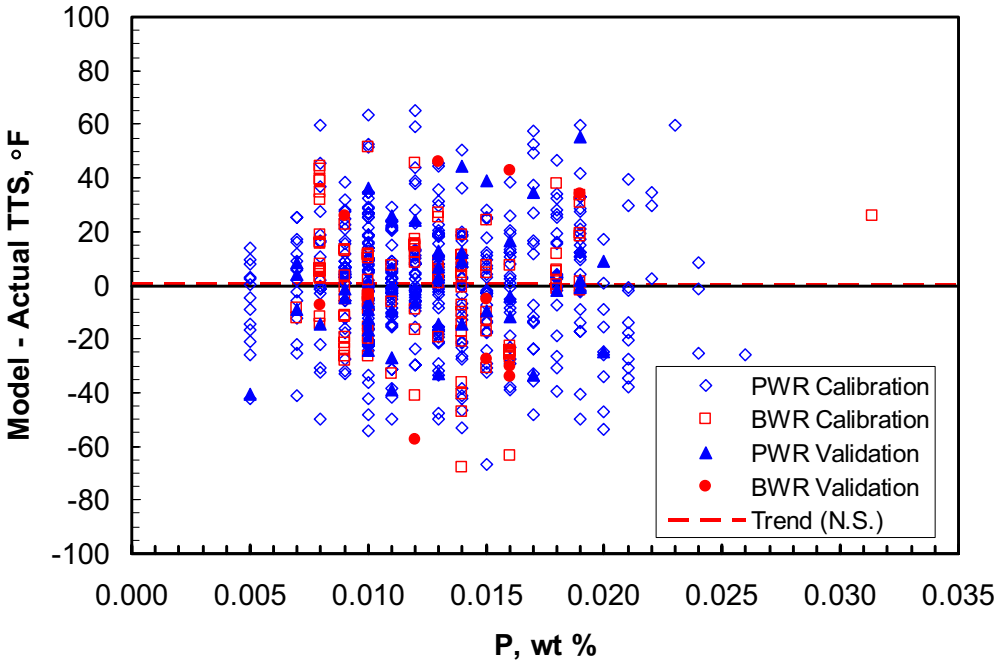

Fig. H.6. Residuals plotted against P, calibration and validation data with Cu > 0.072 wt %.

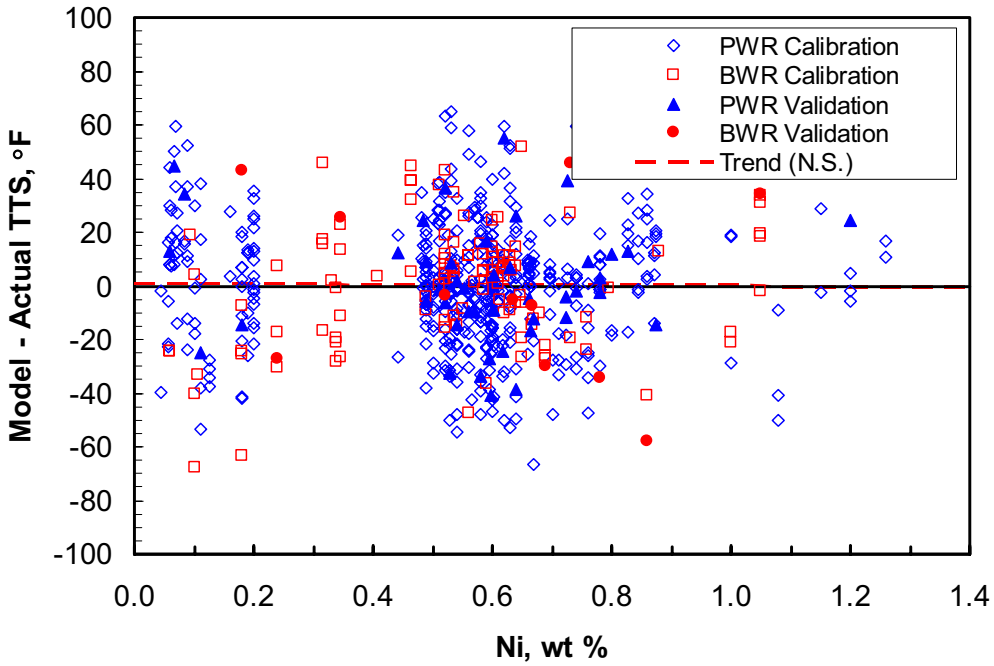

Fig. H.7. Residuals plotted against Ni, calibration and validation data with Cu > 0.072 wt %.

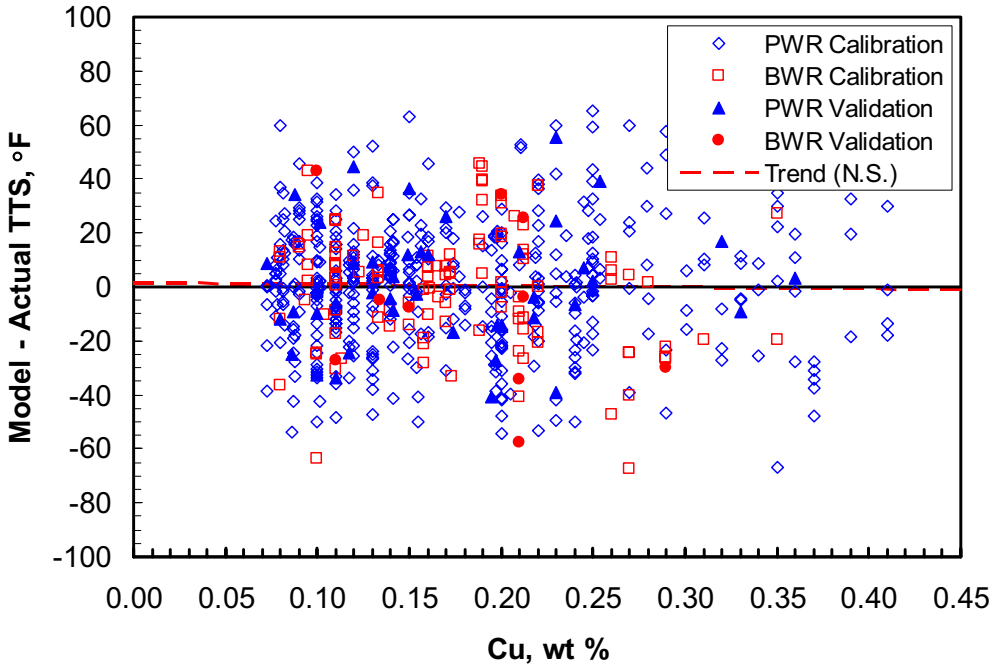

Fig. H.8. Residuals plotted against Cu, calibration and validation data with Cu > 0.072 wt %.

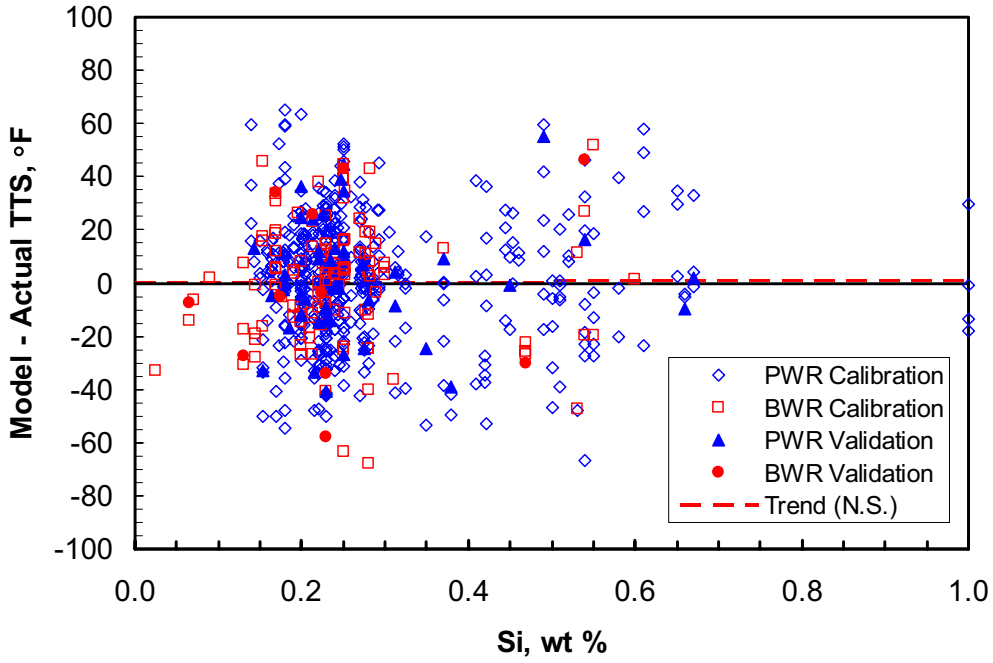

Fig. H.9. Residuals plotted against Si, calibration and validation data with Cu > 0.072 wt %.

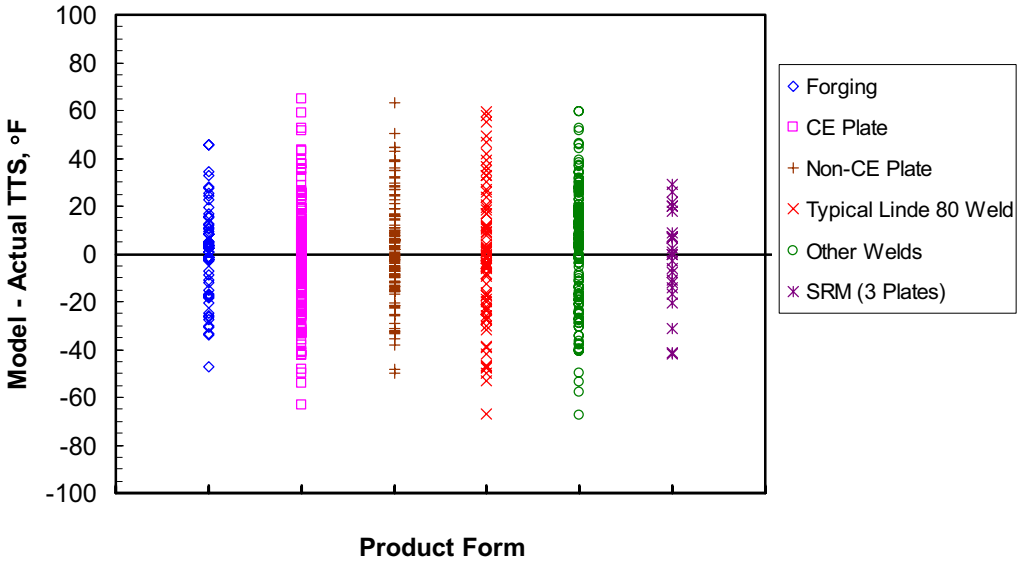

Fig. H.10. Residuals plotted against product form, calibration and validation data with Cu > 0.072 wt %.

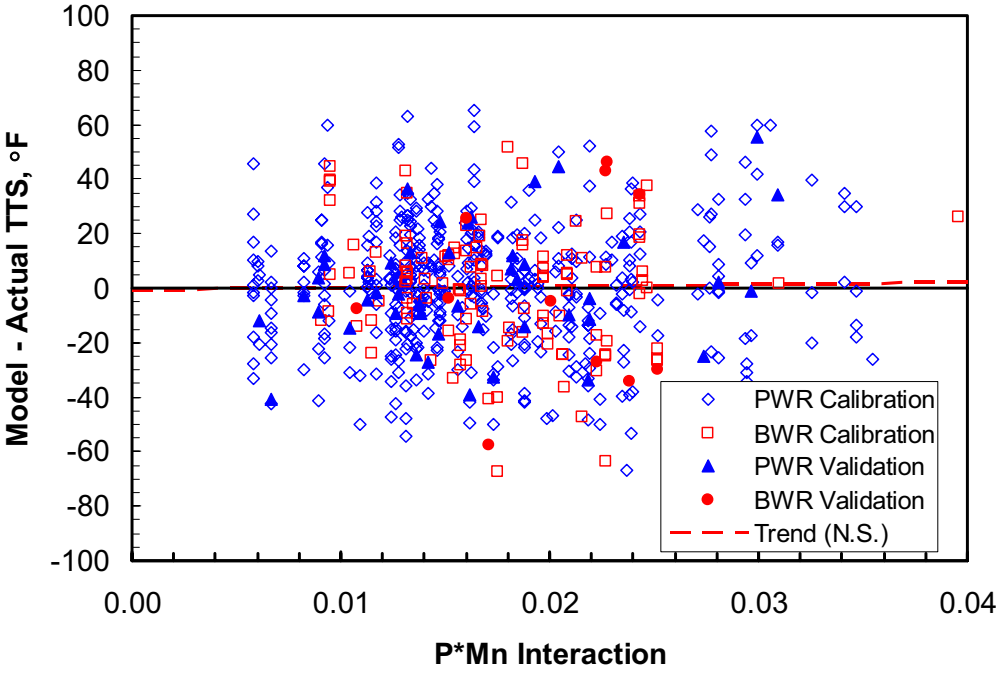

Fig. H.11. Residuals plotted against P*Mn, calibration and validation data with Cu > 0.072 wt %.

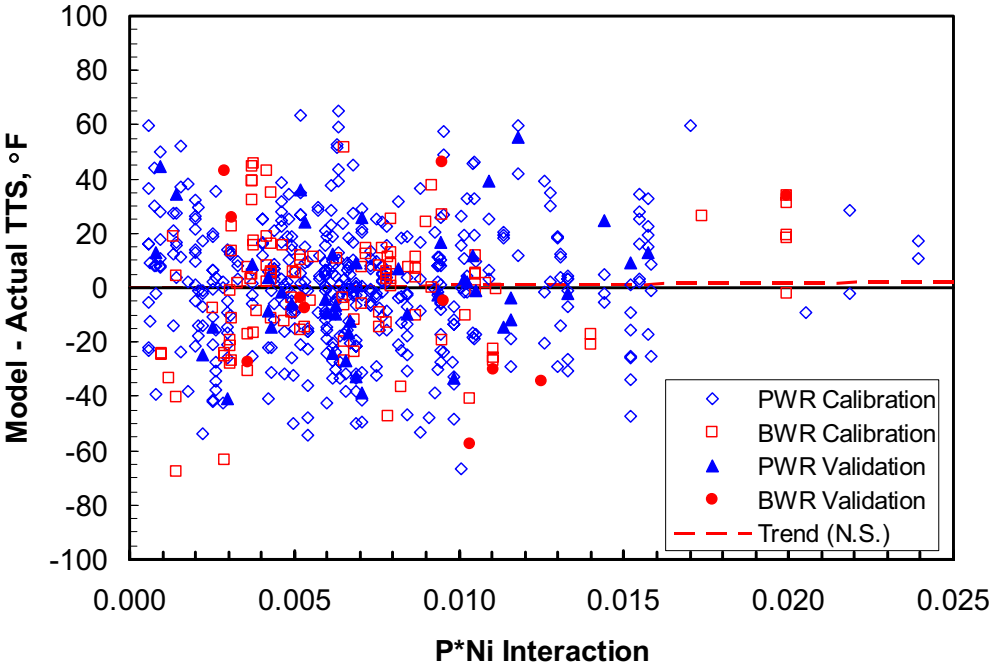

Fig. H.12. Residuals plotted against P*Ni, calibration and validation data with Cu > 0.072 wt %.

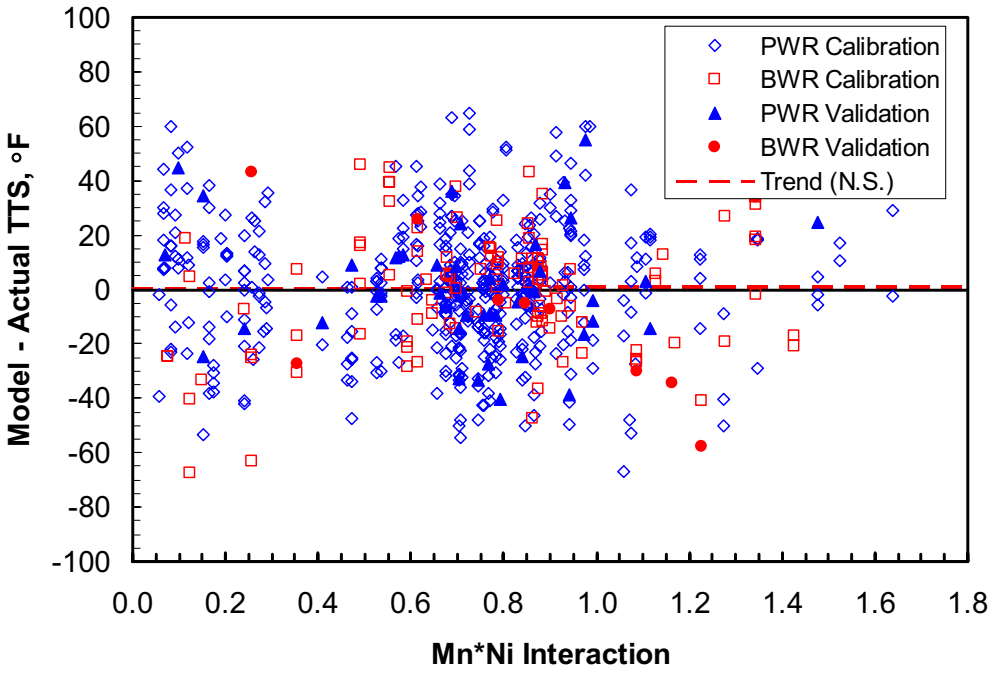

Fig. H.13. Residuals plotted against Mn*Ni, calibration and validation data with Cu > 0.072 wt %.

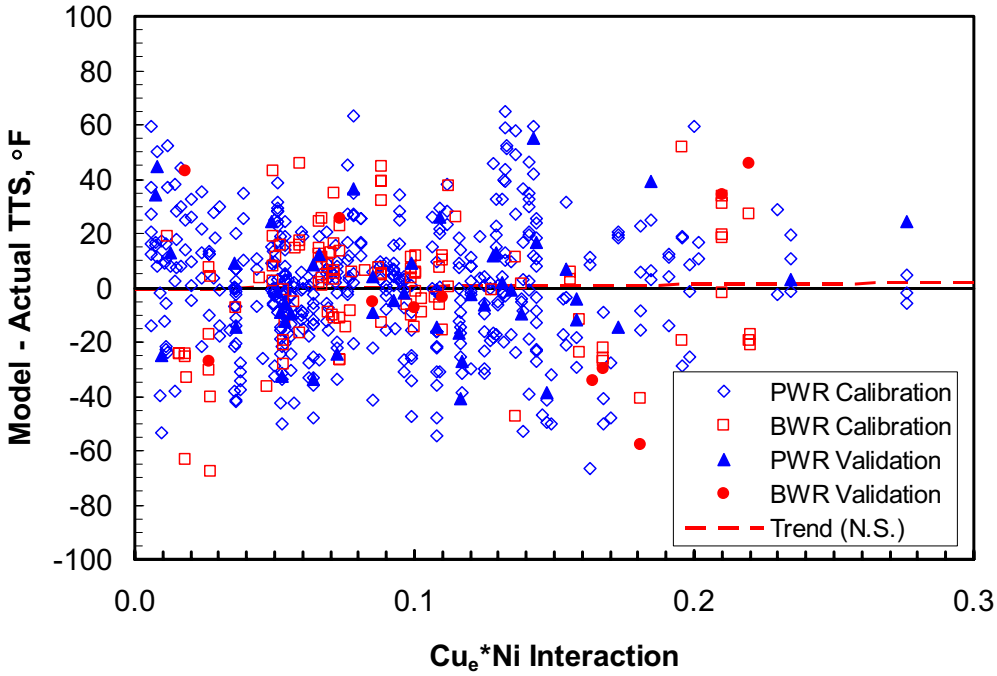

Fig. H.14. Residuals plotted against Cu_e*Ni, calibration and validation data with Cu > 0.072 wt %.

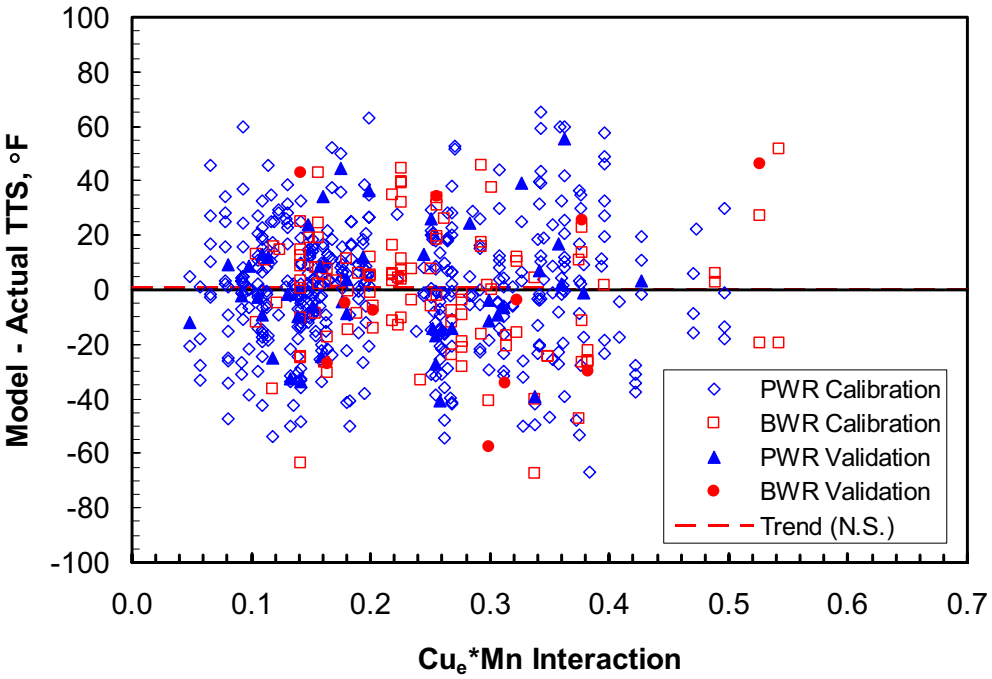

Fig. H.15. Residuals plotted against Cu_e*Mn, calibration and validation data with Cu > 0.072 wt %.

FIRST DRAFT

The UCSB Irradiation Variables Facility Database on Irradiation Induced Yield and Ultimate Tensile Stress Changes in the Reactor Pressure Vessel Steels

Prepared by:
G. R. Odette, T. Yamamoto, D. Klingensmith, D. Gragg and G. E. Lucas
University of California, Santa Barbara

Department of Mechanical Engineering and Department of Materials
University of California, Santa Barbara
Santa Barbara, CA 93106

Final Report

Contract # NRC-04-01-xxx

Prepared for:

Division of Engineering Technology Office of Nuclear Regulatory Research U.S. Nuclear regulatory Commission Washington D.C. 200555-0001 C.

Dr. Mark Kirk Project Monitor

Submitted: April 9, 2007

TABLE OF CONTENTS

1. EXECUTIVE SUMMARY

Irradiation embrittlement of reactor pressure vessels has been a longstanding issue of worldwide concern in regulating nuclear power reactors operating over long periods of planned and extended life. Embrittlement of reactor pressure vessel (RPV) steels is an extremely complex phenomenon, whose magnitude depends on the synergistic interaction of a large number metallurgical and irradiation variables. Irradiation embrittlement is manifested as increases in Charpy impact and fracture toughness reference transition temperatures. However, both of these temperature shifts primarily derive from irradiation-induced increases in the yield and flow stress, which can be measured with good precision using small tensile specimens. Thus the core element of the UCSB irradiation variables (IVAR) program was to measure yield and ultimate stress changes in a large number of RPV steels with controlled, or known, variations in key embrittlement variables.

Specifically, the objective of the IVAR program was to develop a database on irradiation hardening (and microstructure) that provides an accurate and high-resolution map of the individual and combined effects of key RPV steel embrittlement variables. These variables include: irradiation temperature (T_i), neutron flux (ϕ), neutron fluence (ϕt), the alloy chemical composition (Cu, Ni, Mn, P, C, N, Mo, Sn-As-Sb, B), heat treatment (austenitizing, quenching, tempering, stress relief and cooling time-temperature history conditions) and product form (submerged arc welds, plates and split melt model alloys). A total of 57 steel alloys were irradiated in this part of the IVAR program. Other IVAR objectives were to study key embrittlement mechanisms, to explore theoretically predicted phenomena, like late-blooming Mn-Ni rich phases, and to develop a better understanding of deformation and fracture micromechanics in irradiated RPV steels. These mechanism studies included irradiations of a large number of simple model alloys; however, since our major focus is on embrittlement of RPV steels, the model alloy results are also not included in this report.

This document provides a compilation of yield stress ($\Delta\sigma_y$) and ultimate stress ($\Delta\sigma_u$) change data, along with complementary information on alloy and irradiation conditions, for a large set of commercial type and split melt model RPV steels that were irradiated in the UCSB IVAR facility at the University of Michigan Ford Nuclear Reactor (FNR). This is the core part of the large IVAR experimental matrix, which consists of 1537 different combinations of alloy and irradiation conditions. These data do not include an extensive study of the effects of heat treatment on irradiation hardening and dissolved copper content that was reported previously [1], hence, are not presented in this report.

The irradiations were carried out in low, medium and high flux (ϕ) regimes and three irradiation temperatures (T_i) to overlapping ranges of fluences (ϕt) [2,3]. The IVAR facility was conceptually designed by UCSB and the Oak Ridge National laboratory (ORNL) Heavy Section Steel Irradiation (HSSI) Program. The engineering design and construction was carried out by ORNL and the facility was operated by the University of Michigan and ORNL staff for a total of 27,650 reactor hours between 1997 and 2003.

Neutron dosimetry was based on a detailed flux map developed by ORNL for the UCSB IVAR and adjoining ORNL Irradiation-Annealing-Reirradiation (IAR) facilities [3]. The flux map, that was derived from three-dimensional neutron transport calculations using

spectral adjustment procedures to fit multiple activation reaction dosimeter measurements. The data at dosimeter locations throughout the IVAR facility was then fit by physically motivated functions to describe the continuous spatial distribution of the flux. The nominal flux was taken at that at the center of each specimen subcapsule. The corresponding fluence was assumed to be the flux multiplied by the equivalent time of reactor full power operation. We report here flux values for neutrons with energies greater than 1 MeV (> 1MeV), but these can be translated to fluxes with other energy thresholds, as well as to dpa [3]. The range of flux for specimen irradiations is from ≈ 0.7 to 0.98 x 10^{16} n/m^2-s, and the corresponding fluences range from 0.01 to 3.32 x 10^{23} n/m^2. The precision of the flux and fluence estimates are estimated to be about ± 8% at one standard deviation.

Irradiations were carried out at 270, 290 and 310°C. The temperatures in the IVAR facility were monitored by a large number of thermocouples. Detailed heat transfer calculations were used to design and optimize the control system algorithms to maintain the samples at their target temperatures by increasing or decreasing the power to a large number of resistance heaters distributed throughout the IVAR facility [2]. Sensitivity studies indicated the specimen temperatures were maintained within a few degrees of their target values, except for one brief overpower transient. The overall uncertainty in the specimen temperatures is estimated to be about ± 5°C at one standard deviation. Various subsets of the RPV steels were irradiated to total of 40 different ϕ-ϕt-T_i capsule irradiation conditions.

Irradiations were carried out on a set of commercial type steels that included 13 commercial type submerged arc welds (SAW) and 3 base metals. A total of 41 split melt model steels (SMMS) were used to provide systematic and controlled variations in key elements such as Cu, Ni, Mn and P. While the SMMS are small heat model alloys, they were processed to produce microstuctures and mechanical properties that are very similar to those found in actual RPV steels. The SMMS composition matrix also provided a basis for assessing synergisms between the composition variables, such as the effect of Ni-Mn-Cu interactions. The welds and plates were irradiated in the as-received condition. The SMMS were given an austenitize, quench or normalize, temper, stress relieve and cool heat treatment, either in billet sections or equivalent stack-ups of coupons. The SMMS from the LV series were air quenched (normalized) and air cooled after the final stress relief. Those from the CM-series were salt bath quenched and cooled to 300°C at a rate of 8°C per hour following the final stress relief. Two alloys in the base CM and LV matrix were irradiated in the as tempered condition.

Post irradiation tests were carried out on sub-sized dog-bone shaped coupon tensile specimens. The tensile specimens were fabricated by precision die punching 0.5 mm thick coupons. The coupons were cut from sections of weld and plate, and for the SMMS alloys from forged or hot rolled billets. The tensile specimens held in magazine cartridges containing 29 individual lower loading fixtures, for positioning on a semi automated computer controlled load frame. The tensile tests were carried out at ambient temperature at a strain rate of ≈ 10^{-3}/s. The load-extension data (mostly, but not entirely digital) was converted to engineering stress strain data based on cross section area measurements on each specimen. The data presented in this report are based on measurements of the 0.2% offset yield stress (σ_y) and the ultimate tensile stress (σ_u) at

maximum load. Two standard reference material specimens were included in each test cartridge to assure high precision in all measurements. In almost all cases the irradiated σ_{yi} and σ_{ui} were based on the average of multiple tests. The normal ± one standard deviation (SD) uncertainty was determined for each set of specimens in this case. In the few cases, with only one test, no SD uncertainty could be assigned. The average one SD of the measured σ_y and σ_u were ±11.8 MPa and ±13.5 MPa, respectively.

The irradiation induced changes in the yield stress ($\Delta\sigma_y$) and ultimate tensile stress ($\Delta\sigma_u$) data were taken as the difference between the irradiated σ_{yi} and σ_{ui} and unirradiated control values of σ_{yu} and σ_{uu}, respectively. In most cases, the data unirradiated σ_{yu} and σ_{uu} were based on the overall average of multiple tests on a large number (typically 8 to 20) of the as-processed control specimens. However, in some cases there were significant specimen group to-group variations in σ_{yu} and σ_{uu}. This is believed to be primarily due to compositional, microstructural, heat treatment time-temperature history and specimen punching variations for different billet-coupon locations. In order to minimize the effects of such variations, all irradiated specimens could be traced to particular billet and coupon location. In those cases when the variability was significant, the irradiated specimens were paired with groups of unirradiated controls that were taken from nearby billet-coupon locations that showed similar behavior. Microhardness maps were also used to assess property gradients within and between the coupons, as well as on selected specimens. While tedious, this approach to grouping data was effective in reducing the scatter in the $\Delta\sigma_y$ and $\Delta\sigma_u$.

Since the main objective of this program was to provide a comprehensive map of the effects of combinations of material and metallurgical variables on the irradiation hardening of RPV steels, the significance of uncertainties in any individual $\Delta\sigma_y$ data point is greatly reduced compared to typical cases involving only a few materials and irradiation conditions. The database provides an overall “image” or “map” of irradiation hardening behavior, that can be viewed from a wide variety of perspectives, by taking various cross cuts though embrittlement variable space. The cross cuts show smooth and systematic variations in hardening as a function of different variables, as well as similar behavior for alloys with similar compositions. Thus there is a very large effective multiplicity in the IVAR database. Given the massive amount of data, extracting key trends is best done by the use of physically based models. Such a model-based analysis was carried out to assess the synergistic effects of flux, fluence and composition [4]. Another recent analysis compared the IVAR database to predictions of a transition temperature shift model fit to the power reactor surveillance database [5].

2. EXPERIMENTAL AND DATA REDUCTION PROCEDURES

2.1 Description of the IVAR Facility

UCSB and ORNL researchers collaborated in the conceptual design of the IVAR facility. The detailed engineering design and construction was carried out by ORNL and the facility was operated by ORNL and the University of Michigan staff for a total of 27,650 reactor hours between 1997and 2003. Note the following sections borrow information and figures from two detailed ORNL reports on the thermal analysis [2] and

flux mapping [3] of the IVAR facility. As shown in Figure 1a, the IVAR facility was located on the east face of the FNR core, in a cage-like assembly, along with the two other HSSI facilities IAR-1 and IAR-2. The front plate of the assembly acted as a thermal shield to attenuate gamma fluxes, thus reducing heating in the specimens. Measurements taken in the high flux region of the IVAR facility showed the gamma heating resulted in maximum temperatures below 150°C [2]. The specimen target temperatures were achieved by activating an array of resistive heaters coupled with a large number of thermocouples, and an automatic control system that are described below. As shown in Figure 1a, the IVAR and HSSI IAR facilities were mounted on a movable carriage riding on a rail track. This allowed them to be moved to the fixed position at the core face during irradiation, and then moved to a retracted to a position at the end of an irradiation cycle. The facility insertions and retractions were carried out while the reactor operated at full power, with the specimens pre-heated to 90% of their target temperature, greatly minimizing normal start-up and shutdown thermal transients. The entire facility was surrounded by a boral shield that reduced thermal neutron fluxes and, hence, the corresponding radioactivity levels of the samples, by about a factor of 10. The separate high-flux (HF) and intermediate/low-flux (IF/LF) regions are also shown in Figure 1b.

The HF and IF/LF regions are shown more clearly in the perspective drawing in Figure 2 and in the elevation view in Figure 3. The HF specimen basket section is about 63 cm high by 6 cm wide by 4 cm deep. The high flux section accommodated a vertical stack up of nine 50.8 x 50.8 x 12.7 mm specimen subcapsules that were 1 subcapsule wide and 2 subcapsules deep in the horizontal plane. Thus there were a total of 18 full size high flux capsules. There were 2 capsules in both the 270 and 310°C zones and 10 capsules in the 290°C zone. The temperature zones were separated by approximately 2.5 cm gas insulating gaps. The sub-capsule holder basket and housing assembly were made out of stainless steel to minimize heat conduction. The IF/LF specimen basket is 37 cm high, 6 cm wide and 16 cm deep. This accommodates a total vertical stack-up of 4 capsules that is 1 capsule wide and 10 capsule thicknesses deep. The IF/LF specimen basket contained 9 full sub-capsules at both 270°C and 310°C, and 18 at 290°C. There is also space for 4 half-size specimen packets in the IF/LF portion of the facility opposite a thermocouple blade, which is located in the center of the IF basket. A map of the location of the 58 sub-capsule locations is shown in Figure 3.

As is also shown in Figure 2, both the HF and IF/LF specimen baskets were positioned at the bottom of a 6061aluminum sealed thimble that extended to above the top of the reactor pool. The capsule baskets were suspended in position by a cable attached to the shield plug. A low positive pressure helium purge provided for good heat transfer as well as corrosion-oxidation protection. The gas flow was continuously monitored for moisture.

The basic FNR operation cycle involved 12-day irradiation cycles separated by 4-day maintenance and fueling shutdown periods. The subcapsules were inserted and removed, as needed, during the scheduled reactor shutdown periods. This was accomplished by using a transfer cask to move the entire irradiation shied plug and basket assembly to a nearby hot cell for removal and insertion of the specimen subcapsules, which are described in more detail below. The subcapsules were made of 6061 aluminum. Dummy capsule was used to provide a stable neutronic environment when the location was not

occupied by an actual specimen subcapsule. These dummy subcapsules contained masses of steel and aluminum typical of those for a specimen subcapsules.

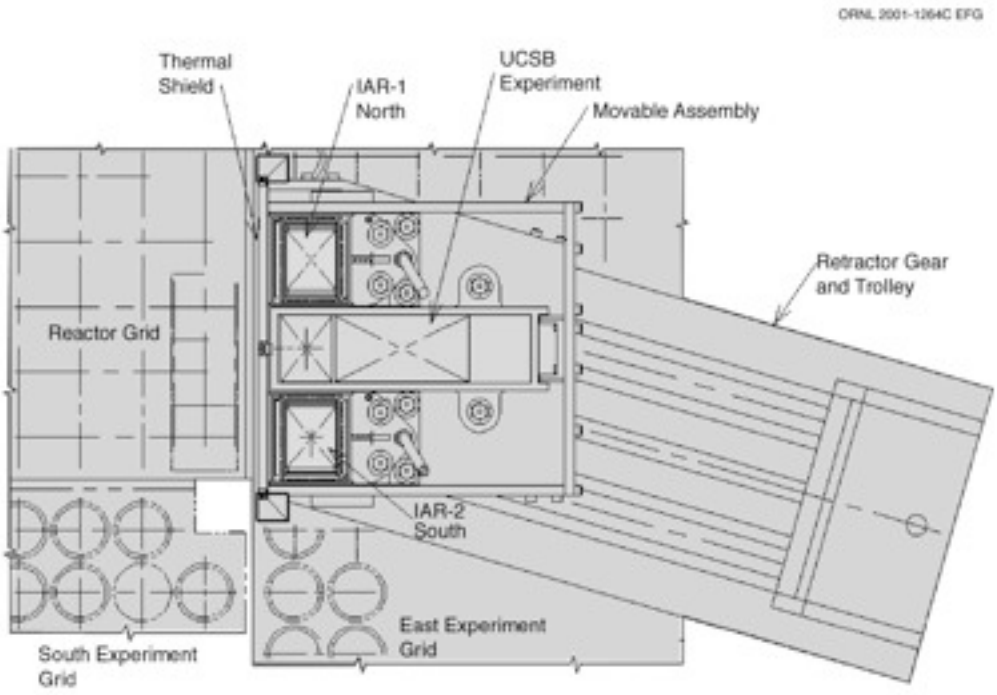

Figure 1a. IVAR and IAR irradiation facility at the east face of the FNR [2].

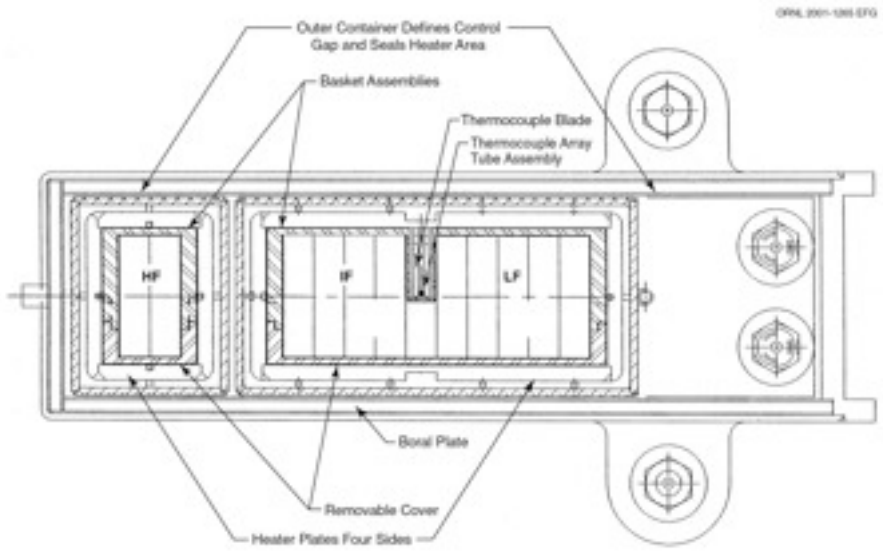

Figure1b. Cross section view through the IVAR facility at the FNR core midplane [2].

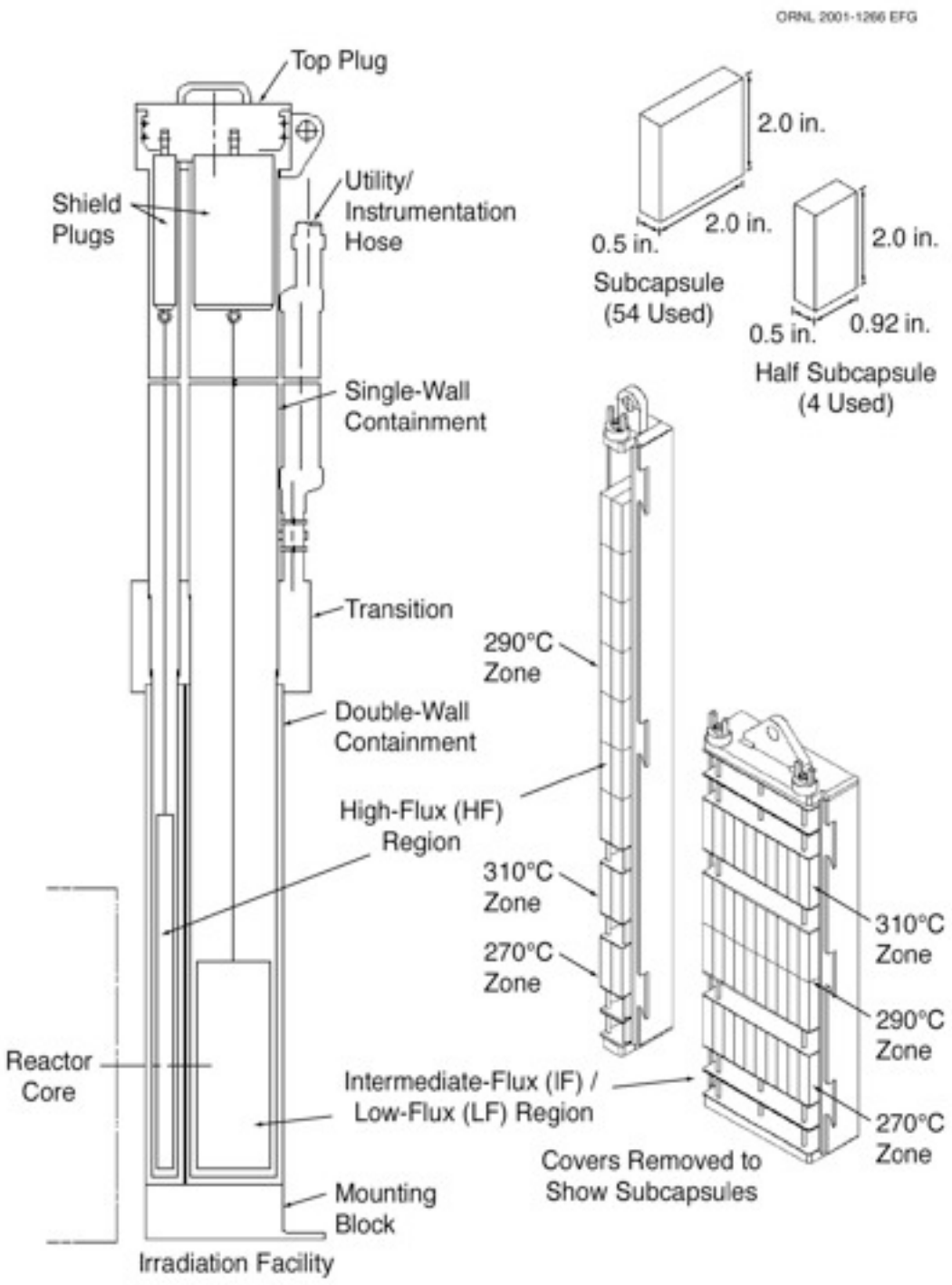

Figure 2. Perspective views of the IVAR facility [2].

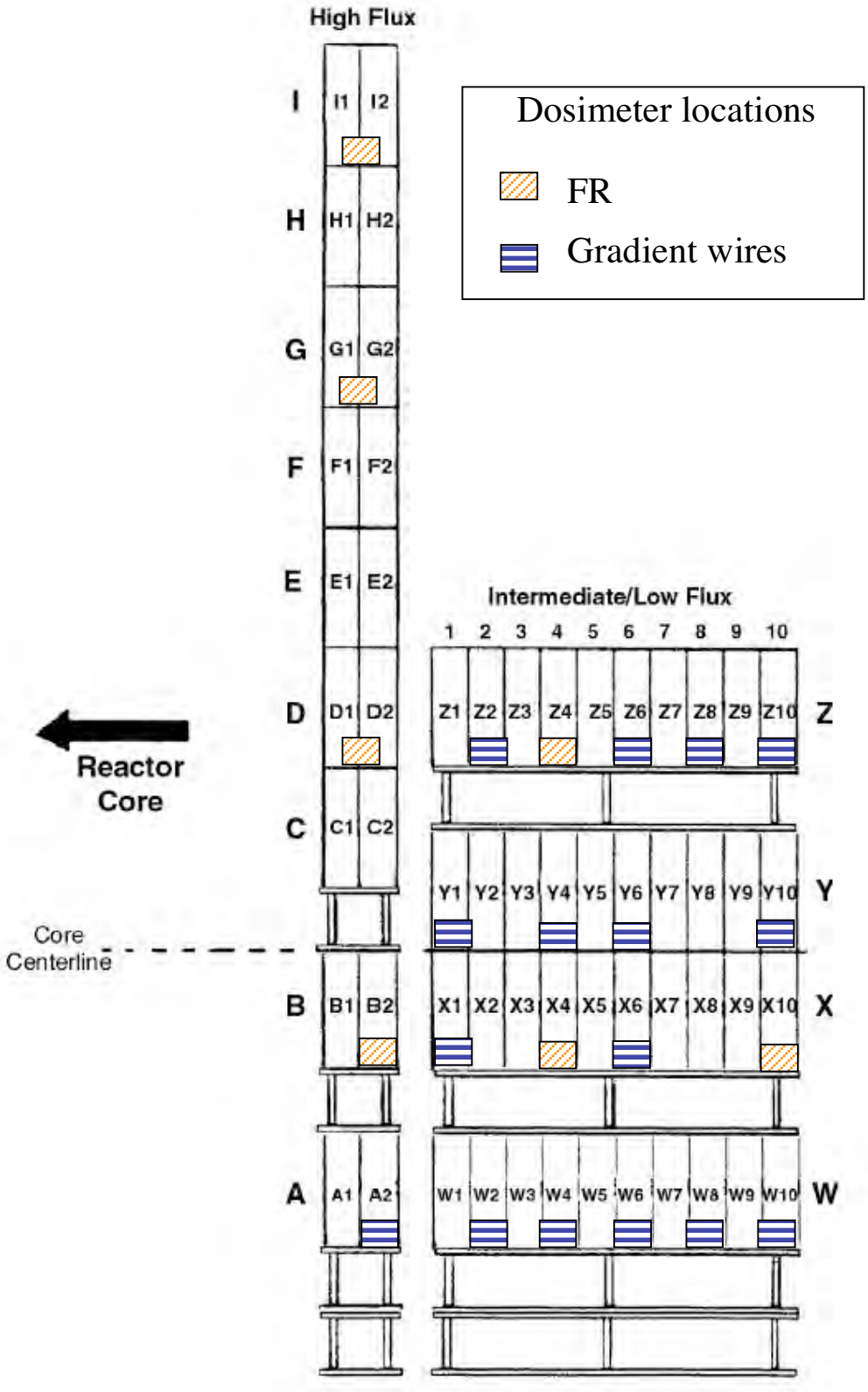

Figure 3 Elevation side view of the IVAR HF and IF/LF facility with the code specifying the subcapsule positions [2]. The boxes show the locations of the dosimeters used in the flux mapping study [3].

2.2 Temperature Monitoring and Control

The thermal analysis and design of the IVAR facility is described in detail in an ORNL report [2]. The main conclusions from that report are summarized here. Since the gamma heating is low, the target specimen temperatures were achieved by controlling the current through 50 electrical resistance heaters, permanently located in 25 separate heater zones in the specimen basket housing, as shown in Figure 4. There were 11 heater zones in the HF housing and 14 heater zones in the IF/LF housing. Temperatures were monitored by 49 permanent thermocouples (28 in HF housing, while 21 in MF/LF). Some of the thermocouples in the IF zone were positioned in blades that ended at the center of the capsule locations.

Heater and thermocouple locations that optimized the temperature distribution throughout both sections of the facility were determined by extensive three-dimensional finite element (FE) heat transfer calculations using the ORNL-in house HEATIG7.2 code [2]. This thermal model incorporated details of the as-built facility configuration. The analysis considered thermal expansion of various components, and modeled the details of the specimen packet and heater plate/thermocouple regions to relate the thermocouple to the specimen temperatures. The analysis included nuclear heating derived from the full neutron field characterization described in the following section. To improve the assumed distribution of nuclear heating in the models, a pre-irradiation experiment was performed in which the facility was placed against the reactor face with no electrical heating. The thermocouple readings for this test were compared to predictions of the thermal model. The assumed nuclear heating distribution was then adjusted to achieve the best match with the thermocouple data. The root mean square deviation between the calculated and observed thermocouple readings was 0.8°C. The control set-point target temperature of all the thermocouples were extracted from the thermal model based on the condition that all the specimen packets were within the desired temperature ranges.

Additional analyses, including more detailed models of the specimen packets, were performed using the optimized temperature control algorithm showed that even with to 50% reductions in either thermal conductivity or nuclear heat generation (separately), the specimen temperatures were maintained within ±5°C. The predictions of the thermal models were also consistent with measurements by thermocouples attached directly to the specimens in the adjoining IAR facilities [2]. Since the complex heat transfer paths were primarily though the capsule holder, basket assembly and capsules, the small amount of gamma heating itself has little local effect on the temperatures of the specimens themselves, although those in the capsule center might run up to a few °C higher than the ones on the front and back bottom. However, given the random positioning, and high effective multiplicity, the specimens for a given alloy, such a small potential temperature variation would have little effect on conclusions derived from an analysis of the IVAR database.

Actual operation and monitoring was performed through a supervisory control and data acquisition (SCADA) system, which consists of the main control computer (SCADA node), electronic heater controllers, electronic flow controllers, and moisture monitoring sensors with a man-machine interface that was remotely accessible at all times. The

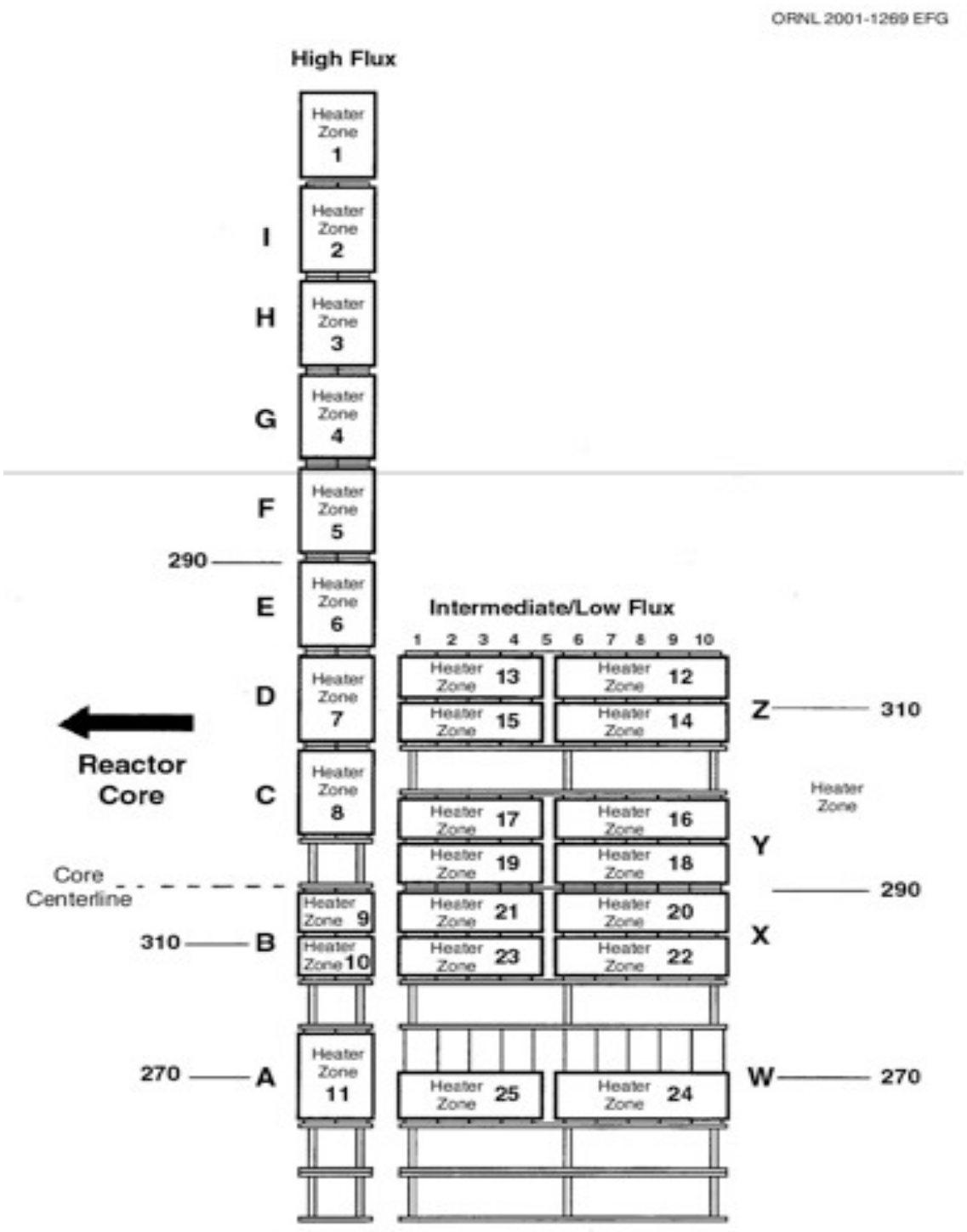

Figure 4 Locations of heater zones in IVAR facility [2]

IVAR SCADA and the SCADA node and those that controlled the HSSI-IAR facilities served as backups for one another. Except for one 45 hour period, related to weather induced power outages, when temperatures in a few locations rose up to 35°C above the setpoints, the temperature control was outstanding. The transient occurred early in the irradiation program (in March after a January start-up) and showed no discernable effects when comparing data that did and did not experience the transient.

Figures 5 (HF) and 6 (MF/LF) show that all the thermocouples operated within ±3°C of their target temperatures. Figure 7, shows the stability of temperatures measured by thermocouples 6, 32, and 46, located in three temperature regions of the facility, during a 10-day period in March, 1999. Figure 8 shows a corresponding expanded view for a 60 min period, demonstrating a short time temperature variation less than 1°C. The average standard deviation of the thermocouple temperatures was about ±3°C around their set point. Alarms were set at ±5°C.

2.3 Dosimetry

This section briefly summarizes the characterization of the neutron field in the IVAR facility carried out by ORNL HSSI program [3]. The characterization consisted of neutron transport calculations, measurements using radiometric monitors and determination of best-estimate irradiation parameters. The best estimates of neutron fluxes were obtained by performing least-squares adjustments of the calculated multi-group neutron spectra based on measured specific activities, or reaction rates, from a large set of radiometric monitors. More detailed information is available in a comprehensive ORNL HSSI dosimetry report [3].

Figure 9 shows a top view of the coordinate system used in the dosimetry study. The vertical origin is at the reactor midplane (z = 0) and the horizontal origin is at the center of the IVAR capsule (x = 0) and the just inside of the thermal shield (y = 0). Two types of neutron dosimeters were used in the experiments: bare Fe, Ni, and Al-0.100%Co gradient wires; and fission radiometric dosimeter sets (FRDs). After irradiation the long gradient wires, often spanning the entire specimen region, were finely sectioned and counted to give a high-resolution map of flux variations with position. The standard FRD contained Co, Fe, Ni, Ti, and Cu wires, as well as NpO_2 and UO_2. The NpO_2 and UO_2 dosimeters were encapsulated in vanadium. The FRDs were located in a 0.89-mm thick gadolinium vials to attenuate thermal neutrons and sealed inside stainless steel tubes. Prior to the initiation of the specimen irradiations, 16 Fe, Ni and Co dosimetry wire sets and 7 FRDs were optimally distributed throughout the IVAR volume and irradiated for 437 full reactor power h. The activation reactions used in the dosimetry for IVAR are summarized in Table 1. The locations of the dosimeter packets are shown in Fig. 3.

The neutron transport calculations were performed with the 3-D TORT code, which was developed for modeling complex geometries and large flux gradients that are characteristic of the IVAR and IAR facilities. The reactor and the HSSI/UCSB capsules were modeled as two separate neutronic regions, using the TORT discontinuous mesh option as is shown in Figure 10. A total of 540,400 space cells (10,808 cells horizontally and 50 planes vertically) formed 217 rectangular "bodies" and 53 material zones. The

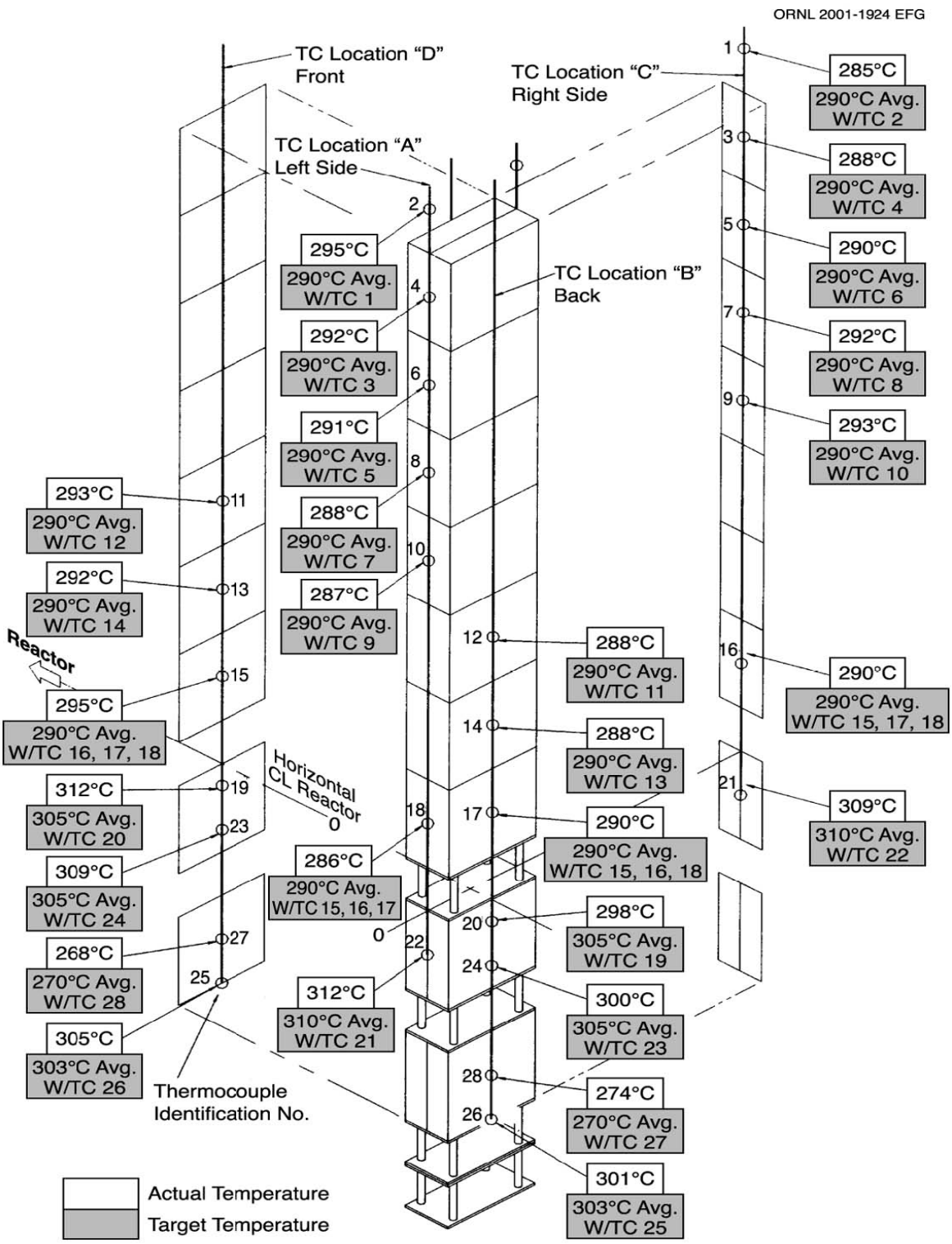

Figure 5 The temperature distribution in the HF region of the HSSI-UCSB facility [2]

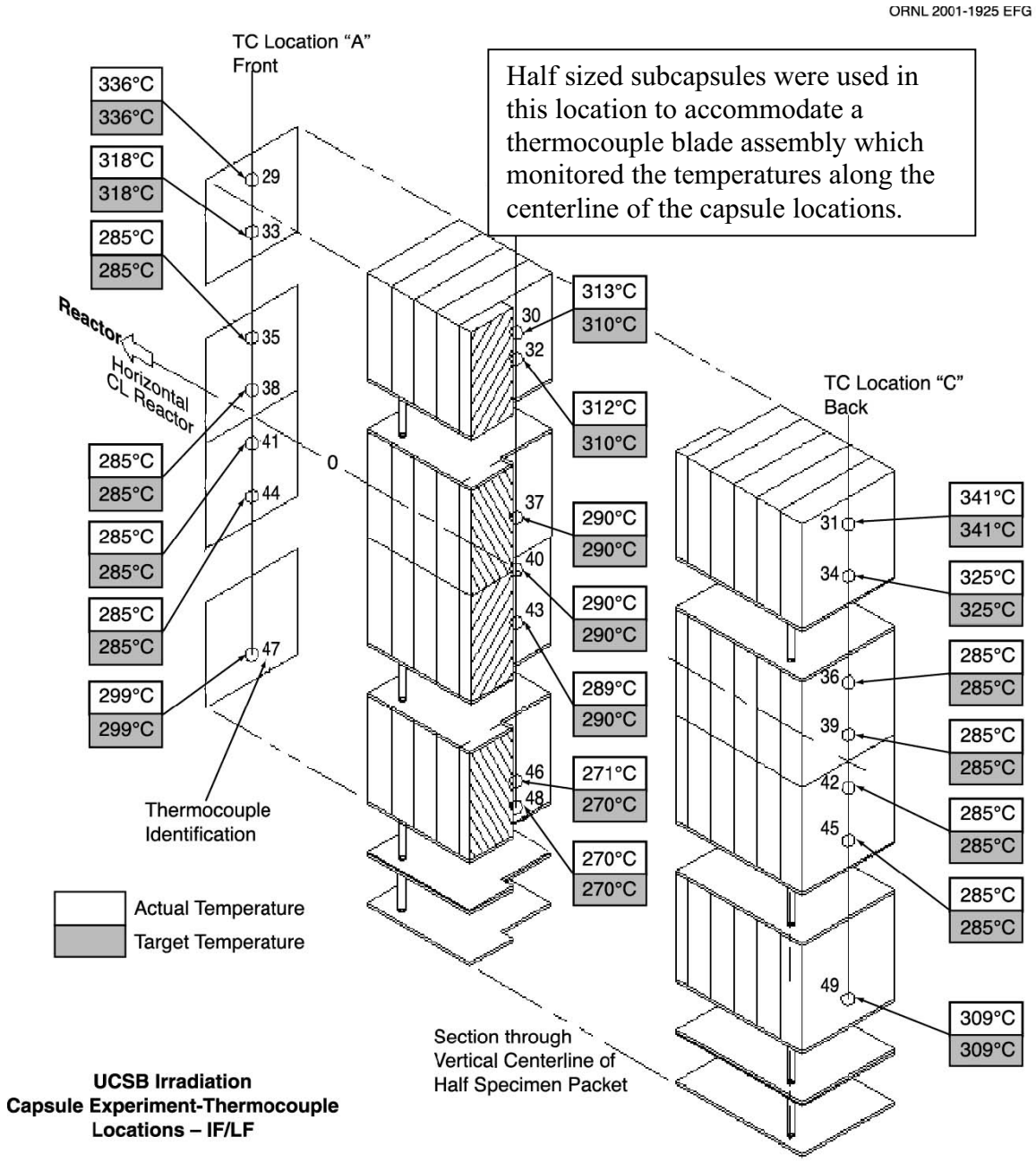

Figure 6 The temperature distribution in the MF/LF region of the HSSI-UCSB facility[2].

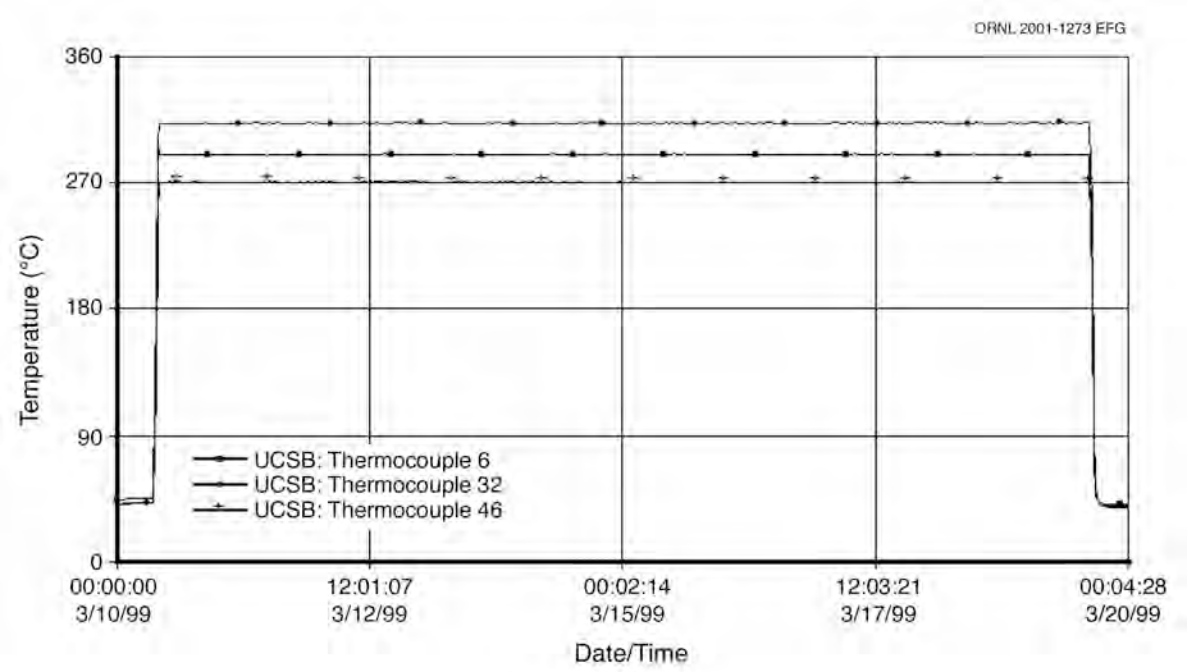

Figure 7 Temperature plots for three thermocouples (one from each temperature zone) in the IVAR facility for a partial-cycle of reactor operation showing excellent temperature control [2].

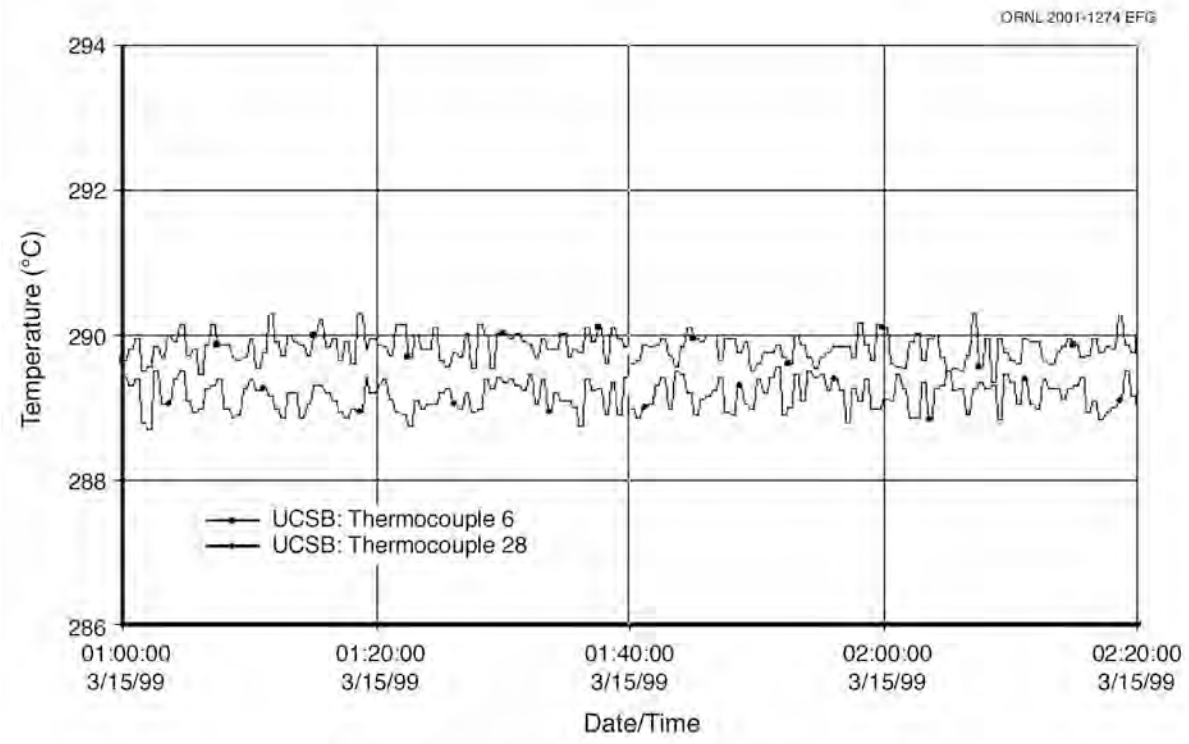

Figure 8 Temperature plots for two thermocouples (same temperature zone) in the IVAR facility for 80 minutes, demonstrating excellent temperature stability and control [2].

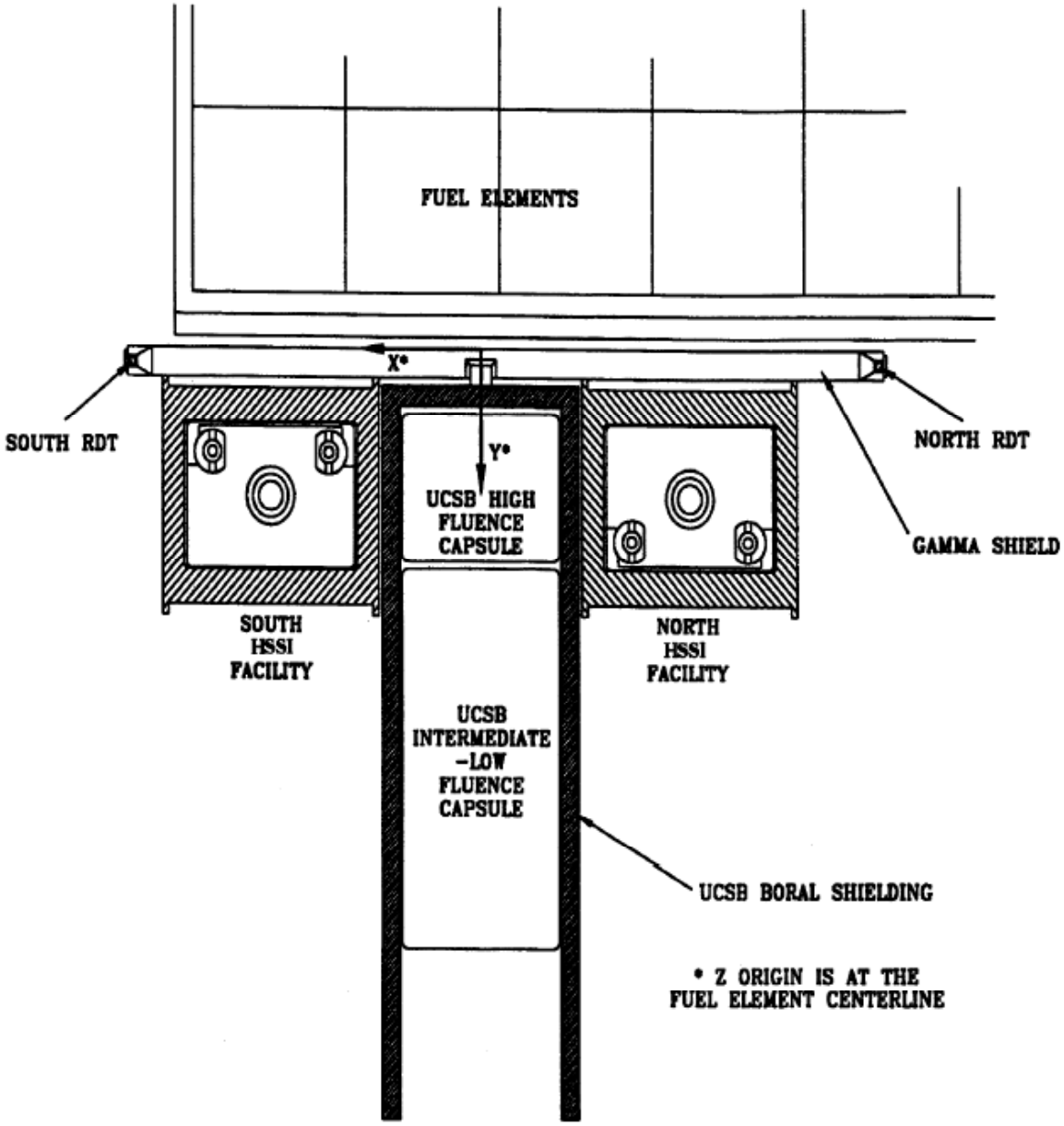

Figure 9 Horizontal cross section of the IVAR and IAR facilities, showing the flux map coordinate system [3].

Table 1 Nuclear Reactions Used in the ORNL Reaction Rate Measurements

Reaction	Dosimeter type
^{46}Ti (n,p) 46Sc	FRDs
^{54}Fe (n,p) ^{54}Mn	Gradient wires, FRDs
^{58}Fe (n,γ) ^{59}Fe	Gradient wires
^{59}Co (n, γ) ^{60}Co	FRDs
^{58}Ni (n,p) ^{58}Co	Gradient wires, FRDs
^{63}Cu (n,α) ^{60}Co	FRDs
^{237}Np (n,f) ^{95}Zr	FRDs
^{237}Np (n,f) ^{103}Ru	FRDs
^{237}Np (n,f) ^{141}Ce	FRDs
^{238}U (n,f) ^{95}Zr	FRDs
^{238}U (n,f) ^{103}Ru	FRDs
^{238}U (n,f) ^{141}Ce	FRDs

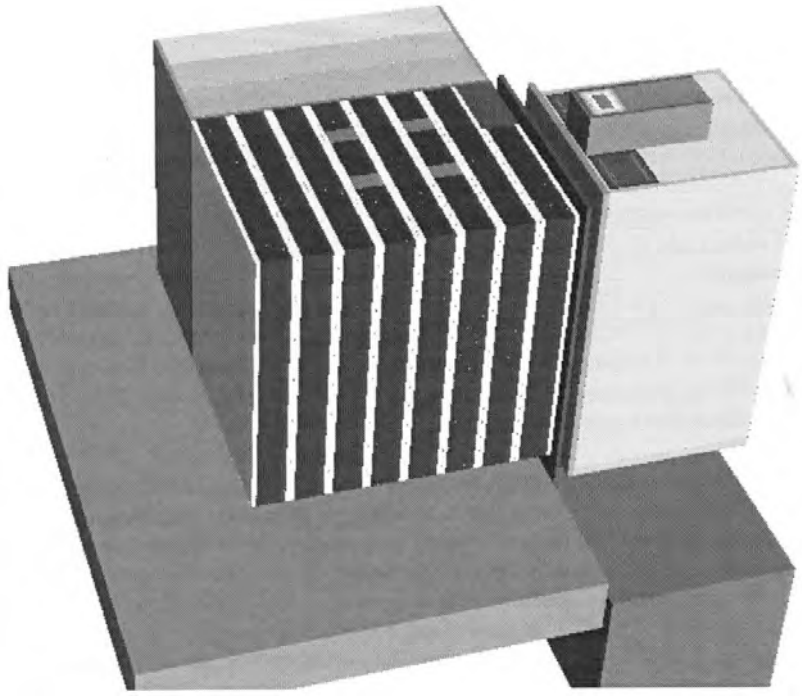

Figure 10 Schematic drawing of the major parts of the TORT geometry model for the neutron transport calculation of the HSSI/UCSB irradiation facilities. The large box region on the left is the FNR core. The irradiation capsules are on the right [3].

Table 2 Threshold ϕ and dpa Spatial Variation Fit Constants [3]

E_t (MeV)	Region	A ($cm^{-2}s^{-1}$)	B_x (cm^{-1})	x_o (cm)	B_z (cm^{-1})	z_o (cm)	λ (cm^{-1})
1	HF	2.520	0.0058	-6.066	0.03976	-0.2434	0.1598
	MF/LF	2.389			0.04360	-1.6090	0.1486
	All	2.464	0.05863	-5.919	0.03952	-0.3017	0.1550
0.5	HF	3.750	0.05689	-6.218	0.04001	-0.3986	0.1401
	MF/LF	4.026			0.04422	-1.5290	0.1451
	All	3.724	0.05706	-6.175	0.03969	-0.4604	0.1384
0.1	HF	5.487	0.05752	-5.963	0.04015	-0.6028	0.1285
	MF/LF	6.371			0.04543	-1.6410	0.1413
	All	5.472	0.0574	-6.008	0.03978	-0.6728	0.1283
dpa	HF	3.516	0.05738	-6.124	0.03984	-0.3932	0.1494
	MF/LF	3.543			0.04453	-1.5740	0.1454
	All	3.451	0.05788	-6.005	0.03957	-0.4556	0.1457

Units: A (cm^2/s), B_y (cm^{-1}), x_o (cm); B_z (cm^{-1}), z_o (cm), λ (cm^{-1})

Table 3 Comparisons of Capsule Dosimeter and ORNL Flux Map Results

Capsule - ϕ	C1/HF ϕ	X?/MF ϕ	X?/LF ϕ
Final ORNL flux map	9.7×10^{15}	3.2×10^{15}	7.0×10^{14}
NIST subcapsule dosimetry	9.7×10^{15}	3.4×10^{15}	6.0×10^{14}

Units: ϕ (n/m^2-s)

calculation was performed in 47 energy groups using the modified SAILOR library cross-sections, including the P approximation to the anisotropic angular scattering dependence and a S directional quadrature set. The transport model used a neutron source determined for the FNR power distribution over three core cycles.

The calculated 47-group (j) neutron energy (E_j) spectrum, $\phi(x,y,z,j)$ were used along with ENDF-B energy dependent reaction cross sections, $\sigma_i(E_j)$, to determine spectral averaged cross sections, $<\sigma_i(x,y,z)>_t$ for neutron with energies greater than a specified threshold energy, $E_j > E_k$, taken as 0.1, 0.5 and 1 MeV, for the various nuclear reactions (i) at the (x,y,z) locations of the dosimeter sets. The spectral averaged reaction cross sections are given by

$$<\sigma_i(x,y,z)>_k = \Sigma_{j\geq k}\phi(x,y,z,j)\sigma_i(j)/\Sigma_{j\geq k}\phi(x,y,z,j) \quad (1)$$

The total flux at x,y,z greater than E_t, $\phi_k(x,y,z)$ is

$$\phi_k(x,y,z) = \Sigma_{j\geq k}\,\phi(x,y,z,j) \quad (2)$$

The reaction rates are related to the threshold fluxes and cross sections as

$$R_i(x,y,z) = <\sigma_i(x,y,z)>_k\phi_k(x,y,z) \quad (3)$$

Measured to calculated $R_i(x,y,z)$ ratios were used to determine the best-estimate $\phi_k(x,y,z)$ at the dosimeter locations. The LSL-M2 code iteratively adjusted the flux spectrum $\phi(x,y,z,j)$, and corresponding $<\sigma_i(x,y,z)>_k$, at the location of each dosimeter set to a least square convergence between all the calculated and measured $R_i(x,y,z)$. A smooth $\phi_k(x,y,z)$ spatial flux function was then least square is fit to the $\phi_k(x,y,z)$ data points as

$$\phi_k(x,y,z) = A\cos[B_x(x-x_0)]\cos[B_z(z-z_0)]\exp(-\lambda y) \quad (4)$$

A total of 256 reaction rates at 129 locations in all three irradiation facilities were used to adjust the calculated neutron fluxes. In addition to the threshold fluxes, the $\phi(x,y,z,k)$ were used to calculate the displacement per atom (dpa) rate in iron using American Society for Testing and Materials (ASTM) E-693 dpa cross sections [6]. The least square fit constants A, B_x, x_0, B_z, z_0, and λ are summarized in Table 2. They were used to calculate the flux (or dpa) at the centers of each subcapsule. The horizontal isoflux profiles at the reactor midplane are shown in Figure 11a. The corresponding axial flux profiles at the centers of the HF, IF and LF are shown in Figure 11b.

In addition to IVAR flux map provided by ORNL, Ni and Fe dosimetry wires were included in all of the IVAR subcapsules. However, only three sets of these were actually counted and analyzed to compare to the ORNL flux map. The activity measurements and analysis were provided by the National Institute of Standards and Technology (NIST) for wires located in the HF, MF and LF regions along the IVAR centerline extending from the reactor core. The results, that are summarized in Table 3, show that the NIST subcapsule flux measurements agree very well with the ORNL flux map. The average deviation from the mean value is ±3.6%.

The fluence for each capsule, m, was taken as the product of flux at its center at ϕt_{km} =

$\phi_k(x_m,y_m,z_m)$ and the capsule full power irradiation time, t_m,

$$\phi t_{km} = \phi_{km} t_m \quad (5)$$

Table 4 summarizes the ϕ_{km} andf ϕt_{km} for E > 1 MeV for all 40 IVAR capsules that provided data included in this report.

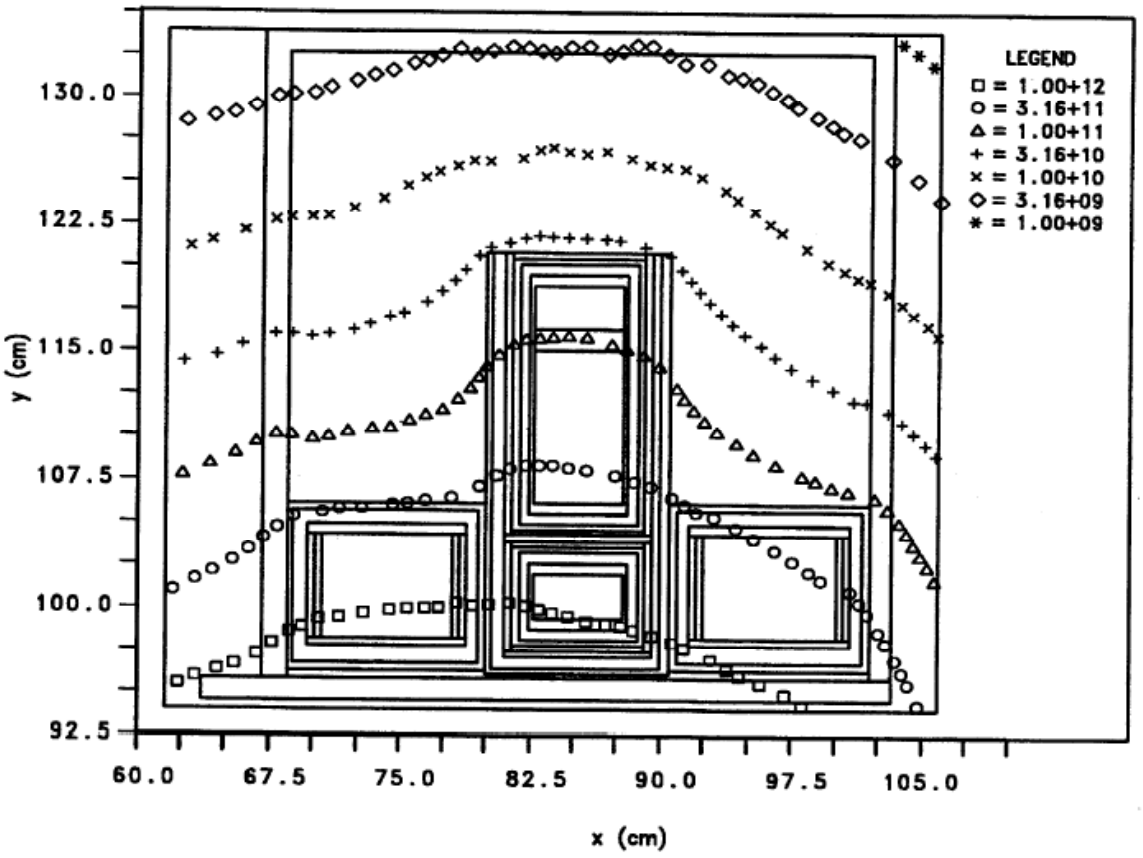

Fig. 11a Isoflux contours (E > 1 MeV) for the IVAR and IAR at the reactor midplane [3].

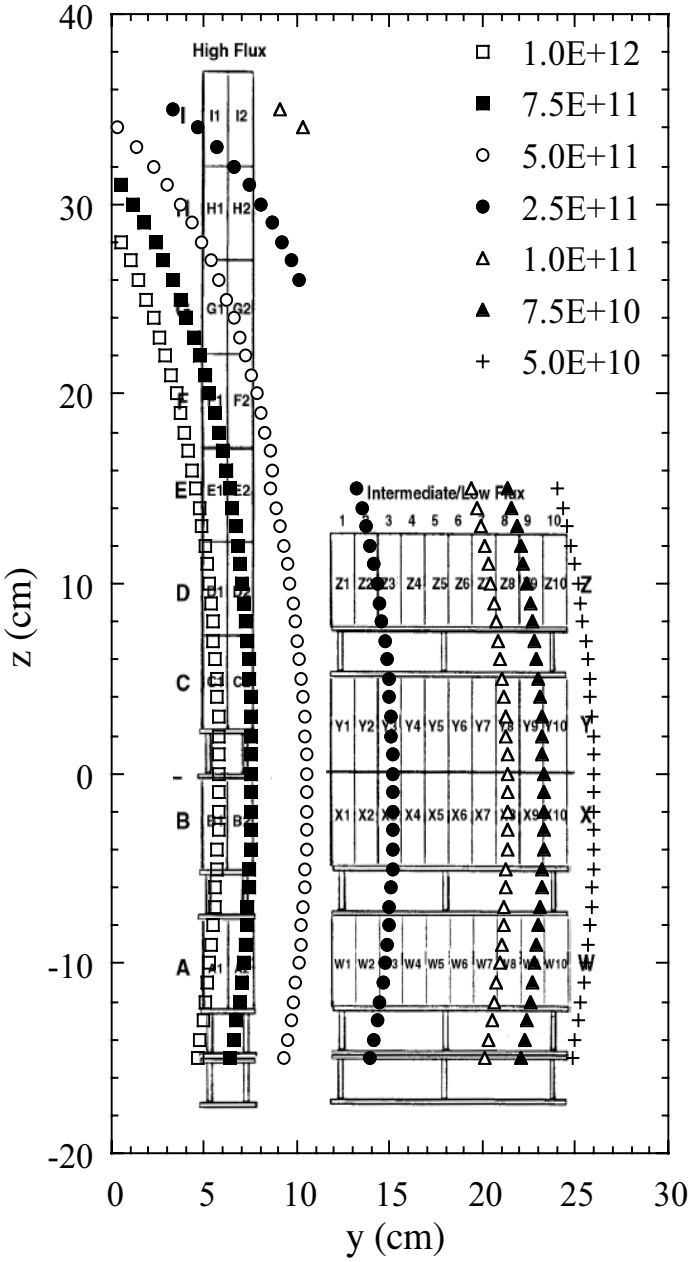

Fig. 11b Vertical isoflux contours (E > 1 MeV) at the center of IVAR facility.

Table 4 IVAR Capsule Irradiation Conditions

Capsule	ϕ-category	ϕ	ϕt	T_i
T1	HF	0.78	0.07	290
T2	HF	0.78	0.18	290
T3	HF	0.78	0.34	290
T4	HF	0.97	0.75	290
T5	HF	0.78	1.36	290
T6	HF	0.97	3.32	290
T7	HF	0.92	0.38	270
T8	HF	0.92	1.52	270
T9	HF	0.98	0.40	310
T10	HF	0.98	1.47	310
T11	MF	0.26	0.04	290
T12	MF	0.32	0.10	290
T13	MF	0.31	0.24	290
T14	MF	0.32	0.48	290
T15	MF	0.26	0.85	290
T16	MF	0.30	1.57	290
T17	MF	0.25	0.43	270
T18	MF	0.36	1.71	270
T19	MF	0.23	0.40	310
T20	MF	0.34	1.60	310
T21	LF	0.10	0.03	290
T22	LF	0.10	0.11	290
T23	LF	0.08	0.24	290
T24	LF	0.08	0.40	290
T25	LF	0.08	0.26	270
T26	LF	0.12	0.41	270
T27	LF	0.07	0.24	310
T28	LF	0.11	0.38	310
T29	HF	0.89	0.44	290
T30	LF	0.07	0.02	290
T31	HF	0.72	0.06	290
T32	MF	0.26	0.02	290
VT1	MF	0.21	0.84	270/290
VT2	MF	0.21	0.84	290/270
SR1	HF	0.97	0.85	290
A1	LF	0.07	0.01	290
A2	LF	0.07	0.01	290
A3	LF	0.07	0.02	290
A4	LF	0.07	0.03	290
A5	HF	0.51	0.04	290

Units: $\phi(10^{16}n/m^2\text{-}s)$, $\phi t(10^{23}n/m^2)$, $T_i(°C)$

2.4 RPV Steel Alloys

The large set of RPV steels investigated in the IVAR program were classified in three general groups:

1. CM-Series SMMS: A set of 31 complex A533B-type split-melt bainitic low alloy steels with composition variants to evaluate the effects of various combinations of Cu (0.0 to 0.8%), Ni (0.0 to 1.6%), Mn (0 to 1.6%) and P (0.005 to 0.040%). The compositions given in the text are nominal. The measured compositions, in weight percent, unless otherwise stated, and heat treatments are shown in Table 5. A total of 31 variants around a base composition were used to evaluate the effects of: a) *combinations* of Cu (0.0 to 0.8%), Ni (0.0 to 1.6%), Mn (0 to 1.6%) and P (0.005 to 0.040%) contents; and, b) *single* variable modifications of Mo, N, C, B and As + Sn + Sb contents. All 31 alloys nominally contained 0.15%C, 0.005%Al and 0.25%Si. The alloys were fabricated by Sheffield University in collaboration with AEA Technology, Harwell and UCSB. They were melted and re-melted in final (approximately) 10-kg ingots followed by hot forging to 18 mm plate. The alloys received a baseline heat treatment consisting of: austenitize at 900°C for 0.5h; salt bath quench to 450°C with a 10 min hold; air cool; temper at 660°C for 4h: air cool; stress relief anneal at 607˚C for 24 h; and programmed cool at 8˚C/h to 300˚C; and air cool. This will be referred to as the standard stress relief (SSR) heat treatment. The SSR yielded prior austenite grain sizes averaging about 50 μm and microstructures ranging from tempered bainite (most CM alloys) to mixed tempered ferrite-bainite. Banding was observed in some alloys. The unirradiated yield stress of the CM-series alloys varied from about 385 to 495MPa, with an average $\sigma_y \approx 470$ MPa.

2. LV-Series SMMS: A second set of 10 complex A533-type split-melt bainitic steels was also used to evaluate the effects of systematic variations in Cu and Ni content. The compositions and heat treatments are also shown in Table 6. The LV-series alloys were fabricated to UCSB specifications by CANMET and supplied by MRK associates. They were melted and remelted in final (approximately) 20-kg ingots hot-rolled to 27-mm plate. The LV-series alloys contain about 1.4%Mn versus a base composition of 1.6%Mn for the CM-series. The baseline heat treatment for the alloys was as follows: austenitize at 900°C for 1 h; air quench (normalize); temper at 664°C for 4 h; air cool; stress relieve at 600°C for 40 h, furnace cool to 300°C; air cool. The microstructures and unirradiated properties of the LV-series and CM-series alloys are very similar. The LV-series steels have been irradiated in previous programs at a variety of conditions, primarily around 300°C, as summarized in more detail elsewhere [7]. The unirradiated yield stress of the LV-series alloys varied from about 470 to 550MPa, with an average $\sigma_y \approx 500$ MPa

3. CWP-Series Welds and Plates: A set of 16 commercial-type welds (13) and base metals (3) was used to link the IVAR results to irradiated tensile and fracture property data for many of these steels from other programs, including surveillance data in some cases. The compositions and heat treatments are given in Table 7. This information was taken from the literature, or based on documentation provided by

Table 5 CM-Series Alloys Chemistries and Heat Treatment

Alloy	Cu	Ni	Mn	Cr	Mo	P	C	Si	S	Notes
CM1	0.01	0.01	1.67	0.04	0.56	0.003	0.13	0.15	0.004	
CM2	0.01	0.01	1.65	0.04	0.56	0.041	0.14	0.16	0.004	
CM3	0.02	0.85	1.60	0.05	0.49	0.006	0.13	0.16	0.000	
CM4	0.02	0.86	1.53	0.05	0.55	0.031	0.16	0.16	0.003	
CM5	0.02	0.86	1.61	0.04	0.53	0.050	0.15	0.16	0.000	
CM6	0.02	1.68	1.50	0.05	0.54	0.007	0.15	0.17	0.003	
CM7	0.00	1.70	1.55	0.05	0.56	0.047	0.16	0.17	0.003	
CM8	0.01	0.86	0.01	0.04	0.55	0.004	0.13	0.14	0.002	
CM9	0.01	0.86	0.85	0.04	0.55	0.003	0.15	0.15	0.003	
CM10	0.02	0.88	1.66	0.05	0.53	0.008	0.16	0.17	0.004	
CM11	0.34	0.85	1.64	0.02	0.53	0.006	0.15	0.18	0.003	
CM12	0.86	0.84	1.65	0.02	0.51	0.006	0.15	0.17	0.003	
CM13	0.11	0.83	1.61	0.00	0.51	0.004	0.15	0.16	0.000	
CM14	0.11	0.83	1.62	0.00	0.52	0.040	0.16	0.17	0.000	
CM15	0.22	0.02	1.59	0.02	0.58	0.002	0.14	0.15	0.003	
CM16	0.22	0.82	1.58	0.00	0.51	0.004	0.16	0.25	0.000	
CM17	0.22	1.59	1.54	0.00	0.50	0.004	0.16	0.25	0.000	
CM18	0.43	0.02	1.70	0.02	0.56	0.002	0.14	0.15	0.003	
CM19	0.42	0.85	1.63	0.01	0.51	0.005	0.16	0.16	0.003	
CM20	0.43	1.69	1.63	0.02	0.50	0.006	0.16	0.16	0.003	
CM21	0.42	0.84	0.01	0.02	0.58	0.002	0.14	0.14	0.003	
CM22	0.42	0.84	0.84	0.02	0.56	0.002	0.14	0.14	0.003	
CM23	0.01	0.83	1.62	0.04	0.55	0.002	0.26	0.15	0.003	
CM24	0.02	0.87	1.65	0.05	0.52	0.006	0.34	0.15	0.003	
CM25	0.01	0.87	1.53	0.05	0.52	0.003	0.14	0.17	0.002	200 appmN
CM26	0.01	0.87	1.66	0.05	0.52	0.006	0.16	0.17	0.003	0.02%Sn+As+Sb
CM27	0.01	0.84	1.60	0.05	0.51	0.002	0.16	0.16	0.003	10 ppmB
CM28	0.42	0.84	1.60	0.02	0.51	0.002	0.16	0.17	0.003	10 ppmB
CM29	0.21	0.02	1.68	0.02	0.02	0.002	0.14	0.14	0.003	
CM30	0.22	0.85	1.64	0.42	0.50	0.006	0.16	0.16	0.003	
CM31	0.01	0.86	1.65	0.05	0.51	0.006	0.16	0.17	0.003	

Compositions in weight %; Other common elements (otherwise noted): N < 50 ppm. Sn/As/Sb ≈ 0.005, Al ≈ 0.01 to 0.03%, B < 1ppm; Heat treatment for CM alloys: austenitize 900°C 30 min/ salt quench 450°C 10 min/ temper 660°C 4hrs air cool/ stress relief 60

Table 6 LV-Series Alloys Chemistries and Heat Treatments

Alloy	Cu	Ni	Mn	Mo	P	C	Si	S
LA	0.40	0.00	1.37	0.55	0.005	0.14	0.22	≤0.015
LB	0.40	0.18	1.35	0.55	0.005	0.14	0.22	≤0.015
LC	0.41	0.86	1.44	0.55	0.005	0.14	0.23	≤0.015
LD	0.38	1.25	1.38	0.55	0.005	0.19	0.23	≤0.015
LG	0.00	0.74	1.37	0.55	0.005	0.16	0.22	≤0.015
LH	0.11	0.74	1.39	0.55	0.005	0.16	0.24	≤0.015
LI	0.20	0.74	1.37	0.55	0.005	0.16	0.24	≤0.015
LJ	0.42	0.81	1.34	0.55	0.005	0.16	0.13	≤0.015
LK	0.80	0.81	1.13	0.55	0.005	0.13	0.13	≤0.015
LO	0.41	0.86	1.44	0.55	0.005	0.14	0.23	≤0.015

Compositions in weight %; Heat treatment for L alloys: austenitized 900∞C/1h; air cool; temper 664ºC/4h; air cool; stress relieved at 600ºC/40h; furnace cooled to 300ºC; air cooled. wth the exception of LO, which was not stress relieved after tempering

Table 7 CWP-Series Alloys Chemistry and Heat Treatment

Alloy	Cu	Ni	Mn	Cr	Mo	P	C	Si	S	HT
A	0.21	0.63	1.69	0.14	0.40	0.014	0.08	0.45	0.013	1
B	0.28	0.69	1.63	0.10	0.40	0.018	0.09	0.54	0.009	2
C	0.06	0.62	1.30	0.08	0.31	0.009	0.08	0.37	0.010	3
62W	0.23	0.60	1.61	0.12	0.39	0.020	0.08	0.59	0.007	4
63W	0.3	0.69	1.65	0.10	0.43	0.016	0.10	0.63	0.011	5
65W	0.22	0.60	1.45	0.09	0.39	0.015	0.08	0.48	0.015	6
67W	0.27	0.69	1.44	0.09	0.39	0.011	0.08	0.50	0.012	7
73W	0.31	0.60	1.56	0.25	0.58	0.005	0.10	0.45	0.005	8
MW	0.27	0.57	1.61	0.10	0.41	0.017	0.08	0.62	0.007	9
HSST02	0.14	0.67	1.55	0.04	0.53	0.009	0.23	0.20	0.014	10
A302B	0.14	0.20	1.20	0.24	0.60	0.015	0.21	0.28	0.017	11
JRQ	0.14	0.82	1.40	0.12	0.50	0.019	0.18	0.25	0.004	12
RWP	0.04	1.65	1.43	0.05	0.39	0.011	0.06	0.50	0.005	13
RWG	0.24	1.71	1.21	0.09	0.35	0.008	0.04	0.60	0.007	13
RWV	0.56	1.66	1.36	0.05	0.41	0.010	0.04	0.38	0.010	13
EPRI C	0.35	0.60	1.55	0.04	0.44	0.005	0.16	0.17	0.009	14

* Compositions in weight %; Heat Treatments: 1. SAW SR 607˚C for 15 h, furnace cooled; 2. SAW SR 607˚C for 23 h, furnace cooled; 3. SAW SR 607˚C for 13.5 h, furnace cooled; 4. SAW SR 593-621˚C for 48h, slow cooled; 5. SAW SR 48 h at 593-621˚C, slow cooled; 6. SAW SR 80 h at 593-621; 7. PWHT, 607˚C for 15 h, furnace cool; 8. PWHT 607˚C, 40h; 9 PWHT 607˚C, 22.5h; 10. Austenitized 913°C 4h/air cool/Austenitized 871°C 4h/air cool/ Temper 663°C 4h/air cool/Stress rel. 621°C 40h/furnace cool; 11. Normalized and tempered; 927°C 6.5h/water quench/885°C 6.5h/water quench/649°C 6.5h/water quench/607°C 6.5 h/furnace cool; 12.Normalized @ 900°C, quenched @ 880°C, tempered at 665˚C for 12 h, SR at 620˚C 40h; 13. Austenitized 920˚C, water quench; tempered 600˚C, 42 h, 650°C, 6h; slow cooled; 14. SAW, PWHT 620˚C, 50h

the supplier. The CWP series consists of: a) three intermediate ≈ 0.6% Ni submerged arc welds (SAW) provided by Babcock and Wilcox (BWA, B and C) with from ≈ 0.06 to 0.28% Cu; b) a set of 6 intermediate ≈ 0.6% Ni SAW (62W-73W and MW) with from ≈ 0.2 to 0.35% Cu supplied by the ORNL HSSI program; c) three high 1.6%Ni SAW with 0.04 to 0.55% Cu supplied by Rolls Royce; d) an intermediate 0.6% Ni SAW used in previous EPRI-sponsored research programs [7] with about 0.35% Cu; e) the intermediate ≈ 0.67% Ni HSST-02 A533B correlation monitor plate with ≈ 0.14% Cu; f) a low ≈ 0.27Ni, 0.15% Cu A302 plate supplied by the ORNL HSSI program; and, g) the intermediate Ni (≈ 0.8%) International Atomic Energy Agency (IAEA) JRQ reference plate with ≈ 0.14% Cu.

Note, he use of SMMS was specifically intended to provide precise and controlled variations in key compositional variables and variable combinations. The SMMS baseline composition, fabrication route, and heat treatment schedule were selected to produce microstructures and mechanical properties that closely match those found in "typical" RPV plates. Thus, the SMMS are similar to their commercial counterparts, except that: (a) they are likely to exhibit less melt-to-melt variability than is characteristic of the wide range of heavy section RPV plates; and (b) the variation of key elements is intentionally wider than in typical commercial steelmaking practice in order to identify variable trends and interactions.

2.5 Heat Treatments and Specimen Preparation

The coupon tensile specimens shown in Figure 12, with a gage section 9 mm x 2 mm x 0.5 mm, were prepared by precision die punching the heat treated coupons precision lapped to 0.5±0.005 mm thick. Punching and tensile testing a calibration alloy after about every 500 IVAR specimens had been punched was used to monitor the quality of the die. The ductility of the annealed 316 stainless sheet calibration alloy was very sensitive to the die quality. When a reduction of ductility was observed, the die assembly was sent to the fabricator for sharpening. This was done several times during the specimen fabrication process.

Tensile specimen fabrication from the CM alloy material involved the procedure shown in Figure 13a. Segments were cut from the as-forged billets and 2mm of surface material was removed from each face. Then the remaining material was EDM sliced into 0.7 mm thick, 70 mm by 35 mm wafers. A stack of four wafers was clamped between two ground 6 mm steel plates. This assembly was placed in a positive pressure helium purged retort furnace at 900°C for 30 minutes. The assembly was then immediately transferred to an adjacent sodium nitrite salt quenching bath at 450°C for 10 minutes, then allowed to air cool. The clamped wafers were then tempered at 664°C for 4 hrs in another positive pressure helium purged retort furnace and air-cooled. The wafers were then commercially precision lapped to a 0.5mm thickness. Tensile specimens were punched in T orientation from the lapped wafers and the end tabs engraved with codes indicating the wafer they were taken from and their location in that wafer. The tensile specimens were then stress relieved in a third positive pressure helium purged retort

furnace at 607°C for 24 hours, followed by slow cooling at 8°C per hour to 300°C and subsequent air cooling.

In the case of the LV alloys, the billets were sectioned and heat-treated intact. After the air quench-normalization, temper and stress relief treatments in positive pressure helium purged retort furnaces described previously, wafers 0.7mm thick were EDM and lapped to 5 mm thickness prior to punching tensile specimens. This procedure produced very uniform unirradiated tensile properties in the LV-series alloys. In the case of the commercial weld and plate alloys, CWP, specimens were fabricated from the material in the as received condition using the same lapping and punching procedure described above. The specimen orientation in the welds is shown in Figure 13b.

2.6 Sub-Capsules and Sub-Capsule Loading

The IVAR facility held 58 full sized 6061T6 aluminum 50.8x50.8x12.52 mm irradiation subcapsules. The capsule consisted of a square frame with a ≈ 1.25 mm (final dimension) lid on each side, secured by 6 stainless steel screws. The capsules were manufactured 0.5 mm oversize in all dimensions, then machined and ground after loading to achieve precise final geometry. Small ventilation holes in the capsule walls allowed for gas circulation.

The irradiation sub-capsules contained tensile specimens, SANS coupons, multi-purpose interstitial pieces from the coupon regions between tensile specimen punch-outs that served as multipurpose specimens. Some capsules also contained fracture toughness specimens, but these are not the focus of this report. High purity iron and nickel dosimetry wires were included in each capsule.

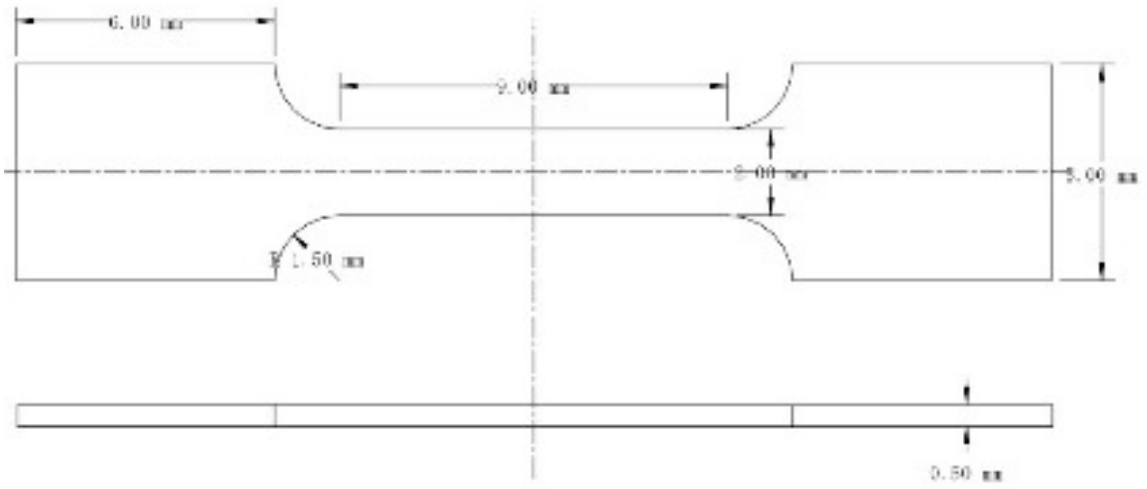

Figure 12 The IVAR tensile specimens.

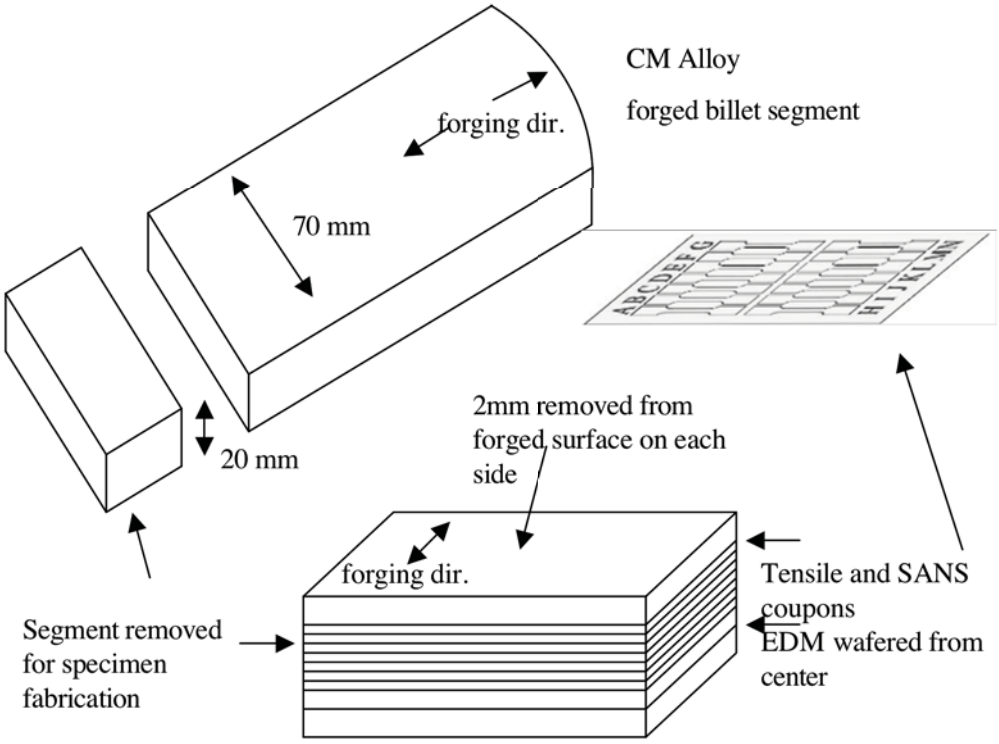

Figure 13a Schematic illustration of the specimen fabrication process and orientation for the forged billet of CM, LV and CWP plate alloys.

.

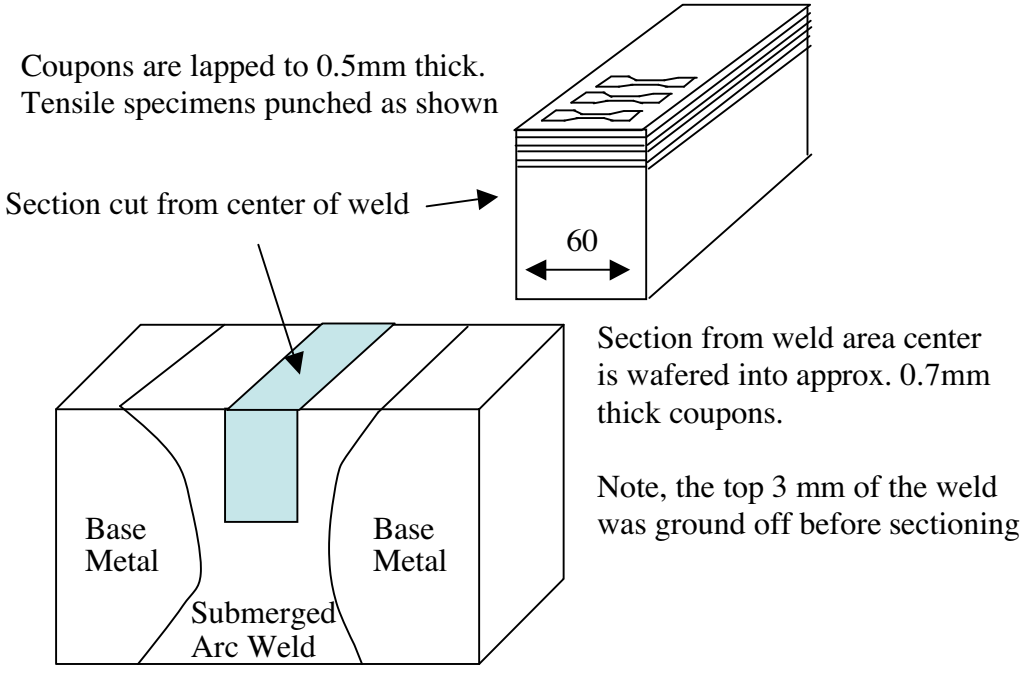

Figure 13b Schematic illustration of the specimen orientation for the CWP welds.

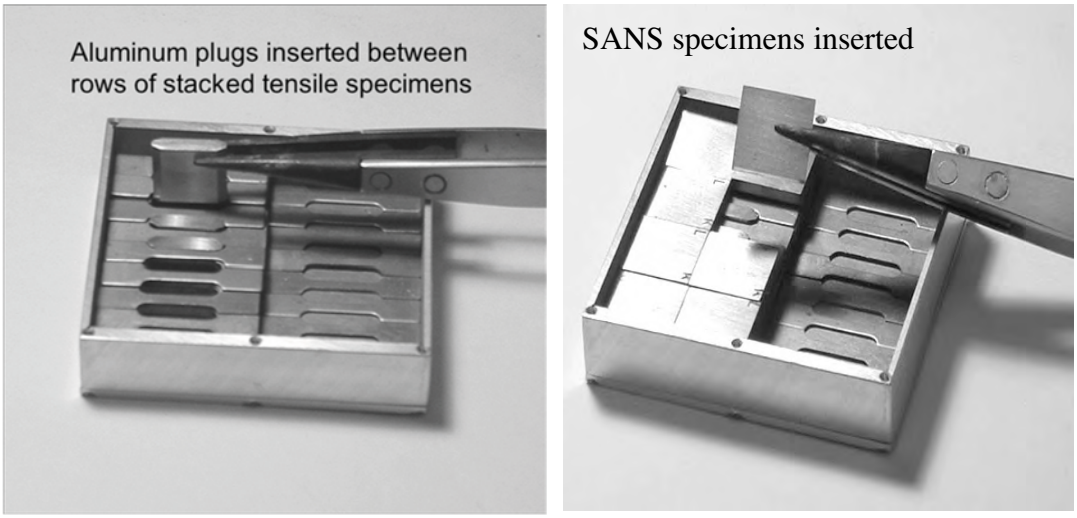

Figure14 Illustration of typical specimen loading configurations for the IVAR subcapsules.

As shown in Figure 14, the capsules were designed to hold two rows of stacks of nine tensile specimens. A typical capsule contained approximately 200 tensile specimens and 32 SANS coupons. Gaps between the tensile stacks were filled with either the multi-purpose coupons described above, or precision machined aluminum plugs. During final capsule assembly, any gaps or variations in tensile stack height were filled with annealed pure aluminum shim. The specimen stack-up was slightly larger than the thickness of the capsule frame. Thus the specimens were press fit loaded by the top and bottom lids. Final assembled capsule volume, including the capsule material, was approximately 50% steel and 50% aluminum (including the inserts). This mix was duplicated in the dummy capsules used in the unoccupied subcapsule sites.

After removal from the irradiation facility the subcapsules were stored at the FNR hot cell for a minimum of 6 months, and often much longer. The capsules were than shipped to UCSB for inspection, disassembly and specimen storage prior to testing in the UCSB warm facility. The specimens were found to remain press fit loaded in their subcapsules after irradiation, and they showed little sign of oxidation or corrosion.

2.7 Tensile Testing

Tests on the flat tensile specimens described above were conducted on a modified computer-controlled, semi-automated Instron 1100 tabletop load frame designed and constructed by UCSB, as shown in Figure 15. Prior to loading, the activated specimens were cleaned using a brief ultrasonic bath in 15% phosphoric acid/ethanol solution, which removed any oxide particles. This treatment also provided a stable oxidation resistant surface finish and greatly reduced contamination during testing (except in the grips themselves activity levels were negligible). Up to 29 specimens were manually loaded in bolt-tightened lower end-tab grips in a magazine cartridge shown in Figure 16. The bottom grips provided good specimen axial alignment. The specimen cartridge was then attached to a precision ball-screw locating stage permanently mounted on the load

frame, which provided precise alignment of the specimens under the upper grip. Each specimen cartridge also included two reference steels with precisely known yield and ultimate stresses to provide a continuous system calibration. Dead weight load cell checks were also performed at intervals throughout the testing period.

As shown in Figure 17, a pneumatically actuated 0.22 MPa hydraulic upper grip assembly attached to the crosshead load cell was used to grip the top end tab of a tensile specimen, after it had been properly positioned by the stage. The upper grips were programmed to release when the load fell 5% below the maximum load, leaving the specimen intact. This minimized friable contamination of the testing chamber, and assured that no fractured tensile end tabs were trapped in the grip. The stage was then moved under computer control to position the next specimen under the top grip, and a new test sequence initiated. The displacements were measured by cross head velocity multiples by time.

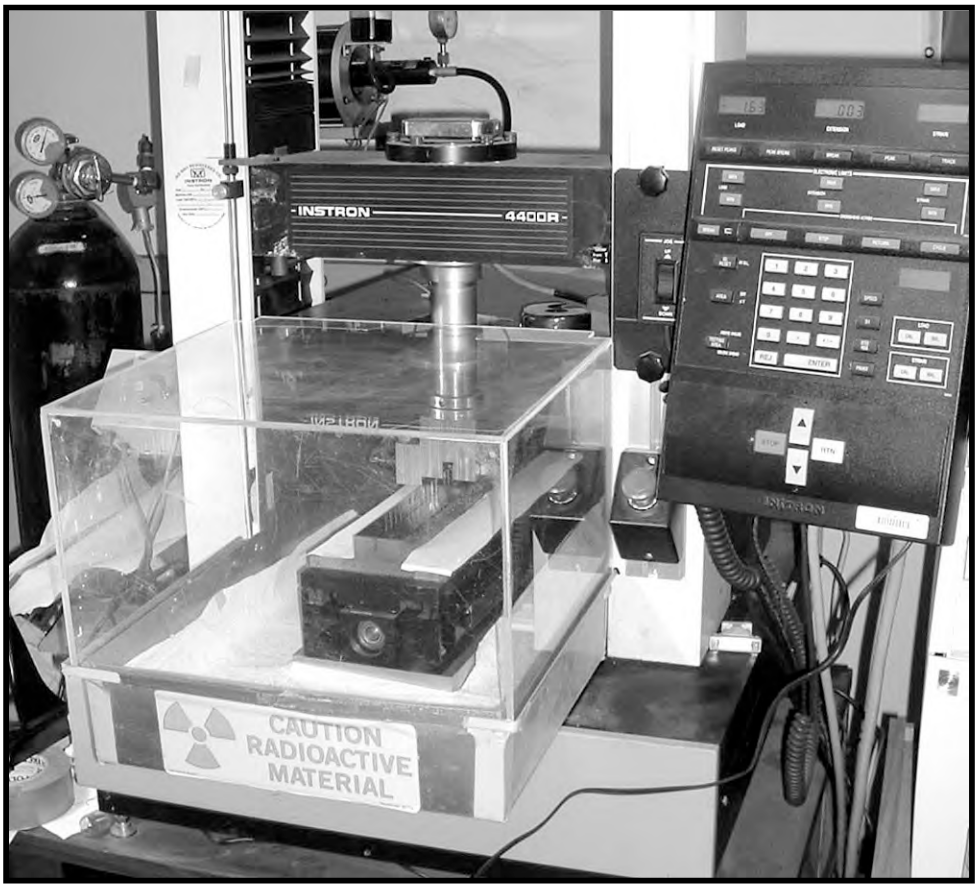

Figure 15 Full view of automated tensile testing system.

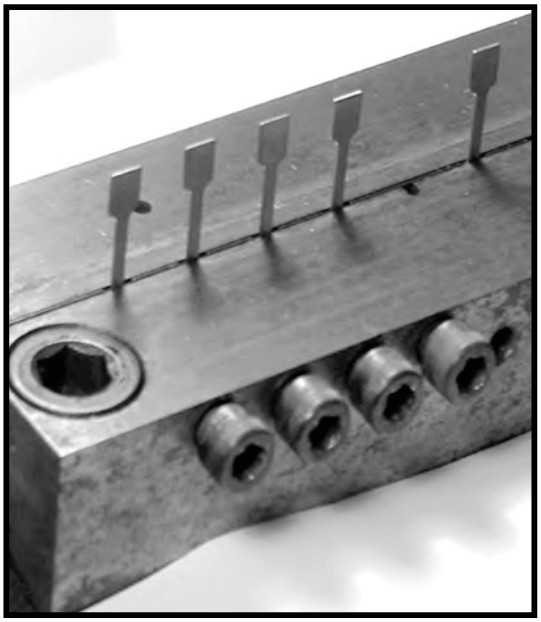

Figure 16 Detail view of lower specimen grip assembly

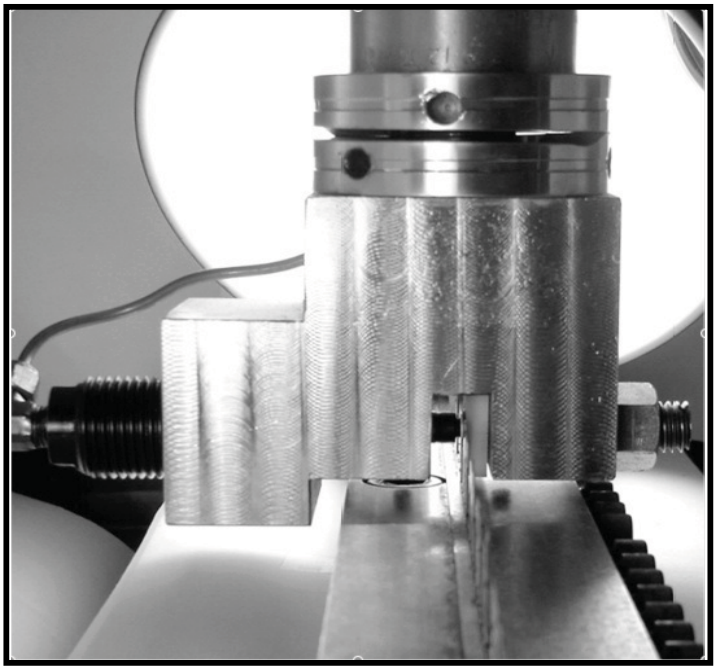

Figure 17 Detail view of the hydraulic upper grip.

The tests were conducted at ambient temperature at a strain rate of ≈ 10^{-3}/s. The majority of the test load-displacement data were digitally recorded and analyzed using dedicated software to obtain 0.2% offset yield stress, σ_y, and ultimate tensile stress at maximum load, σ_u. The loads were converted to engineering stress based on width and thickness measurements on the gauge section of each specimen. The engineering strains were defined as the gauge section extension divided by the original gauge length. The load-displacement curves were visually examined in all cases to assure that the computer-based results were valid. Early in the experimental program some load-displacement data were recorded using a conventional x-y plotter and analyzed manually.

Typical test result plots shown in Fig. 18 for an unirradiated and irradiated alloy. The slope of the initial approximately linear portion of the load-displacement trace was least squares fit. This slope reflects both the steel elasticity and machine compliance, The σ_y is obtained at the cross point of a line with the linear fit shifted by 0.2% strain. The σ_u specified at the maximum load. Except in a very few cases, a minimum of two tensile tests was carried out for each alloy-irradiation condition. Yield stress and ultimate stress change, $\Delta\sigma_y$ and $\Delta\sigma_y$, are then calculated by subtracting the stress values for the corresponding unirradiated control specimens group. The average standard deviation of $\Delta\sigma_y$ and $\Delta\sigma_u$ for all the alloy-irradiation conditions were 11.8 and 13.5 MPa, respectively. Table 8 shows the corresponding average and standard deviations for the various alloy classes.

.

2.8 Data Reduction

Baseline tensile tests on unirradiated material indicated some variability in properties in several of the CM alloys. One systematic variation was associated with the location in the coupon that the specimen had been punched from. In this case, a few specimens that had been taken from the outer edges of the coupon typically had a lower σ_{yu} and σ_{uu} than the majority of specimens taken from the interior region of the coupon. Such variations generally averaged around 15 to 20 MPa, but were much higher in a few cases. The A to N code, shown in Fig. 19, was used to track the specimen coupon location. Some variations in baseline unirradiated tensile properties were also observed for specimens from different billet locations, especially if they were heat-treated at different times. Systematic pairing of the unirradiated-irradiated data by the billet heat treatment group and coupon location also helped reduced scatter of the baseline unirradiated σ_y and σ_u, This approach required dealing with as many as four control specimen groups for individual alloys. The effectiveness of the procedure was demonstrated by the consistency of different sets of paired data for irradiations in the same capsule.

Table 9 summarizes all of the cases in which the average CM baseline σ_y data for an unirradiated specimen group varied by a maximum of more than 15 MPa. Unusual characteristics of some of the alloys are indicated the final column. Table 10 illustrates the effect of pairing grouped data for the CM 22 alloy, which showed the most σ_{yu} variability, for the T16 irradiation. Without pairing the average $\Delta\sigma_y$ is 168.5 ± 29.5 MPa. Assuming the total SD for the $\Delta\sigma_y$ includes the root sum square for the SDs for both σ_{yu} unirradiated groups (7 and 6 MPa) and σ_{yi} (11.9 MPa), $\Delta\sigma_y$ = 168.5 ± 15.1 MPa. Note the

average $\Delta\sigma_y$ is not affected by the grouping in this case. However, in cases with different numbers of grouped irradiated control group data points, this was not always the case. Nevertheless, the effects of grouping on the average $\Delta\sigma_y$ were generally small.

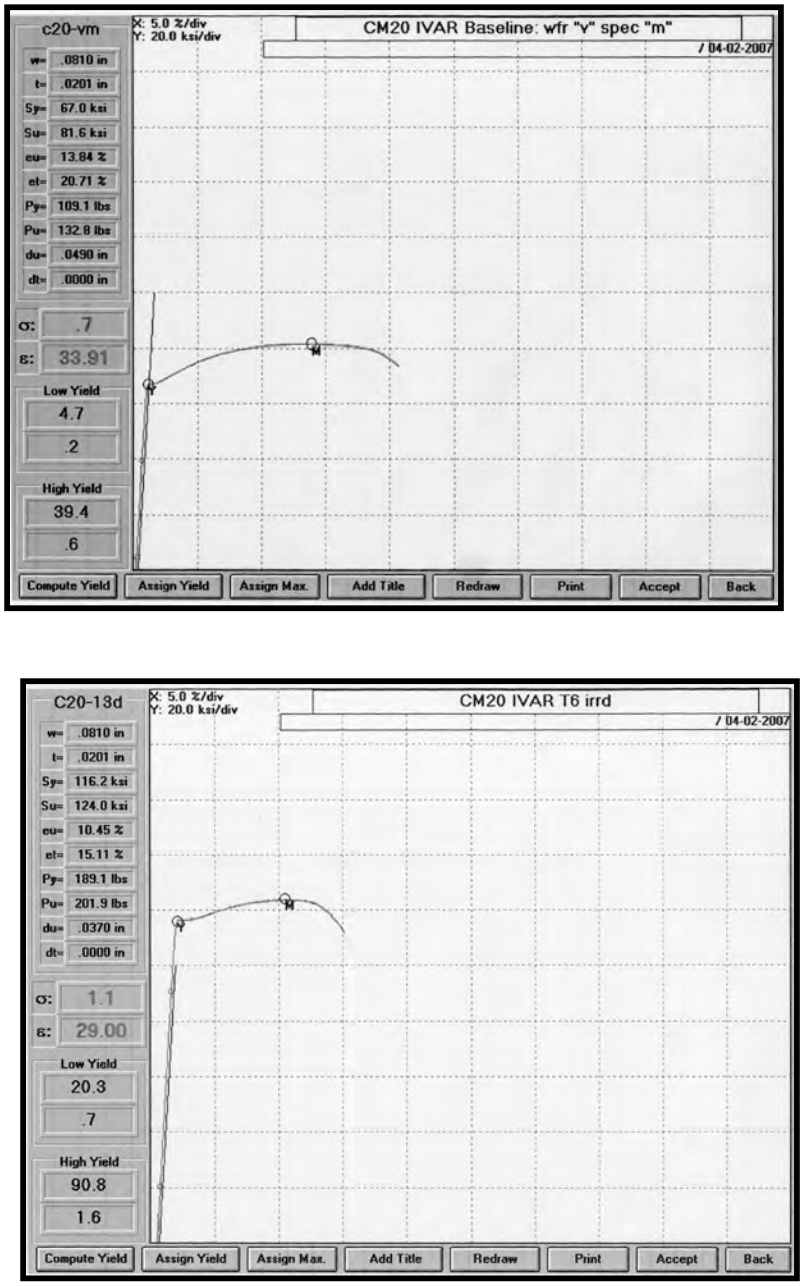

Figure 18. Examples of engineering stress-strain plots of unirradiated (a) and irradiated (b) CM20 specimens from the T6 subcapsule.

Table 8 Average Standard Deviations for $\Delta\sigma_y$ and $\Delta\sigma_u$

	All alloys	CM	LV	CWP
Average SD $\Delta\sigma_y$ (MPa)	11.8±4.5	12.7±3.4	8.4±2.8	12.1±6.1
Average SD $\Delta\sigma_u$ (MPa)	13.5±5.6	16.9±3.7	7.2±2.4	11.2±5.4

Unit: MPa

Table 9 Alloys With Groups of Average Unirradiated σ_ψ Variations of 15 MPa

Alloy	σ_ψ	σ_u	Cu	Ni	Mn	P	Note
CM 22	63	74	0.42	0.84	0.84	0.002	Lower Mn
CM5	56	38	0.02	0.86	1.61	0.050	High P
CM21	34	21	0.42	0.80	0.00	0.002	Low Mn
CM28	27	36	0.42	0.80	1.40	0.002	B added
CM17	27	27	0.22	1.59	1.54	0.004	
CM16	25	35	0.22	0.82	1.58	0.004	
CM23	25	19	0.01	0.83	1.62	0.002	High C
CM14	24	35	0.11	0.83	1.62	0.040	High P
CM10	23	34	0.02	0.88	1.66	0.008	
CM3	19	38	0.02	0.85	1.60	0.006	
CM19	19	24	0.42	0.85	1.63	0.005	
CM11	16	25	0.34	0.85	1.64	0.006	

Units: σ_y and σ_u (MPa), composition (wt.%)
Data from coupon edge specimens are not included

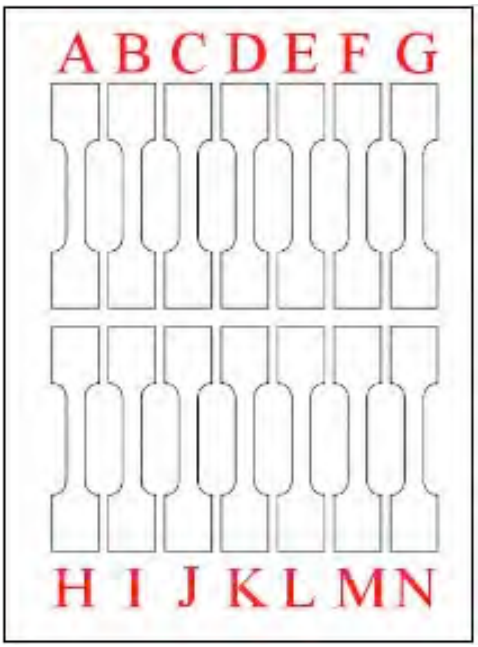

Fig. 19 Coded used to identify IVAR tensile specimen locations in a coupon.

Table 10 Tensile test comparisons from two batches of alloy CM 22 irradiated in the IVAR T16 capsule.

CM22	σ_y	$\Delta\sigma_y$	σ_u	$\Delta\sigma_u$
σ_{yu} Group 1	406±7		482±6	
σ_{yi} Group 1	583	177	638	156
σ_{yu} Group 2	446±6		515±7	
σ_{yi} Group 2	606	160	652	137
Average $\Delta\sigma_y$		168.5±15.1		147±13.5

Units: σ_y, σ_u, $\Delta\sigma_y$ and $\Delta\sigma_y$ (MPa)

3. Summary of the IVAR Irradiations and Organization of the Database

The original IVAR irradiation matrix consisted of 28 subcapsules (T1 to T28) isothermally irradiated over the range of ϕ, ϕt and T_i as described previously. Two additional capsules were used to study the effects of T_i variations (VT1 and VT2). This involved irradiations to a fleunce of $\approx 4.2 \times 10^{22}$ n/m^2 at 270°C (VT1) or 290°C (VT2) followed by an additional irradiation fluence increment of $\approx 4.2 \times 10^{22}$ n/m^2 at 290°C (VT1) or 270°C (VT2). Thus the specimens experience a total fluence of 8.4×10^{23} n/m^2 with low to high and high to low temperature variations. The temperature sequencing was simply accomplished by exchanging capsules between 270 and 290°C MF locations. Another subcapsule (SR1) HF 290°C irradiation to $\approx 10^{23}$ n/m^2 focused on the effect of stress relief heat treatment time and temperature on $\Delta\sigma_y$ and $\Delta\sigma_u$, as well as it's relationship to the start of life dissolved versus pre-precipitated Cu, for a range of alloy compositions. Data for the standard stress relief treatment (SSR) from SR1 irradiation are included in this report. The base IVAR irradiation matrix was subsequently supplemented by 9 additional subcapsules (T29 to T32 and A1 to A5). The primary objective of most of these subcapsules was to clarify embrittlement mechanisms by irradiating a large set of model alloys that were acquired about half way though the IVAR program. However, a number of RPV steel alloys (CM, LV and CWP) were also included in these irradiations and are reported here. Thus we present the IVAR $\Delta\sigma_y$ and $\Delta\sigma_u$ database from 40 subcapsule irradiations representing a total of 1537 combinations of material-irradiation conditions.

The $\Delta\sigma_y$ and $\Delta\sigma_u$ (MPa) data tables are organized by alloy series (CM, LV and CWP) into three Appendices A to C. Each page of data contains a summary of the average $\Delta\sigma_y$ and $\Delta\sigma_u$ data and corresponding 1 SD measures of data scatter for the specified alloy. If no data is entered for an irradiation condition, then it was not included in that particular irradiation. The data tables also include the irradiation capsule designation, flux category (HF, MF and LF), the actual ϕ (10^{16}n/m^2-s, E > 1 MeV), ϕt (10^{23}n/m^2-s, E > 1 MeV) and T_i (°C). The alloy identification code and key element chemistry is included at the top of each data page.

References

[1] G. R. Odette, G. E. Lucas, D. Klingensmith, B.D. Wirth and D. Gragg, The Effects of Composition and Heat Treatment on Hardening and Embrittlment of Reactor Pressure Vessel Steels, NUREG/CR-6778 HT (2003)
[2] D.W. Heatherly, K.R. Thoms, M.T. Hurst, G.E. Giles, "Heavy-Section Steel Irradiation Program's Reusable Irradiation Facilities," ORNL/TM-2002/77 (date)
[3] I. Remec, C. A. Baldwin, E. D. Blakeman and C. J. Fairbanks, "Characterization of The Neutron Field in The HSSI/UCSB Irradiation Facility at The Ford Nuclear Reactor," ORNL/TM-1999/140 (date)
[4] G.R. Odette, T. Yamamoto, D. Klingensmith, "On The Effect of Dose Rate on Irradiation Hardening of RPV Steels," *Phil. Mag*., 85 (2005) pp. 779-797.
[5] E.D. Eason, G.R. Odette, R.K. Nanstad, T. Yamamoto, "A Physically Based Correlation of Irradiation-Induced Transition Temperature Shifts for RPV Steels" NUREG NUREG/CR XXXX (to be published 2007)
[6] ASTM E693-01 " Standard Practice for Characterizing Neutron Exposures in Iron and Low Alloy Steels in Terms of Displacements Per Atom (DPA)," ASTM.
[7] G. R. Odette and G. E. Lucas, Irradiation Embrittlement of LWR Pressure Vessel Steels, EPRI-NP-6114 (1989)

Acknowledgements

To be added – there is a lot to include.

Appendix A

Data Tables for the CM-Series Alloys

	Cu%	Ni%	CM1 Mn%	Mo%	P%			
	0.01	0.01	1.67	0.56	0.003			
Capsule	ϕt	ϕ-code	ϕ	T_i	$\Delta\sigma_y$	±SD	$\Delta\sigma_u$	±SD
A5	0.04	HF	0.51	290	na	-	-	-
T31	0.06	HF	0.72	290	na	-	-	-
T1	0.07	HF	0.78	290	-8	11	-15	16
T2	0.18	HF	0.78	290	-6	13	-14	15
T3	0.34	HF	0.78	290	-4	15	-10	19
T29	0.44	HF	0.89	290	na	-	-	-
T4	0.75	HF	0.97	290	na	-	-	-
SR1	0.85	HF	0.97	290	na	-	-	-
T5	1.36	HF	0.78	290	7	11	-2	9
T6	3.32	HF	0.97	290	-3	12	-20	6
T32	0.02	MF	0.26	290	na	-	-	-
T11	0.04	MF	0.26	290	-3	10	-5	11
T12	0.10	MF	0.32	290	-5	17	-9	6
T13	0.24	MF	0.31	290	na	-	-	-
T14	0.48	MF	0.32	290	-3	12	-17	19
T15	0.85	MF	0.26	290	na	-	-	-
T16	1.57	MF	0.30	290	10	8	1	9
T30	0.02	LF	0.07	290	na	-	-	-
T21	0.03	LF	0.10	290	-16	8	-16	10
T22	0.11	LF	0.10	290	-3	15	-9	19
T23	0.24	LF	0.08	290	na	-	-	-
T24	0.40	LF	0.08	290	-5	11	-17	16
T7	0.38	HF	0.92	270	-6	10	-13	16
T8	1.52	HF	0.92	270	11	10	-1	9
T17	0.43	MF	0.25	270	na	-	-	-
T18	1.71	MF	0.36	270	29	12	24	9
T25	0.26	LF	0.08	270	na	-	-	-
T26	0.41	LF	0.12	270	1	8	-4	9
T9	0.40	HF	0.98	310	-11	8	-22	9
T10	1.47	HF	0.98	310	8	16	-7	17
T19	0.40	MF	0.23	310	na	-	-	-
T20	1.60	MF	0.34	310	7	13	2	14
T27	0.24	LF	0.07	310	na	-	-	-
T28	0.38	LF	0.11	310	6	11	-3	13
VT1	0.84	MF	0.21	270/290	na	-	-	-
VT2	0.84	MF	0.21	290/270	11	14	9	16

* Single test data; "na" - not available; ϕ(10^{16}n/m^2-s); ϕt(10^{23}n/m^2); T_i(°C)

	Cu%	Ni%	CM2 Mn%	Mo%	P%			
	0.01	0.01	1.65	0.56	0.041			
Capsule	ϕt	ϕ-code	ϕ	T_i	$\Delta\sigma_y$	±SD	$\Delta\sigma_u$	±SD
A5	0.04	HF	0.51	290	na	-	-	-
T31	0.06	HF	0.72	290	na	-	-	-
T1	0.07	HF	0.78	290	-10	12	-20	16
T2	0.18	HF	0.78	290	11	12	3	19
T3	0.34	HF	0.78	290	22	14	13	24
T29	0.44	HF	0.89	290	na	-	-	-
T4	0.75	HF	0.97	290	na	-	-	-
SR1	0.85	HF	0.97	290	na	-	-	-
T5	1.36	HF	0.78	290	68	20	59	21
T6	3.32	HF	0.97	290	68	9	60	15
T32	0.02	MF	0.26	290	na	-	-	-
T11	0.04	MF	0.26	290	4	10	1	15
T12	0.10	MF	0.32	290	6	22	5	21
T13	0.24	MF	0.31	290	na	-	-	-
T14	0.48	MF	0.32	290	36	10	25	15
T15	0.85	MF	0.26	290	na	-	-	-
T16	1.57	MF	0.30	290	61	9	50	16
T30	0.02	LF	0.07	290	na	-	-	-
T21	0.03	LF	0.10	290	7	9	5	15
T22	0.11	LF	0.10	290	21	9	10	15
T23	0.24	LF	0.08	290	na	-	-	-
T24	0.40	LF	0.08	290	36	20	23	22
T7	0.38	HF	0.92	270	22	10	11	16
T8	1.52	HF	0.92	270	69	9	58	15
T17	0.43	MF	0.25	270	na	-	-	-
T18	1.71	MF	0.36	270	91	22	92	24
T25	0.26	LF	0.08	270	na	-	-	-
T26	0.41	LF	0.12	270	51	10	43	22
T9	0.40	HF	0.98	310	18	15	9	24
T10	1.47	HF	0.98	310	65	9	57	15
T19	0.40	MF	0.23	310	na	-	-	-
T20	1.60	MF	0.34	310	50	10	36	17
T27	0.24	LF	0.07	310	na	-	-	-
T28	0.38	LF	0.11	310	39	17	30	24
VT1	0.84	MF	0.21	270/290	na	-	-	-
VT2	0.84	MF	0.21	290/270	53	10	41	15

* Single test data; "na" - not available; ϕ(10^{16}n/m^2-s); ϕt(10^{23}n/m^2); T_i(°C)

CM3

Cu%	Ni%	Mn%	Mo%	P%
0.02	0.85	1.60	0.49	0.006

Capsule	ϕt	ϕ-code	ϕ	T_i	$\Delta\sigma_y$	±SD	$\Delta\sigma_u$	±SD
A5	0.04	HF	0.51	290	1	13	-7	17
T31	0.06	HF	0.72	290	na	-	-	-
T1	0.07	HF	0.78	290	7	17	-2	24
T2	0.18	HF	0.78	290	16	12	10	4
T3	0.34	HF	0.78	290	6	13	-17	23
T29	0.44	HF	0.89	290	na	-	-	-
T4	0.75	HF	0.97	290	6	18	-4	12
SR1	0.85	HF	0.97	290	32	12	21	16
T5	1.36	HF	0.78	290	20	12	11	17
T6	3.32	HF	0.97	290	30	12	13	16
T32	0.02	MF	0.26	290	na	-	-	-
T11	0.04	MF	0.26	290	14	16	5	21
T12	0.10	MF	0.32	290	17	18	20	8
T13	0.24	MF	0.31	290	21	21	4	24
T14	0.48	MF	0.32	290	7	16	-6	21
T15	0.85	MF	0.26	290	21	13	8	18
T16	1.57	MF	0.30	290	24	14	16	20
T30	0.02	LF	0.07	290	na	-	-	-
T21	0.03	LF	0.10	290	8	12	2	16
T22	0.11	LF	0.10	290	18	12	8	17
T23	0.24	LF	0.08	290	12	15	9	19
T24	0.40	LF	0.08	290	16	14	8	20
T7	0.38	HF	0.92	270	13	14	5	22
T8	1.52	HF	0.92	270	25	12	13	16
T17	0.43	MF	0.25	270	29	12	19	17
T18	1.71	MF	0.36	270	52	13	35	17
T25	0.26	LF	0.08	270	14	16	-6	16
T26	0.41	LF	0.12	270	21	12	12	16
T9	0.40	HF	0.98	310	-5	15	-11	16
T10	1.47	HF	0.98	310	21	16	8	24
T19	0.40	MF	0.23	310	20	13	16	19
T20	1.60	MF	0.34	310	17	16	4	20
T27	0.24	LF	0.07	310	8	16	1	25
T28	0.38	LF	0.11	310	16	18	12	20
VT1	0.84	MF	0.21	270/290	-2	12	-24	18
VT2	0.84	MF	0.21	290/270	12	21	-9	22

* Single test data; "na" - not available; $\phi(10^{16}n/m^2\text{-}s)$; $\phi t(10^{23}n/m^2)$; $T_i(°C)$

	Cu%	Ni%	CM4 Mn%	Mo%	P%
	0.02	0.86	1.53	0.55	0.031

Capsule	ϕt	ϕ-code	ϕ	T_i	$\Delta\sigma_y$	±SD	$\Delta\sigma_u$	±SD
A5	0.04	HF	0.51	290	na	-	-	-
T31	0.06	HF	0.72	290	na	-	-	-
T1	0.07	HF	0.78	290	21	14	15	19
T2	0.18	HF	0.78	290	28	14	26	15
T3	0.34	HF	0.78	290	26	13	27	16
T29	0.44	HF	0.89	290	na	-	-	-
T4	0.75	HF	0.97	290	na	-	-	-
SR1	0.85	HF	0.97	290	na	-	-	-
T5	1.36	HF	0.78	290	50	13	45	15
T6	3.32	HF	0.97	290	68	13	64	16
T32	0.02	MF	0.26	290	na	-	-	-
T11	0.04	MF	0.26	290	14	33	3	28
T12	0.10	MF	0.32	290	15	17	14	19
T13	0.24	MF	0.31	290	na	-	-	-
T14	0.48	MF	0.32	290	36	14	23	15
T15	0.85	MF	0.26	290	na	-	-	-
T16	1.57	MF	0.30	290	67	13	64	16
T30	0.02	LF	0.07	290	na	-	-	-
T21	0.03	LF	0.10	290	15	22	16	24
T22	0.11	LF	0.10	290	26	19	24	16
T23	0.24	LF	0.08	290	na	-	-	-
T24	0.40	LF	0.08	290	31	14	23	17
T7	0.38	HF	0.92	270	47	13	41	15
T8	1.52	HF	0.92	270	58	13	50	15
T17	0.43	MF	0.25	270	na	-	-	-
T18	1.71	MF	0.36	270	84	16	67	18
T25	0.26	LF	0.08	270	na	-	-	-
T26	0.41	LF	0.12	270	53	25	48	31
T9	0.40	HF	0.98	310	49*	-	49*	-
T10	1.47	HF	0.98	310	54	19	40	26
T19	0.40	MF	0.23	310	na	-	-	-
T20	1.60	MF	0.34	310	43	20	35	24
T27	0.24	LF	0.07	310	na	-	-	-
T28	0.38	LF	0.11	310	42	14	35	18
VT1	0.84	MF	0.21	270/290	na	-	-	-
VT2	0.84	MF	0.21	290/270	72	25	70	37

* Single test data; "na" - not available; ϕ(10^{16}n/m^2-s); ϕt(10^{23}n/m^2); T_i(°C)

CM5

Cu%	Ni%	Mn%	Mo%	P%
0.02	0.86	1.61	0.53	0.035

Capsule	ϕt	ϕ-code	ϕ	T_i	$\Delta\sigma_y$	±SD	$\Delta\sigma_u$	±SD
A5	0.04	HF	0.51	290	na	-	-	-
T31	0.06	HF	0.72	290	na	-	-	-
T1	0.07	HF	0.78	290	2	17	-6	18
T2	0.18	HF	0.78	290	16	12	10	16
T3	0.34	HF	0.78	290	23	13	12	21
T29	0.44	HF	0.89	290	na	-	-	-
T4	0.75	HF	0.97	290	na	-	-	-
SR1	0.85	HF	0.97	290	na	-	-	-
T5	1.36	HF	0.78	290	75	28	79	22
T6	3.32	HF	0.97	290	63	14	56	16
T32	0.02	MF	0.26	290	na	-	-	-
T11	0.04	MF	0.26	290	-1	23	-8	27
T12	0.10	MF	0.32	290	21	15	14	20
T13	0.24	MF	0.31	290	na	-	-	-
T14	0.48	MF	0.32	290	62	24	49	21
T15	0.85	MF	0.26	290	na	-	-	-
T16	1.57	MF	0.30	290	89	25	79	22
T30	0.02	LF	0.07	290	na	-	-	-
T21	0.03	LF	0.10	290	5	16	0	21
T22	0.11	LF	0.10	290	14	32	3	32
T23	0.24	LF	0.08	290	na	-	-	-
T24	0.40	LF	0.08	290	54	21	40	18
T7	0.38	HF	0.92	270	31	24	27	22
T8	1.52	HF	0.92	270	98	21	84	18
T17	0.43	MF	0.25	270	na	-	-	-
T18	1.71	MF	0.36	270	125	21	107	17
T25	0.26	LF	0.08	270	na	-	-	-
T26	0.41	LF	0.12	270	39	10	28	10
T9	0.40	HF	0.98	310	37	27	27	20
T10	1.47	HF	0.98	310	63	21	48	18
T19	0.40	MF	0.23	310	na	-	-	-
T20	1.60	MF	0.34	310	70	39	54	35
T27	0.24	LF	0.07	310	na	-	-	-
T28	0.38	LF	0.11	310	62	21	50	17
VT1	0.84	MF	0.21	270/290	na	-	-	-
VT2	0.84	MF	0.21	290/270	75	22	61	18

* Single test data; "na" - not available; ϕ(10^{16}n/m^2-s); ϕt(10^{23}n/m^2); T_i(°C)

CM6

Cu%	Ni%	Mn%	Mo%	P%
0.02	1.68	1.50	0.54	0.007

Capsule	ϕt	ϕ-code	ϕ	T_i	$\Delta\sigma_y$	±SD	$\Delta\sigma_u$	±SD
A5	0.04	HF	0.51	290	na	-	-	-
T31	0.06	HF	0.72	290	na	-	-	-
T1	0.07	HF	0.78	290	-6	11	-15	13
T2	0.18	HF	0.78	290	1	21	-11	3
T3	0.34	HF	0.78	290	11	20	-2	22
T29	0.44	HF	0.89	290	na	-	-	-
T4	0.75	HF	0.97	290	na	-	-	-
SR1	0.85	HF	0.97	290	na	-	-	-
T5	1.36	HF	0.78	290	49	10	34	10
T6	3.32	HF	0.97	290	55	15	44	21
T32	0.02	MF	0.26	290	na	-	-	-
T11	0.04	MF	0.26	290	3	10	-2	17
T12	0.10	MF	0.32	290	1	9	-8	13
T13	0.24	MF	0.31	290	na	-	-	-
T14	0.48	MF	0.32	290	20	23	4	29
T15	0.85	MF	0.26	290	na	-	-	-
T16	1.57	MF	0.30	290	60	22	36	28
T30	0.02	LF	0.07	290	na	-	-	-
T21	0.03	LF	0.10	290	2	5	-2	10
T22	0.11	LF	0.10	290	10	6	2	9
T23	0.24	LF	0.08	290	na	-	-	-
T24	0.40	LF	0.08	290	37	10	25	10
T7	0.38	HF	0.92	270	9	11	4	17
T8	1.52	HF	0.92	270	50	11	36	12
T17	0.43	MF	0.25	270	na	-	-	-
T18	1.71	MF	0.36	270	190	10	146	14
T25	0.26	LF	0.08	270	na	-	-	-
T26	0.41	LF	0.12	270	39	10	28	10
T9	0.40	HF	0.98	310	14	8	17	11
T10	1.47	HF	0.98	310	28	18	13	24
T19	0.40	MF	0.23	310	na	-	-	-
T20	1.60	MF	0.34	310	35	10	21	11
T27	0.24	LF	0.07	310	na	-	-	-
T28	0.38	LF	0.11	310	25	10	19	10
VT1	0.84	MF	0.21	270/290	na	-	-	-
VT2	0.84	MF	0.21	290/270	69	5	53	10

* Single test data; "na" - not available; ϕ(10^{16}n/m^2-s); ϕt(10^{23}n/m^2); T_i(°C)

CM7

Cu%	Ni%	Mn%	Mo%	P%
0.00	1.70	1.55	0.56	0.047

Capsule	ϕt	ϕ-code	ϕ	T_i	$\Delta\sigma_y$	±SD	$\Delta\sigma_u$	±SD
A5	0.04	HF	0.51	290	na	-	-	-
T31	0.06	HF	0.72	290	na	-	-	-
T1	0.07	HF	0.78	290	10	22	7	27
T2	0.18	HF	0.78	290	15	52	13	58
T3	0.34	HF	0.78	290	33	22	30	27
T29	0.44	HF	0.89	290	na	-	-	-
T4	0.75	HF	0.97	290	na	-	-	-
SR1	0.85	HF	0.97	290	na	-	-	-
T5	1.36	HF	0.78	290	39	14	30	29
T6	3.32	HF	0.97	290	97	15	96	18
T32	0.02	MF	0.26	290	na	-	-	-
T11	0.04	MF	0.26	290	6	27	-4	30
T12	0.10	MF	0.32	290	10	27	3	25
T13	0.24	MF	0.31	290	na	-	-	-
T14	0.48	MF	0.32	290	45	24	40	23
T15	0.85	MF	0.26	290	na	-	-	-
T16	1.57	MF	0.30	290	61	4	53	20
T30	0.02	LF	0.07	290	na	-	-	-
T21	0.03	LF	0.10	290	17	25	27	26
T22	0.11	LF	0.10	290	29	14	28	18
T23	0.24	LF	0.08	290	na	-	-	-
T24	0.40	LF	0.08	290	46	12	39	25
T7	0.38	HF	0.92	270	33	24	30	30
T8	1.52	HF	0.92	270	81	27	69	30
T17	0.43	MF	0.25	270	na	-	-	-
T18	1.71	MF	0.36	270	163	23	150	31
T25	0.26	LF	0.08	270	na	-	-	-
T26	0.41	LF	0.12	270	55	17	50	20
T9	0.40	HF	0.98	310	39	27	36	33
T10	1.47	HF	0.98	310	67	19	55	23
T19	0.40	MF	0.23	310	na	-	-	-
T20	1.60	MF	0.34	310	78	24	70	27
T27	0.24	LF	0.07	310	na	-	-	-
T28	0.38	LF	0.11	310	56	17	51	20
VT1	0.84	MF	0.21	270/290	na	-	-	-
VT2	0.84	MF	0.21	290/270	101	19	97	25

* Single test data; "na" - not available; ϕ(10^{16}n/m^2-s); ϕt(10^{23}n/m^2); T_i(°C)

CM8

Cu%	Ni%	Mn%	Mo%	P%
0.01	0.86	0.01	0.55	0.004

Capsule	ϕt	ϕ-code	ϕ	T_i	$\Delta\sigma_y$	±SD	$\Delta\sigma_u$	±SD
A5	0.04	HF	0.51	290	na	-	-	-
T31	0.06	HF	0.72	290	na	-	-	-
T1	0.07	HF	0.78	290	-9	15	5	18
T2	0.18	HF	0.78	290	-7	11	2	15
T3	0.34	HF	0.78	290	7	6	12	11
T29	0.44	HF	0.89	290	na	-	-	-
T4	0.75	HF	0.97	290	na	-	-	-
SR1	0.85	HF	0.97	290	na	-	-	-
T5	1.36	HF	0.78	290	12	7	1	16
T6	3.32	HF	0.97	290	-2	8	-18	11
T32	0.02	MF	0.26	290	na	-	-	-
T11	0.04	MF	0.26	290	0	12	7	17
T12	0.10	MF	0.32	290	5	9	12	12
T13	0.24	MF	0.31	290	na	-	-	-
T14	0.48	MF	0.32	290	-8	12	-7	14
T15	0.85	MF	0.26	290	na	-	-	-
T16	1.57	MF	0.30	290	26	15	21	17
T30	0.02	LF	0.07	290	na	-	-	-
T21	0.03	LF	0.10	290	2	7	12	11
T22	0.11	LF	0.10	290	6	9	11	12
T23	0.24	LF	0.08	290	na	-	-	-
T24	0.40	LF	0.08	290	7	6	-2	9
T7	0.38	HF	0.92	270	-1	15	-6	22
T8	1.52	HF	0.92	270	14	12	9	16
T17	0.43	MF	0.25	270	na	-	-	-
T18	1.71	MF	0.36	270	35	7	31	12
T25	0.26	LF	0.08	270	na	-	-	-
T26	0.41	LF	0.12	270	11	9	10	10
T9	0.40	HF	0.98	310	4	12	3	11
T10	1.47	HF	0.98	310	18	6	18	10
T19	0.40	MF	0.23	310	na	-	-	-
T20	1.60	MF	0.34	310	-3	22	-6	30
T27	0.24	LF	0.07	310	na	-	-	-
T28	0.38	LF	0.11	310	-5	17	-10	25
VT1	0.84	MF	0.21	270/290	na	-	-	-
VT2	0.84	MF	0.21	290/270	15	6	12	10

* Single test data; "na" - not available; ϕ(10^{16}n/m^2-s); ϕt(10^{23}n/m^2); T_i(°C)

CM9

Cu%	Ni%	Mn%	Mo%	P%
0.01	0.86	0.85	0.55	0.003

Capsule	ϕt	ϕ-code	ϕ	T_i	$\Delta\sigma_y$	±SD	$\Delta\sigma_u$	±SD
A5	0.04	HF	0.51	290	na	-	-	-
T31	0.06	HF	0.72	290	na	-	-	-
T1	0.07	HF	0.78	290	8	8	10	20
T2	0.18	HF	0.78	290	2	8	5	17
T3	0.34	HF	0.78	290	2	9	3	17
T29	0.44	HF	0.89	290	na	-	-	-
T4	0.75	HF	0.97	290	na	-	-	-
SR1	0.85	HF	0.97	290	na	-	-	-
T5	1.36	HF	0.78	290	1	8	-18	17
T6	3.32	HF	0.97	290	20	10	7	20
T32	0.02	MF	0.26	290	na	-	-	-
T11	0.04	MF	0.26	290	-4	11	-11	24
T12	0.10	MF	0.32	290	2	8	2	19
T13	0.24	MF	0.31	290	na	-	-	-
T14	0.48	MF	0.32	290	14	8	10	20
T15	0.85	MF	0.26	290	na	-	-	-
T16	1.57	MF	0.30	290	20	9	13	18
T30	0.02	LF	0.07	290	na	-	-	-
T21	0.03	LF	0.10	290	-1	14	2	25
T22	0.11	LF	0.10	290	-7	9	-12	18
T23	0.24	LF	0.08	290	na	-	-	-
T24	0.40	LF	0.08	290	2	10	-8	22
T7	0.38	HF	0.92	270	11	11	3	24
T8	1.52	HF	0.92	270	11	19	-6	29
T17	0.43	MF	0.25	270	na	-	-	-
T18	1.71	MF	0.36	270	35	10	17	18
T25	0.26	LF	0.08	270	na	-	-	-
T26	0.41	LF	0.12	270	13	8	13	17
T9	0.40	HF	0.98	310	14	8	8	17
T10	1.47	HF	0.98	310	24	8	23	17
T19	0.40	MF	0.23	310	na	-	-	-
T20	1.60	MF	0.34	310	1	10	-11	25
T27	0.24	LF	0.07	310	na	-	-	-
T28	0.38	LF	0.11	310	13	8	5	18
VT1	0.84	MF	0.21	270/290	na	-	-	-
VT2	0.84	MF	0.21	290/270	24	18	16	28

* Single test data; "na" - not available; ϕ(10^{16}n/m^2-s); ϕt(10^{23}n/m^2); T_i(°C)

CM10

Cu%	Ni%	Mn%	Mo%	P%
0.02	0.88	1.66	0.53	0.008

Capsule	ϕt	ϕ-code	ϕ	T_i	$\Delta\sigma_y$	±SD	$\Delta\sigma_u$	±SD
A5	0.04	HF	0.51	290	-3	10	-8	14
T31	0.06	HF	0.72	290	1	17	-10	23
T1	0.07	HF	0.78	290	11	7	14	12
T2	0.18	HF	0.78	290	10	9	8	16
T3	0.34	HF	0.78	290	9	9	6	15
T29	0.44	HF	0.89	290	15	7	2	13
T4	0.75	HF	0.97	290	23	15	17	13
SR1	0.85	HF	0.97	290	na	-	-	-
T5	1.36	HF	0.78	290	29	13	21	19
T6	3.32	HF	0.97	290	18	12	-1	18
T32	0.02	MF	0.26	290	0	16	-8	20
T11	0.04	MF	0.26	290	2	7	2	13
T12	0.10	MF	0.32	290	6	8	4	16
T13	0.24	MF	0.31	290	22	16	17	23
T14	0.48	MF	0.32	290	26	11	18	15
T15	0.85	MF	0.26	290	22	13	12	17
T16	1.57	MF	0.30	290	31	13	20	18
T30	0.02	LF	0.07	290	4	8	-1	15
T21	0.03	LF	0.10	290	2	9	3	15
T22	0.11	LF	0.10	290	10	8	20	14
T23	0.24	LF	0.08	290	10	23	2	27
T24	0.40	LF	0.08	290	22	13	16	18
T7	0.38	HF	0.92	270	9	9	8	13
T8	1.52	HF	0.92	270	23	11	6	15
T17	0.43	MF	0.25	270	34	12	24	15
T18	1.71	MF	0.36	270	53	18	33	23
T25	0.26	LF	0.08	270	26	18	17	27
T26	0.41	LF	0.12	270	25	11	18	16
T9	0.40	HF	0.98	310	4	7	-4	13
T10	1.47	HF	0.98	310	38	13	27	17
T19	0.40	MF	0.23	310	19	16	12	20
T20	1.60	MF	0.34	310	25	12	19	16
T27	0.24	LF	0.07	310	7	13	-6	18
T28	0.38	LF	0.11	310	8	11	-8	15
VT1	0.84	MF	0.21	270/290	34	11	23	16
VT2	0.84	MF	0.21	290/270	30	17	21	24

* Single test data; "na" - not available; $\phi(10^{16}n/m^2\text{-}s)$; $\phi t(10^{23}n/m^2)$; $T_i(°C)$

CM11

Cu%	Ni%	Mn%	Mo%	P%
0.34	0.85	1.64	0.53	0.006

Capsule	ϕt	ϕ-code	ϕ	T_i	$\Delta\sigma_y$	±SD	$\Delta\sigma_u$	±SD
A5	0.04	HF	0.51	290	33	14	18	22
T31	0.06	HF	0.72	290	71	17	55	29
T1	0.07	HF	0.78	290	70	13	57	19
T2	0.18	HF	0.78	290	119	13	103	21
T3	0.34	HF	0.78	290	132	15	108	21
T29	0.44	HF	0.89	290	146	9	125	23
T4	0.75	HF	0.97	290	149	13	131	10
SR1	0.85	HF	0.97	290	153	10	135	7
T5	1.36	HF	0.78	290	180	7	153	11
T6	3.32	HF	0.97	290	168	15	137	19
T32	0.02	MF	0.26	290	38	22	28	36
T11	0.04	MF	0.26	290	56	14	49	22
T12	0.10	MF	0.32	290	110	13	100	20
T13	0.24	MF	0.31	290	189	6	135	12
T14	0.48	MF	0.32	290	172	7	152	12
T15	0.85	MF	0.26	290	189	20	160	17
T16	1.57	MF	0.30	290	197	6	170	12
T30	0.02	LF	0.07	290	53	9	45	14
T21	0.03	LF	0.10	290	65	14	57	19
T22	0.11	LF	0.10	290	124	13	112	21
T23	0.24	LF	0.08	290	165	6	140	14
T24	0.40	LF	0.08	290	175	12	153	14
T7	0.38	HF	0.92	270	162	6	151	16
T8	1.52	HF	0.92	270	198	6	166	11
T17	0.43	MF	0.25	270	198*	-	168*	-
T18	1.71	MF	0.36	270	272	13	225	11
T25	0.26	LF	0.08	270	187	10	167	17
T26	0.41	LF	0.12	270	209	11	180	13
T9	0.40	HF	0.98	310	132	17	125	26
T10	1.47	HF	0.98	310	156	6	133	11
T19	0.40	MF	0.23	310	124	8	108	14
T20	1.60	MF	0.34	310	147	6	118	12
T27	0.24	LF	0.07	310	117	12	98	11
T28	0.38	LF	0.11	310	115	8	89	11
VT1	0.84	MF	0.21	270/290	218	7	189	15
VT2	0.84	MF	0.21	290/270	206	8	173	12

* Single test data; "na" - not available; ϕ(10^{16}n/m^2-s); ϕt(10^{23}n/m^2); T_i(°C)

CM12

Cu%	Ni%	Mn%	Mo%	P%
0.86	0.84	1.65	0.51	0.006

Capsule	ϕt	ϕ-code	ϕ	T_i	$\Delta\sigma_y$	±SD	$\Delta\sigma_u$	±SD
A5	0.04	HF	0.51	290	na	-	-	-
T31	0.06	HF	0.72	290	na	-	-	-
T1	0.07	HF	0.78	290	63	5	54	12
T2	0.18	HF	0.78	290	91	14	71	23
T3	0.34	HF	0.78	290	120	10	95	16
T29	0.44	HF	0.89	290	na	-	-	-
T4	0.75	HF	0.97	290	na	-	-	-
SR1	0.85	HF	0.97	290	143	3	144	11
T5	1.36	HF	0.78	290	144	8	113	23
T6	3.32	HF	0.97	290	149	21	115	37
T32	0.02	MF	0.26	290	na	-	-	-
T11	0.04	MF	0.26	290	52	12	41	24
T12	0.10	MF	0.32	290	91	8	67	11
T13	0.24	MF	0.31	290	na	-	-	-
T14	0.48	MF	0.32	290	139	10	121	8
T15	0.85	MF	0.26	290	na	-	-	-
T16	1.57	MF	0.30	290	167	8	144	12
T30	0.02	LF	0.07	290	na	-	-	-
T21	0.03	LF	0.10	290	43	11	18	21
T22	0.11	LF	0.10	290	114	8	99	19
T23	0.24	LF	0.08	290	na	-	-	-
T24	0.40	LF	0.08	290	139	8	109	15
T7	0.38	HF	0.92	270	136	3	124	12
T8	1.52	HF	0.92	270	165	7	124	14
T17	0.43	MF	0.25	270	na	-	-	-
T18	1.71	MF	0.36	270	242	7	205	13
T25	0.26	LF	0.08	270	na	-	-	-
T26	0.41	LF	0.12	270	169	8	142	19
T9	0.40	HF	0.98	310	124	5	114	13
T10	1.47	HF	0.98	310	126	8	110	5
T19	0.40	MF	0.23	310	na	-	-	-
T20	1.60	MF	0.34	310	110	8	83	5
T27	0.24	LF	0.07	310	na	-	-	-
T28	0.38	LF	0.11	310	86	15	75	18
VT1	0.84	MF	0.21	270/290	176	8	144	11
VT2	0.84	MF	0.21	290/270	167	9	134	8

* Single test data; "na" - not available; ϕ(10^{16}n/m^2-s); ϕt(10^{23}n/m^2); T_i(°C)

CM13

Cu%	Ni%	Mn%	Mo%	P%
0.11	0.83	1.61	0.51	0.004

Capsule	ϕt	ϕ-code	ϕ	T_i	$\Delta\sigma_y$	±SD	$\Delta\sigma_u$	±SD
A5	0.04	HF	0.51	290	na	-	-	-
T31	0.06	HF	0.72	290	na	-	-	-
T1	0.07	HF	0.78	290	16	7	9	11
T2	0.18	HF	0.78	290	28	8	13	16
T3	0.34	HF	0.78	290	37	9	28	14
T29	0.44	HF	0.89	290	na	-	-	-
T4	0.75	HF	0.97	290	46	11	39	18
SR1	0.85	HF	0.97	290	57	11	60	20
T5	1.36	HF	0.78	290	78	15	65	22
T6	3.32	HF	0.97	290	66	8	44	14
T32	0.02	MF	0.26	290	na	-	-	-
T11	0.04	MF	0.26	290	19	12	14	8
T12	0.10	MF	0.32	290	25	3	14	7
T13	0.24	MF	0.31	290	94	14	33	21
T14	0.48	MF	0.32	290	52	17	12	17
T15	0.85	MF	0.26	290	94	11	85	16
T16	1.57	MF	0.30	290	112	15	100	24
T30	0.02	LF	0.07	290	na	-	-	-
T21	0.03	LF	0.10	290	15	9	9	14
T22	0.11	LF	0.10	290	25	4	25	5
T23	0.24	LF	0.08	290	48	11	43	18
T24	0.40	LF	0.08	290	62	6	52	14
T7	0.38	HF	0.92	270	32	19	28	17
T8	1.52	HF	0.92	270	101	14	90	22
T17	0.43	MF	0.25	270	90*	-	70*	-
T18	1.71	MF	0.36	270	180	18	159	31
T25	0.26	LF	0.08	270	72	10	59	17
T26	0.41	LF	0.12	270	85	16	69	21
T9	0.40	HF	0.98	310	34	11	36	3
T10	1.47	HF	0.98	310	57	19	47	26
T19	0.40	MF	0.23	310	35	13	31	16
T20	1.60	MF	0.34	310	46	10	35	17
T27	0.24	LF	0.07	310	25	13	18	19
T28	0.38	LF	0.11	310	37	20	29	31
VT1	0.84	MF	0.21	270/290	78	10	71	17
VT2	0.84	MF	0.21	290/270	98	10	80	18

* Single test data; "na" - not available; $\phi(10^{16}n/m^2\text{-}s)$; $\phi t(10^{23}n/m^2)$; $T_i(°C)$

CM14

Cu%	Ni%	Mn%	Mo%	P%
0.11	0.83	1.62	0.52	0.040

Capsule	ϕt	ϕ-code	ϕ	T_i	$\Delta\sigma_y$	±SD	$\Delta\sigma_u$	±SD
A5	0.04	HF	0.51	290	na	-	-	-
T31	0.06	HF	0.72	290	na	-	-	-
T1	0.07	HF	0.78	290	-2	20	-5	23
T2	0.18	HF	0.78	290	8	22	-2	26
T3	0.34	HF	0.78	290	48	19	44	27
T29	0.44	HF	0.89	290	na	-	-	-
T4	0.75	HF	0.97	290	na	-	-	-
SR1	0.85	HF	0.97	290	na	-	-	-
T5	1.36	HF	0.78	290	85	15	80	15
T6	3.32	HF	0.97	290	94	16	87	20
T32	0.02	MF	0.26	290	na	-	-	-
T11	0.04	MF	0.26	290	21	19	20	26
T12	0.10	MF	0.32	290	24	17	17	20
T13	0.24	MF	0.31	290	na	-	-	-
T14	0.48	MF	0.32	290	63	18	59	20
T15	0.85	MF	0.26	290	na	-	-	-
T16	1.57	MF	0.30	290	105	28	101	32
T30	0.02	LF	0.07	290	na	-	-	-
T21	0.03	LF	0.10	290	1	23	-7	22
T22	0.11	LF	0.10	290	24	17	22	22
T23	0.24	LF	0.08	290	na	-	-	-
T24	0.40	LF	0.08	290	56	16	48	16
T7	0.38	HF	0.92	270	34	17	26	24
T8	1.52	HF	0.92	270	103	16	96	16
T17	0.43	MF	0.25	270	na	-	-	-
T18	1.71	MF	0.36	270	175	25	158	24
T25	0.26	LF	0.08	270	na	-	-	-
T26	0.41	LF	0.12	270	69	14	61	15
T9	0.40	HF	0.98	310	25	17	17	21
T10	1.47	HF	0.98	310	69	22	59	24
T19	0.40	MF	0.23	310	na	-	-	-
T20	1.60	MF	0.34	310	64	17	54	17
T27	0.24	LF	0.07	310	na	-	-	-
T28	0.38	LF	0.11	310	41	16	33	16
VT1	0.84	MF	0.21	270/290	na	-	-	-
VT2	0.84	MF	0.21	290/270	116	21	111	24

* Single test data; "na" - not available; ϕ(10^{16}n/m^2-s); ϕt(10^{23}n/m^2); T_i(°C)

CM15

Cu%	Ni%	Mn%	Mo%	P%
0.22	0.02	1.59	0.58	0.002

Capsule	ϕt	ϕ-code	ϕ	T_i	$\Delta\sigma_y$	±SD	$\Delta\sigma_u$	±SD
A5	0.04	HF	0.51	290	6	10	6	9
T31	0.06	HF	0.72	290	22	12	15	15
T1	0.07	HF	0.78	290	31	7	25	9
T2	0.18	HF	0.78	290	51	12	52	12
T3	0.34	HF	0.78	290	51	10	49	9
T29	0.44	HF	0.89	290	35*	-	20*	-
T4	0.75	HF	0.97	290	45	9	33	16
SR1	0.85	HF	0.97	290	na	-	-	-
T5	1.36	HF	0.78	290	45	6	33	1
T6	3.32	HF	0.97	290	51	7	42	9
T32	0.02	MF	0.26	290	2	11	-5	17
T11	0.04	MF	0.26	290	24	9	22	9
T12	0.10	MF	0.32	290	48	18	48	14
T13	0.24	MF	0.31	290	39	7	22	11
T14	0.48	MF	0.32	290	43	8	33	12
T15	0.85	MF	0.26	290	39	5	28	11
T16	1.57	MF	0.30	290	46	7	39	8
T30	0.02	LF	0.07	290	13	9	10	11
T21	0.03	LF	0.10	290	36	9	36	14
T22	0.11	LF	0.10	290	49	7	48	11
T23	0.24	LF	0.08	290	34	8	22	11
T24	0.40	LF	0.08	290	37	9	29	11
T7	0.38	HF	0.92	270	62	8	61	13
T8	1.52	HF	0.92	270	67	12	50	16
T17	0.43	MF	0.25	270	53	8	42	8
T18	1.71	MF	0.36	270	71	16	54	16
T25	0.26	LF	0.08	270	53	5	41	8
T26	0.41	LF	0.12	270	53	5	41	8
T9	0.40	HF	0.98	310	48	7	44	13
T10	1.47	HF	0.98	310	41	7	27	12
T19	0.40	MF	0.23	310	38	9	29	16
T20	1.60	MF	0.34	310	31	12	21	15
T27	0.24	LF	0.07	310	38	7	27	8
T28	0.38	LF	0.11	310	26	5	17	8
VT1	0.84	MF	0.21	270/290	55	5	45	11
VT2	0.84	MF	0.21	290/270	58	14	46	16

* Single test data; "na" - not available; ϕ(10^{16}n/m^2-s); ϕt(10^{23}n/m^2); T_i(°C)

CM16

Cu%	Ni%	Mn%	Mo%	P%
0.22	0.82	1.58	0.51	0.004

Capsule	ϕt	ϕ-code	ϕ	T_i	$\Delta\sigma_y$	±SD	$\Delta\sigma_u$	±SD
A5	0.04	HF	0.51	290	12	15	-1	24
T31	0.06	HF	0.72	290	29	9	12	15
T1	0.07	HF	0.78	290	34	15	16	24
T2	0.18	HF	0.78	290	72	14	50	25
T3	0.34	HF	0.78	290	99	18	77	25
T29	0.44	HF	0.89	290	110	7	96	13
T4	0.75	HF	0.97	290	124	17	112	18
SR1	0.85	HF	0.97	290	134	22	120	26
T5	1.36	HF	0.78	290	143	19	125	18
T6	3.32	HF	0.97	290	151	16	127	29
T32	0.02	MF	0.26	290	14	14	12	21
T11	0.04	MF	0.26	290	27	20	12	27
T12	0.10	MF	0.32	290	72	21	57	31
T13	0.24	MF	0.31	290	165	13	108	16
T14	0.48	MF	0.32	290	148	14	128	16
T15	0.85	MF	0.26	290	165	14	140	17
T16	1.57	MF	0.30	290	179	13	156	16
T30	0.02	LF	0.07	290	26	9	17	21
T21	0.03	LF	0.10	290	21	16	4	26
T22	0.11	LF	0.10	290	74	15	48	25
T23	0.24	LF	0.08	290	142	13	123	16
T24	0.40	LF	0.08	290	153	14	131	22
T7	0.38	HF	0.92	270	114	29	93	37
T8	1.52	HF	0.92	270	170	13	148	16
T17	0.43	MF	0.25	270	174	14	156	16
T18	1.71	MF	0.36	270	238	14	204	16
T25	0.26	LF	0.08	270	151	15	134	18
T26	0.41	LF	0.12	270	175	14	146	20
T9	0.40	HF	0.98	310	93	14	78	25
T10	1.47	HF	0.98	310	137	13	123	17
T19	0.40	MF	0.23	310	132	7	105	16
T20	1.60	MF	0.34	310	126	16	115	18
T27	0.24	LF	0.07	310	83	13	68	19
T28	0.38	LF	0.11	310	107	14	94	17
VT1	0.84	MF	0.21	270/290	186	17	159	17
VT2	0.84	MF	0.21	290/270	167	16	140	21

* Single test data; "na" - not available; $\phi(10^{16}n/m^2\text{-}s)$; $\phi t(10^{23}n/m^2)$; $T_i(°C)$

CM17

Cu%	Ni%	Mn%	Mo%	P%
0.22	1.59	1.54	0.50	0.004

Capsule	ϕt	ϕ-code	ϕ	T_i	$\Delta\sigma_y$	±SD	$\Delta\sigma_u$	±SD
A5	0.04	HF	0.51	290	10	11	-3	14
T31	0.06	HF	0.72	290	45	23	44	16
T1	0.07	HF	0.78	290	53	8	42	14
T2	0.18	HF	0.78	290	113	8	96	12
T3	0.34	HF	0.78	290	148	9	131	12
T29	0.44	HF	0.89	290	158	2	134	8
T4	0.75	HF	0.97	290	202	11	172	19
SR1	0.85	HF	0.97	290	na	-	-	-
T5	1.36	HF	0.78	290	259	18	219	22
T6	3.32	HF	0.97	290	270	12	237	18
T32	0.02	MF	0.26	290	30	16	24	19
T11	0.04	MF	0.26	290	42	10	36	13
T12	0.10	MF	0.32	290	84	9	67	19
T13	0.24	MF	0.31	290	273	23	144	27
T14	0.48	MF	0.32	290	228	12	193	18
T15	0.85	MF	0.26	290	273	21	235	22
T16	1.57	MF	0.30	290	307	15	264	17
T30	0.02	LF	0.07	290	34	23	36	17
T21	0.03	LF	0.10	290	39	12	30	16
T22	0.11	LF	0.10	290	128	10	107	14
T23	0.24	LF	0.08	290	212	19	186	18
T24	0.40	LF	0.08	290	242	15	215	21
T7	0.38	HF	0.92	270	158	16	141	17
T8	1.52	HF	0.92	270	298	11	252	17
T17	0.43	MF	0.25	270	262	14	229	18
T18	1.71	MF	0.36	270	366	29	313	31
T25	0.26	LF	0.08	270	244	12	217	17
T26	0.41	LF	0.12	270	264	18	226	17
T9	0.40	HF	0.98	310	146	18	132	26
T10	1.47	HF	0.98	310	235	13	199	17
T19	0.40	MF	0.23	310	180	13	156	19
T20	1.60	MF	0.34	310	224	13	192	18
T27	0.24	LF	0.07	310	141	20	117	20
T28	0.38	LF	0.11	310	152	21	127	27
VT1	0.84	MF	0.21	270/290	296	14	262	21
VT2	0.84	MF	0.21	290/270	303	11	268	17

* Single test data; "na" - not available; ϕ(10^{16}n/m^2-s); ϕt(10^{23}n/m^2); T_i(°C)

CM18

Cu%	Ni%	Mn%	Mo%	P%
0.43	0.02	1.70	0.56	0.002

Capsule	ϕt	ϕ-code	ϕ	T_i	$\Delta\sigma_y$	±SD	$\Delta\sigma_u$	±SD
A5	0.04	HF	0.51	290	29*	-	5*	-
T31	0.06	HF	0.72	290	57	2	51	4
T1	0.07	HF	0.78	290	61	9	55	17
T2	0.18	HF	0.78	290	64	10	52	20
T3	0.34	HF	0.78	290	66	8	59	15
T29	0.44	HF	0.89	290	66	18	50	37
T4	0.75	HF	0.97	290	59	11	43	5
SR1	0.85	HF	0.97	290	77	12	66	15
T5	1.36	HF	0.78	290	75	13	61	22
T6	3.32	HF	0.97	290	83	8	64	15
T32	0.02	MF	0.26	290	31	11	15	27
T11	0.04	MF	0.26	290	53	10	42	20
T12	0.10	MF	0.32	290	63	15	45	30
T13	0.24	MF	0.31	290	74	8	62	16
T14	0.48	MF	0.32	290	63	9	47	16
T15	0.85	MF	0.26	290	74	12	62	33
T16	1.57	MF	0.30	290	71	8	52	15
T30	0.02	LF	0.07	290	44	3	38	9
T21	0.03	LF	0.10	290	39	8	21	17
T22	0.11	LF	0.10	290	65	10	59	17
T23	0.24	LF	0.08	290	66	8	61	18
T24	0.40	LF	0.08	290	58	9	47	20
T7	0.38	HF	0.92	270	66	19	52	33
T8	1.52	HF	0.92	270	97	11	69	20
T17	0.43	MF	0.25	270	69	15	46	24
T18	1.71	MF	0.36	270	82	21	64	34
T25	0.26	LF	0.08	270	92	9	80	22
T26	0.41	LF	0.12	270	72	9	57	15
T9	0.40	HF	0.98	310	64	12	51	30
T10	1.47	HF	0.98	310	76	13	64	22
T19	0.40	MF	0.23	310	61	8	56	15
T20	1.60	MF	0.34	310	54	17	29	26
T27	0.24	LF	0.07	310	46	13	25	21
T28	0.38	LF	0.11	310	51	16	46	24
VT1	0.84	MF	0.21	270/290	80	9	57	16
VT2	0.84	MF	0.21	290/270	75	12	57	21

* Single test data; "na" - not available; ϕ(10^{16}n/m^2-s); ϕt(10^{23}n/m^2); T_i(°C)

CM19

Cu%	Ni%	Mn%	Mo%	P%
0.42	0.85	1.63	0.51	0.005

Capsule	ϕt	ϕ-code	ϕ	T_i	$\Delta\sigma_y$	±SD	$\Delta\sigma_u$	±SD
A5	0.04	HF	0.51	290	54	7	35	13
T31	0.06	HF	0.72	290	73	6	555	13
T1	0.07	HF	0.78	290	81	7	65	14
T2	0.18	HF	0.78	290	123	6	103	12
T3	0.34	HF	0.78	290	147	4	124	12
T29	0.44	HF	0.89	290	150	9	129	12
T4	0.75	HF	0.97	290	152	9	124	10
SR1	0.85	HF	0.97	290	165	12	148	17
T5	1.36	HF	0.78	290	170	5	145	14
T6	3.32	HF	0.97	290	190	6	156	12
T32	0.02	MF	0.26	290	36	9	19	15
T11	0.04	MF	0.26	290	70	6	54	13
T12	0.10	MF	0.32	290	124	7	108	14
T13	0.24	MF	0.31	290	188	7	136	12
T14	0.48	MF	0.32	290	171	5	148	13
T15	0.85	MF	0.26	290	188	5	155	12
T16	1.57	MF	0.30	290	198	5	163	12
T30	0.02	LF	0.07	290	53	3	37	8
T21	0.03	LF	0.10	290	72	9	58	13
T22	0.11	LF	0.10	290	141	10	120	13
T23	0.24	LF	0.08	290	168	6	156	15
T24	0.40	LF	0.08	290	178	9	163	13
T7	0.38	HF	0.92	270	169	4	147	15
T8	1.52	HF	0.92	270	205	8	174	20
T17	0.43	MF	0.25	270	214	5	186	12
T18	1.71	MF	0.36	270	268	6	234	13
T25	0.26	LF	0.08	270	191	5	173	13
T26	0.41	LF	0.12	270	201	5	173	16
T9	0.40	HF	0.98	310	131	8	109	16
T10	1.47	HF	0.98	310	153	8	119	12
T19	0.40	MF	0.23	310	132	7	105	6
T20	1.60	MF	0.34	310	143	6	114	16
T27	0.24	LF	0.07	310	114	8	93	16
T28	0.38	LF	0.11	310	110	6	90	16
VT1	0.84	MF	0.21	270/290	214	6	191	13
VT2	0.84	MF	0.21	290/270	192	5	167	15

* Single test data; "na" - not available; ϕ(10^{16}n/m^2-s); ϕt(10^{23}n/m^2); T_i(°C)

CM20

Cu%	Ni%	Mn%	Mo%	P%
0.43	1.69	1.63	0.50	0.006

Capsule	ϕt	ϕ-code	ϕ	T_i	$\Delta\sigma_y$	±SD	$\Delta\sigma_u$	±SD
A5	0.04	HF	0.51	290	62	10	45	16
T31	0.06	HF	0.72	290	92	11	83	17
T1	0.07	HF	0.78	290	111	11	91	17
T2	0.18	HF	0.78	290	183	10	162	17
T3	0.34	HF	0.78	290	224	11	196	16
T29	0.44	HF	0.89	290	226	10	199	16
T4	0.75	HF	0.97	290	250	12	221	11
SR1	0.85	HF	0.97	290	253	10	224	16
T5	1.36	HF	0.78	290	280	22	233	36
T6	3.32	HF	0.97	290	331	14	285	19
T32	0.02	MF	0.26	290	49	10	44	16
T11	0.04	MF	0.26	290	98	10	86	16
T12	0.10	MF	0.32	290	163	11	146	17
T13	0.24	MF	0.31	290	314	10	188	20
T14	0.48	MF	0.32	290	270	11	236	18
T15	0.85	MF	0.26	290	314	11	258	17
T16	1.57	MF	0.30	290	307	13	262	25
T30	0.02	LF	0.07	290	60	16	49	24
T21	0.03	LF	0.10	290	99	10	87	17
T22	0.11	LF	0.10	290	199	11	181	17
T23	0.24	LF	0.08	290	260	11	229	16
T24	0.40	LF	0.08	290	293	12	253	19
T7	0.38	HF	0.92	270	240	13	221	17
T8	1.52	HF	0.92	270	331	16	283	7
T17	0.43	MF	0.25	270	314	10	266	16
T18	1.71	MF	0.36	270	384	10	338	16
T25	0.26	LF	0.08	270	289	10	251	17
T26	0.41	LF	0.12	270	305	13	261	16
T9	0.40	HF	0.98	310	209	12	193	20
T10	1.47	HF	0.98	310	269	13	223	16
T19	0.40	MF	0.23	310	233	10	188	17
T20	1.60	MF	0.34	310	259	13	214	20
T27	0.24	LF	0.07	310	204	13	177	17
T28	0.38	LF	0.11	310	211	10	183	18
VT1	0.84	MF	0.21	270/290	337	14	290	32
VT2	0.84	MF	0.21	290/270	327	11	277	18

* Single test data; "na" - not available; ϕ(10^{16}n/m^2-s); ϕt(10^{23}n/m^2); T_i(°C)

CM21

Cu%	Ni%	Mn%	Mo%	P%
0.42	0.84	0.01	0.58	0.002

Capsule	ϕt	ϕ-code	ϕ	T_i	$\Delta\sigma_y$	±SD	$\Delta\sigma_u$	±SD
A5	0.04	HF	0.51	290	46	11	32	11
T31	0.06	HF	0.72	290	70	11	62	10
T1	0.07	HF	0.78	290	57	11	47	10
T2	0.18	HF	0.78	290	85	14	73	14
T3	0.34	HF	0.78	290	100	14	83	13
T29	0.44	HF	0.89	290	92	12	81	9
T4	0.75	HF	0.97	290	107	12	86	7
SR1	0.85	HF	0.97	290	na	-	-	-
T5	1.36	HF	0.78	290	105	9	86	12
T6	3.32	HF	0.97	290	106	14	88	17
T32	0.02	MF	0.26	290	36	14	19	15
T11	0.04	MF	0.26	290	58	18	42	18
T12	0.10	MF	0.32	290	79	15	66	14
T13	0.24	MF	0.31	290	118	9	95	11
T14	0.48	MF	0.32	290	113	10	97	13
T15	0.85	MF	0.26	290	118	21	104	24
T16	1.57	MF	0.30	290	111	12	98	20
T30	0.02	LF	0.07	290	43	8	36	15
T21	0.03	LF	0.10	290	57	13	47	11
T22	0.11	LF	0.10	290	82	8	71	12
T23	0.24	LF	0.08	290	110	8	98	12
T24	0.40	LF	0.08	290	106	12	93	13
T7	0.38	HF	0.92	270	99	9	83	10
T8	1.52	HF	0.92	270	119	8	104	12
T17	0.43	MF	0.25	270	124	10	109	15
T18	1.71	MF	0.36	270	134	9	110	11
T25	0.26	LF	0.08	270	117	9	100	11
T26	0.41	LF	0.12	270	108	9	92	11
T9	0.40	HF	0.98	310	98	9	83	9
T10	1.47	HF	0.98	310	104	8	88	16
T19	0.40	MF	0.23	310	90	9	72	13
T20	1.60	MF	0.34	310	70	11	58	12
T27	0.24	LF	0.07	310	75	24	63	16
T28	0.38	LF	0.11	310	83	8	70	11
VT1	0.84	MF	0.21	270/290	109	14	85	15
VT2	0.84	MF	0.21	290/270	105	13	93	13

* Single test data; "na" - not available; ϕ(10^{16}n/m^2-s); ϕt(10^{23}n/m^2); T_i(°C)

CM22

Cu%	Ni%	Mn%	Mo%	P%
0.42	0.84	0.84	0.56	0.002

Capsule	ϕt	ϕ-code	ϕ	T_i	$\Delta\sigma_y$	±SD	$\Delta\sigma_u$	±SD
A5	0.04	HF	0.51	290	29	9	14	12
T31	0.06	HF	0.72	290	75	3	60	3
T1	0.07	HF	0.78	290	67	11	53	11
T2	0.18	HF	0.78	290	110	8	97	6
T3	0.34	HF	0.78	290	134	10	124	8
T29	0.44	HF	0.89	290	134	3	122	10
T4	0.75	HF	0.97	290	137	13	114	11
SR1	0.85	HF	0.97	290	na	-	-	-
T5	1.36	HF	0.78	290	151	9	128	12
T6	3.32	HF	0.97	290	165	6	137	7
T32	0.02	MF	0.26	290	37	3	36	5
T11	0.04	MF	0.26	290	57	11	47	16
T12	0.10	MF	0.32	290	92	11	77	9
T13	0.24	MF	0.31	290	156	8	117	9
T14	0.48	MF	0.32	290	154	10	135	10
T15	0.85	MF	0.26	290	156	9	130	12
T16	1.57	MF	0.30	290	169	15	147	16
T30	0.02	LF	0.07	290	45	8	36	14
T21	0.03	LF	0.10	290	54	14	42	10
T22	0.11	LF	0.10	290	113	6	97	15
T23	0.24	LF	0.08	290	153	10	132	9
T24	0.40	LF	0.08	290	151	18	135	16
T7	0.38	HF	0.92	270	139	6	118	8
T8	1.52	HF	0.92	270	191	32	162	26
T17	0.43	MF	0.25	270	175	10	154	10
T18	1.71	MF	0.36	270	240	19	201	16
T25	0.26	LF	0.08	270	164	23	141	22
T26	0.41	LF	0.12	270	189	13	166	15
T9	0.40	HF	0.98	310	117	7	97	13
T10	1.47	HF	0.98	310	140	25	117	19
T19	0.40	MF	0.23	310	115	13	97	12
T20	1.60	MF	0.34	310	110	26	92	17
T27	0.24	LF	0.07	310	113	24	96	30
T28	0.38	LF	0.11	310	94	7	82	12
VT1	0.84	MF	0.21	270/290	173	10	153	7
VT2	0.84	MF	0.21	290/270	179	7	157	13

* Single test data; "na" - not available; ϕ(10^{16}n/m^2-s); ϕt(10^{23}n/m^2); T_i(°C)

CM23

Cu%	Ni%	Mn%	Mo%	P%
0.02	0.83	1.62	0.55	0.002

Capsule	ϕt	ϕ-code	ϕ	T_i	$\Delta\sigma_y$	±SD	$\Delta\sigma_u$	±SD
A5	0.04	HF	0.51	290	na	-	-	-
T31	0.06	HF	0.72	290	na	-	-	-
T1	0.07	HF	0.78	290	10*	-	-5*	-
T2	0.18	HF	0.78	290	-3	17	-4	14
T3	0.34	HF	0.78	290	5	15	2	11
T29	0.44	HF	0.89	290	na	-	-	-
T4	0.75	HF	0.97	290	na	-	-	-
SR1	0.85	HF	0.97	290	na	-	-	-
T5	1.36	HF	0.78	290	17	3	7	5
T6	3.32	HF	0.97	290	26	24	13	20
T32	0.02	MF	0.26	290	na	-	-	-
T11	0.04	MF	0.26	290	3	35	-2	23
T12	0.10	MF	0.32	290	-2	15	-2	12
T13	0.24	MF	0.31	290	na	-	-	-
T14	0.48	MF	0.32	290	12	7	7	6
T15	0.85	MF	0.26	290	na	-	-	-
T16	1.57	MF	0.30	290	6	5	11	5
T30	0.02	LF	0.07	290	na	-	-	-
T21	0.03	LF	0.10	290	-6	15	-4	9
T22	0.11	LF	0.10	290	19	31	10	13
T23	0.24	LF	0.08	290	na	-	-	-
T24	0.40	LF	0.08	290	14	6	6	6
T7	0.38	HF	0.92	270	20	23	15	21
T8	1.52	HF	0.92	270	24*	-	19*	-
T17	0.43	MF	0.25	270	na	-	-	-
T18	1.71	MF	0.36	270	25	14	15	17
T25	0.26	LF	0.08	270	na	-	-	-
T26	0.41	LF	0.12	270	19*	-	21*	-
T9	0.40	HF	0.98	310	-13	15	-13	11
T10	1.47	HF	0.98	310	13*	-	13*	-
T19	0.40	MF	0.23	310	na	-	-	-
T20	1.60	MF	0.34	310	15	3	7	4
T27	0.24	LF	0.07	310	na	-	-	-
T28	0.38	LF	0.11	310	13	5	8	5
VT1	0.84	MF	0.21	270/290	na	-	-	-
VT2	0.84	MF	0.21	290/270	29	7	23	6

* Single test data; "na" - not available; ϕ(10^{16}n/m^2-s); ϕt(10^{23}n/m^2); T_i(°C)

CM24

Cu%	Ni%	Mn%	Mo%	P%
0.02	0.87	1.65	0.52	0.006

Capsule	ϕt	ϕ-code	ϕ	T_i	$\Delta\sigma_y$	±SD	$\Delta\sigma_u$	±SD
A5	0.04	HF	0.51	290	na	-	-	-
T31	0.06	HF	0.72	290	na	-	-	-
T1	0.07	HF	0.78	290	-2	13	-7	13
T2	0.18	HF	0.78	290	-5	17	-14	17
T3	0.34	HF	0.78	290	-3	12	-11	12
T29	0.44	HF	0.89	290	na	-	-	-
T4	0.75	HF	0.97	290	na	-	-	-
SR1	0.85	HF	0.97	290	na	-	-	-
T5	1.36	HF	0.78	290	14	13	-4	25
T6	3.32	HF	0.97	290	13	14	4	12
T32	0.02	MF	0.26	290	na	-	-	-
T11	0.04	MF	0.26	290	-4	17	-7	21
T12	0.10	MF	0.32	290	-5	14	-16	14
T13	0.24	MF	0.31	290	na	-	-	-
T14	0.48	MF	0.32	290	17	12	9	24
T15	0.85	MF	0.26	290	na	-	-	-
T16	1.57	MF	0.30	290	16	5	11	5
T30	0.02	LF	0.07	290	na	-	-	-
T21	0.03	LF	0.10	290	6	16	6	13
T22	0.11	LF	0.10	290	-3	16	-13	14
T23	0.24	LF	0.08	290	na	-	-	-
T24	0.40	LF	0.08	290	5	15	-4	29
T7	0.38	HF	0.92	270	1	13	-9	13
T8	1.52	HF	0.92	270	12*	-	-8*	-
T17	0.43	MF	0.25	270	na	-	-	-
T18	1.71	MF	0.36	270	32	12	13	7
T25	0.26	LF	0.08	270	na	-	-	-
T26	0.41	LF	0.12	270	24	13	18	22
T9	0.40	HF	0.98	310	0	12	-10	12
T10	1.47	HF	0.98	310	27*	-	25*	-
T19	0.40	MF	0.23	310	na	-	-	-
T20	1.60	MF	0.34	310	22	12	18	12
T27	0.24	LF	0.07	310	na	-	-	-
T28	0.38	LF	0.11	310	18	12	12	22
VT1	0.84	MF	0.21	270/290	na	-	-	-
VT2	0.84	MF	0.21	290/270	23	13	2	30

* Single test data; "na" - not available; ϕ(10^{16}n/m^2-s); ϕt(10^{23}n/m^2); T_i(°C)

CM25

Cu%	Ni%	Mn%	Mo%	P%
0.01	0.87	1.53	0.52	0.003

Capsule	ϕt	ϕ-code	ϕ	T_i	$\Delta\sigma_y$	±SD	$\Delta\sigma_u$	±SD
A5	0.04	HF	0.51	290	na	-	-	-
T31	0.06	HF	0.72	290	na	-	-	-
T1	0.07	HF	0.78	290	6	7	-1	14
T2	0.18	HF	0.78	290	10	9	0	15
T3	0.34	HF	0.78	290	8	31	4	45
T29	0.44	HF	0.89	290	na	-	-	-
T4	0.75	HF	0.97	290	na	-	-	-
SR1	0.85	HF	0.97	290	na	-	-	-
T5	1.36	HF	0.78	290	33	11	2	22
T6	3.32	HF	0.97	290	22	20	4	28
T32	0.02	MF	0.26	290	na	-	-	-
T11	0.04	MF	0.26	290	-7	24	-12	30
T12	0.10	MF	0.32	290	11	9	3	17
T13	0.24	MF	0.31	290	na	-	-	-
T14	0.48	MF	0.32	290	18	7	12	28
T15	0.85	MF	0.26	290	na	-	-	-
T16	1.57	MF	0.30	290	30	9	21	21
T30	0.02	LF	0.07	290	na	-	-	-
T21	0.03	LF	0.10	290	2	8	0	14
T22	0.11	LF	0.10	290	15	9	1	19
T23	0.24	LF	0.08	290	na	-	-	-
T24	0.40	LF	0.08	290	18	9	8	14
T7	0.38	HF	0.92	270	8	16	2	27
T8	1.52	HF	0.92	270	34	19	23	30
T17	0.43	MF	0.25	270	na	-	-	-
T18	1.71	MF	0.36	270	24	7	14	18
T25	0.26	LF	0.08	270	na	-	-	-
T26	0.41	LF	0.12	270	26	19	12	23
T9	0.40	HF	0.98	310	16	8	13	21
T10	1.47	HF	0.98	310	25	7	15	15
T19	0.40	MF	0.23	310	na	-	-	-
T20	1.60	MF	0.34	310	23	10	7	19
T27	0.24	LF	0.07	310	na	-	-	-
T28	0.38	LF	0.11	310	23	7	11	14
VT1	0.84	MF	0.21	270/290	na	-	-	-
VT2	0.84	MF	0.21	290/270	35	8	32	14

* Single test data; "na" - not available; ϕ(10^{16}n/m^2-s); ϕt(10^{23}n/m^2); T_i(°C)

CM26

Cu%	Ni%	Mn%	Mo%	P%
0.01	0.87	1.66	0.52	0.006

Capsule	ϕt	ϕ-code	ϕ	T_i	$\Delta\sigma_y$	±SD	$\Delta\sigma_u$	±SD
A5	0.04	HF	0.51	290	na	-	-	-
T31	0.06	HF	0.72	290	na	-	-	-
T1	0.07	HF	0.78	290	3	17	-7	22
T2	0.18	HF	0.78	290	7	24	-1	31
T3	0.34	HF	0.78	290	14	8	5	8
T29	0.44	HF	0.89	290	na	-	-	-
T4	0.75	HF	0.97	290	na	-	-	-
SR1	0.85	HF	0.97	290	na	-	-	-
T5	1.36	HF	0.78	290	25	12	27	17
T6	3.32	HF	0.97	290	34	17	16	14
T32	0.02	MF	0.26	290	na	-	-	-
T11	0.04	MF	0.26	290	-2	10	-9	12
T12	0.10	MF	0.32	290	5	11	-6	11
T13	0.24	MF	0.31	290	na	-	-	-
T14	0.48	MF	0.32	290	12	20	8	20
T15	0.85	MF	0.26	290	na	-	-	-
T16	1.57	MF	0.30	290	13	13	5	17
T30	0.02	LF	0.07	290	na	-	-	-
T21	0.03	LF	0.10	290	6	8	-7	8
T22	0.11	LF	0.10	290	-2	21	-12	24
T23	0.24	LF	0.08	290	na	-	-	-
T24	0.40	LF	0.08	290	5	6	-13	14
T7	0.38	HF	0.92	270	13	16	19	21
T8	1.52	HF	0.92	270	30*	-	31*	-
T17	0.43	MF	0.25	270	na	-	-	-
T18	1.71	MF	0.36	270	33	10	19	12
T25	0.26	LF	0.08	270	na	-	-	-
T26	0.41	LF	0.12	270	11	16	7	17
T9	0.40	HF	0.98	310	15	7	9	8
T10	1.47	HF	0.98	310	39*	-	36*	-
T19	0.40	MF	0.23	310	na	-	-	-
T20	1.60	MF	0.34	310	24	6	24	9
T27	0.24	LF	0.07	310	na	-	-	-
T28	0.38	LF	0.11	310	17	21	16	28
VT1	0.84	MF	0.21	270/290	na	-	-	-
VT2	0.84	MF	0.21	290/270	na	-	-	-

* Single test data; "na" - not available; ϕ(10^{16}n/m^2-s); ϕt(10^{23}n/m^2); T_i(°C)

CM27

Cu%	Ni%	Mn%	Mo%	P%
0.02	0.84	1.60	0.51	0.002

Capsule	ϕt	ϕ-code	ϕ	T_i	$\Delta\sigma_y$	±SD	$\Delta\sigma_u$	±SD
A5	0.04	HF	0.51	290	na	-	-	-
T31	0.06	HF	0.72	290	na	-	-	-
T1	0.07	HF	0.78	290	-7	16	-8	19
T2	0.18	HF	0.78	290	12	18	5	19
T3	0.34	HF	0.78	290	-12	16	-20	18
T29	0.44	HF	0.89	290	na	-	-	-
T4	0.75	HF	0.97	290	na	-	-	-
SR1	0.85	HF	0.97	290	na	-	-	-
T5	1.36	HF	0.78	290	19	9	8	8
T6	3.32	HF	0.97	290	21	9	5	11
T32	0.02	MF	0.26	290	na	-	-	-
T11	0.04	MF	0.26	290	12	17	3	19
T12	0.10	MF	0.32	290	1	16	-4	19
T13	0.24	MF	0.31	290	na	-	-	-
T14	0.48	MF	0.32	290	4	10	-6	12
T15	0.85	MF	0.26	290	na	-	-	-
T16	1.57	MF	0.30	290	28	10	13	13
T30	0.02	LF	0.07	290	na	-	-	-
T21	0.03	LF	0.10	290	12	16	12	19
T22	0.11	LF	0.10	290	6	23	-3	24
T23	0.24	LF	0.08	290	na	-	-	-
T24	0.40	LF	0.08	290	9	9	1	9
T7	0.38	HF	0.92	270	-5	17	3	16
T8	1.52	HF	0.92	270	3*	-	-11*	-
T17	0.43	MF	0.25	270	na	-	-	-
T18	1.71	MF	0.36	270	24	11	5	12
T25	0.26	LF	0.08	270	na	-	-	-
T26	0.41	LF	0.12	270	16	8	2	9
T9	0.40	HF	0.98	310	17	8	8	8
T10	1.47	HF	0.98	310	23*	-	13*	-
T19	0.40	MF	0.23	310	na	-	-	-
T20	1.60	MF	0.34	310	5	5	-13	8
T27	0.24	LF	0.07	310	na	-	-	-
T28	0.38	LF	0.11	310	8	8	-3	11
VT1	0.84	MF	0.21	270/290	na	-	-	-
VT2	0.84	MF	0.21	290/270	na	-	-	-

* Single test data; "na" - not available; ϕ(10^{16}n/m^2-s); ϕt(10^{23}n/m^2); T_i(°C)

CM28

Cu%	Ni%	Mn%	Mo%	P%
0.42	0.84	1.60	0.51	0.002

Capsule	ϕt	ϕ-code	ϕ	T_i	$\Delta\sigma_y$	±SD	$\Delta\sigma_u$	±SD
A5	0.04	HF	0.51	290	na	-	-	-
T31	0.06	HF	0.72	290	na	-	-	-
T1	0.07	HF	0.78	290	58	12	37	21
T2	0.18	HF	0.78	290	129	17	116	13
T3	0.34	HF	0.78	290	141	16	123	22
T29	0.44	HF	0.89	290	na	-	-	-
T4	0.75	HF	0.97	290	na	-	-	-
SR1	0.85	HF	0.97	290	na	-	-	-
T5	1.36	HF	0.78	290	184	10	160	15
T6	3.32	HF	0.97	290	184	17	156	20
T32	0.02	MF	0.26	290	na	-	-	-
T11	0.04	MF	0.26	290	64	16	51	13
T12	0.10	MF	0.32	290	115	16	97	21
T13	0.24	MF	0.31	290	na	-	-	-
T14	0.48	MF	0.32	290	186	10	165	11
T15	0.85	MF	0.26	290	na	-	-	-
T16	1.57	MF	0.30	290	203	10	171	11
T30	0.02	LF	0.07	290	na	-	-	-
T21	0.03	LF	0.10	290	77	17	67	24
T22	0.11	LF	0.10	290	128	12	111	18
T23	0.24	LF	0.08	290	na	-	-	-
T24	0.40	LF	0.08	290	169	11	142	12
T7	0.38	HF	0.92	270	158	20	130	40
T8	1.52	HF	0.92	270	202	13	170	13
T17	0.43	MF	0.25	270	na	-	-	-
T18	1.71	MF	0.36	270	267	15	221	14
T25	0.26	LF	0.08	270	na	-	-	-
T26	0.41	LF	0.12	270	213	10	182	11
T9	0.40	HF	0.98	310	115	14	99	27
T10	1.47	HF	0.98	310	170	11	143	12
T19	0.40	MF	0.23	310	na	-	-	-
T20	1.60	MF	0.34	310	154	10	124	11
T27	0.24	LF	0.07	310	na	-	-	-
T28	0.38	LF	0.11	310	129	13	109	15
VT1	0.84	MF	0.21	270/290	na	-	-	-
VT2	0.84	MF	0.21	290/270	223	16	194	17

* Single test data; "na" - not available; ϕ(10^{16}n/m^2-s); ϕt(10^{23}n/m^2); T_i(°C)

CM29

Cu%	Ni%	Mn%	Mo%	P%
0.21	0.02	1.68	0.02	0.002

Capsule	ϕt	ϕ-code	ϕ	T_i	$\Delta\sigma_y$	±SD	$\Delta\sigma_u$	±SD
A5	0.04	HF	0.51	290	na	-	-	-
T31	0.06	HF	0.72	290	na	-	-	-
T1	0.07	HF	0.78	290	55	15	57	25
T2	0.18	HF	0.78	290	61	28	48	41
T3	0.34	HF	0.78	290	76	14	64	35
T29	0.44	HF	0.89	290	na	-	-	-
T4	0.75	HF	0.97	290	na	-	-	-
SR1	0.85	HF	0.97	290	na	-	-	-
T5	1.36	HF	0.78	290	79	9	56	12
T6	3.32	HF	0.97	290	80	30	66	45
T32	0.02	MF	0.26	290	na	-	-	-
T11	0.04	MF	0.26	290	38	24	17	24
T12	0.10	MF	0.32	290	55	21	55	32
T13	0.24	MF	0.31	290	na	-	-	-
T14	0.48	MF	0.32	290	74	7	59	13
T15	0.85	MF	0.26	290	na	-	-	-
T16	1.57	MF	0.30	290	81	12	60	16
T30	0.02	LF	0.07	290	na	-	-	-
T21	0.03	LF	0.10	290	36	17	40	32
T22	0.11	LF	0.10	290	57	16	44	25
T23	0.24	LF	0.08	290	na	-	-	-
T24	0.40	LF	0.08	290	64	7	42	15
T7	0.38	HF	0.92	270	63	19	47	22
T8	1.52	HF	0.92	270	89*	-	53*	-
T17	0.43	MF	0.25	270	na	-	-	-
T18	1.71	MF	0.36	270	108	8	67	12
T25	0.26	LF	0.08	270	na	-	-	-
T26	0.41	LF	0.12	270	88	10	75	12
T9	0.40	HF	0.98	310	64	25	59	35
T10	1.47	HF	0.98	310	86*	-	71*	-
T19	0.40	MF	0.23	310	na	-	-	-
T20	1.60	MF	0.34	310	76	7	59	12
T27	0.24	LF	0.07	310	na	-	-	-
T28	0.38	LF	0.11	310	48	8	23	13
VT1	0.84	MF	0.21	270/290	na	-	-	-
VT2	0.84	MF	0.21	290/270	na	-	-	-

* Single test data; "na" - not available; ϕ(10^{16}n/m^2-s); ϕt(10^{23}n/m^2); T_i(°C)

CM30

Cu%	Ni%	Mn%	Mo%	P%
0.22	0.86	1.64	0.50	0.006

Capsule	ϕt	ϕ-code	ϕ	T_i	$\Delta\sigma_y$	±SD	$\Delta\sigma_u$	±SD
A5	0.04	HF	0.51	290	na	-	-	-
T31	0.06	HF	0.72	290	na	-	-	-
T1	0.07	HF	0.78	290	33	3	18	5
T2	0.18	HF	0.78	290	72	10	55	17
T3	0.34	HF	0.78	290	92	8	76	14
T29	0.44	HF	0.89	290	na	-	-	-
T4	0.75	HF	0.97	290	na	-	-	-
SR1	0.85	HF	0.97	290	na	-	-	-
T5	1.36	HF	0.78	290	135	10	116	11
T6	3.32	HF	0.97	290	170	13	141	20
T32	0.02	MF	0.26	290	na	-	-	-
T11	0.04	MF	0.26	290	30	10	24	16
T12	0.10	MF	0.32	290	69	9	57	14
T13	0.24	MF	0.31	290	na	-	-	-
T14	0.48	MF	0.32	290	138	10	119	13
T15	0.85	MF	0.26	290	na	-	-	-
T16	1.57	MF	0.30	290	165	11	138	13
T30	0.02	LF	0.07	290	na	-	-	-
T21	0.03	LF	0.10	290	35	10	27	16
T22	0.11	LF	0.10	290	87	12	67	23
T23	0.24	LF	0.08	290	na	-	-	-
T24	0.40	LF	0.08	290	141	9	115	12
T7	0.38	HF	0.92	270	110	16	89	24
T8	1.52	HF	0.92	270	178*	-	145*	-
T17	0.43	MF	0.25	270	na	-	-	-
T18	1.71	MF	0.36	270	227	11	188	17
T25	0.26	LF	0.08	270	na	-	-	-
T26	0.41	LF	0.12	270	173	11	150	15
T9	0.40	HF	0.98	310	91	13	79	18
T10	1.47	HF	0.98	310	132*	-	110*	-
T19	0.40	MF	0.23	310	na	-	-	-
T20	1.60	MF	0.34	310	122	10	98	15
T27	0.24	LF	0.07	310	na	-	-	-
T28	0.38	LF	0.11	310	101	10	91	16
VT1	0.84	MF	0.21	270/290	na	-	-	-
VT2	0.84	MF	0.21	290/270	na	-	-	-

* Single test data; "na" - not available; ϕ(10^{16}n/m^2-s); ϕt(10^{23}n/m^2); T_i(°C)

CM31

Cu%	Ni%	Mn%	Mo%	P%
0.01	0.80	1.65	0.51	0.006

Capsule	ϕt	ϕ-code	ϕ	T_i	$\Delta\sigma_y$	±SD	$\Delta\sigma_u$	±SD
A5	0.04	HF	0.51	290	na	-	-	-
T31	0.06	HF	0.72	290	na	-	-	-
T1	0.07	HF	0.78	290	0	8	-5	16
T2	0.18	HF	0.78	290	7	9	-6	12
T3	0.34	HF	0.78	290	11	7	6	9
T29	0.44	HF	0.89	290	na	-	-	-
T4	0.75	HF	0.97	290	na	-	-	-
SR1	0.85	HF	0.97	290	na	-	-	-
T5	1.36	HF	0.78	290	24	6	12	9
T6	3.32	HF	0.97	290	25	12	16	17
T32	0.02	MF	0.26	290	na	-	-	-
T11	0.04	MF	0.26	290	5	12	-1	20
T12	0.10	MF	0.32	290	3	6	-4	9
T13	0.24	MF	0.31	290	na	-	-	-
T14	0.48	MF	0.32	290	12	6	-3	12
T15	0.85	MF	0.26	290	na	-	-	-
T16	1.57	MF	0.30	290	25*	6	15*	9
T30	0.02	LF	0.07	290	na	-	-	-
T21	0.03	LF	0.10	290	6	13	6	18
T22	0.11	LF	0.10	290	7	6	0	11
T23	0.24	LF	0.08	290	na	-	-	-
T24	0.40	LF	0.08	290	21*	-	11*	-
T7	0.38	HF	0.92	270	5	7	-5	9
T8	1.52	HF	0.92	270	30*	-	17*	-
T17	0.43	MF	0.25	270	na	-	-	-
T18	1.71	MF	0.36	270	30	6	7	9
T25	0.26	LF	0.08	270	na	-	-	-
T26	0.41	LF	0.12	270	24	7	14	11
T9	0.40	HF	0.98	310	4	8	-1	2
T10	1.47	HF	0.98	310	23*	-	12*	-
T19	0.40	MF	0.23	310	na	-	-	-
T20	1.60	MF	0.34	310	15	6	0	9
T27	0.24	LF	0.07	310	na	-	-	-
T28	0.38	LF	0.11	310	15	7	2	14
VT1	0.84	MF	0.21	270/290	na	-	-	-
VT2	0.84	MF	0.21	290/270	na	-	-	-

* Single test data; "na" - not available; ϕ(10^{16}n/m^2-s); ϕt(10^{23}n/m^2); T_i(°C)

Appendix B

Data Tables for the LV-Series Alloys

	Cu%	Ni%	LA Mn%	Mo%	P%
	0.40	0.00	1.37	0.55	0.005

Capsule	ϕt	ϕ-code	ϕ	T_i	$\Delta\sigma_y$	±SD	$\Delta\sigma_u$	±SD
A5	0.04	HF	0.51	290	40	8	29	8
T31	0.06	HF	0.72	290	na	-	-	-
T1	0.07	HF	0.78	290	54	13	43	11
T2	0.18	HF	0.78	290	63	17	53	14
T3	0.34	HF	0.78	290	84	9	74	6
T29	0.44	HF	0.89	290	na	-	-	-
T4	0.75	HF	0.97	290	80	15	73	12
T5	1.36	HF	0.78	290	84	8	71	8
T6	3.32	HF	0.97	290	96	10	81	9
T32	0.02	MF	0.26	290	na	-	-	-
T11	0.04	MF	0.26	290	59	8	49	8
T12	0.10	MF	0.32	290	64	13	49	13
T13	0.24	MF	0.31	290	73	13	62	11
T14	0.48	MF	0.32	290	80	10	74	9
T15	0.85	MF	0.26	290	76	19	66	17
T16	1.57	MF	0.30	290	90	14	79	16
A1	0.006	LF	0.07	290	27*	-	19*	-
A2	0.01	LF	0.07	290	38*	-	29*	-
A3	0.02	LF	0.07	290	57*	-	42*	-
T30	0.02	LF	0.07	290	na	-	-	-
A4	0.03	LF	0.07	290	na	-	-	-
T21	0.03	LF	0.10	290	55	7	45	9
T22	0.11	LF	0.10	290	70	10	63	9
T23	0.24	LF	0.08	290	75	7	68	7
T24	0.40	LF	0.08	290	64	18	58	19
T7	0.38	HF	0.92	270	88	6	76	6
T8	1.52	HF	0.92	270	96	25	81	23
T17	0.43	MF	0.25	270	107	8	93	10
T18	1.71	MF	0.36	270	120	10	99	12
T25	0.26	LF	0.08	270	87	6	77	6
T26	0.41	LF	0.12	270	102*	-	90*	-
T9	0.40	HF	0.98	310	68	8	61	9
T10	1.47	HF	0.98	310	84	9	74	8
T19	0.40	MF	0.23	310	51	12	45	12
T20	1.60	MF	0.34	310	83	6	69	6
T27	0.24	LF	0.07	310	55	8	49	9
T28	0.38	LF	0.11	310	55	8	49	8
VT1	0.84	MF	0.21	270/290	97	9	83	8
VT2	0.84	MF	0.21	290/270	84	6	74	7

* Single test data; "na" - not available; $\phi(10^{16}n/m^2\text{-}s)$; $\phi t(10^{23}n/m^2)$; $T_i(°C)$

	Cu%	Ni%	LB Mn%	Mo%	P%
	0.40	0.18	1.35	0.55	0.005

Capsule	ϕt	ϕ-code	ϕ	T_i	$\Delta\sigma_y$	±SD	$\Delta\sigma_u$	±SD
A5	0.04	HF	0.51	290	na	-	-	-
T31	0.06	HF	0.72	290	na	-	-	-
T1	0.07	HF	0.78	290	73	9	64	7
T2	0.18	HF	0.78	290	87	9	85	7
T3	0.34	HF	0.78	290	96	9	91	7
T29	0.44	HF	0.89	290	na	-	-	-
T4	0.75	HF	0.97	290	80	14	77	8
T5	1.36	HF	0.78	290	98	13	90	12
T6	3.32	HF	0.97	290	100	9	95	12
T32	0.02	MF	0.26	290	na	-	-	-
T11	0.04	MF	0.26	290	52	9	51	9
T12	0.10	MF	0.32	290	85	9	80	7
T13	0.24	MF	0.31	290	91*	-	91*	-
T14	0.48	MF	0.32	290	94	12	87	10
T15	0.85	MF	0.26	290	86	12	81	10
T16	1.57	MF	0.30	290	89	9	85	7
A1	0.006	LF	0.07	290	na	-	-	-
A2	0.01	LF	0.07	290	na	-	-	-
A3	0.02	LF	0.07	290	na	-	-	-
T30	0.02	LF	0.07	290	na	-	-	-
A4	0.03	LF	0.07	290	na	-	-	-
T21	0.03	LF	0.10	290	64	9	56	7
T22	0.11	LF	0.10	290	84	9	79	7
T23	0.24	LF	0.08	290	80	10	77	7
T24	0.40	LF	0.08	290	79	9	79	7
T7	0.38	HF	0.92	270	94	11	91	12
T8	1.52	HF	0.92	270	114	12	102	10
T17	0.43	MF	0.25	270	124	10	112	8
T18	1.71	MF	0.36	270	136	10	115	8
T25	0.26	LF	0.08	270	97	9	91	7
T26	0.41	LF	0.12	270	110	9	99	7
T9	0.40	HF	0.98	310	73	11	74	8
T10	1.47	HF	0.98	310	78	10	75	7
T19	0.40	MF	0.23	310	51	13	54	10
T20	1.60	MF	0.34	310	71	9	69	7
T27	0.24	LF	0.07	310	54	9	52	7
T28	0.38	LF	0.11	310	51	7	53	7
VT1	0.84	MF	0.21	270/290	111	11	100	9
VT2	0.84	MF	0.21	290/270	102	9	93	8

* Single test data; "na" - not available; $\phi(10^{16}n/m^2\text{-}s)$; $\phi t(10^{23}n/m^2)$; $T_i(°C)$

Cu	Ni	LC Mn	Mo%	P%
0.41	0.86	1.44	0.55	0.005

Capsule	ϕt	ϕ-code	ϕ	T_i	$\Delta\sigma_y$	±SD	$\Delta\sigma_u$	±SD
A5	0.04	HF	0.51	290	51	5	38	5
T31	0.06	HF	0.72	290	59	8	51	4
T1	0.07	HF	0.78	290	73	6	55	5
T2	0.18	HF	0.78	290	116	4	98	5
T3	0.34	HF	0.78	290	150	4	133	5
T29	0.44	HF	0.89	290	154	5	140	4
T4	0.75	HF	0.97	290	145	5	136	7
T5	1.36	HF	0.78	290	174	5	155	5
T6	3.32	HF	0.97	290	193	4	169	6
T32	0.02	MF	0.26	290	38	5	33	4
T11	0.04	MF	0.26	290	66	5	51	6
T12	0.10	MF	0.32	290	111	5	95	5
T13	0.24	MF	0.31	290	155	6	134	5
T14	0.48	MF	0.32	290	169	6	155	5
T15	0.85	MF	0.26	290	188*	-	170*	-
T16	1.57	MF	0.30	290	198	5	176	5
A1	0.006	LF	0.07	290	31	4	21	4
A2	0.01	LF	0.07	290	42	3	30	7
A3	0.02	LF	0.07	290	61	4	46	4
T30	0.02	LF	0.07	290	53	5	37	5
A4	0.03	LF	0.07	290	75	5	59	5
T21	0.03	LF	0.10	290	71	6	55	5
T22	0.11	LF	0.10	290	129	5	111	5
T23	0.24	LF	0.08	290	168	6	152	5
T24	0.40	LF	0.08	290	176	4	163	5
T7	0.38	HF	0.92	270	155	5	137	4
T8	1.52	HF	0.92	270	212	5	181	4
T17	0.43	MF	0.25	270	214	5	183	4
T18	1.71	MF	0.36	270	257	5	220	5
T25	0.26	LF	0.08	270	187	5	169	5
T26	0.41	LF	0.12	270	202	4	177	5
T9	0.40	HF	0.98	310	127	9	114	9
T10	1.47	HF	0.98	310	161	6	138	5
T19	0.40	MF	0.23	310	132	5	117	5
T20	1.60	MF	0.34	310	148	7	129	9
T27	0.24	LF	0.07	310	119	4	107	4
T28	0.38	LF	0.11	310	122	4	112	4
VT1	0.84	MF	0.21	270/290	205	6	183	5
VT2	0.84	MF	0.21	290/270	200	5	177	5

* Single test data; "na" - not available; $\phi(10^{16}n/m^2\text{-}s)$; $\phi t(10^{23}n/m^2)$; $T_i(°C)$

Cu	Ni	LD Mn	Mo%	P%
0.38	1.25	1.38	0.55	0.005

Capsule	ϕt	ϕ-code	ϕ	T_i	$\Delta\sigma_y$	±SD	$\Delta\sigma_u$	±SD
A5	0.04	HF	0.51	290	50	8	32	4
T31	0.06	HF	0.72	290	61	3	48	4
T1	0.07	HF	0.78	290	64	5	47	3
T2	0.18	HF	0.78	290	125	4	102	3
T3	0.34	HF	0.78	290	163	4	126	3
T29	0.44	HF	0.89	290	165	7	149	4
T4	0.75	HF	0.97	290	170	6	158	3
T5	1.36	HF	0.78	290	216	4	186	5
T6	3.32	HF	0.97	290	245	3	212	4
T32	0.02	MF	0.26	290	36	4	23	5
T11	0.04	MF	0.26	290	64	4	46	3
T12	0.10	MF	0.32	290	112	4	92	5
T13	0.24	MF	0.31	290	175	4	149	4
T14	0.48	MF	0.32	290	200	3	177	3
T15	0.85	MF	0.26	290	233	3	205	4
T16	1.57	MF	0.30	290	252	4	219	3
A1	0.006	LF	0.07	290	34*	-	25*	-
A2	0.01	LF	0.07	290	na	-	-	-
A3	0.02	LF	0.07	290	62*	-	32*	-
T30	0.02	LF	0.07	290	51	3	32	3
A4	0.03	LF	0.07	290	80*	-	60	-
T21	0.03	LF	0.10	290	73	5	55	4
T22	0.11	LF	0.10	290	138	4	116	5
T23	0.24	LF	0.08	290	198	4	172	7
T24	0.40	LF	0.08	290	215	5	191	5
T7	0.38	HF	0.92	270	166	5	144	5
T8	1.52	HF	0.92	270	253	5	211	5
T17	0.43	MF	0.25	270	242	3	202	3
T18	1.71	MF	0.36	270	305	3	261	4
T25	0.26	LF	0.08	270	217	3	189	4
T26	0.41	LF	0.12	270	231	3	202	3
T9	0.40	HF	0.98	310	145	3	126	3
T10	1.47	HF	0.98	310	199	5	168	6
T19	0.40	MF	0.23	310	164	3	140	3
T20	1.60	MF	0.34	310	195	6	166	4
T27	0.24	LF	0.07	310	146	3	131	3
T28	0.38	LF	0.11	310	158	3	141	3
VT1	0.84	MF	0.21	270/290	246	6	212	6
VT2	0.84	MF	0.21	290/270	240	4	207	6

* Single test data; "na" - not available; ϕ(10^{16}n/m^2-s); ϕt(10^{23}n/m^2); T_i(°C)

Cu	Ni	LG Mn	Mo%	P%
0.01	0.74	1.37	0.55	0.005

Capsule	ϕt	ϕ-code	ϕ	T_i	$\Delta\sigma_y$	±SD	$\Delta\sigma_u$	±SD
A5	0.04	HF	0.51	290	24	8	13	7
T31	0.06	HF	0.72	290	na	-	-	-
T1	0.07	HF	0.78	290	20	9	8	9
T2	0.18	HF	0.78	290	25	7	14	6
T3	0.34	HF	0.78	290	30	7	19	7
T29	0.44	HF	0.89	290	na	-	-	-
T4	0.75	HF	0.97	290	33	9	28	9
T5	1.36	HF	0.78	290	40	8	29	7
T6	3.32	HF	0.97	290	49*	-	42*	-
T32	0.02	MF	0.26	290	na	-	-	-
T11	0.04	MF	0.26	290	25	7	15	6
T12	0.10	MF	0.32	290	26	8	17	7
T13	0.24	MF	0.31	290	38	8	26	7
T14	0.48	MF	0.32	290	35	7	27	6
T15	0.85	MF	0.26	290	41	7	32	6
T16	1.57	MF	0.30	290	42	7	33	6
A1	0.006	LF	0.07	290	na	-	-	-
A2	0.01	LF	0.07	290	na	-	-	-
A3	0.02	LF	0.07	290	na	-	-	-
T30	0.02	LF	0.07	290	na	-	-	-
A4	0.03	LF	0.07	290	na	-	-	-
T21	0.03	LF	0.10	290	20	9	10	10
T22	0.11	LF	0.10	290	30	7	19	6
T23	0.24	LF	0.08	290	34	10	23	9
T24	0.40	LF	0.08	290	33	11	23	9
T7	0.38	HF	0.92	270	32	7	21	6
T8	1.52	HF	0.92	270	49	7	38	7
T17	0.43	MF	0.25	270	49	9	38	7
T18	1.71	MF	0.36	270	57	8	37	12
T25	0.26	LF	0.08	270	42	8	24	10
T26	0.41	LF	0.12	270	49	7	35	7
T9	0.40	HF	0.98	310	29	7	21	6
T10	1.47	HF	0.98	310	38	8	29	9
T19	0.40	MF	0.23	310	35	7	28	7
T20	1.60	MF	0.34	310	33	7	29	6
T27	0.24	LF	0.07	310	32	8	24	10
T28	0.38	LF	0.11	310	32	7	26	6
VT1	0.84	MF	0.21	270/290	35	7	25	7
VT2	0.84	MF	0.21	290/270	36	11	23	12

* Single test data; "na" - not available; ϕ(10^{16}n/m^2-s); ϕt(10^{23}n/m^2); T_i(°C)

Cu	Ni	LH Mn	Mo%	P%
0.11	0.74	1.39	0.55	0.005

Capsule	ϕt	ϕ-code	ϕ	T_i	$\Delta\sigma_y$	±SD	$\Delta\sigma_u$	±SD
A5	0.04	HF	0.51	290	13	4	11	3
T31	0.06	HF	0.72	290	na	-	-	-
T1	0.07	HF	0.78	290	20	4	16	3
T2	0.18	HF	0.78	290	24	4	22	2
T3	0.34	HF	0.78	290	28	4	24	4
T29	0.44	HF	0.89	290	na	-	-	-
T4	0.75	HF	0.97	290	37	4	34	2
T5	1.36	HF	0.78	290	60	4	52	2
T6	3.32	HF	0.97	290	70	4	62	2
T32	0.02	MF	0.26	290	na	-	-	-
T11	0.04	MF	0.26	290	18	8	18	8
T12	0.10	MF	0.32	290	26	5	22	3
T13	0.24	MF	0.31	290	36	4	36	2
T14	0.48	MF	0.32	290	46	4	42	2
T15	0.85	MF	0.26	290	61	4	56	2
T16	1.57	MF	0.30	290	74	5	67	3
A1	0.006	LF	0.07	290	na	-	-	-
A2	0.01	LF	0.07	290	na	-	-	-
A3	0.02	LF	0.07	290	na	-	-	-
T30	0.02	LF	0.07	290	na	-	-	-
A4	0.03	LF	0.07	290	na	-	-	-
T21	0.03	LF	0.10	290	18	5	16	4
T22	0.11	LF	0.10	290	21	5	20	2
T23	0.24	LF	0.08	290	40	5	37	3
T24	0.40	LF	0.08	290	47	5	40	3
T7	0.38	HF	0.92	270	31	4	27	2
T8	1.52	HF	0.92	270	81	5	69	3
T17	0.43	MF	0.25	270	77	4	60	7
T18	1.71	MF	0.36	270	123	5	98	2
T25	0.26	LF	0.08	270	58	4	52	3
T26	0.41	LF	0.12	270	65	5	54	3
T9	0.40	HF	0.98	310	19	8	19	8
T10	1.47	HF	0.98	310	40	4	40	2
T19	0.40	MF	0.23	310	18	5	17	6
T20	1.60	MF	0.34	310	38	13	39	3
T27	0.24	LF	0.07	310	25	6	25	4
T28	0.38	LF	0.11	310	21	5	19	3
VT1	0.84	MF	0.21	270/290	73	4	64	3
VT2	0.84	MF	0.21	290/270	73	4	64	2

* Single test data; "na" - not available; $\phi(10^{16}n/m^2\text{-}s)$; $\phi t(10^{23}n/m^2)$; $T_i(°C)$

Cu	Ni	LI Mn	Mo%	P%
0.20	0.74	1.37	0.55	0.005

Capsule	ϕt	ϕ-code	ϕ	T_i	$\Delta\sigma_y$	±SD	$\Delta\sigma_u$	±SD
A5	0.04	HF	0.51	290	25	8	14	10
T31	0.06	HF	0.72	290	na	-	-	-
T1	0.07	HF	0.78	290	42	11	20	7
T2	0.18	HF	0.78	290	68	7	51	8
T3	0.34	HF	0.78	290	82	6	66	7
T29	0.44	HF	0.89	290	na	-	-	-
T4	0.75	HF	0.97	290	105	12	91	13
T5	1.36	HF	0.78	290	115	6	96	7
T6	3.32	HF	0.97	290	139	13	119	15
T32	0.02	MF	0.26	290	na	-	-	-
T11	0.04	MF	0.26	290	38	10	25	11
T12	0.10	MF	0.32	290	66	7	51	8
T13	0.24	MF	0.31	290	104	6	85	7
T14	0.48	MF	0.32	290	107	13	93	8
T15	0.85	MF	0.26	290	132	6	114	7
T16	1.57	MF	0.30	290	137	12	117	10
A1	0.006	LF	0.07	290	na	-	-	-
A2	0.01	LF	0.07	290	na	-	-	-
A3	0.02	LF	0.07	290	na	-	-	-
T30	0.02	LF	0.07	290	na	-	-	-
A4	0.03	LF	0.07	290	na	-	-	-
T21	0.03	LF	0.10	290	39	9	29	9
T22	0.11	LF	0.10	290	79	6	62	7
T23	0.24	LF	0.08	290	106	6	89	8
T24	0.40	LF	0.08	290	125	6	113	7
T7	0.38	HF	0.92	270	95	6	80	7
T8	1.52	HF	0.92	270	146	7	124	7
T17	0.43	MF	0.25	270	146	10	124	9
T18	1.71	MF	0.36	270	200	10	163	8
T25	0.26	LF	0.08	270	127	10	105	9
T26	0.41	LF	0.12	270	133	6	106	7
T9	0.40	HF	0.98	310	70	6	60	7
T10	1.47	HF	0.98	310	116	6	97	7
T19	0.40	MF	0.23	310	76	6	66	7
T20	1.60	MF	0.34	310	96	8	85	7
T27	0.24	LF	0.07	310	66	7	57	7
T28	0.38	LF	0.11	310	75	6	65	7
VT1	0.84	MF	0.21	270/290	146	13	128	17
VT2	0.84	MF	0.21	290/270	143	7	122	7

* Single test data; "na" - not available; ϕ(10^{16}n/m^2-s); ϕt(10^{23}n/m^2); T_i(°C)

Cu	Ni	LJ Mn	Mo%	P%
0.42	0.81	1.34	0.55	0.005

Capsule	ϕt	ϕ-code	ϕ	T_i	$\Delta\sigma_y$	±SD	$\Delta\sigma_u$	±SD
A5	0.04	HF	0.51	290	48	13	31	7
T31	0.06	HF	0.72	290	na	-	-	-
T1	0.07	HF	0.78	290	68	12	47	5
T2	0.18	HF	0.78	290	111	12	91	4
T3	0.34	HF	0.78	290	122	13	103	5
T29	0.44	HF	0.89	290	na	-	-	-
T4	0.75	HF	0.97	290	141	12	117	4
T5	1.36	HF	0.78	290	154	12	130	6
T6	3.32	HF	0.97	290	158	12	134	10
T32	0.02	MF	0.26	290	na	-	-	-
T11	0.04	MF	0.26	290	56	12	39	4
T12	0.10	MF	0.32	290	101	12	83	4
T13	0.24	MF	0.31	290	139*	-	121*	-
T14	0.48	MF	0.32	290	154	13	132	6
T15	0.85	MF	0.26	290	162	13	140	8
T16	1.57	MF	0.30	290	167	12	139	5
A1	0.006	LF	0.07	290	na	-	-	-
A2	0.01	LF	0.07	290	na	-	-	-
A3	0.02	LF	0.07	290	na	-	-	-
T30	0.02	LF	0.07	290	na	-	-	-
A4	0.03	LF	0.07	290	na	-	-	-
T21	0.03	LF	0.10	290	58	12	42	6
T22	0.11	LF	0.10	290	114	13	96	8
T23	0.24	LF	0.08	290	142	12	124	4
T24	0.40	LF	0.08	290	151	13	133	5
T7	0.38	HF	0.92	270	136	12	116	4
T8	1.52	HF	0.92	270	183	12	150	5
T17	0.43	MF	0.25	270	188	12	162	5
T18	1.71	MF	0.36	270	225	12	182	4
T25	0.26	LF	0.08	270	172	12	151	4
T26	0.41	LF	0.12	270	176	12	150	5
T9	0.40	HF	0.98	310	110	12	93	5
T10	1.47	HF	0.98	310	136	12	111	4
T19	0.40	MF	0.23	310	103	12	86	5
T20	1.60	MF	0.34	310	120	12	99	4
T27	0.24	LF	0.07	310	94	12	79	8
T28	0.38	LF	0.11	310	97	13	76	7
VT1	0.84	MF	0.21	270/290	182	13	157	7
VT2	0.84	MF	0.21	290/270	169	12	157	5

* Single test data; "na" - not available; ϕ(10^{16}n/m^2-s); ϕt(10^{23}n/m^2); T_i(°C)

Cu	Ni	LK Mn	Mo%	P%
0.80	0.81	1.13	0.55	0.005

Capsule	ϕt	ϕ-code	ϕ	T_i	$\Delta\sigma_y$	±SD	$\Delta\sigma_u$	±SD
A5	0.04	HF	0.51	290	41	8	36	7
T31	0.06	HF	0.72	290	na	-	-	-
T1	0.07	HF	0.78	290	64	8	55	6
T2	0.18	HF	0.78	290	85	13	77	10
T3	0.34	HF	0.78	290	105	10	95	9
T29	0.44	HF	0.89	290	na	-	-	-
T4	0.75	HF	0.97	290	112	8	102	8
T5	1.36	HF	0.78	290	122	13	106	15
T6	3.32	HF	0.97	290	128	9	109	9
T32	0.02	MF	0.26	290	na	-	-	-
T11	0.04	MF	0.26	290	54	8	46	6
T12	0.10	MF	0.32	290	88	8	78	7
T13	0.24	MF	0.31	290	110*	-	113*	-
T14	0.48	MF	0.32	290	129	11	119	13
T15	0.85	MF	0.26	290	137	10	118	6
T16	1.57	MF	0.30	290	127	9	111	8
A1	0.006	LF	0.07	290	na	-	-	-
A2	0.01	LF	0.07	290	na	-	-	-
A3	0.02	LF	0.07	290	na	-	-	-
T30	0.02	LF	0.07	290	na	-	-	-
A4	0.03	LF	0.07	290	na	-	-	-
T21	0.03	LF	0.10	290	50	11	42	9
T22	0.11	LF	0.10	290	85	8	72	7
T23	0.24	LF	0.08	290	122	10	110	7
T24	0.40	LF	0.08	290	120	17	111	8
T7	0.38	HF	0.92	270	114	9	105	7
T8	1.52	HF	0.92	270	150	8	132	7
T17	0.43	MF	0.25	270	162	14	142	14
T18	1.71	MF	0.36	270	203	14	171	13
T25	0.26	LF	0.08	270	137	14	125	15
T26	0.41	LF	0.12	270	152	19	135	19
T9	0.40	HF	0.98	310	72	8	67	9
T10	1.47	HF	0.98	310	125	19	130	35
T19	0.40	MF	0.23	310	71	17	74	8
T20	1.60	MF	0.34	310	89	8	84	10
T27	0.24	LF	0.07	310	70	9	66	6
T28	0.38	LF	0.11	310	64	12	57	10
VT1	0.84	MF	0.21	270/290	164	9	147	9
VT2	0.84	MF	0.21	290/270	148	8	135	6

* Single test data; "na" - not available; ϕ(10^{16}n/m^2-s); ϕt(10^{23}n/m^2); T_i(°C)

	Cu	Ni	L0 Mn	Mo%	P%
	0.41	0.86	1.44	0.55	0.005

Capsule	ϕt	ϕ-code	ϕ	T_i	$\Delta\sigma_y$	±SD	$\Delta\sigma_u$	±SD
A5	0.04	HF	0.51	290	32	9	25	8
T31	0.06	HF	0.72	290	na	-	-	-
T1	0.07	HF	0.78	290	62	11	54	8
T2	0.18	HF	0.78	290	124	10	119	9
T3	0.34	HF	0.78	290	168	10	155	10
T29	0.44	HF	0.89	290	na	-	-	-
T4	0.75	HF	0.97	290	185	9	170	8
T5	1.36	HF	0.78	290	196	11	181	9
T6	3.32	HF	0.97	290	221	11	189	9
T32	0.02	MF	0.26	290	na	-	-	-
T11	0.04	MF	0.26	290	56	10	47	11
T12	0.10	MF	0.32	290	96	9	89	8
T13	0.24	MF	0.31	290	148*	-	149*	-
T14	0.48	MF	0.32	290	182	9	173	8
T15	0.85	MF	0.26	290	199	10	186	11
T16	1.57	MF	0.30	290	212	9	197	8
A1	0.006	LF	0.07	290	na	-	-	-
A2	0.01	LF	0.07	290	na	-	-	-
A3	0.02	LF	0.07	290	na	-	-	-
T30	0.02	LF	0.07	290	na	-	-	-
A4	0.03	LF	0.07	290	na	-	-	-
T21	0.03	LF	0.10	290	55	10	48	9
T22	0.11	LF	0.10	290	121	17	112	14
T23	0.24	LF	0.08	290	174	10	159	9
T24	0.40	LF	0.08	290	188	9	179	8
T7	0.38	HF	0.92	270	155	10	148	8
T8	1.52	HF	0.92	270	225	10	200	9
T17	0.43	MF	0.25	270	226	10	197	8
T18	1.71	MF	0.36	270	279	9	249	8
T25	0.26	LF	0.08	270	194	9	179	8
T26	0.41	LF	0.12	270	212	9	188	8
T9	0.40	HF	0.98	310	150	9	146	8
T10	1.47	HF	0.98	310	187*	-	169*	-
T19	0.40	MF	0.23	310	142	9	136	9
T20	1.60	MF	0.34	310	165	9	152	8
T27	0.24	LF	0.07	310	125	9	120	8
T28	0.38	LF	0.11	310	129	9	125	8
VT1	0.84	MF	0.21	270/290	221	10	201	10
VT2	0.84	MF	0.21	290/270	218	12	198	11

* Single test data; "na" - not available; ϕ(10^{16}n/m^2-s); ϕt(10^{23}n/m^2); T_i(°C)

Appendix C

Data Tables for the CWP-Series Alloys

EPRI C

Cu%	Ni%	Mn%	Mo%	P%
0.35	0.60	1.30	0.44	0.005

Capsule	ϕt	ϕ-code	ϕ	T_i	$\Delta\sigma_y$	±SD	$\Delta\sigma_u$	±SD
T31	0.06	HF	0.72	290°C	62	8	47	8
T1	0.07	HF	0.84	290°C	79	5	61	8
T2	0.19	HF	0.84	290°C	111	5	95	8
T3	0.34	HF	0.78	290°C	128	7	117	8
T29	0.44	HF	0.89	290°C	na	-	-	-
T4	0.78	HF	1.00	290°C	120	6	105	9
T5	1.36	HF	0.78	290°C	140	5	119	8
T6	3.32	HF	0.97	290°C	151	6	128	9
T32	0.02	MF	0.26	290°C	42	8	28	10
T11	0.04	MF	0.27	290°C	69	5	50	8
T12	0.10	MF	0.32	290°C	106	5	89	8
T13	0.25	MF	0.32	290°C	129	5	117	8
T14	0.48	MF	0.32	290°C	138	5	121	8
T15	0.85	MF	0.26	290°C	146*	-	127*	-
T16	1.57	MF	0.30	290°C	145	5	121	8
T30	0.02	LF	0.07	290°C	45	7	29	9
T21	0.03	LF	0.11	290°C	69	5	49	9
T22	0.10	LF	0.11	290°C	124	8	110	12
T23	0.24	LF	0.08	290°C	145	6	130	8
T24	0.40	LF	0.08	290°C	145	5	121	8
T7	0.38	HF	0.92	270°C	137	5	117	14
T8	1.52	HF	0.92	270°C	162	6	136	8
T17	0.43	MF	0.25	270°C	175	7	153	8
T18	1.71	MF	0.36	270°C	212	5	173	8
T25	0.26	LF	0.08	270°C	162	6	142	8
T26	0.41	LF	0.12	270°C	160	5	139	9
T9	0.40	HF	0.98	310°C	116	9	106	9
T10	1.47	HF	0.98	310°C	129	5	110	8
T19	0.40	MF	0.23	310°C	102	5	88	8
T20	1.60	MF	0.34	310°C	113	6	100	8
T27	0.24	LF	0.08	310°C	90	7	81	9
T28	0.38	LF	0.11	310°C	90	5	75	8
VT1	0.84	MF	0.21	270°/290°	168	7	146	9
VT2	0.84	MF	0.21	290°/270°	161	5	137	9

* Single test data; "na" - not available; $\phi(10^{16}n/m^2\text{-}s)$; $\phi t(10^{23}n/m^2)$; $T_i(°C)$

Cu%	Ni%	MW Mn%	Mo%	P%
0.27	0.57	1.61	0.41	0.017

Capsule	ϕt	ϕ-code	ϕ	T_i	$\Delta\sigma_y$	±SD	$\Delta\sigma_u$	±SD
T31	0.06	HF	0.72	290°C	na	-	-	-
T1	0.07	HF	0.84	290°C	49	12	29	10
T2	0.19	HF	0.84	290°C	74	9	55	9
T3	0.34	HF	0.78	290°C	103	14	84	10
T29	0.44	HF	0.89	290°C	na	-	-	-
T4	0.78	HF	1.00	290°C	na	-	-	-
T5	1.36	HF	0.78	290°C	138	11	115	9
T6	3.32	HF	0.97	290°C	na	-	-	-
T32	0.02	MF	0.26	290°C	na	-	-	-
T11	0.04	MF	0.27	290°C	43	9	27	9
T12	0.10	MF	0.32	290°C	59	8	39	8
T13	0.25	MF	0.32	290°C	na	-	-	-
T14	0.48	MF	0.32	290°C	119	9	99	10
T15	0.85	MF	0.26	290°C	na	-	-	-
T16	1.57	MF	0.30	290°C	160	11	136	10
T30	0.02	LF	0.07	290°C	na	-	-	-
T21	0.03	LF	0.11	290°C	36	9	32	9
T22	0.10	LF	0.11	290°C	71	9	54	9
T23	0.24	LF	0.08	290°C	na	-	-	-
T24	0.40	LF	0.08	290°C	127	9	109	11
T7	0.38	HF	0.92	270°C	na	-	-	-
T8	1.52	HF	0.92	270°C	na	-	-	-
T17	0.43	MF	0.25	270°C	na	-	-	-
T18	1.71	MF	0.36	270°C	na	-	-	-
T25	0.26	LF	0.08	270°C	na	-	-	-
T26	0.41	LF	0.12	270°C	na	-	-	-
T9	0.40	HF	0.98	310°C	na	-	-	-
T10	1.47	HF	0.98	310°C	na	-	-	-
T19	0.40	MF	0.23	310°C	na	-	-	-
T20	1.60	MF	0.34	310°C	na	-	-	-
T27	0.24	LF	0.08	310°C	na	-	-	-
T28	0.38	LF	0.11	310°C	na	-	-	-
VT1	0.84	MF	0.21	270°/290°	na	-	-	-
VT2	0.84	MF	0.21	290°/270°	na	-	-	-

* Single test data; "na" - not available; f(10^{16}n/m^2-s); ft(10^{23}n/m^2); T_i(°C)

A weld

Cu%	Ni%	Mn%	Mo%	P%
0.24	0.63	1.69	0.40	0.014

Capsule	ϕt	ϕ-code	ϕ	T_i	$\Delta\sigma_y$	±SD	$\Delta\sigma_u$	±SD
T31	0.06	HF	0.72	290°C	na	-	-	-
T1	0.07	HF	0.84	290°C	35	19	23	10
T2	0.19	HF	0.84	290°C	69	19	76	22
T3	0.34	HF	0.78	290°C	91	17	78	11
T29	0.44	HF	0.89	290°C	na	-	-	-
T4	0.78	HF	1.00	290°C	na	-	-	-
T5	1.36	HF	0.78	290°C	113	16	94	10
T6	3.32	HF	0.97	290°C	129	16	118	11
T32	0.02	MF	0.26	290°C	na	-	-	-
T11	0.04	MF	0.27	290°C	31	20	18	14
T12	0.10	MF	0.32	290°C	51	23	40	11
T13	0.25	MF	0.32	290°C	na	-	-	-
T14	0.48	MF	0.32	290°C	106	15	92	10
T15	0.85	MF	0.26	290°C	na	-	-	-
T16	1.57	MF	0.30	290°C	126	25	110	20
T30	0.02	LF	0.07	290°C	na	-	-	-
T21	0.03	LF	0.11	290°C	33	15	19	10
T22	0.10	LF	0.11	290°C	75	16	61	10
T23	0.24	LF	0.08	290°C	na	-	-	-
T24	0.40	LF	0.08	290°C	100	16	90	10
T7	0.38	HF	0.92	270°C	89	15	76	10
T8	1.52	HF	0.92	270°C	148	16	123	11
T17	0.43	MF	0.25	270°C	na	-	-	-
T18	1.71	MF	0.36	270°C	165	15	141	10
T25	0.26	LF	0.08	270°C	na	-	-	-
T26	0.41	LF	0.12	270°C	119	16	104	10
T9	0.40	HF	0.98	310°C	86	28	82	22
T10	1.47	HF	0.98	310°C	109	15	95	10
T19	0.40	MF	0.23	310°C	na	-	-	-
T20	1.60	MF	0.34	310°C	81	15	73	10
T27	0.24	LF	0.08	310°C	na	-	-	-
T28	0.38	LF	0.11	310°C	70	17	63	16
VT1	0.84	MF	0.21	270°/290°	131	29	116	22
VT2	0.84	MF	0.21	290°/270°	141	22	121	15

* Single test data; "na" - not available; ϕ(10^{16}n/m^2-s); ϕt(10^{23}n/m^2); T_i(°C)

B weld

Cu%	Ni%	Mn%	Mo%	P%
0.35	0.69	1.63	0.40	0.018

Capsule	ϕt	ϕ-code	ϕ	T_i	$\Delta\sigma_y$	±SD	$\Delta\sigma_u$	±SD
T31	0.06	HF	0.72	290°C	na	-	-	-
T1	0.07	HF	0.84	290°C	na	-	-	-
T2	0.19	HF	0.84	290°C	na	-	-	-
T3	0.34	HF	0.78	290°C	116	13	100	6
T29	0.44	HF	0.89	290°C	na	-	-	-
T4	0.78	HF	1.00	290°C	na	-	-	-
T5	1.36	HF	0.78	290°C	132	12	107	7
T6	3.32	HF	0.97	290°C	169	18	140	13
T32	0.02	MF	0.26	290°C	na	-	-	-
T11	0.04	MF	0.27	290°C	na	-	-	-
T12	0.10	MF	0.32	290°C	na	-	-	-
T13	0.25	MF	0.32	290°C	na	-	-	-
T14	0.48	MF	0.32	290°C	115	12	100	8
T15	0.85	MF	0.26	290°C	na	-	-	-
T16	1.57	MF	0.30	290°C	135	12	117	9
T30	0.02	LF	0.07	290°C	na	-	-	-
T21	0.03	LF	0.11	290°C	na	-	-	-
T22	0.10	LF	0.11	290°C	na	-	-	-
T23	0.24	LF	0.08	290°C	na	-	-	-
T24	0.40	LF	0.08	290°C	132	12	111	7
T7	0.38	HF	0.92	270°C	118	14	96	12
T8	1.52	HF	0.92	270°C	148	12	125	6
T17	0.43	MF	0.25	270°C	na	-	-	-
T18	1.71	MF	0.36	270°C	192	13	154	7
T25	0.26	LF	0.08	270°C	na	-	-	-
T26	0.41	LF	0.12	270°C	141	13	114	18
T9	0.40	HF	0.98	310°C	101	14	86	6
T10	1.47	HF	0.98	310°C	115	13	97	8
T19	0.40	MF	0.23	310°C	na	-	-	-
T20	1.60	MF	0.34	310°C	120	11	96	6
T27	0.24	LF	0.08	310°C	na	-	-	-
T28	0.38	LF	0.11	310°C	92	12	75	8
VT1	0.84	MF	0.21	270°/290°	160	18	132	12
VT2	0.84	MF	0.21	290°/270°	151	11	128	7

* Single test data; "na" - not available; ϕ(10^{16}n/m^2-s); ϕt(10^{23}n/m^2); T_i(°C)

C weld

Cu%	Ni%	Mn%	Mo%	P%
0.06	0.62	1.30	0.31	0.009

Capsule	ϕt	ϕ-code	ϕ	T_i	$\Delta\sigma_y$	±SD	$\Delta\sigma_u$	±SD
T31	0.06	HF	0.72	290°C	na	-	-	-
T1	0.07	HF	0.84	290°C	38	13	25	15
T2	0.19	HF	0.84	290°C	na	-	-	-
T3	0.34	HF	0.78	290°C	na	-	-	-
T29	0.44	HF	0.89	290°C	na	-	-	-
T4	0.78	HF	1.00	290°C	na	-	-	-
T5	1.36	HF	0.78	290°C	33	7	29	6
T6	3.32	HF	0.97	290°C	81	15	67	14
T32	0.02	MF	0.26	290°C	na	-	-	-
T11	0.04	MF	0.27	290°C	na	-	-	-
T12	0.10	MF	0.32	290°C	24	9	14	9
T13	0.25	MF	0.32	290°C	na	-	-	-
T14	0.48	MF	0.32	290°C	39	9	31	6
T15	0.85	MF	0.26	290°C	na	-	-	-
T16	1.57	MF	0.30	290°C	43	16	40	11
T30	0.02	LF	0.07	290°C	na	-	-	-
T21	0.03	LF	0.11	290°C	26	13	20	7
T22	0.10	LF	0.11	290°C	45	6	34	6
T23	0.24	LF	0.08	290°C	na	-	-	-
T24	0.40	LF	0.08	290°C	44	25	39	17
T7	0.38	HF	0.92	270°C	50	7	38	7
T8	1.52	HF	0.92	270°C	50	17	42	16
T17	0.43	MF	0.25	270°C	na	-	-	-
T18	1.71	MF	0.36	270°C	53	10	39	7
T25	0.26	LF	0.08	270°C	na	-	-	-
T26	0.41	LF	0.12	270°C	47	17	37	13
T9	0.40	HF	0.98	310°C	42	10	37	7
T10	1.47	HF	0.98	310°C	43	23	42	12
T19	0.40	MF	0.23	310°C	na	-	-	-
T20	1.60	MF	0.34	310°C	58	7	48	6
T27	0.24	LF	0.08	310°C	na	-	-	-
T28	0.38	LF	0.11	310°C	22	14	23	10
VT1	0.84	MF	0.21	270°/290°	47	9	38	8
VT2	0.84	MF	0.21	290°/270°	48	9	34	8

* Single test data; "na" - not available; ϕ(10^{16}n/m^2-s); ϕt(10^{23}n/m^2); T_i(°C)

Cu%	Ni%	62W Mn%	Mo%	P%
0.21	0.54	1.51	0.38	0.016

Capsule	ϕt	ϕ-code	ϕ	T_i	$\Delta\sigma_y$	±SD	$\Delta\sigma_u$	±SD
T31	0.06	HF	0.72	290°C	46	8	28	8
T1	0.07	HF	0.84	290°C	45	8	29	8
T2	0.19	HF	0.84	290°C	70	8	51	8
T3	0.34	HF	0.78	290°C	107	8	82	9
T29	0.44	HF	0.89	290°C	na	-	-	-
T4	0.78	HF	1.00	290°C	94	9	73	8
T5	1.36	HF	0.78	290°C	107	8	77	8
T6	3.32	HF	0.97	290°C	149	11	120	13
T32	0.02	MF	0.26	290°C	31	8	14	8
T11	0.04	MF	0.27	290°C	37	10	25	8
T12	0.10	MF	0.32	290°C	67	14	42	14
T13	0.25	MF	0.32	290°C	77	12	61	11
T14	0.48	MF	0.32	290°C	98	8	78	9
T15	0.85	MF	0.26	290°C	115*	-	90*	-
T16	1.57	MF	0.30	290°C	129	9	98	8
T30	0.02	LF	0.07	290°C	14	17	7	13
T21	0.03	LF	0.11	290°C	32	8	20	8
T22	0.10	LF	0.11	290°C	80	17	62	11
T23	0.24	LF	0.08	290°C	99	9	76	8
T24	0.40	LF	0.08	290°C	111	9	85	9
T7	0.38	HF	0.92	270°C	83	16	64	18
T8	1.52	HF	0.92	270°C	131	16	97	15
T17	0.43	MF	0.25	270°C	114	10	89	10
T18	1.71	MF	0.36	270°C	167	9	130	8
T25	0.26	LF	0.08	270°C	112	8	85	9
T26	0.41	LF	0.12	270°C	115	11	87	10
T9	0.40	HF	0.98	310°C	87	8	75	9
T10	1.47	HF	0.98	310°C	112	8	90	11
T19	0.40	MF	0.23	310°C	73	11	52	9
T20	1.60	MF	0.34	310°C	93	9	66	8
T27	0.24	LF	0.08	310°C	62	16	51	8
T28	0.38	LF	0.11	310°C	77	8	59	11
VT1	0.84	MF	0.21	270°/290°	134	10	115	10
VT2	0.84	MF	0.21	290°/270°	141	9	113	8

* Single test data; "na" - not available; ϕ(10^{16}n/m^2-s); ϕt(10^{23}n/m^2); T_i(°C)

Cu%	Ni%	63W Mn%	Mo%	P%
0.30	0.69	1.65	0.43	0.016

Capsule	ϕt	ϕ-code	ϕ	T_i	$\Delta\sigma_y$	±SD	$\Delta\sigma_u$	±SD
T31	0.06	HF	0.72	290°C	60	11	44	8
T1	0.07	HF	0.84	290°C	64	7	49	5
T2	0.19	HF	0.84	290°C	109	17	88	9
T3	0.34	HF	0.78	290°C	130	13	115	10
T29	0.44	HF	0.89	290°C	na	-	-	-
T4	0.78	HF	1.00	290°C	135	7	118	6
T5	1.36	HF	0.78	290°C	162	10	137	6
T6	3.32	HF	0.97	290°C	201	11	173	6
T32	0.02	MF	0.26	290°C	39	7	23	5
T11	0.04	MF	0.27	290°C	53	10	36	7
T12	0.10	MF	0.32	290°C	83	13	68	6
T13	0.25	MF	0.32	290°C	119	10	112	5
T14	0.48	MF	0.32	290°C	145	8	124	5
T15	0.85	MF	0.26	290°C	171*	-	143*	-
T16	1.57	MF	0.30	290°C	183*	-	154*	-
T30	0.02	LF	0.07	290°C	33	7	22	5
T21	0.03	LF	0.11	290°C	56	10	40	7
T22	0.10	LF	0.11	290°C	111	10	93	7
T23	0.24	LF	0.08	290°C	139	7	116	5
T24	0.40	LF	0.08	290°C	155	7	137	5
T7	0.38	HF	0.92	270°C	118	12	104	8
T8	1.52	HF	0.92	270°C	194	9	165	6
T17	0.43	MF	0.25	270°C	166	7	144	5
T18	1.71	MF	0.36	270°C	228	10	186	7
T25	0.26	LF	0.08	270°C	157	7	132	5
T26	0.41	LF	0.12	270°C	165	10	141	6
T9	0.40	HF	0.98	310°C	127	10	114	5
T10	1.47	HF	0.98	310°C	145	8	129	8
T19	0.40	MF	0.23	310°C	123	9	104	6
T20	1.60	MF	0.34	310°C	134	10	114	7
T27	0.24	LF	0.08	310°C	96	7	84	5
T28	0.38	LF	0.11	310°C	112	7	96	5
VT1	0.84	MF	0.21	270°/290°	188	9	159	9
VT2	0.84	MF	0.21	290°/270°	184	8	158	5

* Single test data; "na" - not available; ϕ(10^{16}n/m^2-s); ϕt(10^{23}n/m^2); T_i(°C)

Cu%	Ni%	65W Mn%	Mo%	P%
0.22	0.60	1.45	0.39	0.015

Capsule	ϕt	ϕ-code	ϕ	T_i	$\Delta\sigma_y$	±SD	$\Delta\sigma_u$	±SD
T31	0.06	HF	0.72	290°C	39	12	25	10
T1	0.07	HF	0.84	290°C	45	8	29	8
T2	0.19	HF	0.84	290°C	64	7	52	6
T3	0.34	HF	0.78	290°C	82	8	72	6
T29	0.44	HF	0.89	290°C	na	-	-	-
T4	0.78	HF	1.00	290°C	100	11	86	8
T5	1.36	HF	0.78	290°C	117	7	100	6
T6	3.32	HF	0.97	290°C	139	15	121	12
T32	0.02	MF	0.26	290°C	25	11	18	7
T11	0.04	MF	0.27	290°C	35	10	23	9
T12	0.10	MF	0.32	290°C	64	10	48	9
T13	0.25	MF	0.32	290°C	81	8	71	6
T14	0.48	MF	0.32	290°C	95	10	84	7
T15	0.85	MF	0.26	290°C	124*	-	107*	-
T16	1.57	MF	0.30	290°C	129	8	109	8
T30	0.02	LF	0.07	290°C	36	8	26	6
T21	0.03	LF	0.11	290°C	27	13	21	9
T22	0.10	LF	0.11	290°C	73	7	61	6
T23	0.24	LF	0.08	290°C	90	10	75	8
T24	0.40	LF	0.08	290°C	99	9	86	7
T7	0.38	HF	0.92	270°C	84	7	77	12
T8	1.52	HF	0.92	270°C	141	13	117	8
T17	0.43	MF	0.25	270°C	114	9	95	8
T18	1.71	MF	0.36	270°C	163	11	131	12
T25	0.26	LF	0.08	270°C	109	7	91	7
T26	0.41	LF	0.12	270°C	104	13	88	9
T9	0.40	HF	0.98	310°C	83	7	77	7
T10	1.47	HF	0.98	310°C	118	12	102	10
T19	0.40	MF	0.23	310°C	82	9	70	9
T20	1.60	MF	0.34	310°C	89	11	77	9
T27	0.24	LF	0.08	310°C	66	8	54	8
T28	0.38	LF	0.11	310°C	77	7	64	7
VT1	0.84	MF	0.21	270°/290°	138	8	121	6
VT2	0.84	MF	0.21	290°/270°	144	16	122	14

* Single test data; "na" - not available; $\phi(10^{16}n/m^2\text{-}s)$; $\phi t(10^{23}n/m^2)$; $T_i(°C)$

67W

Cu%	Ni%	Mn%	Mo%	P%
0.27	0.59	1.44	0.39	0.011

Capsule	ϕt	ϕ-code	ϕ	T_i	$\Delta\sigma_y$	±SD	$\Delta\sigma_u$	±SD
T31	0.06	HF	0.72	290°C	26	16	18	15
T1	0.07	HF	0.84	290°C	40	22	33	20
T2	0.19	HF	0.84	290°C	67	19	54	21
T3	0.34	HF	0.78	290°C	70	16	61	15
T29	0.44	HF	0.89	290°C	na	-	-	-
T4	0.78	HF	1.00	290°C	67	17	57	15
T5	1.36	HF	0.78	290°C	89	18	73	17
T6	3.32	HF	0.97	290°C	120	20	106	19
T32	0.02	MF	0.26	290°C	20	19	15	22
T11	0.04	MF	0.27	290°C	45	18	33	16
T12	0.10	MF	0.32	290°C	44	16	33	15
T13	0.25	MF	0.32	290°C	62	18	62	17
T14	0.48	MF	0.32	290°C	79	26	69	21
T15	0.85	MF	0.26	290°C	100*	-	85*	-
T16	1.57	MF	0.30	290°C	99	22	86	23
T30	0.02	LF	0.07	290°C	27	17	19	16
T21	0.03	LF	0.11	290°C	24	22	18	17
T22	0.10	LF	0.11	290°C	53	20	45	15
T23	0.24	LF	0.08	290°C	66	16	55	16
T24	0.40	LF	0.08	290°C	79	20	71	20
T7	0.38	HF	0.92	270°C	65	16	51	15
T8	1.52	HF	0.92	270°C	106	16	87	16
T17	0.43	MF	0.25	270°C	79	17	70	15
T18	1.71	MF	0.36	270°C	146	16	123	15
T25	0.26	LF	0.08	270°C	92	16	78	15
T26	0.41	LF	0.12	270°C	97	16	81	15
T9	0.40	HF	0.98	310°C	63	19	57	16
T10	1.47	HF	0.98	310°C	84	17	71	15
T19	0.40	MF	0.23	310°C	55	16	47	17
T20	1.60	MF	0.34	310°C	81	17	72	19
T27	0.24	LF	0.08	310°C	56	16	49	15
T28	0.38	LF	0.11	310°C	47	19	43	20
VT1	0.84	MF	0.21	270°/290°	120	17	104	16
VT2	0.84	MF	0.21	290°/270°	122	17	102	16

* Single test data; "na" - not available; ϕ(10^{16}n/m^2-s); ϕt(10^{23}n/m^2); T_i(°C)

Cu%	Ni%	73W Mn%	Mo%	P%
0.31	0.60	1.56	0.58	0.017

Capsule	ϕt	ϕ-code	ϕ	T_i	$\Delta\sigma_y$	±SD	$\Delta\sigma_u$	±SD
T31	0.06	HF	0.72	290°C	51	15	35	16
T1	0.07	HF	0.84	290°C	67	16	49	15
T2	0.19	HF	0.84	290°C	98	18	84	13
T3	0.34	HF	0.78	290°C	129	13	113	12
T29	0.44	HF	0.89	290°C	na	-	-	-
T4	0.78	HF	1.00	290°C	132	14	103	11
T5	1.36	HF	0.78	290°C	154	14	131	14
T6	3.32	HF	0.97	290°C	165	13	143	12
T32	0.02	MF	0.26	290°C	28	13	15	12
T11	0.04	MF	0.27	290°C	64	13	48	12
T12	0.10	MF	0.32	290°C	91	13	76	12
T13	0.25	MF	0.32	290°C	127	13	98	9
T14	0.48	MF	0.32	290°C	147	15	127	13
T15	0.85	MF	0.26	290°C	167*	-	148*	-
T16	1.57	MF	0.30	290°C	164	15	143	15
T30	0.02	LF	0.07	290°C	38	13	26	13
T21	0.03	LF	0.11	290°C	60	13	45	12
T22	0.10	LF	0.11	290°C	112	14	96	13
T23	0.24	LF	0.08	290°C	150	16	129	14
T24	0.40	LF	0.08	290°C	131	13	112	12
T7	0.38	HF	0.92	270°C	118	14	100	15
T8	1.52	HF	0.92	270°C	173	14	147	13
T17	0.43	MF	0.25	270°C	169	15	142	13
T18	1.71	MF	0.36	270°C	212	15	179	15
T25	0.26	LF	0.08	270°C	139	13	119	13
T26	0.41	LF	0.12	310°C	152	13	135	12
T9	0.40	HF	0.98	310°C	116	16	110	13
T10	1.47	HF	0.98	310°C	144	13	123	12
T19	0.40	MF	0.23	310°C	120	13	106	13
T20	1.60	MF	0.34	310°C	130	16	113	14
T27	0.24	LF	0.08	310°C	84	14	74	13
T28	0.38	LF	0.11	310°C	90	15	80	14
VT1	0.84	MF	0.21	270°/290°	172	15	147	14
VT2	0.84	MF	0.21	290°/270°	155	13.0	128	13

* Single test data; "na" - not available; ϕ(10^{16}n/m^2-s); ϕt(10^{23}n/m^2); T_i(°C)

RWV

Cu%	Ni%	Mn%	Mo%	P%
0.24	1.71	1.21	0.35	0.008

Capsule	ϕt	ϕ-code	ϕ	T_i	$\Delta\sigma_y$	±SD	$\Delta\sigma_u$	±SD
T31	0.06	HF	0.72	290°C	45	7	34	8
T1	0.07	HF	0.84	290°C	61	8	40	9
T2	0.19	HF	0.84	290°C	89	8	69	9
T3	0.34	HF	0.78	290°C	128	6	108	8
T29	0.44	HF	0.89	290°C	137	13	118	16
T4	0.78	HF	1.00	290°C	na	-	-	-
T5	1.36	HF	0.78	290°C	197	6	175	8
T6	3.32	HF	0.97	290°C	na	-	-	-
T32	0.02	MF	0.26	290°C	41	7	30	9
T11	0.04	MF	0.27	290°C	47	8	34	8
T12	0.10	MF	0.32	290°C	74	6	53	8
T13	0.25	MF	0.32	290°C	na	-	-	-
T14	0.48	MF	0.32	290°C	161	14	142	15
T15	0.85	MF	0.26	290°C	na	-	-	-
T16	1.57	MF	0.30	290°C	245	24	216	16
T30	0.02	LF	0.07	290°C	37*		36*	-
T21	0.03	LF	0.11	290°C	54	6	41	8
T22	0.10	LF	0.11	290°C	105	6	86	8
T23	0.24	LF	0.08	290°C	na	-	-	-
T24	0.40	LF	0.08	290°C	192	6	172	8
T7	0.38	HF	0.92	270°C	na	-	-	-
T8	1.52	HF	0.92	270°C	246	9	214	11
T17	0.43	MF	0.25	270°C	na	-	-	-
T18	1.71	MF	0.36	270°C	na	-	-	-
T25	0.26	LF	0.08	270°C	na	-	-	-
T26	0.41	LF	0.12	270°C	na	-	-	-
T9	0.40	HF	0.98	310°C	na	-	-	-
T10	1.47	HF	0.98	310°C	203	9	179	8
T19	0.40	MF	0.23	310°C	na	-	-	-
T20	1.60	MF	0.34	310°C	na	-	-	-
T27	0.24	LF	0.08	310°C	na	-	-	-
T28	0.38	LF	0.11	310°C	na	-	-	-
VT1	0.84	MF	0.21	270°/290°	na	-	-	-
VT2	0.84	MF	0.21	290°/270°	na	-	-	-

* Single test data; "na" - not available; ϕ(10^{16}n/m^2-s); ϕt(10^{23}n/m^2); T_i(°C)

RWP

Cu%	Ni%	Mn%	Mo%	P%
0.04	1.68	1.43	0.39	0.011

Capsule	ϕt	ϕ-code	ϕ	T_i	$\Delta\sigma_y$	±SD	$\Delta\sigma_u$	±SD
T31	0.06	HF	0.72	290°C	na	-	-	-
T1	0.07	HF	0.84	290°C	25	3	19	3
T2	0.19	HF	0.84	290°C	29	5	25	4
T3	0.34	HF	0.78	290°C	36	3	33	3
T29	0.44	HF	0.89	290°C	na	-	-	-
T4	0.78	HF	1.00	290°C	na	-	-	-
T5	1.36	HF	0.78	290°C	60	3	52	3
T6	3.32	HF	0.97	290°C	na	-	-	-
T32	0.02	MF	0.26	290°C	na	-	-	-
T11	0.04	MF	0.27	290°C	22	3	15	3
T12	0.10	MF	0.32	290°C	17	4	12	3
T13	0.25	MF	0.32	290°C	na	-	-	-
T14	0.48	MF	0.32	290°C	42	4	37	3
T15	0.85	MF	0.26	290°C	na	-	-	-
T16	1.57	MF	0.30	290°C	75	3	64	5
T30	0.02	LF	0.07	290°C	na	-	-	-
T21	0.03	LF	0.11	290°C	18	5	13	7
T22	0.10	LF	0.11	290°C	31	5	23	5
T23	0.24	LF	0.08	290°C	na	-	-	-
T24	0.40	LF	0.08	290°C	49	3	45	4
T7	0.38	HF	0.92	270°C	na	-	-	-
T8	1.52	HF	0.92	270°C	70	4	60	3
T17	0.43	MF	0.25	270°C	na	-	-	-
T18	1.71	MF	0.36	270°C	na	-	-	-
T25	0.26	LF	0.08	270°C	na	-	-	-
T26	0.41	LF	0.12	270°C	na	-	-	-
T9	0.40	HF	0.98	310°C	na	-	-	-
T10	1.47	HF	0.98	310°C	54	3	49	3
T19	0.40	MF	0.23	310°C	na	-	-	-
T20	1.60	MF	0.34	310°C	na	-	-	-
T27	0.24	LF	0.08	310°C	na	-	-	-
T28	0.38	LF	0.11	310°C	na	-	-	-
VT1	0.84	MF	0.21	270°/290°	na	-	-	-
VT2	0.84	MF	0.21	290°/270°	na	-	-	-

* Single test data; "na" - not available; ϕ(10^{16}n/m^2-s); ϕt(10^{23}n/m^2); T_i(°C)

Cu%	Ni%	RWV Mn%	Mo%	P%
0.60	1.72	1.36	0.41	0.010

Capsule	ϕt	ϕ-code	ϕ	T_i	$\Delta\sigma_y$	±SD	$\Delta\sigma_u$	±SD
T31	0.06	HF	0.72	290°C	114	5	104	4
T1	0.07	HF	0.84	290°C	na	-	-	-
T2	0.19	HF	0.84	290°C	na	-	-	-
T3	0.34	HF	0.78	290°C	na	-	-	-
T29	0.44	HF	0.89	290°C	263	4	243	3
T4	0.78	HF	1.00	290°C	na	-	-	-
T5	1.36	HF	0.78	290°C	334	8	296	8
T6	3.32	HF	0.97	290°C	na	-	-	-
T32	0.02	MF	0.26	290°C	67	3	62	6
T11	0.04	MF	0.27	290°C	na	-	-	-
T12	0.10	MF	0.32	290°C	na	-	-	-
T13	0.25	MF	0.32	290°C	na	-	-	-
T14	0.48	MF	0.32	290°C	299	8	270	10
T15	0.85	MF	0.26	290°C	na	-	-	-
T16	1.57	MF	0.30	290°C	364	8	324	8
T30	0.02	LF	0.07	290°C	86	7	74	8
T21	0.03	LF	0.11	290°C	na	-	-	-
T22	0.10	LF	0.11	290°C	na	-	-	-
T23	0.24	LF	0.08	290°C	na	-	-	-
T24	0.40	LF	0.08	290°C	319	9	289	9
T7	0.38	HF	0.92	270°C	na	-	-	-
T8	1.52	HF	0.92	270°C	366	8	320	8
T17	0.43	MF	0.25	270°C	na	-	-	-
T18	1.71	MF	0.36	270°C	na	-	-	-
T25	0.26	LF	0.08	270°C	na	-	-	-
T26	0.41	LF	0.12	270°C	na	-	-	-
T9	0.40	HF	0.98	310°C	na	-	-	-
T10	1.47	HF	0.98	310°C	314	11	282	9
T19	0.40	MF	0.23	310°C	na	-	-	-
T20	1.60	MF	0.34	310°C	na	-	-	-
T27	0.24	LF	0.08	310°C	na	-	-	-
T28	0.38	LF	0.11	310°C	na	-	-	-
VT1	0.84	MF	0.21	270°/290°	na	-	-	-
VT2	0.84	MF	0.21	290°/270°	na	-	-	-

* Single test data; "na" - not available; ϕ(10^{16}n/m^2-s); ϕt(10^{23}n/m^2); T_i(°C)

HSST 02

Cu%	Ni%	Mn%	Mo%	P%
0.14	0.67	1.55	0.53	0.009

Capsule	ϕt	ϕ-code	ϕ	T_i	$\Delta\sigma_y$	±SD	$\Delta\sigma_u$	±SD
T31	0.06	HF	0.72	290°C	46	18	23	24
T1	0.07	HF	0.84	290°C	46	4	30	4
T2	0.19	HF	0.84	290°C	71	5	61	4
T3	0.34	HF	0.78	290°C	101	9	84	9
T29	0.44	HF	0.89	290°C	na	-	-	-
T4	0.78	HF	1.00	290°C	97	11	81	5
T5	1.36	HF	0.78	290°C	117	15	91	6
T6	3.32	HF	0.97	290°C	144	6	110	26
T32	0.02	MF	0.26	290°C	48	7	32	6
T11	0.04	MF	0.27	290°C	49	5	33	5
T12	0.10	MF	0.32	290°C	54	19	39	15
T13	0.25	MF	0.32	290°C	90	4	75	4
T14	0.48	MF	0.32	290°C	113	11	95	9
T15	0.85	MF	0.26	290°C	112*	-	84*	-
T16	1.57	MF	0.30	290°C	136	5	113	6
T30	0.02	LF	0.07	290°C	39	5	23	4
T21	0.03	LF	0.11	290°C	50	5	34	5
T22	0.10	LF	0.11	290°C	78	5	61	4
T23	0.24	LF	0.08	290°C	93	5	75	5
T24	0.40	LF	0.08	290°C	112	5	96	6
T7	0.38	HF	0.92	270°C	81	8	65	4
T8	1.52	HF	0.92	270°C	140	5	115	4
T17	0.43	MF	0.25	270°C	136	4	114	4
T18	1.71	MF	0.36	270°C	190	5	156	5
T25	0.26	LF	0.08	270°C	107	4	86	4
T26	0.41	LF	0.12	270°C	129	5	107	7
T9	0.40	HF	0.98	310°C	88	7	76	9
T10	1.47	HF	0.98	310°C	123	12	107	8
T19	0.40	MF	0.23	310°C	84	5	70	5
T20	1.60	MF	0.34	310°C	96	6	76	10
T27	0.24	LF	0.08	310°C	76	5	64	5
T28	0.38	LF	0.11	310°C	77	4	63	4
VT1	0.84	MF	0.21	270°/290°	137	8	115	15
VT2	0.84	MF	0.21	290°/270°	137	4	110	4

* Single test data; "na" - not available; ϕ(10^{16}n/m^2-s); ϕt(10^{23}n/m^2); T_i(°C)

JRQ

Cu%	Ni%	Mn%	Mo%	P%
0.14	0.82	1.40	0.50	0.019

Capsule	ϕt	ϕ-code	ϕ	T_i	$\Delta\sigma_y$	±SD	$\Delta\sigma_u$	±SD
T31	0.06	HF	0.72	290°C	28	12	23	11
T1	0.07	HF	0.84	290°C	20	9	19	10
T2	0.19	HF	0.84	290°C	39	8	37	11
T3	0.34	HF	0.78	290°C	52	9	50	10
T29	0.44	HF	0.89	290°C	na	-	-	-
T4	0.78	HF	1.00	290°C	59	8	55	10
T5	1.36	HF	0.78	290°C	na	-	-	-
T6	3.32	HF	0.97	290°C	129	9	115	10
T32	0.02	MF	0.26	290°C	15	8	12	10
T11	0.04	MF	0.27	290°C	13	10	11	12
T12	0.10	MF	0.32	290°C	30	10	22	12
T13	0.25	MF	0.32	290°C	53	9	46	14
T14	0.48	MF	0.32	290°C	na	-	-	-
T15	0.85	MF	0.26	290°C	92*	-	82*	-
T16	1.57	MF	0.30	290°C	na	-	-	-
T30	0.02	LF	0.07	290°C	13	8	16	11
T21	0.03	LF	0.11	290°C	16	10	13	14
T22	0.10	LF	0.11	290°C	38	10	36	10
T23	0.24	LF	0.08	290°C	60	11	57	11
T24	0.40	LF	0.08	290°C	52	23	46	23
T7	0.38	HF	0.92	270°C	61	15	55	16
T8	1.52	HF	0.92	270°C	121	8	106	10
T17	0.43	MF	0.25	270°C	89	9	77	10
T18	1.71	MF	0.36	270°C	na	-	-	-
T25	0.26	LF	0.08	270°C	75	9	64	13
T26	0.41	LF	0.12	270°C	89	10	73	11
T9	0.40	HF	0.98	310°C	38	8	38	12
T10	1.47	HF	0.98	310°C	79	9	69	11
T19	0.40	MF	0.23	310°C	43	8	41	10
T20	1.60	MF	0.34	310°C	72	9	62	12
T27	0.24	LF	0.08	310°C	32	8	25	12
T28	0.38	LF	0.11	310°C	40	8	42	10
VT1	0.84	MF	0.21	270°/290°	108	9	98	10
VT2	0.84	MF	0.21	290°/270°	117	10	106	13

* Single test data; "na" - not available; ϕ(10^{16}n/m^2-s); ϕt(10^{23}n/m^2); T_i(°C)

A302

Cu%	Ni%	Mn%	Mo%	P%
0.14	0.02	1.20	0.60	0.015

Capsule	ϕt	ϕ-code	ϕ	T_i	$\Delta\sigma_y$	±SD	$\Delta\sigma_u$	±SD
T31	0.06	HF	0.72	290°C	7	19	2	19
T1	0.07	HF	0.84	290°C	12	23	9	23
T2	0.19	HF	0.84	290°C	13	25	6	22
T3	0.34	HF	0.78	290°C	31	19	25	20
T29	0.44	HF	0.89	290°C	na	-	-	-
T4	0.78	HF	1.00	290°C	23	18	24	19
T5	1.36	HF	0.78	290°C	36	18	29	19
T6	3.32	HF	0.97	290°C	53	20	45	20
T32	0.02	MF	0.26	290°C	26*	-	19*	-
T11	0.04	MF	0.27	290°C	27	50	11	40
T12	0.10	MF	0.32	290°C	10	19	0	20
T13	0.25	MF	0.32	290°C	71	24	56	22
T14	0.48	MF	0.32	290°C	42	6	33	8
T15	0.85	MF	0.26	290°C	41*	-	30*	-
T16	1.57	MF	0.30	290°C	66	27	58	22
T30	0.02	LF	0.07	290°C	45	67	34	53
T21	0.03	LF	0.11	290°C	3	2	-3	3
T22	0.10	LF	0.11	290°C	58	49	43	38
T23	0.24	LF	0.08	290°C	na	-	-	-
T24	0.40	LF	0.08	290°C	52	23	46	23
T7	0.38	HF	0.92	270°C	15	28	1	28
T8	1.52	HF	0.92	270°C	67	18	57	19
T17	0.43	MF	0.25	270°C	na	-	-	-
T18	1.71	MF	0.36	270°C	73*	-	56*	-
T25	0.26	LF	0.08	270°C	na	-	-	-
T26	0.41	LF	0.12	270°C	55	32	48	25
T9	0.40	HF	0.98	310°C	21	30	17	28
T10	1.47	HF	0.98	310°C	39	30	32	28
T19	0.40	MF	0.23	310°C	23	25	16	20
T20	1.60	MF	0.34	310°C	47	25	41	23
T27	0.24	LF	0.08	310°C	89	29	68	25
T28	0.38	LF	0.11	310°C	47	38	35	31
VT1	0.84	MF	0.21	270°/290°	62	19	57	21
VT2	0.84	MF	0.21	290°/270°	47	19	27	28

* Single test data; "na" - not available; $\phi(10^{16}n/m^2\text{-}s)$; $\phi t(10^{23}n/m^2)$; $T_i(°C)$

Appendix C

Comparison of the Predictions of CM-3(2) to the IVAR and RADAMO Databases

Table of IVAR Chemistry Values

Alloy	Product Form	Composition [wt-%]				
		Cu	Ni	Mn	P	Si
62W	Weld	0.23	0.6	1.61	0.02	0.59
63W	Weld	0.3	0.69	1.65	0.016	0.63
65W	Weld	0.22	0.6	1.45	0.015	0.48
67W	Weld	0.27	0.69	1.44	0.011	0.5
73W	Weld	0.31	0.6	1.56	0.005	0.45
A302	Plate	0.14	0.2	1.2	0.015	0.28
A508	Forging	0.06	0.8	1.3	0.005	0.01
BW-A	Weld	0.21	0.63	1.69	0.014	0.45
BW-B	Weld	0.28	0.69	1.63	0.018	0.54
BW-C	Weld	0.06	0.62	1.3	0.009	0.37
CM1	SMMS	0.01	0.01	1.67	0.003	0.15
CM10	SMMS	0.02	0.88	1.66	0.008	0.17
CM11	SMMS	0.34	0.85	1.64	0.006	0.18
CM12	SMMS	0.86	0.84	1.65	0.006	0.17
CM13	SMMS	0.11	0.83	1.61	0.004	0.16
CM14	SMMS	0.11	0.83	1.62	0.04	0.17
CM15	SMMS	0.22	0.02	1.59	0.002	0.15
CM16	SMMS	0.22	0.82	1.58	0.004	0.25
CM17	SMMS	0.22	1.59	1.54	0.004	0.25
CM18	SMMS	0.43	0.02	1.7	0.002	0.15
CM19	SMMS	0.42	0.85	1.63	0.005	0.16
CM2	SMMS	0.01	0.01	1.65	0.041	0.16
CM20	SMMS	0.43	1.69	1.63	0.006	0.16
CM21	SMMS	0.42	0.84	0.01	0.002	0.14
CM22	SMMS	0.42	0.84	0.84	0.002	0.14
CM23	SMMS	0.01	0.83	1.62	0.002	0.15
CM24	SMMS	0.02	0.87	1.65	0.006	0.15
CM25	SMMS	0.01	0.87	1.53	0.003	0.17
CM26	SMMS	0.01	0.87	1.66	0.006	0.17
CM27	SMMS	0.01	0.84	1.6	0.002	0.16
CM28	SMMS	0.42	0.84	1.6	0.002	0.17
CM29	SMMS	0.21	0.02	1.68	0.002	0.14
CM3	SMMS	0.02	0.85	1.6	0.006	0.16
CM30	SMMS	0.22	0.85	1.64	0.006	0.16
CM31	SMMS	0.01	0.86	1.65	0.006	0.17
CM4	SMMS	0.02	0.86	1.53	0.031	0.16
CM5	SMMS	0.02	0.86	1.61	0.05	0.16
CM6	SMMS	0.02	1.68	1.5	0.007	0.17
CM7	SMMS	0	1.7	1.55	0.047	0.17

Alloy	Product Form	Composition [wt-%]				
		Cu	Ni	Mn	P	Si
CM8	SMMS	0.01	0.86	0.01	0.004	0.14
CM9	SMMS	0.01	0.86	0.85	0.003	0.15
EPRI-C	Weld	0.4	0.6	1.36	0.006	0.51
HSST02	Plate	0.14	0.67	1.55	0.009	0.2
JRQ	Plate	0.14	0.82	1.4	0.019	0.25
LA	SMMS	0.4	0	1.37	0.005	0.22
LB	SMMS	0.4	0.18	1.35	0.005	0.22
LC	SMMS	0.41	0.86	1.44	0.005	0.23
LD	SMMS	0.38	1.25	1.38	0.005	0.23
LG	SMMS	0	0.74	1.37	0.005	0.22
LH	SMMS	0.11	0.74	1.39	0.005	0.24
LI	SMMS	0.2	0.74	1.37	0.005	0.24
LJ	SMMS	0.42	0.81	1.34	0.005	0.13
LK	SMMS	0.8	0.81	1.13	0.005	0.13
LO	SMMS	0.41	0.86	1.44	0.005	0.23
Midland	Weld	0.27	0.57	1.61	0.017	0.62
Palisades	Weld	0.2	1.2	1.3	0.01	0.18
RR-WG	Weld	0.24	1.71	1.21	0.008	0.6
RR-WP	Weld	0.04	1.65	1.43	0.011	0.5
RR-WV	Weld	0.56	1.66	1.36	0.01	0.38

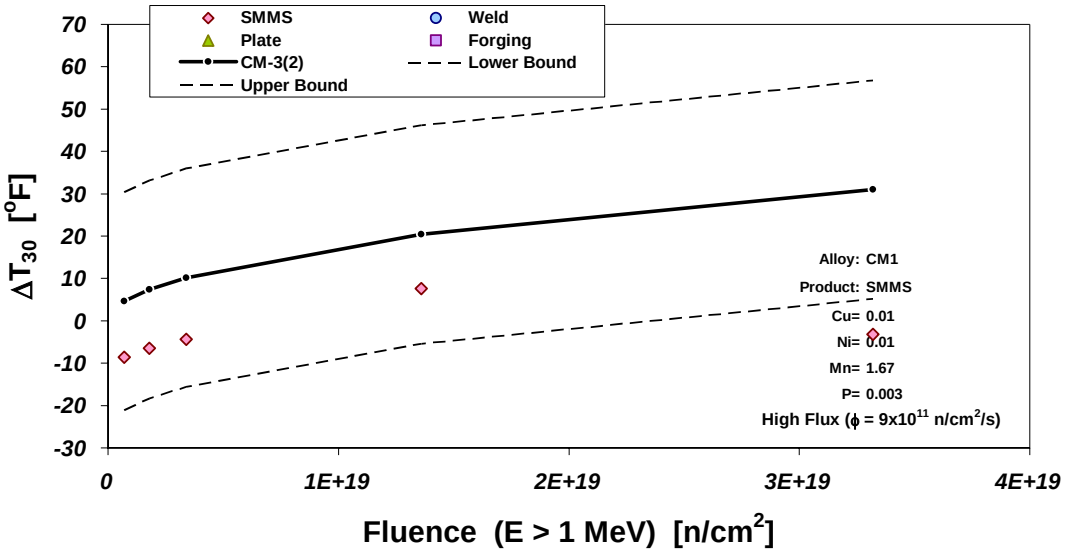
SMMS
Weld
Plate
Forging
CM-3(2)
Lower Bound
Upper Bound
Alloy: CM1
Product: SMMS
Cu= 0.01
Ni= 0.01
Mn= 1.67
P= 0.003
High Flux (ϕ = 9x10^11 n/cm^2/s)
ΔT30 [°F]
70
60
50
40
30
20
10
0
-10
-20
-30
0
1E+19
2E+19
3E+19
4E+19
Fluence (E > 1 MeV) [n/cm^2]

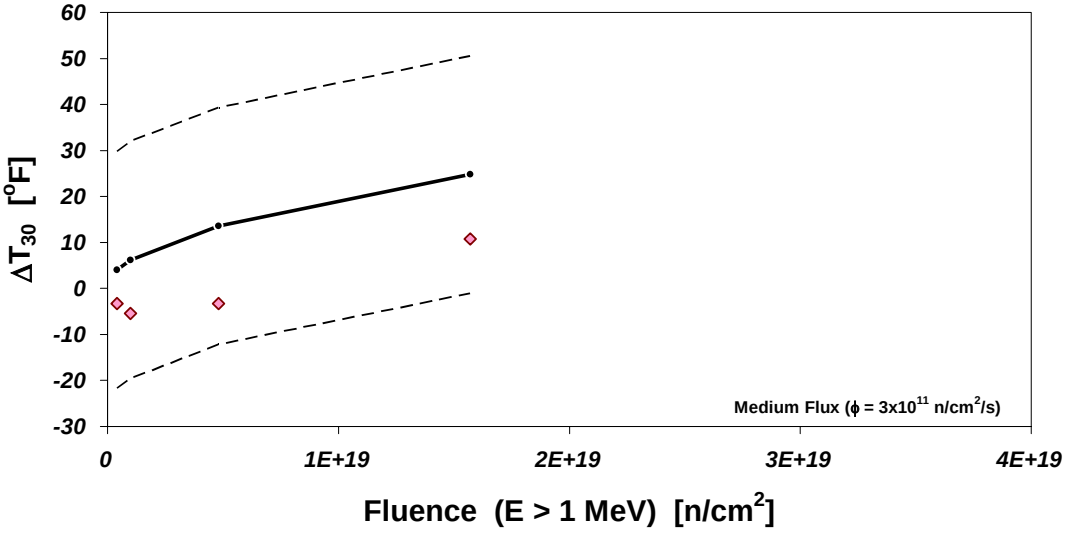
Medium Flux (ϕ = 3x10^11 n/cm^2/s)
ΔT30 [°F]
60
50
40
30
20
10
0
-10
-20
-30
0
1E+19
2E+19
3E+19
4E+19
Fluence (E > 1 MeV) [n/cm^2]

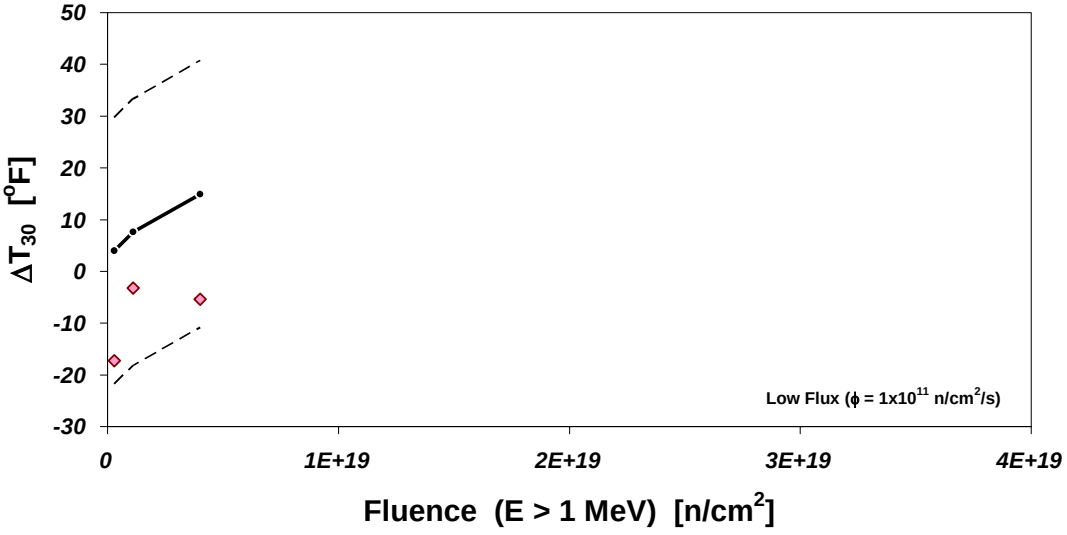
Low Flux (ϕ = 1x10^11 n/cm^2/s)
ΔT30 [°F]
50
40
30
20
10
0
-10
-20
-30
0
1E+19
2E+19
3E+19
4E+19
Fluence (E > 1 MeV) [n/cm^2]

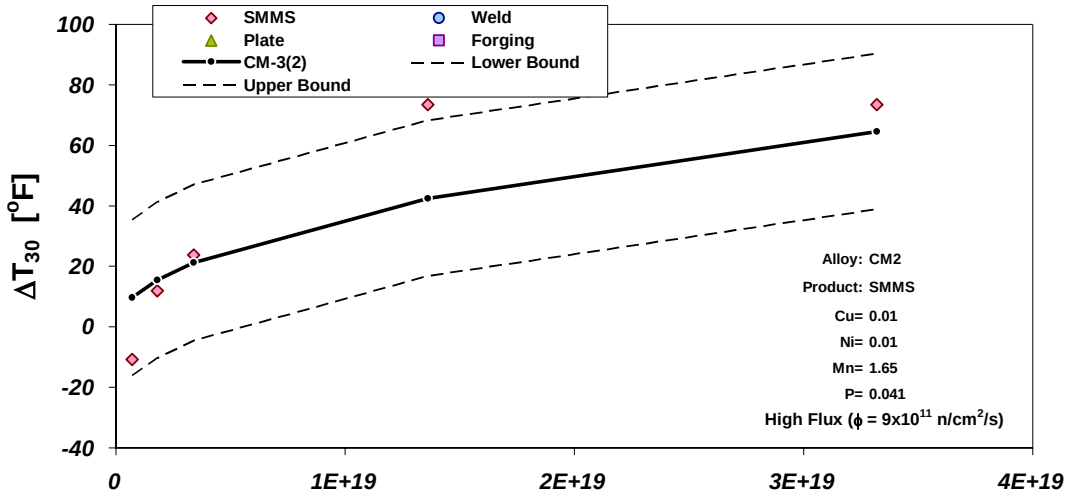
SMMS
Weld
Plate
Forging
CM-3(2)
Lower Bound
Upper Bound
Alloy: CM2
Product: SMMS
Cu= 0.01
Ni= 0.01
Mn= 1.65
P= 0.041
High Flux (ϕ = 9x10^11 n/cm^2/s)
ΔT30 [°F]
100
80
60
40
20
0
-20
-40
0
1E+19
2E+19
3E+19
4E+19
Fluence (E > 1 MeV) [n/cm^2]

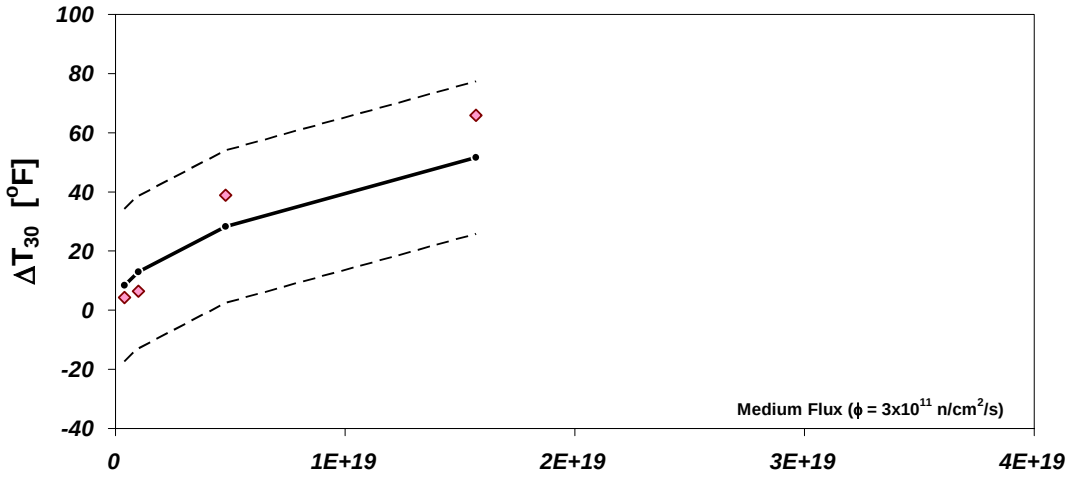
Medium Flux (ϕ = 3x10^11 n/cm^2/s)
ΔT30 [°F]
100
80
60
40
20
0
-20
-40
0
1E+19
2E+19
3E+19
4E+19
Fluence (E > 1 MeV) [n/cm^2]

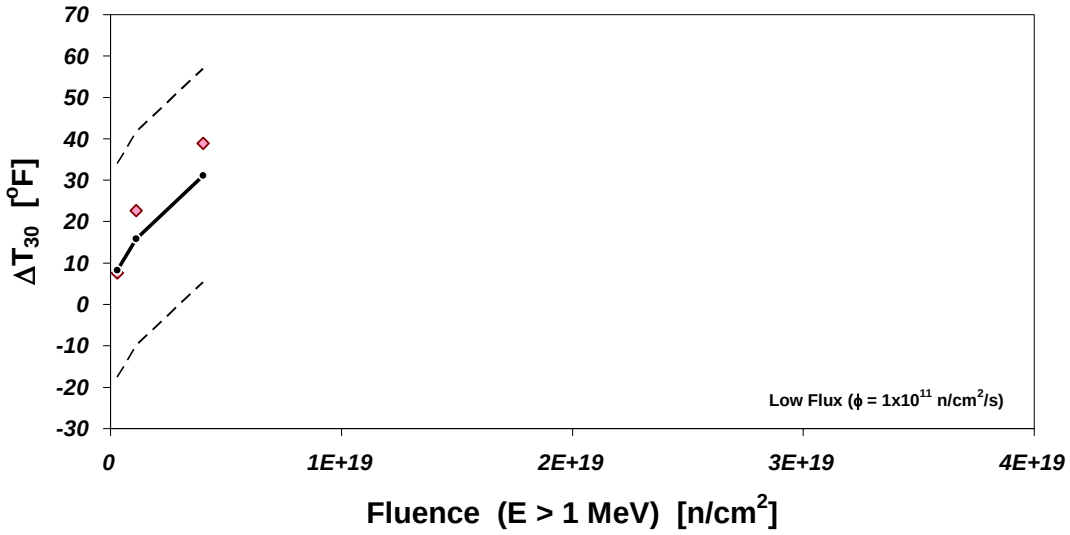
Low Flux (ϕ = 1x10^11 n/cm^2/s)
ΔT30 [°F]
70
60
50
40
30
20
10
0
-10
-20
-30
0
1E+19
2E+19
3E+19
4E+19
Fluence (E > 1 MeV) [n/cm^2]

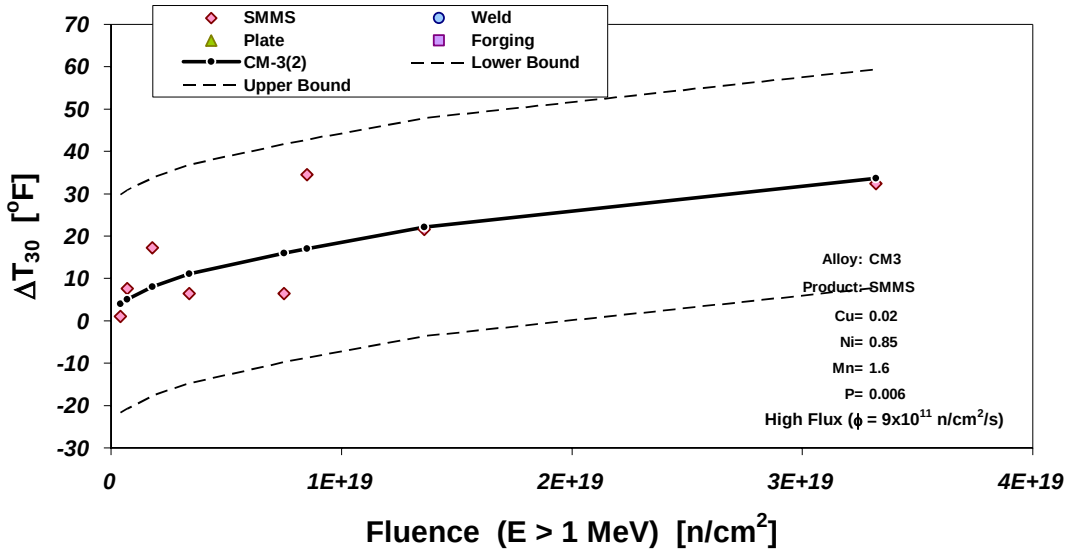
SMMS
Weld
Plate
Forging
CM-3(2)
Lower Bound
Upper Bound
Alloy: CM3
Product: SMMS
Cu= 0.02
Ni= 0.85
Mn= 1.6
P= 0.006
High Flux (ϕ = 9x10^11 n/cm^2/s)
ΔT30 [°F]
70
60
50
40
30
20
10
0
-10
-20
-30
0
1E+19
2E+19
3E+19
4E+19
Fluence (E > 1 MeV) [n/cm^2]

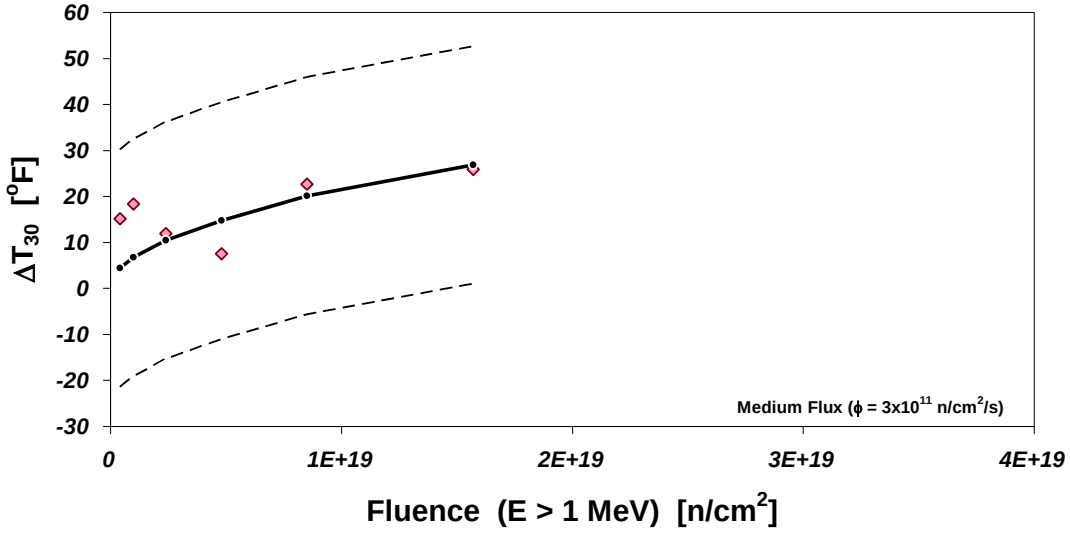
Medium Flux (ϕ = 3x10^11 n/cm^2/s)
ΔT30 [°F]
60
50
40
30
20
10
0
-10
-20
-30
0
1E+19
2E+19
3E+19
4E+19
Fluence (E > 1 MeV) [n/cm^2]

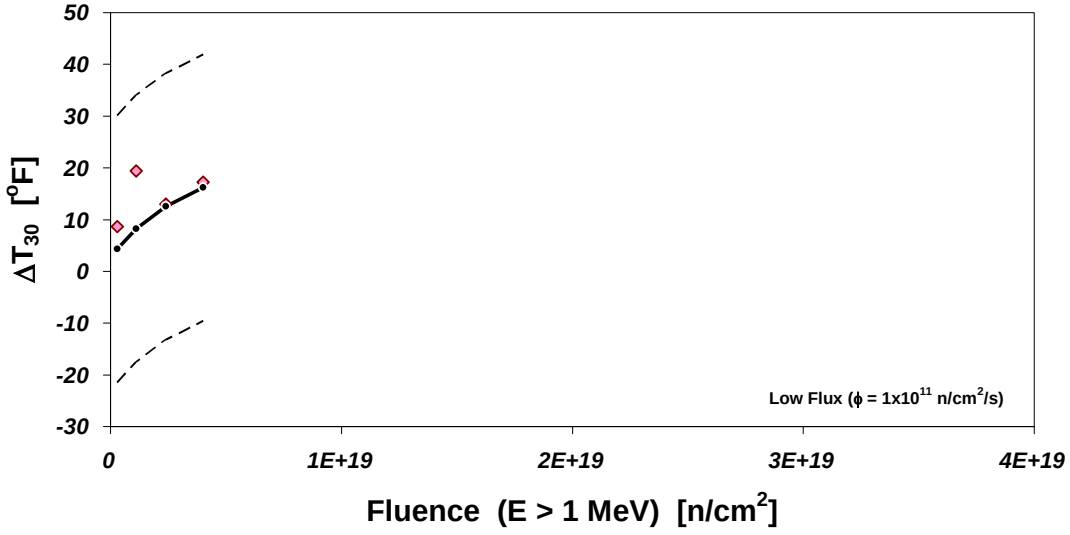
Low Flux (ϕ = 1x10^11 n/cm^2/s)
ΔT30 [°F]
50
40
30
20
10
0
-10
-20
-30
0
1E+19
2E+19
3E+19
4E+19
Fluence (E > 1 MeV) [n/cm^2]

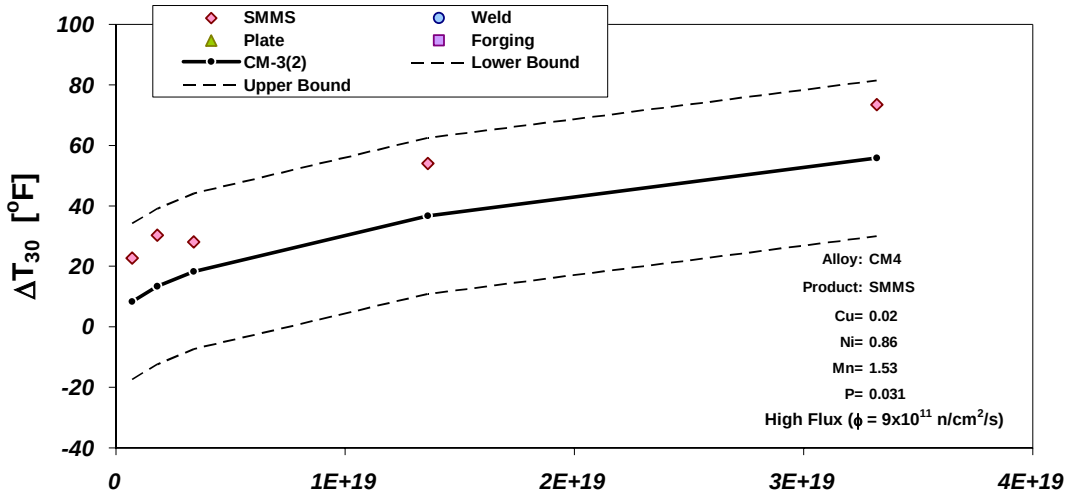
SMMS
Weld
Plate
Forging
CM-3(2)
Lower Bound
Upper Bound
100
80
60
40
20
0
-20
-40
ΔT30 [°F]
Alloy: CM4
Product: SMMS
Cu= 0.02
Ni= 0.86
Mn= 1.53
P= 0.031
High Flux (ϕ = 9x10^11 n/cm^2/s)
0
1E+19
2E+19
3E+19
4E+19
Fluence (E > 1 MeV) [n/cm^2]

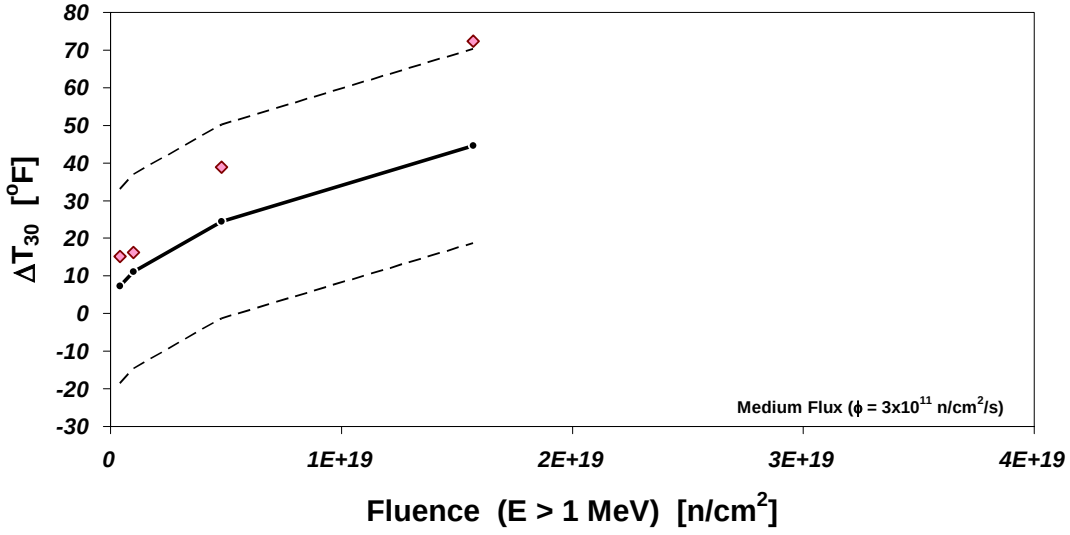
80
70
60
50
40
30
20
10
0
-10
-20
-30
ΔT30 [°F]
Medium Flux (ϕ = 3x10^11 n/cm^2/s)
0
1E+19
2E+19
3E+19
4E+19
Fluence (E > 1 MeV) [n/cm^2]

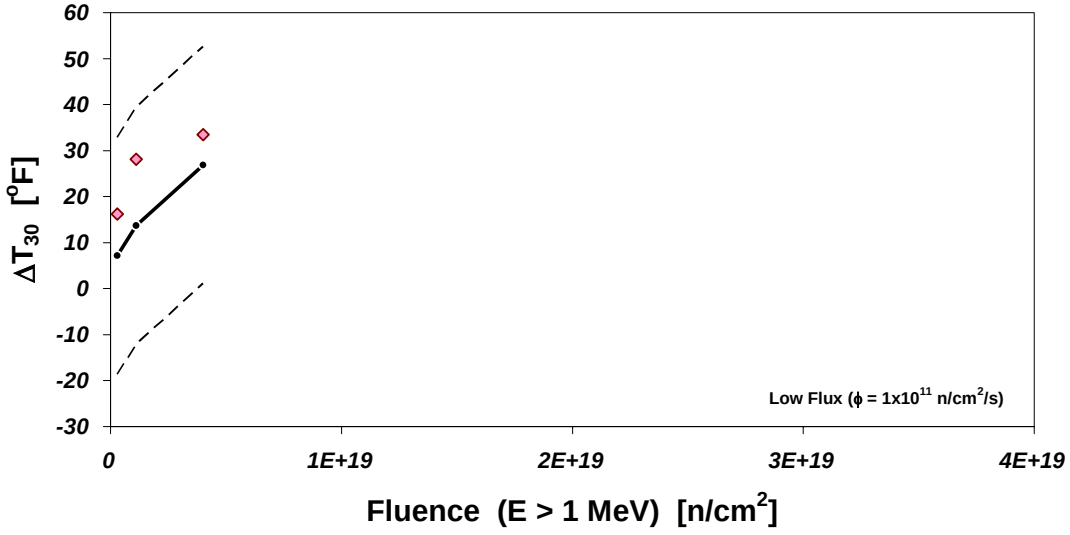
60
50
40
30
20
10
0
-10
-20
-30
ΔT30 [°F]
Low Flux (ϕ = 1x10^11 n/cm^2/s)
0
1E+19
2E+19
3E+19
4E+19
Fluence (E > 1 MeV) [n/cm^2]

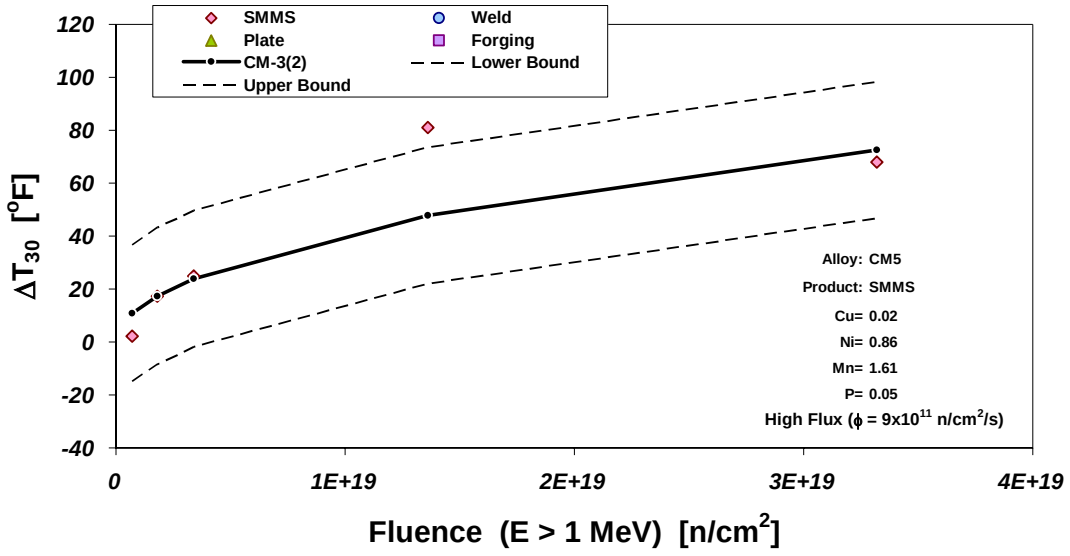
SMMS
Weld
Plate
Forging
CM-3(2)
Lower Bound
Upper Bound
ΔT30 [°F]
Alloy: CM5
Product: SMMS
Cu= 0.02
Ni= 0.86
Mn= 1.61
P= 0.05
High Flux (ϕ = 9x10^11 n/cm^2/s)
Fluence (E > 1 MeV) [n/cm^2]

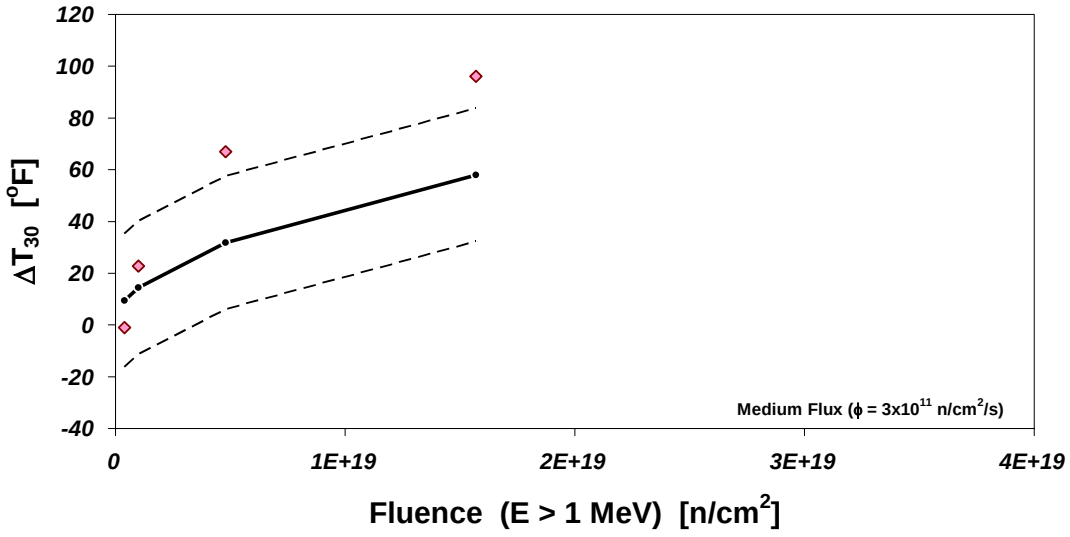
ΔT30 [°F]
Medium Flux (ϕ = 3x10^11 n/cm^2/s)
Fluence (E > 1 MeV) [n/cm^2]

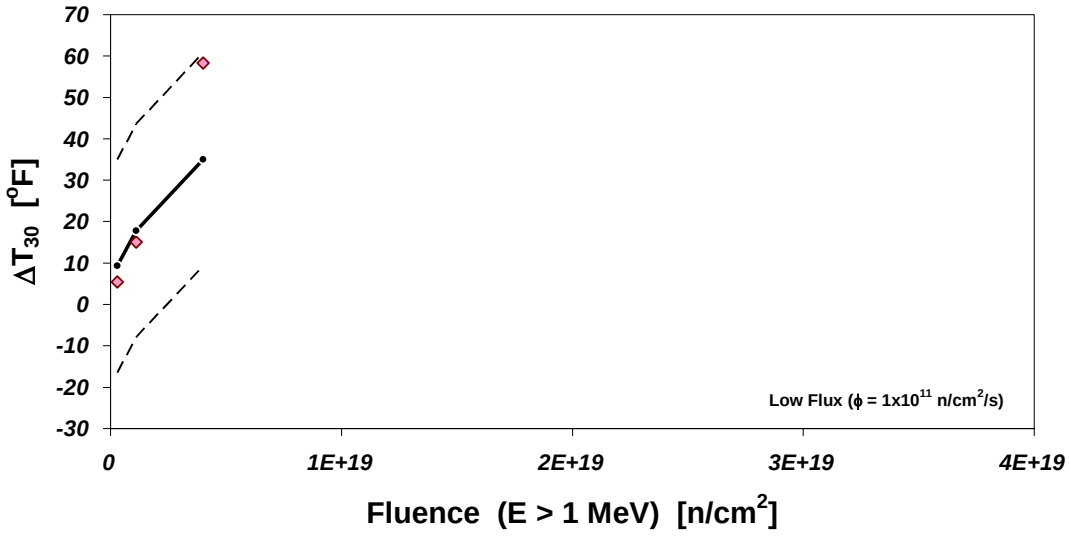
ΔT30 [°F]
Low Flux (ϕ = 1x10^11 n/cm^2/s)
Fluence (E > 1 MeV) [n/cm^2]

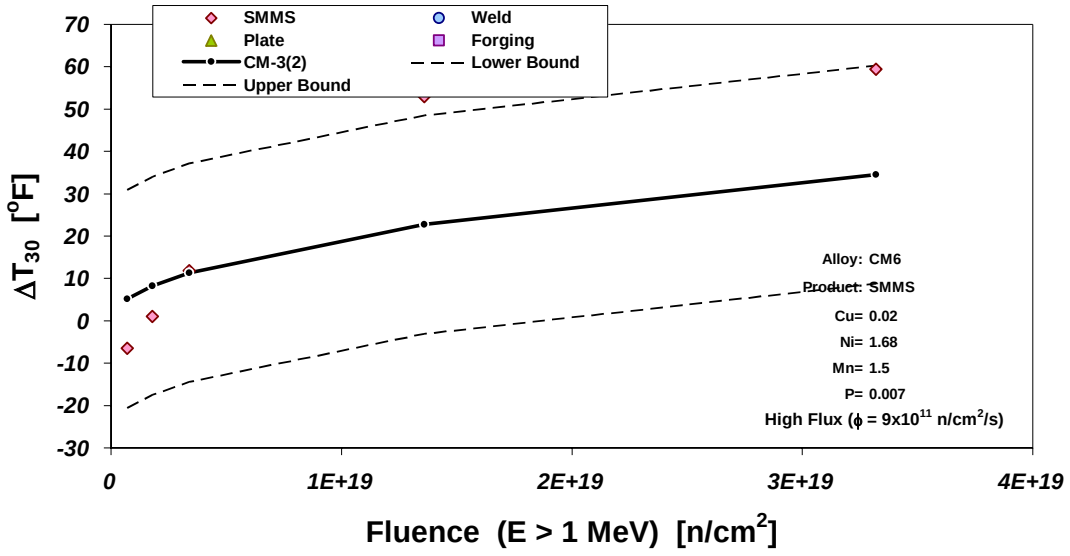
SMMS
Weld
Plate
Forging
CM-3(2)
Lower Bound
Upper Bound
Alloy: CM6
Product: SMMS
Cu= 0.02
Ni= 1.68
Mn= 1.5
P= 0.007
High Flux (ϕ = 9x10^11 n/cm^2/s)
ΔT30 [°F]
70
60
50
40
30
20
10
0
-10
-20
-30
0
1E+19
2E+19
3E+19
4E+19
Fluence (E > 1 MeV) [n/cm^2]

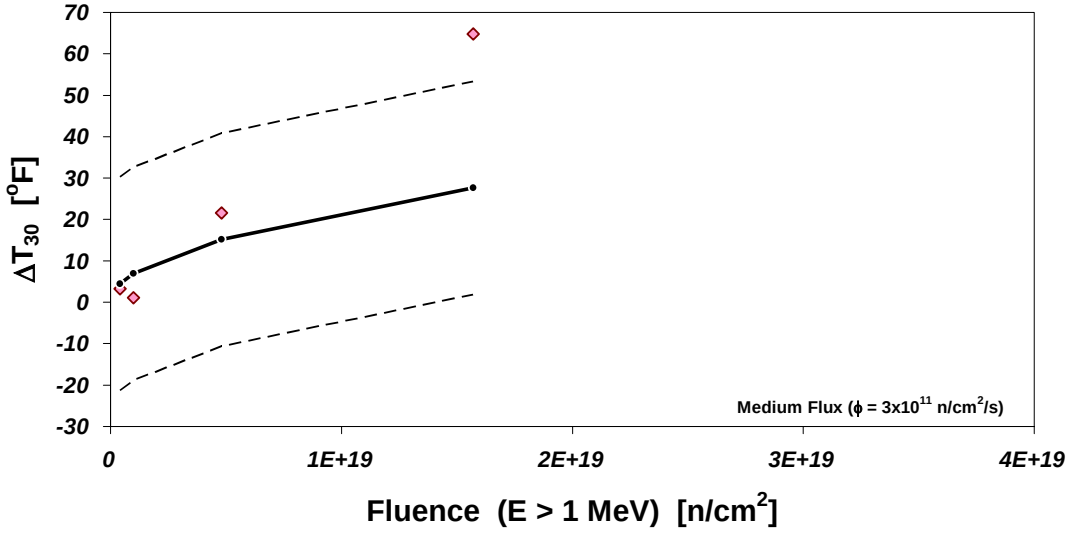
Medium Flux (ϕ = 3x10^11 n/cm^2/s)
ΔT30 [°F]
70
60
50
40
30
20
10
0
-10
-20
-30
0
1E+19
2E+19
3E+19
4E+19
Fluence (E > 1 MeV) [n/cm^2]

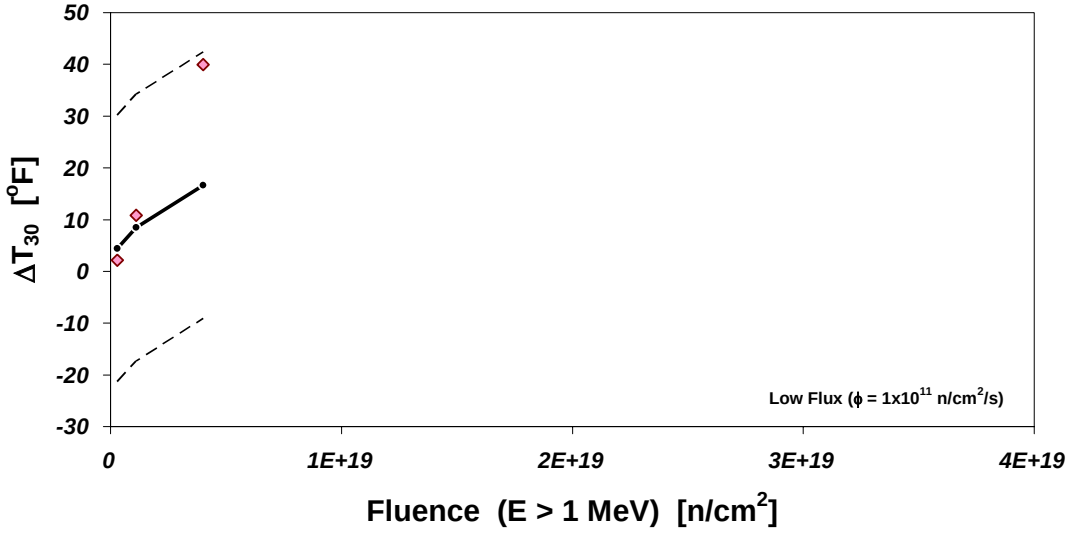
Low Flux (ϕ = 1x10^11 n/cm^2/s)
ΔT30 [°F]
50
40
30
20
10
0
-10
-20
-30
0
1E+19
2E+19
3E+19
4E+19
Fluence (E > 1 MeV) [n/cm^2]

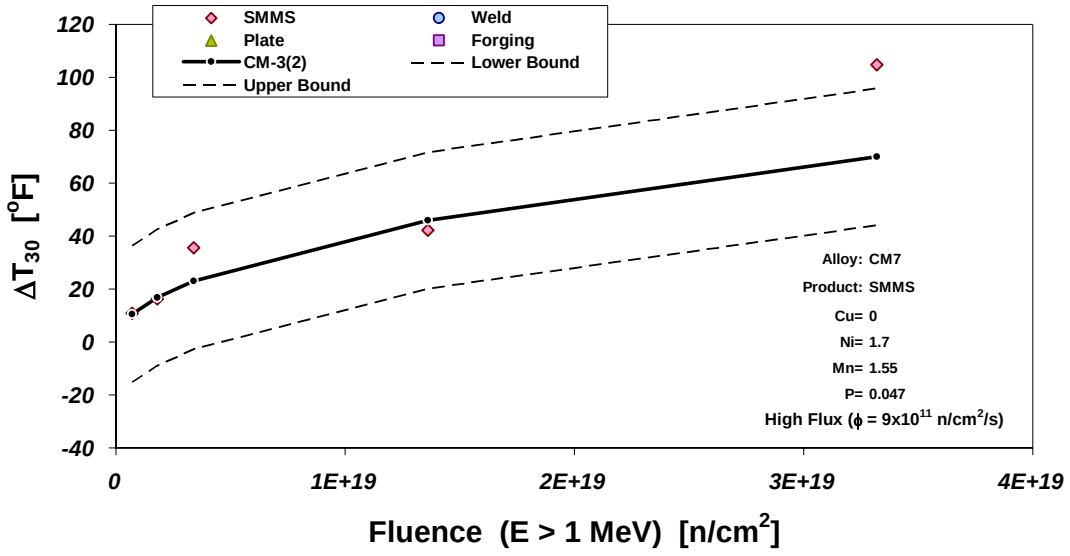
SMMS
Weld
Plate
Forging
CM-3(2)
Lower Bound
Upper Bound
Alloy: CM7
Product: SMMS
Cu= 0
Ni= 1.7
Mn= 1.55
P= 0.047
High Flux (ϕ = 9x10^11 n/cm^2/s)
ΔT30 [°F]
Fluence (E > 1 MeV) [n/cm^2]

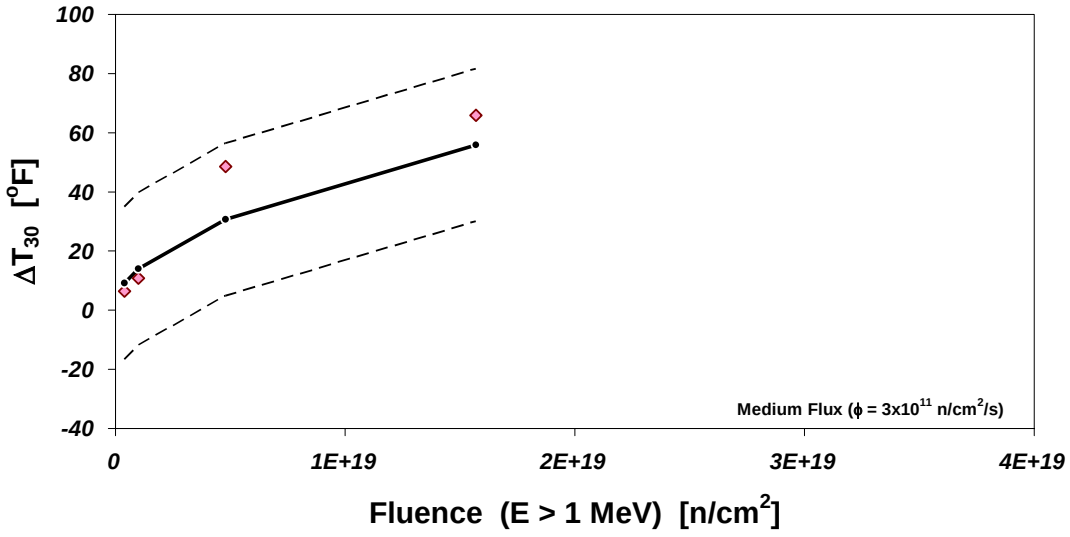
Medium Flux (ϕ = 3x10^11 n/cm^2/s)
ΔT30 [°F]
Fluence (E > 1 MeV) [n/cm^2]

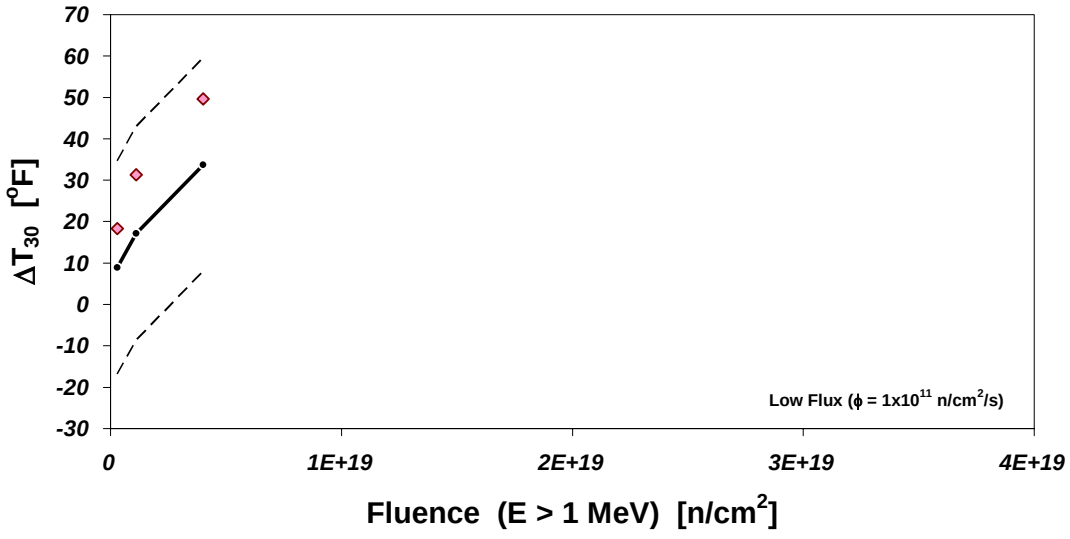
Low Flux (ϕ = 1x10^11 n/cm^2/s)
ΔT30 [°F]
Fluence (E > 1 MeV) [n/cm^2]

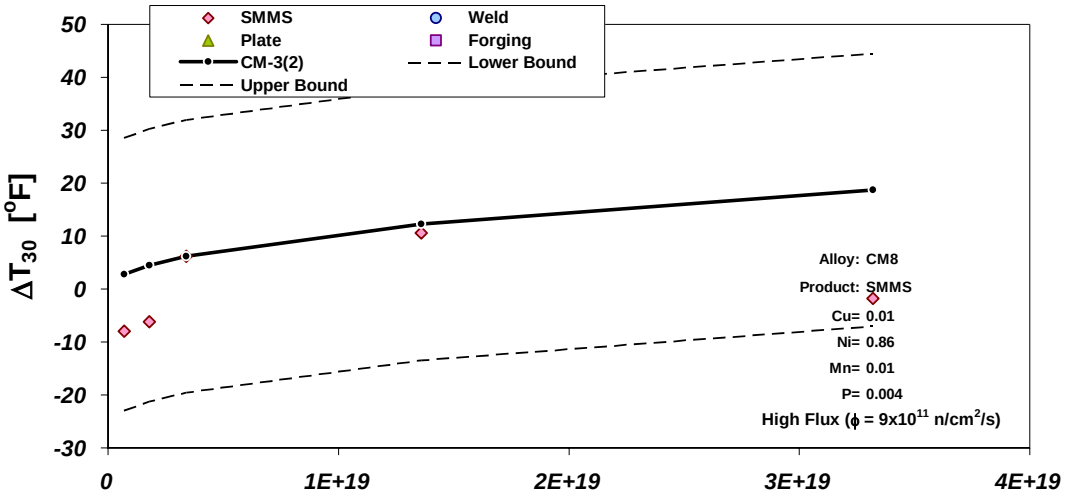
SMMS
Weld
Plate
Forging
CM-3(2)
Lower Bound
Upper Bound
Alloy: CM8
Product: SMMS
Cu= 0.01
Ni= 0.86
Mn= 0.01
P= 0.004
High Flux (ϕ = 9x10^11 n/cm^2/s)
ΔT30 [°F]
50
40
30
20
10
0
-10
-20
-30
0
1E+19
2E+19
3E+19
4E+19
Fluence (E > 1 MeV) [n/cm^2]

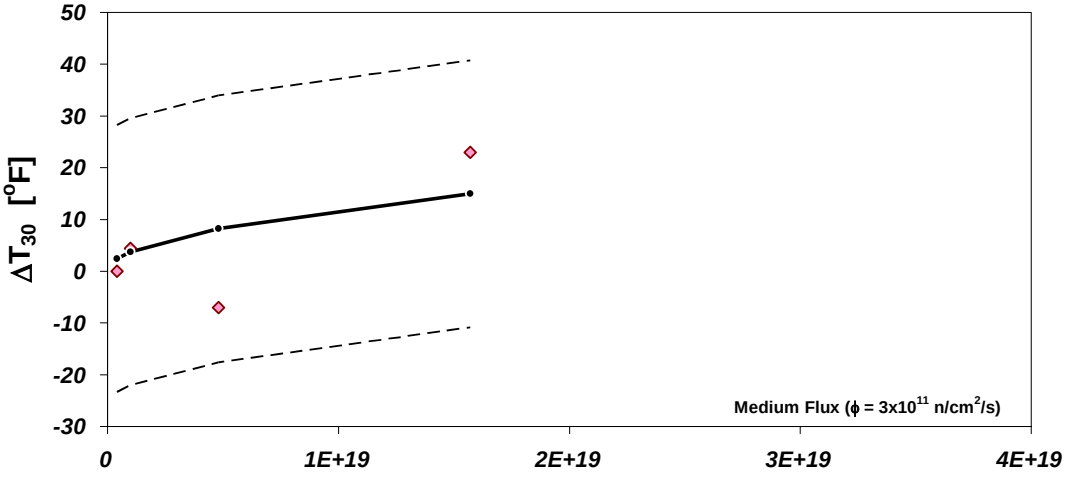
Medium Flux (ϕ = 3x10^11 n/cm^2/s)
ΔT30 [°F]
50
40
30
20
10
0
-10
-20
-30
0
1E+19
2E+19
3E+19
4E+19
Fluence (E > 1 MeV) [n/cm^2]

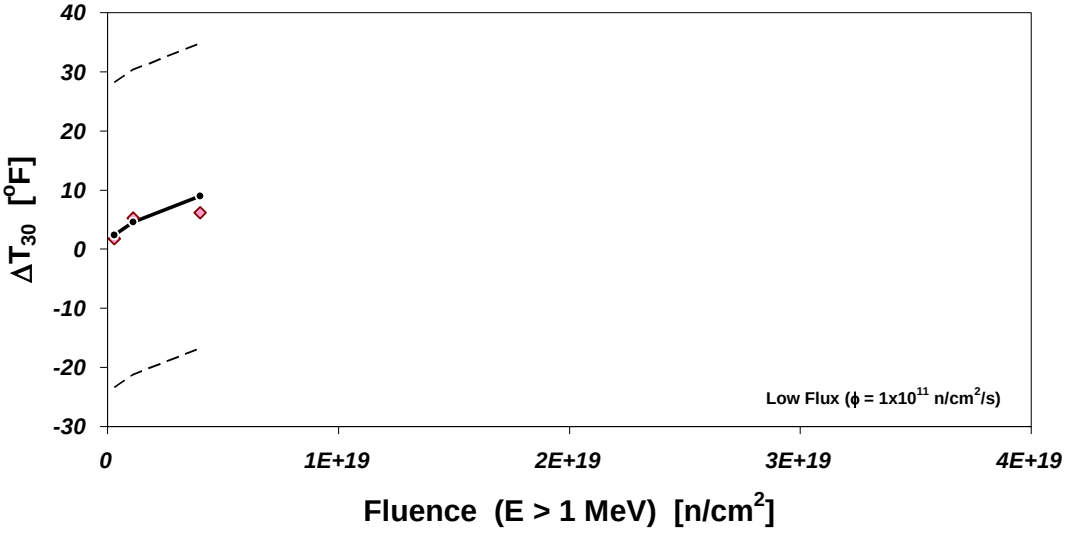
Low Flux (ϕ = 1x10^11 n/cm^2/s)
ΔT30 [°F]
40
30
20
10
0
-10
-20
-30
0
1E+19
2E+19
3E+19
4E+19
Fluence (E > 1 MeV) [n/cm^2]

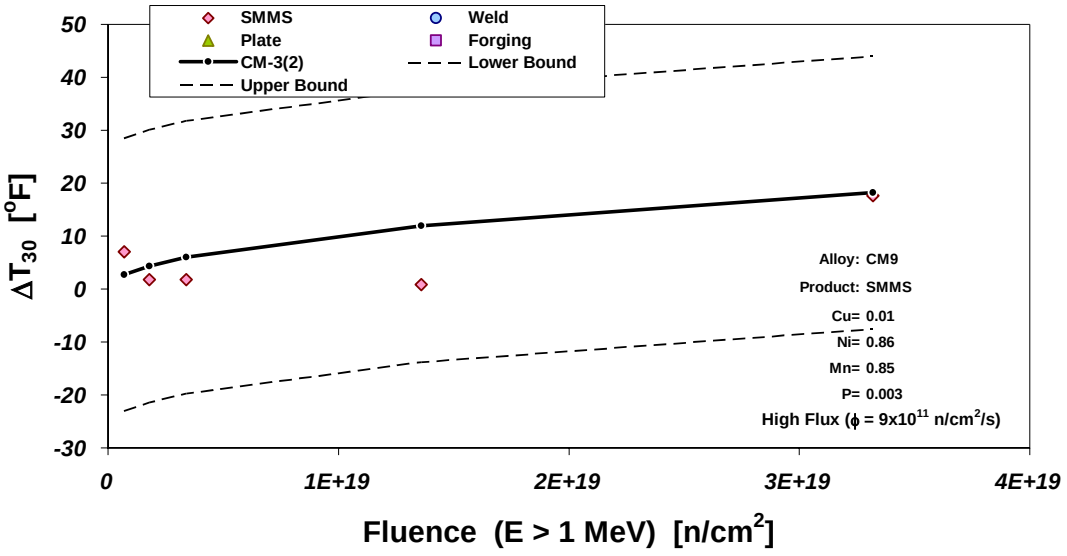
SMMS
Weld
Plate
Forging
CM-3(2)
Lower Bound
Upper Bound
Alloy: CM9
Product: SMMS
Cu= 0.01
Ni= 0.86
Mn= 0.85
P= 0.003
High Flux (ϕ = 9x10^11 n/cm^2/s)
ΔT30 [°F]
50
40
30
20
10
0
-10
-20
-30
0
1E+19
2E+19
3E+19
4E+19
Fluence (E > 1 MeV) [n/cm^2]

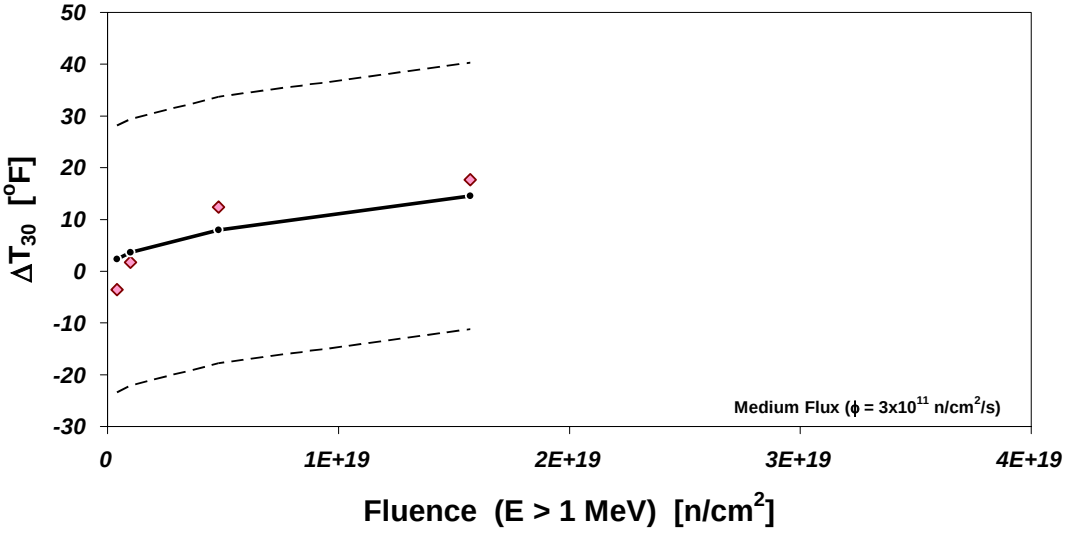
Medium Flux (ϕ = 3x10^11 n/cm^2/s)
ΔT30 [°F]
50
40
30
20
10
0
-10
-20
-30
0
1E+19
2E+19
3E+19
4E+19
Fluence (E > 1 MeV) [n/cm^2]

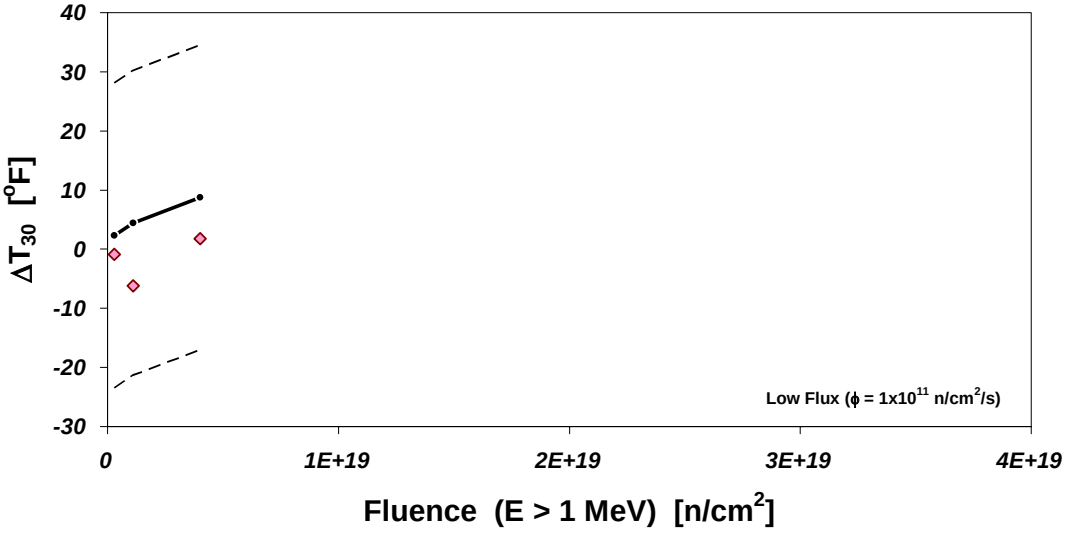
Low Flux (ϕ = 1x10^11 n/cm^2/s)
ΔT30 [°F]
40
30
20
10
0
-10
-20
-30
0
1E+19
2E+19
3E+19
4E+19
Fluence (E > 1 MeV) [n/cm^2]

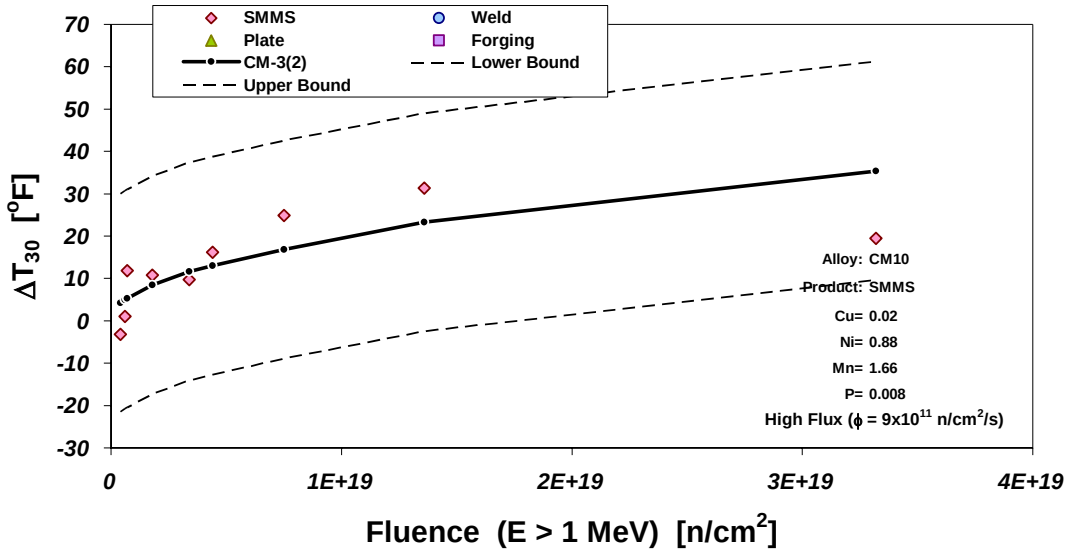
SMMS
Weld
Plate
Forging
CM-3(2)
Lower Bound
Upper Bound
Alloy: CM10
Product: SMMS
Cu= 0.02
Ni= 0.88
Mn= 1.66
P= 0.008
High Flux (ϕ = 9x10^11 n/cm^2/s)
ΔT30 [°F]
Fluence (E > 1 MeV) [n/cm^2]

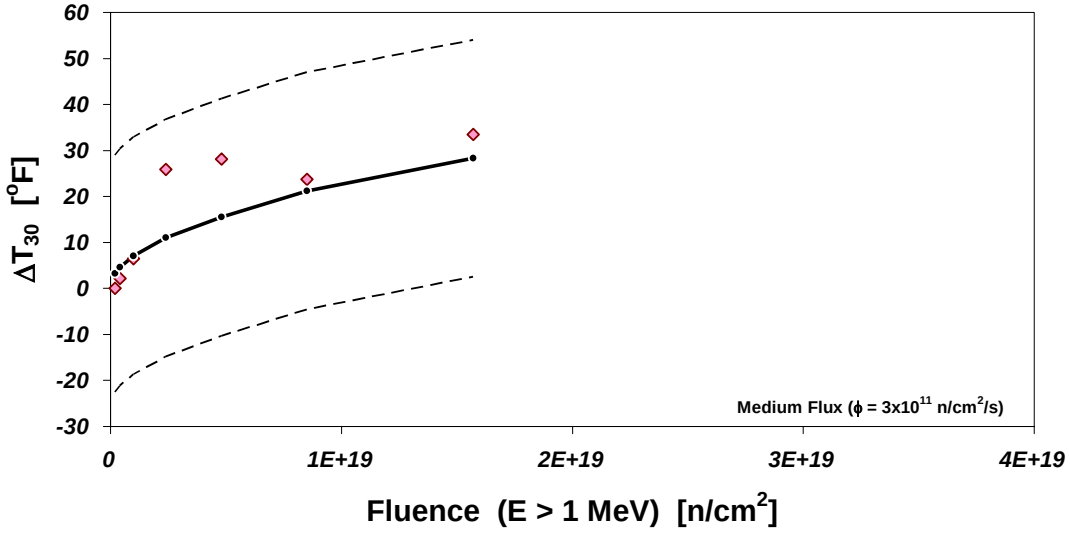
Medium Flux (ϕ = 3x10^11 n/cm^2/s)
ΔT30 [°F]
Fluence (E > 1 MeV) [n/cm^2]

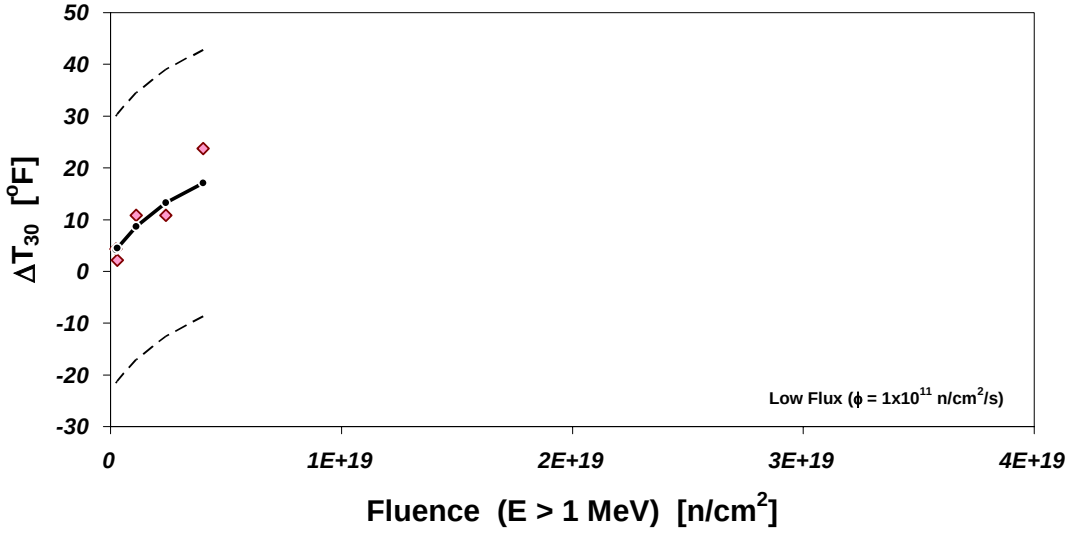
Low Flux (ϕ = 1x10^11 n/cm^2/s)
ΔT30 [°F]
Fluence (E > 1 MeV) [n/cm^2]

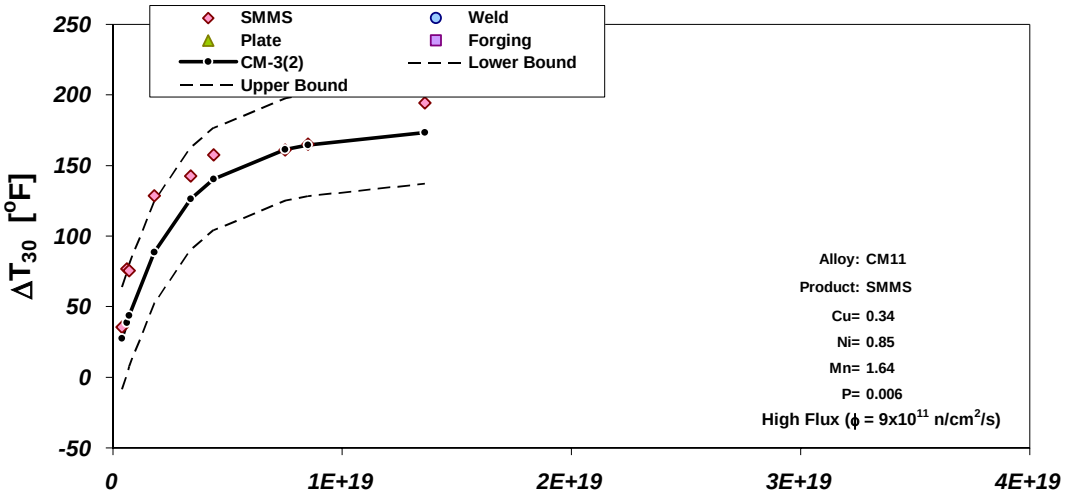
SMMS
Weld
Plate
Forging
CM-3(2)
Lower Bound
Upper Bound
Alloy: CM11
Product: SMMS
Cu= 0.34
Ni= 0.85
Mn= 1.64
P= 0.006
High Flux (ϕ = 9x10^11 n/cm^2/s)
ΔT30 [°F]
250
200
150
100
50
0
-50
0
1E+19
2E+19
3E+19
4E+19
Fluence (E > 1 MeV) [n/cm^2]

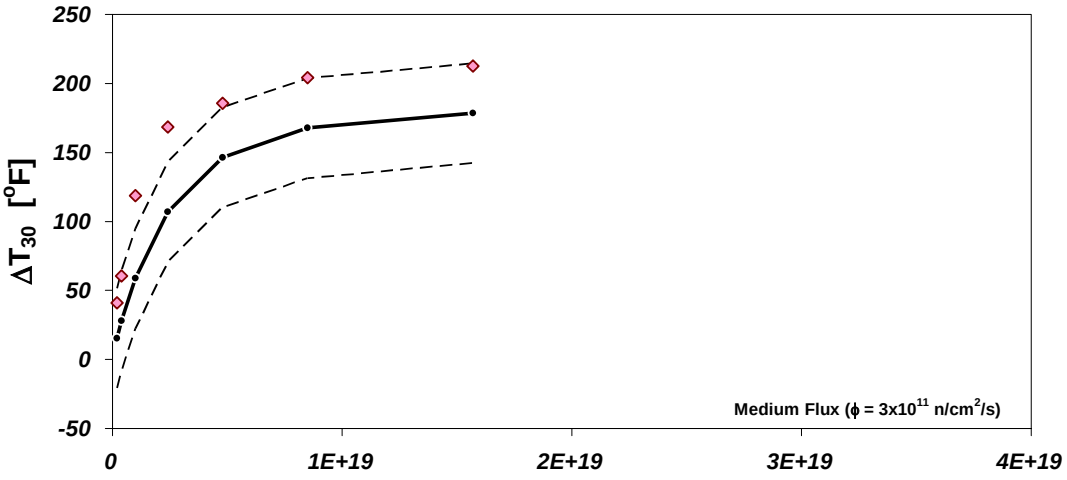
Medium Flux (ϕ = 3x10^11 n/cm^2/s)
ΔT30 [°F]
250
200
150
100
50
0
-50
0
1E+19
2E+19
3E+19
4E+19
Fluence (E > 1 MeV) [n/cm^2]

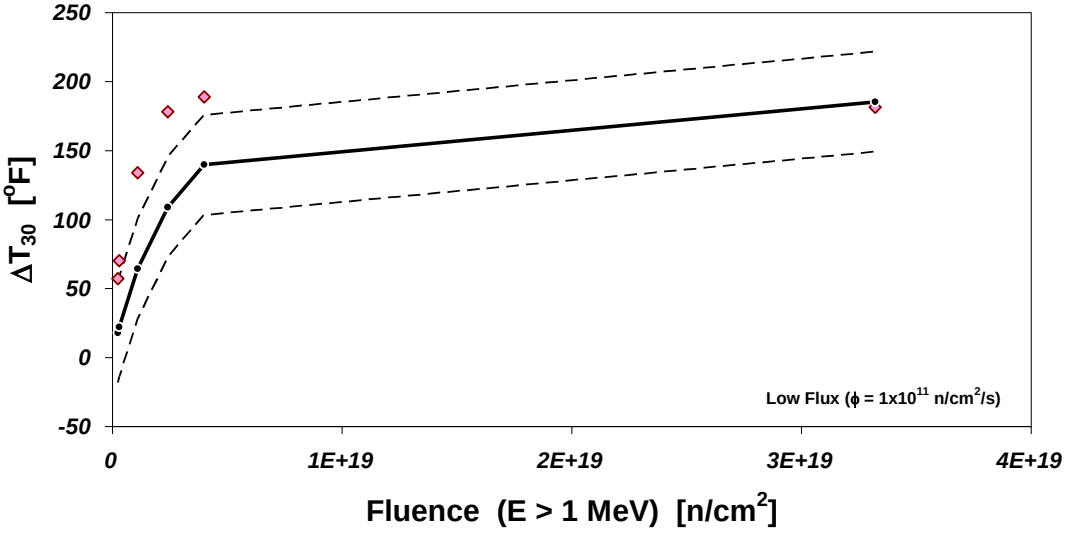
Low Flux (ϕ = 1x10^11 n/cm^2/s)
ΔT30 [°F]
250
200
150
100
50
0
-50
0
1E+19
2E+19
3E+19
4E+19
Fluence (E > 1 MeV) [n/cm^2]

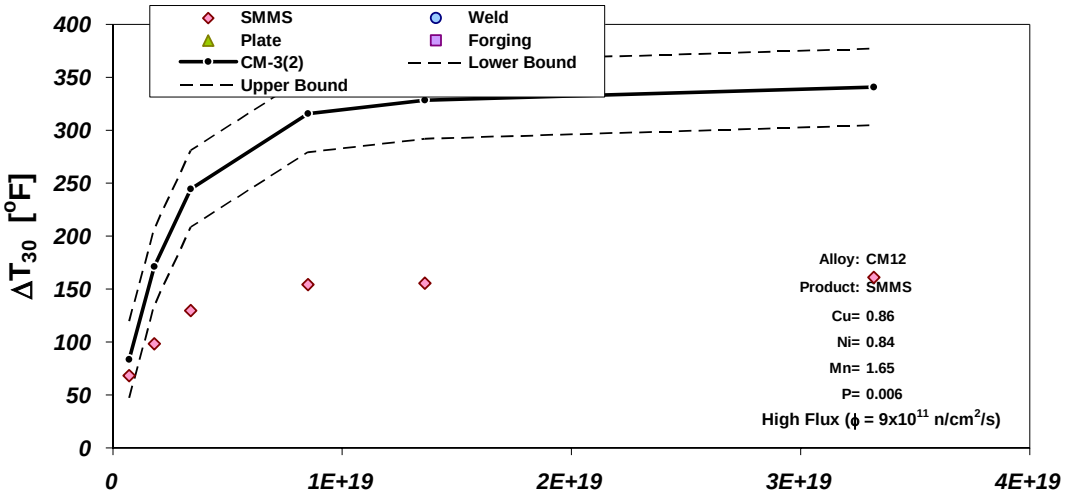
SMMS
Weld
Plate
Forging
CM-3(2)
Lower Bound
Upper Bound
Alloy: CM12
Product: SMMS
Cu= 0.86
Ni= 0.84
Mn= 1.65
P= 0.006
High Flux (ϕ = 9x10^11 n/cm^2/s)
ΔT30 [°F]
0
50
100
150
200
250
300
350
400
0
1E+19
2E+19
3E+19
4E+19
Fluence (E > 1 MeV) [n/cm^2]

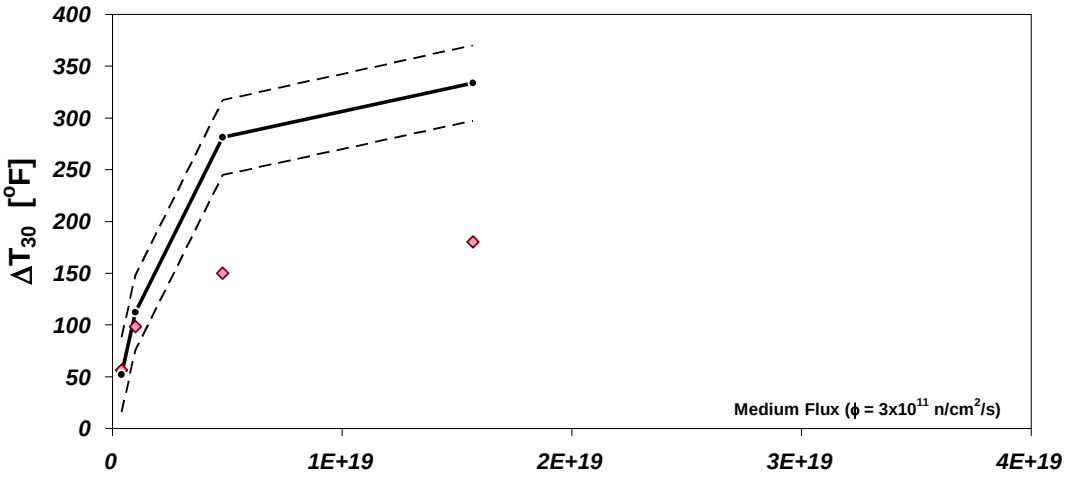
Medium Flux (ϕ = 3x10^11 n/cm^2/s)
ΔT30 [°F]
0
50
100
150
200
250
300
350
400
0
1E+19
2E+19
3E+19
4E+19
Fluence (E > 1 MeV) [n/cm^2]

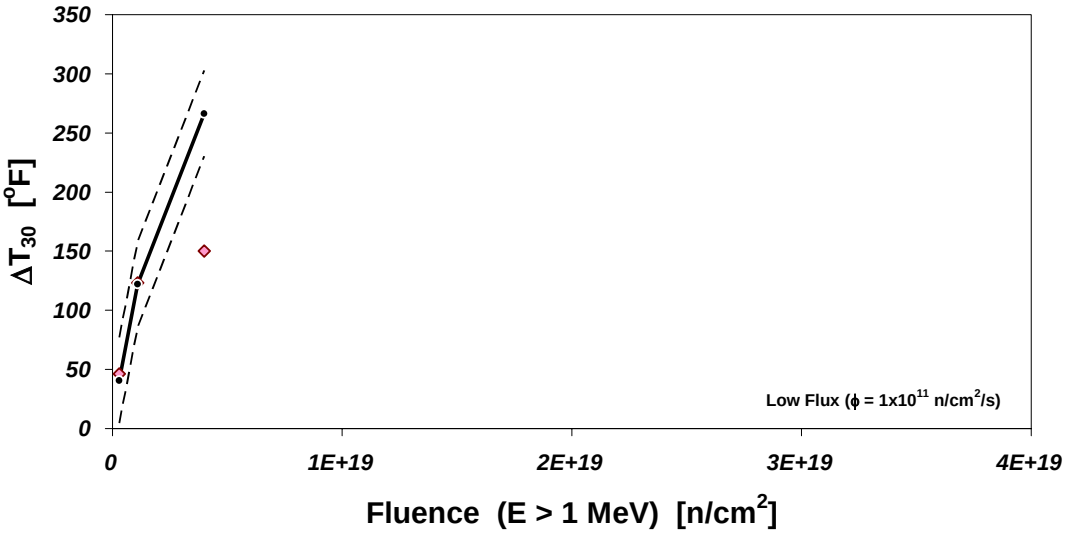
Low Flux (ϕ = 1x10^11 n/cm^2/s)
ΔT30 [°F]
0
50
100
150
200
250
300
350
0
1E+19
2E+19
3E+19
4E+19
Fluence (E > 1 MeV) [n/cm^2]

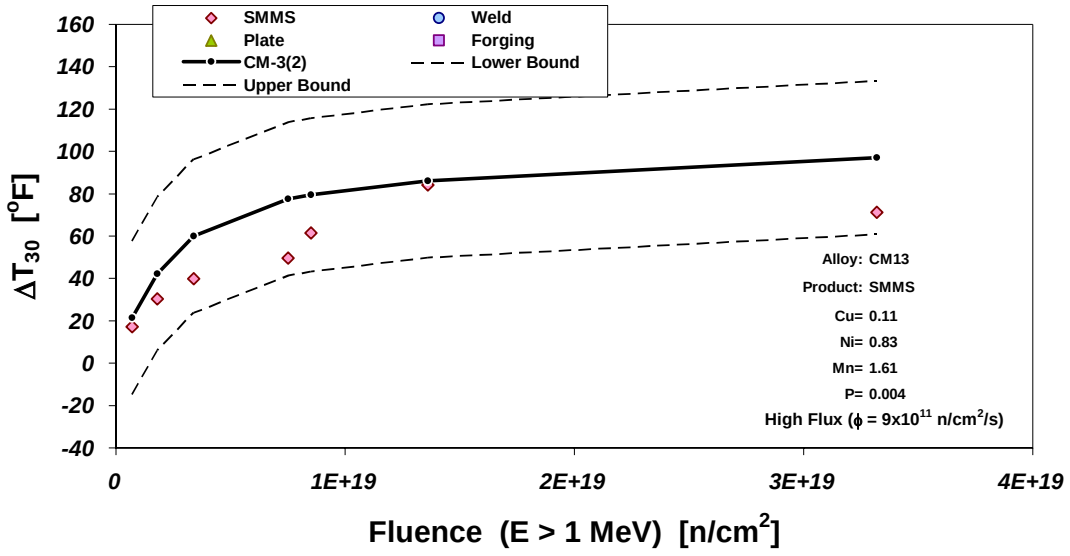
SMMS
Weld
Plate
Forging
CM-3(2)
Lower Bound
Upper Bound
Alloy: CM13
Product: SMMS
Cu= 0.11
Ni= 0.83
Mn= 1.61
P= 0.004
High Flux (ϕ = 9x10^11 n/cm^2/s)
ΔT30 [°F]
Fluence (E > 1 MeV) [n/cm^2]

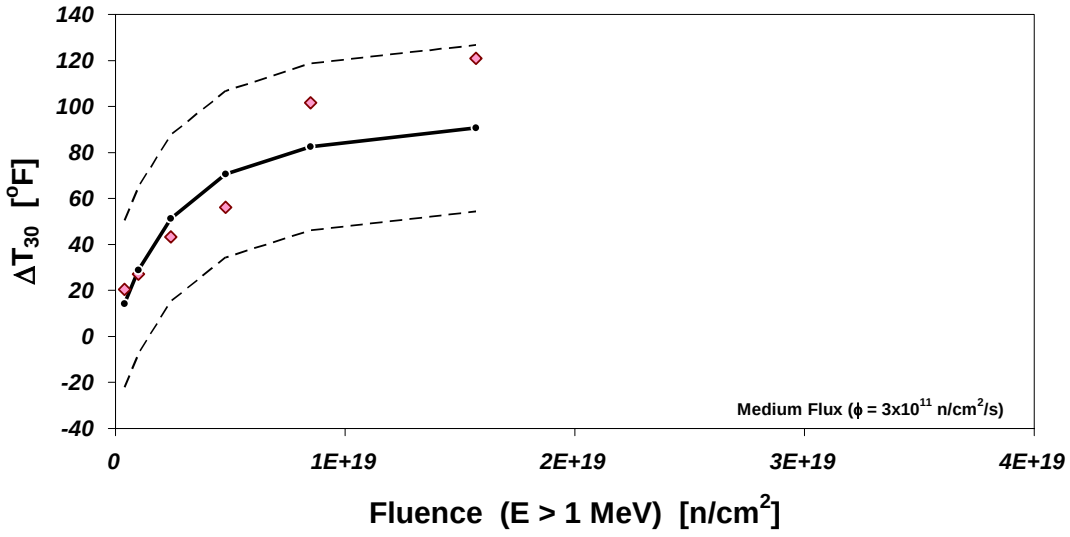
Medium Flux (ϕ = 3x10^11 n/cm^2/s)
ΔT30 [°F]
Fluence (E > 1 MeV) [n/cm^2]

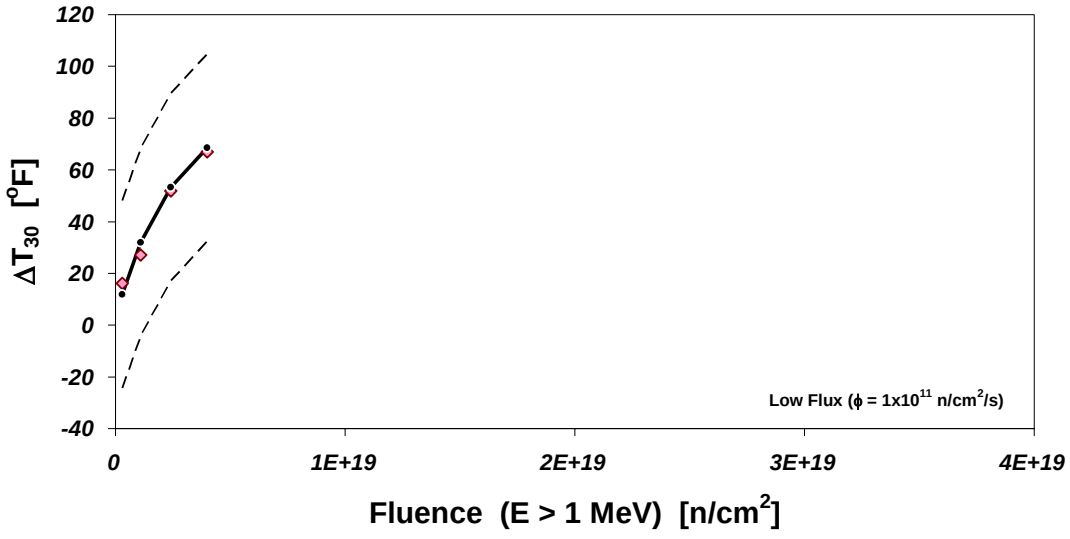
Low Flux (ϕ = 1x10^11 n/cm^2/s)
ΔT30 [°F]
Fluence (E > 1 MeV) [n/cm^2]

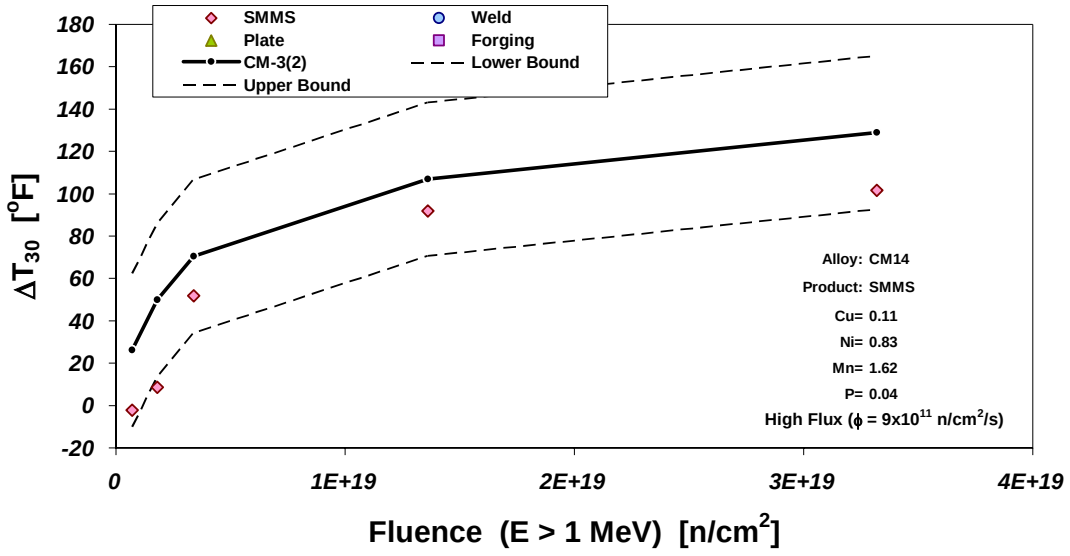
SMMS
Weld
Plate
Forging
CM-3(2)
Lower Bound
Upper Bound
Alloy: CM14
Product: SMMS
Cu= 0.11
Ni= 0.83
Mn= 1.62
P= 0.04
High Flux (ϕ = 9x10^11 n/cm^2/s)
ΔT30 [°F]
180
160
140
120
100
80
60
40
20
0
-20
0
1E+19
2E+19
3E+19
4E+19
Fluence (E > 1 MeV) [n/cm^2]

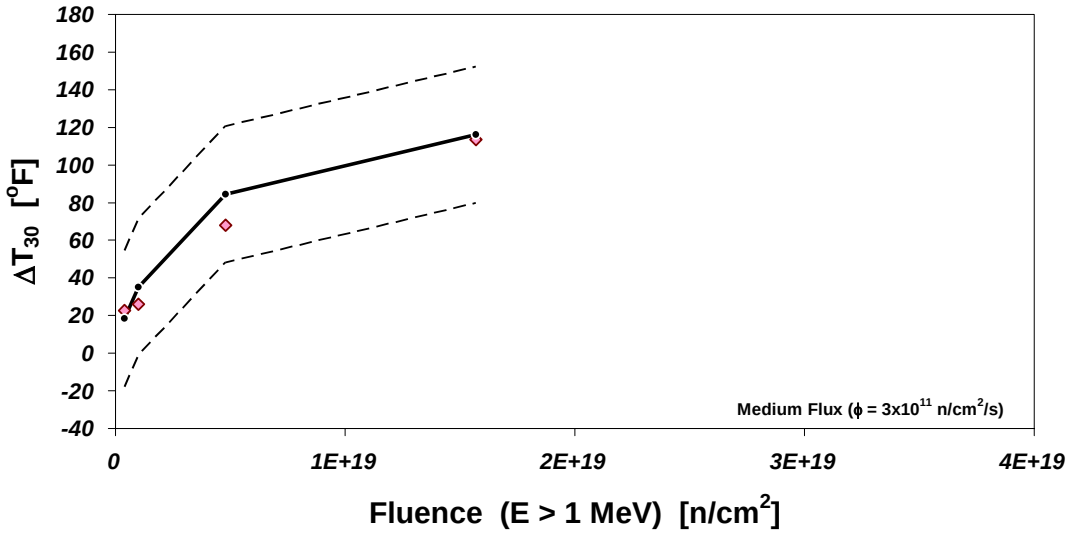
Medium Flux (ϕ = 3x10^11 n/cm^2/s)
ΔT30 [°F]
180
160
140
120
100
80
60
40
20
0
-20
-40
0
1E+19
2E+19
3E+19
4E+19
Fluence (E > 1 MeV) [n/cm^2]

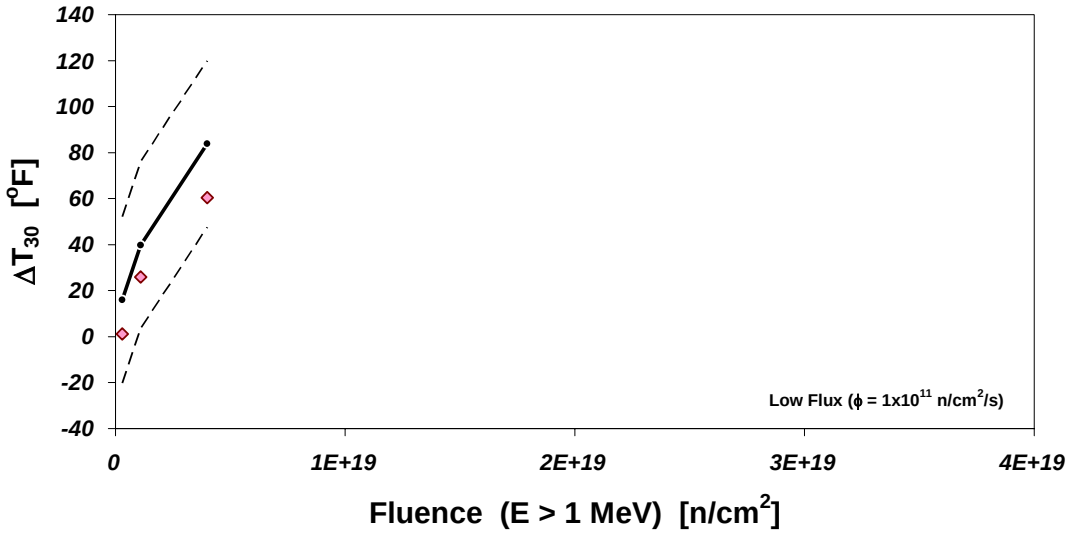
Low Flux (ϕ = 1x10^11 n/cm^2/s)
ΔT30 [°F]
140
120
100
80
60
40
20
0
-20
-40
0
1E+19
2E+19
3E+19
4E+19
Fluence (E > 1 MeV) [n/cm^2]

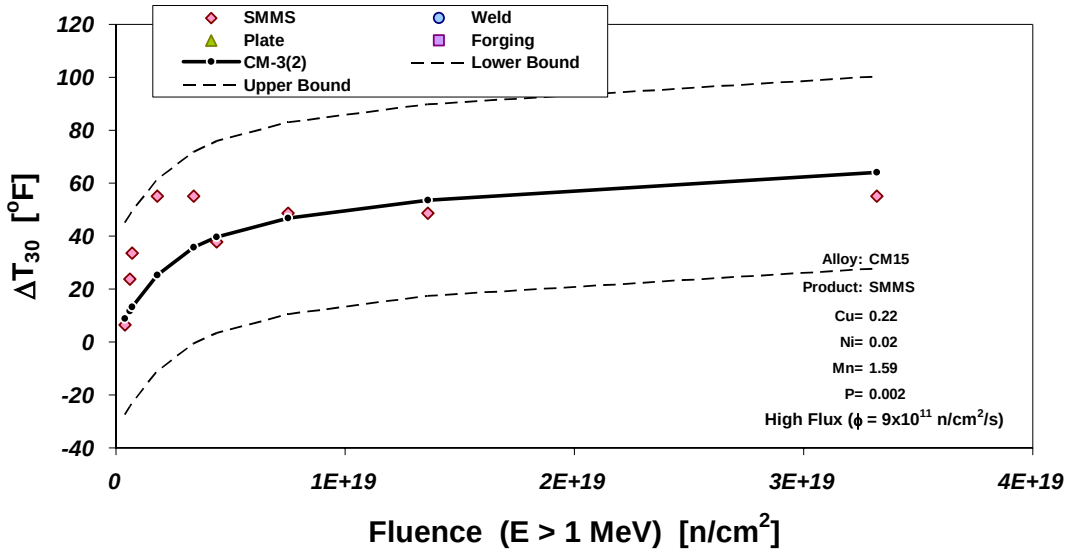
SMMS
Weld
Plate
Forging
CM-3(2)
Lower Bound
Upper Bound
Alloy: CM15
Product: SMMS
Cu= 0.22
Ni= 0.02
Mn= 1.59
P= 0.002
High Flux (ϕ = 9x10^11 n/cm^2/s)
ΔT30 [°F]
120
100
80
60
40
20
0
-20
-40
0
1E+19
2E+19
3E+19
4E+19
Fluence (E > 1 MeV) [n/cm^2]

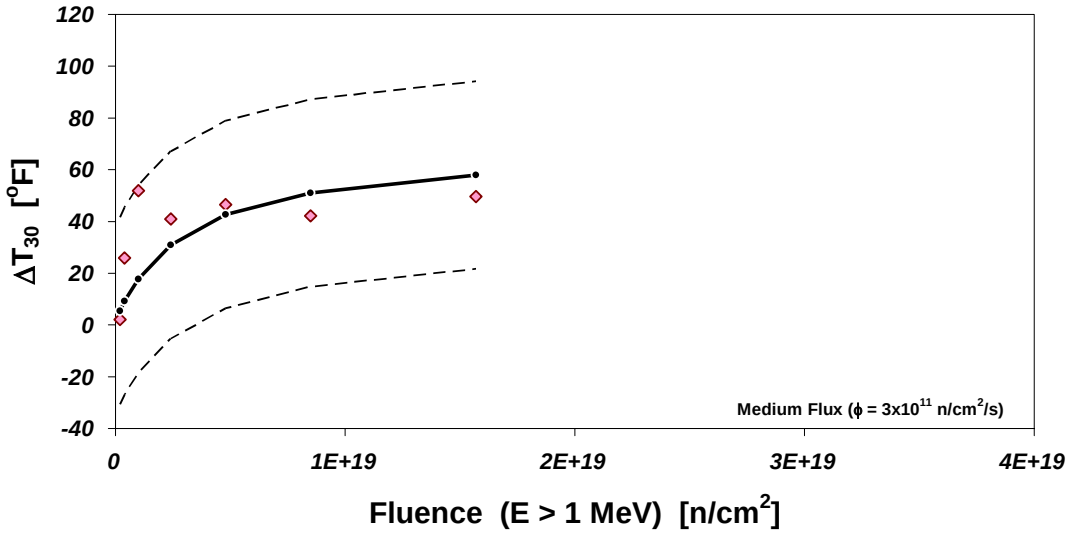
Medium Flux (ϕ = 3x10^11 n/cm^2/s)
ΔT30 [°F]
120
100
80
60
40
20
0
-20
-40
0
1E+19
2E+19
3E+19
4E+19
Fluence (E > 1 MeV) [n/cm^2]

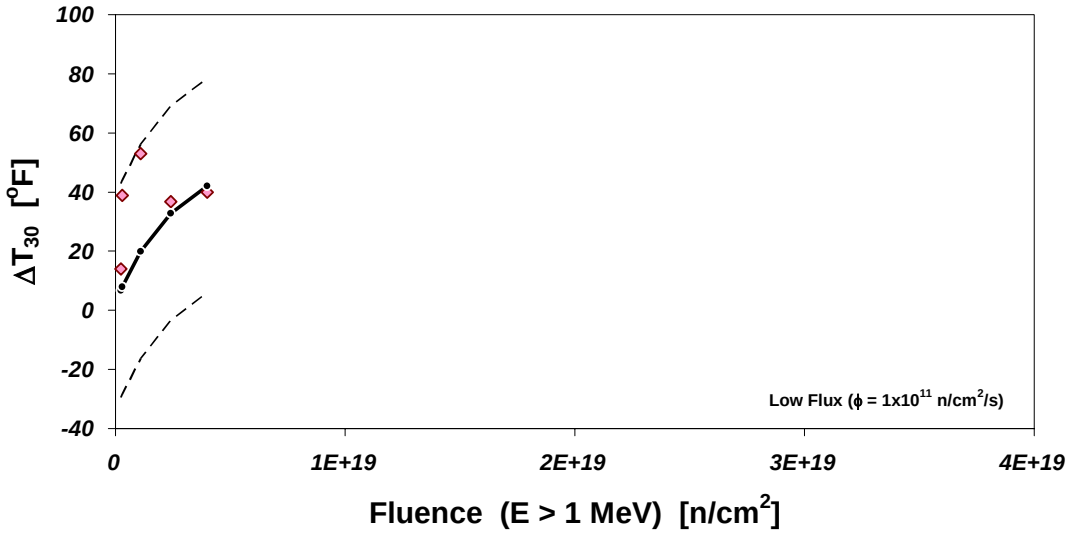
Low Flux (ϕ = 1x10^11 n/cm^2/s)
ΔT30 [°F]
100
80
60
40
20
0
-20
-40
0
1E+19
2E+19
3E+19
4E+19
Fluence (E > 1 MeV) [n/cm^2]

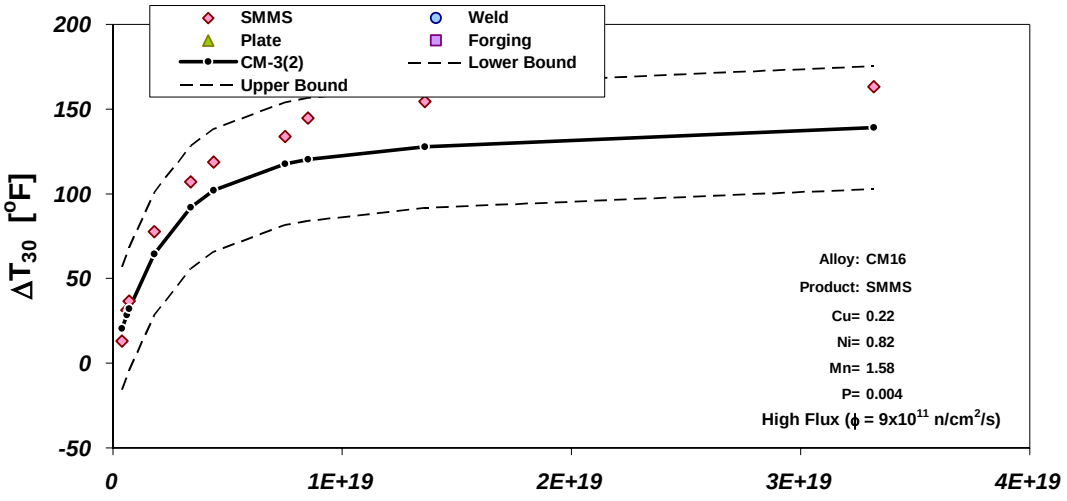
SMMS
Weld
Plate
Forging
CM-3(2)
Lower Bound
Upper Bound
Alloy: CM16
Product: SMMS
Cu= 0.22
Ni= 0.82
Mn= 1.58
P= 0.004
High Flux (ϕ = 9x10^11 n/cm^2/s)
ΔT30 [°F]
200
150
100
50
0
-50
0
1E+19
2E+19
3E+19
4E+19
Fluence (E > 1 MeV) [n/cm^2]

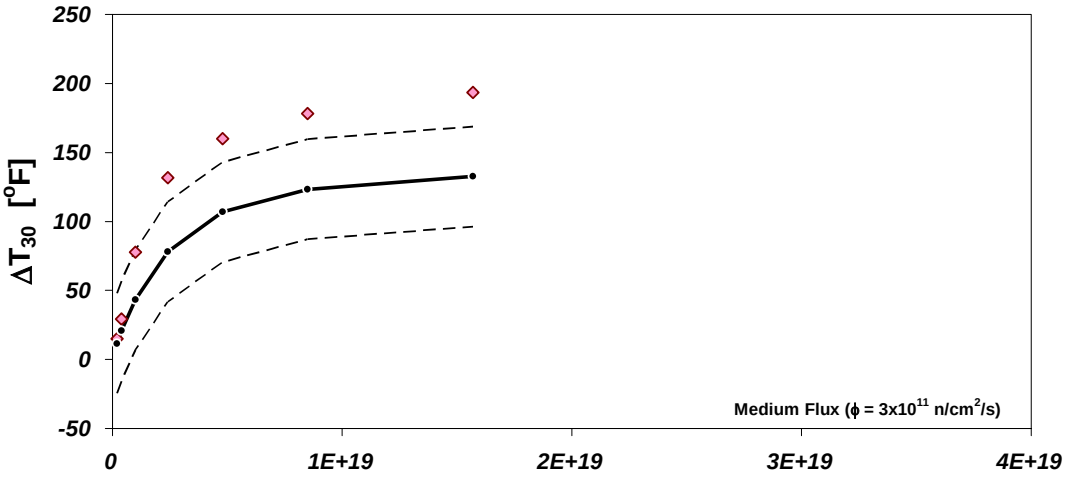
Medium Flux (ϕ = 3x10^11 n/cm^2/s)
ΔT30 [°F]
250
200
150
100
50
0
-50
0
1E+19
2E+19
3E+19
4E+19
Fluence (E > 1 MeV) [n/cm^2]

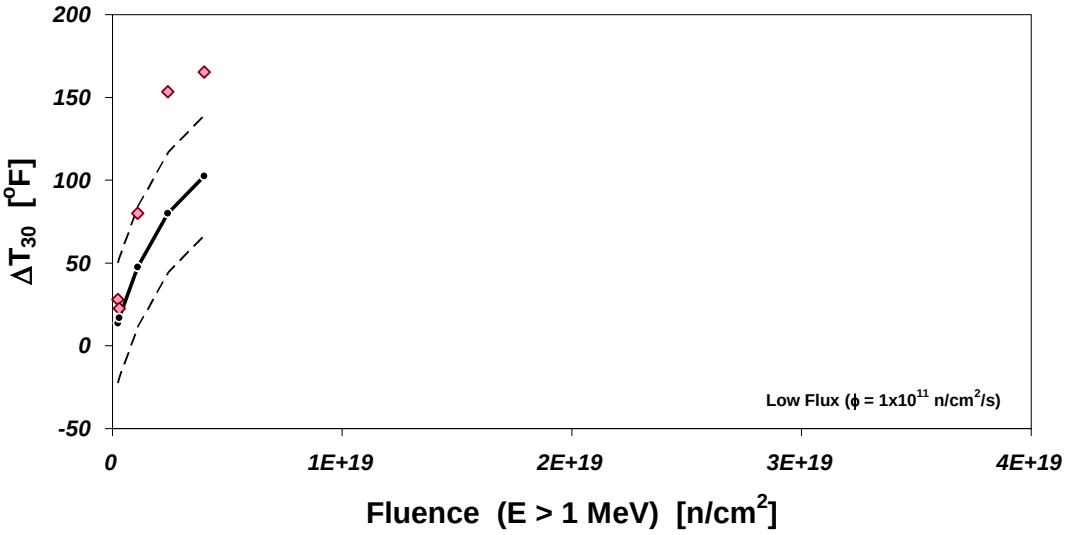
Low Flux (ϕ = 1x10^11 n/cm^2/s)
ΔT30 [°F]
200
150
100
50
0
-50
0
1E+19
2E+19
3E+19
4E+19
Fluence (E > 1 MeV) [n/cm^2]

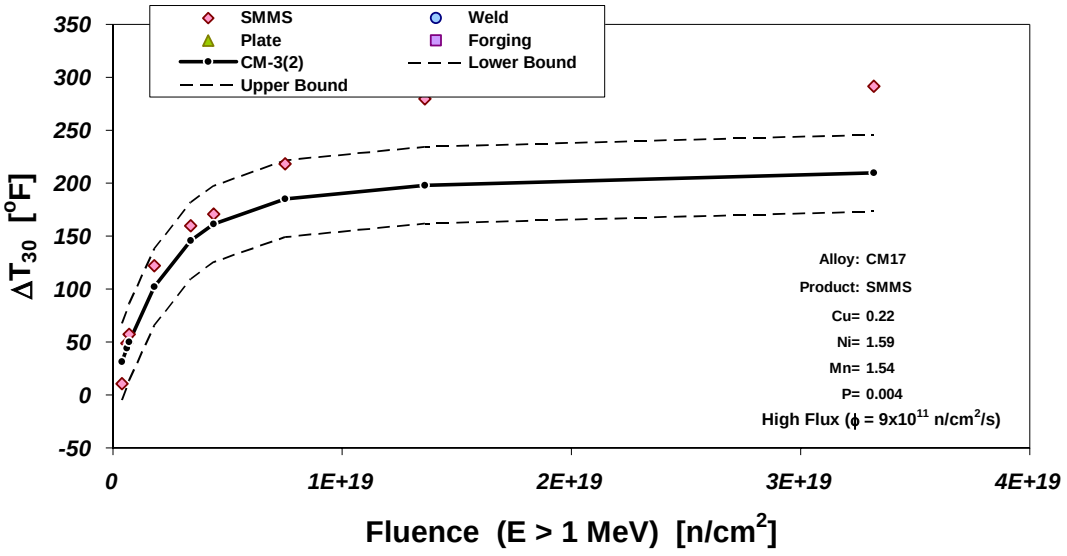
SMMS
Weld
Plate
Forging
CM-3(2)
Lower Bound
Upper Bound
Alloy: CM17
Product: SMMS
Cu= 0.22
Ni= 1.59
Mn= 1.54
P= 0.004
High Flux (ϕ = 9x10^11 n/cm^2/s)
ΔT30 [°F]
350
300
250
200
150
100
50
0
-50
0
1E+19
2E+19
3E+19
4E+19
Fluence (E > 1 MeV) [n/cm^2]

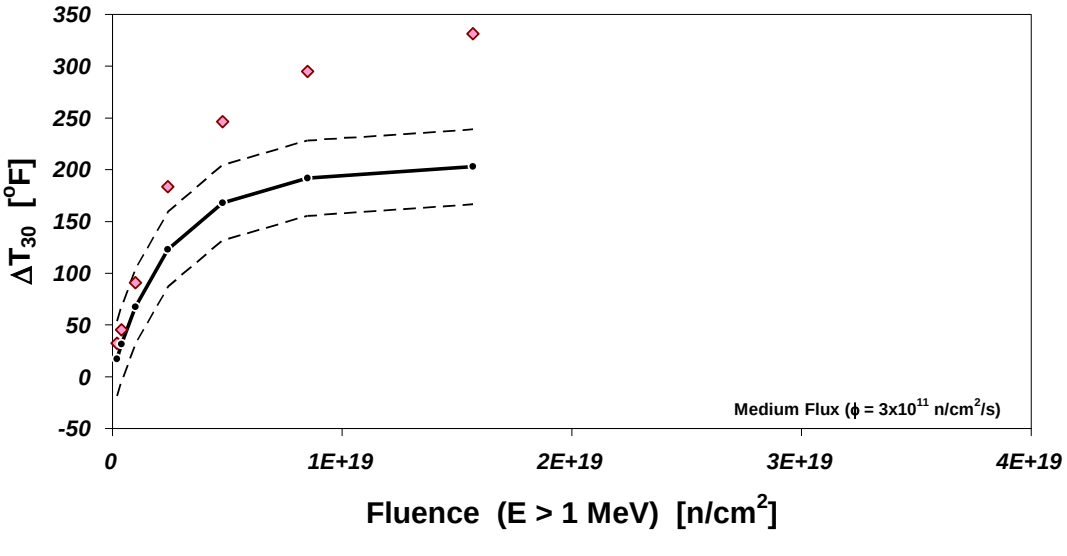
Medium Flux (ϕ = 3x10^11 n/cm^2/s)
ΔT30 [°F]
350
300
250
200
150
100
50
0
-50
0
1E+19
2E+19
3E+19
4E+19
Fluence (E > 1 MeV) [n/cm^2]

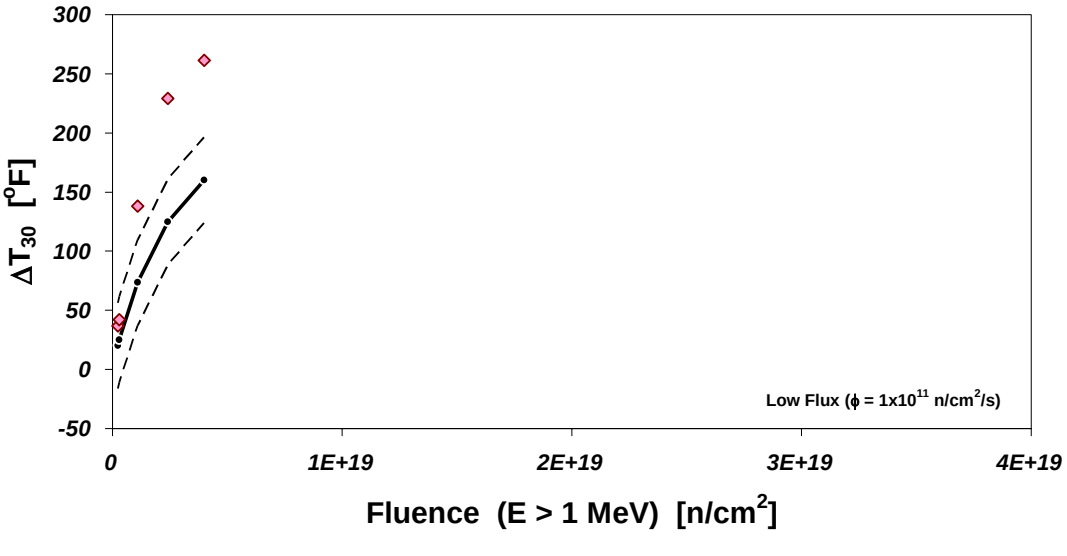
Low Flux (ϕ = 1x10^11 n/cm^2/s)
ΔT30 [°F]
300
250
200
150
100
50
0
-50
0
1E+19
2E+19
3E+19
4E+19
Fluence (E > 1 MeV) [n/cm^2]

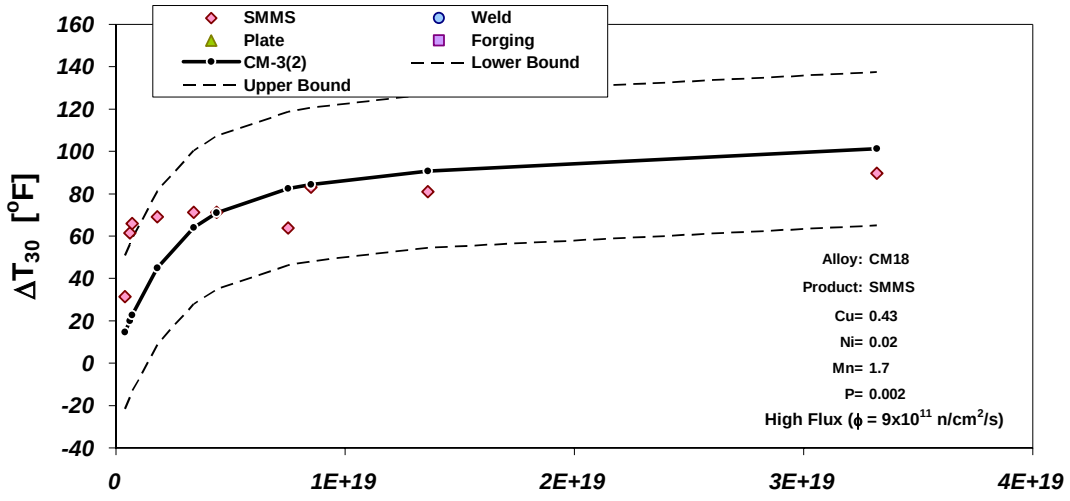
SMMS
Weld
Plate
Forging
CM-3(2)
Lower Bound
Upper Bound
Alloy: CM18
Product: SMMS
Cu= 0.43
Ni= 0.02
Mn= 1.7
P= 0.002
High Flux (ϕ = 9x10^11 n/cm^2/s)
ΔT30 [°F]
160
140
120
100
80
60
40
20
0
-20
-40
0
1E+19
2E+19
3E+19
4E+19
Fluence (E > 1 MeV) [n/cm^2]

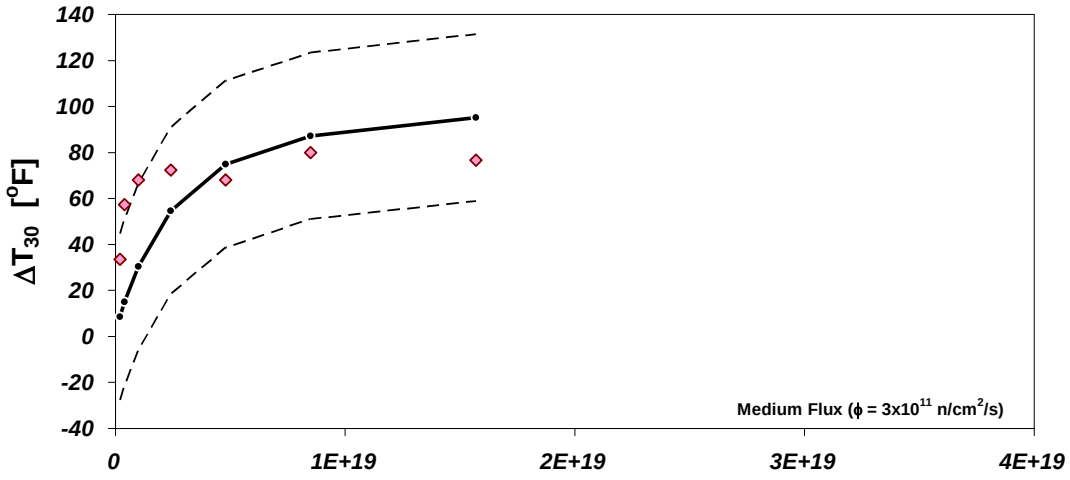
Medium Flux (ϕ = 3x10^11 n/cm^2/s)
ΔT30 [°F]
140
120
100
80
60
40
20
0
-20
-40
0
1E+19
2E+19
3E+19
4E+19
Fluence (E > 1 MeV) [n/cm^2]

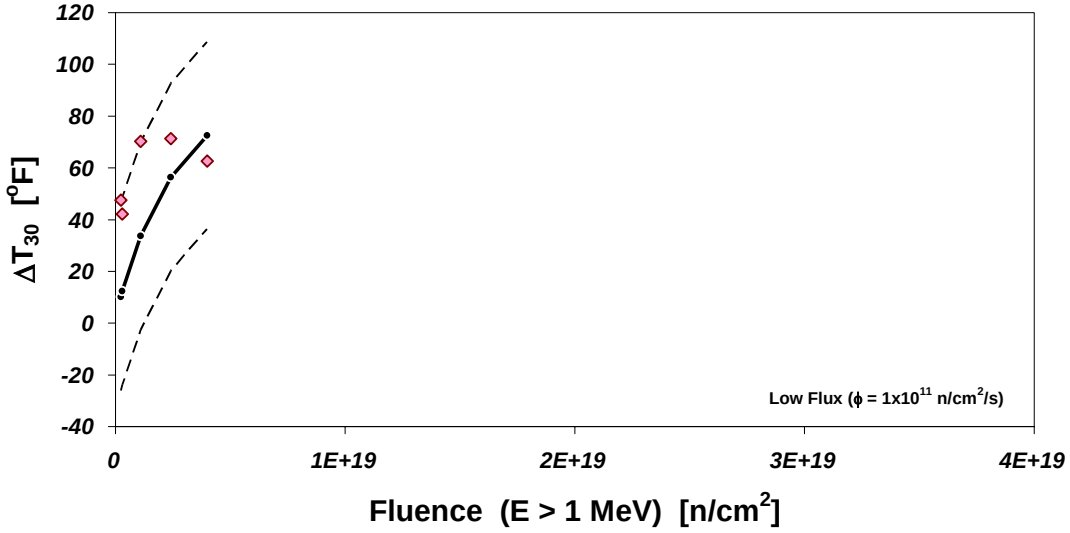
Low Flux (ϕ = 1x10^11 n/cm^2/s)
ΔT30 [°F]
120
100
80
60
40
20
0
-20
-40
0
1E+19
2E+19
3E+19
4E+19
Fluence (E > 1 MeV) [n/cm^2]

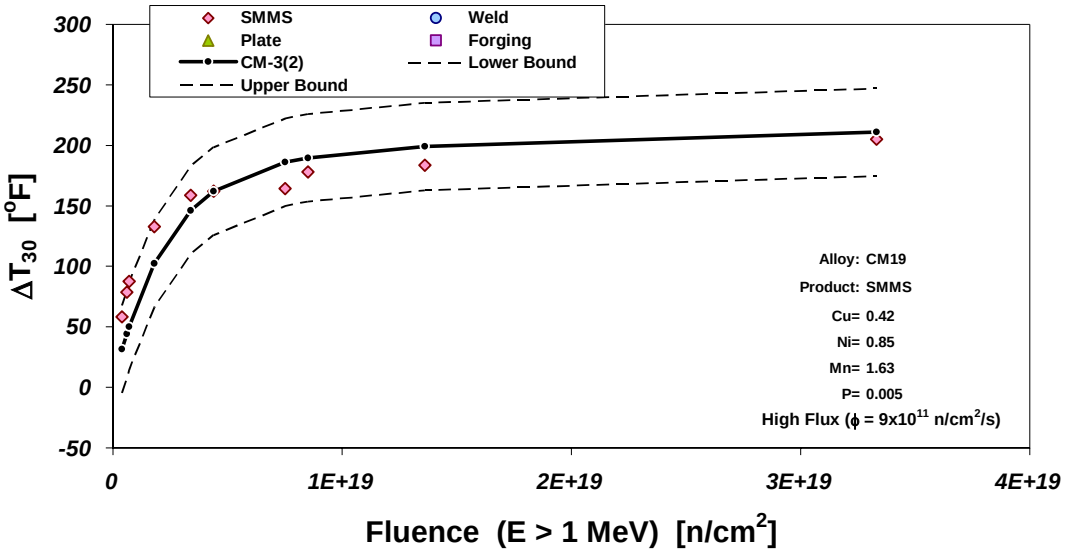
SMMS
Weld
Plate
Forging
CM-3(2)
Lower Bound
Upper Bound
Alloy: CM19
Product: SMMS
Cu= 0.42
Ni= 0.85
Mn= 1.63
P= 0.005
High Flux (ϕ = 9x10^11 n/cm^2/s)
ΔT30 [°F]
300
250
200
150
100
50
0
-50
0
1E+19
2E+19
3E+19
4E+19
Fluence (E > 1 MeV) [n/cm^2]

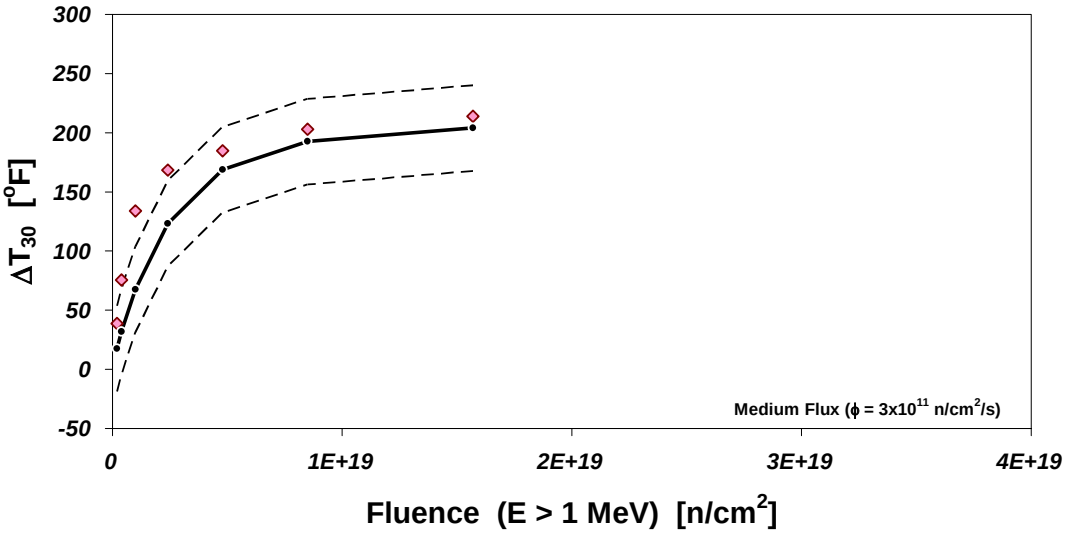
Medium Flux (ϕ = 3x10^11 n/cm^2/s)
ΔT30 [°F]
300
250
200
150
100
50
0
-50
0
1E+19
2E+19
3E+19
4E+19
Fluence (E > 1 MeV) [n/cm^2]

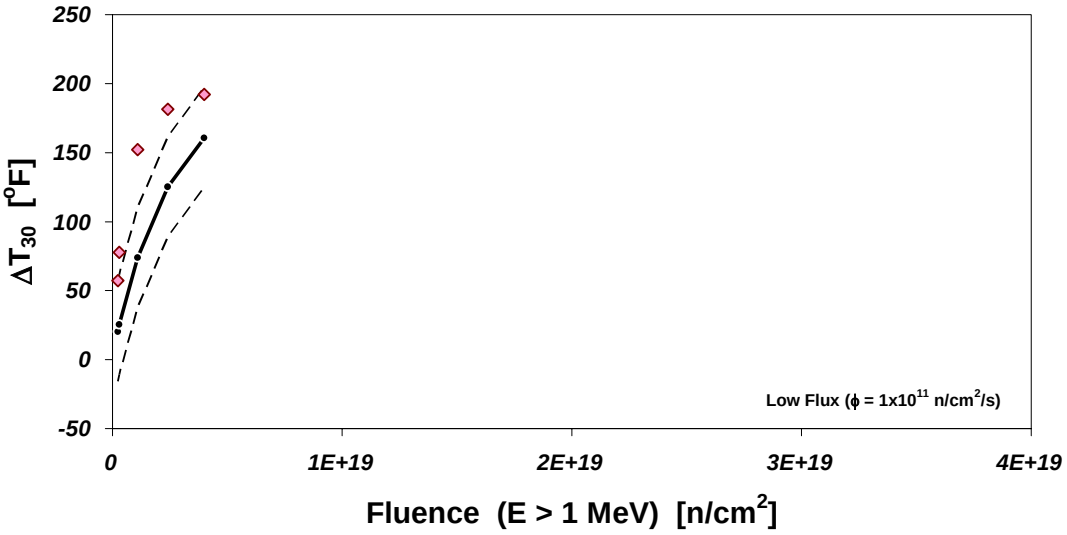
Low Flux (ϕ = 1x10^11 n/cm^2/s)
ΔT30 [°F]
250
200
150
100
50
0
-50
0
1E+19
2E+19
3E+19
4E+19
Fluence (E > 1 MeV) [n/cm^2]

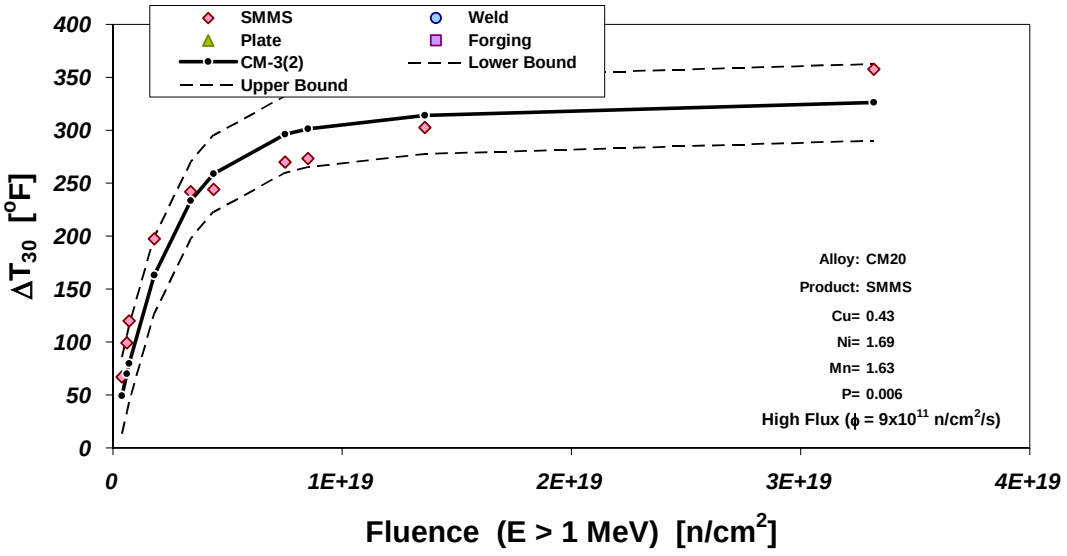
SMMS
Weld
Plate
Forging
CM-3(2)
Lower Bound
Upper Bound
Alloy: CM20
Product: SMMS
Cu= 0.43
Ni= 1.69
Mn= 1.63
P= 0.006
High Flux (ϕ = 9x10^11 n/cm^2/s)
ΔT30 [°F]
400
350
300
250
200
150
100
50
0
0
1E+19
2E+19
3E+19
4E+19
Fluence (E > 1 MeV) [n/cm^2]

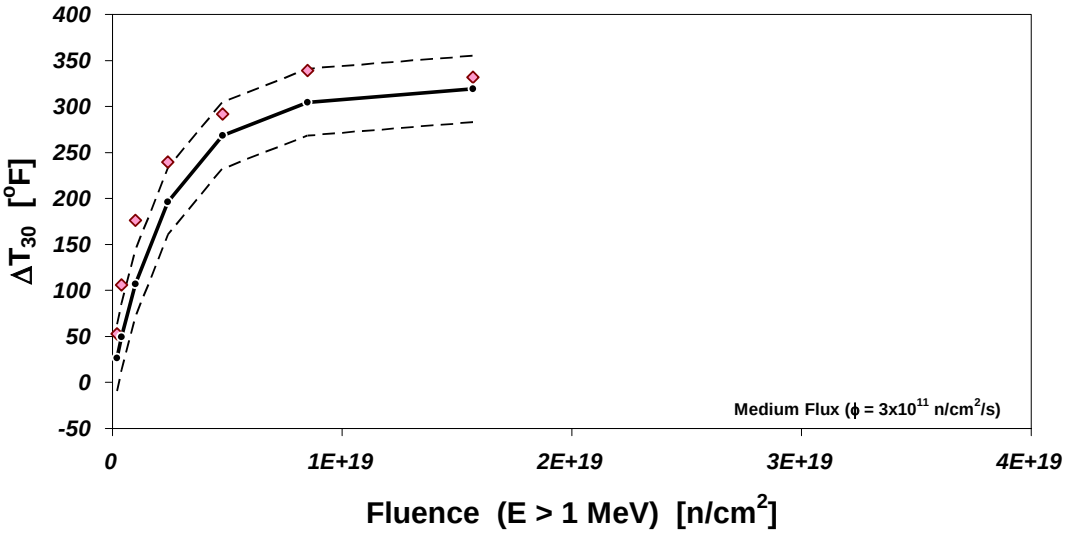
Medium Flux (ϕ = 3x10^11 n/cm^2/s)
ΔT30 [°F]
400
350
300
250
200
150
100
50
0
-50
0
1E+19
2E+19
3E+19
4E+19
Fluence (E > 1 MeV) [n/cm^2]

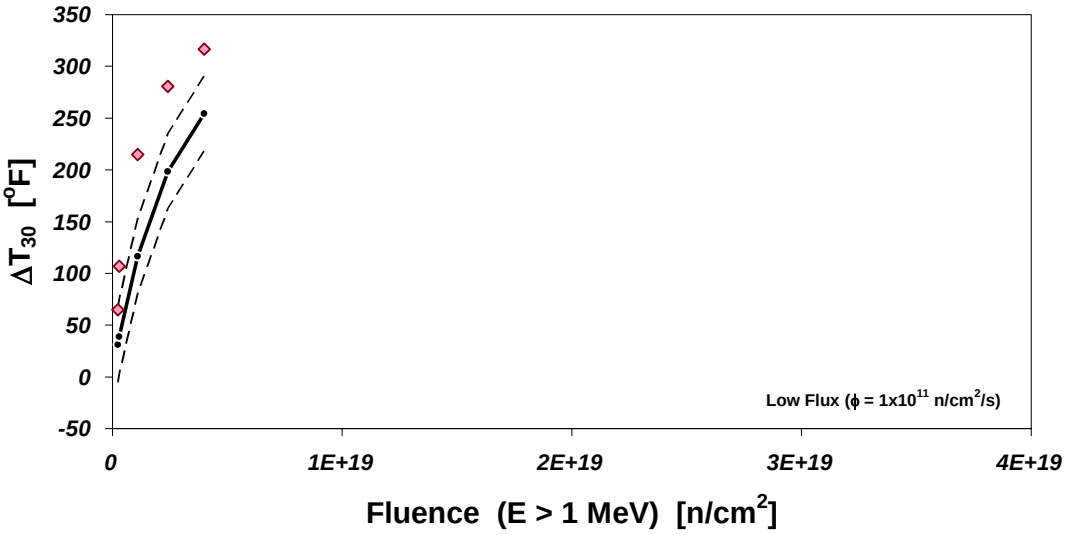
Low Flux (ϕ = 1x10^11 n/cm^2/s)
ΔT30 [°F]
350
300
250
200
150
100
50
0
-50
0
1E+19
2E+19
3E+19
4E+19
Fluence (E > 1 MeV) [n/cm^2]

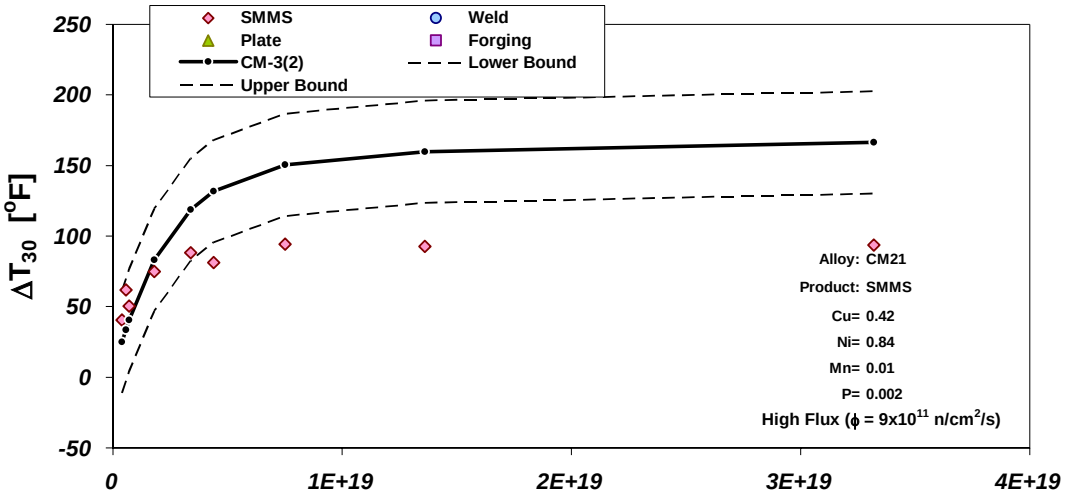
SMMS
Weld
Plate
Forging
CM-3(2)
Lower Bound
Upper Bound
ΔT30 [°F]
250
200
150
100
50
0
-50
0
1E+19
2E+19
3E+19
4E+19
Alloy: CM21
Product: SMMS
Cu= 0.42
Ni= 0.84
Mn= 0.01
P= 0.002
High Flux (ϕ = 9x10^11 n/cm^2/s)
Fluence (E > 1 MeV) [n/cm^2]

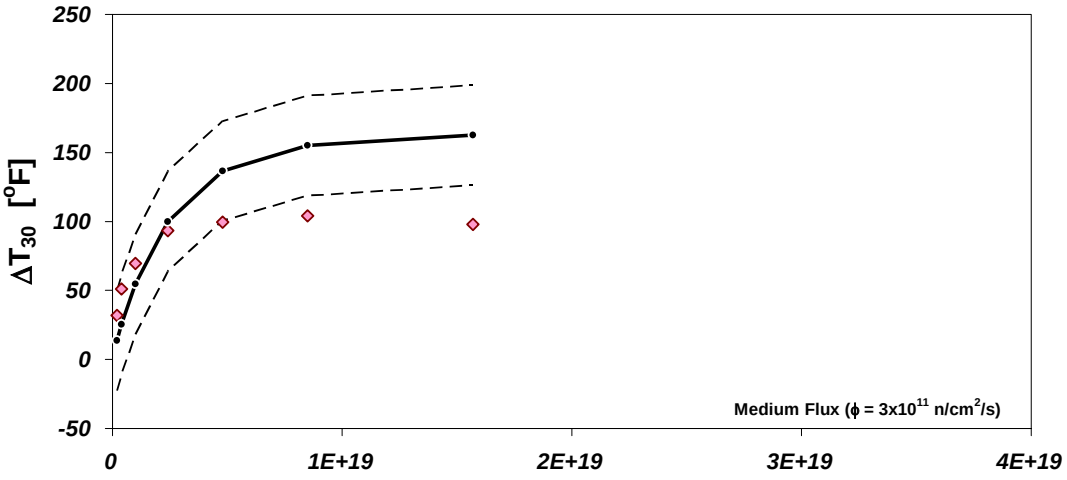
ΔT30 [°F]
250
200
150
100
50
0
-50
0
1E+19
2E+19
3E+19
4E+19
Medium Flux (ϕ = 3x10^11 n/cm^2/s)
Fluence (E > 1 MeV) [n/cm^2]

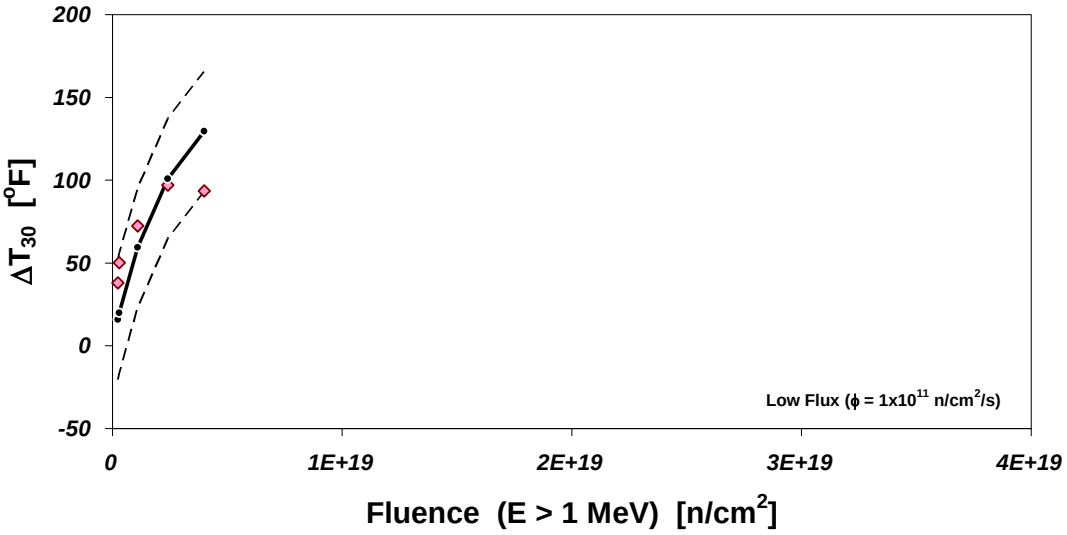
ΔT30 [°F]
200
150
100
50
0
-50
0
1E+19
2E+19
3E+19
4E+19
Low Flux (ϕ = 1x10^11 n/cm^2/s)
Fluence (E > 1 MeV) [n/cm^2]

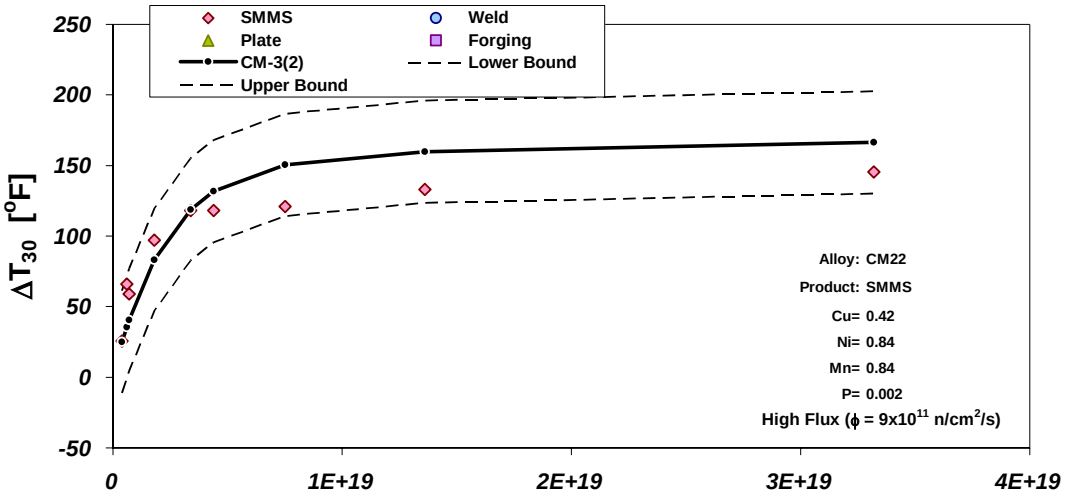
SMMS
Weld
Plate
Forging
CM-3(2)
Lower Bound
Upper Bound
Alloy: CM22
Product: SMMS
Cu= 0.42
Ni= 0.84
Mn= 0.84
P= 0.002
High Flux (ϕ = 9x10^11 n/cm^2/s)
ΔT30 [°F]
250
200
150
100
50
0
-50
0
1E+19
2E+19
3E+19
4E+19
Fluence (E > 1 MeV) [n/cm^2]

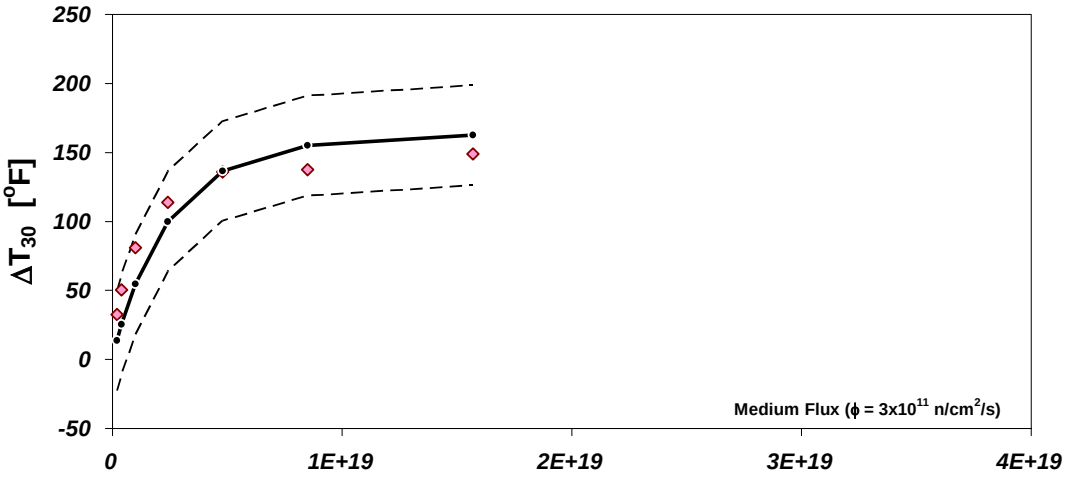
Medium Flux (ϕ = 3x10^11 n/cm^2/s)
ΔT30 [°F]
250
200
150
100
50
0
-50
0
1E+19
2E+19
3E+19
4E+19
Fluence (E > 1 MeV) [n/cm^2]

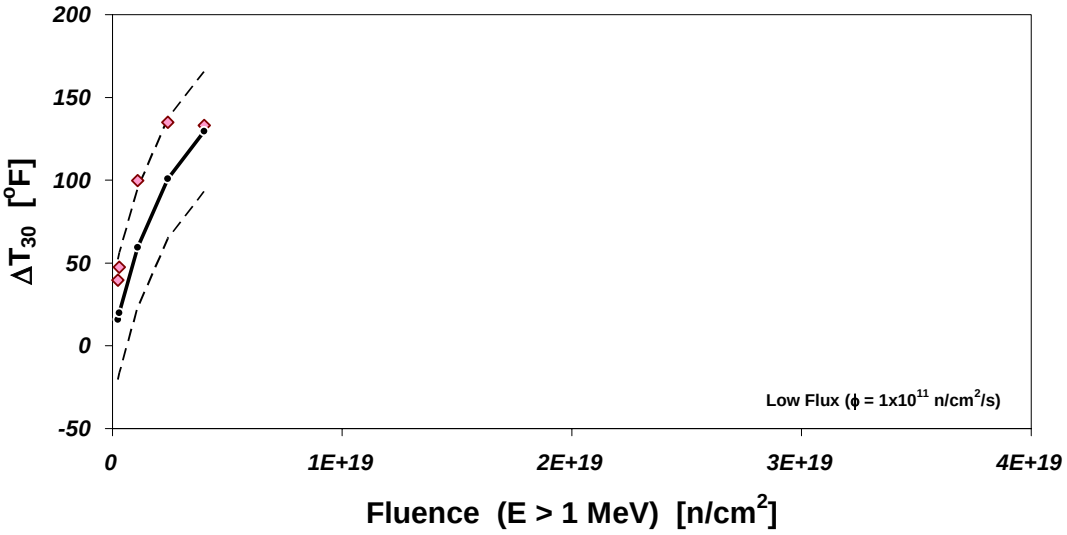
Low Flux (ϕ = 1x10^11 n/cm^2/s)
ΔT30 [°F]
200
150
100
50
0
-50
0
1E+19
2E+19
3E+19
4E+19
Fluence (E > 1 MeV) [n/cm^2]

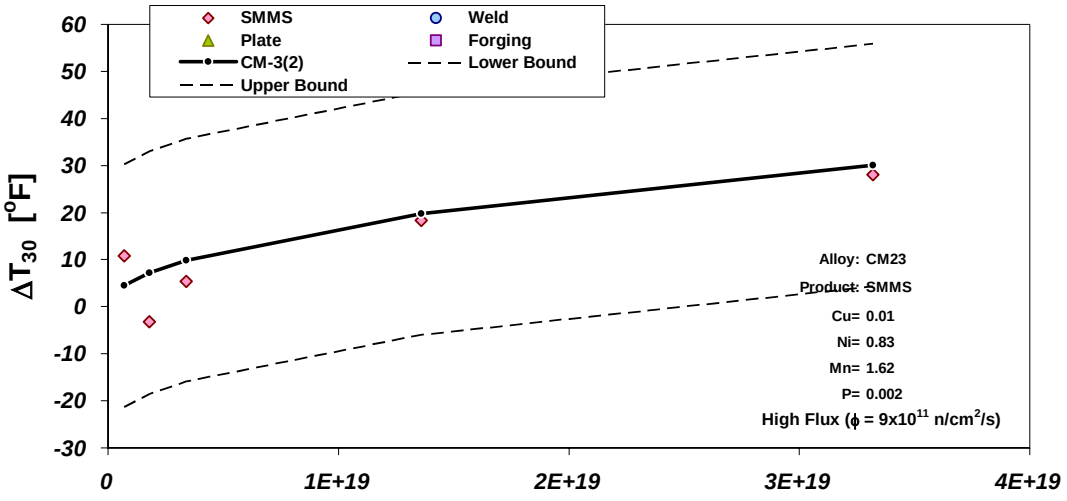
SMMS
Weld
Plate
Forging
CM-3(2)
Lower Bound
Upper Bound
Alloy: CM23
Product: SMMS
Cu= 0.01
Ni= 0.83
Mn= 1.62
P= 0.002
High Flux (ϕ = 9x10^11 n/cm^2/s)
ΔT30 [°F]
Fluence (E > 1 MeV) [n/cm^2]

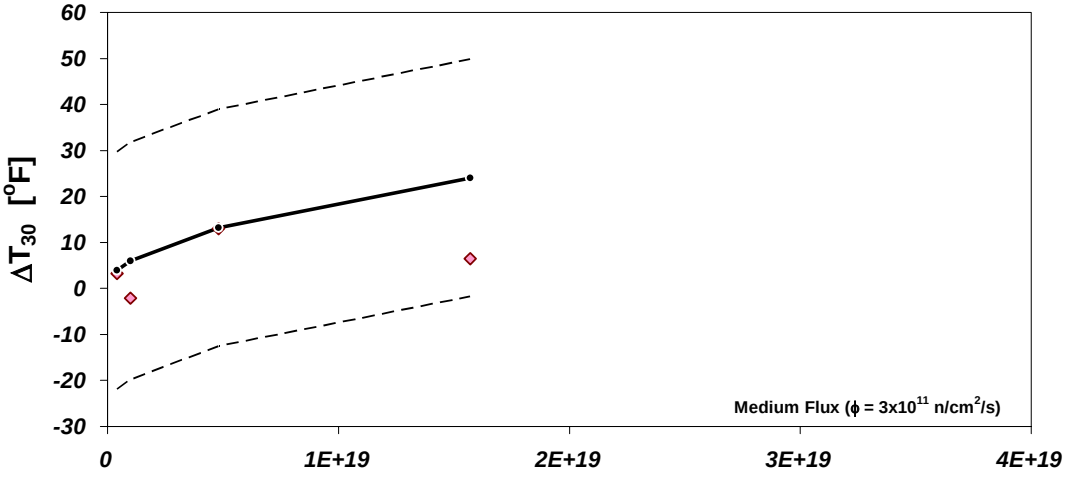
Medium Flux (ϕ = 3x10^11 n/cm^2/s)
ΔT30 [°F]
Fluence (E > 1 MeV) [n/cm^2]

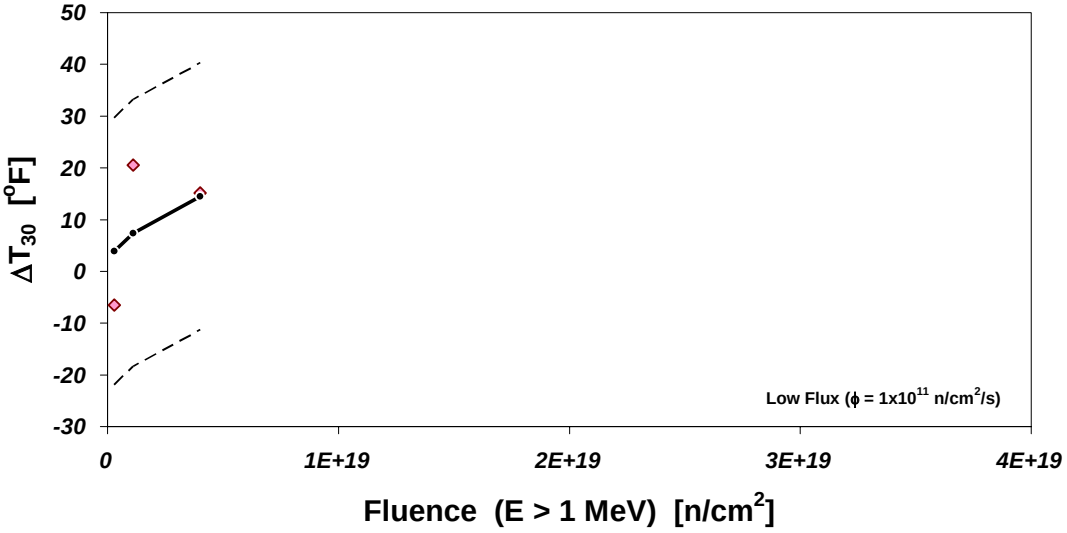
Low Flux (ϕ = 1x10^11 n/cm^2/s)
ΔT30 [°F]
Fluence (E > 1 MeV) [n/cm^2]

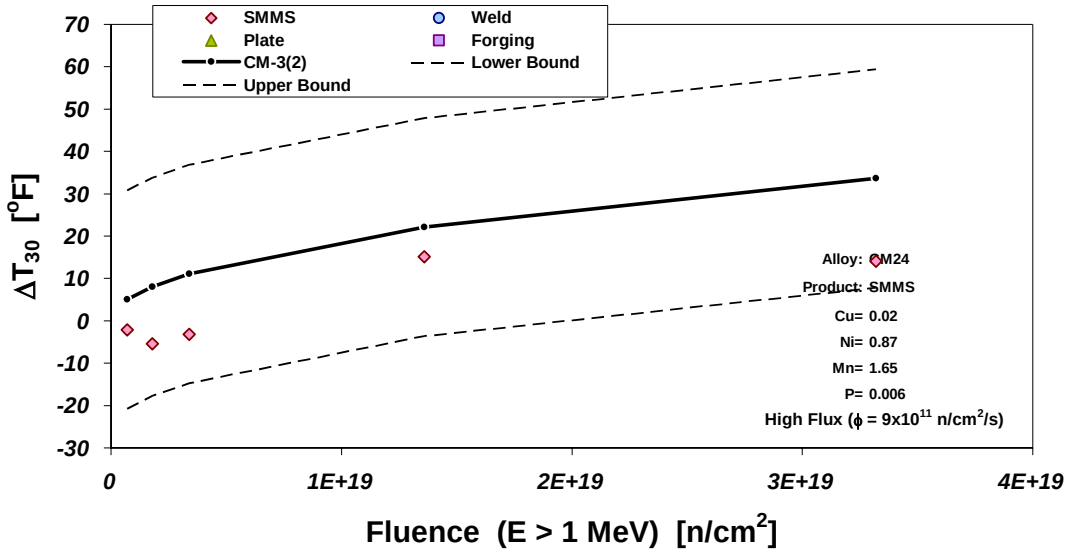
SMMS
Weld
Plate
Forging
CM-3(2)
Lower Bound
Upper Bound
Alloy: CM24
Product: SMMS
Cu= 0.02
Ni= 0.87
Mn= 1.65
P= 0.006
High Flux (ϕ = 9x10^11 n/cm^2/s)
ΔT30 [°F]
70
60
50
40
30
20
10
0
-10
-20
-30
0
1E+19
2E+19
3E+19
4E+19
Fluence (E > 1 MeV) [n/cm^2]

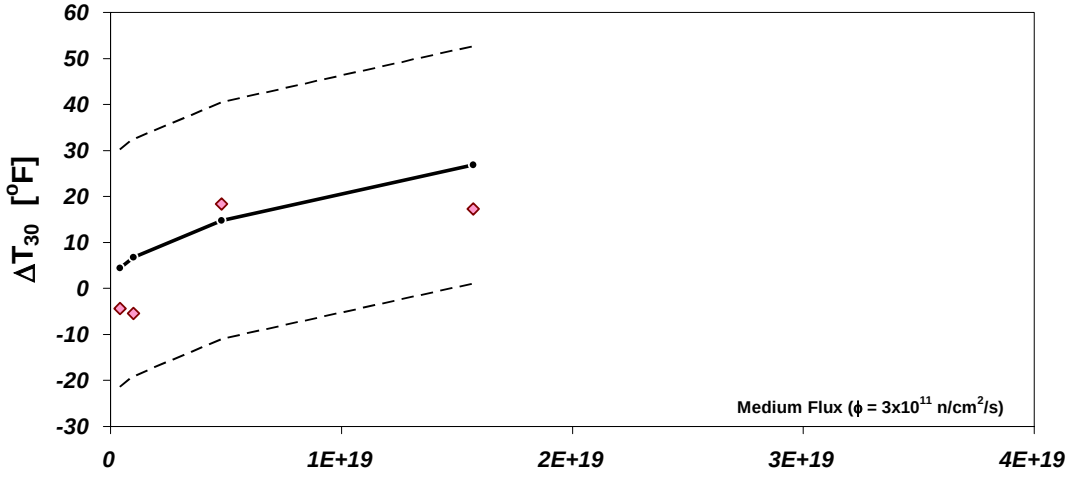
Medium Flux (ϕ = 3x10^11 n/cm^2/s)
ΔT30 [°F]
60
50
40
30
20
10
0
-10
-20
-30
0
1E+19
2E+19
3E+19
4E+19
Fluence (E > 1 MeV) [n/cm^2]

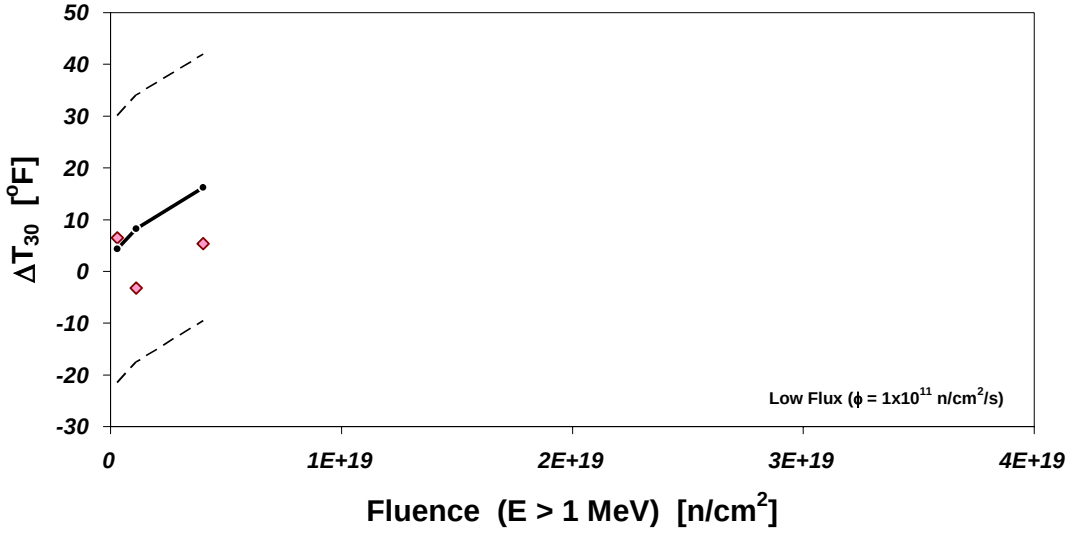
Low Flux (ϕ = 1x10^11 n/cm^2/s)
ΔT30 [°F]
50
40
30
20
10
0
-10
-20
-30
0
1E+19
2E+19
3E+19
4E+19
Fluence (E > 1 MeV) [n/cm^2]

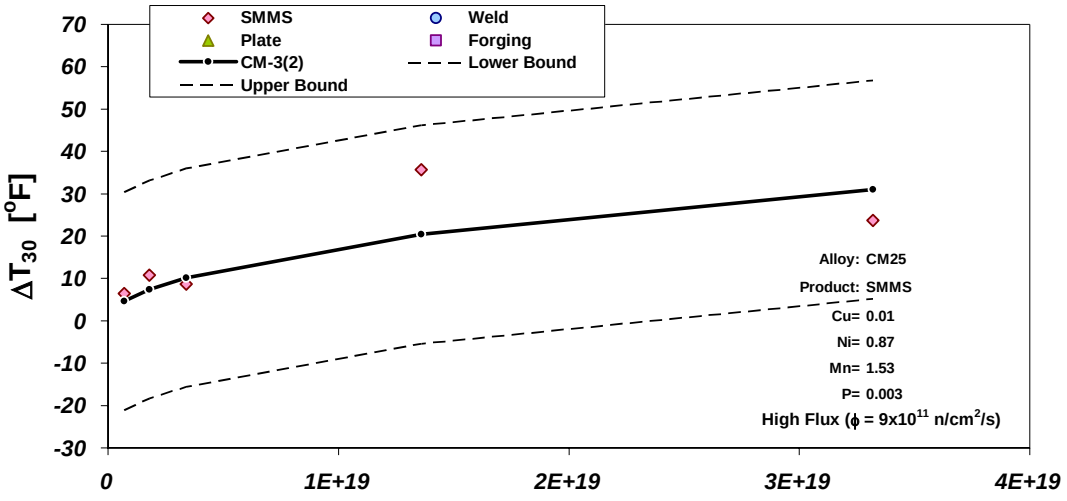
SMMS
Weld
Plate
Forging
CM-3(2)
Lower Bound
Upper Bound
70
60
50
40
30
20
10
0
-10
-20
-30
ΔT30 [°F]
Alloy: CM25
Product: SMMS
Cu= 0.01
Ni= 0.87
Mn= 1.53
P= 0.003
High Flux (ϕ = 9x10^11 n/cm^2/s)
0
1E+19
2E+19
3E+19
4E+19
Fluence (E > 1 MeV) [n/cm^2]

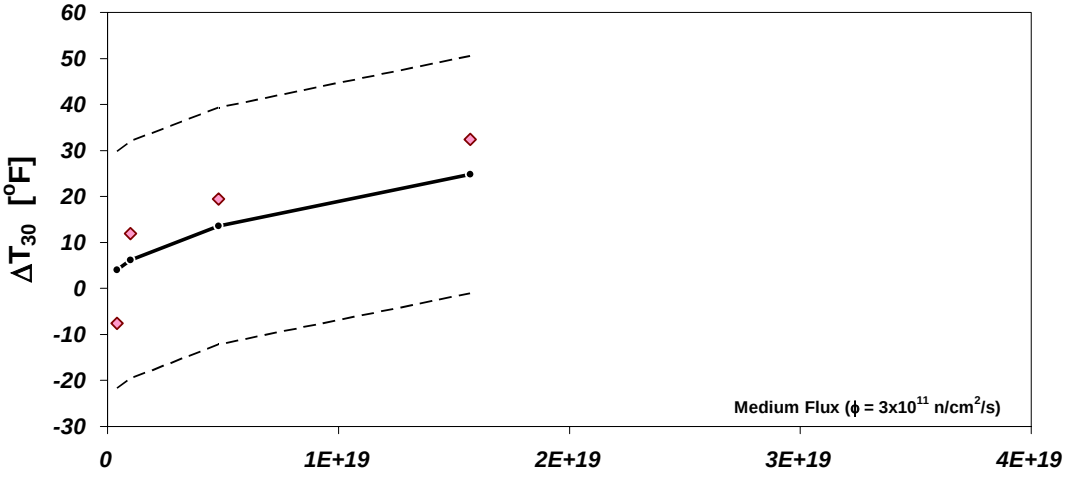
60
50
40
30
20
10
0
-10
-20
-30
ΔT30 [°F]
Medium Flux (ϕ = 3x10^11 n/cm^2/s)
0
1E+19
2E+19
3E+19
4E+19
Fluence (E > 1 MeV) [n/cm^2]

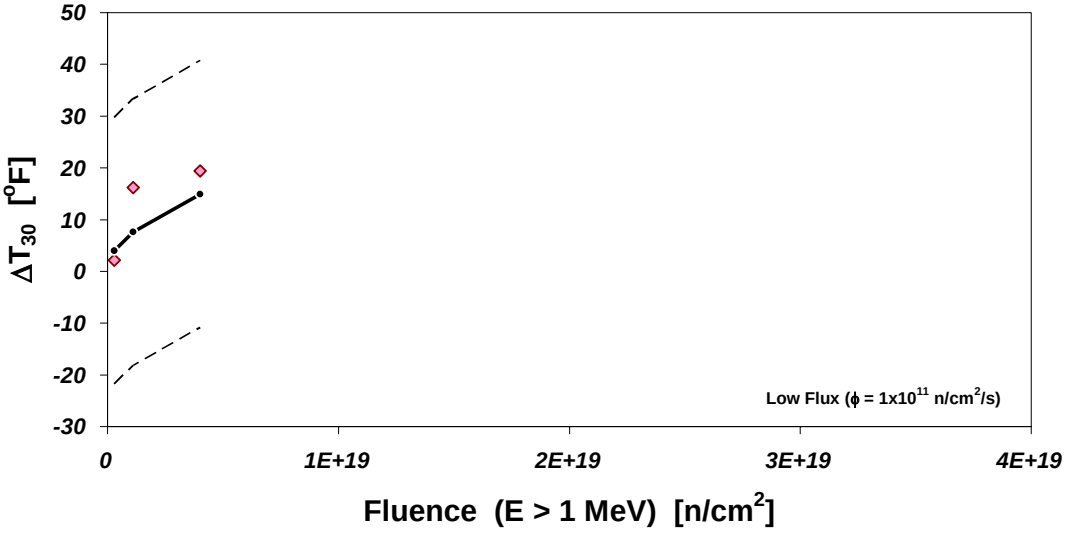
50
40
30
20
10
0
-10
-20
-30
ΔT30 [°F]
Low Flux (ϕ = 1x10^11 n/cm^2/s)
0
1E+19
2E+19
3E+19
4E+19
Fluence (E > 1 MeV) [n/cm^2]

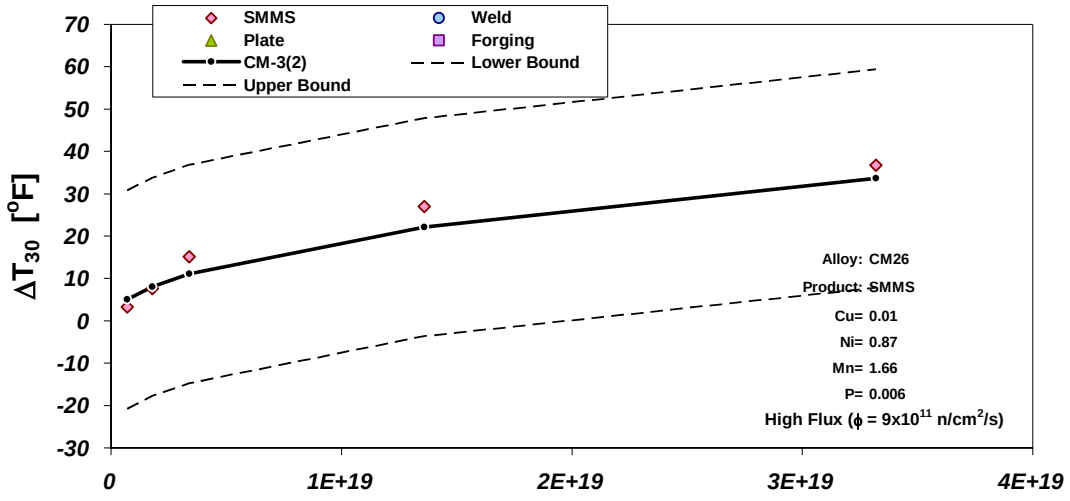
SMMS
Weld
Plate
Forging
CM-3(2)
Lower Bound
Upper Bound
70
60
50
40
30
20
10
0
-10
-20
-30
ΔT30 [°F]
Alloy: CM26
Product: SMMS
Cu= 0.01
Ni= 0.87
Mn= 1.66
P= 0.006
High Flux (ϕ = 9x10^11 n/cm^2/s)
0
1E+19
2E+19
3E+19
4E+19
Fluence (E > 1 MeV) [n/cm^2]

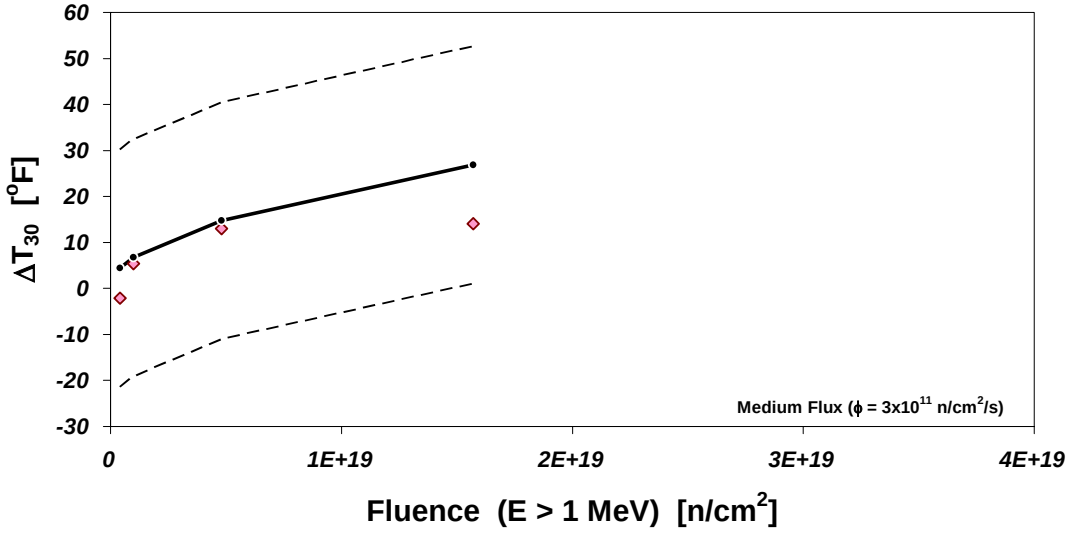
60
50
40
30
20
10
0
-10
-20
-30
ΔT30 [°F]
Medium Flux (ϕ = 3x10^11 n/cm^2/s)
0
1E+19
2E+19
3E+19
4E+19
Fluence (E > 1 MeV) [n/cm^2]

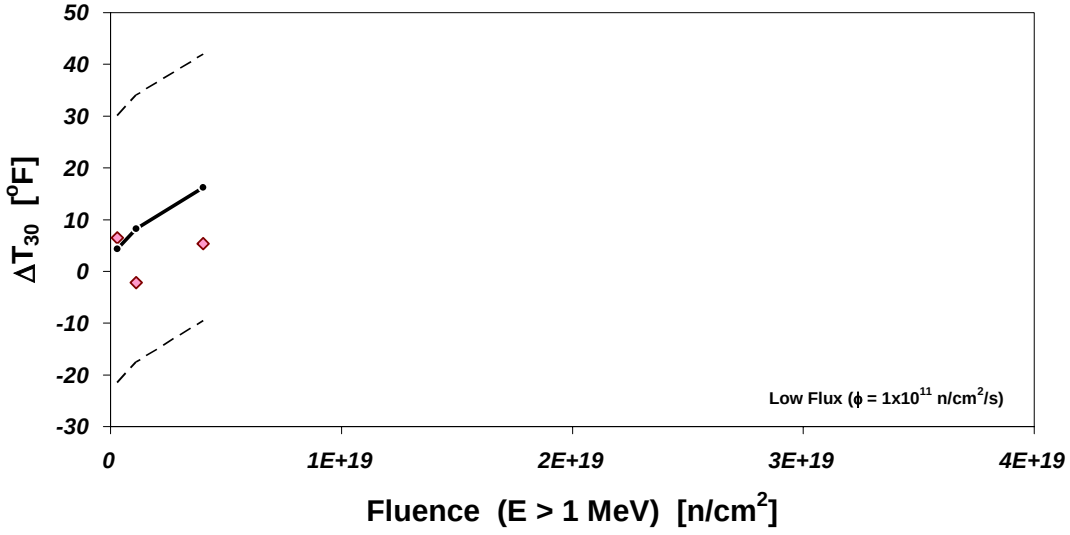
50
40
30
20
10
0
-10
-20
-30
ΔT30 [°F]
Low Flux (ϕ = 1x10^11 n/cm^2/s)
0
1E+19
2E+19
3E+19
4E+19
Fluence (E > 1 MeV) [n/cm^2]

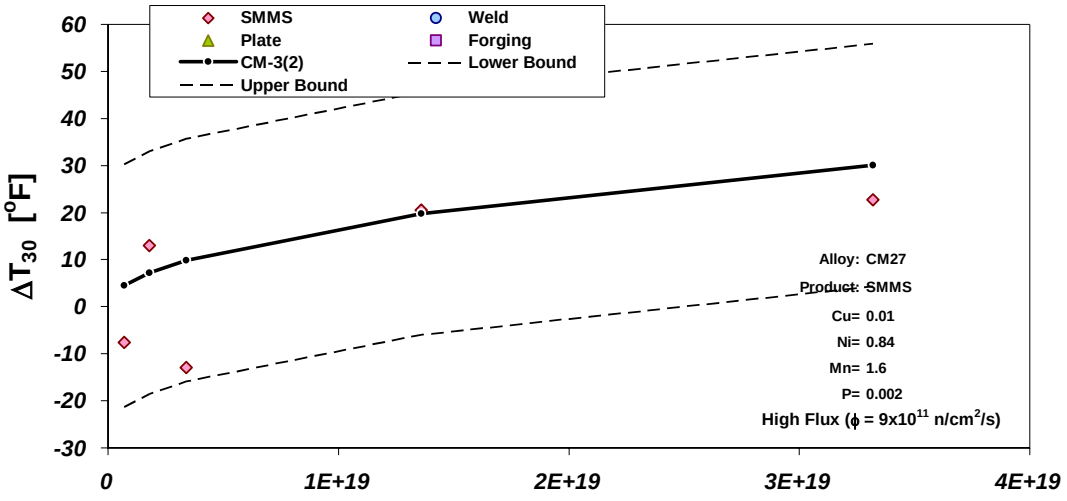
SMMS
Weld
Plate
Forging
CM-3(2)
Lower Bound
Upper Bound
Alloy: CM27
Product: SMMS
Cu= 0.01
Ni= 0.84
Mn= 1.6
P= 0.002
High Flux (ϕ = 9x10^11 n/cm^2/s)
ΔT30 [°F]
60
50
40
30
20
10
0
-10
-20
-30
0
1E+19
2E+19
3E+19
4E+19
Fluence (E > 1 MeV) [n/cm^2]

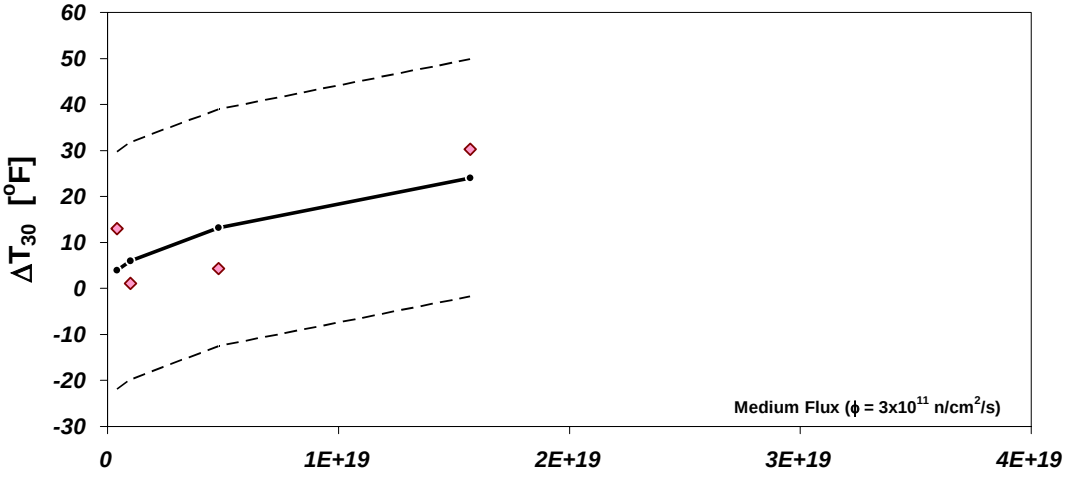
Medium Flux (ϕ = 3x10^11 n/cm^2/s)
ΔT30 [°F]
60
50
40
30
20
10
0
-10
-20
-30
0
1E+19
2E+19
3E+19
4E+19
Fluence (E > 1 MeV) [n/cm^2]

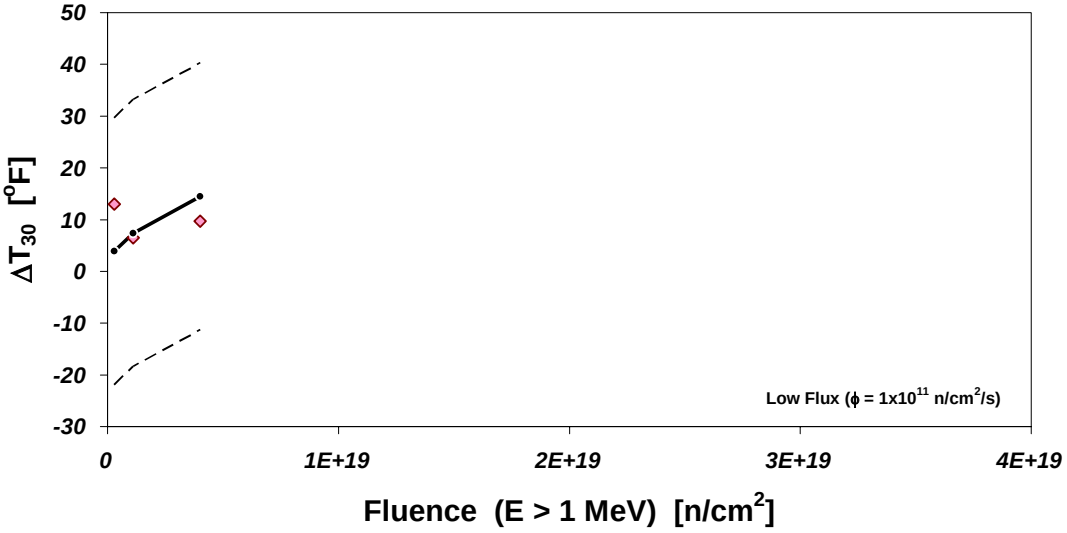
Low Flux (ϕ = 1x10^11 n/cm^2/s)
ΔT30 [°F]
50
40
30
20
10
0
-10
-20
-30
0
1E+19
2E+19
3E+19
4E+19
Fluence (E > 1 MeV) [n/cm^2]

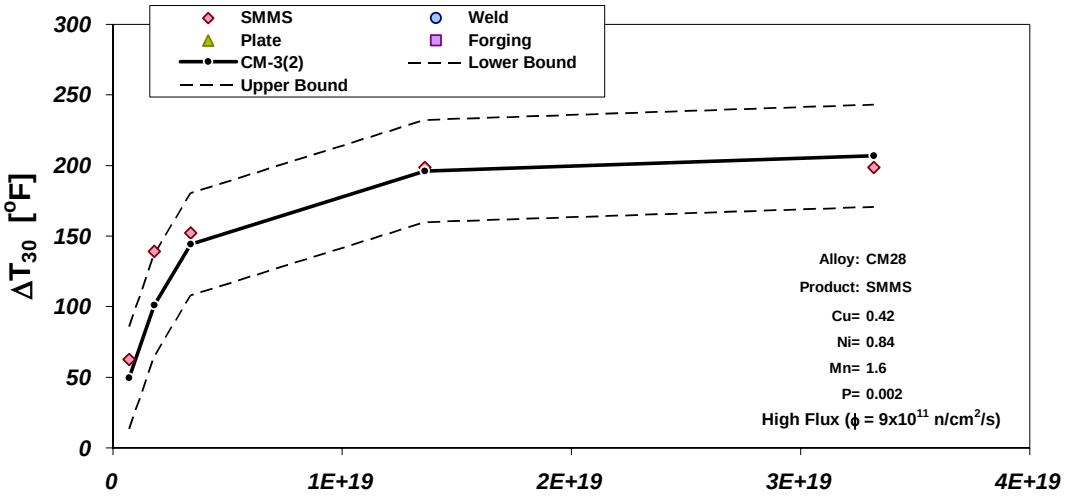
SMMS
Weld
Plate
Forging
CM-3(2)
Lower Bound
Upper Bound
ΔT30 [°F]
300
250
200
150
100
50
0
Alloy: CM28
Product: SMMS
Cu= 0.42
Ni= 0.84
Mn= 1.6
P= 0.002
High Flux (ϕ = 9x10^11 n/cm^2/s)
0
1E+19
2E+19
3E+19
4E+19
Fluence (E > 1 MeV) [n/cm^2]

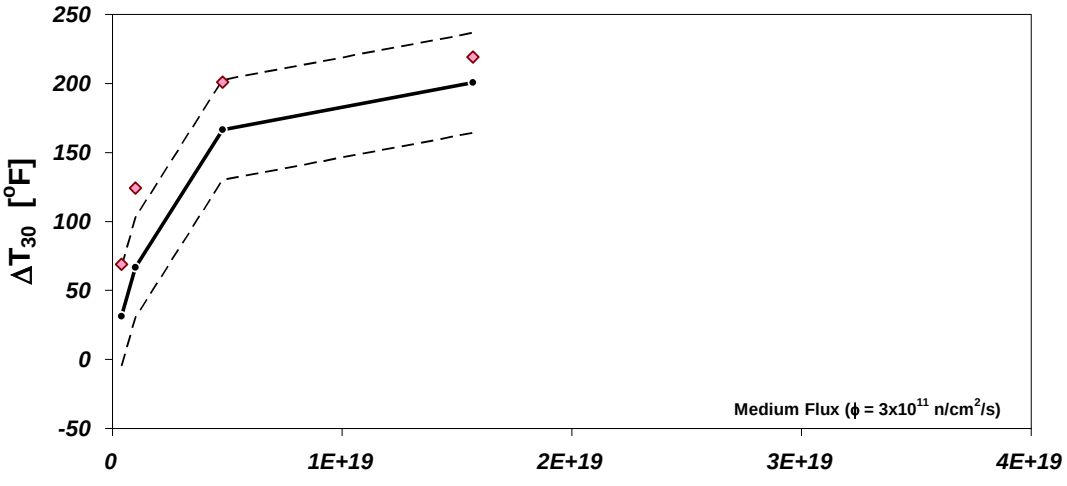
ΔT30 [°F]
250
200
150
100
50
0
-50
Medium Flux (ϕ = 3x10^11 n/cm^2/s)
0
1E+19
2E+19
3E+19
4E+19
Fluence (E > 1 MeV) [n/cm^2]

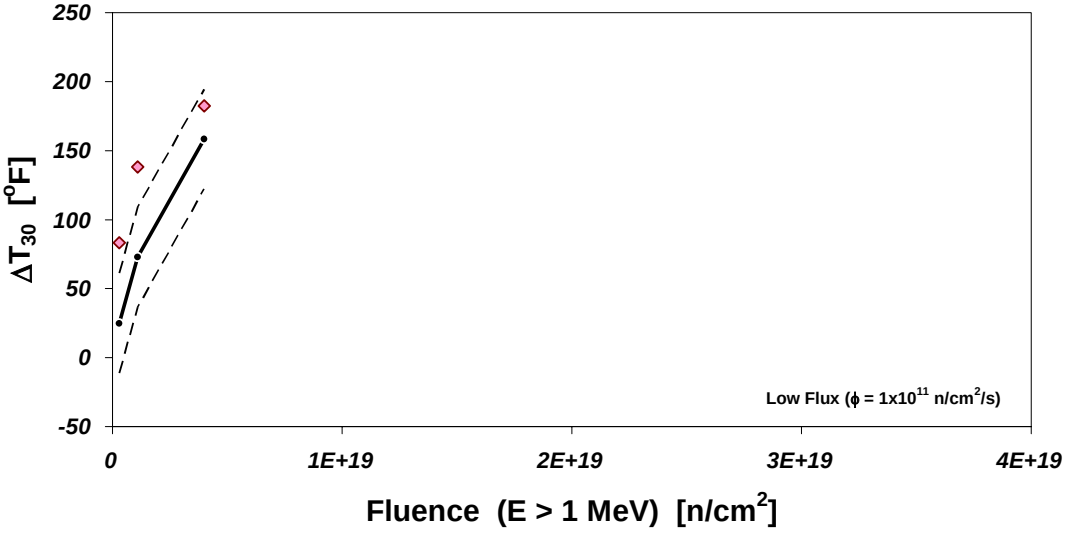
ΔT30 [°F]
250
200
150
100
50
0
-50
Low Flux (ϕ = 1x10^11 n/cm^2/s)
0
1E+19
2E+19
3E+19
4E+19
Fluence (E > 1 MeV) [n/cm^2]

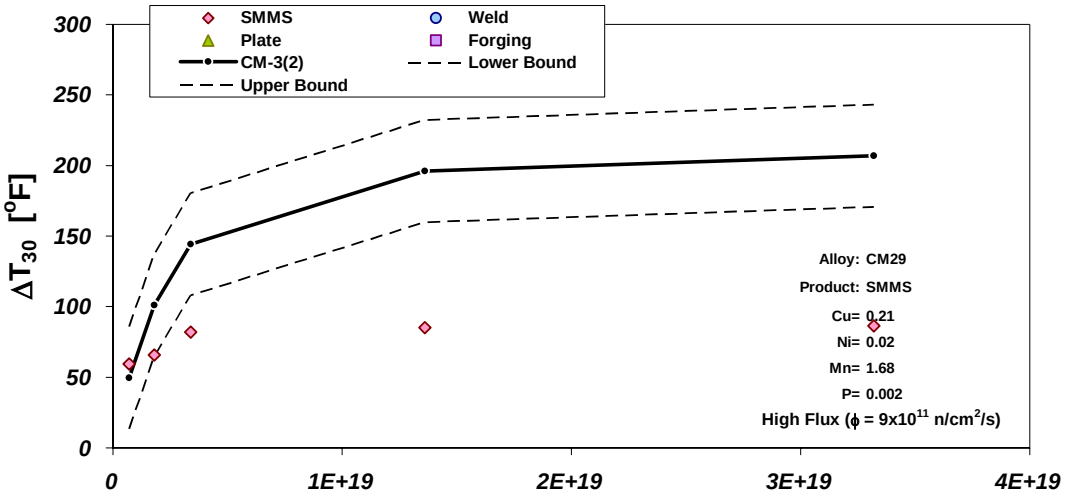
SMMS
Weld
Plate
Forging
CM-3(2)
Lower Bound
Upper Bound
Alloy: CM29
Product: SMMS
Cu= 0.21
Ni= 0.02
Mn= 1.68
P= 0.002
High Flux (ϕ = 9x10^11 n/cm^2/s)
ΔT30 [°F]
300
250
200
150
100
50
0
0
1E+19
2E+19
3E+19
4E+19
Fluence (E > 1 MeV) [n/cm^2]

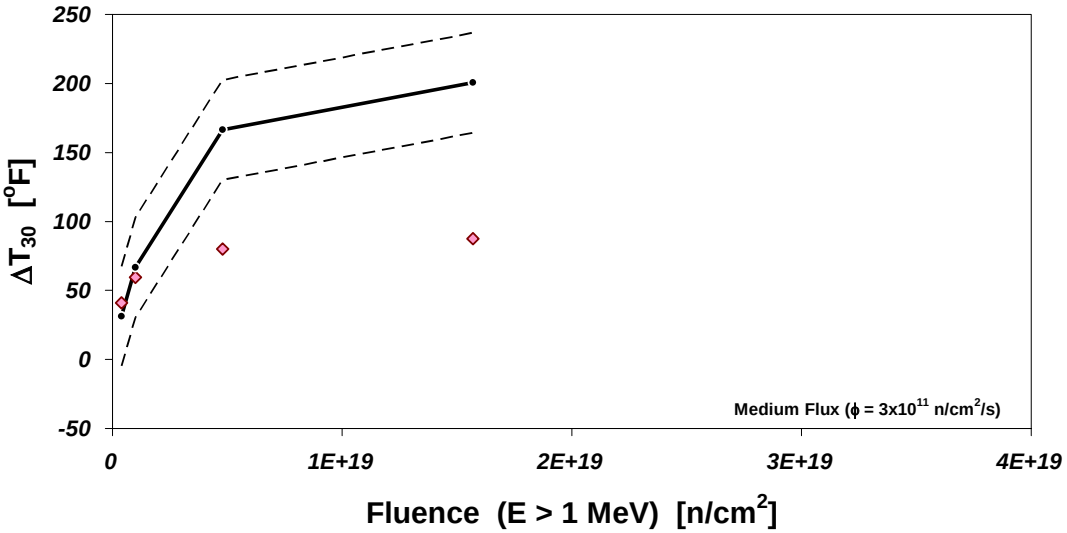
Medium Flux (ϕ = 3x10^11 n/cm^2/s)
ΔT30 [°F]
250
200
150
100
50
0
-50
0
1E+19
2E+19
3E+19
4E+19
Fluence (E > 1 MeV) [n/cm^2]

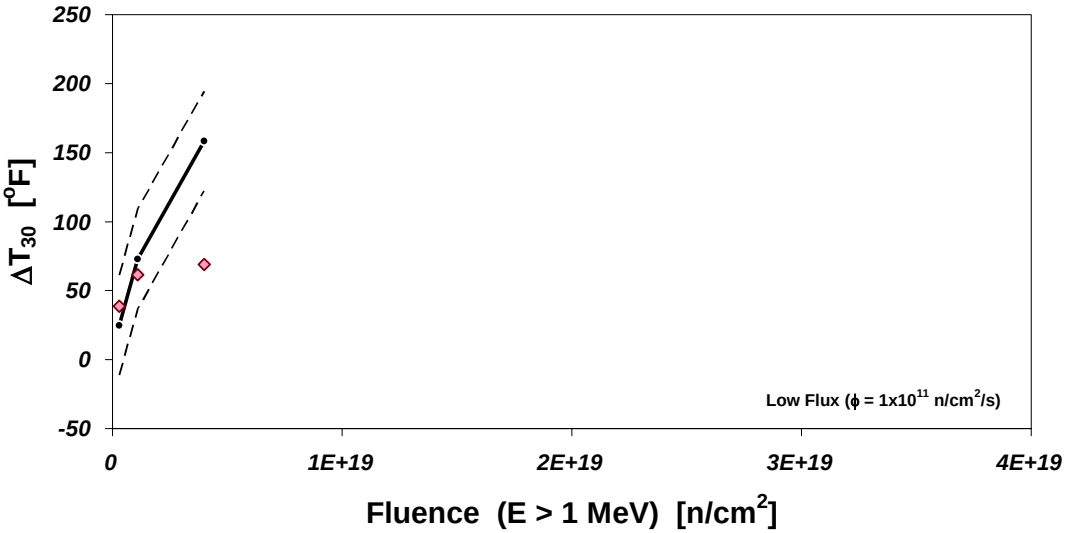
Low Flux (ϕ = 1x10^11 n/cm^2/s)
ΔT30 [°F]
250
200
150
100
50
0
-50
0
1E+19
2E+19
3E+19
4E+19
Fluence (E > 1 MeV) [n/cm^2]

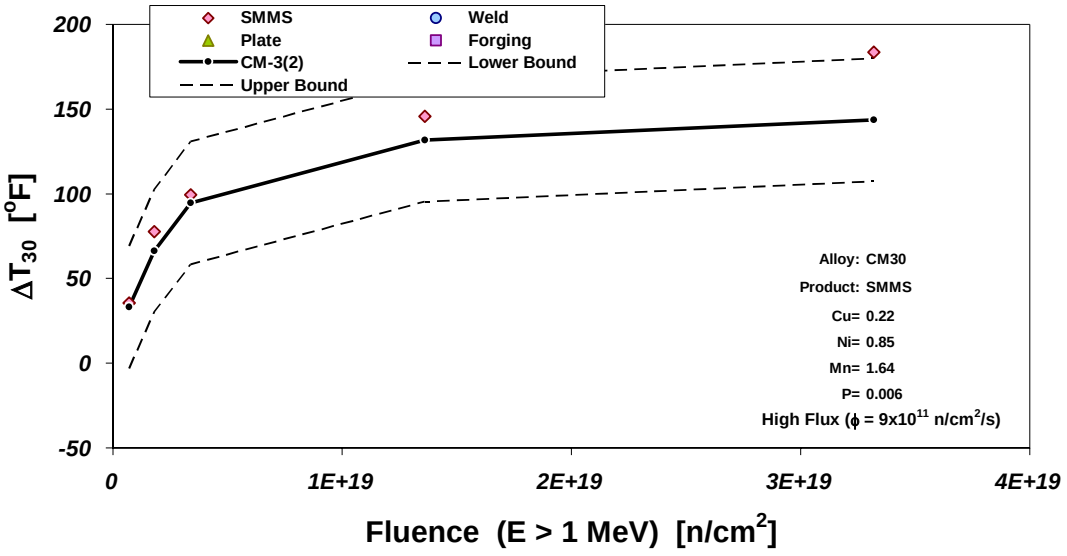
SMMS
Weld
Plate
Forging
CM-3(2)
Lower Bound
Upper Bound
Alloy: CM30
Product: SMMS
Cu= 0.22
Ni= 0.85
Mn= 1.64
P= 0.006
High Flux (ϕ = 9x10^11 n/cm^2/s)
ΔT30 [°F]
200
150
100
50
0
-50
0
1E+19
2E+19
3E+19
4E+19
Fluence (E > 1 MeV) [n/cm^2]

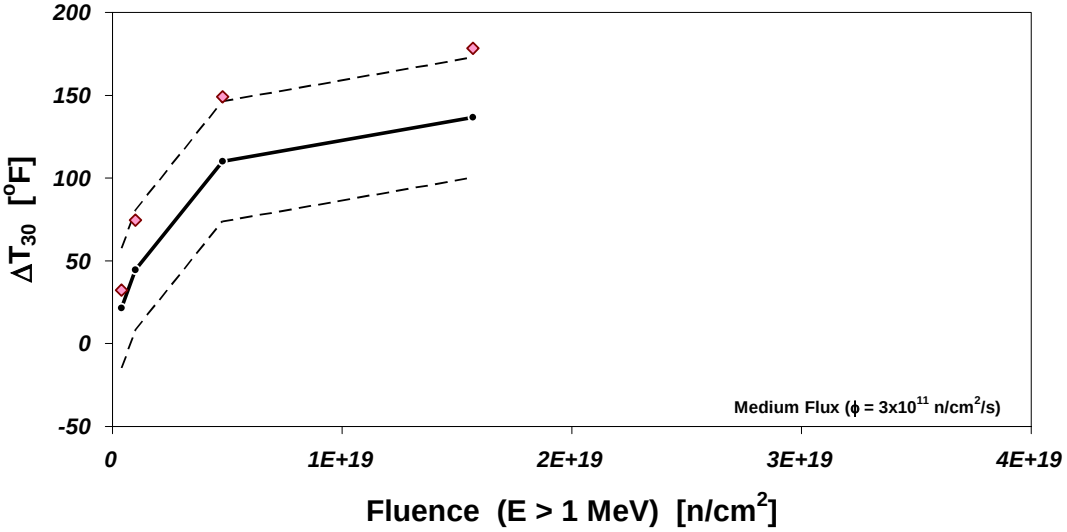
Medium Flux (ϕ = 3x10^11 n/cm^2/s)
ΔT30 [°F]
200
150
100
50
0
-50
0
1E+19
2E+19
3E+19
4E+19
Fluence (E > 1 MeV) [n/cm^2]

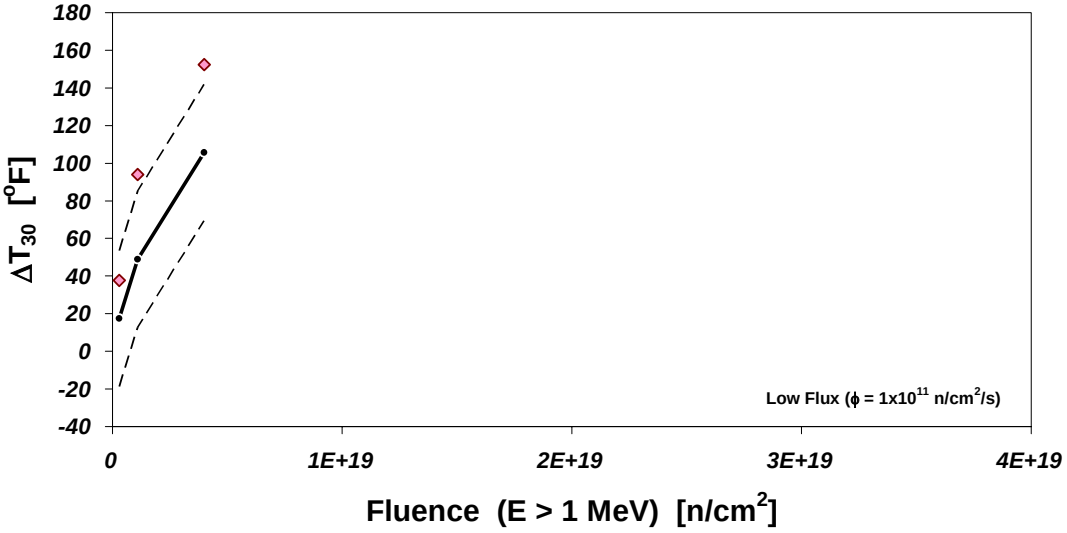
Low Flux (ϕ = 1x10^11 n/cm^2/s)
ΔT30 [°F]
180
160
140
120
100
80
60
40
20
0
-20
-40
0
1E+19
2E+19
3E+19
4E+19
Fluence (E > 1 MeV) [n/cm^2]

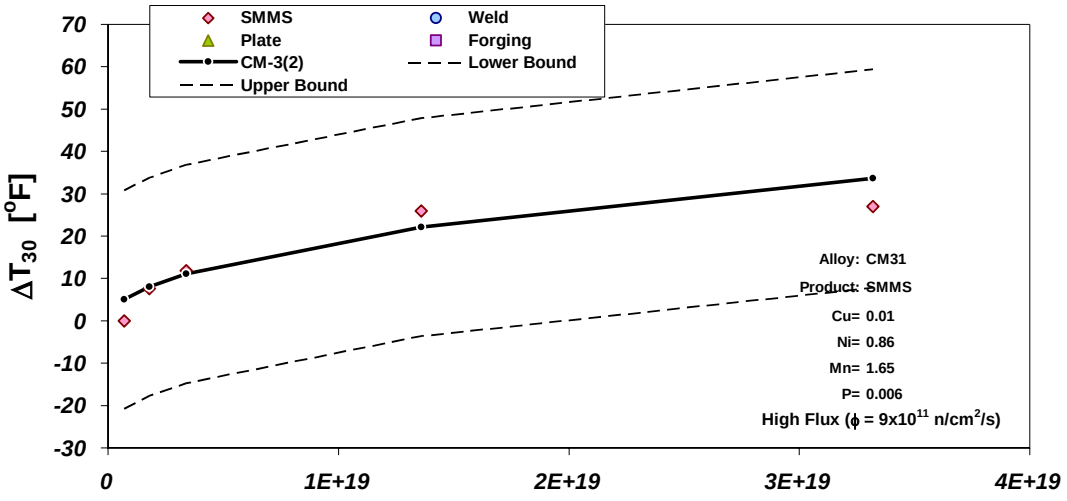
SMMS
Weld
Plate
Forging
CM-3(2)
Lower Bound
Upper Bound
Alloy: CM31
Product: SMMS
Cu= 0.01
Ni= 0.86
Mn= 1.65
P= 0.006
High Flux (ϕ = 9x10^11 n/cm^2/s)
ΔT30 [°F]
70
60
50
40
30
20
10
0
-10
-20
-30
0
1E+19
2E+19
3E+19
4E+19
Fluence (E > 1 MeV) [n/cm^2]

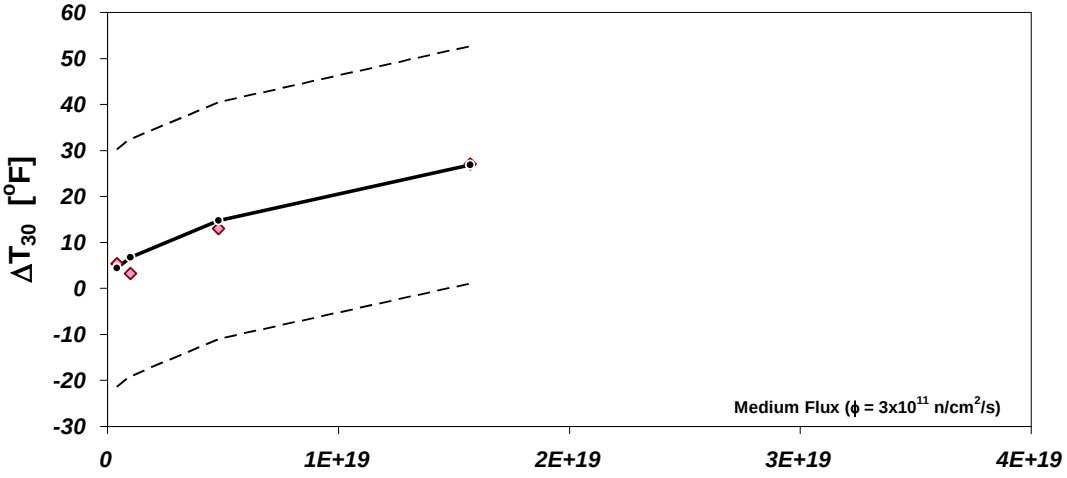
Medium Flux (ϕ = 3x10^11 n/cm^2/s)
ΔT30 [°F]
60
50
40
30
20
10
0
-10
-20
-30
0
1E+19
2E+19
3E+19
4E+19
Fluence (E > 1 MeV) [n/cm^2]

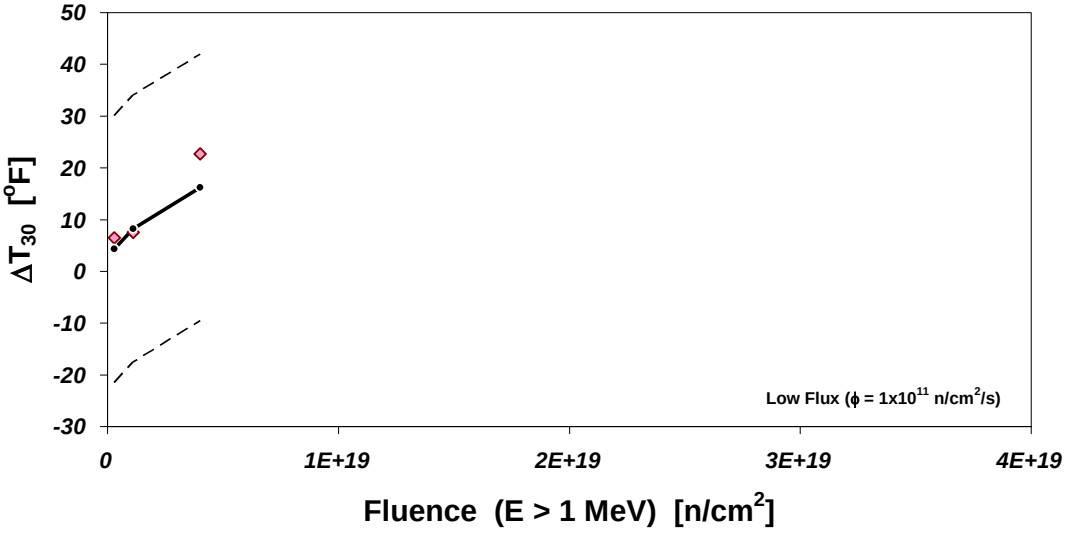
Low Flux (ϕ = 1x10^11 n/cm^2/s)
ΔT30 [°F]
50
40
30
20
10
0
-10
-20
-30
0
1E+19
2E+19
3E+19
4E+19
Fluence (E > 1 MeV) [n/cm^2]

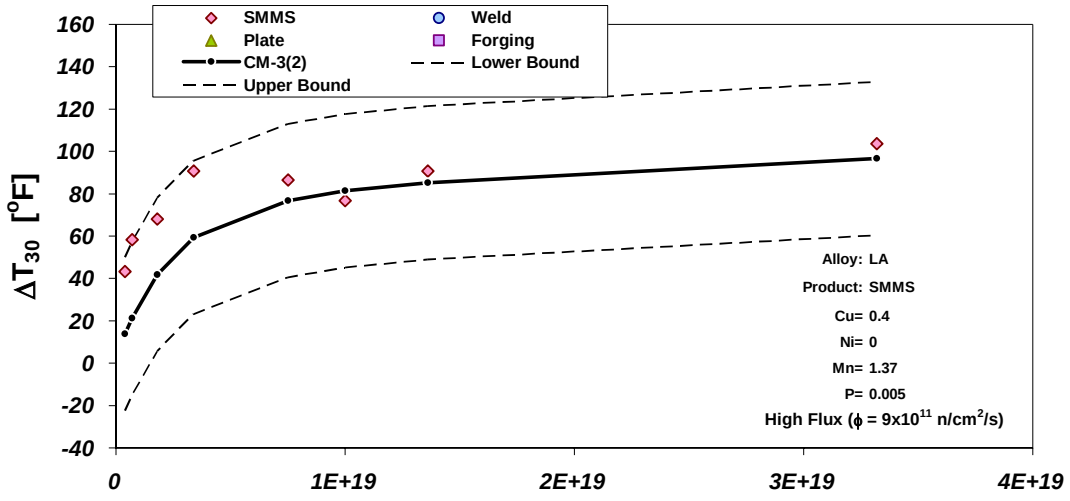
SMMS
Weld
Plate
Forging
CM-3(2)
Lower Bound
Upper Bound
ΔT30 [°F]
Alloy: LA
Product: SMMS
Cu= 0.4
Ni= 0
Mn= 1.37
P= 0.005
High Flux (ϕ = 9x10^11 n/cm^2/s)
Fluence (E > 1 MeV) [n/cm^2]

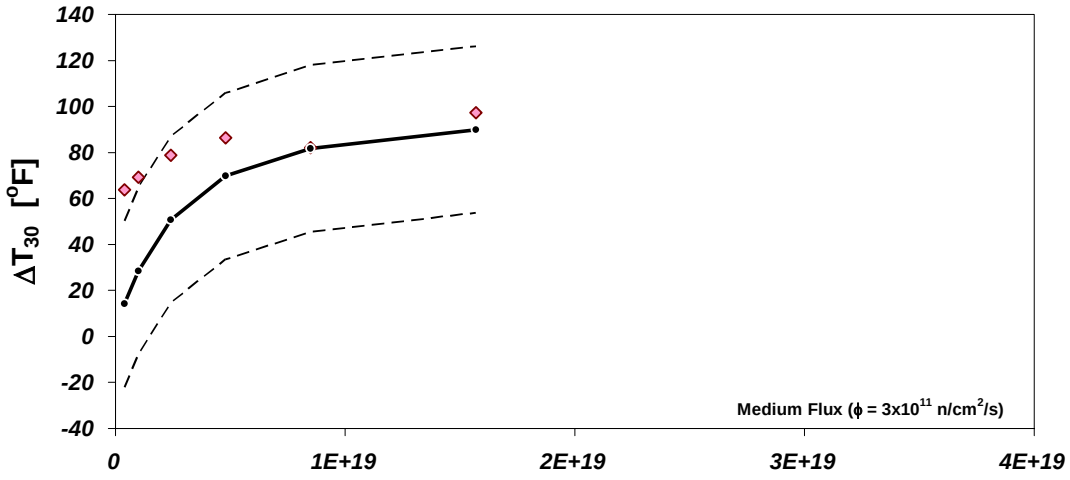
ΔT30 [°F]
Medium Flux (ϕ = 3x10^11 n/cm^2/s)
Fluence (E > 1 MeV) [n/cm^2]

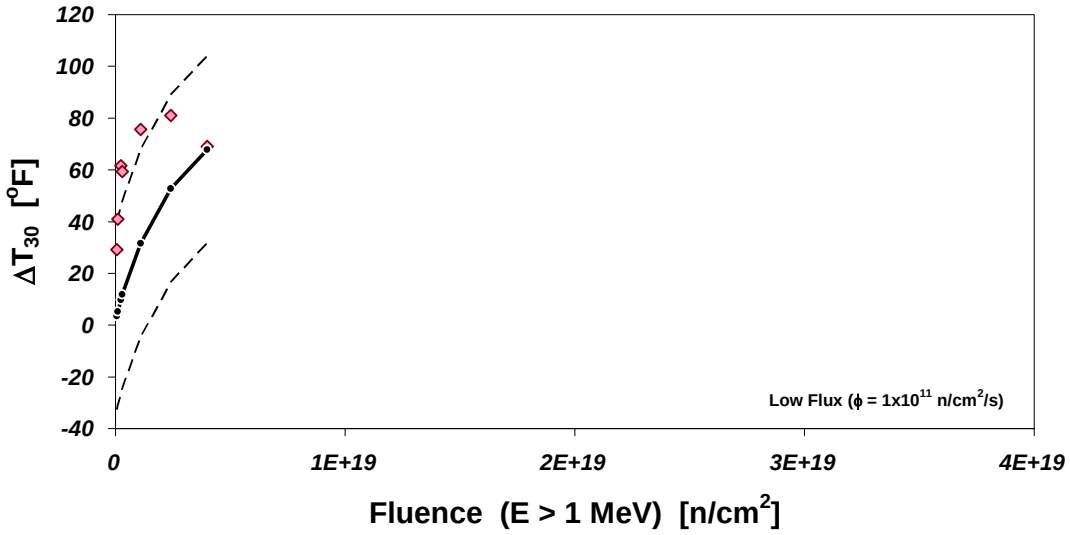
ΔT30 [°F]
Low Flux (ϕ = 1x10^11 n/cm^2/s)
Fluence (E > 1 MeV) [n/cm^2]

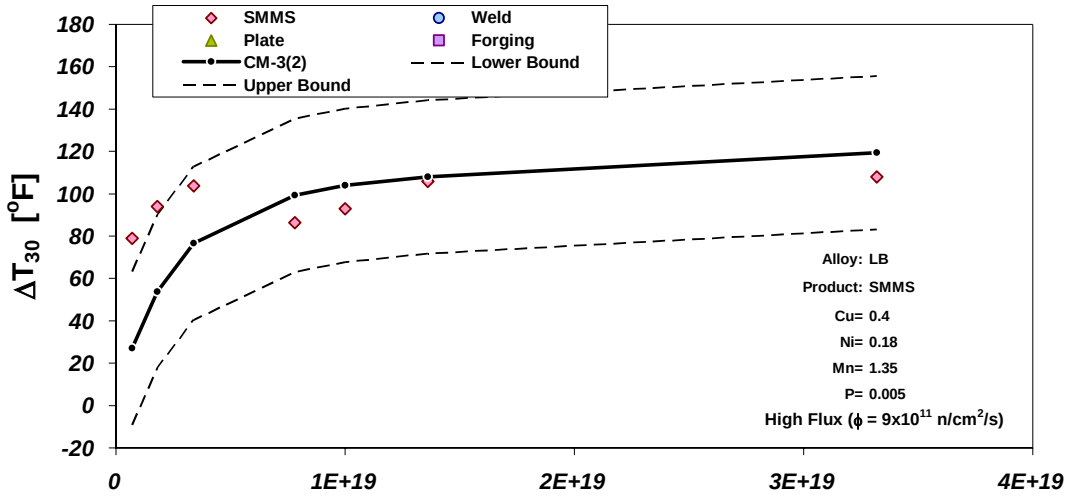
SMMS
Weld
Plate
Forging
CM-3(2)
Lower Bound
Upper Bound
ΔT30 [°F]
Alloy: LB
Product: SMMS
Cu= 0.4
Ni= 0.18
Mn= 1.35
P= 0.005
High Flux (ϕ = 9x10^11 n/cm^2/s)
Fluence (E > 1 MeV) [n/cm^2]

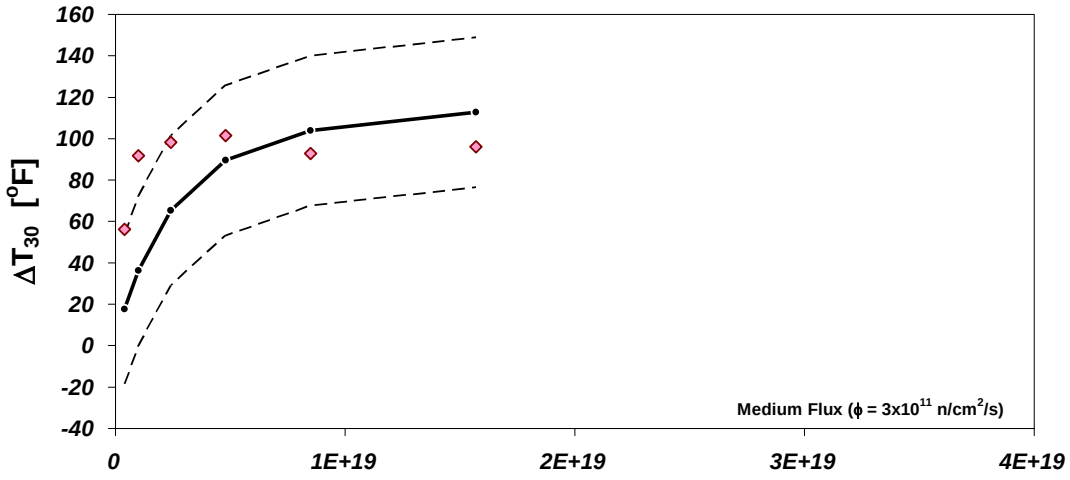
ΔT30 [°F]
Medium Flux (ϕ = 3x10^11 n/cm^2/s)
Fluence (E > 1 MeV) [n/cm^2]

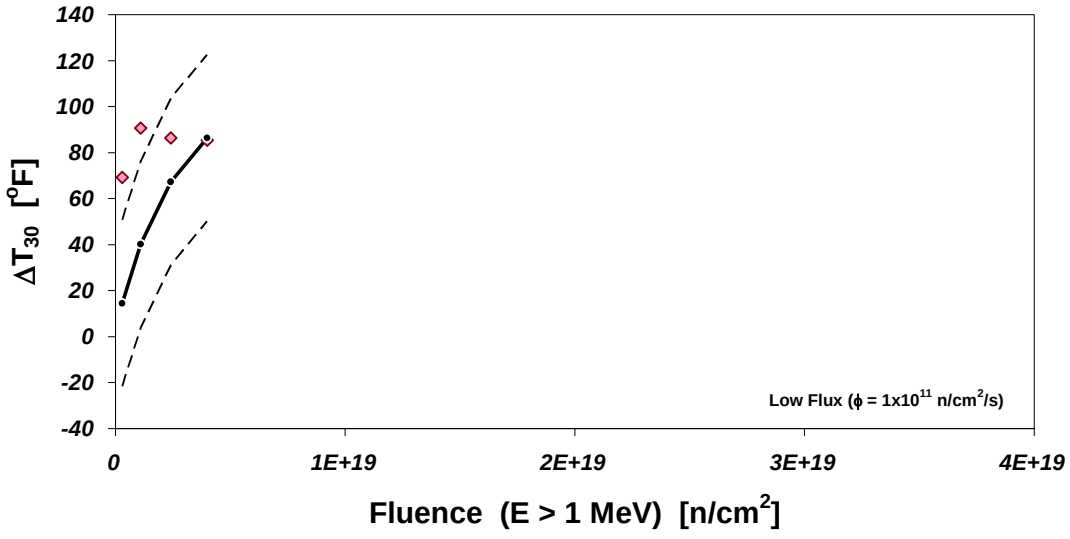
ΔT30 [°F]
Low Flux (ϕ = 1x10^11 n/cm^2/s)
Fluence (E > 1 MeV) [n/cm^2]

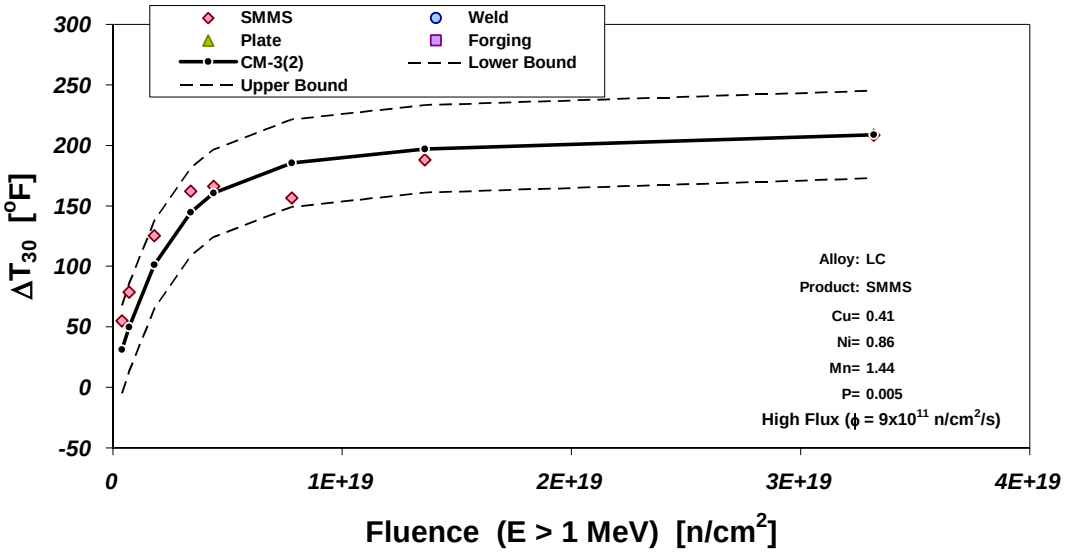
SMMS
Weld
Plate
Forging
CM-3(2)
Lower Bound
Upper Bound
Alloy: LC
Product: SMMS
Cu= 0.41
Ni= 0.86
Mn= 1.44
P= 0.005
High Flux (ϕ = 9x10^11 n/cm^2/s)
ΔT30 [°F]
300
250
200
150
100
50
0
-50
0
1E+19
2E+19
3E+19
4E+19
Fluence (E > 1 MeV) [n/cm^2]

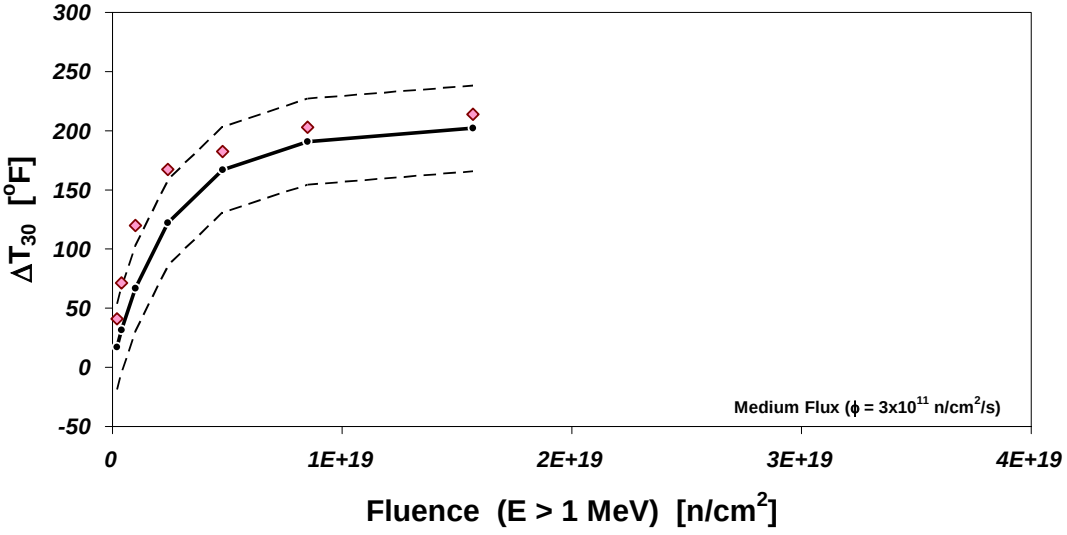
Medium Flux (ϕ = 3x10^11 n/cm^2/s)
ΔT30 [°F]
300
250
200
150
100
50
0
-50
0
1E+19
2E+19
3E+19
4E+19
Fluence (E > 1 MeV) [n/cm^2]

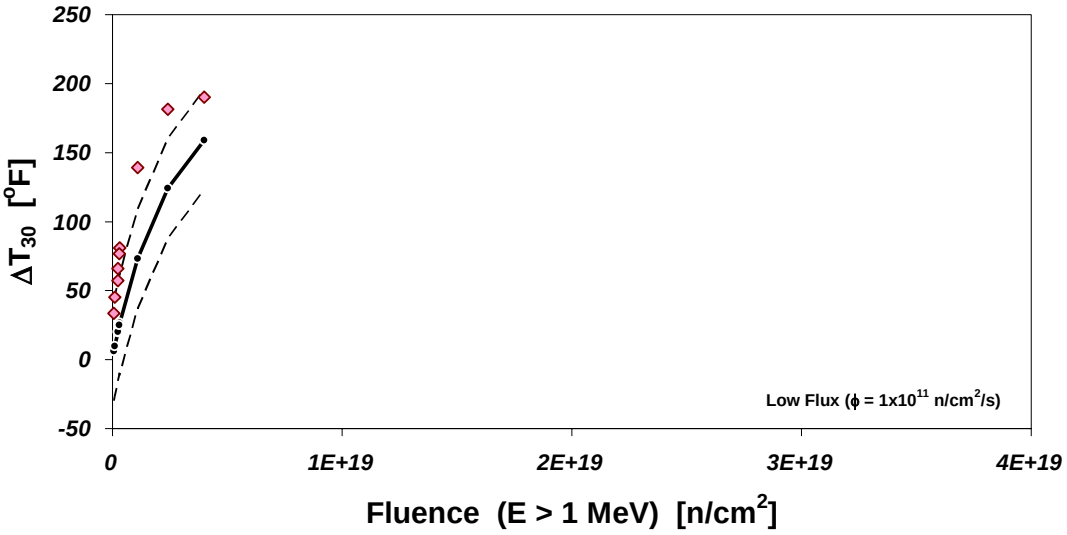
Low Flux (ϕ = 1x10^11 n/cm^2/s)
ΔT30 [°F]
250
200
150
100
50
0
-50
0
1E+19
2E+19
3E+19
4E+19
Fluence (E > 1 MeV) [n/cm^2]

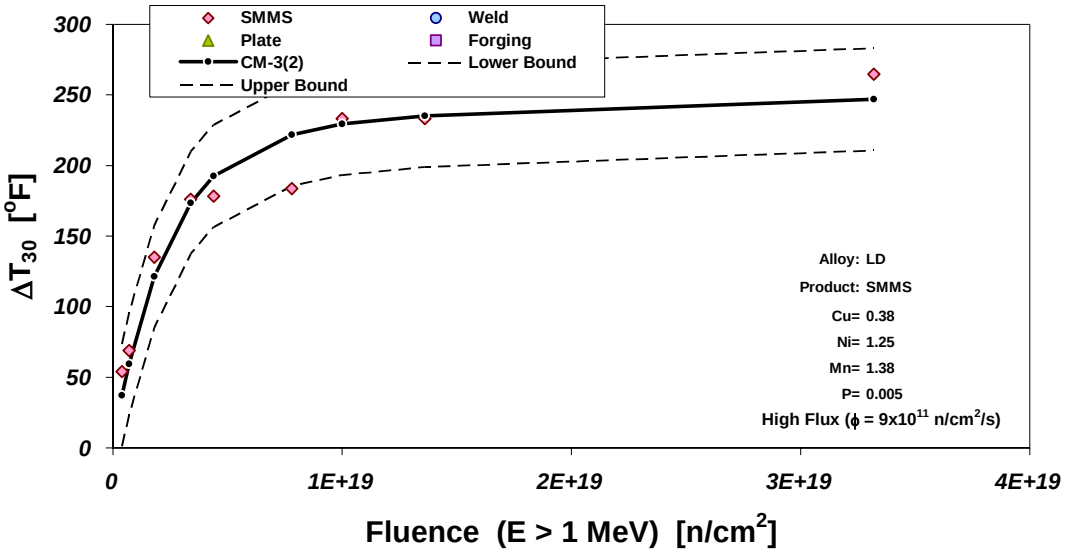
SMMS
Weld
Plate
Forging
CM-3(2)
Lower Bound
Upper Bound
Alloy: LD
Product: SMMS
Cu= 0.38
Ni= 1.25
Mn= 1.38
P= 0.005
High Flux (ϕ = 9x10^11 n/cm^2/s)
ΔT30 [°F]
300
250
200
150
100
50
0
0
1E+19
2E+19
3E+19
4E+19
Fluence (E > 1 MeV) [n/cm^2]

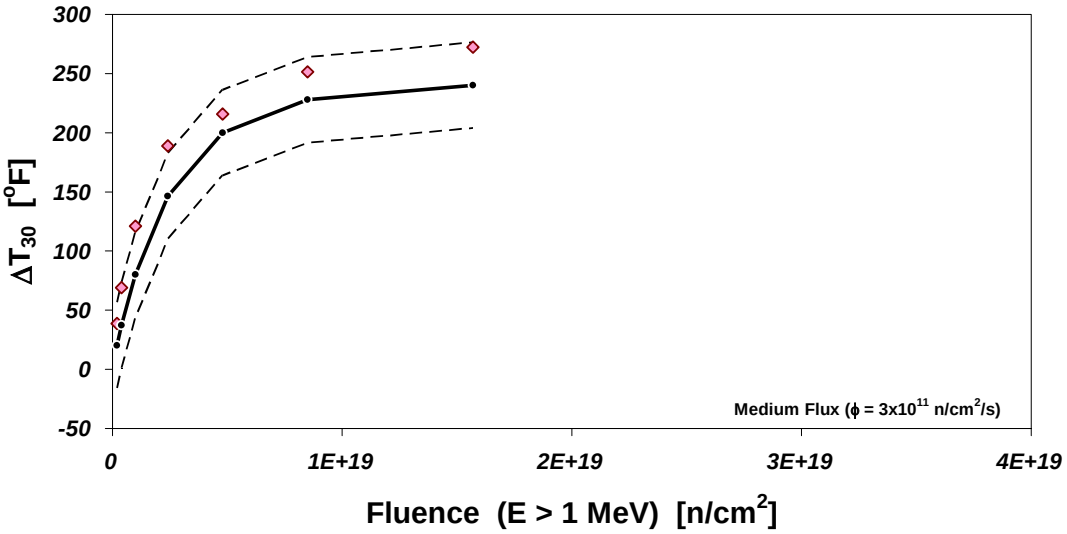
Medium Flux (ϕ = 3x10^11 n/cm^2/s)
ΔT30 [°F]
300
250
200
150
100
50
0
-50
0
1E+19
2E+19
3E+19
4E+19
Fluence (E > 1 MeV) [n/cm^2]

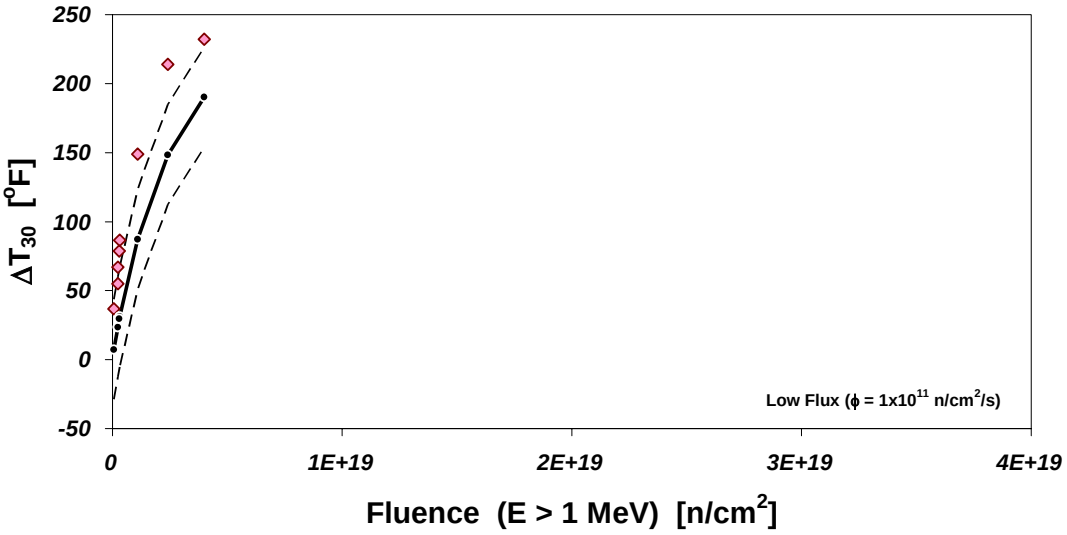
Low Flux (ϕ = 1x10^11 n/cm^2/s)
ΔT30 [°F]
250
200
150
100
50
0
-50
0
1E+19
2E+19
3E+19
4E+19
Fluence (E > 1 MeV) [n/cm^2]

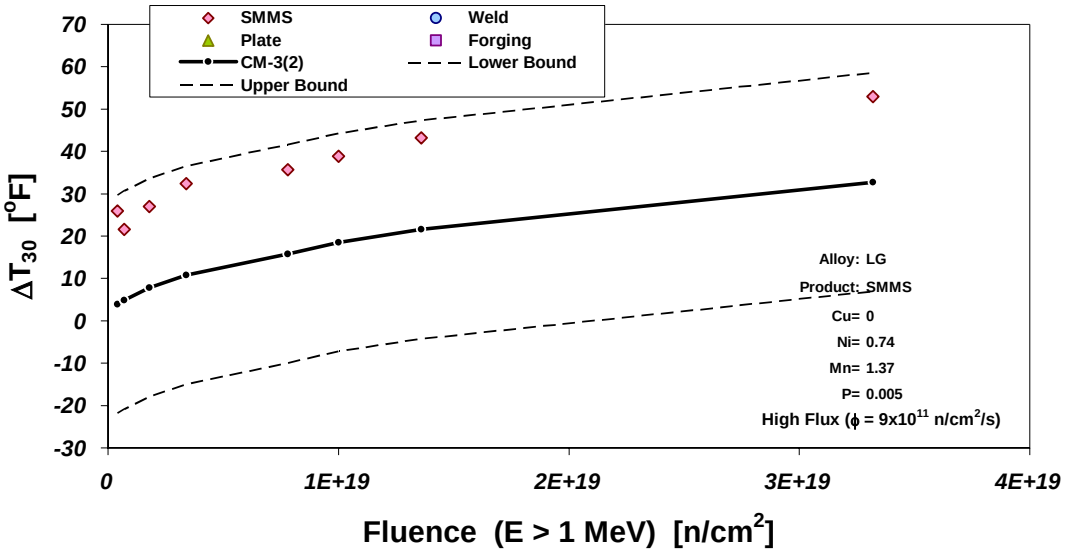
SMMS
Weld
Plate
Forging
CM-3(2)
Lower Bound
Upper Bound
Alloy: LG
Product: SMMS
Cu= 0
Ni= 0.74
Mn= 1.37
P= 0.005
High Flux (ϕ = 9x10^11 n/cm^2/s)
ΔT30 [°F]
Fluence (E > 1 MeV) [n/cm^2]

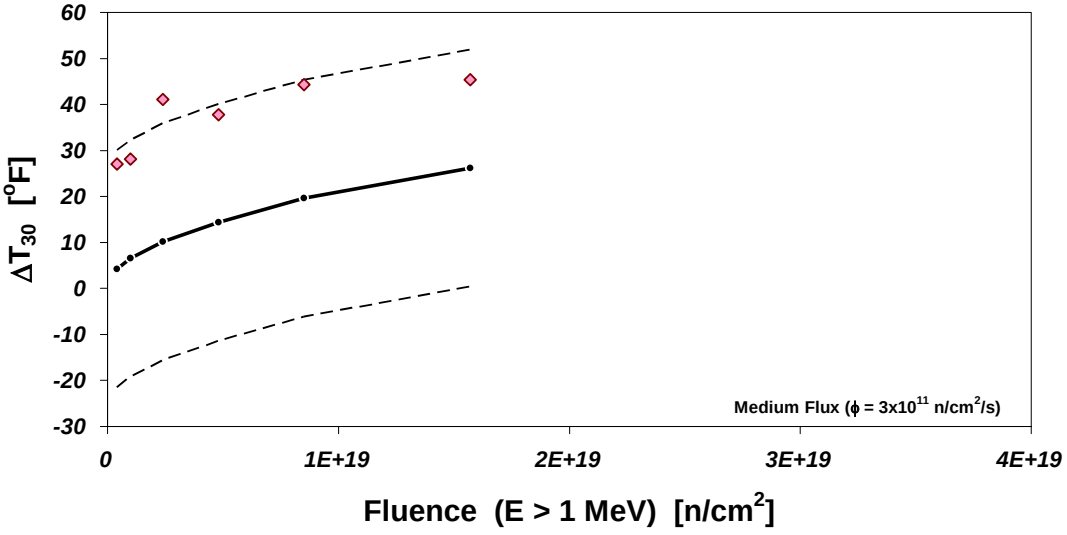
Medium Flux (ϕ = 3x10^11 n/cm^2/s)
ΔT30 [°F]
Fluence (E > 1 MeV) [n/cm^2]

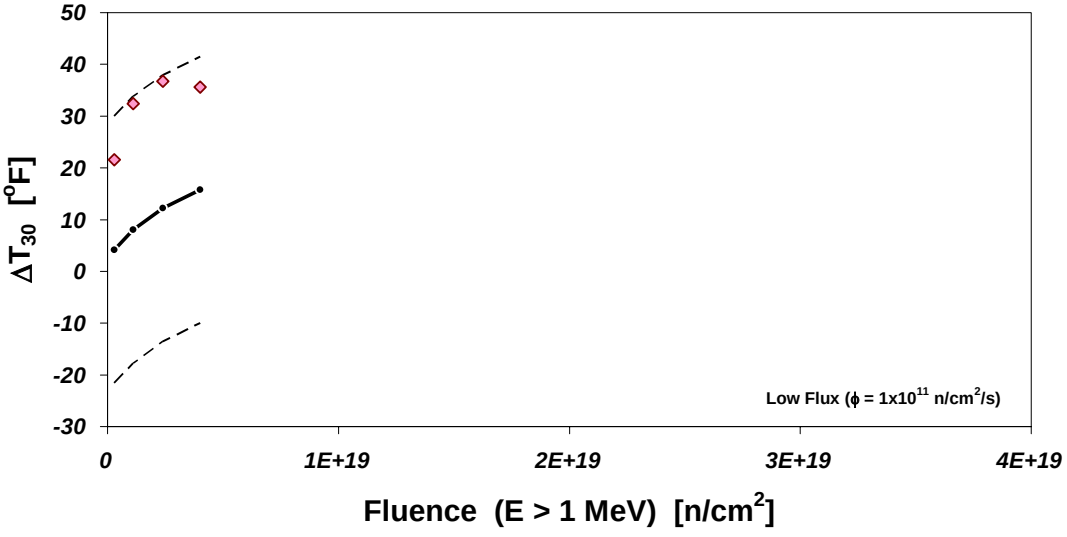
Low Flux (ϕ = 1x10^11 n/cm^2/s)
ΔT30 [°F]
Fluence (E > 1 MeV) [n/cm^2]

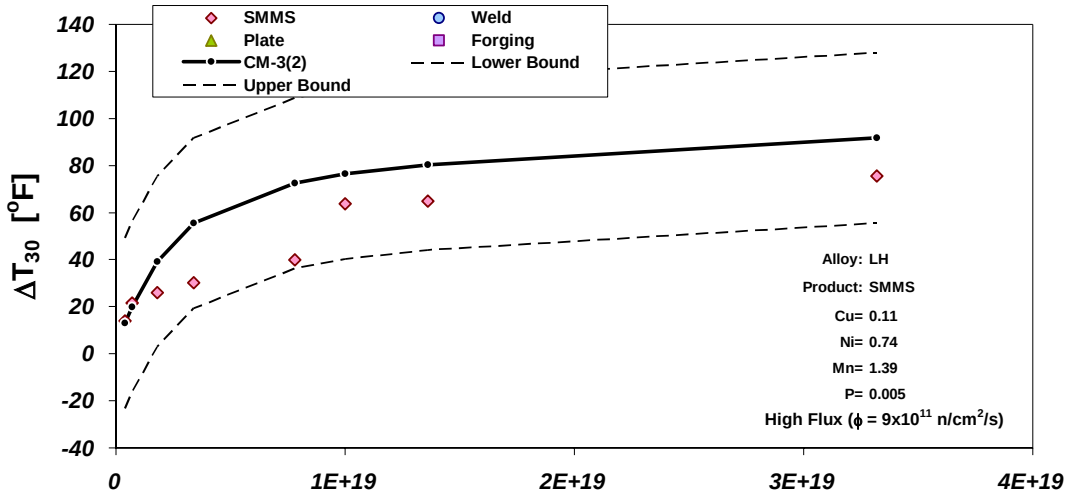
SMMS
Weld
Plate
Forging
CM-3(2)
Lower Bound
Upper Bound
ΔT30 [°F]
Alloy: LH
Product: SMMS
Cu= 0.11
Ni= 0.74
Mn= 1.39
P= 0.005
High Flux (ϕ = 9x10^11 n/cm^2/s)
Fluence (E > 1 MeV) [n/cm^2]

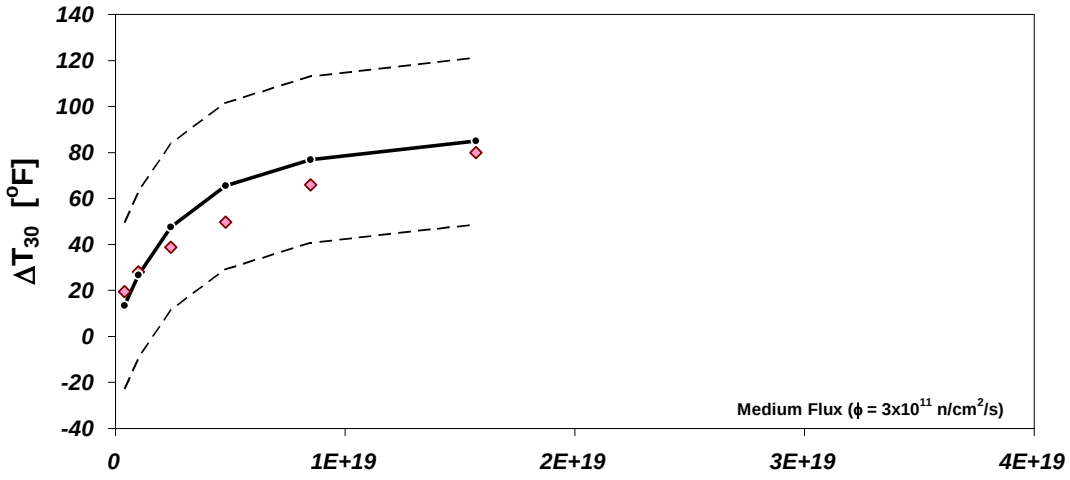
ΔT30 [°F]
Medium Flux (ϕ = 3x10^11 n/cm^2/s)
Fluence (E > 1 MeV) [n/cm^2]

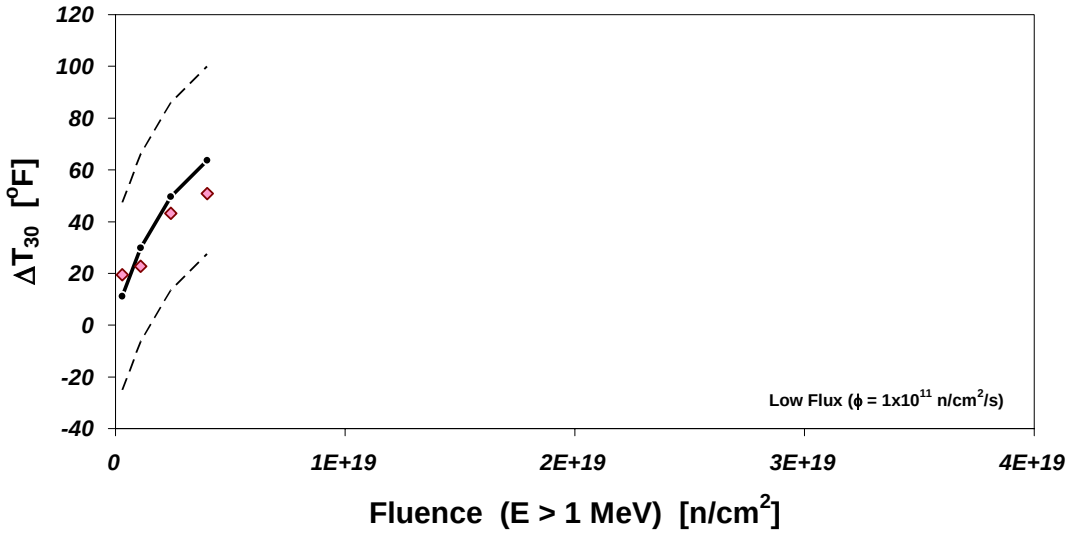
ΔT30 [°F]
Low Flux (ϕ = 1x10^11 n/cm^2/s)
Fluence (E > 1 MeV) [n/cm^2]

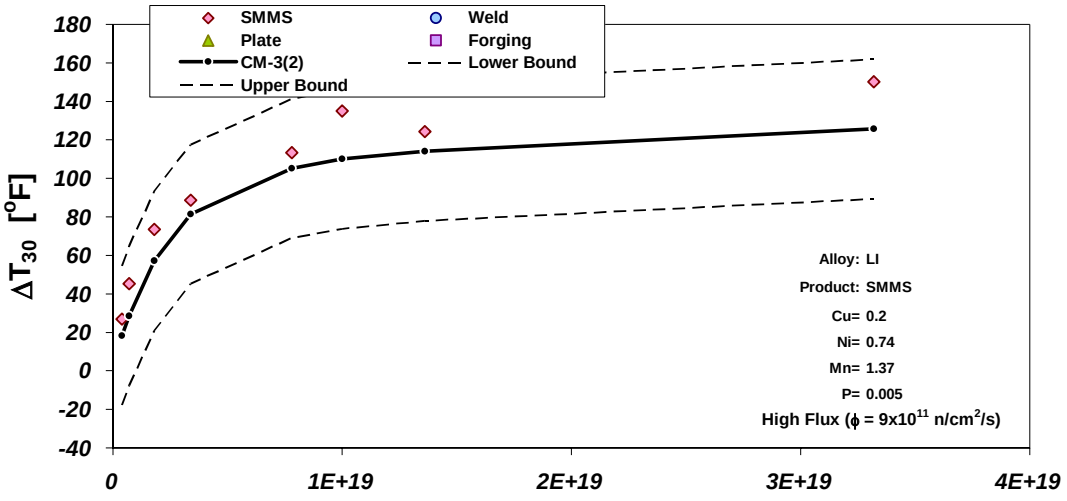
SMMS
Weld
Plate
Forging
CM-3(2)
Lower Bound
Upper Bound
Alloy: LI
Product: SMMS
Cu= 0.2
Ni= 0.74
Mn= 1.37
P= 0.005
High Flux (ϕ = 9x10^11 n/cm^2/s)
ΔT30 [°F]
180
160
140
120
100
80
60
40
20
0
-20
-40
0
1E+19
2E+19
3E+19
4E+19
Fluence (E > 1 MeV) [n/cm^2]

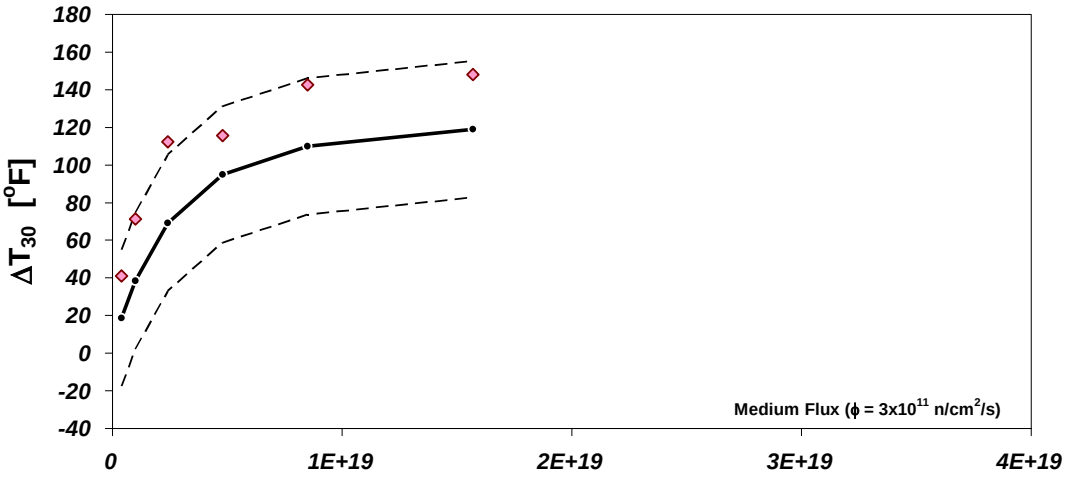
Medium Flux (ϕ = 3x10^11 n/cm^2/s)
ΔT30 [°F]
180
160
140
120
100
80
60
40
20
0
-20
-40
0
1E+19
2E+19
3E+19
4E+19
Fluence (E > 1 MeV) [n/cm^2]

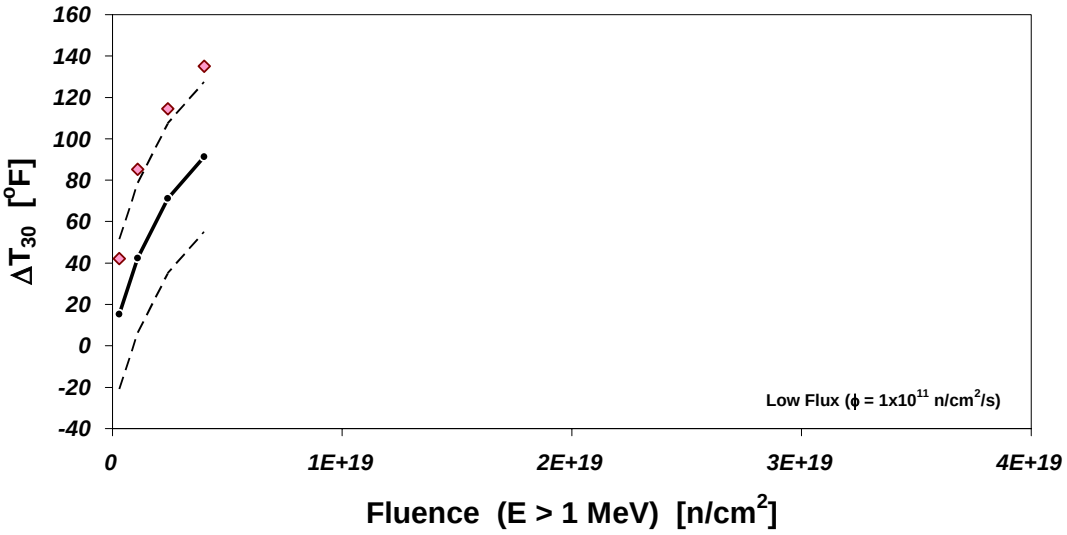
Low Flux (ϕ = 1x10^11 n/cm^2/s)
ΔT30 [°F]
160
140
120
100
80
60
40
20
0
-20
-40
0
1E+19
2E+19
3E+19
4E+19
Fluence (E > 1 MeV) [n/cm^2]

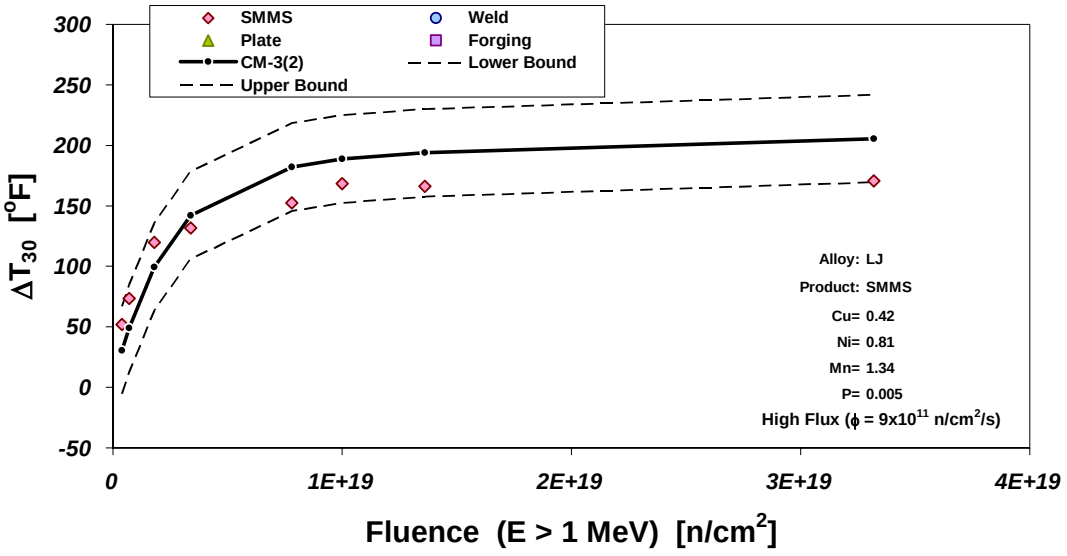
SMMS
Weld
Plate
Forging
CM-3(2)
Lower Bound
Upper Bound
Alloy: LJ
Product: SMMS
Cu= 0.42
Ni= 0.81
Mn= 1.34
P= 0.005
High Flux (ϕ = 9x10^11 n/cm^2/s)
ΔT30 [°F]
300
250
200
150
100
50
0
-50
0
1E+19
2E+19
3E+19
4E+19
Fluence (E > 1 MeV) [n/cm^2]

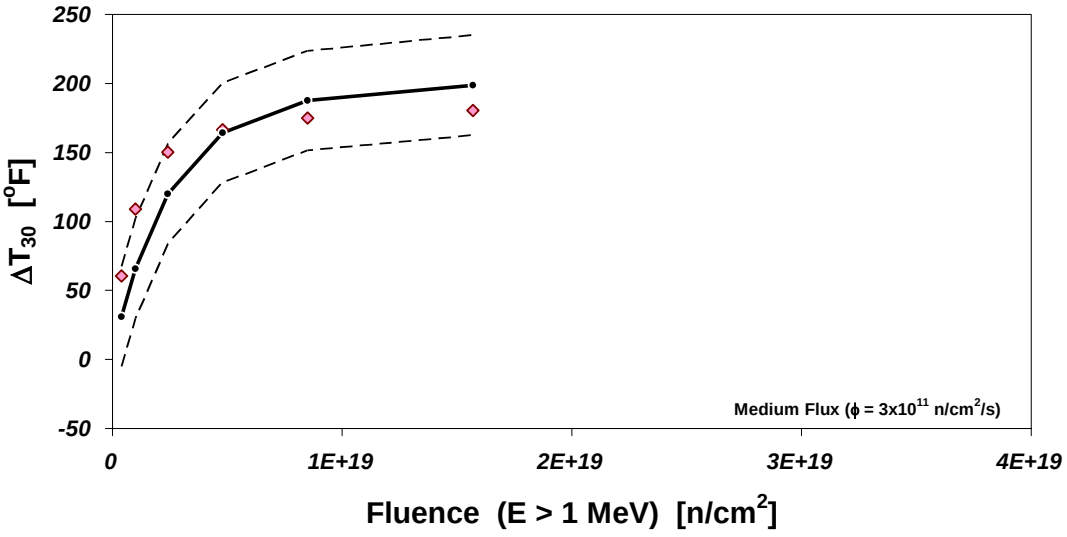
Medium Flux (ϕ = 3x10^11 n/cm^2/s)
ΔT30 [°F]
250
200
150
100
50
0
-50
0
1E+19
2E+19
3E+19
4E+19
Fluence (E > 1 MeV) [n/cm^2]

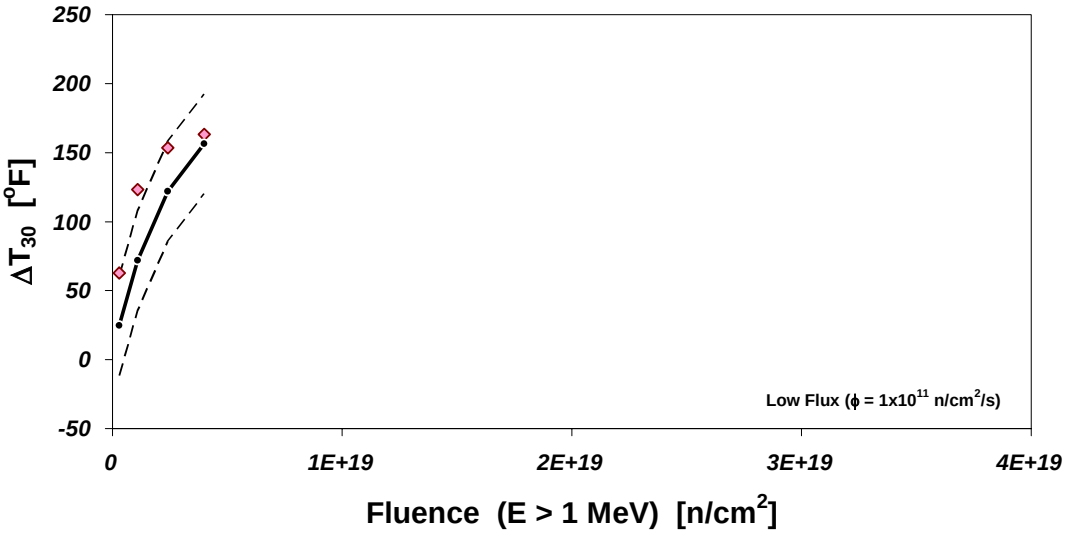
Low Flux (ϕ = 1x10^11 n/cm^2/s)
ΔT30 [°F]
250
200
150
100
50
0
-50
0
1E+19
2E+19
3E+19
4E+19
Fluence (E > 1 MeV) [n/cm^2]

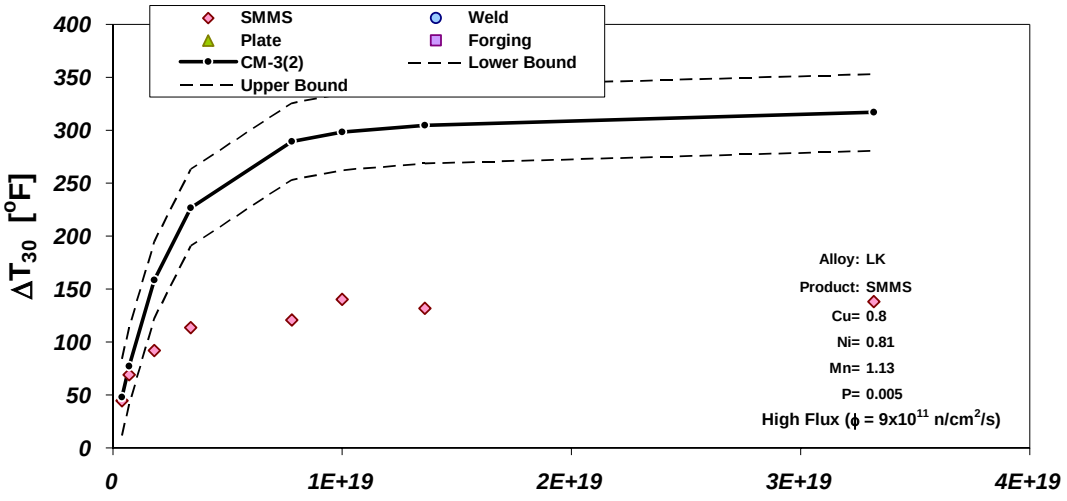
SMMS
Weld
Plate
Forging
CM-3(2)
Lower Bound
Upper Bound
Alloy: LK
Product: SMMS
Cu= 0.8
Ni= 0.81
Mn= 1.13
P= 0.005
High Flux (ϕ = 9x10^11 n/cm^2/s)
ΔT30 [°F]
0
50
100
150
200
250
300
350
400
0
1E+19
2E+19
3E+19
4E+19
Fluence (E > 1 MeV) [n/cm^2]

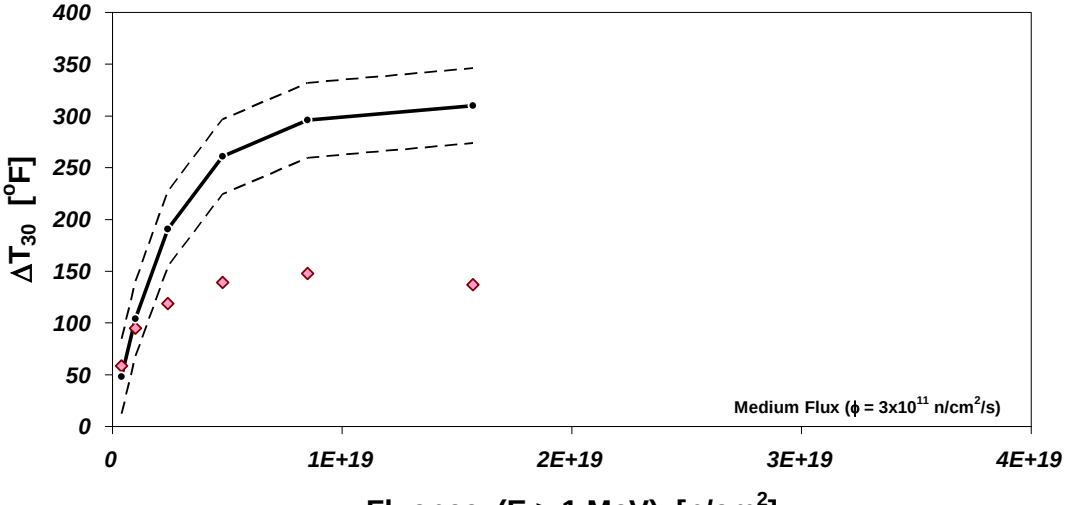
Medium Flux (ϕ = 3x10^11 n/cm^2/s)
ΔT30 [°F]
0
50
100
150
200
250
300
350
400
0
1E+19
2E+19
3E+19
4E+19
Fluence (E > 1 MeV) [n/cm^2]

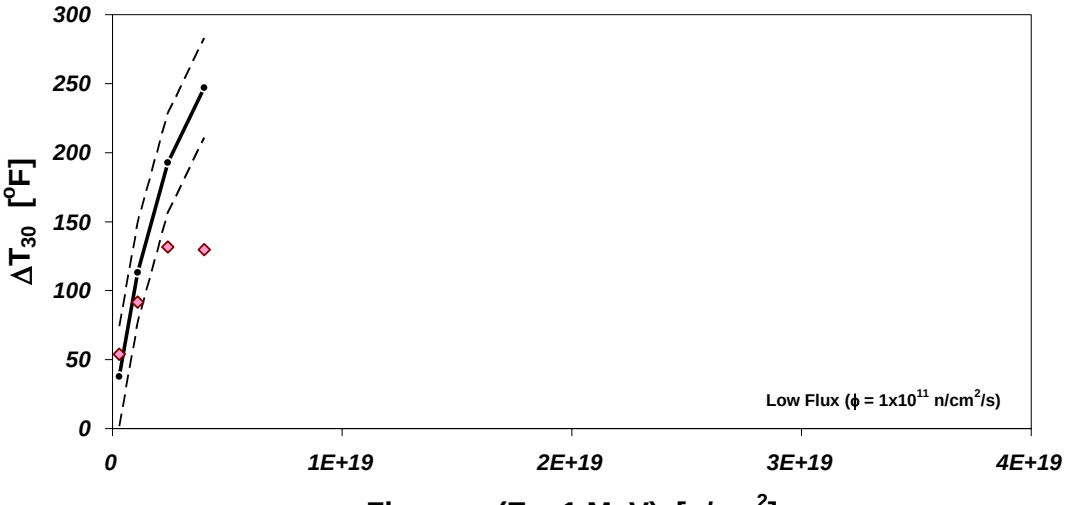
Low Flux (ϕ = 1x10^11 n/cm^2/s)
ΔT30 [°F]
0
50
100
150
200
250
300
0
1E+19
2E+19
3E+19
4E+19
Fluence (E > 1 MeV) [n/cm^2]

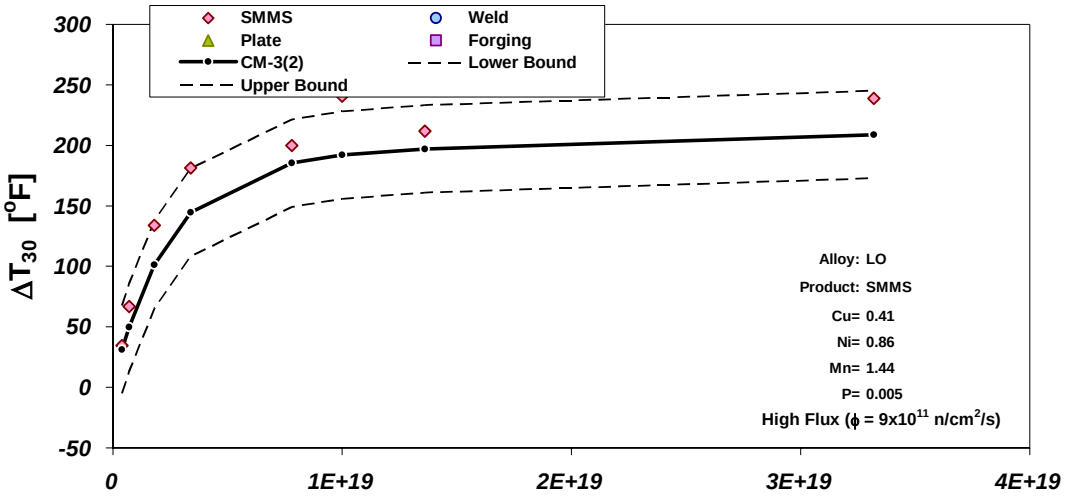
SMMS
Weld
Plate
Forging
CM-3(2)
Lower Bound
Upper Bound
Alloy: LO
Product: SMMS
Cu= 0.41
Ni= 0.86
Mn= 1.44
P= 0.005
High Flux (ϕ = 9x10^11 n/cm^2/s)
ΔT30 [°F]
300
250
200
150
100
50
0
-50
0
1E+19
2E+19
3E+19
4E+19
Fluence (E > 1 MeV) [n/cm^2]

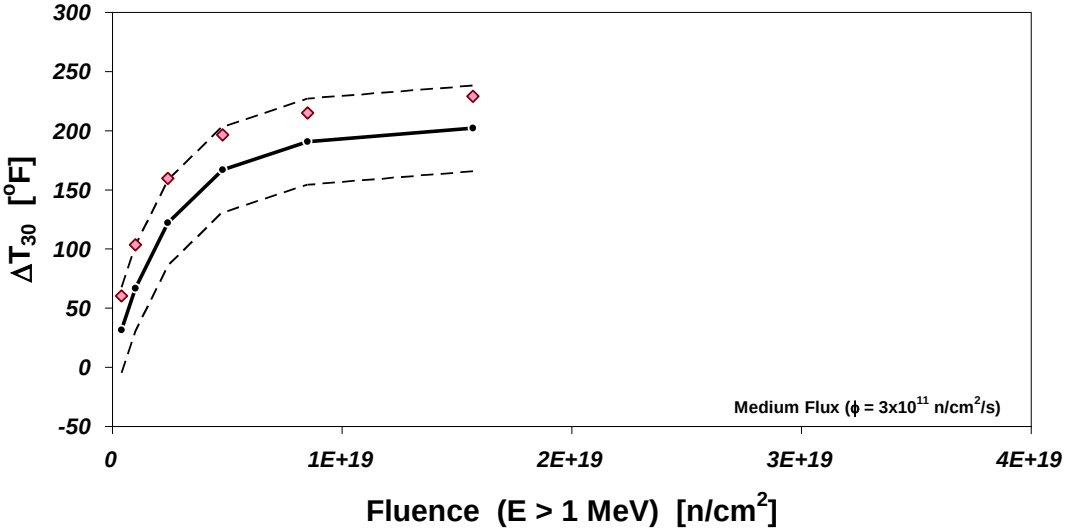
Medium Flux (ϕ = 3x10^11 n/cm^2/s)
ΔT30 [°F]
300
250
200
150
100
50
0
-50
0
1E+19
2E+19
3E+19
4E+19
Fluence (E > 1 MeV) [n/cm^2]

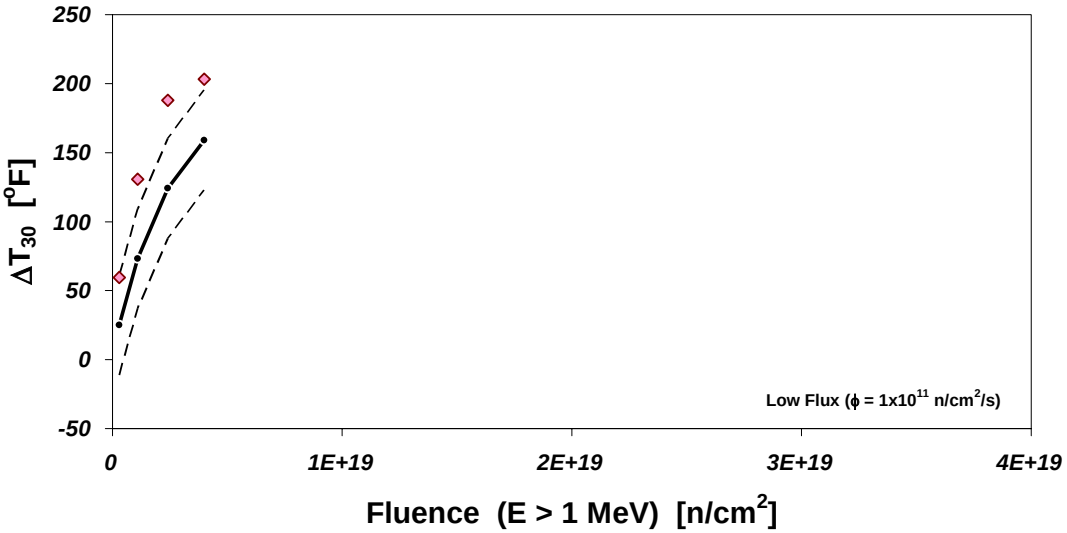
Low Flux (ϕ = 1x10^11 n/cm^2/s)
ΔT30 [°F]
250
200
150
100
50
0
-50
0
1E+19
2E+19
3E+19
4E+19
Fluence (E > 1 MeV) [n/cm^2]

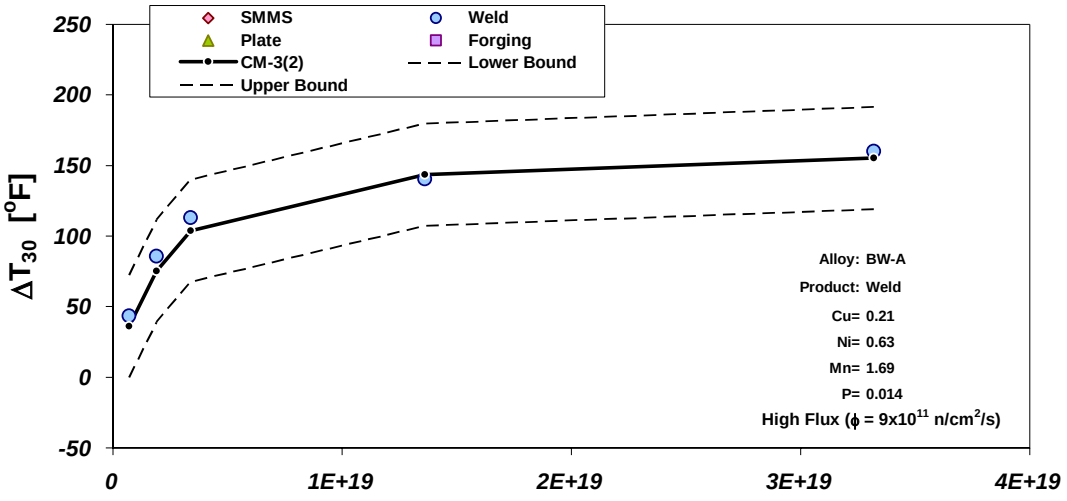
SMMS
Weld
Plate
Forging
CM-3(2)
Lower Bound
Upper Bound
250
200
150
100
50
0
-50
ΔT30 [°F]
Alloy: BW-A
Product: Weld
Cu= 0.21
Ni= 0.63
Mn= 1.69
P= 0.014
High Flux (ϕ = 9x10^11 n/cm^2/s)
0
1E+19
2E+19
3E+19
4E+19
Fluence (E > 1 MeV) [n/cm^2]

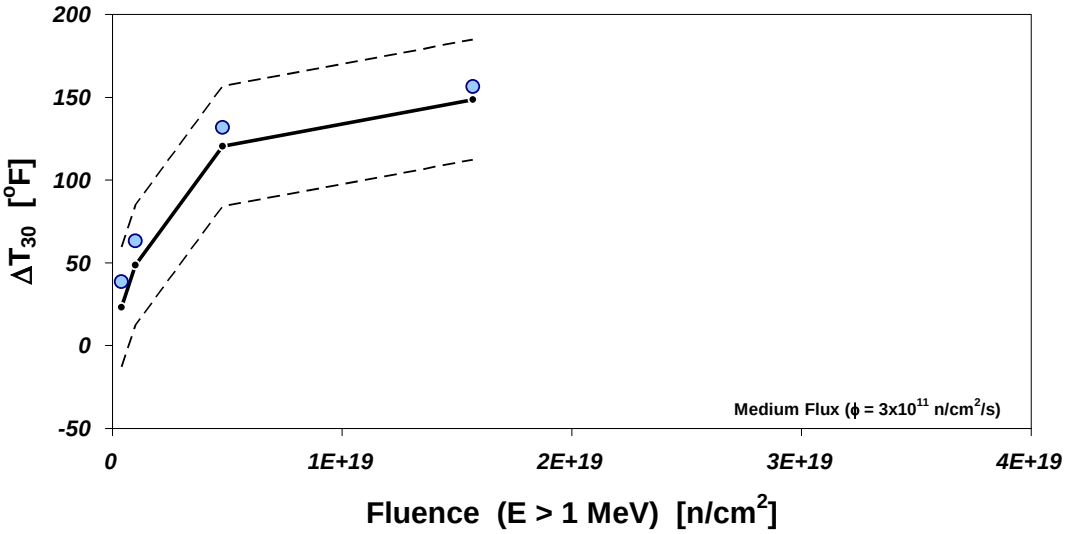
200
150
100
50
0
-50
ΔT30 [°F]
Medium Flux (ϕ = 3x10^11 n/cm^2/s)
0
1E+19
2E+19
3E+19
4E+19
Fluence (E > 1 MeV) [n/cm^2]

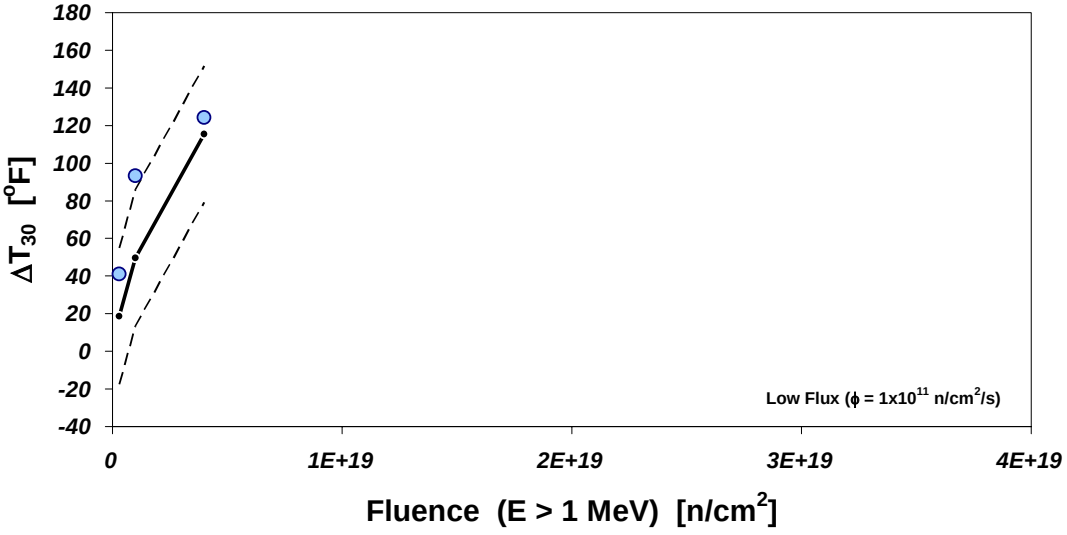
180
160
140
120
100
80
60
40
20
0
-20
-40
ΔT30 [°F]
Low Flux (ϕ = 1x10^11 n/cm^2/s)
0
1E+19
2E+19
3E+19
4E+19
Fluence (E > 1 MeV) [n/cm^2]

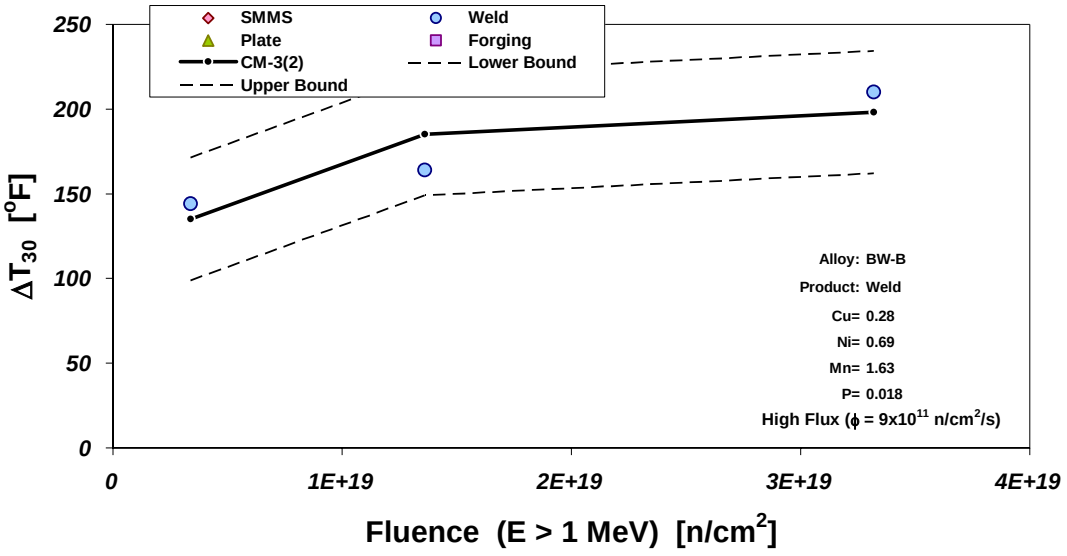
SMMS
Weld
Plate
Forging
CM-3(2)
Lower Bound
Upper Bound
Alloy: BW-B
Product: Weld
Cu= 0.28
Ni= 0.69
Mn= 1.63
P= 0.018
High Flux (ϕ = 9x10^11 n/cm^2/s)
ΔT30 [°F]
Fluence (E > 1 MeV) [n/cm^2]
0
50
100
150
200
250
0
1E+19
2E+19
3E+19
4E+19

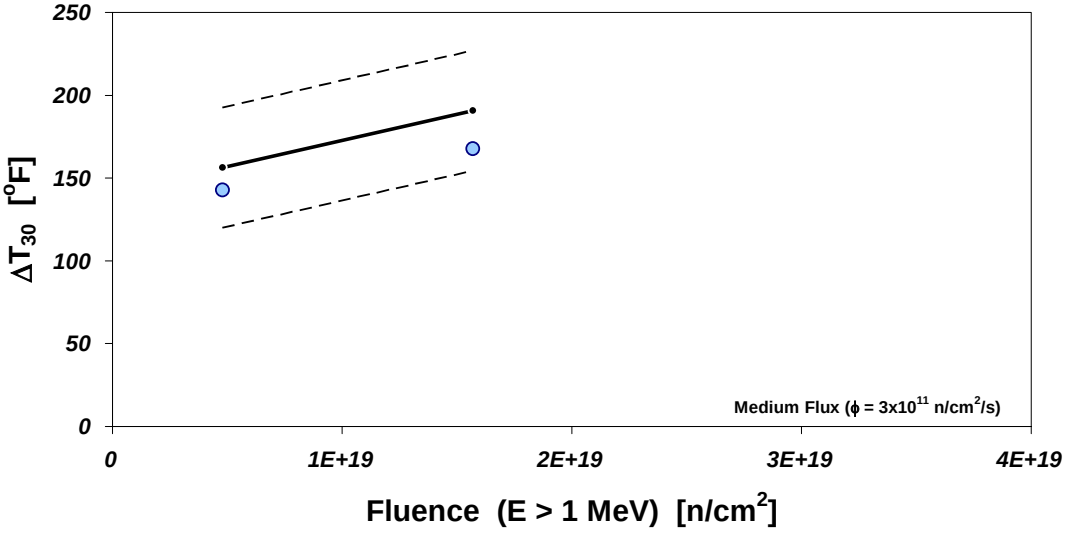
Medium Flux (ϕ = 3x10^11 n/cm^2/s)
ΔT30 [°F]
Fluence (E > 1 MeV) [n/cm^2]
0
50
100
150
200
250
0
1E+19
2E+19
3E+19
4E+19

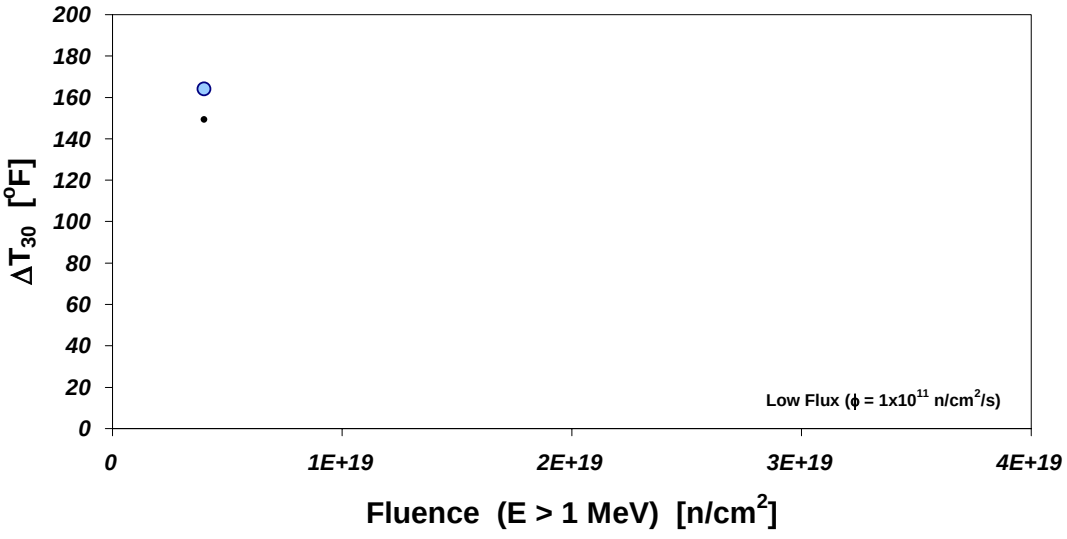
Low Flux (ϕ = 1x10^11 n/cm^2/s)
ΔT30 [°F]
Fluence (E > 1 MeV) [n/cm^2]
0
20
40
60
80
100
120
140
160
180
200
0
1E+19
2E+19
3E+19
4E+19

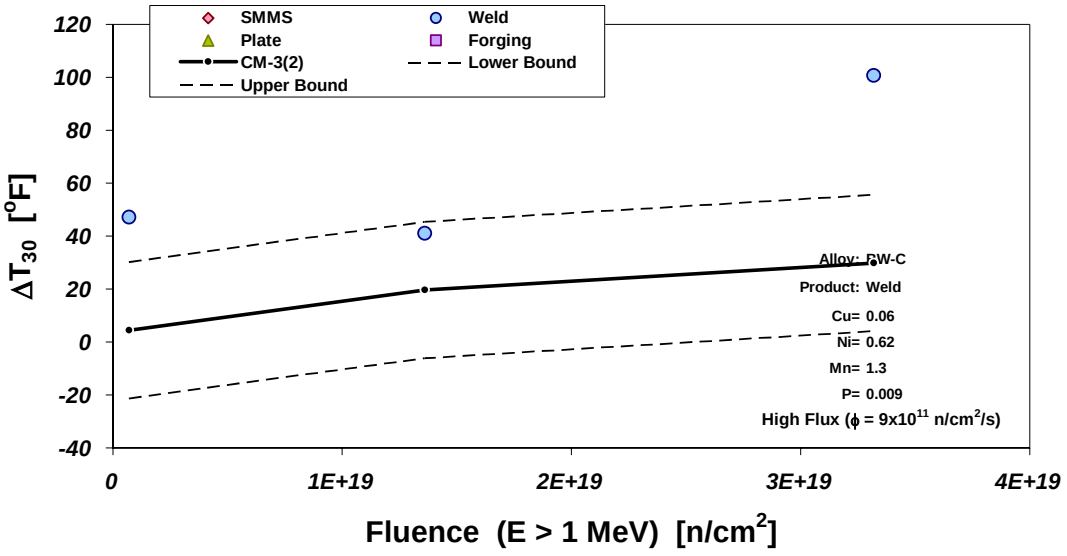
SMMS
Weld
Plate
Forging
CM-3(2)
Lower Bound
Upper Bound
Alloy: PWW-C
Product: Weld
Cu= 0.06
Ni= 0.62
Mn= 1.3
P= 0.009
High Flux (ϕ = 9x10^11 n/cm^2/s)
ΔT30 [°F]
120
100
80
60
40
20
0
-20
-40
0
1E+19
2E+19
3E+19
4E+19
Fluence (E > 1 MeV) [n/cm^2]

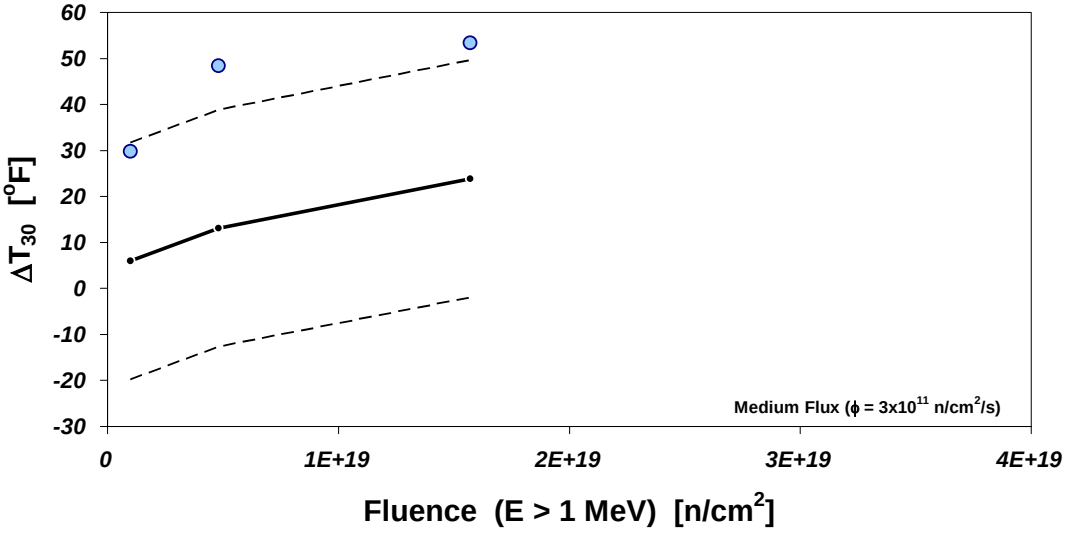
Medium Flux (ϕ = 3x10^11 n/cm^2/s)
ΔT30 [°F]
60
50
40
30
20
10
0
-10
-20
-30
0
1E+19
2E+19
3E+19
4E+19
Fluence (E > 1 MeV) [n/cm^2]

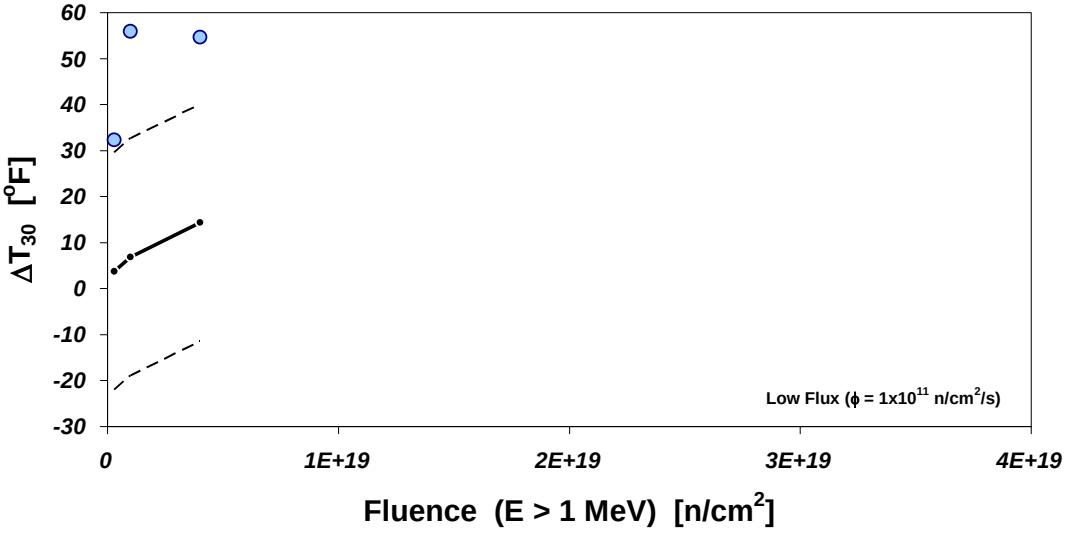
Low Flux (ϕ = 1x10^11 n/cm^2/s)
ΔT30 [°F]
60
50
40
30
20
10
0
-10
-20
-30
0
1E+19
2E+19
3E+19
4E+19
Fluence (E > 1 MeV) [n/cm^2]

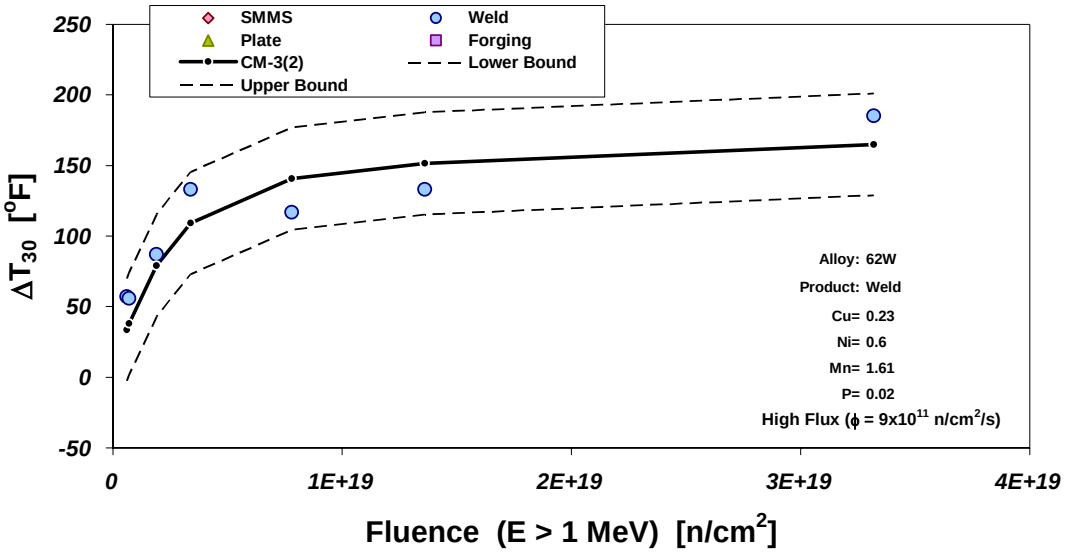
SMMS
Weld
Plate
Forging
CM-3(2)
Lower Bound
Upper Bound
250
200
150
100
50
0
-50
ΔT30 [°F]
Alloy: 62W
Product: Weld
Cu= 0.23
Ni= 0.6
Mn= 1.61
P= 0.02
High Flux (ϕ = 9x10^11 n/cm^2/s)
0
1E+19
2E+19
3E+19
4E+19
Fluence (E > 1 MeV) [n/cm^2]

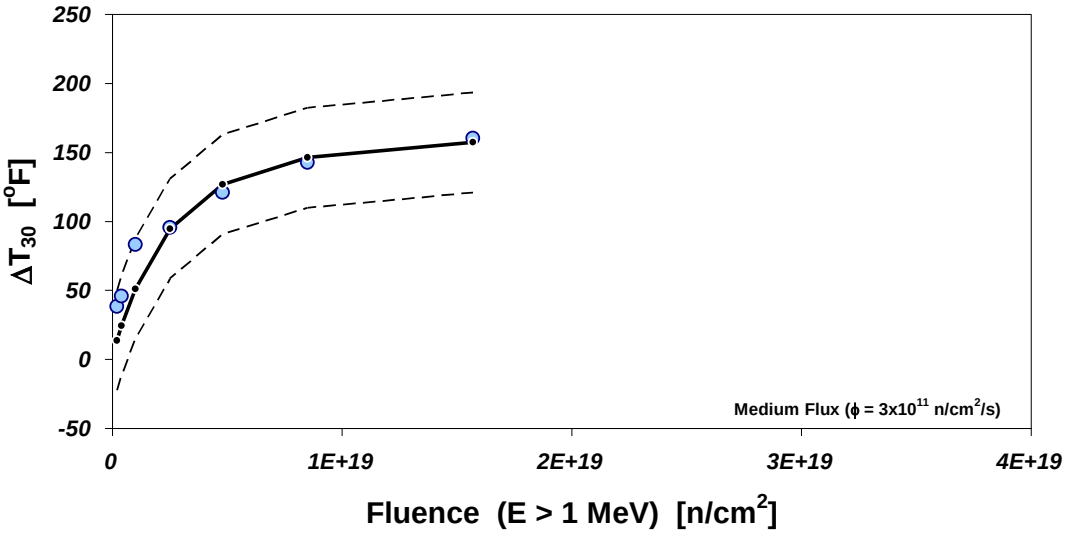
250
200
150
100
50
0
-50
ΔT30 [°F]
Medium Flux (ϕ = 3x10^11 n/cm^2/s)
0
1E+19
2E+19
3E+19
4E+19
Fluence (E > 1 MeV) [n/cm^2]

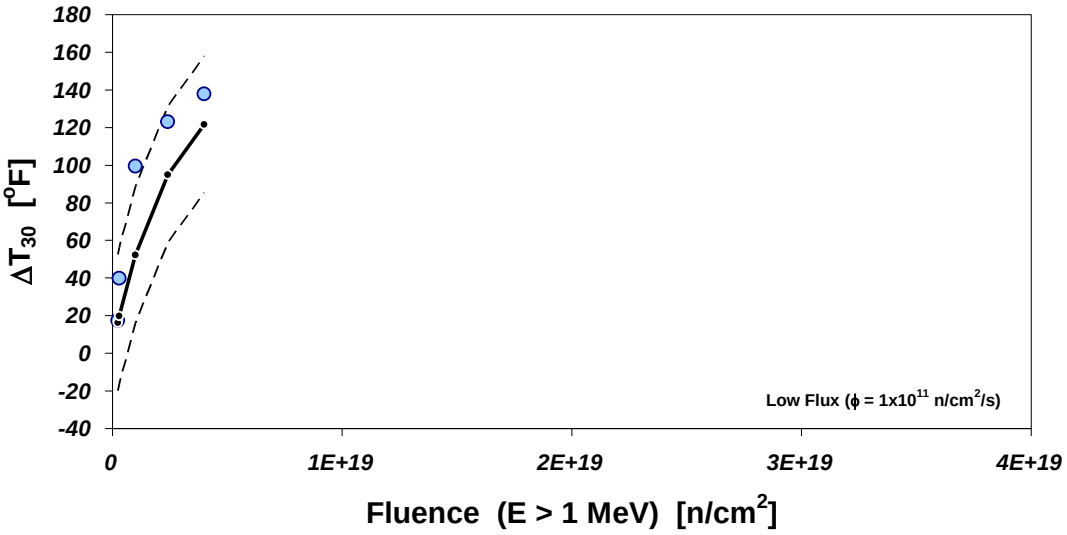
180
160
140
120
100
80
60
40
20
0
-20
-40
ΔT30 [°F]
Low Flux (ϕ = 1x10^11 n/cm^2/s)
0
1E+19
2E+19
3E+19
4E+19
Fluence (E > 1 MeV) [n/cm^2]

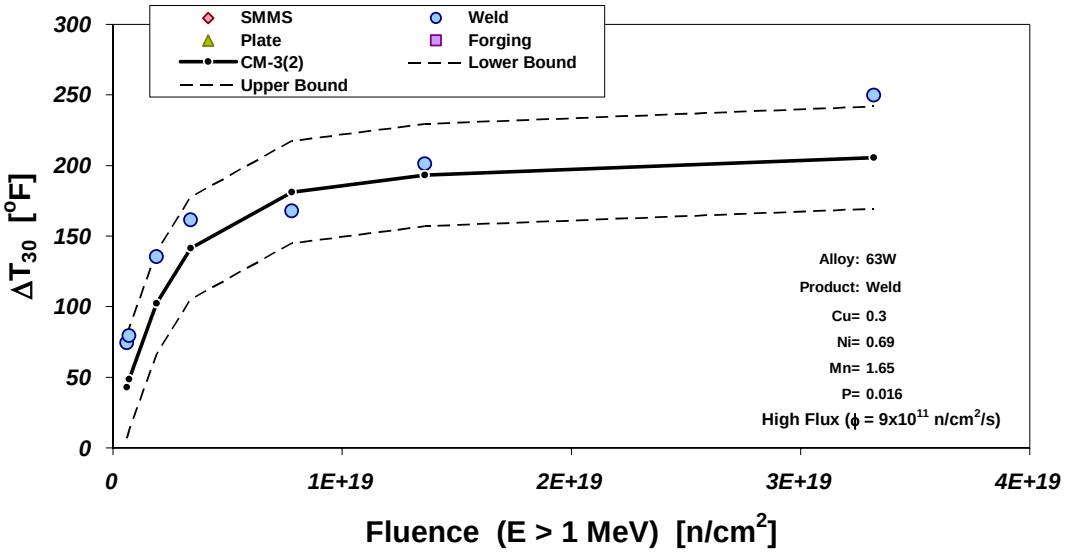
SMMS
Weld
Plate
Forging
CM-3(2)
Lower Bound
Upper Bound
ΔT30 [°F]
300
250
200
150
100
50
0
Alloy: 63W
Product: Weld
Cu= 0.3
Ni= 0.69
Mn= 1.65
P= 0.016
High Flux (ϕ = 9x10^11 n/cm^2/s)
0
1E+19
2E+19
3E+19
4E+19
Fluence (E > 1 MeV) [n/cm^2]

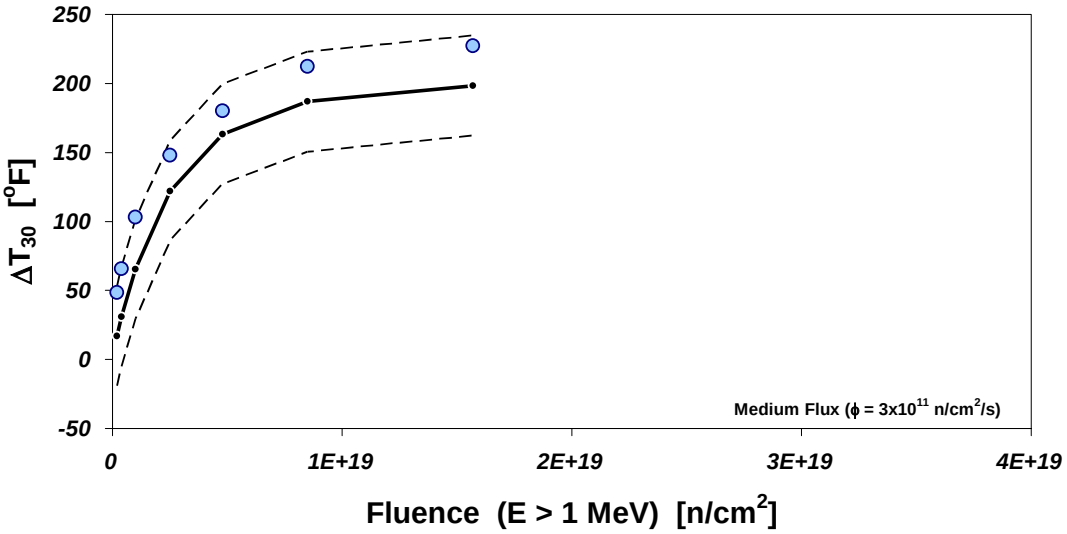
ΔT30 [°F]
250
200
150
100
50
0
-50
Medium Flux (ϕ = 3x10^11 n/cm^2/s)
0
1E+19
2E+19
3E+19
4E+19
Fluence (E > 1 MeV) [n/cm^2]

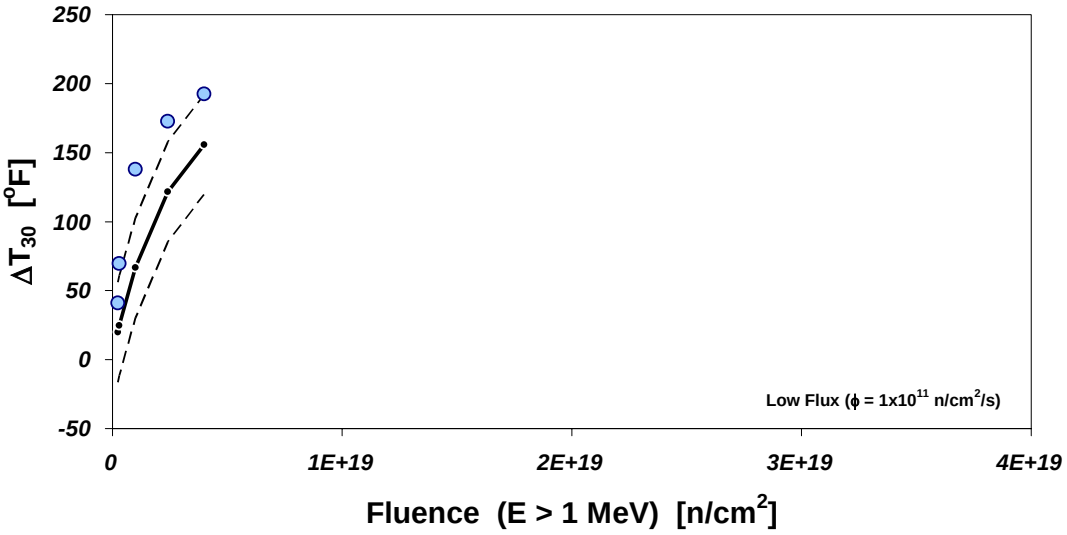
ΔT30 [°F]
250
200
150
100
50
0
-50
Low Flux (ϕ = 1x10^11 n/cm^2/s)
0
1E+19
2E+19
3E+19
4E+19
Fluence (E > 1 MeV) [n/cm^2]

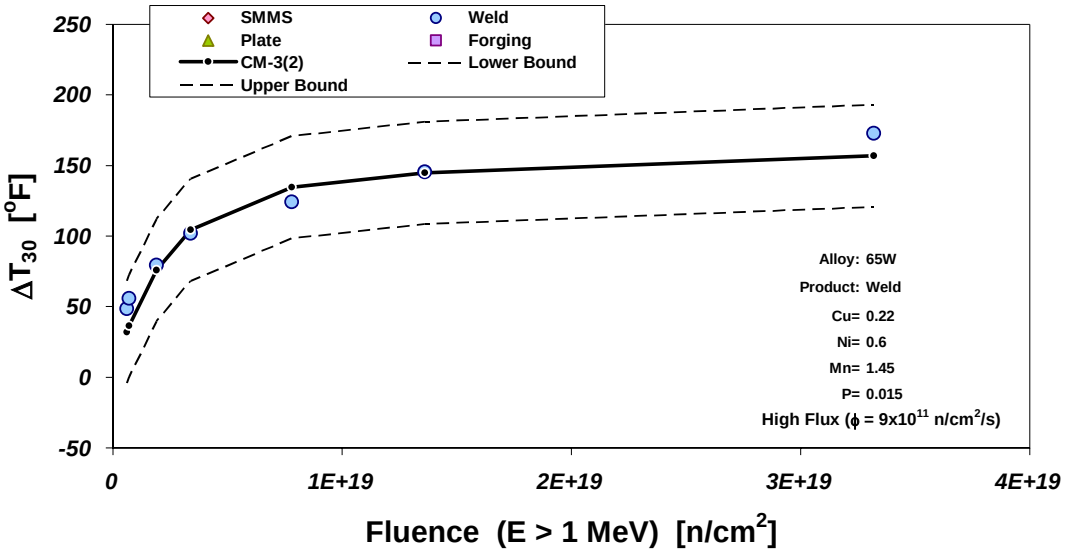
SMMS
Weld
Plate
Forging
CM-3(2)
Lower Bound
Upper Bound
ΔT30 [°F]
250
200
150
100
50
0
-50
0
1E+19
2E+19
3E+19
4E+19
Alloy: 65W
Product: Weld
Cu= 0.22
Ni= 0.6
Mn= 1.45
P= 0.015
High Flux (ϕ = 9x10^11 n/cm^2/s)
Fluence (E > 1 MeV) [n/cm^2]

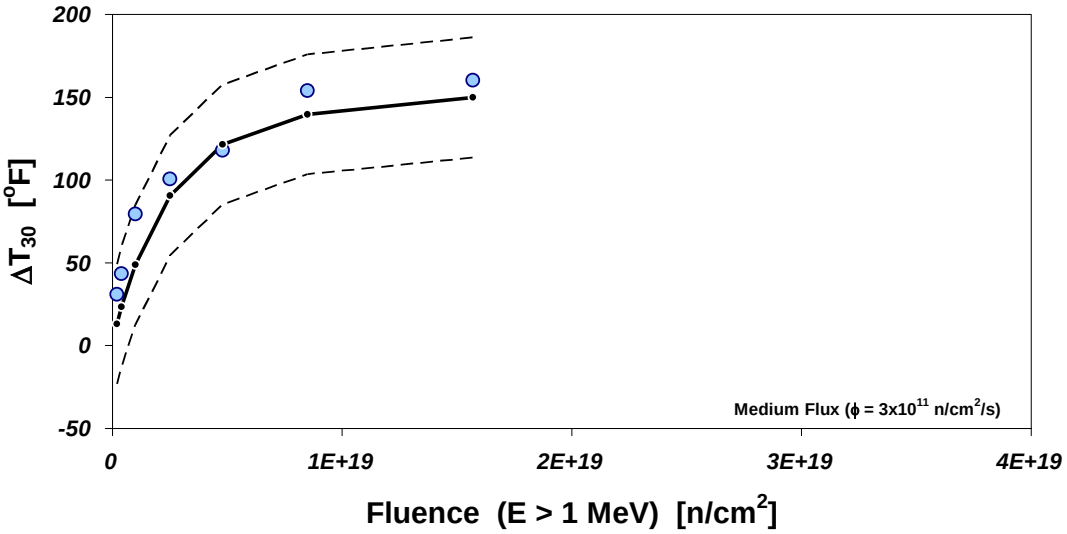
ΔT30 [°F]
200
150
100
50
0
-50
0
1E+19
2E+19
3E+19
4E+19
Medium Flux (ϕ = 3x10^11 n/cm^2/s)
Fluence (E > 1 MeV) [n/cm^2]

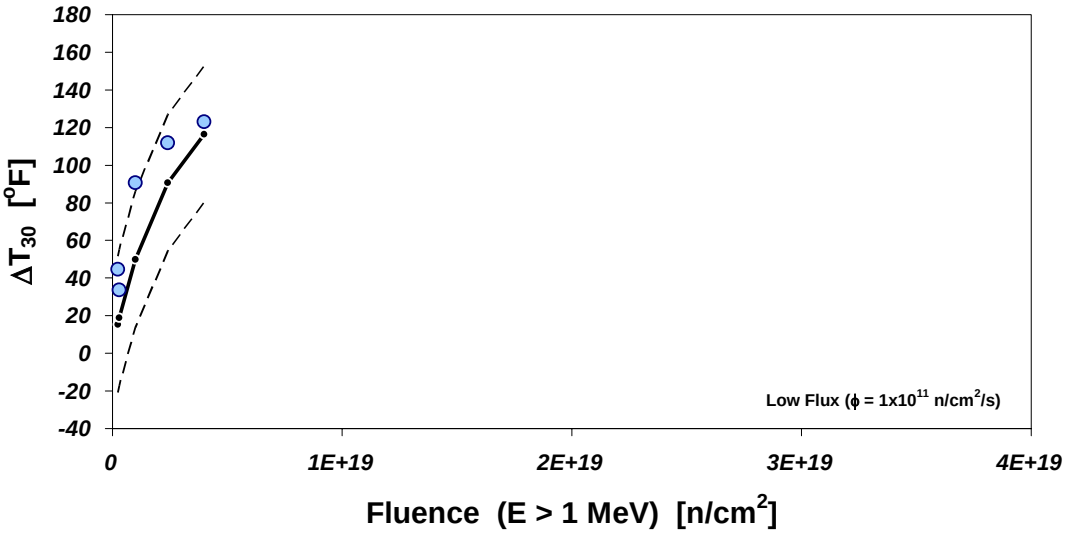
ΔT30 [°F]
180
160
140
120
100
80
60
40
20
0
-20
-40
0
1E+19
2E+19
3E+19
4E+19
Low Flux (ϕ = 1x10^11 n/cm^2/s)
Fluence (E > 1 MeV) [n/cm^2]

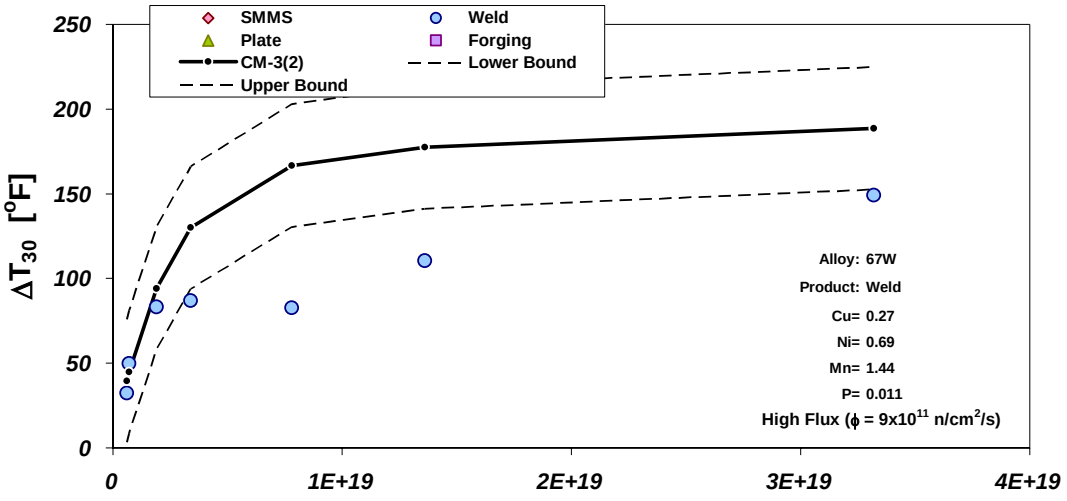
SMMS
Weld
Plate
Forging
CM-3(2)
Lower Bound
Upper Bound
Alloy: 67W
Product: Weld
Cu= 0.27
Ni= 0.69
Mn= 1.44
P= 0.011
High Flux (ϕ = 9x10^11 n/cm^2/s)
ΔT30 [°F]
250
200
150
100
50
0
0
1E+19
2E+19
3E+19
4E+19
Fluence (E > 1 MeV) [n/cm^2]

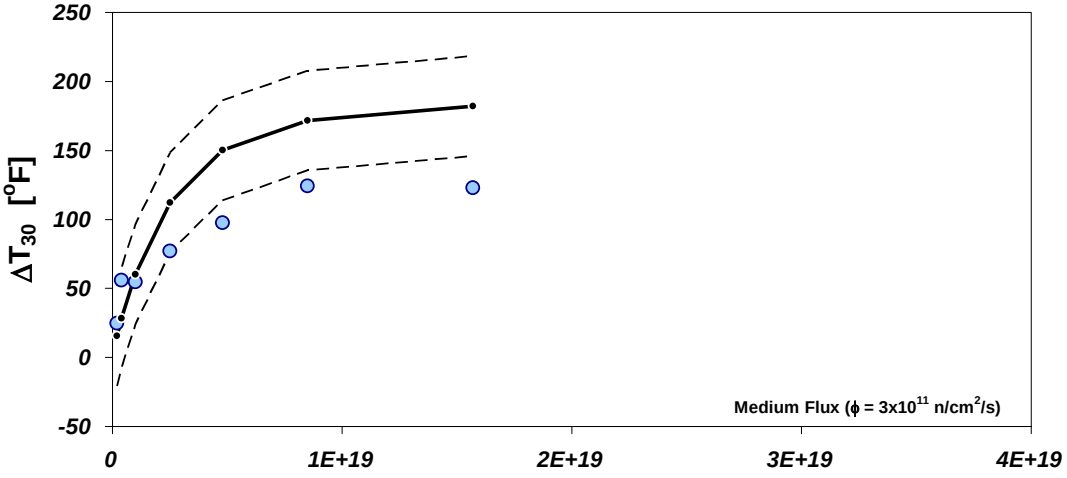
Medium Flux (ϕ = 3x10^11 n/cm^2/s)
ΔT30 [°F]
250
200
150
100
50
0
-50
0
1E+19
2E+19
3E+19
4E+19
Fluence (E > 1 MeV) [n/cm^2]

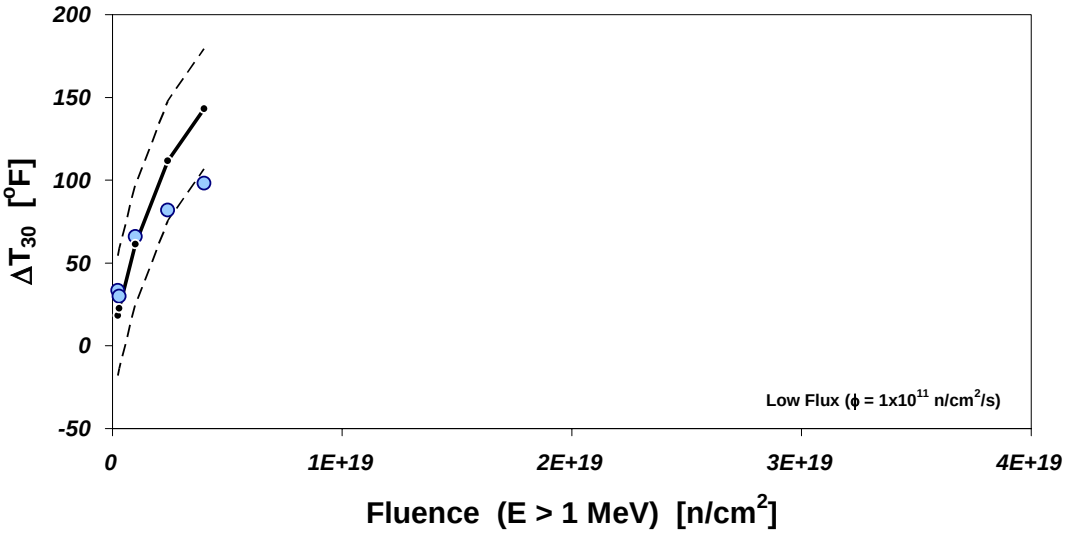
Low Flux (ϕ = 1x10^11 n/cm^2/s)
ΔT30 [°F]
200
150
100
50
0
-50
0
1E+19
2E+19
3E+19
4E+19
Fluence (E > 1 MeV) [n/cm^2]

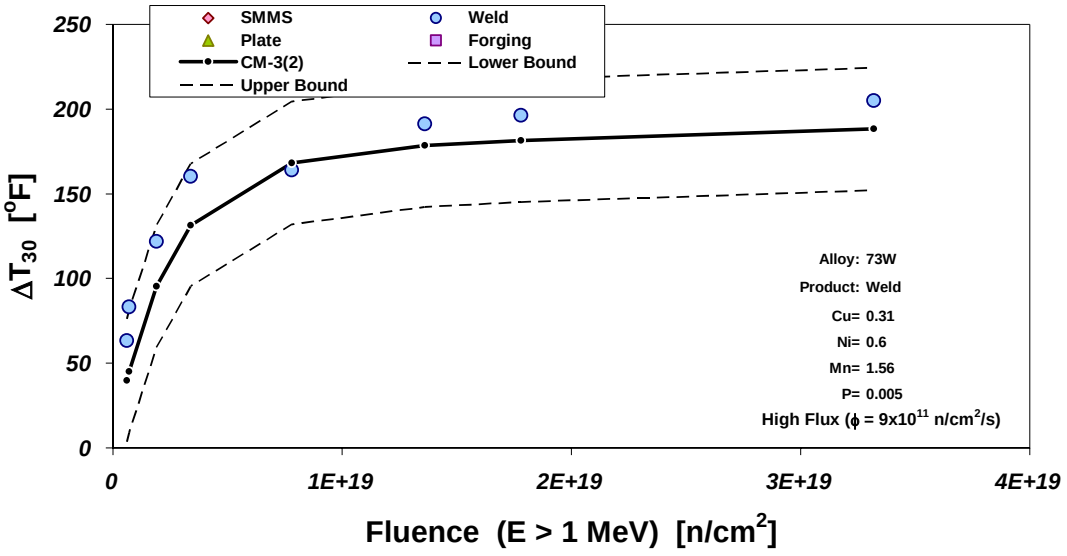
SMMS
Weld
Plate
Forging
CM-3(2)
Lower Bound
Upper Bound
Alloy: 73W
Product: Weld
Cu= 0.31
Ni= 0.6
Mn= 1.56
P= 0.005
High Flux (ϕ = 9x10^11 n/cm^2/s)
ΔT30 [°F]
Fluence (E > 1 MeV) [n/cm^2]
250
200
150
100
50
0
0
1E+19
2E+19
3E+19
4E+19

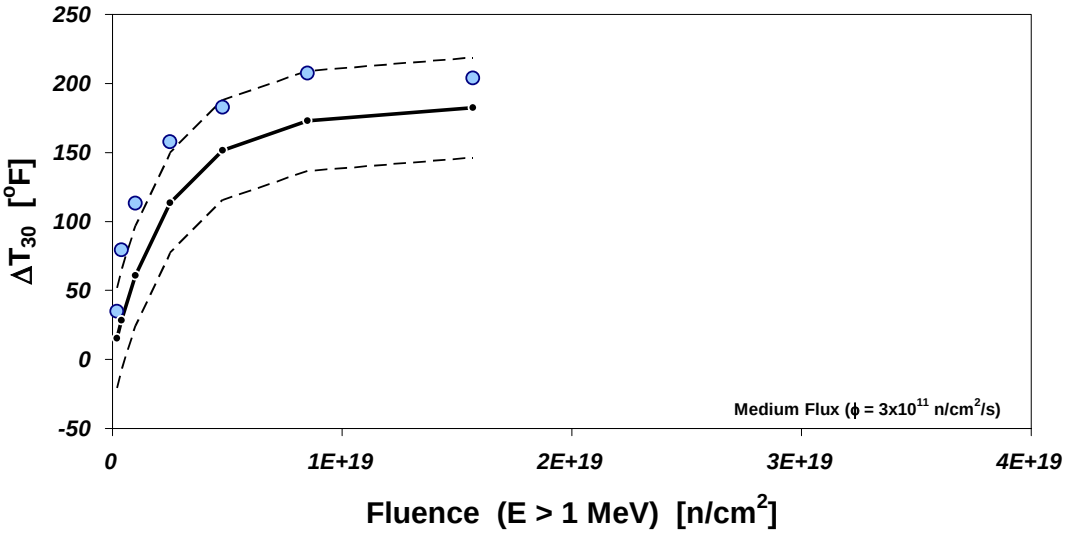
Medium Flux (ϕ = 3x10^11 n/cm^2/s)
ΔT30 [°F]
Fluence (E > 1 MeV) [n/cm^2]
250
200
150
100
50
0
-50
0
1E+19
2E+19
3E+19
4E+19

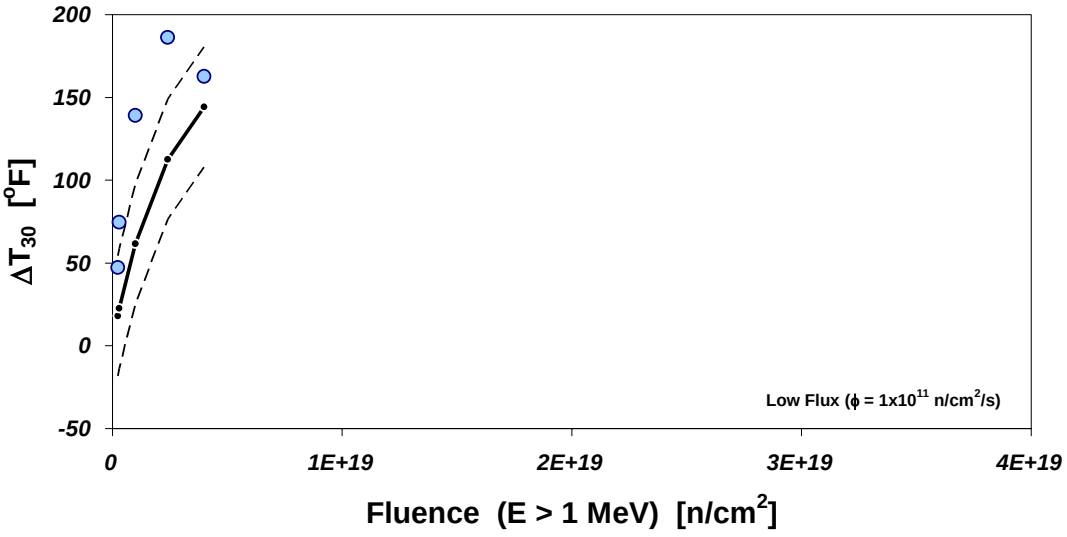
Low Flux (ϕ = 1x10^11 n/cm^2/s)
ΔT30 [°F]
Fluence (E > 1 MeV) [n/cm^2]
200
150
100
50
0
-50
0
1E+19
2E+19
3E+19
4E+19

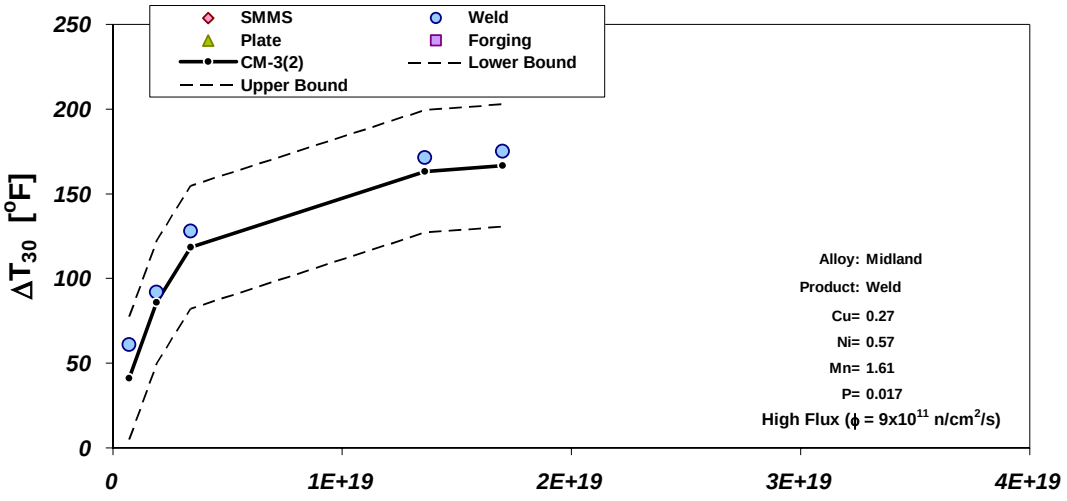
SMMS
Weld
Plate
Forging
CM-3(2)
Lower Bound
Upper Bound
250
200
150
100
50
0
ΔT30 [°F]
Alloy: Midland
Product: Weld
Cu= 0.27
Ni= 0.57
Mn= 1.61
P= 0.017
High Flux (ϕ = 9x10^11 n/cm^2/s)
0
1E+19
2E+19
3E+19
4E+19
Fluence (E > 1 MeV) [n/cm^2]

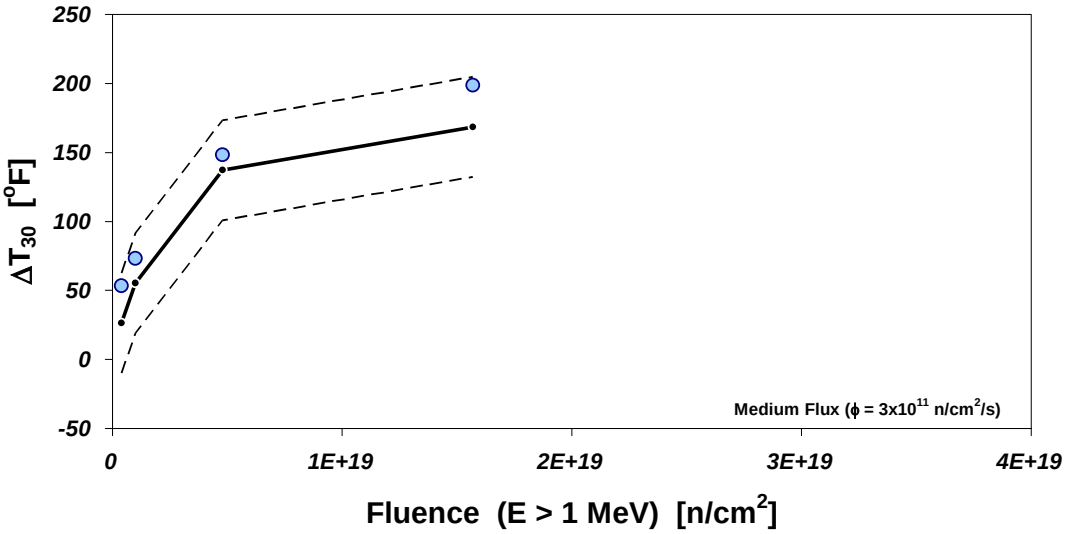
250
200
150
100
50
0
-50
ΔT30 [°F]
Medium Flux (ϕ = 3x10^11 n/cm^2/s)
0
1E+19
2E+19
3E+19
4E+19
Fluence (E > 1 MeV) [n/cm^2]

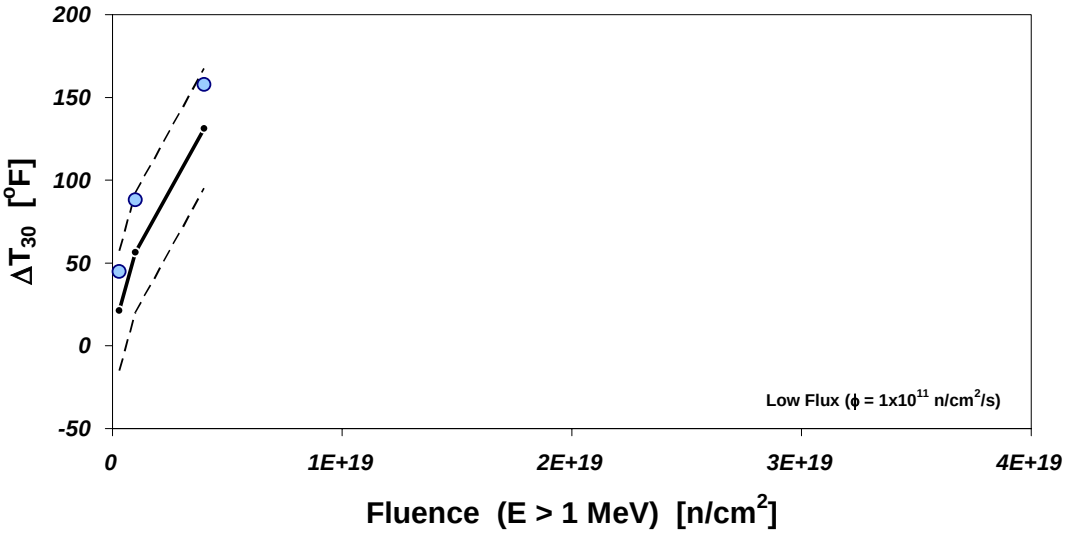
200
150
100
50
0
-50
ΔT30 [°F]
Low Flux (ϕ = 1x10^11 n/cm^2/s)
0
1E+19
2E+19
3E+19
4E+19
Fluence (E > 1 MeV) [n/cm^2]

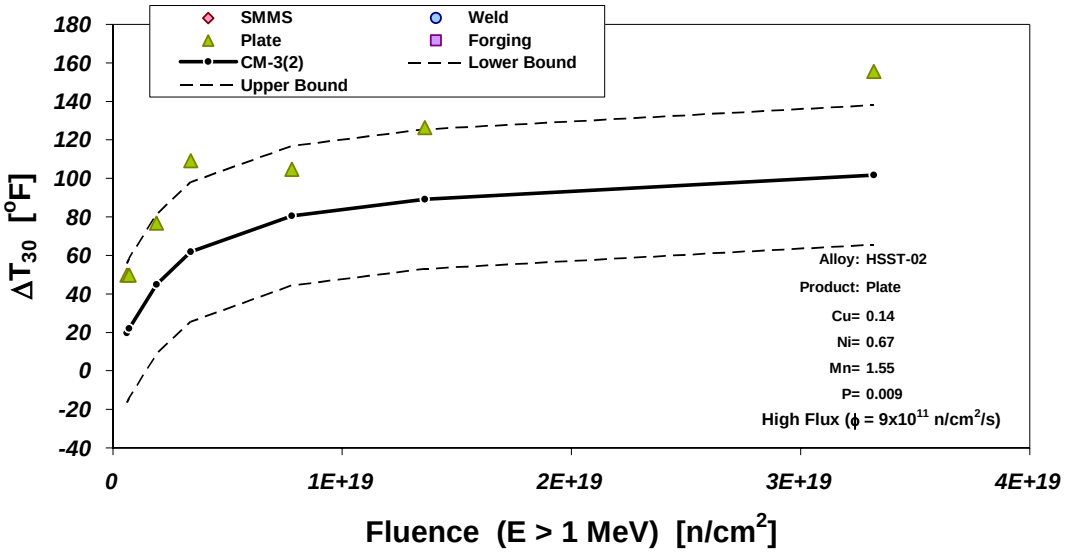
SMMS
Weld
Plate
Forging
CM-3(2)
Lower Bound
Upper Bound
Alloy: HSST-02
Product: Plate
Cu= 0.14
Ni= 0.67
Mn= 1.55
P= 0.009
High Flux (ϕ = 9x10^11 n/cm^2/s)
ΔT30 [°F]
Fluence (E > 1 MeV) [n/cm^2]

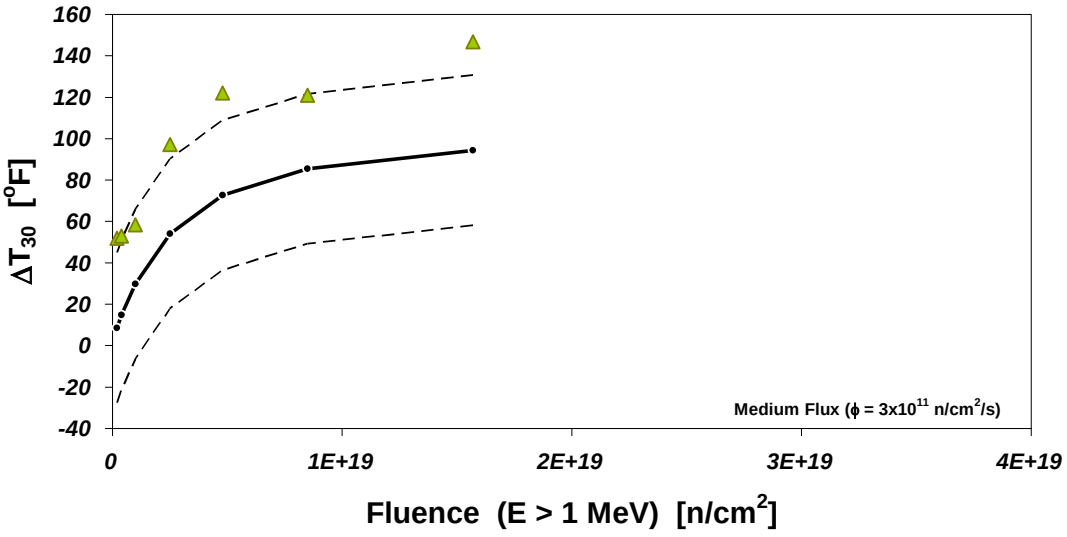
Medium Flux (ϕ = 3x10^11 n/cm^2/s)
ΔT30 [°F]
Fluence (E > 1 MeV) [n/cm^2]

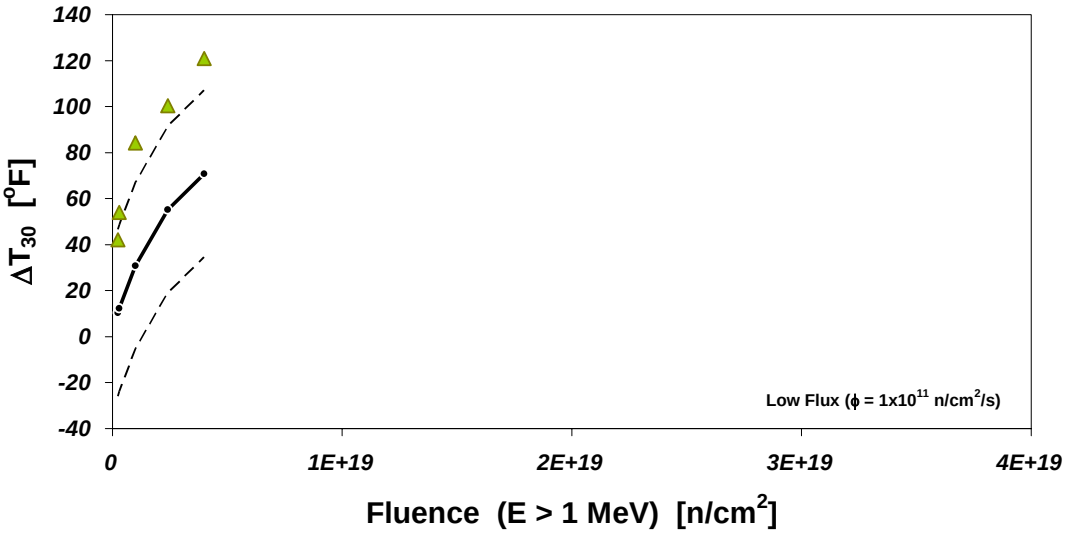
Low Flux (ϕ = 1x10^11 n/cm^2/s)
ΔT30 [°F]
Fluence (E > 1 MeV) [n/cm^2]

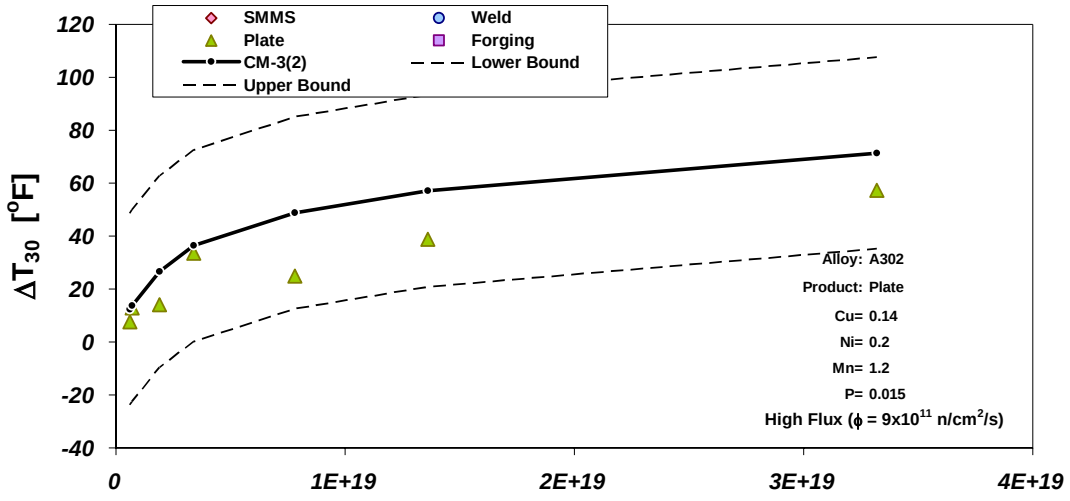
SMMS
Weld
Plate
Forging
CM-3(2)
Lower Bound
Upper Bound
120
100
80
60
40
20
0
-20
-40
ΔT30 [°F]
Alloy: A302
Product: Plate
Cu= 0.14
Ni= 0.2
Mn= 1.2
P= 0.015
High Flux (ϕ = 9x10^11 n/cm^2/s)
0
1E+19
2E+19
3E+19
4E+19
Fluence (E > 1 MeV) [n/cm^2]

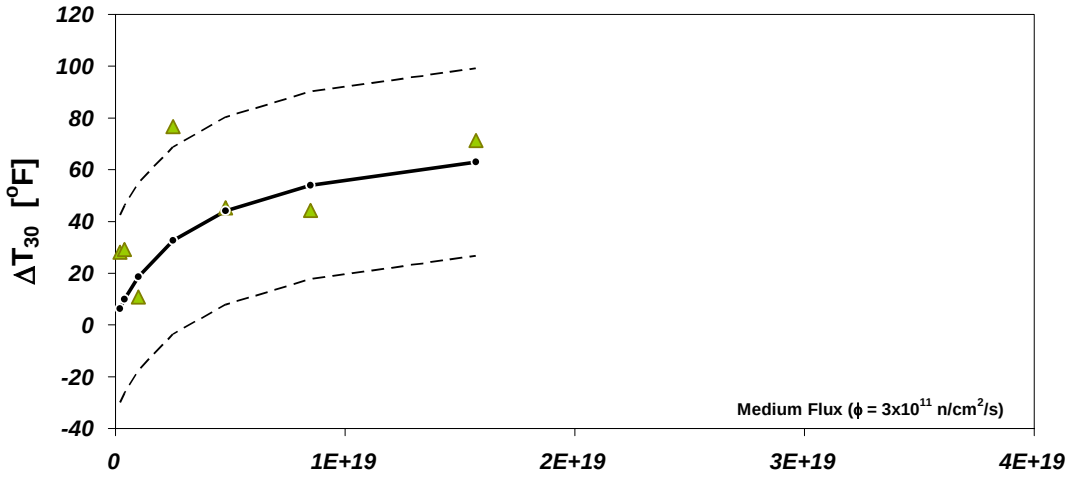
120
100
80
60
40
20
0
-20
-40
ΔT30 [°F]
Medium Flux (ϕ = 3x10^11 n/cm^2/s)
0
1E+19
2E+19
3E+19
4E+19
Fluence (E > 1 MeV) [n/cm^2]

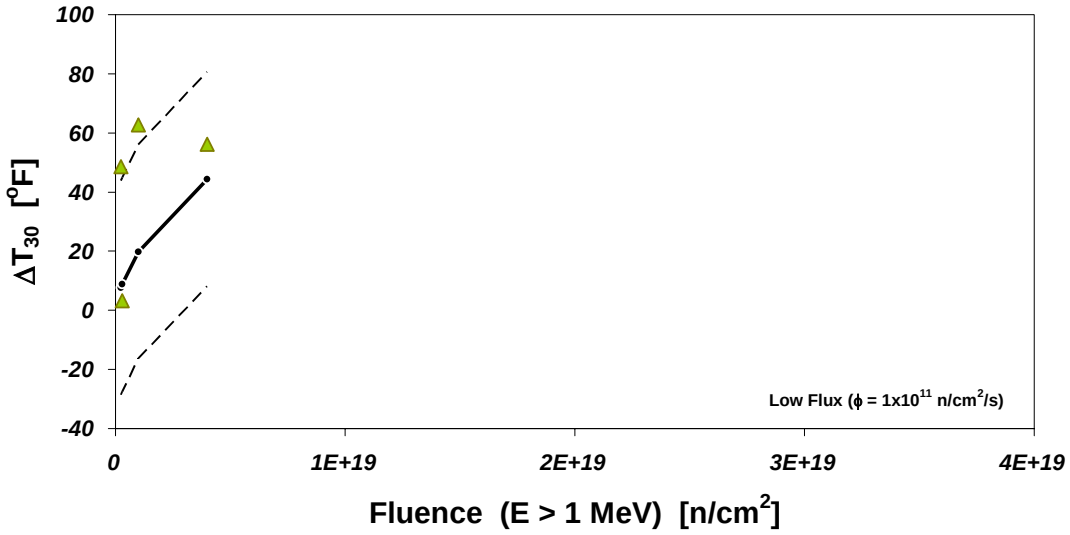
100
80
60
40
20
0
-20
-40
ΔT30 [°F]
Low Flux (ϕ = 1x10^11 n/cm^2/s)
0
1E+19
2E+19
3E+19
4E+19
Fluence (E > 1 MeV) [n/cm^2]

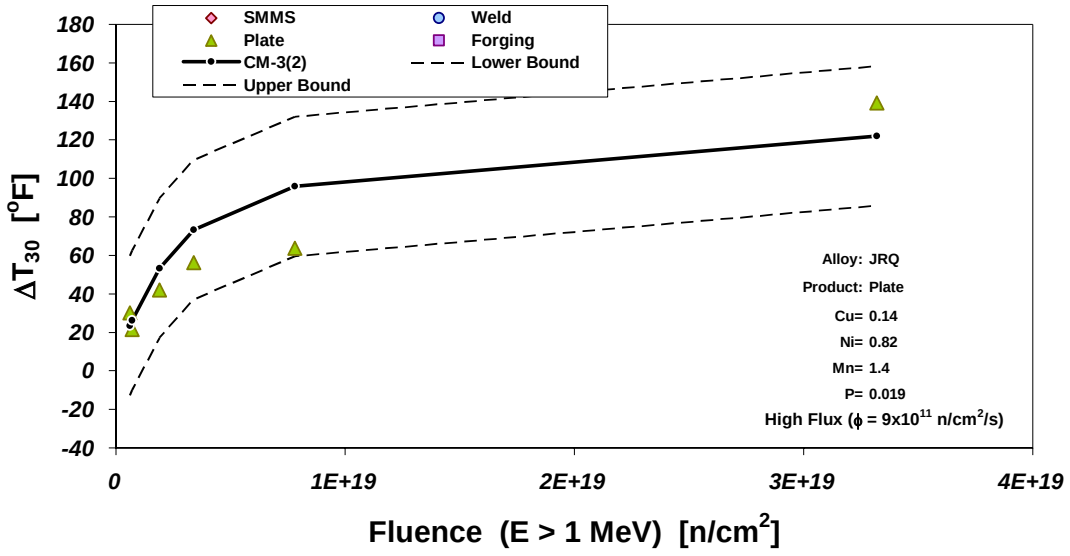
SMMS
Weld
Plate
Forging
CM-3(2)
Lower Bound
Upper Bound
Alloy: JRQ
Product: Plate
Cu= 0.14
Ni= 0.82
Mn= 1.4
P= 0.019
High Flux (ϕ = 9x10^11 n/cm^2/s)
ΔT30 [°F]
180
160
140
120
100
80
60
40
20
0
-20
-40
0
1E+19
2E+19
3E+19
4E+19
Fluence (E > 1 MeV) [n/cm^2]

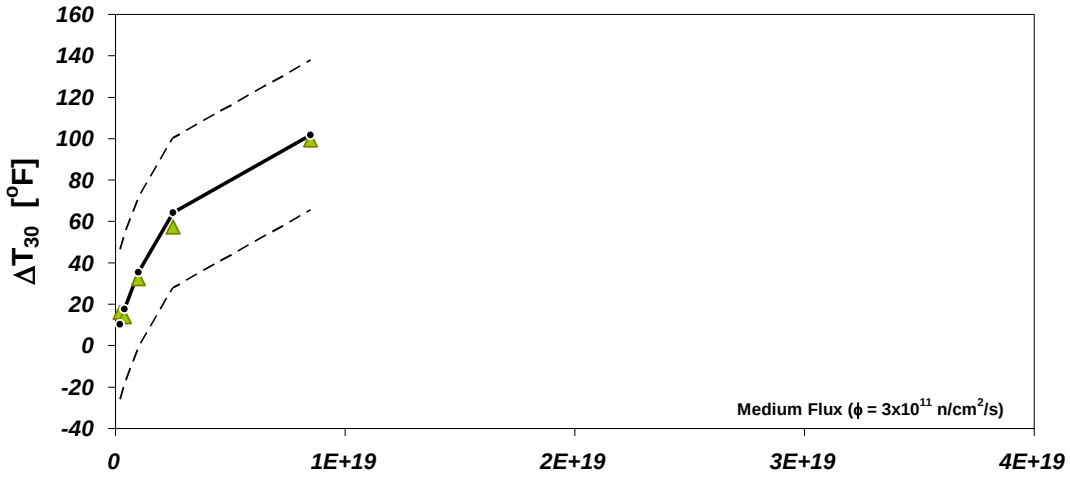
Medium Flux (ϕ = 3x10^11 n/cm^2/s)
ΔT30 [°F]
160
140
120
100
80
60
40
20
0
-20
-40
0
1E+19
2E+19
3E+19
4E+19
Fluence (E > 1 MeV) [n/cm^2]

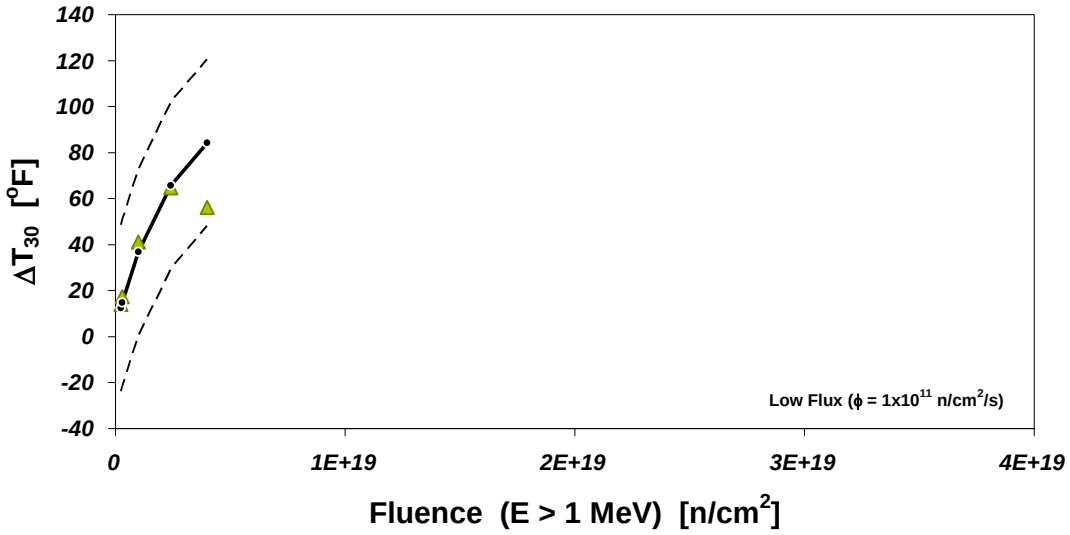
Low Flux (ϕ = 1x10^11 n/cm^2/s)
ΔT30 [°F]
140
120
100
80
60
40
20
0
-20
-40
0
1E+19
2E+19
3E+19
4E+19
Fluence (E > 1 MeV) [n/cm^2]

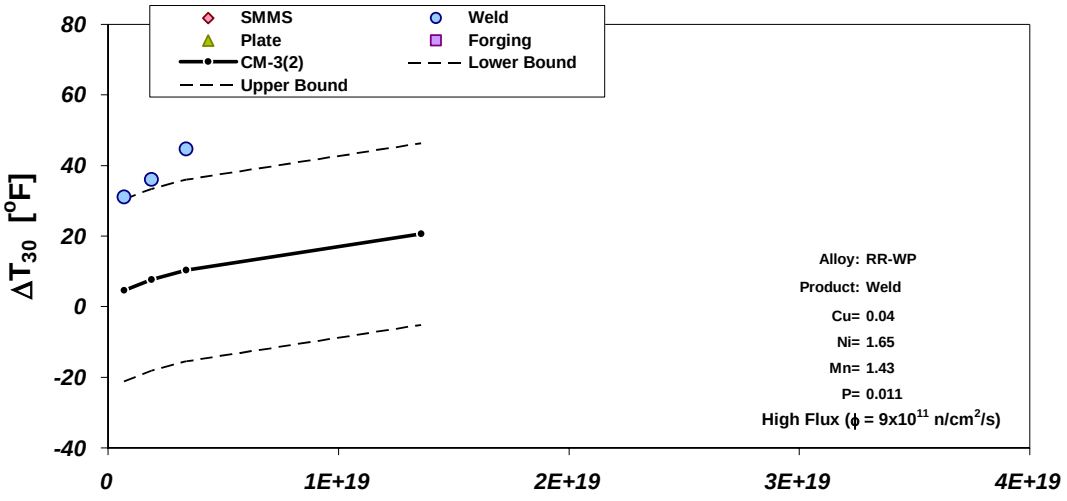
SMMS
Weld
Plate
Forging
CM-3(2)
Lower Bound
Upper Bound
80
60
40
20
0
-20
-40
ΔT30 [°F]
Alloy: RR-WP
Product: Weld
Cu= 0.04
Ni= 1.65
Mn= 1.43
P= 0.011
High Flux (ϕ = 9x10^11 n/cm^2/s)
0
1E+19
2E+19
3E+19
4E+19
Fluence (E > 1 MeV) [n/cm^2]

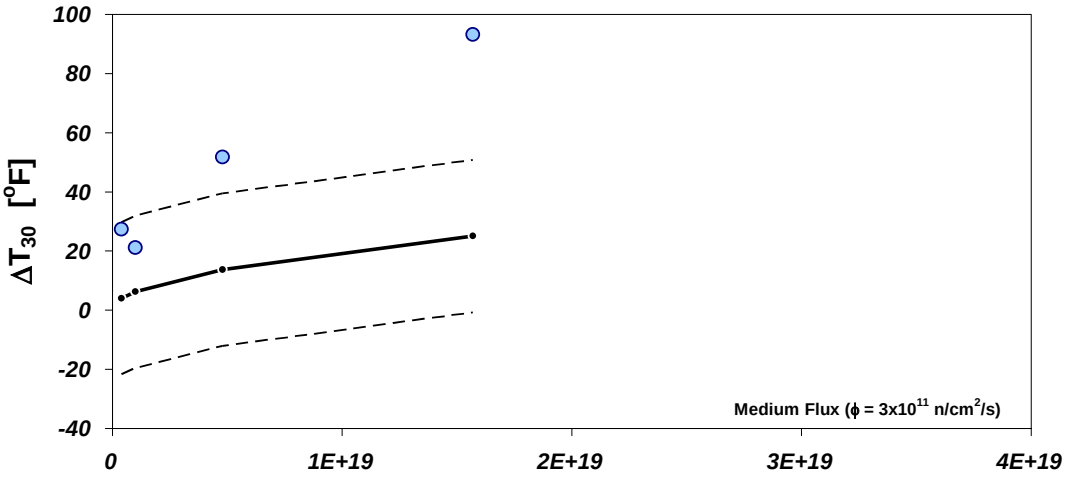
100
80
60
40
20
0
-20
-40
ΔT30 [°F]
Medium Flux (ϕ = 3x10^11 n/cm^2/s)
0
1E+19
2E+19
3E+19
4E+19
Fluence (E > 1 MeV) [n/cm^2]

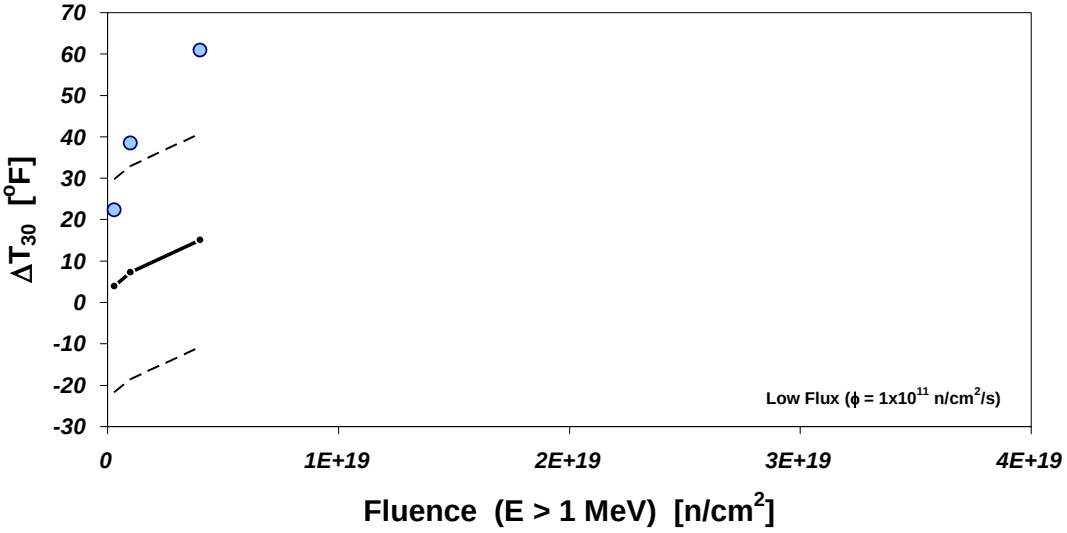
70
60
50
40
30
20
10
0
-10
-20
-30
ΔT30 [°F]
Low Flux (ϕ = 1x10^11 n/cm^2/s)
0
1E+19
2E+19
3E+19
4E+19
Fluence (E > 1 MeV) [n/cm^2]

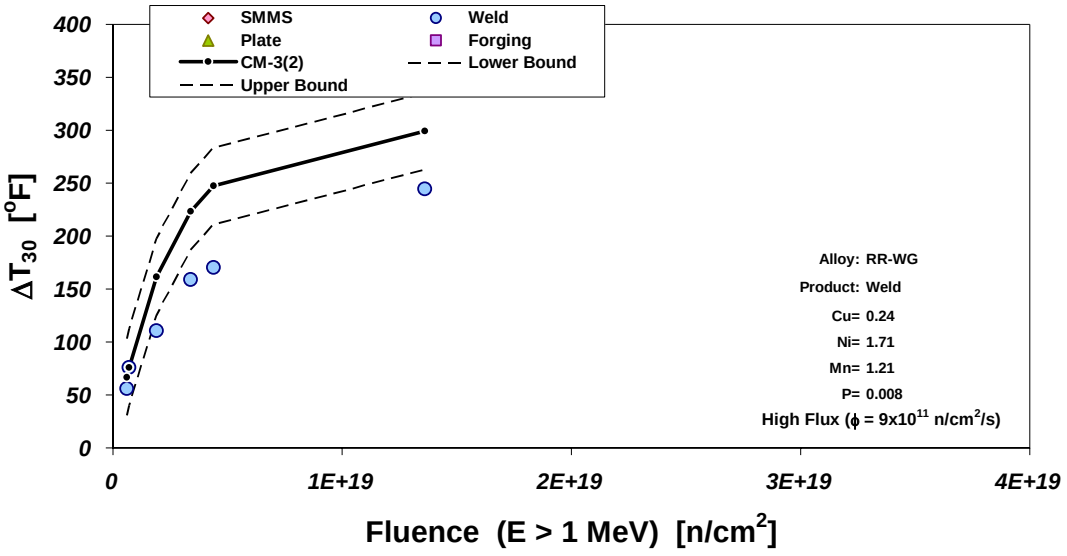
SMMS
Weld
Plate
Forging
CM-3(2)
Lower Bound
Upper Bound
Alloy: RR-WG
Product: Weld
Cu= 0.24
Ni= 1.71
Mn= 1.21
P= 0.008
High Flux (ϕ = 9x10^11 n/cm^2/s)
ΔT30 [°F]
400
350
300
250
200
150
100
50
0
0
1E+19
2E+19
3E+19
4E+19
Fluence (E > 1 MeV) [n/cm^2]

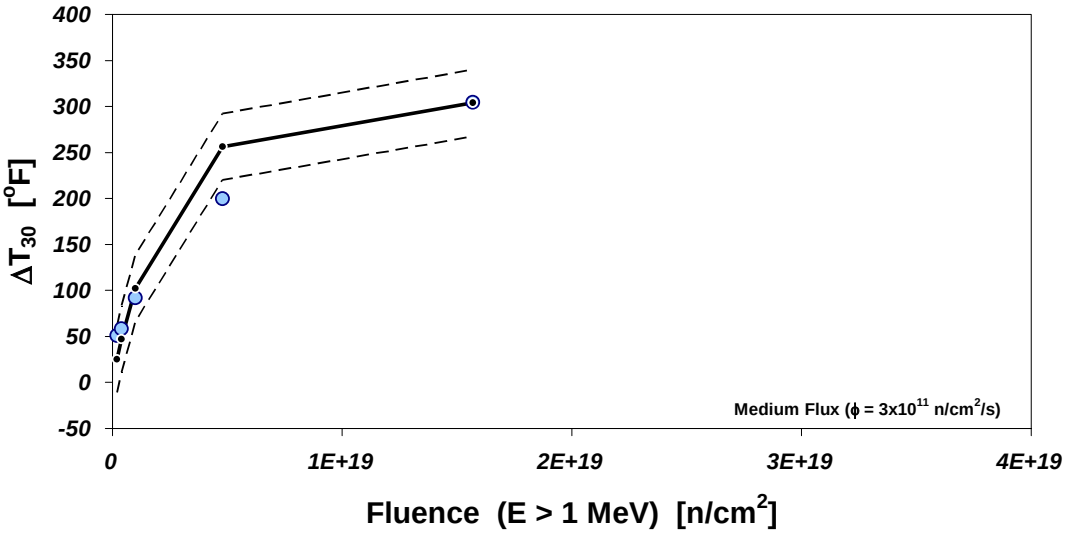
Medium Flux (ϕ = 3x10^11 n/cm^2/s)
ΔT30 [°F]
400
350
300
250
200
150
100
50
0
-50
0
1E+19
2E+19
3E+19
4E+19
Fluence (E > 1 MeV) [n/cm^2]

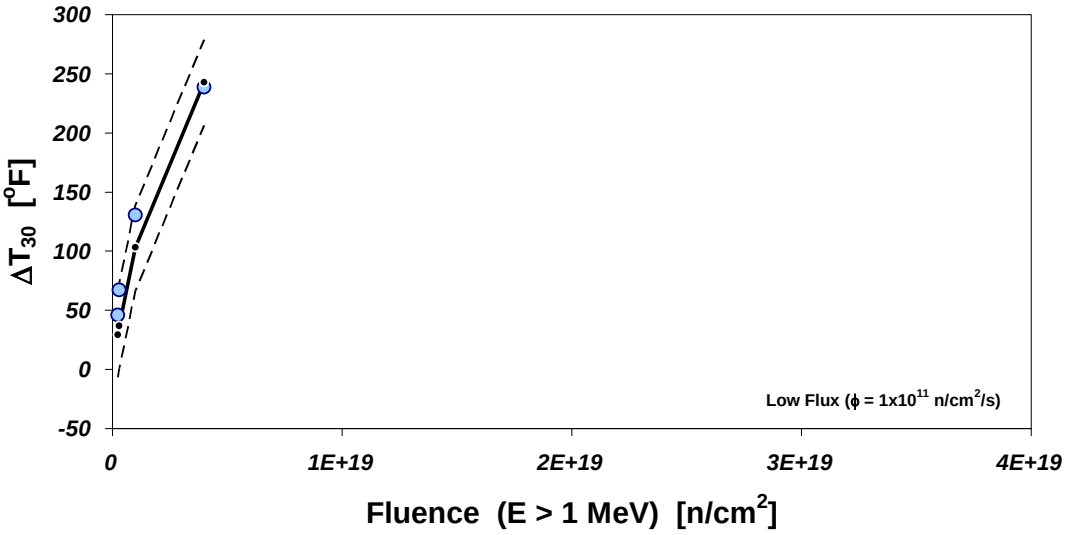
Low Flux (ϕ = 1x10^11 n/cm^2/s)
ΔT30 [°F]
300
250
200
150
100
50
0
-50
0
1E+19
2E+19
3E+19
4E+19
Fluence (E > 1 MeV) [n/cm^2]

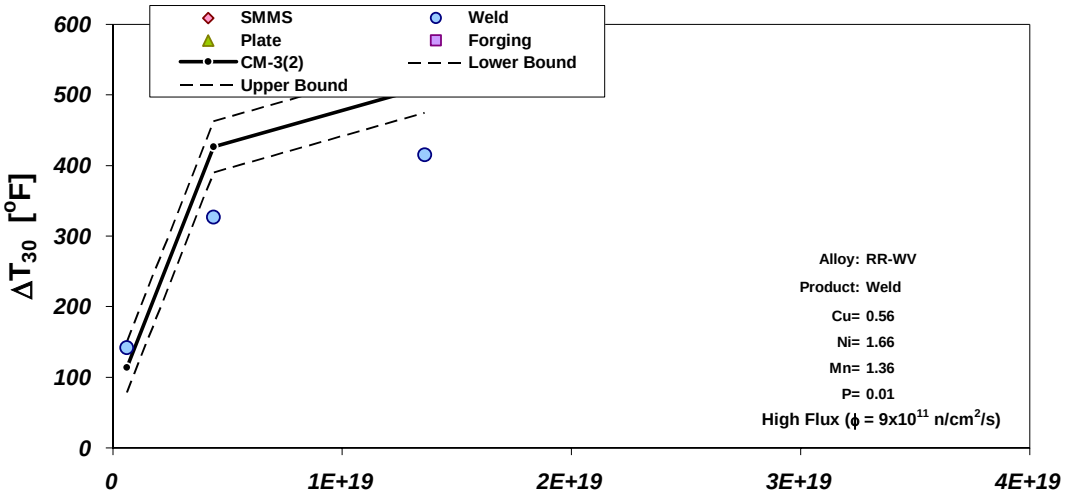
SMMS
Weld
Plate
Forging
CM-3(2)
Lower Bound
Upper Bound
Alloy: RR-WV
Product: Weld
Cu= 0.56
Ni= 1.66
Mn= 1.36
P= 0.01
High Flux (ϕ = 9x10^11 n/cm^2/s)
ΔT30 [°F]
0
100
200
300
400
500
600
0
1E+19
2E+19
3E+19
4E+19
Fluence (E > 1 MeV) [n/cm^2]

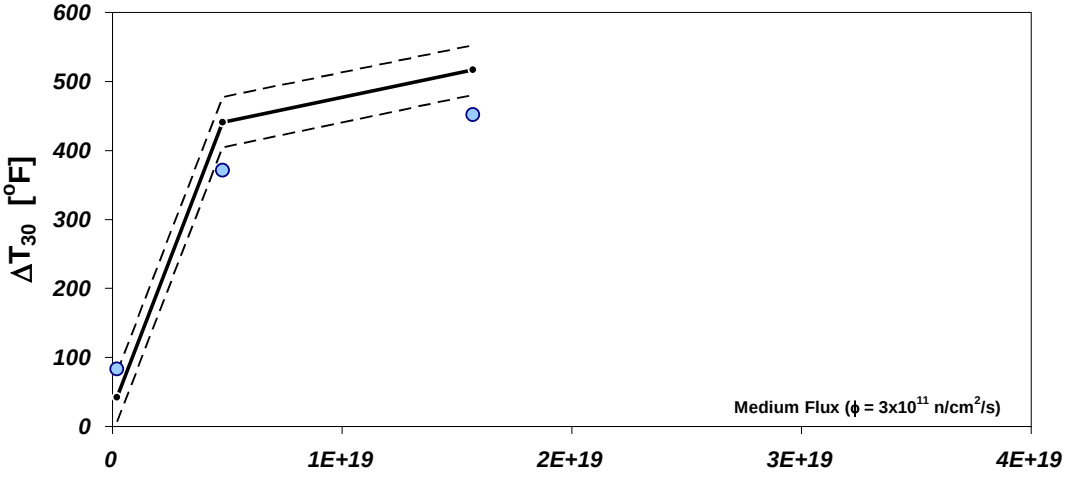
Medium Flux (ϕ = 3x10^11 n/cm^2/s)
ΔT30 [°F]
0
100
200
300
400
500
600
0
1E+19
2E+19
3E+19
4E+19
Fluence (E > 1 MeV) [n/cm^2]

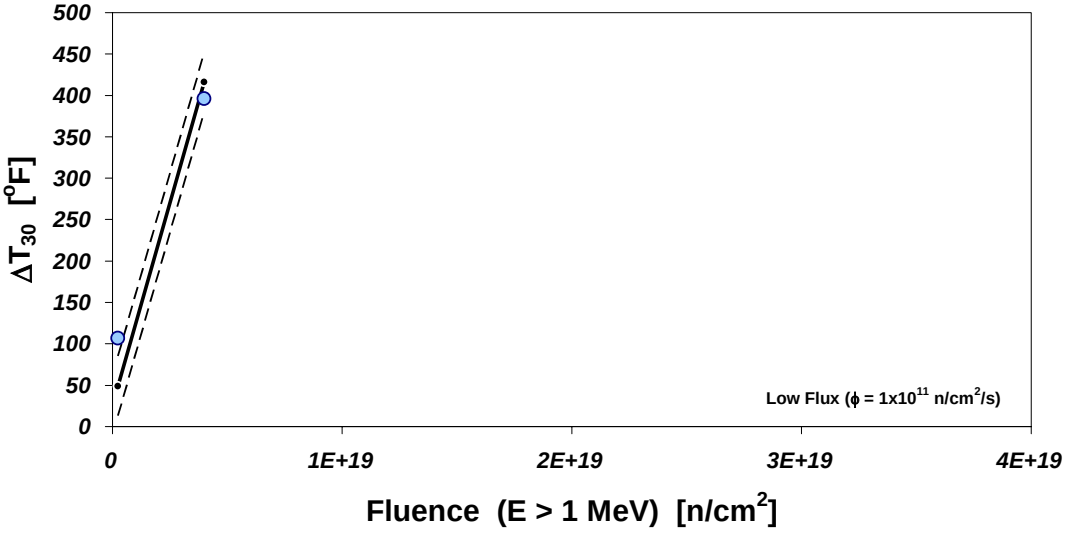
Low Flux (ϕ = 1x10^11 n/cm^2/s)
ΔT30 [°F]
0
50
100
150
200
250
300
350
400
450
500
0
1E+19
2E+19
3E+19
4E+19
Fluence (E > 1 MeV) [n/cm^2]

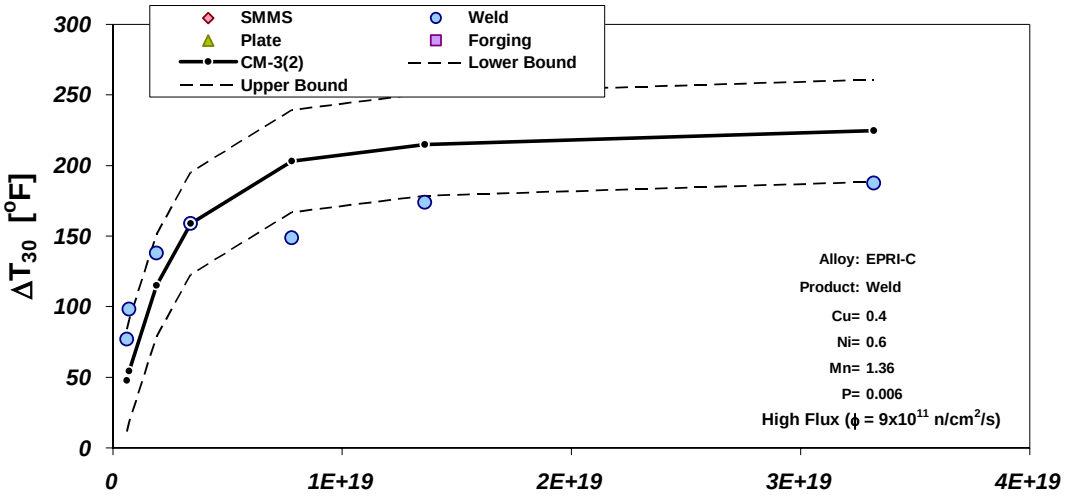
SMMS
Weld
Plate
Forging
CM-3(2)
Lower Bound
Upper Bound
Alloy: EPRI-C
Product: Weld
Cu= 0.4
Ni= 0.6
Mn= 1.36
P= 0.006
High Flux (ϕ = 9x10^11 n/cm^2/s)
ΔT30 [°F]
300
250
200
150
100
50
0
0
1E+19
2E+19
3E+19
4E+19
Fluence (E > 1 MeV) [n/cm^2]

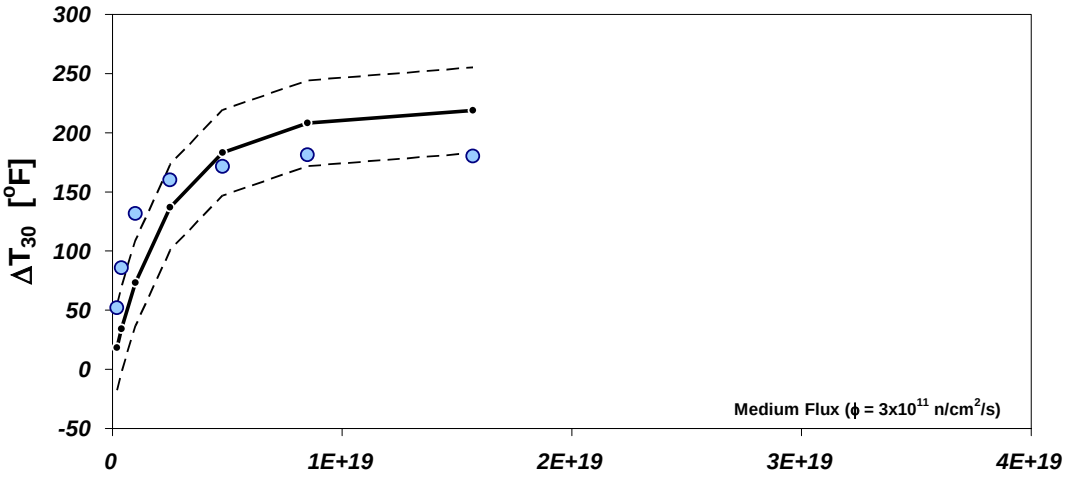
Medium Flux (ϕ = 3x10^11 n/cm^2/s)
ΔT30 [°F]
300
250
200
150
100
50
0
-50
0
1E+19
2E+19
3E+19
4E+19
Fluence (E > 1 MeV) [n/cm^2]

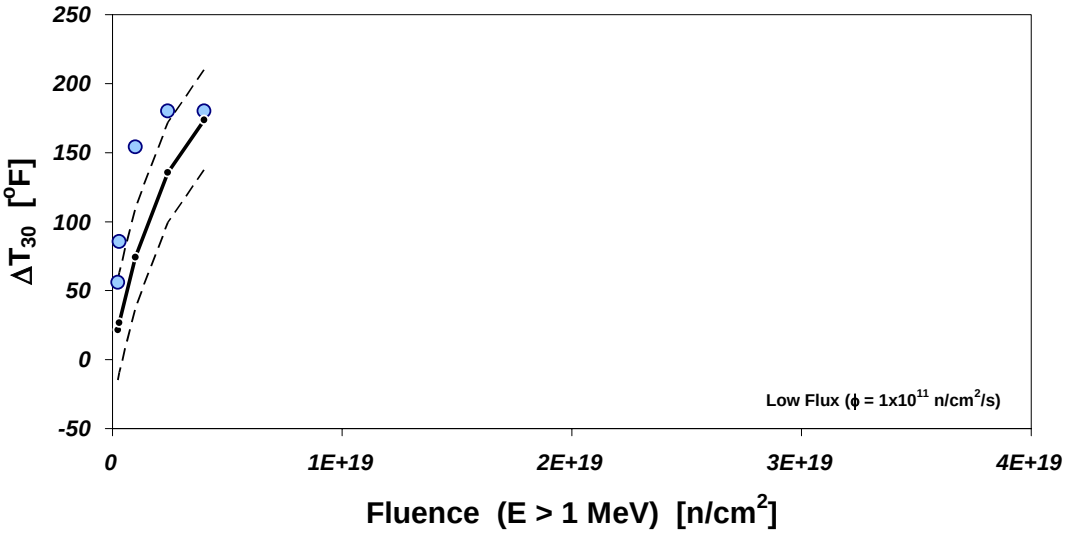
Low Flux (ϕ = 1x10^11 n/cm^2/s)
ΔT30 [°F]
250
200
150
100
50
0
-50
0
1E+19
2E+19
3E+19
4E+19
Fluence (E > 1 MeV) [n/cm^2]

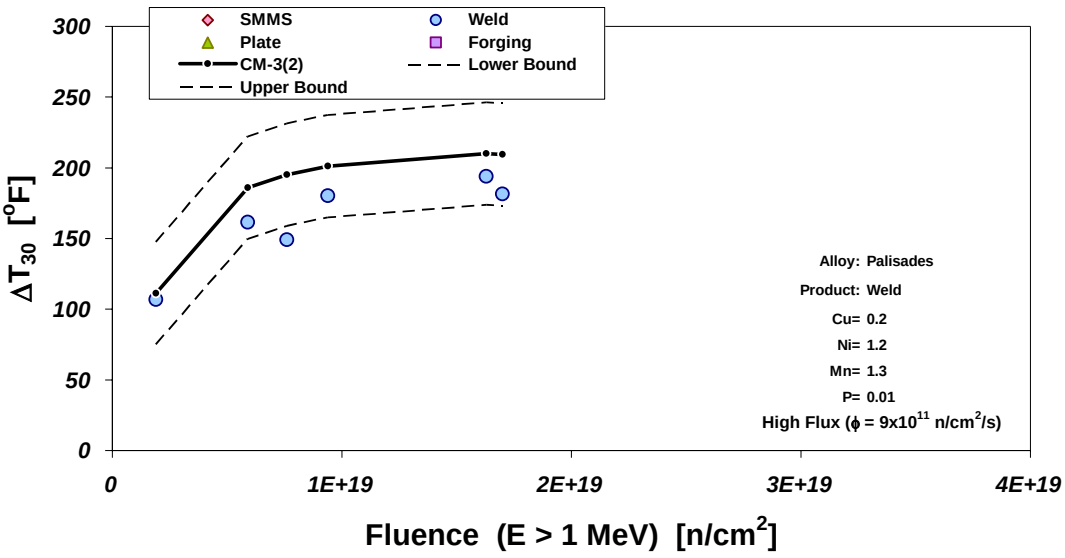

No data reported in IVAR at medium or flow flux for this alloy.

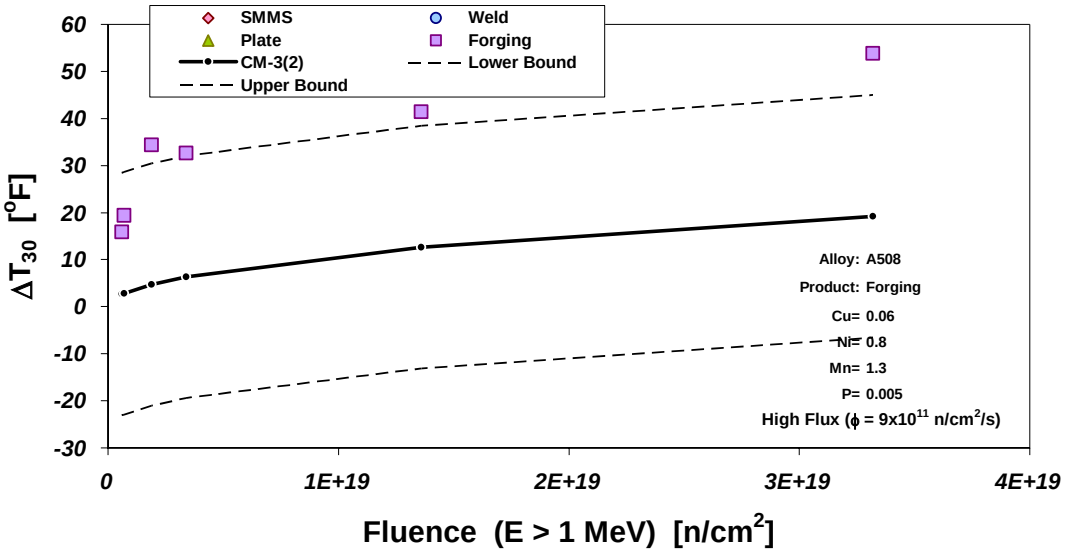
SMMS
Weld
Plate
Forging
CM-3(2)
Lower Bound
Upper Bound
Alloy: A508
Product: Forging
Cu= 0.06
Ni= 0.8
Mn= 1.3
P= 0.005
High Flux (ϕ = 9x10^11 n/cm^2/s)
ΔT30 [°F]
Fluence (E > 1 MeV) [n/cm^2]

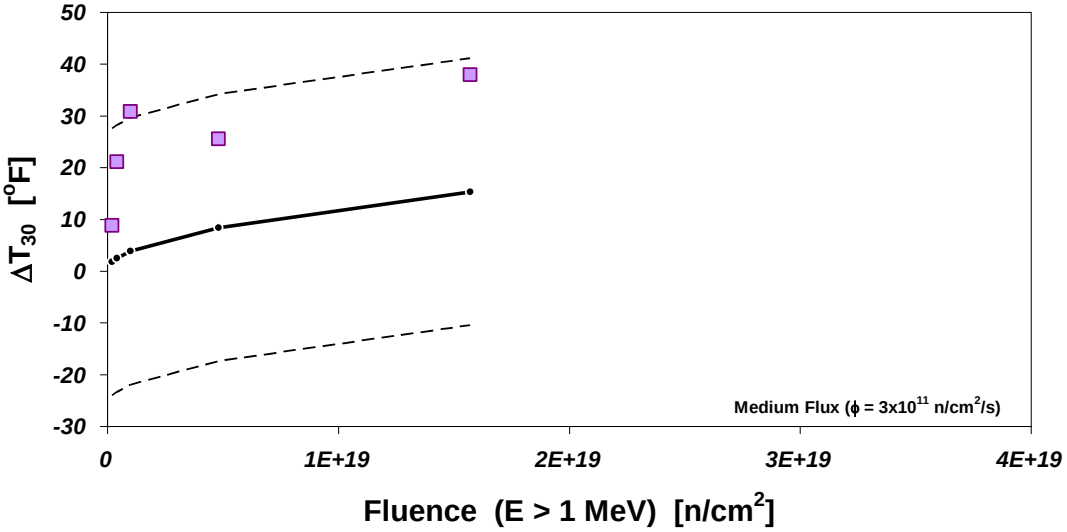
Medium Flux (ϕ = 3x10^11 n/cm^2/s)
ΔT30 [°F]
Fluence (E > 1 MeV) [n/cm^2]

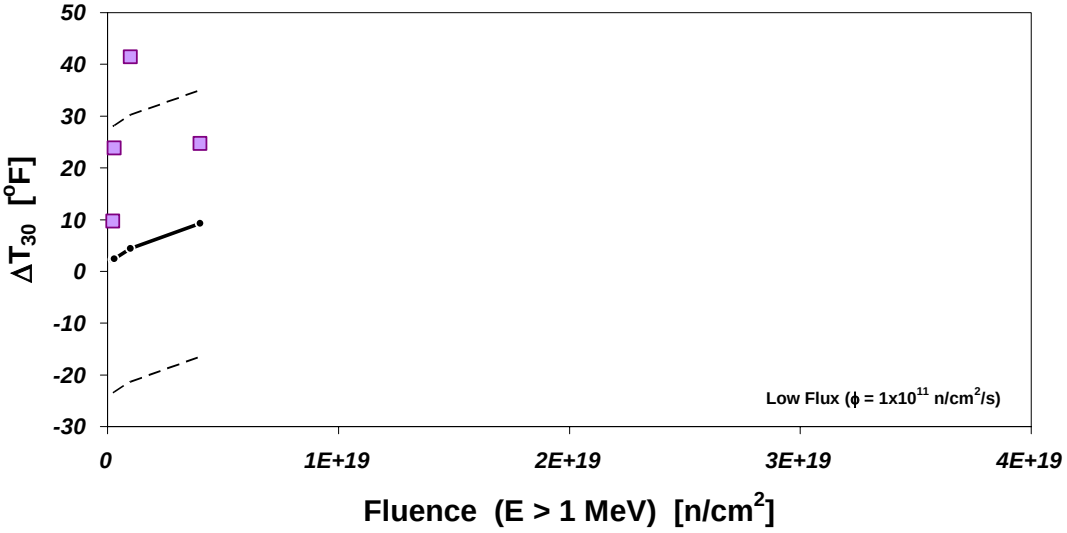
Low Flux (ϕ = 1x10^11 n/cm^2/s)
ΔT30 [°F]
Fluence (E > 1 MeV) [n/cm^2]

Table of RADAMO Chemistry Values

Alloy	Product Form	Composition [wt-%]				
		Cu	Ni	Mn	P	Si
16MND5	forging	0.065	0.69	1.37	0.013	0.04
18MND5-BM	plate	0.13	0.64	1.55	0.008	0.25
18MND5-W	weld	0.12	1.01	1.3	0.021	0.19
20MnMoNi55	forging	0.11	0.8	1.29	0.007	0.2
72W	weld	0.23	0.6	1.6	0.006	0.44
73W	weld	0.31	0.6	1.56	0.005	0.45
A508-B	forging	0.05	0.75	1.43	0.008	0.28
A508-W	weld	0.07	0.83	1.57	0.015	0.22
HSST-03	plate	0.12	0.62	1.36	0.011	0.26
JRQ	plate	0.14	0.84	1.42	0.017	0.24
VVER-1000B	plate	0.05	1.26	0.46	0.008	0.3
VVER-1000W	weld	0.06	1.7	0.73	0.006	0.14
VVER-440B	plate	0.08	0.12	0.4	0.012	0.29
VVER-440W	weld	0.13	0.12	0.97	0.032	0.5

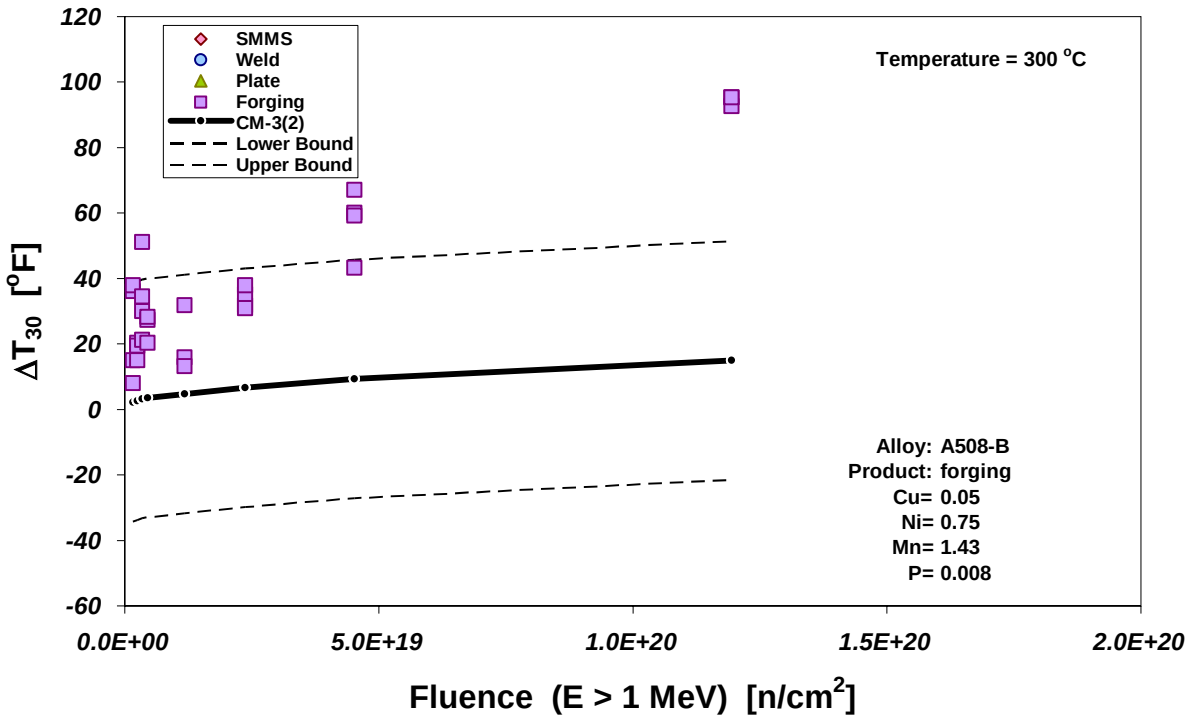
SMMS
Weld
Plate
Forging
CM-3(2)
Lower Bound
Upper Bound
Temperature = 300 °C
Alloy: A508-B
Product: forging
Cu= 0.05
Ni= 0.75
Mn= 1.43
P= 0.008
ΔT30 [°F]
120
100
80
60
40
20
0
-20
-40
-60
0.0E+00
5.0E+19
1.0E+20
1.5E+20
2.0E+20
Fluence (E > 1 MeV) [n/cm2]

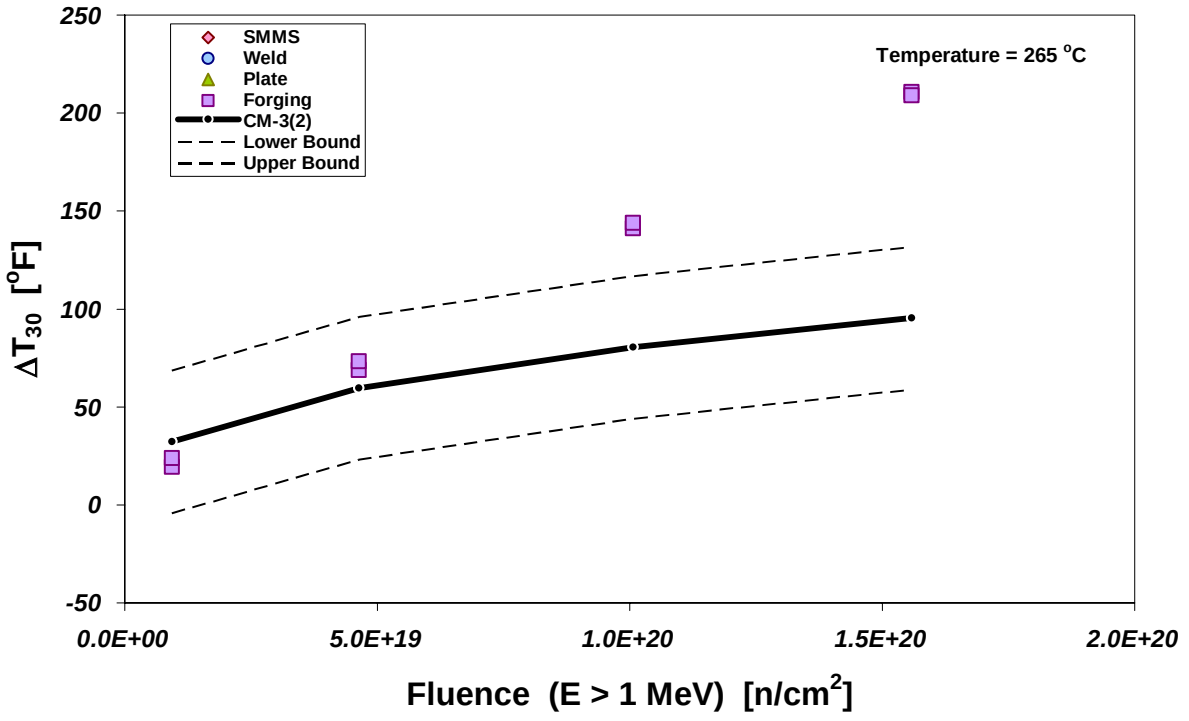
SMMS
Weld
Plate
Forging
CM-3(2)
Lower Bound
Upper Bound
Temperature = 265 °C
ΔT30 [°F]
250
200
150
100
50
0
-50
0.0E+00
5.0E+19
1.0E+20
1.5E+20
2.0E+20
Fluence (E > 1 MeV) [n/cm2]

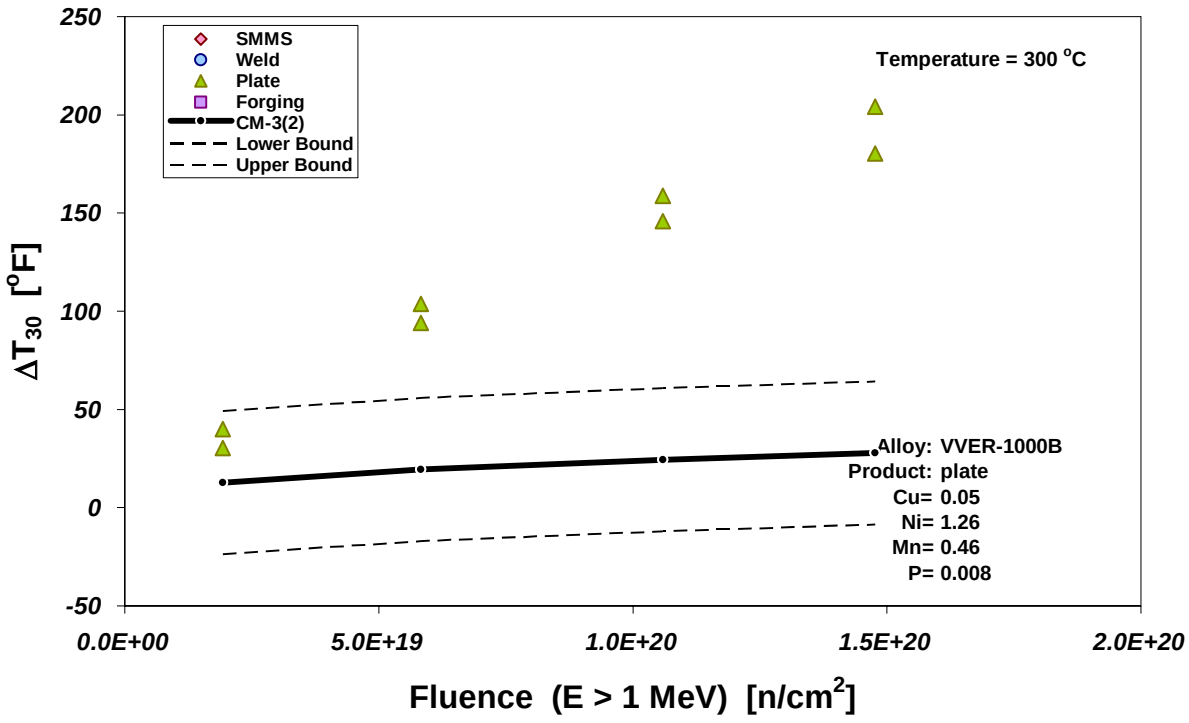
SMMS
Weld
Plate
Forging
CM-3(2)
Lower Bound
Upper Bound
Temperature = 300 °C
Alloy: VVER-1000B
Product: plate
Cu= 0.05
Ni= 1.26
Mn= 0.46
P= 0.008
ΔT30 [°F]
250
200
150
100
50
0
-50
0.0E+00
5.0E+19
1.0E+20
1.5E+20
2.0E+20
Fluence (E > 1 MeV) [n/cm2]

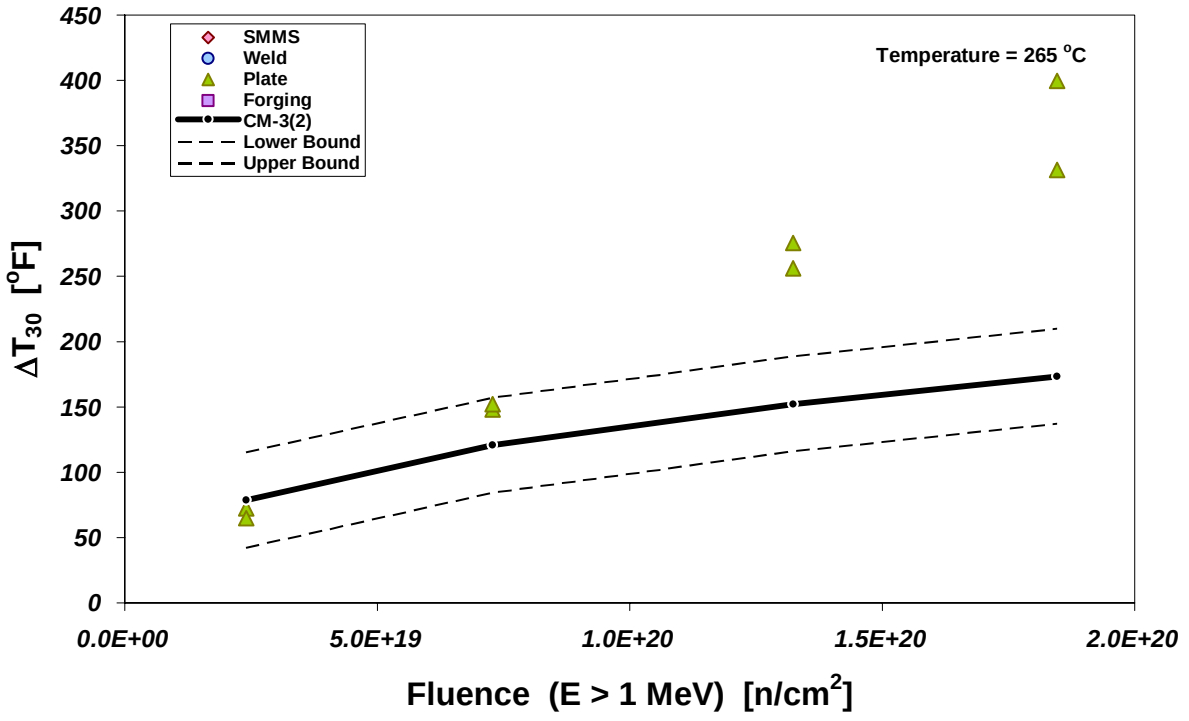
SMMS
Weld
Plate
Forging
CM-3(2)
Lower Bound
Upper Bound
Temperature = 265 °C
ΔT30 [°F]
450
400
350
300
250
200
150
100
50
0
0.0E+00
5.0E+19
1.0E+20
1.5E+20
2.0E+20
Fluence (E > 1 MeV) [n/cm2]

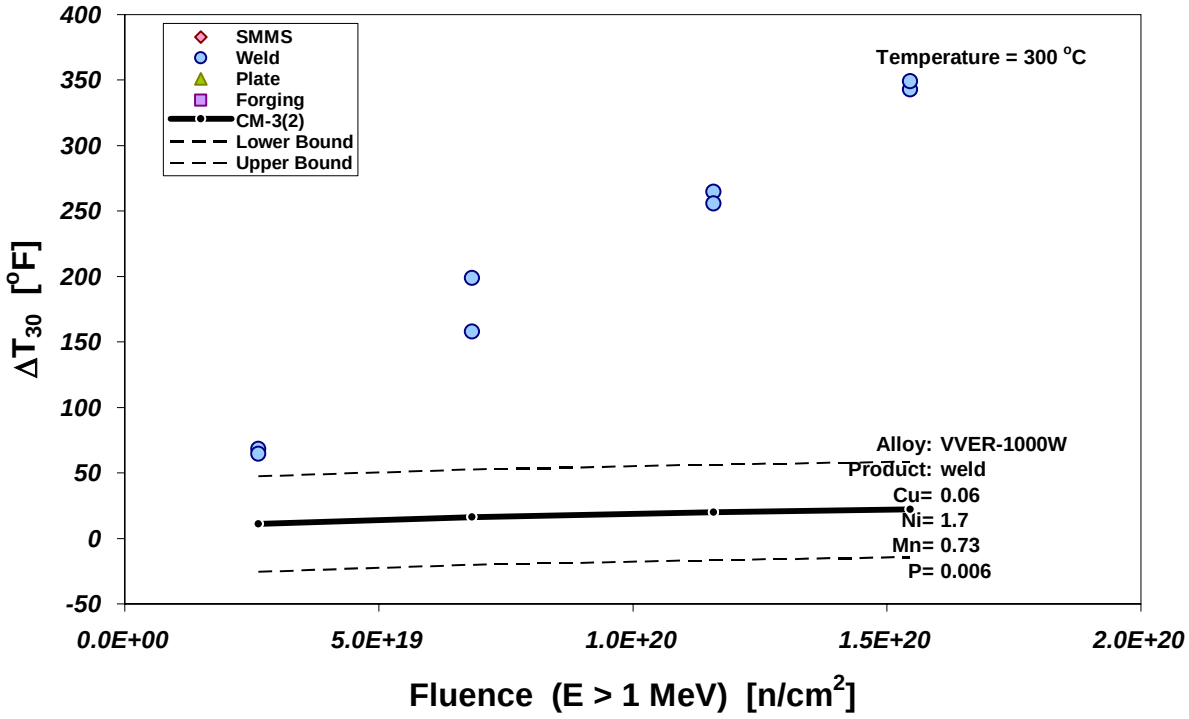
SMMS
Weld
Plate
Forging
CM-3(2)
Lower Bound
Upper Bound
Temperature = 300 °C
Alloy: VVER-1000W
Product: weld
Cu= 0.06
Ni= 1.7
Mn= 0.73
P= 0.006
ΔT30 [°F]
400
350
300
250
200
150
100
50
0
-50
0.0E+00
5.0E+19
1.0E+20
1.5E+20
2.0E+20
Fluence (E > 1 MeV) [n/cm2]

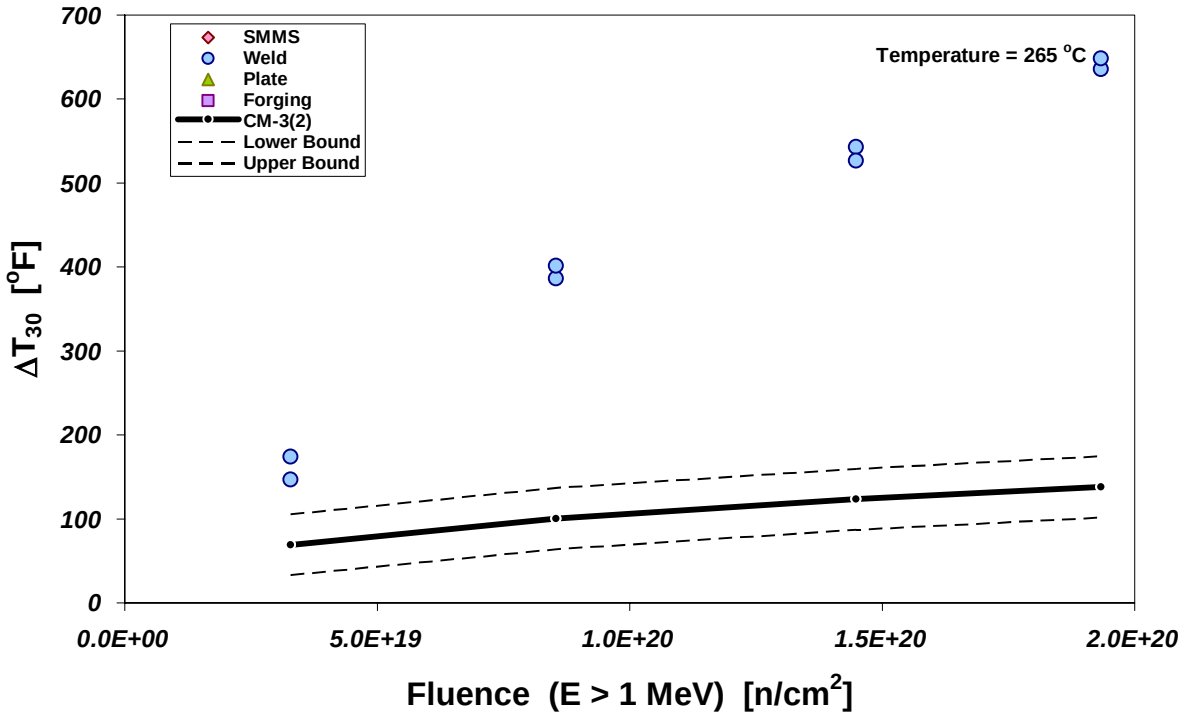
SMMS
Weld
Plate
Forging
CM-3(2)
Lower Bound
Upper Bound
Temperature = 265 °C
ΔT30 [°F]
700
600
500
400
300
200
100
0
0.0E+00
5.0E+19
1.0E+20
1.5E+20
2.0E+20
Fluence (E > 1 MeV) [n/cm2]

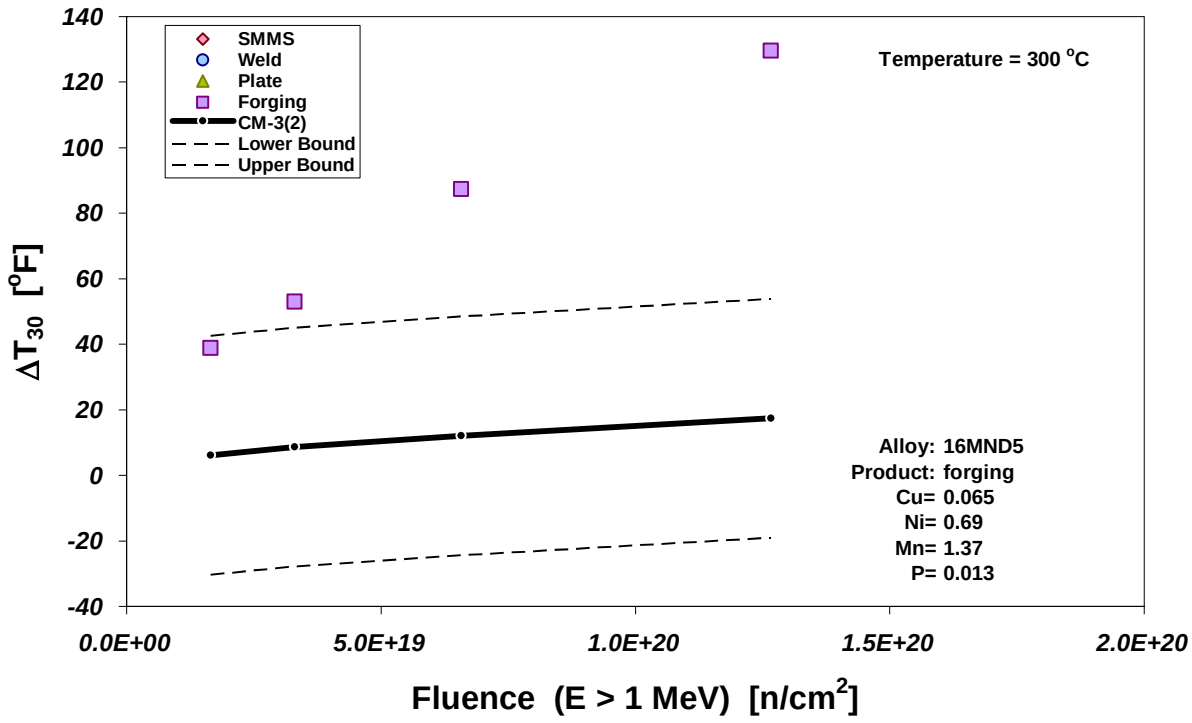

No data reported in RADAMO at 265 °C for this alloy.

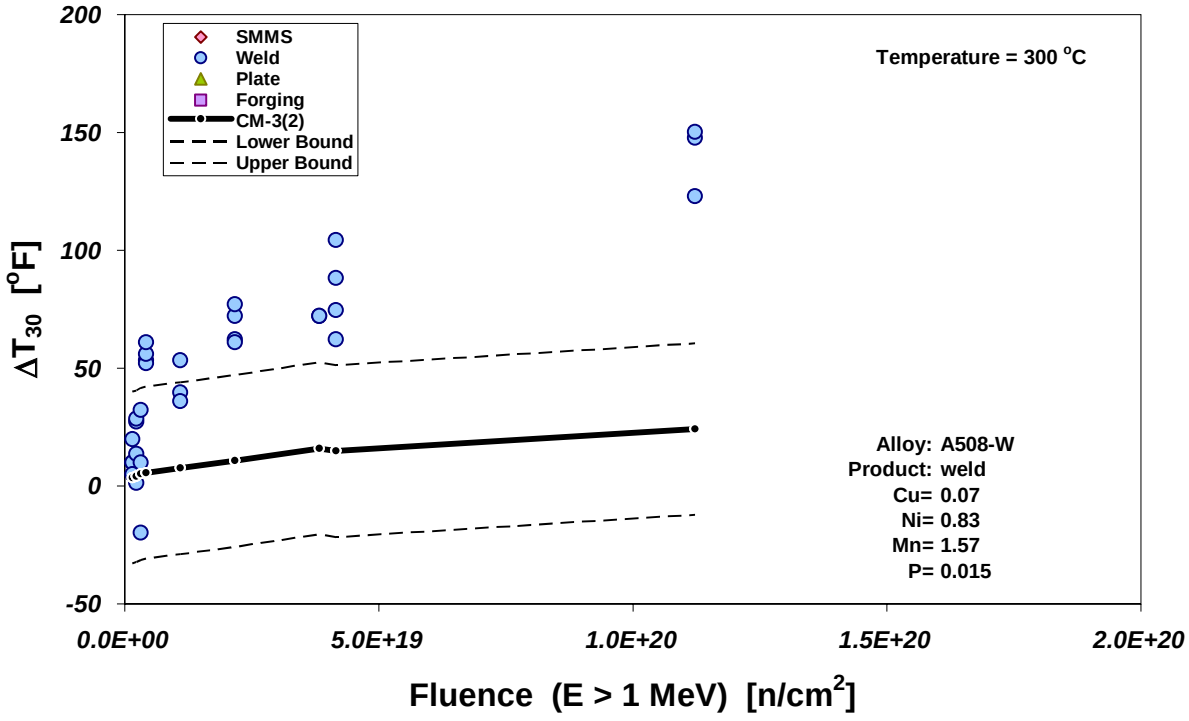
SMMS
Weld
Plate
Forging
CM-3(2)
Lower Bound
Upper Bound
Temperature = 300 °C
Alloy: A508-W
Product: weld
Cu= 0.07
Ni= 0.83
Mn= 1.57
P= 0.015
ΔT30 [°F]
200
150
100
50
0
-50
0.0E+00
5.0E+19
1.0E+20
1.5E+20
2.0E+20
Fluence (E > 1 MeV) [n/cm2]

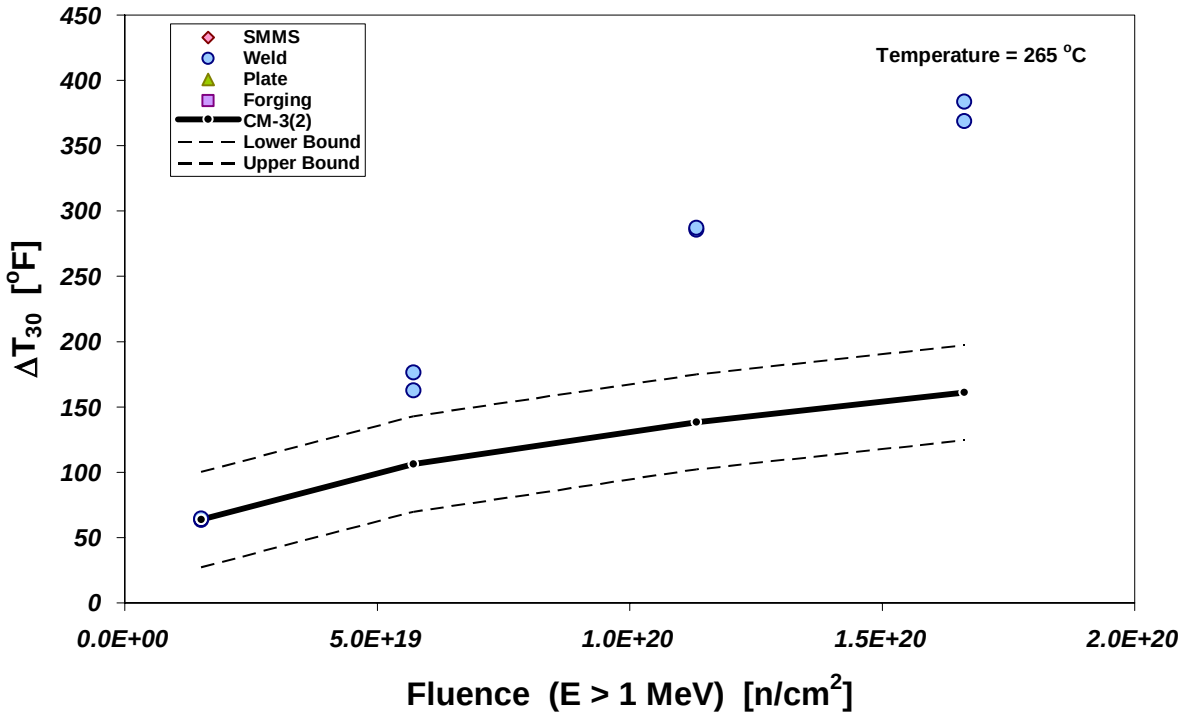
SMMS
Weld
Plate
Forging
CM-3(2)
Lower Bound
Upper Bound
Temperature = 265 °C
ΔT30 [°F]
450
400
350
300
250
200
150
100
50
0
0.0E+00
5.0E+19
1.0E+20
1.5E+20
2.0E+20
Fluence (E > 1 MeV) [n/cm2]

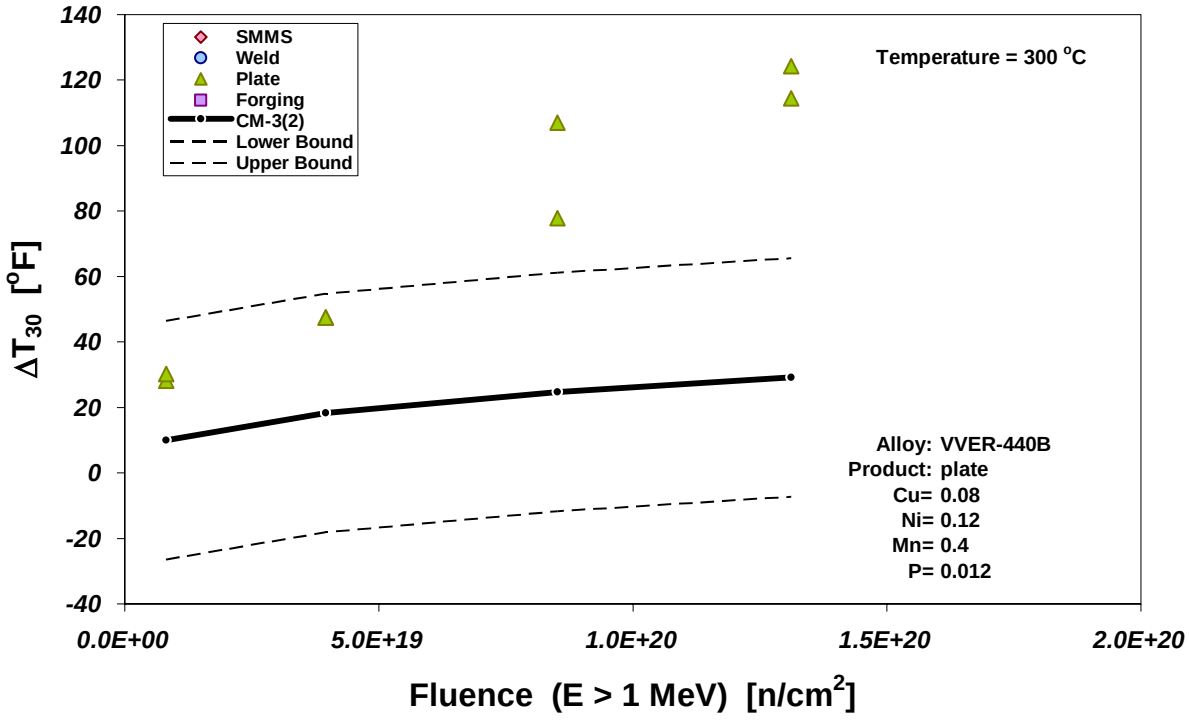
SMMS
Weld
Plate
Forging
CM-3(2)
Lower Bound
Upper Bound
Temperature = 300 °C
Alloy: VVER-440B
Product: plate
Cu= 0.08
Ni= 0.12
Mn= 0.4
P= 0.012
ΔT30 [°F]
140
120
100
80
60
40
20
0
-20
-40
0.0E+00
5.0E+19
1.0E+20
1.5E+20
2.0E+20
Fluence (E > 1 MeV) [n/cm2]

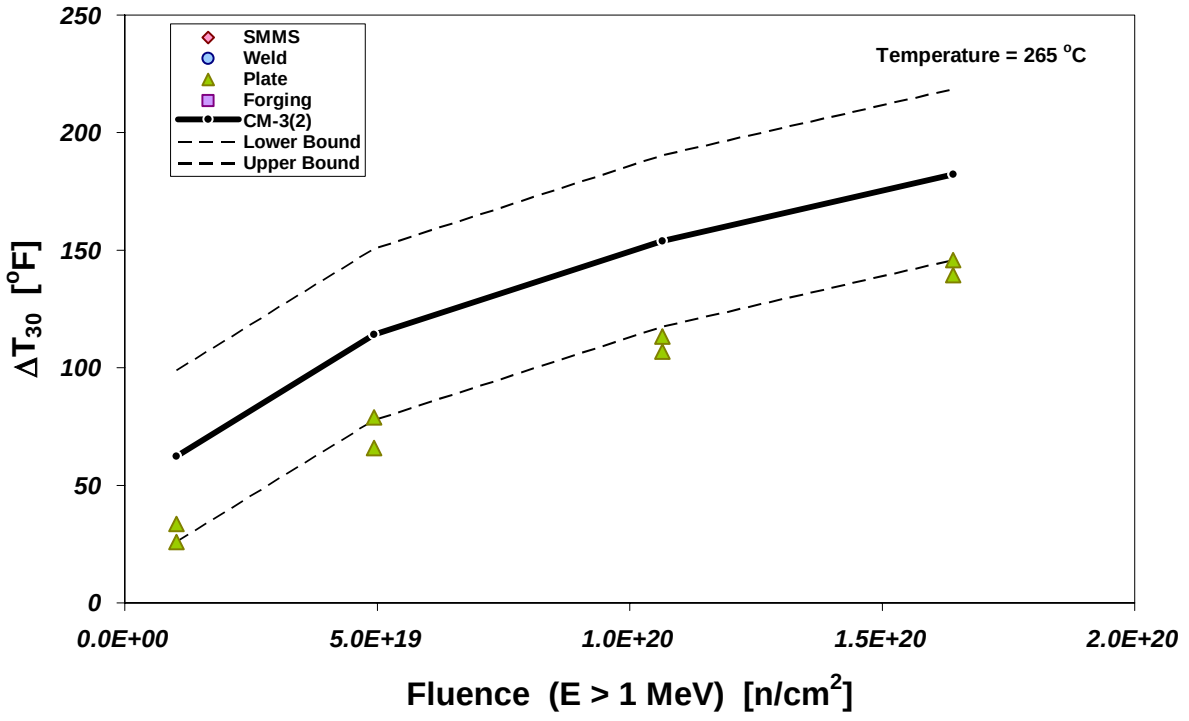
SMMS
Weld
Plate
Forging
CM-3(2)
Lower Bound
Upper Bound
Temperature = 265 °C
ΔT30 [°F]
250
200
150
100
50
0
0.0E+00
5.0E+19
1.0E+20
1.5E+20
2.0E+20
Fluence (E > 1 MeV) [n/cm2]

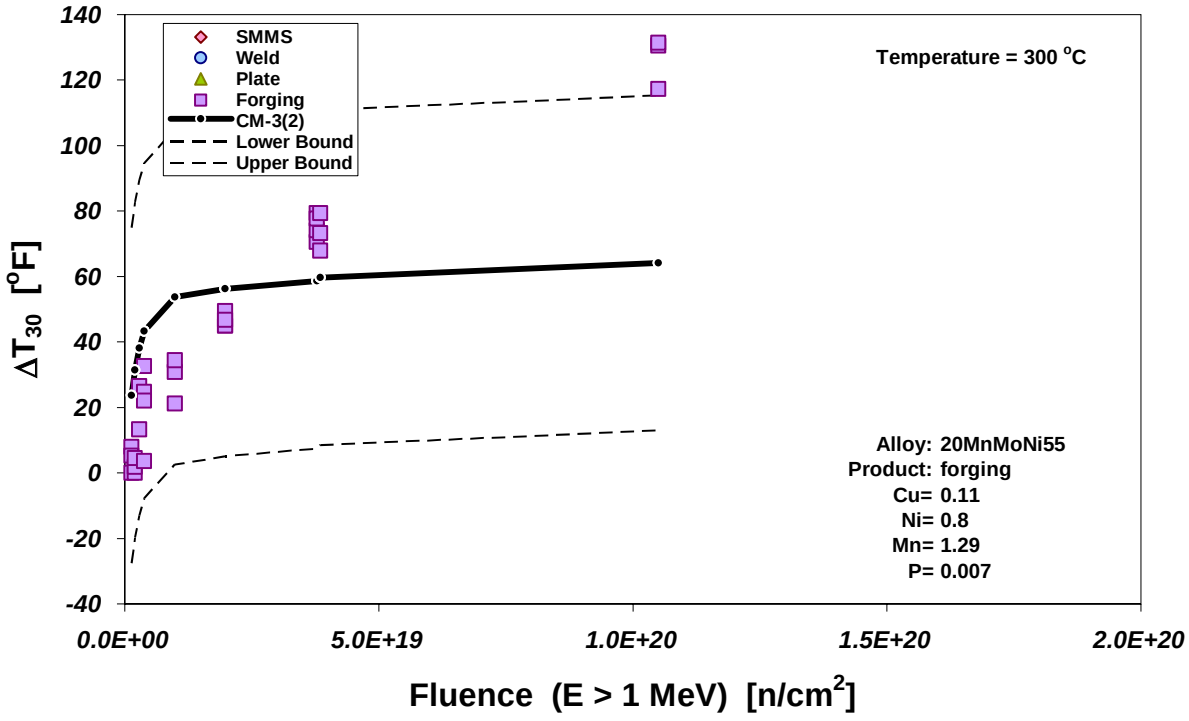
SMMS
Weld
Plate
Forging
CM-3(2)
Lower Bound
Upper Bound
Temperature = 300 °C
Alloy: 20MnMoNi55
Product: forging
Cu= 0.11
Ni= 0.8
Mn= 1.29
P= 0.007
ΔT30 [°F]
140
120
100
80
60
40
20
0
-20
-40
0.0E+00
5.0E+19
1.0E+20
1.5E+20
2.0E+20
Fluence (E > 1 MeV) [n/cm2]

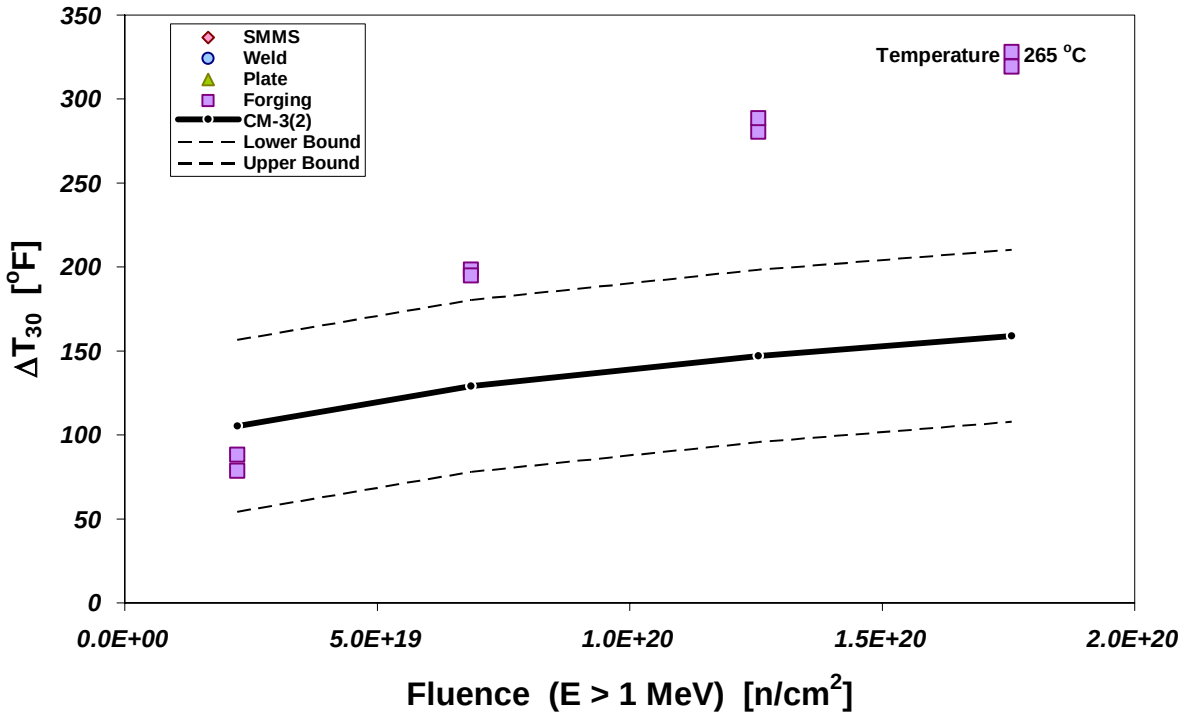
SMMS
Weld
Plate
Forging
CM-3(2)
Lower Bound
Upper Bound
Temperature 265 °C
ΔT30 [°F]
350
300
250
200
150
100
50
0
0.0E+00
5.0E+19
1.0E+20
1.5E+20
2.0E+20
Fluence (E > 1 MeV) [n/cm2]

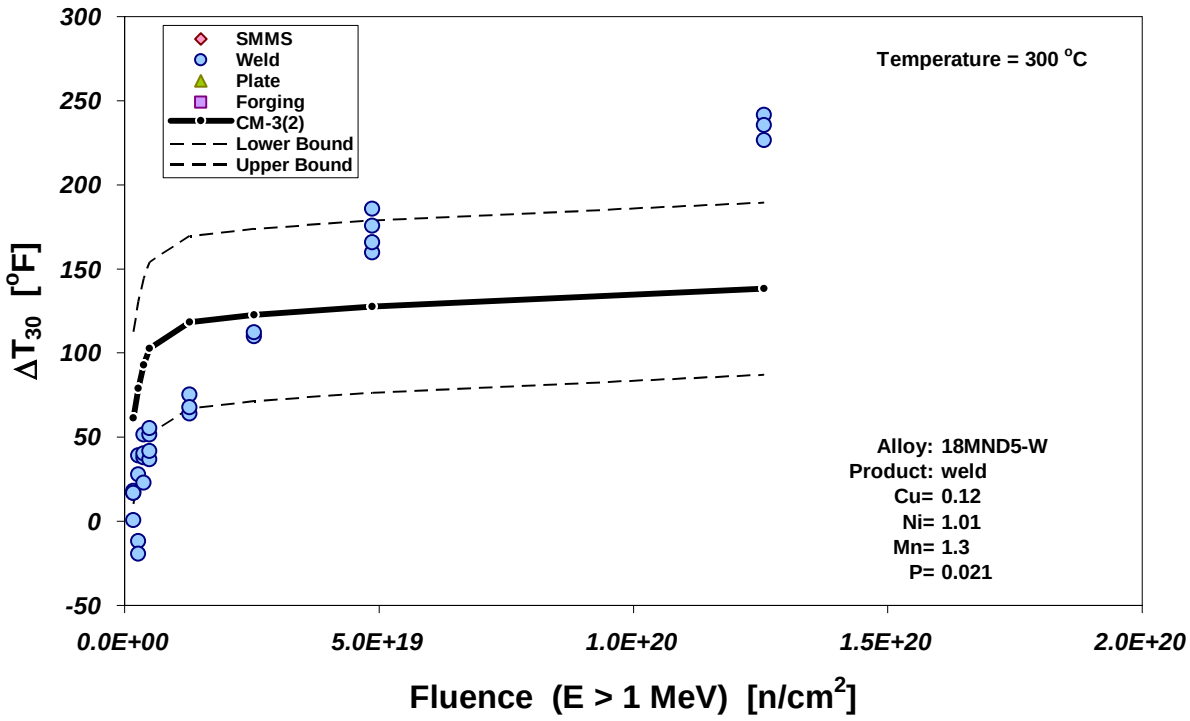

No data reported in RADAMO at 265 °C for this alloy.

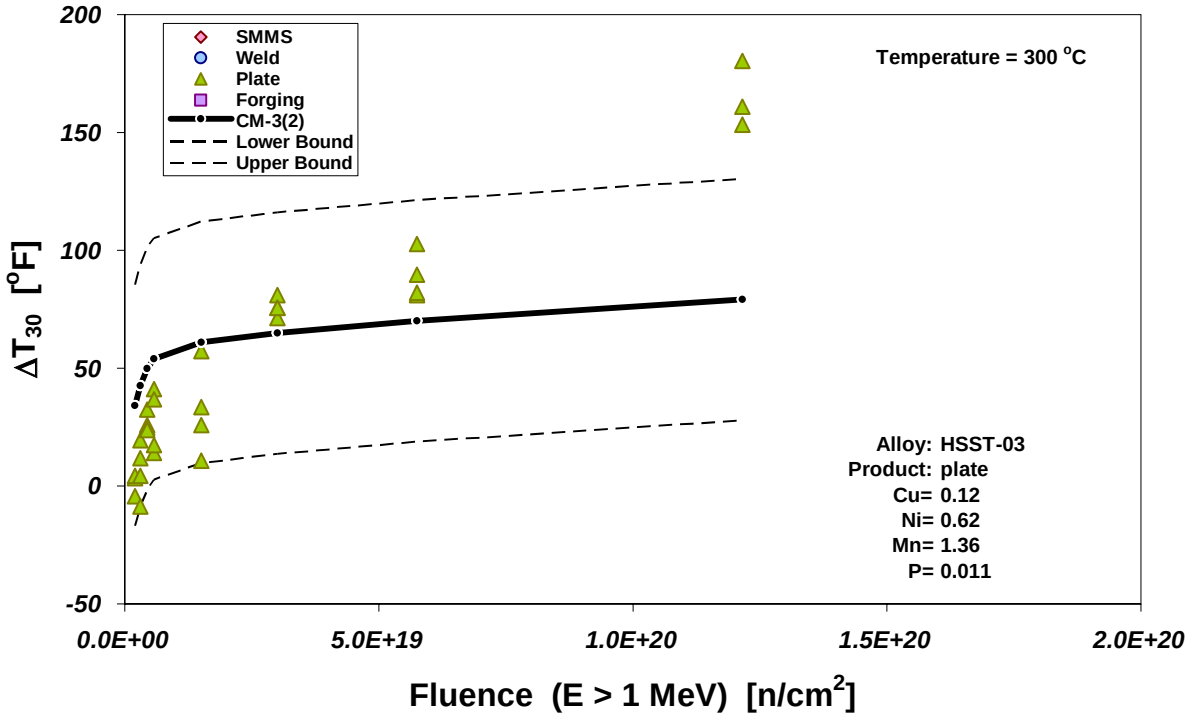
SMMS
Weld
Plate
Forging
CM-3(2)
Lower Bound
Upper Bound
Temperature = 300 °C
Alloy: HSST-03
Product: plate
Cu= 0.12
Ni= 0.62
Mn= 1.36
P= 0.011
ΔT30 [°F]
200
150
100
50
0
-50
0.0E+00
5.0E+19
1.0E+20
1.5E+20
2.0E+20
Fluence (E > 1 MeV) [n/cm2]

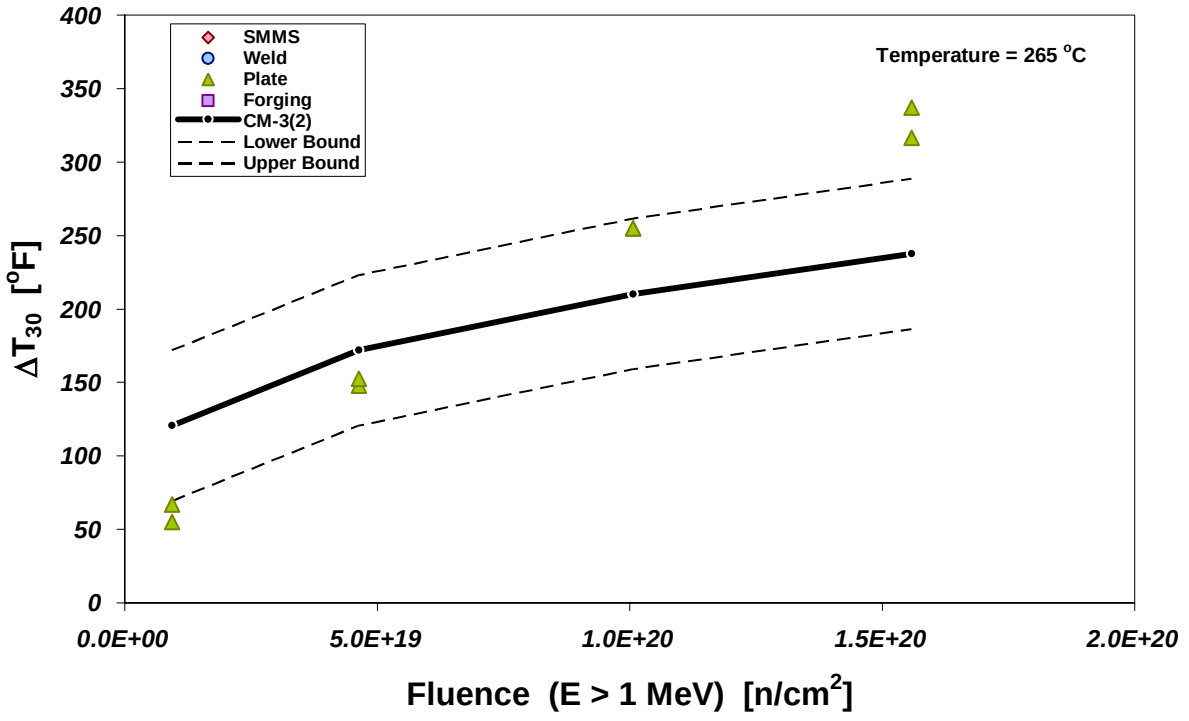
SMMS
Weld
Plate
Forging
CM-3(2)
Lower Bound
Upper Bound
Temperature = 265 °C
ΔT30 [°F]
400
350
300
250
200
150
100
50
0
0.0E+00
5.0E+19
1.0E+20
1.5E+20
2.0E+20
Fluence (E > 1 MeV) [n/cm2]

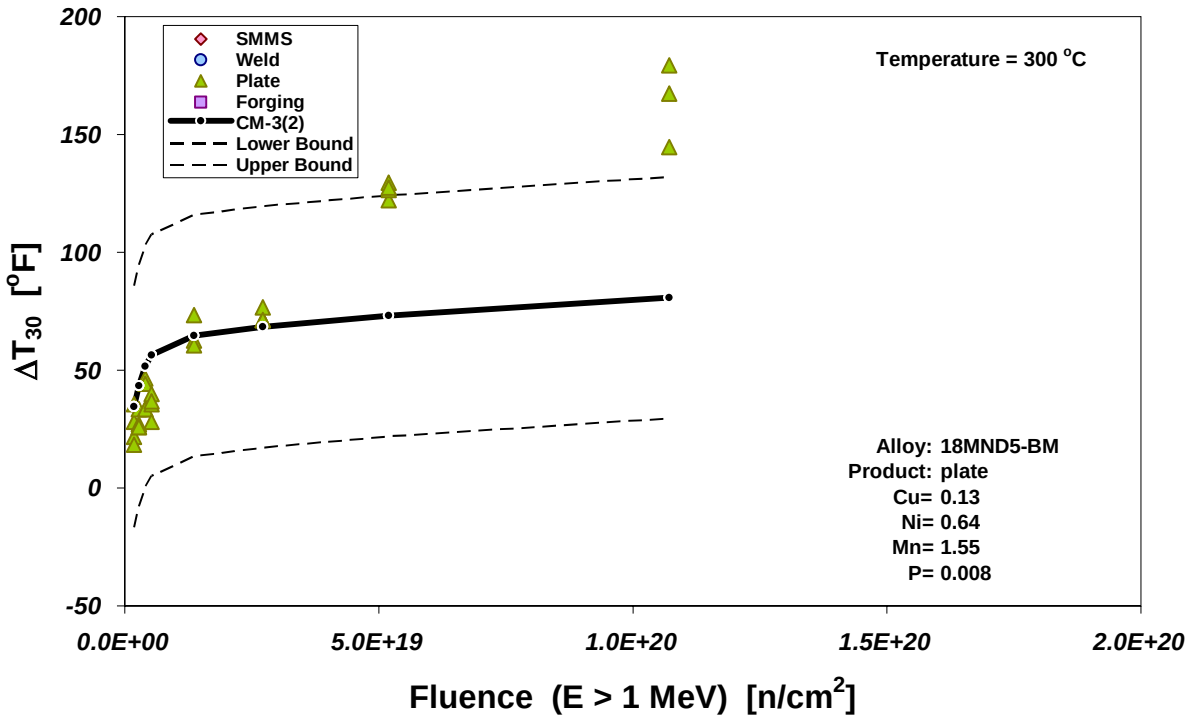
SMMS
Weld
Plate
Forging
CM-3(2)
Lower Bound
Upper Bound
Temperature = 300 °C
Alloy: 18MND5-BM
Product: plate
Cu= 0.13
Ni= 0.64
Mn= 1.55
P= 0.008
ΔT30 [°F]
200
150
100
50
0
-50
0.0E+00
5.0E+19
1.0E+20
1.5E+20
2.0E+20
Fluence (E > 1 MeV) [n/cm2]

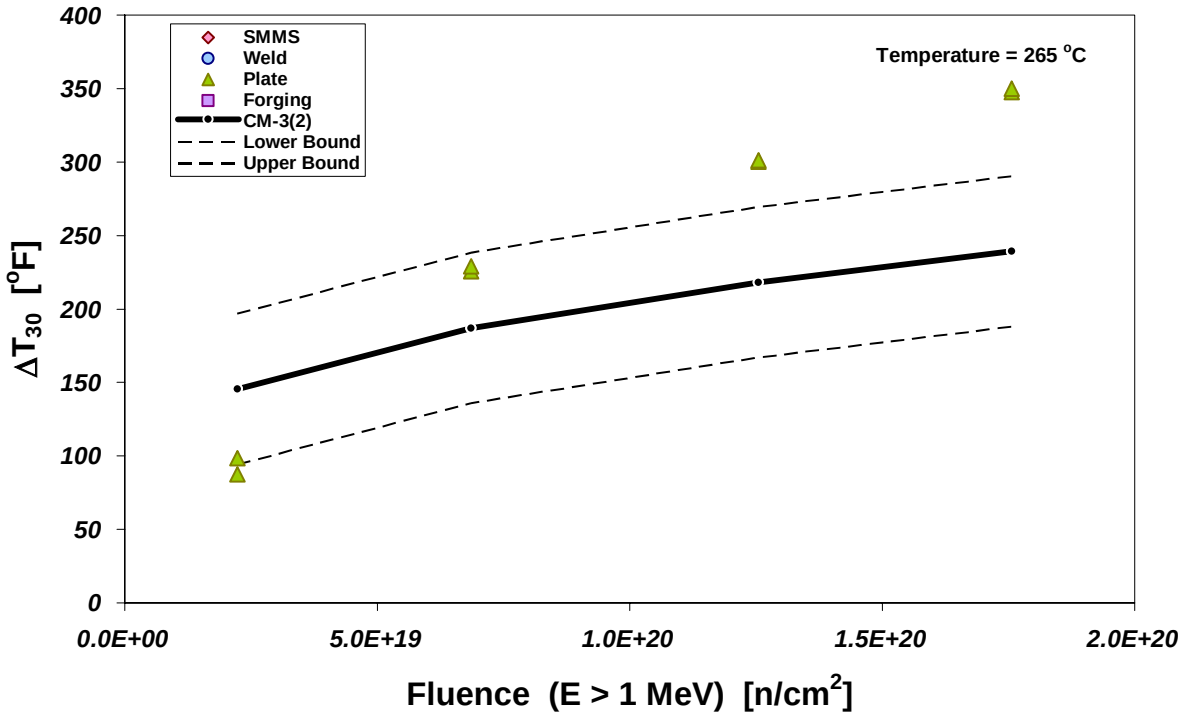
SMMS
Weld
Plate
Forging
CM-3(2)
Lower Bound
Upper Bound
Temperature = 265 °C
ΔT30 [°F]
400
350
300
250
200
150
100
50
0
0.0E+00
5.0E+19
1.0E+20
1.5E+20
2.0E+20
Fluence (E > 1 MeV) [n/cm2]

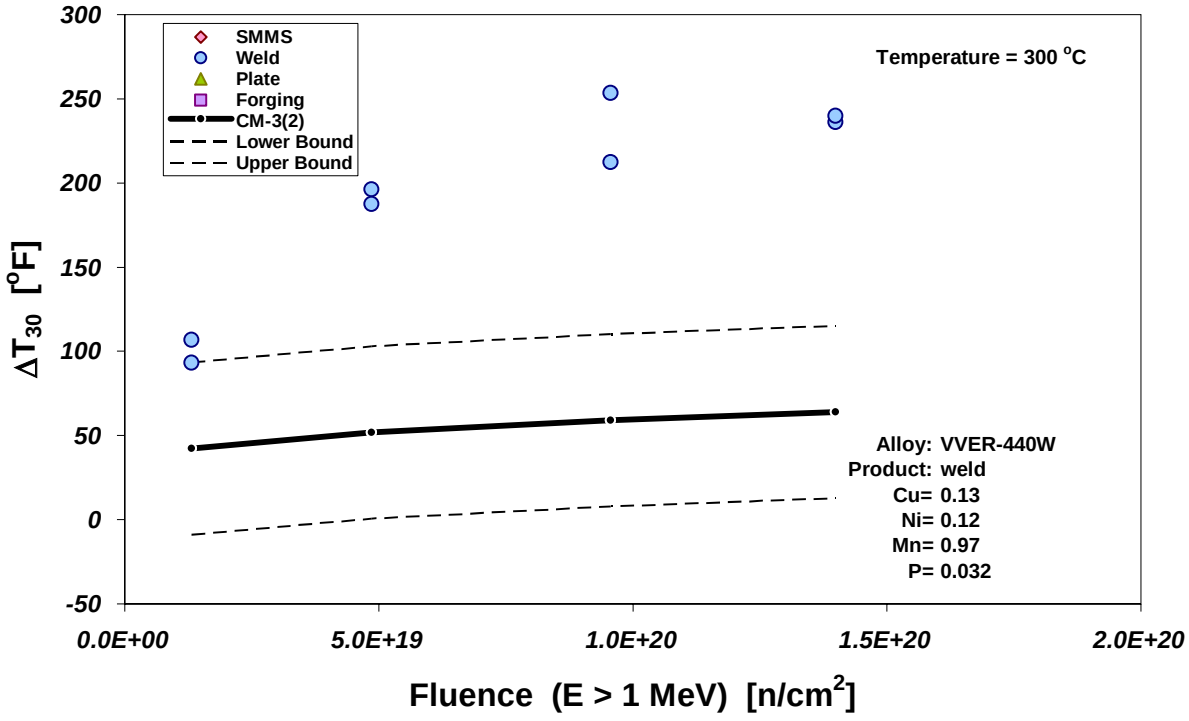
SMMS
Weld
Plate
Forging
CM-3(2)
Lower Bound
Upper Bound
Temperature = 300 °C
Alloy: VVER-440W
Product: weld
Cu= 0.13
Ni= 0.12
Mn= 0.97
P= 0.032
ΔT30 [°F]
300
250
200
150
100
50
0
-50
0.0E+00
5.0E+19
1.0E+20
1.5E+20
2.0E+20
Fluence (E > 1 MeV) [n/cm2]

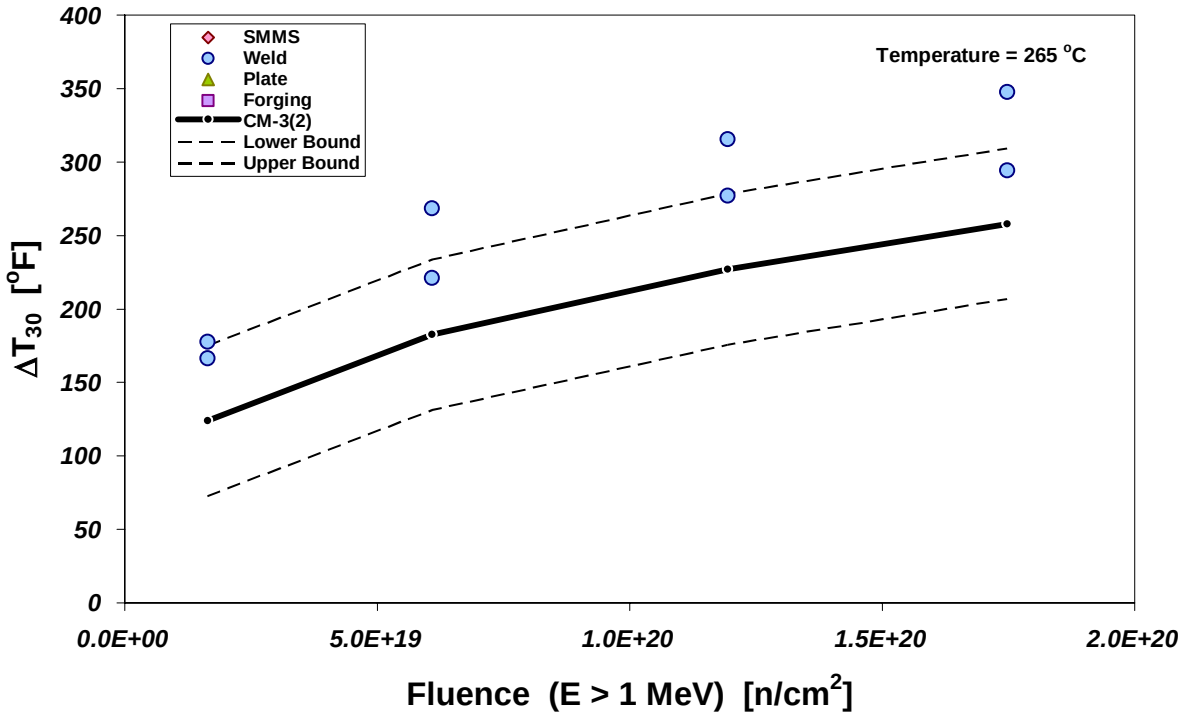
SMMS
Weld
Plate
Forging
CM-3(2)
Lower Bound
Upper Bound
Temperature = 265 °C
ΔT30 [°F]
400
350
300
250
200
150
100
50
0
0.0E+00
5.0E+19
1.0E+20
1.5E+20
2.0E+20
Fluence (E > 1 MeV) [n/cm2]

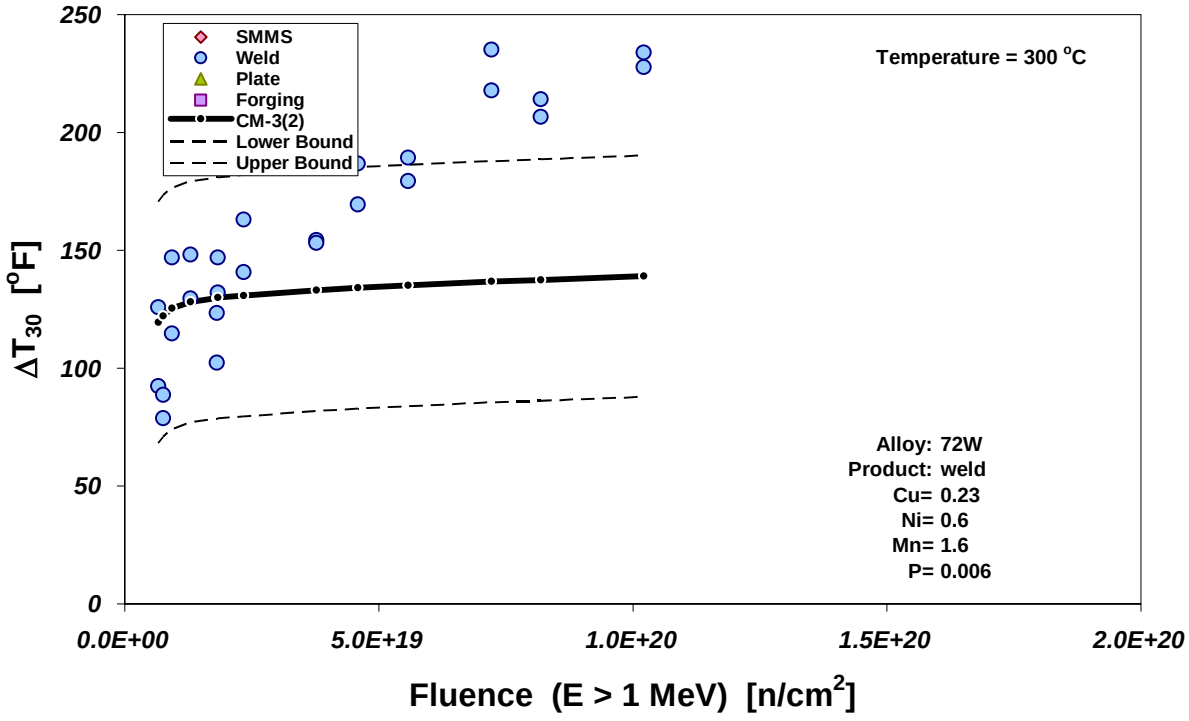
SMMS
Weld
Plate
Forging
CM-3(2)
Lower Bound
Upper Bound
Temperature = 300 °C
Alloy: 72W
Product: weld
Cu= 0.23
Ni= 0.6
Mn= 1.6
P= 0.006
ΔT30 [°F]
250
200
150
100
50
0
0.0E+00
5.0E+19
1.0E+20
1.5E+20
2.0E+20
Fluence (E > 1 MeV) [n/cm2]

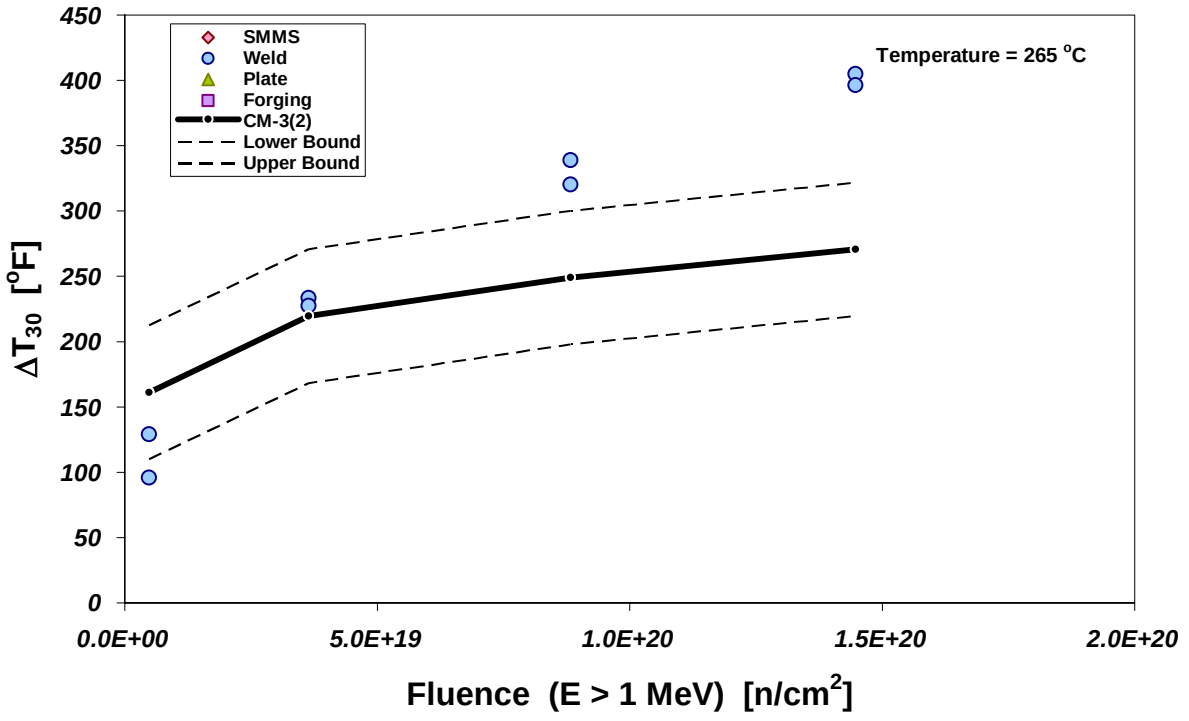
SMMS
Weld
Plate
Forging
CM-3(2)
Lower Bound
Upper Bound
Temperature = 265 °C
ΔT30 [°F]
450
400
350
300
250
200
150
100
50
0
0.0E+00
5.0E+19
1.0E+20
1.5E+20
2.0E+20
Fluence (E > 1 MeV) [n/cm2]

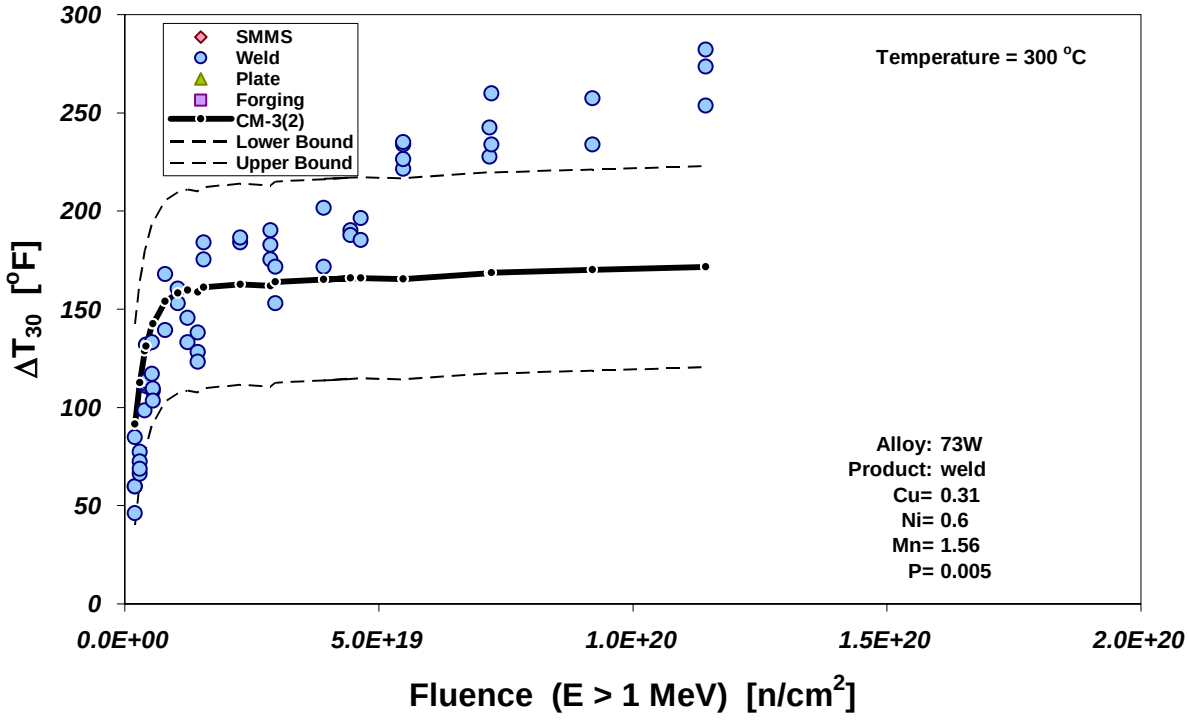
SMMS
Weld
Plate
Forging
CM-3(2)
Lower Bound
Upper Bound
Temperature = 300 °C
Alloy: 73W
Product: weld
Cu= 0.31
Ni= 0.6
Mn= 1.56
P= 0.005
ΔT30 [°F]
300
250
200
150
100
50
0
0.0E+00
5.0E+19
1.0E+20
1.5E+20
2.0E+20
Fluence (E > 1 MeV) [n/cm2]

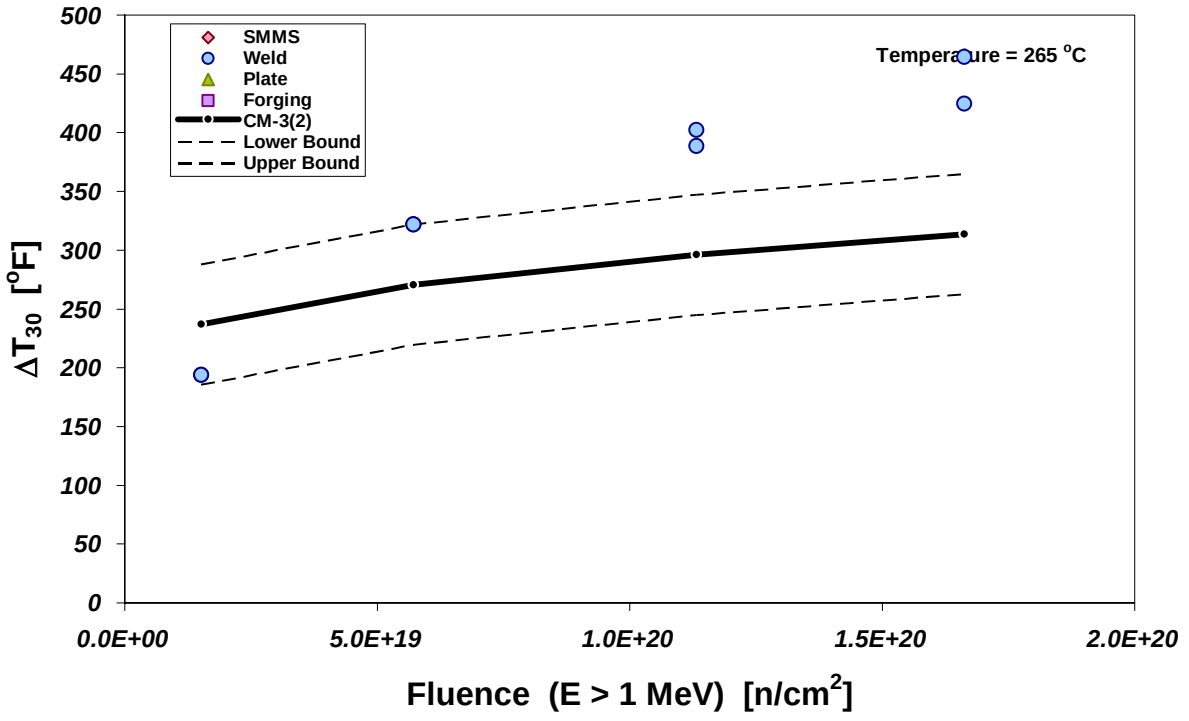
SMMS
Weld
Plate
Forging
CM-3(2)
Lower Bound
Upper Bound
Temperature = 265 °C
ΔT30 [°F]
500
450
400
350
300
250
200
150
100
50
0
0.0E+00
5.0E+19
1.0E+20
1.5E+20
2.0E+20
Fluence (E > 1 MeV) [n/cm2]

Appendix D

Comparison of the Predictions of RM-6(2) to the IVAR and RADAMO Databases

Table of IVAR Chemistry Values

Alloy	Product Form	Composition [wt-%]				
		Cu	Ni	Mn	P	Si
62W	Weld	0.23	0.6	1.61	0.02	0.59
63W	Weld	0.3	0.69	1.65	0.016	0.63
65W	Weld	0.22	0.6	1.45	0.015	0.48
67W	Weld	0.27	0.69	1.44	0.011	0.5
73W	Weld	0.31	0.6	1.56	0.005	0.45
A302	Plate	0.14	0.2	1.2	0.015	0.28
A508	Forging	0.06	0.8	1.3	0.005	0.01
BW-A	Weld	0.21	0.63	1.69	0.014	0.45
BW-B	Weld	0.28	0.69	1.63	0.018	0.54
BW-C	Weld	0.06	0.62	1.3	0.009	0.37
CM1	SMMS	0.01	0.01	1.67	0.003	0.15
CM10	SMMS	0.02	0.88	1.66	0.008	0.17
CM11	SMMS	0.34	0.85	1.64	0.006	0.18
CM12	SMMS	0.86	0.84	1.65	0.006	0.17
CM13	SMMS	0.11	0.83	1.61	0.004	0.16
CM14	SMMS	0.11	0.83	1.62	0.04	0.17
CM15	SMMS	0.22	0.02	1.59	0.002	0.15
CM16	SMMS	0.22	0.82	1.58	0.004	0.25
CM17	SMMS	0.22	1.59	1.54	0.004	0.25
CM18	SMMS	0.43	0.02	1.7	0.002	0.15
CM19	SMMS	0.42	0.85	1.63	0.005	0.16
CM2	SMMS	0.01	0.01	1.65	0.041	0.16
CM20	SMMS	0.43	1.69	1.63	0.006	0.16
CM21	SMMS	0.42	0.84	0.01	0.002	0.14
CM22	SMMS	0.42	0.84	0.84	0.002	0.14
CM23	SMMS	0.01	0.83	1.62	0.002	0.15
CM24	SMMS	0.02	0.87	1.65	0.006	0.15
CM25	SMMS	0.01	0.87	1.53	0.003	0.17
CM26	SMMS	0.01	0.87	1.66	0.006	0.17
CM27	SMMS	0.01	0.84	1.6	0.002	0.16
CM28	SMMS	0.42	0.84	1.6	0.002	0.17
CM29	SMMS	0.21	0.02	1.68	0.002	0.14
CM3	SMMS	0.02	0.85	1.6	0.006	0.16
CM30	SMMS	0.22	0.85	1.64	0.006	0.16
CM31	SMMS	0.01	0.86	1.65	0.006	0.17
CM4	SMMS	0.02	0.86	1.53	0.031	0.16
CM5	SMMS	0.02	0.86	1.61	0.05	0.16
CM6	SMMS	0.02	1.68	1.5	0.007	0.17
CM7	SMMS	0	1.7	1.55	0.047	0.17

Alloy	Product Form	Composition [wt-%]				
		Cu	Ni	Mn	P	Si
CM8	SMMS	0.01	0.86	0.01	0.004	0.14
CM9	SMMS	0.01	0.86	0.85	0.003	0.15
EPRI-C	Weld	0.4	0.6	1.36	0.006	0.51
HSST02	Plate	0.14	0.67	1.55	0.009	0.2
JRQ	Plate	0.14	0.82	1.4	0.019	0.25
LA	SMMS	0.4	0	1.37	0.005	0.22
LB	SMMS	0.4	0.18	1.35	0.005	0.22
LC	SMMS	0.41	0.86	1.44	0.005	0.23
LD	SMMS	0.38	1.25	1.38	0.005	0.23
LG	SMMS	0	0.74	1.37	0.005	0.22
LH	SMMS	0.11	0.74	1.39	0.005	0.24
LI	SMMS	0.2	0.74	1.37	0.005	0.24
LJ	SMMS	0.42	0.81	1.34	0.005	0.13
LK	SMMS	0.8	0.81	1.13	0.005	0.13
LO	SMMS	0.41	0.86	1.44	0.005	0.23
Midland	Weld	0.27	0.57	1.61	0.017	0.62
Palisades	Weld	0.2	1.2	1.3	0.01	0.18
RR-WG	Weld	0.24	1.71	1.21	0.008	0.6
RR-WP	Weld	0.04	1.65	1.43	0.011	0.5
RR-WV	Weld	0.56	1.66	1.36	0.01	0.38

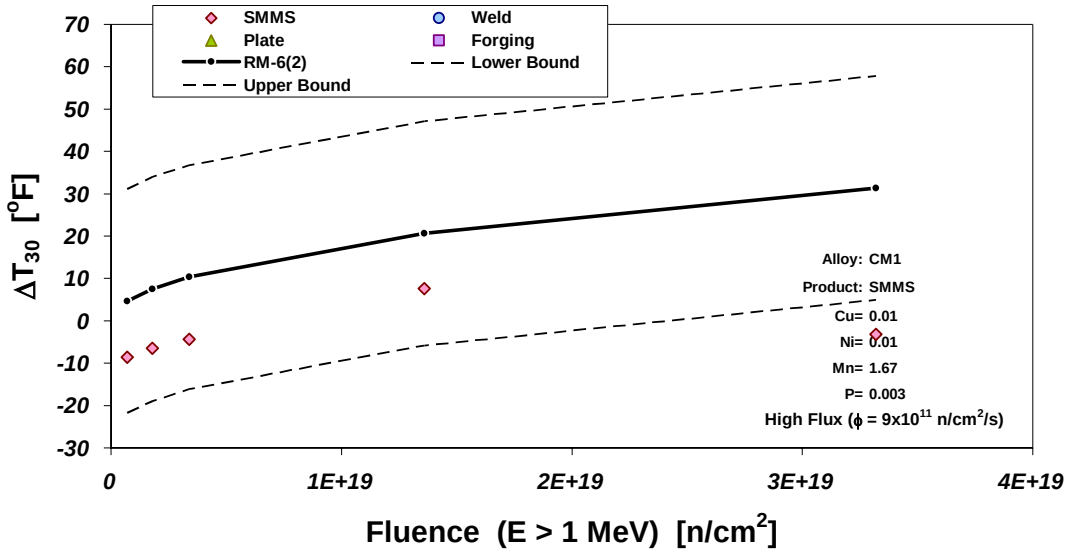
SMMS
Weld
Plate
Forging
RM-6(2)
Lower Bound
Upper Bound
Alloy: CM1
Product: SMMS
Cu= 0.01
Ni= 0.01
Mn= 1.67
P= 0.003
High Flux (ϕ = 9x10^11 n/cm^2/s)
ΔT30 [°F]
70
60
50
40
30
20
10
0
-10
-20
-30
0
1E+19
2E+19
3E+19
4E+19
Fluence (E > 1 MeV) [n/cm^2]

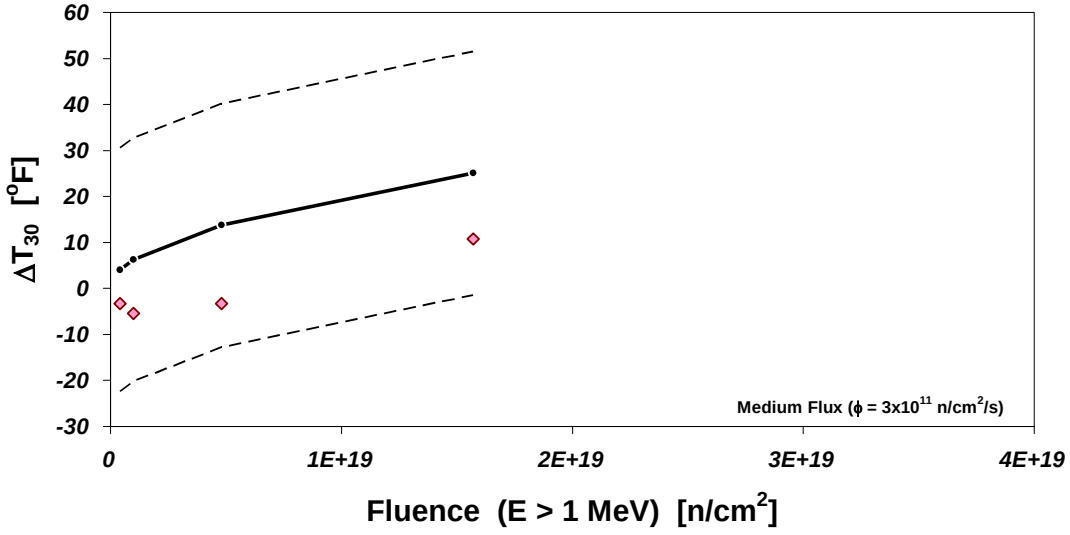
Medium Flux (ϕ = 3x10^11 n/cm^2/s)
ΔT30 [°F]
60
50
40
30
20
10
0
-10
-20
-30
0
1E+19
2E+19
3E+19
4E+19
Fluence (E > 1 MeV) [n/cm^2]

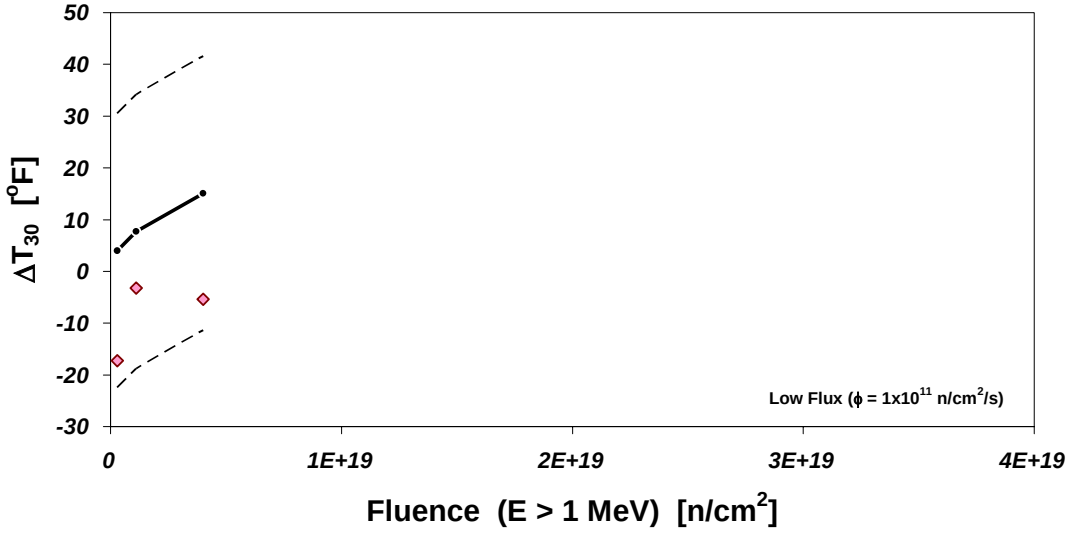
Low Flux (ϕ = 1x10^11 n/cm^2/s)
ΔT30 [°F]
50
40
30
20
10
0
-10
-20
-30
0
1E+19
2E+19
3E+19
4E+19
Fluence (E > 1 MeV) [n/cm^2]

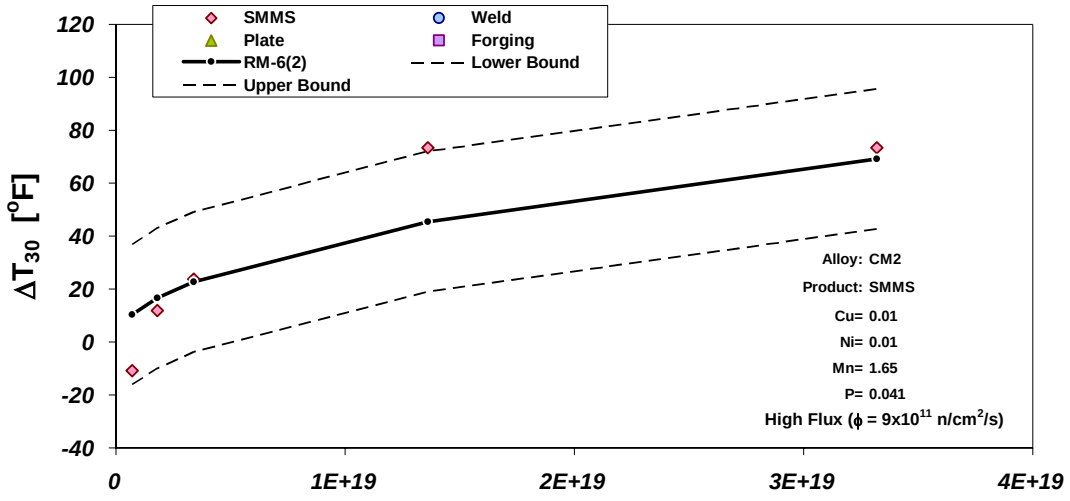
SMMS
Weld
Plate
Forging
RM-6(2)
Lower Bound
Upper Bound
Alloy: CM2
Product: SMMS
Cu= 0.01
Ni= 0.01
Mn= 1.65
P= 0.041
High Flux (ϕ = 9x10^11 n/cm^2/s)
ΔT30 [°F]
120
100
80
60
40
20
0
-20
-40
0
1E+19
2E+19
3E+19
4E+19
Fluence (E > 1 MeV) [n/cm^2]

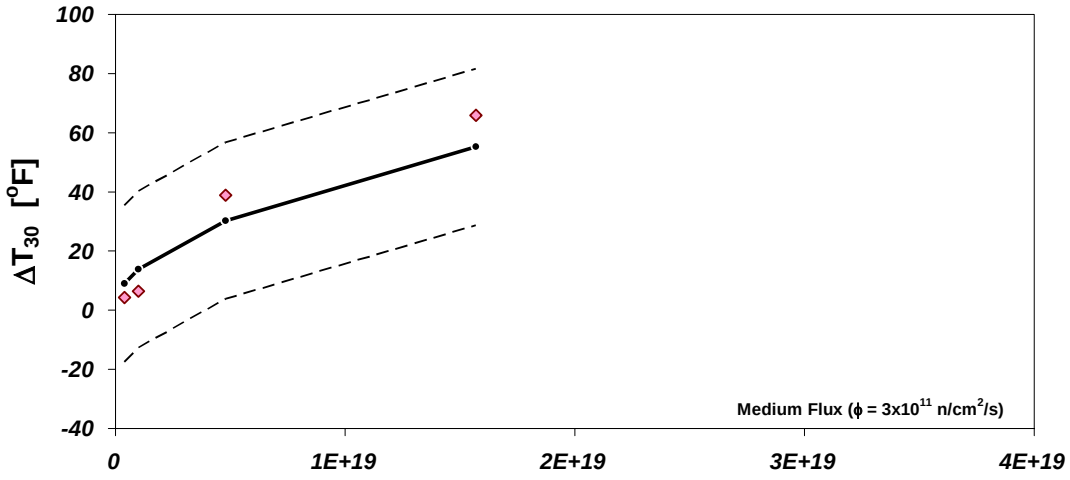
Medium Flux (ϕ = 3x10^11 n/cm^2/s)
ΔT30 [°F]
100
80
60
40
20
0
-20
-40
0
1E+19
2E+19
3E+19
4E+19
Fluence (E > 1 MeV) [n/cm^2]

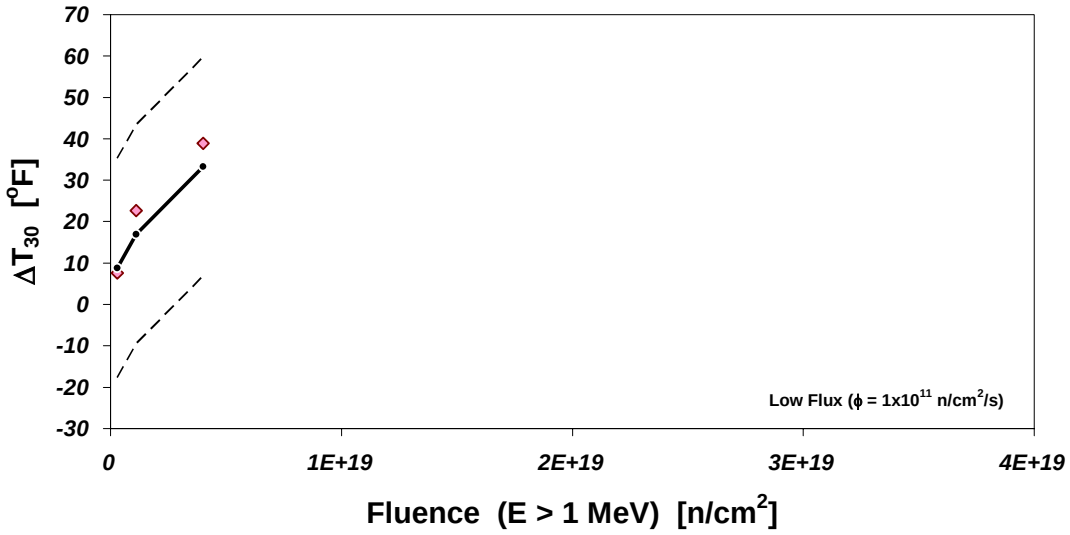
Low Flux (ϕ = 1x10^11 n/cm^2/s)
ΔT30 [°F]
70
60
50
40
30
20
10
0
-10
-20
-30
0
1E+19
2E+19
3E+19
4E+19
Fluence (E > 1 MeV) [n/cm^2]

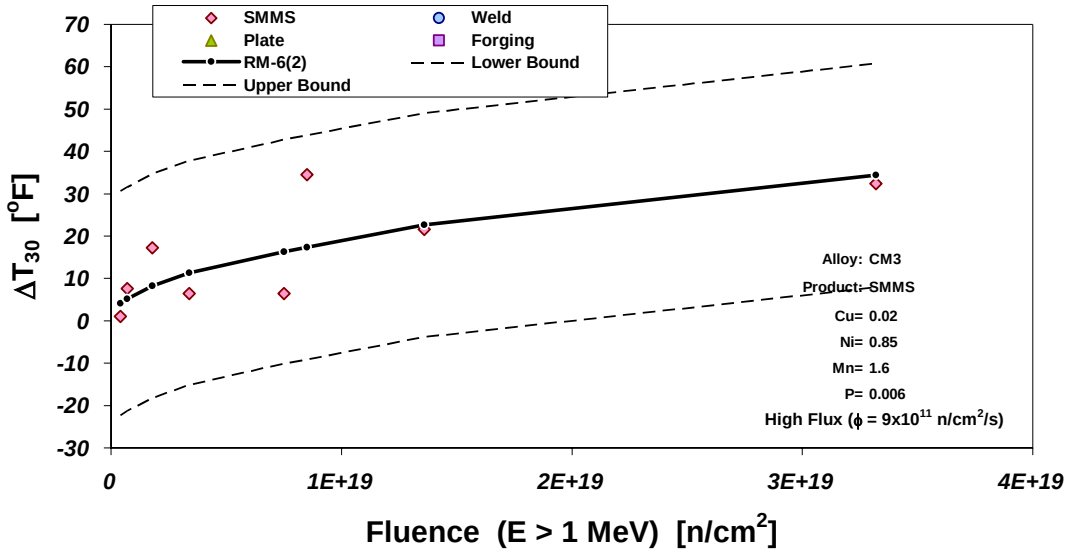
SMMS
Weld
Plate
Forging
RM-6(2)
Lower Bound
Upper Bound
Alloy: CM3
Product: SMMS
Cu= 0.02
Ni= 0.85
Mn= 1.6
P= 0.006
High Flux (ϕ = 9x10^11 n/cm^2/s)
ΔT30 [°F]
70
60
50
40
30
20
10
0
-10
-20
-30
0
1E+19
2E+19
3E+19
4E+19
Fluence (E > 1 MeV) [n/cm^2]

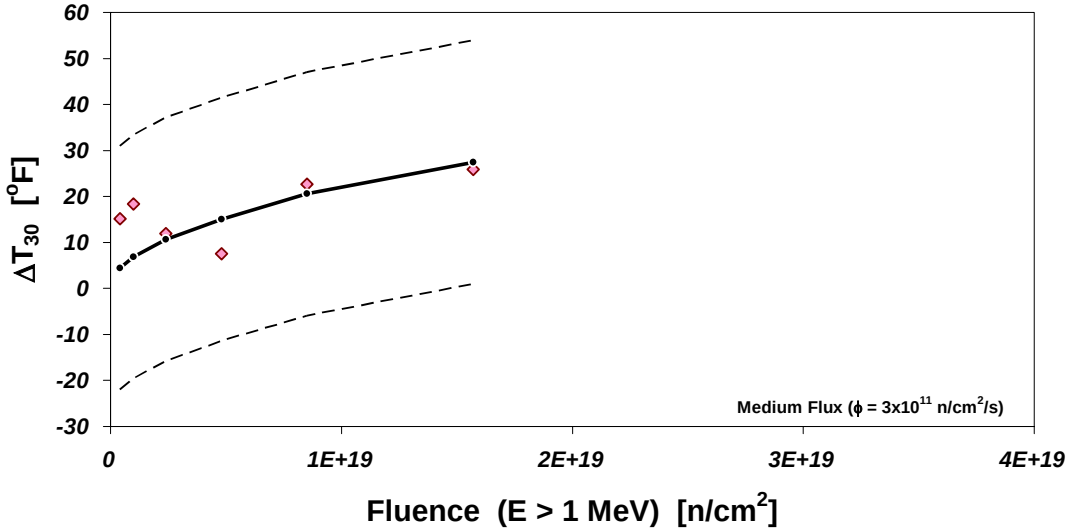
Medium Flux (ϕ = 3x10^11 n/cm^2/s)
ΔT30 [°F]
60
50
40
30
20
10
0
-10
-20
-30
0
1E+19
2E+19
3E+19
4E+19
Fluence (E > 1 MeV) [n/cm^2]

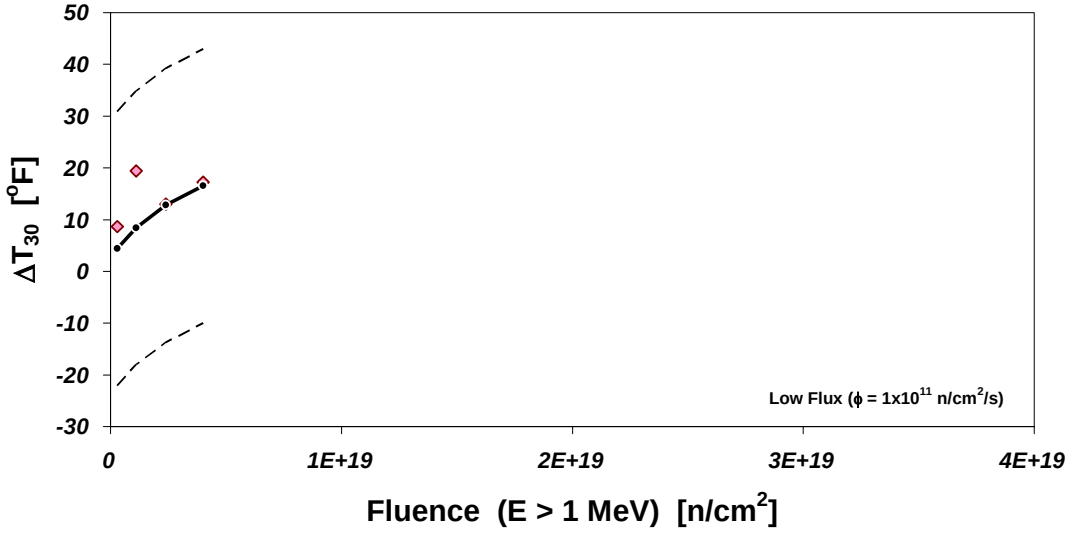
Low Flux (ϕ = 1x10^11 n/cm^2/s)
ΔT30 [°F]
50
40
30
20
10
0
-10
-20
-30
0
1E+19
2E+19
3E+19
4E+19
Fluence (E > 1 MeV) [n/cm^2]

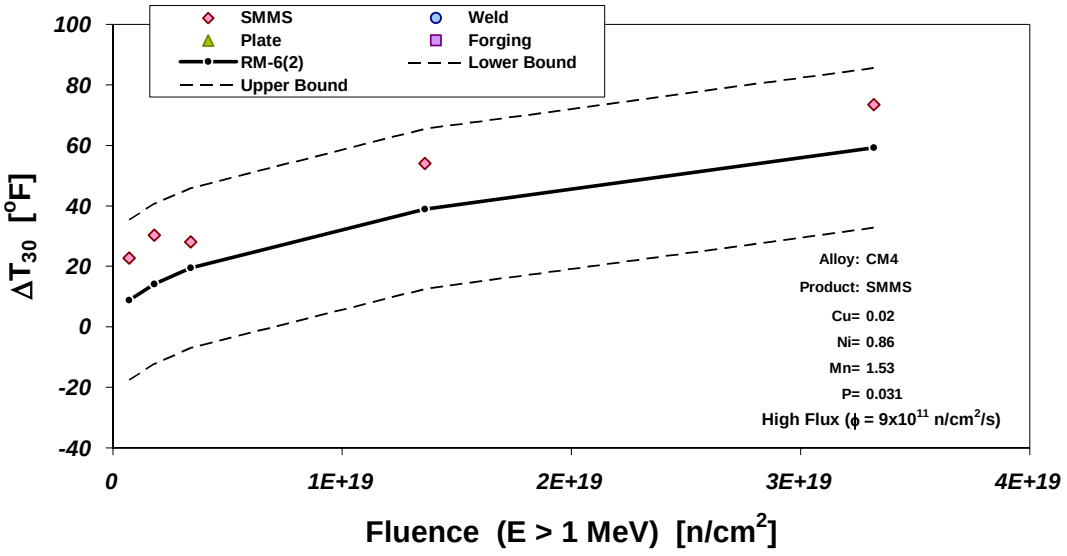
SMMS
Weld
Plate
Forging
RM-6(2)
Lower Bound
Upper Bound
100
80
60
40
20
0
-20
-40
ΔT30 [°F]
Alloy: CM4
Product: SMMS
Cu= 0.02
Ni= 0.86
Mn= 1.53
P= 0.031
High Flux (ϕ = 9x10^11 n/cm^2/s)
0
1E+19
2E+19
3E+19
4E+19
Fluence (E > 1 MeV) [n/cm^2]

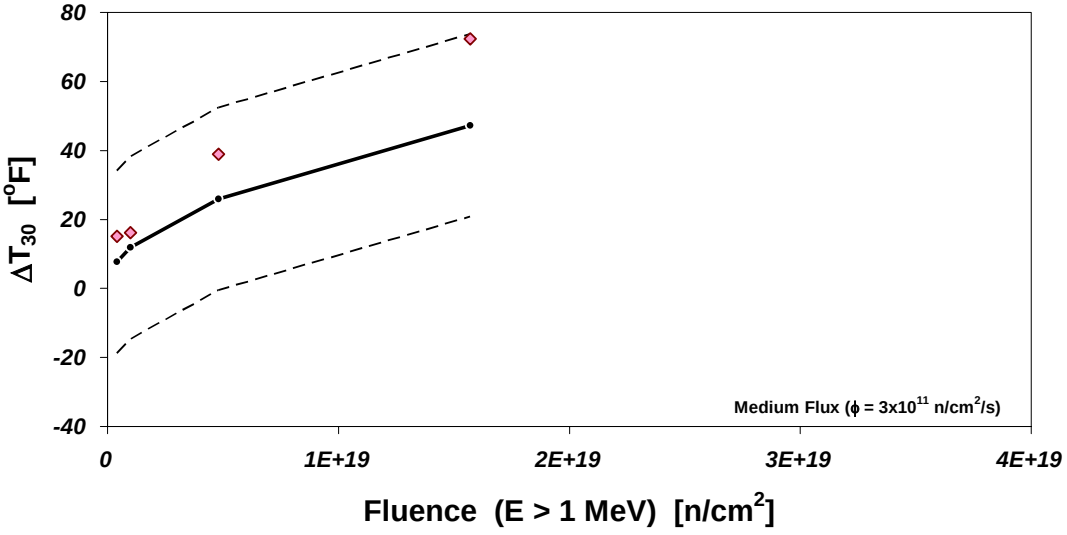
80
60
40
20
0
-20
-40
ΔT30 [°F]
Medium Flux (ϕ = 3x10^11 n/cm^2/s)
0
1E+19
2E+19
3E+19
4E+19
Fluence (E > 1 MeV) [n/cm^2]

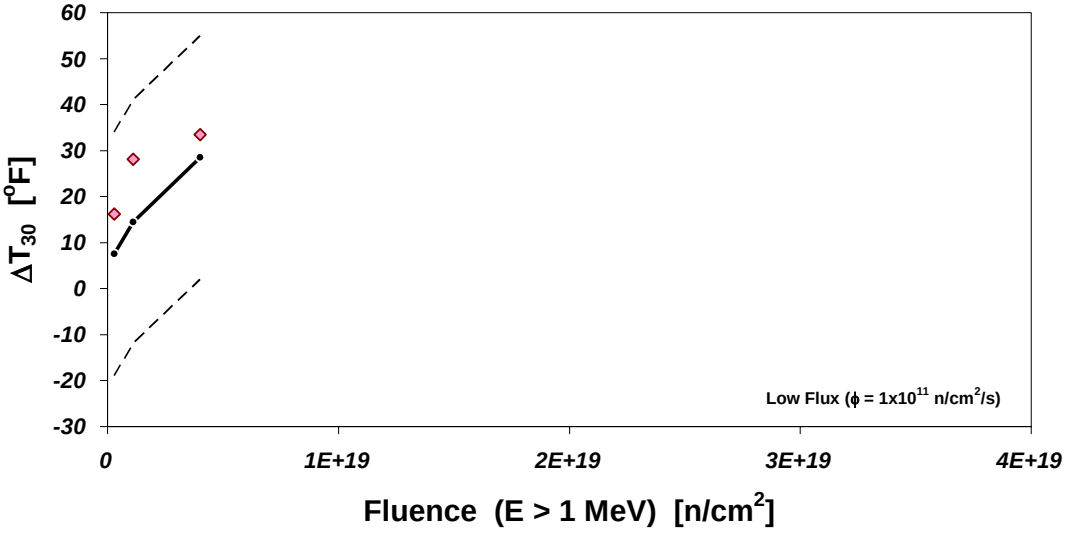
60
50
40
30
20
10
0
-10
-20
-30
ΔT30 [°F]
Low Flux (ϕ = 1x10^11 n/cm^2/s)
0
1E+19
2E+19
3E+19
4E+19
Fluence (E > 1 MeV) [n/cm^2]

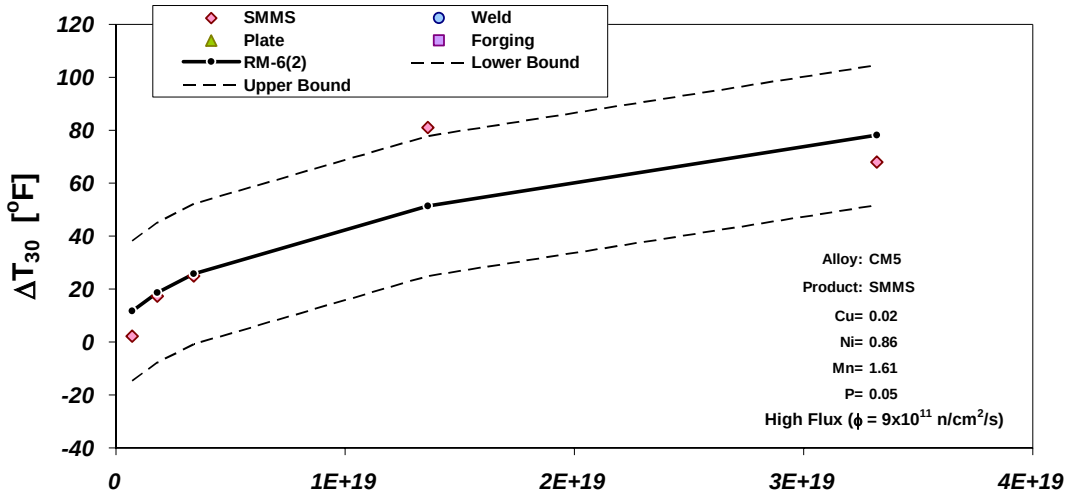
SMMS
Weld
Plate
Forging
RM-6(2)
Lower Bound
Upper Bound
Alloy: CM5
Product: SMMS
Cu= 0.02
Ni= 0.86
Mn= 1.61
P= 0.05
High Flux (ϕ = 9x10^11 n/cm^2/s)
ΔT30 [°F]
120
100
80
60
40
20
0
-20
-40
0
1E+19
2E+19
3E+19
4E+19
Fluence (E > 1 MeV) [n/cm^2]

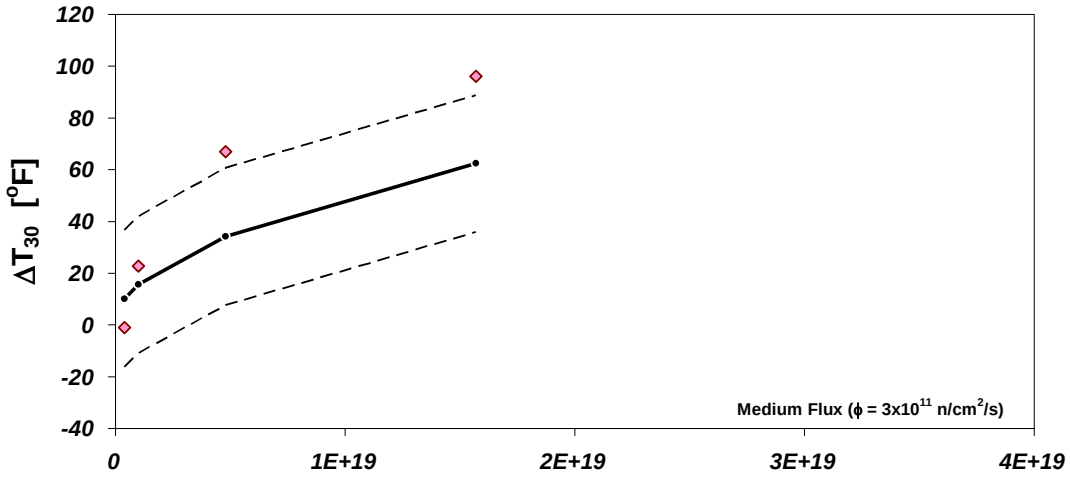
Medium Flux (ϕ = 3x10^11 n/cm^2/s)
ΔT30 [°F]
120
100
80
60
40
20
0
-20
-40
0
1E+19
2E+19
3E+19
4E+19
Fluence (E > 1 MeV) [n/cm^2]

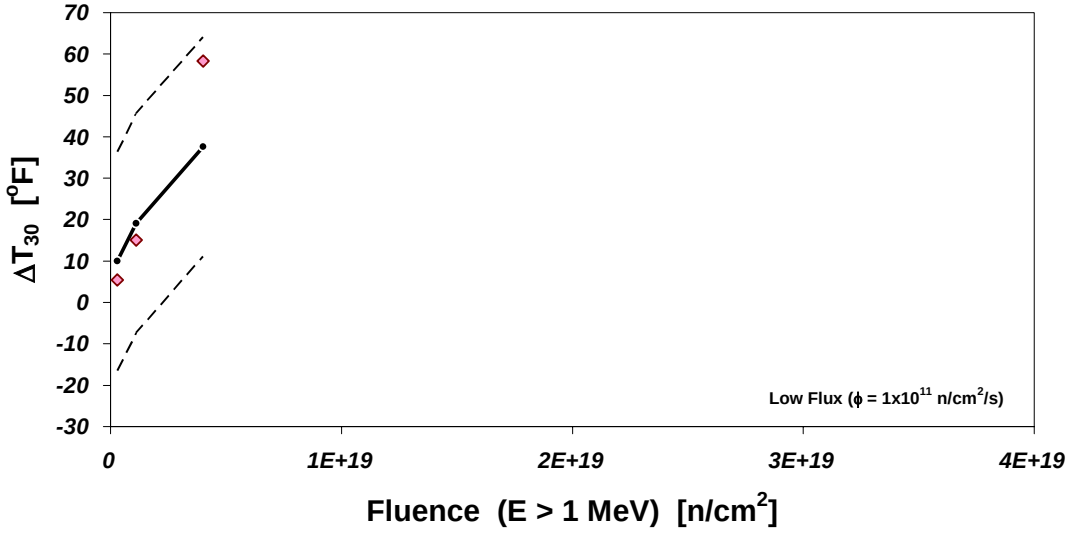
Low Flux (ϕ = 1x10^11 n/cm^2/s)
ΔT30 [°F]
70
60
50
40
30
20
10
0
-10
-20
-30
0
1E+19
2E+19
3E+19
4E+19
Fluence (E > 1 MeV) [n/cm^2]

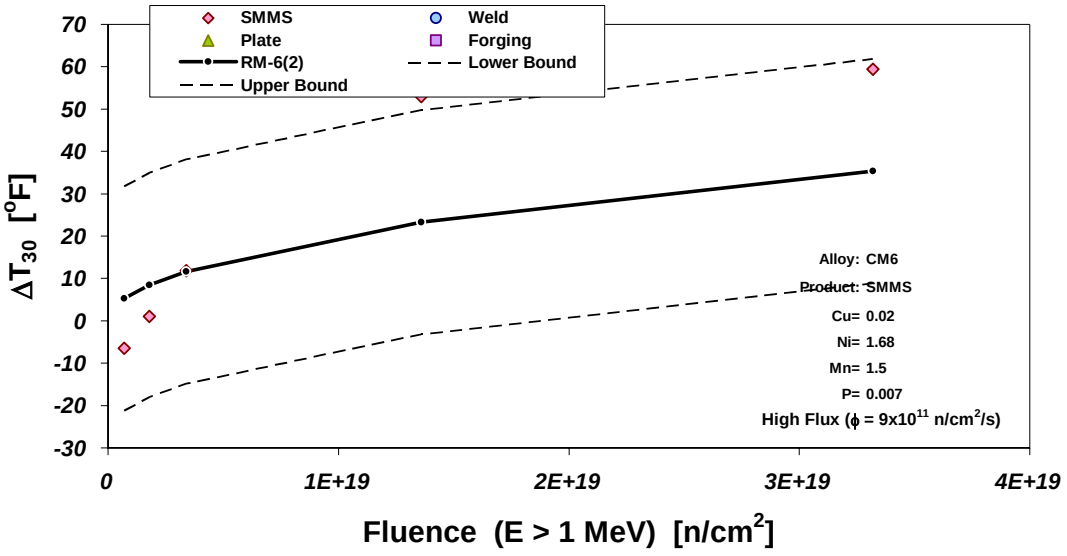
SMMS
Weld
Plate
Forging
RM-6(2)
Lower Bound
Upper Bound
Alloy: CM6
Product: SMMS
Cu= 0.02
Ni= 1.68
Mn= 1.5
P= 0.007
High Flux (ϕ = 9x10^11 n/cm^2/s)
ΔT30 [°F]
70
60
50
40
30
20
10
0
-10
-20
-30
0
1E+19
2E+19
3E+19
4E+19
Fluence (E > 1 MeV) [n/cm^2]

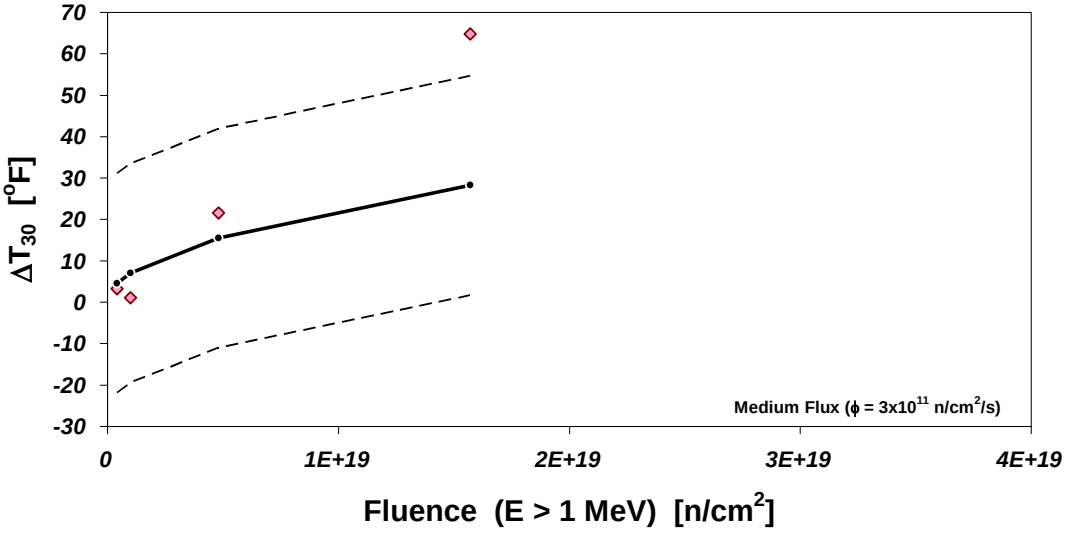
Medium Flux (ϕ = 3x10^11 n/cm^2/s)
ΔT30 [°F]
70
60
50
40
30
20
10
0
-10
-20
-30
0
1E+19
2E+19
3E+19
4E+19
Fluence (E > 1 MeV) [n/cm^2]

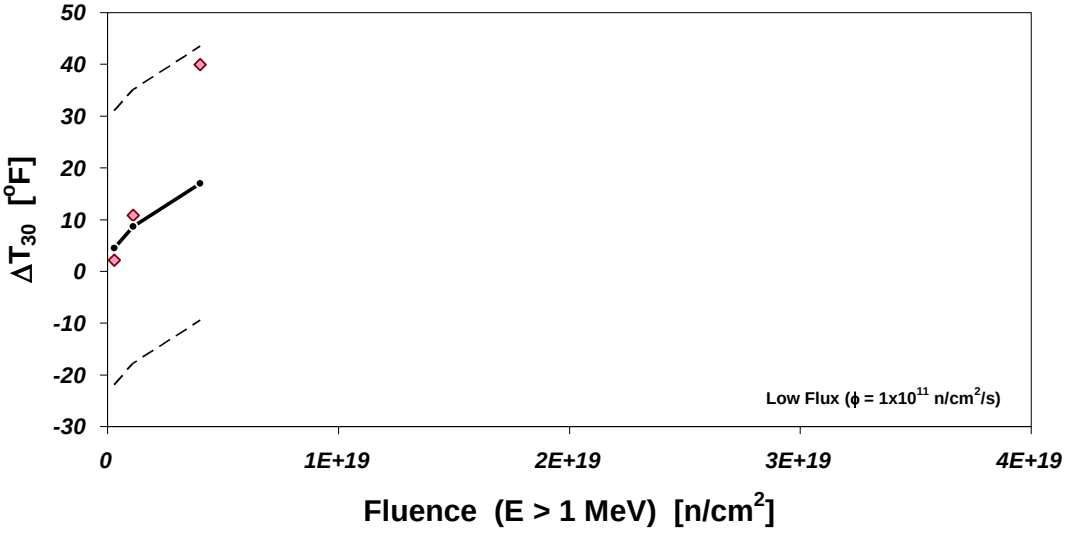
Low Flux (ϕ = 1x10^11 n/cm^2/s)
ΔT30 [°F]
50
40
30
20
10
0
-10
-20
-30
0
1E+19
2E+19
3E+19
4E+19
Fluence (E > 1 MeV) [n/cm^2]

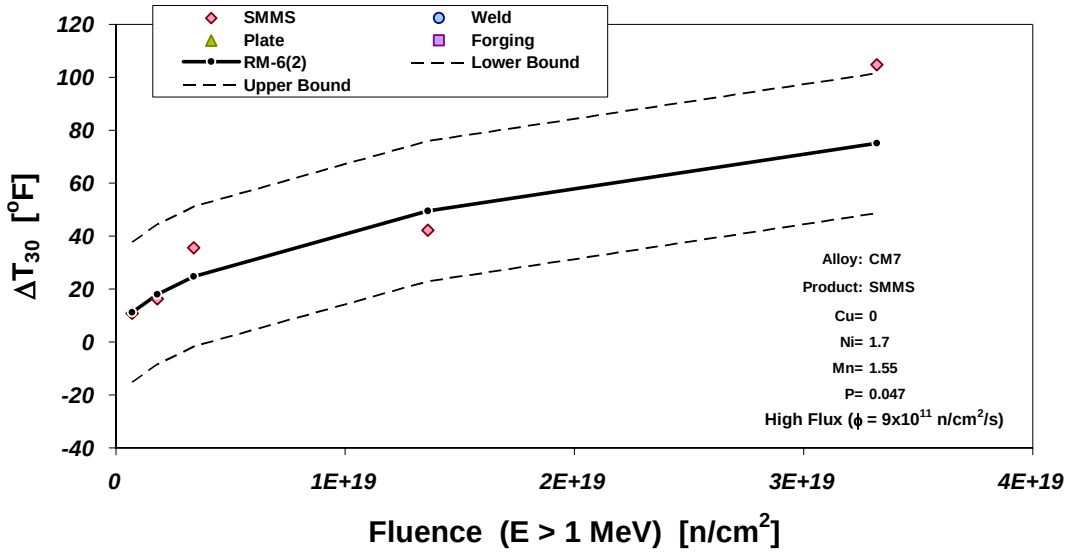
SMMS
Weld
Plate
Forging
RM-6(2)
Lower Bound
Upper Bound
Alloy: CM7
Product: SMMS
Cu= 0
Ni= 1.7
Mn= 1.55
P= 0.047
High Flux (ϕ = 9x10^11 n/cm^2/s)
ΔT30 [°F]
120
100
80
60
40
20
0
-20
-40
0
1E+19
2E+19
3E+19
4E+19
Fluence (E > 1 MeV) [n/cm^2]

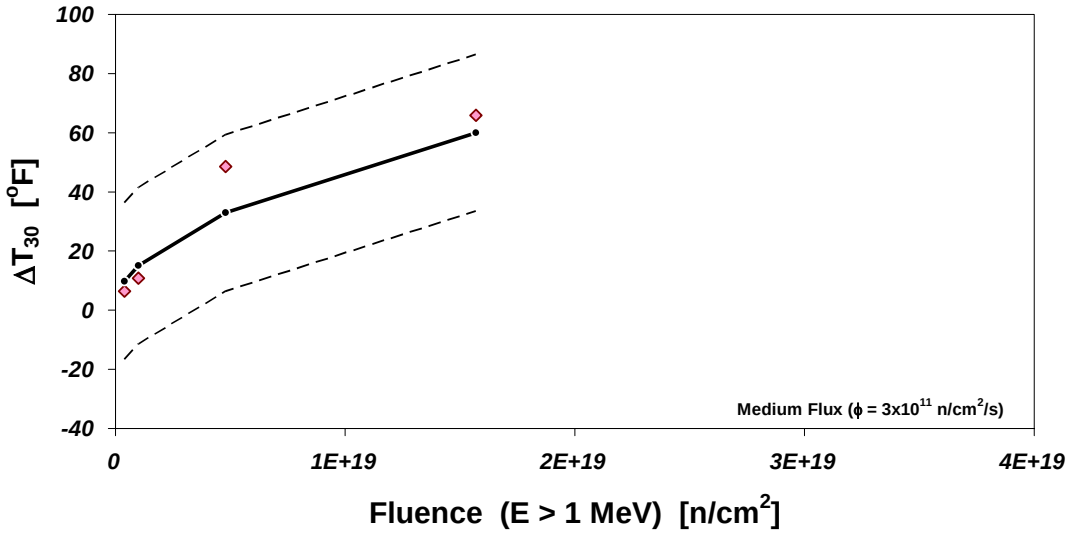
Medium Flux (ϕ = 3x10^11 n/cm^2/s)
ΔT30 [°F]
100
80
60
40
20
0
-20
-40
0
1E+19
2E+19
3E+19
4E+19
Fluence (E > 1 MeV) [n/cm^2]

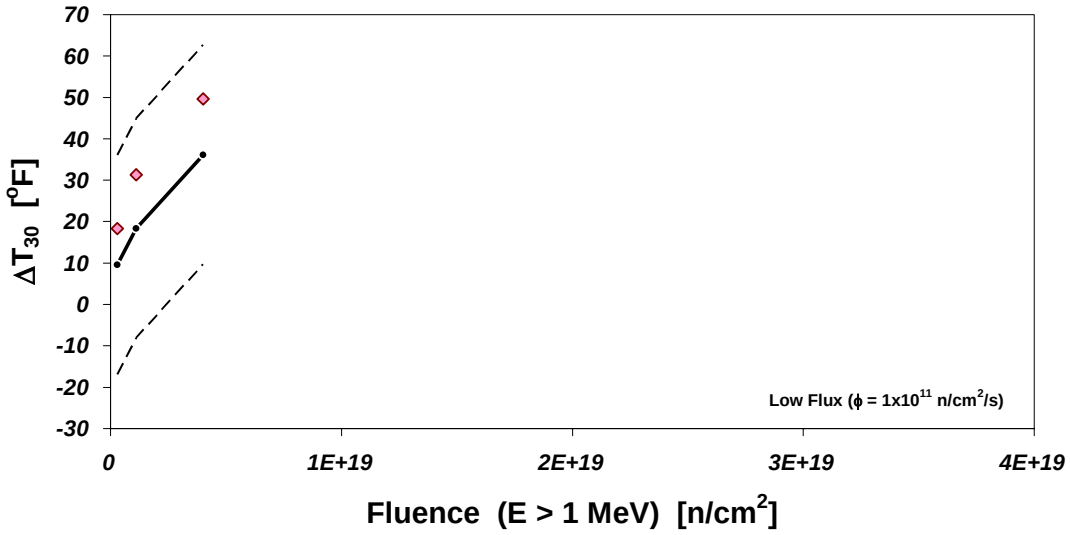
Low Flux (ϕ = 1x10^11 n/cm^2/s)
ΔT30 [°F]
70
60
50
40
30
20
10
0
-10
-20
-30
0
1E+19
2E+19
3E+19
4E+19
Fluence (E > 1 MeV) [n/cm^2]

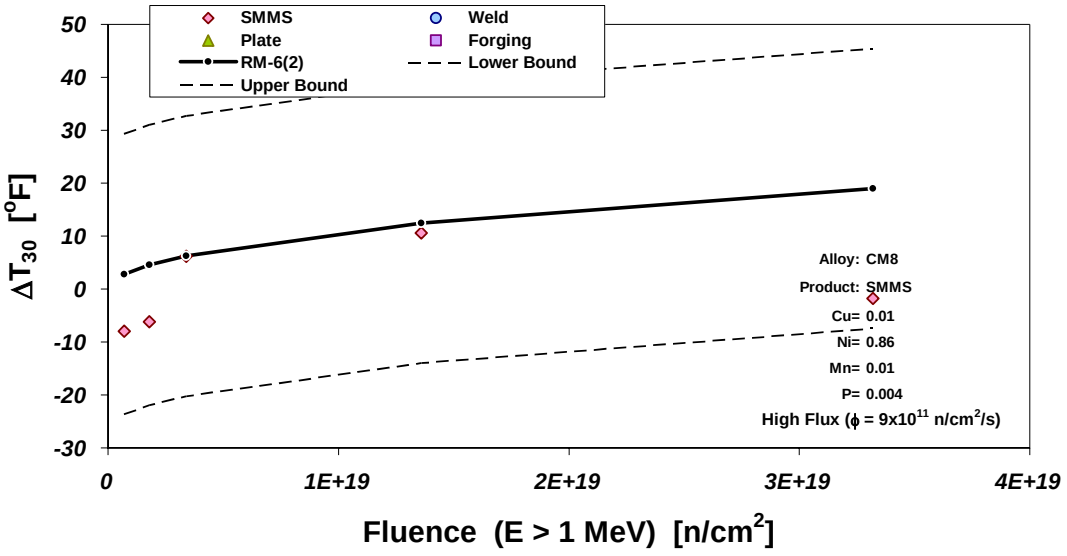
SMMS
Weld
Plate
Forging
RM-6(2)
Lower Bound
Upper Bound
Alloy: CM8
Product: SMMS
Cu= 0.01
Ni= 0.86
Mn= 0.01
P= 0.004
High Flux (ϕ = 9x10^11 n/cm^2/s)
ΔT30 [°F]
50
40
30
20
10
0
-10
-20
-30
0
1E+19
2E+19
3E+19
4E+19
Fluence (E > 1 MeV) [n/cm^2]

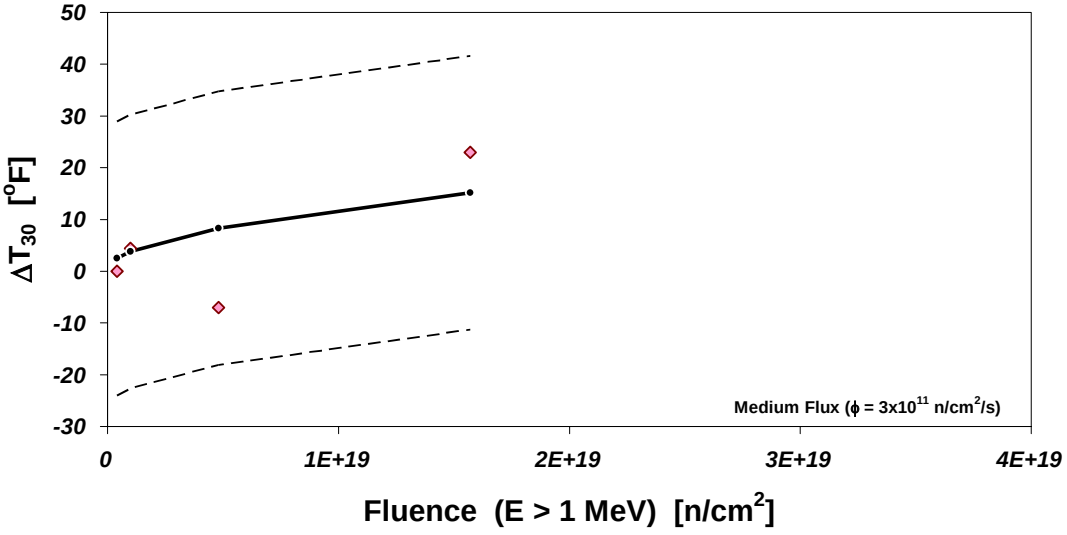
Medium Flux (ϕ = 3x10^11 n/cm^2/s)
ΔT30 [°F]
50
40
30
20
10
0
-10
-20
-30
0
1E+19
2E+19
3E+19
4E+19
Fluence (E > 1 MeV) [n/cm^2]

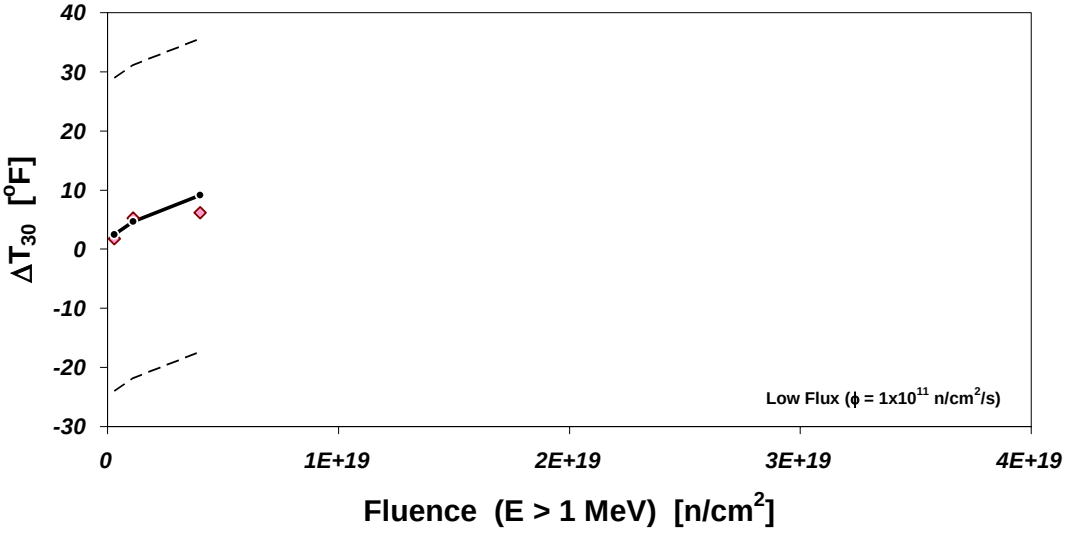
Low Flux (ϕ = 1x10^11 n/cm^2/s)
ΔT30 [°F]
40
30
20
10
0
-10
-20
-30
0
1E+19
2E+19
3E+19
4E+19
Fluence (E > 1 MeV) [n/cm^2]

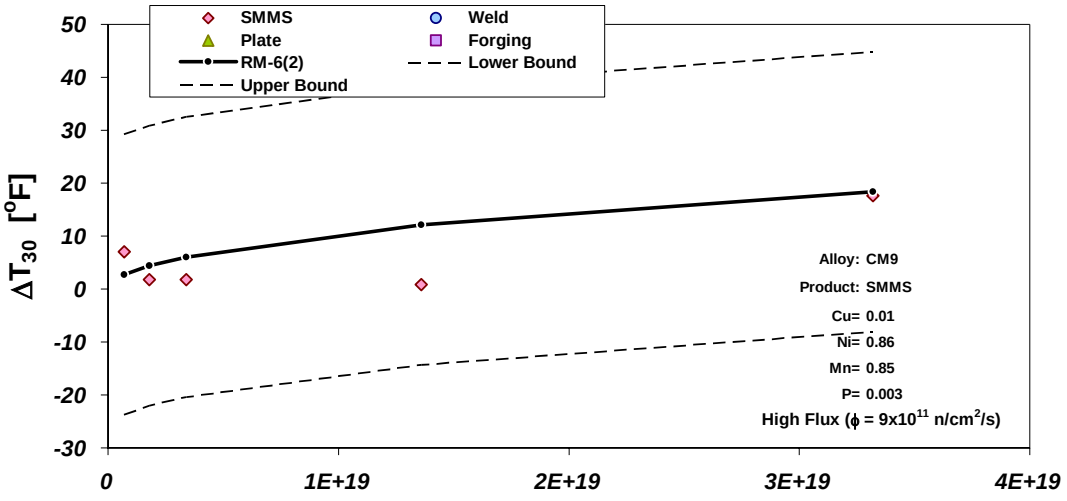
SMMS
Weld
Plate
Forging
RM-6(2)
Lower Bound
Upper Bound
Alloy: CM9
Product: SMMS
Cu= 0.01
Ni= 0.86
Mn= 0.85
P= 0.003
High Flux (ϕ = 9x10^11 n/cm^2/s)
ΔT30 [°F]
50
40
30
20
10
0
-10
-20
-30
0
1E+19
2E+19
3E+19
4E+19
Fluence (E > 1 MeV) [n/cm^2]

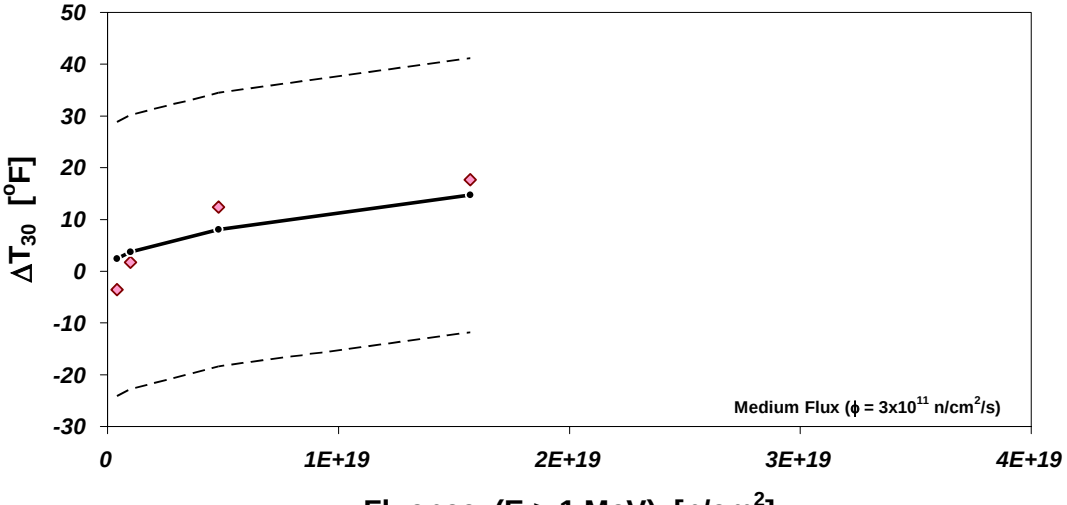
Medium Flux (ϕ = 3x10^11 n/cm^2/s)
ΔT30 [°F]
50
40
30
20
10
0
-10
-20
-30
0
1E+19
2E+19
3E+19
4E+19
Fluence (E > 1 MeV) [n/cm^2]

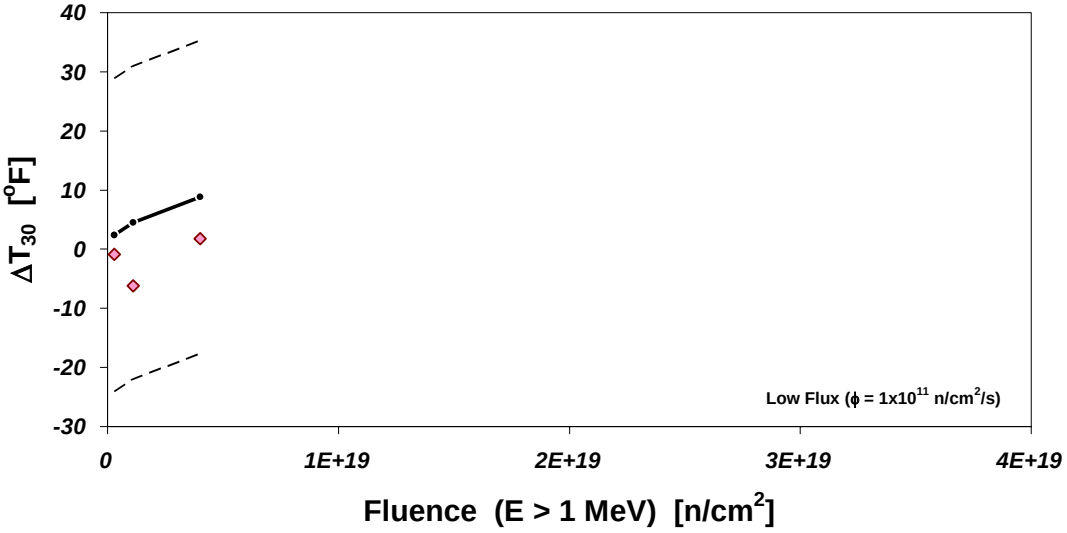
Low Flux (ϕ = 1x10^11 n/cm^2/s)
ΔT30 [°F]
40
30
20
10
0
-10
-20
-30
0
1E+19
2E+19
3E+19
4E+19
Fluence (E > 1 MeV) [n/cm^2]

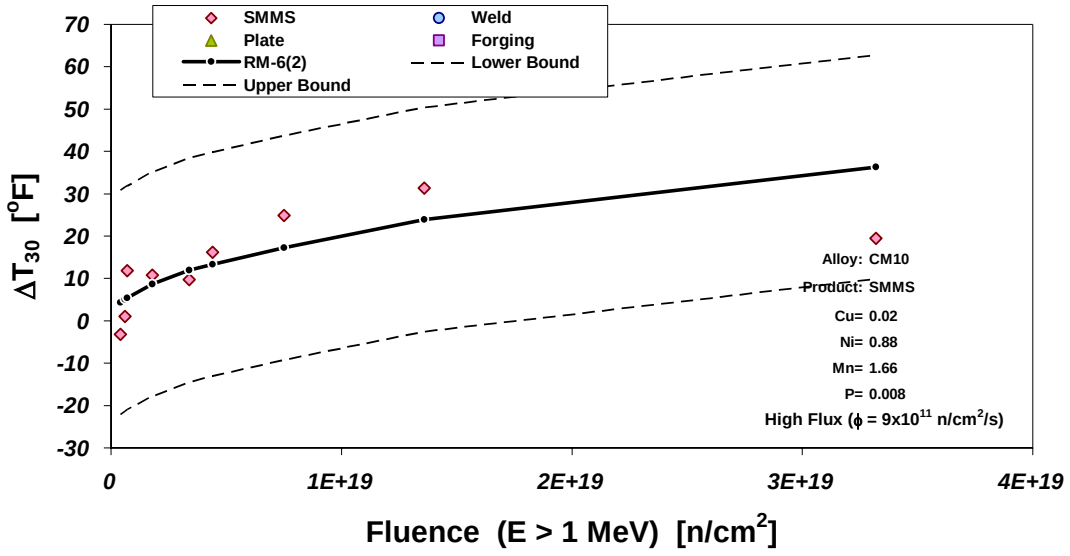
SMMS
Weld
Plate
Forging
RM-6(2)
Lower Bound
Upper Bound
Alloy: CM10
Product: SMMS
Cu= 0.02
Ni= 0.88
Mn= 1.66
P= 0.008
High Flux (ϕ = 9x10^11 n/cm^2/s)
ΔT30 [°F]
70
60
50
40
30
20
10
0
-10
-20
-30
0
1E+19
2E+19
3E+19
4E+19
Fluence (E > 1 MeV) [n/cm^2]

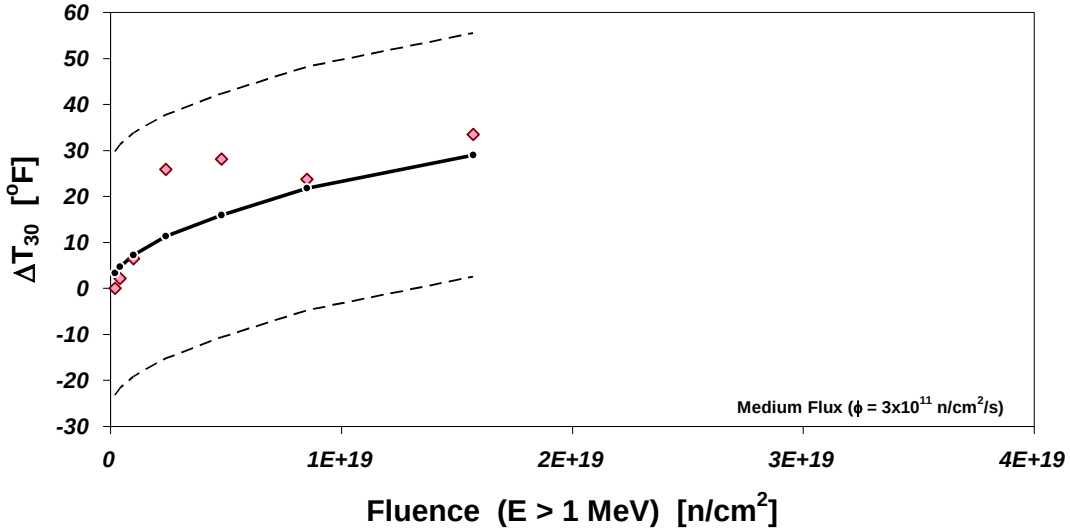
Medium Flux (ϕ = 3x10^11 n/cm^2/s)
ΔT30 [°F]
60
50
40
30
20
10
0
-10
-20
-30
0
1E+19
2E+19
3E+19
4E+19
Fluence (E > 1 MeV) [n/cm^2]

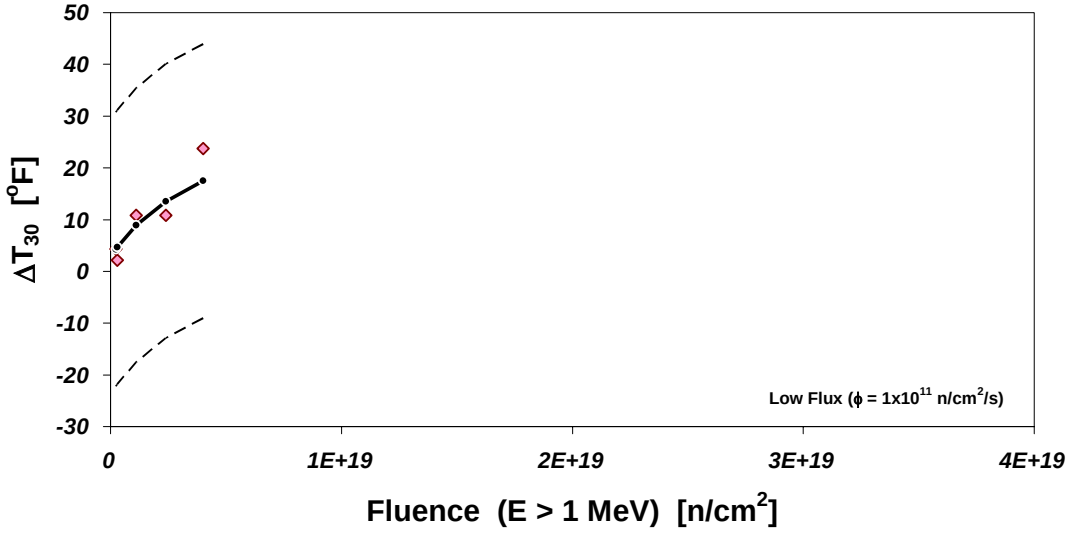
Low Flux (ϕ = 1x10^11 n/cm^2/s)
ΔT30 [°F]
50
40
30
20
10
0
-10
-20
-30
0
1E+19
2E+19
3E+19
4E+19
Fluence (E > 1 MeV) [n/cm^2]

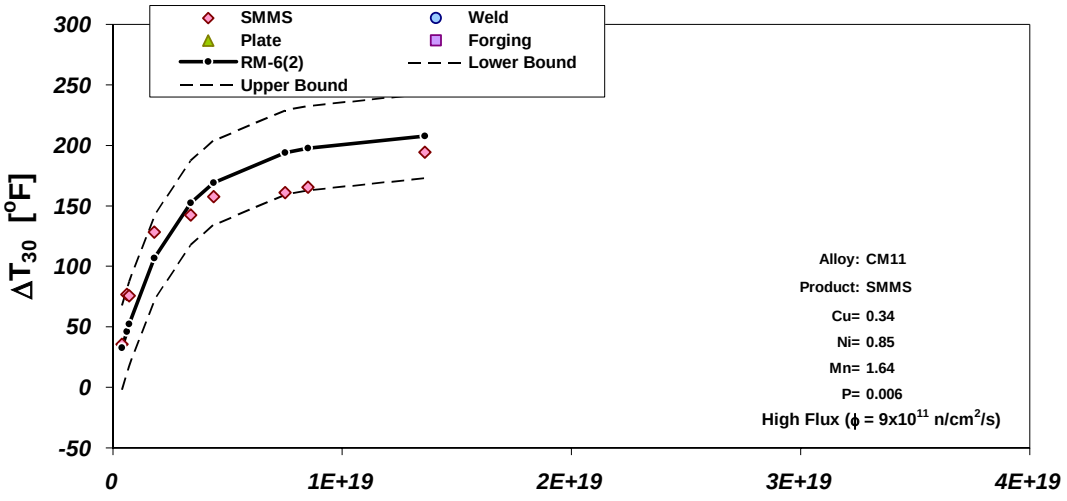
SMMS
Weld
Plate
Forging
RM-6(2)
Lower Bound
Upper Bound
Alloy: CM11
Product: SMMS
Cu= 0.34
Ni= 0.85
Mn= 1.64
P= 0.006
High Flux (ϕ = 9x10^11 n/cm^2/s)
ΔT30 [°F]
300
250
200
150
100
50
0
-50
0
1E+19
2E+19
3E+19
4E+19
Fluence (E > 1 MeV) [n/cm^2]

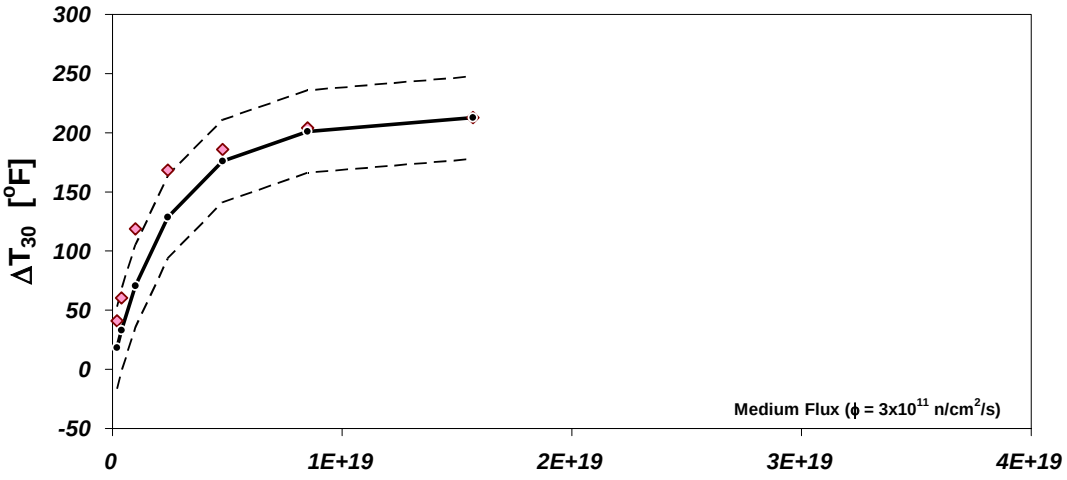
Medium Flux (ϕ = 3x10^11 n/cm^2/s)
ΔT30 [°F]
300
250
200
150
100
50
0
-50
0
1E+19
2E+19
3E+19
4E+19
Fluence (E > 1 MeV) [n/cm^2]

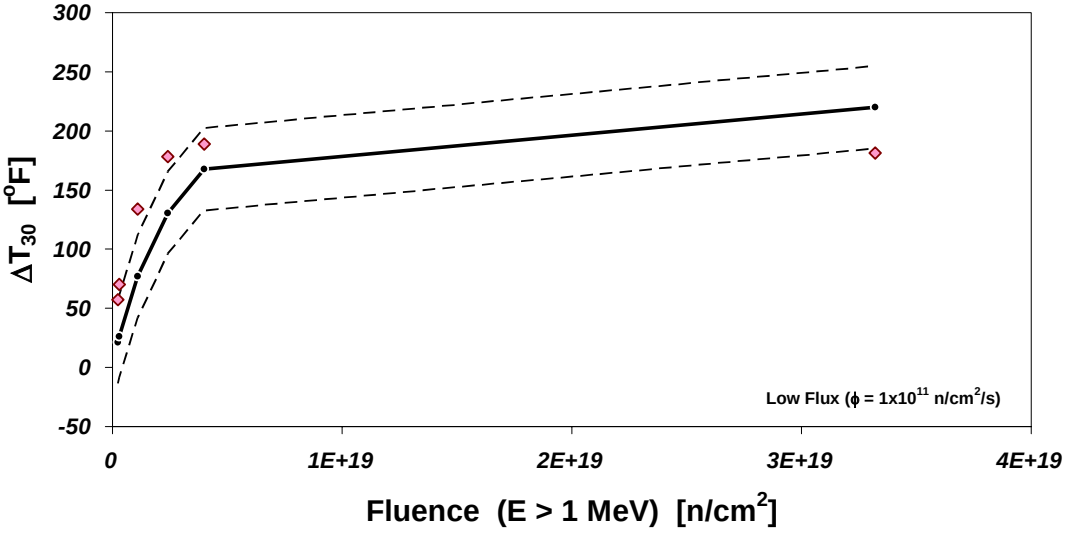
Low Flux (ϕ = 1x10^11 n/cm^2/s)
ΔT30 [°F]
300
250
200
150
100
50
0
-50
0
1E+19
2E+19
3E+19
4E+19
Fluence (E > 1 MeV) [n/cm^2]

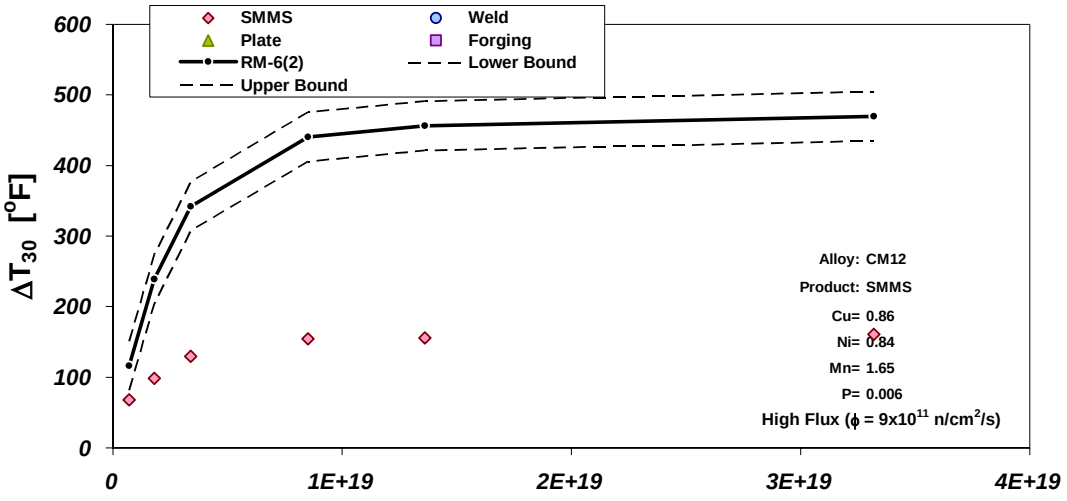
SMMS
Weld
Plate
Forging
RM-6(2)
Lower Bound
Upper Bound
Alloy: CM12
Product: SMMS
Cu= 0.86
Ni= 0.84
Mn= 1.65
P= 0.006
High Flux (ϕ = 9x10^11 n/cm^2/s)
ΔT30 [°F]
Fluence (E > 1 MeV) [n/cm^2]

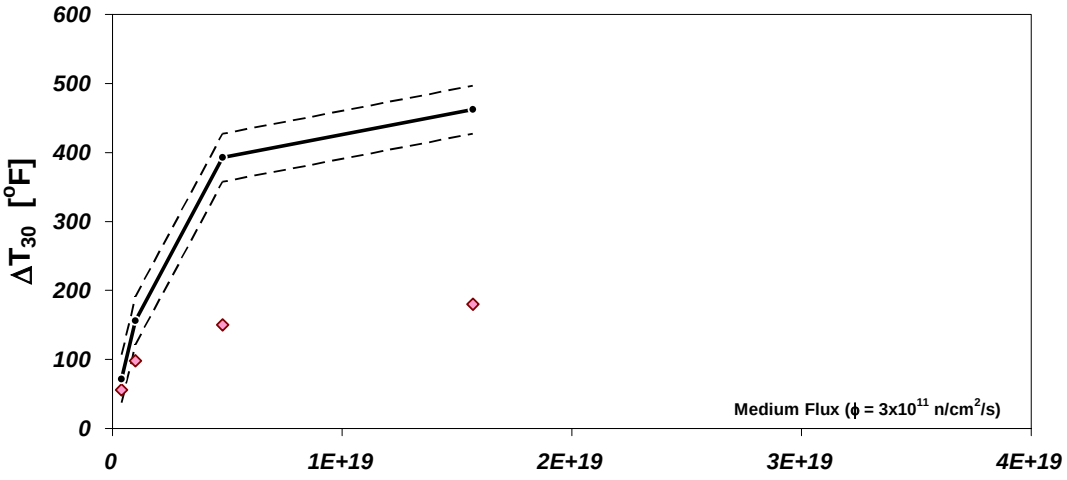
Medium Flux (ϕ = 3x10^11 n/cm^2/s)
ΔT30 [°F]
Fluence (E > 1 MeV) [n/cm^2]

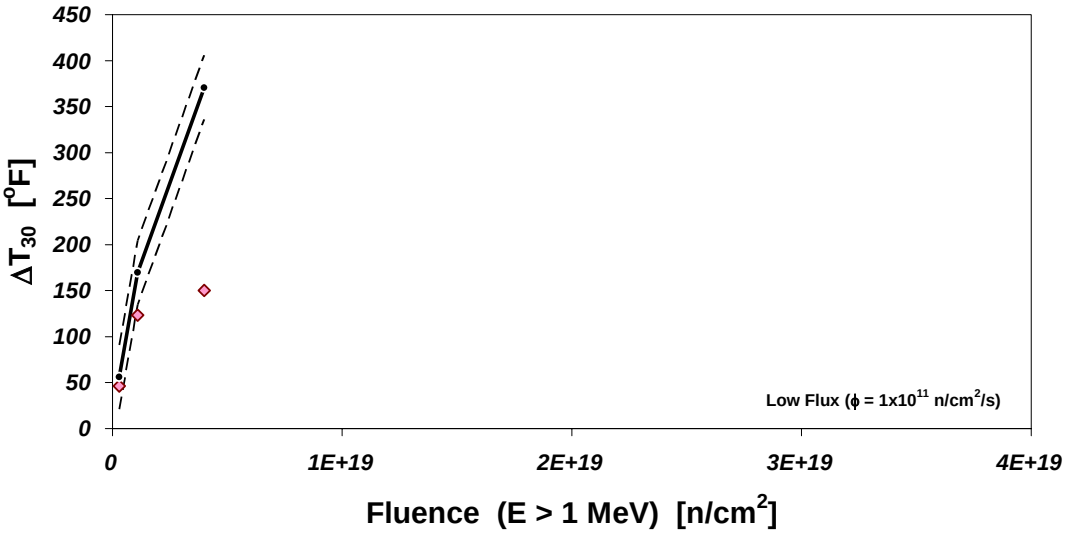
Low Flux (ϕ = 1x10^11 n/cm^2/s)
ΔT30 [°F]
Fluence (E > 1 MeV) [n/cm^2]

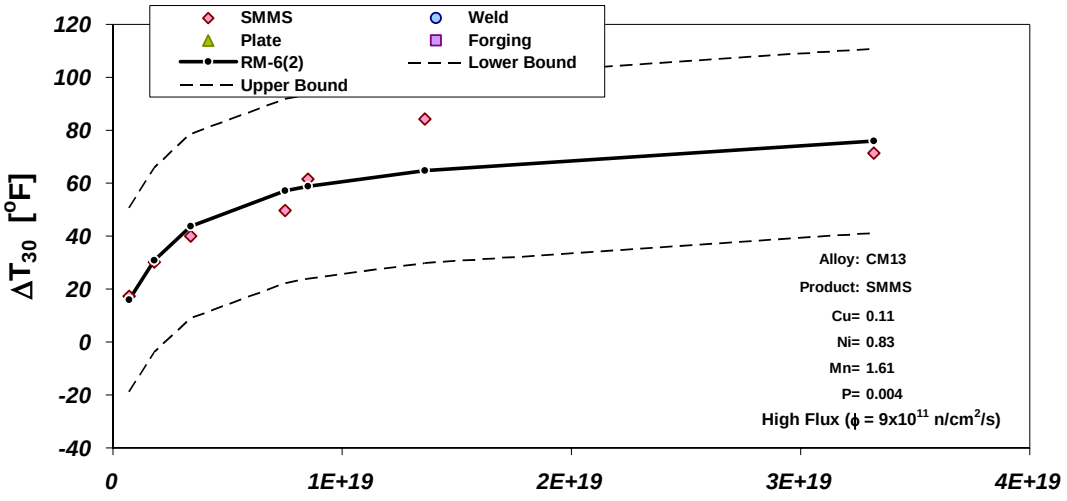
SMMS
Weld
Plate
Forging
RM-6(2)
Lower Bound
Upper Bound
Alloy: CM13
Product: SMMS
Cu= 0.11
Ni= 0.83
Mn= 1.61
P= 0.004
High Flux (ϕ = 9x10^11 n/cm^2/s)
ΔT30 [°F]
120
100
80
60
40
20
0
-20
-40
0
1E+19
2E+19
3E+19
4E+19
Fluence (E > 1 MeV) [n/cm^2]

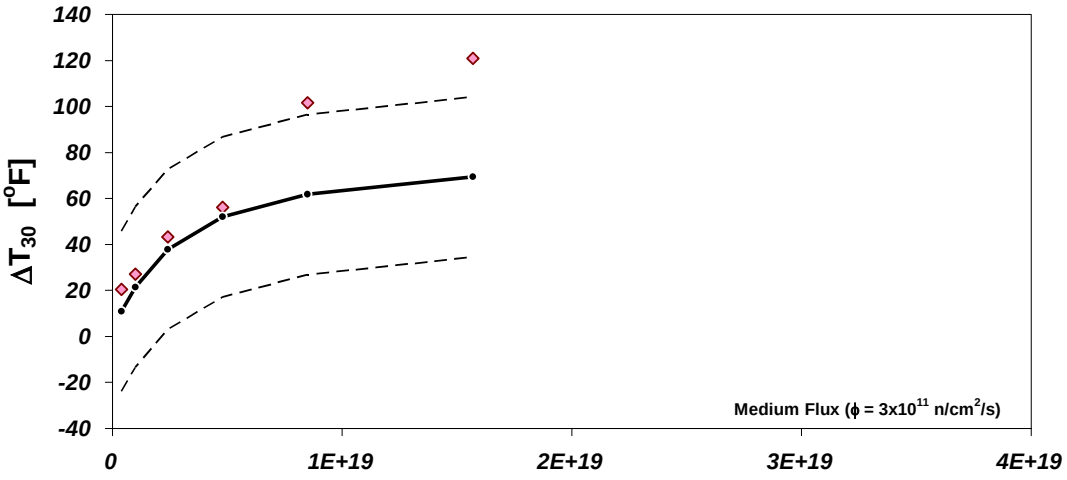
Medium Flux (ϕ = 3x10^11 n/cm^2/s)
ΔT30 [°F]
140
120
100
80
60
40
20
0
-20
-40
0
1E+19
2E+19
3E+19
4E+19
Fluence (E > 1 MeV) [n/cm^2]

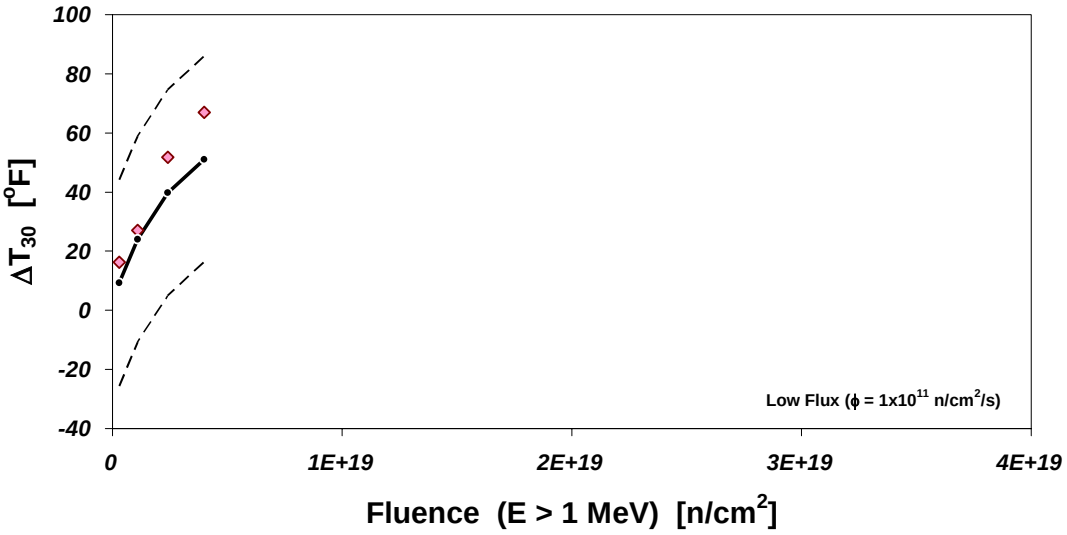
Low Flux (ϕ = 1x10^11 n/cm^2/s)
ΔT30 [°F]
100
80
60
40
20
0
-20
-40
0
1E+19
2E+19
3E+19
4E+19
Fluence (E > 1 MeV) [n/cm^2]

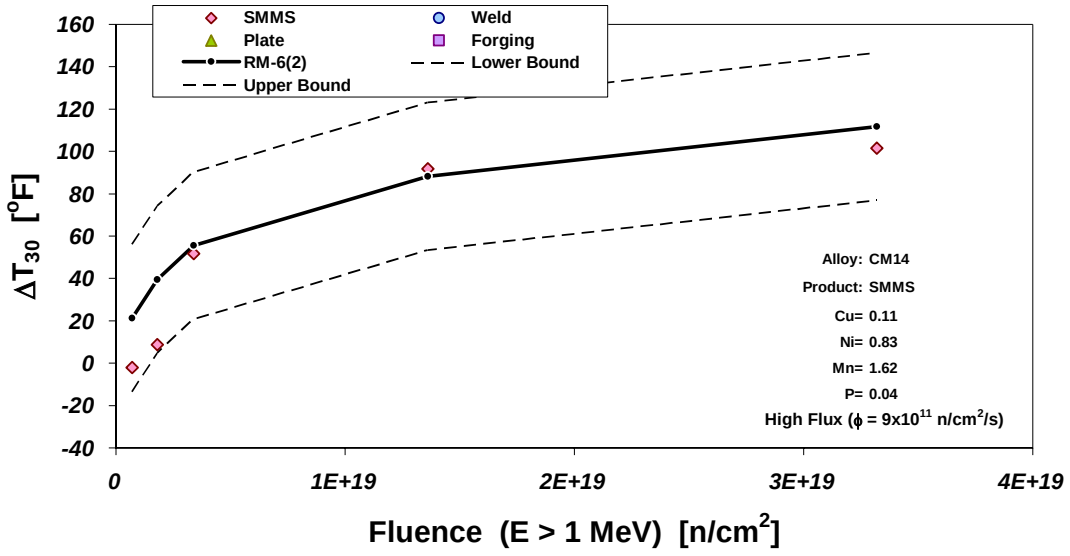
SMMS
Weld
Plate
Forging
RM-6(2)
Lower Bound
Upper Bound
Alloy: CM14
Product: SMMS
Cu= 0.11
Ni= 0.83
Mn= 1.62
P= 0.04
High Flux (ϕ = 9x10^11 n/cm^2/s)
ΔT30 [°F]
160
140
120
100
80
60
40
20
0
-20
-40
0
1E+19
2E+19
3E+19
4E+19
Fluence (E > 1 MeV) [n/cm^2]

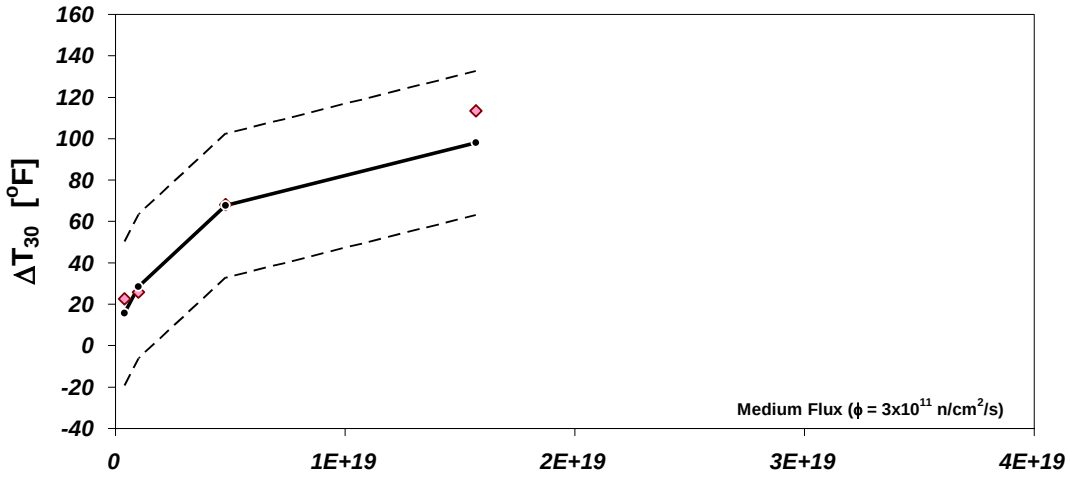
Medium Flux (ϕ = 3x10^11 n/cm^2/s)
ΔT30 [°F]
160
140
120
100
80
60
40
20
0
-20
-40
0
1E+19
2E+19
3E+19
4E+19
Fluence (E > 1 MeV) [n/cm^2]

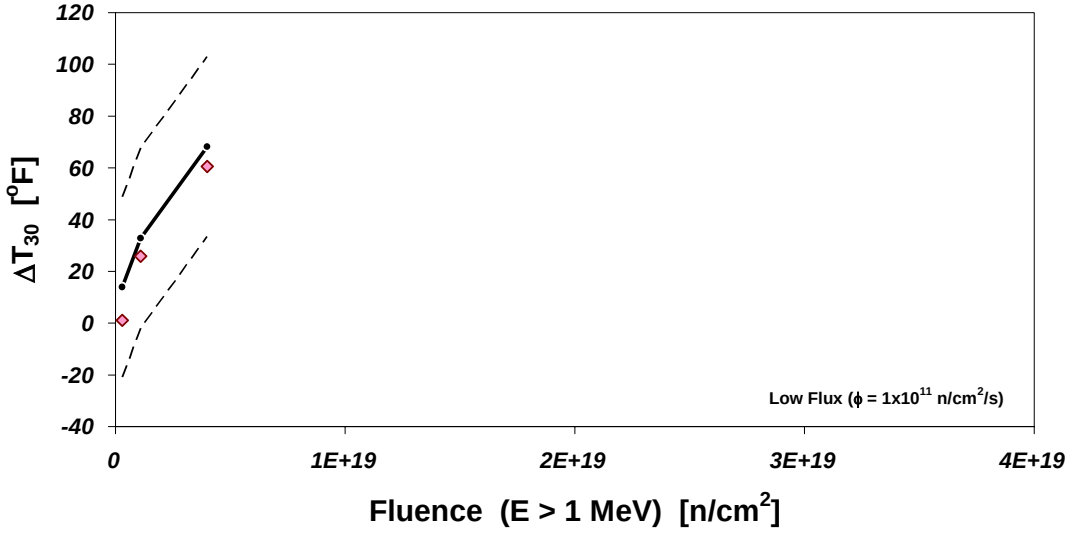
Low Flux (ϕ = 1x10^11 n/cm^2/s)
ΔT30 [°F]
120
100
80
60
40
20
0
-20
-40
0
1E+19
2E+19
3E+19
4E+19
Fluence (E > 1 MeV) [n/cm^2]

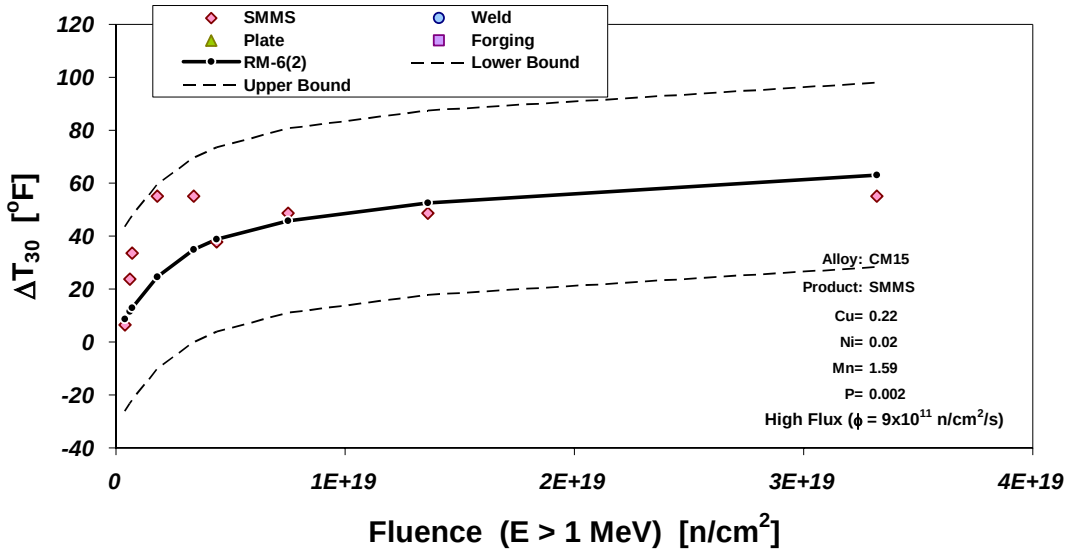
SMMS
Weld
Plate
Forging
RM-6(2)
Lower Bound
Upper Bound
Alloy: CM15
Product: SMMS
Cu= 0.22
Ni= 0.02
Mn= 1.59
P= 0.002
High Flux (ϕ = 9x10^11 n/cm^2/s)
ΔT30 [°F]
120
100
80
60
40
20
0
-20
-40
0
1E+19
2E+19
3E+19
4E+19
Fluence (E > 1 MeV) [n/cm^2]

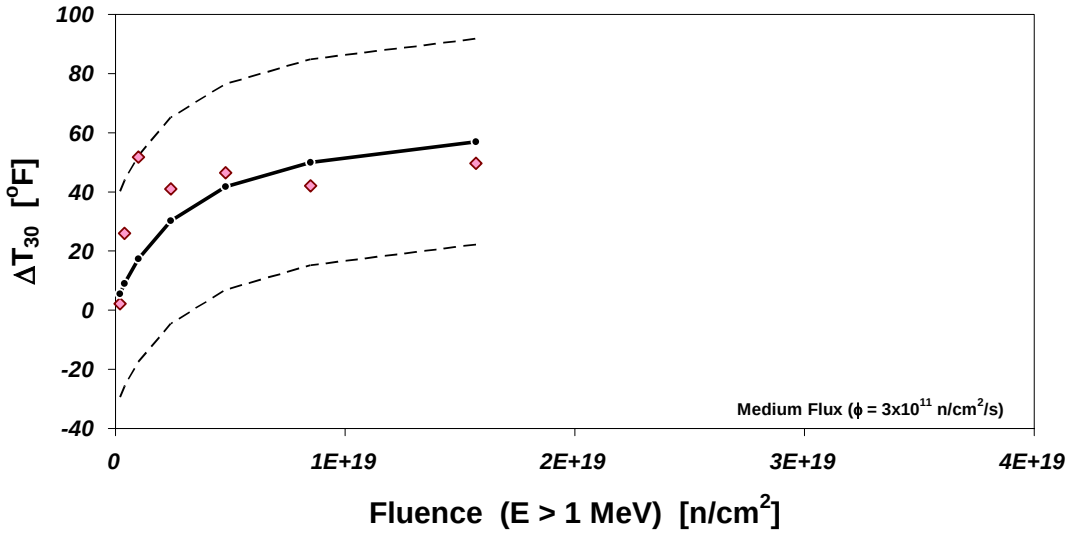
Medium Flux (ϕ = 3x10^11 n/cm^2/s)
ΔT30 [°F]
100
80
60
40
20
0
-20
-40
0
1E+19
2E+19
3E+19
4E+19
Fluence (E > 1 MeV) [n/cm^2]

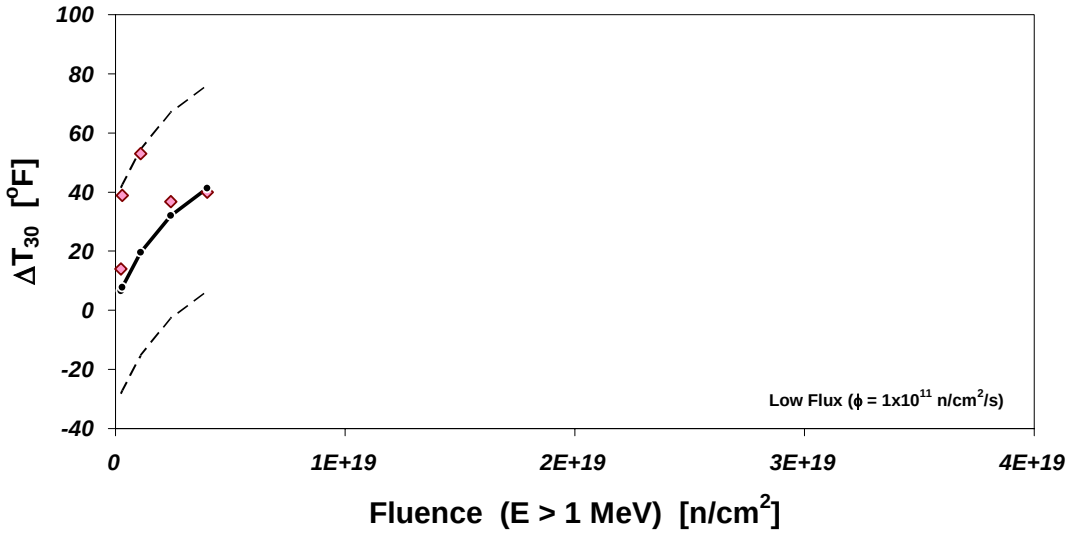
Low Flux (ϕ = 1x10^11 n/cm^2/s)
ΔT30 [°F]
100
80
60
40
20
0
-20
-40
0
1E+19
2E+19
3E+19
4E+19
Fluence (E > 1 MeV) [n/cm^2]

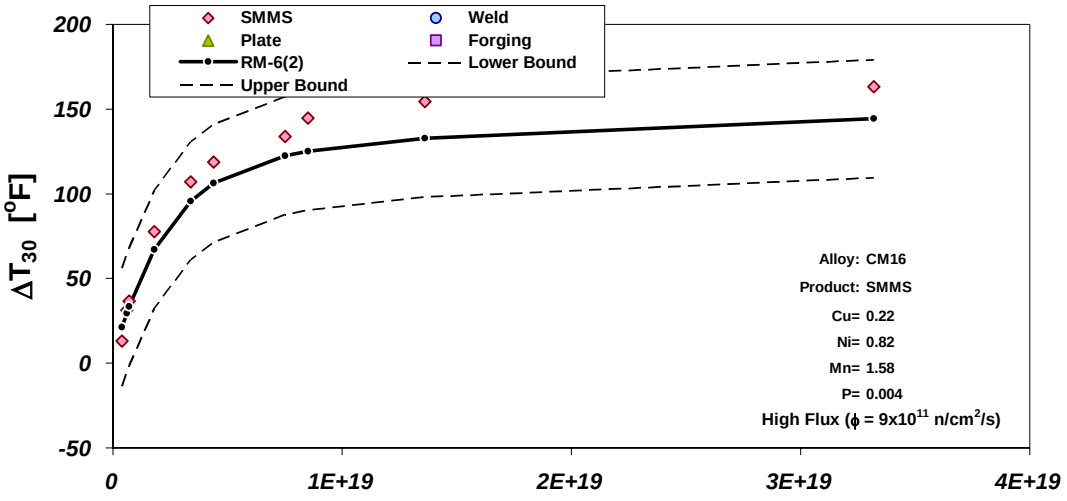
SMMS
Weld
Plate
Forging
RM-6(2)
Lower Bound
Upper Bound
200
150
100
50
0
-50
ΔT30 [°F]
Alloy: CM16
Product: SMMS
Cu= 0.22
Ni= 0.82
Mn= 1.58
P= 0.004
High Flux (ϕ = 9x10^11 n/cm^2/s)
0
1E+19
2E+19
3E+19
4E+19
Fluence (E > 1 MeV) [n/cm^2]

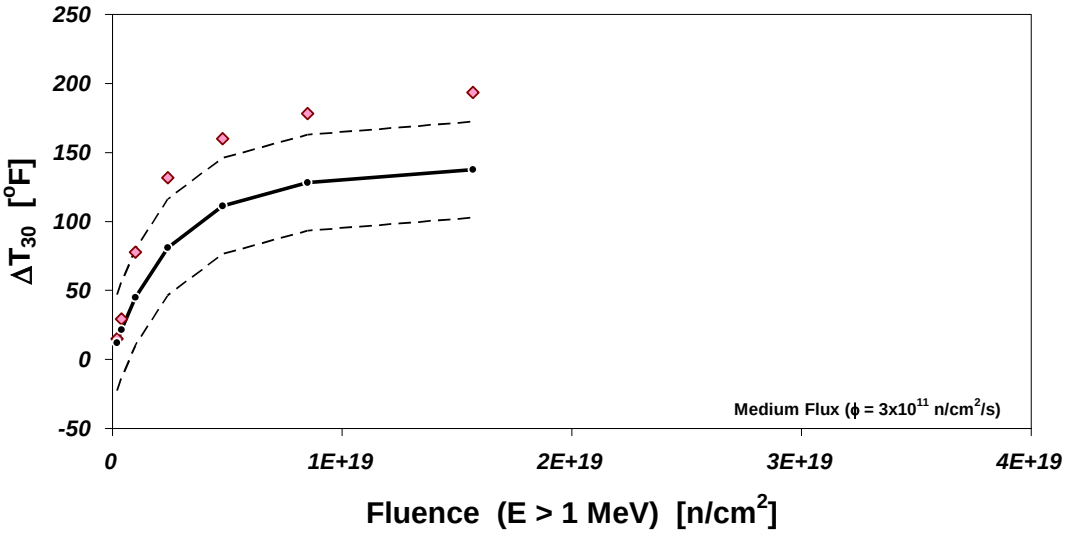
250
200
150
100
50
0
-50
ΔT30 [°F]
Medium Flux (ϕ = 3x10^11 n/cm^2/s)
0
1E+19
2E+19
3E+19
4E+19
Fluence (E > 1 MeV) [n/cm^2]

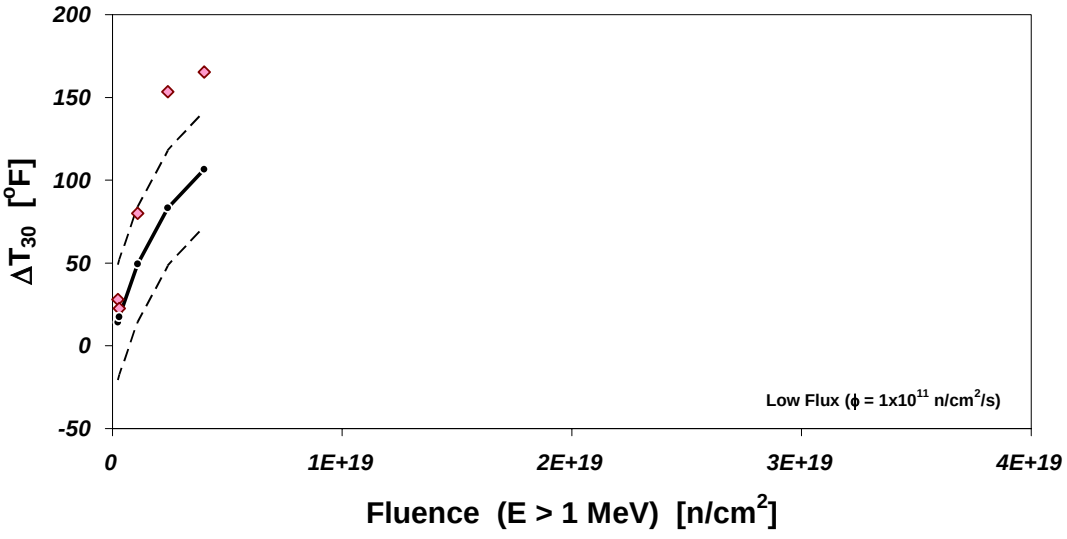
200
150
100
50
0
-50
ΔT30 [°F]
Low Flux (ϕ = 1x10^11 n/cm^2/s)
0
1E+19
2E+19
3E+19
4E+19
Fluence (E > 1 MeV) [n/cm^2]

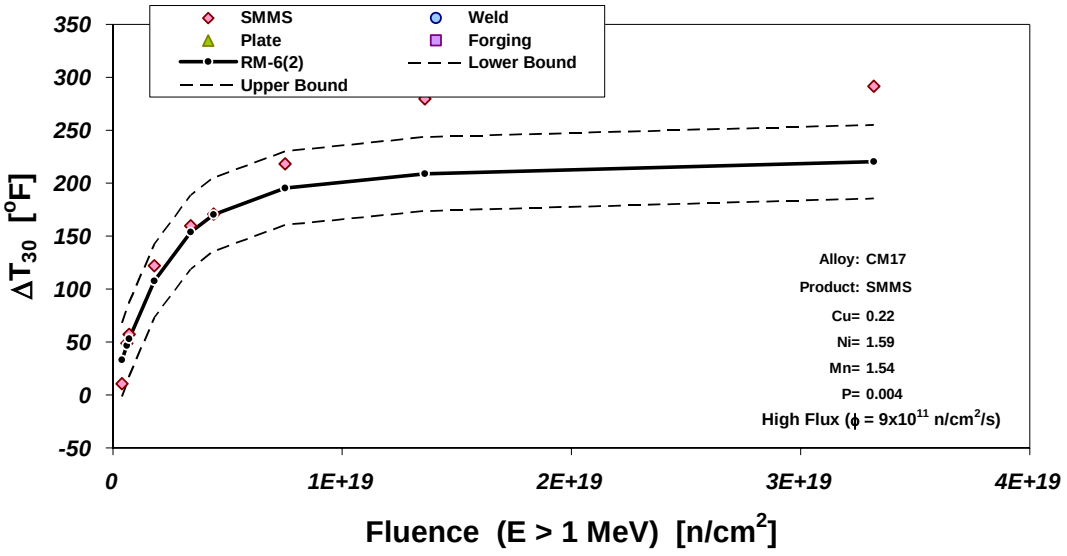
SMMS
Weld
Plate
Forging
RM-6(2)
Lower Bound
Upper Bound
Alloy: CM17
Product: SMMS
Cu= 0.22
Ni= 1.59
Mn= 1.54
P= 0.004
High Flux (ϕ = 9x10^11 n/cm^2/s)
ΔT30 [°F]
350
300
250
200
150
100
50
0
-50
0
1E+19
2E+19
3E+19
4E+19
Fluence (E > 1 MeV) [n/cm^2]

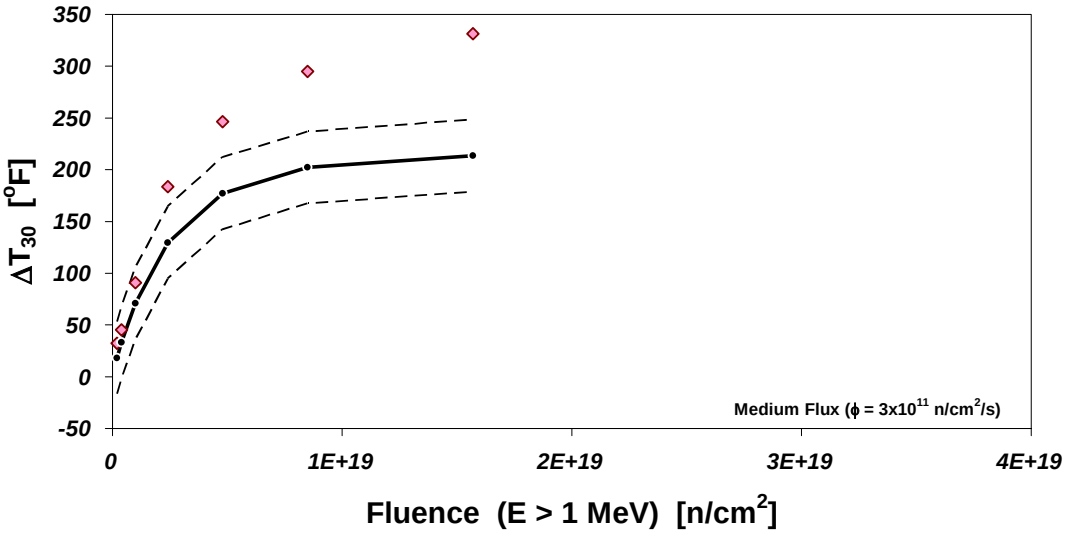
Medium Flux (ϕ = 3x10^11 n/cm^2/s)
ΔT30 [°F]
350
300
250
200
150
100
50
0
-50
0
1E+19
2E+19
3E+19
4E+19
Fluence (E > 1 MeV) [n/cm^2]

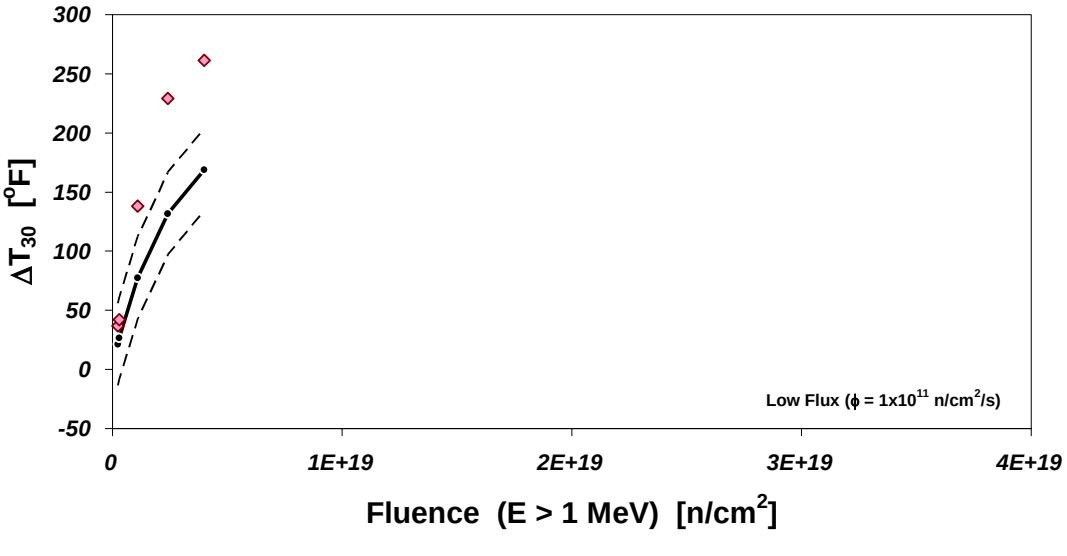
Low Flux (ϕ = 1x10^11 n/cm^2/s)
ΔT30 [°F]
300
250
200
150
100
50
0
-50
0
1E+19
2E+19
3E+19
4E+19
Fluence (E > 1 MeV) [n/cm^2]

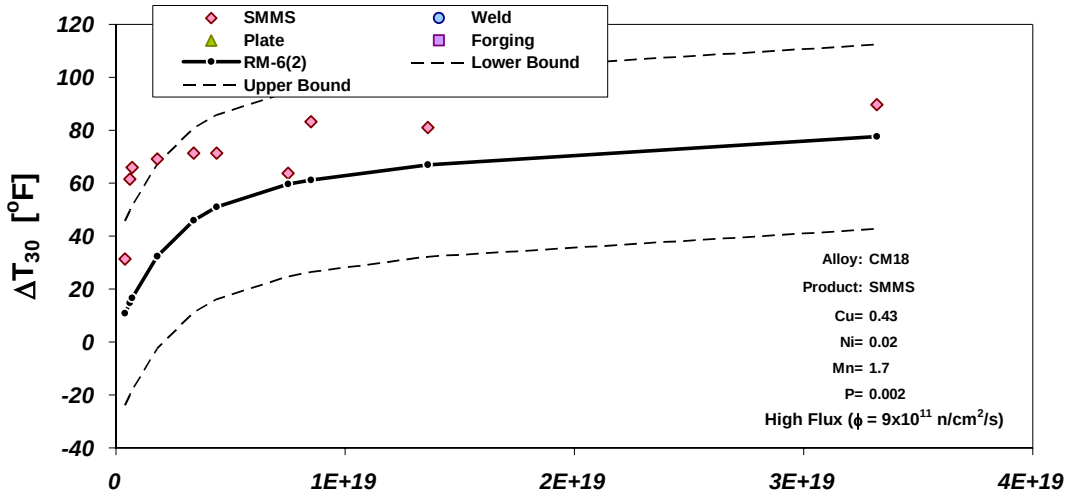
SMMS
Weld
Plate
Forging
RM-6(2)
Lower Bound
Upper Bound
Alloy: CM18
Product: SMMS
Cu= 0.43
Ni= 0.02
Mn= 1.7
P= 0.002
High Flux (ϕ = 9x10^11 n/cm^2/s)
ΔT30 [°F]
120
100
80
60
40
20
0
-20
-40
0
1E+19
2E+19
3E+19
4E+19
Fluence (E > 1 MeV) [n/cm^2]

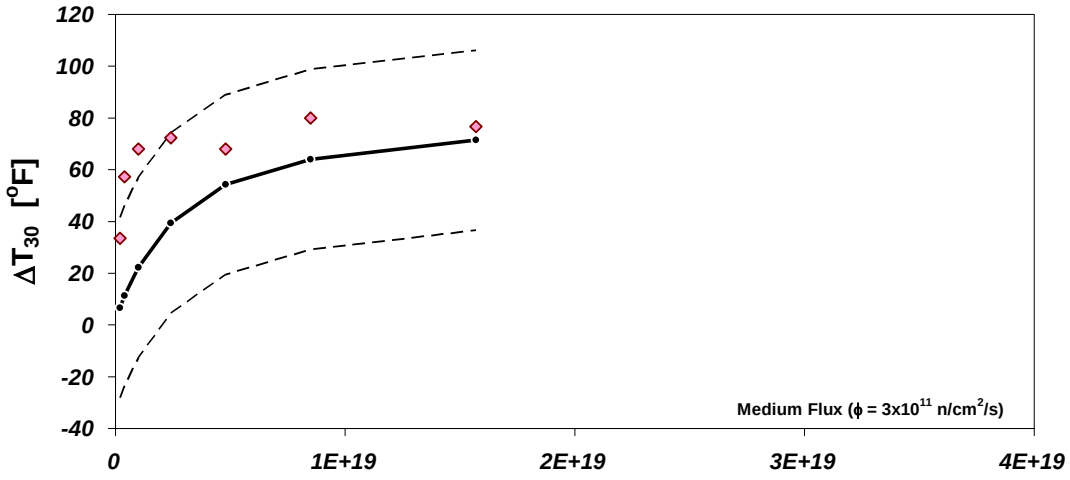
Medium Flux (ϕ = 3x10^11 n/cm^2/s)
ΔT30 [°F]
120
100
80
60
40
20
0
-20
-40
0
1E+19
2E+19
3E+19
4E+19
Fluence (E > 1 MeV) [n/cm^2]

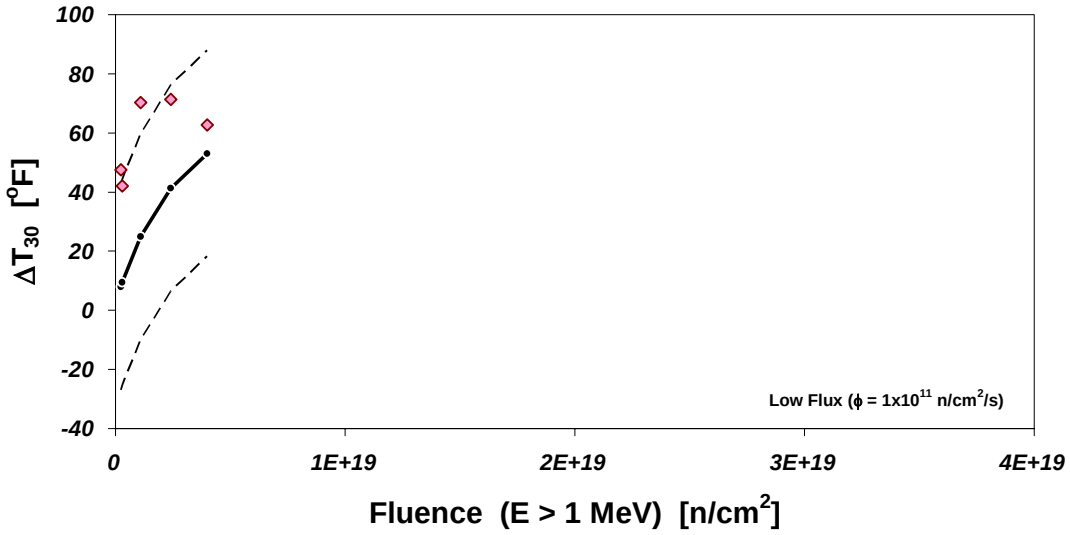
Low Flux (ϕ = 1x10^11 n/cm^2/s)
ΔT30 [°F]
100
80
60
40
20
0
-20
-40
0
1E+19
2E+19
3E+19
4E+19
Fluence (E > 1 MeV) [n/cm^2]

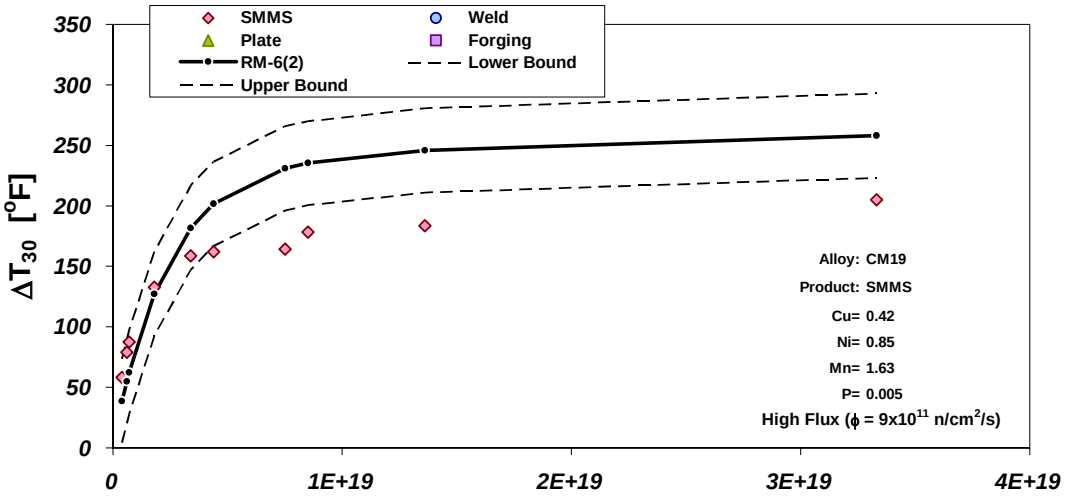
SMMS
Weld
Plate
Forging
RM-6(2)
Lower Bound
Upper Bound
Alloy: CM19
Product: SMMS
Cu= 0.42
Ni= 0.85
Mn= 1.63
P= 0.005
High Flux (ϕ = 9x10^11 n/cm^2/s)
ΔT30 [°F]
350
300
250
200
150
100
50
0
0
1E+19
2E+19
3E+19
4E+19
Fluence (E > 1 MeV) [n/cm^2]

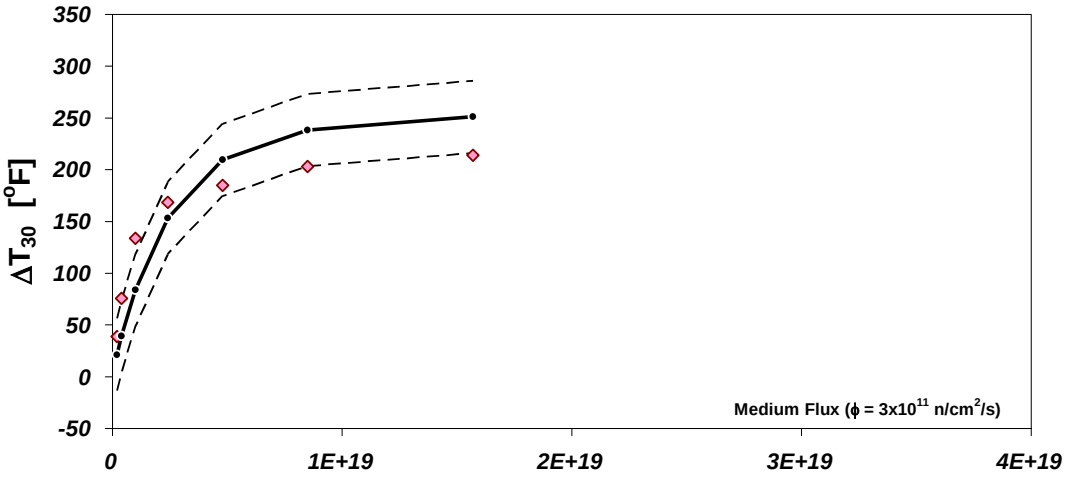
Medium Flux (ϕ = 3x10^11 n/cm^2/s)
ΔT30 [°F]
350
300
250
200
150
100
50
0
-50
0
1E+19
2E+19
3E+19
4E+19
Fluence (E > 1 MeV) [n/cm^2]

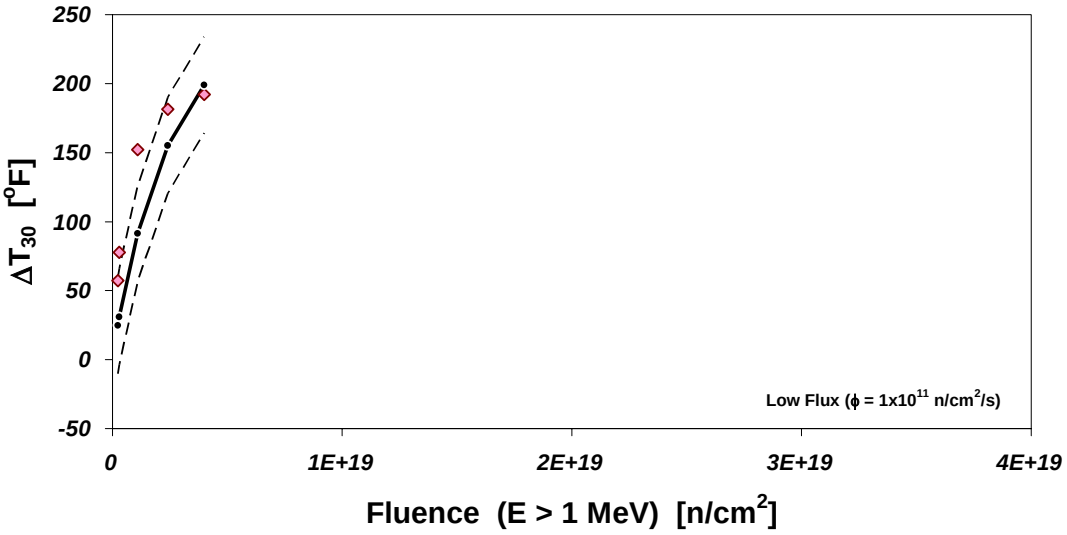
Low Flux (ϕ = 1x10^11 n/cm^2/s)
ΔT30 [°F]
250
200
150
100
50
0
-50
0
1E+19
2E+19
3E+19
4E+19
Fluence (E > 1 MeV) [n/cm^2]

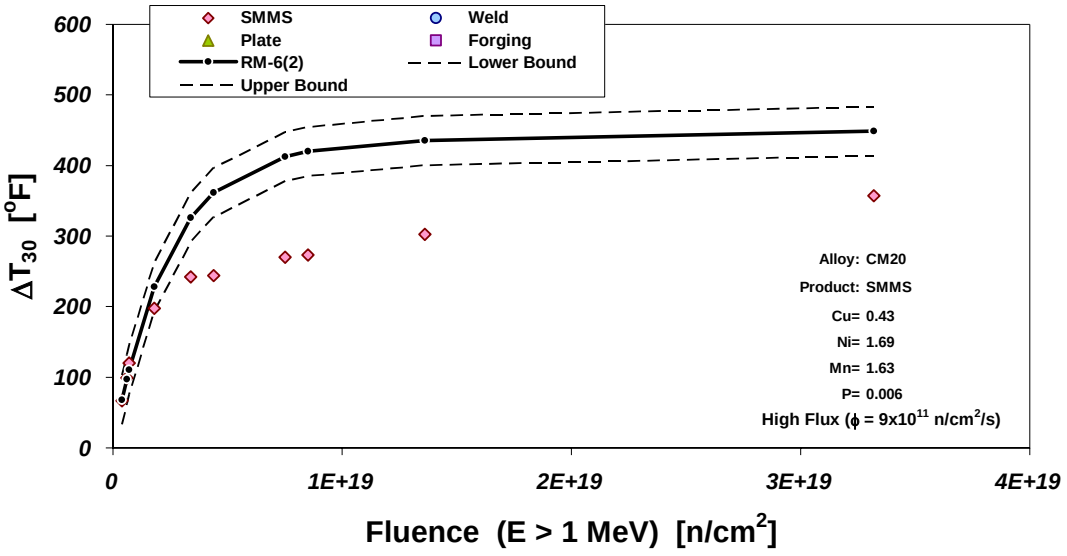
SMMS
Weld
Plate
Forging
RM-6(2)
Lower Bound
Upper Bound
Alloy: CM20
Product: SMMS
Cu= 0.43
Ni= 1.69
Mn= 1.63
P= 0.006
High Flux (ϕ = 9x10^11 n/cm^2/s)
ΔT30 [°F]
0
100
200
300
400
500
600
0
1E+19
2E+19
3E+19
4E+19
Fluence (E > 1 MeV) [n/cm^2]

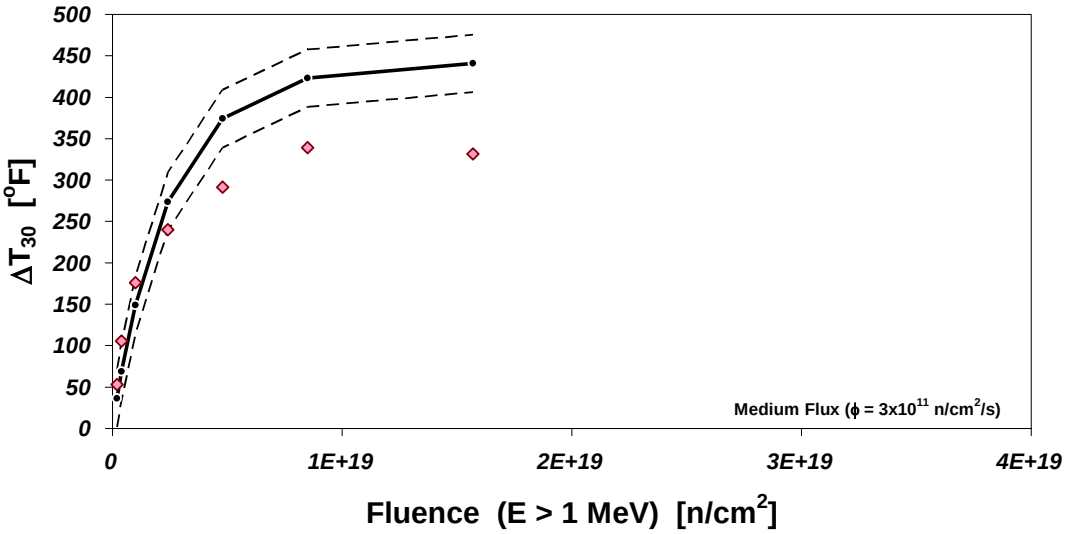
Medium Flux (ϕ = 3x10^11 n/cm^2/s)
ΔT30 [°F]
0
50
100
150
200
250
300
350
400
450
500
0
1E+19
2E+19
3E+19
4E+19
Fluence (E > 1 MeV) [n/cm^2]

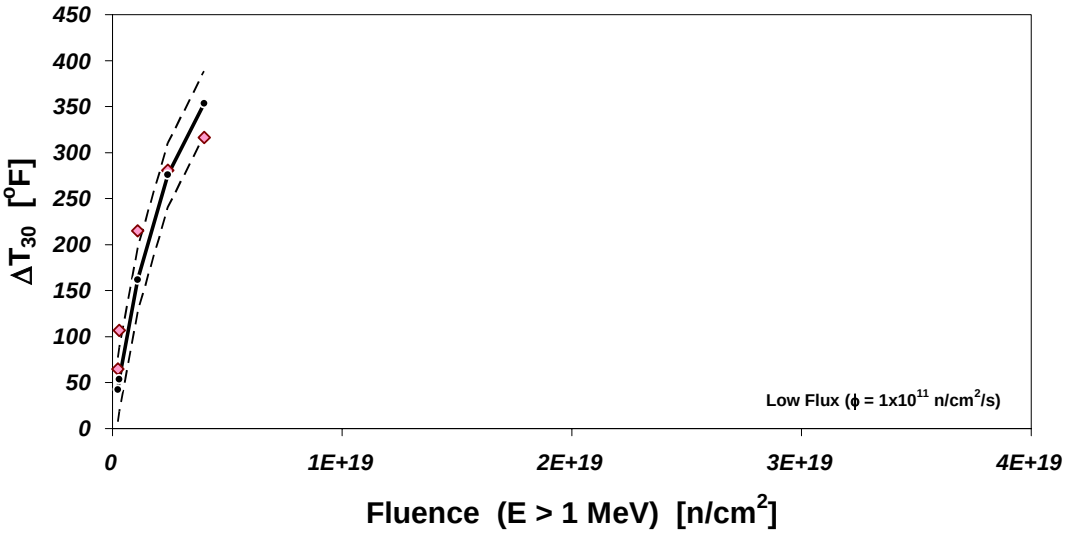
Low Flux (ϕ = 1x10^11 n/cm^2/s)
ΔT30 [°F]
0
50
100
150
200
250
300
350
400
450
0
1E+19
2E+19
3E+19
4E+19
Fluence (E > 1 MeV) [n/cm^2]

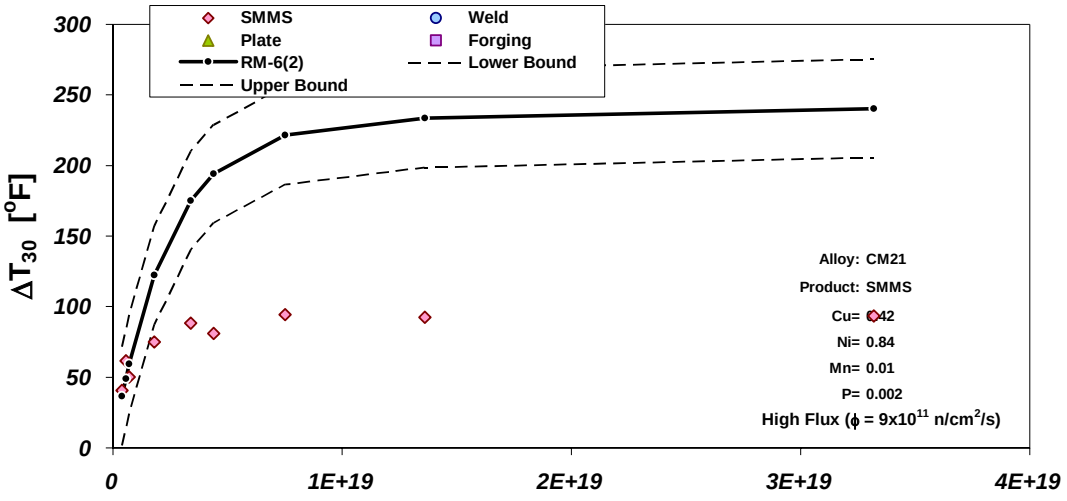
SMMS
Weld
Plate
Forging
RM-6(2)
Lower Bound
Upper Bound
Alloy: CM21
Product: SMMS
Cu= 0.42
Ni= 0.84
Mn= 0.01
P= 0.002
High Flux (ϕ = 9x10^11 n/cm^2/s)
ΔT30 [°F]
300
250
200
150
100
50
0
0
1E+19
2E+19
3E+19
4E+19
Fluence (E > 1 MeV) [n/cm^2]

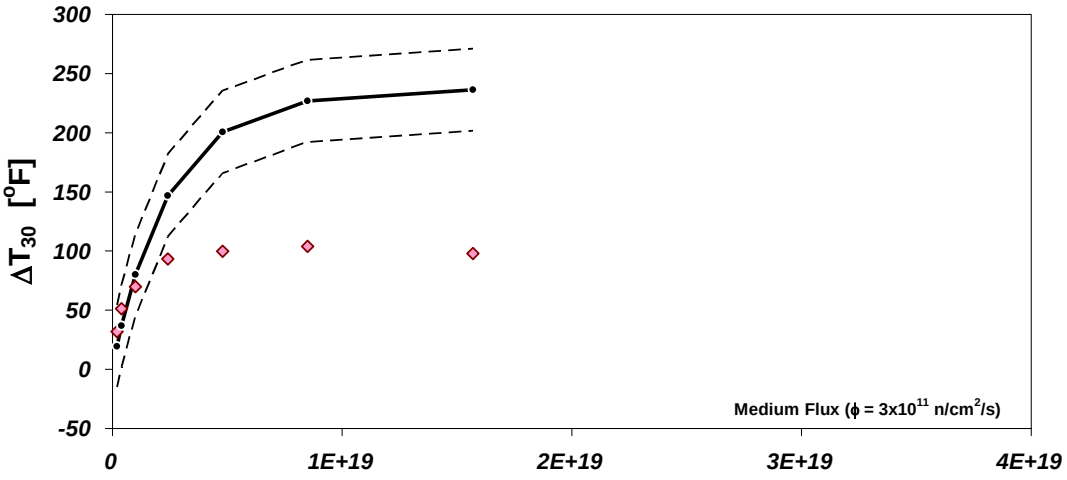
Medium Flux (ϕ = 3x10^11 n/cm^2/s)
ΔT30 [°F]
300
250
200
150
100
50
0
-50
0
1E+19
2E+19
3E+19
4E+19
Fluence (E > 1 MeV) [n/cm^2]

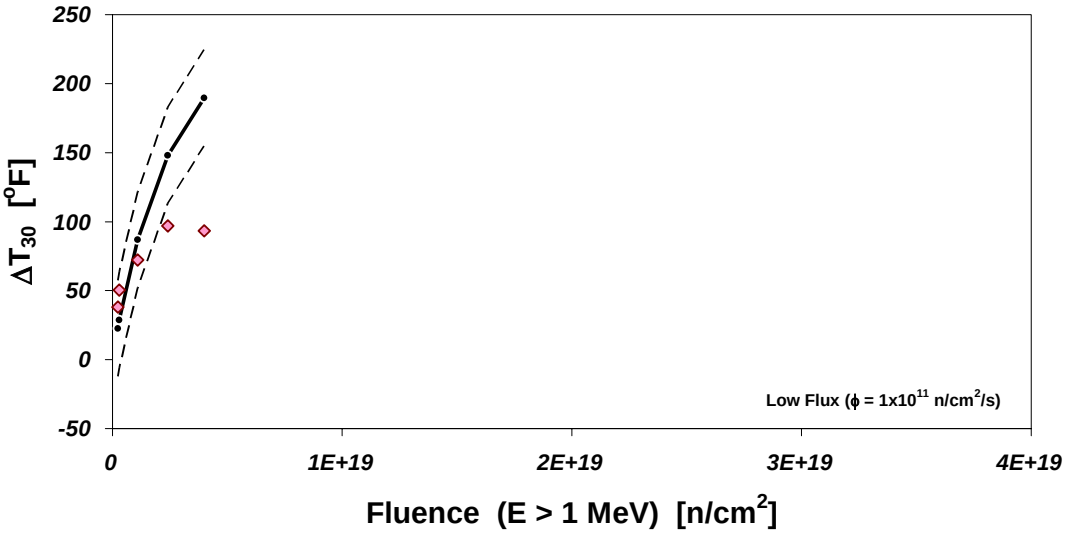
Low Flux (ϕ = 1x10^11 n/cm^2/s)
ΔT30 [°F]
250
200
150
100
50
0
-50
0
1E+19
2E+19
3E+19
4E+19
Fluence (E > 1 MeV) [n/cm^2]

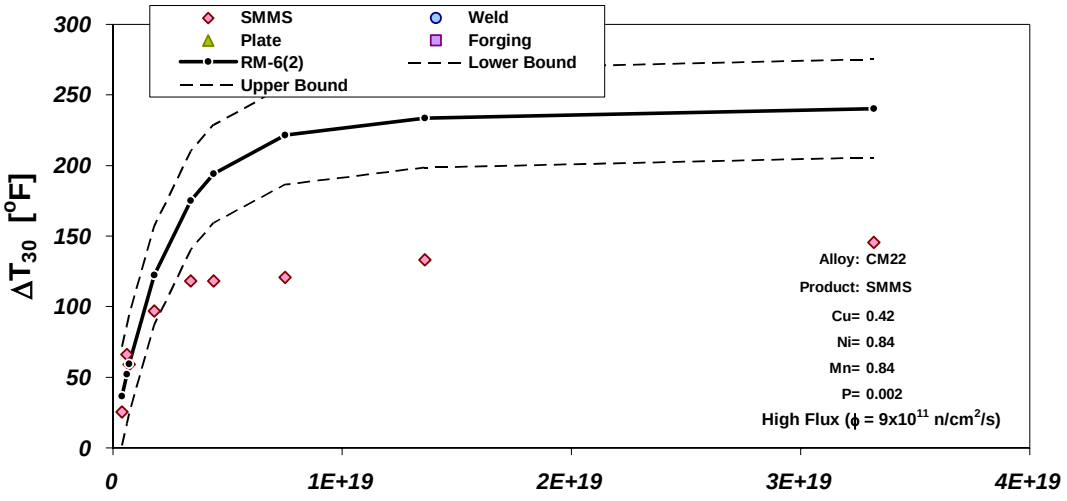
SMMS
Weld
Plate
Forging
RM-6(2)
Lower Bound
Upper Bound
ΔT30 [°F]
300
250
200
150
100
50
0
Alloy: CM22
Product: SMMS
Cu= 0.42
Ni= 0.84
Mn= 0.84
P= 0.002
High Flux (ϕ = 9x10^11 n/cm^2/s)
0
1E+19
2E+19
3E+19
4E+19
Fluence (E > 1 MeV) [n/cm^2]

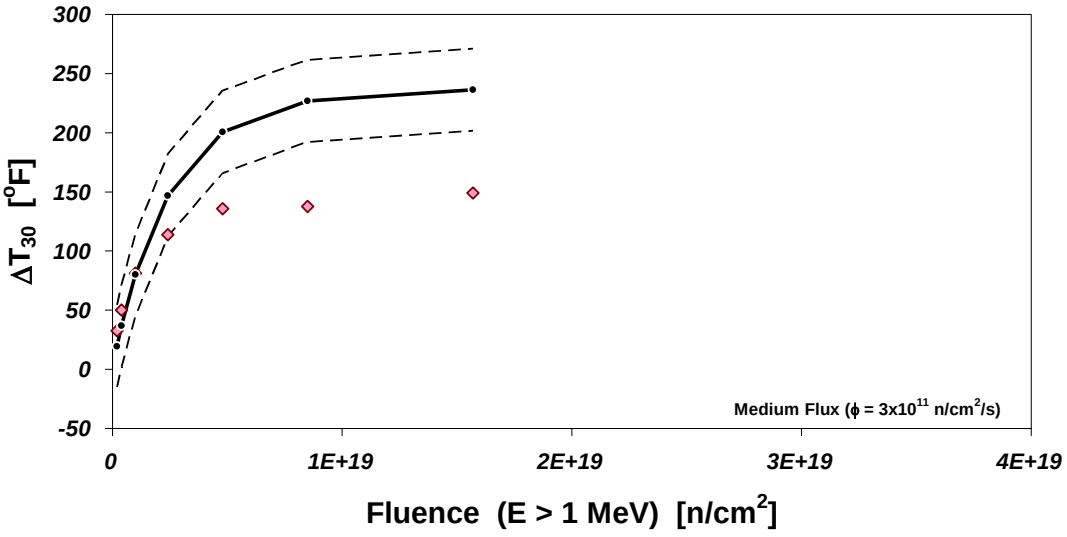
ΔT30 [°F]
300
250
200
150
100
50
0
-50
Medium Flux (ϕ = 3x10^11 n/cm^2/s)
0
1E+19
2E+19
3E+19
4E+19
Fluence (E > 1 MeV) [n/cm^2]

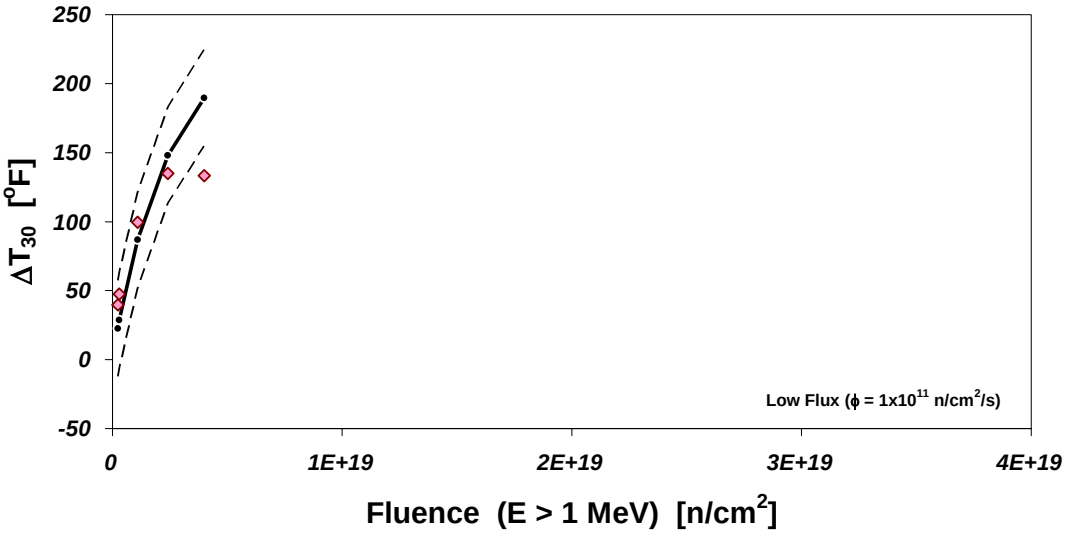
ΔT30 [°F]
250
200
150
100
50
0
-50
Low Flux (ϕ = 1x10^11 n/cm^2/s)
0
1E+19
2E+19
3E+19
4E+19
Fluence (E > 1 MeV) [n/cm^2]

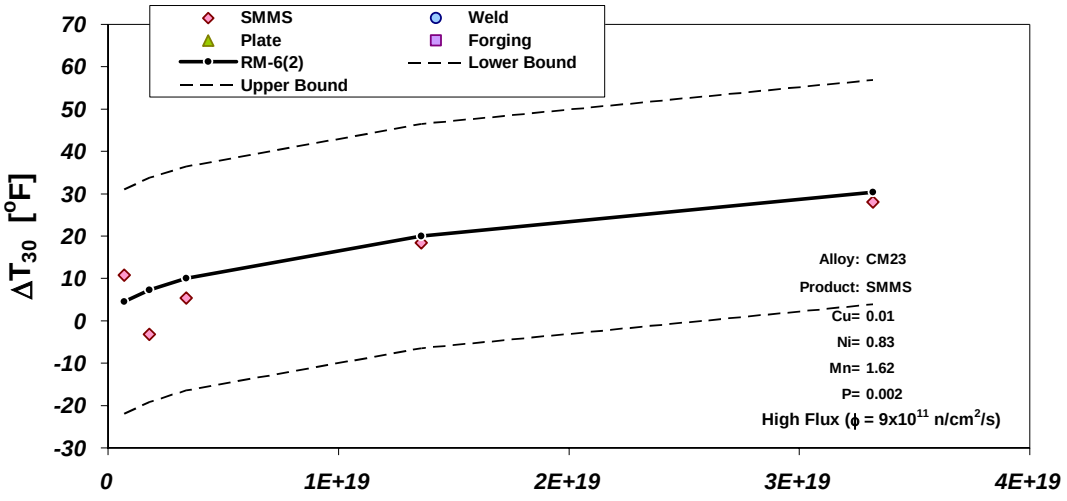
SMMS
Weld
Plate
Forging
RM-6(2)
Lower Bound
Upper Bound
Alloy: CM23
Product: SMMS
Cu= 0.01
Ni= 0.83
Mn= 1.62
P= 0.002
High Flux (ϕ = 9x10^11 n/cm^2/s)
ΔT30 [°F]
70
60
50
40
30
20
10
0
-10
-20
-30
0
1E+19
2E+19
3E+19
4E+19
Fluence (E > 1 MeV) [n/cm^2]

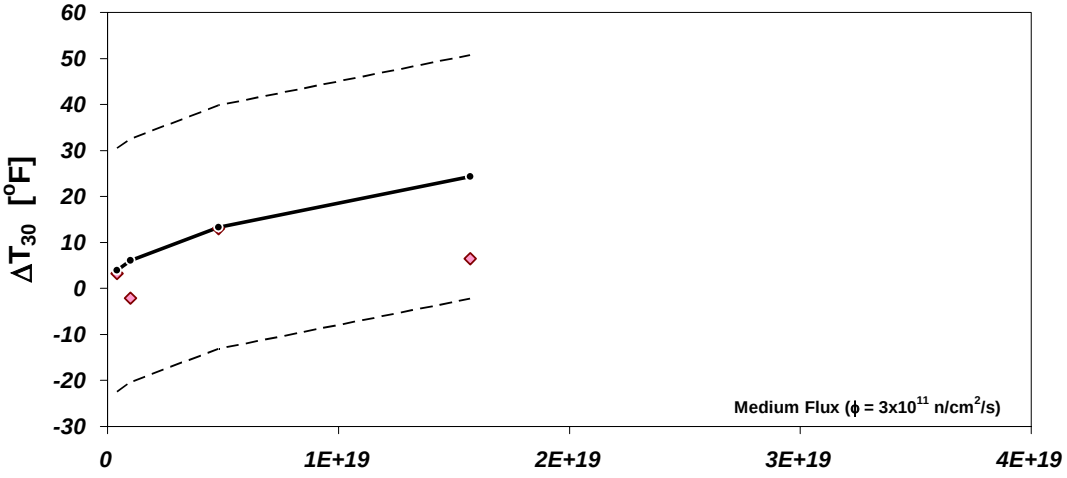
Medium Flux (ϕ = 3x10^11 n/cm^2/s)
ΔT30 [°F]
60
50
40
30
20
10
0
-10
-20
-30
0
1E+19
2E+19
3E+19
4E+19
Fluence (E > 1 MeV) [n/cm^2]

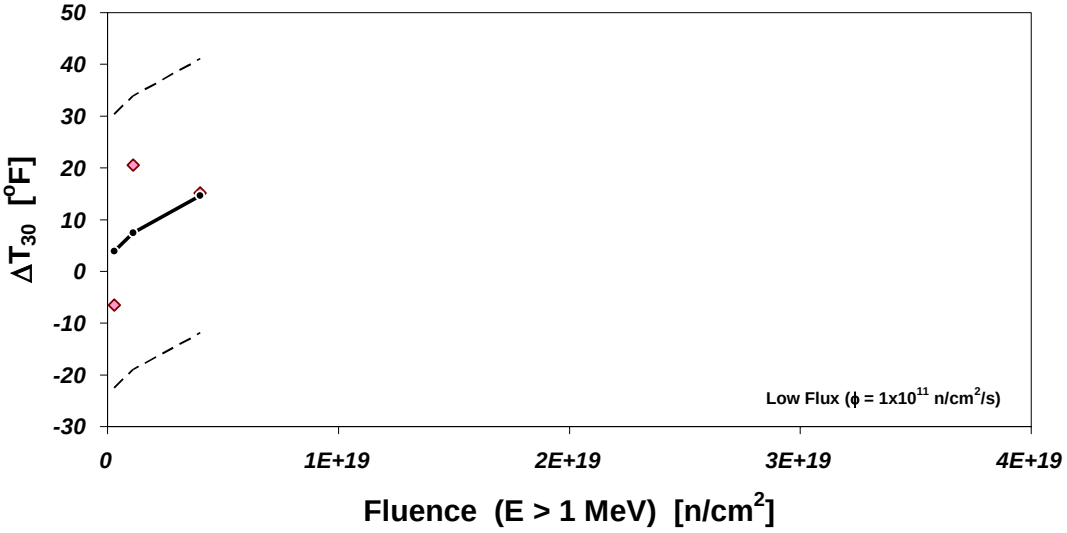
Low Flux (ϕ = 1x10^11 n/cm^2/s)
ΔT30 [°F]
50
40
30
20
10
0
-10
-20
-30
0
1E+19
2E+19
3E+19
4E+19
Fluence (E > 1 MeV) [n/cm^2]

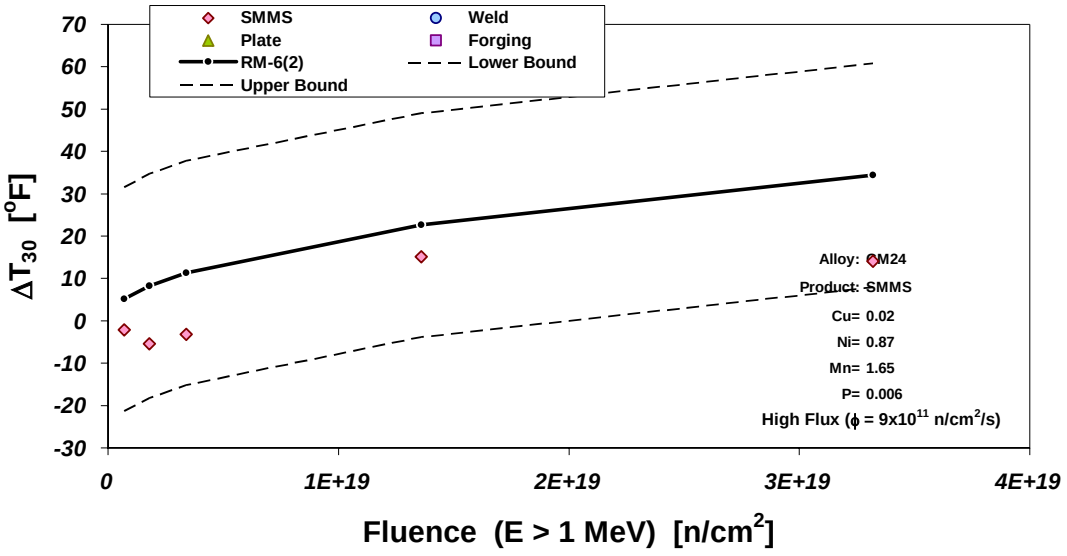
SMMS
Weld
Plate
Forging
RM-6(2)
Lower Bound
Upper Bound
Alloy: CM24
Product: SMMS
Cu= 0.02
Ni= 0.87
Mn= 1.65
P= 0.006
High Flux (ϕ = 9x10^11 n/cm^2/s)
ΔT30 [°F]
70
60
50
40
30
20
10
0
-10
-20
-30
0
1E+19
2E+19
3E+19
4E+19
Fluence (E > 1 MeV) [n/cm^2]

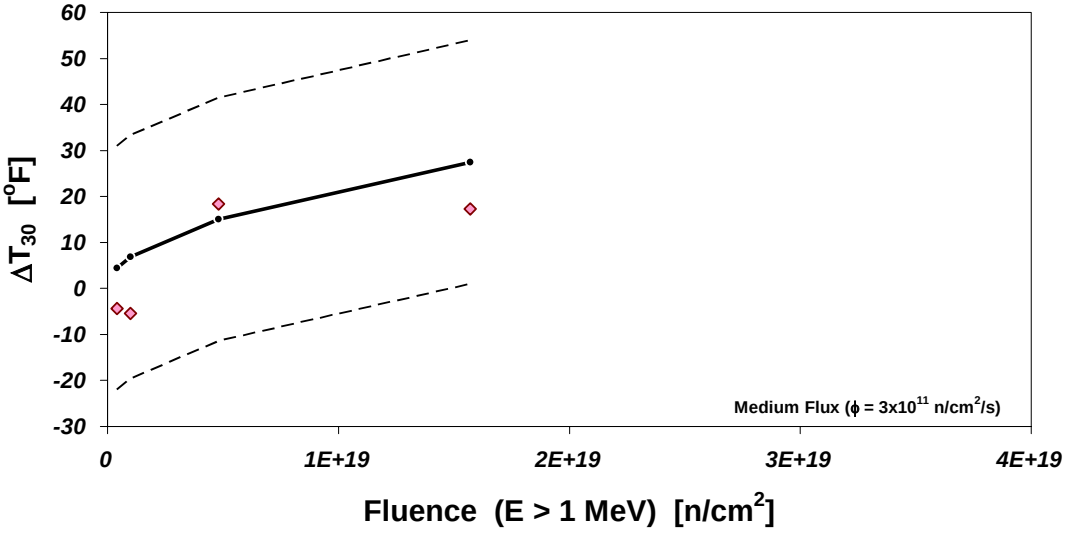
Medium Flux (ϕ = 3x10^11 n/cm^2/s)
ΔT30 [°F]
60
50
40
30
20
10
0
-10
-20
-30
0
1E+19
2E+19
3E+19
4E+19
Fluence (E > 1 MeV) [n/cm^2]

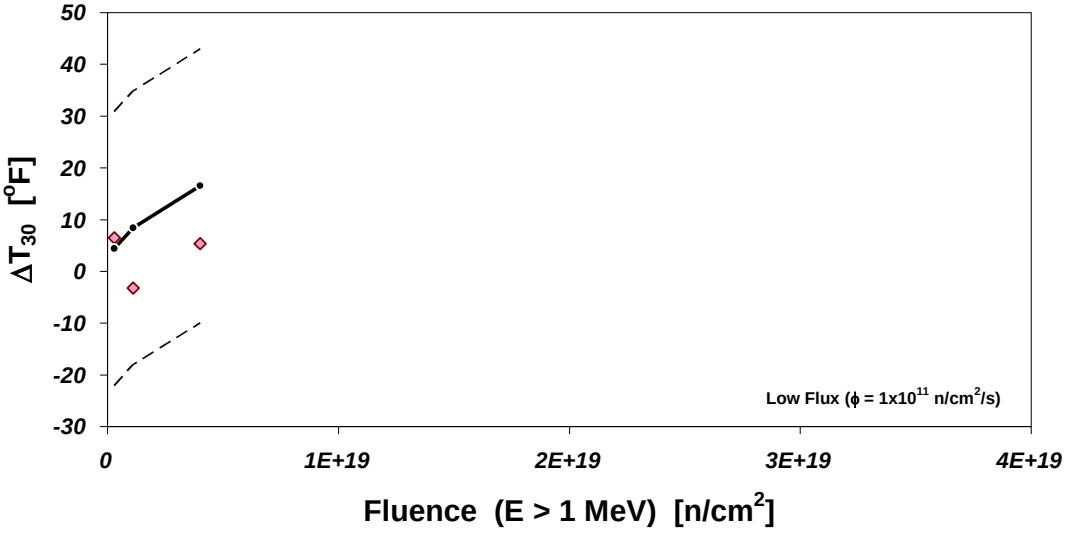
Low Flux (ϕ = 1x10^11 n/cm^2/s)
ΔT30 [°F]
50
40
30
20
10
0
-10
-20
-30
0
1E+19
2E+19
3E+19
4E+19
Fluence (E > 1 MeV) [n/cm^2]

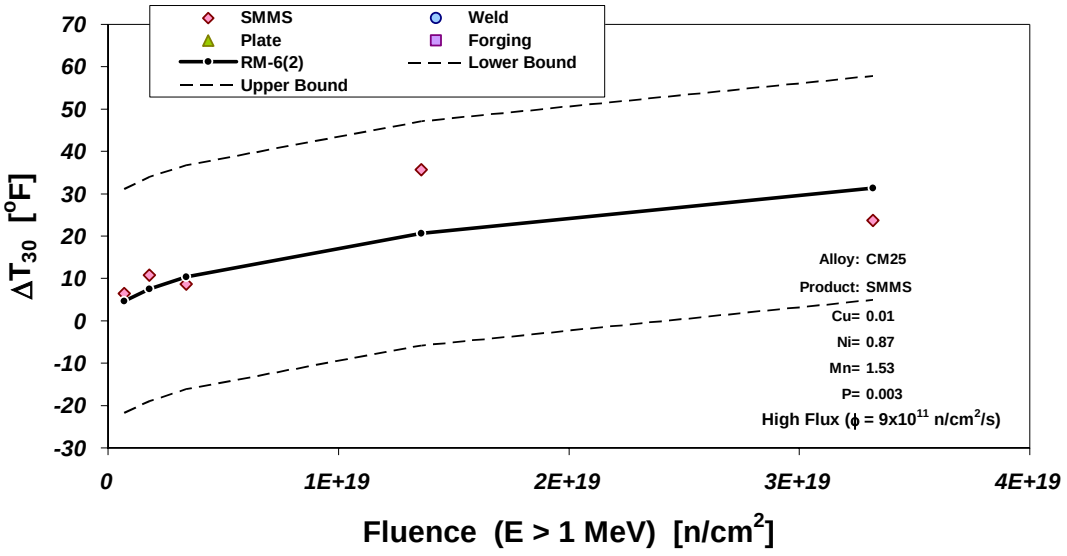
SMMS
Weld
Plate
Forging
RM-6(2)
Lower Bound
Upper Bound
70
60
50
40
30
20
10
0
-10
-20
-30
ΔT30 [°F]
Alloy: CM25
Product: SMMS
Cu= 0.01
Ni= 0.87
Mn= 1.53
P= 0.003
High Flux (ϕ = 9x10^11 n/cm^2/s)
0
1E+19
2E+19
3E+19
4E+19
Fluence (E > 1 MeV) [n/cm^2]

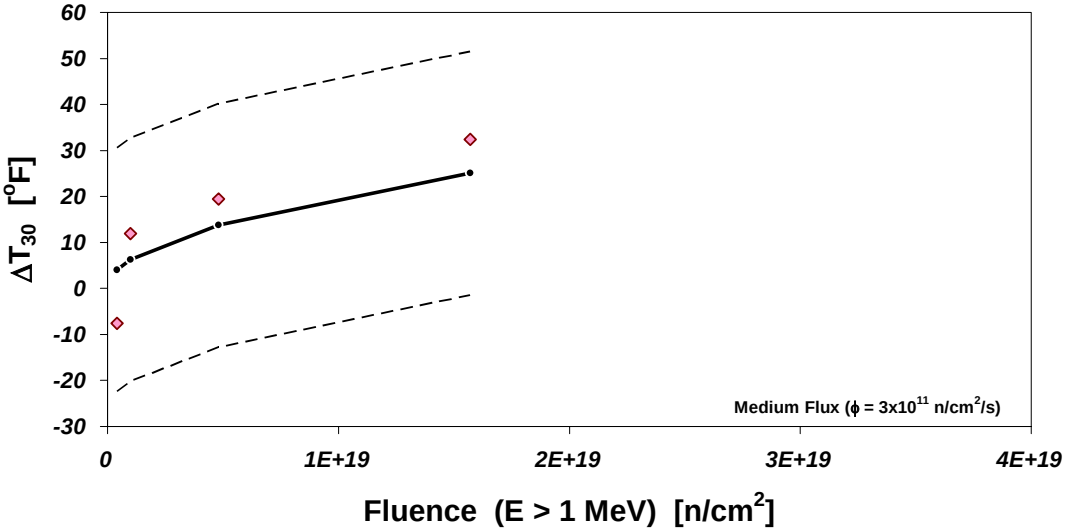
60
50
40
30
20
10
0
-10
-20
-30
ΔT30 [°F]
Medium Flux (ϕ = 3x10^11 n/cm^2/s)
0
1E+19
2E+19
3E+19
4E+19
Fluence (E > 1 MeV) [n/cm^2]

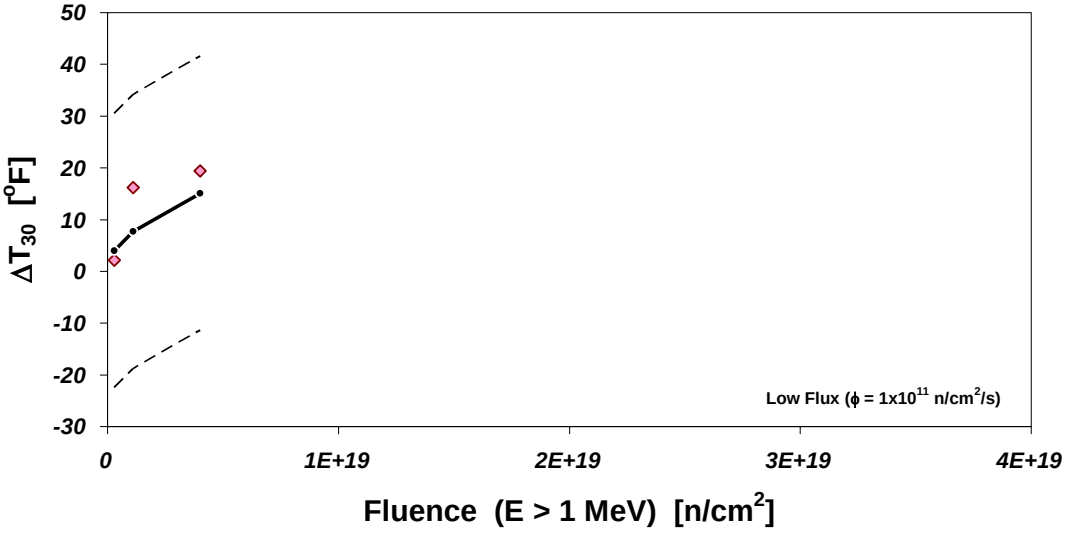
50
40
30
20
10
0
-10
-20
-30
ΔT30 [°F]
Low Flux (ϕ = 1x10^11 n/cm^2/s)
0
1E+19
2E+19
3E+19
4E+19
Fluence (E > 1 MeV) [n/cm^2]

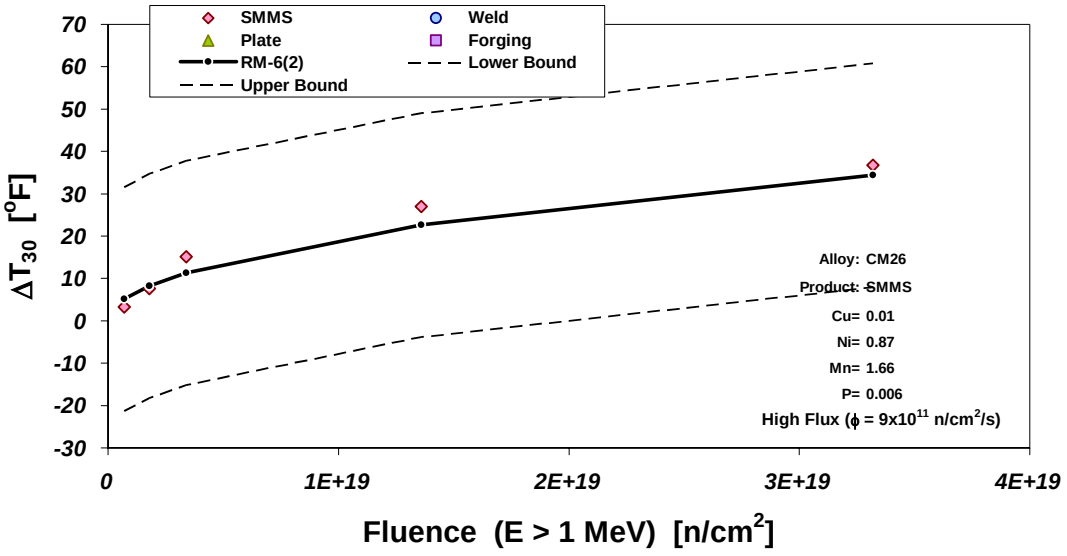
SMMS
Weld
Plate
Forging
RM-6(2)
Lower Bound
Upper Bound
Alloy: CM26
Product: SMMS
Cu= 0.01
Ni= 0.87
Mn= 1.66
P= 0.006
High Flux (ϕ = 9x10^11 n/cm^2/s)
ΔT30 [°F]
70
60
50
40
30
20
10
0
-10
-20
-30
0
1E+19
2E+19
3E+19
4E+19
Fluence (E > 1 MeV) [n/cm^2]

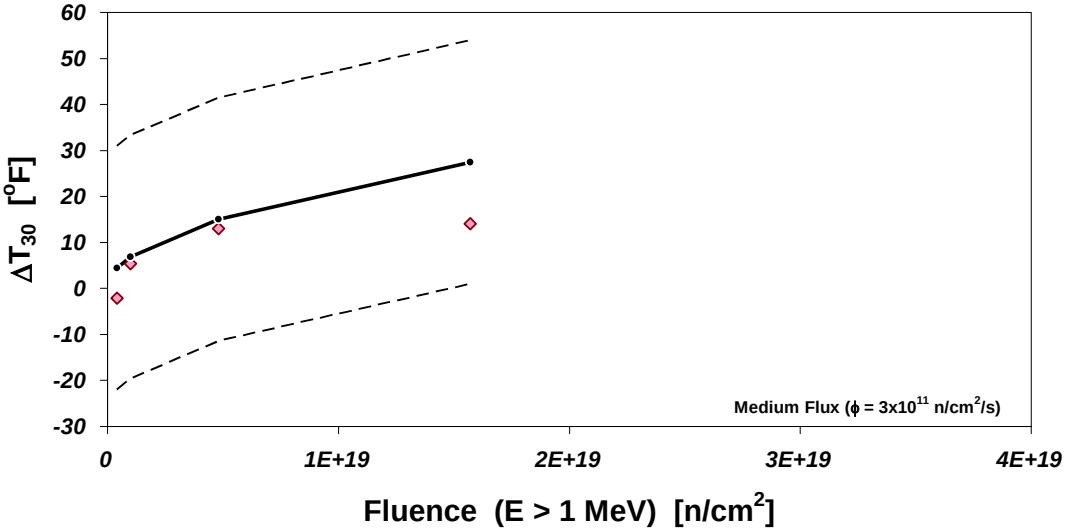
Medium Flux (ϕ = 3x10^11 n/cm^2/s)
ΔT30 [°F]
60
50
40
30
20
10
0
-10
-20
-30
0
1E+19
2E+19
3E+19
4E+19
Fluence (E > 1 MeV) [n/cm^2]

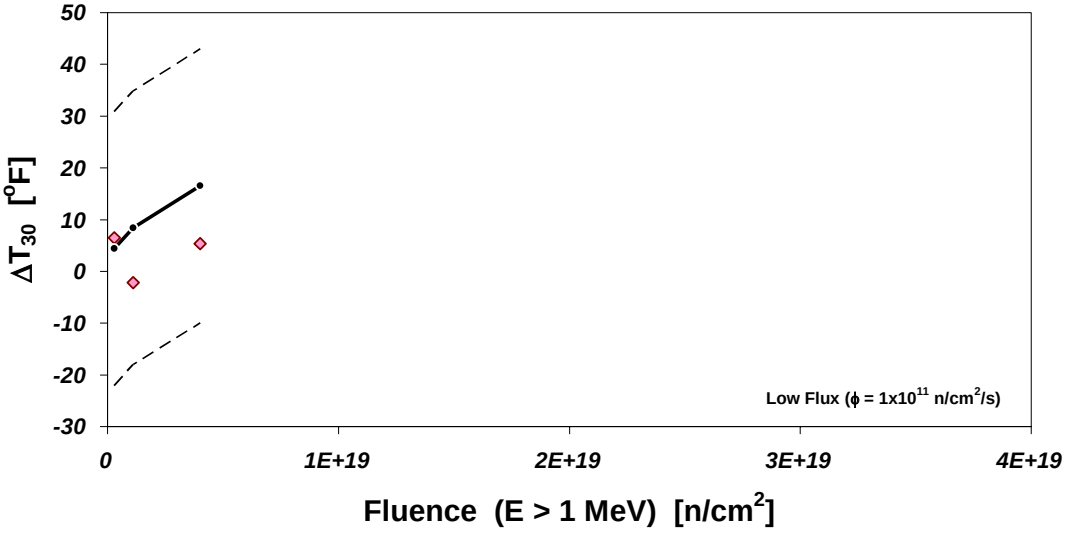
Low Flux (ϕ = 1x10^11 n/cm^2/s)
ΔT30 [°F]
50
40
30
20
10
0
-10
-20
-30
0
1E+19
2E+19
3E+19
4E+19
Fluence (E > 1 MeV) [n/cm^2]

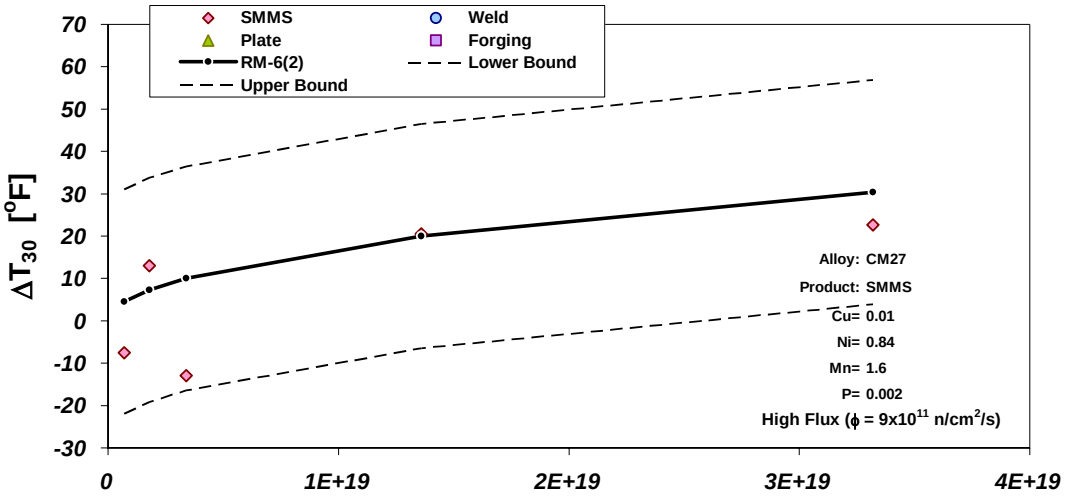
SMMS
Weld
Plate
Forging
RM-6(2)
Lower Bound
Upper Bound
Alloy: CM27
Product: SMMS
Cu= 0.01
Ni= 0.84
Mn= 1.6
P= 0.002
High Flux (ϕ = 9x10^11 n/cm^2/s)
ΔT30 [°F]
70
60
50
40
30
20
10
0
-10
-20
-30
0
1E+19
2E+19
3E+19
4E+19
Fluence (E > 1 MeV) [n/cm^2]

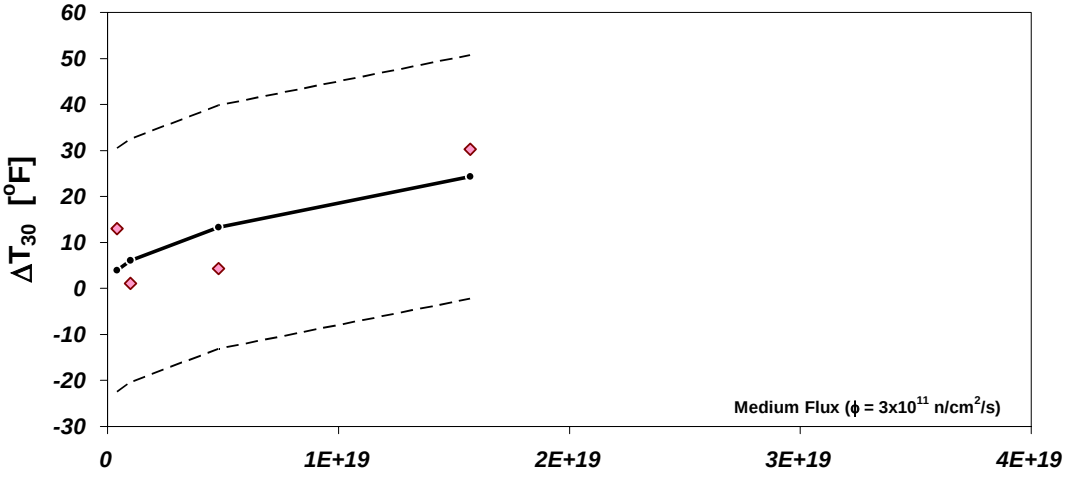
Medium Flux (ϕ = 3x10^11 n/cm^2/s)
ΔT30 [°F]
60
50
40
30
20
10
0
-10
-20
-30
0
1E+19
2E+19
3E+19
4E+19
Fluence (E > 1 MeV) [n/cm^2]

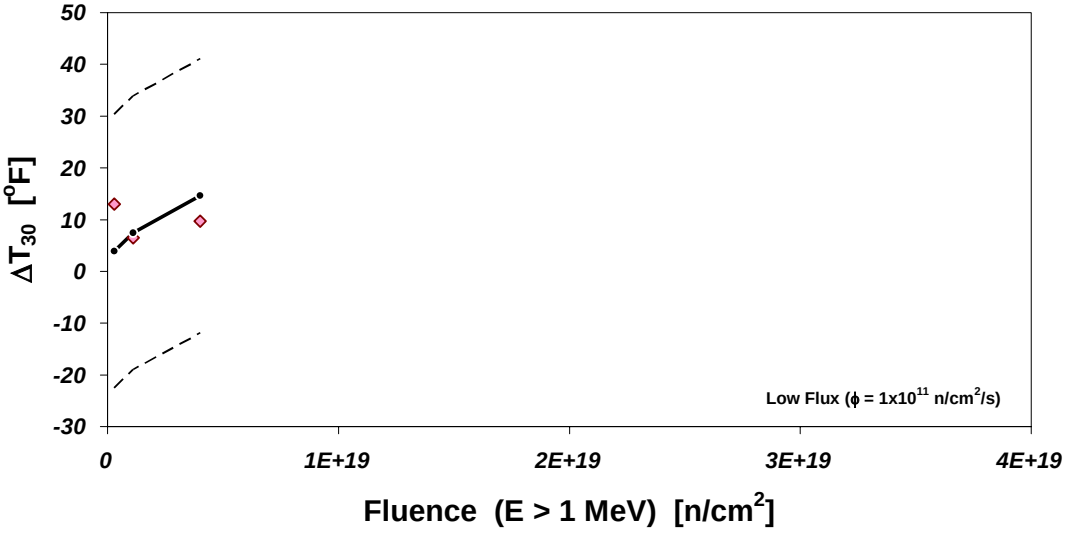
Low Flux (ϕ = 1x10^11 n/cm^2/s)
ΔT30 [°F]
50
40
30
20
10
0
-10
-20
-30
0
1E+19
2E+19
3E+19
4E+19
Fluence (E > 1 MeV) [n/cm^2]

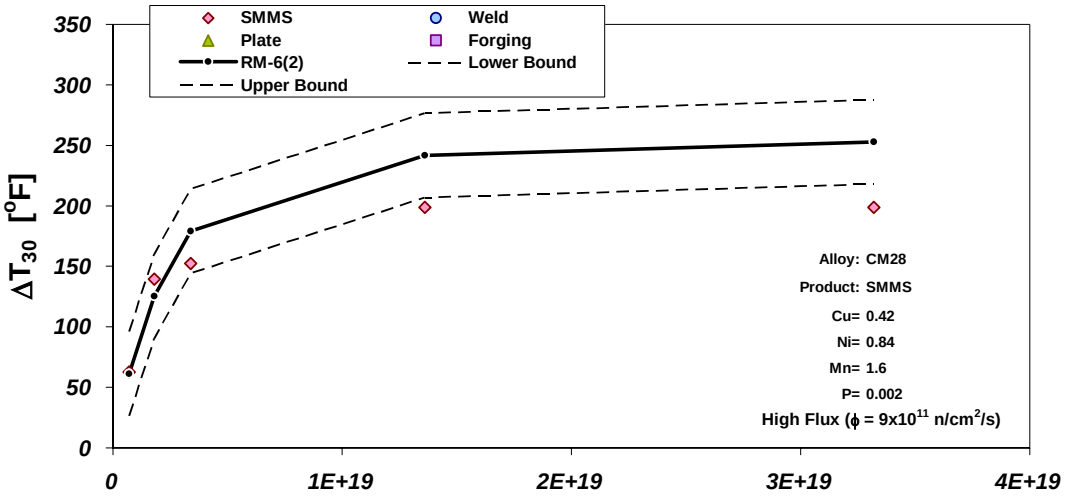
SMMS
Weld
Plate
Forging
RM-6(2)
Lower Bound
Upper Bound
ΔT30 [°F]
350
300
250
200
150
100
50
0
Alloy: CM28
Product: SMMS
Cu= 0.42
Ni= 0.84
Mn= 1.6
P= 0.002
High Flux (ϕ = 9x10^11 n/cm^2/s)
0
1E+19
2E+19
3E+19
4E+19
Fluence (E > 1 MeV) [n/cm^2]

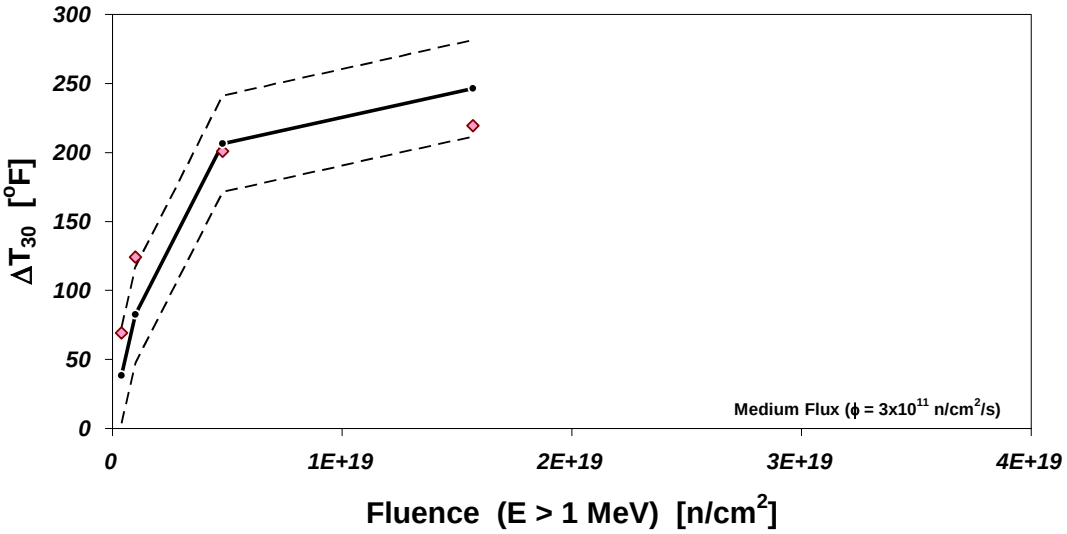
ΔT30 [°F]
300
250
200
150
100
50
0
Medium Flux (ϕ = 3x10^11 n/cm^2/s)
0
1E+19
2E+19
3E+19
4E+19
Fluence (E > 1 MeV) [n/cm^2]

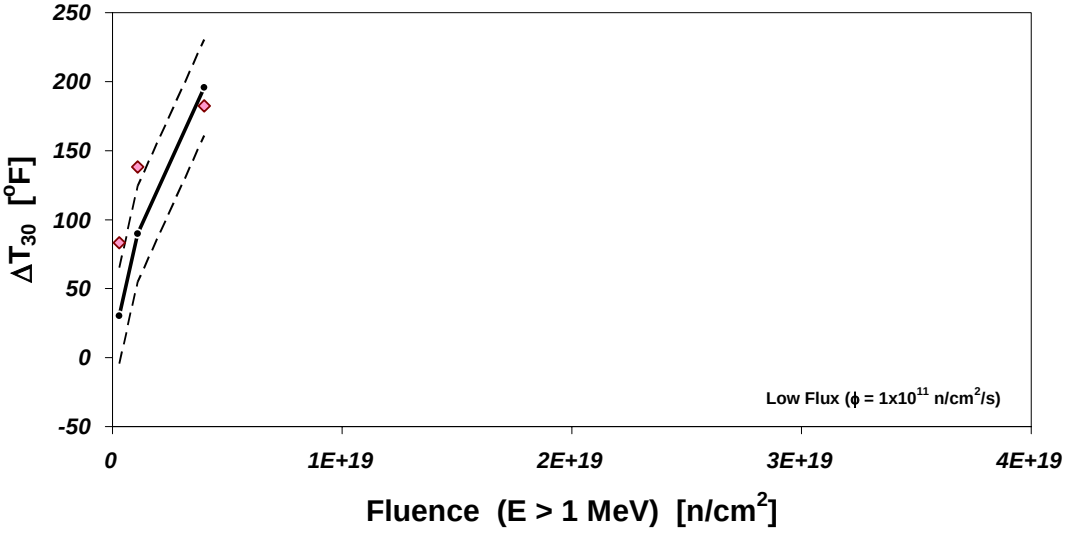
ΔT30 [°F]
250
200
150
100
50
0
-50
Low Flux (ϕ = 1x10^11 n/cm^2/s)
0
1E+19
2E+19
3E+19
4E+19
Fluence (E > 1 MeV) [n/cm^2]

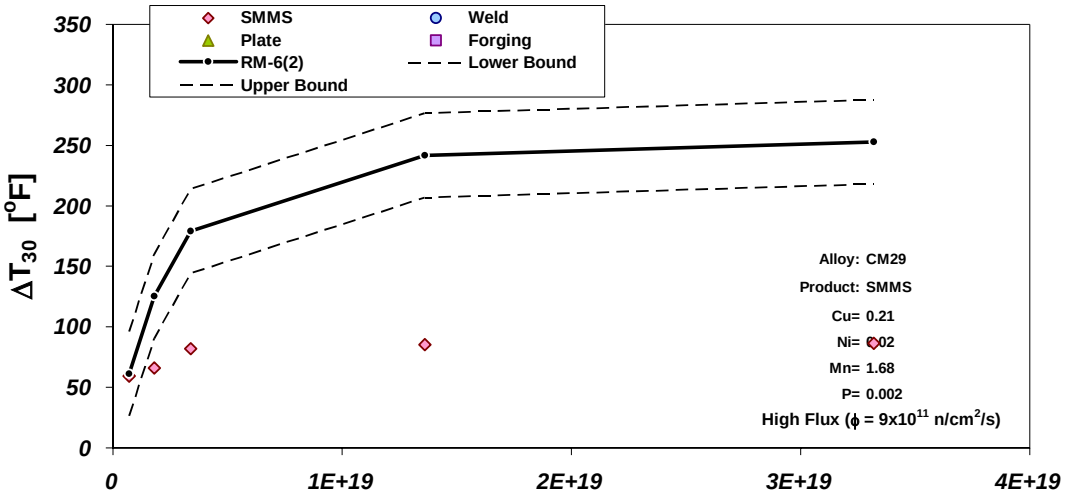
SMMS
Weld
Plate
Forging
RM-6(2)
Lower Bound
Upper Bound
Alloy: CM29
Product: SMMS
Cu= 0.21
Ni= .02
Mn= 1.68
P= 0.002
High Flux (ϕ = 9x10^11 n/cm^2/s)
ΔT30 [°F]
350
300
250
200
150
100
50
0
0
1E+19
2E+19
3E+19
4E+19
Fluence (E > 1 MeV) [n/cm^2]

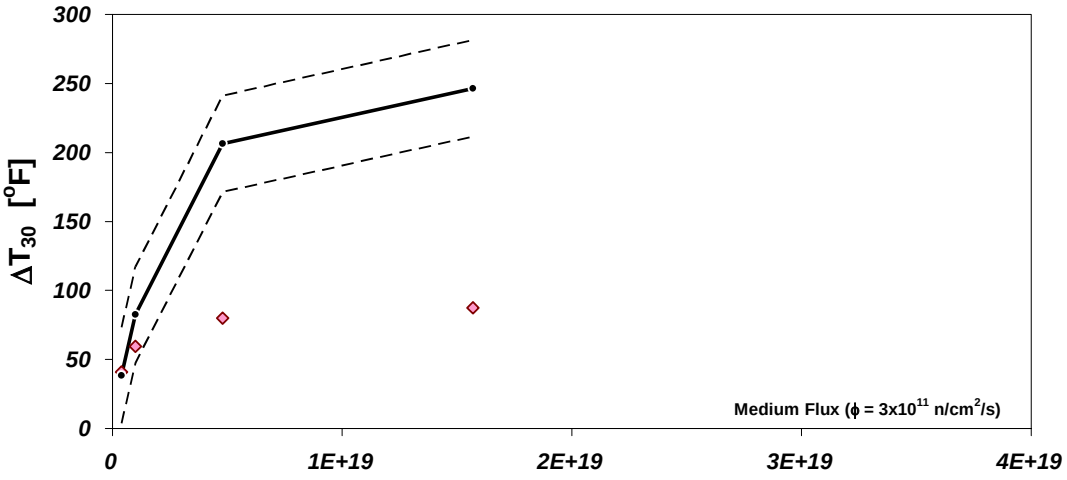
Medium Flux (ϕ = 3x10^11 n/cm^2/s)
ΔT30 [°F]
300
250
200
150
100
50
0
0
1E+19
2E+19
3E+19
4E+19
Fluence (E > 1 MeV) [n/cm^2]

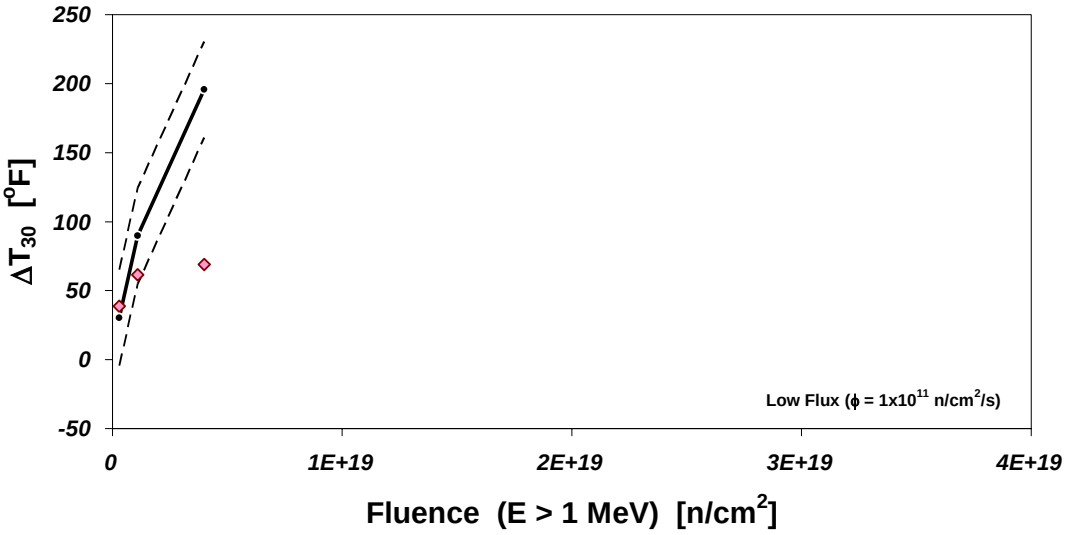
Low Flux (ϕ = 1x10^11 n/cm^2/s)
ΔT30 [°F]
250
200
150
100
50
0
-50
0
1E+19
2E+19
3E+19
4E+19
Fluence (E > 1 MeV) [n/cm^2]

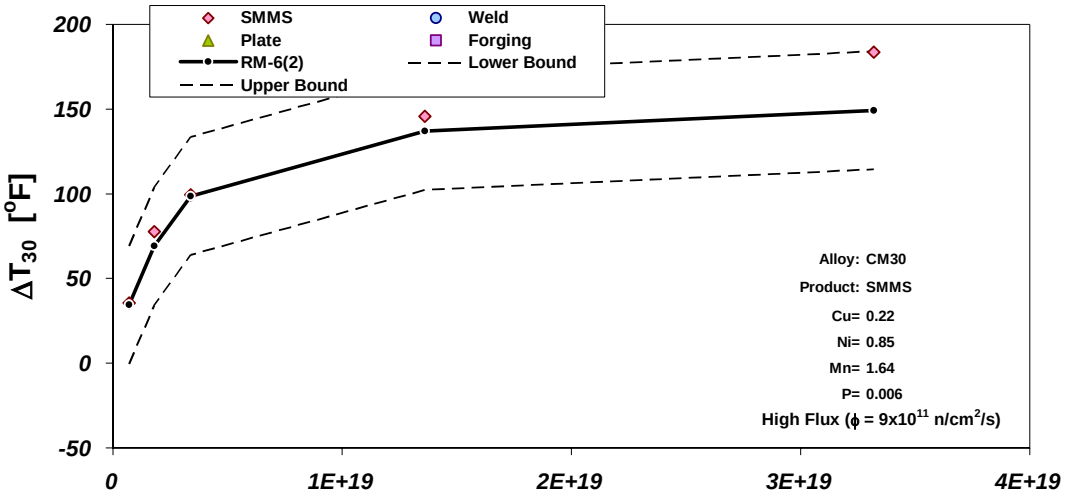
SMMS
Weld
Plate
Forging
RM-6(2)
Lower Bound
Upper Bound
200
150
100
50
0
-50
ΔT30 [°F]
Alloy: CM30
Product: SMMS
Cu= 0.22
Ni= 0.85
Mn= 1.64
P= 0.006
High Flux (ϕ = 9x10^11 n/cm^2/s)
0
1E+19
2E+19
3E+19
4E+19
Fluence (E > 1 MeV) [n/cm^2]

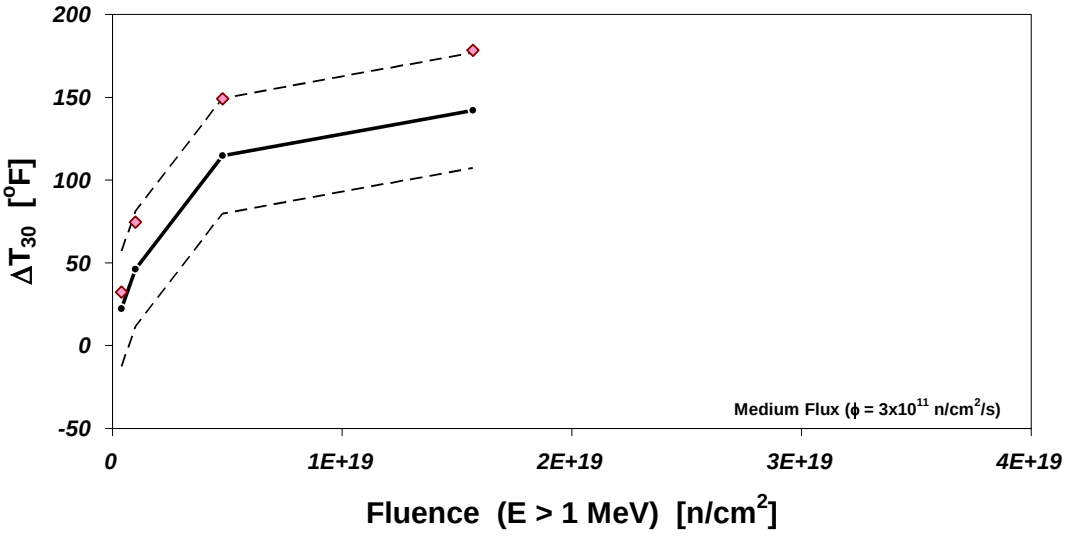
200
150
100
50
0
-50
ΔT30 [°F]
Medium Flux (ϕ = 3x10^11 n/cm^2/s)
0
1E+19
2E+19
3E+19
4E+19
Fluence (E > 1 MeV) [n/cm^2]

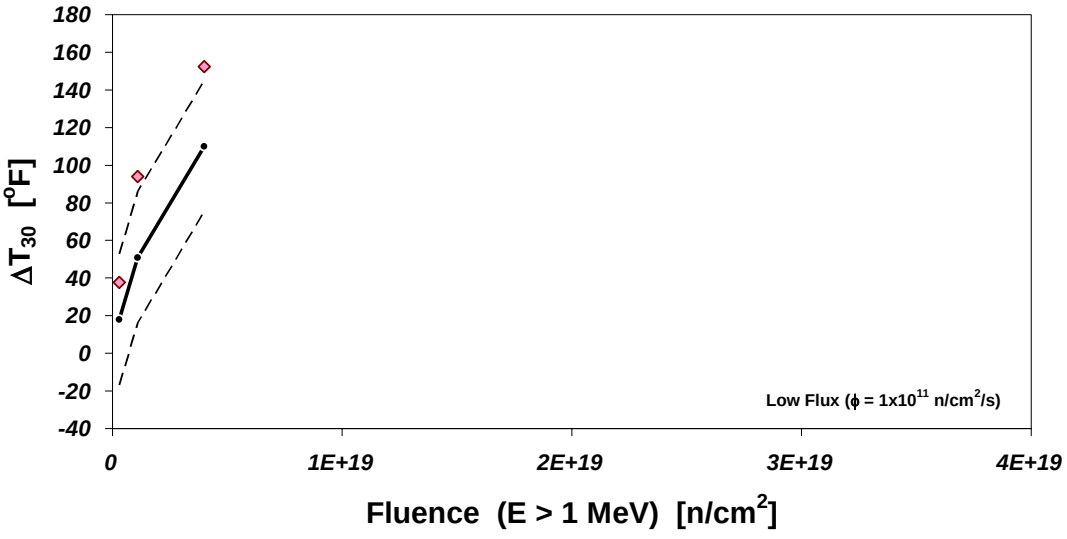
180
160
140
120
100
80
60
40
20
0
-20
-40
ΔT30 [°F]
Low Flux (ϕ = 1x10^11 n/cm^2/s)
0
1E+19
2E+19
3E+19
4E+19
Fluence (E > 1 MeV) [n/cm^2]

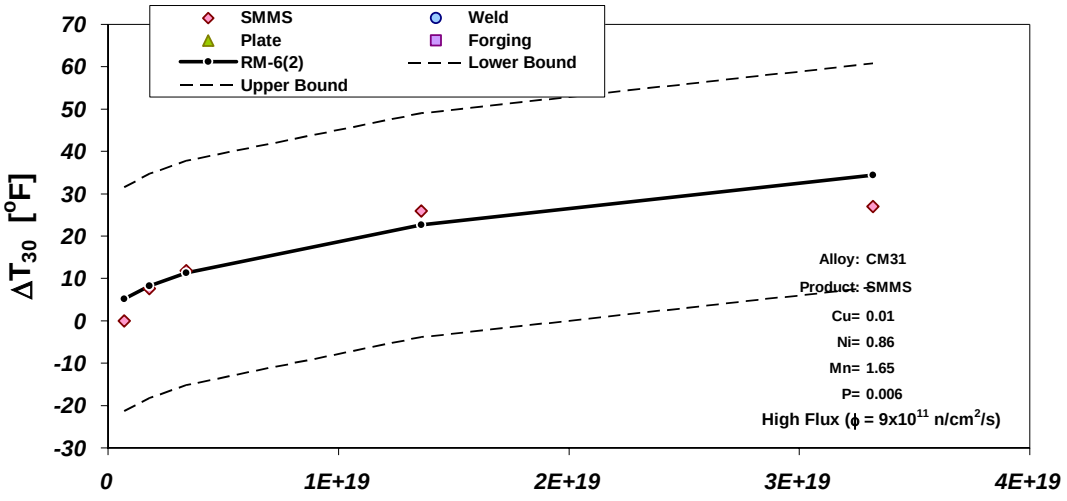
SMMS
Weld
Plate
Forging
RM-6(2)
Lower Bound
Upper Bound
Alloy: CM31
Product: SMMS
Cu= 0.01
Ni= 0.86
Mn= 1.65
P= 0.006
High Flux (ϕ = 9x10^11 n/cm^2/s)
ΔT30 [°F]
70
60
50
40
30
20
10
0
-10
-20
-30
0
1E+19
2E+19
3E+19
4E+19
Fluence (E > 1 MeV) [n/cm^2]

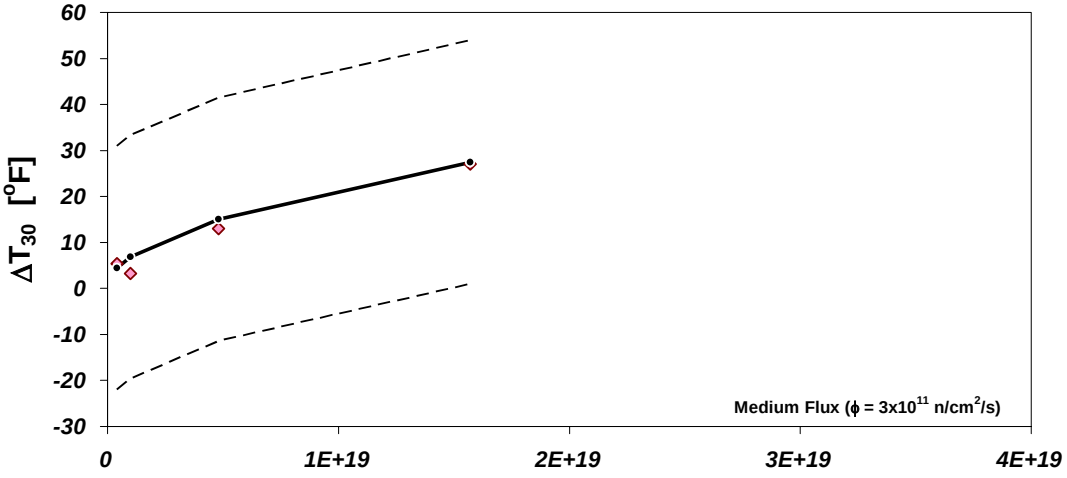
Medium Flux (ϕ = 3x10^11 n/cm^2/s)
ΔT30 [°F]
60
50
40
30
20
10
0
-10
-20
-30
0
1E+19
2E+19
3E+19
4E+19
Fluence (E > 1 MeV) [n/cm^2]

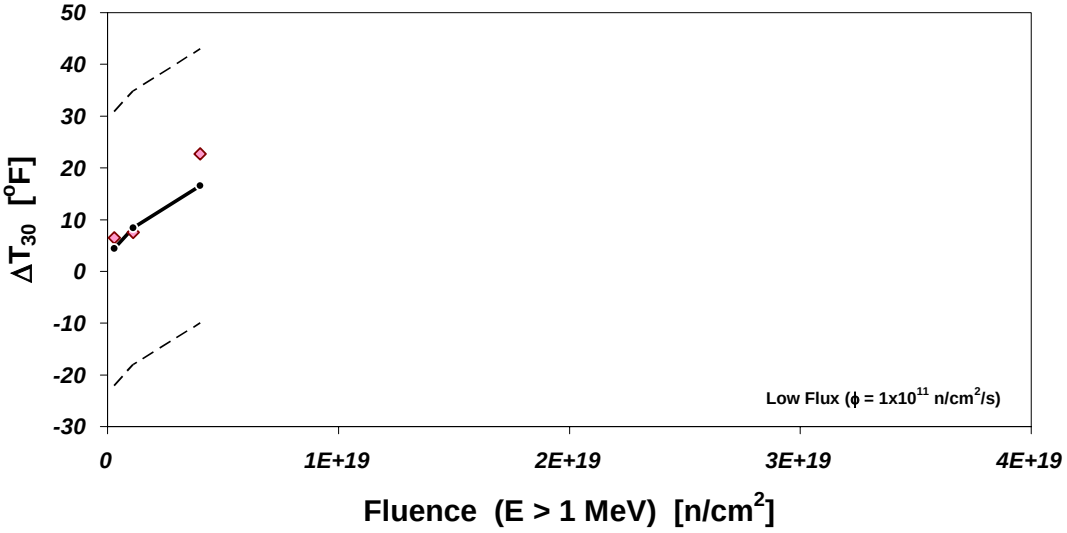
Low Flux (ϕ = 1x10^11 n/cm^2/s)
ΔT30 [°F]
50
40
30
20
10
0
-10
-20
-30
0
1E+19
2E+19
3E+19
4E+19
Fluence (E > 1 MeV) [n/cm^2]

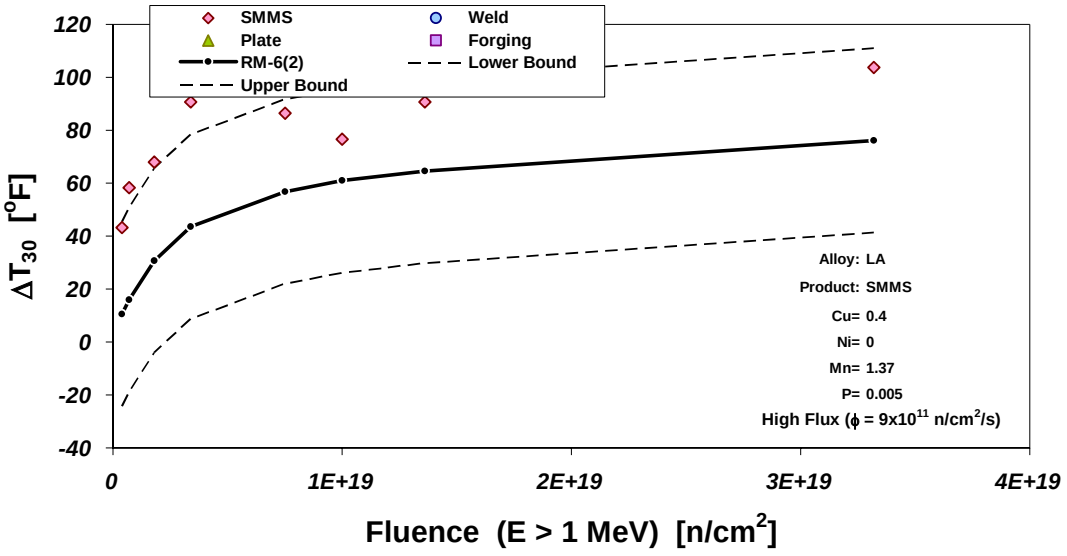
SMMS
Weld
Plate
Forging
RM-6(2)
Lower Bound
Upper Bound
Alloy: LA
Product: SMMS
Cu= 0.4
Ni= 0
Mn= 1.37
P= 0.005
High Flux (ϕ = 9x10^11 n/cm^2/s)
ΔT30 [°F]
Fluence (E > 1 MeV) [n/cm^2]

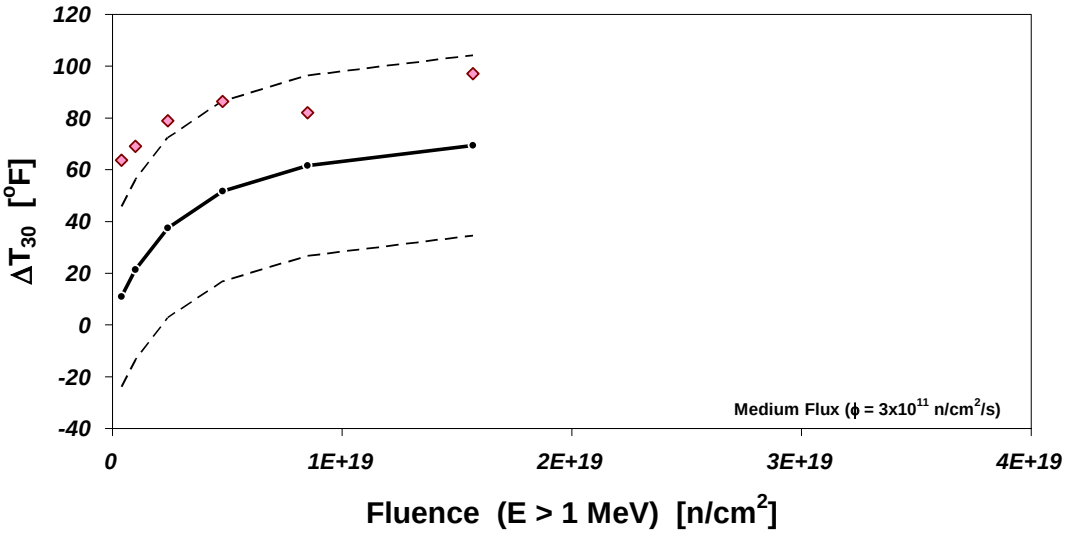
Medium Flux (ϕ = 3x10^11 n/cm^2/s)
ΔT30 [°F]
Fluence (E > 1 MeV) [n/cm^2]

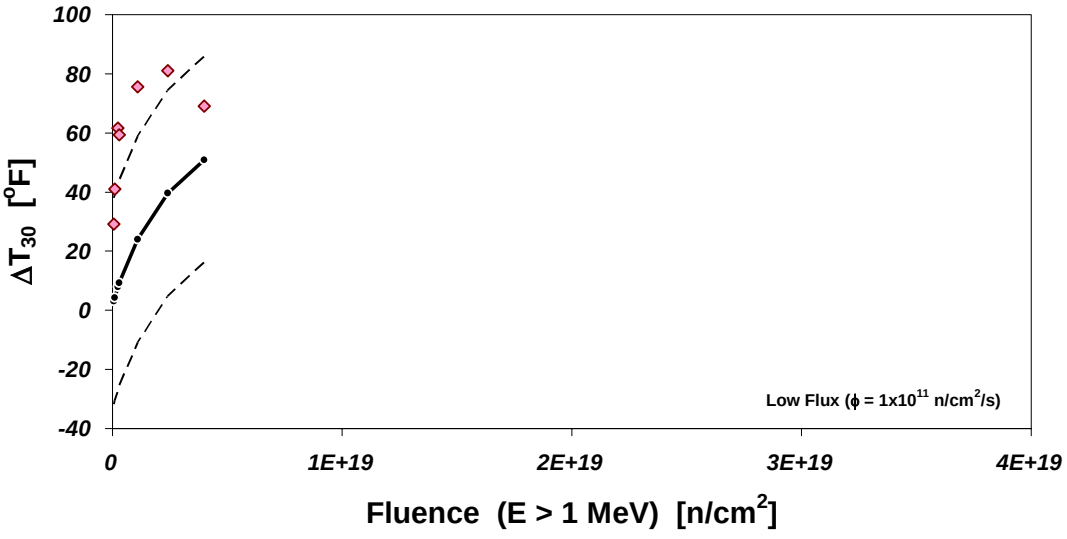
Low Flux (ϕ = 1x10^11 n/cm^2/s)
ΔT30 [°F]
Fluence (E > 1 MeV) [n/cm^2]

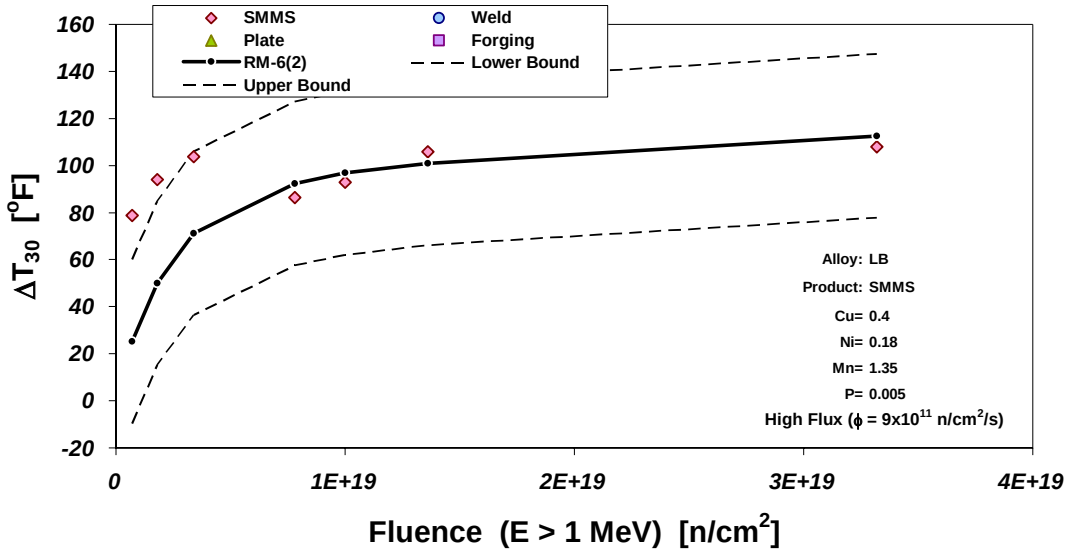
SMMS
Weld
Plate
Forging
RM-6(2)
Lower Bound
Upper Bound
ΔT30 [°F]
160
140
120
100
80
60
40
20
0
-20
0
1E+19
2E+19
3E+19
4E+19
Fluence (E > 1 MeV) [n/cm2]
Alloy: LB
Product: SMMS
Cu= 0.4
Ni= 0.18
Mn= 1.35
P= 0.005
High Flux (ϕ = 9x10^11 n/cm^2/s)

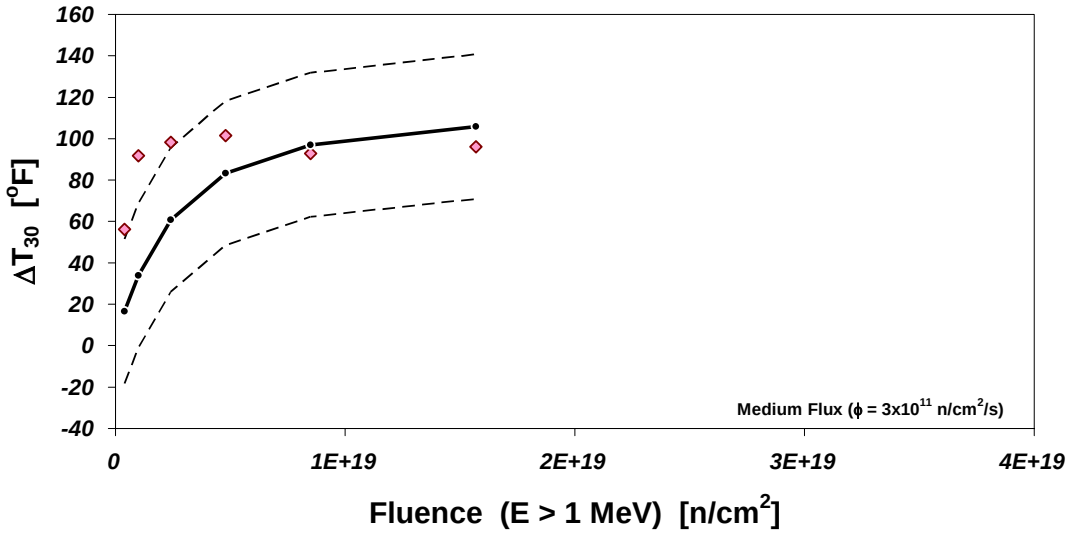
ΔT30 [°F]
160
140
120
100
80
60
40
20
0
-20
-40
0
1E+19
2E+19
3E+19
4E+19
Fluence (E > 1 MeV) [n/cm2]
Medium Flux (ϕ = 3x10^11 n/cm^2/s)

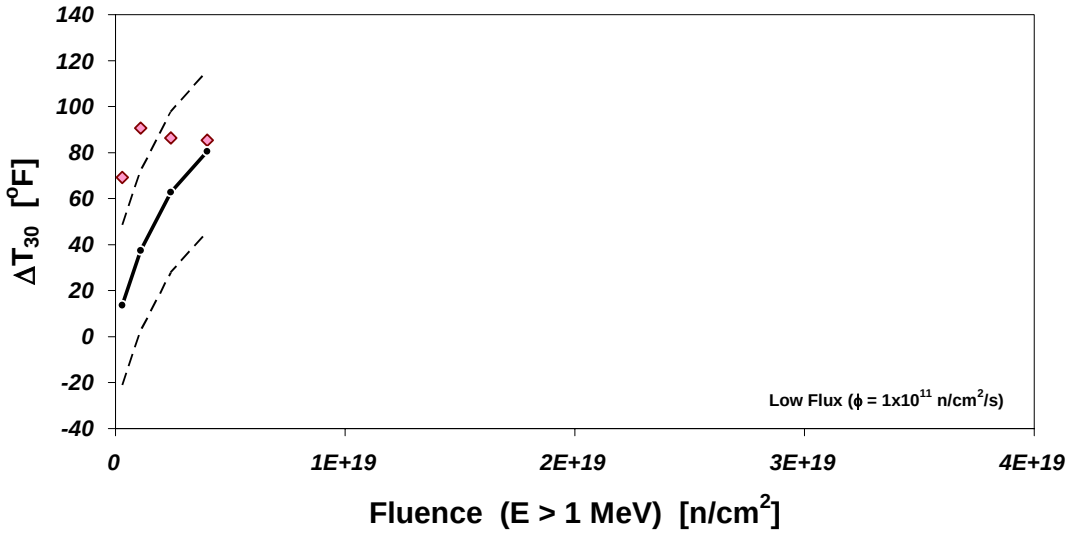
ΔT30 [°F]
140
120
100
80
60
40
20
0
-20
-40
0
1E+19
2E+19
3E+19
4E+19
Fluence (E > 1 MeV) [n/cm2]
Low Flux (ϕ = 1x10^11 n/cm^2/s)

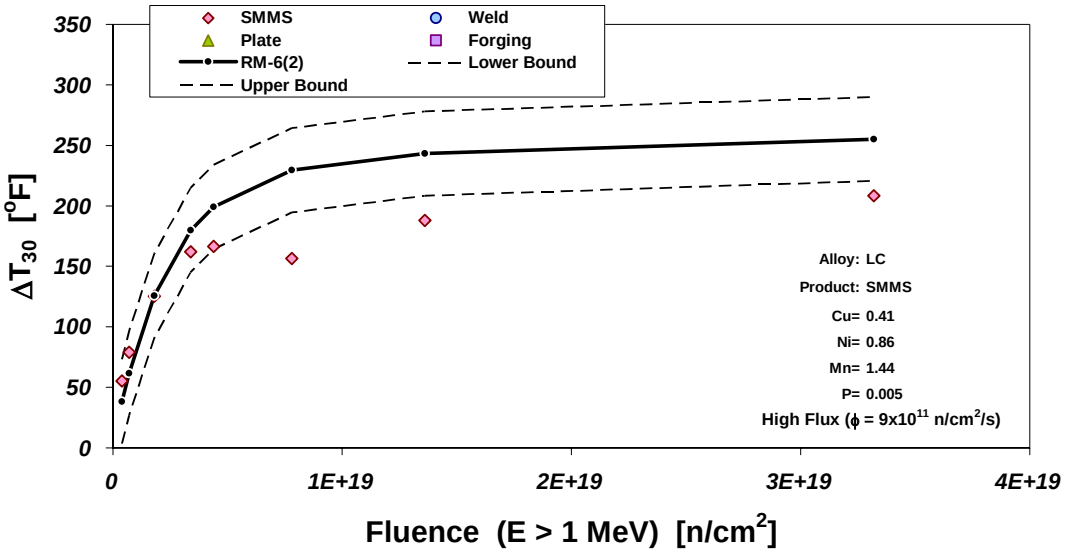
SMMS
Weld
Plate
Forging
RM-6(2)
Lower Bound
Upper Bound
Alloy: LC
Product: SMMS
Cu= 0.41
Ni= 0.86
Mn= 1.44
P= 0.005
High Flux (ϕ = 9x10^11 n/cm^2/s)
ΔT30 [°F]
Fluence (E > 1 MeV) [n/cm^2]
0
50
100
150
200
250
300
350
0
1E+19
2E+19
3E+19
4E+19

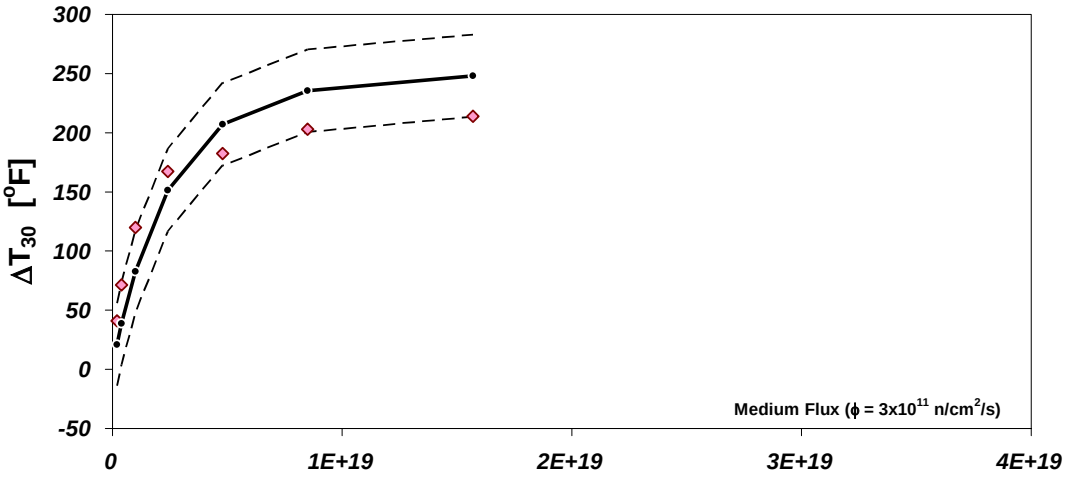
Medium Flux (ϕ = 3x10^11 n/cm^2/s)
ΔT30 [°F]
Fluence (E > 1 MeV) [n/cm^2]
-50
0
50
100
150
200
250
300
0
1E+19
2E+19
3E+19
4E+19

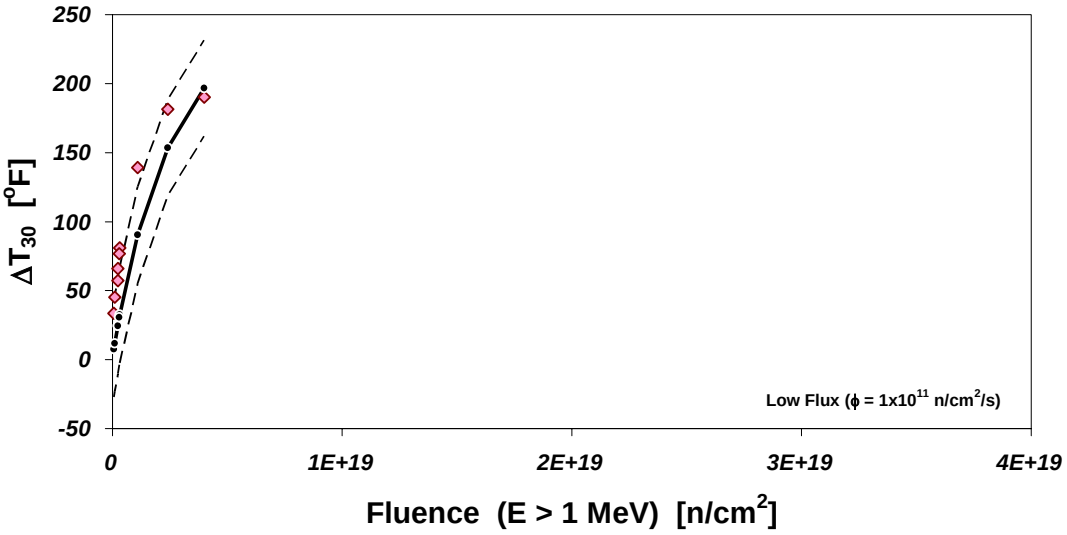
Low Flux (ϕ = 1x10^11 n/cm^2/s)
ΔT30 [°F]
Fluence (E > 1 MeV) [n/cm^2]
-50
0
50
100
150
200
250
0
1E+19
2E+19
3E+19
4E+19

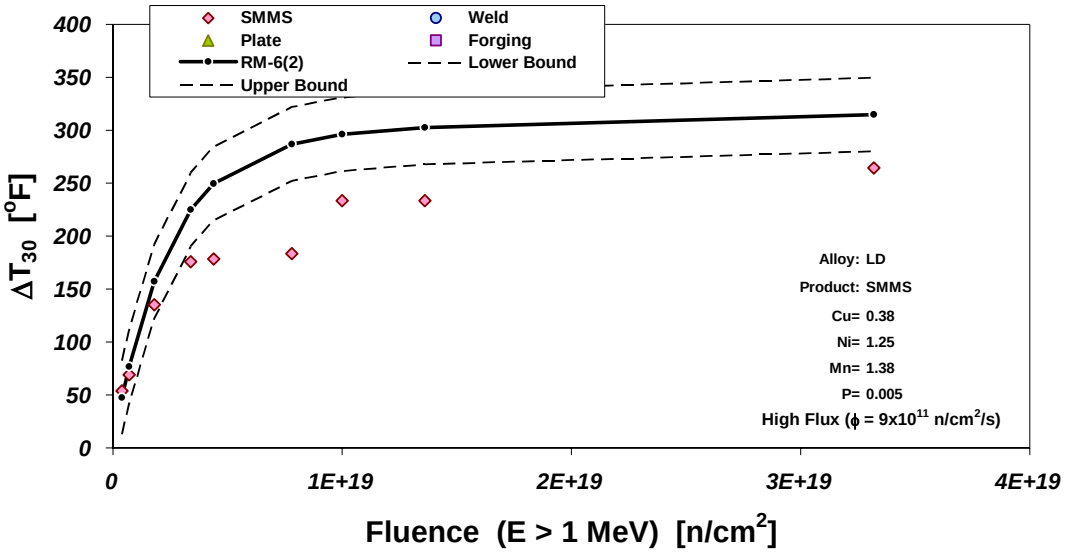
SMMS
Weld
Plate
Forging
RM-6(2)
Lower Bound
Upper Bound
Alloy: LD
Product: SMMS
Cu= 0.38
Ni= 1.25
Mn= 1.38
P= 0.005
High Flux (ϕ = 9x10^11 n/cm^2/s)
ΔT30 [°F]
Fluence (E > 1 MeV) [n/cm^2]
400
350
300
250
200
150
100
50
0
0
1E+19
2E+19
3E+19
4E+19

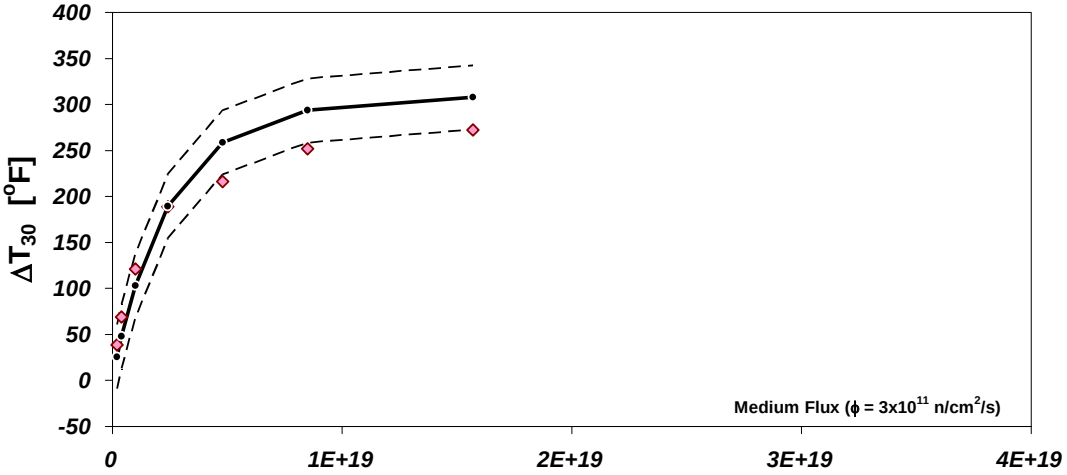
Medium Flux (ϕ = 3x10^11 n/cm^2/s)
ΔT30 [°F]
Fluence (E > 1 MeV) [n/cm^2]
400
350
300
250
200
150
100
50
0
-50
0
1E+19
2E+19
3E+19
4E+19

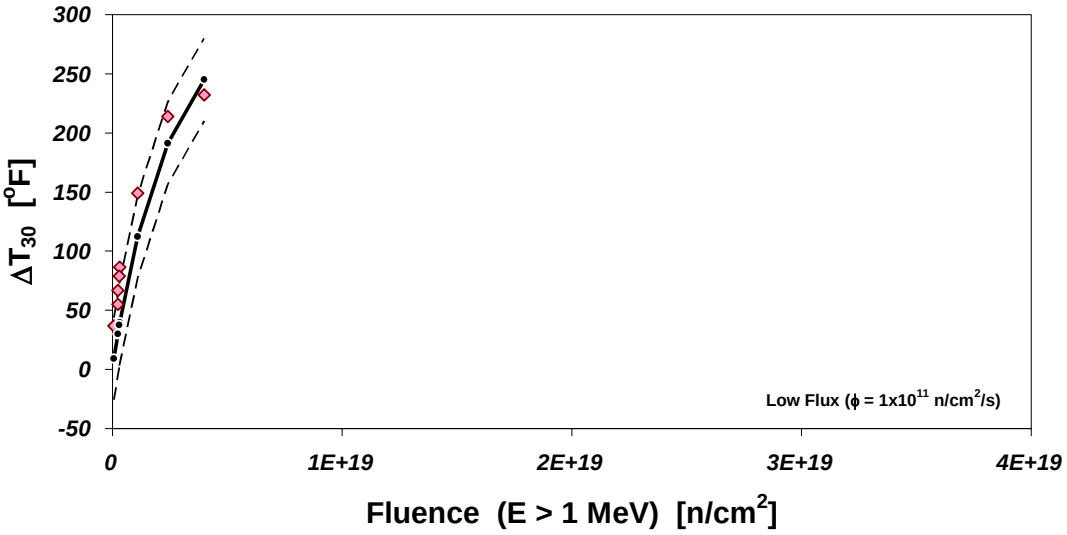
Low Flux (ϕ = 1x10^11 n/cm^2/s)
ΔT30 [°F]
Fluence (E > 1 MeV) [n/cm^2]
300
250
200
150
100
50
0
-50
0
1E+19
2E+19
3E+19
4E+19

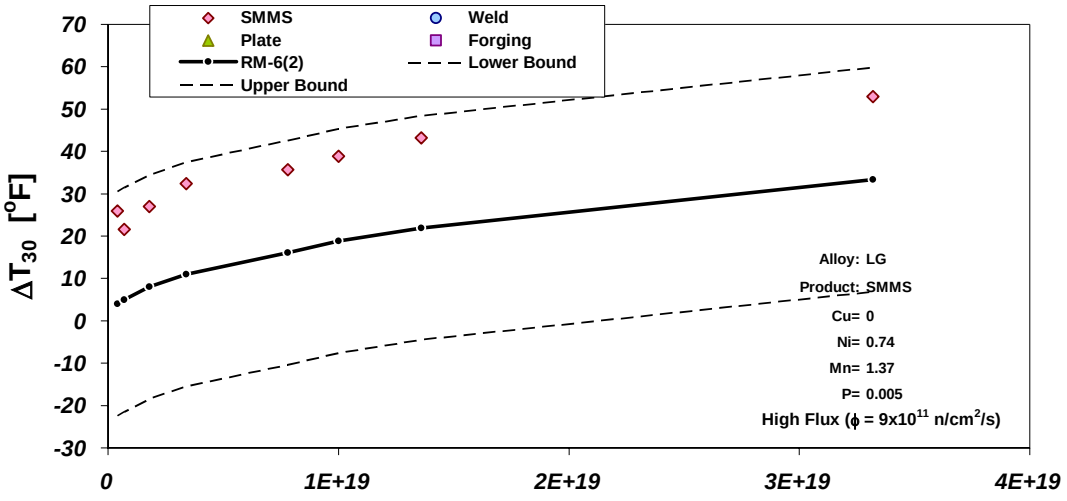
SMMS
Weld
Plate
Forging
RM-6(2)
Lower Bound
Upper Bound
Alloy: LG
Product: SMMS
Cu= 0
Ni= 0.74
Mn= 1.37
P= 0.005
High Flux (ϕ = 9x10^11 n/cm^2/s)
ΔT30 [°F]
70
60
50
40
30
20
10
0
-10
-20
-30
0
1E+19
2E+19
3E+19
4E+19
Fluence (E > 1 MeV) [n/cm^2]

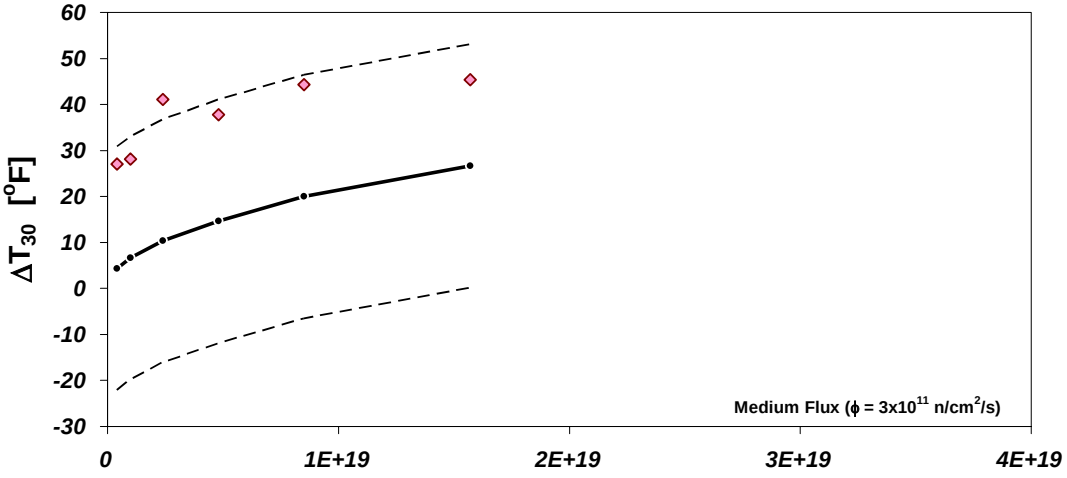
Medium Flux (ϕ = 3x10^11 n/cm^2/s)
ΔT30 [°F]
60
50
40
30
20
10
0
-10
-20
-30
0
1E+19
2E+19
3E+19
4E+19
Fluence (E > 1 MeV) [n/cm^2]

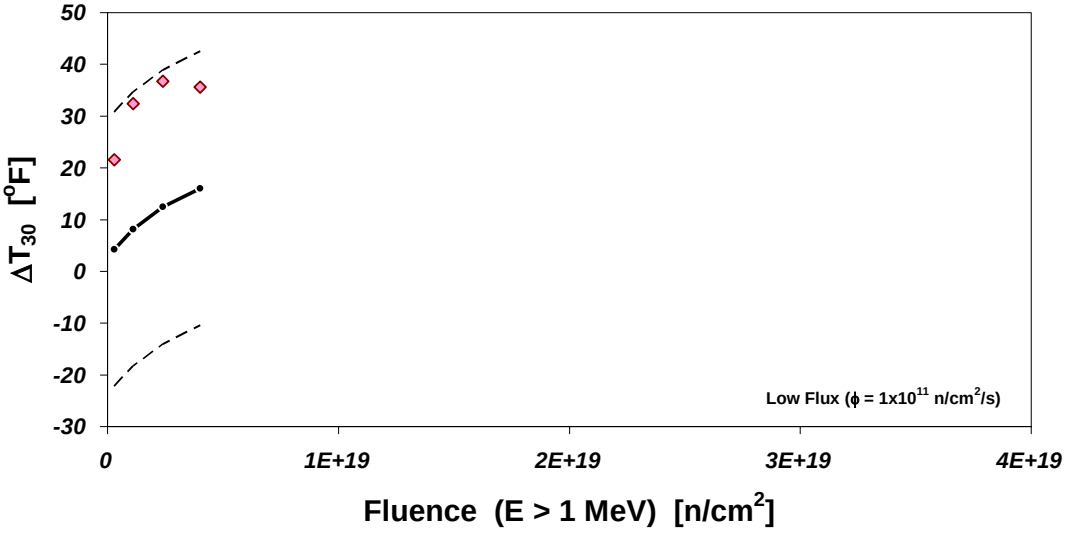
Low Flux (ϕ = 1x10^11 n/cm^2/s)
ΔT30 [°F]
50
40
30
20
10
0
-10
-20
-30
0
1E+19
2E+19
3E+19
4E+19
Fluence (E > 1 MeV) [n/cm^2]

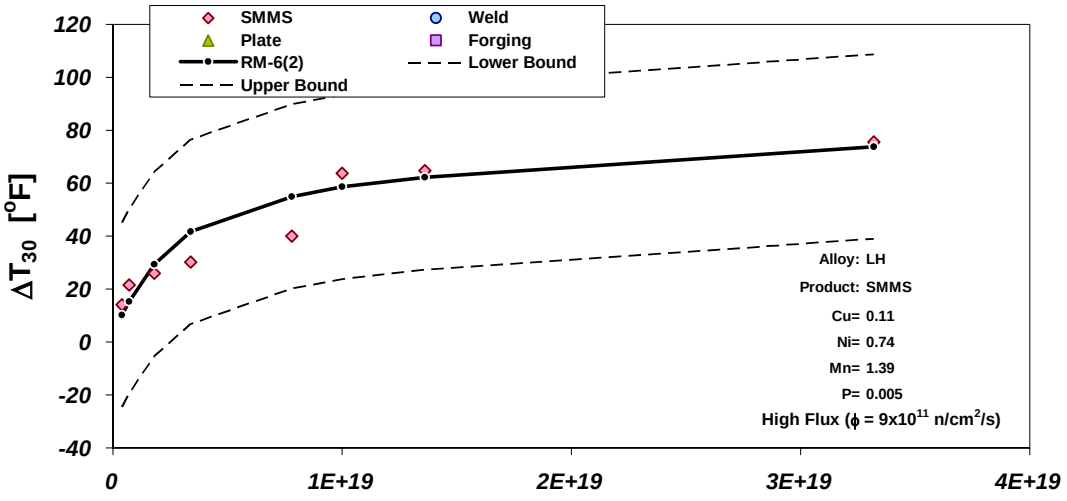
SMMS
Weld
Plate
Forging
RM-6(2)
Lower Bound
Upper Bound
Alloy: LH
Product: SMMS
Cu= 0.11
Ni= 0.74
Mn= 1.39
P= 0.005
High Flux (ϕ = 9x10^11 n/cm^2/s)
ΔT30 [°F]
Fluence (E > 1 MeV) [n/cm^2]
120
100
80
60
40
20
0
-20
-40
0
1E+19
2E+19
3E+19
4E+19

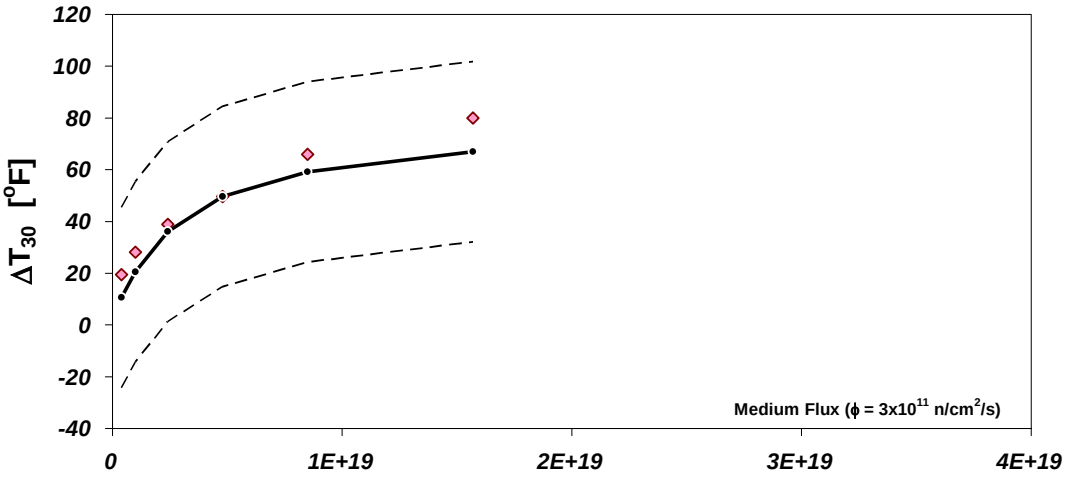
Medium Flux (ϕ = 3x10^11 n/cm^2/s)
ΔT30 [°F]
Fluence (E > 1 MeV) [n/cm^2]
120
100
80
60
40
20
0
-20
-40
0
1E+19
2E+19
3E+19
4E+19

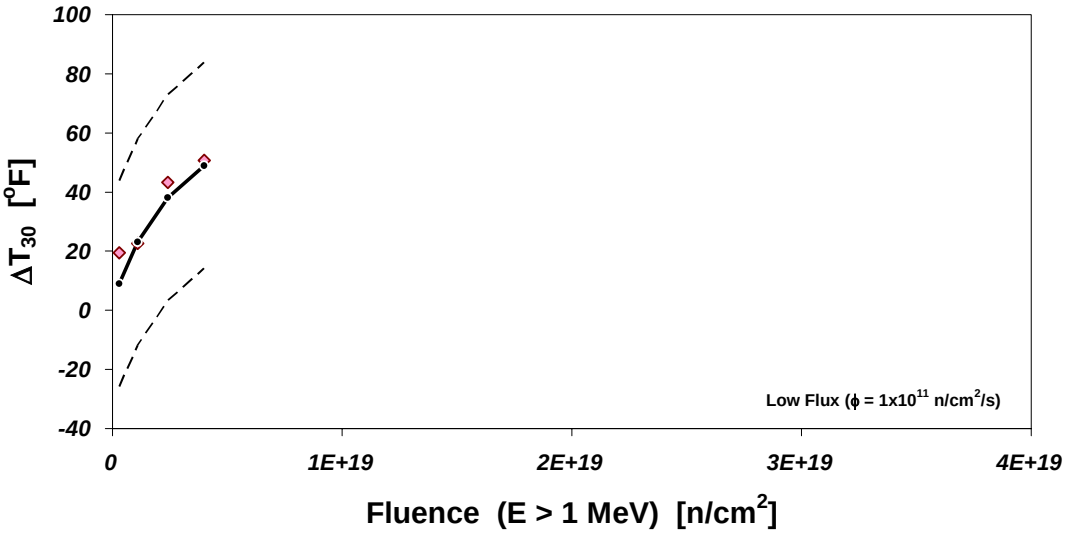
Low Flux (ϕ = 1x10^11 n/cm^2/s)
ΔT30 [°F]
Fluence (E > 1 MeV) [n/cm^2]
100
80
60
40
20
0
-20
-40
0
1E+19
2E+19
3E+19
4E+19

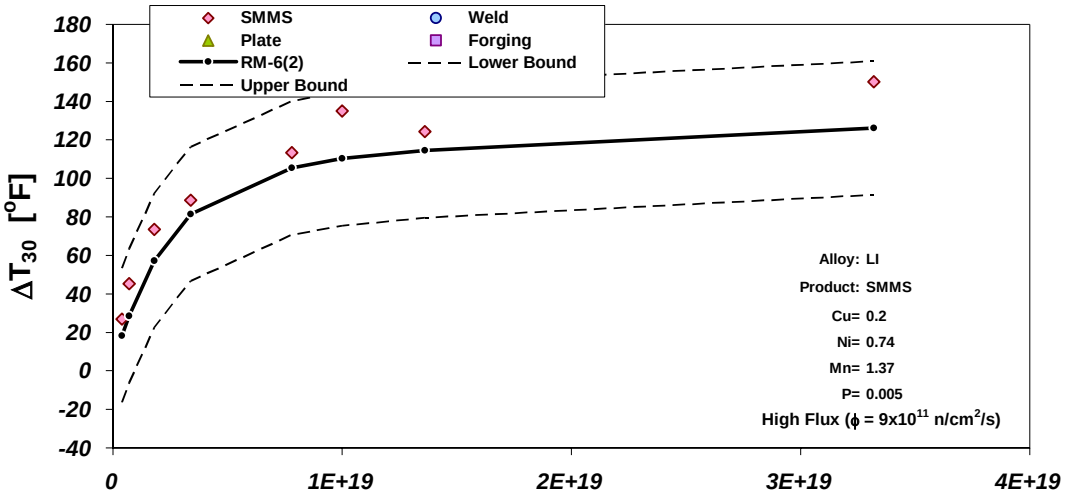
SMMS
Weld
Plate
Forging
RM-6(2)
Lower Bound
Upper Bound
Alloy: LI
Product: SMMS
Cu= 0.2
Ni= 0.74
Mn= 1.37
P= 0.005
High Flux (ϕ = 9x10^11 n/cm^2/s)
ΔT30 [°F]
180
160
140
120
100
80
60
40
20
0
-20
-40
0
1E+19
2E+19
3E+19
4E+19
Fluence (E > 1 MeV) [n/cm^2]

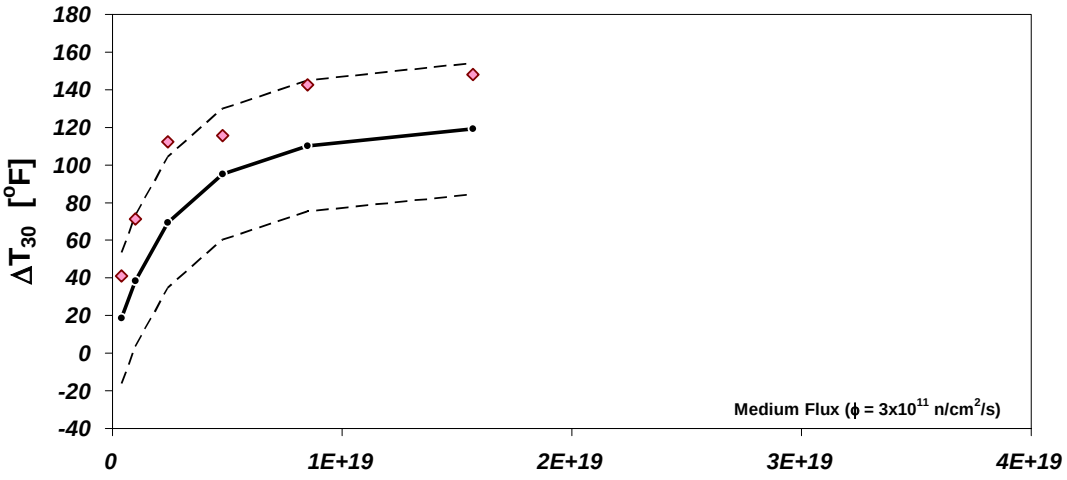
Medium Flux (ϕ = 3x10^11 n/cm^2/s)
ΔT30 [°F]
180
160
140
120
100
80
60
40
20
0
-20
-40
0
1E+19
2E+19
3E+19
4E+19
Fluence (E > 1 MeV) [n/cm^2]

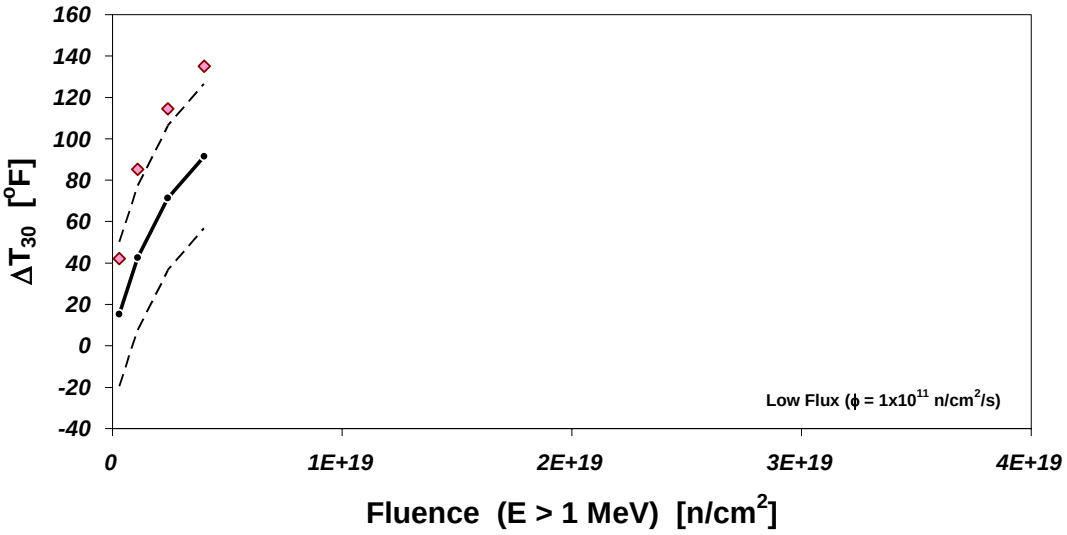
Low Flux (ϕ = 1x10^11 n/cm^2/s)
ΔT30 [°F]
160
140
120
100
80
60
40
20
0
-20
-40
0
1E+19
2E+19
3E+19
4E+19
Fluence (E > 1 MeV) [n/cm^2]

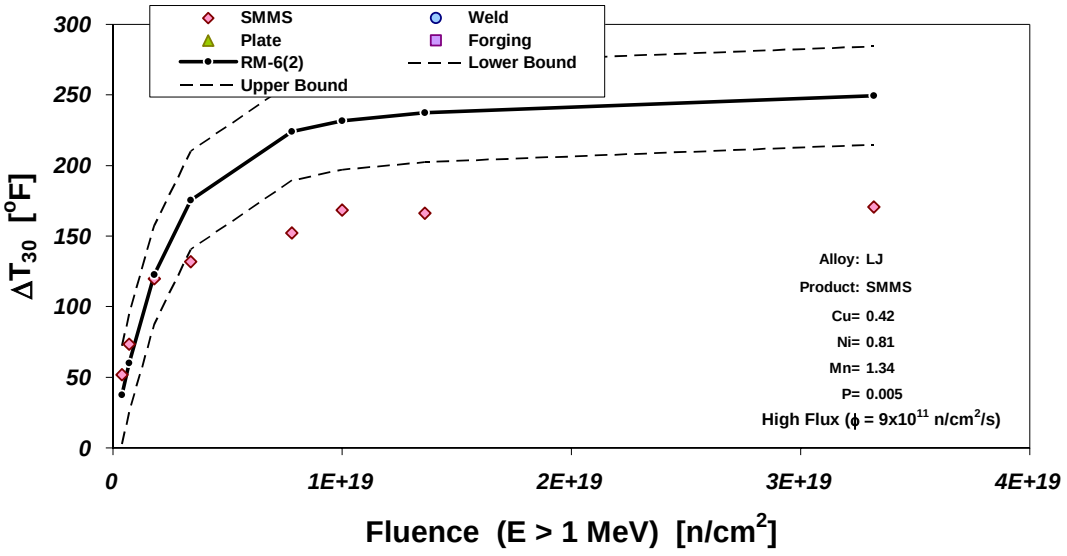
SMMS
Weld
Plate
Forging
RM-6(2)
Lower Bound
Upper Bound
Alloy: LJ
Product: SMMS
Cu= 0.42
Ni= 0.81
Mn= 1.34
P= 0.005
High Flux (ϕ = 9x10^11 n/cm^2/s)
ΔT30 [°F]
300
250
200
150
100
50
0
0
1E+19
2E+19
3E+19
4E+19
Fluence (E > 1 MeV) [n/cm^2]

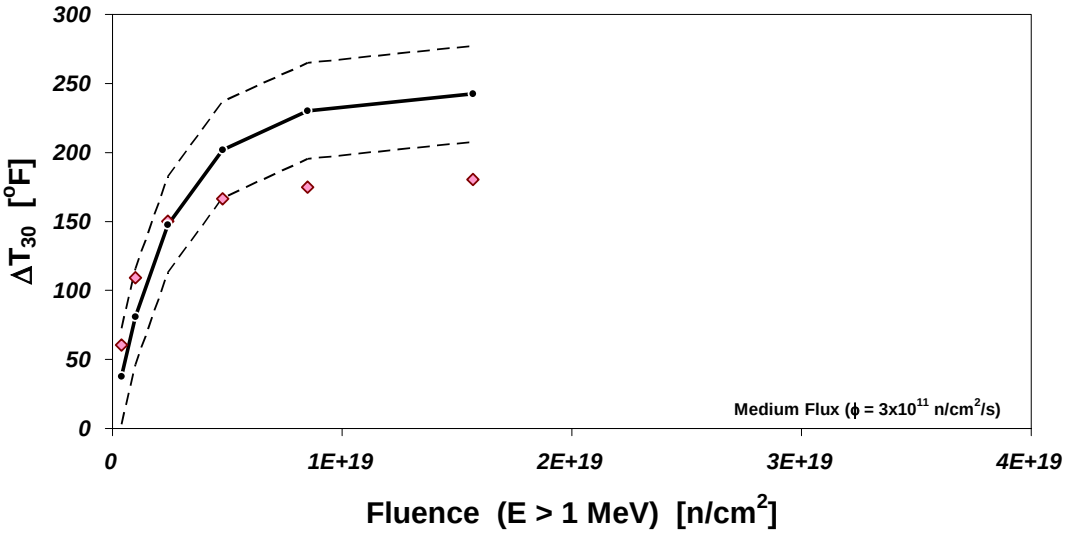
Medium Flux (ϕ = 3x10^11 n/cm^2/s)
ΔT30 [°F]
300
250
200
150
100
50
0
0
1E+19
2E+19
3E+19
4E+19
Fluence (E > 1 MeV) [n/cm^2]

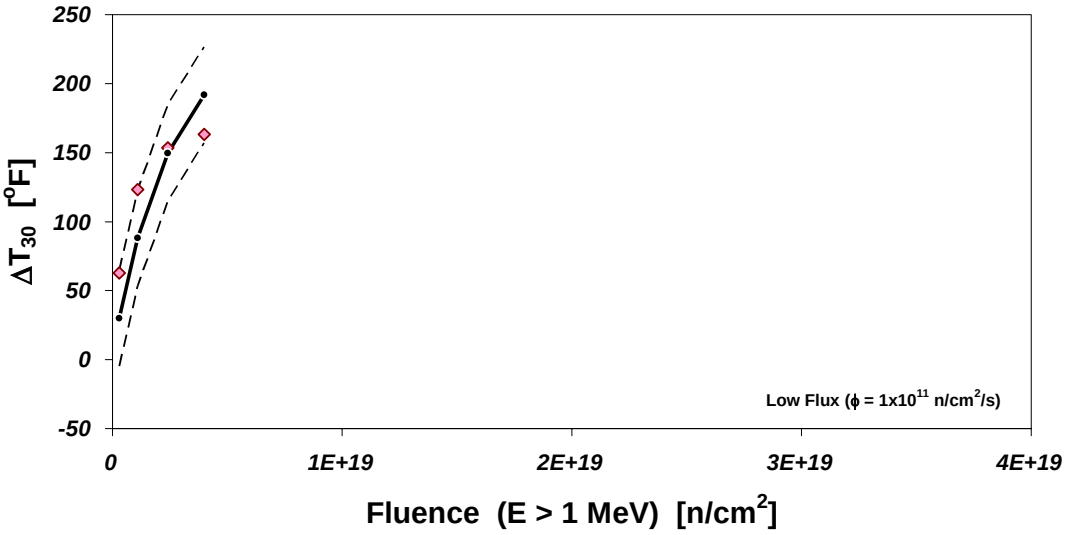
Low Flux (ϕ = 1x10^11 n/cm^2/s)
ΔT30 [°F]
250
200
150
100
50
0
-50
0
1E+19
2E+19
3E+19
4E+19
Fluence (E > 1 MeV) [n/cm^2]

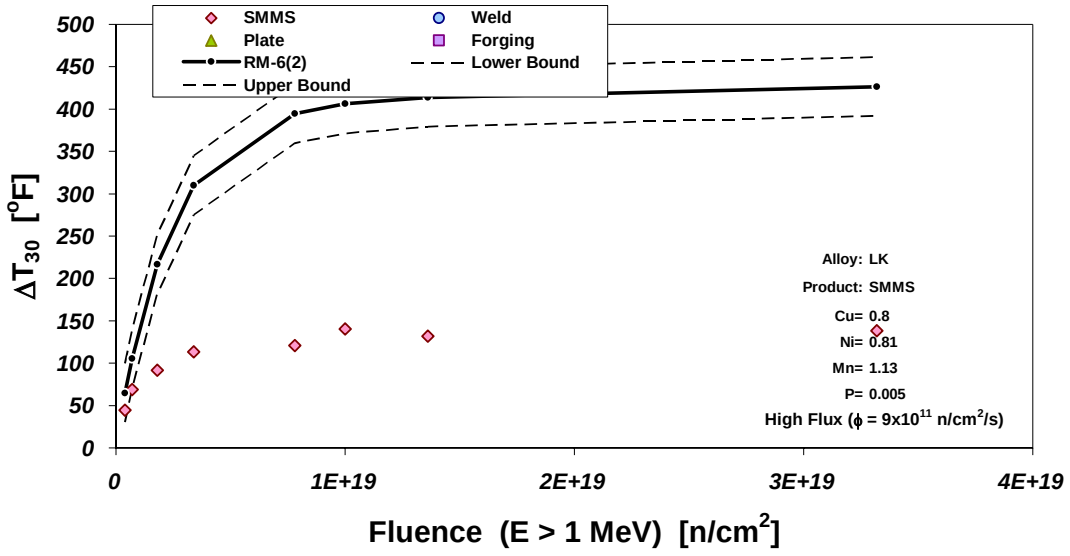
SMMS
Weld
Plate
Forging
RM-6(2)
Lower Bound
Upper Bound
Alloy: LK
Product: SMMS
Cu= 0.8
Ni= 0.81
Mn= 1.13
P= 0.005
High Flux (ϕ = 9x10^11 n/cm^2/s)
ΔT30 [°F]
Fluence (E > 1 MeV) [n/cm^2]
0
50
100
150
200
250
300
350
400
450
500
0
1E+19
2E+19
3E+19
4E+19

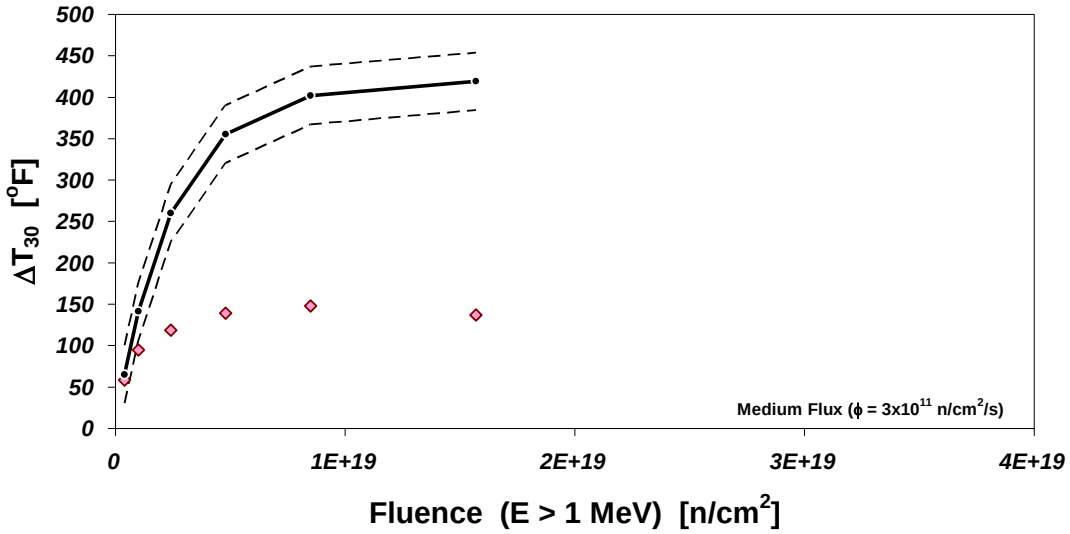
Medium Flux (ϕ = 3x10^11 n/cm^2/s)
ΔT30 [°F]
Fluence (E > 1 MeV) [n/cm^2]
0
50
100
150
200
250
300
350
400
450
500
0
1E+19
2E+19
3E+19
4E+19

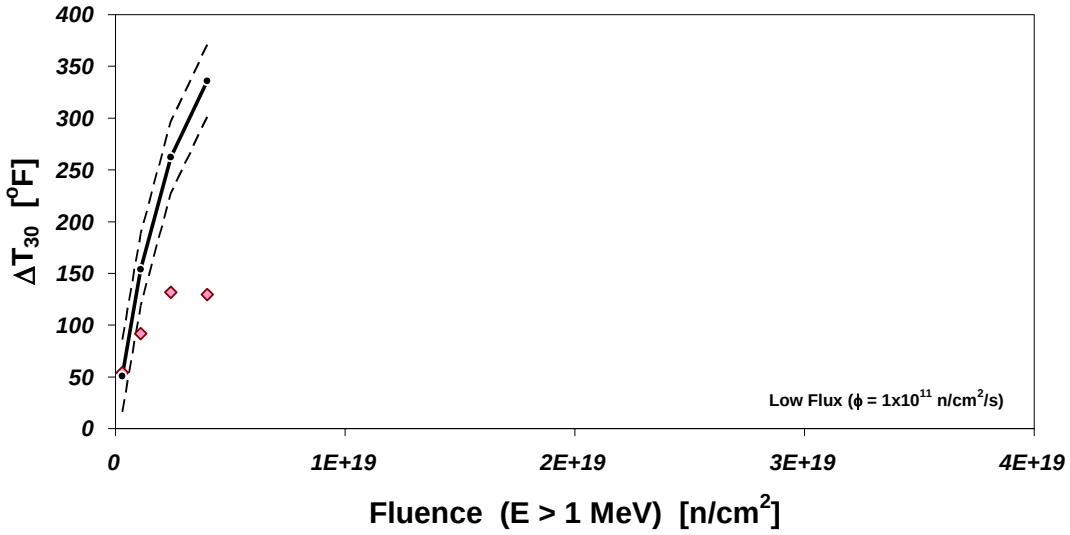
Low Flux (ϕ = 1x10^11 n/cm^2/s)
ΔT30 [°F]
Fluence (E > 1 MeV) [n/cm^2]
0
50
100
150
200
250
300
350
400
0
1E+19
2E+19
3E+19
4E+19

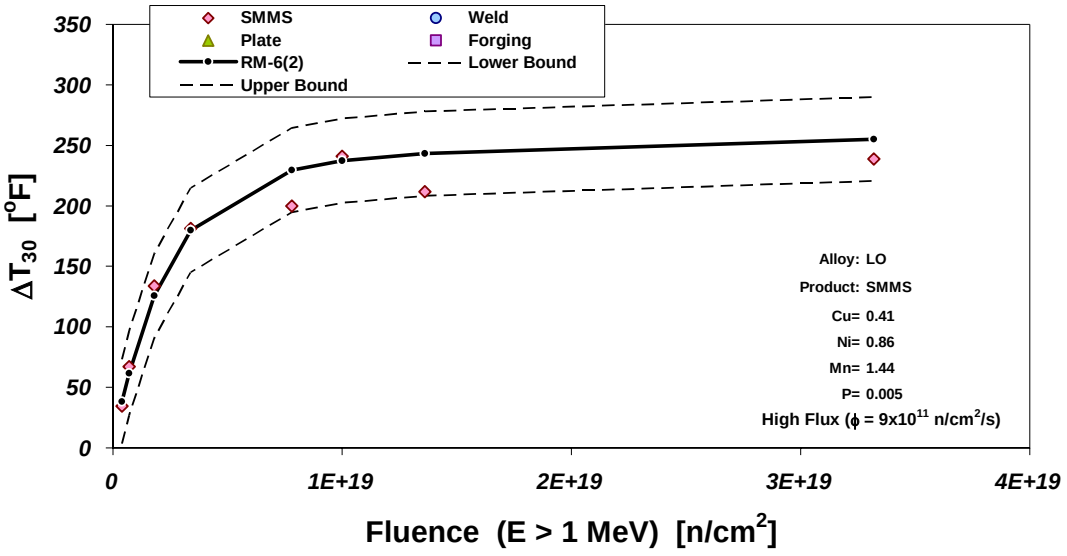
SMMS
Weld
Plate
Forging
RM-6(2)
Lower Bound
Upper Bound
Alloy: LO
Product: SMMS
Cu= 0.41
Ni= 0.86
Mn= 1.44
P= 0.005
High Flux (ϕ = 9x10^11 n/cm^2/s)
ΔT30 [°F]
Fluence (E > 1 MeV) [n/cm^2]
0
50
100
150
200
250
300
350
0
1E+19
2E+19
3E+19
4E+19

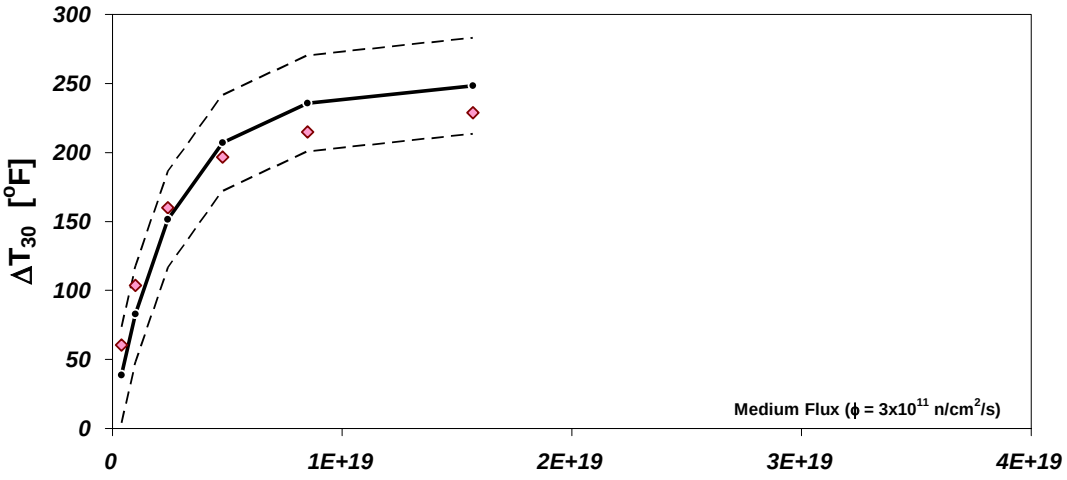
Medium Flux (ϕ = 3x10^11 n/cm^2/s)
ΔT30 [°F]
Fluence (E > 1 MeV) [n/cm^2]
0
50
100
150
200
250
300
0
1E+19
2E+19
3E+19
4E+19

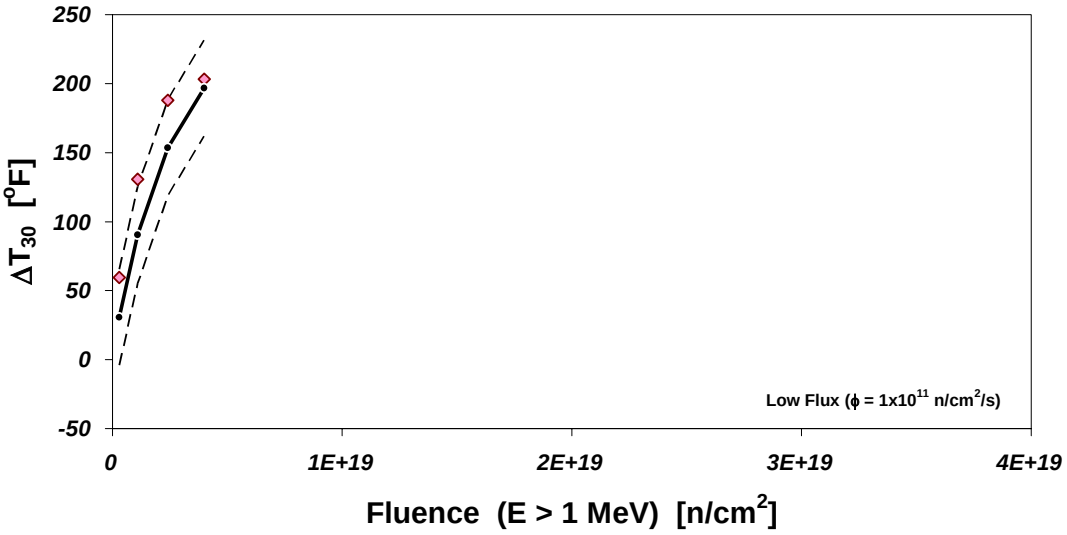
Low Flux (ϕ = 1x10^11 n/cm^2/s)
ΔT30 [°F]
Fluence (E > 1 MeV) [n/cm^2]
-50
0
50
100
150
200
250
0
1E+19
2E+19
3E+19
4E+19

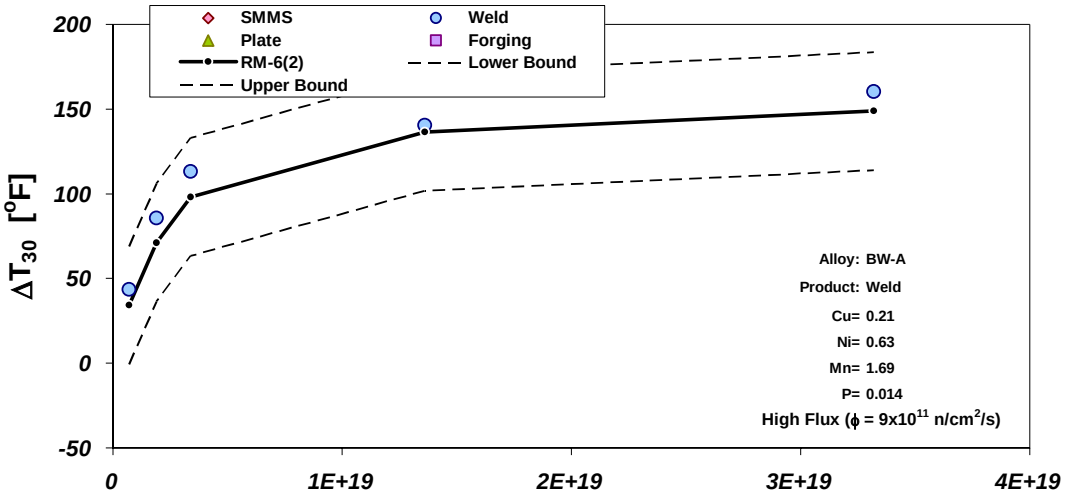
SMMS
Weld
Plate
Forging
RM-6(2)
Lower Bound
Upper Bound
Alloy: BW-A
Product: Weld
Cu= 0.21
Ni= 0.63
Mn= 1.69
P= 0.014
High Flux (ϕ = 9x10^11 n/cm^2/s)
ΔT30 [°F]
200
150
100
50
0
-50
0
1E+19
2E+19
3E+19
4E+19
Fluence (E > 1 MeV) [n/cm^2]

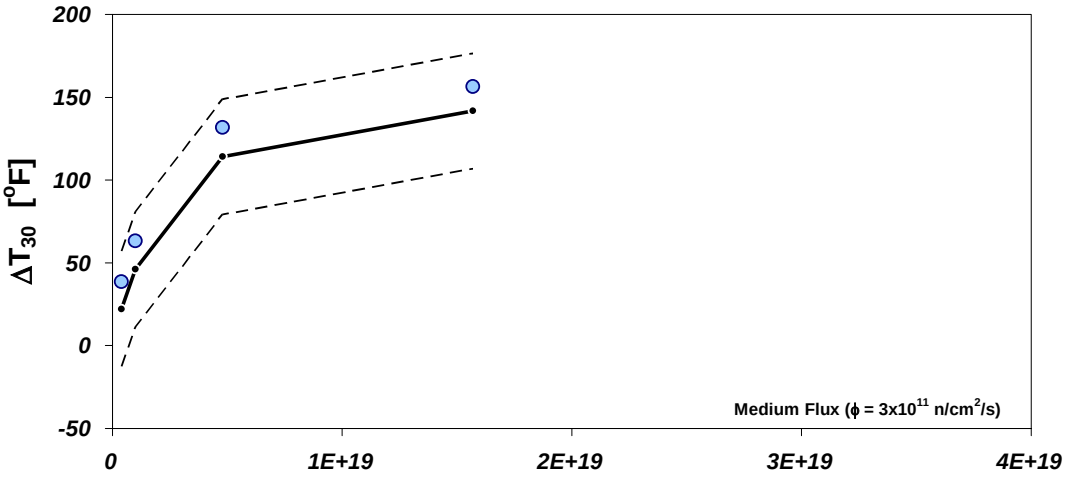
Medium Flux (ϕ = 3x10^11 n/cm^2/s)
ΔT30 [°F]
200
150
100
50
0
-50
0
1E+19
2E+19
3E+19
4E+19
Fluence (E > 1 MeV) [n/cm^2]

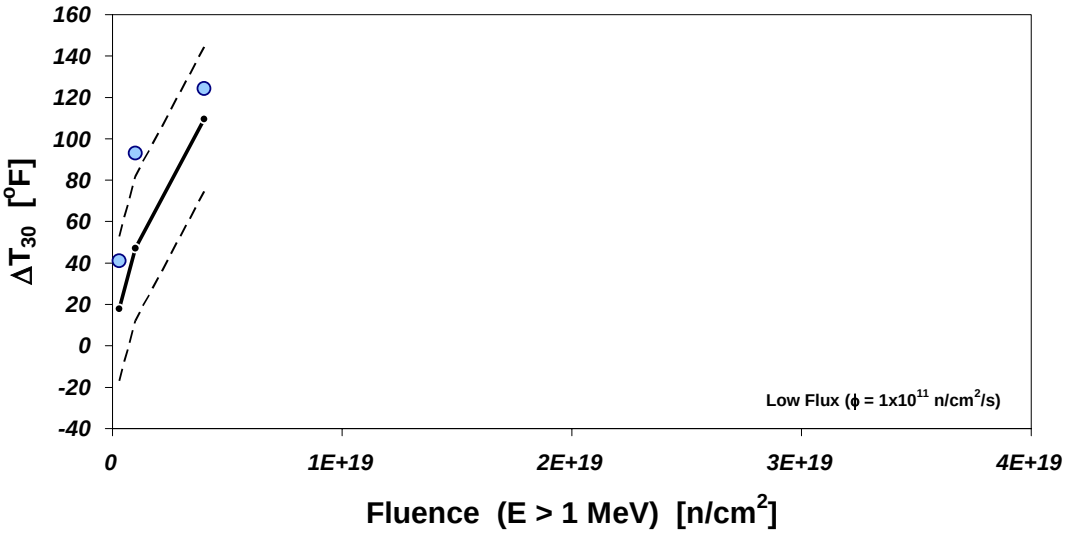
Low Flux (ϕ = 1x10^11 n/cm^2/s)
ΔT30 [°F]
160
140
120
100
80
60
40
20
0
-20
-40
0
1E+19
2E+19
3E+19
4E+19
Fluence (E > 1 MeV) [n/cm^2]

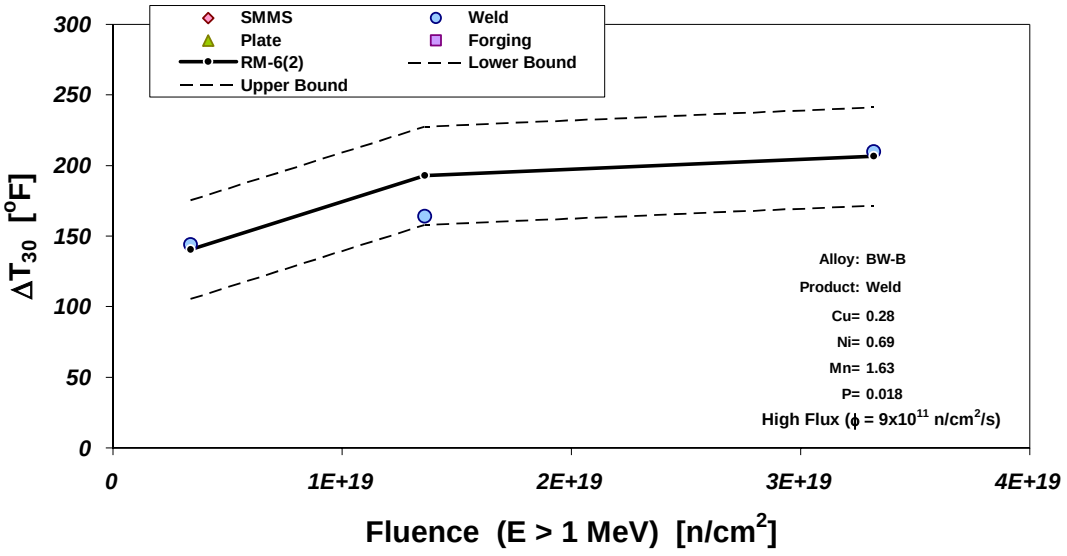
SMMS
Weld
Plate
Forging
RM-6(2)
Lower Bound
Upper Bound
Alloy: BW-B
Product: Weld
Cu= 0.28
Ni= 0.69
Mn= 1.63
P= 0.018
High Flux (ϕ = 9x10^11 n/cm^2/s)
ΔT30 [°F]
Fluence (E > 1 MeV) [n/cm^2]
0
50
100
150
200
250
300
0
1E+19
2E+19
3E+19
4E+19

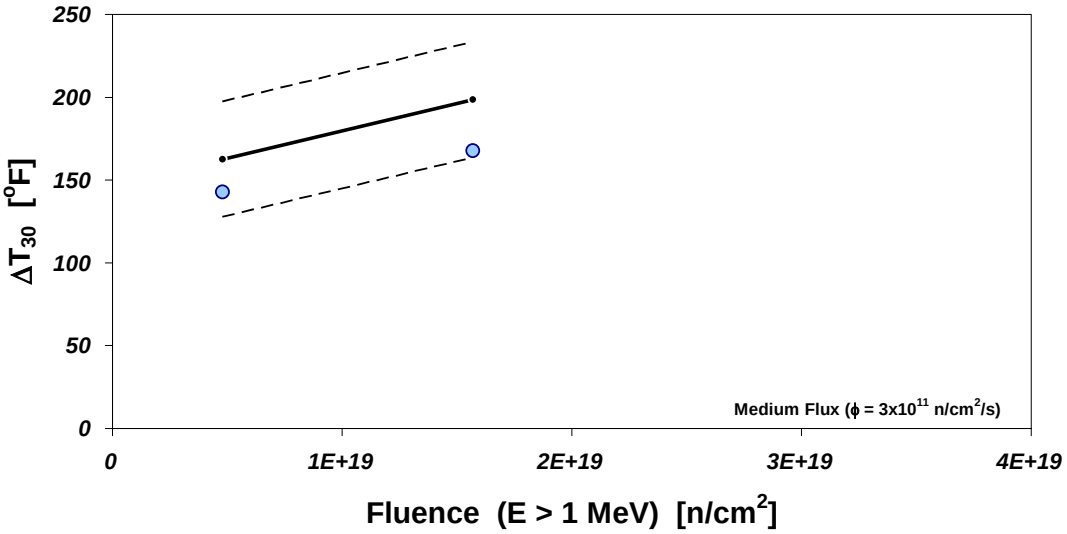
Medium Flux (ϕ = 3x10^11 n/cm^2/s)
ΔT30 [°F]
Fluence (E > 1 MeV) [n/cm^2]
0
50
100
150
200
250
0
1E+19
2E+19
3E+19
4E+19

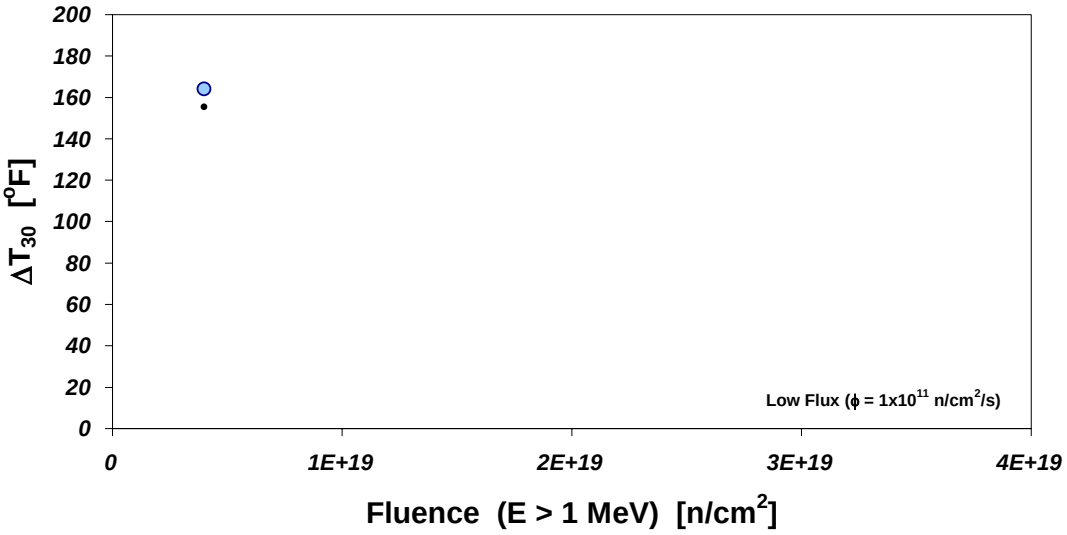
Low Flux (ϕ = 1x10^11 n/cm^2/s)
ΔT30 [°F]
Fluence (E > 1 MeV) [n/cm^2]
0
20
40
60
80
100
120
140
160
180
200
0
1E+19
2E+19
3E+19
4E+19

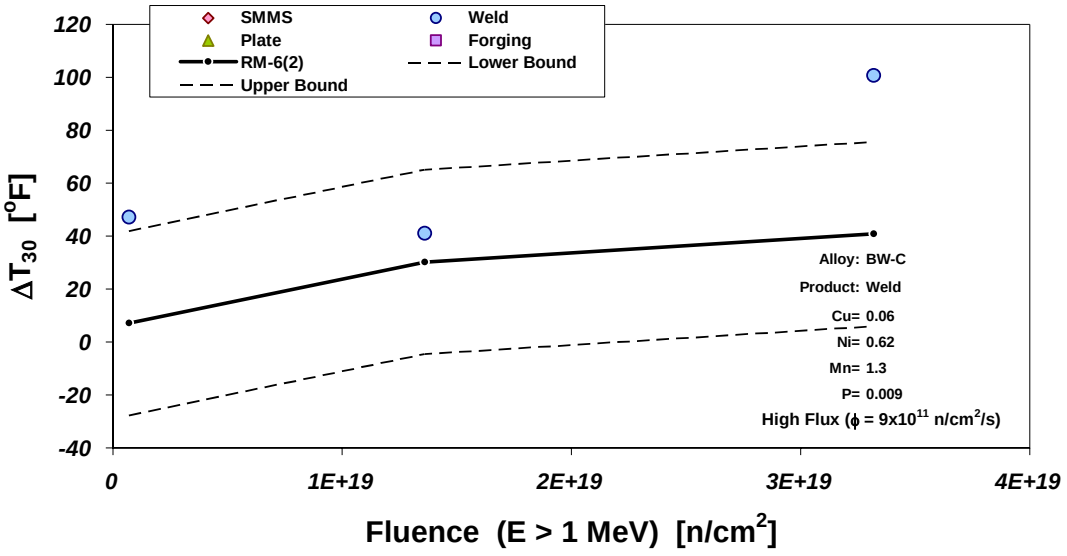
SMMS
Weld
Plate
Forging
RM-6(2)
Lower Bound
Upper Bound
Alloy: BW-C
Product: Weld
Cu= 0.06
Ni= 0.62
Mn= 1.3
P= 0.009
High Flux (ϕ = 9x10^11 n/cm^2/s)
ΔT30 [°F]
120
100
80
60
40
20
0
-20
-40
0
1E+19
2E+19
3E+19
4E+19
Fluence (E > 1 MeV) [n/cm^2]

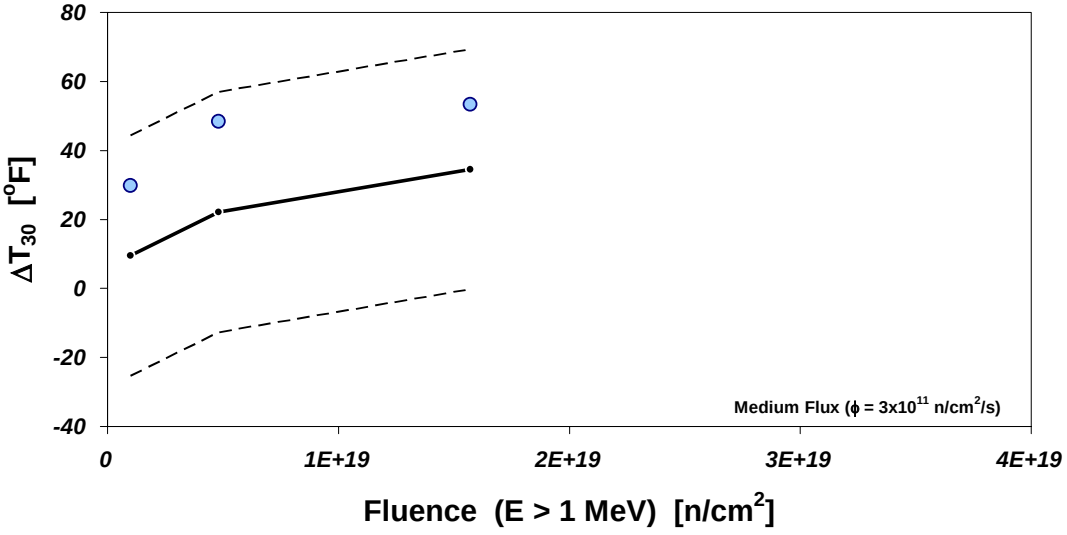
Medium Flux (ϕ = 3x10^11 n/cm^2/s)
ΔT30 [°F]
80
60
40
20
0
-20
-40
0
1E+19
2E+19
3E+19
4E+19
Fluence (E > 1 MeV) [n/cm^2]

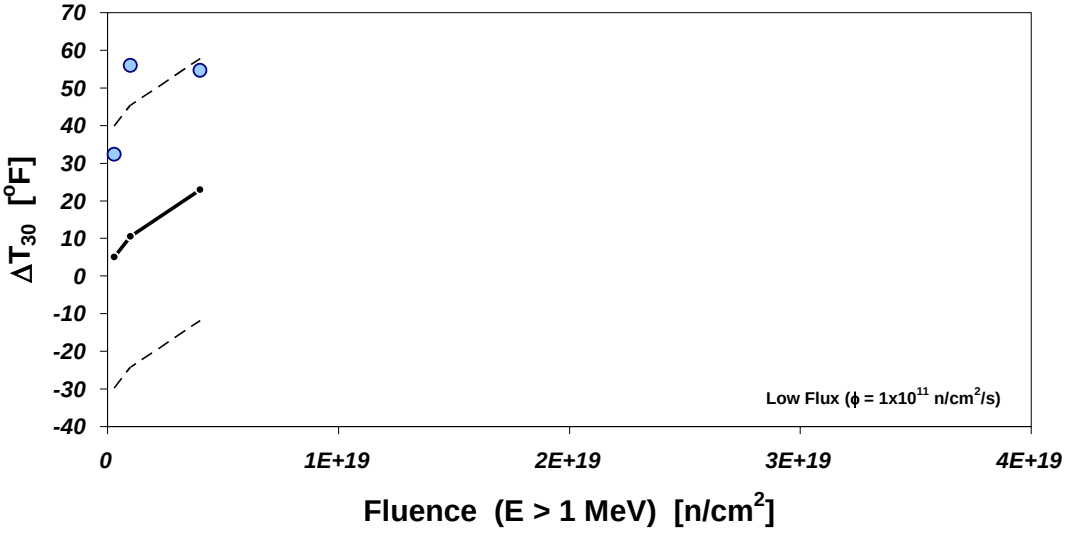
Low Flux (ϕ = 1x10^11 n/cm^2/s)
ΔT30 [°F]
70
60
50
40
30
20
10
0
-10
-20
-30
-40
0
1E+19
2E+19
3E+19
4E+19
Fluence (E > 1 MeV) [n/cm^2]

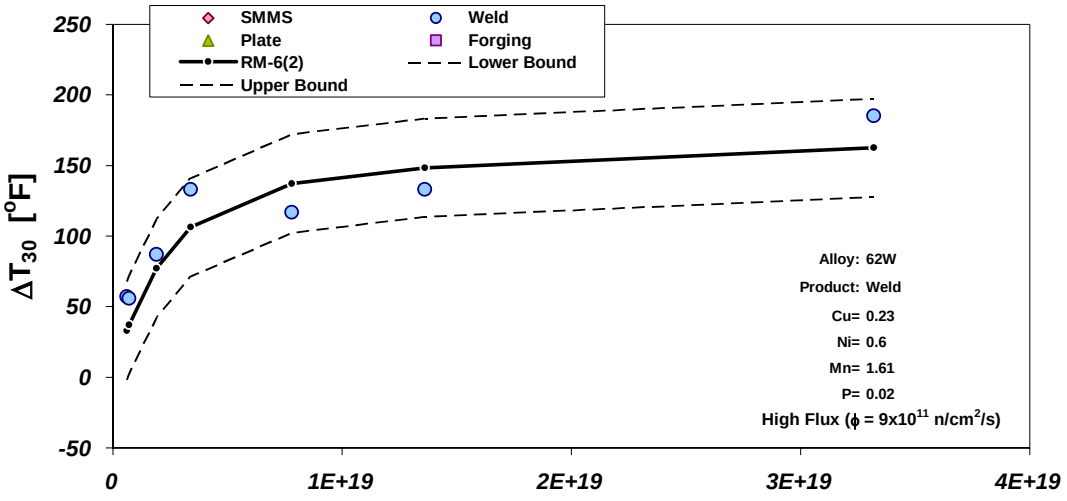
SMMS
Weld
Plate
Forging
RM-6(2)
Lower Bound
Upper Bound
250
200
150
100
50
0
-50
ΔT30 [°F]
Alloy: 62W
Product: Weld
Cu= 0.23
Ni= 0.6
Mn= 1.61
P= 0.02
High Flux (ϕ = 9x10^11 n/cm^2/s)
0
1E+19
2E+19
3E+19
4E+19
Fluence (E > 1 MeV) [n/cm^2]

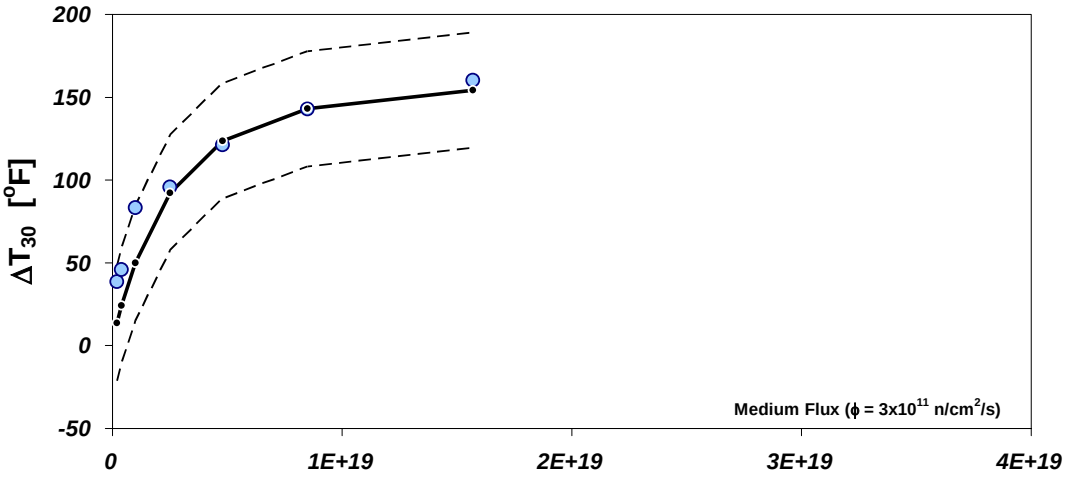
200
150
100
50
0
-50
ΔT30 [°F]
Medium Flux (ϕ = 3x10^11 n/cm^2/s)
0
1E+19
2E+19
3E+19
4E+19
Fluence (E > 1 MeV) [n/cm^2]

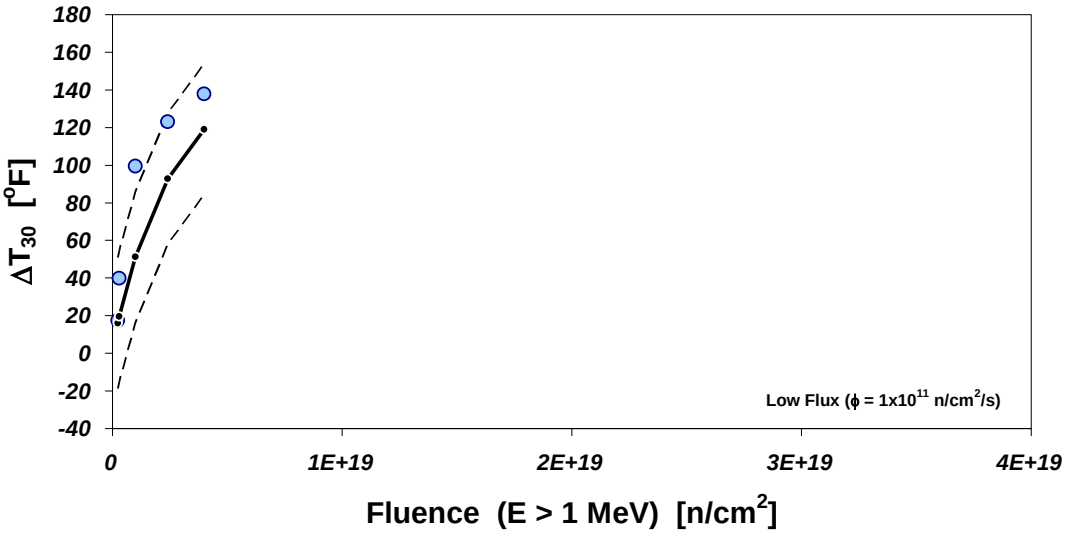
180
160
140
120
100
80
60
40
20
0
-20
-40
ΔT30 [°F]
Low Flux (ϕ = 1x10^11 n/cm^2/s)
0
1E+19
2E+19
3E+19
4E+19
Fluence (E > 1 MeV) [n/cm^2]

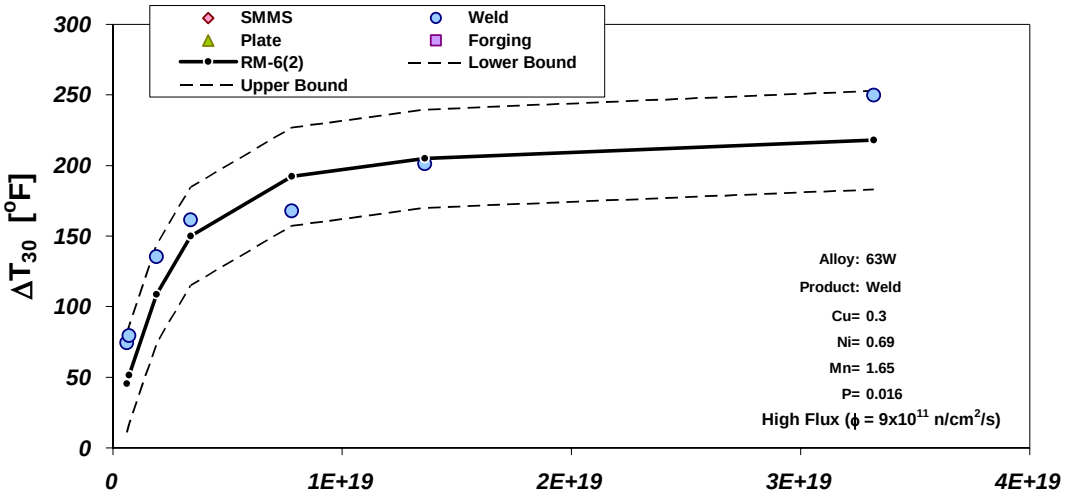
SMMS
Weld
Plate
Forging
RM-6(2)
Lower Bound
Upper Bound
Alloy: 63W
Product: Weld
Cu= 0.3
Ni= 0.69
Mn= 1.65
P= 0.016
High Flux (ϕ = 9x10^11 n/cm^2/s)
ΔT30 [°F]
300
250
200
150
100
50
0
0
1E+19
2E+19
3E+19
4E+19
Fluence (E > 1 MeV) [n/cm^2]

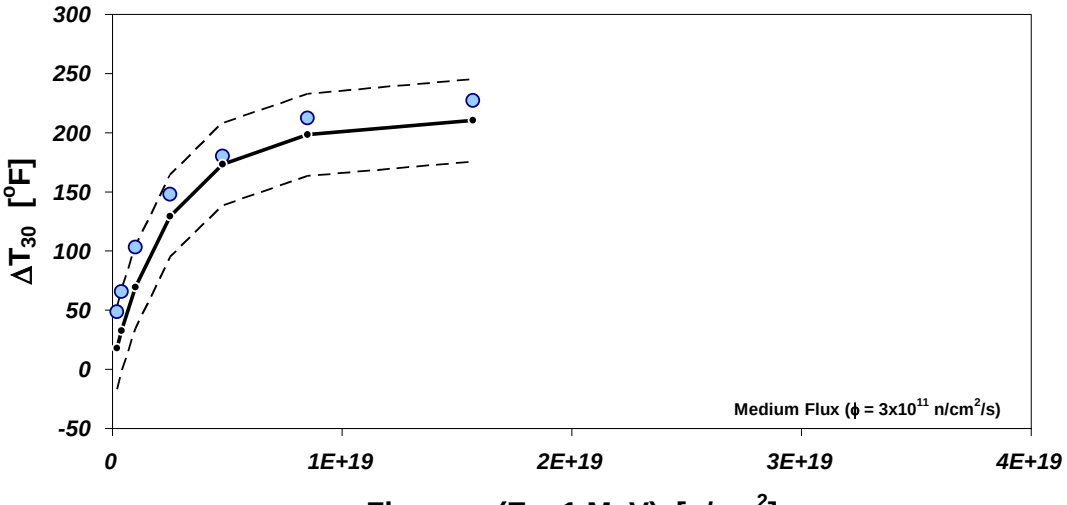
Medium Flux (ϕ = 3x10^11 n/cm^2/s)
ΔT30 [°F]
300
250
200
150
100
50
0
-50
0
1E+19
2E+19
3E+19
4E+19
Fluence (E > 1 MeV) [n/cm^2]

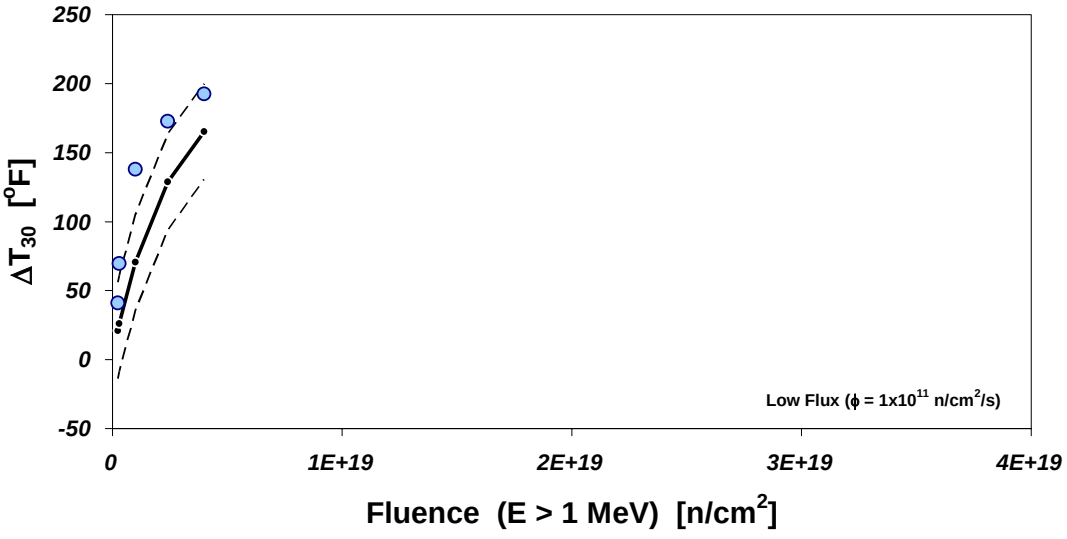
Low Flux (ϕ = 1x10^11 n/cm^2/s)
ΔT30 [°F]
250
200
150
100
50
0
-50
0
1E+19
2E+19
3E+19
4E+19
Fluence (E > 1 MeV) [n/cm^2]

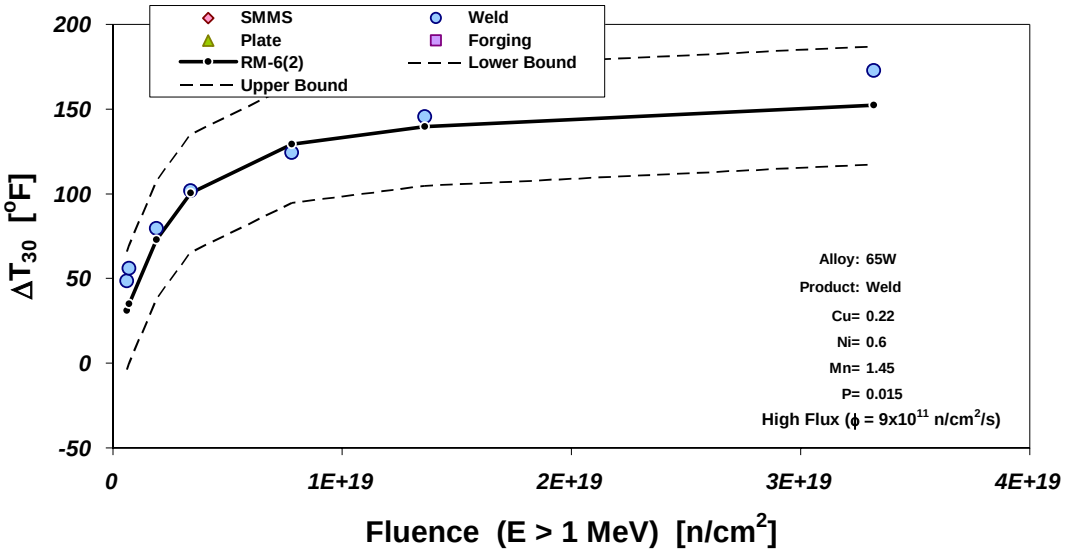
SMMS
Weld
Plate
Forging
RM-6(2)
Lower Bound
Upper Bound
200
150
100
50
0
-50
ΔT30 [°F]
Alloy: 65W
Product: Weld
Cu= 0.22
Ni= 0.6
Mn= 1.45
P= 0.015
High Flux (ϕ = 9x10^11 n/cm^2/s)
0
1E+19
2E+19
3E+19
4E+19
Fluence (E > 1 MeV) [n/cm^2]

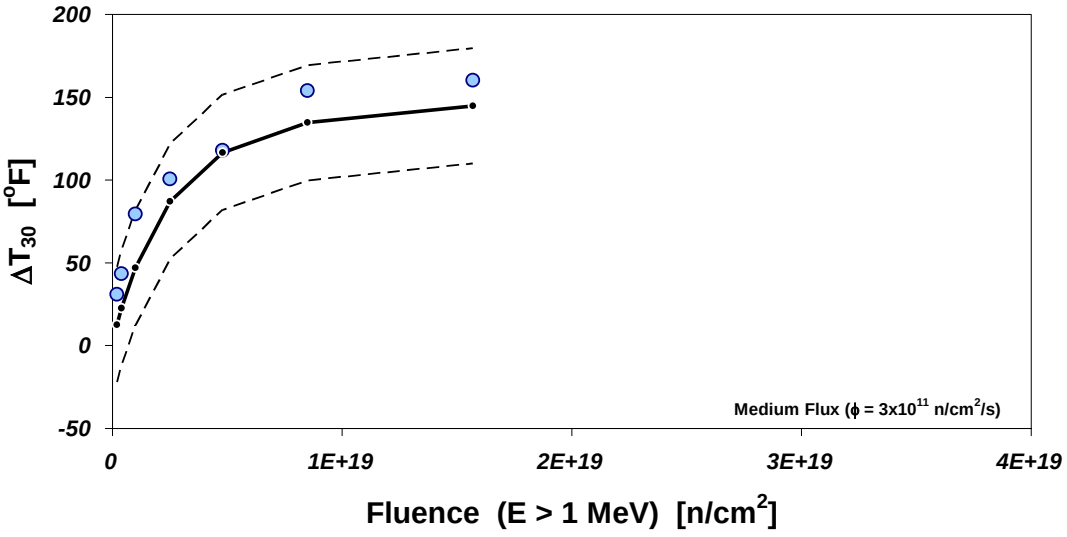
200
150
100
50
0
-50
ΔT30 [°F]
Medium Flux (ϕ = 3x10^11 n/cm^2/s)
0
1E+19
2E+19
3E+19
4E+19
Fluence (E > 1 MeV) [n/cm^2]

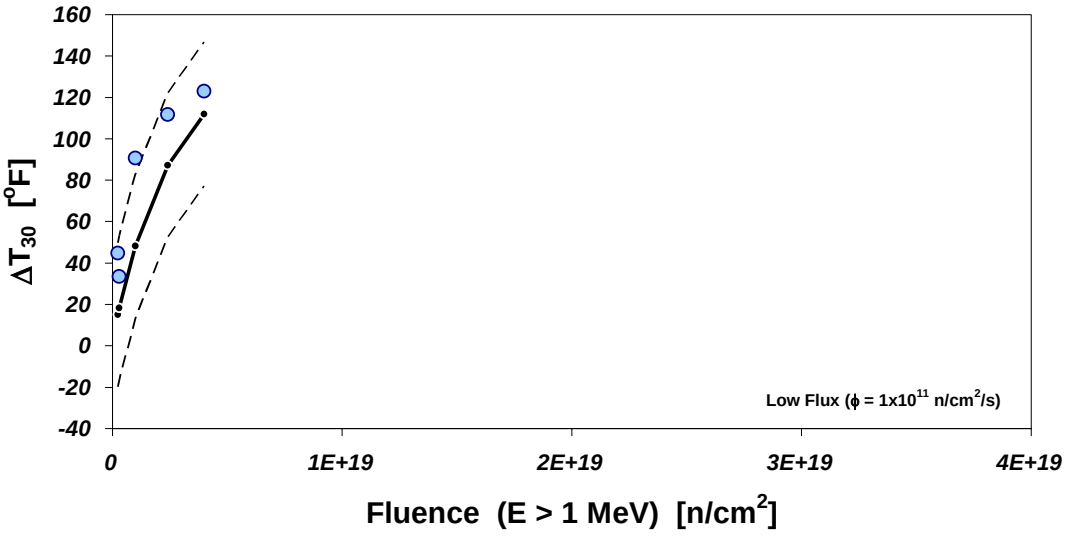
160
140
120
100
80
60
40
20
0
-20
-40
ΔT30 [°F]
Low Flux (ϕ = 1x10^11 n/cm^2/s)
0
1E+19
2E+19
3E+19
4E+19
Fluence (E > 1 MeV) [n/cm^2]

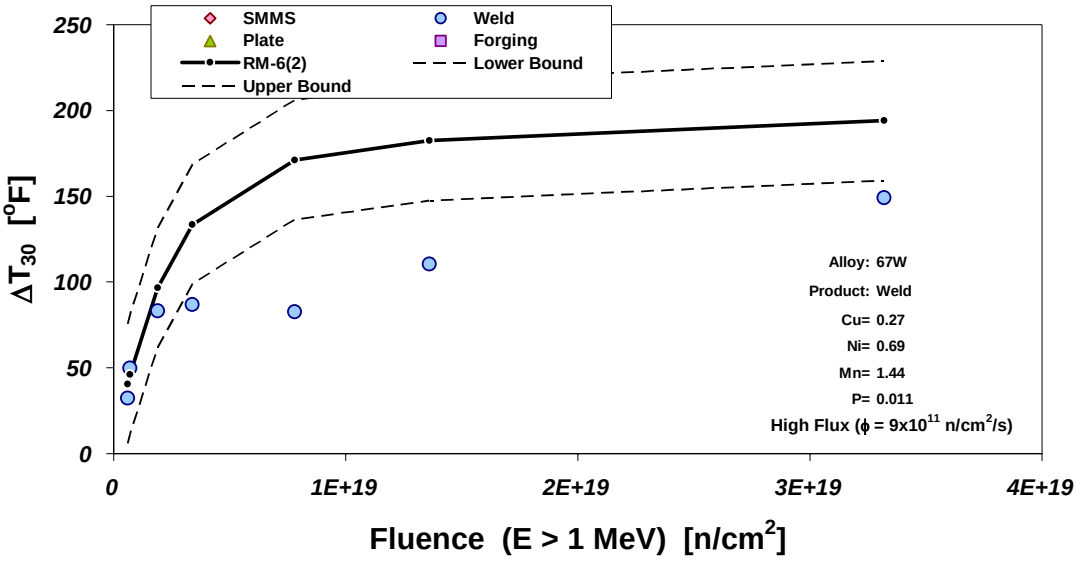
SMMS
Weld
Plate
Forging
RM-6(2)
Lower Bound
Upper Bound
Alloy: 67W
Product: Weld
Cu= 0.27
Ni= 0.69
Mn= 1.44
P= 0.011
High Flux (ϕ = 9x10^11 n/cm^2/s)
ΔT30 [°F]
250
200
150
100
50
0
0
1E+19
2E+19
3E+19
4E+19
Fluence (E > 1 MeV) [n/cm^2]

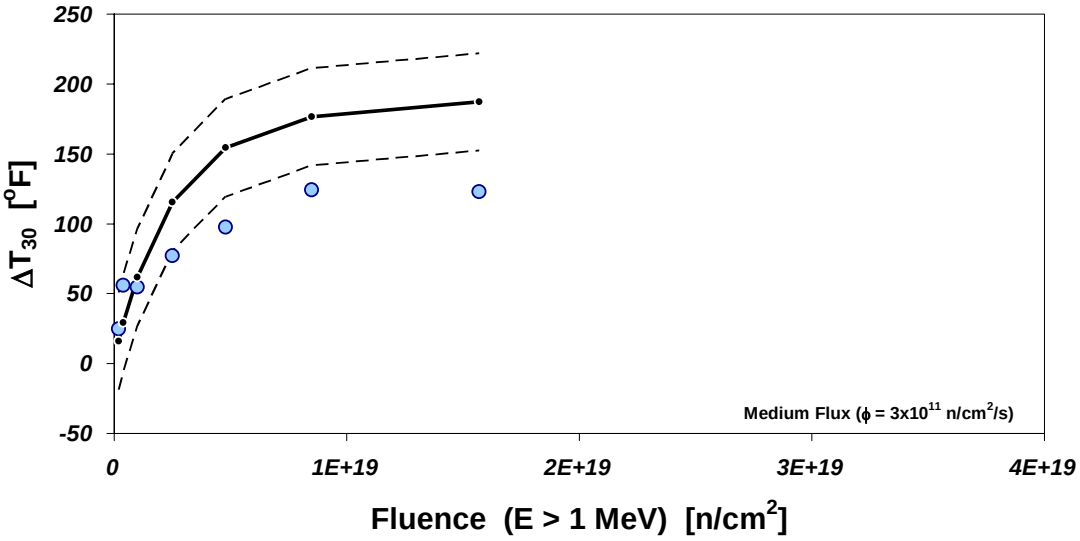
Medium Flux (ϕ = 3x10^11 n/cm^2/s)
ΔT30 [°F]
250
200
150
100
50
0
-50
0
1E+19
2E+19
3E+19
4E+19
Fluence (E > 1 MeV) [n/cm^2]

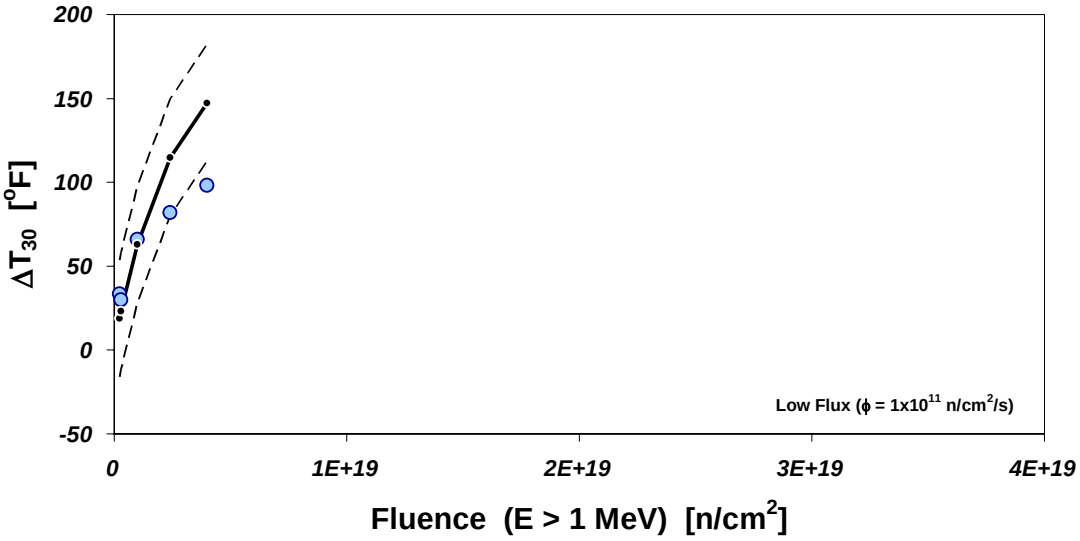
Low Flux (ϕ = 1x10^11 n/cm^2/s)
ΔT30 [°F]
200
150
100
50
0
-50
0
1E+19
2E+19
3E+19
4E+19
Fluence (E > 1 MeV) [n/cm^2]

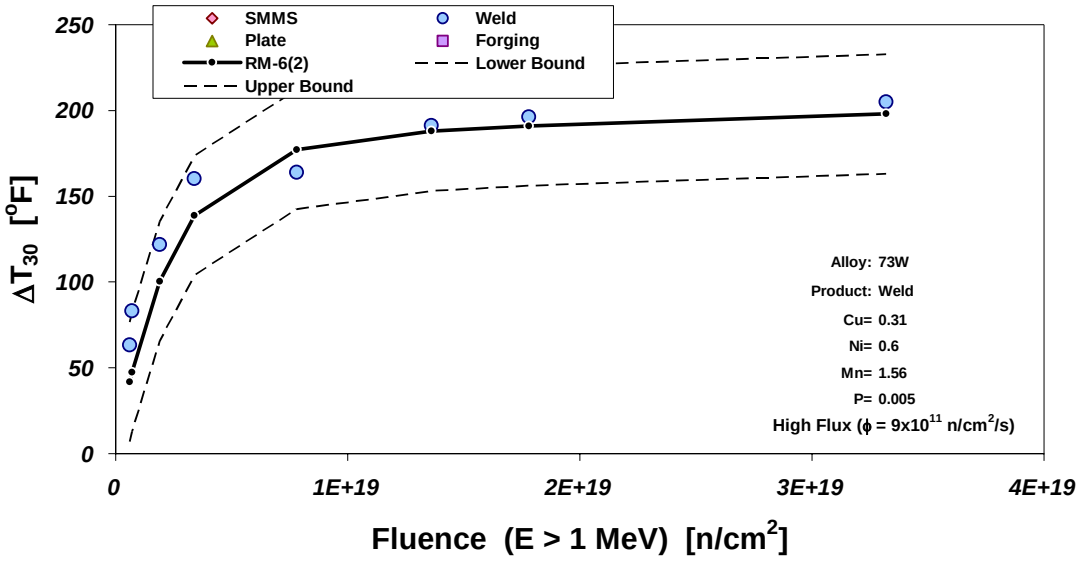
SMMS
Weld
Plate
Forging
RM-6(2)
Lower Bound
Upper Bound
Alloy: 73W
Product: Weld
Cu= 0.31
Ni= 0.6
Mn= 1.56
P= 0.005
High Flux (ϕ = 9x10^11 n/cm^2/s)
ΔT30 [°F]
250
200
150
100
50
0
0
1E+19
2E+19
3E+19
4E+19
Fluence (E > 1 MeV) [n/cm^2]

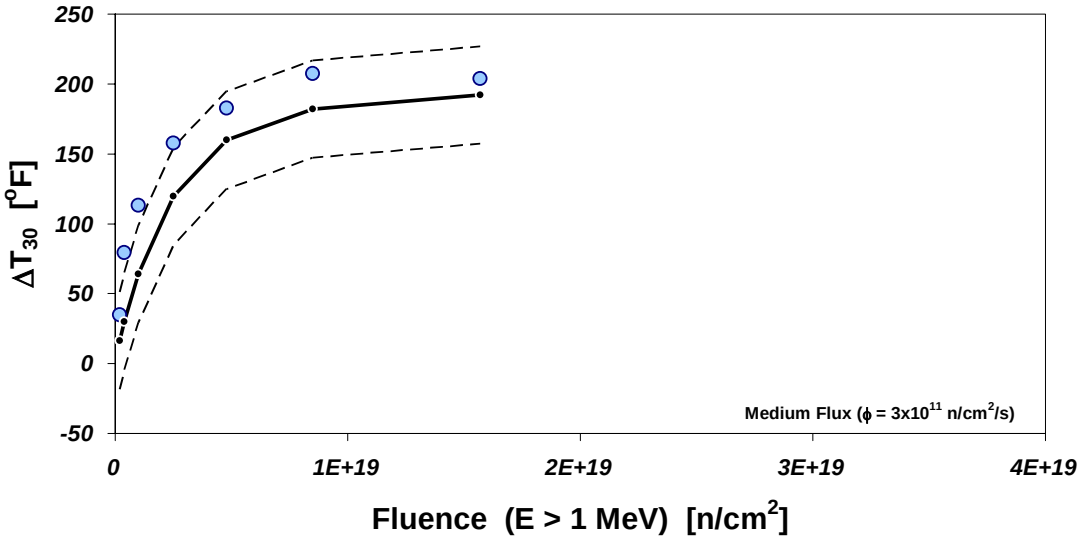
Medium Flux (ϕ = 3x10^11 n/cm^2/s)
ΔT30 [°F]
250
200
150
100
50
0
-50
0
1E+19
2E+19
3E+19
4E+19
Fluence (E > 1 MeV) [n/cm^2]

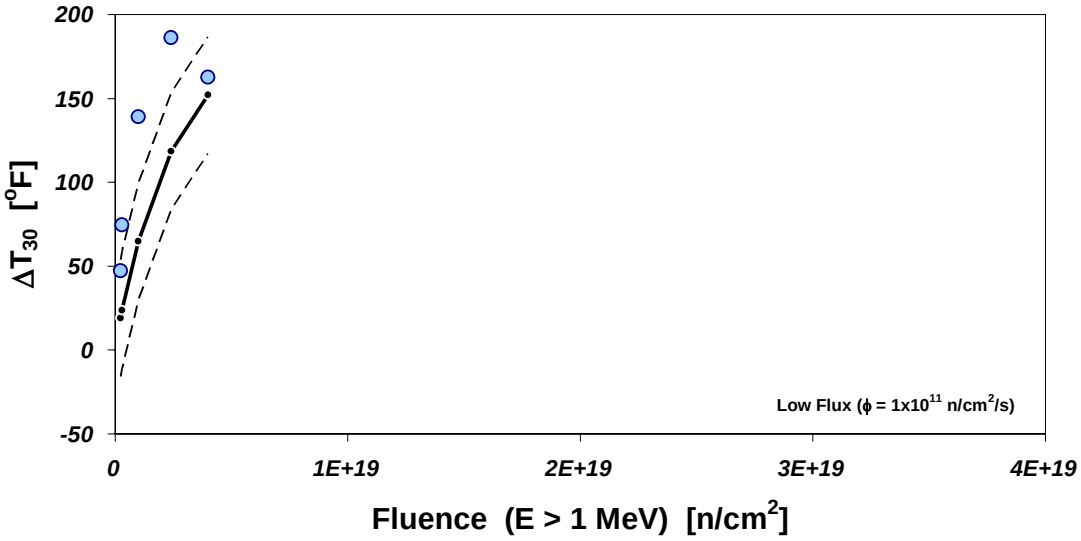
Low Flux (ϕ = 1x10^11 n/cm^2/s)
ΔT30 [°F]
200
150
100
50
0
-50
0
1E+19
2E+19
3E+19
4E+19
Fluence (E > 1 MeV) [n/cm^2]

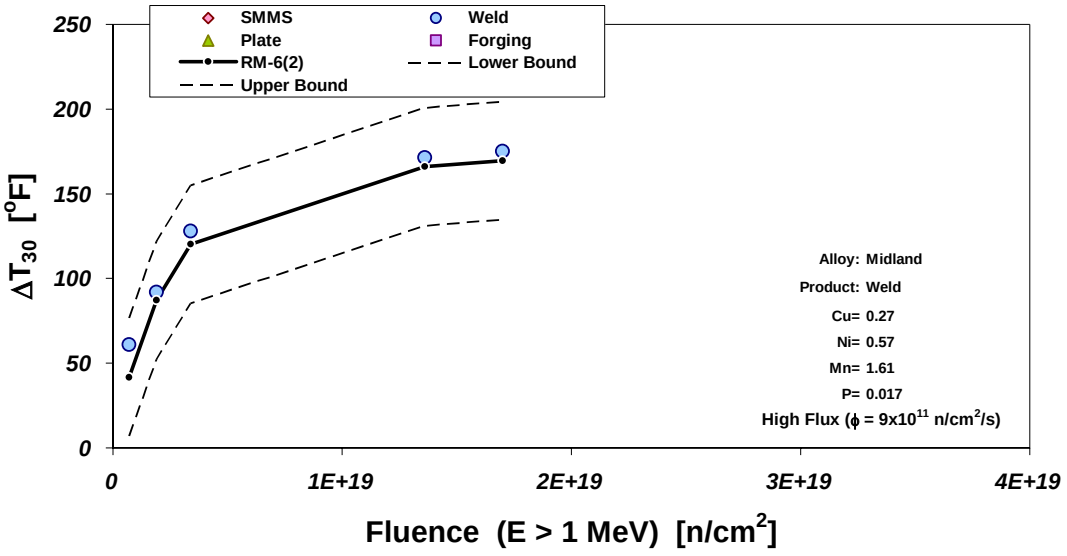
SMMS
Weld
Plate
Forging
RM-6(2)
Lower Bound
Upper Bound
Alloy: Midland
Product: Weld
Cu= 0.27
Ni= 0.57
Mn= 1.61
P= 0.017
High Flux (ϕ = 9x10^11 n/cm^2/s)
ΔT30 [°F]
250
200
150
100
50
0
0
1E+19
2E+19
3E+19
4E+19
Fluence (E > 1 MeV) [n/cm^2]

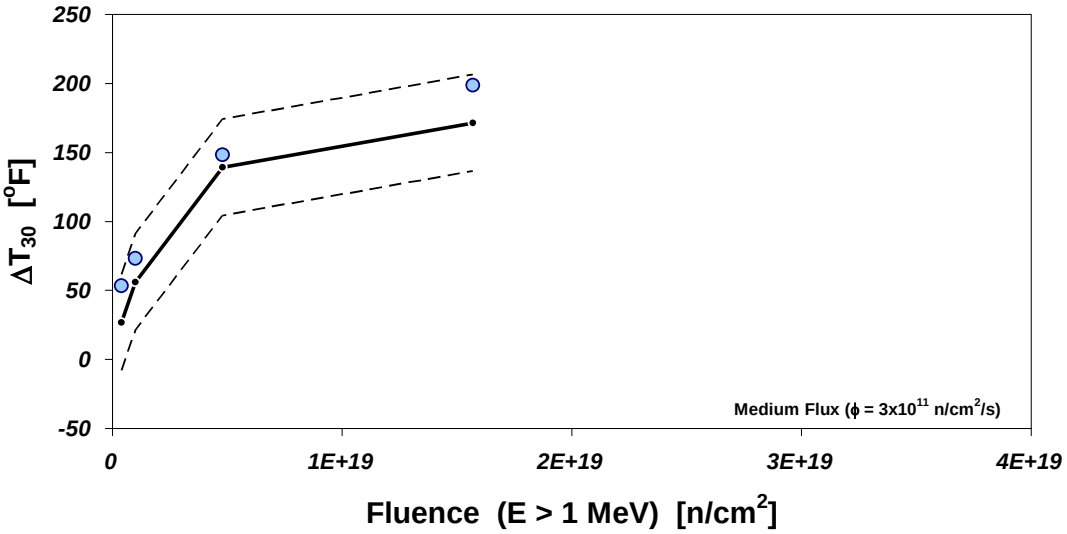
Medium Flux (ϕ = 3x10^11 n/cm^2/s)
ΔT30 [°F]
250
200
150
100
50
0
-50
0
1E+19
2E+19
3E+19
4E+19
Fluence (E > 1 MeV) [n/cm^2]

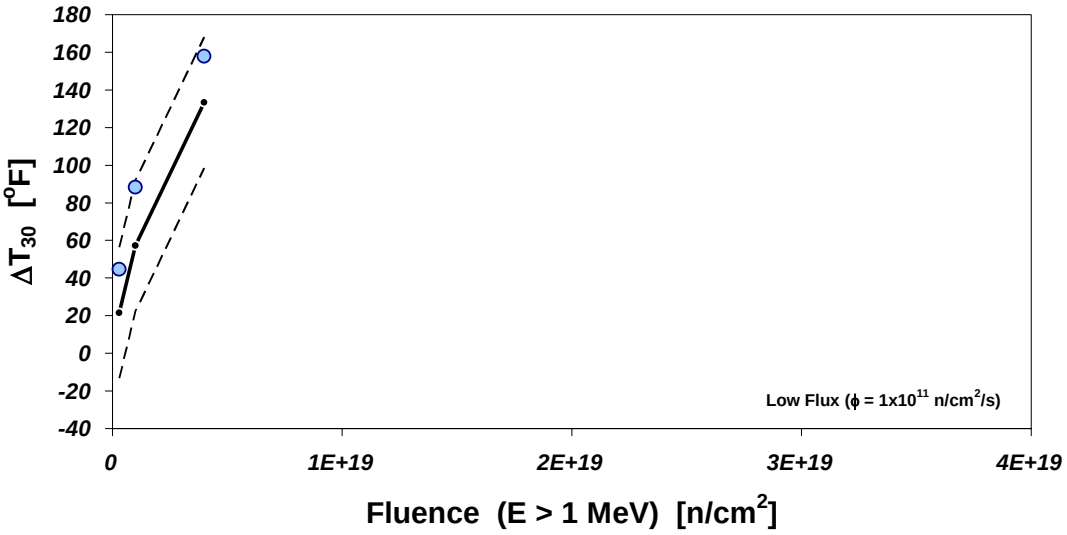
Low Flux (ϕ = 1x10^11 n/cm^2/s)
ΔT30 [°F]
180
160
140
120
100
80
60
40
20
0
-20
-40
0
1E+19
2E+19
3E+19
4E+19
Fluence (E > 1 MeV) [n/cm^2]

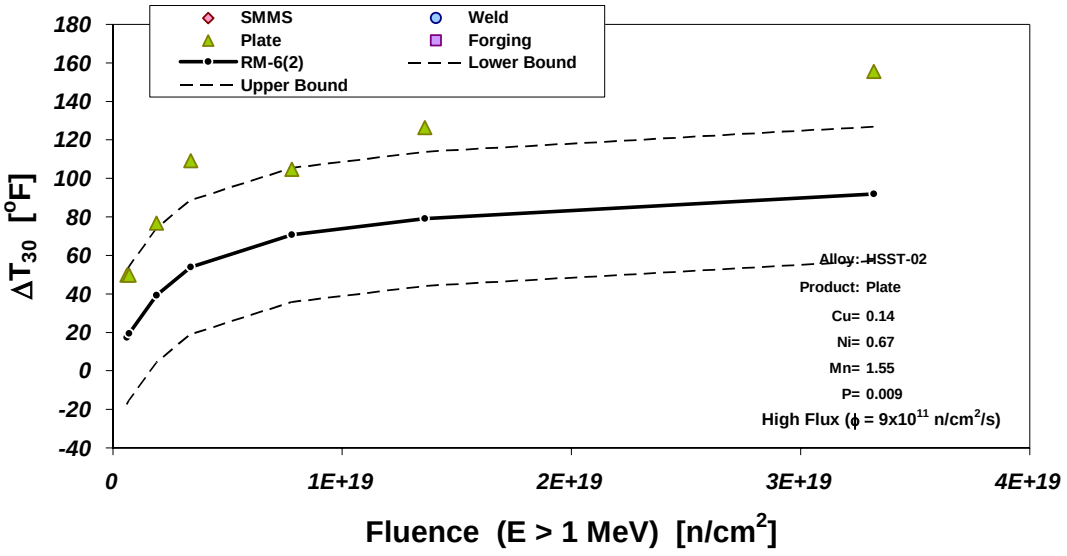
SMMS
Weld
Plate
Forging
RM-6(2)
Lower Bound
Upper Bound
Alloy: HSST-02
Product: Plate
Cu= 0.14
Ni= 0.67
Mn= 1.55
P= 0.009
High Flux (ϕ = 9x10^11 n/cm^2/s)
ΔT30 [°F]
Fluence (E > 1 MeV) [n/cm^2]

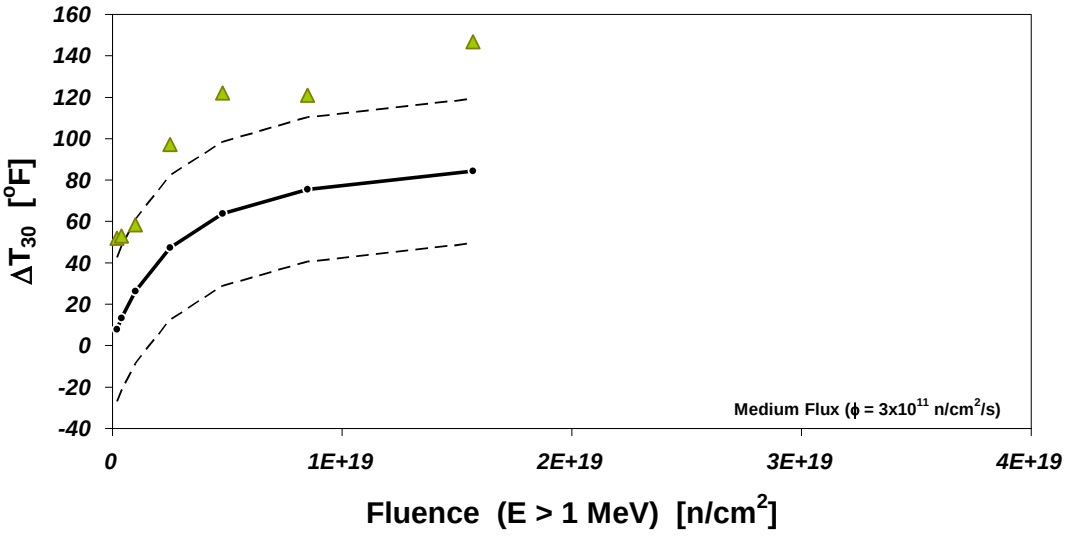
Medium Flux (ϕ = 3x10^11 n/cm^2/s)
ΔT30 [°F]
Fluence (E > 1 MeV) [n/cm^2]

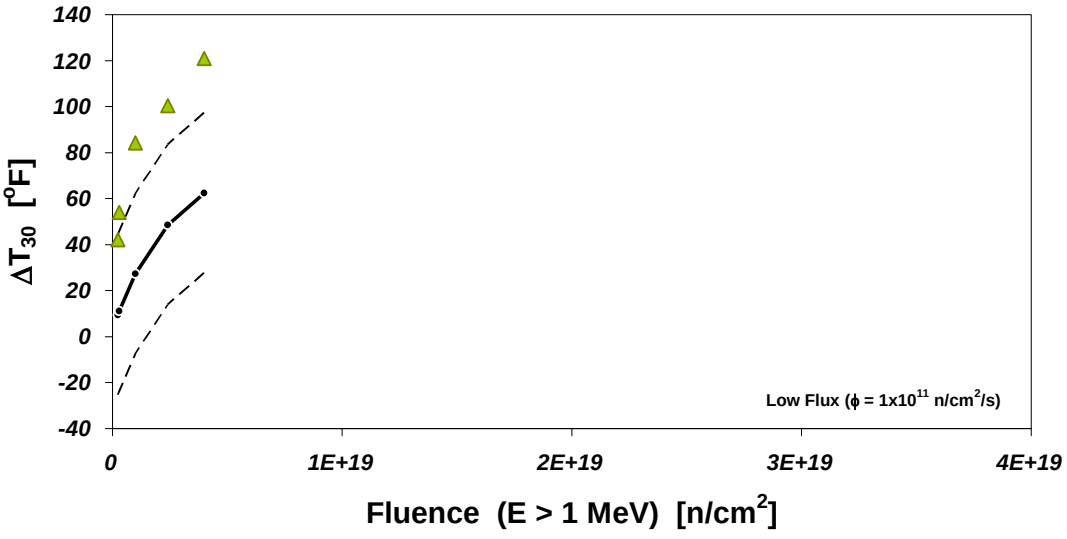
Low Flux (ϕ = 1x10^11 n/cm^2/s)
ΔT30 [°F]
Fluence (E > 1 MeV) [n/cm^2]

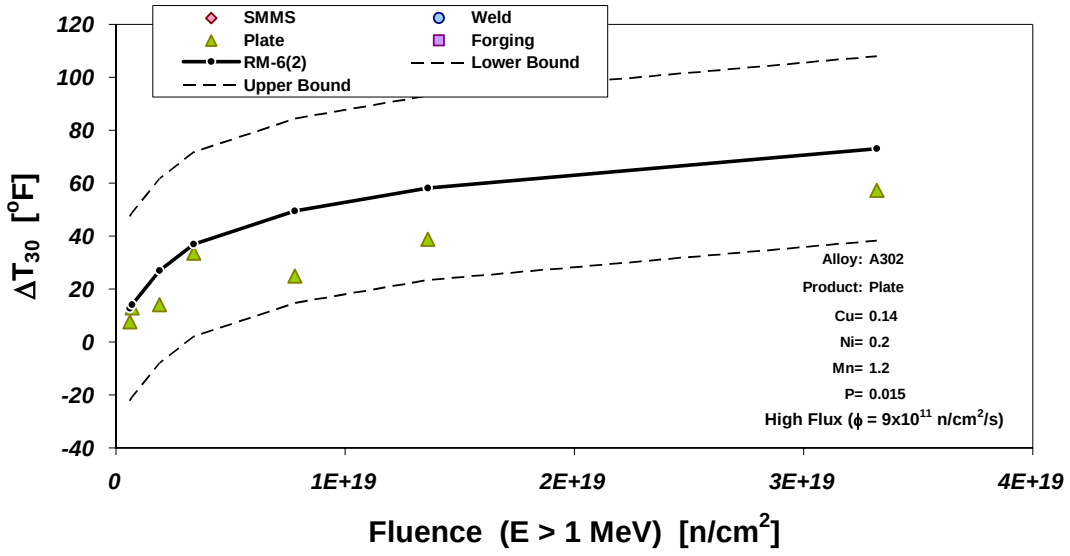
SMMS
Weld
Plate
Forging
RM-6(2)
Lower Bound
Upper Bound
120
100
80
60
40
20
0
-20
-40
ΔT30 [°F]
Alloy: A302
Product: Plate
Cu= 0.14
Ni= 0.2
Mn= 1.2
P= 0.015
High Flux (ϕ = 9x10^11 n/cm^2/s)
0
1E+19
2E+19
3E+19
4E+19
Fluence (E > 1 MeV) [n/cm^2]

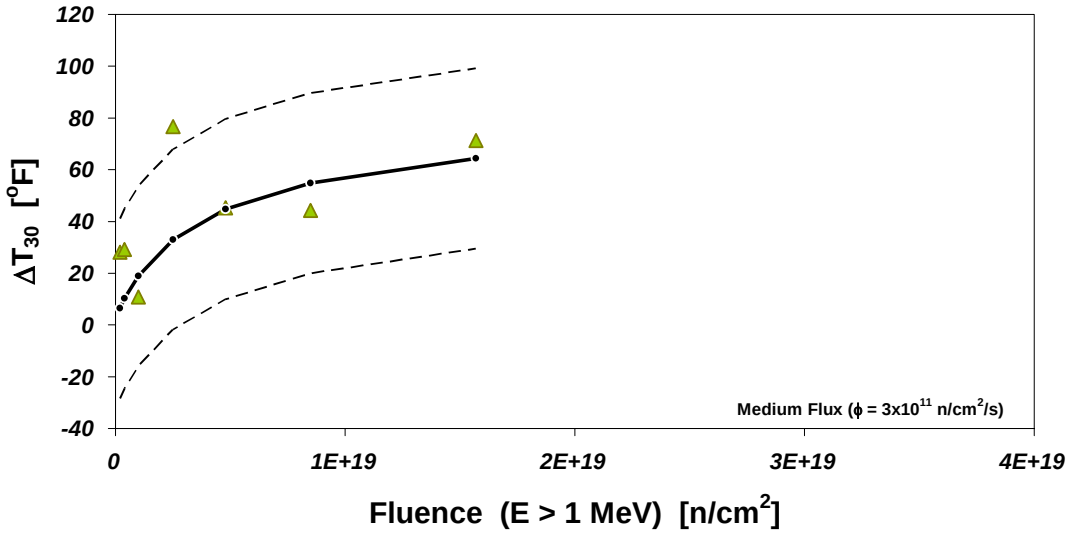
120
100
80
60
40
20
0
-20
-40
ΔT30 [°F]
Medium Flux (ϕ = 3x10^11 n/cm^2/s)
0
1E+19
2E+19
3E+19
4E+19
Fluence (E > 1 MeV) [n/cm^2]

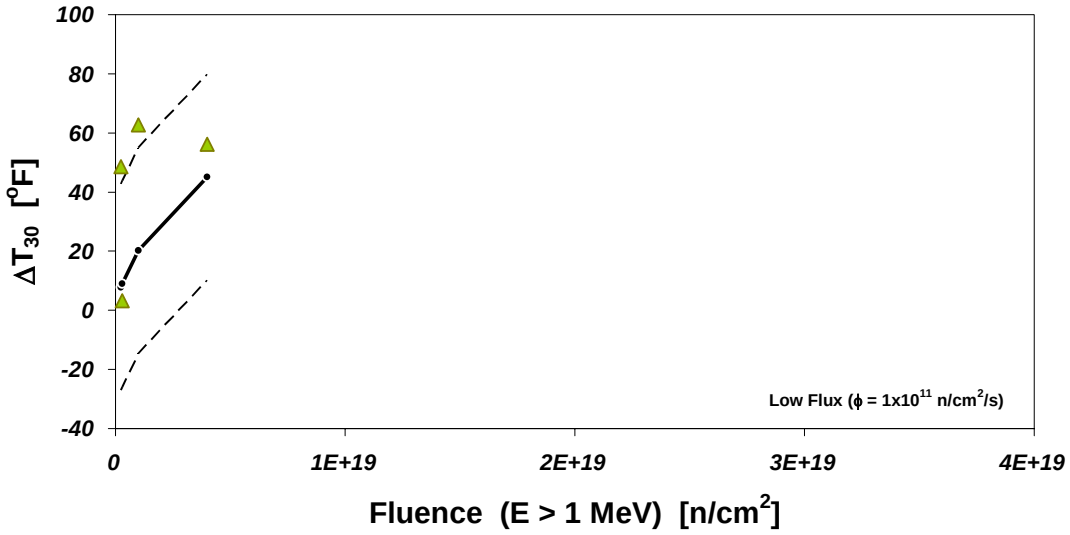
100
80
60
40
20
0
-20
-40
ΔT30 [°F]
Low Flux (ϕ = 1x10^11 n/cm^2/s)
0
1E+19
2E+19
3E+19
4E+19
Fluence (E > 1 MeV) [n/cm^2]

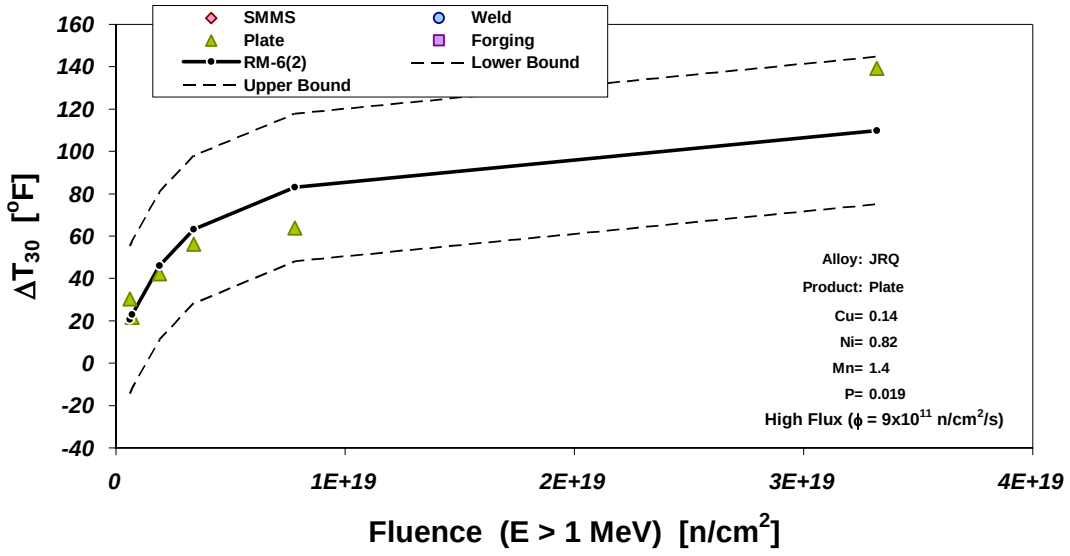
SMMS
Weld
Plate
Forging
RM-6(2)
Lower Bound
Upper Bound
Alloy: JRQ
Product: Plate
Cu= 0.14
Ni= 0.82
Mn= 1.4
P= 0.019
High Flux (ϕ = 9x10^11 n/cm^2/s)
ΔT30 [°F]
160
140
120
100
80
60
40
20
0
-20
-40
0
1E+19
2E+19
3E+19
4E+19
Fluence (E > 1 MeV) [n/cm^2]

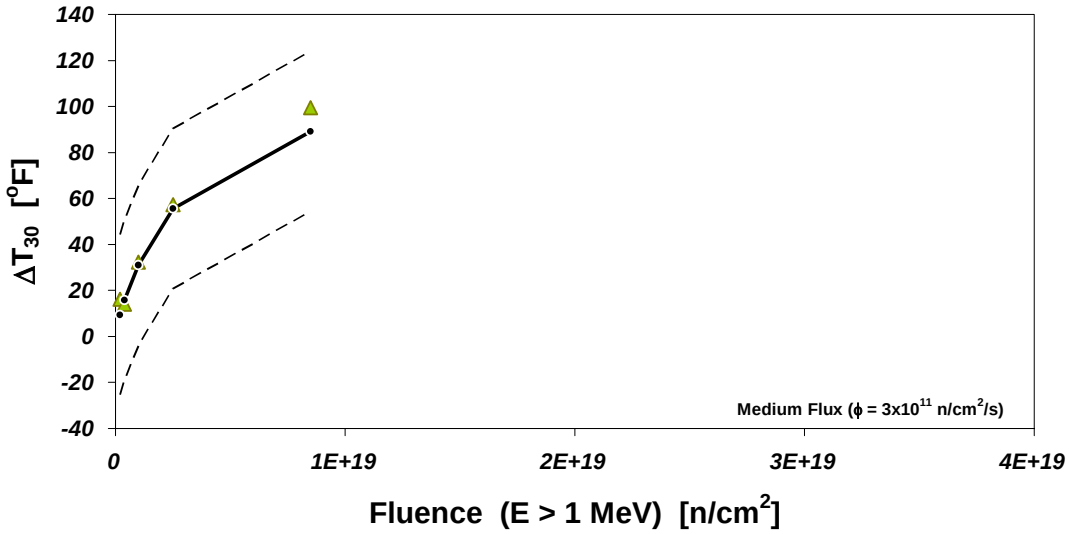
Medium Flux (ϕ = 3x10^11 n/cm^2/s)
ΔT30 [°F]
140
120
100
80
60
40
20
0
-20
-40
0
1E+19
2E+19
3E+19
4E+19
Fluence (E > 1 MeV) [n/cm^2]

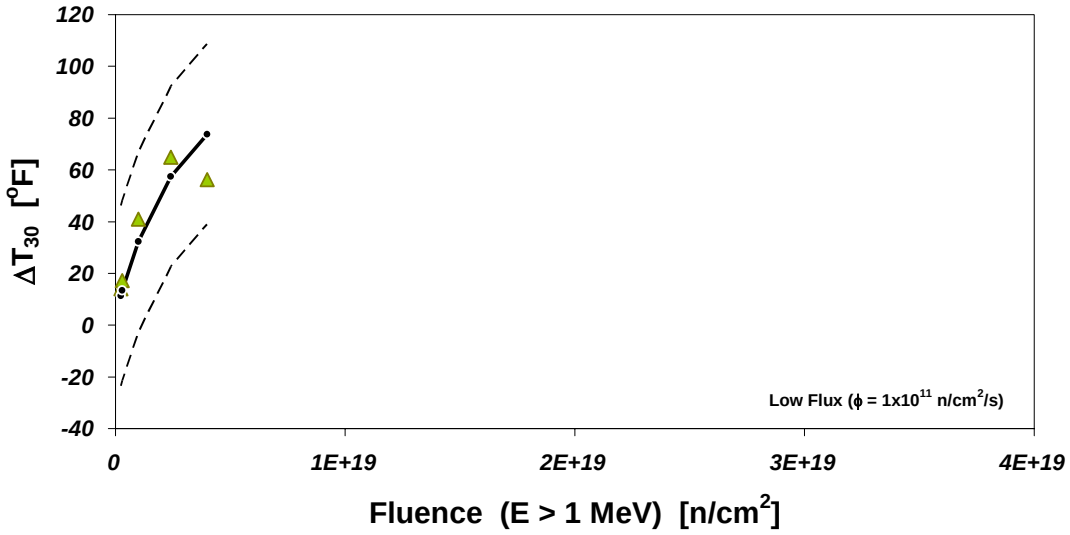
Low Flux (ϕ = 1x10^11 n/cm^2/s)
ΔT30 [°F]
120
100
80
60
40
20
0
-20
-40
0
1E+19
2E+19
3E+19
4E+19
Fluence (E > 1 MeV) [n/cm^2]

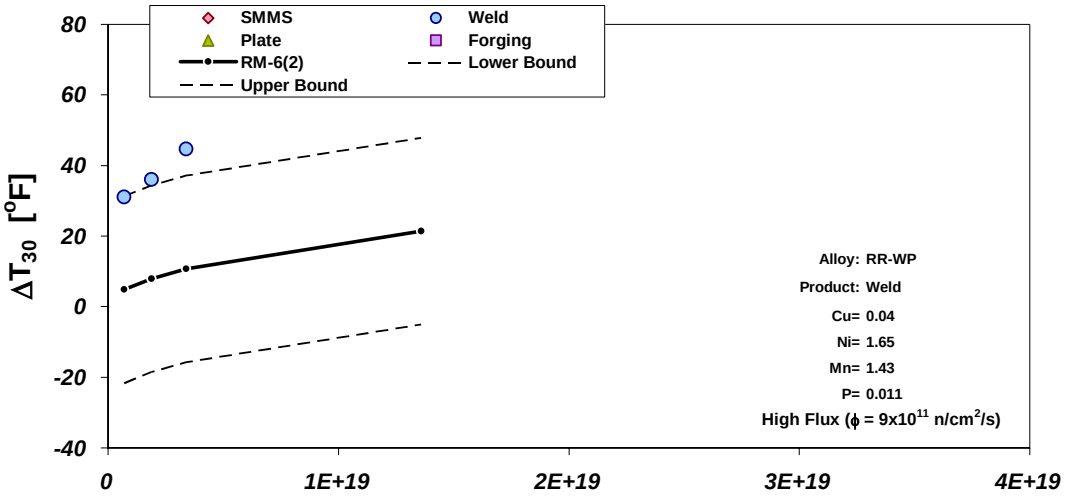
SMMS
Weld
Plate
Forging
RM-6(2)
Lower Bound
Upper Bound
80
60
40
20
0
-20
-40
ΔT30 [°F]
Alloy: RR-WP
Product: Weld
Cu= 0.04
Ni= 1.65
Mn= 1.43
P= 0.011
High Flux (ϕ = 9x10^11 n/cm^2/s)
0
1E+19
2E+19
3E+19
4E+19
Fluence (E > 1 MeV) [n/cm^2]

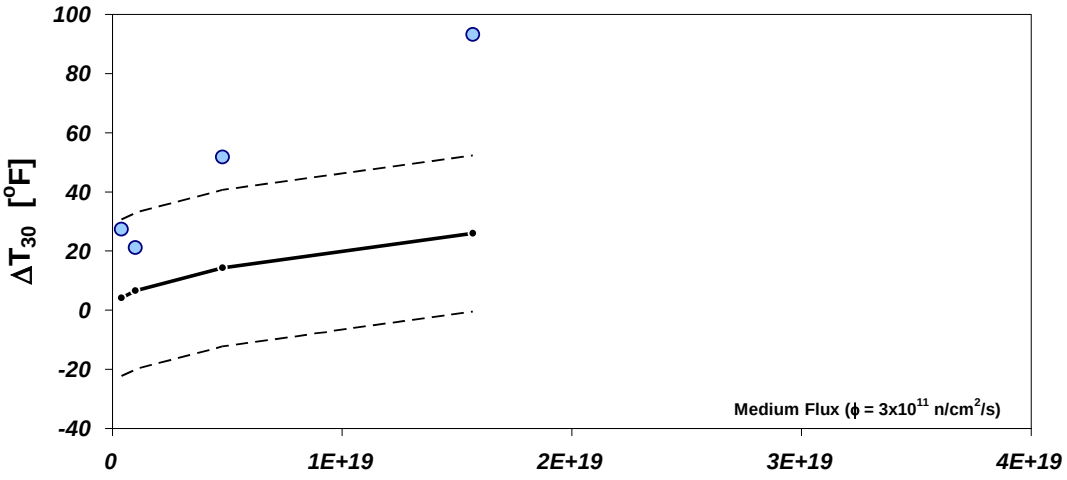
100
80
60
40
20
0
-20
-40
ΔT30 [°F]
Medium Flux (ϕ = 3x10^11 n/cm^2/s)
0
1E+19
2E+19
3E+19
4E+19
Fluence (E > 1 MeV) [n/cm^2]

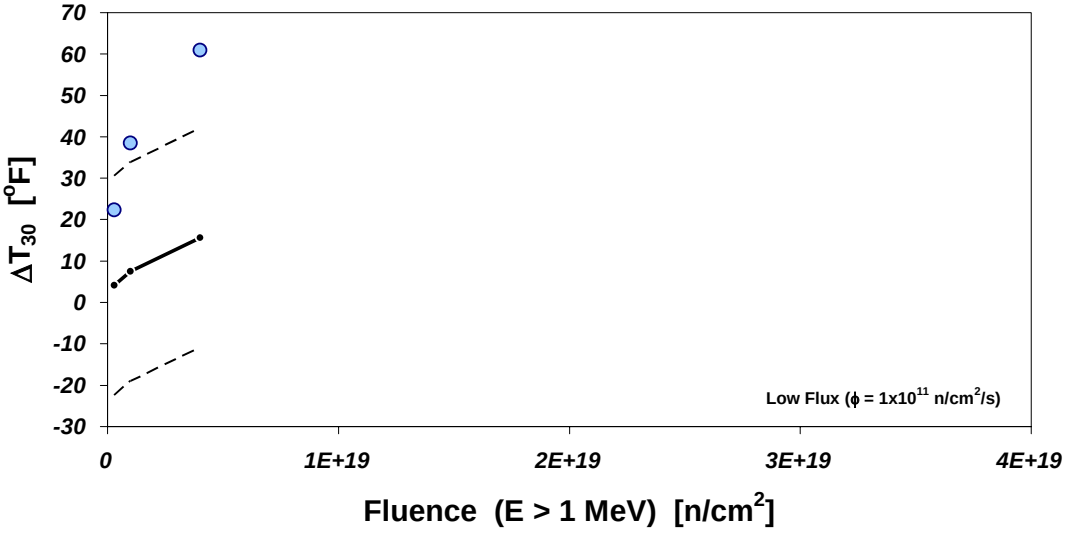
70
60
50
40
30
20
10
0
-10
-20
-30
ΔT30 [°F]
Low Flux (ϕ = 1x10^11 n/cm^2/s)
0
1E+19
2E+19
3E+19
4E+19
Fluence (E > 1 MeV) [n/cm^2]

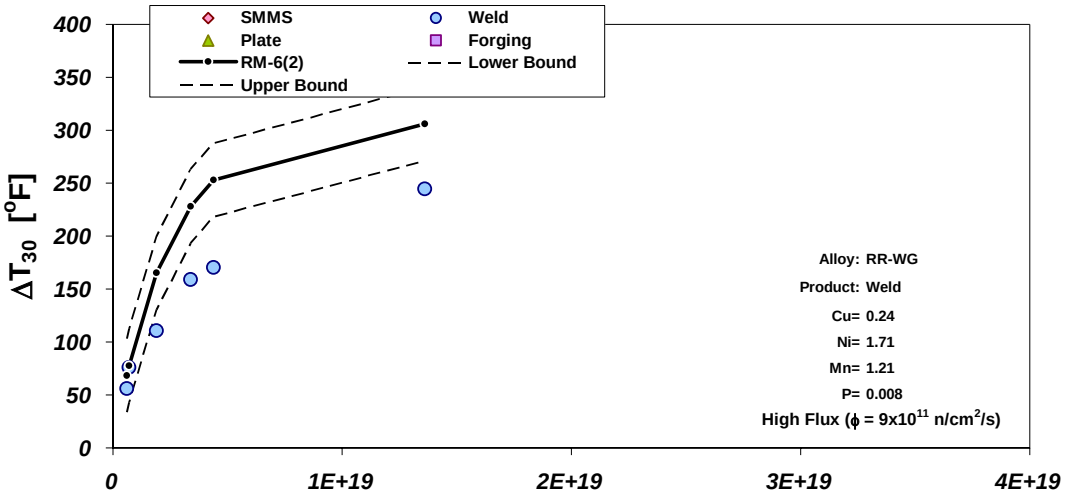
SMMS
Weld
Plate
Forging
RM-6(2)
Lower Bound
Upper Bound
Alloy: RR-WG
Product: Weld
Cu= 0.24
Ni= 1.71
Mn= 1.21
P= 0.008
High Flux (ϕ = 9x10^11 n/cm^2/s)
ΔT30 [°F]
400
350
300
250
200
150
100
50
0
0
1E+19
2E+19
3E+19
4E+19
Fluence (E > 1 MeV) [n/cm^2]

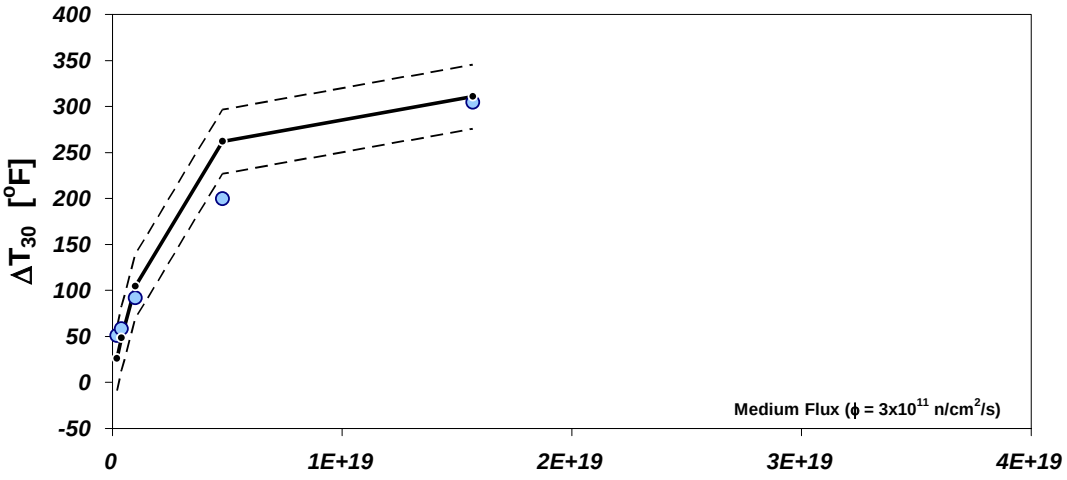
Medium Flux (ϕ = 3x10^11 n/cm^2/s)
ΔT30 [°F]
400
350
300
250
200
150
100
50
0
-50
0
1E+19
2E+19
3E+19
4E+19
Fluence (E > 1 MeV) [n/cm^2]

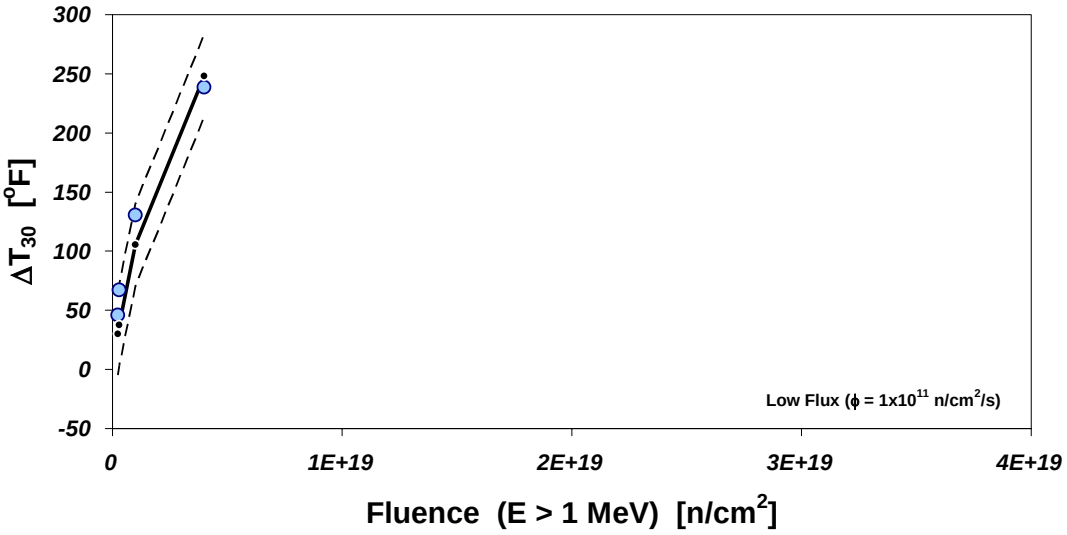
Low Flux (ϕ = 1x10^11 n/cm^2/s)
ΔT30 [°F]
300
250
200
150
100
50
0
-50
0
1E+19
2E+19
3E+19
4E+19
Fluence (E > 1 MeV) [n/cm^2]

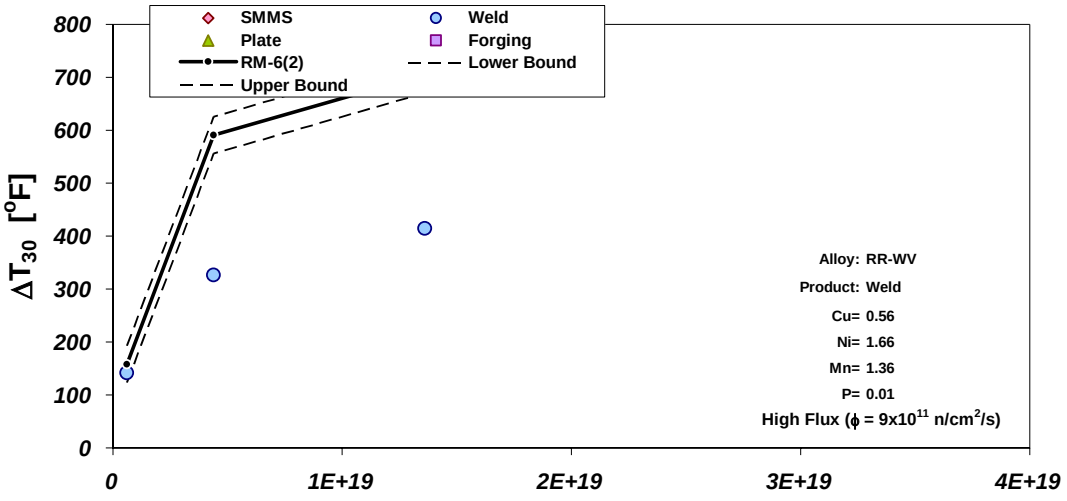
SMMS
Weld
Plate
Forging
RM-6(2)
Lower Bound
Upper Bound
Alloy: RR-WV
Product: Weld
Cu= 0.56
Ni= 1.66
Mn= 1.36
P= 0.01
High Flux (ϕ = 9x10^11 n/cm^2/s)
ΔT30 [°F]
0
100
200
300
400
500
600
700
800
0
1E+19
2E+19
3E+19
4E+19
Fluence (E > 1 MeV) [n/cm^2]

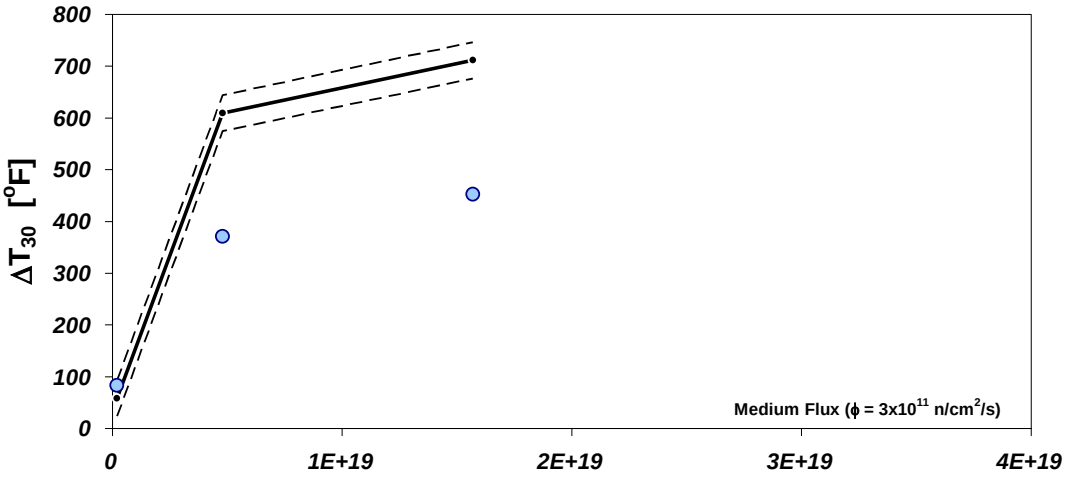
Medium Flux (ϕ = 3x10^11 n/cm^2/s)
ΔT30 [°F]
0
100
200
300
400
500
600
700
800
0
1E+19
2E+19
3E+19
4E+19
Fluence (E > 1 MeV) [n/cm^2]

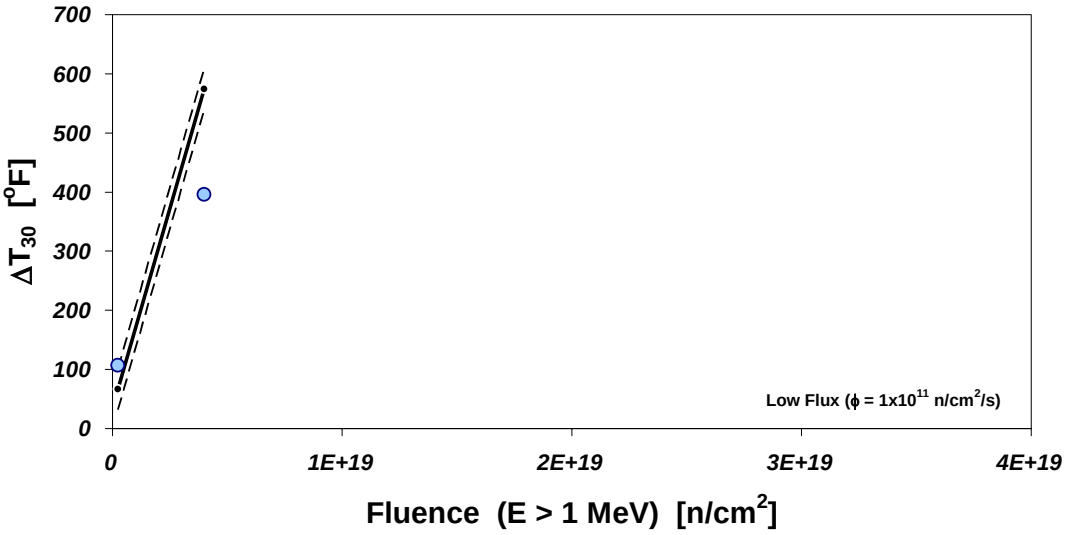
Low Flux (ϕ = 1x10^11 n/cm^2/s)
ΔT30 [°F]
0
100
200
300
400
500
600
700
0
1E+19
2E+19
3E+19
4E+19
Fluence (E > 1 MeV) [n/cm^2]

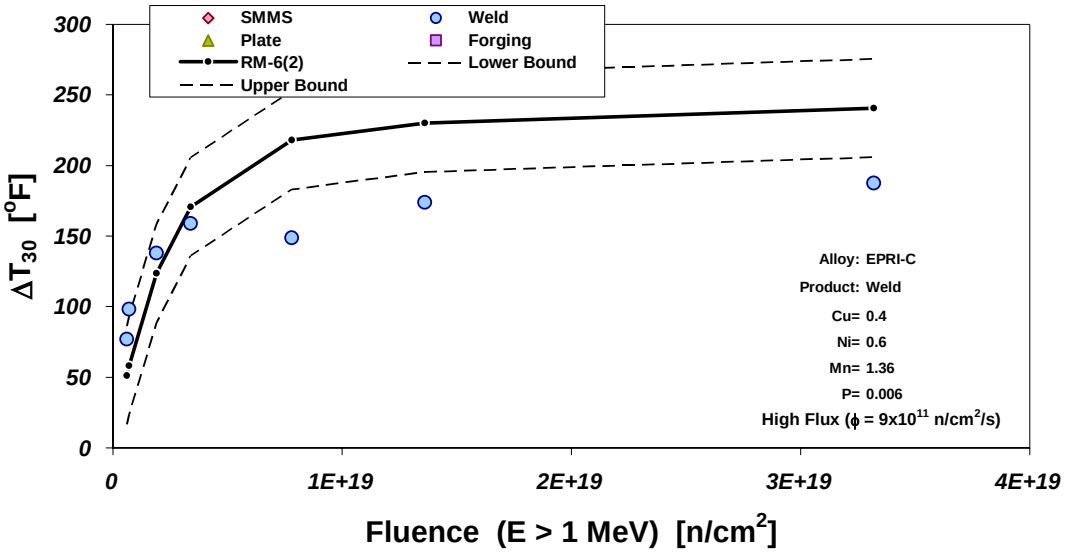
SMMS
Weld
Plate
Forging
RM-6(2)
Lower Bound
Upper Bound
Alloy: EPRI-C
Product: Weld
Cu= 0.4
Ni= 0.6
Mn= 1.36
P= 0.006
High Flux (ϕ = 9x10^11 n/cm^2/s)
ΔT30 [°F]
300
250
200
150
100
50
0
0
1E+19
2E+19
3E+19
4E+19
Fluence (E > 1 MeV) [n/cm^2]

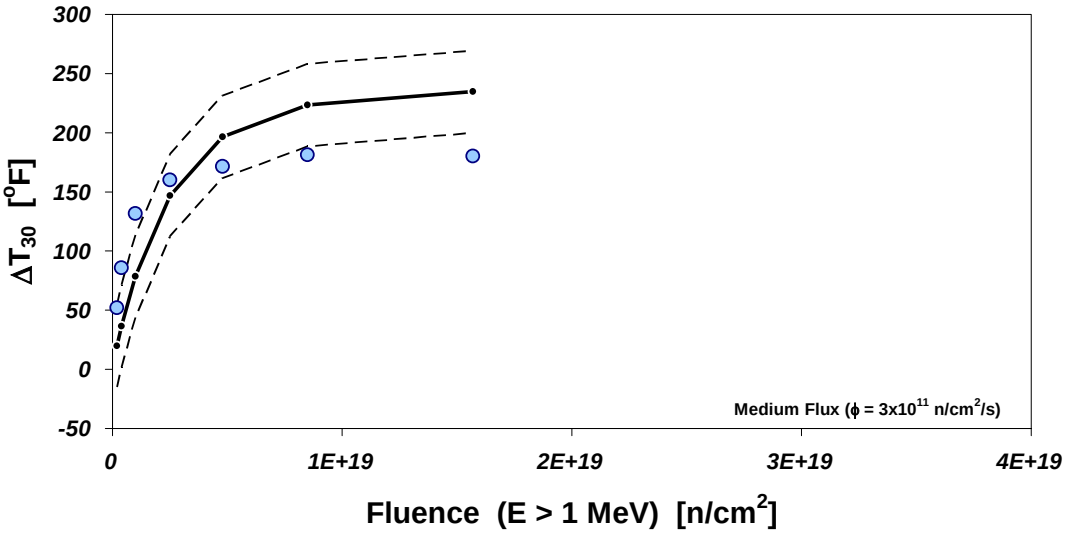
Medium Flux (ϕ = 3x10^11 n/cm^2/s)
ΔT30 [°F]
300
250
200
150
100
50
0
-50
0
1E+19
2E+19
3E+19
4E+19
Fluence (E > 1 MeV) [n/cm^2]

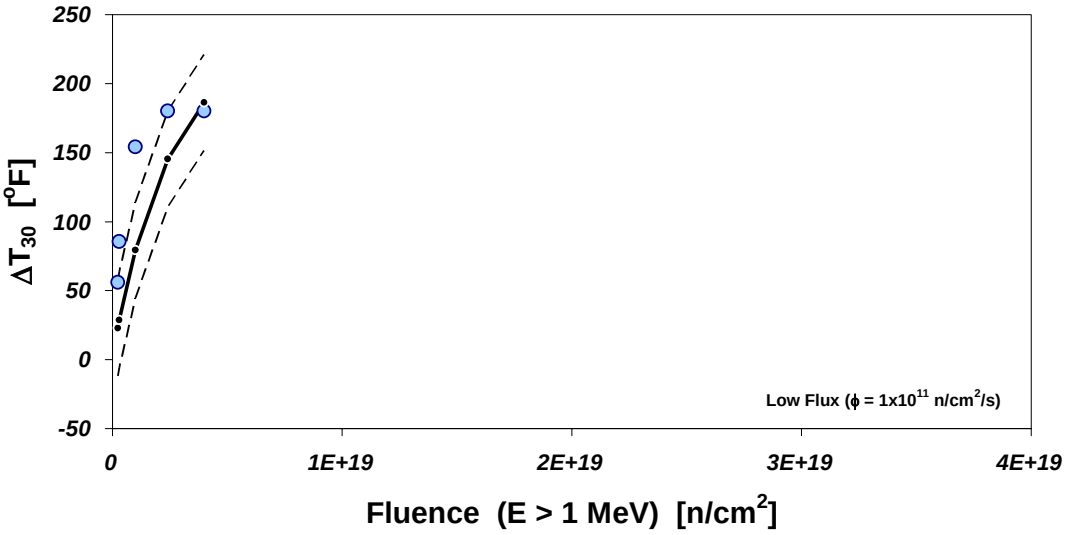
Low Flux (ϕ = 1x10^11 n/cm^2/s)
ΔT30 [°F]
250
200
150
100
50
0
-50
0
1E+19
2E+19
3E+19
4E+19
Fluence (E > 1 MeV) [n/cm^2]

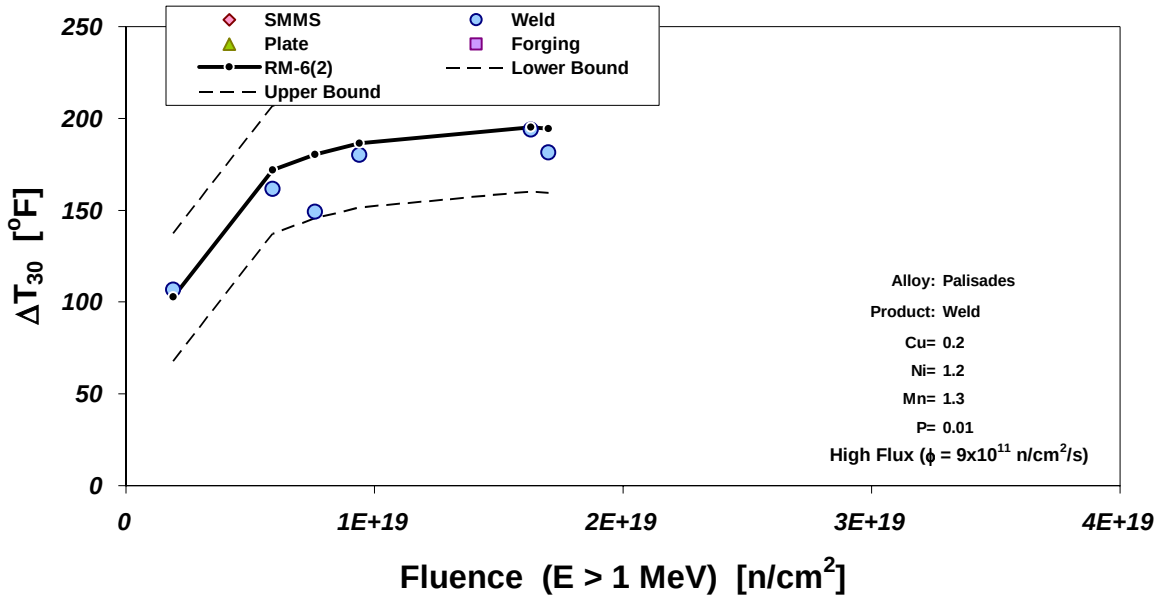

No data reported in IVAR at medium or low flux for this alloy.

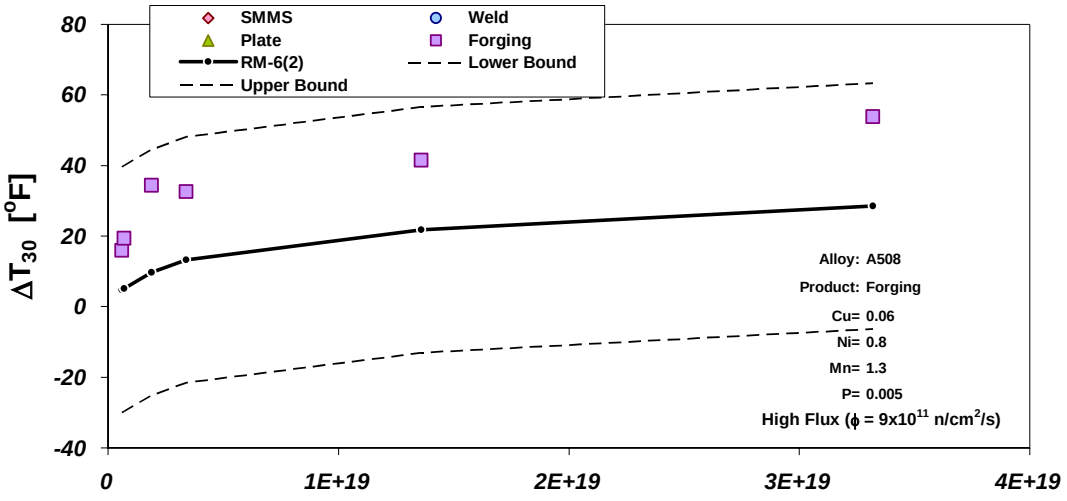
SMMS
Weld
Plate
Forging
RM-6(2)
Lower Bound
Upper Bound
Alloy: A508
Product: Forging
Cu= 0.06
Ni= 0.8
Mn= 1.3
P= 0.005
High Flux (ϕ = 9x10^11 n/cm^2/s)
ΔT30 [°F]
80
60
40
20
0
-20
-40
0
1E+19
2E+19
3E+19
4E+19
Fluence (E > 1 MeV) [n/cm^2]

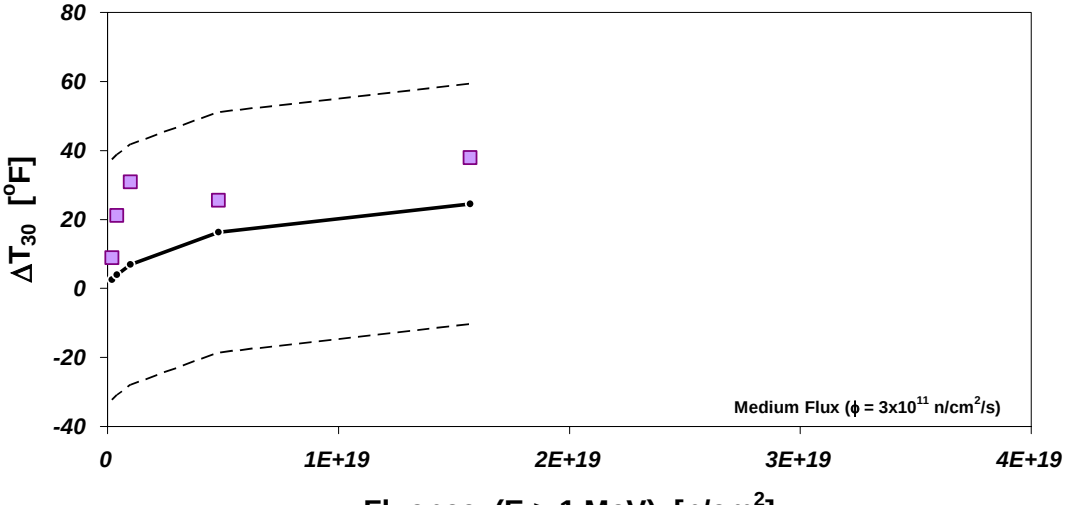
Medium Flux (ϕ = 3x10^11 n/cm^2/s)
ΔT30 [°F]
80
60
40
20
0
-20
-40
0
1E+19
2E+19
3E+19
4E+19
Fluence (E > 1 MeV) [n/cm^2]

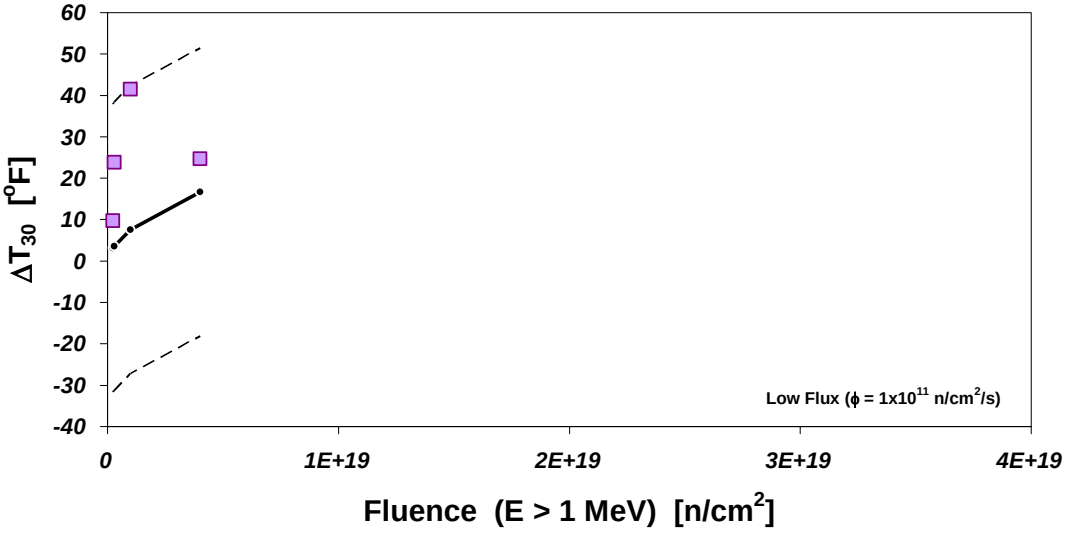
Low Flux (ϕ = 1x10^11 n/cm^2/s)
ΔT30 [°F]
60
50
40
30
20
10
0
-10
-20
-30
-40
0
1E+19
2E+19
3E+19
4E+19
Fluence (E > 1 MeV) [n/cm^2]

Table of RADAMO Chemistry Values

Alloy	Product Form	Composition [wt-%]				
		Cu	Ni	Mn	P	Si
16MND5	forging	0.065	0.69	1.37	0.013	0.04
18MND5-BM	plate	0.13	0.64	1.55	0.008	0.25
18MND5-W	weld	0.12	1.01	1.3	0.021	0.19
20MnMoNi55	forging	0.11	0.8	1.29	0.007	0.2
72W	weld	0.23	0.6	1.6	0.006	0.44
73W	weld	0.31	0.6	1.56	0.005	0.45
A508-B	forging	0.05	0.75	1.43	0.008	0.28
A508-W	weld	0.07	0.83	1.57	0.015	0.22
HSST-03	plate	0.12	0.62	1.36	0.011	0.26
JRQ	plate	0.14	0.84	1.42	0.017	0.24
VVER-1000B	plate	0.05	1.26	0.46	0.008	0.3
VVER-1000W	weld	0.06	1.7	0.73	0.006	0.14
VVER-440B	plate	0.08	0.12	0.4	0.012	0.29
VVER-440W	weld	0.13	0.12	0.97	0.032	0.5

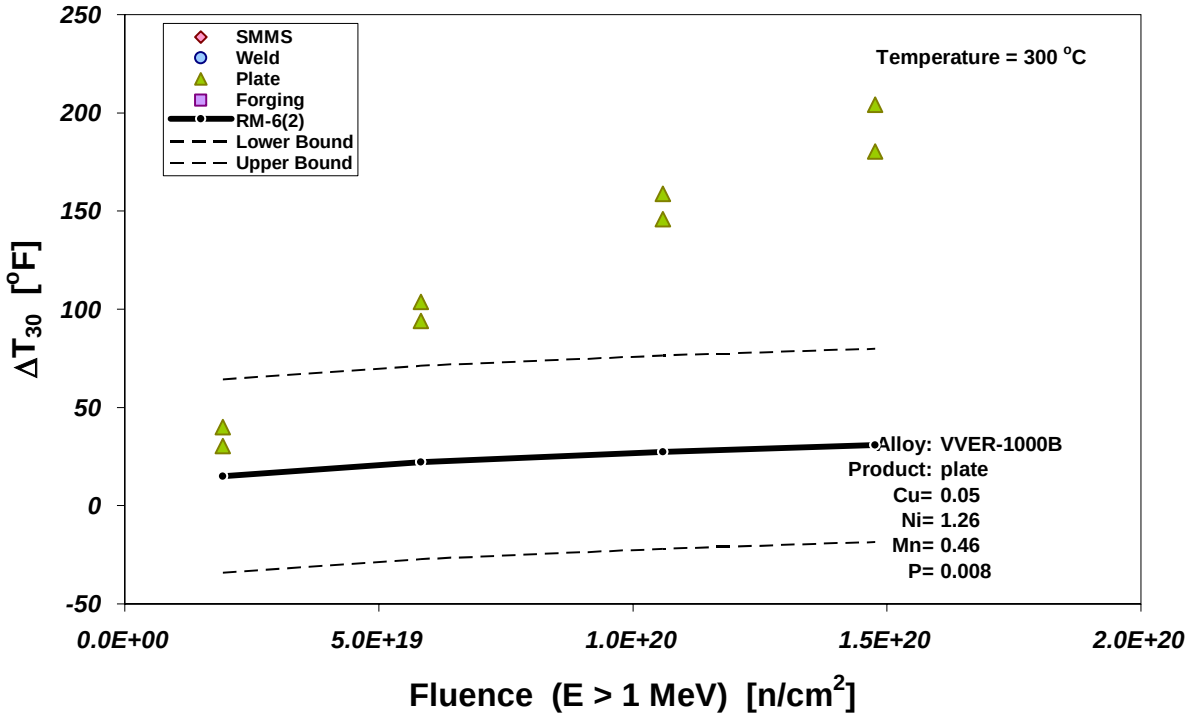
SMMS
Weld
Plate
Forging
RM-6(2)
Lower Bound
Upper Bound
Temperature = 300 °C
Alloy: VVER-1000B
Product: plate
Cu= 0.05
Ni= 1.26
Mn= 0.46
P= 0.008
250
200
150
100
50
0
-50
0.0E+00
5.0E+19
1.0E+20
1.5E+20
2.0E+20
ΔT30 [°F]
Fluence (E > 1 MeV) [n/cm2]

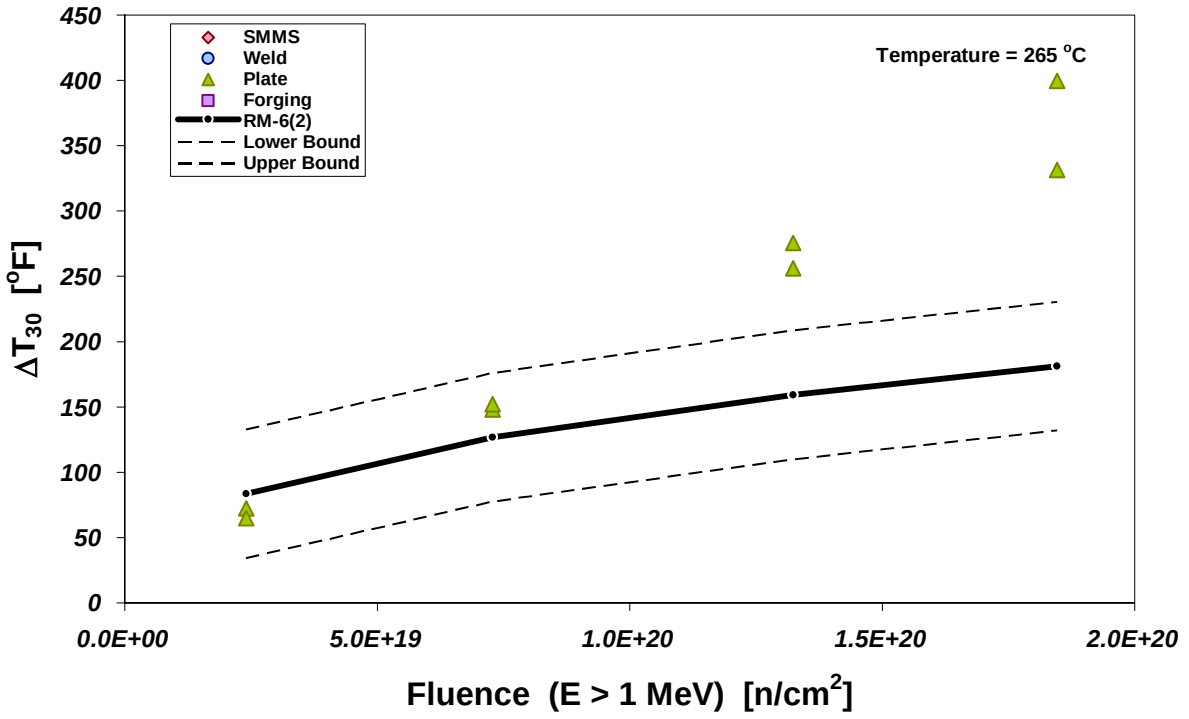
SMMS
Weld
Plate
Forging
RM-6(2)
Lower Bound
Upper Bound
Temperature = 265 °C
450
400
350
300
250
200
150
100
50
0
0.0E+00
5.0E+19
1.0E+20
1.5E+20
2.0E+20
ΔT30 [°F]
Fluence (E > 1 MeV) [n/cm2]

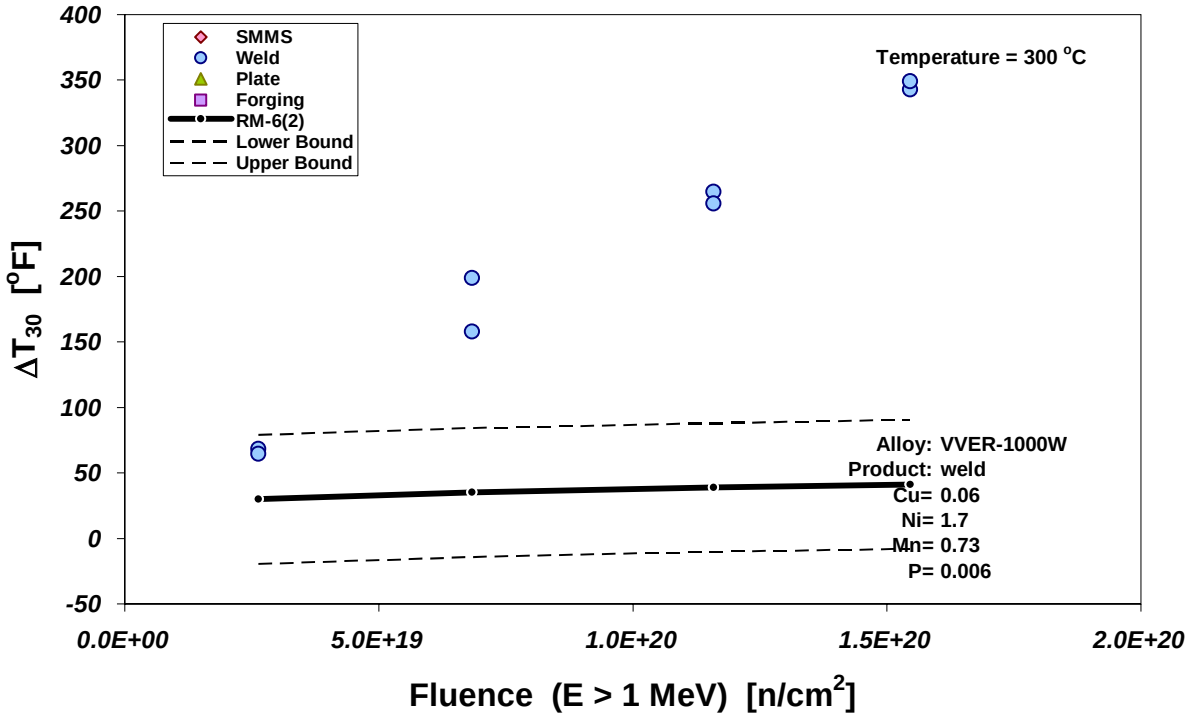
SMMS
Weld
Plate
Forging
RM-6(2)
Lower Bound
Upper Bound
Temperature = 300 °C
Alloy: VVER-1000W
Product: weld
Cu= 0.06
Ni= 1.7
Mn= 0.73
P= 0.006
ΔT30 [°F]
400
350
300
250
200
150
100
50
0
-50
0.0E+00
5.0E+19
1.0E+20
1.5E+20
2.0E+20
Fluence (E > 1 MeV) [n/cm2]

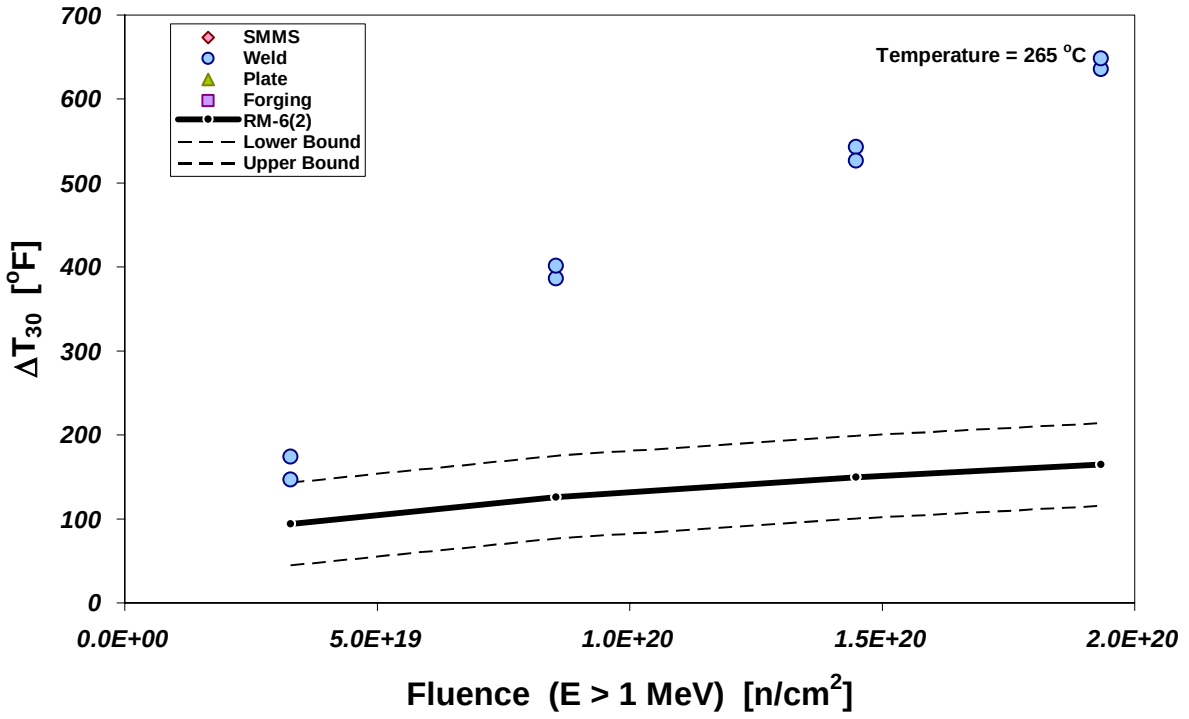
SMMS
Weld
Plate
Forging
RM-6(2)
Lower Bound
Upper Bound
Temperature = 265 °C
ΔT30 [°F]
700
600
500
400
300
200
100
0
0.0E+00
5.0E+19
1.0E+20
1.5E+20
2.0E+20
Fluence (E > 1 MeV) [n/cm2]

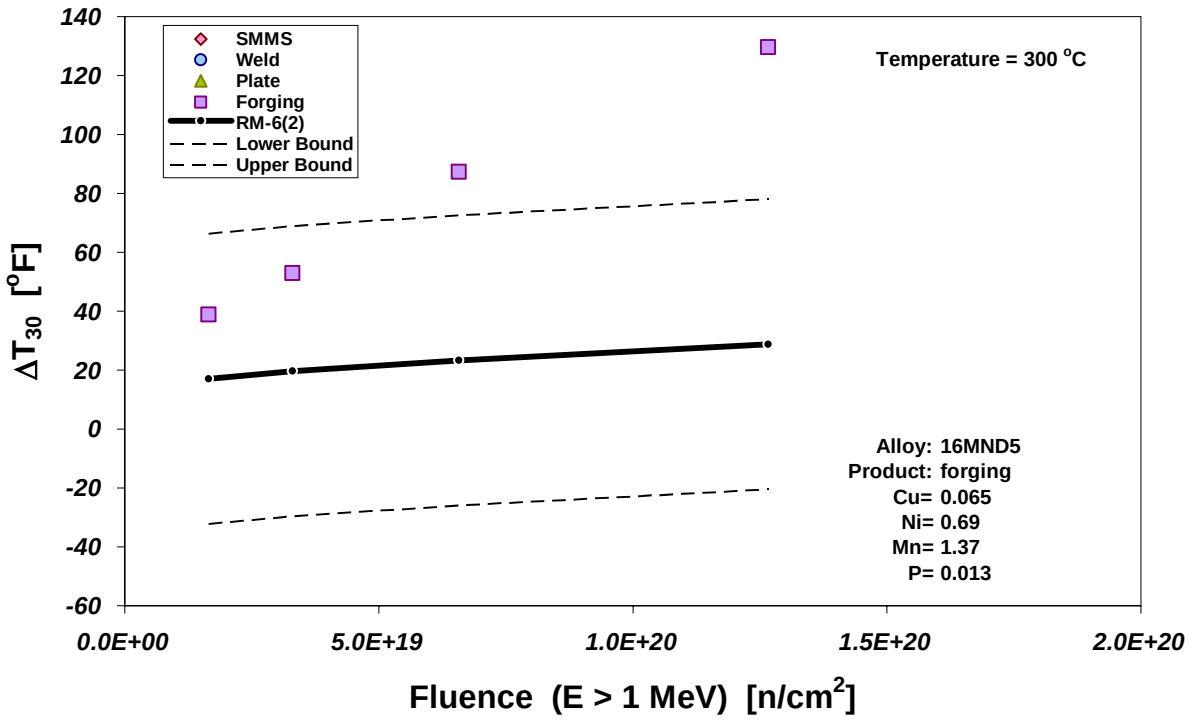

No data reported in RADAMO at 265 °C for this alloy.

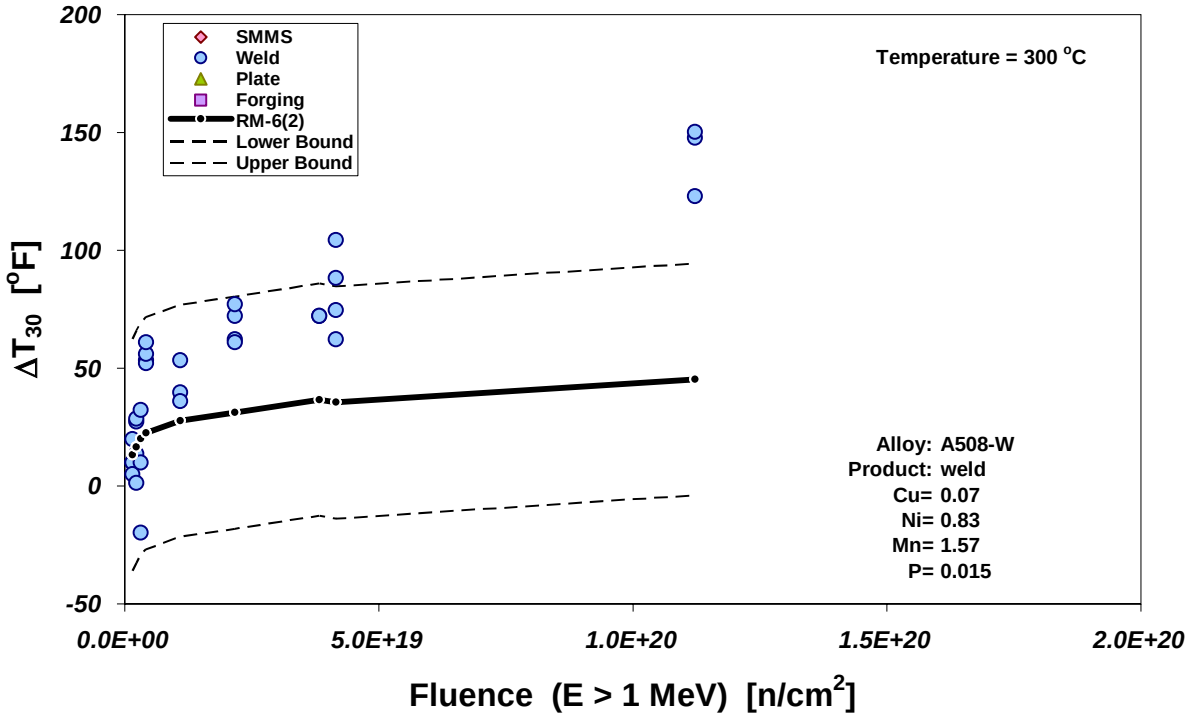
SMMS
Weld
Plate
Forging
RM-6(2)
Lower Bound
Upper Bound
Temperature = 300 °C
Alloy: A508-W
Product: weld
Cu= 0.07
Ni= 0.83
Mn= 1.57
P= 0.015
ΔT30 [°F]
200
150
100
50
0
-50
0.0E+00
5.0E+19
1.0E+20
1.5E+20
2.0E+20
Fluence (E > 1 MeV) [n/cm2]

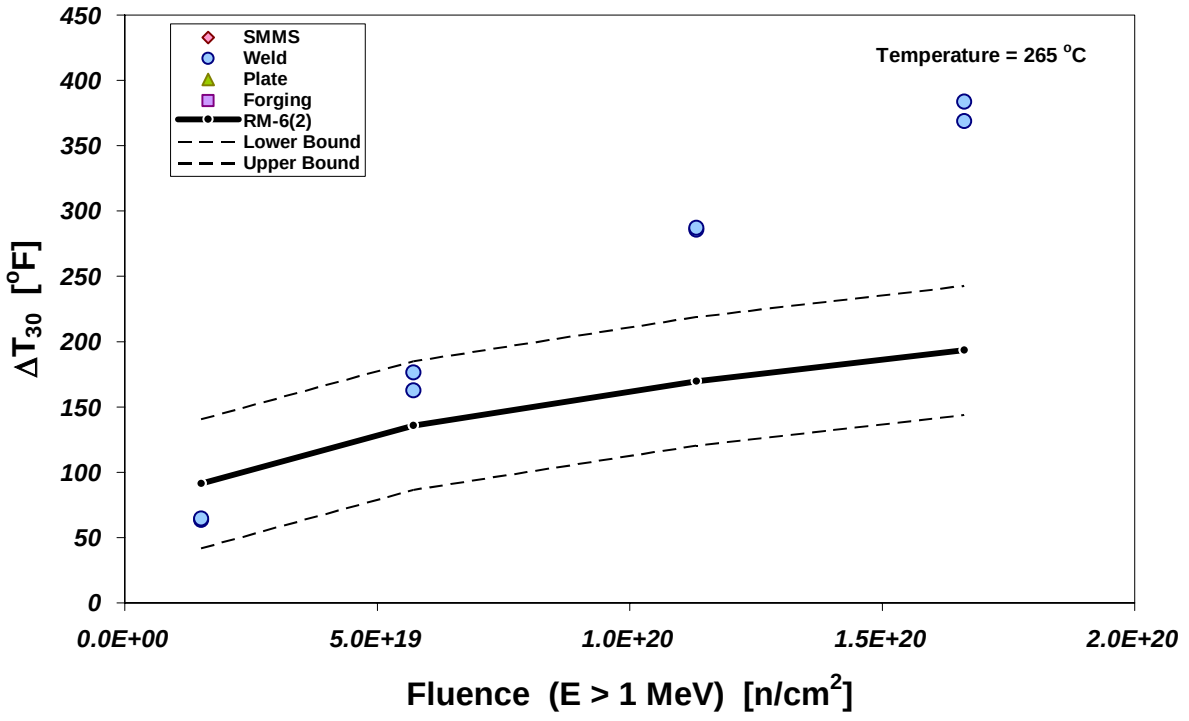
SMMS
Weld
Plate
Forging
RM-6(2)
Lower Bound
Upper Bound
Temperature = 265 °C
ΔT30 [°F]
450
400
350
300
250
200
150
100
50
0
0.0E+00
5.0E+19
1.0E+20
1.5E+20
2.0E+20
Fluence (E > 1 MeV) [n/cm2]

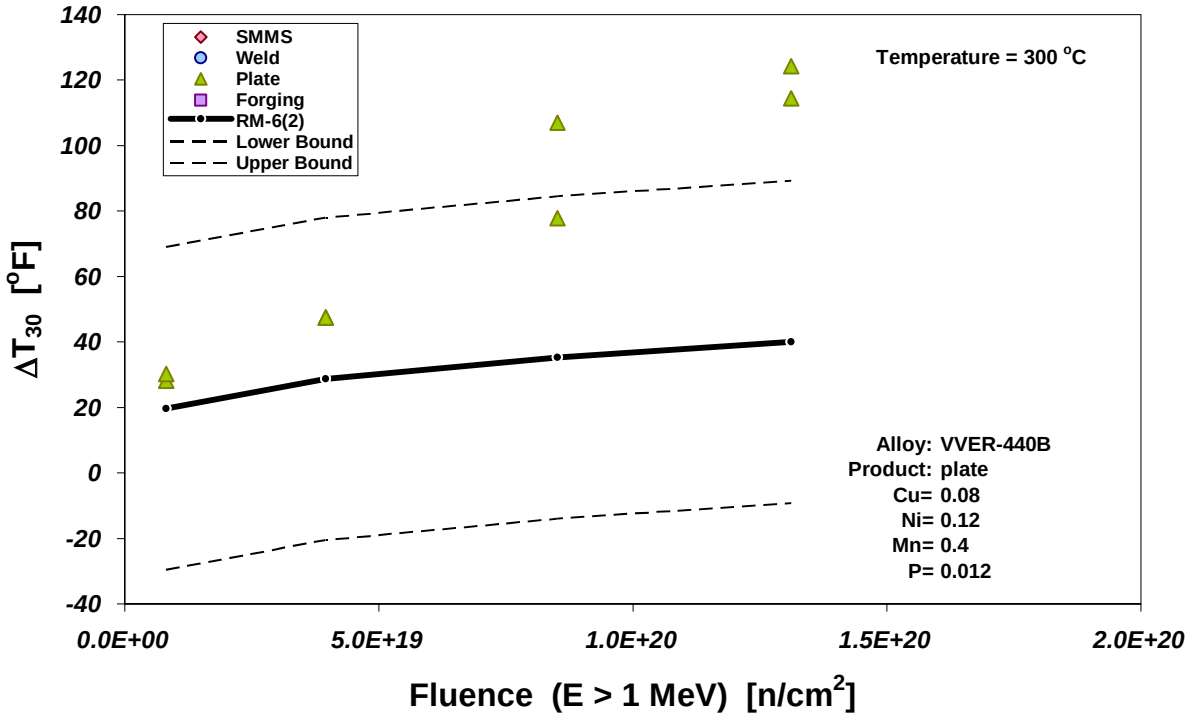
SMMS
Weld
Plate
Forging
RM-6(2)
Lower Bound
Upper Bound
Temperature = 300 °C
Alloy: VVER-440B
Product: plate
Cu= 0.08
Ni= 0.12
Mn= 0.4
P= 0.012
ΔT30 [°F]
140
120
100
80
60
40
20
0
-20
-40
0.0E+00
5.0E+19
1.0E+20
1.5E+20
2.0E+20
Fluence (E > 1 MeV) [n/cm2]

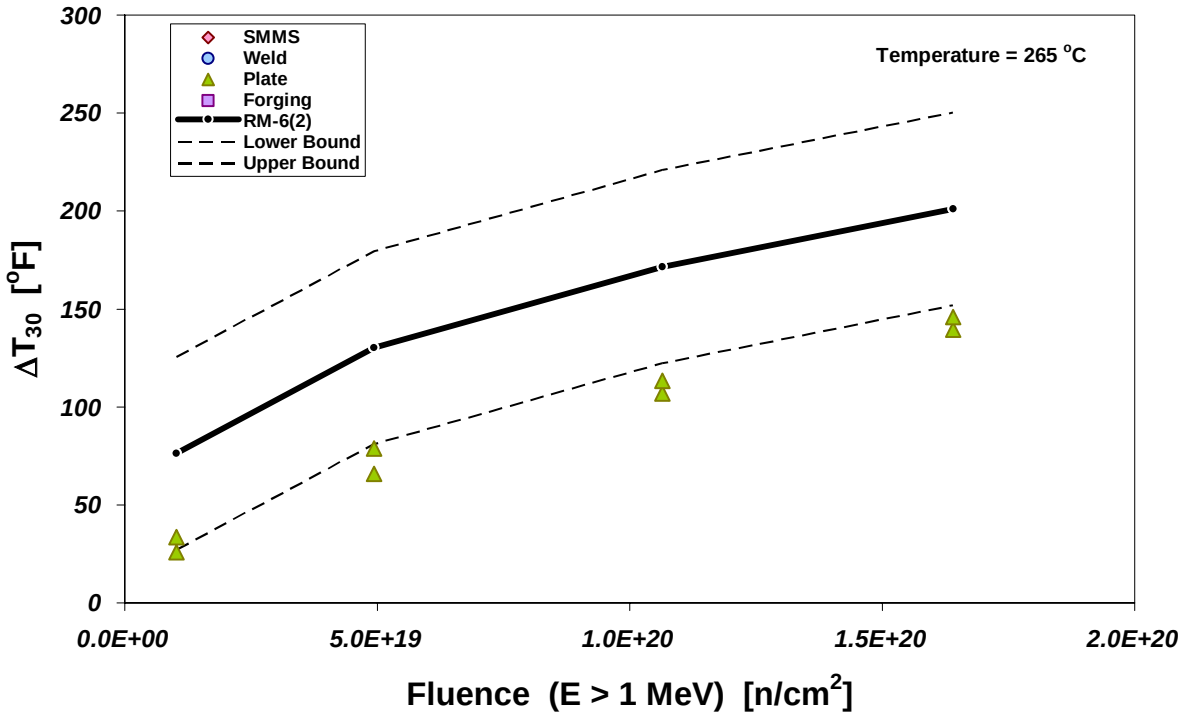
SMMS
Weld
Plate
Forging
RM-6(2)
Lower Bound
Upper Bound
Temperature = 265 °C
ΔT30 [°F]
300
250
200
150
100
50
0
0.0E+00
5.0E+19
1.0E+20
1.5E+20
2.0E+20
Fluence (E > 1 MeV) [n/cm2]

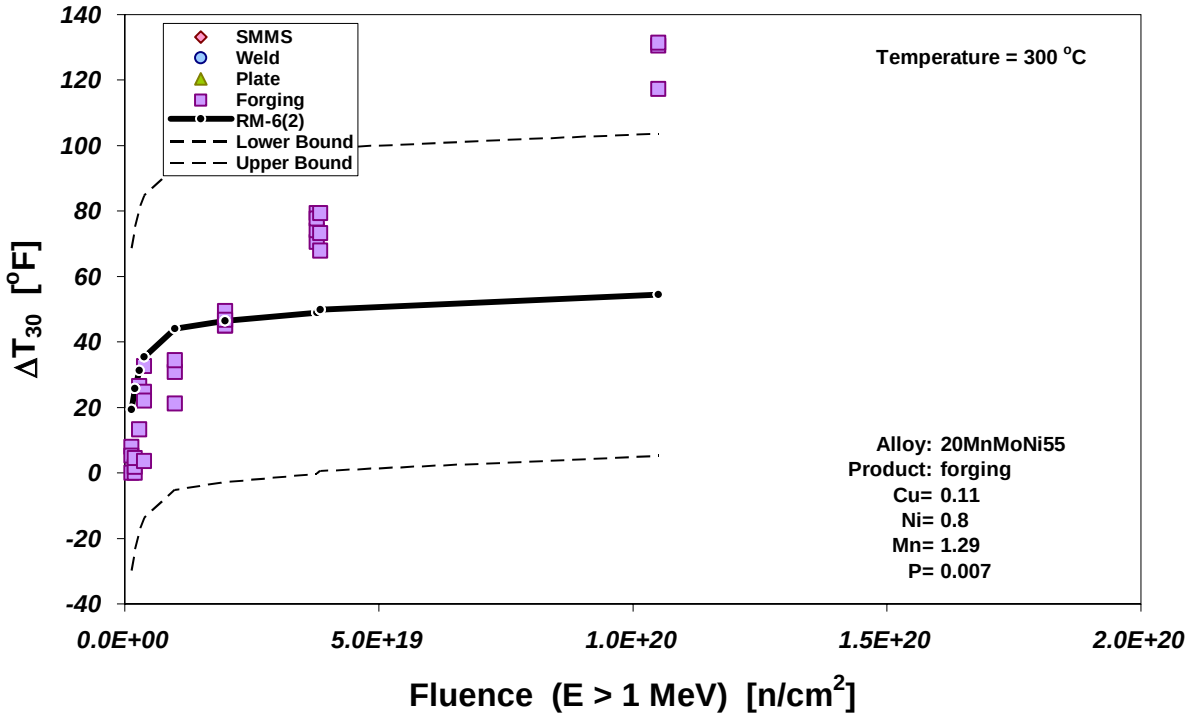
SMMS
Weld
Plate
Forging
RM-6(2)
Lower Bound
Upper Bound
Temperature = 300 °C
Alloy: 20MnMoNi55
Product: forging
Cu= 0.11
Ni= 0.8
Mn= 1.29
P= 0.007
ΔT30 [°F]
140
120
100
80
60
40
20
0
-20
-40
0.0E+00
5.0E+19
1.0E+20
1.5E+20
2.0E+20
Fluence (E > 1 MeV) [n/cm2]

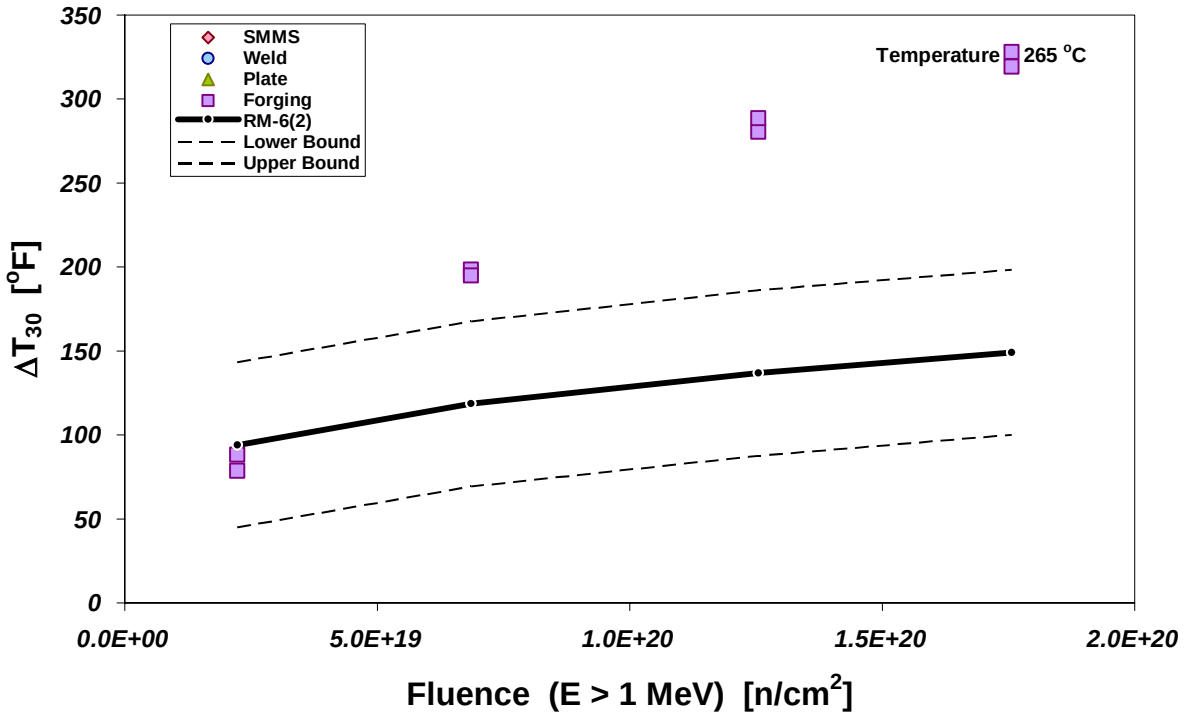
SMMS
Weld
Plate
Forging
RM-6(2)
Lower Bound
Upper Bound
Temperature 265 °C
ΔT30 [°F]
350
300
250
200
150
100
50
0
0.0E+00
5.0E+19
1.0E+20
1.5E+20
2.0E+20
Fluence (E > 1 MeV) [n/cm2]

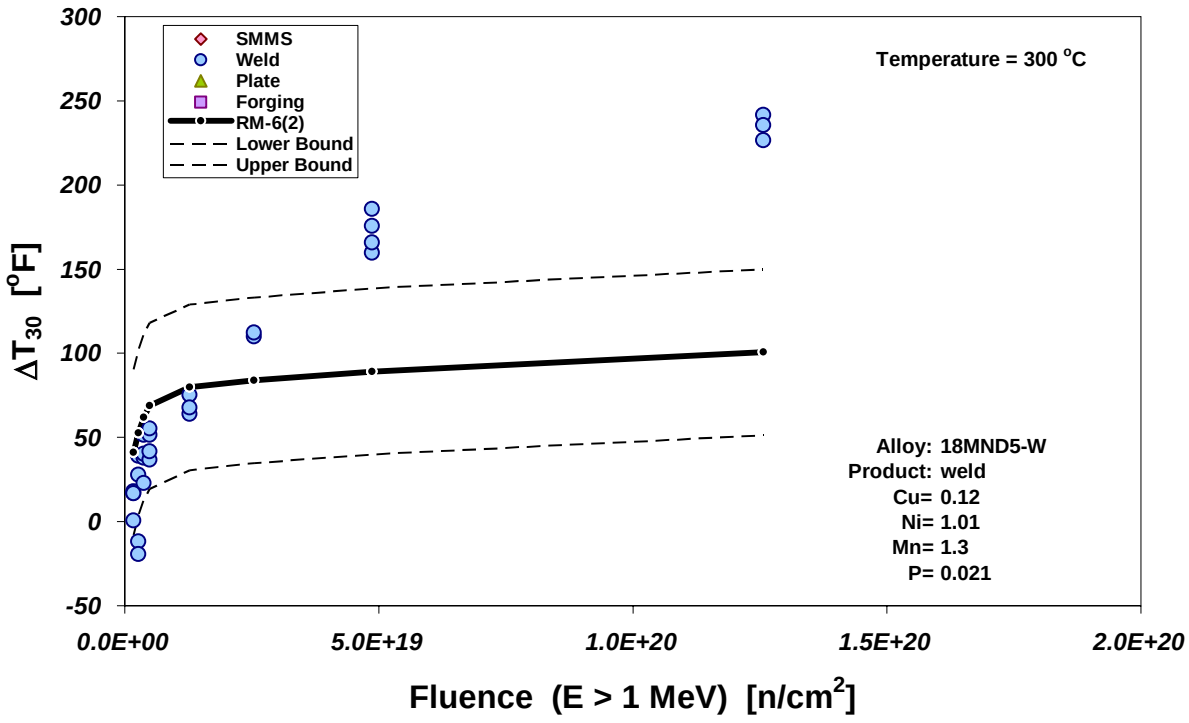

No data reported in RADAMO at 265 °C for this alloy.

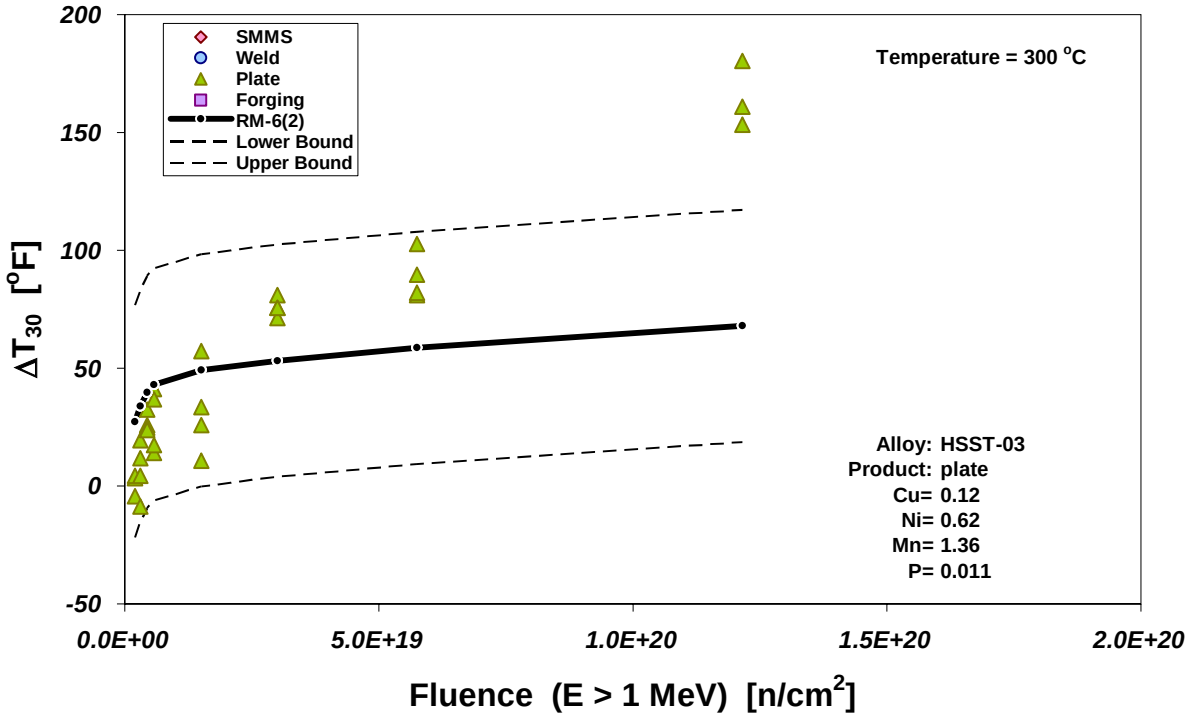
SMMS
Weld
Plate
Forging
RM-6(2)
Lower Bound
Upper Bound
Temperature = 300 °C
Alloy: HSST-03
Product: plate
Cu= 0.12
Ni= 0.62
Mn= 1.36
P= 0.011
200
150
100
50
0
-50
0.0E+00
5.0E+19
1.0E+20
1.5E+20
2.0E+20
ΔT30 [°F]
Fluence (E > 1 MeV) [n/cm2]

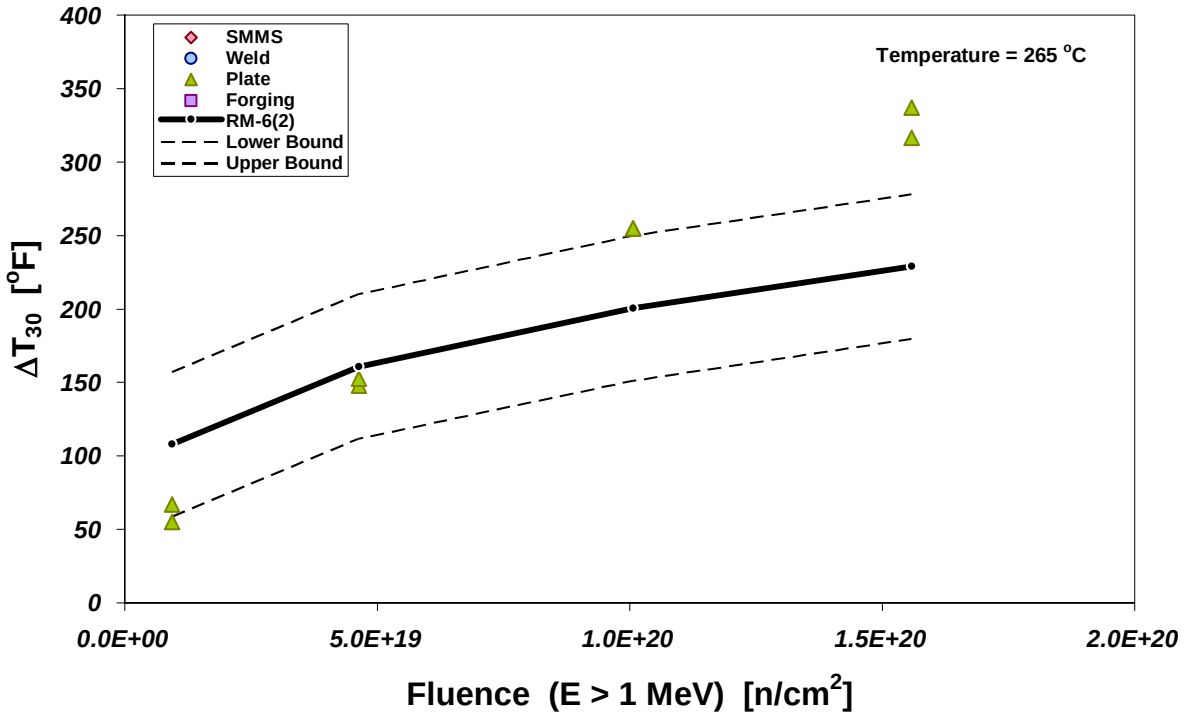
SMMS
Weld
Plate
Forging
RM-6(2)
Lower Bound
Upper Bound
Temperature = 265 °C
400
350
300
250
200
150
100
50
0
0.0E+00
5.0E+19
1.0E+20
1.5E+20
2.0E+20
ΔT30 [°F]
Fluence (E > 1 MeV) [n/cm2]

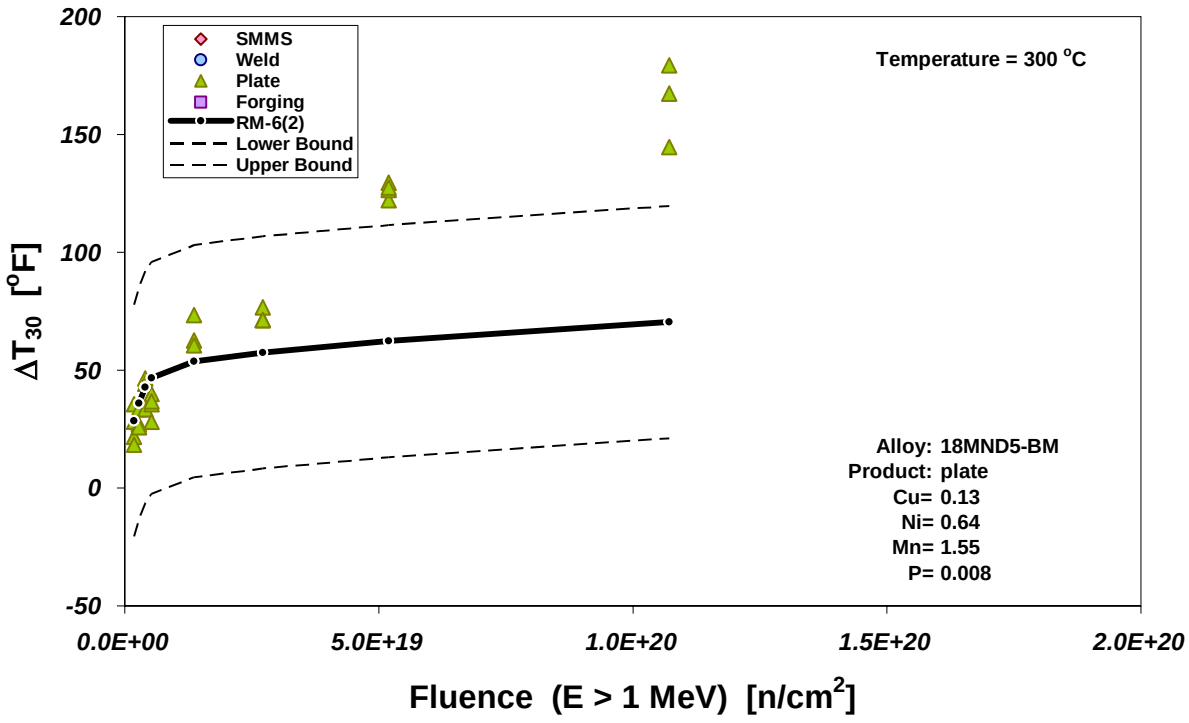
SMMS
Weld
Plate
Forging
RM-6(2)
Lower Bound
Upper Bound
Temperature = 300 °C
Alloy: 18MND5-BM
Product: plate
Cu= 0.13
Ni= 0.64
Mn= 1.55
P= 0.008
ΔT30 [°F]
200
150
100
50
0
-50
0.0E+00
5.0E+19
1.0E+20
1.5E+20
2.0E+20
Fluence (E > 1 MeV) [n/cm2]

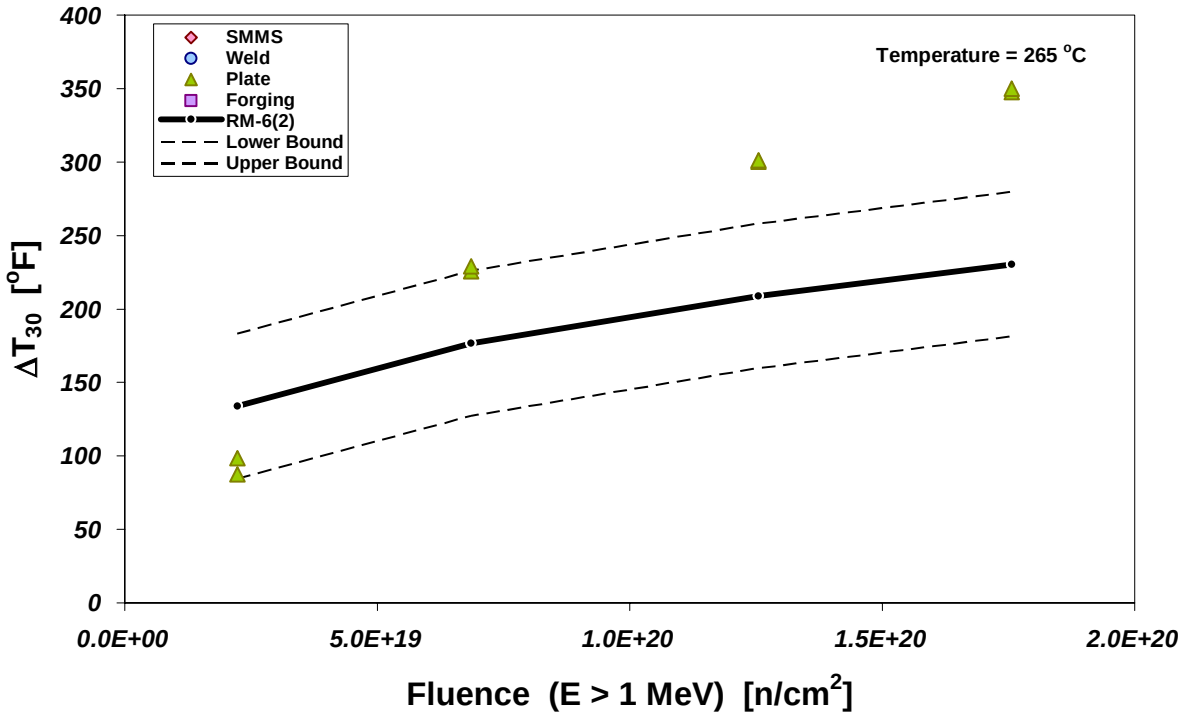
SMMS
Weld
Plate
Forging
RM-6(2)
Lower Bound
Upper Bound
Temperature = 265 °C
ΔT30 [°F]
400
350
300
250
200
150
100
50
0
0.0E+00
5.0E+19
1.0E+20
1.5E+20
2.0E+20
Fluence (E > 1 MeV) [n/cm2]

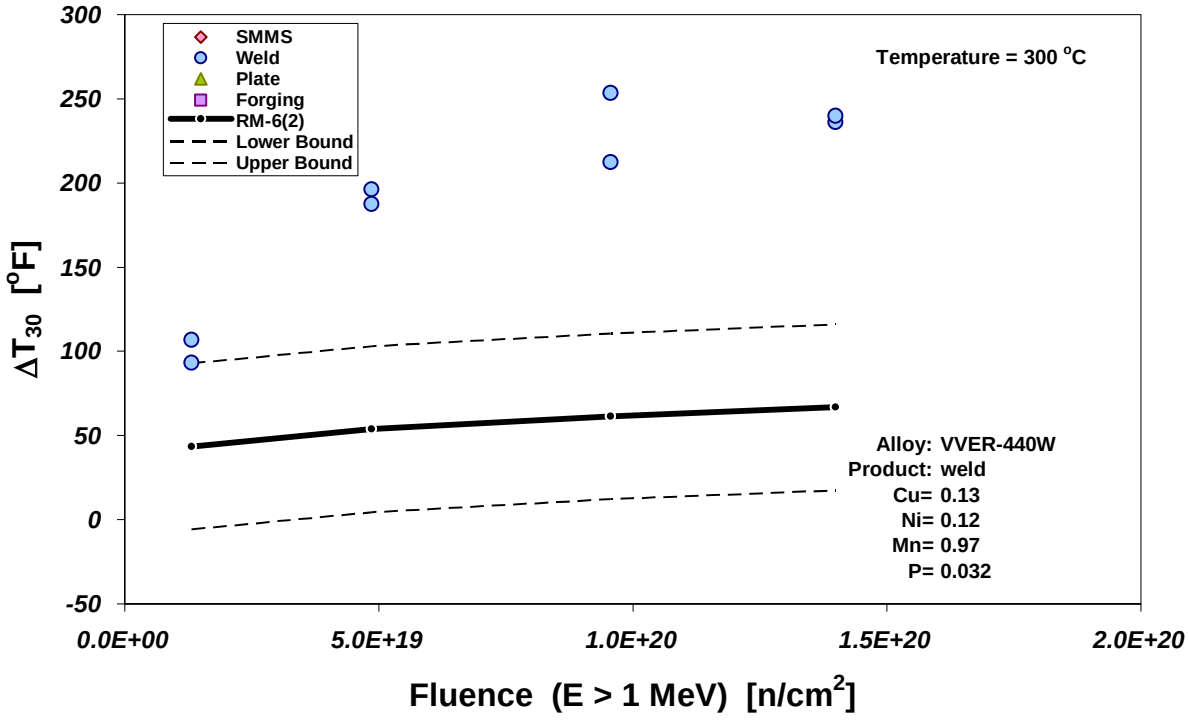
SMMS
Weld
Plate
Forging
RM-6(2)
Lower Bound
Upper Bound
Temperature = 300 °C
Alloy: VVER-440W
Product: weld
Cu= 0.13
Ni= 0.12
Mn= 0.97
P= 0.032
ΔT30 [°F]
300
250
200
150
100
50
0
-50
0.0E+00
5.0E+19
1.0E+20
1.5E+20
2.0E+20
Fluence (E > 1 MeV) [n/cm2]

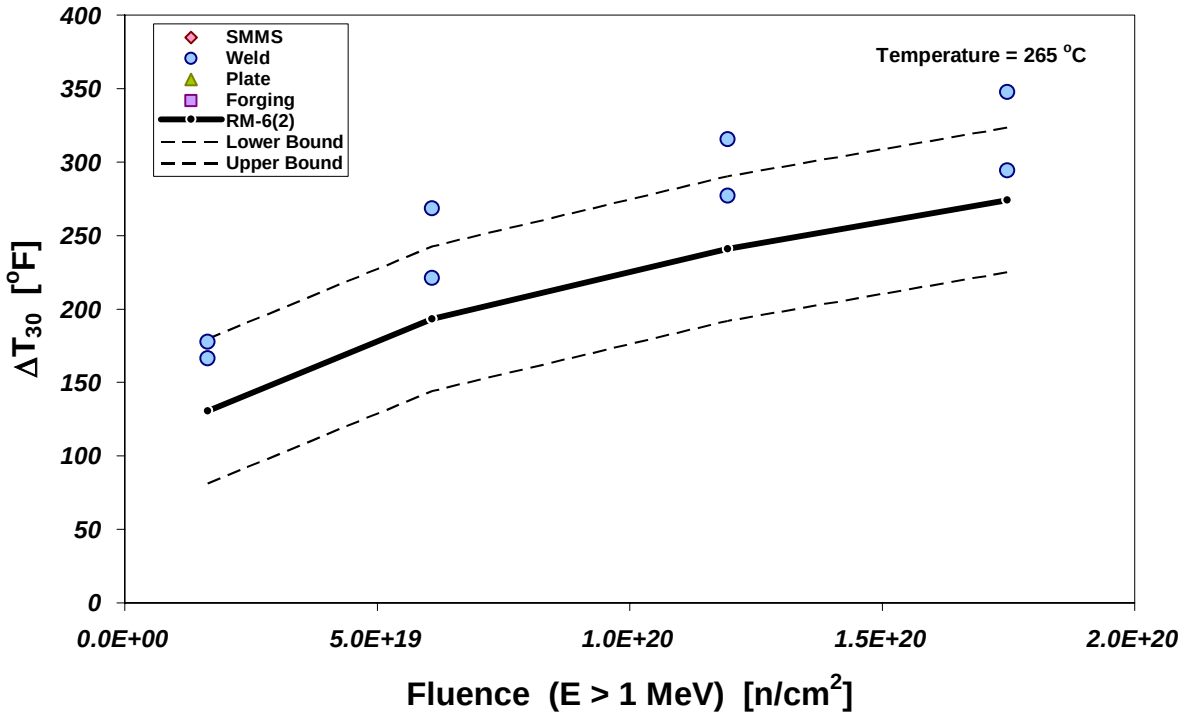
SMMS
Weld
Plate
Forging
RM-6(2)
Lower Bound
Upper Bound
Temperature = 265 °C
ΔT30 [°F]
400
350
300
250
200
150
100
50
0
0.0E+00
5.0E+19
1.0E+20
1.5E+20
2.0E+20
Fluence (E > 1 MeV) [n/cm2]

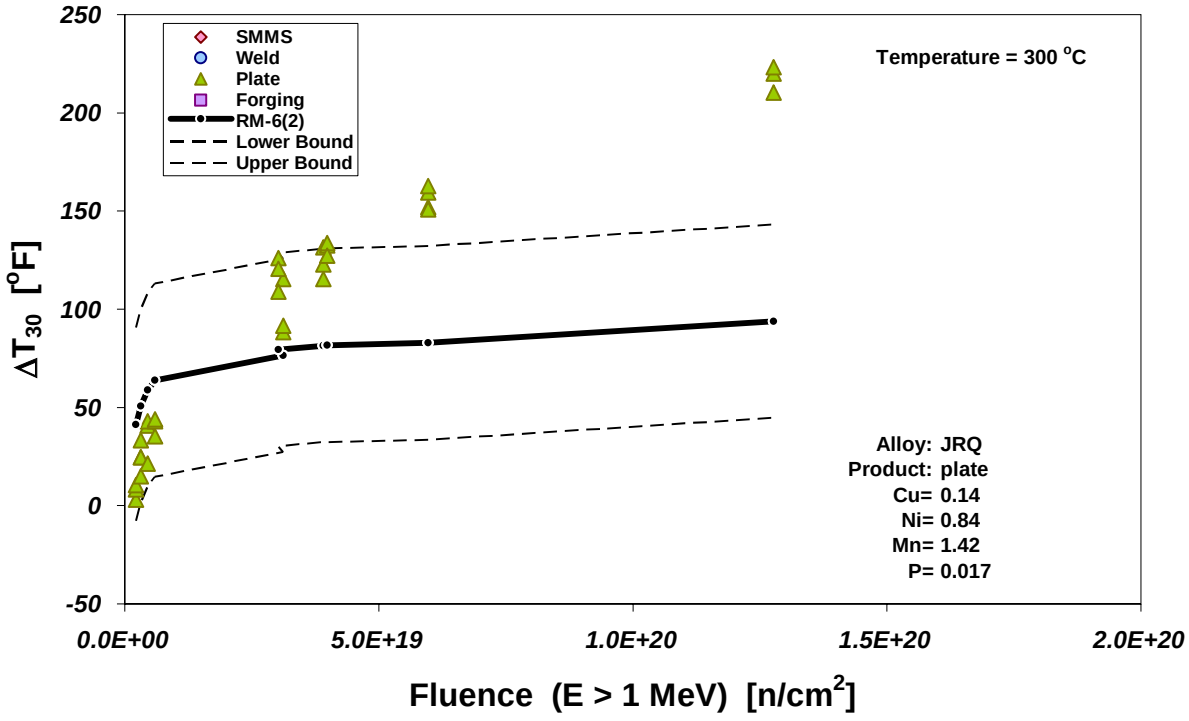
SMMS
Weld
Plate
Forging
RM-6(2)
Lower Bound
Upper Bound
Temperature = 300 °C
Alloy: JRQ
Product: plate
Cu= 0.14
Ni= 0.84
Mn= 1.42
P= 0.017
ΔT30 [°F]
250
200
150
100
50
0
-50
0.0E+00
5.0E+19
1.0E+20
1.5E+20
2.0E+20
Fluence (E > 1 MeV) [n/cm2]

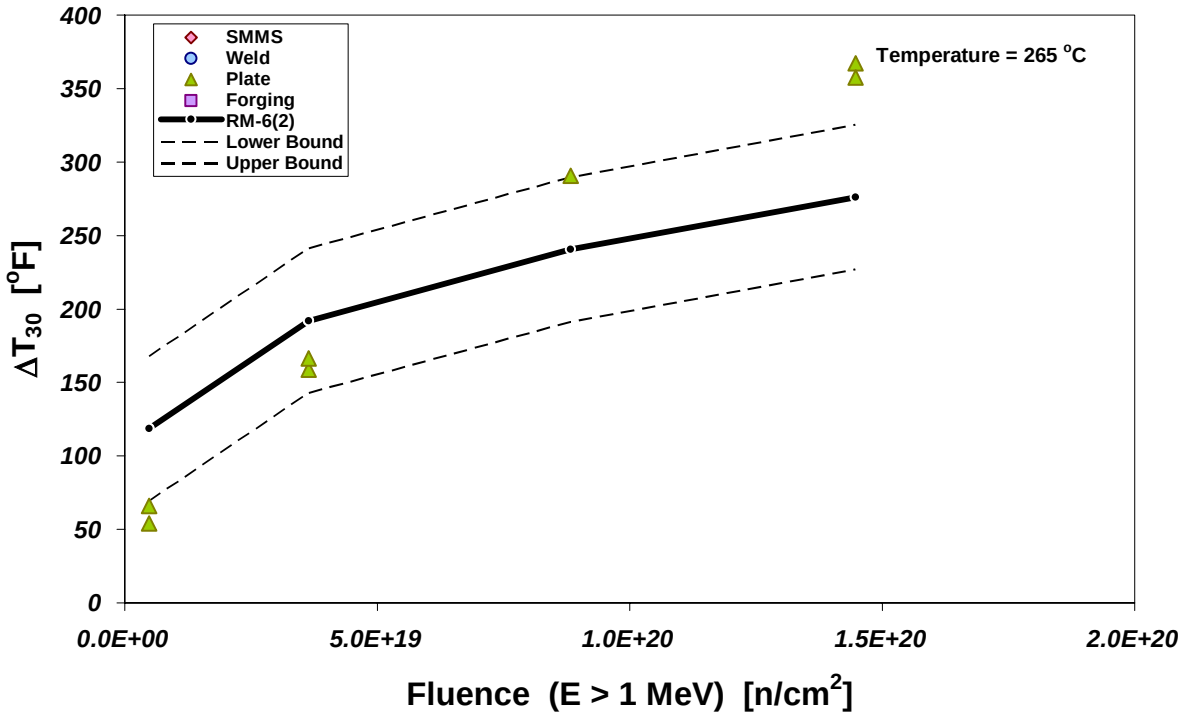
SMMS
Weld
Plate
Forging
RM-6(2)
Lower Bound
Upper Bound
Temperature = 265 °C
ΔT30 [°F]
400
350
300
250
200
150
100
50
0
0.0E+00
5.0E+19
1.0E+20
1.5E+20
2.0E+20
Fluence (E > 1 MeV) [n/cm2]

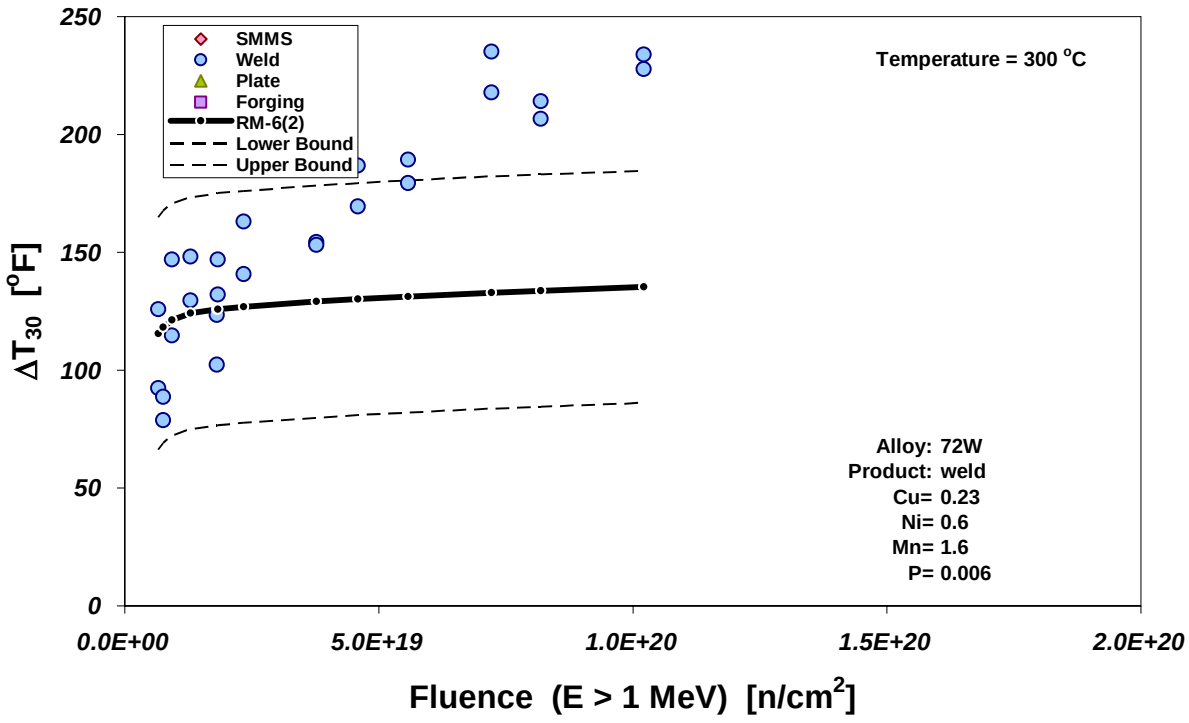
SMMS
Weld
Plate
Forging
RM-6(2)
Lower Bound
Upper Bound
Temperature = 300 °C
Alloy: 72W
Product: weld
Cu= 0.23
Ni= 0.6
Mn= 1.6
P= 0.006
ΔT30 [°F]
250
200
150
100
50
0
0.0E+00
5.0E+19
1.0E+20
1.5E+20
2.0E+20
Fluence (E > 1 MeV) [n/cm2]

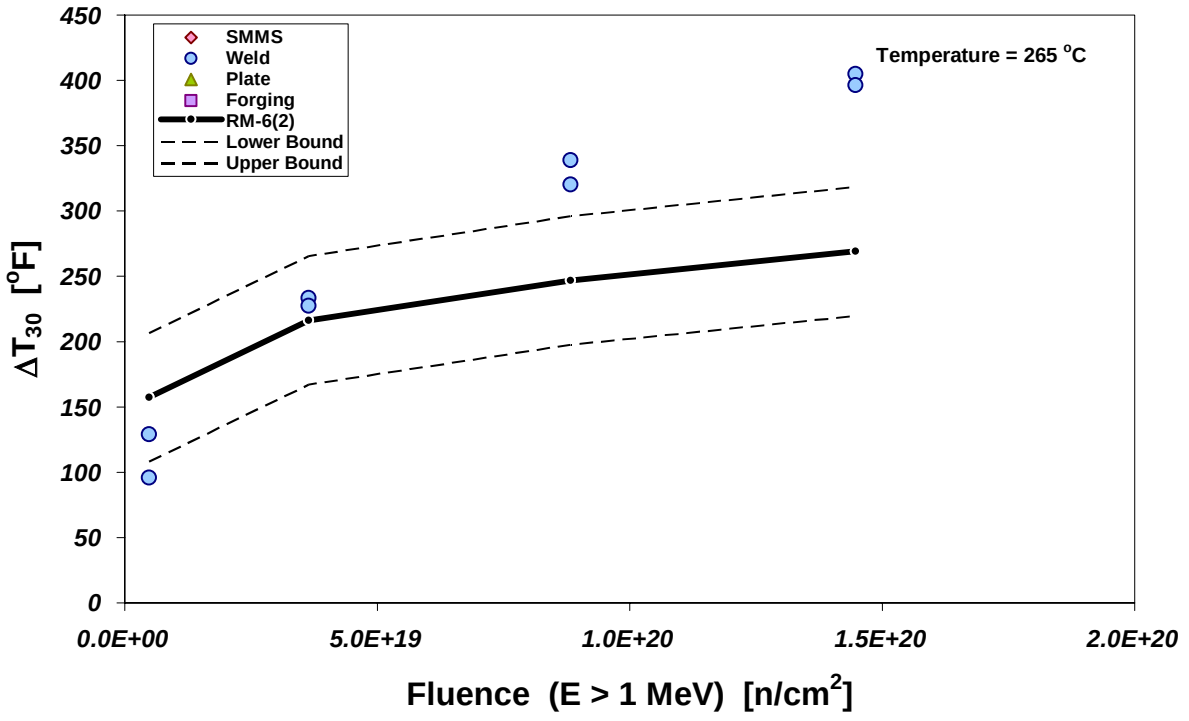
SMMS
Weld
Plate
Forging
RM-6(2)
Lower Bound
Upper Bound
Temperature = 265 °C
ΔT30 [°F]
450
400
350
300
250
200
150
100
50
0
0.0E+00
5.0E+19
1.0E+20
1.5E+20
2.0E+20
Fluence (E > 1 MeV) [n/cm2]

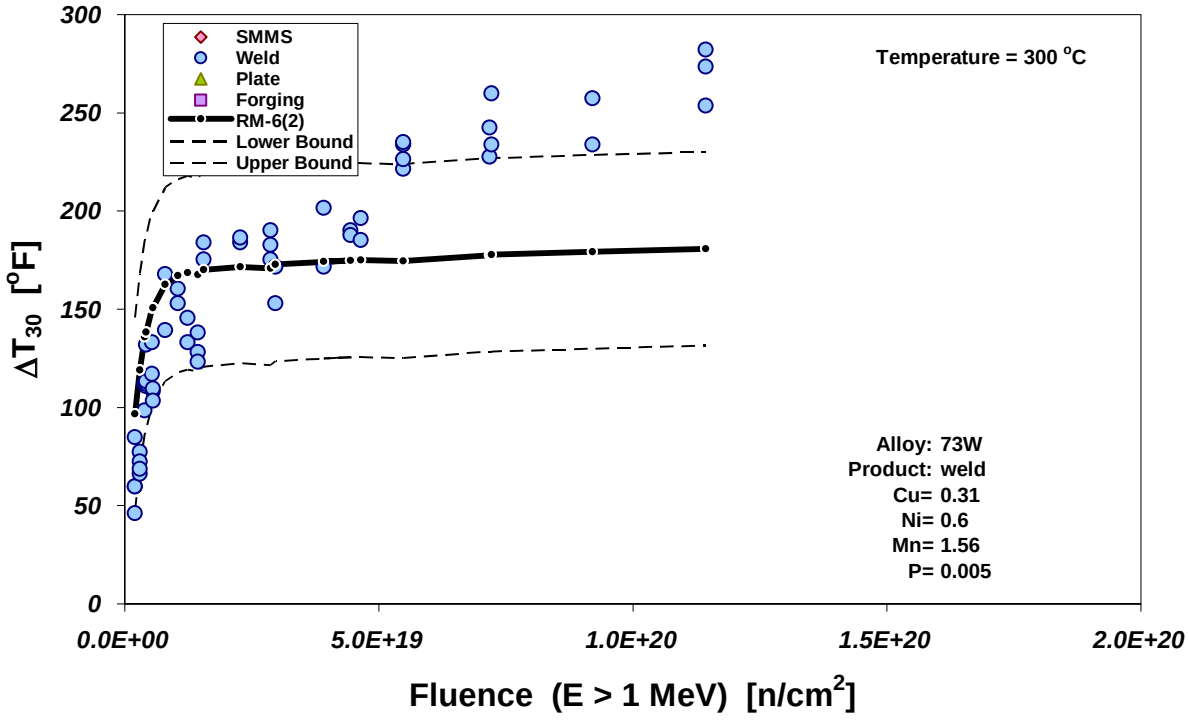
SMMS
Weld
Plate
Forging
RM-6(2)
Lower Bound
Upper Bound
Temperature = 300 °C
Alloy: 73W
Product: weld
Cu= 0.31
Ni= 0.6
Mn= 1.56
P= 0.005
ΔT30 [°F]
300
250
200
150
100
50
0
0.0E+00
5.0E+19
1.0E+20
1.5E+20
2.0E+20
Fluence (E > 1 MeV) [n/cm2]

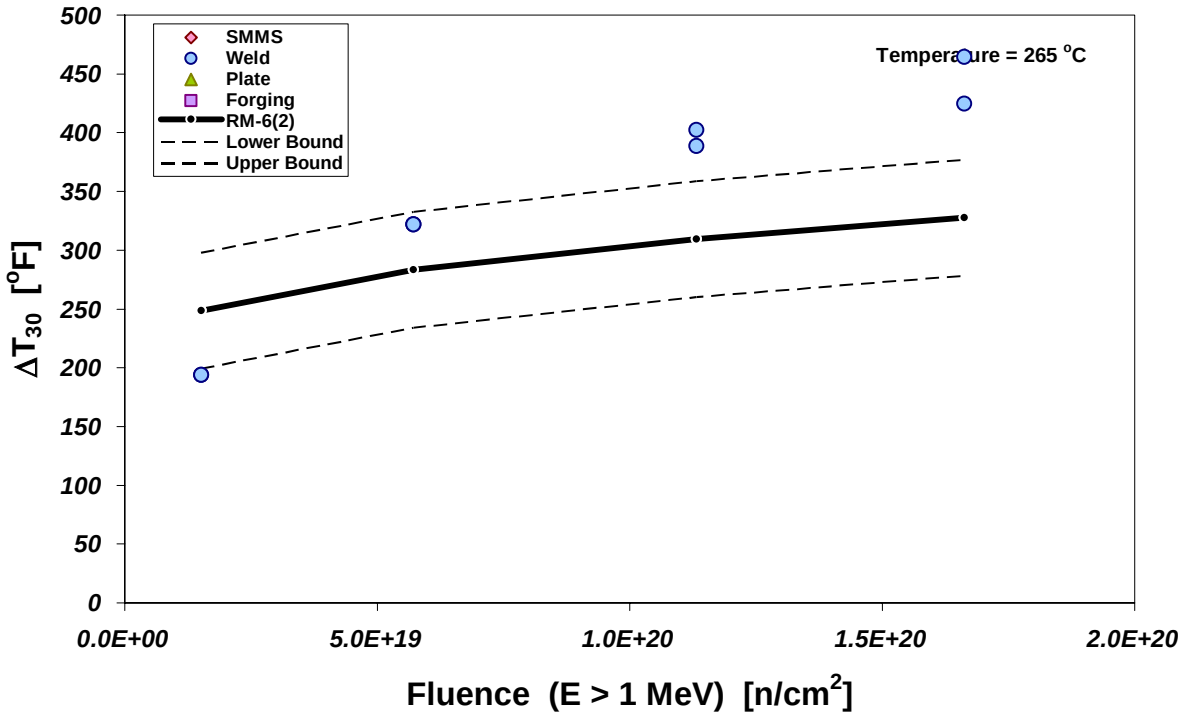
SMMS
Weld
Plate
Forging
RM-6(2)
Lower Bound
Upper Bound
Temperature = 265 °C
ΔT30 [°F]
500
450
400
350
300
250
200
150
100
50
0
0.0E+00
5.0E+19
1.0E+20
1.5E+20
2.0E+20
Fluence (E > 1 MeV) [n/cm2]

Appendix E

Comparison of the Predictions of the RADAMO Trend Curve to Empirical Databases

Note: All graphs include PRP term, unless stated otherwise.

Residuals vs. Fluence

RADAMO vs. RADAMO

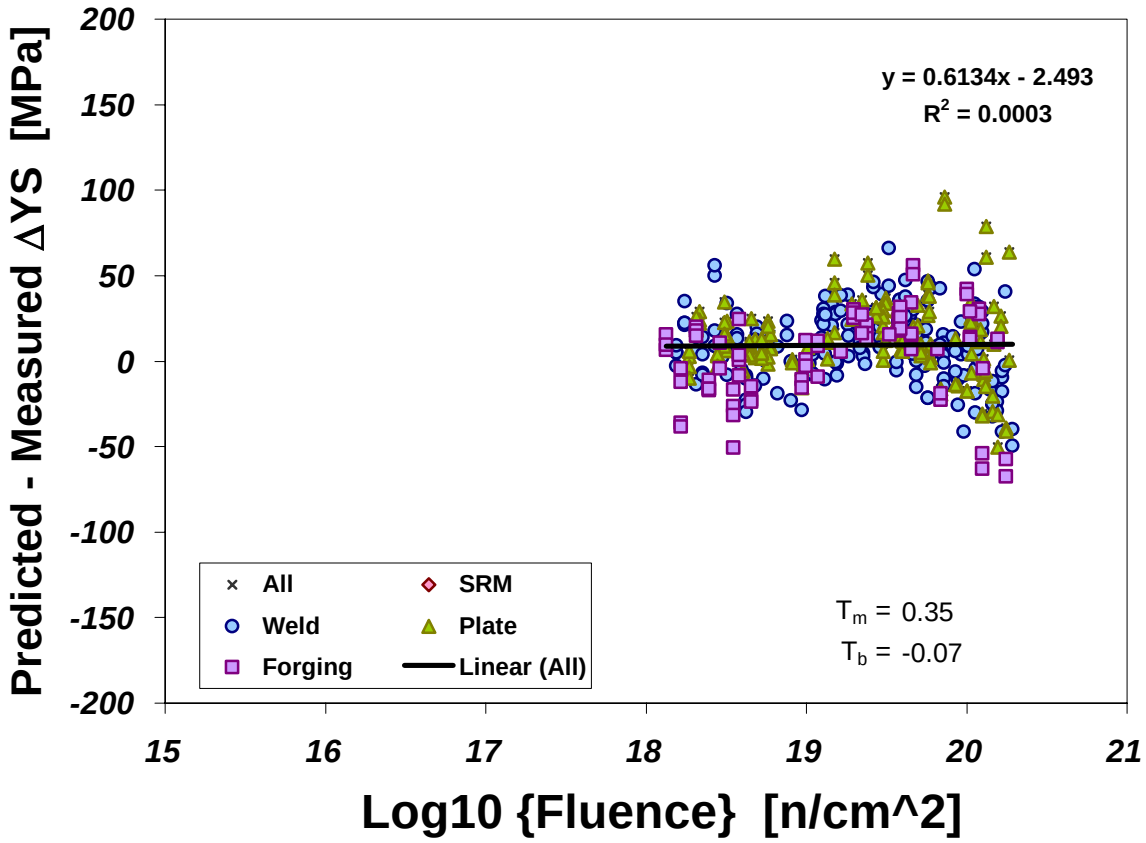

RADAMO vs. US-LWR

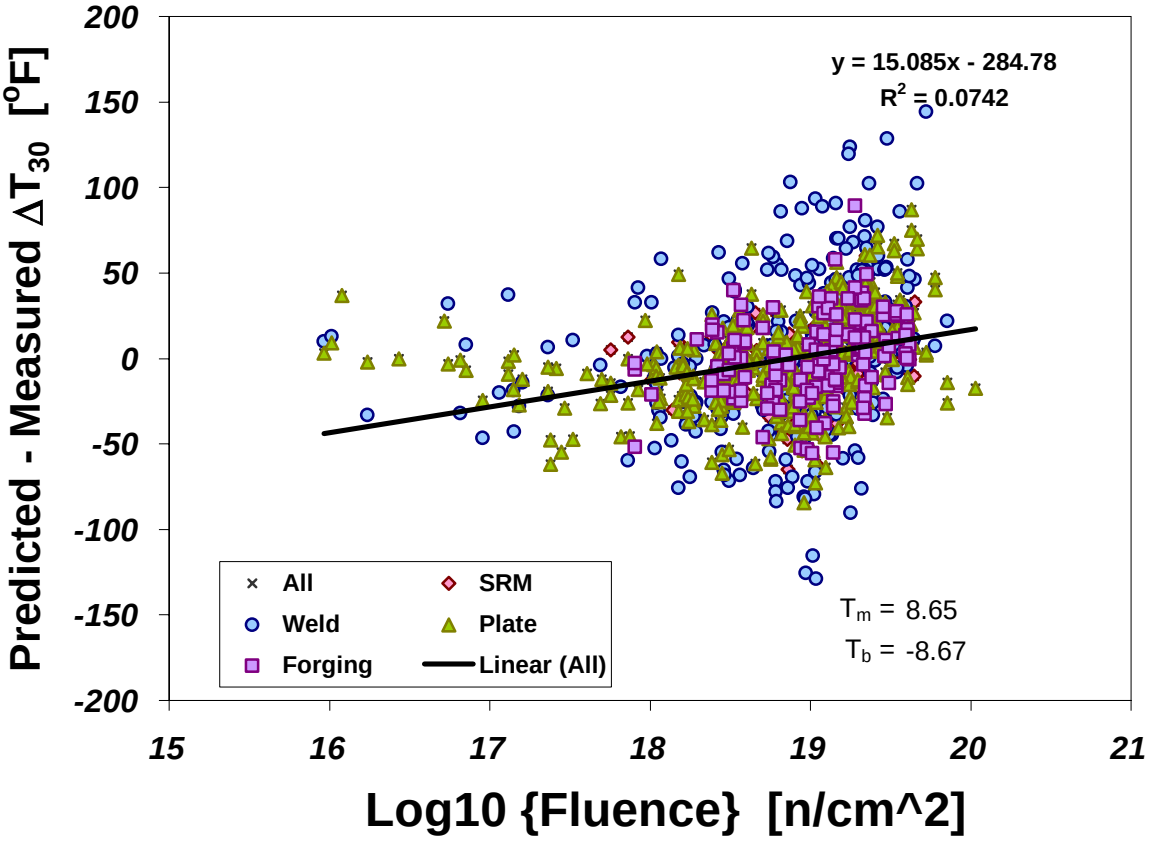

Residuals vs. Fluence

RADAMO vs. IVAR

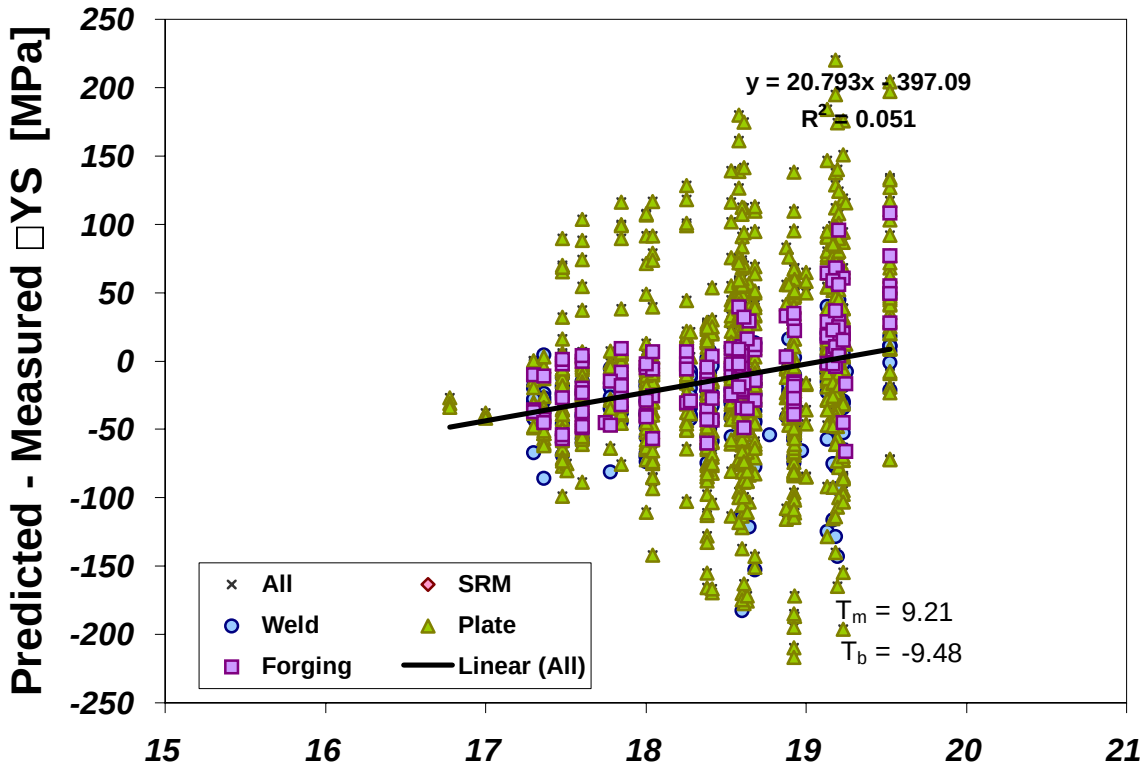

RADAMO vs. French

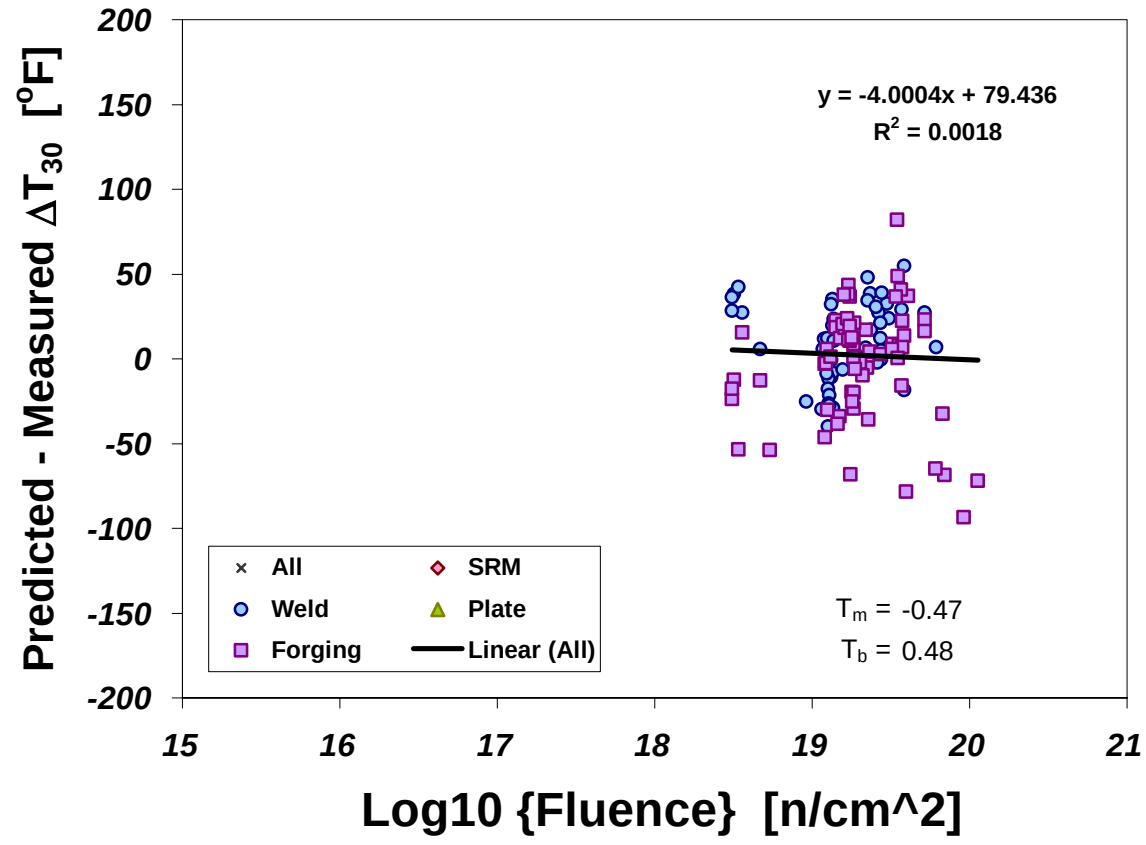

Residuals vs. Fluence

RADAMO vs. JNES$_{TEST}$

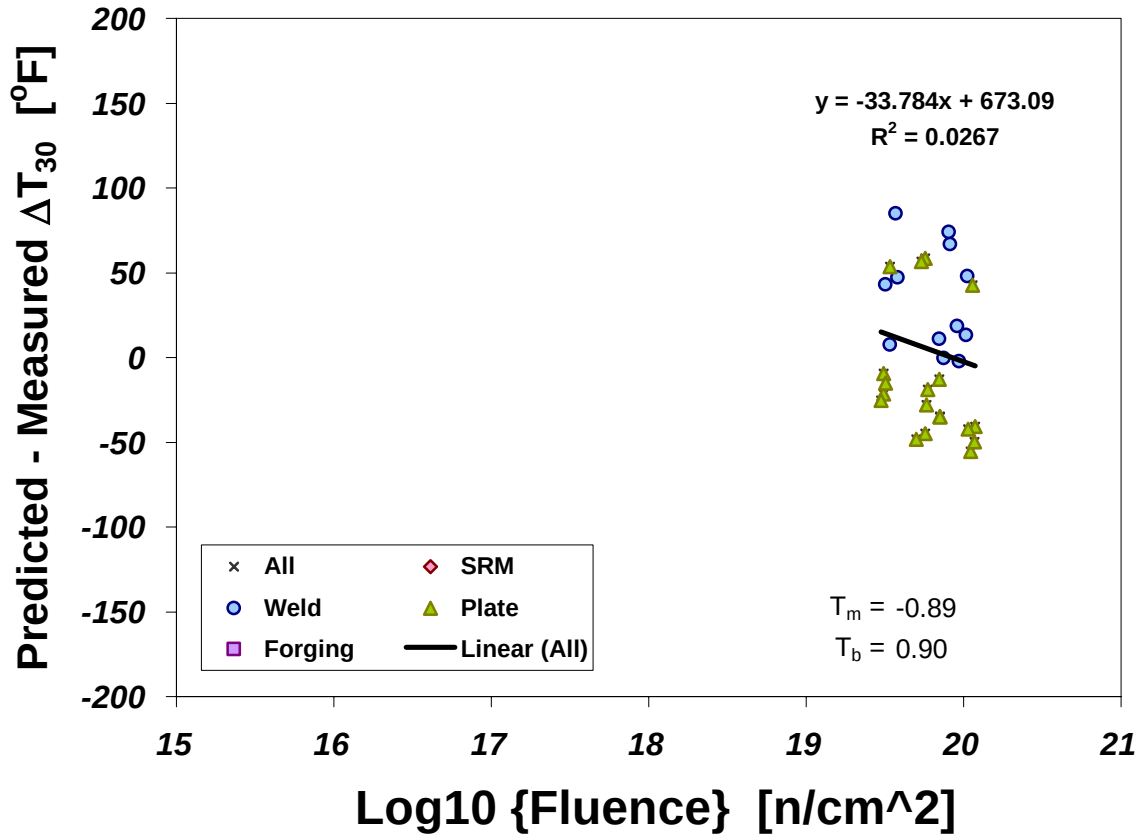

RADAMO vs. JNES$_{RPV}$

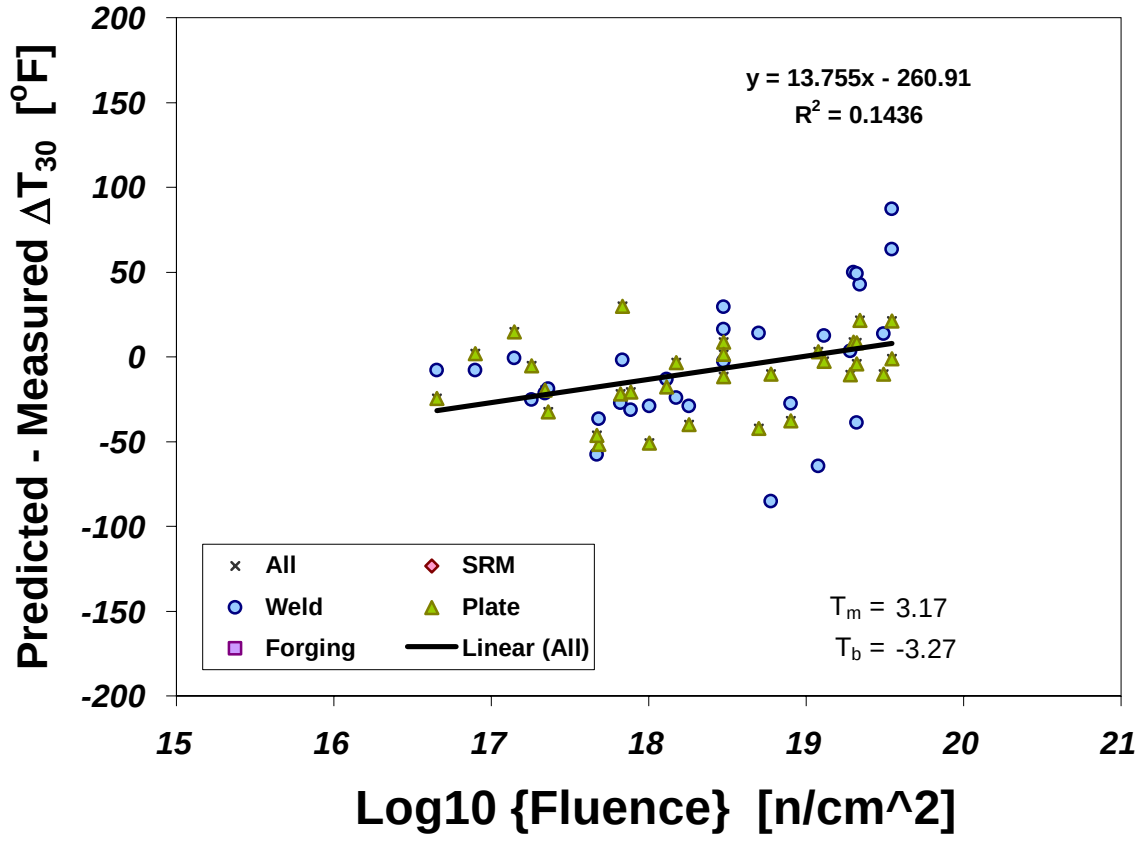

Residuals vs. Flux

RADAMO vs. RADAMO

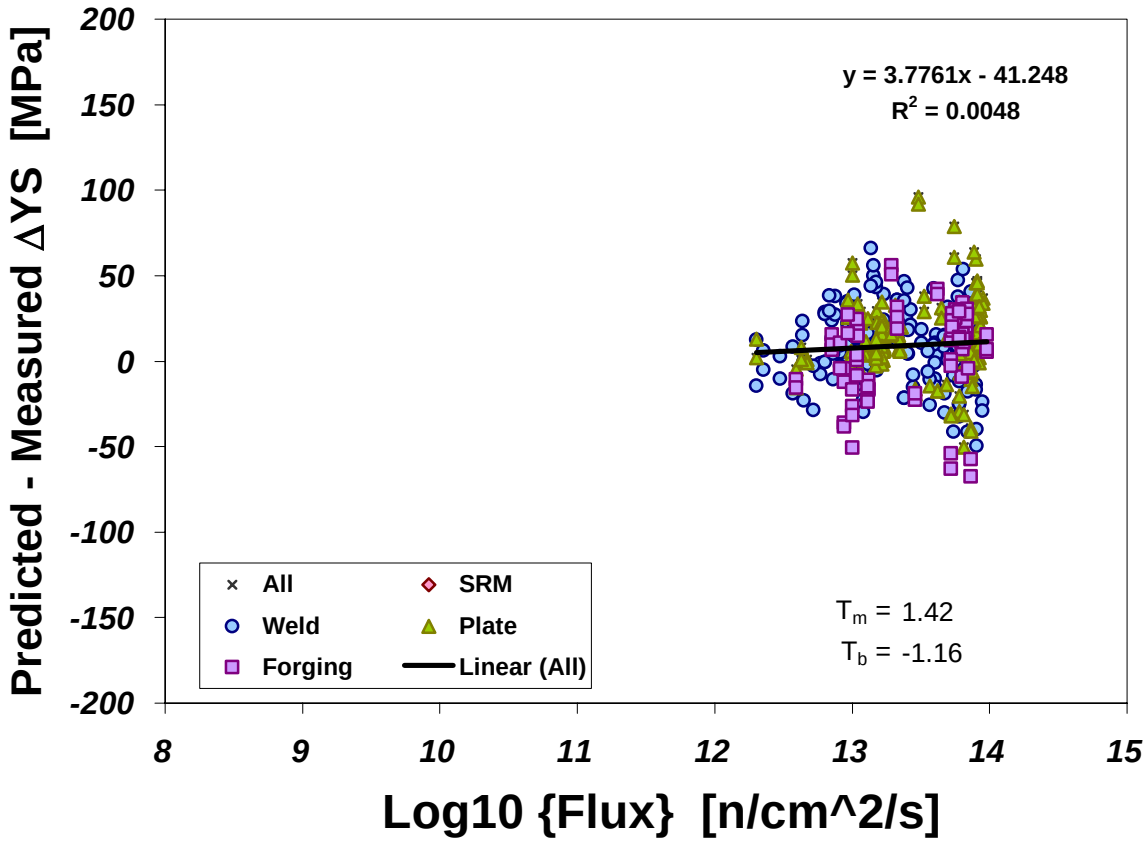

RADAMO vs. US-LWR

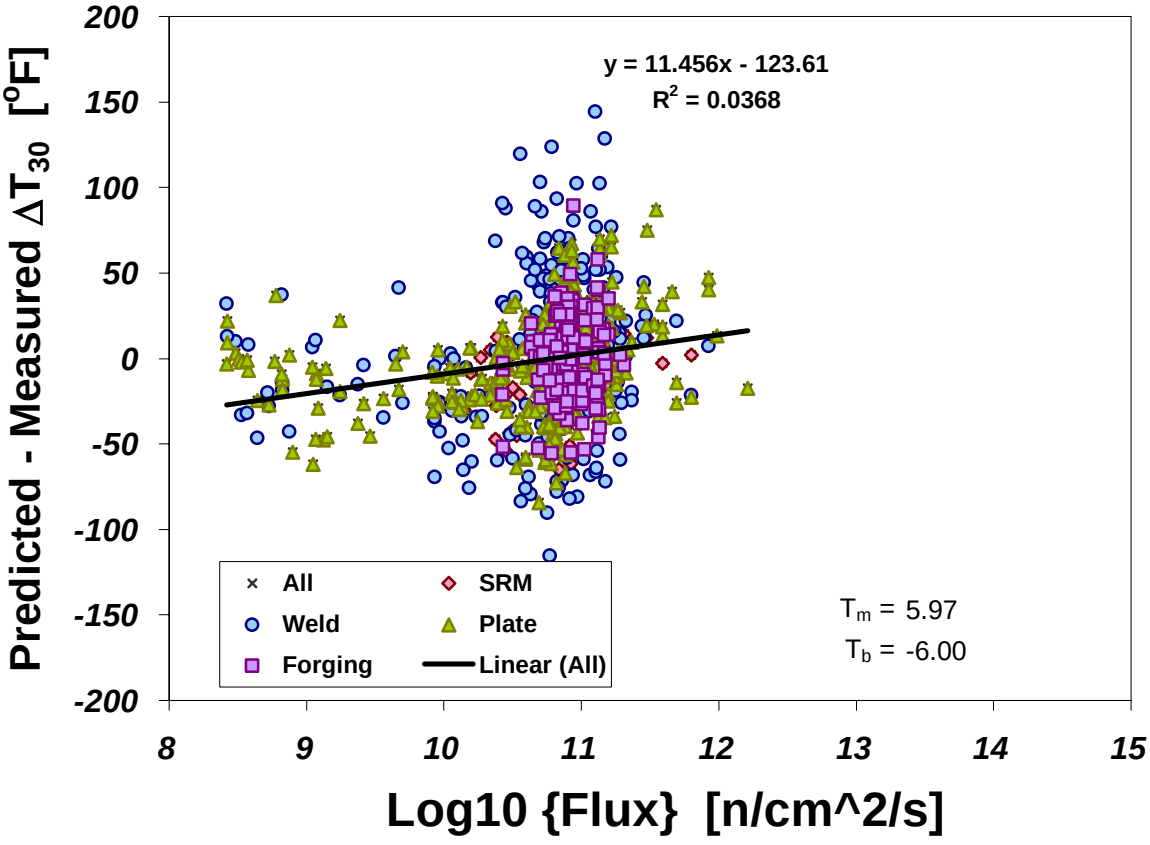

Residuals vs. Flux

RADAMO vs. IVAR

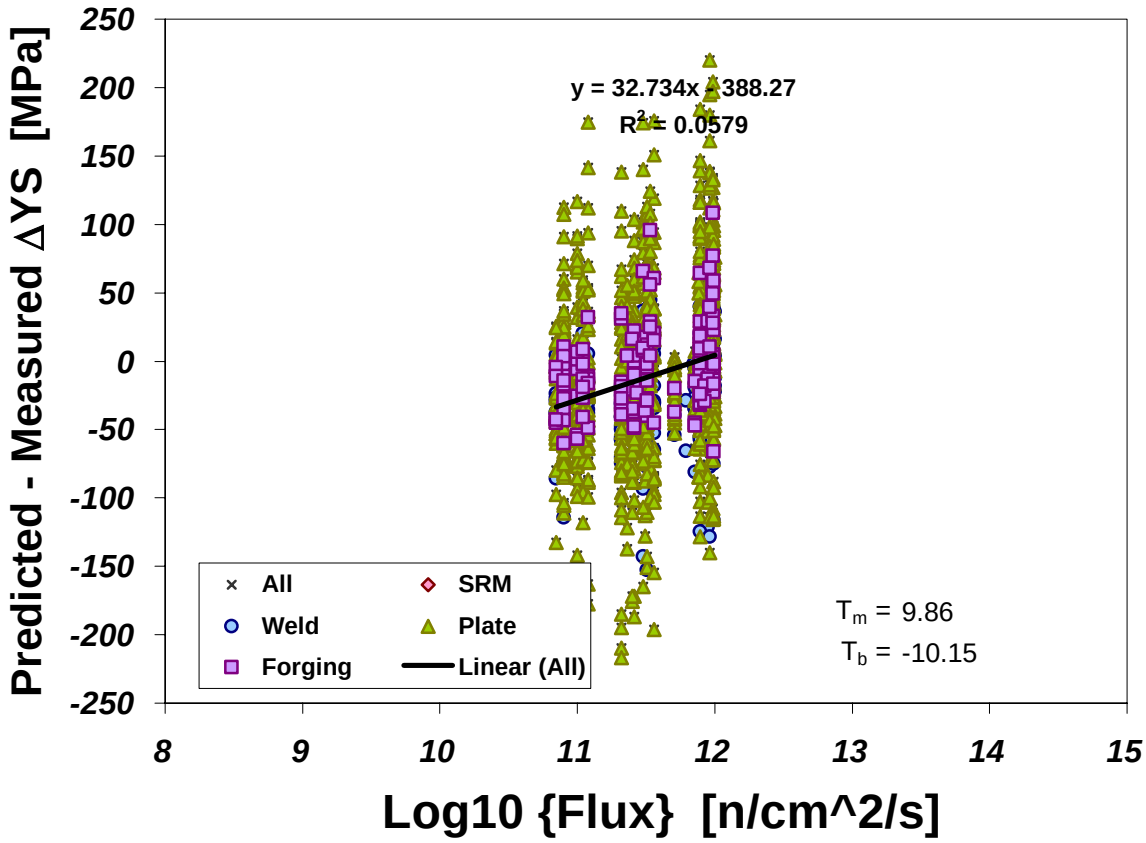

RADAMO vs. French

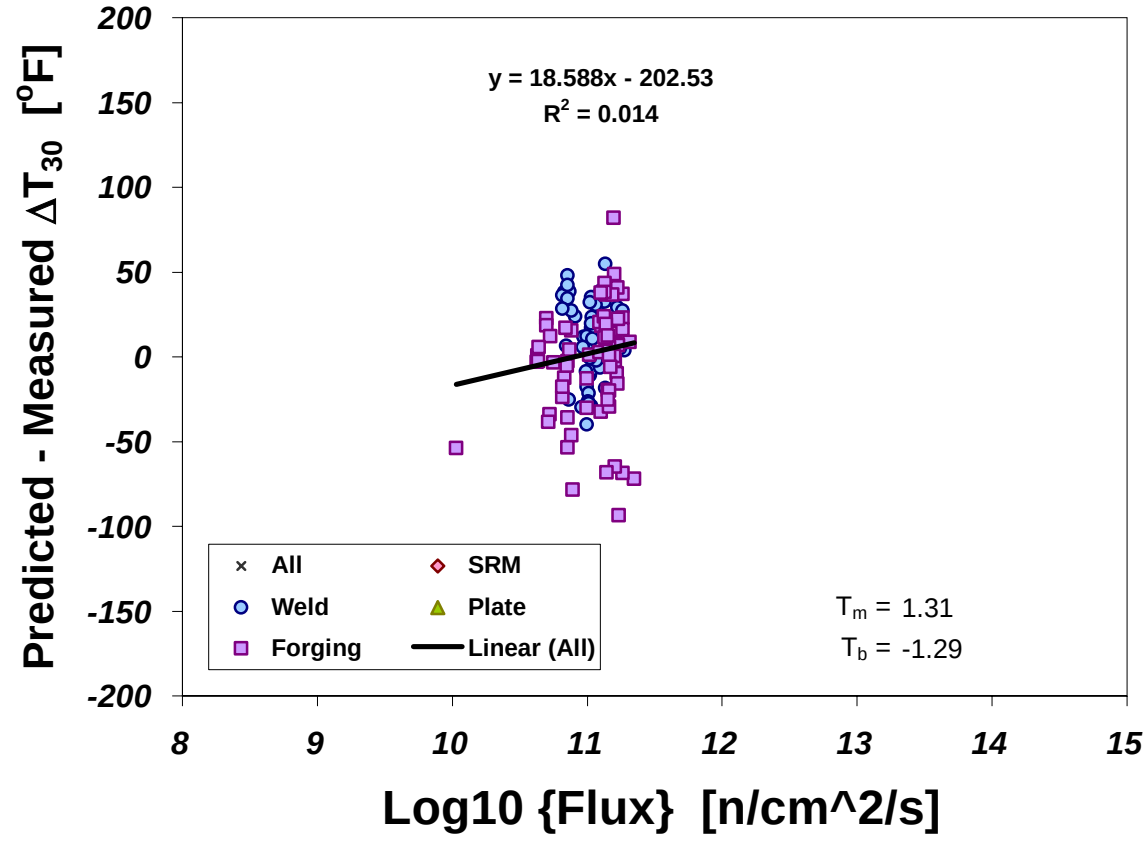

Residuals vs. Flux

RADAMO vs. $JNES_{TEST}$

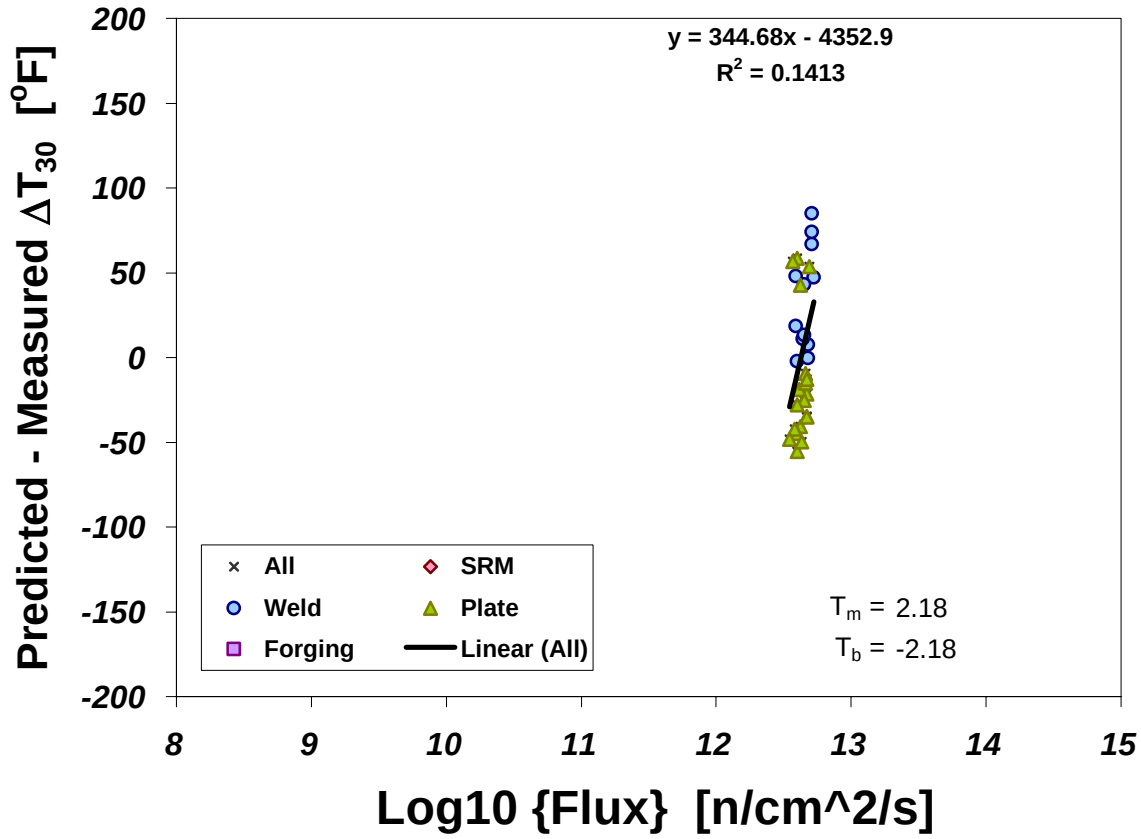

RADAMO vs. $JNES_{RPV}$

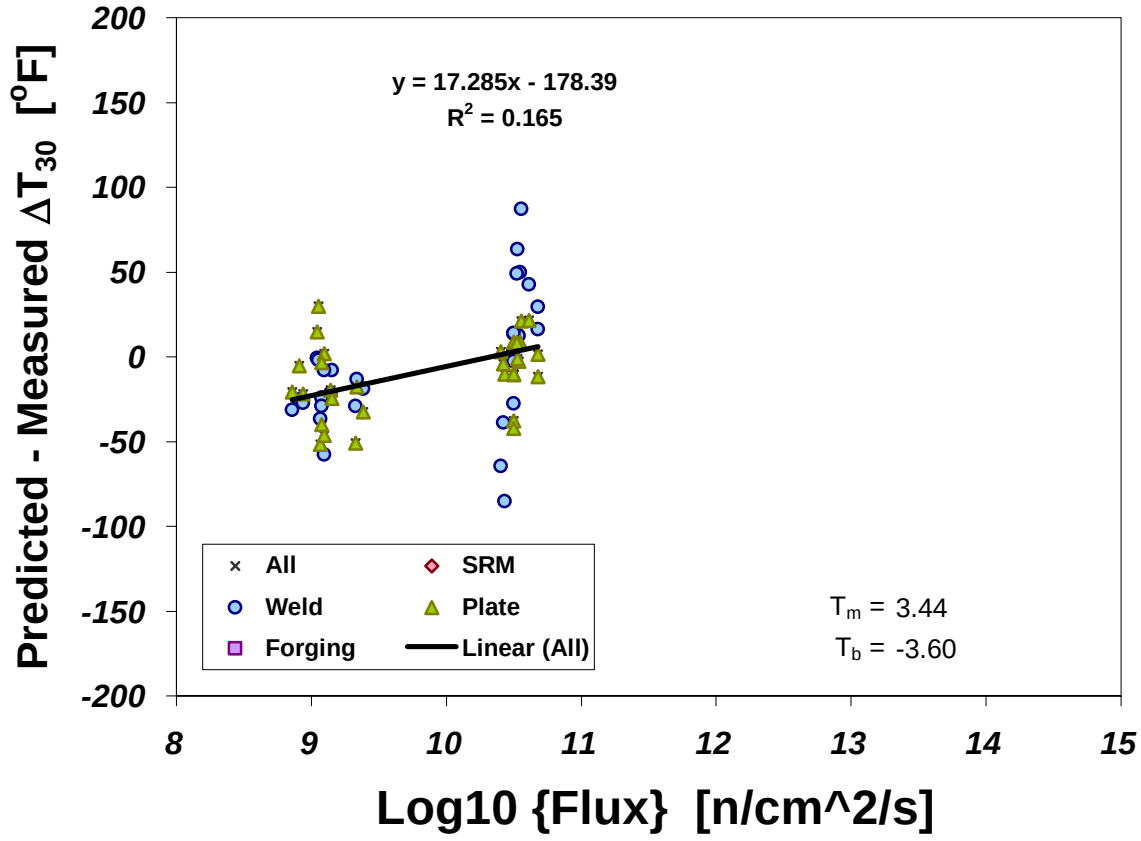

Residuals vs. Temperature

RADAMO vs. RADAMO

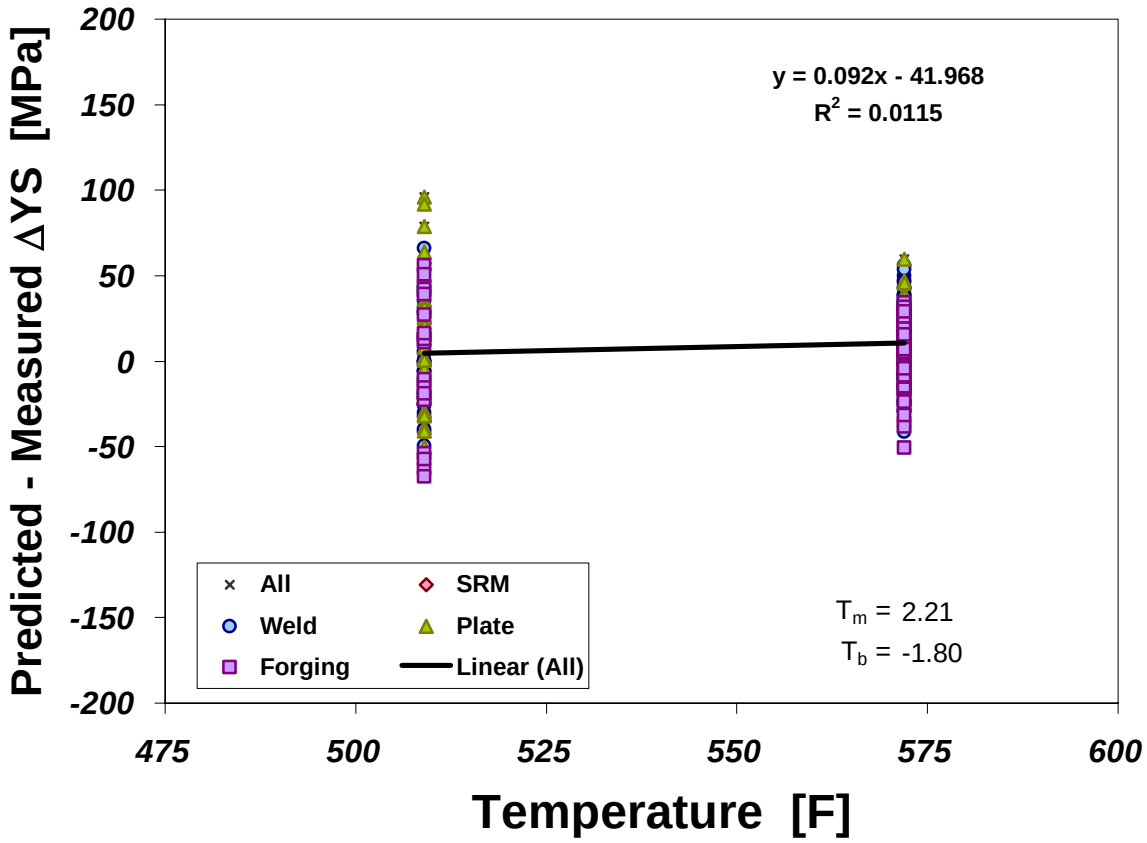

RADAMO vs. US-LWR

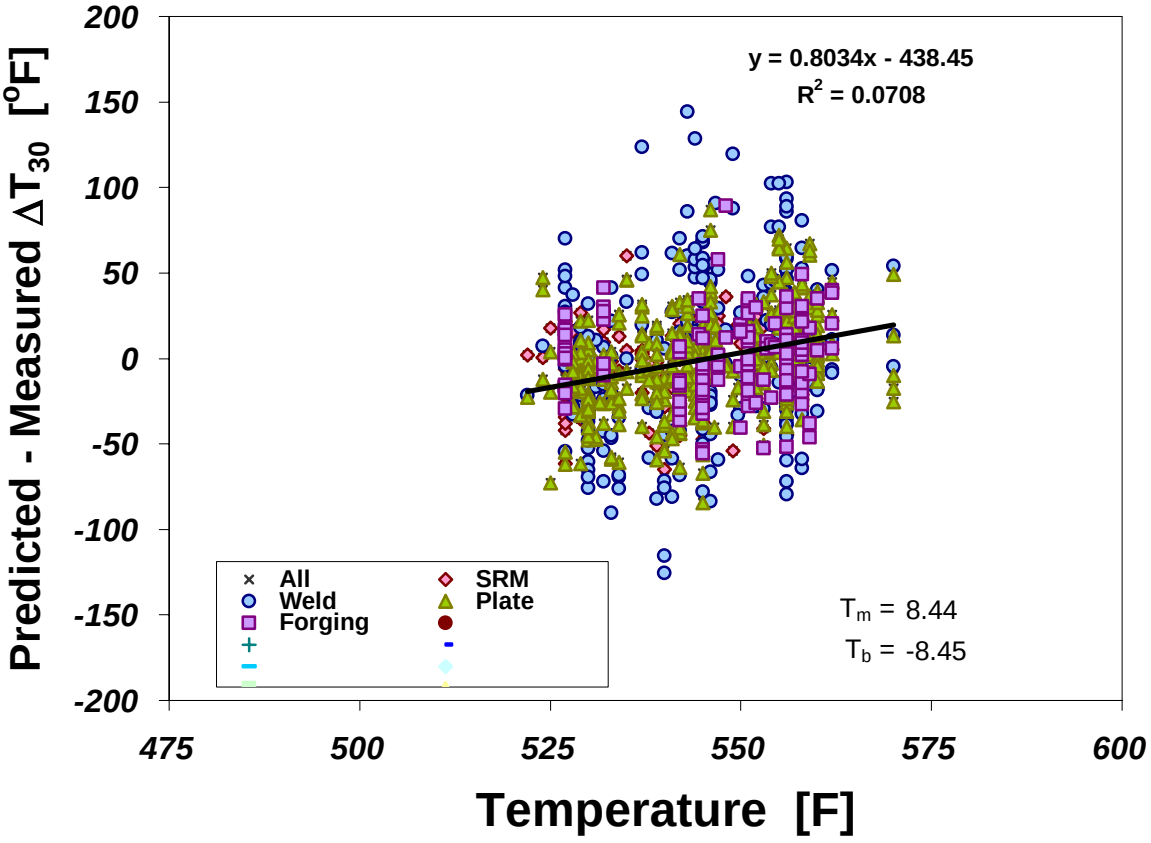

Residuals vs. Temperature

RADAMO vs. IVAR

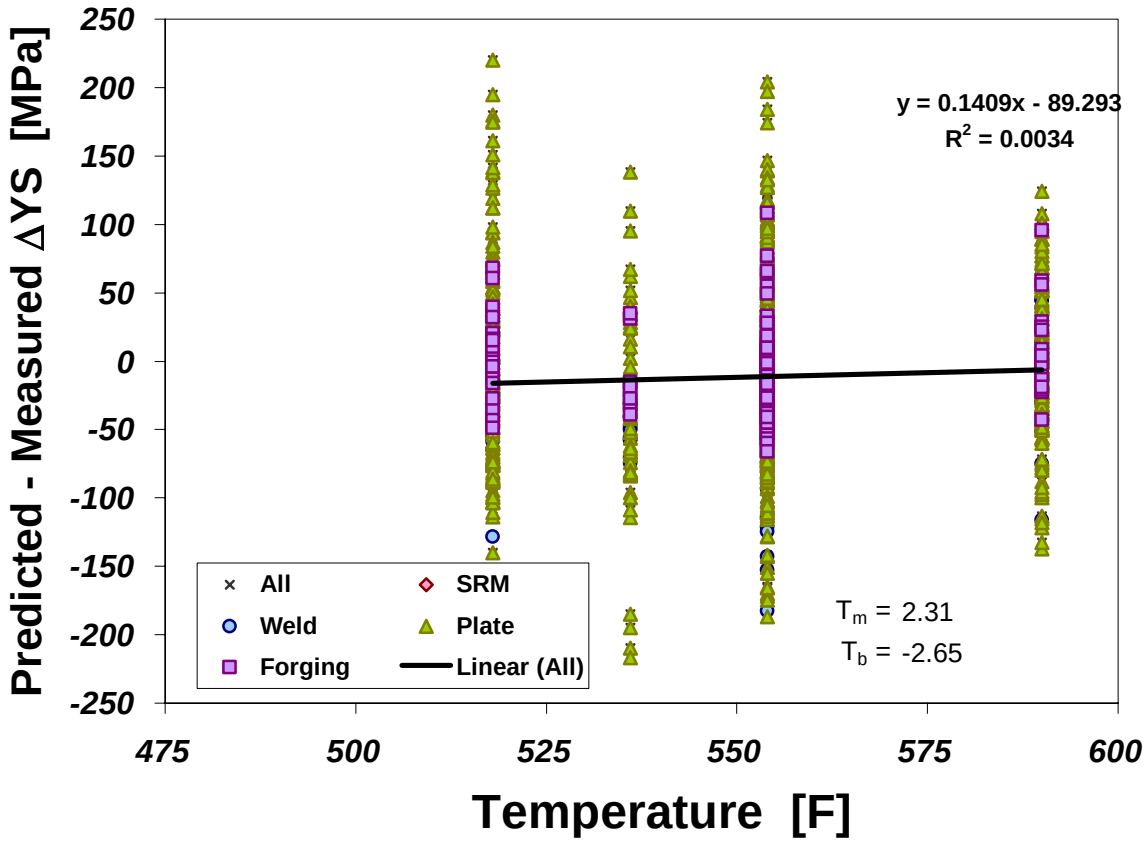

RADAMO vs. French

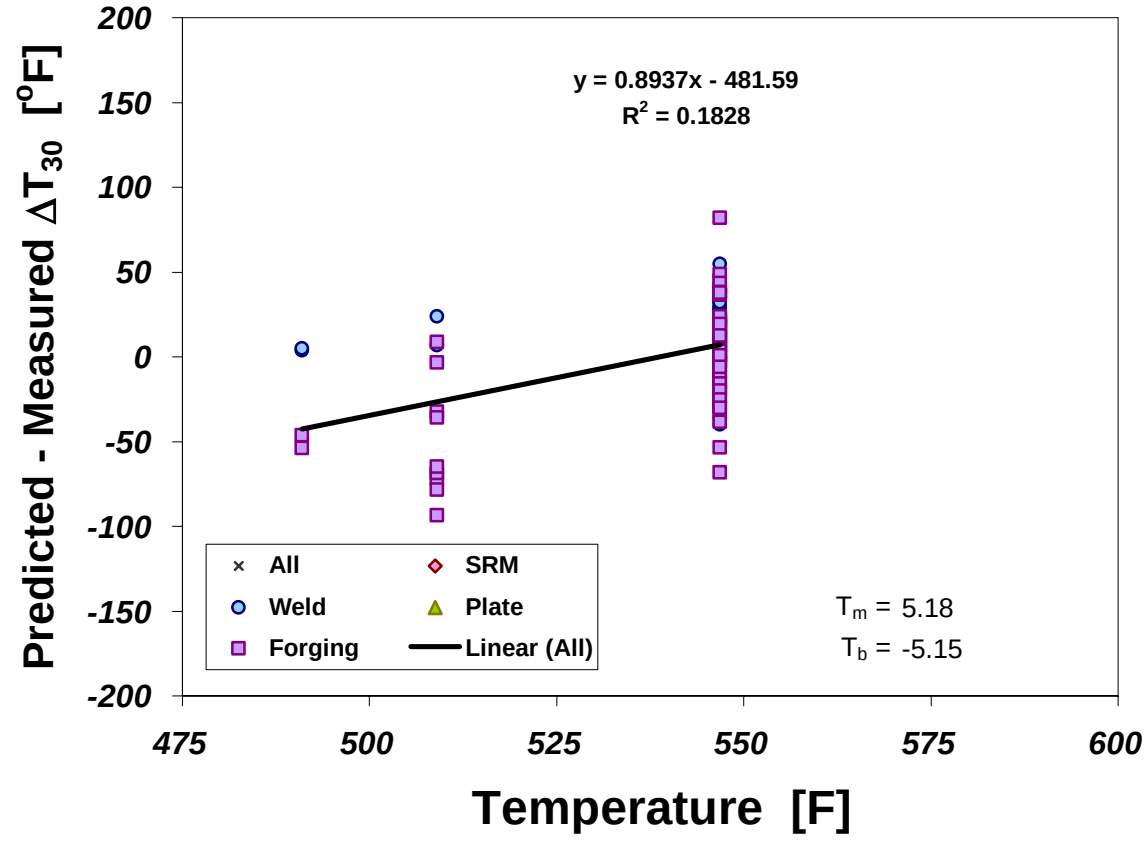

Residuals vs. Temperature

RADAMO vs. $JNES_{TEST}$

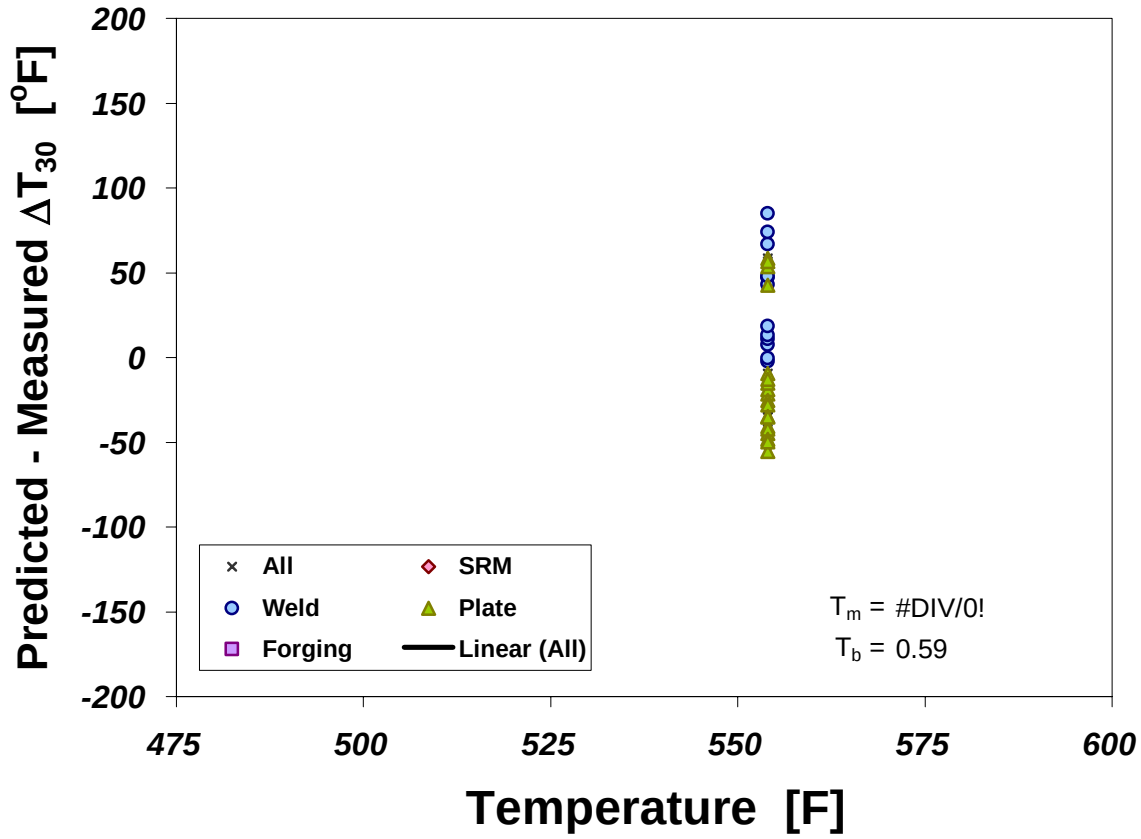

RADAMO vs. $JNES_{RPV}$

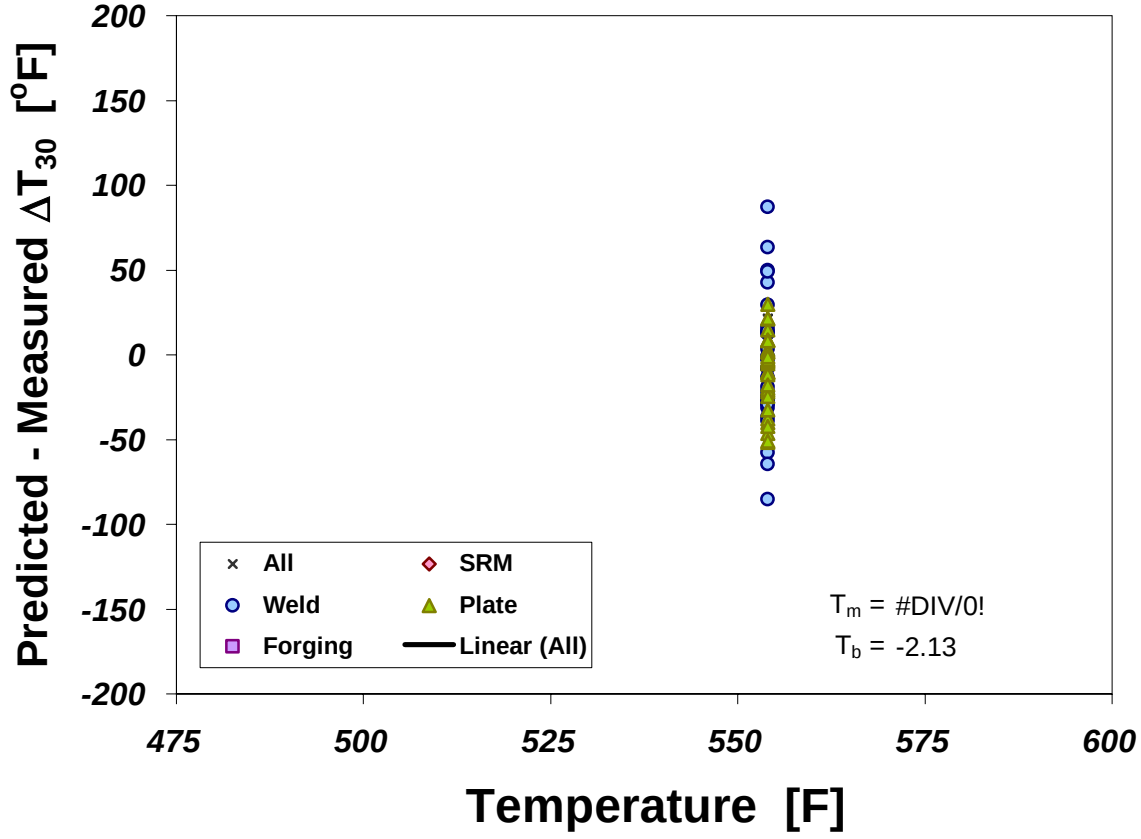

Residuals vs. Copper

RADAMO vs. RADAMO

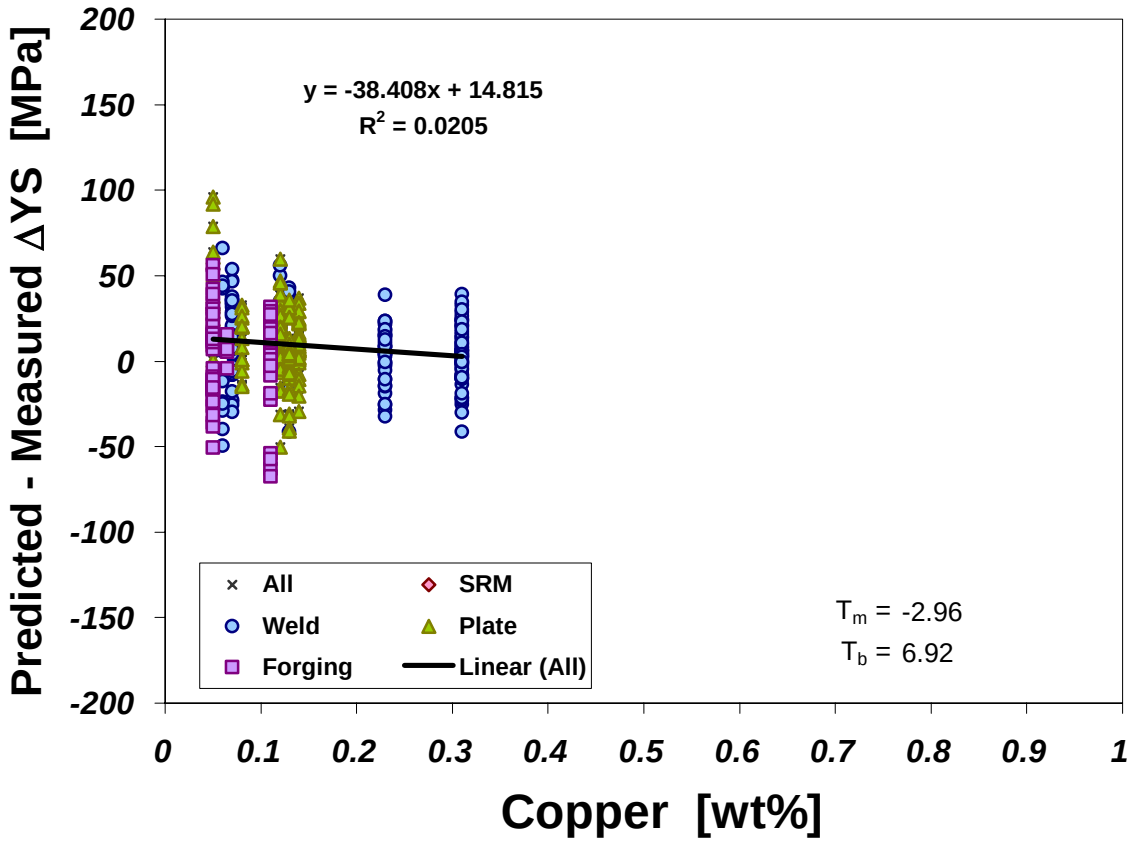

RADAMO vs. US-LWR

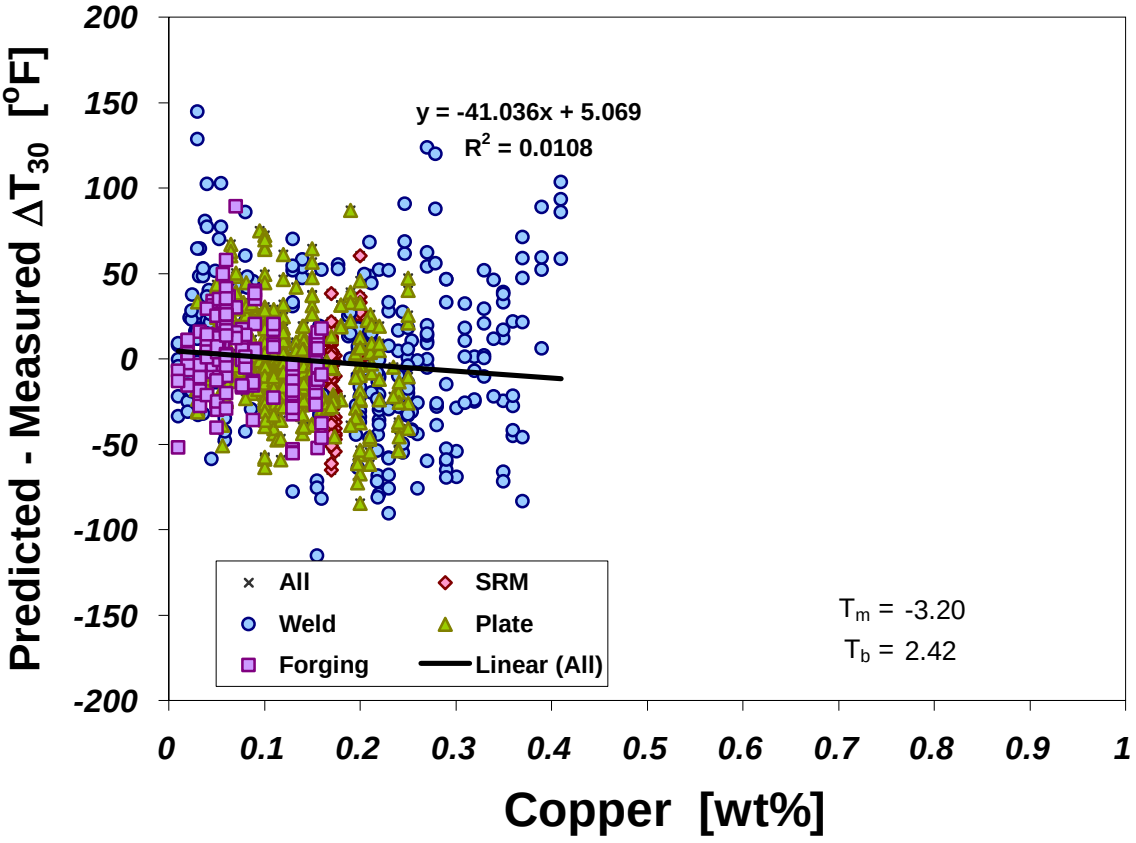

Residuals vs. Copper

RADAMO vs. IVAR

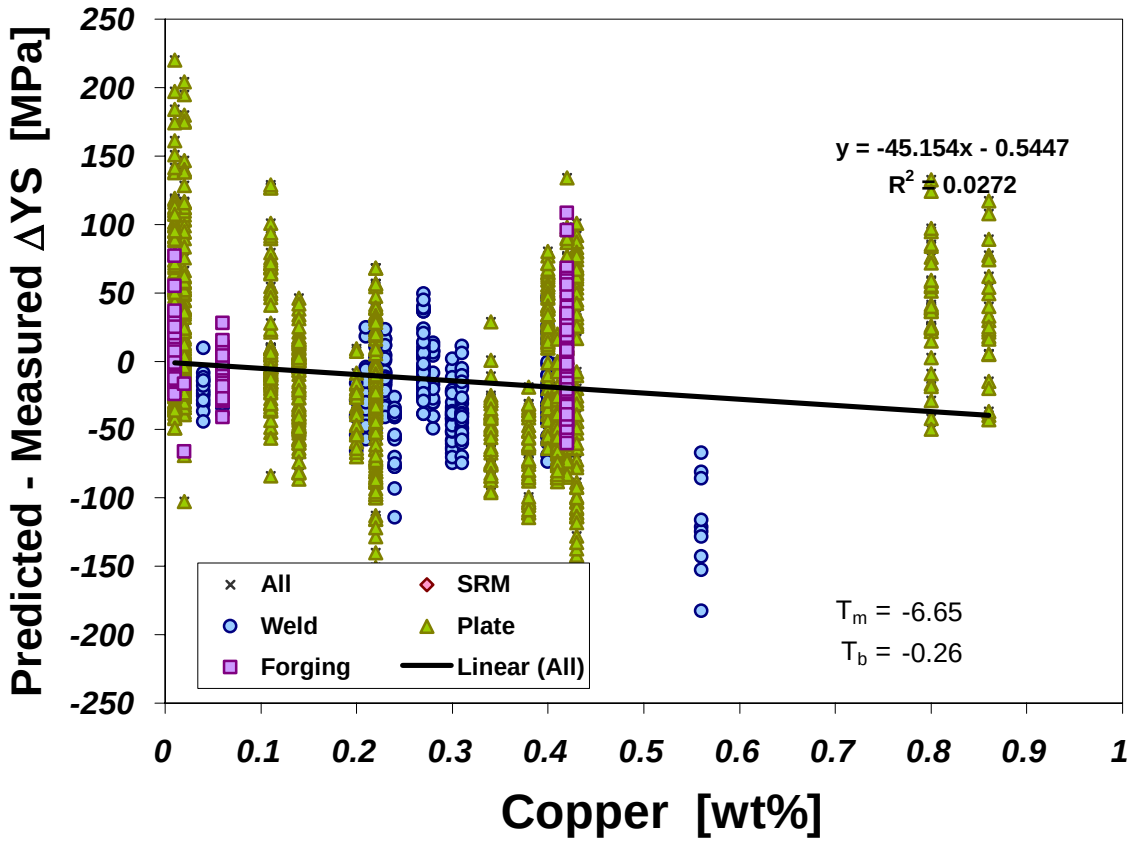

RADAMO vs. French

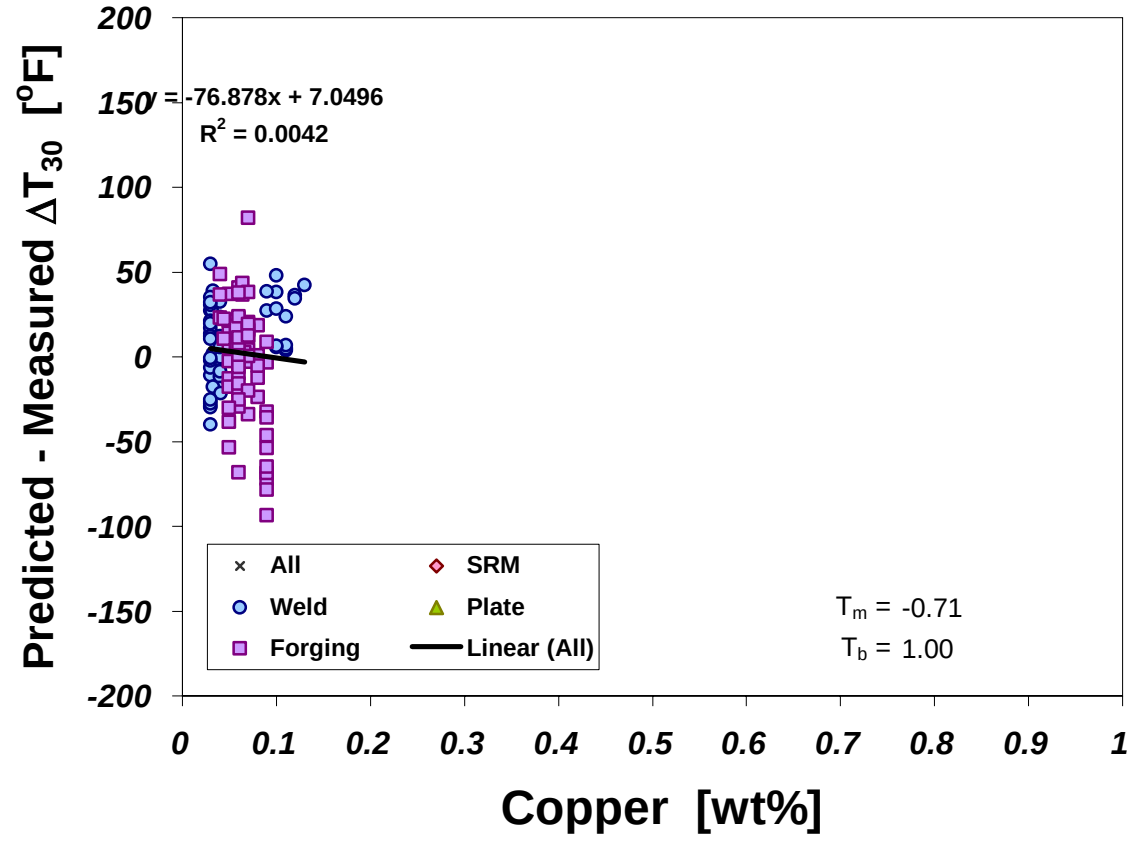

Residuals vs. Copper

RADAMO vs. $JNES_{TEST}$

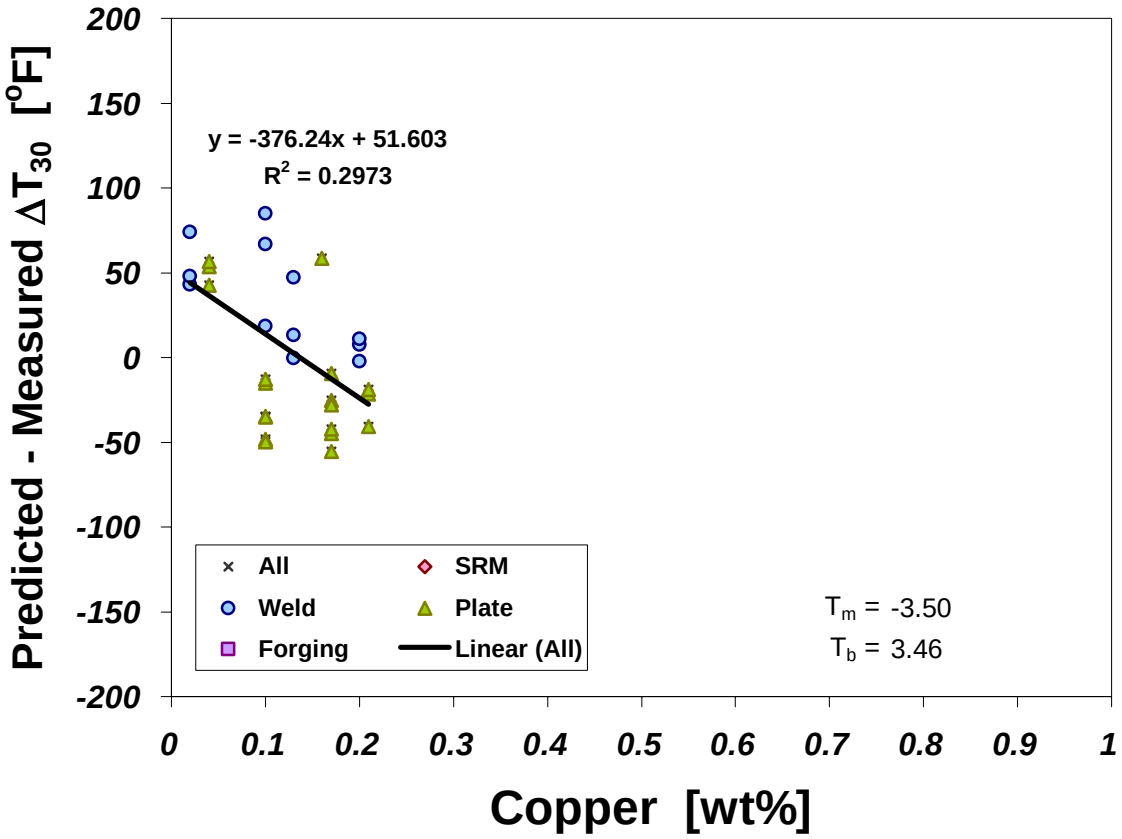

RADAMO vs. $JNES_{RPV}$

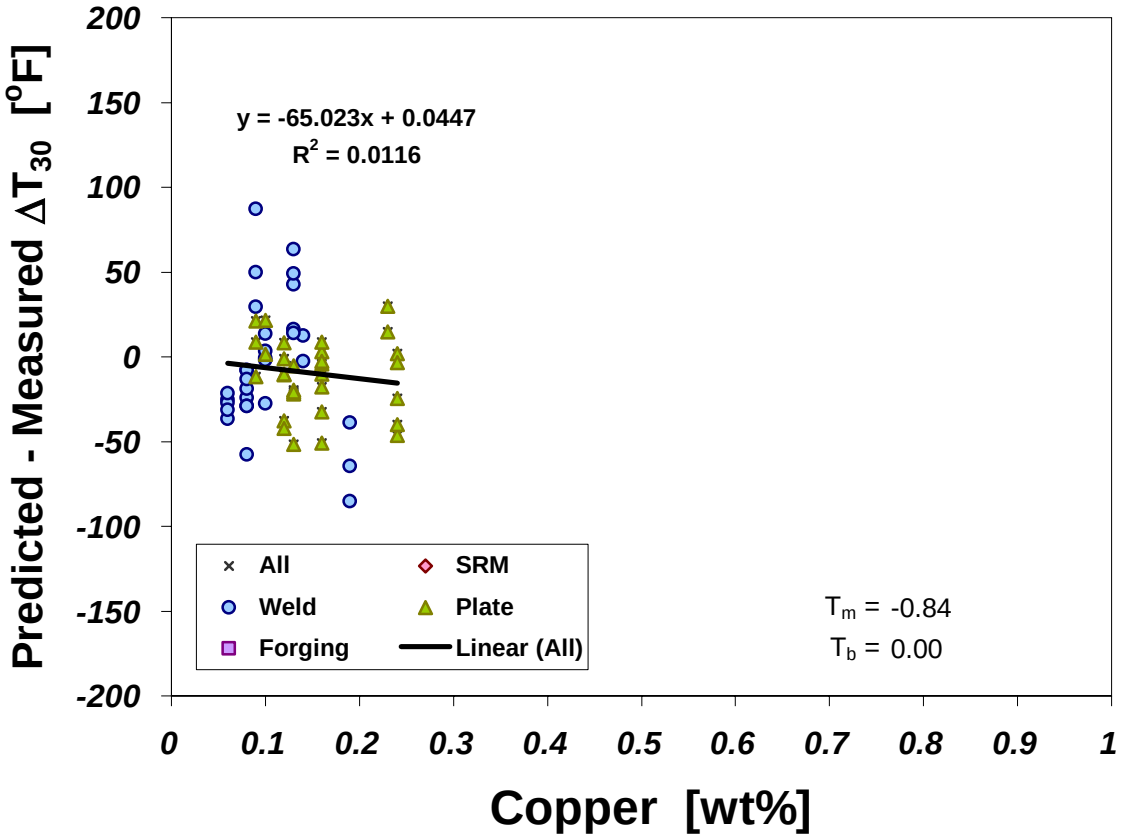

Residuals vs. Nickel

RADAMO vs. RADAMO

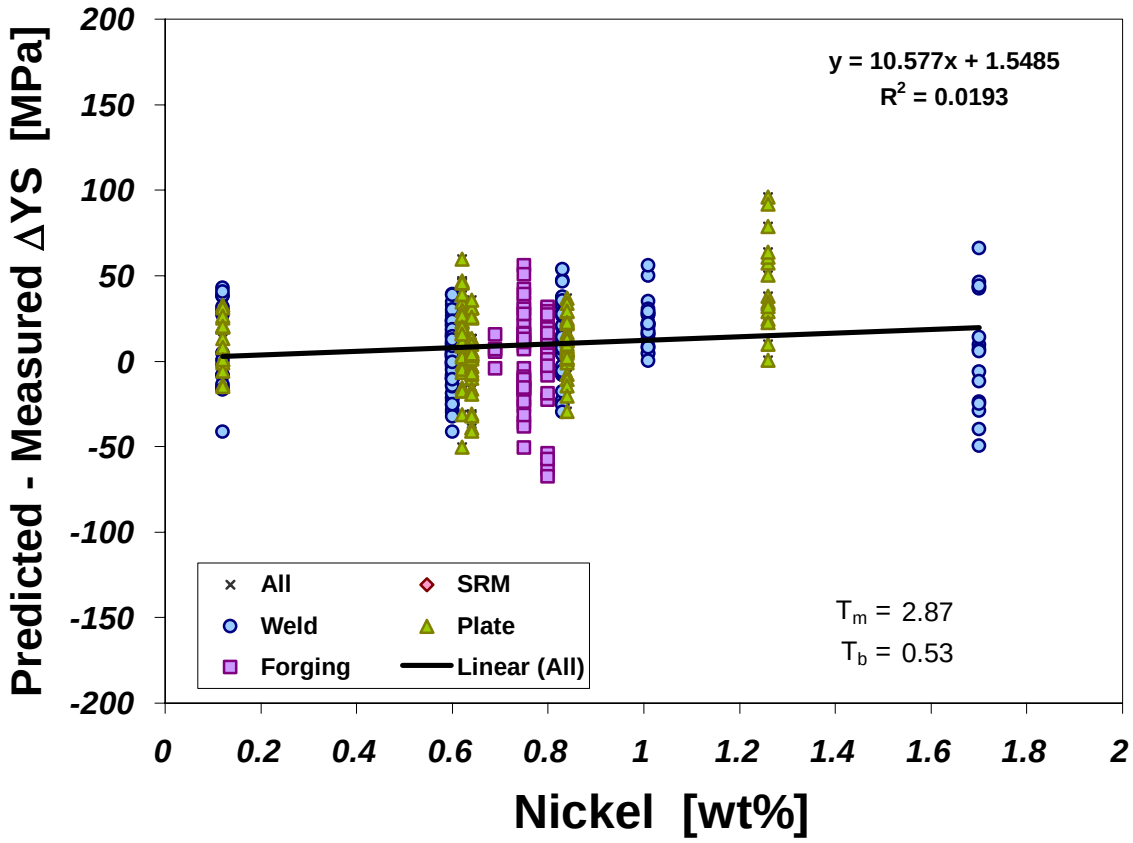

RADAMO vs. US-LWR

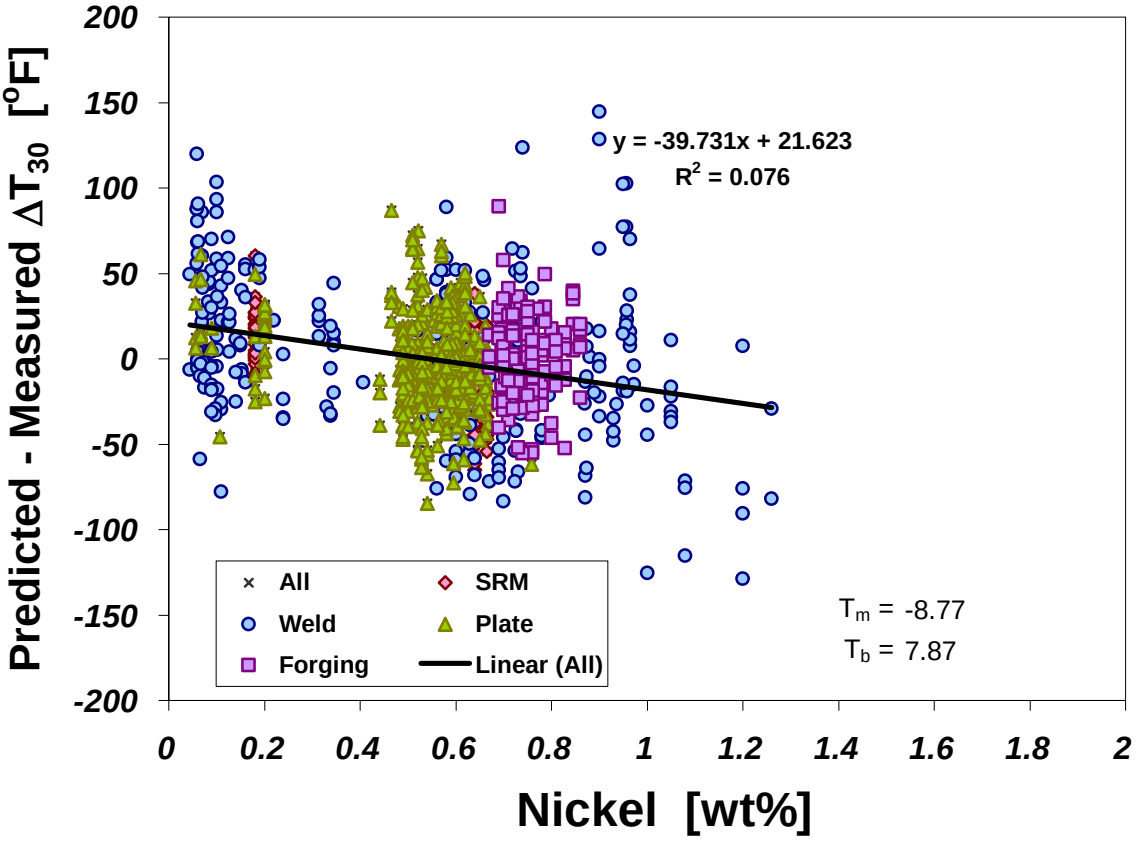

Residuals vs. Nickel

RADAMO vs. IVAR

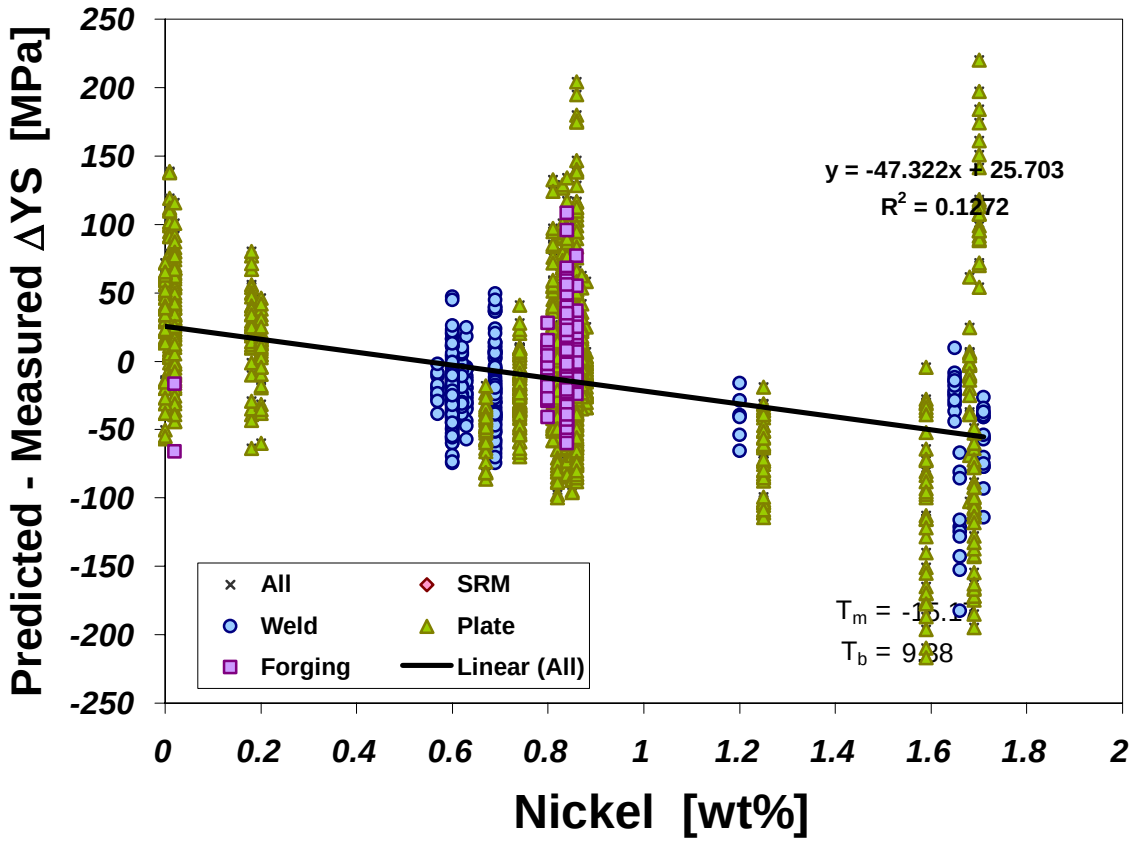

RADAMO vs. French

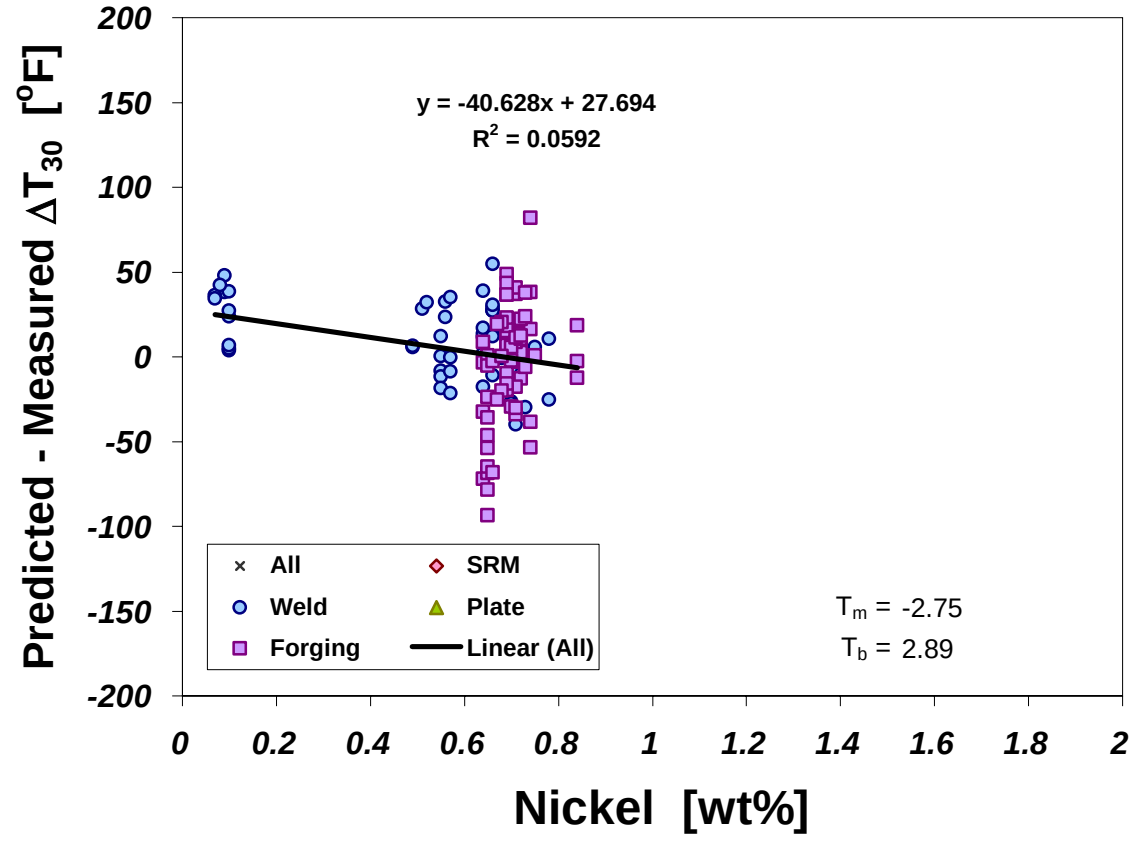

Residuals vs. Nickel

RADAMO vs. JNES$_{TEST}$

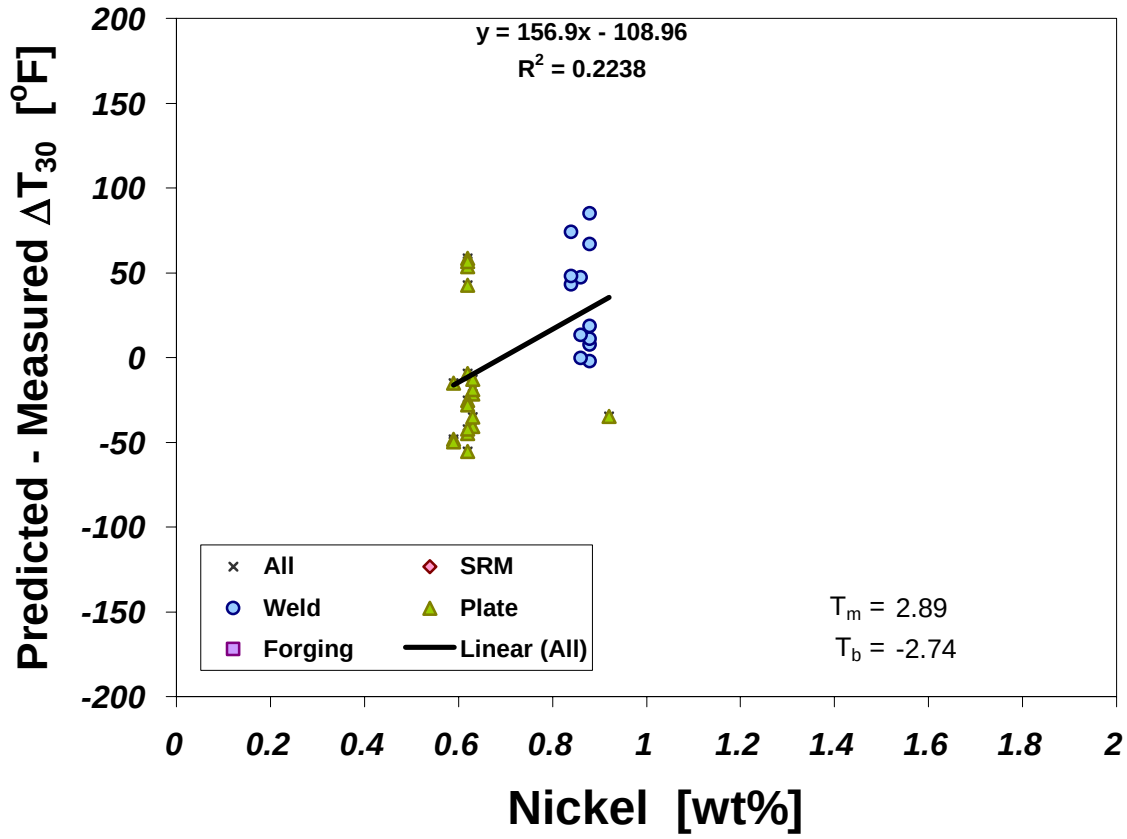

RADAMO vs. JNES$_{RPV}$

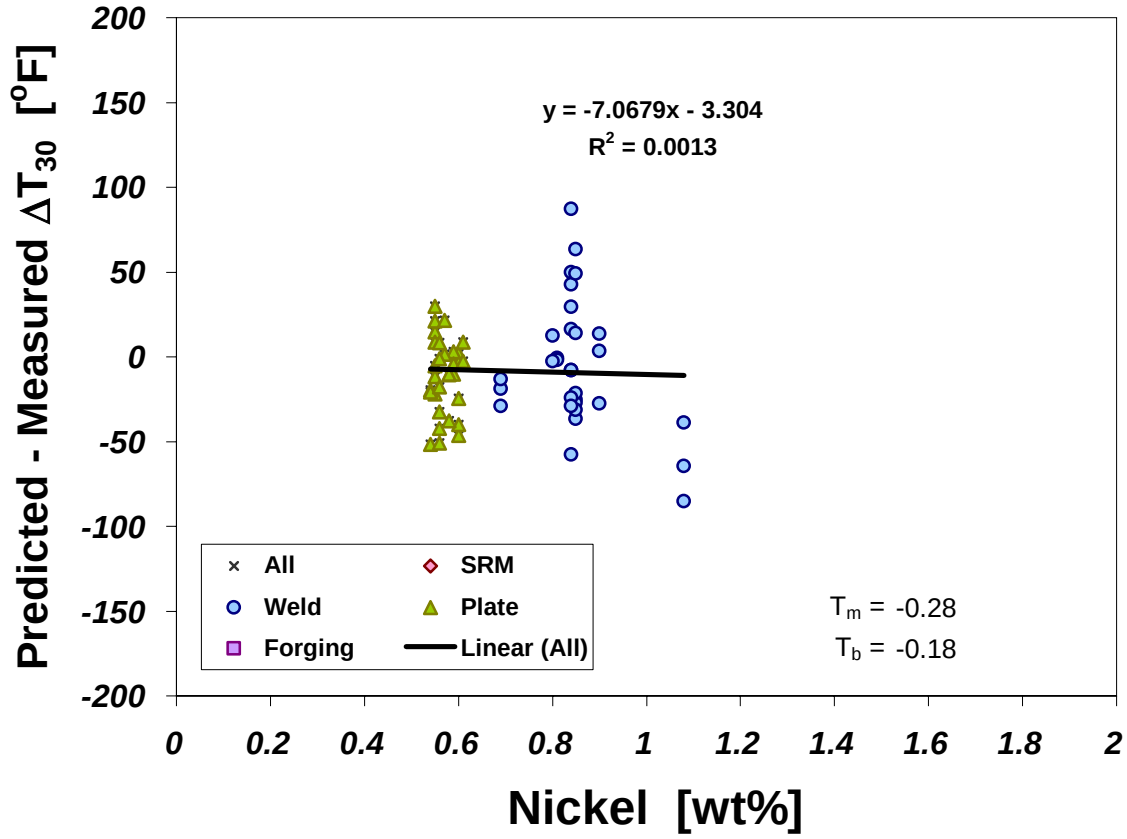

Residuals vs. Phosphorus

WITH PRP TERM

RADAMO vs. RADAMO

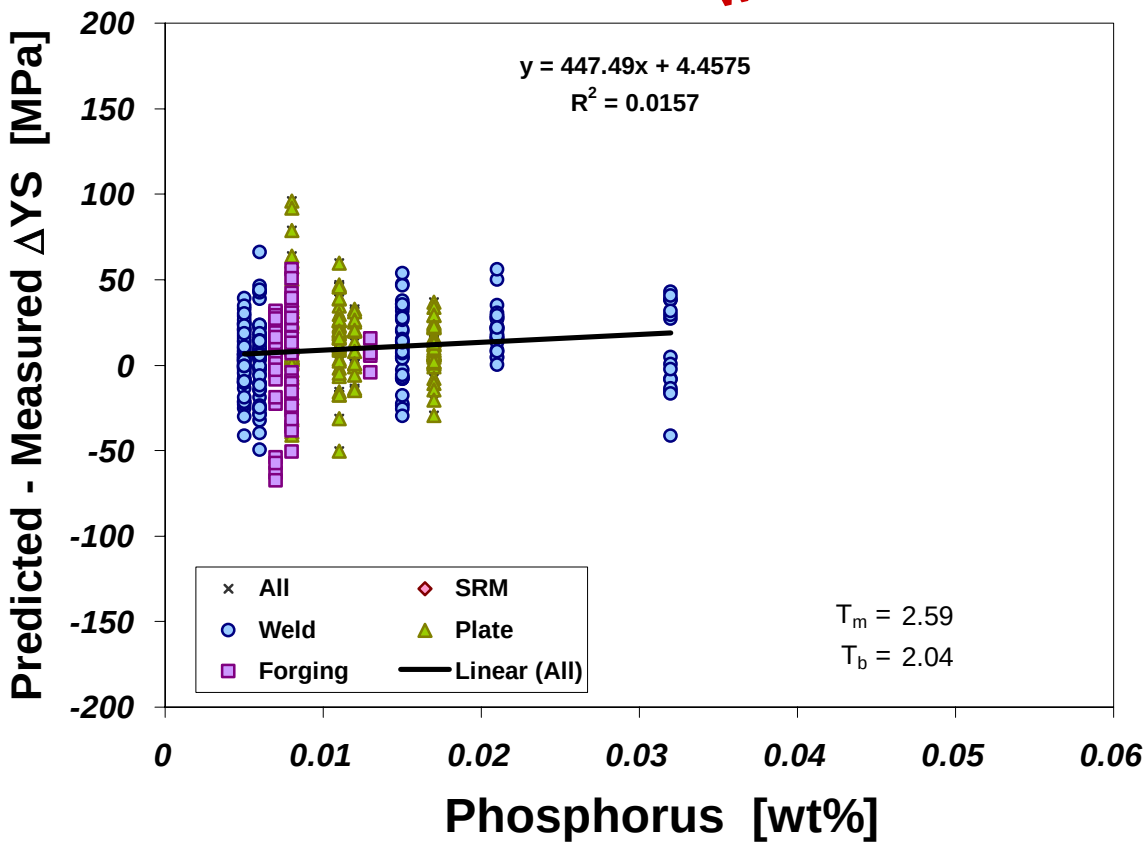

RADAMO vs. US-LWR

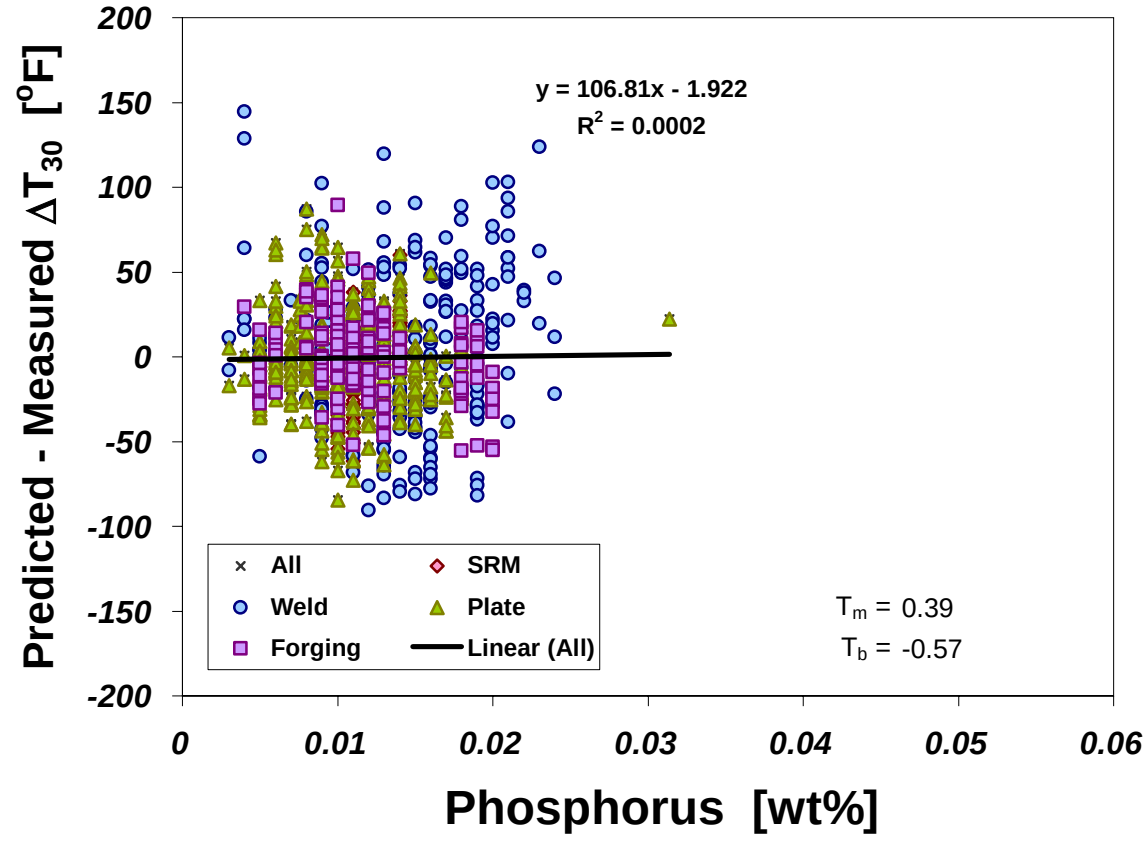

Residuals vs. Phosphorus

WITH PRP TERM

RADAMO vs. IVAR

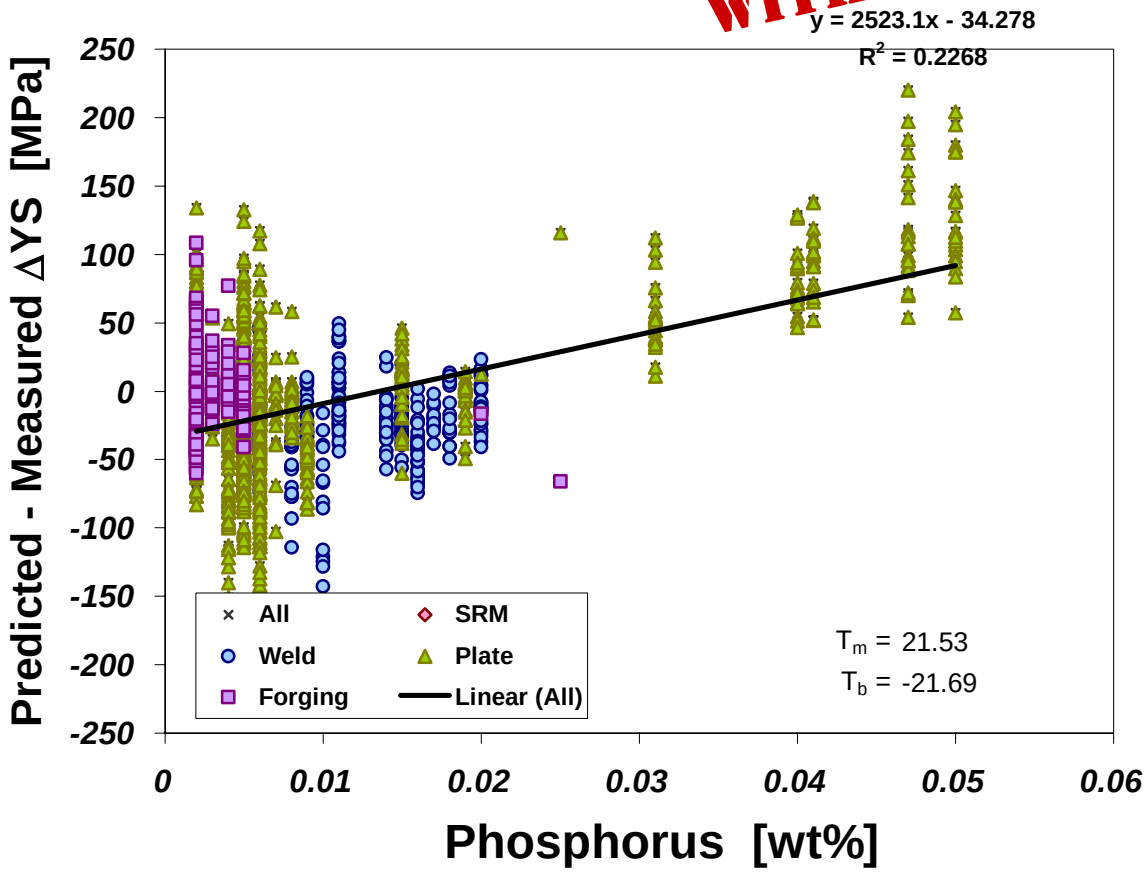

RADAMO vs. French

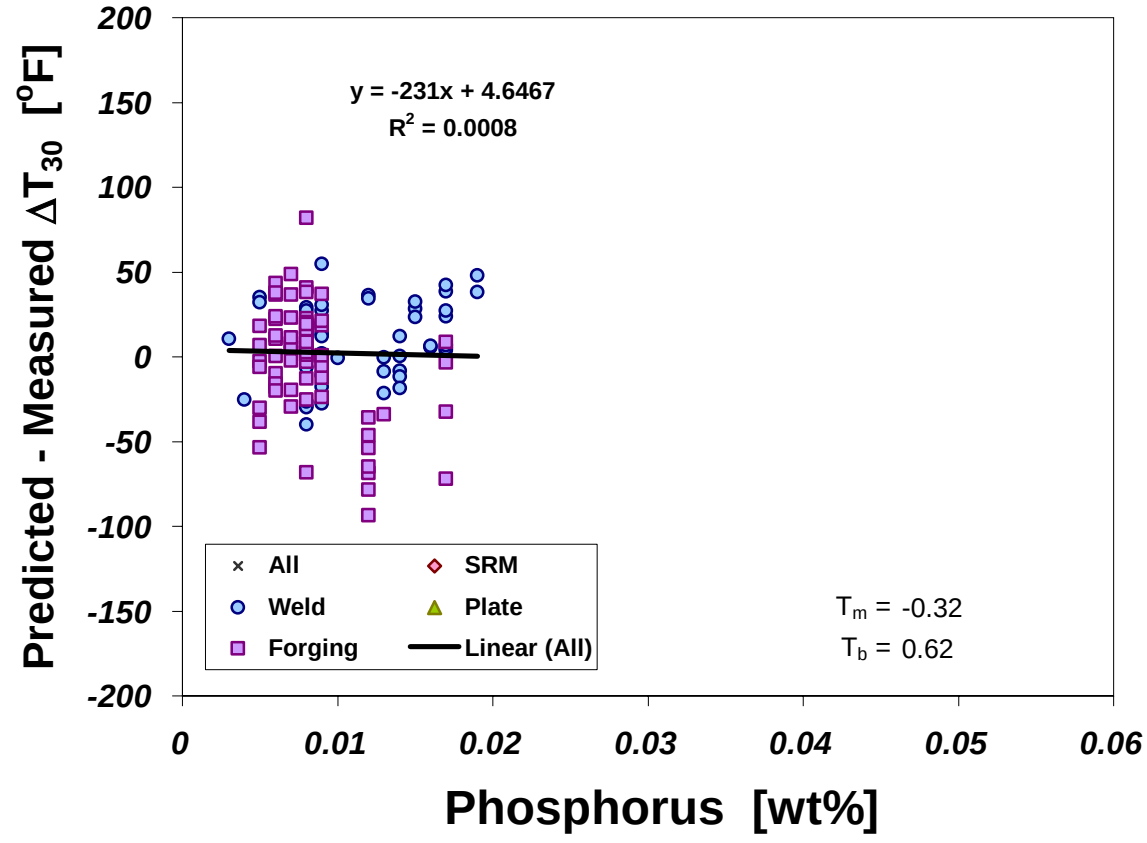

Residuals vs. Phosphorus

WITH PRP TERM

RADAMO vs. $JNES_{TEST}$

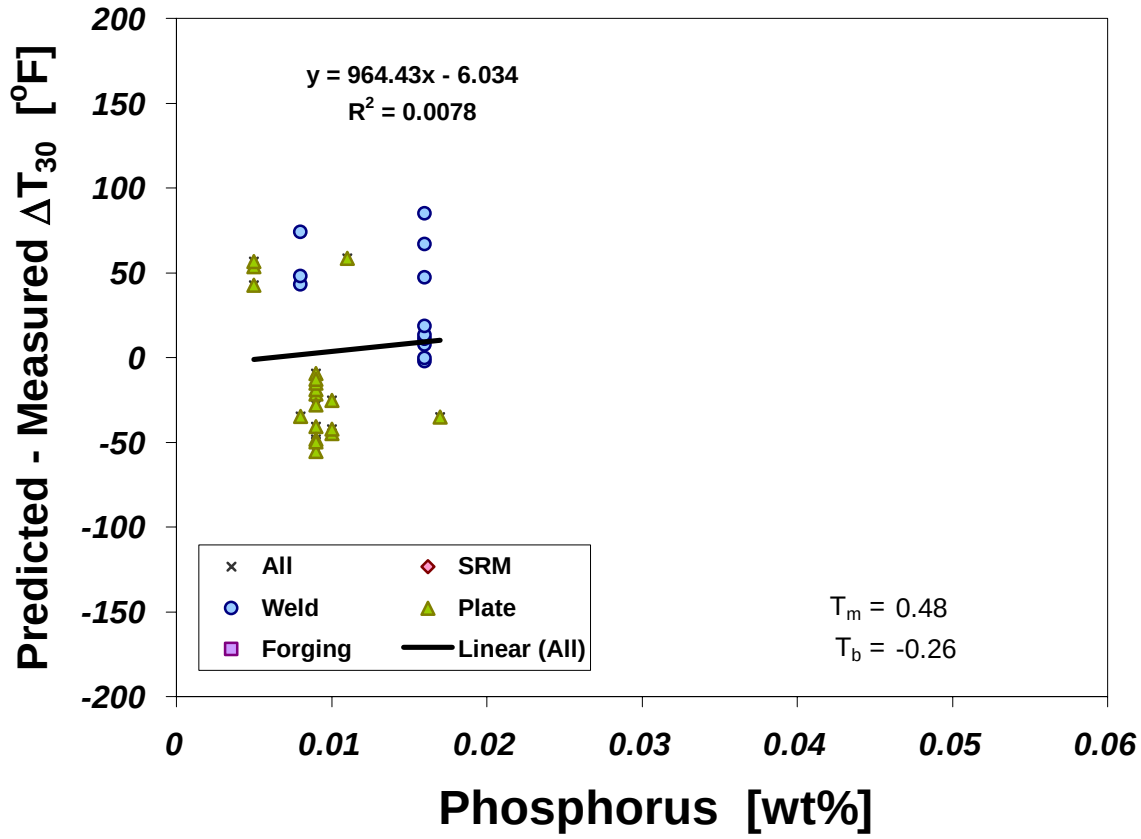

RADAMO vs. $JNES_{RPV}$

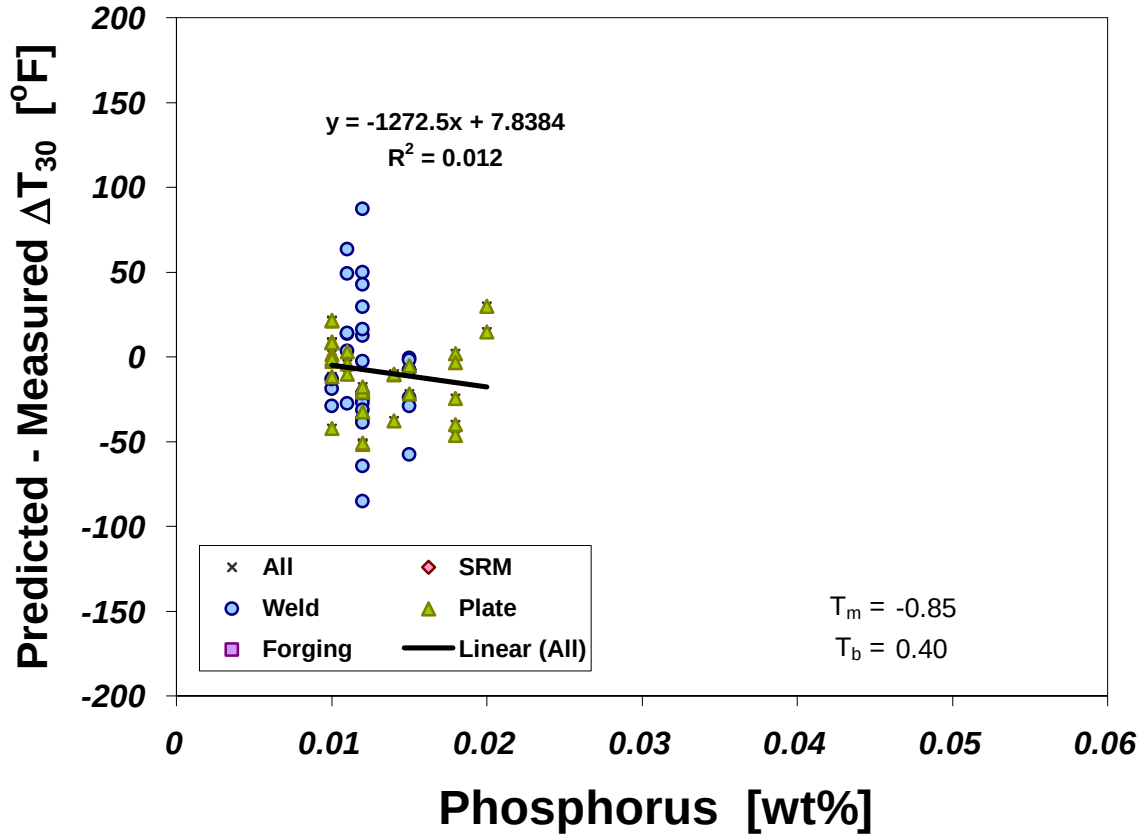

Residuals vs. Phosphorus

NO PRP TERM

RADAMO vs. RADAMO

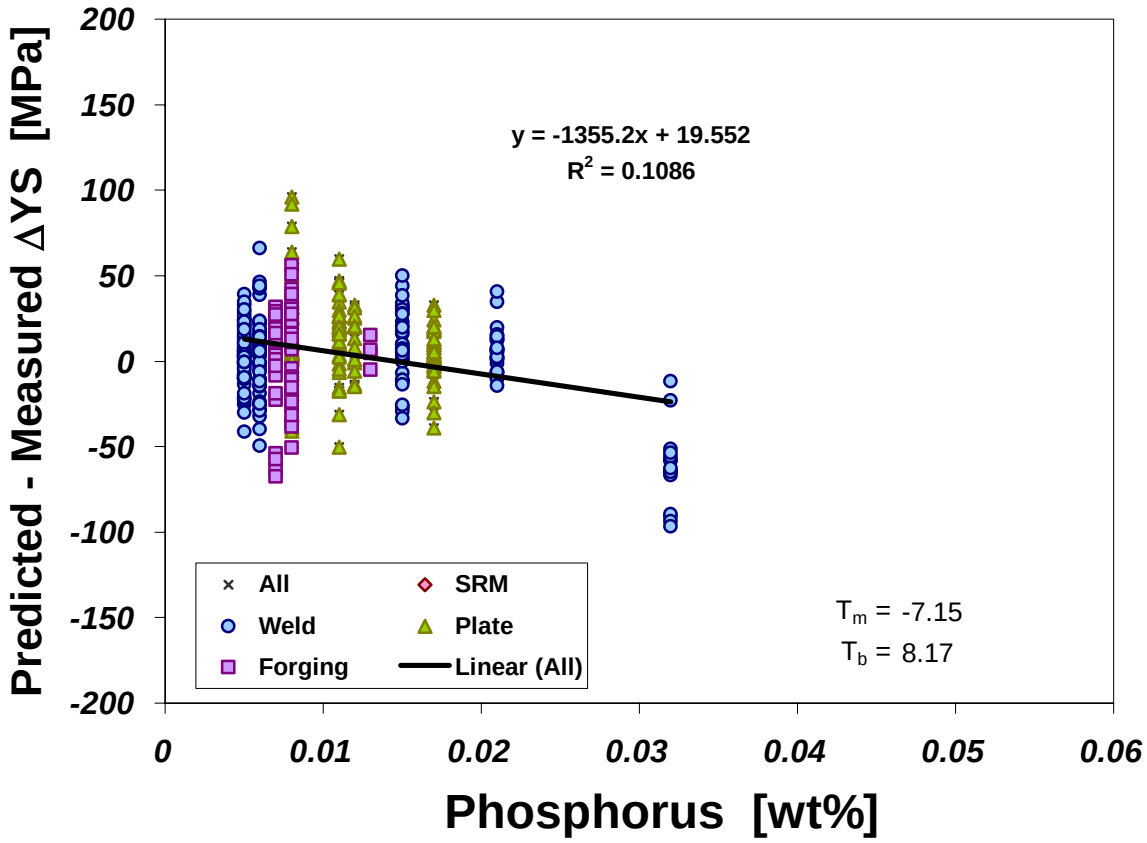

RADAMO vs. US-LWR

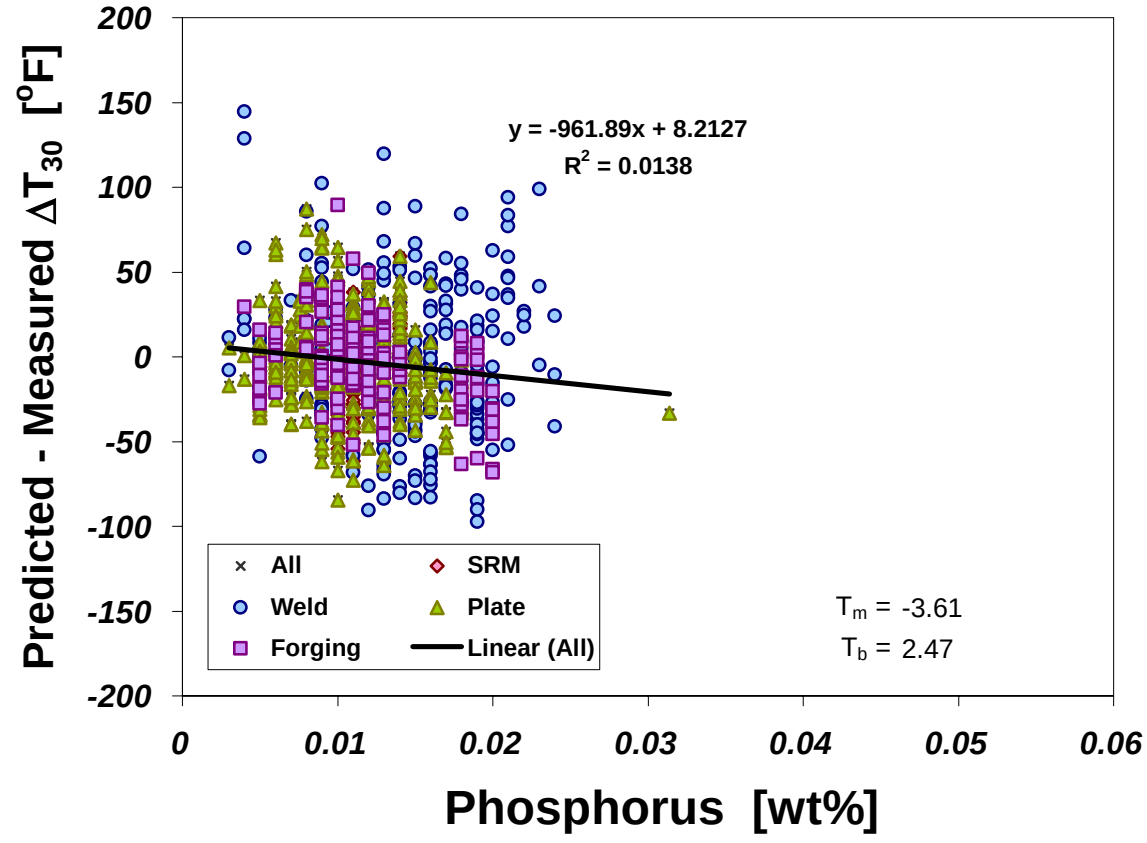

Residuals vs. Phosphorus

NO PRP TERM

RADAMO vs. IVAR

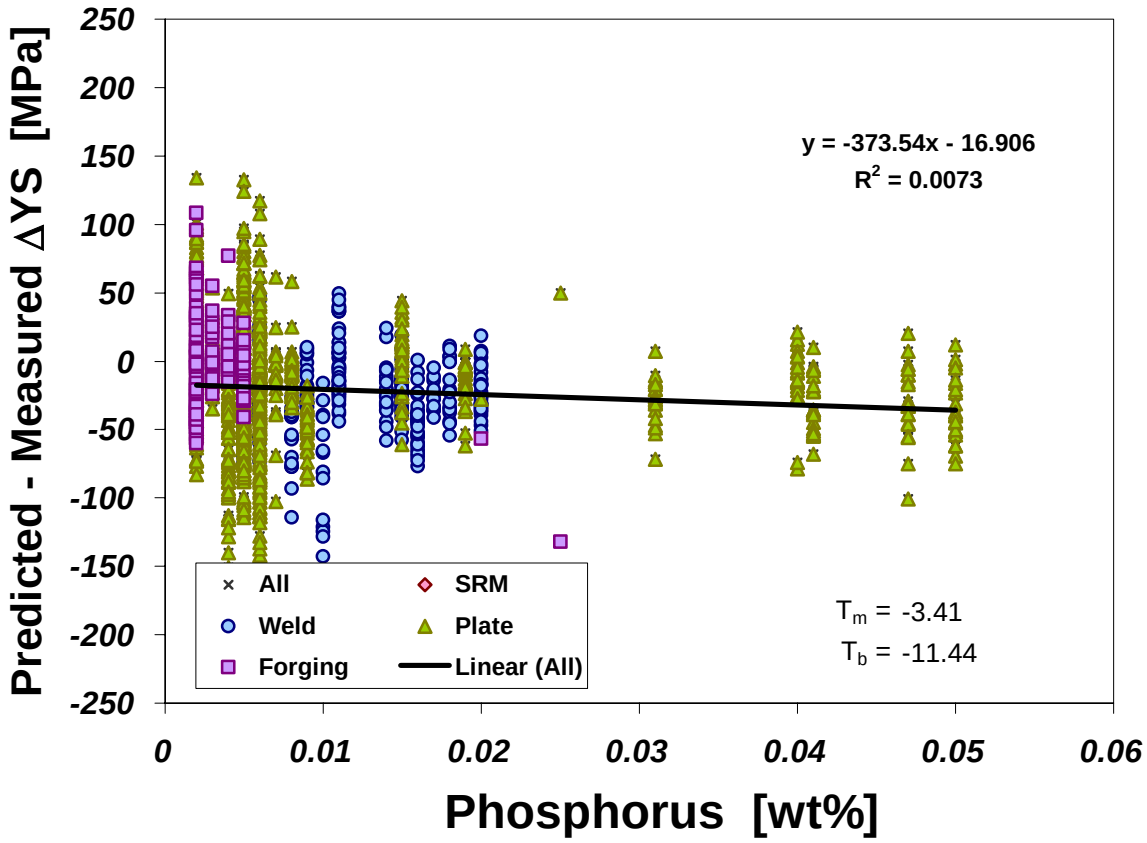

RADAMO vs. French

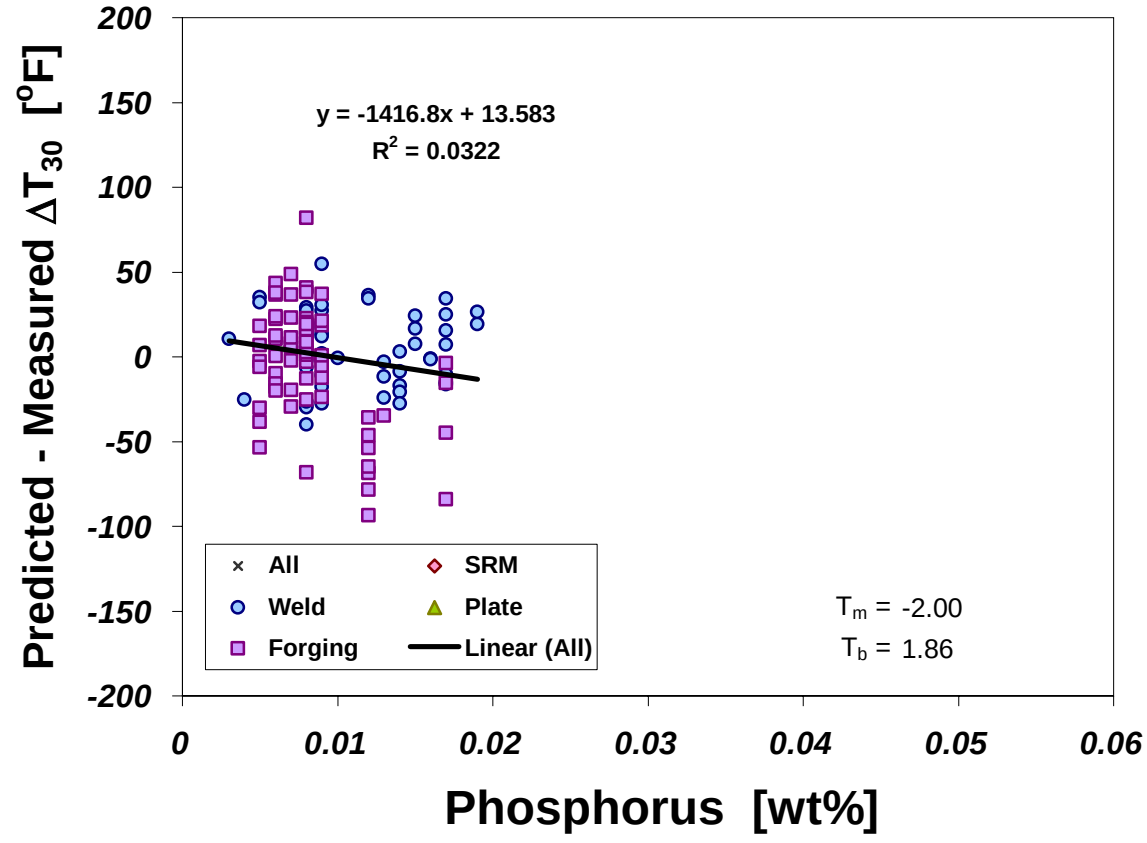

Residuals vs. Phosphorus

NO PRP TERM

RADAMO vs. $JNES_{TEST}$

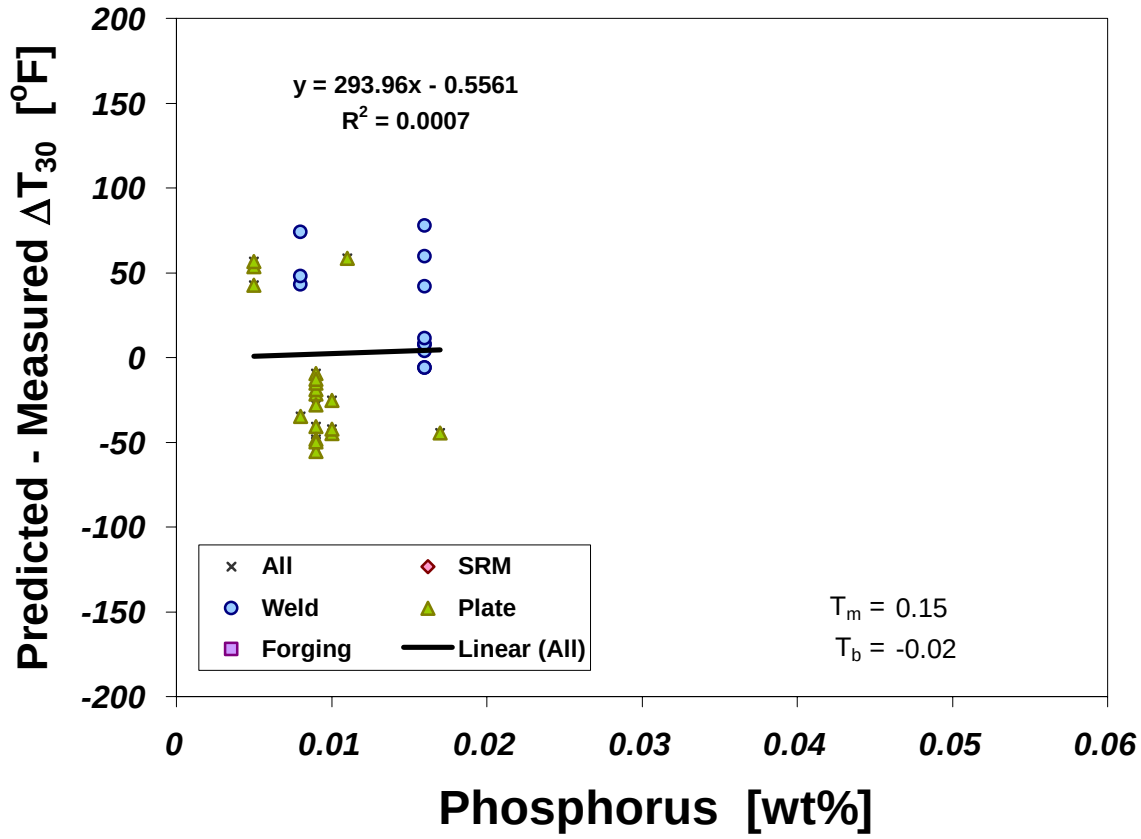

RADAMO vs. $JNES_{RPV}$

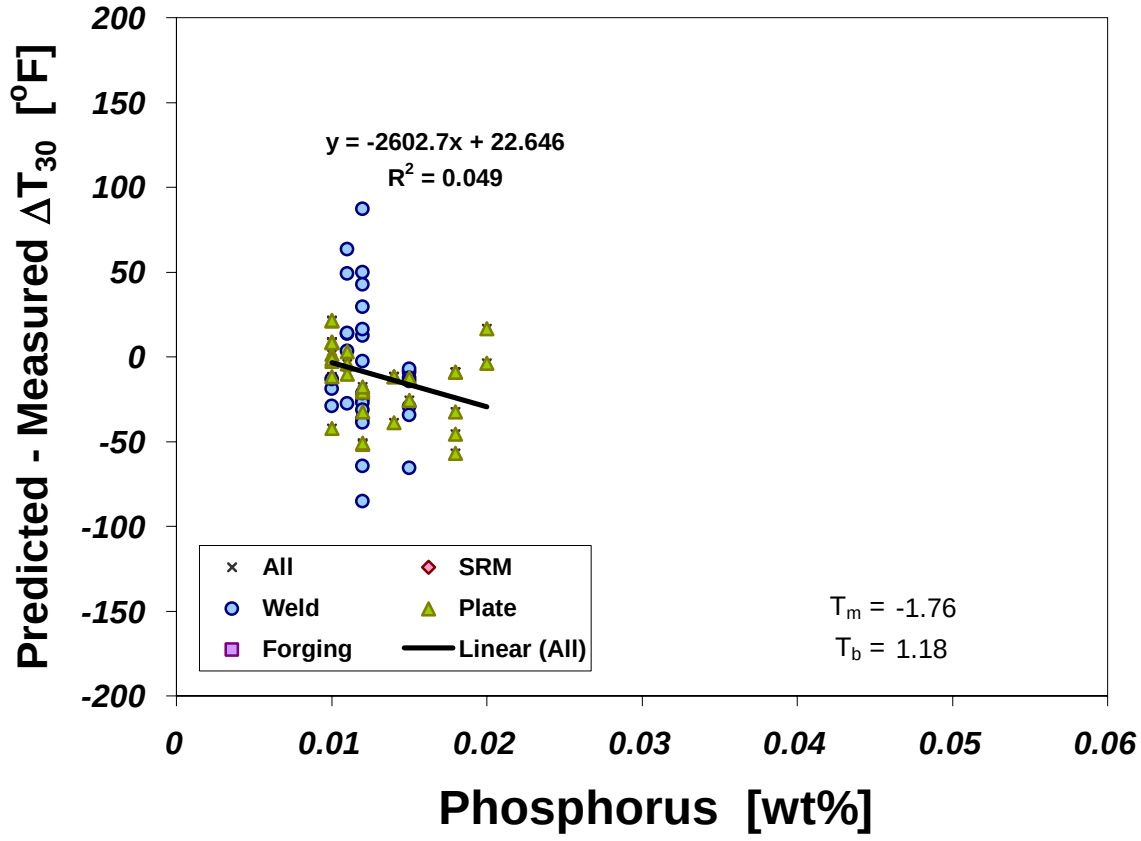

Residuals vs. Manganese

RADAMO vs. RADAMO

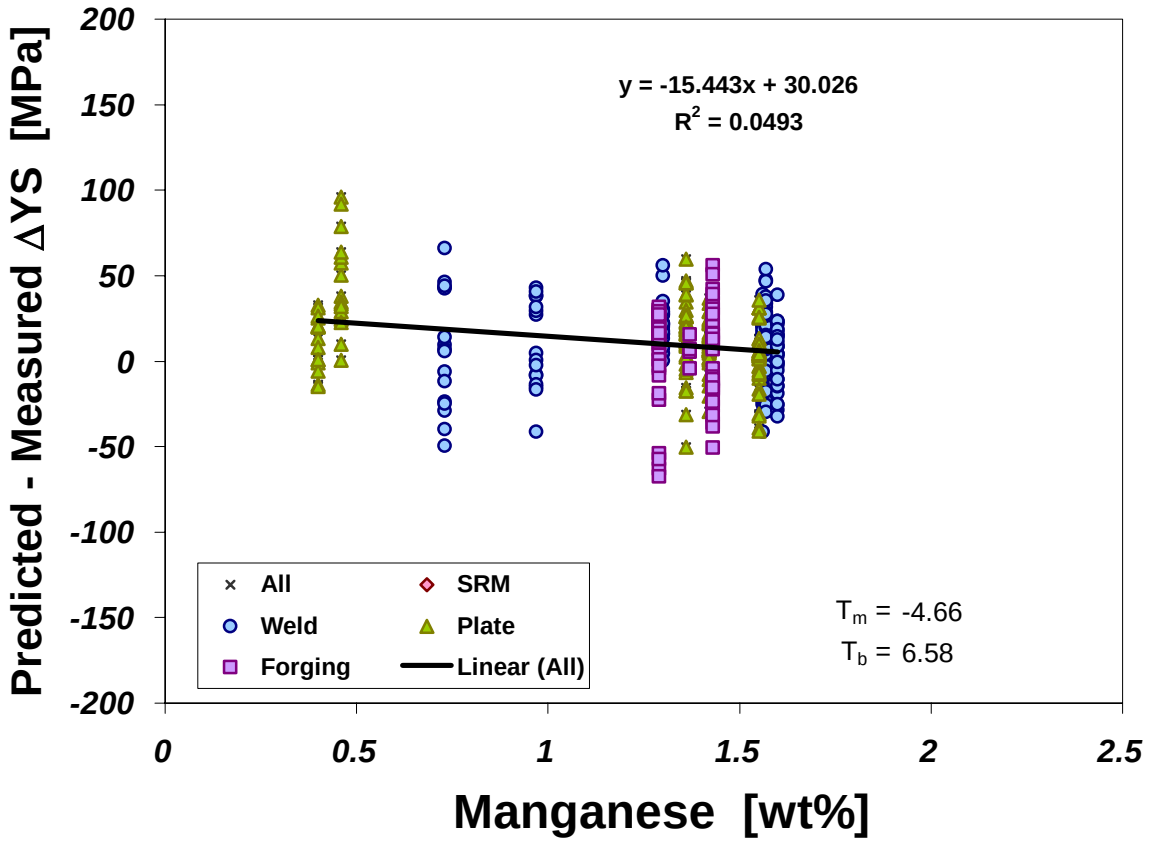

RADAMO vs. US-LWR

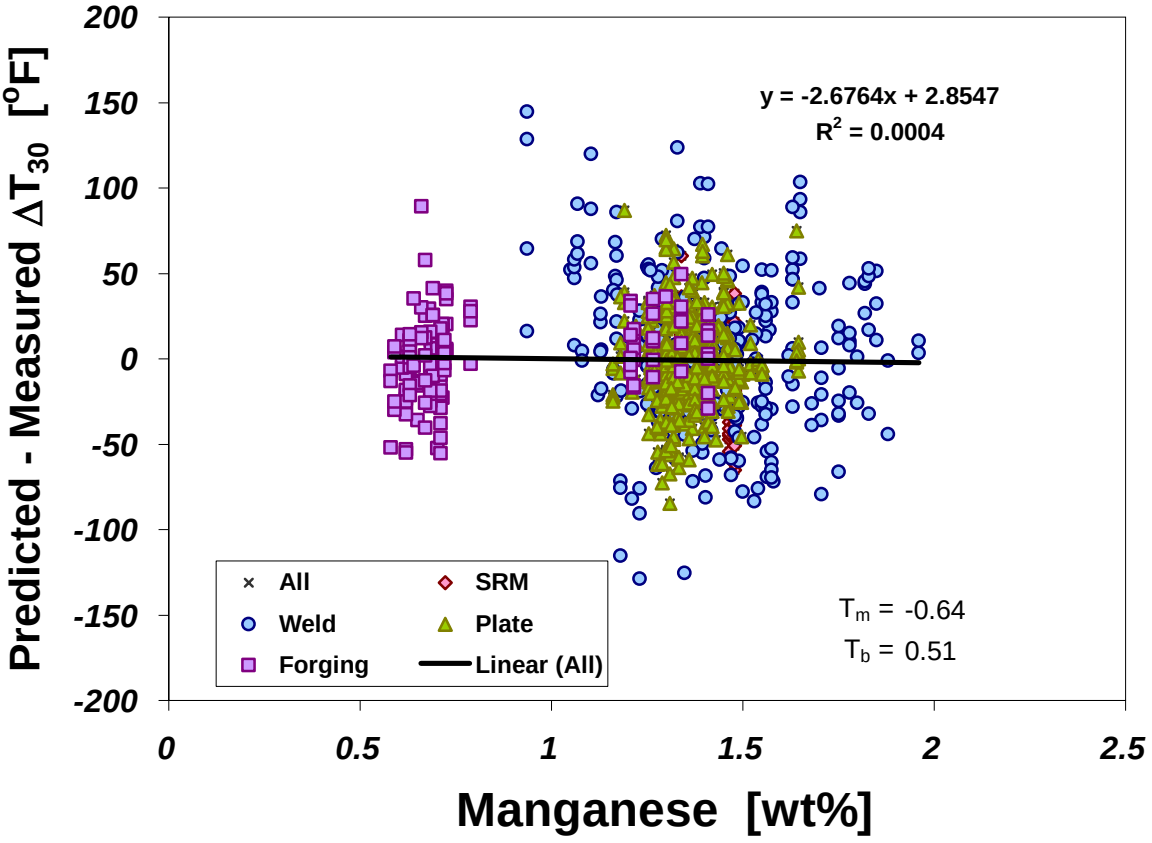

Residuals vs. Manganese

RADAMO vs. IVAR

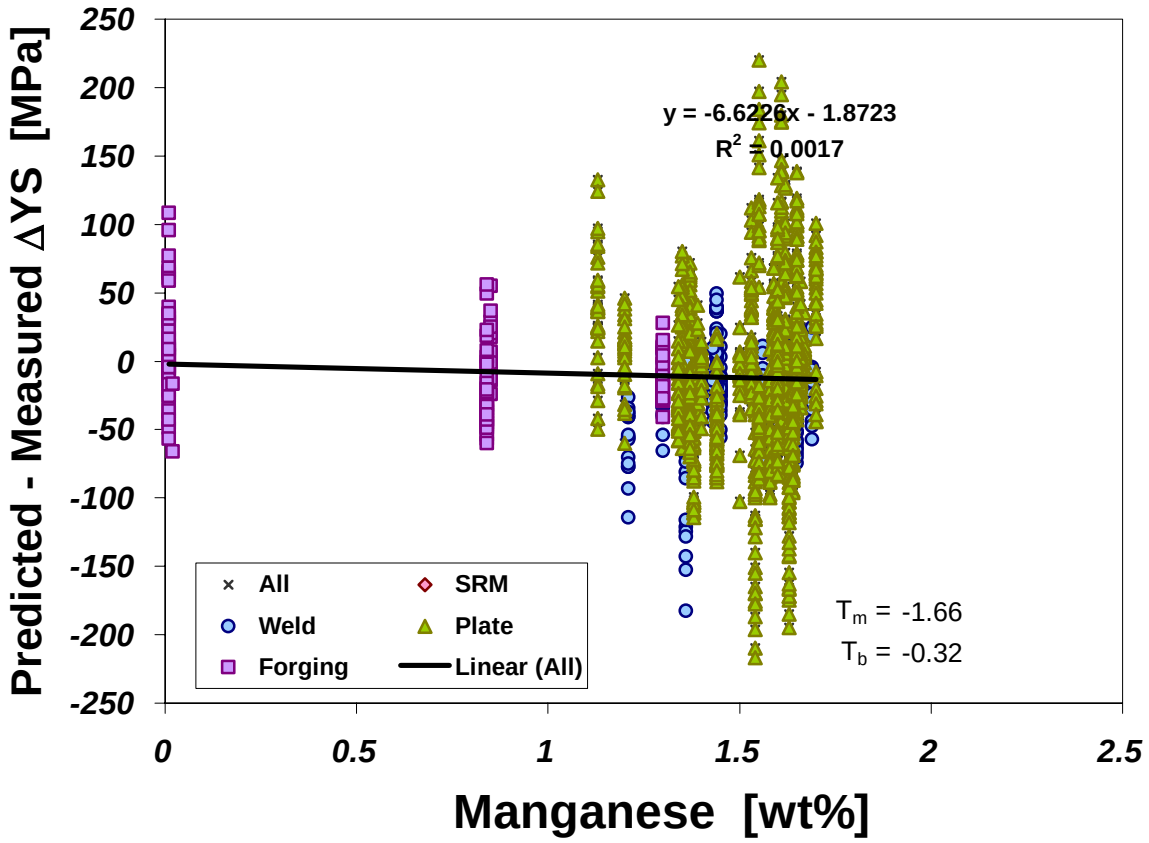

RADAMO vs. French

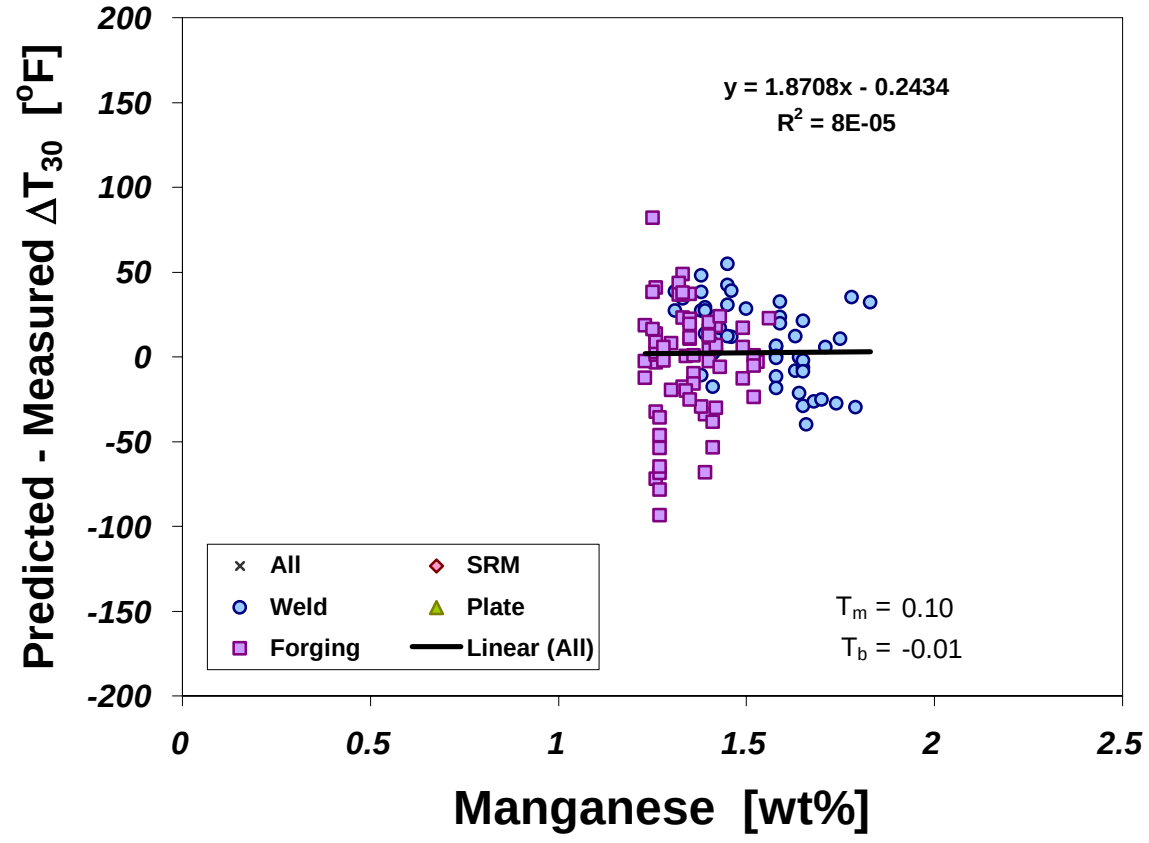

Residuals vs. Manganese

RADAMO vs. JNES$_{TEST}$

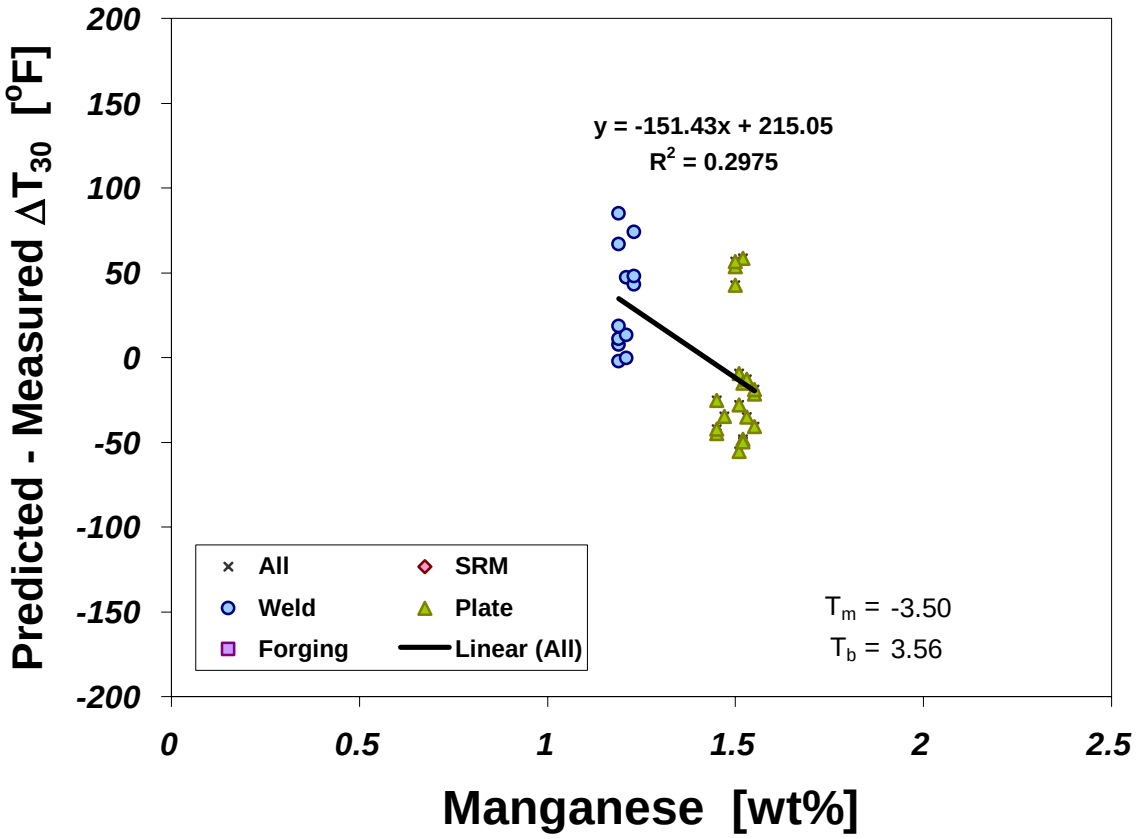

RADAMO vs. JNES$_{RPV}$

Mn not reported

Residuals vs. Silicon

RADAMO vs. RADAMO

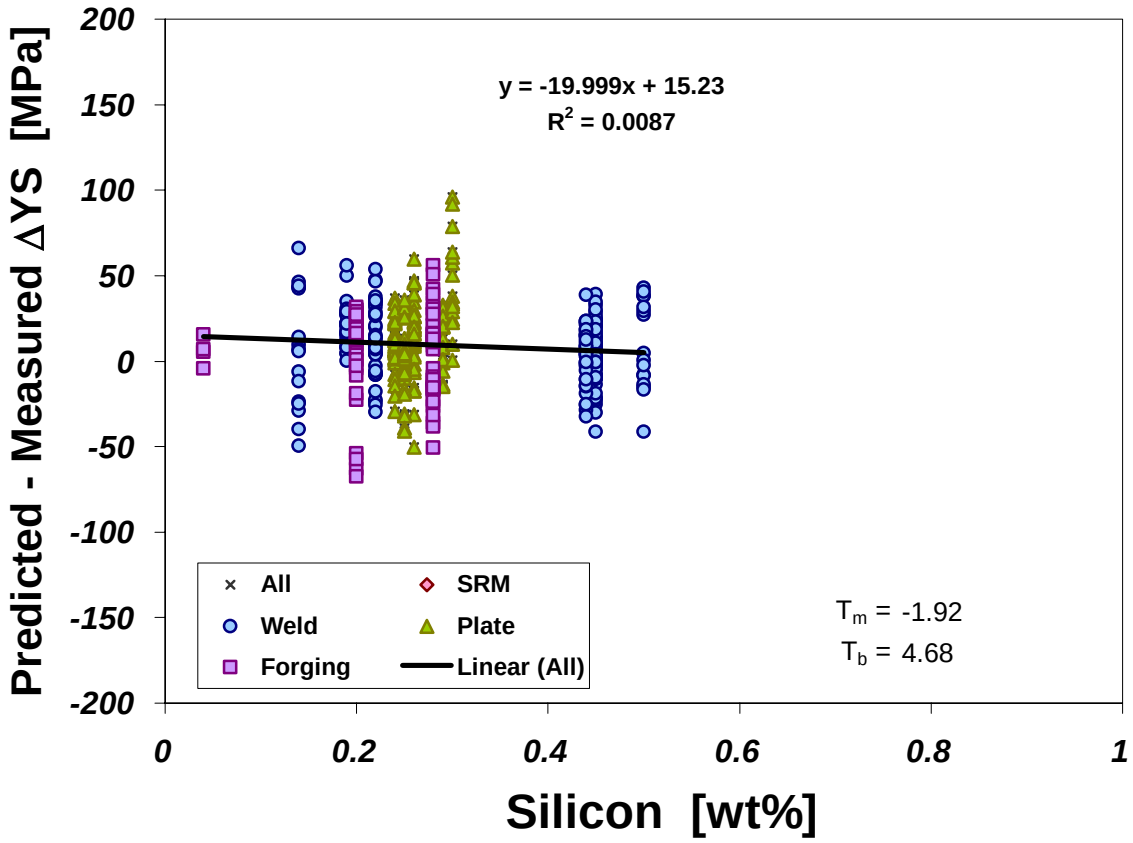

RADAMO vs. US-LWR

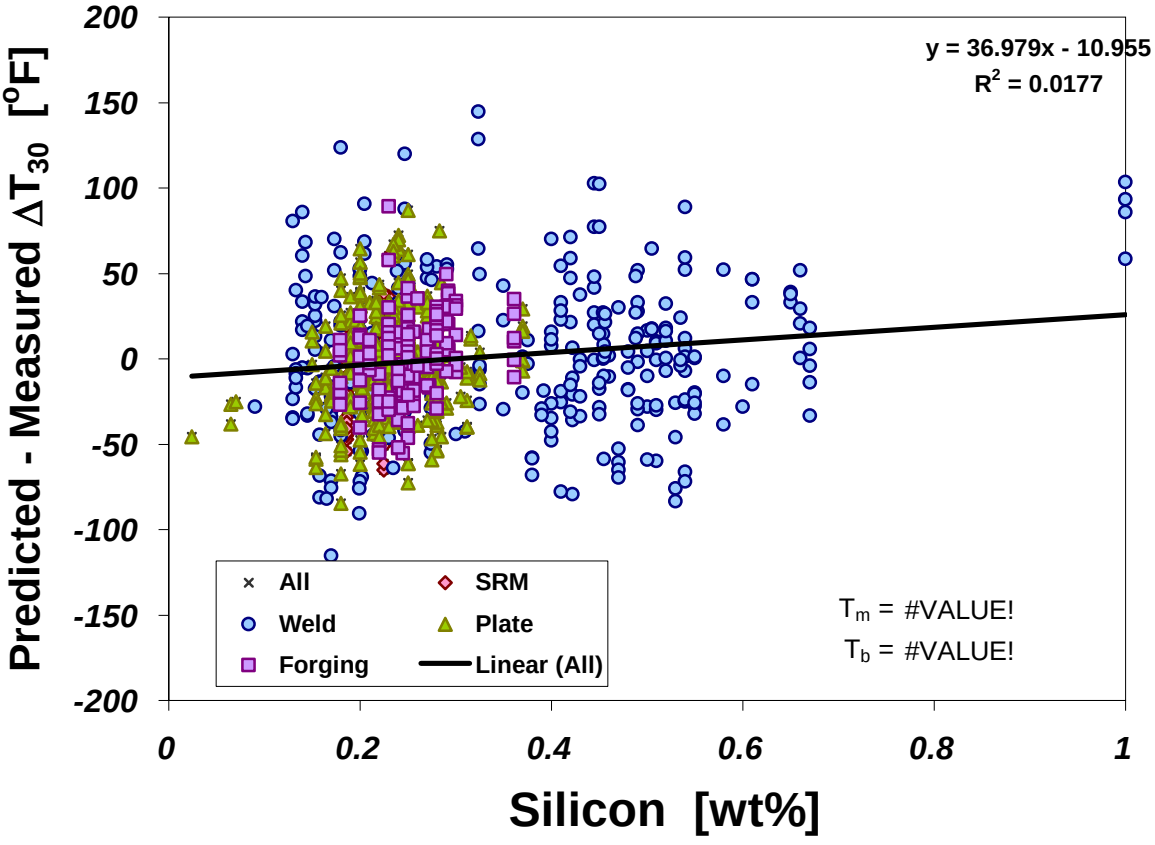

Residuals vs. Silicon

RADAMO vs. IVAR

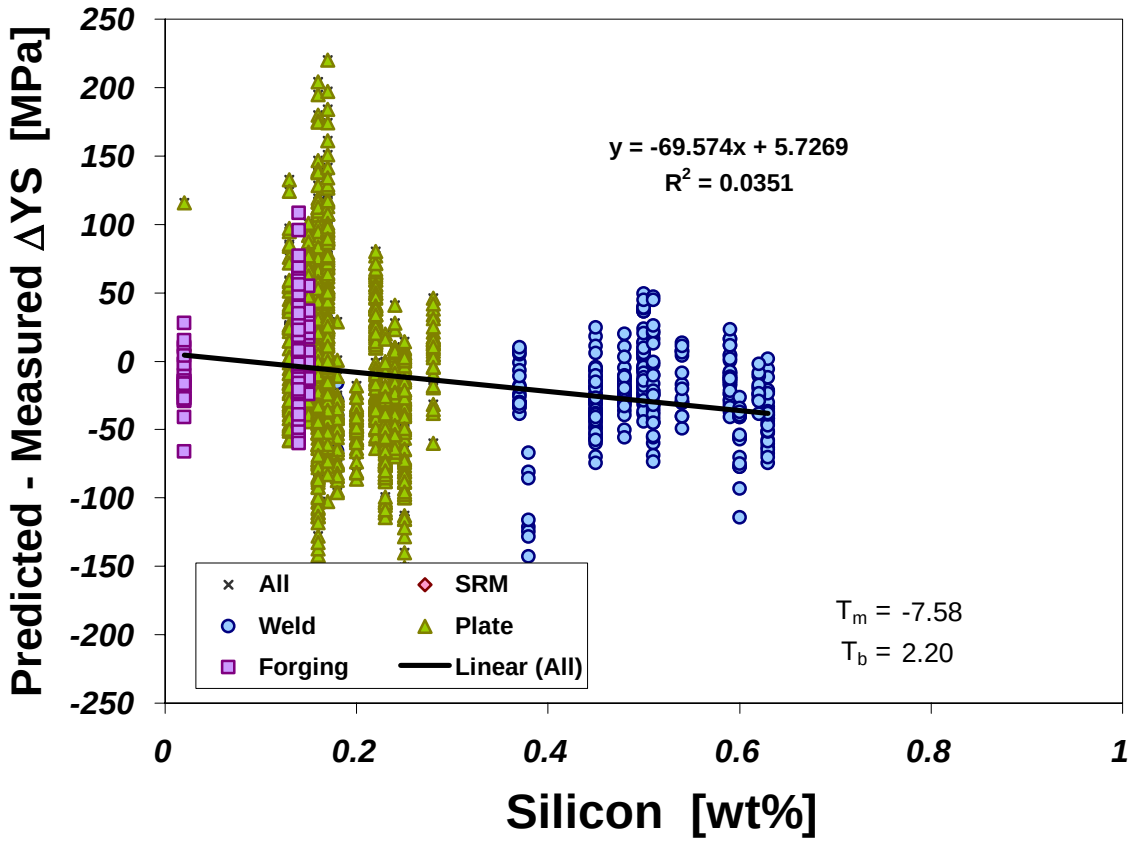

RADAMO vs. French

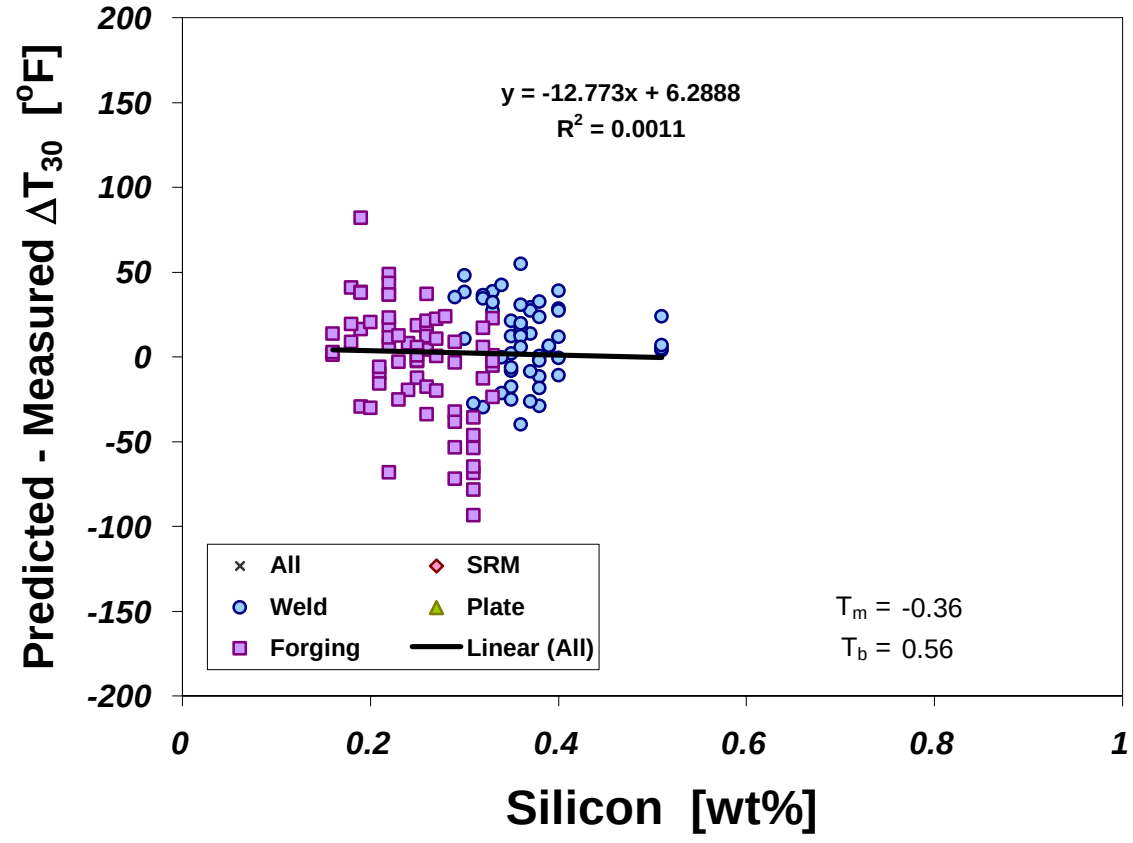

Residuals vs. Silicon

RADAMO vs. JNES$_{TEST}$

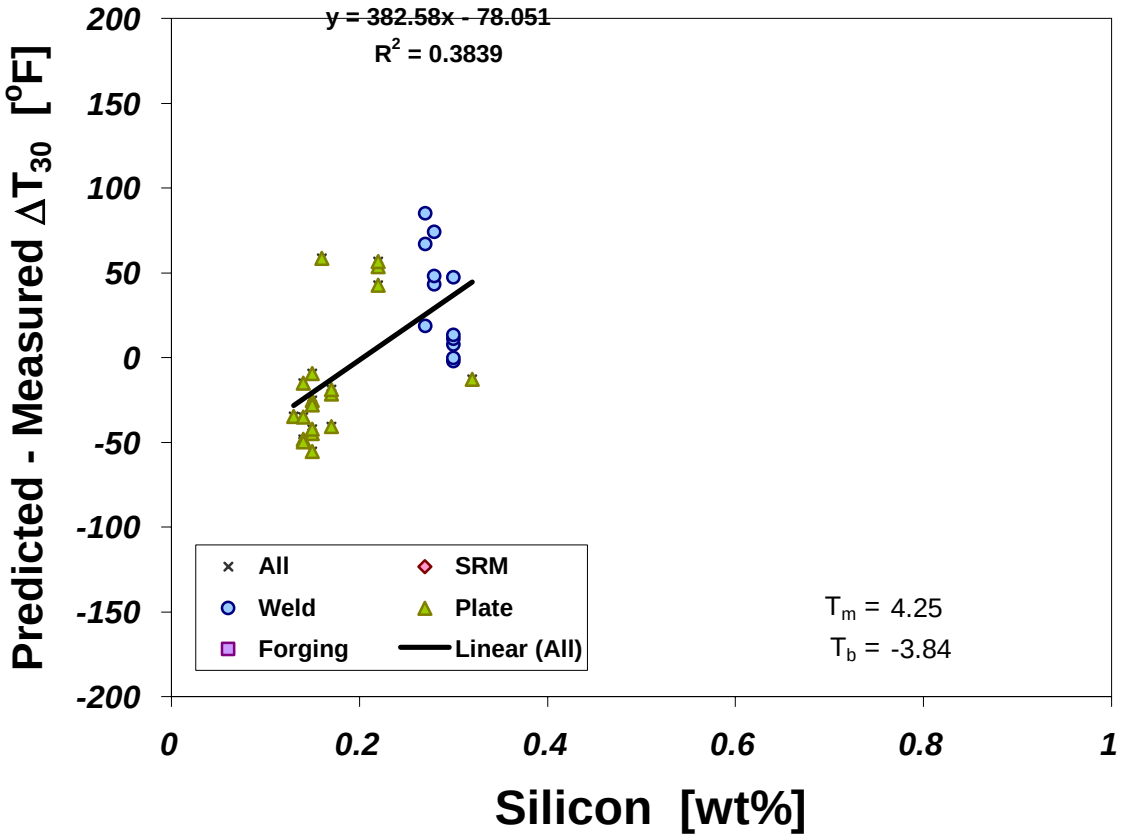

RADAMO vs. JNES$_{RPV}$

Si not reported

Appendix F

STUDIECENTRUM VOOR KERNENERGIE
CENTRE D'ÉTUDE DE L'ÉNERGIE NUCLÉAIRE

RESTRICTED CONTRACT REPORT
SCK•CEN-R-4325

Irradiation of Heavy-Section Steel Irradiation (HSSI) Program Specimens in the BR2 Reactor: the FRISCO-R Experiment

E. Lucon

Contract: CO-90-05-1906-00

April, 2006

RMO
SCK•CEN
Boeretang 200
2400 Mol
Belgium

Distribution list

Name	Institute	Number
R. Nanstad	ORNL, TN (US)	1
T. Rosseel	ORNL, TN (US)	3
M. Sokolov	ORNL, TN (US)	1
E. Lucon	RMO, SCK•CEN	1
M. Scibetta	RMO, SCK•CEN	1
E. van Walle	RMO, SCK•CEN	1
	RPV Steel & Fusion Materials Group	5
M. Wéber	TCH, SCK•CEN	1
J. Wagemans	RF&M-DR, SCK•CEN	1
	Secretariaat RMO	3

		Date	Approval
Author:	E. Lucon		
Verified by:	J. Schuurmans		
Approved by:	E. van Walle		

RESTRICTED CONTRACT REPORT
SCK•CEN-R-4325

Irradiation of Heavy-Section Steel Irradiation (HSSI) Program Specimens in the BR2 Reactor: the FRISCO-R Experiment

E. Lucon

Contract: CO-90-05-1906-00

April, 2006
Status: Confidential

RMO
SCK•CEN
Boeretang 200
2400 Mol
Belgium

Summary

Tensile, half-size Charpy and miniature Compact Tension specimens of six RPV steels have been irradiated in the BR2 reactor in the framework of the HSSI Program, funded by the USNRC at Oak Ridge National Laboratory.

A set of samples from Palisades Weld have been irradiated in IPS-2 for one BR2 cycle (03/2005) up to an average fast neutron fluence of 1.05×10^{20} n/cm² or 0.158 dpa. The corresponding average fast flux was 4.81×10^{13} n/cm²·s.

The remaining sets of samples have been irradiated in IPS-3 during two BR2 cycles (03-04/2005). For Midland Beltline Weld, Palisades Weld, 73W and JRQ the average fast neutron fluence reached was 6.45×10^{19} n/cm² or 0.097 dpa, corresponding to an average fast flux of 1.93×10^{13} n/ cm²·s. In the case of HSST-02, for which mini C(T) were also irradiated, the average values for fast fluence, dpa and fast flux were respectively 7.20×10^{19} n/cm², 0.108 dpa and 2.16×10^{13} n/ cm²·s.

Keywords

RPV steels, HSSI Program, Palisades Weld, Midland Beltline Weld, 73W, JRQ, HSST-02, fast neutron fluence, fast neutron flux, dpa.

TABLE OF CONTENTS

1. Introduction

The primary goal of the Heavy-Section Steel Irradiation (HSSI) Program is to provide a thorough, quantitative assessment of the effects of neutron irradiation on the material behavior, and in particular the fracture toughness properties, of typical pressure vessel steels as they relate to light-water reactor pressure vessel (RPV) integrity. The program includes studies of the effects of irradiation on the degradation of mechanical and fracture properties of vessel materials augmented by enhanced examinations and modeling of the accompanying microstructural changes. Effects of specimen size; material chemistry; product form and microstructure; irradiation fluence, flux, temperature, and spectrum; and post-irradiation mitigation are being examined on a wide range of fracture properties. Results from the HSSI studies are incorporated into codes and standards directly applicable to resolving major regulatory issues that involve RPV irradiation embrittlement such as pressurized-thermal shock, operating pressure-temperature limits, low-temperature over pressurization, and the specialized problems associated with low upper-shelf welds.

The HSSI Program, funded by the U.S. Nuclear Regulatory Commission (USNRC) at Oak Ridge National Laboratory (ORNL), has contracted with SCK•CEN on a project aimed at investigating the effects of relatively high, fast neutron flux on RPV steels.

The irradiation campaign, denominated FRISCO-R (**F**usion and **R**eactor Materials **I**rradiation **S**CK•CEN/**O**RNL – **R**PV steels), was performed during the last three cycles of the Belgian Reactor 2 (BR2) in the period July/December 2005.

All specimens, with the exception mentioned below, have been irradiated in the in-pile section 3 (IPS-3) of BR2 during cycles 04/2005 and 05/2005, at an equivalent fission flux of approximately 2×10^{13} n/(cm²·s), E > 1 MeV. In this document, we will refer to this part of the experiment as *lower flux irradiation*.

Samples from Palisades Weld were also irradiated in the in-pile section 2 (IPS-2) of BR2 during cycle 03/2005, at an equivalent fission flux of approximately 5×10^{13} n/(cm²·s), E > 1 MeV. In this document, we will refer to this part of the experiment as *higher flux irradiation*.

2. Irradiation conditions

The lower flux irradiation has been conducted between Oct 12 and Dec 20, 2005 at a water temperature between 295 and 300 °C in the K311 channel (IPS-3) of the CALLISTO rig in the BR2 reactor. In order to achieve uniform irradiation conditions (fluence and flux) in the radial direction, the rig has been rotated by 180° between the first and the second cycle.

The higher flux irradiation has been conducted between July 29 and Aug 26, 2005 at the same water temperature (295-300 °C) in the D180 channel (IPS-2) of the CALLISTO rig.

For both irradiations, the parameters relative to the coolant have been chosen in conformity with the technical specification of PWR primary water chemistry:

- Temperature 295-300 °C
- Boron (boric acid) ± 550 ppm
- Lithium (lithium hydroxide) 1.8 ppm ≤ [Li] ≤ 2.2 ppm
- pH $7.00 \leq pH_{25°C} \leq 7.08$ or $7.26 \leq pH_{300°C} \leq 7.34$
- Dissolved hydrogen 25 ccSTP/kg ≤ $[H_2]$ ≤ 35 ccSTP/kg

The specimens were in direct contact with the water.

3. Materials and specimens irradiated

Five different reactor pressure vessel (RPV) steels have been irradiated in the FRISCO-R experiment: Palisades Weld (PW), Midland Beltline Weld (MBW), HSST-02, 73W and JRQ.

For each steel, the following samples have been irradiated:

- 6 miniature tensile specimens with cylindrical cross section and the following nominal dimensions:
  - overall length L = 24 mm;
  - length of reduced section A = 12 mm;
  - diameter of reduced section D = 2.4 mm;
  - heads M4;
- 12 half-size Charpy-V specimens to be tested for fracture toughness, with the following nominal dimensions:
  - thickness B = 5 mm;
  - width W = 10 mm;
  - length L = 55 mm;
- 1 atom probe blank (nominal dimensions 7 × 7 × 0.5 mm³);
- 1 SANS blank (nominal dimensions 7 × 7 × 0.25 mm³).

For Palisades Weld, two series of specimens as detailed above were irradiated, one at higher flux in IPS-2 and one at lower flux in IPS-3.

Additionally, 12 miniature Compact Tension specimens of HSST-02 steel have been irradiated with the following nominal dimensions:

- height H =10 mm;
- width W = 10 mm;
- thickness B = 4.2 mm.

Technical drawings of the samples are given in Annex 1 (tensile), Annex 2 (half-size Charpy) and Annex 3 (miniature C(T)).

The chemical composition of the five RPV steels is given in Table 1; Table 2 shows their tensile properties at room temperature. Information contained in both Tables has been provided by ORNL.

Table 1 - Chemical composition of the RPV steels irradiated in the FRISCO-R experiment.

Material	C	Mn	Si	S	P	Cr	V	Cu	Mo	Ni	W	Al
MBW	-	1.607	0.622	-	0.017	-	-	0.256	-	0.574	-	-
PW	0.11	1.25	0.18	0.017	0.014	0.04	0.003	0.20	0.55	1.2	-	-
HSST-02	0.23	1.55	0.20	0.014	0.009	0.04	0.003	0.14	0.53	0.67	<0.01	0.019
73W	0.10	1.56	0.45	0.005	0.005	0.25	-	0.31	0.58	0.60	<0.01	0.005
JRQ	0.18	1.42	0.24	0.004	0.017	0.12	0.002	0.14	0.51	0.84	<0.01	0.014

Table 2 -Room temperature tensile properties of the RPV steels irradiated in the FRISCO-R experiment.

Material	Yield strength [MPa]	Tensile strength [MPa]	Total elongation [%]	Reduction of area [%]
MBW	407	586	n/a	n/a
PW	470	580	n/a	n/a
HSST-02	466	614	21	66
73W	490	599	22	68
JRQ	487	627	25	74

4. Pre-irradiation operations

Samples were sent from ORNL to SCK•CEN before irradiation. Most of them had been dimensionally checked before shipping; dimensional controls on the remaining specimens were performed at SCK•CEN. All dimensional measurements are provided in Annex 4.

It can be remarked that 50% of the half-size Charpy specimens of 73W were received in fatigue precracked condition; all the remaining fracture toughness samples will be precracked after irradiation.

Before loading, the half-size Charpy specimens have been assembled two by two by welding small 10 × 10 mm² plates at each end. After irradiation, the plates have been removed by milling and the samples separated.

5. Fluence and flux evaluation

The estimation of neutron fluences and fluxes experienced by the specimens is based upon the power of BR2, the axial position of the samples in the rig and the duration of the irradiation cycles.

The maximum fast neutron fluences and fluxes (E > 1 MeV) relative to the center channel of the CALLISTO rig (channel E) and the BR2 midplane (axial position Z = -72 mm) have been calculated using the code GEXBR2-TRPT3, which has been developed and validated by SCK•CEN and is based on neutron transport theory. The calculated values are:

- Higher flux irradiation: Cycle 03/2005, IPS-2
  Reference power: 57 MW
  $\Phi = 1.93 \times 10^{20}$ n/cm² (E > 1 MeV) – 0.29 dpa
  Irradiation time: 25 days or 2.18549×10^{6} sec
  Flux = 8.83×10^{13} n/(cm²·s) (E > 1 MeV)
- Lower flux irradiation: Cycles 04-05/2005, IPS-3
  Reference power: 60 MW
  $\Phi = 0.79 \times 10^{20}$ n/cm² (E > 1 MeV) – 0.12 dpa
  Irradiation time: 39 days or 3.33582×10^{6} sec
  Flux = 2.37×10^{13} n/(cm²·s) (E > 1 MeV)

These values are rigorously valid only for samples located at the position of highest flux (midplane) and in the center channel of the rig (channel E); cosinusoidal axial distribution functions [1] have been used to evaluate the fluence and flux associated to each individual specimen.

In addition, 9 activation dosimeters made of pure iron (disks with diameter = 9 mm and thickness = 0.5 mm) were loaded in the CALLISTO rig and placed inside the boxes containing the tensile samples. Fluences and fluxes measured by the dosimeters have been used to adjust the values calculated using the neutron transport code. Details of the dosimetry measurements are given in the Technical Note presented in Annex 5.

The values of fast fluence, fast flux and dpa associated to each irradiated specimen are reported in the next section.

6. Loading plan; values of fluence, flux and dpa

The needles containing the specimens irradiated in IPS-2 have been loaded into the CALLISTO shroud tube CAL 17; the needles containing the specimens irradiated in IPS-3 have been loaded into the shroud tube CAL 22.

All loading and unloading operations have been performed in the BR2 hot cells; other operations in the reactor pool were standard manipulations.

6.1 Higher flux irradiation – Palisades Weld (IPS-2, cycle 03/2005)

The loading plan[1] is given in Table 3 for the Palisades Weld (PW) specimens irradiated in channels D and F of IPS-2 during cycle 03/2005, with the values of fast fluence, fast flux and dpa calculated for each individual sample.

The mean values of fast fluence, fast flux and dpa associated to the entire specimen set and to each type of specimen (tensile and half-size Charpy) are presented in Table 4.

Table 3 - Loading plan, fluence, flux and dpa values for the samples of Palisades Weld (PW) irradiated in IPS-2 during cycle 03/2005.

Channel	Axial level (mm)	Specimen type	Specimen id	Fast fluence 10^{20} n/cm²	Fast flux 10^{13} n/cm²·s	dpa
D	-422	Half-size Charpy	BH1	0.91	4.17	0.137
			BH2			
	-357		BX1	1.28	5.84	0.191
			BX2			
	213		BX3	1.28	5.84	0.191
			BX4			
	278		BX5	0.91	4.17	0.137
			BX6			
F	-422	Half-size Charpy	BX7	0.87	3.98	0.130
			BX8			
	-357		BX9	1.22	5.57	0.183
			BX10			
	209.5	AP + SANS		1.24	5.66	0.183
	246.5	Tensile	BX1	1.04	4.75	0.156
			BX2			
			BX3			
	271.5	Tensile	BX4	0.91	4.14	0.136
			BX5			
			BX6			

[1] The axial level in Table 3 refers to the midplane of the specimens.

Table 4 - Mean values of fluence, flux and dpa calculated for the PW specimens irradiated in IPS-2 during cycle 03/2005.

Specimen type	Mean fast fluence n/cm², E > 1 MeV	Mean fast flux n/cm²·s, E > 1 MeV	Mean dpa
Tensile	0.97×10^{20}	4.45×10^{13}	0.146
Half-size Charpy	1.08×10^{20}	4.93×10^{13}	0.161
All	$\mathbf{1.05 \times 10^{20}}$	$\mathbf{4.81 \times 10^{13}}$	**0.158**

6.2 Lower flux irradiation (IPS-3, cycles 04-05/2005)

6.2.1 Midland Beltline Weld

The loading plan for channel A (Midland Beltline Weld specimens) is given in Table 5, with the values of fast fluence, fast flux and dpa calculated for each individual sample.

The mean values of fast fluence, fast flux and dpa associated to the entire specimen set and to each type of specimen (tensile and half-size Charpy) are presented in Table 6.

Table 5 - Loading plan, fluence, flux and dpa values for the samples of Midland Beltline Weld (MBW) irradiated in IPS-3 during cycles 04-05/2005.

Channel	Axial level (mm)	Specimen type	Specimen id	Fluence 10^{19} n/cm²	Flux 10^{13} n/cm²·s	dpa
A	-302.5	Half-size Charpy	MW01	5.21	1.56	0.078
			MW02			
	-244.5	Tensile	MW1	6.12	1.84	0.092
			MW2			
			MW3			
	-182.5	Half-size Charpy	MW03	6.88	2.06	0.103
			MW04			
	-117.5		WQ5	7.34	2.20	0.110
			WQ6			
	-75	AP + SANS		7.44	2.23	0.111
	-32.5	Half-size Charpy	MW07	7.36	2.21	0.110
			MW08			
	32.5		MW09	6.94	2.08	0.104
			MW10			
	92.5	Tensile	MW04	6.24	1.87	0.094
			MW05			
			MW06			
	152.5	Half-size Charpy	MW11	5.31	1.59	0.080
			MW12			

Table 6 - Mean values of fluence, flux and dpa calculated for the MBW specimens irradiated in IPS-3 during cycles 04-05/2005.

Specimen type	Mean fast fluence n/cm², E > 1 MeV	Mean fast flux n/cm²·s, E > 1 MeV	Mean dpa
Tensile	6.18×10^{19}	1.85×10^{13}	0.093
Half-size Charpy	6.51×10^{19}	1.95×10^{13}	0.098
All	$\mathbf{6.45 \times 10^{19}}$	$\mathbf{1.93 \times 10^{13}}$	**0.097**

6.2.2 Palisades Weld

The loading plan for channel B (Palisades Weld specimens) is given in Table 7, with the values of fast fluence, fast flux and dpa calculated for each individual sample.

The mean values of fast fluence, fast flux and dpa associated to the entire specimen set and to each type of specimen (tensile and half-size Charpy) are presented in Table 8.

Table 7 - Loading plan, fluence, flux and dpa values for the samples of Palisades Weld (PW) irradiated in IPS-3 during cycles 04-05/2005.

Channel	Axial level (mm)	Specimen type	Specimen id	Fluence 10^{19} n/cm²	Flux 10^{13} n/cm²·s	dpa
B	-302.5	Half-size Charpy	BH13	5.21	1.56	0.078
			BH14			
	-244.5	Tensile	BX7	6.12	1.84	0.092
			BX9			
			BX10			
	-182.5	Half-size Charpy	BH15	6.88	2.06	0.103
			BH16			
	-117.5		BH17	7.34	2.20	0.110
			BH18			
	-75	AP + SANS		7.44	2.23	0.111
	-32.5	Half-size Charpy	BH19	7.36	2.21	0.110
			BH20			
	32.5		BH21	6.94	2.08	0.104
			BH22			
	92.5	Tensile	BH11	6.24	1.87	0.094
			BX5A			
			BX6A			
	152.5	Half-size Charpy	BH23	5.31	1.59	0.080
			BH24			

Table 8 - Mean values of fluence, flux and dpa calculated for the PW specimens irradiated in IPS-3 during cycles 04-05/2005.

Specimen type	Mean fast fluence n/cm², E > 1 MeV	Mean fast flux n/cm²·s, E > 1 MeV	Mean dpa
Tensile	6.18×10^{19}	1.85×10^{13}	0.093
Half-size Charpy	6.51×10^{19}	1.95×10^{13}	0.098
All	**6.45×10^{19}**	**1.93×10^{13}**	**0.097**

6.2.3 73W

The loading plan for channel D (73W specimens) is given in Table 9, with the values of fast fluence, fast flux and dpa calculated for each individual sample.

The mean values of fast fluence, fast flux and dpa associated to the entire specimen set and to each type of specimen (tensile and half-size Charpy) are presented in Table 10.

Table 9 - Loading plan, fluence, flux and dpa values for the samples of 73W irradiated in IPS-3 during cycles 04-05/2005.

Channel	Axial level (mm)	Specimen type	Specimen id	Fluence 10^{19} n/cm²	Flux 10^{13} n/cm²·s	dpa
D	-302.5	Half-size Charpy	73W5	5.21	1.56	0.078
			73W6			
	-244.5	Tensile	73W1	6.12	1.84	0.092
			73W2			
			73W3			
	-182.5	Half-size Charpy	73W7	6.88	2.06	0.103
			73W9			
	-117.5		73W12	7.34	2.20	0.110
			73W18			
	-75	AP + SANS		7.44	2.23	0.111
	-32.5	Half-size Charpy	73WQ1A	7.36	2.21	0.110
			73WQ2A			
	32.5		73WQ3A	6.94	2.08	0.104
			73WQ4A			
	92.5	Tensile	73W4	6.24	1.87	0.094
			MW5			
			MW6			
	152.5	Half-size Charpy	73WQ5A	5.31	1.59	0.080
			73WQ6A			

Table 10 - Mean values of fluence, flux and dpa calculated for the 73W specimens irradiated in IPS-3 during cycles 04-05/2005.

Specimen type	Mean fast fluence n/cm², E > 1 MeV	Mean fast flux n/cm²·s, E > 1 MeV	Mean dpa
Tensile	6.18×10^{19}	1.85×10^{13}	0.093
Half-size Charpy	6.51×10^{19}	1.95×10^{13}	0.098
All	**6.45×10^{19}**	**1.93×10^{13}**	**0.097**

6.2.4 JRQ

The loading plan for channel E (JRQ specimens) is given in Table 11, with the values of fast fluence, fast flux and dpa calculated for each individual sample.

The mean values of fast fluence, fast flux and dpa associated to the entire specimen set and to each type of specimen (tensile and half-size Charpy) are presented in Table 12.

Table 11 - Loading plan, fluence, flux and dpa values for the samples of JRQ irradiated in IPS-3 during cycles 04-05/2005.

Channel	Axial level (mm)	Specimen type	Specimen id	Fluence 10^{19} n/cm²	Flux 10^{13} n/cm²·s	dpa
E	-302.5	Half-size Charpy	JRQ1	5.21	1.56	0.078
			JRQ2			
	-244.5	Tensile	J1	6.12	1.84	0.092
			J2			
			J3			
	-182.5	Half-size Charpy	JRQ3	6.88	2.06	0.103
			JRQ4			
	-117.5		JRQ5	7.34	2.20	0.110
			JRQ6			
	-75	AP + SANS		7.44	2.23	0.111
	-32.5	Half-size Charpy	JRQ7	7.36	2.21	0.110
			JRQ8			
	32.5		JRQ9	6.94	2.08	0.104
			JRQ10			
	92.5	Tensile	J4	6.24	1.87	0.094
			JRQ-Q5			
			JRQ-Q6			
	152.5	Half-size Charpy	TRQ11	5.31	1.59	0.080
			TRQ12			

Table 12 - Mean values of fluence, flux and dpa calculated for the JRQ specimens irradiated in IPS-3 during cycles 04-05/2005.

Specimen type	Mean fast fluence n/cm², E > 1 MeV	Mean fast flux n/cm²·s, E > 1 MeV	Mean dpa
Tensile	6.18×10^{19}	1.85×10^{13}	0.093
Half-size Charpy	6.51×10^{19}	1.95×10^{13}	0.098
All	**6.45×10^{19}**	**1.93×10^{13}**	**0.097**

6.2.5 HSST-02

The loading plan for channel I (HSST-02 specimens) is given in Table 13, with the values of fast fluence, fast flux and dpa calculated for each individual sample.

The mean values of fast fluence, fast flux and dpa associated to the entire specimen set and to each type of specimen (tensile, half-size Charpy and mini C(T)) are presented in Table 14.

Table 13 - Loading plan, fluence, flux and dpa values for the samples of HSST-02 irradiated in IPS-3 during cycles 04-05/2005.

Channel	Axial level (mm)	Specimen type	Specimen id	Fluence 10^{19} n/cm²	Flux 10^{13} n/cm²·s	dpa
I	-336	Half-size Charpy	2D01	4.88	1.46	0.073
			2D02			
	-276	Tensile	2D1	5.96	1.79	0.089
			2D2			
			2D3			
	-216	Half-size Charpy	2D03	6.87	2.06	0.103
			2D04			
	-151		2D05	7.55	2.26	0.113
			2D06			
	-86.75[2]	Mini C(T)	2D01 ↓ 2D12	7.84	2.35	0.118
	-45	AP + SANS		7.82	2.34	0.117
	-2.5	Half-size Charpy	2D07	7.62	2.28	0.114
			2D08			
	62.5		2D09	6.99	2.10	0.105
			2D10			
	122.5	Tensile	2D4	6.12	1.84	0.092
			2D5			
			2D6			
	182.5	Half-size Charpy	2D11	5.06	1.52	0.076
			2D12			

Table 14 - Mean values of fluence, flux and dpa calculated for the HSST-02 specimens irradiated in IPS-3 during cycles 04-05/2005.

Specimen type	Mean fast fluence n/cm², E > 1 MeV	Mean fast flux n/cm²·s, E > 1 MeV	Mean dpa
Tensile	6.04×10^{19}	1.81×10^{13}	0.091
Half-size Charpy	6.49×10^{19}	1.95×10^{13}	0.097
Mini C(T)	7.84×10^{19}	2.35×10^{13}	0.118
All	$\mathbf{7.20 \times 10^{19}}$	$\mathbf{2.16 \times 10^{13}}$	**0.108**

[2] The value refers to the middle position of the mini C(T) specimen set (between specimen 2D06 and 2D07).

7. Post-irradiation operations

After irradiation, the samples have been unloaded in the BR2 hot cells and transferred to the Laboratory for High and Medium Activity (LHMA) of SCK•CEN, where they are currently kept in storage in view of being tested and/or dispatched back to ORNL.

Acknowledgements

The collaboration of the personnel of the BR2 and TCH departments of SCK•CEN for all pre- and post-irradiation operations is acknowledged. Personal thanks to Marcel Wéber who followed the preparation and execution of the irradiation campaign.

Reference

[1] R. Chaouadi, *A Simple Equation to Estimate the Neutron Flux Distribution in the Callisto Loop of the BR2 Reactor*, SCK•CEN Open Report BLG-866, January 2001.

Appendix F

ANNEX 1

Technical drawing of the sub-size tensile specimen

Appendix F

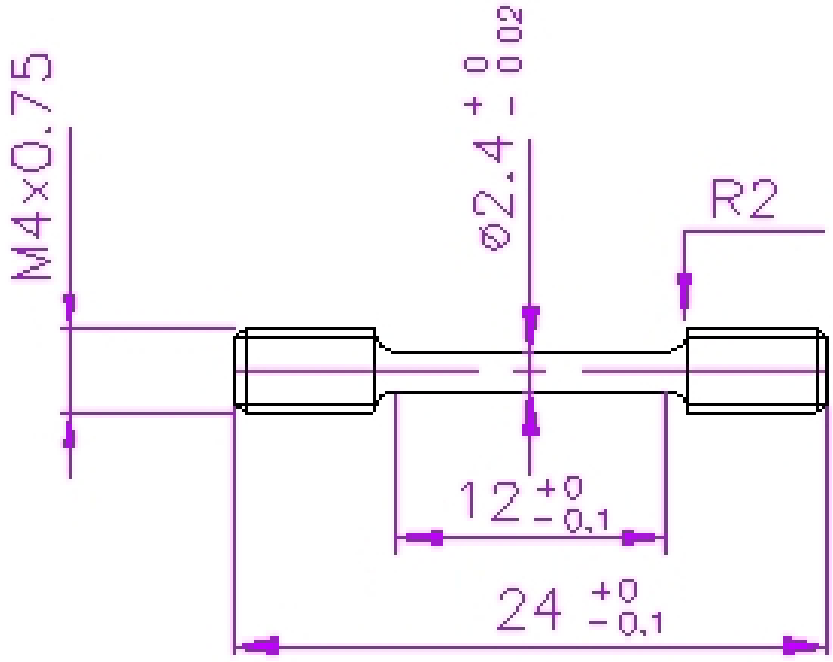
M4x0.75
Ø2.4 +0.02 +0
R2
12 +0 -0.1
24 +0 -0.1

Appendix F

ANNEX 2

Technical drawing of the half-size Charpy specimen

Appendix F

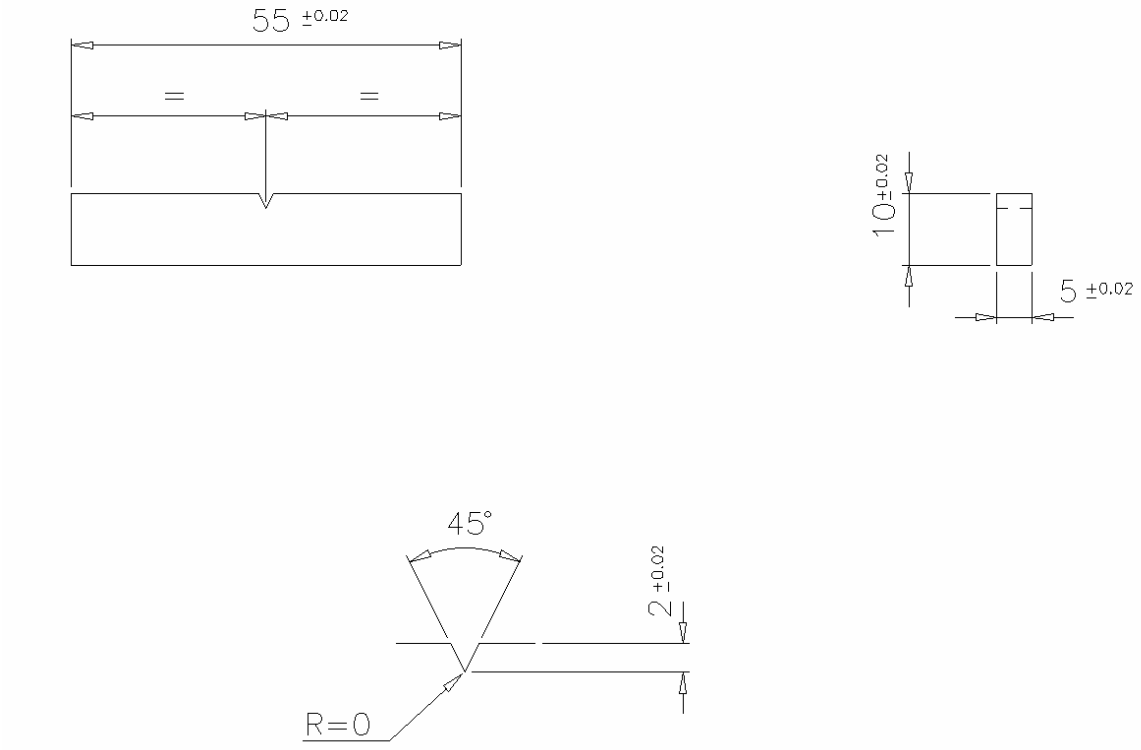
55 ±0.02
=
=
10±0.02
5 ±0.02
45°
2±0.02
R=0

Appendix F

ANNEX 3

Technical drawing of the miniature C(T) specimen

Appendix F

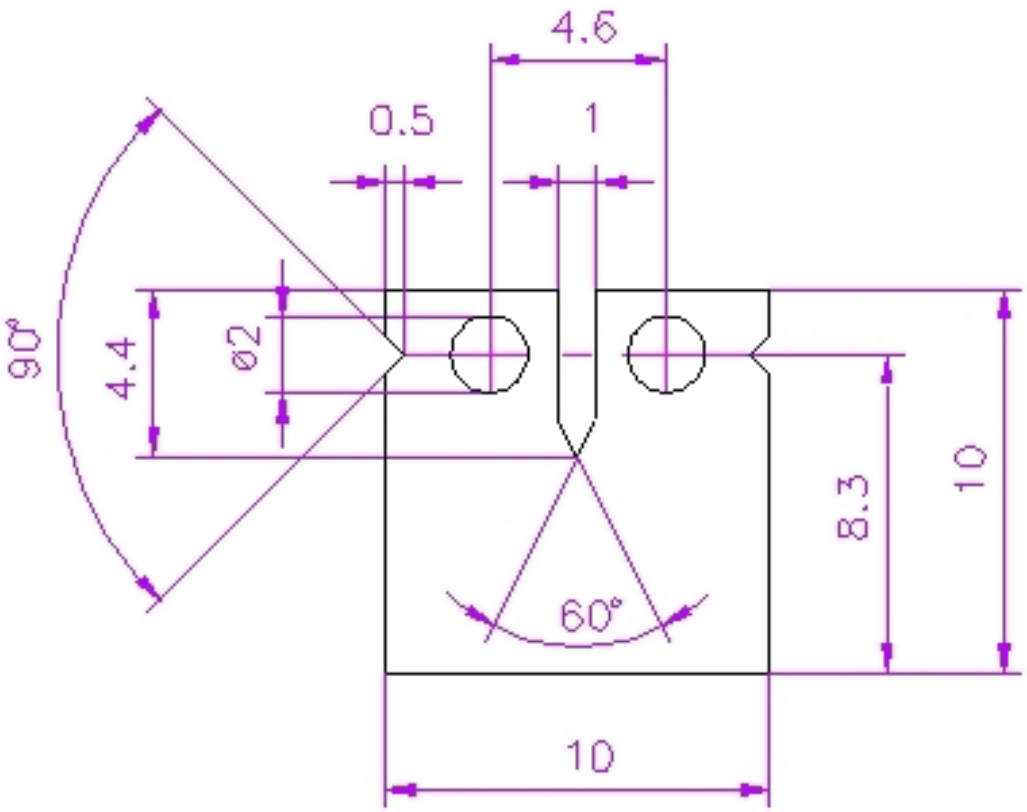

Thickness 4.2

Appendix F

ANNEX 4

Dimensional measurements of the FRISCO-R specimens

Appendix F

MATERIAL : Palisades weld (low fluence)

Specimen type: half-size Charpy (not precracked)

Specimen id	Length		Width		Thickness		Notch depth	
	(in)	(mm)	(in)	(mm)	(in)	(mm)	(in)	(mm)
BH13	2.165	54.991	0.3943	10.0152	0.1945	4.9403	0.0790	2.0066
BH14	2.165	54.991	0.3943	10.0152	0.1945	4.9403	0.0790	2.0066
BH15	2.165	54.991	0.3943	10.0152	0.1945	4.9403	0.0790	2.0066
BH16	2.165	54.991	0.3943	10.0152	0.1945	4.9403	0.0785	1.9939
BH17	2.165	54.991	0.3943	10.0152	0.1945	4.9403	0.0790	2.0066
BH18	2.165	54.991	0.3943	10.0152	0.1945	4.9403	0.0790	2.0066
BH19	2.165	54.991	0.3943	10.0152	0.1945	4.9403	0.0790	2.0066
BH20	2.165	54.991	0.3943	10.0152	0.1945	4.9403	0.0790	2.0066
BH21	2.165	54.991	0.3943	10.0152	0.1945	4.9403	0.0790	2.0066
BH22	2.165	54.991	0.3943	10.0152	0.1945	4.9403	0.0790	2.0066
BH23	2.165	54.991	0.3943	10.0152	0.1945	4.9403	0.0790	2.0066
BH24	2.165	54.991	0.3943	10.0152	0.1945	4.9403	0.0790	2.0066

Specimen type: atom probe blank

Specimen id	Thickness		Width		Height	
	(in)	(mm)	(in)	(mm)	(in)	(mm)
1	0.0197	0.49911	0.278	7.0612	0.275	6.9850

Specimen type: SANS blank

Specimen id	Thickness		Width		Height	
	(in)	(mm)	(in)	(mm)	(in)	(mm)
1	0.0098	0.24765	0.277	7.0358	0.275	6.9850

Specimen type: sub-size tensile

Specimen id	Overall length		Gage diameter		Gage length		Fillet radius
	(in)	(mm)	(in)	(mm)	(in)	(mm)	
BX5A		23.987		2.382		12.065	OK
BX6A		23.970		2.399		12.139	OK
BX7	0.942	23.9268	0.0940	2.3876	0.4700	11.9380	OK
BX9	0.943	23.9522	0.0943	2.3952	0.4700	11.9380	OK
BX10	0.943	23.9522	0.0943	2.3952	0.4710	11.9634	OK
BX11	0.944	23.9776	0.0942	2.3927	0.4690	11.9126	OK

MATERIAL : Midland Weld

Specimen type: half-size Charpy

Specimen id	Length		Width		Thickness		Notch depth	
	(in)	(mm)	(in)	(mm)	(in)	(mm)	(in)	(mm)
MW-01	2.1650	54.991	0.3937	10.0000	0.1968	4.9987	0.0790	2.0066
MW-02	2.1650	54.991	0.3937	10.0000	0.1968	4.9987	0.0790	2.0066
MW-03	2.1650	54.991	0.3937	10.0000	0.1968	4.9987	0.0790	2.0066
MW-04	2.1650	54.991	0.3937	10.0000	0.1968	4.9987	0.0790	2.0066
MW-05	2.1650	54.991	0.3937	10.0000	0.1968	4.9987	0.0790	2.0066
MW-06	2.1650	54.991	0.3937	10.0000	0.1968	4.9987	0.0790	2.0066
MW-07	2.1650	54.991	0.3937	10.0000	0.1968	4.9987	0.0790	2.0066
MW-08	2.1650	54.991	0.3937	10.0000	0.1969	5.0013	0.0790	2.0066
MW-09	2.1650	54.991	0.3937	10.0000	0.1969	5.0013	0.0790	2.0066
MW-10	2.1650	54.991	0.3937	10.0000	0.1968	4.9987	0.0790	2.0066
MW-11	2.1650	54.991	0.3937	10.0000	0.1968	4.9987	0.0790	2.0066
MW-12	2.1650	54.991	0.3937	10.0000	0.1969	5.0013	0.0790	2.0066

Specimen type: atom probe blank

Specimen id	Thickness		Width		Height	
	(in)	(mm)	(in)	(mm)	(in)	(mm)
1	0.0195	0.4953	0.276	7.0104	0.275	6.9850

Specimen type: SANS blank

Specimen id	Thickness		Width		Height	
	(in)	(mm)	(in)	(mm)	(in)	(mm)
1	0.0100	0.254	0.276	7.0104	0.276	7.0104

Specimen type: sub-size tensile

Specimen id	Overall length		Gage diameter		Gage length		Fillet radius
	(in)	(mm)	(in)	(mm)	(in)	(mm)	
MW-1	0.9452	24.0081	0.0945	2.4003	0.4700	11.9380	OK
MW-2	0.9440	23.9776	0.0948	2.4079	0.4695	11.9253	OK
MW-3	0.9447	23.9954	0.0951	2.4155	0.4715	11.9761	OK
MW-4	0.9452	24.0081	0.0929	2.3597	0.4720	11.9888	OK
MW-5		23.994		2.383		11.983	OK
MW-6		24.008		2.391		11.998	OK

MATERIAL : 73W

Specimen type: half-size Charpy (not precracked)

Specimen id	Length		Width		Thickness		Notch depth	
	(in)	(mm)	(in)	(mm)	(in)	(mm)	(in)	(mm)
73WQ1A	2.1652	54.9961	0.3940	10.0076	0.1973	5.0114	0.0790	2.0066
73WQ2A	2.1652	54.9961	0.3940	10.0076	0.1975	5.0165	0.0790	2.0066
73WQ3A	2.1652	54.9961	0.3940	10.0076	0.1975	5.0165	0.0790	2.0066
73WQ4A	2.1652	54.9961	0.3940	10.0076	0.1973	5.0114	0.0790	2.0066
73WQ5A	2.1652	54.9961	0.3940	10.0076	0.1975	5.0165	0.0790	2.0066
73WQ6A	2.1652	54.9961	0.3940	10.0076	0.1975	5.0165	0.0790	2.0066

Specimen type: half-size Charpy (already precracked)

Specimen id	Length		Width		Thickness		Notch depth	
	(in)	(mm)	(in)	(mm)	(in)	(mm)	(in)	(mm)
73W-05	2.1664	55.0266	0.3938	10.0025	0.1775	4.5085	0.0785	1.9939
73W-06	2.1660	55.0164	0.3938	10.0025	0.1775	4.5085	0.0785	1.9939
73W-07	2.1662	55.0215	0.3938	10.0025	0.1775	4.5085	0.0785	1.9939
73W-09	2.1670	55.0418	0.3938	10.0025	0.1775	4.5085	0.0785	1.9939
73W-12	2.1666	55.0316	0.3938	10.0025	0.1775	4.5085	0.0785	1.9939
73W-18	2.1668	55.0367	0.3943	10.0152	0.1775	4.5085	0.0785	1.9939

Specimen type: atom probe blank

Specimen id	Thickness		Width		Height	
	(in)	(mm)	(in)	(mm)	(in)	(mm)
1	0.0197	0.50038	0.276	7.0104	0.276	7.0104

Specimen type: SANS blank

Specimen id	Thickness		Width		Height	
	(in)	(mm)	(in)	(mm)	(in)	(mm)
1	0.0100	0.254	0.275	6.9850	0.276	7.0104

Specimen type: sub-size tensile

Specimen id	Overall length		Gage diameter		Gage length		Fillet radius
	(in)	(mm)	(in)	(mm)	(in)	(mm)	
73W-1	0.9464	24.0386	0.0948	2.4079	0.4700	11.9380	OK
73W-2	0.9469	24.0513	0.0952	2.4181	0.4705	11.9507	OK
73W-3	0.9459	24.0259	0.0947	2.4054	0.4690	11.9126	OK
73W-4	0.9468	24.0487	0.0948	2.4079	0.4690	11.9126	OK
73WQ5		24.024		2.398		11.977	OK
73WQ6		23.969		2.394		12.041	OK

MATERIAL : JRQ

Specimen type: half-size Charpy

Specimen id	Length		Width		Thickness		Notch depth	
	(in)	(mm)	(in)	(mm)	(in)	(mm)	(in)	(mm)
JRQ-01	2.1650	54.991	0.3942	10.0127	0.1972	5.0089	0.0790	2.0066
JRQ-02	2.1650	54.991	0.3943	10.0152	0.1972	5.0089	0.0790	2.0066
JRQ-03	2.1650	54.991	0.3943	10.0152	0.1972	5.0089	0.0790	2.0066
JRQ-04	2.1650	54.991	0.3942	10.0127	0.1972	5.0089	0.0790	2.0066
JRQ-05	2.1650	54.991	0.3942	10.0127	0.1970	5.0038	0.0790	2.0066
JRQ-06	2.1650	54.991	0.3943	10.0152	0.1972	5.0089	0.0790	2.0066
JRQ-07	2.1650	54.991	0.3942	10.0127	0.1972	5.0089	0.0790	2.0066
JRQ-08	2.1650	54.991	0.3943	10.0152	0.1970	5.0038	0.0790	2.0066
JRQ-09	2.1650	54.991	0.3943	10.0152	0.1970	5.0038	0.0790	2.0066
JRQ-10	2.1650	54.991	0.3943	10.0152	0.1972	5.0089	0.0790	2.0066
JRQ-11	2.1650	54.991	0.3942	10.0127	0.1972	5.0089	0.0790	2.0066
JRQ-12	2.1650	54.991	0.3942	10.0127	0.1972	5.0089	0.0790	2.0066

Specimen type: atom probe blank

Specimen id	Thickness		Width		Height	
	(in)	(mm)	(in)	(mm)	(in)	(mm)
1	0.0198	0.50292	0.273	6.9342	0.275	6.9850

Specimen type: SANS blank

Specimen id	Thickness		Width		Height	
	(in)	(mm)	(in)	(mm)	(in)	(mm)
1	0.0100	0.254	0.273	6.9342	0.274	6.9596

Specimen type: sub-size tensile

Specimen id	Overall length		Gage diameter		Gage length		Fillet radius
	(in)	(mm)	(in)	(mm)	(in)	(mm)	
JRQ-1	0.9461	24.0309	0.0948	2.4079	0.4680	11.8872	OK
JRQ-2	0.9462	24.0335	0.0948	2.4079	0.4690	11.9126	OK
JRQ-3	0.9466	24.0436	0.0951	2.4155	0.4670	11.8618	OK
JRQ-4	0.9470	24.0538	0.0948	2.4079	0.4695	11.9253	OK
JRQ-Q5		23.954		2.393		11.929	OK
JRQ-Q6		23.982		2.389		12.092	OK

Appendix F

MATERIAL : HSST Plate 02

Specimen type: half-size Charpy

Specimen id	Length (in)	Length (mm)	Width (in)	Width (mm)	Thickness (in)	Thickness (mm)	Notch depth (in)	Notch depth (mm)
2D01	2.1637	54.9580	0.3942	10.0127	0.1970	5.0038	0.0790	2.0066
2D02	2.1634	54.9504	0.3942	10.0127	0.1970	5.0038	0.0790	2.0066
2D03	2.1633	54.9478	0.3942	10.0127	0.1970	5.0038	0.0790	2.0066
2D04	2.1635	54.9529	0.3942	10.0127	0.1970	5.0038	0.0790	2.0066
2D05	2.1635	54.9529	0.3942	10.0127	0.1970	5.0038	0.0790	2.0066
2D06	2.1635	54.9529	0.3942	10.0127	0.1970	5.0038	0.0790	2.0066
2D07	2.1633	54.9478	0.3942	10.0127	0.1970	5.0038	0.0790	2.0066
2D08	2.1631	54.9427	0.3943	10.0152	0.1970	5.0038	0.0790	2.0066
2D09	2.1635	54.9529	0.3943	10.0152	0.1970	5.0038	0.0790	2.0066
2D10	2.1632	54.9453	0.3942	10.0127	0.1970	5.0038	0.0790	2.0066
2D11	2.1638	54.9605	0.3942	10.0127	0.1970	5.0038	0.0790	2.0066
2D12	2.1638	54.9605	0.3942	10.0127	0.1970	5.0038	0.0790	2.0066

Specimen type: miniature C(T)

Specimen id	Width (in)	Width (mm)	Thickness (in)	Thickness (mm)
2D01	0.3260	8.2804	0.1660	4.2164
2D02	0.3260	8.2804	0.1659	4.2139
2D03	0.3260	8.2804	0.1657	4.2088
2D04	0.3260	8.2804	0.1658	4.2113
2D05	0.3260	8.2804	0.1657	4.2088
2D06	0.3260	8.2804	0.1662	4.2215
2D07	0.3260	8.2804	0.1657	4.2088
2D08	0.3260	8.2804	0.1660	4.2164
2D09	0.3260	8.2804	0.1657	4.2088
2D10	0.3260	8.2804	0.1659	4.2139
2D11	0.3260	8.2804	0.1659	4.2139
2D12	0.3260	8.2804	0.1657	4.2088

Specimen type: atom probe blank

Specimen id	Thickness (in)	Thickness (mm)	Width (in)	Width (mm)	Height (in)	Height (mm)
1	0.0198	0.5029	0.276	7.0104	0.276	7.0104

Specimen type: SANS blank

Specimen id	Thickness (in)	Thickness (mm)	Width (in)	Width (mm)	Height (in)	Height (mm)
1	0.0100	0.254	0.276	7.0104	0.276	7.0104

Specimen type: sub-size tensile

Specimen id	Overall length (in)	Overall length (mm)	Gage diameter (in)	Gage diameter (mm)	Gage length (in)	Gage length (mm)	Fillet radius
2D1	0.9446	23.9928	0.0953	2.4206	0.4680	11.8872	OK
2D2	0.9462	24.0335	0.0948	2.4079	0.4695	11.9253	OK
2D3	0.9440	23.9776	0.0949	2.4105	0.4985	12.6619	OK
2D4	0.9458	24.0233	0.0948	2.4079	0.4680	11.8872	OK
2D5		23.965		2.393		11.776	OK
2D6		24.000		2.383		11.876	OK

Appendix F

Dimensional measurements:

Date: 01/06/2005
Programma: FRISCO
Material: Palisades weld HF
Operator: Paul Wouters
Measuring: Profile projector PJ300
Remark: measuring unit mm

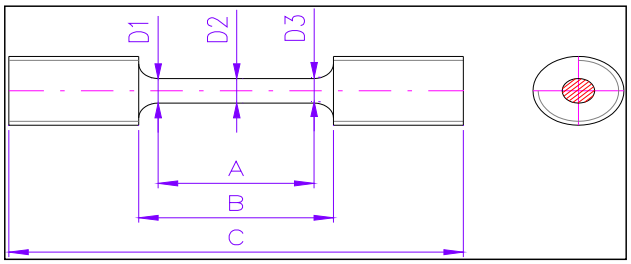

	Sp. Id	A	C	D1	D2 0°	D2 90°	D2average	D3
1	BX1	12.010	23.960	2.405	2.393	2.394	2.393	2.401
2	BX2	12.003	23.975	2.403	2.389	2.388	2.388	2.390
3	BX3	12.000	23.950	2.398	2.392	2.396	2.394	2.410
4	BX4	12.002	23.926	2.403	2.399	2.400	2.399	2.421
5	BX5	12.003	23.896	2.416	2.395	2.399	2.397	2.408
6	BX6	12.000	23.949	2.417	2.392	2.396	2.394	2.403

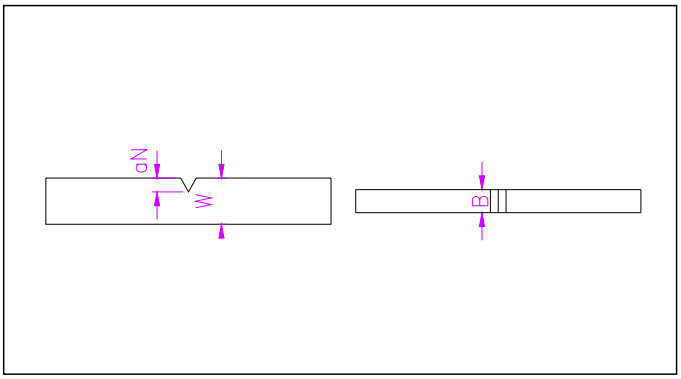

Measuring: Profile projector PJ300

	Sp. Id	W	B	aN
1	BH1	10.010	4.941	1.993
2	BH2	10.004	4.939	1.993
3	BX1	10.014	4.942	1.972
4	BX2	10.016	4.940	1.977
5	BX3	10.019	4.943	1.975
6	BX4	10.017	4.941	1.999
7	BX5	10.018	4.943	1.996
8	BX6	10.014	4.944	1.987
9	BX7	10.016	4.944	2.027
10	BX8	10.028	4.947	1.991
11	BX9	10.023	4.944	1.998
12	BX10	10.013	4.943	1.996

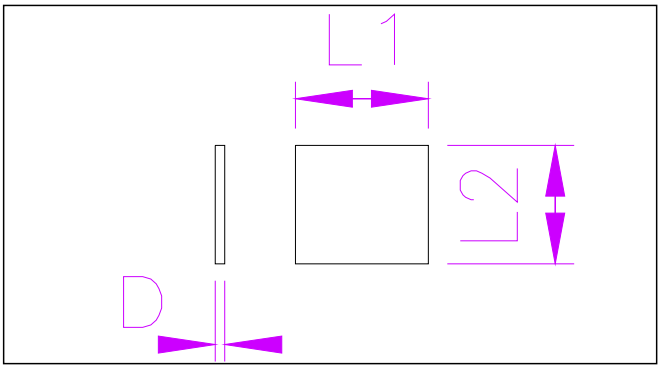

Measuring: Profile projector PJ300
D with Mitutoyo IP54

	Sp. Id	L1	L2	D
1	Sans Blank	7.049	6.992	0.245
2	Atom Probe	7.053	6.983	0.5

ANNEX 5

Dosimetry measurements

(Technical Note RF&M/Vwi/vwi 32.D049011-205/06 04)

Appendix F

Appendix F

To:	Cc:
☐ H. Aït Abderrahim	☐ S. Kalcheva
☐ W. Claes	☐ V. Kuzminov
☐ E. Koonen	☐ J. Oeyen
☐ E. Lucon	☐ B. Ponsard
☐ M. Weber	☐ J. Wagemans
	☐ W. Haeck

SCK•CEN
STUDIECENTRUM VOOR KERNENERGIE
CENTRE D'ÉTUDE DE L'ÉNERGIE NUCLÉAIRE

Reactorfysica & Myrrha

Willekens Victor - (33 22 15)
Technical-Scientific Cooperator

Technical note
Neutron dosimetry, experiment FRISCO-R

	Name	Date	Signature
Author:	Willekens Marcel (33 22 15)	2006-04-12	
Review by:	Wagemans Jan (33 22 14)	12-4-2006	

Introduction

The Heavy-Section Steel Irradition Programme, funded by the U.S. Nuclear Regulatory Comission at Oak Ridge National Laboratory, has proposed to collaborate with SCK•CEN on a project to investigate the effects of relatively high fast neutron flux on reactor pressure vessel steels and on fusion materials. FRISCO stands for **F**usion and **R**eactor material **I**rradiation **S**CK•**C**EN- **O**RNL.
The specimens from the FRISCO-R experiment are made of different RPV steels.

The specimens were inserted in capsules which were assembled to a needle. These needles were loaded in the CALLISTO loop IPS2 or IPS3. Six needles were loaded with Fe dosimeters. The Fe dosimeters were inserted at the end of the specimens set in each capsule (see annex Figures 1A and 1B). Both dosimeters are small discs made of pure iron. One irradiation cycle is foreseen for needle F in IPS2 and two cycles for the needles in IPS3. This report describes how the fission flux and fluence is determined from the activity measurements of the dosimeters that have been irradiated during cycle 03A/2005 or cycles 04B & 04C & 05A/2005.

Irradiation

The irradiation was performed in the BR2 reactor in channel D180 (IPS2) and K311 (IPS3) of the CALLISTO loop at a nominal temperature of 295°C. The basket containing the FRISCO-R samples was rotated 180° between cycles 04C and 05A/2005 in order to get the most uniform fluence at the different specimen positions.

Fe activation dosimeters are used for the determination of the fast neutron flux and fluence. The dosimeters are discs with a diameter of 9 mm and a thickness of 0.5 mm.

Appendix F

Table 1 summarises the identification, dosimeter name, needle number, axial position in the reactor, irradiation cycle and rig (IPS).

Table 1: Overview of the dosimeters.

Identification name	Dosimeter number	Needle	Reactor position	Irradiation cycle	Irradiation rig
FRIS-5	NFE9	F	-246.5	03A/2005	IPS 2
FRIS-6	NFE10	A	-255.5	04BC&05A/2005	IPS 3
FRIS-7	NFE11	A	+104.5	04BC&05A/2005	IPS 3
FRIS-8	NFE13	B	-255.5	04BC&05A/2005	IPS 3
FRIS-9	NFE14	B	+104.5	04BC&05A/2005	IPS 3
FRIS-12	NFE19	D	-255.5	04BC&05A/2005	IPS 3
FRIS-13	NFE20	D	+104.5	04BC&05A/2005	IPS 3
FRIS-14	NFE22	E	-255.5	04BC&05A/2005	IPS 3
FRIS-15	NFE23	E	+104.5	04BC&05A/2005	IPS 3
FRIS-10	NFE16	I	-289.0	04BC&05A/2005	IPS 3
FRIS-11	NFE17	I	+134.5	04BC&05A/2005	IPS 3

The irradiation history is given in Table 2.

Table 2: Irradiation history.

BR2 cycle	Start date of the irradiation	End date of the irradiation	Nominal Power (MW)	Duration (days)
03A/2005	2005-07-29 07:05	2005-08-23 21:15	57	25.48
04B/2005	2005-10-12 07:45	2005-10-20 10:11	60	8.02
04C/2005	2005-10-22 11:10	2005-11-02 18:42	60	11.31
05A/2005	2005-11-29 07:45	2005-12-19 00:48	60	19.39

A plot of the irradiation history is given in the annex (Figures 2 & 3).

Dismantling of the dosimeters

The capsule with the dosimeters was unloaded in the hot cells of BR2. All the dosimeters were recovered.

Results

The equivalent fission flux was calculated from the ^{54}Mn activity formed by the following reaction:

$$^{54}Fe(n,p)^{54}Mn$$

The neutron flux was calculated using the ^{235}U fission spectrum averaged $^{54}Fe(n,p)^{54}Mn$ cross-section $\langle\sigma\rangle = 81.7$ mb adopted from [1] (the $^{54}Fe(n,p)$ reaction having an effective threshold energy of 2.80 MeV [1]).

Appendix F

The determined equivalent fission fluxes and fluences are given in Table 3 and Figure 4. All neutron fluxes are calculated at reference power 60.0 MW, except for rod F (IPS2).

Table 3: Dosimetry results obtained from the ^{54}Mn activity measurements.

Identification number	Needle	Reactor position (mm)	Spec. activity (Bq/g)	Reaction rate (s^{-1})	Eq. fis. flux (n/cm²/s)	Eq. fis. fluence (n/cm²)
NFE10	A	-255.5	6.95E+07	1.39E-12	1.70E+13	5.68E+19
NFE11		104.5	7.80E+07	1.56E-12	1.91E+13	6.38E+19
NFE13	B	-255.5	6.93E+07	1.39E-12	1.70E+13	5.67E+19
NFE14		104.5	7.68E+07	1.54E-12	1.88E+13	6.28E+19
NFE16	I	-289.0	6.53E+07	1.31E-12	1.60E+13	5.34E+19
NFE17		134.5	7.83E+07	1.57E-12	1.92E+13	6.40E+19
NFE19	D	-255.5	6.68E+07	1.34E-12	1.64E+13	5.46E+19
NFE20		104.5	7.58E+07	1.52E-12	1.86E+13	6.20E+19
NFE22	E	-255.5	6.70E+07	1.34E-12	1.64E+13	5.48E+19
NFE23		104.5	7.74E+07	1.55E-12	1.90E+13	6.33E+19
NFE9*	F	246.5	1.33E+08	3.88E-12	4.75E+13	1.04E+20

* irradiated in IPS2, cycle 03A/2005, reference power 57MW

The uncertainty (1σ) on the specific activity < 3%.
Due to the rotation of the basket between cycle 04C and 05A/2005 (IPS3), an error is introduced in the neutron flux (fluence) determination for all needles except needle E. In view of the short irradiation duration and the ^{54}Mn half-life of 312 days, this error is estimated to be ≤ 5%.

Table 4 summarises how the equivalent fission flux (EFF) can be converted to flux > 0.1 MeV, flux > 0.5 MeV and flux > 1 MeV[2, 3].

Table 4: Fast neutron flux conversion factors.

Irradiation rig	(flux > 0.1 MeV)/EFF	(flux > 0.5 MeV)/EFF	(flux > 1 MeV)/EFF
IPS 2	2.54	1.61	1.03
IPS 3	2.64	1.63	1.03

In order to obtain dpa rates, multiply the neutron flux > 1 MeV by [2, 3]:

- 1440 barn for IPS 2;
- 1490 barn for IPS 3.

References

[1] "Nuclear Date Guide for Reactor Neutron Metrology" J.H.Baard et al. , Kluwer (1989).
[2] V. Kuzminov, SCK•CEN Technical Note BR2-SCU/VK/F04302/fluxes-dpa/23.06.04.
[3] V. Kuzminov, private communication.

Appendix F

ANNEX

Fig 1A: Position of the dosimeters in needle F for experiment FRISCO-R (IPS2).

FRISCO: cycle 03A/2005 in Callisto IPS2

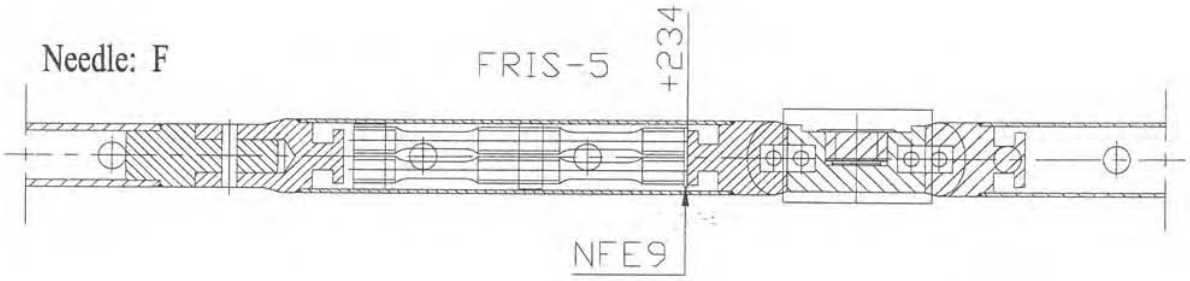

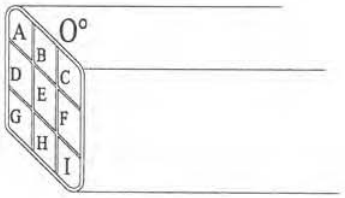

Appendix F

Fig 1B: Position of the dosimeters in the different needles for experiment FRISCO-R (IPS3).

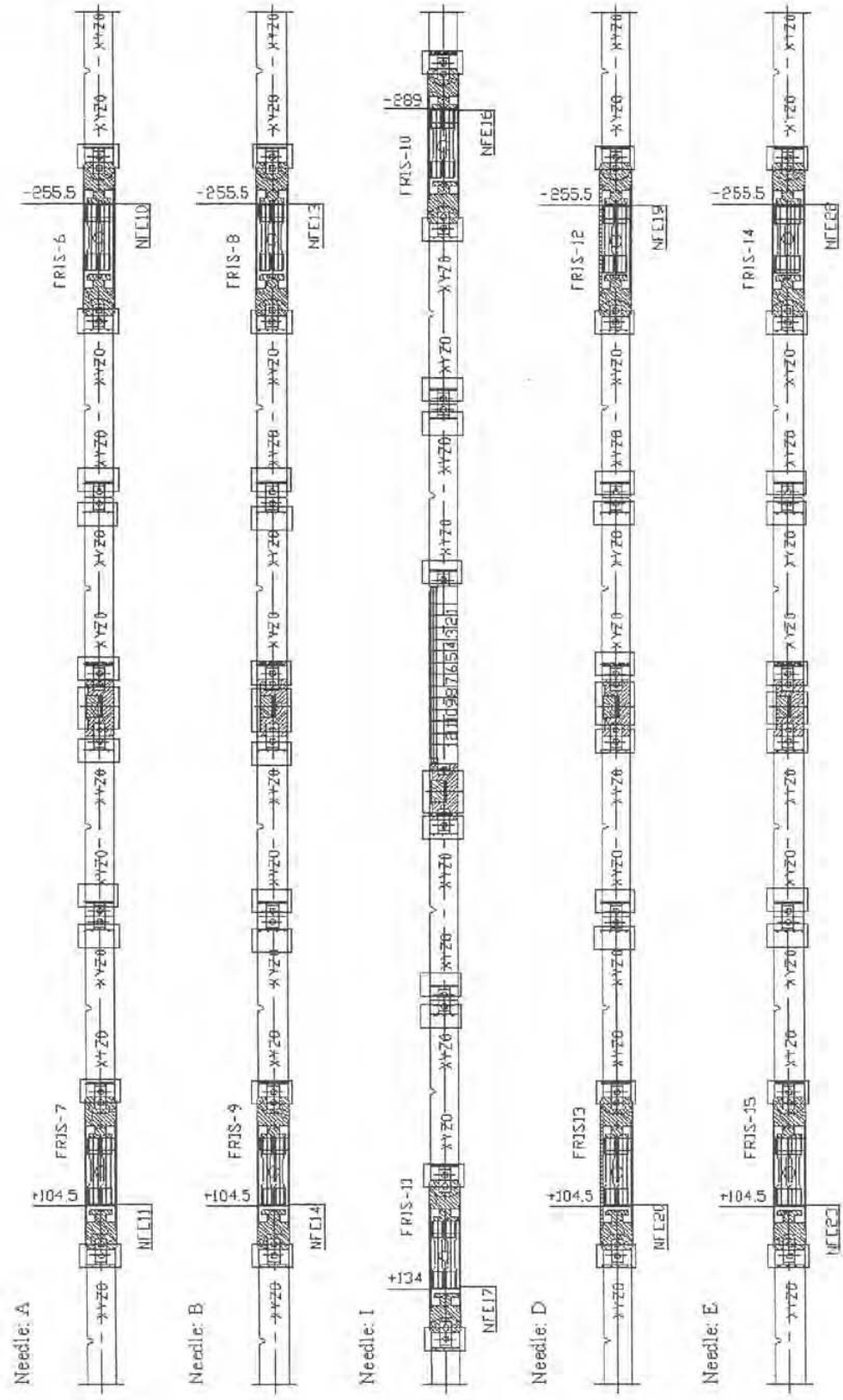

Fig.2 Irradiation history for experiment FRISCO-R in the BR2 reactor (cycle 03A/2005).

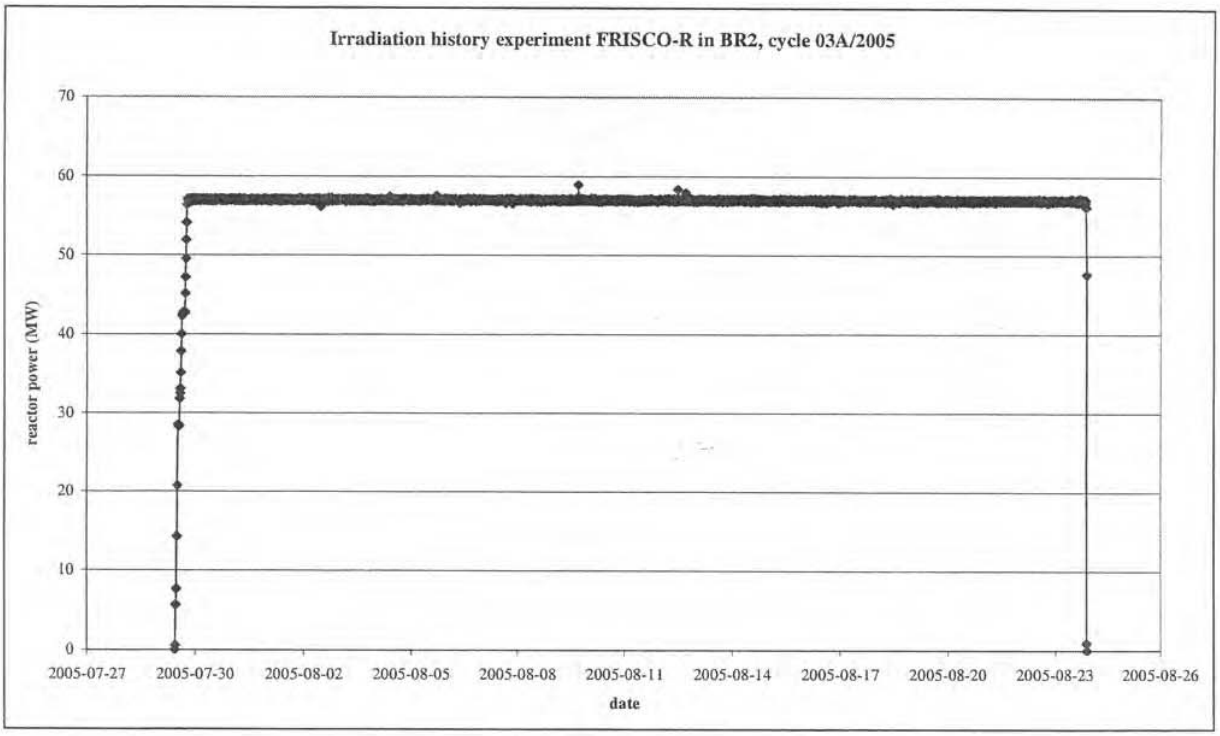

Fig.3 Irradiation history for experiment FRISCO-R in the BR2 reactor (cycles 04BC&05A/2005).

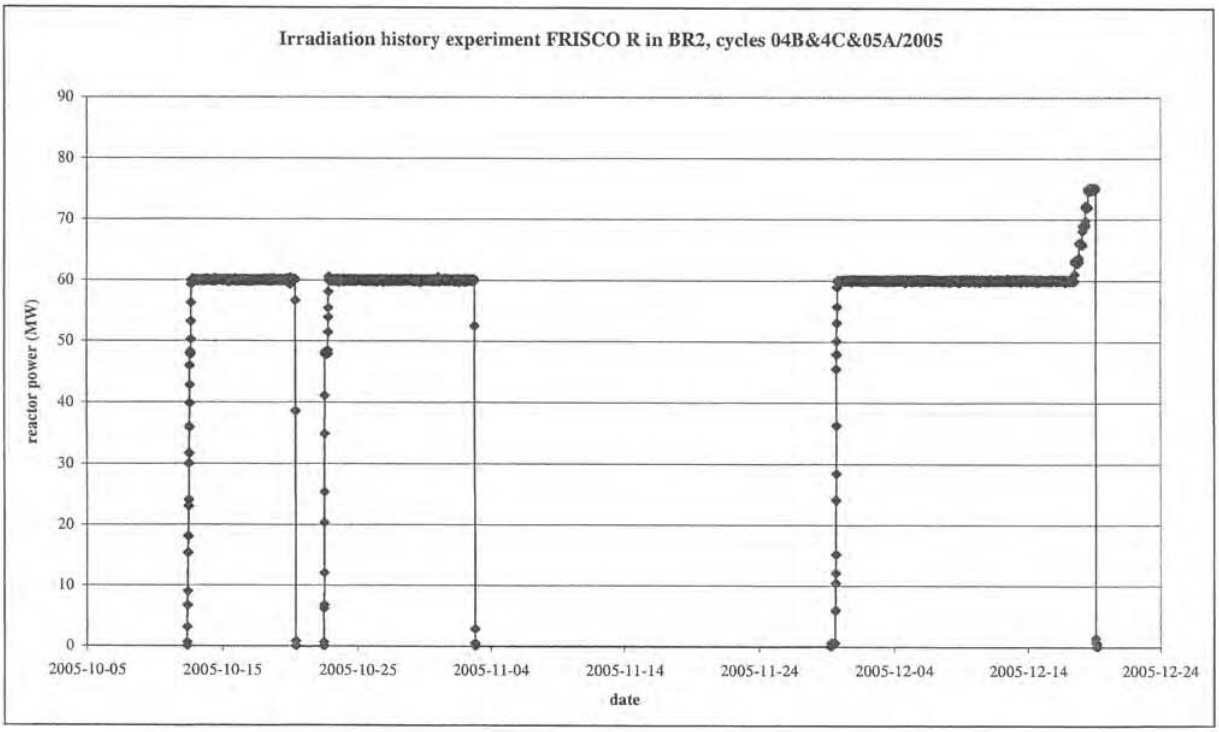

Appendix F

Fig.4 The neutron flux results determined from the activity measurements.

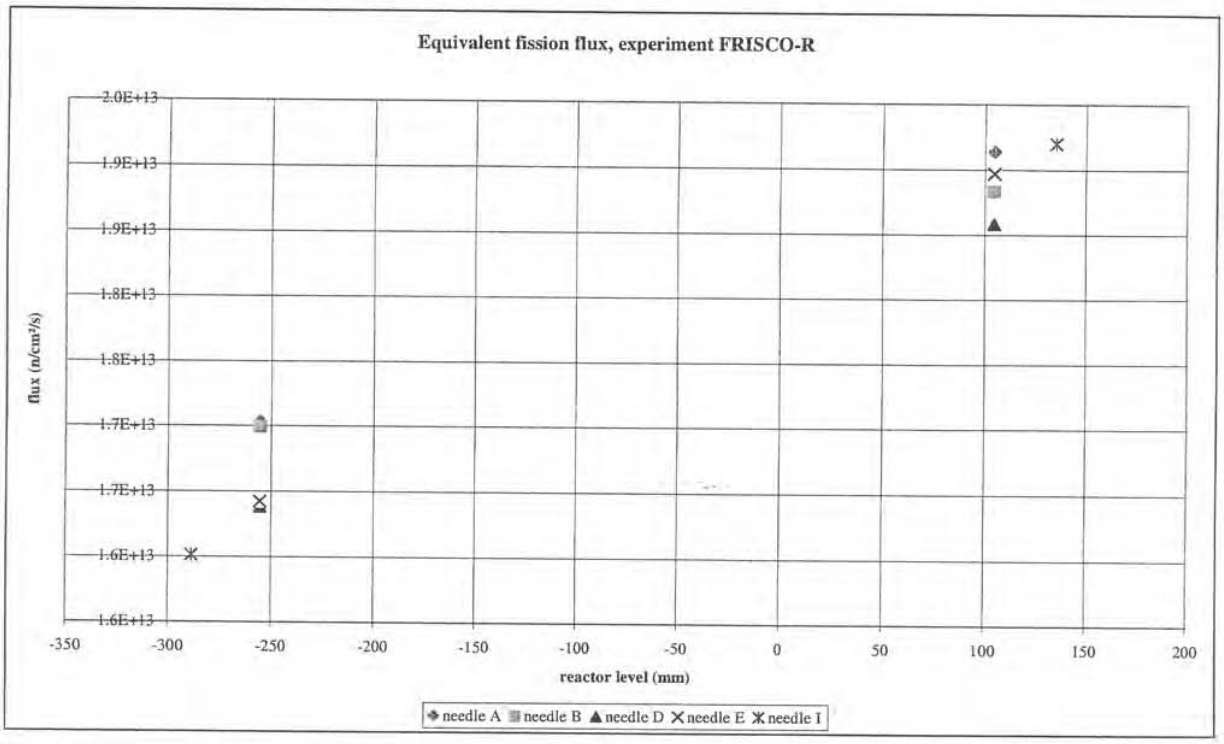

NRC FORM 335
(2-89)
NRCM 1102,
3201,3202

U.S. NUCLEAR REGULATORY COMMISSION

BIBLIOGRAPHIC DATA SHEET

(See instructions on the reverse)

1. REPORT NUMBER
(Assigned by NRC, Add Vol., Supp., Rev., and Addendum Numbers, if anv.1

NUREG-xxxx

2. TITLE AND SUBTITLE

Technical Basis for Revision of Regulatory Guide 1.99: NRC Guidance on Methods to Estimate the Effects of Radiation Embrittlement on the Charpy V-Notch Impact Toughness of Reactor Vessel Materials

3. DATE REPORT PUBLISHED

MONTH	YEAR
September	2007

4. FIN OR GRANT NUMBER

5. AUTHOR(S)

Mark T EricksonKirk

6. TYPE OF REPORT

long

7. PERIOD COVERED *(Inclusive Dates)*

Sep 2006 to Sep 2007

8. PERFORMING ORGANIZATION - NAME AND ADDRESS *(If NRC, provide Division, Office or Region, U.S. Nuclear Regulatory Commission, and mailing address; if contractor, provide name and mailing address.)*

Division of Fuel, Engineering, and Radiological Research
Office of Nuclear Regulatory Research
U.S. Nuclear Regulatory Commission
Washington, DC 2055-0001

9. SPONSORING ORGANIZATION - NAME AND ADDRESS *(If NRC, type "Same as above"; if contractor, provide NRC Division, Office or Region, U.S. Nuclear Regulatory Commission, and mailing address.)*

Division of Fuel, Engineering, and Radiological Research
Office of Nuclear Regulatory Research
U.S. Nuclear Regulatory Commission
Washington, DC 2055-0001

10. SUPPLEMENTARY NOTES

1 1. ABSTRACT *(200 words or less)*

Revision 2 of Regulatory Guide 1.99, “Radiation Embrittlement of Reactor Vessel Materials,” was promulgated in May 1988 [RG199R2]. This guide details methods that are acceptable to the staff by which licensees can estimate the effects of radiation on the Charpy V-notch (CVN) impact energy (CVE) of the ferritic steels used in the construction of the beltline region of a nuclear reactor pressure vessel (RPV). Radiation damage reduces the ability of these materials to carry load without failure. Consequently, the effects of radiation damage need to be accounted for in any assessment of the operating safety of the RPV structure. Since 1988 considerable advances have been made in both the physical understanding of radiation damage process and in the empirical quantification of the effect these processes have on the mechanical properties of RPV steels. This report summarizes these advances in the state of knowledge and amalgamates them into a technical basis for an up-to-date version of RG1.99.

12. KEY WORDS/DESCRIPTORS *(List words or phrases that will assist researchers in locating the report.)*

Neutron irradiation embrittlement, reactor pressure vessel, steel, trend curves, Charpy V-notch

13. AVAILABILITY STATEMENT

unlimited

14. SECURITY CLASSIFICATION

(This Page)
unclassified

(This Report)
unclassified

15. NUMBER OF PAGES

lots

16. PRICE

priceless